

Fluid Mechanics and Its Applications

Kostas J. Spyrou · Vadim L. Belenky ·  
Toru Katayama · Igor Bačkalov ·  
Alberto Francescutto *Editors*

# Contemporary Ideas on Ship Stability

From Dynamics to Criteria

 Springer

# **Fluid Mechanics and Its Applications**

**Founding Editor**

René Moreau

Volume 134

**Series Editor**

André Thess, German Aerospace Center, Institute of Engineering  
Thermodynamics, Stuttgart, Germany

The purpose of this series is to focus on subjects in which fluid mechanics plays a fundamental role. As well as the more traditional applications of aeronautics, hydraulics, heat and mass transfer etc., books will be published dealing with topics, which are currently in a state of rapid development, such as turbulence, suspensions and multiphase fluids, super and hypersonic flows and numerical modelling techniques. It is a widely held view that it is the interdisciplinary subjects that will receive intense scientific attention, bringing them to the forefront of technological advancement. Fluids have the ability to transport matter and its properties as well as transmit force, therefore fluid mechanics is a subject that is particularly open to cross fertilisation with other sciences and disciplines of engineering. The subject of fluid mechanics will be highly relevant in such domains as chemical, metallurgical, biological and ecological engineering. This series is particularly open to such new multidisciplinary domains. The median level of presentation is the first year graduate student. Some texts are monographs defining the current state of a field; others are accessible to final year undergraduates; but essentially the emphasis is on readability and clarity.

**Springer and Professor Thess welcome book ideas from authors. Potential authors who wish to submit a book proposal should contact Dr. Mayra Castro, Senior Editor, Springer Heidelberg, e-mail: [mayra.castro@springer.com](mailto:mayra.castro@springer.com)**

Indexed by SCOPUS, EBSCO Discovery Service, OCLC, ProQuest Summon, Google Scholar and SpringerLink


Kostas J. Spyrou · Vadim L. Belenky ·  
Toru Katayama · Igor Bačkalov ·  
Alberto Francescutto  
Editors


# Contemporary Ideas on Ship Stability

From Dynamics to Criteria

 Springer

*Editors*

Kostas J. Spyrou   
School of Naval Architecture and Marine  
Engineering  
National Technical University of Athens  
Athens, Greece

Toru Katayama   
Osaka Metropolitan University  
Sakai, Osaka, Japan

Alberto Francescutto  
Department of Engineering  
and Architecture  
University of Trieste  
Trieste, Italy

Vadim L. Belenky  
Carderock Division  
Naval Surface Warfare Center  
West Bethesda, MD, USA

Igor Bačkalov   
Development Centre for Ship Technology  
and Transport Systems  
Duisburg, Germany

ISSN 0926-5112

ISSN 2215-0056 (electronic)

Fluid Mechanics and Its Applications

ISBN 978-3-031-16328-9

ISBN 978-3-031-16329-6 (eBook)

<https://doi.org/10.1007/978-3-031-16329-6>

© The Editor(s) (if applicable) and The Author(s), under exclusive license to Springer Nature Switzerland AG 2023

This work is subject to copyright. All rights are solely and exclusively licensed by the Publisher, whether the whole or part of the material is concerned, specifically the rights of translation, reprinting, reuse of illustrations, recitation, broadcasting, reproduction on microfilms or in any other physical way, and transmission or information storage and retrieval, electronic adaptation, computer software, or by similar or dissimilar methodology now known or hereafter developed.

The use of general descriptive names, registered names, trademarks, service marks, etc. in this publication does not imply, even in the absence of a specific statement, that such names are exempt from the relevant protective laws and regulations and therefore free for general use.

The publisher, the authors, and the editors are safe to assume that the advice and information in this book are believed to be true and accurate at the date of publication. Neither the publisher nor the authors or the editors give a warranty, expressed or implied, with respect to the material contained herein or for any errors or omissions that may have been made. The publisher remains neutral with regard to jurisdictional claims in published maps and institutional affiliations.

This Springer imprint is published by the registered company Springer Nature Switzerland AG  
The registered company address is: Gewerbestrasse 11, 6330 Cham, Switzerland

# Foreword

Ship stability has been investigated for so many years in order to achieve prevention of capsizing of intact and damaged ships. However, it has not yet been fully established for practical implementation. Ship stability requires us to deal with stochastic prediction problems of rare events in nonlinear dynamical systems under random environments. A ship has the restoring moment but only within a limited range, so the system should be regarded as strongly nonlinear. The wind and waves that the ship meets are random processes. Most currently operated ships are safe, but capsizing may still occur in some exceptional cases. In the case of other areas of ship dynamics, the situations are different. Seakeeping of ships under random environments can be modelled as linear or weakly nonlinear so that the linear superposition procedures can work well. Manoeuvring of ships deals with nonlinear systems, but the random environment is not essential. In ship stability, however, some room still remains for further discussion and challenge.

The relevant experts have formed an international forum to tackle the ship stability problem scientifically. This forum runs a series of conferences, i.e. *The International Conference on the Stability of Ships and Ocean Vehicles* and workshops, i.e. *The International Ship Stability Workshop*. For the conference, papers are submitted and then reviewed. If they are accepted, they are ready for conveying the novel research findings to the audience. On the other hand, at the workshop, papers are invited for facilitating discussion among the participants. It means that discussion among the experts is more important at the workshop. However, some of the workshop papers certainly have potential values to contribute towards the scientific progress of ship stability and regulatory development of international stability criteria for practical applications. Therefore, books are regularly published by collecting archive papers, with further revisions and careful reviews, among those presented at the workshops. Occasionally, some papers from the conferences were also included.

The first book was published based on the first four workshops: the second book on the following six workshops as well as two conferences; the third book on two workshops and one conference. These three books were welcomed by the ship stability research community as well as by the industry. Following these successful publications, the fourth book is herewith prepared covering the most recent five workshops,

i.e. the 13th Stability Workshop (Brest, 2013), the 14th Workshop (Kuala Lumpur, 2014), the 15th Workshop (Stockholm, 2016), the 16th Workshop (Belgrade, 2017) and the 17th Workshop (Helsinki, 2019). This new book is expected to be used by researchers of ship stability as well as by practical users of the international ship stability criteria recently developed by the International Maritime Organization (IMO), which are known as the Second Generation Intact Stability Criteria.

We would like to express our gratitude to all editorial committee members, particularly to Professor Kostas Spyrou for his role as the main editor of this book. The thanks extend to all expert reviewers and authors as well as the organizers and sponsors of the relevant workshops.

Osaka, Japan

Naoya Umeda  
On behalf of the International Standing  
Committee for the International  
Conference on the Stability and Safety  
of Ships and Ocean Vehicles

# Contents

## Introduction

<b>Contemporary Ideas on Ship Stability: From Dynamics to Criteria—An Overview</b> .....	3
Kostas J. Spyrou	

## Development of Second-Generation IMO Intact Stability Criteria

<b>The Second Generation Intact Stability Criteria—Achievements and Remaining Issues</b> .....	21
Naoya Umeda and Alberto Francescutto	

<b>Safety Level of the IMO Second Generation Intact Stability Criteria</b> ...	35
William S. Peters, Vadim Belenky, and Kostas J. Spyrou	

<b>Second Generation Intact Stability Criteria—Robustness and Consistency Analysis</b> .....	59
--	----

Carsten Schrøter, Marie Lützen, Henrik Erichsen, Jørgen Juncher Jensen, Hans Otto Kristensen, Preben Hagelskjær Lauridsen, Onur Tunccan, and Jens Peter Baltersen

<b>On Regulatory Consistency of Criteria for Dead Ship Condition and Pure Loss of Stability</b> .....	73
William S. Peters and Vadim Belenky	

<b>Simplifications in Direct Stability Assessment</b> .....	93
V. Shigunov	

<b>Regulatory Use of Nonlinear Dynamics: An Overview</b> .....	113
William S. Peters, Vadim Belenky, and Kostas J. Spyrou	

## History of Stability Criteria

<b>Rahola Criterion and the Development of the Intact Stability Code</b> .....	131
Alberto Francescutto	



<b>Improvements on Current Methods of Probabilistic Assessment of Ship Stability</b>	
<b>Study on Short-Term Prediction of Roll in Beam Sea</b> .....	143
Toru Katayama, Mai Kankaku, Atsuo Maki, Kei Sugimoto, and Yusuke Fukumoto	
<b>An Efficient Formulation of the Critical Wave Groups Method for the Assessment of Ship Stability in Beam Seas</b> .....	157
Panayiotis A. Anastopoulos and Kostas J. Spyrou	
<b>On Extending Multifidelity Uncertainty Quantification Methods from Non-rare to Rare Problems</b> .....	175
Brendan Brown and Vladas Pipiras	
<b>Evaluation of Probabilistic Methods and Interpretation of Results</b>	
<b>Review of Probabilistic Methods for Direct Dynamic Stability of Ships in Random Seaway</b> .....	189
Clève Wandji	
<b>Verification, Validation and Accreditation in the Context of the IMO Second Generation Intact Stability Criteria and the Role of Specific Intended Uses in This Process</b> .....	211
Arthur M. Reed	
<b>Statistical Validation of the Split-Time Method with Volume-Based Numerical Simulation</b> .....	225
Kenneth Weems, Vadim Belenky, Bradley Campbell, and Vladas Pipiras	
<b>Effectiveness of the Generalized Pareto Distribution for Characterizing Ship Tendency for Capsize</b> .....	245
Panayiotis A. Anastopoulos and Kostas J. Spyrou	
<b>Envelope Peaks Over Threshold (EPOT) Application and Verification</b> .....	265
Bradley Campbell, Kenneth Weems, Vadim Belenky, Vladas Pipiras, and Themis Sapsis	
<b>Interpretation of Results of Numerical Simulation</b> .....	291
Arthur M. Reed	
<b>Parametric Roll, Operational Measures and Stability Monitoring</b>	
<b>A Case Study on Operational Measures for Avoiding Parametric Rolling</b> .....	307
Hirotada Hashimoto, Yuuki Taniguchi, and Michio Fujii	

<b>Wave Radar Application to the Simplified Parametric Roll Operational Guidance at Actual Sea</b> .....	323
Takehiro Yano, Naoya Umeda, Keiichi Hirayama, Mitsunori Baba, and Masahiro Sakai	
<b>On the Application of Artificial Neural Networks for the Real Time Prediction of Parametric Roll Resonance</b> .....	335
Marcos Míguez González, Vicente Díaz Casás, Fernando López Peña, and Luis Pérez Rojas	
<b>Application of Real-Time Estimation Techniques for Stability Monitoring of Fishing Vessels</b> .....	351
Lucía Santiago Caamaño, Marcos Míguez González, Roberto Galeazzi, Ulrik D. Nielsen, and Vicente Díaz Casás	
<b>Real-Time Estimation of Natural Roll Frequency for the Stability Guidance of Fishing Vessels</b> .....	367
Marcos Míguez González, Gabriele Bulian, Lucía Santiago Caamaño, Sandra Allegue García, and Vicente Díaz Casás	
<b>Surf-Riding and Broaching-to</b>	
<b>Estimates of the Probability of Surf-Riding in Irregular Seas</b> .....	387
Kostas J. Spyrou, Nikos Themelis, and Ioannis Kontolefas	
<b>Abnormal High Speed Ship Motions in Two-Frequency and Multi-Frequency Following Waves</b> .....	401
Kostas J. Spyrou, Ioannis Kontolefas, and Nikos Themelis	
<b>Critical Distance on a Phase Plane as a Metric for the Likelihood of Surf-Riding in Irregular Waves</b> .....	413
Vadim Belenky, Kostas Spyrou, and Kenneth Weems	
<b>Modeling Broaching-to and Capsizing with Extreme Value Theory</b> .....	435
Vadim Belenky, Kenneth Weems, Kostas Spyrou, Vladas Pipiras, and Themistocles Sapsis	
<b>Roll Damping</b>	
<b>Estimation of Force Coefficients for Bilge Keel and Skin Friction Roll Damping of Ships by CFD Simulations</b> .....	461
Sven Wassermann and Moustafa Abdel-Maksoud	
<b>Study on Bilge Keel Component of Roll Damping for Non-periodic Motion</b> .....	475
Jun Umeda, Toru Katayama, Hirotada Hashimoto, and Burak Yıldız	
<b>On Application of Standard Methods for Roll Damping Prediction to Ships with High Block Coefficient</b> .....	493
Stefan Rudaković and Igor Bačkalov	

<b>A Pragmatic Approach to Roll Damping</b> .....	509
Jakub Cichowicz and Dracos Vassalos	
<b>Damaged Stability</b>	
<b>Regulatory, Design, Operational and Emergency Response Measures for Improving the Damage Survivability of Existing RoPax</b> .....	529
Dracos Vassalos, Evangelos Boulougouris, Luis Guarin, and Andrzej Jasionowski	
<b>The Inertia Contributions Due to Floodwater Mass</b> .....	545
Gyeong Joong Lee, Arthur M. Reed, Frans van Walree, Andrew Peters, Paola Gualeni, Toru Katayama, and WenYang Duan	
<b>Air Pressure Scale Effects During Damage Model Tests</b> .....	555
Gyeong Joong Lee, Arthur M. Reed, Frans van Walree, Andrew Peters, Paola Gualeni, Toru Katayama, and WenYang Duan	
<b>A Framework for Probabilistic Damage Stability Assessment of Passenger Ships Considering Collision, Grounding and Contact Accidents</b> .....	565
Gabriele Bulian, Mike Cardinale, George Dafermos, Eleftheria Eliopoulou, Alberto Francescutto, Rainer Hamann, Daniel Lindroth, Henning Luhmann, Pekka Ruponen, and George Zaraphonitis	
<b>Cruise Ship Survivability in Waves</b> .....	589
Georgios Atzamos, Dracos Vassalos, Jakub Cichowicz, Donald Paterson, and Evangelos Boulougouris	
<b>Model Experiments</b>	
<b>Overview of Model Test Procedures for Stability Under Dead Ship Condition and Pure Loss of Stability in Astern Waves</b> .....	609
Naoya Umeda, Daichi Kawaida, Yuto Ito, Yohei Tsutsumi, Akihiko Matsuda, and Daisuke Terada	
<b>Model Experiments of an Offshore Supply Vessel Running in Astern Waves</b> .....	625
Naoya Umeda, Sreenath Subramaniam, Aqmil Alway, Akihiko Matsuda, Atsuo Maki, Satoshi Usada, and Daisuke Terada	
<b>Characteristics of Capsizing Phenomena of Fishing Vessels</b> .....	643
Akihiko Matsuda, Daisuke Terada, and Hirohada Hashimoto	

**Accident Investigation**

**Experimental Investigations into Accidents of Two Japanese Fishing Vessels** ..... 661  
Harukuni Taguchi, Akihiko Matsuda, and Kuniaki Shoji

**Cargo Liquefaction**

**Liquefaction of Sand and Olive Pomace Cargo and Its Effect on the Stability of a Bulk-Carrier** ..... 679  
I. A. Koromila, C. C. Spandonidis, and K. J. Spyrou

**Offshore Structures**

**Experimental and Numerical Investigation on Parametrically-Excited Motions of a Mono-Column Platform in Waves** ..... 693  
Claudio A. Rodríguez, Julio C. F. Polo, and Marcelo A. S. Neves

**Special Craft**

**Validation of Simulation Tools for a RHIB Operating in Heavy Seas** .... 713  
Frans van Walree and William L. Thomas

**Impulsive Loads on and Water Ingress in a Landing Craft: Model Tests and Simulations** ..... 733  
F. van Walree and D. Sgarioto

# Introduction

# Contemporary Ideas on Ship Stability: From Dynamics to Criteria—An Overview



Kostas J. Spyrou

**Abstract** In this introductory chapter of the book “Contemporary Ideas on Ship Stability: From Dynamics to Criteria” are summarised the 42 research contributions that appear as individual chapters of the book. They are classified in 13 sections covering the following topics: Development of second generation IMO intact stability criteria; history of stability criteria; improvements on current methods of probabilistic assessment of ship stability; evaluation of probabilistic methods and interpretation of results; parametric roll, operational measures and stability monitoring; surf-riding and broaching-to; roll damping; damaged stability; model experiments; accident investigation; cargo liquefaction; offshore structures; special craft.

**Keywords** Ship stability · Ship dynamics · IMO criteria · Ship safety

## 1 Introduction

This book is intended to update the community of naval architects/maritime engineers for the latest research advances on the technical topic of ship dynamic stability. Its publication could not have been timelier, since it coincides with the finalization of the works at the International Maritime Organization (IMO) towards establishing criteria reflecting current knowledge that can adequately ensure the stability safety of ships in intact condition [1, 2]. This important work lasted at IMO for several years and, in some cases, advanced scientific methodologies were employed. The new criteria went through evaluations that of course will be continued for sufficient time until full confidence on their effectiveness has been built. A glimpse into this background work that the new criteria relied upon, is offered by the present book. However, the book covers also other important areas of current stability research such as are, the stability of ships in damaged condition, stochastic stability assessment, instability phenomena, stability monitoring, roll damping, cargo liquefaction, stability of special craft and stability of floating platforms.

---

K. J. Spyrou (✉)

School of Naval Architecture and Marine Engineering, National Technical University of Athens, 9 Iroon Polytechniou, 15780 Zographos, Athens, Greece  
e-mail: [k.spyrou@central.ntua.gr](mailto:k.spyrou@central.ntua.gr)

From a modern perspective, ship stability assessment requires advanced and balanced capabilities which are, actually, still developing. These can be identified as satisfying two quite separate needs. The first refers to the mathematical modeling of the ship hydromechanics associated with extreme ship motion phenomena. The second, refers to the rigorous assessment of ship dynamics. These capabilities cannot become real without properly accounting for the effects of nonlinearities, as well as, for the stochastic nature of the excitations due to the physical environment in which a ship operates. The title of the book is intended to emphasize the strong connection of the new criteria with in-depth considerations of ship dynamics using modern methodologies.

The next chapters have ensued from selected works presented in five recent International Ship Stability Workshops, held in Brest in 2013, in Kuala Lumpur in 2014, in Stockholm in 2016, in Belgrade in 2017 and in Helsinki in 2019. However, in comparison to their initial status, most of these contributions were expanded and corrected. Single blind evaluation by at least two experts has been applied to all chapters before these were accepted to appear in this book. It has been tried the sequence of the chapters to appear natural, although of course this matter is quite subjective.

The reader is advised to consider also the two previous books on ship stability, published in the same Springer series on Fluid Mechanics and Its Applications (see [3] and [4]). The three books are quite supplementary and they offer an excellent view of the progress achieved on the topic of ship stability in the last 15 years or so.

The works selected for the present book were classified in 13 sections. In the next is provided a brief description of these sections.

## **2 Development of Second Generation IMO Intact Stability Criteria**

In this section are contained 6 chapters, all referring to the development of the Second Generation Intact Stability Criteria (SGISC).

Chapter 2 was authored by two of the coordinators of the efforts at IMO towards the new criteria. However, it was written a few months before criteria's finalization. For this reason, in this chapter are discussed also a few issues that were unsettled at the time of writing. The major task during the final period was the completion of the Explanatory Notes which are intended to offer insights about the scientific background of the new criteria and also some assistance for their application. The Criteria are arranged at three levels, escalating from simple checks, at level 1, to demanding evaluations at level 3. Check at the first level is the starting point. Success at any level means a pass and no need of further evaluations at higher level. Whilst the vulnerability criteria comprising the first two levels have a definitive form, the direct assessment procedure comprising the third level exists only as a specification. Direct assessment is the highest and most costly level of the assessment. Normally, it

will be needed for those ships that, failing to satisfy the level 1 requirements, failed also at level 2. Direct assessment should rely on specialized numerical codes and/or model experiments, the development of which should fit to a specification. Insights in relation to this matter are provided also in this chapter. Another matter discussed is the development of operational measures for ships that either do not satisfy the criteria at all; or it is not desired to go through third level testing. The chapter ends with a plea to relevant stakeholders for testing the new stability criteria and reporting back the results.

In Chap. 3 is touched the relation between the new criteria and the safety level achieved for a ship fulfilling the criteria. The matter is neither simple nor straightforward. The safety level associated with a certain criterion is the probability of failure with regard to the failure mode addressed by this criterion, assuming that the ship marginally satisfies the criterion. It is a question however how this probability can be estimated. In particular, how such calculation can be combined with the vulnerability assessment procedures described in the new criteria. In the chapter are presented also some ideas about the connection of these criteria with the main approaches promoted at IMO for the development of new criteria, as are, the *Goal Based Standards* approach and *Formal Safety Assessment*.

In Chap. 4 is described a systematic evaluation of the criteria per failure mode (namely: pure loss of stability, parametric roll, dead ship condition, excessive acceleration and surf-riding/ broaching-to), from the perspective of the construction of GM limit curves, for a practical range of ship drafts. Inconsistencies observed with regard to the traditional ship design procedure of drawing the GM limit curves should not be surprising and they do not necessarily reflect deficiencies of the criteria. 17 vessels of different types were tested. These tests were based however on the 2015–2016 version of the criteria which was amended later. Nevertheless, some interesting insights are offered about the stability performance of several existing vessels. The authors propose to incorporate suitable calculation routines with the new criteria on the vessels' loading computers, in order to be easy to check (e.g. upon vessel's departure) whether her stability is sufficient.

In Chap. 5 is addressed the quite fundamental topic of the consistency of the level 1 and level 2 vulnerability criteria, for two stability failure modes: dead ship condition and pure loss of stability. Consistency for the dead ship condition should receive particular attention since this failure mode is covered also in the mandatory part of the 2008 Intact Stability Code (ISC) of IMO. Actually, what appears at SGISC for dead ship condition as level 1, is similar to the weather criterion of the 2008 ISC. Therefore, a consistency check essentially would tell whether SGISC and 2008 ISC are compatible. However, the assessment procedure for the dead ship condition, level 2, involves calculation of the long-term probability of stability failure; while level 1 follows the more deterministic logic (with some probabilistic inputs) of the weather criterion. As the weather criterion cannot receive a unique probabilistic interpretation, some inconsistency is likely to be found. More generally, the authors propose that, for better consistency, it would be preferable the level 1 and level 2 procedures to rely on similar basic mathematical models, setting however the safety for level 1 above that of level 2.



Chapter 6 deals with the third level requirements of the new criteria comprising the so called direct stability assessment. These entail detailed mathematical modeling and extensive simulations, intended to supply data for estimating the vessel's probability of stability failure. In these simulations however, one comes across the computational issue of the rarity of ship capsizes. It implies that excessive (and basically unavailable) time would be required for reaching an acceptably accurate estimate of the probability of failure. In this chapter are investigated a few known methods for reducing (to practical level) the excessive time requirement of the simulations. One aspect discussed, is the assumption that roll stability failures could be classified as *stationary Poisson processes*. Stochastic systems belonging to this category, receive a well-known mathematical description of their rate (in time) of failure events. In the chapter is discussed further whether the failure rate could be empirically extrapolated with regard to wave height, for conditions of rarer capsizes (milder conditions). Nevertheless, as the different cases still appear numerous, it is proposed in the chapter to confine the assessment to a small set of scenarios.

Chapter 7 is intended to explain the scientific background of the level two vulnerability criterion proposed for the surf-riding and broaching-to failure mode, in the context of the IMO Second Generation Intact Stability Criteria. This criterion is a good example where an advanced technique from the field of nonlinear dynamics was used for predicting the realization of surf-riding behavior. It is the so-called "Melnikov method" which is applicable for predicting analytically the occurrence of a global bifurcation phenomenon, known as "homoclinic connection". This phenomenon causes a critical transformation in the dynamical system's phase space where, specifically, a limit-cycle (representing the oscillatory surging motion of a vessel in high following waves) collides with an unstable fixed point representing an unstable surf-riding condition. The event incurs global attraction to a nearby existing stable fixed point representing the stable surf-riding condition. The chapter explains, from naval architecture perspective, the steps of the calculation process coming with this criterion.

### 3 History of Stability Criteria

The single chapter of this section (Chap. 8) provides a historical account of the developments towards the current stability criteria. Two main different points of view existed during the twentieth century about the suitable form of the ship stability criteria. The first, relied on a statistical approach which was however profoundly empirical with no physics of a ship's motion behavior in waves involved. The doctoral thesis of Rahola, published in 1939, has been the origin of this approach. It involved only the GZ characteristics for calm water and relied on an analysis that was intended to achieve empirical discrimination between safe and unsafe vessels. The second had relied on Moseley's idea of energy balance between the work of the excitation and the capacity of the vessel to store it as potential energy. This approach, has led to the well-known *weather criterion* of ship stability for the so-called dead ship condition. The

paper offers a detailed account of regulatory developments with regard to these two stability criteria philosophies, including their evolution into the current International Intact Ship Stability Code.

## **4 Improvements on Current Methods of Probabilistic Assessment of Ship Stability**

In the 3 chapters of this section are discussed possible improvements on current methods of probabilistic assessment of large amplitude ship rolling. These improvements can make a method more accurate and rigorous; or they can make its application more efficient, reducing considerably the time required for its application without significant loss of accuracy.

In the presence of the well-known restoring and damping nonlinearities, the probability density function (pdf) of roll angle and roll velocity will depart from the Gaussian form when the roll motions are not small. It is obvious that availability of an effective method of computation of this non-standard pdf, depending on the vessel's form, is very useful. This matter is addressed in Chap. 9, the authors showing how a suitable non-Gaussian pdf could be derived for a short-term ship stability assessment procedure (relating, for example, to a particular journey) that incorporates the nonlinear effects. The method is based on earlier work and requires, as input information, roll angle's variance and the inertial, damping and restoring data of the vessel. Comparison of the non-Gaussian pdf against model Monte-Carlo simulations, and also against experimental results, are also included in the Chapter for evaluation of the method.

In Chap. 10 is proposed a simplified version of the so called "critical wave groups method". This method relies on short-term focused simulations and it can reduce drastically the required simulation time in comparison to the Monte-Carlo or other numerical methods. For this reason it has been discussed extensively in recent years for dealing with the rarity problem of ship capsizing. The simplification discussed in this Chapter concerns the selection of the initial conditions of the vessel and also the selection of a small set of sea conditions where it is highly probable to observe roll resonance. The computational advantage of the first simplification is quite obvious though its validity is subject to conditions. As for the second simplification, it can reduce seriously the required number of simulations. Because, for types of failure where resonance is the underlying factor, the main contribution to the probability of failure essentially comes from waves having periods close to the natural period of the vessel.

Chapter 11 touches upon the fidelity and consistency issues of the data that are used in stability assessment procedures. A known fact is that, often, there is variability on the level of fidelity of the input data as these may come from different sources, being the output of models of different complexity. Some may be empirical, while other may be derived with some account of the problem's physics. For

determining the uncertainty of the outcome of an assessment procedure, is usually required the estimation of average values, a task however that is not suitable for stochastic processes where the attention is focused on their rare extremes. In this chapter is proposed to exploit extreme value theory for overcoming this, applied simultaneously to data deriving from low- and high-fidelity models.

## 5 Evaluation of Probabilistic Methods and Interpretation of Results

Several methods have been proposed for characterizing, probabilistically, a vessel's stability. These methods need to be thoroughly evaluated and also, their application to real ships should be transparent and verifiable. One category of methods, treated in Chap. 12, employs direct counting of simulated stability failure events. A few quantities can be identified as the proper statistical representatives of the roll responses. It is quite enlightening to grasp how these statistical quantities are related with each other. For example, how the exceedances in time of a certain threshold (up-crossing rate) connects with the maximum value observed within a fixed time period; and further, with the time to failure; etc. These relations depend on whether the ship is directly or indirectly excited in roll (as in the parametric roll case) and on whether nonlinearity or other effects are present.

The success of the Second Generation Intact Stability Criteria depends on various matters; but of course, most crucial is that compliance reflects *objectively* the stability safety of a vessel. This raises the issue of validation. Confidence on the new criteria will be built gradually via their extensive application to a wide range of ships, during the trial period specified by IMO. For the level 1 and 2 criteria, it is also needed that the correct implementation by the user (who could be the designer or the developer of software) of the prescribed algorithms is, in some way, verified. At the third level however, where only a guideline has been produced by IMO, much more freedom is granted to the developer with regard to the actual content of the calculation procedures. For such complicated software it becomes then vital to be established formal accreditation procedures by authorized entities. The issues involved in such matters are discussed in Chap. 13.

In Chap. 14 is considered the statistical validation of the split-time method of stability assessment, through comparisons against numerical simulations. The split-time method is one of the first methods proposed for handling the computational obstacle of the rarity of ship capsizes. This is, basically, a numerical extrapolation technique; meaning that the aim is, from a known form of the probability distribution for a certain roll angle range, to deduce the form of the distribution for an adjacently located range of angles where sufficient data is probably not available. A key idea behind the "split-time", is the execution of a campaign of automated motion perturbation simulations, initiated from the angle of the up-crossing threshold. Via these simulations is determined the critical roll rate (at up-crossing) which leads to capsizes.

A novelty of the work described in this Chapter is that, the split-time formulation is combined with simulations accounting effectively for the well-known inseparability issue of the nonlinear hydrostatic and Froude-Krylov forces for large roll angles.

Another idea that has been around for some time is that, the Generalized Pareto Distribution (GPD), which is a distribution used for modeling exceedances over thresholds, could provide a solution for calculating the probability of exceeding very high roll angles representing borderline safety conditions. This would be equivalent to overcoming the rarity problem. However, the evaluation of this technique, described in Chap. 15, reveals that issues exist, rendering, at least for the current time, the practical application of the method quite ambiguous. Actually, attention needs to be paid also to other important facts. One is that, capsize is an escape phenomenon (i.e. exceedance with no return) out of the system's safety domain. Another, is the "data-driven" nature of the method. Such data may not be fully available for a ship that is still at the design stage. Of course, with further research these issues might be overcome. Comparisons against direct Monte-Carlo simulation and also against the critical wave groups method are included also in this chapter. Even this comparison was found to present its own difficulties. For example, Monte-Carlo cannot produce sufficient data, in reasonable time, at the extreme angle range and the comparison can only be rough.

The fitting of a Generalized Pareto Distribution (GPD) is invoked also in the context of the so-called Envelope-Peak-Over-Threshold (EPOT) method which is the subject of Chap. 16. Here again the target is, to predict roll statistics above a selected threshold value. The EPOT was introduced a few years ago as a variant of the more widely known Peak-Over-Threshold (POT) approach. POT requires however independent data in order to apply the GPD fit, which is not satisfied by a series of successive roll peaks. To overcome this, EPOT incorporates the envelope of the roll response. As the peaks of the envelope are usually found quite far apart, independence of the data used in the extrapolation can be reasonably assumed. This chapter is particularly focused on the statistical validation and assessment of the EPOT method. Distribution tail extrapolations based not only on GPD but also on Pareto are evaluated, with some practically useful conclusions drawn about their observed validity.

This discussion is essentially continued in the final chapter of the Section (Chap. 17). Here can be found a useful outline of the so called "non-rare" problem of statistical characterization of extreme motions (first for the linear case which is very straightforward; and then for the nonlinear which presents some issues); and also of the rare problem as approached via the split-time method. When the focus is on motion extremes, the tail of the distribution contains the essential information; and yet substantial difficulties can arise for predicting the tail if there is rarity and nonlinearity. The author proposes the Generalized Pareto Distribution and also the Pareto Distribution as a good basis for deriving the tail, in combination with the application of a POT or an EPOT technique.

## 6 Parametric Roll, Operational Measures and Stability Monitoring

Parametric roll is one of the most widely publicized types of dynamic instability of ships. Design requirements for avoiding parametric roll are part of the recently finalized Second Generation Intact Stability Criteria. A feature of the Second Generation Intact Stability Criteria is that, ships failing to satisfy the requirements of the vulnerability criteria or of the direct assessment, they can still operate if their owners accept to adopt for these a restricted operational profile. These operational measures as they are called, are comprised of the setting of vessel-specific operational limitations and an associated operational guidance. In Chap. 18, is presented a case study demonstrating how these can be developed for the specific failure model of parametric roll. The operational limitations discussed in the chapter employ the significant wave height as the single limiting parameter. Adoption of such limitations for a vessel means, as discussed in the chapter, consequences for the selection of navigation routes and for the duration of the journeys.

As already said, the Second Generation Intact Stability Criteria will go through a trial period and evaluation; therefore it is likely that incidents of instability, such as parametric roll, will continue to arise for some time. To help avoid these as much as possible, technological aids that can mitigate a vessel's propensity to stability failure should therefore be considered. In Chap. 19 is presented an interesting study involving real-time measurements of encountered waves by wave radar and, in parallel, measurement of the roll motions by a gyro sensor, for a Ropax vessel. By these systems, one could compute and continually check whether parametric roll is likely to appear, by following procedures as described in the vulnerability criteria or in any other reliable parametric roll prediction method.

Artificial neural networks (ANN) are widely applied nowadays in several fields. These are basically computer algorithms, which after going through a "training" stage, they can predict, in many cases quite well, the behavior of a complex system without having to recourse to the solution of first-principle equations involving the physics of the system. This presents, of course, serious advantages, subject to the condition that rare phenomena such as the stability failures can be duly accounted. In Chap. 20 is presented a concept where an ANN is trained using roll motion data obtained from a mathematical model. Then the ANN is evaluated for its capability to alert for parametric roll, by being used in model experiments in a wave basin.

Real-time estimation of ship stability representative quantities is important and it usually relies on signal processing techniques. In Chap. 21 are evaluated, comparatively, two such techniques, applied in order to extract the roll natural frequency of a stern trawler operating in waves, with quite promising results. For these evaluations, data was obtained from simulations of the trawler in irregular seas; and in addition, from model experiments of the trawler in regular waves. The practical implementation of a real-time stability monitoring system onboard is also discussed, from the perspective of a change detector. That is a system alerting for unacceptable change

of the monitored stability quantity at some parts of the journey so that action can be taken by the Master.

A similar purpose is served by Chap. 22, with aim of the work to monitor accurately the metacentric height during a ship's operation, again however via a natural roll frequency's estimation. Here, a methodology based on spectral analysis of the roll motion is developed, with the authors concluding that further evaluations and improvements will be required for this promising method, in order to contain the prediction error within acceptable limits.

## 7 Surf-Riding and Broaching-To

Broaching-to due to surf-riding is one of the failure modes accounted in the new IMO criteria. The second level vulnerability criterion for this particular mode assumes that a moderately fast moving vessel is met, from the stern, by a steep and long regular wave which pushes her into the surf-riding mode. Surf-riding in irregular waves still remains a scientifically open, state-of-art, topic of research. An issue to be dealt-with is that, by moving away from the simplistic consideration of monochromatic sea, the phase space flow of the dynamical system becomes time-dependent. It is then likely that other, beyond those already known, dynamic phenomena can arise, that are uniquely identified with the irregularity of the seaway. It is not yet well understood how these can impact on the probability of ship motion instability. These are matters elaborated in the following two chapters of this book.

In Chap. 23 are discussed two different calculation schemes that can be used in order to estimate the probability of surf-riding in irregular seas. The first scheme is derived from an analysis of system dynamics. Specifically, it is set up in order to identify special points in the phase space that one could characterize as the irregular sea counterparts of the surf-riding equilibria. The surf-riding equilibria are basically positions of a ship in a regular wave field, where the sum of the forces acting on the ship, in the longitudinal direction, is null. Such points are unlikely to exist, with finite duration, in an irregular sea and some new concept needs to be invented, as explained in the chapter. The second scheme is more empirical, targeting the so called "high-run" phenomena that are, extraordinary increases of vessel speed above a predefined threshold. This work, as also those which follow in this section, drive towards the creation of a theory for surf-riding in irregular seas. The two schemes discussed provide different perspectives of the problem. But it is interesting that the probability estimations by the two can be compared against each other, so that efficient probability estimation procedures can be built in the longer term.

Another facet of basically the same problem is the effect of the frequency content of the wave excitation on the surge behavior (always assuming a ship operating in steep following waves). This is looked into in Chap. 24, on the basis of, first, a deterministic, and then, a stochastic approach. In the first, an extra frequency is added to an initially monochromatic "sea", revealing two types of oscillatory surf-riding and also the possibility of chaotic surge motions. In the second, a filter is applied

on a JONSWAP wave frequency spectrum that has capacity to turn, gradually, the sea from initially monochromatic to highly irregular, while maintaining its energy content. This scheme helps one to perceive the qualitative transformation of the phase space, as excitation's irregularity is gradually intensified by spreading the wave energy to a wide range of frequencies.

In the final two chapters of this section are described applications of the split-time concept, already presented in earlier paragraphs, however then in the context of other instability modes. In Chap. 25 is explained how the split-time method could be used towards setting up a metric for the estimation of the probability of surf-riding in irregular waves. The proposed metric is basically the distance between ship's location in phase space and the instantaneous boundary separating the surging and surf-riding types of motion. These require however to invoke the concept of surf-riding "pseudo-equilibria" which are points in phase space where the sum of the forces is null, without however including the inertia force. Another interesting concept invoked for the implementation of this metric is that of instantaneous wave celerity. It is used in order to mathematically setup the condition of surf-riding, assumed to be realized when surge velocity exceeds the instantaneous celerity.

In the final chapter of this section (Chap. 26) is found another application of the split-time method, focused this time on the estimation of the probability of broaching-to in association with earlier occurrence of surf-riding. The scheme targets unintended deviations of yaw from the desired course. The proposed metric is based on the phase space distance between the phase space location of the ship when the yaw deviation is initiated, and a nearby stable surf-riding pseudo-equilibrium.

## 8 Roll Damping

An increase of roll damping is very effective towards mitigating resonant roll motions. However, prediction of roll damping is still a difficult and multi-faceted problem. Some of the different elements of the problem are addressed in this section.

In Chap. 27 is found a CFD approach for predicting the bilge-keel component of roll damping. A quite fundamental setup is examined, based on an ellipsoid with flat plates attached resembling bilge keels. The practical purpose is to develop simple expressions, via the CFD analysis, for the normal-to-the-plate force, parameterized (as done in the past) with respect to the Keulegan-Carpenter number ( $KC$ ) reflecting the relative importance of the drag forces over the inertia forces. In the same chapter is found an investigation on the skin friction damping component, proposing an improvement over the widely applied prediction formula of Ikeda.

Bilge-keel damping is also the object of Chap. 28, with special focus however on this damping force developing during non-periodic roll motion of the hull, as typically realized in irregular seas. The CFD approach that is employed here seems to provide useful insights about key characteristics of the flow around the hull and the bilge-keels. A type of memory effect is found, influencing the evolution of the vortices. This enhances, in turn, the experienced damping during the hull's roll motion. A

closer account into the phenomena of the flow is a very important direction of future research.

Roll damping's prediction for a particular category of vessels, inland vessels (mainly those operating in rivers) is the focus of Chap. 29. The very full hull form and shallow draft (beam to draft ratio over 4) of these vessels means that, common semi-empirical methods that are used for predicting roll damping may be not applicable. The authors identify a particular discrepancy for the eddy-making component of roll damping (which could actually be relevant also for a few ocean-going vessels) when the block coefficient is higher than 0.84. For this reason, they propose an adjustment of Ikeda's simplified formula in order to extend its range of applicability.

A very different perspective of roll damping is the matter of Chap. 30 where the initial target was to deduce the form of the motion equations for a rolling, partly submerged, semi-cylindrical body. A set of roll damping experiments was the starting point of the investigation, carried out in order to determine the hydrodynamic reaction forces on the cylinder. These were then utilized in an Euler–Lagrange formulation, for the purpose of deriving a system of equations for roll and sway motions that could represent the key system dynamics. Interesting suggestions about the variation of the damping coefficients in terms of the frequency of oscillation are offered, for the intact as well as for the damaged cylinder.

## 9 Damaged Stability

Maintaining stability safety for adequate time after accidental flooding of compartments, is vital for a ship. However, the accurate prediction of the dynamic behavior of a damaged ship in waves is one of the most difficult tasks. This topic receives traditionally very high public attention because flooding accidents, in particular of large passenger ships, are often quite devastating, resulting in great loss of life. Nevertheless, in this topic of stability research are still found several challenges. Among these are, the modeling from first principles of compartments' flooding and the incurred effect on ship behavior; the probabilistic formulation accounting for the random characteristics of a hull damage; ship design for maximizing resistance to capsizing post flooding; the management of post-accident operations (what is usually called *emergency response*); and others.

In Chap. 31 are discussed possible measures for improving the damaged survivability of existing RO/RO passenger vessels. In focus are the options for improving damaged stability in case IMO decided to raise the standard, by increasing the value of the required subdivision index and to apply it also to existing vessels. Some interesting concepts, as for example the vulnerability screening of a ship, are discussed which can be the basis for determining more clearly the risk mitigation options associated with flooding.

In Chaps. 32 and 33 is reviewed the mathematical modeling of two particular factors that can influence system dynamics in the case of flooding, both relating with the agility of floodwater in a compartment. In Chap. 32 is investigated how



floodwater's mass should be accounted when calculating the inertia of a combined ship-floodwater system. The authors subdivide the problem into one of water entering the ship, one of a partly flooded compartment and, finally, that of the fully flooded compartment. Most difficult appears the second, where, depending on circumstances, the effect of floodwater on the ship dynamics can range from semi-static to fully dynamic. As for a fully flooded compartment, the authors bring to our attention that, whilst for acceleration along straight line the floodwater can be treated like a solid of same density filling the same compartment, for rotational acceleration the moment of inertia is smaller, because some part of the water does not quite follow ship's rotation.

An effect on the flooding process arises if some quantity of air is trapped in the damaged compartment. Why such entrapment of air happens, and how flooding is affected, can be investigated of course by model experiments. However, it is then needed to grasp how these findings could be scaled up to the full ship. In Chap. 33 is treated this matter in comparative manner considering, on the one hand, a flooded compartment with trapped air; and on the other, the same compartment with air venting. The scale effect on flooding seems to be substantial when air is trapped but quite negligible for compartment with large vents.

In Chap. 34 is extended the scope of the standard probabilistic modeling of the damages that is used in the current IMO damaged stability regulations. The additional aspects that are treated here and were not accounted earlier, are, bottom groundings and side groundings/contacts. The authors apply an automated scheme which is based on Monte Carlo simulations for generating the damages in accordance to the predefined probability distributions of their position and extent. This scheme does not require to examine compartments' breaching in the customary sequential manner on the basis of ship division to transverse vertical zones. This is the reason for the approach to have become known as "non-zonal".

In the final chapter of this section (Chap. 35) are taken steps towards a specialized method for the assessment of the damaged survivability of cruise ships. Whilst cruise ships do not have the open deck like RO/RO's, their flooding can be also very devastating. Therefore, their survivability after damage is of highest priority. Here can be found a proposed formula for the survivability factor  $s$  that could be used for the probabilistic assessment of damaged stability of cruise ships in waves. It was derived from extensive simulations on cruise ships of various sizes and also from static calculations. These have targeted to determine the critical significant wave height given the residual (after damage) stability properties of the cruise ship.

## 10 Model Experiments

In the framework of "direct assessment" of the Second Generation Intact Stability Criteria, model experiments can play an important role. Either by being the direct assessment method of choice; or, by being used for validating predictions from

numerical simulations. In Chap. 36 are offered some comparisons between simulations and experiments with regard to two failure modes: dead ship stability and pure loss of stability. A whole lot of details can affect these comparisons and the authors draw attention, mainly, on the representativeness of the wind generation conditions (as regards the dead ship failure mode); and on issues relating to the comparability of the incident waves between simulation and experiment (for pure-loss).

A matter that received attention during the preparation of the Second Generation Intact Stability Criteria was to ensure the consistency of the criteria between the 3 different levels of assessment. An inconsistency for example arises when, a ship that satisfied the level 1 criterion with regard to a certain failure mode, failed at the level 2. Of course such a test would not be formally needed because success at one level implies success, in principle, at all higher levels. Inconsistencies of this kind are inherent to a rating system where the procedures do not rely exactly on the same theory, where only the level of the involved theoretical detail would have been responsible for any differences. The interesting matter of inconsistency in the criteria is touched once more, in Chap. 37, for an offshore supply vessel which exhibited it with regard to pure loss of stability. Due to their low weather deck, these vessels are actually not very typical. However, through experiments the authors found that the source of the problem was the effect of water entrapment on the deck.

In Chap. 38 are described free-running model tests in extreme wave conditions, with main objective to identify whether characteristic designs of Japanese and European fishing vessels present similar vulnerability to the various capsize modes. Indeed, behavioral differences are identified, with European fishing vessels appearing less prone to the usual instabilities. For the latter however, the authors observed a dangerous sub-harmonic roll behavior in following and stern quartering seas.

## 11 Accident Investigation

Stability accident investigation is important because lessons can be learnt for avoiding similar accidents in the future. Sometimes, the causes stand out and they can be attributed, for example, to a failure in the chain of command on board; or to some equipment failure. However, in others, it is needed to carry out deeper analysis including model experiments. In Chap. 39 are described such model experiments that were carried out in Japan, for the purpose of clarifying the causes of the loss of two fishing vessels, a purse seiner and a stern trawler, whose capsizes cost several people's lives. For both, flooding of the deck and of internal spaces was the key effect. The purse seiner capsized while sea-anchored, after successively hit by two isolated big waves. The stern trawler capsized while sailing in head seas.

## 12 Cargo Liquefaction

When realized en route in a ship carrying bulky cargo, the phenomenon of “cargo liquefaction” can be very dangerous, representing the primary cause behind the losses of bulk carriers in recent years. The key effect is that, a seemingly solid cargo is turned into a movable one. Unprocessed or little processed mineral sands, and also other moisture-containing cargos, are prone to liquefaction. The phenomenon happens when moisture carried on the surface of the cargo particles migrates due to vibrations and ship motions, forming wet pockets inside the cargo and a fluid layer on the cargo’s surface. Liquefaction can render the cargo to behave fully or partly like a fluid cargo with free surface. In Chap. 40 are presented experiments with a “shaking table” equipment, that were intended to offer insights for the transformation of a cargo of wet granular materials during liquefaction. The tested materials were, sand and olive pomace, for several moisture contents. The effect incurred by liquefaction on a bulk-carrier’s stability is also discussed in this chapter.

## 13 Offshore Structures

The dynamic stability safety of floating structures in harsh environments is of paramount importance for the effective exploitation of the oceans’ energy and subsea resources. In the single chapter appearing in this section (Chap. 41) are described and discussed model experiments on a mono-column structure in regular and irregular waves. The authors have observed the possibility the column to exhibit parametric resonant motions in roll and pitch, sometimes with transfer of energy between these two modes. The excessive motions seem to be caused by the mooring system’s configuration, calling therefore for attention on the role that the moorings can play for a floating structure’s dynamic stability.

## 14 Special Craft

The final section of the book contains contributions concerning special craft. The first part (Chap. 42) refers to a topic that, at first glance, is of particular interest to the Navies, although it could receive also wider attention. Comparative simulation and experimental studies are described for a rigid hulled inflatable boat (RHIB), operating in heavy seas. A key point in studies focusing on the behavior of not so usual boat forms, is whether (and to what extent) true capability exists for predicting their motions. The chapter provides some insights about the limits of good prediction capability for an RHIB, from the perspective of a specific existing simulation code. Actually the boat exhibited capsizing incidents that were caused by breaking waves encountered in the stern quartering direction.

In the final chapter of the book (Chap. 43) is described one more study that is of main interest for the Navies. The focus is on landing craft motions, and moreover, on their impulsive loads and water ingress that could be experienced during their operation in heavy seas. Simulation results for predicting these phenomena are compared with corresponding experimental results.

**Acknowledgements** The selection of the chapters was collective responsibility of the editorial team. To ensure the technical quality of these chapters, a review committee was established. In this respect, the important contribution of the following reviewers is recognized: P. Anastopoulos, M. Angelou, I. Backalov, V. Belenky, H. Bruhns, G. Bulian, J. Cichowicz, J.O. de Kat, E. Eliopoulou, A. Francescutto, M.M. González, H. Hashimoto, T. Katayama, M. Levine, W.M. Lin, A. Maki, T. Manderbacka, L. Pérez -Rojas, P. Ruponen, V. Shigunov, T. Smith, K. Spyrou, N. Themelis, N. Umeda, D. Vassalos, G. Zaraphonitis. Special thanks are due to Dr. Vadim Belenky, member of the editorial team, for coordinating part of the review process and for supporting the Editor-in-Chief in several respects, during the preparation of the book.

## References

1. IMO (2020) Interim guidelines on the second generation intact stability criteria. MSC.1/Circ.1627. 10 Dec 2020
2. IMO (2022) Explanatory notes to the interim guidelines on second generation intact stability criteria. MSC.1/Circ.1652
3. Neves MAS, Belenky VL, de Kat JO, Spyrou K, Umeda N (eds) (2011) Contemporary ideas on ship stability and capsizing in waves. Fluid mechanics and its applications series. Springer Science+Business Media B.V. ISBN: 978-94-007-1481-6
4. Belenky VL, Spyrou K, van Walree F, Neves MAS, Umeda N (eds) (2019) Contemporary ideas on ship stability. Risk of capsizing. Fluid mechanics and its applications series, Springer Nature Switzerland AG 2019. ISBN: 978-3-030-00514-6

# **Development of Second-Generation IMO Intact Stability Criteria**

# The Second Generation Intact Stability Criteria—Achievements and Remaining Issues



Naoya Umeda and Alberto Francescutto

**Abstract** The paper summarises background and current status of the development of the second generation intact stability criteria at the International Maritime Organization (IMO). The decisions at the IMO so far together with the implementation scheme for the vulnerability criteria, the guidelines for the direct assessment procedures and for operational measures. The remaining issues, mostly related to the finalization of the explanatory notes are presented.

**Keywords** IMO · Intact stability · Pure loss of stability · Parametric roll · Broaching · Dead ship stability · Excessive acceleration

## 1 Introduction

The second generation intact stability criteria development launched in 2001 was a part of the revision of the Intact Stability Code at the IMO [4]. The existing intact stability code known as IS Code 2008 [6] consists of the purely empirical criteria based on Rahola's work, which was adopted at the IMO in 1968, and the semi-empirical criterion using energy balance of simplified ship roll model in irregular beam wind and waves, which was adopted at the IMO in 1985. In the empirical criteria casualty data of ships having their length of 100 m or less were used for obtaining the relationship between GZ curve parameters and ship stability safety. In the semi-empirical criterion casualty data of ships by 1950s were used to determine the critical value of average wind velocity, i.e. 26 m/s. Since they are directly or indirectly based on casualty data of ships existing before their development, these two criteria could be regarded as the first generation criteria. As a result, the applicability of these existing criteria to current ships cannot be straightforwardly guaranteed. The current

---

N. Umeda  
Osaka University, Osaka, Japan  
e-mail: [umeda@naoe.eng.osaka-u.ac.jp](mailto:umeda@naoe.eng.osaka-u.ac.jp)

A. Francescutto (✉)  
University of Trieste, Trieste, Italy  
e-mail: [francesc@units.it](mailto:francesc@units.it)

major ship types, such as containerships, car carriers, RoPax ships, were not so easily found in 1950s and the sizes of these ships, particularly containerships and cruise ships, are drastically increasing year by year. To properly guarantee the stability safety for contemporary ships, new criteria are required, which have been named as the second generation intact stability criteria.

The adopted approach for the second generation intact stability criteria is physics-based and multi-layered. Since the progress of ship design is faster than accumulating accident data, empirical approaches are not practical for innovative ship designs. They are not in line, moreover, with the new philosophy adopted by IMO for the formulation of new criteria, i.e., Formal Safety Assessment and Goal-Based Approaches. If criteria are based on physics, limitation of their applicability can be significantly reduced. Current ship dynamics together with ship hydrodynamics seem to be sufficient for assessing safety of intact ships by using numerical simulation in the time domain and scaled model experiments. However, the use of such advanced tools for practical purpose cannot be mandated because these tools require experts, qualified experimental facilities and time. Since the IS Code shall be applied to all passenger and cargo ships of 24 m or larger, the number of experts and experimental facilities are definitely insufficient. Since intact stability could be related to both details of hull form and basic specifications of the contract, the use of advanced tools could be impractical for the early design stage. Therefore, it was agreed that, if a ship complies with simplified criteria, the application of advanced tools can be exempted. Here the simplified criteria as lower-level ones should be still physics-based, but with a larger margin of safety. As a result, the framework of the whole criteria can avoid inconsistent judgement in which a ship complying with the lower level criterion could fail to comply with the higher level criterion. During the discussion, the lower level criteria were made to consist of two levels of different complexity: level 1 assessment only requires very simple calculations, while level 2 assessment requires a spread sheet-type calculation. These are named as “vulnerability criteria”. On the contrary, the assessment using an advanced tool, named “direct stability assessment”, requires a computer and, occasionally experimental facilities.

This set of intact stability criteria consider with five major failure modes, i.e. pure loss of stability, parametric roll, broaching, dead ship stability and excessive acceleration.

In case that a ship fails to comply with these criteria, the ship could be allowed to navigate with operational guidelines based on the direct stability assessment procedures or operational limitations based on the level 2 vulnerability criteria.

By the 7th session of the Sub-Committee on Ship Design and Construction (SDC) in February 2020, the interim guidelines for all five vulnerability criteria were agreed and published as an MSC Circular [8] including the interim standards, which specify the required safety levels. The standards have been selected in a way to reduce the number of “false positives” (ships/loading conditions that do not pass the lower level criterion but pass the higher one, and, more important, to limit the possibility of “false negatives”, i.e. cases which pass the first level assessment but would not pass the higher ones. At the same time, also the interim guidelines for direct stability

assessment and interim guidelines for operational measures were agreed. For supplementing the descriptions of calculation procedures in vulnerability criteria for each failure mode, the development of explanatory notes is in an advanced status, with a limited number of remaining issues. This paper illustrates the rationale behind the subdivision of criteria in levels. The few remaining issues in the vulnerability criteria, interim guidelines for direct stability assessment, for operational limitation and their guidelines and explanatory notes are also highlighted.

## 2 Pure Loss of Stability

When a wave crest is near midship section, the roll restoring moment is usually reduced. This is due to the variation of the waterplane through particular features of hull geometry like transom stern and/or bow flare. If the ship runs with high speed in following seas, this reduction continues longer than in head waves. If the ship speed is slightly lower than the surf-riding threshold, the ship speed increases at a wave crest so that the duration of the reduced restoring moment could be extremely long. If the ship with high speed significantly heels because of reduction of restoring moment, asymmetry of the underwater submerged volume could induce a hydrodynamic yaw moment, which could act as external heel moment on a wave crest amidships.

Therefore, in a numerical simulation model for this failure mode, not only the reduction of GZ curve but also the effect of surge motion and roll-yaw coupling should be taken into account.

Based on this understanding, the level 2 vulnerability criterion for this mode has a requirement of the forward ship speed. If the Froude number defined with calm-water velocity exceeds 0.24, the ship could be vulnerable to this failure mode. This is because it is already established that the surf-riding threshold is the nominal Froude number of 0.3, which is determined with the wave steepness of 1/10. Then the level 2 criterion requires the GZ calculation for a ship in longitudinal waves in which the wavelength is equal to the ship length as a conservative assumption. Since an actual wavelength can be different, the steepness used here is adjusted with this equivalent wave and ocean wave spectrum, which is the specified significant wave height and the mean wave period, by using the least square method in space. This procedure is well known as Grim's effective wave concept.

Once the GZ curve in the equivalent wave is obtained, it will be compared with an external heeling moment due to forward velocity. Two criteria, namely CR1 and CR2, have been introduced. CR1 is based on the equilibrium heeling angle of inclination between the restoring moment and the external moment with a binary output being 0 or 1 if the heel angle is smaller or larger than  $15^\circ$  for a passenger ship and  $25^\circ$  for a cargo ship, in which case the ship is judged to be vulnerable to this failure mode. CR2 is based on the angle of vanishing stability without external moment again with a binary output, being 0 or 1 if the vanishing angle is smaller or larger than  $30^\circ$ , in which case the ship is also judged to be vulnerable. This procedure is repeated for all combinations of significant wave height and mean wave period, which appear in



a wave scatter table normally in the North Atlantic. Then the value of the maximum between the weighted averages of CR1 and CR2, which means the probability of dangerous sea states for this failure mode in the specified water area, is used for the final judgement in the level 2 assessment. If the attained value is larger than the required value, set to 0.06, the ship is judged to be vulnerable to this failure mode.

The critical Froude number and heel angles are determined with the recent accidents of RoPax and RoRo ships, which can be presumed to be relevant to this failure mode. The required value was determined with many sample calculation results for existing and coming passenger and cargo ships.

The level 1 criterion was obtained by simplifying the level 2 assessment. While the speed requirement is the same as for the level 2 assessment, the GZ calculation in waves is replaced with the GM calculation in waves. Furthermore, a method for a fast approximate calculation of  $GM_{\min}$  is provided. Here  $GM_{\min}$  in waves can be calculated only with a conventional hydrostatic table and very simple calculations so that workload of ship designers is minimal. Regarding the relationship with actual ocean waves, the representative wave steepness is determined using the wave scatter diagram, which is  $s_w = 0.0334$  for the North Atlantic. The required value for the  $GM_{\min}$  in waves has been set to 0.05 m. This means that the effect of ship speed is ignored. Generally speaking, GM well represents GZ at least at smaller angle, with the exception of ships having a large beam to depth ratio.

During the development stage of these criteria, most sample calculations were executed with the approximate method for GM in waves, which appeared to be reasonably conservative with respect to the direct hydrostatic calculation. As a result, the outcomes of the level 1 assessment are more conservative than those of the level 2 assessment. However, it was experienced that, using the direct hydrostatic calculation, the level 1 assessment occasionally occurs to be less conservative than the level 2 assessment so that some “false negative” cases appear for ships having large beam to depth ratio. Typical examples are ships having extended low weather decks, such as offshore supply vessels. These ships often comply with level 1 criterion but fail to comply with the level 2 assessment. On the other hand, the physical model experiments indicate that such ship may not suffer the stability failure because of water on deck, which could induce anti-roll tank effects [5]. Thus, the criteria for pure loss of stability may not be applied to a vessel with an extended low weather deck.

### 3 Parametric Roll

Contrary to the restoring reduction at wave crest amidship mentioned above, the restoring moment could increase at the wave trough amidship. As a result, a ship in waves may experience the restoring variation with time. Under certain conditions, this restoring variation could induce violent roll motion, with a maximum amplitude which can be much larger than beam-sea resonance. This phenomenon can be categorised as parametric resonance. Using a coupled heave-roll-pitch model in the

time domain, it is possible to accurately predict parametric roll resonance in irregular longitudinal waves. Such numerical simulation can be used as a tool for direct stability assessment.

For vulnerability level 2 criteria, an uncoupled roll model is used for the sake of simplicity. Ignoring dynamic coupling effect with vertical motion normally could result in over-estimation of restoring variation in head waves so that it is expected to provide conservative predictions in the level 2 criteria. It is noteworthy here that roll damping moment, including bilge keels effect, is estimated by using simplified Ikeda's semi-empirical method or experimental data.

In the case of the uncoupled roll model, the occurrence zone of parametric roll can be analytically evaluated through the use of an averaging method [14]. These estimations for typical 16 regular waves constitute the first check of the level 2 criteria, leading to the calculation of a first index C1 for which the standard was set to 0.06.

However, since the zone for the parametric roll occurrence is very wide for slender ships such as containerships, we have to evaluate amplitude of parametric roll for our final judgement even in the level 2 criteria, which is named as the second check, leading to a second criterion C2. If we apply an averaging method or equivalent to the uncoupled roll model, the amplitudes of parametric roll can be estimated almost immediately including stability of the coexisting solutions. Here GM is assumed to vary with time, but nonlinear characters of GZ curve are kept as that in calm water. For accurately modelling a hydrostatically calculated GZ curve, numerical simulations of the uncoupled roll model in the time domain can be recommended. Thus, the SDC agreed to use the numerical simulation. In this case, calculated results could depend on initial conditions so that user-friendly guidelines could be helpful if developed.

This procedure for estimating the roll amplitude is repeated for all combinations of the significant wave height and the mean wave period, which appear in a wave scatter table normally in the North Atlantic, as well as 12 different encounter wave periods. Then their weighted average, which means the probability of dangerous sea states for this failure mode in the specified water area, is used for the final judgement in the level 2 criteria. The attained value according to this criterion, called C2, has to be lower or equal than the required value, which has been set to 0.025, based on the result of accident containership the ship is judged to be vulnerable to this failure mode.

For the level 1 criterion, the procedure used in the level 2 criteria is further simplified. If we ignore nonlinearity in both GZ and roll damping and use the mean of GM variation, the formula of the averaging method can be restricted to a simple estimation formula as a function of GM variation amplitude  $\delta GM$  and roll damping. Regarding the relationship with actual ocean waves, the representative wave steepness is determined using the wave scatter diagram, which is 0.0167 for the North Atlantic. Further simplifying Ikeda's simplified method and hydrostatic GM estimation, we can calculate the attained value in the level 1 assessment only with a hydrostatic table, bilge keel area ratio and very simple calculations. The standard in terms of  $\delta GM/GM$  depends on the roll damping due to shipshape and bilge keels area.

It does not appear that there are remaining issues in the formulation of both levels of this criterion.

## 4 Surf-Riding/Broaching

Even a directionally stable ship in calm water can be directionally unstable at following wave downslope. If surf-riding occurs, a ship can be captured at wave downslope so that the ship could fail to keep its straight course in stern quartering waves even with its maximum steering effort. This is known as broaching. Because of surf-riding, the forward ship speed is high. As a result, yaw angular velocity due to directional instability could result in violent centrifugal force, which could induce extremely large heel.

Probability of stability failure due to broaching can be predicted by combining a probabilistic wave theory and a coupled surge-sway-yaw-roll numerical model with accurately estimated manoeuvring coefficients. This could be utilised as a tool for direct stability assessment. Obviously, accurate estimation of manoeuvring coefficients cannot be mandated for all ships covered by IMO instruments.

Thus, the SDC already agreed for the vulnerability criteria to deal with surf-riding in place of broaching. If we avoid surf-riding, the possibility of stability failure due to broaching is small enough. It should be underlined that typical surf-riding can be dealt even with an uncoupled surge model in following waves so that we do not have to estimate manoeuvring coefficients.

In the level 2 criterion, critical nominal speeds for surf-riding of a self-propelled ship in regular following waves are estimated for various wavelengths and wave heights by a perturbation method starting with its solution without surge damping [9, 11, 12]. Then the occurrence probability of waves that the ship can be surf-ridden is calculated with a stochastic wave theory and the North Atlantic wave statistics. Finally, the probability of surf-riding occurrence when a ship meets one local wave is calculated and compared with the acceptable safety level [13]. Based on sample calculation results for relevant ships, the acceptable safety level has been set to be 0.005. It is noteworthy here that accurate prediction of calm-water resistance up to wave celerity is required, and the acceptable safety level depends on prediction accuracy of wave-induced surge force.

For avoiding such difficulties and designers' workloads, the level 1 criterion was developed with sample calculation results for various ships under the wave steepness of 1/10 with measured wave-induced surge force and calm-water resistance. As a result, we concluded that, if the nominal Froude number is smaller than 0.3, surf-riding is not likely to be met. This criterion and standard are the same as those in the ship-independent operational guidance in the MSC. 1/Circ. 1228. In addition, with calculated results based on the level 2 assessment, it was also concluded that, if the ship length is larger than 200 m, the ship is out of the scope of this failure mode. This is because ocean waves are too short for such longer ships to be surf-ridden. If a ship fails to comply with level 1 vulnerability, instead of to go to level 2 assessment, can

be subjected to the procedures of ship handling on how to avoid dangerous conditions for surf-riding/broaching, as recommended in section 4.2.1 the MSC.1/Circ.1228, subject to the approval of the Administration.

## 5 Stability in Dead Ship Condition

If a ship loses all propulsion power or a shipmaster decides to stop engine power for avoiding other dangerous phenomena with the forward velocity, the ship would drift under beam wind and wave conditions for longer duration. Although its wave heading depends on its under-water and above-water shape, the beam wind and wave condition could be regarded as a worst situation [15]. This is known as dead ship condition, and the weather criterion was originally developed for this condition but with a simplified energy balance analysis. However, the weather criterion is believed to excessively limit the freedom of designing contemporary ships such as large cruise ships. Thus, new criteria for this failure mode were developed.

Probability of stability failure under this condition can be estimated with the Monte Carlo numerical simulation in irregular beam wind and waves by using a sway-heave-roll-pitch model. This could be utilised as a tool for direct stability assessment, but the actually small value of probability could require so many realisations for accurately obtaining the probability for a practical ship.

The use of an analytical solution of uncoupled roll model is a way to reduce computation time significantly. In the level 2 criterion, the SDC agreed to use linear GZ curve up to the critical heel angle. Above the critical angle, the GZ is assumed to be zero. Here the critical heel angle is determined to keep the area of original GZ curve up to the angle of vanishing stability, which is responsible for dynamic ship stability, as the same as the approximate GZ. Thanks to linear GZ, there is no difficulty for calculating the probability of stability failure in irregular beam wind and waves with a wave scatter diagram [3]. Here the roll damping and the roll exciting moment can be estimated with simplified Ikeda's method and the Froude-Krylov approach assuming rectangular hull sections, respectively. If the calculated probability for the relevant water area is larger than the acceptable safety level, the ship is judged to be vulnerable to this failure mode. The value of acceptable safety level, represented by the long-term probability index that measures the vulnerability of the ship to a stability failure in the dead ship condition based on the probability of occurrence of short-term environmental conditions, as specified in the text of the regulation has been set to 0.06, based on the sample calculations using existing and actually designed ships.

Regarding the level 1 criterion, the SDC also agreed to use the current weather criterion but with the extended wave table that was already adopted in the MSC.1/Circ. 1200 for the experiment-supported weather criterion. This is because the current weather criterion can be regarded as a simplified version of the level 2 methodology with several assumptions for wind gustiness, wave irregularity and so on.

Like the case of pure loss of stability, also for dead ship stability the provisions given above apply to all ships, except for ships with an extended low weather deck due to increased likelihood of water on deck or deck-in-water.

It has to be noted, furthermore, that reference environmental conditions to be used in the assessment of level 2 may be modified when introducing operational limitations permitting operation in specific operational areas or routes and, if appropriate, specific season, according to the Interim guidelines for operational measures.

For this failure mode, major remaining issues are the development of guidelines for alternative roll damping estimation using CFD (computational fluid dynamics) and of the effective wave slope coefficient for ships different from monohulls for the level 2 assessment.

The development of second generation intact stability criteria, and in particular the set concerning this failure mode, for which a mandatory criterion already exists, opens potential problems of compatibility and conflict since the use of new vulnerability criteria could change the safety level guaranteed by the current weather criterion.

Actually, the level 1 vulnerability for dead ship differs slightly from the existing weather criterion. This difference is indeed limited to the tail of weather conditions, represented by the wave steepness. It was already incorporated in the interim guidelines for alternative assessment of the weather criterion as contained in MSC.1/Circ.1200. To have a better insight on this, and to fix an appropriate value for the standard, some sample calculations using many existing ships having wider loading conditions were executed [7].

Firstly, the calculated attained values, i.e.  $C$  values, have been plotted as a function of the metacentric height,  $GM$ , as shown in Fig. 1. It does not appear any clear correlation between  $GM$  and  $C$ , which corresponds to a capsizing probability index for a ship in beam wind and waves. Although larger  $GM$  is expected to provide better stability, the existence of roll resonance, which occurs at the ship-dependent natural roll period, results in no distinct correlation.

Secondly, the calculated  $C$  values have been plotted as a function of the ratio of the heeling energy and residual restoring energy,  $b/a$ , in the level 1 assessment as shown in Fig. 2. In this figure, broadly speaking, the values of  $C$  decrease with the increasing

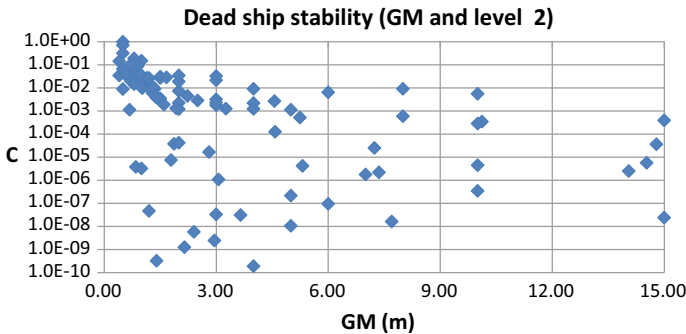
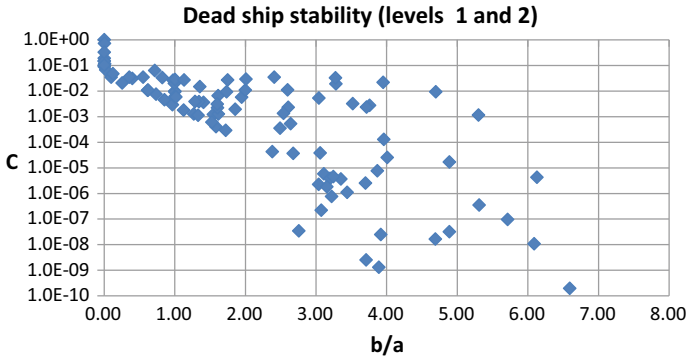


Fig. 1 Relationship between the metacentric height and the  $C$  value in the level 2 criterion [7]



**Fig. 2** Relationship between the  $b/a$  in the level 1 criterion and the  $C$  value in the level 2 criterion [7]

value of  $b/a$ . This is because both methods deal with stability failure mode in beam wind and waves. If we look into detail, some scatters can be found in the  $b/a$  region between 1.1 and 5.5. This is probably due to the difference in estimation accuracy of roll motions between the two different modelling. An almost vertical trend of  $C$  can be found when  $b/a$  is close to zero. This is because the level 1 assessment assumes only one stationary sea state for determining loss of static balance between GZ and wind heeling lever and the level 2 assessment uses many different sea states and their occurrence probability included in the wave scatter table for the same purpose.

It appeared that with the use of standard value in the range 0.04–0.06, no “false negative” case exists at least in these sample ships. In other words, some ships failing to comply with the current weather criterion can be regarded as non-vulnerable for dead ship stability failure keeping the safety level that the current weather criterion requires. It is expected that a complete answer to this problem will come from the extensive application of the full set of second generation intact stability criteria in the interim period.

## 6 Excessive Acceleration

If GM is excessively large, the natural roll period can be too small so that large acceleration under synchronous resonance could act on crew or cargoes. Since actual fatal accidents for modern containerships under ballast conditions were reported [1, 2], this situation was also included as a stability failure. However, the problem to be solved is almost linear so that a standard sea keeping tool can be used with acceptable acceleration value. This could be a tool for direct stability assessment. However, there is a different-type difficulty. A conservative estimation here could require too small GM, which can be smaller than GM required by other stability criteria.

Therefore, the vulnerability criteria should be more conservative than the direct stability assessment but its margin should be smallest. In the level 2 criterion, the uncoupled roll model in short-crested irregular waves without forward velocity is used because beam seas can be regarded as a worst situation. By using the linear response operator, wave spectrum, the Froude-Krylov wave exciting moment and the equivalent linearization of roll damping, the variance of lateral acceleration can be calculated. Then, assuming the Rayleigh distribution of roll amplitude, critical acceleration value and the wave scatter table, the long-term probability of lateral acceleration exceeding its critical value can be obtained. If it is larger than the acceptable level, the ship is judged as vulnerable to this failure mode. Here the critical acceleration value is set as  $9.81 \text{ m/s}^2$ , and the standard was set to 0.00039, based on the result of accident containership.

For the level 1 criterion, the level 2 procedure is simplified by approximating the wave frequency in the numerator with the natural roll frequency. As a result, we can obtain a simple formula without integral, which depends on the wave steepness from the weather criterion and roll damping coefficient. Here the roll damping and wave excitation are estimated by simplified methods. The critical acceleration was set to  $4.64 \text{ m/s}^2$ .

## 7 Operational Limitation and Guidance

It can be easily presumed that a safety level estimated with a perfect direct stability assessment, i.e. the safety level estimation by using a time-domain numerical simulation in irregular external forcing, if available, could be below the actual accident rate. This is because operators might avoid existing dangers by avoiding some dangerous wave and operational conditions. Thus ignoring operational aspects cannot be justified. On the other hand, the outcomes from the level 2 criterion and the direct stability assessment can be useful to improve the operator's actions to avoid dangers. Therefore, the SDC agreed to allow the ship operation if the ship is judged as vulnerable to a failure in the level 2 assessment but the operational limitation based on the level 2 application outcomes is provided. Similarly, operational guidance based on the direct stability assessment can be used for a ship failed to pass the direct stability assessment.

The Interim guidelines for operational limitations and guidance have also been finalized in the frame of SDC 7. These interim guidelines consider the following ship specific operational measures:

1. Operational limitations which define the limits on a ship's operation in a considered loading condition, consist in Operational limitations related to areas or routes and season which permit operation in specific operational areas or routes and, if appropriate, the specific season, and in Operational limitations related to maximum significant wave height which permit operation in conditions up to a maximum significant wave height;

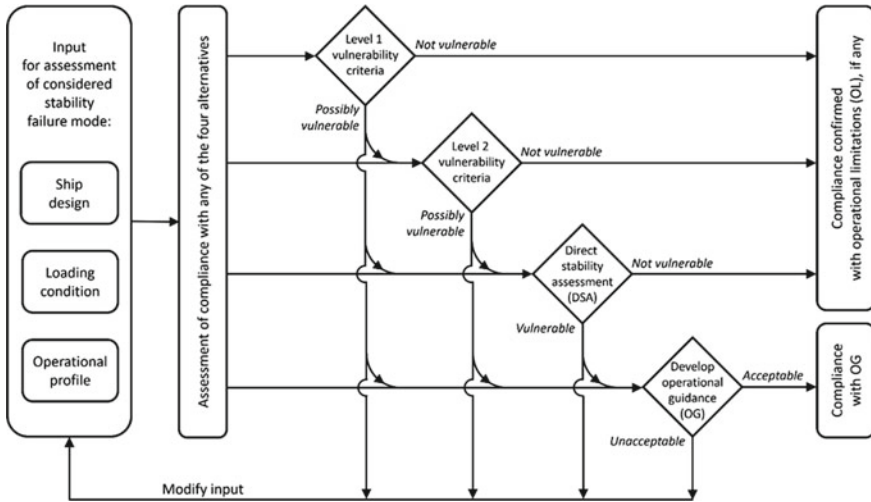


**Fig. 3** Simplified scheme of the application structure of the second generation intact stability criteria [8]

- Operational guidance which defines the combinations of ship speed and heading relative to mean wave direction that are not recommended and that should be avoided in each relevant sea state.

Operational limitations and operational guidance should provide at least the same level of safety as that provided by the procedures and standards given by the interim guidelines for vulnerability criteria or the direct stability assessment. In particular, the safety level of those loading conditions that fail vulnerability or direct design assessment requirements should become sufficient if almost all combinations of the sailing condition and sea state that are not recommended by these operational measures are removed from the design assessment.

The application structure of the second generation intact stability criteria is roughly illustrated in Fig. 3 as a reference. The actual application should be based on the interim guidelines [8]

## 8 Guidelines for Direct Stability Assessment

The interim guidelines provide specifications for direct stability assessment procedures for all the five stability failure modes. As for the vulnerability criteria, these procedures should not apply to both the dead ship condition and pure loss of stability failure modes to ships with an extended low weather deck. Only major general features of these interim guidelines are reported here.



Direct stability assessment procedures are intended to employ the latest technology while being sufficiently practical to be uniformly accepted and applied using currently available infrastructure and are designed to ensure a safety level corresponding to the average stability failure rate not exceeding  $2.6 \times 10^{-3}$  per ship per year. In this frame, the failure event is defined as:

1. Exceedance of roll angle, defined as  $40^\circ$ , angle of vanishing stability in calm water or angle of submergence of unprotected openings in calm water, whichever is less; or
2. Exceedance of lateral acceleration of  $9.81 \text{ m/s}^2$ , at the highest location along the length of the ship where passengers or crew may be present.

Active means of motion reduction, such as active anti-roll fins and anti-roll tanks, can significantly reduce roll motions in a seaway. However, the safety of the ship should be ensured in cases of failure of such devices. Therefore, such devices should be assumed in the assessment to be inactive or retracted, if they are retractable.

The procedure for direct stability assessment consists of two major components:

1. a method that adequately replicates ship motions in wind and waves; and
2. a prescribed procedure that identifies the process by which input values are obtained for the assessment, how the output values are processed, and how the results are evaluated.

Requirements for a method that adequately predicts ship motions, verification procedures for particular stability failure modes, requirements for qualitative and quantitative validation of software for numerical simulation of ship motions are included in the interim guidelines together with details on the different probability-based or deterministic methodologies and the simplified design situations for each stability failure mode.

## **9 Implementation of the Second Generation Intact Stability Criteria and of the Related Explanatory Notes for the Second Generation Intact Stability Criteria**

The set of Second generation intact stability criteria, consisting of the vulnerability criteria of levels 1 and 2 for all five failure modes together with the Interim guidelines for direct stability assessment procedures and the Interim guidelines for operational measures was agreed at SDC 7 and were approved as an MSC Circular [8]. It was agreed to keep the Interim guidelines under review, taking into account experience in the design and operation of ships gained during their application.

The IMO member States are invited to use the Interim guidelines as complementary measures when applying the requirements of the mandatory criteria of part A of the Intact Stability Code, to bring them to the attention of all parties concerned, in

particular shipbuilders, shipmasters, shipowners, ship operators and shipping companies, and to recount their experience gained through the trial use of these Interim guidelines to the IMO.

Work is in progress intersessionally based on document IMO SDC 4/5/1, to finalise the explanatory notes for all five failure modes, including worked examples, operational limitations and guidance and guidelines for direct stability assessment at SDC 8 in 2022.

## 10 Conclusions

The interim guidelines of second generation intact stability criteria was approved as MSC Circular (MSC.1/Circ. 1627) in 2020 for the IMO Member States to test their feasibility and effectiveness. Their detailed procedures for using the interim guidelines and the technical background would be published as its explanatory notes later as another MSC Circular. These would open the door to use contemporary technical methodologies as actual regulations of ship safety. This could be the performance-oriented criteria that the Part A of the 2008 IS Code noted to be developed. For this purpose, the member states together with the relevant stakeholders should be encouraged to test these new stability criteria.

**Acknowledgements** This work was supported by a Grant-in Aid for Scientific Research from the Japan Society for Promotion of Science (JSPS KAKENHI Grant Number 15H02327). It was partly carried out as a research activity of Goal-based Stability Criteria Project of Japan Ship Technology Research Association in the fiscal years of 2015 funded by the Nippon Foundation. The authors appreciate Miss Naho Yamashita for her effective assistance in the sample calculation.

## References

1. BSU (2009) Fatal accident on board the CMV CHICAGO EXPRESS during typhoon “HAGUPIT” on 24 September 2008 off the coast of Hong Kong, Investigation Report 510/08, 1 November 2009
2. BSU (2011) Fatal accident on board the CMV CCNI GUAYAS during typhoon “KOPPU” on 15 September 2009 in the sea area off Hong Kong, Investigation Report 391/09 1 June 2011
3. Bulian G, Francescutto A (2004) A simplified modular approach for the prediction of the roll motion due to the combined action of wind and waves. *J Engineering for the Maritime Environment* 218(M3):189–212
4. Francescutto A (2015) Intact stability criteria of ships—past, present and future. In: Proceedings of the 12th international conference on stability of ships and ocean vehicles, glasgow, pp 1199–1209
5. Htun SS, Umeda N, Sakai M, Matsuda A, Terada D (2019) Water-on-deck effects on roll motions of an offshore supply vessel in regular stern quartering waves. *Ocean Engineering* 188
6. IMO (2009) International code on intact stability, 2008
7. IMO (2015) Information collected by the correspondence group on intact stability regarding second generation intact stability criteria. SDC 3/INF.10

8. IMO (2020) Interim guidelines on the second generation intact stability criteria. MSC.1/Circ.1627
9. Kan M (1990) Surging of large amplitude and surf-riding of ships in following seas. Selected Papers in Naval Architecture and Ocean Engineering, vol 28, Society of Naval Architects of Japan, Tokyo
10. Kawahara Y, Maekawa K, Ikeda Y (2009) A simple prediction formula of a roll damping of conventional cargo ships on the basis of Ikeda's method and its limitation. In: Proceedings of 10th international conference on stability of ships and ocean vehicles, St. Petersburg, pp 387–398
11. Maki A, Umeda N, Renilson M, Ueta T (2010) Analytical formulae for predicting the surf-riding threshold for a ship in following seas. *J Marine Science and Technology* 15(3):218–229
12. Spyrou KJ (2006) Asymmetric surging of ships in following seas and its repercussions for safety. *Nonlinear Dyn* 43:149–172
13. Umeda N (1990) Probabilistic study on surf-riding of a ship in irregular following seas. In: Proceedings of 4th international conference on stability of ships and ocean vehicles, Naples, Italy, pp 336–343
14. Umeda N, Hashimoto H, Vassalos D, Urano S, Okou K (2004) Nonlinear dynamics on parametric roll resonance with realistic numerical modelling. *Int Shipbuild Prog* 51(2/3):205–220
15. Umeda N, Koga S, Ueda J, Maeda E, Tsukamoto I, Paroka D (2007) Methodology for calculating capsizing probability for a ship under dead ship condition. In: Proceedings of the 9th international ship stability workshop, Hamburg, pp 1.2.1–1.2.19

# Safety Level of the IMO Second Generation Intact Stability Criteria



William S. Peters, Vadim Belenky, and Kostas J. Spyrou

**Abstract** The safety level of a criterion is defined as a probability that a failure will occur, if the criterion is met exactly, i.e. without any surplus. This chapter considers how the safety level can be evaluated, in principle, for the vulnerability assessment included in the Second Generation Intact Stability Criteria (SGISC). The chapter also provides a review of the background literature for the SGISC and considers the alignment of SGISC with Goal Based Standards and Formal Safety Assessment.

**Keywords** Intact stability · Safety level · Goal-based standards

## 1 Introduction

Goal-based standards (GBS) represent a significant paradigm-shift in regulation philosophy and practice. Instead of prescribing the means of achieving safety, GBS formulates the objective, leaving the freedom of achieving this objective to a designer (see, e.g. [28, 43]). GBS may be considered as the natural regulatory framework for deploying a risk-based or probabilistic approach. Indeed, for stability in particular, the probability of stability failure, as a universal indicator of danger, is a natural metric of the goal of safety and is naturally aligned with the GBS.

For example, the IMO Guidelines for the approval of alternatives and equivalents as provided in various IMO instruments [34] acknowledges that approval risk assessment and reliability analysis by Administrations is an increasingly acceptable practice, especially for novel designs. Also, risk analysis is an important part of a

---

W. S. Peters

US Coast Guard Office of Design and Engineering Standards, Washington, DC, USA  
e-mail: [william.s.peters@uscg.mil](mailto:william.s.peters@uscg.mil)

V. Belenky (✉)

David Taylor Model Basin (NSWCCD), West Bethesda, MD, USA  
e-mail: [vadim.belenky@navy.mil](mailto:vadim.belenky@navy.mil)

K. J. Spyrou

School of Naval Architecture, National Technical University of Athens, Athens, Greece  
e-mail: [spyrou@deslab.ntua.gr](mailto:spyrou@deslab.ntua.gr)

formal safety assessment (FSA), which is considered for use in the IMO rule-making process.

A comprehensive (and still up-to-date) review of a risk-based approach to intact stability can be found in [42]. The most difficult problem is the calculation of probability of stability failure in an absolute sense. In other words, what does the term “probability of stability failure” mean?

Stability failures in realistic sea conditions are rare and cannot be assessed by direct numerical simulation of reasonable fidelity. This problem of rarity (as defined in the Interim Guidelines on the second generation intact stability criteria, see [32]) inevitably generates need of using statistical extrapolation schemes. The ability to determine the probability of stability failure in an absolute sense means that an extrapolation method is capable of recovering the value of the probability of stability failure that would be observed from numerous lengthy data sets [72].

The derivation of probability of stability failure in an absolute sense allows consideration of intact-stability hazards together with other hazards, like fires, machinery failures etc., making intact stability fully assessable with risk analysis and FSA.

The next question is how the alignment with GBS propagates through the multi-tiered structure of the second generation intact stability criteria (SGISC). Since probabilistic criteria are expected to be used for direct stability assessment, such alignment appears quite trivial at the tier 3 of the SGISC. Indeed, probability of stability failure produced by the direct stability assessment directly “plugs-in” into FSA and risk analysis. This is more difficult however for vulnerability criteria, as there is less information available and the calculation methods are much simpler than the direct assessment. It is especially difficult for vulnerability criteria level 1. To address this challenge, a brief review of the physical background of the SGISC vulnerability criteria is carried out and an attempt is made to reveal their connection to a general probabilistic framework. Before this however, the background of the probabilistic formulation by means of which the stability failure modes can be assessed is explained.

The Interim Guidelines on the SGISC [32] define an intact stability failure as an event that includes the occurrence of very large roll (heel, list) angles or excessive rigid body accelerations, which may result in capsizing or impairs normal operation of the ship and could be dangerous to crew, passengers, cargo or ship equipment. The Interim Guidelines address five dynamic stability failure modes, including the dead ship condition, excessive acceleration, pure loss of stability, parametric rolling, and surf-riding/broaching.

## 2 Probabilistic Framework

Waves and wind are stochastic processes. Therefore, any stability failures caused by wind or waves are random events and they can be characterized by their probability of occurrence.

An objective of safe operation of a ship is the absence of stability failures during a ship's lifetime. The symbol  $X$  is used to denote a random event, the occurrence of at least one stability failure during a ship's lifetime. Then the complimentary event  $\bar{X}$  is that no stability failures occur during a ship's lifetime. The bar above the symbol identifies it as a complimentary random event, i.e., that the event  $X$  does not occur. The likelihood of achieving this objective is characterized by the probability that no stability failure occurs during a ship's lifetime,  $P(\bar{X})$ .

Stability failure is a random event and it might occur at any interval of time while the ship is in operation. The objective of safe operation is achieved when no stability failure occurs at any of the time intervals comprising the entire time of ship operation. Let us represent these intervals by a series of discrete time instances. Then the probability of failure is expressed as:

$$P(\bar{X}) = P_1(\bar{X}) \cdot P_2(\bar{X}) \cdot \dots \cdot P_N(\bar{X}) = \prod_{i=1}^N P_i(\bar{X}). \quad (1)$$

For a particular ship, the probability,  $P_i(\bar{X})$  that no stability failure occurs in association to the  $i$ th time instant depends on the environmental (i.e., significant wave height, mean wind velocity, mean zero-crossing period of wave, etc.) and operational conditions (loading, speed, heading relative to the waves, etc.). Further justification of the probabilistic framework can be found in Chap. 1 of [9].

The short-term formulation is relevant for consideration of a particular sea state, i.e., when the significant wave height and the mean zero-crossing period can be associated with a particular cell of a scatter table (e.g. [30]).

For a ship at a given loading condition, heading and speed, the probability,  $P_i(\bar{X})$  remains constant for each time interval. Then the probability of no stability failure under the conditions of a realization of a sea state with significant wave height  $H_S$  and mean zero-crossing period  $T_Z$  is:

$$P(\bar{X}|H_S, T_Z) = (P_i(\bar{X}))^n, \quad (2)$$

where  $P_i(\bar{X})$  is a probability that there will be no stability failure at a brief time period around some time instant;  $n$  is the number of such time instants.

As is obvious, the probability of no stability failure depends on time; the longer the time of exposure, the higher the probability of failure.

Equation (2) is interpreted as a particular case of the binomial distribution, which expresses the probability that a random event occurs  $k$  times out of  $n$  attempts—the probability of  $k$  failures occurring in  $n$  instants of time:

$$P(k) = C(n, k)p^k q^{n-k}, \quad (3)$$

where  $C(n, k)$  is the number of  $k$  combinations out  $n$  without repetitions,  $p$  is the probability of stability failure at any given instant of time and  $q$  is the probability of the complimentary event, (i.e., that stability failure does not occur at any instant of

time):

$$p = P_i(X); \quad q = 1 - P_i(X) = P_i(\bar{X}). \quad (4)$$

The Poisson distribution is the limit case of the binomial distribution for a large number of time instants, while the duration of each time instant is small:

$$P(k) = \frac{(\lambda T)^k}{k!} \cdot \exp(-\lambda T), \quad (5)$$

where  $T$  is a finite duration of time, while the condition  $(H_S, T_Z)$  exists and  $\lambda$  is the rate of random events (stability failures) per unit of time. The probability of no stability failures while the condition  $(H_S, T_Z)$  holds is given by the case  $k = 0$ :

$$P(\bar{X}|H_S, T_Z) = \exp(-\lambda T). \quad (6)$$

The probability of the complimentary event—at least one stability failure during time  $T$  is interpreted as the CDF of the time before the first event occurs. It is an exponential distribution with parameter  $\lambda$ :

$$P(X|H_S, T_Z) = CDF(T) = 1 - \exp(-\lambda T). \quad (7)$$

There are three assumptions, associated with the short-term formulation:

- Stability failures are independent random events;
- The probability of occurrence of a stability failure at a particular instant of time is infinitely small;
- Only one stability failure can occur at a particular instant of time.

The first assumption is inherited from (1), while the two others are the result of the limit transition from (3) to (5). A probabilistic model of random events using these three assumptions is known as a “Poisson flow of events”.

The value of the stability failure rate  $\lambda$  depends on a ship’s speed, heading and loading condition. The methods for the numerical evaluation of  $\lambda$  are failure-mode-specific. A key point is that  $\lambda$  is assumed constant for a particular speed, heading, loading and the environmental conditions  $(H_S, T_Z)$ .

The lifetime of a ship is presented as a sequence of sea states described in a scatter table with  $N_S$  significant wave heights and  $N_T$  zero-crossing mean periods. Equation (1) for the probability of no stability failures over the lifetime of a ship, using (6),  $T_{LT}$  is rewritten as:

$$P(\bar{X}) = \prod_{i=1}^{N_S} \prod_{j=1}^{N_T} \exp(-\lambda_{i,j} T_{LT} f_{i,j}) = \exp(-\lambda_a T_{LT}), \quad (8)$$

where  $f_{i,j}$  is the statistical frequency for the  $i$ th significant wave height and the  $j$ th mean zero-crossing period;  $\lambda_a$  is the rate of stability failures, averaged over the scatter table:

$$\lambda_a = \sum_{i=1}^{N_s} \sum_{j=1}^{N_T} f_{i,j} \hat{\lambda}_{i,j}. \quad (9)$$

The probability of at least one stability failure is expressed through the complementary probability to (8):

$$P(X) = 1 - \exp(-\lambda_a T_{LT}). \quad (10)$$

The criteria for different stability failure modes use different probabilistic formulations, but all of them are based on Eqs. (7), (9) and (10).

The safety level of the stability criterion is a measure of how remote the possibility of stability failure is if a ship meets the standard used with the criterion. Hence, the safety level of a vulnerability criterion is measured as a probability of stability failure of a ship that passes that standard. The idea to measure reliability of an intact stability criterion with a probability of stability failure while the criterion is satisfied exactly is not new, e.g. [69]. The English version is available in subsection 1.1 of [9], where the safety level is referred as a “guarantee”.

While formulating the framework for the SGISC, two types of criteria were envisioned: deterministic and probabilistic [7]. A probabilistic criterion yields an estimate of probability of failure, the standard has a meaning as the acceptable probability of failure. Thus, determining the safety level of a probabilistic criterion is straightforward—it is equal to the standard.

To evaluate the safety level of a deterministic criterion, a random variable (or variables) needs to be found (or assumed) in a criterion’s equation. A distribution for this random variation is to be determined or assumed. Then, the criterion’s equation can be treated as a deterministic function of a random argument(s) and a distribution of the criterion value can be found. The safety level  $SL$  is determined as a probability of exceedance of a standard;

$$SL = P(C \geq St) = \int_{St}^{\infty} pdf(C) dC, \quad (11)$$

where  $C$  is a criteria and  $St$  is a standard.

Level 1 vulnerability criteria are deterministic, while all the level 2 vulnerability criteria are probabilistic. For three failure modes (excessive acceleration, pure loss of stability and surf-riding), wave steepness can be identified as a random variable that defines the safety level. Detailed consideration is given further in the text, while the distribution of wave steepness is described here.

Consider a short-term problem: a sea state is given where both the significant wave height  $H_s$  and the zero-crossing period  $T_z$  are known. A spectral density of wave



elevations  $s_w$  is also defined. The availability of a joint probability density function (PDF) of the wave amplitude and the wave period is very useful for deriving the probability of stability failure since both of these variables affect ship stability. Such a PDF was proposed, for example, by [48] on the basis of normalized quantities,  $H_w/(2\sqrt{2m_0})$  for wave amplitude; and  $\tau = T_w/T_{01}$  for wave period:

$$T_{01} = 2\pi \frac{m_0}{m_1}; m_n = \int_0^{\infty} s_w(\omega) \omega^n d\omega, \quad (12)$$

where  $n$  is an order of the spectral moment. The period, corresponding to the mean frequency is related to the mean zero-crossing frequency through the spectral moment, see e.g. [47]  $T_z = 2\pi \sqrt{m_0/m_2}$ . The joint distribution of  $a$  and  $\tau$  is expressed as:

$$pdf(a, \tau) = \frac{2k_N}{v\sqrt{\pi}} \left(\frac{a}{\tau}\right)^2 \cdot \exp\left\{-a^2 \left[1 + \frac{1}{v^2} \left(1 - \frac{1}{\tau}\right)^2\right]\right\} \quad (13)$$

where  $k_N$  is a normalizing factor taking into account the positivity of period and amplitude, while  $v$  is a spectral width parameter:

$$k_N = \frac{1}{2} \cdot \frac{\sqrt{1+v^2}}{1+\sqrt{1+v^2}}; \quad v^2 = \frac{m_0 m_1}{m_1^2} - 1. \quad (14)$$

Using the dispersion relation in deep water between a wave length  $\lambda_w$  and a wave period  $T_w = \sqrt{2\pi\lambda_w/g}$  (where  $g$  is the gravity acceleration), the PDF (13) can be re-written for the wave length  $\lambda_w$  and the wave steepness  $s = H_w/\lambda_w$ , using well-known formulae for distribution of deterministic function of random arguments (see e.g. Sect. 6.7 of [65]—the derivation is not difficult as it is essentially a substitution of the variables:

$$pdf(\lambda_w, s) = k_{N1} \lambda_w^{3/2} s^2 \cdot \exp\left\{-2 \left(\frac{\lambda_w \cdot s}{H_s}\right)^2 \left[1 + \frac{1}{v^2} \left(1 - T_{01} \sqrt{\frac{g}{2\pi\lambda_w}}\right)^2\right]\right\}, \quad (15)$$

where the constant  $k_{N1}$  is defined through the normalizing factor  $k_N$ :

$$k_{N1} = \frac{8T_{01}\sqrt{g}}{\pi v H_s^3} k_N. \quad (16)$$

The distribution of the wave steepness is the marginal distribution of (15); it cannot be expressed in elementary functions:

$$pdf(s) = \int_0^{\infty} pdf(\lambda_w, s) d\lambda_w. \quad (17)$$

A probability that the wave steepness exceeds a critical value  $s_{cr}$  for a given sea state is defined with a significant wave height  $H_s$  and a zero-crossing period  $T_z$ :

$$P(s > s_{cr} | H_s, T_z) = \int_{s_{cr}}^{s=1/7} pdf(s | H_s, T_z) ds. \quad (18)$$

The critical wave steepness  $s_{cr}$  is defined for each failure mode, while  $s = 1/7$  is the breaking wave limit.

All the level 2 vulnerability criteria are formulated as long-term probabilistic criteria, i.e. weight-averaged over all possible sea states using statistical weights from a wave scatter table (such as [30]). Thus, it makes sense to evaluate the safety level of the level 1 vulnerability criteria also as an average of the short-term value over a scatter table:

$$SL = P_a = \sum_{i=1}^{N_s} \sum_{j=1}^{N_T} f_{i,j} P(s > s_{cr} | H_{Si}, T_{Zj}), \quad (19)$$

where  $f_{i,j}$  is the statistical frequency for the  $i$ th significant wave height  $H_{Si}$  and the  $j$ th mean zero-crossing period  $T_{Zj}$ .

### 3 Dead Ship Condition

The dead ship condition corresponds to the assumed situation considered by the severe wind and rolling criterion (also known as weather criterion), which is formulated in Sect. 2.3 of part A of the 2008 IS Code [31]. As it follows from its name, the main propulsion is assumed not to be available. As a result, a ship drifts under the action of wind and waves. A position of a ship relative to wind is defined by the distribution of the windage area. A conventional steam-era ship, with approximately symmetric windage area forward and aft, usually takes a near beam seas position. For modern ship types, this assumption is made in order to maximize the projected area and therefore the heeling moment. Gustly wind makes the ship to heel and roll motions have a non-zero mean. A hydrodynamic drag, generated by the drift creates an additional heeling moment and contributes to the roll mean value.

The objective of an assessment of stability in the dead ship condition is to ensure that a vessel can withstand the action of wind and waves; this is taken to mean that a roll angle does not exceed a prescribed limit. Three important elements are included in the dead ship condition assumed situation:

- A large roll angle is associated with the failure, while capsizing is not considered;

- A ship is subjected to the combined actions of wind and waves; and
- The dynamics of ship motions must be considered.

The weather criterion considers a specific instance when a ship experiences a peak roll angle to the windward side (roll back angle) and followed with the application of a wind gust. The dynamic roll angle is found with the energy balance method, which assumes that the work of the heeling moment is equal to the increase of the potential energy of heeling. The drift-generated drag is included in the lever of the wind heeling moment.

A diploma thesis explored the possibility of a probabilistic interpretation of the weather criterion [83]. It was realized, however, that this turns out to be quite ambiguous as the applied excitations follow a rather idealized structure.

The development and background for the vulnerability assessment of the SGISC are described in Bulian and Francescutto [12–14]. The level 1 vulnerability criteria is essentially the weather criterion with an extended table for the natural roll period [paragraph 2.2.2.4, 32]. The probabilistic interpretation of the level 1 criteria is a challenge and can be addressed only in a statistical sense, a detailed consideration of this problem is given by [62].

The level 2 vulnerability criteria has a probabilistic formulation through the random exceedance of a prescribed limit from either side of the ship. The exceedance or upcrossing of a threshold is defined as a random event when the current value of a stochastic process equals the leeward threshold  $\varphi_{fail+}$  and the first derivative is positive ( $\varphi(t) = \varphi_{fail+} \cap \dot{\varphi}(t) > 0$ ). The general formula for the rate of exceedance or upcrossing of  $\varphi_{fail+}$  is:

$$\lambda_{fail+} = \int_0^{\infty} \dot{\varphi} \cdot pdf(\varphi = \varphi_{fail+}, \dot{\varphi}) d\dot{\varphi}, \quad (20)$$

where  $pdf(\varphi = \varphi_{fail+}, \dot{\varphi})$  is a joint PDF of the roll angle and the roll rate computed at the level of stability failure in the leeward direction.

The failure or exceedance through the windward side is expressed through the downcrossing of the level  $\varphi_{fail-}$ . The rate of downcrossing is expressed in a similar way to (11), but under the condition of a negative roll rate:

$$\lambda_{fail-} = \int_{-\infty}^0 \dot{\varphi} \cdot pdf(\varphi = \varphi_{fail-}, \dot{\varphi}) d\dot{\varphi}. \quad (21)$$

The failure in the dead ship condition is the exceedance of either  $\varphi_{fail+}$  or  $\varphi_{fail-}$ , which is an assumption that both exceedances are rare (i.e., that this does not happen within the time interval of the auto-correlation of ship motion being significant). This failure is expressed through a simple sum of (11) and (13);

$$\lambda_{DS}(H_S, T_Z) = \int_0^{\infty} \dot{\varphi} \cdot pdf(\varphi = \varphi_{fail+}, \dot{\varphi}) d\dot{\varphi}$$

$$+ \int_{-\infty}^0 \dot{\varphi} \cdot pdf(\varphi = \varphi_{fail-}, \dot{\varphi}) d\dot{\varphi}. \quad (22)$$

The short term solution (13) requires knowledge of the joint distribution of roll angles and rates that needs to include large roll angles.

The evaluation of the joint distribution of roll angles and rates including large roll angles is a non-trivial task. The distribution is non-Gaussian and its shape depends on the hull geometry (mostly on the freeboard that effects the shape of the GZ curve (e.g. subsection 8.6.2 of [9]). For a non-Gaussian distribution, the roll angles and roll rates may be dependent while uncorrelated because only stochastic processes with a normal joint distribution are independent when they are uncorrelated. However, there are some indications that the assumption of independence of the roll angles and roll rates is applicable for beam seas [8]. A method for modeling the non-Gaussian distribution of large roll angles through Fokker-Plank-Kolmogorov equation was proposed by Maki [49, 50]. The influence of the hull geometry on the PDF is preserved despite the existence of white noise excitation. The actual PDF is obtained by scaling with the results of a numerical simulation.

An approximate approach was proposed by Bulian and Francescutto [12–14] and it was used for the level 2 vulnerability criterion of the dead ship condition stability failure mode. The idea is to use a linear roll process and to adjust a level of failure to account for nonlinearity. The values of this equivalent level of failure are computed from the first integral equations, which express the energy balance over one quarter of a period of roll oscillation.

## 4 Excessive Accelerations

The second generation intact stability criteria extends the definition of an intact stability failure to the lateral acceleration that exceeds a prescribed limit [paragraph 1.1.2.2.3 of 32]. The lateral accelerations were a main factor in two fatal accidents with the container carriers *Chicago Express* in September of 2008 [6] and *Guayas* in September of 2009 [5]. Fatalities and injuries were sustained by crew members who fell and were thrown across the navigation bridge in the course of these accidents. Both accidents occurred in stormy conditions in which large roll angles were observed. Both cases were characterized by a very high GM value (7.7 m and 5.6 m, respectively). Synchronous roll resonance is believed to be the main reason for both accidents. The situation was exacerbated by a decrease of roll damping (caused by slow speed) and by the high location of the navigation bridge. Development of the vulnerability assessment is described in [70], while the validation of a direct stability assessment for this failure mode is addressed in [45].

The criteria consider the highest point on a ship where passengers or crew may be present. The evaluation of the acceleration at the point is based on the kinematics of a point of a rigid body involved in an arbitrary motion.

For mathematical models with reduced degrees of freedom, further simplifications are appropriate [see Appendix 3, 36]. Roll acceleration combined with the lateral component of the gravity acceleration is considered to be the main factor causing the failure. Separation of the contribution of the roll acceleration from the contribution of other motions leads to the following equation for the lateral acceleration:

$$a_{ALat} = (a_{z0} - g)\sin\varphi + z_A\ddot{\varphi} + a_{y0}\cos\varphi. \quad (23)$$

The contribution from other degrees of freedom is accounted as horizontal  $a_{y0}$  and vertical  $a_{z0}$  components of the acceleration caused by motions other than roll, expressed in an earth-fixed coordinate system; where  $z_A$  is the coordinate of the point of interest expressed in ship-fixed coordinate system. Note that a difference in (23) and formula (1) in Ref. [Appendix 3, 36] is caused by the difference in coordinate systems applied.

A further simplification of (23) involves a linear assumption for roll motion. For both known accidents involving excessive accelerations, the maxima of the GZ curve were located above  $50^\circ$ . Therefore, the observed roll angles ( $20^\circ$ – $30^\circ$ ) were in the nearly linear range. The assumption of linearity could be justified by the fact that the excessive accelerations are expected in case of high metacentric heights, when the GZ curve is dominated by the “initial stability” in the expected range of roll angles.

The assumption of linearity of the GZ curve allows the use of frequency-domain models for irregular roll motions. The response amplitude operator (RAO) for lateral acceleration is expressed through the magnitude of the lateral acceleration, which is derived from (23). Further simplifications include expressing the influence of other degrees of freedom through a location coefficient  $k_L$ , which takes into account the simultaneous action of roll, yaw and pitch motions:

$$a_{ALat}(\omega) = \varphi_a(\omega)k_L(g + \omega^2 z_A). \quad (24)$$

where  $\omega$  is a wave frequency; a formula for  $k_L$  is given in paragraph 2.3.2.1 of [32]. Formula (24) is used for the vulnerability assessment on both level 1 and level 2; further simplifications for level 1 are aimed at the elements of roll motions.

Level 1 vulnerability criterion is a deterministic criterion and uses a characteristic roll angle that depends on wave steepness. The wave steepness is interpreted as a random variable and is used for the safety level evaluation, see Eq. (19). Table 2.3.2.1 in [32] provides values of wave steepness as a function of the natural roll period. These values of wave steepness can be considered as critical for use in Eq. (19).

The well-justified linear assumption for roll motions leads to a normal distribution of lateral accelerations for the considered failure mode scenario (i.e., when the GM value is large). The rate of the upcrossing,  $\lambda_{Lat}$ , of the acceptable level of lateral acceleration,  $R_2 = 9.81 \text{ m/s}^2$ , is expressed as

$$\lambda_{Lat} = \frac{1}{2\pi} \frac{\sigma_{\dot{a}_{ALat}}}{\sigma_{a_{ALat}}} \exp\left(-\frac{R_2^2}{2\sigma_{a_{ALat}}^2}\right), \quad (25)$$

where  $\sigma_{a_{ALat}}$  is the standard deviation of lateral accelerations, while  $\sigma_{\dot{a}_{ALat}}$  is the standard deviation of a temporal derivative of the lateral acceleration.

There are certain difficulties in the frequency-domain evaluation of the standard deviation of a temporal derivative of the lateral acceleration. This is related to the accepted formulation of the spectral density of wave elevations that may have a convergence problem when used with high-order frequency derivatives. To avoid this problem, the level 2 vulnerability criterion kept only the exponential part of Eq. (25) and the standard  $R_{EA2} = 0.00039$  was calibrated for this truncated formula. This calibration requires additional consideration for evaluation of the safety level for the excessive acceleration vulnerability criteria level, which remains as future work.

## 5 Pure Loss of Stability

At a given draft, the ship waterplane may be narrow at the bow and stern, while near the midship section it is relatively full. At the same time, the waterplane is full at the full depth level. These basic geometry features may lead to decreased stability while a crest of a longitudinal wave is located near the midship section. Sometimes, this loss of stability may be so significant (even completely negative) that a ship capsizes or heels over to a large angle. This type of stability failure is referred as “pure loss of stability on a wave crest” or just “pure loss of stability”. A universally accepted theory describing a failure caused by pure loss of stability is not available at this writing.

The fact that stability decreases when a ship is located in the wave crest has been known to naval architecture for well over a century [64]. It was observed on a segmented model in 1949 [46]. However, practical calculation methods were not available until the 1960s [57]. A decade later, it was recognized as a separate mode of stability failure [60] while observing capsizing due to this phenomenon in free-running model experiments in San Francisco Bay. Kan et al. [20] de Kat and Thomas [39] and others also demonstrated capsizing due to pure loss of stability by free-running model experiments in seakeeping and maneuvering basins.

There are a number of single large roll accidents in which pure loss of stability may have been a trigger: the rail ferry *Aratere* in March 2006 [55], the ro-ro ship *M/V Finnbirch* in November 2006 [82], the fast ferry *M/V Ariake* in November 2009 [38], and the container ship *M/V Svendborg Maersk* in February 2014 [18].

The main feature of pure loss of stability is the significant change of the stiffness of the dynamical system. The stiffness may even become completely negative, which has the effect of turning a dynamical system into a “repeller” (see e.g., [4] or [81]).

Key elements of the GZ curve can be assessed as stochastic processes in irregular waves. The first attempt to describe the behavior of the instantaneous GM was made by [21] using a Gaussian distribution. Later, [11] applied it to describe pure loss of stability. However, it was found that the behavior of stability elements in irregular waves is too complex to be described by a normal distribution [10]. This complex

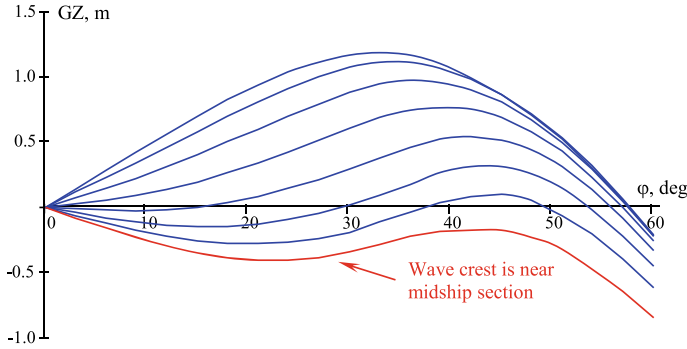


**Fig. 1** GZ curve variation in wave

probabilistic behavior of the stability elements in irregular waves makes the [23] effective wave the preferable practical solution. The accuracy of Grim’s effective wave was studied by [88, 86] and found sufficient for practical use. To account for surging [86] “modulated” Grim effective wave, it allows modeling the effect of increased timing of decreased stability.

The background of the vulnerability assessment for pure loss of stability is described in [44] and [90]. A low-freeboard extended weather deck has a significant influence on the physics of pure loss of stability failure because this feature can allow a large volume of green water on the ship that changes the dynamics of the ship and the stability variation may not be sole factor causing a stability failure. The results of experimental and numerical studies can be found in [91] and [29].

The essential feature of pure loss of stability is a negative stability experienced by a ship during a certain interval of time. Figure 1 shows an example of the variation of the GZ curve computed for a 260 m long containership with a draft of 8.4 m encountering a following wave of a length equal to the ship length. The height of the vertical center of gravity is assumed as the maximum to satisfy the 2008 IS Code [31], part A, which corresponds to a GM of 0.39 m.

The roll stiffness, shown by the GZ curve, changes from positive to negative and then from negative to positive during the passing of a longitudinal wave (i.e. a “wave pass”). The solution of the roll equation experiences drastic changes with these stiffness variations. To understand this better, consider an equation of roll motion that includes the variation of the restoring arm  $GZ(\varphi, t)$ , depicted in Fig. 1.

$$(I_{xx} + A_{44})\ddot{\varphi} + B_{44}\dot{\varphi} + \Delta g GZ(\varphi, t) = 0, \quad (26)$$

where  $A_{44}$  is the added mass in roll,  $B_{44}$  is the roll damping.

The drastic changes can be illustrated with the solutions of the linear equations for positive and negative stiffness. For the positive stiffness, the linear roll equation and its solution are well known:

$$(I_x + A_{44})\ddot{\varphi} + B_{44}\dot{\varphi} + \Delta g GM\varphi = 0, \quad (27)$$

$$\varphi = \varphi_A \sin(\omega_d t + \varepsilon), \quad (28)$$

where  $\varphi_A$  and  $\varepsilon$  are arbitrary constants, depending on initial conditions and  $\omega_d = \sqrt{\omega_0^2 - \delta^2}$  is the frequency of small damped roll oscillations,  $\omega_0$  is the natural roll frequency and  $\delta = B_{44}/2(I_x + A_{44})$  is the roll damping coefficient.

The solution of the linear roll equation with the negative stiffness is quite different because it is exponential rather than oscillatory where the eigenvalues  $\lambda_{1,2} = -\delta \pm \sqrt{\omega_1^2 + \delta^2}$  are real where  $\omega_1^2$  is a stiffness coefficient:  $\omega_1^2 = \Delta g |GM_1| / (I_x + A_{44})$  (frequency is no longer relevant as  $GM_1 < 0$ )

$$(I_x + A_{44})\ddot{\varphi} + B_{44}\dot{\varphi} - \Delta g |GM_1| \varphi = 0, \quad (29)$$

$$\varphi = C_1 \exp(\lambda_1 t) + C_2 \exp(\lambda_2 t), \quad (30)$$

where  $C_{1,2}$  are arbitrary constants which depend on the initial conditions. Dynamical system described by the (29) is known as “repeller”.

One of the eigenvalues of the solution (30) is negative, but the other one is positive. The solution (30) is unlimited. The time  $t_f$  necessary to reach a large roll angle  $\varphi_f$  is approximated by neglecting the exponential function with the negative eigenvalue:

$$t_f = \frac{1}{\lambda_1} \ln \left( \frac{\varphi_f}{C_1} \right). \quad (31)$$

The linear solution (30) is only appropriate for a qualitative description because the actual phenomenon includes large amplitudes of roll and time-dependent stiffness. An equivalent linear stiffness may be derived by balancing the potential energy that corresponds to the initial time-dependent stiffness with the potential energy of a linear system. This approach further may lead to an analytical formulation for dynamics of pure loss of stability in regular waves, see Spyrou [77]. However, the level 2 vulnerability assessment of SGISC in [32] does not include any mathematical model of dynamics and instead focuses on the stability variation in waves. Following the ideas presented in Spyrou [77], alternative vulnerability criteria were proposed that include dynamical considerations, see [62].

The level 1 vulnerability criteria for pure loss of stability is described in Sect. 2.4.2 of [32]. This is essentially a simplified calculation of GM with the ship assumed to be situated with the crest of a longitudinal wave at amidships. The critical value of the wave steepness is set to 0.0334 and can be used in Eq. (19) to evaluate the safety level.



## 6 Parametric Roll

Parametric roll resonance is an amplification of roll motion caused by periodic variation of stability in longitudinal waves.

The large-scale container loss that occurred on the container carrier M/V APL China in October 1998 was attributed to parametric roll beyond reasonable doubt [22]. Parametric roll can be also suspected as cause of accident of M/V Pacific Sun [54]. Beyond the IMO, the problem of parametric roll has been addressed by classification societies [1, 16] and the International Towing Tank Conference [37].

The theoretical possibility of parametric roll was studied in [58] and the observation of this phenomenon in a model test is described in [59].

The background for vulnerability assessment for parametric roll is described in Spyrou [75], Bulian and Francescutto [15, 14] and Sakai et al. [67]. The probabilistic treatment for the level 2 vulnerability criteria is based on the application of the Grim's effective wave [23] where the calculation of the encounter wave period for the Grim effective wave is considered in [66].

The Mathieu equation is the simplest mathematical model of parametric roll and it has been extensively used to analyze this phenomenon (e.g. [61]).

$$\frac{d^2x}{d\tau^2} + (p + q \cdot \cos(\tau)) \cdot x = 0, \quad (32)$$

where the variable  $x$  is related to roll motion through an exponential formula (to eliminate damping),  $\tau$  is non-dimensional time,  $p$  and  $q$  are numerical parameters related to calm water  $GM$  and the magnitude of the  $GM$  variation in waves, respectively.

The Mathieu equation is a linear differential equation with variable coefficients, but its solution cannot be expressed with elementary functions. The solution is considered to be a specialized function, known as the Mathieu function. It is tabulated and is included in advanced mathematical software packages. The Mathieu functions may exhibit two types of behavior: bounded and unbounded, each depending on values of the parameters  $p$  and  $q$ . A graphical representation of this dependence is known as Ince-Strutt diagram. Formulae for the approximation of the boundaries between the bounded and unbounded types of Mathieu functions can be found in [27].

Due to its linear nature, the Mathieu equation cannot yield an amplitude of steady-state parametric roll. To evaluate roll amplitude caused by parametric roll, the nonlinearity of a GZ curve must be included, see e.g. [61]. To avoid the complexity of a nonlinear differential equation, Spyrou [75] proposed to use a transient solution of the Mathieu equation to formulate a criterion and a standard for development of dangerous parametric roll:

$$\frac{\delta GM_1}{GM} \leq 2 \frac{\ln f + \ln 2}{\pi n} + \frac{4\delta}{\omega_0}, \quad (33)$$

where  $\delta GM_1$  is an amplitude of variation of the metacentric height,  $\delta$  is roll damping coefficient,  $\omega_0$  is natural roll frequency, and  $f$  is an amplification factor of parametric

resonance achieved during  $n$  roll oscillations. Two factors are included in the standard, which are shown on the right-hand side of Eq. (33): damping  $\delta$  and amplification  $f$ .

The level 1 vulnerability criterion for parametric roll and its appropriate standard is described in section 2.5.2 of [32]. With the exception of ships with sharp bilges, the standard  $R_{PR}$  in paragraph 2.5.2.1 of [32] consists of two components:

$$R_{PR} = 0.17 + C_{bk}, \quad (34)$$

where the value  $C_{bk}$  accounts for the contribution of the bilge keels and is computed as a function of the area of the bilge keels, length, beam and midship section coefficient.

The value 0.17 may be attributed to the transient and roll damping of the bare hull and appendages other than bilge keels. To estimate a safety level for the parametric roll criterion, a conservative assumption can be taken that the entire value of 0.17 is attributed to the transient. For the initiation of parametric roll, the amplification factor has to be more than 1.0, but this is another conservative assumption. According to Eq. (33), the value 0.17 will be achieved during approximately 2.6 roll oscillations, which is equal to approximately 5 wave encounters.

Further consideration requires a probabilistic characterization of encountering several waves of certain parameters. The wave group approach seems to be the most natural one. First, the application of the wave group approach to ship dynamics was proposed by Spyrou and Themelis [80]. This was followed by an application of this approach to a long-term probabilistic assessment of stability during the voyage [84] as well as the application to broaching [89] and parametric roll [52]. For the current state-of-the-art on wave groups, see [2, 26] as well as [71].

Since the wave group is defined as  $N_W$  waves that exceed a certain threshold  $a_G$ , the event of the encounter of a wave group can be considered as the upcrossing of the threshold followed by  $N_W - 1$  waves with peaks exceeding the threshold. If the threshold is set high enough, the event of the encounter can be considered to follow Poisson flow with the rate:

$$\xi_G(N_W) = \xi_G(a_G) P\left(\bigcup_{i=2}^{N_W} (a_i > a_G)\right), \quad (35)$$

where the  $\xi(a_G)$  is a rate of upcrossing of the threshold  $a_G$  by the water surface. Assuming a normal distribution for wave elevations, the rate is expressed as

$$\xi_G(a_G) = \frac{1}{2\pi} \sqrt{\frac{V_D}{V_W}} \exp\left(-\frac{a_G^2}{2V_W}\right), \quad (36)$$

where  $V_W$  is the variance of the wave elevation and  $V_D$  is the variance of the derivative of wave elevations. Further modeling of the wave group follows [84].

The properties of wave amplitudes are described using envelope theory. The assumption that only amplitudes of two consecutive waves are dependent is made

because the autocorrelation function of the wave envelope usually goes to zero within two mean periods. With this, the set of amplitudes of consecutive waves can be represented by a Markov chain and the rate of encounter of a wave group with  $N_W$  waves can be written as

$$\xi_G(N_W) = \xi_G(a_G)(P(a_2 > a_G|a_1)a_G)^{N_W-1}. \quad (37)$$

The conditional probability that the second wave exceeds the threshold  $a_G$  as the first wave exceeds it as well is calculated from the joint distribution of two consecutive amplitudes available from envelope theory:

$$f(a_1, a_2) = \frac{a_1 a_2}{V_W^2 p^2} \exp\left(-\frac{a_1^2 + a_2^2}{2V_W p^2}\right) \mathbf{I}_0\left(\frac{a_1 a_2 \sqrt{1-p^2}}{2V_W p^2}\right), \quad (38)$$

where  $\mathbf{I}_0$  is the modified Bessel function of the first kind and zero order (the standard function is included in most mathematical handbooks and software packages) and  $p$  is the parameter derived from the spectrum:

$$p = \sqrt{1 - k^2 - r^2}, \quad (39)$$

where  $k()$  and  $r()$  are the autocorrelation function and the result of the sine transformation of the wave spectrum density  $s_w(\omega)$ , which is computed for the time lag  $\tau$  that is equal to a period corresponding to the mean frequency  $\tau = T_{01}$ :

$$k(\tau) = \int_0^\infty s_w(\omega) \cos(\omega\tau) d\omega; \quad r(\tau) = \int_0^\infty s_w(\omega) \sin(\omega\tau) d\omega. \quad (40)$$

The formulation of the level 1 vulnerability criterion in paragraph 2.5.2.2 uses the wave steepness value  $s_{PR} = 0.0167$ . For the wave length equal to ship length,  $a_G = 0.5s_{PR}L$ . If the wave length that causes significant stability variation is between  $\lambda_{w1}$  and  $\lambda_{w2}$  (say, between 1 and 2 ship length), then a rate encounter of a wave capable of causing parametric roll can be approximated as:

$$\xi_G(N_W) = (P(a_2 > a_G|a_1)a_G)^{N_W-1} \int_{\lambda_{w1}}^{\lambda_{w2}} \xi_G(0.5s_{PR}\lambda_w) \text{pdf}(\lambda_w) d\lambda_w, \quad (41)$$

where  $\text{pdf}(\lambda_w)$  is the marginal pdf for wave lengths.

Equation (41) describes the short-term rate of encounter of wave groups capable of causing parametric roll according to the level 1 vulnerability criteria. This equation preserves the dependence on time. If the safety level is needed in a time-independent form (like Eq. 11), then the rate of encounter (11) may be substituted by a probability of exceedance of the wave amplitude using the Rayleigh distribution:

$$p_G(N_W) = (P(a_2 > a_G | a_1) a_G)^{N_W - 1} \int_{\lambda_{w1}}^{\lambda_{w2}} p_G(0.5 s_{PR} \lambda_w) \text{pdf}(\lambda_w) d\lambda_w;$$

$$p_G(a_G) = \frac{a_G}{2\pi V_W} \exp\left(-\frac{a_G^2}{2V_W}\right). \quad (42)$$

The long-term safety level is computed by averaging Eq. (41) or (42) over all the sea states represented in the wave scatter table.

The level 2 vulnerability criteria is described in Sect. 2.5.3 of [32]. Both C1 and C2 are probabilistic criteria; the safety level is equal to the corresponding standard identified in paragraph 2.5.3.1 of [32].

## 7 Surf-Riding and Broaching

Broaching (a shortening of “broaching-to”) is a violent uncontrollable turn (or large yaw rate) that occurs despite maximum steering efforts to maintain course that are often accompanied with a dangerously large heel angle that leads to a partial or total stability failure. Surf-riding is a transition from a periodic surging motion to a situation where the ship takes on the speed of the wave. Surf-riding is the most common pre-requisite for broaching, but it is not the only one [74].

Broaching-to is believed to be a primary reason behind the capsizing of the Papua New Guinean passenger ship *M/V Rabaul Queen* on the route from Kimbe to Lae on February 2nd, 2012, which caused the death of at least 142 and possible as many as 161 persons [3].

As a phenomenon, broaching was known as a major threat from the age of sail [79]. The scientific description of broaching and surf-riding date to the middle of the twentieth century [19, 17, 92, 93]. The early phase plane analysis [53] pointed towards the true nature of the phenomena. The development of nonlinear dynamics [25], together with the analysis of surf-riding experiments [40] prompted the modern understanding of the physics of surf-riding and broaching [73, 74, 78, 85].

A recommendation on the avoidance of surf-riding is included in [33], which is the same criterion that was used for the level 1 vulnerability assessment based on [87]. The level 2 vulnerability assessment is based on the Melnikov analysis [56]. The initial application of linearized resistance is described in Kan [41], while versions that include nonlinear resistance is available in [51, 76] and [68]. These versions, however, used an assumption of small damping in the surge equation. Wu et al. [93] theoretically demonstrated the validity of the small damping assumption.

The physics of surf-riding and the justification of the criteria are described in another chapter of this book [63]. The level-1 vulnerability criterion is described in Sect. 2.6.1 of [32]. The criterion was developed by assuming the wave steepness to be 0.1, which means that the safety level can be computed using Eq. (19). The level 2 vulnerability criterion is described in 2.6.2 of [32]. Because this is a probabilistic criterion, its safety level is equal to its standard, which is defined in paragraph 2.6.3.2 of [32].

## 8 Final Remarks

This chapter has summarized the scientific background of the IMO second generation intact stability criteria (SGISC). In particular, the implementation of the concept of “safety level” in the SGISC, that is the probability of failure if a criterion is satisfied, has been analyzed.

There are two types of the criteria in SGISC: probabilistic and deterministic. An assessment of the safety level of a probabilistic criterion is straightforward since it equals the associated standard. Evaluation of the safety level for a deterministic criterion is more challenged because the random elements need to be identified in the criterion’s formulation. While the criterion may be treated as a deterministic function of random variables, the details, however, may not be so straight forward.

The SGISC covers five intact stability failure modes: dead ship condition, excessive accelerations, pure loss of stability parametric roll, surf-riding and broaching. For the level 2 vulnerability criteria, the derivation of the safety level is simple, since for all failure modes these criteria are probabilistic. However, as all the level 1 criteria are deterministic, the safety level for these criteria requires probabilistic interpretation as follows:

- For the dead ship condition failure mode, there is no robust probabilistic interpretation;
- For excessive accelerations, pure loss of stability and surf-riding failure modes, the probabilistic consideration is that of wave steepness; and
- For the parametric roll failure mode, a combination of a simplified wave group method and a probabilistic consideration of wave steepness is needed.

Considerations of the safety level of these criteria are still quite abstract, but a detailed numerical analysis remains for the future work.

**Acknowledgements** The work described in this chapter has been partially funded by the Office of Design and Engineering Standards of the US Coast Guard (CG-ENG) under the guidance of Mr. J. Sirkar and the Office of Naval Research, under the supervision of Dr. L. P. Purtell, Dr. K-H. Kim, Dr. T. Fu and Dr. W-M. Lin. Earlier contributions related to this work have been supported by Mr. J. Webster (NAVSEA).

This chapter relied in parts of the IMO information paper [35] developed by the 29th ITTC Stability in Wave Committee, chaired by V. Belenky having as other members Dr. J.-F. Leguen (secretary), Prof. E. Boulougouris, Dr. S-K. Cho, Dr. P. Fan, Prof. J. Lu, Mr. A. Matsuda, and Dr. A. Oliva-Remola. The help of Dr. A. Reed (David Taylor Model Basin / NSWCCD) with the clarity of the text is greatly appreciated. Discussions on wave groups with Dr. C. Bassler (then David Taylor Model Basin / NSWCCD) was helpful.

## References

1. ABS (2019) Guide for the assessment of parametric roll resonance in the design of container carriers. American Bureau of Shipping, Houston, TX
2. Anastopoulos PA, Spyrou KJ (2019) Evaluation of the critical wave group method in calculating the probability of ship capsizing in beam seas. *Ocean Eng* 187:106213
3. Andrew W (2012) Report of the commission of inquiry into the sinking of *Rabaul Queen*. 28 June 2012 [https://www.academia.edu/29381006/Commission\\_of\\_Inquiry\\_into\\_the\\_sinking\\_of\\_Rabaul\\_Queen\\_COMMISSION\\_OF\\_INQUIRY\\_INTO\\_THE\\_SINKING\\_OF\\_RABAU\\_L\\_QUEEN](https://www.academia.edu/29381006/Commission_of_Inquiry_into_the_sinking_of_Rabaul_Queen_COMMISSION_OF_INQUIRY_INTO_THE_SINKING_OF_RABAU_L_QUEEN)
4. Andronov AA, Vitt AA, Khaikin SE (1966) Theory of oscillators. Pergamon Press, New York
5. BSU (2011) Fatal accident on board the CMV CCNI GUAYAS during Typhoon “KOPPU” on 15 September 2009 in the sea area off Hong Kong, Investigation Report 391/09 1 June 2011.
6. BSU (2009) Fatal accident on board the CMV CHICAGO EXPRESS during typhoon “HAGUPIT” on 24 September 2008 off the coast of Hong Kong, Investigation Report 510/08, 1 Nov 2009
7. Belenky V, de Kat JO, Umeda N (2008) Towards performance-based criteria for intact stability. *Mar Technol* 45(2):101–123
8. Belenky V, Weems KM (2019) Dependence of roll and roll rate in nonlinear ship motions in following and stern quartering seas. In: Belenky V, Spyrou K, van Walree F, Neves MAS, Umeda N (eds) Contemporary ideas on ship stability. Risk of capsizing, Chap. 27. Springer, pp 455–473. ISBN 978–3–030–00514–6
9. Belenky VL, Sevastianov NB (2007) Stability and safety of ships: risk of capsizing, 2nd edn. SNAME, Jersey City. ISBN: 0–939773–61–9
10. Belenky V, Weems (2008) Probabilistic qualities of stability change in waves. In: Proceedings of 10th international ship stability workshop, Daejeon, Korea
11. Bulian G (2010) Checking vulnerability to pure loss of stability in long-crested following waves: a probabilistic approach. *Ocean Eng* 37:1007–1026
12. Bulian G, Francescutto A (2004) A simplified modular approach for the prediction of the roll motion due to the combined action of wind and waves. *J Engineering for the Maritime Environment* 218(M3):189–212. <https://doi.org/10.1243/1475090041737958>
13. Bulian G, Francescutto A (2011) Effect of roll modelling in beam waves under multi-frequency excitation. *Ocean Eng* 38:1448–1463. <https://doi.org/10.1016/j.oceaneng.2011.07.004>
14. Bulian G, Francescutto A (2011) Considerations on parametric roll and dead ship conditions for the development of second generation intact stability criteria. 12th international ship stability workshop. DC, USA, Washington, pp 7–18
15. Bulian G, Francescutto A (2010) A simplified regulatory-oriented method for relative assessment of susceptibility to parametric roll inception at the early design stage. In: Proceedings of 4th international maritime conference on design for safety and 3rd workshop on risk-based approaches in the marine industries—Part I, Trieste, Italy, pp 93–106
16. Bureau Veritas (2019) Parametric roll assessment. Rule Note NR 667 DT R00 E
17. Du Cane P, Goodrich GJ (1962) The following sea, broaching and surging. *Trans RINA* 104:109–140
18. Danish Maritime Accident Investigation Board (2014) Marine accident report Svendborg Maersk heavy weather damage on 14 February 2014
19. Davidson KSM (1948) A note on the steering of ships in following seas. In: Proceedings of 7th international congress applied mechanics, London
20. de Kat JO, Thomas III WL (1998) Extreme rolling, broaching and capsizing—model tests and simulations of a steered ship in waves. In: Proceedings of 22nd symposium on naval hydrodynamics, Washington, DC, USA
21. Dunwoody AB (1989) Roll of a ship in astern seas—metacentric height spectra. *J Ship Res* 33(3):221–228

22. France WM, Levadou M, Treakle TW, Paulling JR, Michel K, Moore C (2003) An investigation of head-sea parametric rolling and its influence on container lashing systems. *Marine Tech* 40(1):1–19
23. Grim O (1961) Beitrag zu dem Problem der Sicherheit des Schiffes im Seegang. *Schiff und Hafen*, Heft 6:490–491
24. Grim O (1951) Das Schiff von Achtern Auflaufender. *Ja der Schiffbautechnischen Ges* 4:264–287
25. Guckenheimer J, Holmes PJ (1983) *Nonlinear oscillations, dynamical systems and bifurcations of vector fields*. Springer, Berlin
26. Guth S, Sapsis T (2021) Stochastically-preluded wave-groups for efficient statistical characterization of systems subjected to random waves. *Proc. 1st international conf. of the Stability and Safety of Ship and Ocean Vehicles STABS 2021*, Glasgow, UK
27. Hayashi C (1985) *Nonlinear oscillation in physical systems*, Princeton, New Jersey. ISBN 0-691-08383-5
28. Hoppe H (2005) Goal-based standards—a new approach to the international regulation of ship construction. *WMU J. of Maritime Affairs* 4(2):169–180
29. Htun SS, Umeda N, Sakai M, Matsuda A, Terada D (2019) Water-on-deck effects on roll motions of an offshore supply vessel in regular stern quartering waves. *Ocean Engineering* 188
30. IACS Recommendation No. 34 (2001) Standard Wave Data. Nov 2001
31. IMO IS Code (2008) International code on intact stability. London, UK, v+160 p
32. IMO MCS.1/Circ.1627 (2020) Interim guidelines on the second generation intact stability criteria. London, 10 Dec 2020
33. IMO MSC.1/Circ.1228 (2007) Revised guidance for avoiding dangerous situations in adverse weather and sea conditions, London, 8 p
34. IMO MSC.1/Circ.1455 (2013) Guidelines for approval of alternatives and equivalents as provided in various IMO instruments, London, June 2013
35. IMO SDC 8/INF.2 (2021) Physical background and mathematical models for stability failures of the second generation intact stability criteria. Submitted by ITTC, London
36. IMO SLF 54/INF.12 (2011) Development of second generation intact stability criteria. Information collected by the intersessional correspondence group. Submitted by Japan London, Nov 2011
37. ITTC (2021) International towing tank conference recommended procedure 7.5-02-07-04.3. Predicting the occurrence and magnitude of parametric rolling
38. Japan Transport Safety Board (2011) *Ferry ARIAKE Hull Heeling Ship Accident Investigation Report*, MA2011–2.
39. Kan M, Saruta T, Taguchi H (1994) Comparative model tests on capsizing of ships in quartering seas. In: *Proceedings of 5th international conference on stability of ships and ocean vehicles*, Melbourne, vol 3, pp 1–20
40. Kan M (1990) A guideline to avoid the dangerous surf-riding. In: *Proceedings of 4th international conference on stability of ships and ocean vehicles*, Naples, Italy, pp 90–97
41. Kan M (1990a) Surging of large amplitude and surf-riding of ships in following seas. *Selected papers in naval architecture and ocean engineering*, vol 28. Society of Naval Architects of Japan, Tokyo
42. Kobylinski LK, Kastner S (2003) *Stability and safety of ships: regulation and operation*. Elsevier, Amsterdam, p 454
43. Kobylinski L (2007) Goal-based stability standards. In: *Proceedings of 9th international ship stability workshop*, Hamburg, Germany
44. Kubo H, Umeda N, Yamane K, Matsuda A (2012) Pure loss of stability in Astern Seas—is it really pure? *Proceedings of 6th Asia-Pacific workshop on marine hydrodynamics*, Johor, pp 307–312
45. Kuroda T, Hara S, Houtani H, Ota D (2019) Direct stability assessment for excessive acceleration failure mode and validation by model test. *Ocean Engineering* 187. <https://doi.org/10.1016/j.oceaneng.2019.106137>

46. Leguen J-F, Creismeas P, Dartois H, Billard J-Y (2019) “Analyse critique d’essais de stabilité sur maquettes réalisées au Bassin d’essais de s carènes dans les années 50” Apport ajout et intérêt moderne, ATMA 2019
47. Lewis EV (ed) (1989) Principles of naval architecture. Vol. 3: Motions in Waves and Controllability. SNAME, Jersey City, 429 p. ISBN 0-939773-02-3
48. Longuet-Higgins MS (1983) On the joint distribution of wave periods and amplitudes in a random wave field. Proc R Soc London A 389:241–258
49. Maki A (2017) Estimation method of the capsizing probability in irregular beam seas using non-Gaussian probability density function. J Mar Sci Technol 22(2):351–360. <https://doi.org/10.1007/s00773-016-0415-9>
50. Maki A, Umeda N, Matsuda A, Yoshizumi H (2019) Non-Gaussian PDF of ship roll motion in irregular beam sea and wind conditions-Comparison between theory and experiment. Ocean Eng 188:106278
51. Maki A, Umeda N, Renilson M, Ueta T (2010) Analytical formulae for predicting the surf-riding threshold for a ship in following seas. J Marine Science and Technology 15(3):218–229
52. Maki A, Umeda N, Shiotani S, Kobayashi E (2011) Parametric rolling prediction in irregular seas using combination, of deterministic ship dynamics and probabilistic wave theory. J Marine Science Technology 16:294–310
53. Makov YL (1969) Some results of theoretical analysis of surf-riding in following seas. Trans. Krylov Society, Maneuverability and Seakeeping of Ships. vol. 126, Sudostroenie publishing, Leningrad, pp 124–128 (in Russian)
54. Marine Accident Investigation Branch (2009), Report on the Investigation of Heavy Weather Encountered by the Cruise ship Pacific Sun 200 miles North-North East of North Cape, New Zealand on 30 July 2008, Resulting in Injuries to 77 Passengers and Crew, Report No 14/2009, Southampton, UK, June 2009
55. Maritime New Zealand (2007) Passenger freight ferry Aratere heavy weather incident resulting in cargo shift on 3 March 2006, Report 06–201 New Zealand Transport Accident Investigation Commission
56. Melnikov VK (1963) On the stability of a center for time-periodic perturbations. Trans Moscow Math Soc 12:3–52 (in Russian)
57. Paulling JR (1961) The transverse stability of a ship in a longitudinal seaway. J Ship Research 4(4):37–49
58. Paulling JR, Rosenberg RM (1959) On unstable ship motions resulting from nonlinear coupling. J Ship Research 3(1):36–46
59. Paulling JR, Kastner S, Schaffran S (1972) Experimental studies of capsizing of intact ships in heavy seas. US Coast Guard, Technical report, 58 p (Also IMO Doc. STAB/7, 1973)
60. Paulling JR, Oakley OH, Wood PD (1975) Ship capsizing in heavy seas: the correlation of theory and experiments. In: Proceedings of 1st international conference on stability of ships and ocean vehicles, Glasgow
61. Peters W, Belenky V, Bassler C, Spyrou K, Umeda N, Bulian G, Altmayer B (2011) The second generation of intact stability criteria an overview of development. SNAME Trans 119:225–264
62. Peters W, Belenky V (2023) On regulatory consistency of criteria for dead ship condition and pure loss of stability. In: Spyrou K, Belenky V, Katayama T, Bačkalov I, Francescutto A (eds) Contemporary ideas on ship stability—from dynamics to criteria, Chap. 5, Springer, ISBN 978-3-031-16328-9, pp. 73–92
63. Peters W, Belenky V, Spyrou K (2023) Regulatory use of nonlinear dynamics: an overview. In: Spyrou K, Belenky V, Katayama T, Bačkalov I, Francescutto A (eds) Contemporary ideas on ship stability—from dynamics to criteria, Chap. 7, Springer, ISBN 978-3-031-16328-9, pp. 113–127
64. Pollard J, Dudebout A (1892) Theorie du Navire, vol 3, Paris
65. Ross S (1997) A first course in probability, Prentice Hall, Upper Saddle Rive NJ, 514 p. ISBN 0-13746314-6
66. Sakai M, Umeda N, Maki A (2019) Encounter frequency effect on the simplified design criteria against parametric roll. Ocean Eng 182:21–27



67. Sakai M, Umeda N, Yano T, Maki A, Yamashita N, Matsuda A, Terada D (2018) Averaging methods for estimating parametric roll in longitudinal and oblique waves. *J Marine Science and Technology* 23(3):413–424
68. Sakai M, Maki A, Murakami T, Umeda N (2017) Analytical solution of critical speed for surf-riding in the light of melnikov analysis. In: *Proc. Conf. of the Japan Society of Naval Architects and Ocean Engineers* 24:311–314
69. Sevastianov NB (1968) Comparison and evaluation of different systems of stability standards. *Sudostroenie*, No 6, Leningrad, pp 3–5 (in Russian)
70. Shigunov V, Rathje H, El Moctar O, Altmayer B (2011) On the consideration of lateral accelerations in ship design rules. In: *Proceedings of 12th international ship stability workshop*, Washington DC, USA, pp 34–42
71. Silva K, Xu W, Maki K (2021) Efficient sampling strategies for a critical wave group implementation using computational fluid dynamics and neural networks. *Proceedings of 1st international conference of the stability and safety of ship and ocean vehicles STABS 2021*, Glasgow, UK
72. Smith TC (2019) Validation approach for statistical extrapolation. In: Belenky V, Neves M, Spyrou K, Umeda N, van Walree F (eds) *Contemporary ideas on ship stability. Risk of Capsizing*, Chap. 34. Springer, pp 573–589. ISBN 978-3-030-00514-6
73. Spyrou KJ (1996) Dynamic instability in quartering seas: the behavior of a ship during broaching. *J Ship Res* 40(1):46–59
74. Spyrou KJ (1997) Dynamic instability in quartering seas-part III: nonlinear effects on periodic motions. *J Ship Res* 41(3):210–223
75. Spyrou KJ (2005) Design criteria for parametric rolling. *Oceanic Engineering International* 9(1):11–27
76. Spyrou KJ (2006) Asymmetric surging of ships in following seas and its repercussions for safety. *Nonlinear Dyn* 43:149–172
77. Spyrou KJ (2009) Pure-loss of stability revisited: analytical design aid. Internal Report of National Technical University of Athens, Greece
78. Spyrou KJ (2017) Homoclinic phenomena in ship motions. *J Ship Research* 61(3):107–130
79. Spyrou KJ (2009a) Perceptions of broaching-to: discovering the past. In: *Proceedings of 10th international conference on stability of ships and ocean vehicles*, St. Petersburg, Russia, pp 357–368
80. Spyrou KJ, Themelis N (2005) Probabilistic assessment of intact stability. In: *Proceedings of 8th international ship stability workshop*, Istanbul, Turkey
81. Strogatz SH (1994) *Nonlinear dynamics and chaos with applications to physics, biology, chemistry, and engineering (studies in nonlinearity)*. Perseus Books, Cambridge
82. Swedish Accident Investigation (2008) Loss of M/S Finnbirch between Oland and Gotland 1 November 2006, Report RS 2008:03e, Case S-130/06
83. Thanou AA (2010) Probabilistic consideration of the weather criterion of ship stability. Final year diploma thesis (supervised by K. J. Spyrou). National Technical University of Athens, Greece
84. Themelis N, Spyrou KJ (2007) Probabilistic assessment of ship stability. *Trans SNAME* 115:181–206
85. Umeda N (1999) Nonlinear dynamics on ship capsize due to broaching in following and quartering seas. *J Marine Science and Technology* 4:16–26
86. Umeda N, Yamakoshi Y (1994) Probability of ship capsizing due to pure loss of stability in quartering seas. *Naval Architecture and Ocean Engineering* 30:73–85
87. Umeda N (1990) Probabilistic study on surf-riding of a ship in irregular following seas. In: *Proceedings of 4th international conference on stability of ships and ocean vehicles*, Naples, Italy. pp 336–343
88. Umeda N, Yamakoshi Y (1986) Experimental study on pure loss of stability in regular and irregular following seas. In: *Proceedings of 3rd international conference on stability of ships and ocean vehicles*, Gdansk, Poland, vol 1, pp 93–99
89. Umeda N, Shuto M, Maki A (2007) Theoretical prediction of broaching probability for a ship in irregular astern seas. In: *Proceedings of 9th international ship stability workshop*, Hamburg

90. Umeda N, Sakurada A, Yamane K, Kubo H (2013) A RoPax ship accident due to pure loss of stability on a wave crest and intact stability criteria. In: Proceedings of design for safety conference
91. Umeda N, Alway A, Sakai S, Matsuda A, Terada D (2016) Model experiment of an offshore supply vessel running in astern waves. In: Proceedings of 15th international ship stability workshop, Stockholm, Sweden, pp 11–16
92. Wahab R, Swaan WA (1964) Coursekeeping and broaching of ships in following seas. *J Ship Res* 7(4):1–15
93. Wu W, Spyrou KJ, McCue L (2010) Improved prediction of the threshold of surf-riding of a ship in steep following seas. *Ocean Eng* 37:1103–1110

# Second Generation Intact Stability Criteria—Robustness and Consistency Analysis



**Carsten Schrøter, Marie Lützen, Henrik Erichsen, Jørgen Juncher Jensen, Hans Otto Kristensen, Preben Hagelskjær Lauridsen, Onur Tunccan, and Jens Peter Baltersen**

**Abstract** The formulation of the Second Generation of Intact Stability Criteria was finalized by the International Maritime Organization (IMO) in 2020. The criteria have been developed for a future incorporation into the 2008 IS Code, however they require testing before using them as a mandatory criterion. Member states are by IMO invited to use the Interim Guidelines and report back the experience. The criteria are formulated for five failure modes, each of which is analyzed by two vulnerability levels and, if needed, a direct numerical simulation. The present paper summarizes results testing the vulnerability levels in these new stability criteria. The calculations are carried out for 17 ships using the full matrix of operational

---

C. Schrøter  
Knud E. Hansen A/S, Elsinore, Denmark  
e-mail: [cas@knudehansen.com](mailto:cas@knudehansen.com)

M. Lützen (✉)  
University of Southern Denmark, Odense, Denmark  
e-mail: [mlut@iti.sdu.dk](mailto:mlut@iti.sdu.dk)

H. Erichsen · O. Tunccan  
Lloyds Register Marine, Copenhagen, Denmark  
e-mail: [henrik.erichsen@lr.org](mailto:henrik.erichsen@lr.org)

O. Tunccan  
e-mail: [onur.tunccan@lr.org](mailto:onur.tunccan@lr.org)

J. J. Jensen  
Technical University of Denmark, Lyngby, Denmark  
e-mail: [jjj@mek.dtu.dk](mailto:jjj@mek.dtu.dk)

H. O. Kristensen  
HOK Marineconsult ApS, Copenhagen, Denmark  
e-mail: [hokmarine@mail.dk](mailto:hokmarine@mail.dk)

P. H. Lauridsen  
OSK-ShipTech A/S, Aarhus, Denmark  
e-mail: [pl@osk-shiptech.com](mailto:pl@osk-shiptech.com)

J. P. Baltersen  
DFDS A/S, Copenhagen, Denmark  
e-mail: [jebal@dfds.com](mailto:jebal@dfds.com)

draughts, trims and GM values. Each failure mode criterion is examined individually regarding construction of a GM limit curve for the full range of operational draughts. The consistency of the outcomes has been analyzed, and finally examined whether the new criteria tend to be more or less conservative compared to the present rules by evaluating approved loading conditions. The analyses were performed in 2016 and based on criteria developed in 2015 and 2016 and amended by the Sub-Committee on Ship Design and Construction of IMO. Work performed in IMO up to Spring 2020 relevant for the analysis is described.

**Keywords** IMO · Second generation intact stability criteria · Sample calculations · GM limit curves

## 1 Introduction

The Second Generation of Intact Stability Criteria, which differ very much from the formulations in the current IS Code 2008 [3], is based on first principles with the stability examined for the ship sailing in waves. The new intact stability criteria are formulated for five failure modes: pure loss of stability, parametric roll, dead ship condition, excessive acceleration and surf-riding/broaching. Each of these failure modes is divided into three levels—two vulnerability levels and a third level, which consists of numerical simulations of the ship's behavior in waves.

Several papers have already presented results for specific vessels. Tompuri et al. [8] discuss in details computational methods to be used in the Second Generation Intact Stability Criteria, focusing on level 1 and level 2 procedures for parametric roll, pure loss of stability and surf-riding/broaching. They also provide detailed calculations and sensitivity analyses for a specific RoPax Vessel and stress the need for software able to do the extensive calculations. The detailed discussions attached to Tompuri et al. [8] give a very valuable insight in the current status of development of the new criteria.

The present paper summarizes results performed for testing the Second Generation of Intact Stability Criteria. The paper deals with all five failure modes, with the first four modes evaluated for level 1 and 2 whereas the last criterion, surf-riding/broaching, is evaluated for the first level only. The calculations are carried out for 17 ships for the full matrix of operational draughts (light service condition to summer draught), trims (even keel and two extreme trims forward and aft) and GM values. The results are presented as GM limit curves from the two levels and compared with the approved GM limit curve from the stability book.

The criteria used in the present calculations are based on Second Generation Intact Stability Criteria as amended in February 2015 and January 2016 by the Sub-Committee on Ship Design and Construction of IMO. Furthermore, the explanatory notes from [5], Annex 3–7 are consulted.

- Pure loss of stability ([4] Annex 1 (2.10.2.1 + 2.10.2.3))
- Parametric roll ([4] Annex 2 (2.11.2.1 + 2.11.2.3))

- Surf-riding /Broaching ([4] Annex 3)
- Dead ship condition ([5] Annex 1)
- Excessive acceleration ([5] Annex 2)

Three types of analysis have been performed:

1. Each criterion has been examined individually for the possibility of obtaining usable results for construction of a GM limit curve for the full range of operational draughts.
2. The relationship between level 1 and level 2—the requirement that level 1 is more restrictive in GM limits than level 2 has been examined.
3. Will the new regulation be more or less conservative? The analysis has been performed for approved loading conditions.

### ***1.1 Subsequent Discussions in IMO***

Since the formulations investigated and presented in this paper an SDC working group and an intersessional correspondence group has developed and agreed on formulations for the stability criteria for the assessment of dynamic stability failure modes in waves as instructed.

At SDC 7 in 2020 the proposal from the working group was brought forward to SDC and accepted as MSC circular: Interim guidelines on the second generation intact stability criteria [7]. The document contains formulations not only for Guidelines on vulnerability criteria, as addressed in this paper, but also “Guidelines for direct stability failure assessment” and “Guidelines for operational measures” to complete the work with all levels as agreed. In fact, most of the work and studies done after 2017 has been focusing on the direct stability failure assessment and operational measures to be able to finalize the text to the scheduled deadline.

However, in the text of the draft MSC Circ. it is made clear that the robustness of the new criteria is not the same for the different stability failure modes and they require testing before using them as mandatory criteria. For that reason, Member States are invited to use the Interim guidelines as complementary measures when applying the requirements of the mandatory criteria and to give feedback to IMO. Based on the feedback the Organization will be able to subsequently refine the Second Generation Intact Stability Criteria.

A modification to the application logic is made as illustrated in Figs. 1 and 2.

While the previous application logic was sequential (following the arrows in the routing scheme) the modified approach allows the user to be guided by a sequential logic of the Interim guidelines, but it is also acceptable that the users apply any alternative design assessment or operational measure option. For example, a user may wish to immediately commence with the application of direct stability assessment procedures without passing through Levels 1 and 2 of the vulnerability criteria or develop operational measures without performing design assessment. In this case the

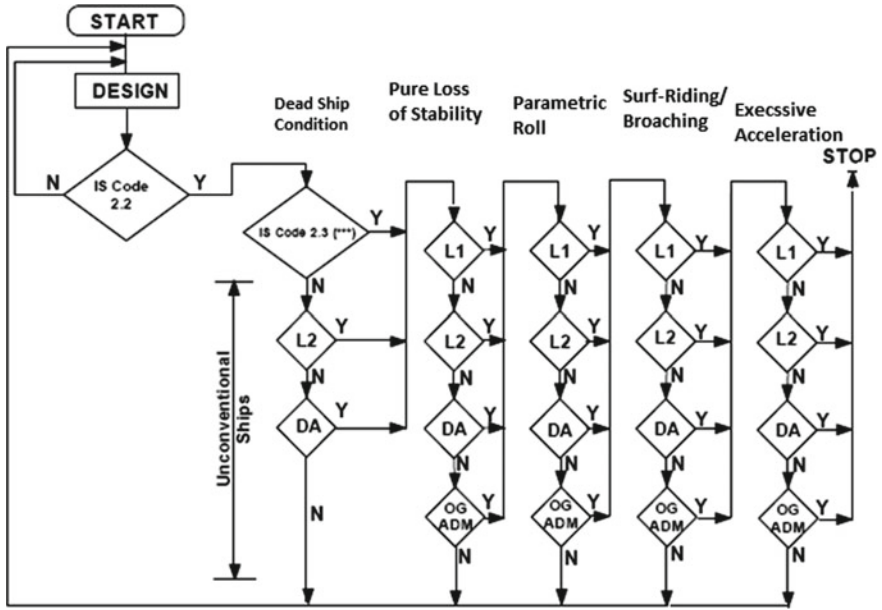


Fig. 1 Previous application logic (SDC 2 and SDC 3)

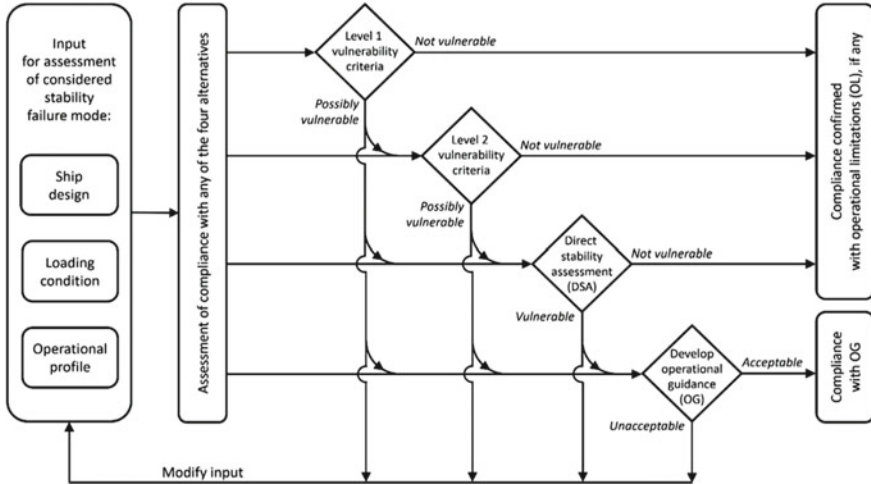


Fig. 2 Modified application logic (SDC 7—draft MSC Circ.)

documentation result of Levels 1 and 2 of the vulnerability criteria is irrelevant and need not to be presented.

This draft MSC Circular was submitted to MSC but the agenda item has not yet been addressed at present time due postponement of the meeting because of the Covid-19 situation.

Examples of assessments and interpretation of the Guidelines on vulnerability criteria will be addressed in the Explanatory notes that is at present time (August 2021) under development with the aim of finalizing at SDC8 in 2022. It is the intention to do a separate draft MSC Circ. to be submitted to MSC for acceptance.

## 2 Sample Ships

The sample ships used for the calculation comprise 17 existing vessels. They include eight RoRo ships (six passenger and two cargo vessels); two installation vessels (jack-up vessels); three supply vessels—one standby vessel, one cable layer and one anchor handler; one bulk carrier and three container vessels. The sample ship particulars can be seen in Table 1.

**Table 1** Principal particulars of the sample ships

Id	Type	L [m]	Fn	Built
1	RoRo passenger	159.3	0.303	2016
2	RoRo passenger	135.0	0.262	1997
3	RoRo passenger	183.6	0.298	2009
4	RoRo passenger	92.3	0.246	2010
5	RoRo passenger	88.8	0.298	2013
6	RoRo passenger	39.6	0.287	2011
7	Ro-Ro cargo	180.5	0.261	2009
8	Ro-Ro cargo	185.9	0.241	2014
9	Installation vessel	155.6	0.170	2009
10	Installation vessel	79.3	0.169	2011
11	Supply standby	39.2	0.315	2011
12	Supply cable layer	120.4	0.175	2016
13	Supply anchor handler	81.6	0.310	2000
14	Bulk carrier	174.6	0.173	2012
15	Container ship	382.6	0.208	2006
16	Container ship	324.6	0.222	1997
17	Feeder vessel	154.1	0.250	1991

### 3 Analysis

The analysis is performed for the full matrix of operational draughts from light ship to summer draught and for three trims—even keel and two extreme trims forward and aft. The calculations are carried out for the five modes of stability failure:

- Pure loss of stability
- Parametric roll
- Dead ship
- Excessive acceleration
- Surf-riding/Broaching

All calculations have been carried out using NAPA stability software XNAPA Release B137 2016.0 sgis. This is the same software as used in Tompuri et al. [8]. A more detailed description of the analysis can be seen in an information paper submitted to SDC 4 [6].

All modes are evaluated for criteria levels 1 and 2, except the last failure mode, where only level 1 is carried out. This last criterion, surf-riding/broaching is a function of length and speed of the vessel and does not depend on GM of the vessel. The criterion pure loss of stability applies only to ships for which the Froude number exceeds 0.24.

In the mode ‘Pure loss of stability’ in criteria level 2, ships with low weather deck/low buoyant hull can give some unexpected results. The problem is possibly caused by a loss of stability on the wave crest combined with water accumulated on the weather deck, see Fig. 3. How to deal with this is not yet defined in the explanatory notes.

However, as the whole idea with the criteria is to understand the ships behavior to certain stability failure modes in waves, the hull form is some cases slightly modified, resulting in a more ‘appropriate’ hull form including all parts that provides buoyancy, even though they are not fully watertight due to freeing ports, mooring holes etc.

#### 3.1 Construction of Limiting GM Curves

Each criterion is examined for the possibility of obtaining usable results for construction of a GM limit curve for the full range of operational draughts. A summary of the results is shown in Table 2.



**Fig. 3** Illustration of “water on deck” problem





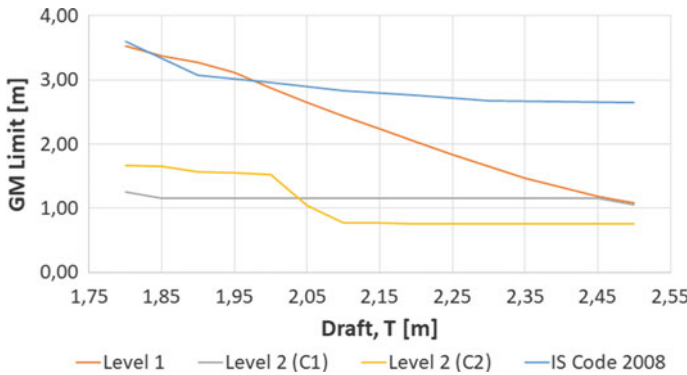


Fig. 4 GM limit (T), Ship no. 6. Parametric roll—Trim Aft

GM [m]	T [m] ->														
	1,80	1,85	1,90	1,95	2,00	2,05	2,10	2,15	2,20	2,25	2,30	2,35	2,40	2,45	2,50
0,50	0,999723	0,999829	0,999723	0,999723	0,999784	0,99967	0,99967	0,999776	0,981413	0,944753	0,908074	0,907975	0,886717	0,889628	0,944701
0,60	0,401473	0,364694	0,361204	0,328152	0,300658	0,283079	0,273732	0,275306	0,225042	0,213733	0,195643	0,194949	0,195595	0,196629	0,204251
0,70	0,215928	0,165096	0,175596	0,175266	0,175206	0,140461	0,151135	0,150762	0,138891	0,149063	0,136287	0,145698	0,136399	0,147018	0,136335
0,80	0,067038	0,067038	0,067038	0,030251	0,030251	0,030177	0,030171	0,007609	0,005674	0,005674	0,005674	0,005686	0,001864	0,002227	0,002245
0,90	0,000534	0,012973	8,94E-05	2,39E-05	2,39E-05	0	0	0	0	0,000006	0	0,000006	2,99E-05	0,000006	0,000101
1,00	0,197816	0,194187	0,095044	0,098178	0,093651	0,081699	0,03876	0,013907	0,004161	0,000837	0,000137	2,39E-05	0,000006	0,000006	0,000006
1,10	0,146763	0,096828	0,052496	0,050534	0,050101	0,020118	0,007909	0,003346	0,001991	0,005639	0,005106	0,004137	0,00146	0	0
1,20	0,043295	0,024114	0,012728	0,021842	0,019676	0,019084	0,015468	0,014867	0,030147	0,022974	0,013974	0,012894	0,004137	0,002922	0,000528
1,30	0,019541	0,044308	0,044299	0,035102	0,023469	0,030476	0,043653	0,043646	0,030411	0,014422	0,005021	0,001367	0,001358	0,000249	8,21E-05
1,40	0,068124	0,076644	0,07618	0,05439	0,054279	0,054277	0,051917	0,030382	0,013203	0,004226	0,001367	0,000303	9,34E-05	2,43E-05	2,61E-05
1,50	0,056533	0,079934	0,078108	0,07688	0,06791	0,037428	0,015637	0,005355	0,001438	0,000459	8,91E-05	0,000006	0,000006	0	0
1,60	0,084153	0,080295	0,048096	0,046692	0,031957	0,015002	0,005364	0,001527	5,51E-05	2,39E-05	0	0	0	0	0
1,70	0,048589	0,037025	0,015895	0,015086	0,005983	0,00222	0,000532	8,91E-05	0,000006	0	0	0	0	0	0
1,80	0,015895	0,005993	0,004396	0,002213	0,000797	0,000162	2,39E-05	0	0	0	0	0	0	0	0
1,90	0,001924	0,000791	0,000241	8,91E-05	2,39E-05	0	0	0	0	0	0	0	0	0	0
2,00	0,000156	0,000006	0	0	0	0	0	0	0	0	0	0	0	0	0

Fig. 5 Matrix (T, GM), Ship no. 6. Parametric roll, Level 2 (C2)—Trim Aft

It must also be noted that the Ikeda [1] parameter limits are exceeded for all vessels at certain draughts—especially in the criteria for dead ship condition and excessive acceleration. How this affects the results is not clear and it should be examined to which extent the roll damping results are reliable when extrapolating outside the parameter range for which Ikeda’s empirical equations are valid.

### 3.2 Inconsistency Between Level 1 and Level 2

When analyzing the results from level 1 and level 2, it is expected that level 1 is more restrictive in GM limits than level 2. As the failure mode surf-riding/broaching is not based on a GM evaluation, it is not included in this analysis. For vessels exposed to

resonance phenomenon and thereby different conditions of failures for same draught, the highest GM value is chosen.

The results from the analysis are shown in Table 3. The green color indicates that there is a proper relationship between the levels i.e. level 1 is more conservative than level 2 for all operational draughts. The red color indicates the opposite—if the whole or a part of the GM limit curve for level 2 is more restrictive than level 1, the cell is marked red. When it was not possible to obtain results for one of the levels, the consistency between the levels could not be evaluated; this is indicated with white or blue cells in the table.

**Table 3** Evaluation of the failure mode criteria—inconsistency between level 1 and level 2

Green	OK GM limit for L1 > GM for L2 (except for excessive acceleration, where it is opposite)
Red	Not OK - GM limit for L1 < GM for L2 (except for excessive acceleration, where it is opposite)
Blue (light)	No results - Computational problems for one or both levels
Grey	No results - no GM limit curve available due to inconsistency in results
White	No results - criterion does not apply to ship (Fn lower than 0.24)

	Pure loss of stability			Parametric roll C1			Parametric roll C2			Dead ship			Excessive acc.		
	Aft	Even	Fwd	Aft	Even	Fwd	Aft	Even	Fwd	Aft	Even	Fwd	Aft	Even	Fwd
1	Red	Red	Red	Green	Green	Green	Green	Green	Green	Green	Green	Green	Green	Green	Green
2	Red	Red	Red	Red	Green	Green	Green	Green	Green	Red	Green	Red	Green	Green	Green
3	Red	Red	Red	Green	Green	Green	Green	Green	Green	Grey	Grey	Grey	Green	Green	Green
4	White	White	White	Red	Red	Red	Green	Green	Green	Green	Green	Green	Green	Green	Green
5	Blue	Red	Red	Green	Green	Red	Blue	Red	Red	Red	Red	Red	Red	Red	Green
6	Red	Red	Red	Green	Green	Green	Green	Green	Green	Red	Red	Red	Green	Green	Green
7	Red	Red	Red	Green	Green	Green	Green	Green	Green	Blue	Blue	Blue	Green	Green	Green
8	Red	Red	Red	Red	Red	Red	Green	Green	Green	Green	Green	Green	Green	Green	Green
9	White	White	White	Green	Green	Green	Green	Green	Green	Green	Green	Green	Green	Green	Green
10	White	White	White	Blue	Blue	Blue	Red	Red	Red	Red	Red	Red	Green	Green	Green
11	Red	Red	Red	Blue	Blue	Blue	Red	Red	Red	Red	Red	Red	Red	Red	Red
12	White	White	White	Red	Red	Red	Red	Red	Red	Red	Red	Red	Green	Green	Green
13	Red	Red	Red	Red	Red	Red	Green	Green	Green	Red	Red	Red	Red	Red	Red
14	White	White	White	Green	Green	Green	Blue	Blue	Blue	Blue	Blue	Blue	Green	Green	Green
15	White	White	White	Green	Green	Green	Blue	Blue	Blue	Blue	Blue	Blue	Green	Green	Green
16	White	White	White	Green	Green	Green	Blue	Blue	Blue	Blue	Blue	Blue	Green	Green	Green
17	Red	Red	Red	Green	Green	Green	Green	Green	Green	Red	Red	Red	Green	Green	Green

Green: OK—GM limit for L1 > GM for L2 (except for excessive acceleration, where it is opposite)  
 Red: Not OK—GM limit for L1 < GM for L2 (except for excessive acceleration, where it is opposite)  
 Blue (light): No results—Computational problems for one or both levels  
 Grey: No results—no GM limit curve available due to inconsistency in results  
 White: No results—criterion does not apply to ship (Fn lower than 0.24)

Table 3 shows that in nearly half of the cases, level 2 results are more conservative than level 1; for the criterion pure loss of stability, it is the case for all vessels.

### 3.3 Loading Condition Analysis

The analysis is performed for approved operational loading conditions taken from the ship stability booklet. The results are summarized in Table 4.

**Table 4** Evaluation of loading conditions

Green	All loading conditions comply with the criteria
Red	One or more loading conditions do not comply with the new criteria. The number in the cell indicates the percentage of loading conditions not complying.
Blue	No useful results for GM limit (whole or part of curve).
White	Not calculated – criterion does not apply to ship (Fn lower than 0.24)

	Pure loss of stability		Parametric roll			Dead ship		Excessive acc.	
	L1	L2	L1	L2 C1	L2 C2	L1	L2	L1	L2
1		37							
2								100	
3			100	100				100	100
4							100	100	100
5							100	33	
6							100	100	100
7	77	77	100	92	77			23	23
8								13	
9							100	100	100
10						100			
11	100	100				33	100	100	100
12							25	55	18
13		55				9	72		27
14								74	52
15			50	12				25	
16			100	100					
17	50	67						82	33

Green: All loading conditions comply with the criteria

Red: One or more loading conditions do not comply with the new criteria. The number in the cell indicates the percentage of loading conditions not complying

Blue: No useful results for GM limit (whole or part of curve)

White: Not calculated—criterion does not apply to ship (Fn lower than 0.24)

## 4 Discussions

A series of 17 existing vessels have been evaluated against Second Generation Intact Stability Criteria as amended in February 2015 and January 2016 by the Sub-Committee on Ship Design and Construction of IMO.

Three analysis have been performed.

- Inconsistency analysis
- GM limit curves
- Approved loading condition check

### 4.1 *Inconsistency Analysis*

The relationship between level 1 and level 2—the requirement that level 1 is more restrictive in GM limits than level 2 has been examined. The analysis showed that none of the vessels shows a consistent result when applying level 2 versus level 1 analysis for all failure modes, see Table 3. For more than half of the cases the limiting GM required by level 2 would be higher (more restrictive) than for level 1 analysis, which is not the intention.

### 4.2 *GM Limit Curves and Approved Loading Condition Check*

Each criterion has been examined individually for the possibility of obtaining usable results for construction of a GM limit curve for the full range of operational draughts, see Table 2. With one or two exceptions for the vessels considered, it is not possible to derive the GM curve. This is the case for the parametric roll and dead ship failure modes, i.e. at a given draught multiple permissible GM values would be obtained for most of the vessels.

It must be noted that the new draft MSC Circ. does not include or consider a GM limit curve as it is required in the vessel's stability booklet following current regulation. The new criteria is based on calculation of the actual loading condition of the vessel.

When evaluated at realistic operational GM (or KG) conditions allowed according to the current intact and damage stability criteria—loading conditions from the vessel's stability booklet, none of the vessels satisfies all of the SGISC failure modes, see Table 4. The majority of vessels satisfy some of the failure modes under certain loading conditions. Some of the vessels satisfy the parametric roll criteria for all loading conditions considered. Very few vessels satisfy the excessive acceleration criterion in any loading condition.

### **4.3 *Evaluating Stability Criteria Based on Current Loading Condition***

According to SOLAS chapter II-1 [2], the master must be provided with reliable information on the ship's stability that is necessary to enable him to get exact guidance in a fast and simple manner about the ship's stability under various operating conditions.

As the new criteria is not suitable for implementation in an intact or combined intact and damage stability limit curve, it requires a loading computer that can handle the SGISC requirements as direct calculation of all intact stability criteria in each loading case during the entire voyage. This loading computer is not available at the market of today. But this is assumed to be possible, as it basically can be based on the same available philosophy as used today, apart from implementing the calculation routines behind SGISC. However, with the nature of some of the criteria to form "islands" of noncompliance rather than a well-defined border between safe and unsafe area (equals a limit curve), the user must be guided towards a more holistic review of the expected entire voyage in order to see if unsafe areas are passed on the way. In other words, a kind of 3D limit figure instead of a 2D limit curve must be introduced and made visible for the user. It is foreseen, that if this shall become operationally safe, precise guidelines on number of steps, intended change in tank-configuration etc. during the voyage etc. shall be pre-defined and verified against the SGISC criteria. In case changes are made from the pre-planned voyage/tank configuration etc., revised calculations must be carried out and verified for compliance.

Another concern linked to the direct calculations and the 3D limit figure is that over a longer voyage, the vessels draught, trim and GM will change, thus also cause the 3D "landscape" to change and the unsafe "islands" might very well change, leading to an even more complicated matrix of loading condition variations to be checked. Obviously, the longer voyage/larger consumption, the larger change in the foundation for evaluation of the stability.

Adding further to the complexity is the increasing usage of other operational support systems like weather routing and trim optimization—systems that are also providing guidance to the operation/ballasting of the vessel, not seldomly varying over the length of a voyage. That input also needs to be considered when assessing the voyage from a stability compliance perspective.

All in all, something that is manageable but understood to require quite some new thinking in terms of development of enhanced instructions to the user (navigator) related to voyage planning and guidelines to graphical user interface development for the supplier of the new type of loading computer.

## 5 Conclusions

A series of 17 existing vessels have been evaluated against the current version of Second Generation Intact Stability Criteria (SGISC). These criteria comprise five failure modes: Pure loss of stability, parametric roll, dead ship, excessive acceleration and surfripping/broaching. Results have been analyzed for different loading and trim conditions in terms of limiting GM curves.

Conclusions from the analyses are that using conventional GM limiting curves are not possible when applying SGISC. The vessel must be equipped with a loading computer having the SGISC routines implemented. These computers, which are not available at the market of today, must besides evaluating the actual condition of the ship also be able to consider all conditions encountered during an entire voyage.

**Acknowledgements** The work described in this paper has been financed by The Danish Maritime Fund.

The work was carried out by a consortium consisting of: Project group: IDA Maritime, The Society of Engineers, OSK-ShipTech A/S, Knud E. Hansen A/S, Odense Maritime Technology A/S, Maersk Maritime Technology, Lloyds Register Marine, Technical University of Denmark and University of Southern Denmark.

The work has been assisted by an advisory board consisting of: American Bureau of Shipping, ABS, Maersk Maritime Technology, MMT, Baltic and International Maritime Council, BIMCO, DFDS, and Danish Maritime Authority.

## References

1. Ikeda Y, Himeno Y, Tanaka N (1978) A prediction method for ship roll damping. Report of Department of Naval Architecture, University of Osaka Prefecture, Report no. 00405
2. IMO (1974) International convention for the safety of life at sea (SOLAS). [www.imo.org/en/About/Conventions/ListOfConventions/Pages/International-Convention-for-the-Safety-of-Life-at-Sea-\(SOLAS\)-1974.aspx](http://www.imo.org/en/About/Conventions/ListOfConventions/Pages/International-Convention-for-the-Safety-of-Life-at-Sea-(SOLAS)-1974.aspx). Accessed 15 July 2020
3. IMO (2008) The international code on intact stability (IS Code 2008)
4. IMO (2015) SDC 2/WP.4, development of second generation intact stability criteria. Report of the working group, London, UK
5. IMO (2016) SDC 3/WP.5, development of second generation intact stability criteria. Report of the working group, London, UK
6. IMO (2016) SDC 4/INF.9, sample ship calculation results, Submitted by Denmark, London, UK
7. IMO (2020) MSC.1/Circ.1627, Interim guidelines on the second generation intact stability criteria
8. Tompuri, M, Ruponen P, Forss M, Lindroth D (2015) Application of the second generation intact stability criteria in initial ship design. Transactions—Society of Naval Architects and Marine Engineers 122:20–45

# On Regulatory Consistency of Criteria for Dead Ship Condition and Pure Loss of Stability



William S. Peters and Vadim Belenky

**Abstract** The chapter examines different aspects of consistency between the levels 1 and 2 of the vulnerability assessment within the IMO second generation intact stability criteria (SGISC). Both the dead ship condition and the pure loss of stability failure modes are considered. The most important aspect of consistency for the dead ship condition is its possible influence on the integrity of the existing mandatory stability regulations since the consistency between the levels of vulnerability criteria is, in fact, representative of consistency between the 2008 IS Code and the SGISC. The chapter describes a possible solution for the between-the-levels consistency of the pure loss of stability failure mode. The main idea is to assess the safety level of the deterministic criterion for the level 1 vulnerability criteria. Then, the standard for the probabilistic level 2 vulnerability criteria must be set to a higher level than the assessed level 1 safety level (as the level 2 criterion is meant to be less conservative than the level 1 criterion). For this approach to work, both levels 1 and 2 should use the same mathematical models of the stability failure or, at least, the model for level 1 should be inherently more conservative compared to the level 2.

**Keywords** Dead-ship condition · Pure loss of stability · Second generation intact stability criteria (SGISC) · Vulnerability criteria · Weather criterion · 2008 IS Code

## 1 Introduction

The tiered structure of the second generation intact stability criteria (SGISC) that has been developed by the International Maritime Organization (IMO) allows effective management of the complexity of calculations. If the vulnerability of a ship to a particular mode of dynamic stability failure is not indicated on the lower level, there

---

W. S. Peters

US Coast Guard Office of Design and Engineering Standards, Washington, DC, USA

e-mail: [william.s.peters@uscg.mil](mailto:william.s.peters@uscg.mil)

V. Belenky (✉)

David Taylor Model Basin (NSWCCD), West Bethesda, MD, USA

e-mail: [vadim.belenky@navy.mil](mailto:vadim.belenky@navy.mil)



is no need for further assessment. On the other hand, the criteria for the same mode of failure must be consistent for the different levels: if the level 1 assessment shows no vulnerability, so also should be the result of the level 2 assessment.

Unfortunately, this is not always the case. Systematic sample calculations show these inconsistencies are fairly frequent, e.g. see [1]. This chapter considers between-level inconsistency for the dead ship condition and the pure loss of stability modes of stability failures.

## 2 Dead Ship Condition

The vulnerability criteria for the dead ship condition are described in Sect. 2.2 of the IMO Interim Guidelines on the Second Generation Intact Stability Criteria [2]. There are several aspects of consistency of the vulnerability criteria for the dead ship condition: application consistency, probabilistic consistency and physical consistency.

### 2.1 Application Consistency

The dead ship condition is the only mode of failure included in the second generation intact stability criteria that also is covered in Part A of the 2008 IS Code [3]. The severe wind and rolling criterion (weather criterion), described in the Sect. 2.3 of the 2008 IS Code [3], has loading condition limitations for use of the formula and a table for the calculation of the roll back angle in paragraph 2.3.5. These limitations are described in paragraph 2.3.5 and include the breadth to draft ratio, the  $KG$  to draft ratio and the natural roll period.

For loading conditions beyond these applicability limitations, MSC Circular 1200 [4] describes an alternative way to obtain the roll-back angle through the performance of model tests. However, the assessment of the weather criterion and how it is satisfied is unchanged.

The level 1 vulnerability criterion of the second generation intact stability criteria uses the extended natural roll period table from [4], which means that the limitations for two other parameters (beam over draft and  $KG$  over draft) remain to be addressed at the level 2 assessment. The level 2 assessment is a probabilistic long-term criterion based on an averaged upcrossing rate, it does not provide the roll back angle outside the applicability range of the weather criterion. Therefore, the level 2 assessment is essentially an alternative outside the current stability regulatory framework contained in the 2008 IS Code [3].

## 2.2 Probabilistic Consistency

The level 1 vulnerability criterion is the weather criterion with an extended table for the roll period. The consistency problem essentially focuses on the probabilistic interpretation of the weather criterion. The problem attracted attention of naval architects long ago (e.g. [5]) abridged version available in [6].

IMO document SDC 7/INF.3 [7] describes a probabilistic study that addresses the inconsistency between the levels of vulnerability criteria for the dead ship condition stability failure mode. The sample size is 74 data points (loading conditions), which is based on 32 ships. All the data points in the sample satisfied the following conditions:

- Weather criterion is fully applicable:  $B/d \leq 3.5$ ,  $0.3 \leq KG/d - 1 \leq 0.5$  and  $T \leq 20$  s.
- Area  $a$  exactly equals area  $b$  or the static angle equals to  $16^\circ$ .

The critical state of the weather criterion was achieved by adjusting  $KG$  and/or the windage area.

The distribution of ship length (which is related to the size of ship) in the sample is not necessarily the same as that of the world fleet. To make the present calculations representative of the world fleet, the criterion values are weighted to reproduce a distribution of ship lengths of the world fleet covered by IMO instruments. Figure 1 shows distributions (in a form of histograms) of lengths ( $LBP$ ) of the sample ships (transparent bars) and the world fleet covered by IMO instruments (solid bars). The latter distribution is based on data obtained from the USCG Marine Information for Safety and Law Enforcement (MISLE) system (some of this information is publicly available through the USCG Maritime Information Exchange: <https://cgmix.uscg.mil>). While the weighting on the basis of the ship length only may not give a fully representative picture, yet it provides some indication for distribution of dimensions of the world fleet.

Figure 2 shows a histogram of the level 2 criteria value, which is computed as described in Sect. 2.2 of Interim Guidelines. The “weighted data” refers to the data

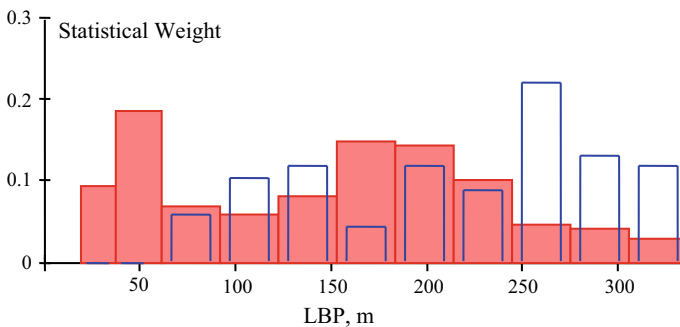


**Fig. 1** Distribution of ship lengths in the sample (transparent bars) and in the world fleet covered by IMO instruments (solid bars)

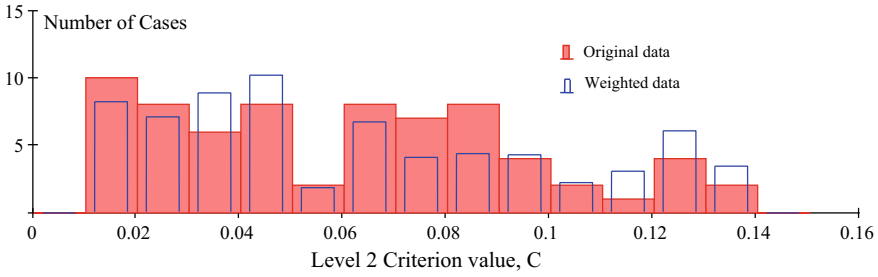


**Fig. 2** Distribution of the level 2 criterion value  $C$  based on original and weighted data. Four outliers are not shown at  $C = 0.21, 0.24, 0.33$  and  $0.55$

adjusted by the statistical weight to match the distribution of ship lengths in the world fleet shown in Fig. 1. The inconsistency between the levels manifests itself in the form of a distribution, while consistency would look like a deterministic value.

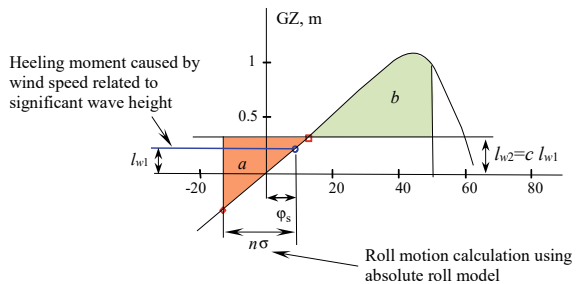
### 2.3 Physical Consistency

A possible source of inconsistency between the levels is the difference in the mathematical model describing stability failure in a dead ship condition. SDC 7/INF.3 [7] contains a formulation of an alternative level 2 criterion, which uses the same general scheme of application as the weather criterion, but in which the input parameters are given a probabilistic interpretation, see Fig. 3.

The alternative level 2 criterion for a sea state described by the  $i$ th cell of a scatter table (e.g. from [8]) with a significant wave height  $H_S$  and a mean-zero-crossing period  $T_z$ :

$$\begin{aligned}
 C_{S,i} &= 0 \text{ if } a \leq b \text{ and } \varphi_s \leq 16^\circ \text{ or } \varphi_s \leq 0.8\varphi_d \\
 C_{S,i} &= 1 \text{ otherwise}
 \end{aligned}
 \tag{1}$$

**Fig. 3** The formulation of the alternative level 2 vulnerability criterion



where  $a$  and  $b$  are defined as similar to that given in paragraph 2.3 of the 2008 IS Code [3], Part A, and illustrated in Fig. 3.  $\varphi_d$  is the angle of deck immersion. The other parameters in Fig. 3 are:

$$l_{w1} = (P \cdot A \cdot Z)/(m \cdot g) \quad (2)$$

where  $A$  is the longitudinal projected area of the portion of the ship and deck cargo above the waterline,  $Z$  is the vertical distance from the center of  $A$  to the center of underwater lateral area or approximately to a point at one half of the mean draft,  $m$  is the mass of the ship, and  $g$  is the acceleration due to gravity.  $P$  is the pressure, which is computed as:

$$P = (\rho_A U_{Wm}^2/2) \cdot C_m \quad (3)$$

where  $C_m$  is the wind heeling moment coefficient and is taken as 1.22 from paragraph 2.2.3.2.2 of the Interim Guidelines;  $\rho_A$  is the density of air at sea surface. The mean wind speed  $U_{Wm}$  is also taken from paragraph 2.2.3.2.2 of Interim Guidelines as well as the rest of the gusty wind model.

$$U_{Wm} = (H_S/0.06717)^{2/3} \quad (4)$$

The angle of roll,  $\varphi_1$ , is calculated as the product of a factor,  $n$ , and the standard deviation of absolute roll motion,  $\sigma_\varphi$ :

$$\sigma_\varphi = \left( \int_0^\infty (S_{\alpha e}(\omega) + S_{mw}(\omega)) H^2(\omega) d\omega \right)^{1/2} \quad (5)$$

where  $H(\omega)$  is the RAO of roll motion using absolute coordinates:

$$H^2(\omega) = \frac{\omega_{0S}^4}{(\omega_{0S}^2 + \omega^2)^2 + (2\delta_{\varphi e} \cdot \omega)^2} \quad (6)$$

where  $\omega_{0S}$  is a modified-roll natural frequency computed at the heel angle caused by the steady wind at the considered cell of the scatter table,  $\omega$  is the circular frequency, and  $\delta_{\varphi e}$  is the equivalent linear roll-damping, computed with any accepted or prescribed linearization method.  $S_{\alpha e}(\omega)$  is the spectral density of roll excitation, caused by irregular waves while  $S_{mw}(\omega)$  is the roll excitation caused by gusty wind and is expressed as

$$S_{mw}(\omega) = \rho_A C_m U_{Wm} A \cdot Z \cdot S_v(\omega) \quad (7)$$

where  $S_v(\omega)$  is the spectral density of wind velocities caused by random gusts:

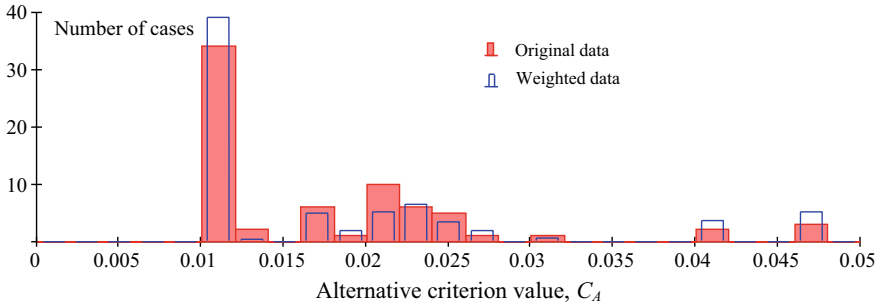


**Fig. 4** Distribution of the alternative criterion value based on original and weighted data. Three outliers are not shown at  $C_A = 0.077$ ,  $0.089$  and  $0.291$

$$S_v(\omega) = 0.012 \frac{U_{Wm}^2}{\omega} \cdot \frac{X_D^3(\omega)}{(1 + X_D^2(\omega))^{4/3}};$$

$$X_D(\omega) = \frac{600 \cdot \omega}{\pi \cdot U_{Wm}}. \quad (8)$$

The value of the alternative criterion is averaged over all  $N$  sea states included in a scatter table with a statistical weight  $W_i$ , as formulated in paragraph 2.2.3.2 of the Interim Guidelines:

$$C_A = \sum_{i=1}^N W_i C_{Si} \quad (9)$$

Applying the alternative criterion helped to decrease the amount of inconsistency, but did not resolve it completely. As applied to the data sample described in the previous subsection, it still produced a distribution, see Fig. 4.

The most prominent feature of the histogram in Fig. 4 is the bar around the criterion value  $C_A = 0.011$ , which equals to 34. There are 31 cases where the static angle was the limiting value in the criterion (i.e.,  $\varphi_S \leq \min(16^\circ, \varphi_d)$ ) rather than the ratio of area  $b$  to area  $a$ . These cases are not random and should be processed separately to determine the distribution fit.

## 2.4 Controlled Inconsistency

The inconsistency between the levels of the vulnerability criteria seems to be originated from an attempt to account for the stochasticity of waves and wind. The alternative criterion is essentially a probabilistic interpretation of certain elements of the level 1 criterion; but that was not sufficient to resolve the inconsistency.

If the inconsistency cannot be removed, consideration is given to control it by setting a standard with a probability of inconsistency to not exceed a given value. The histograms in Figs. 2 and 4 are approximated with a log-normal distribution to accommodate apparent asymmetry. These are then used to set the standard with a specified “probability of inconsistency” that may be treated in a similar way as safety level. The log-normal distribution is determined from:

$$PDF(x) = \left[ 1 / \left( x \cdot s \sqrt{2\pi} \right) \right] \exp \left[ - (\ln(x) - \mu)^2 / (2s^2) \right] \quad (10)$$

where symbols  $\mu$  and  $s$  stand for the location and scale parameters of the log-normal distribution, respectively. These parameters can be computed through the mean value and standard deviation, which are estimated over the sample population for the values of the current level 2 and alternative criteria.

$$\hat{\mu}_C = \ln \left( \hat{E}_C \sqrt{1 + \hat{\sigma}_{CA}^2 / \hat{E}_C^2} \right); \quad \hat{\mu}_{CA} = \ln \left( \hat{E}_{CA} \sqrt{1 + \hat{\sigma}_{CA}^2 / \hat{E}_{CA}^2} \right) \quad (11)$$

$$\hat{s}_C = \sqrt{\ln \left( 1 + \hat{\sigma}_C^2 / \hat{E}_C^2 \right)}; \quad \hat{s}_{CA} = \sqrt{\ln \left( 1 + \hat{\sigma}_{CA}^2 / \hat{E}_{CA}^2 \right)} \quad (12)$$

where  $\hat{\mu}_C$  and  $\hat{s}_C$  are the location and scale parameters, which are estimated for the criterion value  $C$ , while  $\hat{E}_C$  and  $\hat{\sigma}_C$  are the estimates of the mean value and the standard deviation of the criterion value  $C$ . The symbols  $\hat{\mu}_{CA}$  and  $\hat{s}_{CA}$  are the location and scale parameters, respectively, which are estimated for the alternative criterion value  $C_A$ , while  $\hat{E}_{CA}$  and  $\hat{\sigma}_{CA}$  are the estimates of the mean value and the standard deviation of the alternative criterion value  $C_A$ . Note that these estimates are weighted to account for the distribution of length of ships, covered by IMO instruments, see Fig. 1.

The distribution (10) is fitted with the level 2 or alternative criteria value, which is computed for the critical state of the level 1 criteria. Given the probability of inconsistency  $P_C$ , a possible standard for the criterion  $C$  is computed for a quantile of the distribution (10), corresponding to the probability  $P_C$ :

$$St = \exp \left[ Q_N \left( P_C; \hat{E}_C, \hat{\sigma}_C \right) \right] \quad (13)$$

where  $Q_N$  is a normal quantile corresponding to probability  $P_C$  with the mean value  $\hat{E}_C$  and standard deviation  $\hat{\sigma}_C$ . A possible standard for the alternative criterion  $C_A$  is computed taking into account that some cases yield a deterministic value:

$$St_A = W_R \exp \left[ Q_N \left( P_C; \hat{E}_{CA}, \hat{\sigma}_{CA} \right) \right] + W_D St_D \quad (14)$$

where  $W_R = 0.495$  is the weight of the random values of  $C_A$ ,  $W_D = 0.505$  is the weight of deterministic values of  $C_A$ , and  $St_D = 0.011$  is the deterministic value of  $C_A$  corresponding to the cases in which the static angle is the limiting factor.

Equations (13) and (14) include estimates that are random numbers (the estimates are identified by use of the “hat” symbol: e.g.  $\hat{x}$ ). Thus, these equations are deterministic functions of random variables. Given the number of data points available in the sample, the distribution of the mean value and the standard deviation estimates is assumed to be normal. The mean values of these distributions are equal to the estimates themselves:

$$\mathbb{E}(\hat{E}_C) = \hat{E}_C; \mathbb{E}(\hat{E}_{CA}) = \hat{E}_{CA}; \mathbb{E}(\hat{\sigma}_C) = \hat{\sigma}_C; \mathbb{E}(\hat{\sigma}_{CA}) = \hat{\sigma}_{CA} \quad (15)$$

where  $\mathbb{E}(\dots)$  is a mean value operator. The variances of the mean value estimates are computed as follows:

$$Var(\hat{E}_C) = \hat{\sigma}_C^2 \sum_{i=1}^N W_i^2; \quad Var(\hat{E}_{CA}) = \hat{\sigma}_{CA}^2 \sum_{i=1}^N W_i^2; \quad (16)$$

A randomness of the mean value estimate is taken into account for the computation of the variance of the variance:

$$Var(\hat{\sigma}_C^2) = \sum_{i=1}^N W_i^2 (\hat{\sigma}_{C^2}^2 - 4\hat{E}_C (\hat{E}_{C^3} + \hat{E}_C^3)) \quad (17)$$

$$Var(\hat{\sigma}_{CA}^2) = \sum_{i=1}^N W_i^2 (\hat{\sigma}_{CA^2}^2 - 4\hat{E}_{CA} (\hat{E}_{CA^3} + \hat{E}_{CA}^3)) \quad (18)$$

where  $\hat{\sigma}_{C^2}$  and  $\hat{\sigma}_{CA^2}$  are the estimates of the standard deviation of the squares of the criteria values of  $C$  and  $C_A$ , and  $\hat{E}_{C^3}$  and  $\hat{E}_{CA^3}$  are the mean value estimates of cubes of these values.

The boundaries of the confidence interval for the mean value estimates  $\hat{E}_C$  and  $\hat{E}_{CA}$  are computed with standard normal quantiles corresponding to the selected confidence probability. This analysis used the *de-facto* industry standard of 95% with the normal standard quantile of 1.96 for the double-sided confidence interval. These boundaries are substituted into the equations for the parameters (11, 12) of lognormal distribution (10) producing a total of four pairs of parameters. These four pairs are used in Eq. (13) for the level 2 criterion  $C$  and Eq. (14) for the alternative criterion  $C_A$ . The largest value among those pairs sets the upper boundary of the possible standard  $St$  and  $St_A$ , while the smallest value sets its lower boundary. Such an approach to the calculation of the confidence interval is sometimes referred as a “boundary method”, for which its justification can be found in Sect. 4.4 of [9].

## 2.5 Factoring-In Applicability of the Linear Assumptions

Both the current level 2 vulnerability criterion and the alternative criterion include a calculation of the standard deviation of roll motion using a linear assumption. The assumption is applicable when most roll angles are sufficiently small that the GZ curve can be approximated with a line, i.e. not too close to the angle of the maximum GZ. This idea can be expressed as:

$$\varphi_{SW} + k \cdot \sigma_{\varphi W} < \varphi_{\max} \quad (19)$$

where  $k$  is a factor that defines how strictly the assumption of linearity is supported,  $\varphi_{\max}$  is the angle of the maximum GZ,  $\varphi_{SW}$  is a long-term weight-averaged static angle, while  $\sigma_{\varphi W}$  is the weighted-averaged standard deviation of roll angles.

Both values  $\varphi_{SW}$  and  $\sigma_{\varphi W}$  are computed for high sea state states where large roll motions are possible. Per Eqs. (3) and (4), the wind pressure, used in the weather criterion ( $P = 504$  Pa), corresponds to row 8 ( $H_S = 8.91$  m) of the scatter table in IACS Recommendation 34. Therefore, every sea state that exceed this significant wave height (i.e.,  $H_S$  values of 9.5 m through 16.5 m) can be assumed to be a “high sea state” for the purpose of this analysis. The weight-averaged static angle  $\varphi_{SW}$ , corresponding to high sea states is computed as:

$$\varphi_{SW} = \frac{\sum_{i=h}^{NH_S} \sum_{j=1}^{NT_Z} W_{i,j} \varphi_S(H_{Si}, T_{Zj})}{\sum_{i=h}^{NH_S} \sum_{j=1}^{NT_Z} W_{i,j}} \quad (20)$$

where  $NH_S$  is the number of “high sea states” and  $\varphi_S(H_{Si}, T_{Zj})$  is a static heel angle computed as described in the Sect. 2.2.3 of MSC.1/Circ.1627 [2] for each significant wave height  $H_S$  and a zero-crossing mean period  $T_Z$  while  $W_{ij}$  is the weight of the sea state defined by the rows  $i$  and column  $j$  of the scatter table of IACS Recommendation 34. The weighted-averaged standard deviation  $\sigma_{\varphi W}$ , which corresponds to high sea states, is computed as:

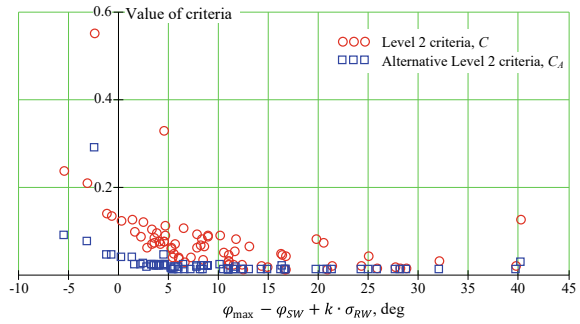
$$\sigma_{\varphi W} = \frac{\sum_{i=h}^{NH_S} \sum_{j=1}^{NT_Z} W_{i,j} \sigma_{\varphi}(H_{Si}, T_{Zj})}{\sum_{i=h}^{NH_S} \sum_{j=1}^{NT_Z} W_{i,j}} \quad (21)$$

where  $\sigma_{\varphi}(H_{Si}, T_{Zj})$  is a standard deviation computed with Eq. (5).

The application of the applicability limitation (19) is illustrated in Fig. 5. Values of the current level 2 and the alternative criteria are plotted against the limitation (19) for all 74 sample points. The value of  $k$  used is 1.2. The cases to be excluded correspond to negative values of the limitation, which in this case totals 4 for the current and the alternative criteria.



**Fig. 5** Application of the linear roll assumption

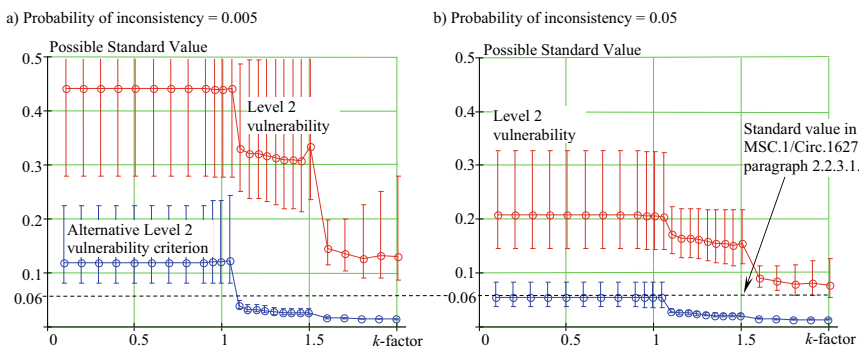


### 2.6 Setting a Standard with Controlled Inconsistency

There are two elements to consider when setting a standard to a specified probability of inconsistency. The first element is an uncertainty of the estimates computed with Eqs. (13) and (14), which are quantified with a confidence interval. The second element is the linear roll assumption applicability, which is expressed with the  $k$ -factor in Eq. (19).

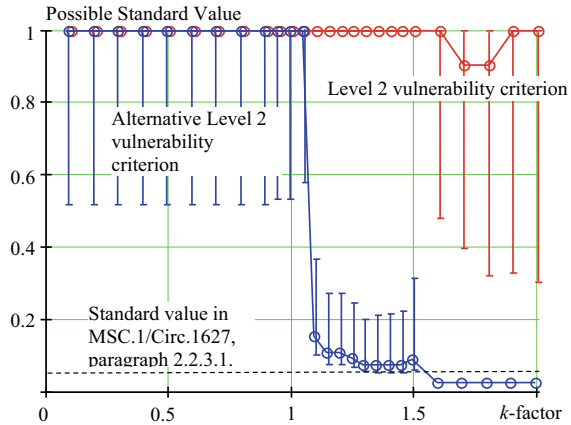
Figure 6 shows the influence of these elements on the possible standard for the level 2 vulnerability criterion and its alternative. The standard value is plotted versus the  $k$ -factor, while the probability of inconsistency is set to 0.005 in Fig. 6a and to 0.05 in Fig. 6b.

Figure 6 shows that to decrease the probability of inconsistency, either the standard should be relaxed or a more stringent requirement for the applicability of linear roll calculations should be implemented. The alternative criterion seems to perform better than the original level 2 criterion. This is an expected outcome since the alternative



**Fig. 6** Possible standard as a function of degree of applicability of linear roll assumption ( $k$ -factor): confidence interval for alternative criterion above  $k$ -factor 1.2 is too small to show. **a** Probability of inconsistency 0.005. **b** Probability of inconsistency 0.05

**Fig. 7** A possible standard as a function of the degree of applicability of the linear roll assumption ( $k$ -factor) computed for a small probability of inconsistency ( $10^{-10}$ )



scenario is closer to that used in the level 1 criterion. At the same time, however, the level 2 criterion can be considered to be more advanced since it is based on the formal application of upcrossing theory.

What if the inconsistency is not accepted? Fig. 7 shows possible standards for the probability of inconsistency that are close to zero ( $10^{-10}$ ). The current level 2 criterion cannot provide a complete consistency. However, the alternative criterion can be consistent if its application is limited to small-to-moderate roll motions that correspond to a  $k$ -factor of 1.1 and above.

Plots for more values of the probability of inconsistency are available from SDC 7/INF.3 [7]. Figure 8 shows the probability of inconsistency for the alternative level 2 criterion that has to be accepted for a given application limitation that is presented with a  $k$ -factor for the standard of 0.06, [paragraph 2.2.3.1., 2]. The upper boundaries of the confidence interval for the alternative level-2 criterion were used to plot the lines in Fig. 8. The consistency between the levels cannot be achieved with the current level 2 criterion. However, consistency is possible if a set of alternative criteria are used with applicability limited to the cases in which roll motion can be assumed within the linear range of the  $GZ$  curve.

This result is expected. A probabilistic interpretation of the weather criterion (and, therefore, the level 1 vulnerability criterion for the dead ship condition) is possible in terms of probabilistic characterization of motion parameters, e.g. [5]. However, probabilistic interpretation of the criteria does not imply constancy in term of the standard, i.e. that it will yield results that are consistent with the weather criterion. An early attempt to compute the probability of capsizing on a set of sample ships each of which have a critical  $KG$  condition has shown a vast variation of the results [10]. Thanou [11] concluded that a consistent probabilistic interpretation of the weather criterion is not viable.

Since the current level 2 criterion can be interpreted as more theoretically advanced in comparison to the weather criterion, the probabilistic inconsistencies are likely to originate from the scenario used in the weather criterion. Thus, it makes sense to

**Fig. 8** The probability of inconsistency for the alternative level 2 criterion as a function of the degree of applicability of the linear roll assumption ( $k$ -factor) for a standard of 0.06



change the role of the level 2 vulnerability criteria to be considered rather as an independent assessment of the safety level in the dead ship condition. The independent application of two (or more) sets of criteria that address the same stability failure mode does not require consistency between them.

### 3 Pure Loss of Stability

A theoretical reason for inconsistency between levels 1 and 2 of the vulnerability criteria for the pure loss of stability failure mode can be considered similarly as for the dead ship condition. The level 1 criterion is essentially a  $GM$ -value that is approximated for a wave with a steepness of 0.0334 in which the wave length is considered to be equal to the ship length [paragraph 2.4.2.2, 2]. The level 2 criterion is an estimate of a long-term probability that either the static angle caused by a specified heeling moment or the angle of vanishing stability exceeds required boundary values. Both angles are computed for the worst  $GZ$  curve while a longitudinal wave passes the ship (i.e., a wave pass). Thus, the level 1 criterion is deterministic and the level 2 criterion is probabilistic. This difference, by itself, can lead to an inconsistency between the levels unless special provisions are considered.

#### 3.1 Probabilistic Consistency

To gain insight into the probabilistic aspect of inconsistency, a notional pure-loss-of-stability criterion is considered: a static or dynamic angle of heel that is obtained when a specified heeling moment is applied using the worst  $GZ$  curve that occurs during a wave pass. This criterion is applied for both level 1 and level 2. To compute this criterion, one needs to know both wave length and wave height.

Grim's effective wave is used to represent a stability variation in a particular sea state. Since the length of Grim's effective wave is equal to the ship length, there is only one random variable remaining—the wave height. Thus, for a given ship length, each cell of a wave scatter table (e.g., IACS Recommendation 34—see [Table 2.7.2.1.2, 2]) corresponds to a particular value of the effective wave height,  $H_{eff}$ :

$$H_{eff} \approx 5.97\sqrt{V_H} \quad (22)$$

where  $V_H$  is the variance of the effective wave:

$$V_H = \int_{\omega_1}^{\omega_2} RAO_{eff}^2(\omega) s(\omega|H_S, T_z) d\omega \quad (23)$$

Here,  $s(\omega|H_S, T_z)$  is a spectral density of the wave elevations,  $\omega$  is a frequency,  $\omega_{1,2}$  are the limits of integration,  $H_S$  is the significant wave height,  $T_z$  is the mean wave zero-crossing period, and  $RAO_{eff}$  is the RAO of the effective wave amplitude:

$$RAO_{eff}(\omega) = \frac{\omega^2 L g^{-1} \cdot \sin(0.5\omega^2 L g^{-1})}{\pi^2 - 0.5\omega^2 L g^{-1}} \quad (24)$$

where  $L$  is the ship length and  $g$  is the acceleration due to gravity.

To find a safety level of the notional criterion, a probability of encounter of specific environmental conditions need to be characterized; consider a scatter table (e.g. [8]). Each cell of the scatter table also corresponds to a statistical frequency, one can easily compute an estimate of the cumulative distribution function (CDF) by sorting the effective wave heights in ascending order and integrating all the statistical frequencies below the current value:

$$P(H_{eff}) = P(H_S, T_z) \quad (25)$$

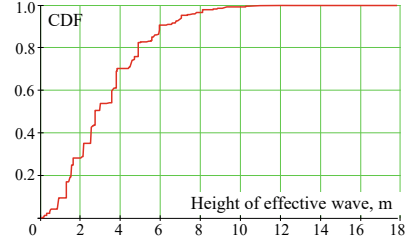
$$P_1(H_{eff}) = \text{sort}(P(H_{eff}), H_{eff}) \quad (26)$$

$$CDF(H_{eff}) = \int_0^{H_{eff}} P_1(h) dh \quad (27)$$

As an example, a CDF, computed for a ship length of 260 m, is shown in Fig. 9. This CDF also can be interpreted as showing a dependence between the safety level for the level 1 criterion and a wave steepness for a ship with length of 260 m. The safety level of a deterministic criterion is a probability that a ship with a loading condition satisfying this criterion will nevertheless experience a failure. As the ship stability is subject of random environmental factors, the safety level theoretically cannot be zero.

For example, set the safety factor to 1%. In this case, the effective wave height corresponding to the 99 percentile equals approximately 9.2 m for a ship length of

**Fig. 9** An estimate of the CDF of the effective wave height computed for a ship length  $L = 260$  m



260 m. Thus, the steepness of the effective wave is  $9.2 \text{ m}/260 \text{ m} = 0.035$ . If the ship satisfies the level 1 criterion for the wave steepness of 0.035, there is only a probability of 1% over the ship's lifetime that the stability will not be sufficient to withstand the pure loss of stability failure. By keeping the safety level constant, one can obtain another wave stiffness for a length, which tends to an idea of the level 1 wave steepness that depends on a ship length. Originally, this idea was proposed in IMO document SDC 5/6/5 [12].

It is assumed here that the heeling moment is created by a steady wind. The relation of mean wind speed  $U_{wm}$  is taken from [2, paragraph 2.2.3.2.2]:

$$U_{wm} = \left( \frac{H_s}{0.06717} \right)^{2/3} \quad (28)$$

Based on this, the aerodynamic pressure  $p_A$  can be computed as:

$$p_A = \frac{\rho_A U_{wm}^2}{2} \cdot C_m \quad (29)$$

where  $C_m$  is the wind heeling moment coefficient ( $C_m = 1.22$ ) and  $\rho_A$  is the density of air [2, paragraph 2.2.3.2.2].

This pressure is also a random variable, as it depends on the significant wave height. As each value of the significant wave height in the scatter diagram has an associated statistical frequency, one can compute the CDF for the significant wave height:

$$CDF(H_s) = \int_0^{H_s} P_H(h) dh \quad (30)$$

where  $P_H$  is a statistical frequency of the significant wave height, which is available from a wave scatter table (e.g., [8]). The CDF of the wind pressure is essentially a rescaling of the CDF (30) with the formula (29), see Fig. 10.

The values of mean wind pressure can be expressed as a function of the safety level (SL):

$$SL = 1 - CDF \quad (31)$$

**Fig. 10** A CDF for the mean wind pressure

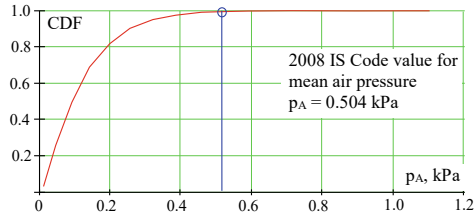


Figure 10 shows the wind pressure value of 0.504 kPa that is used in the weather criterion [3, Sect. 2.3]. The CDF for this value is interesting because it is actually quite high—equal to 0.993 when the scatter diagram from IACS Recommendation 34 is used. So, the safety level is 0.007.

Setting the safety level for the level 1 criterion defines both the wave steepness and the wind pressure. Beyond these, there are no more random parameters involved in the level 1 criterion. Now, if the standard for level 2 criterion is established above the safety level for the level 1 criterion, the criteria always will be consistent between the two levels.

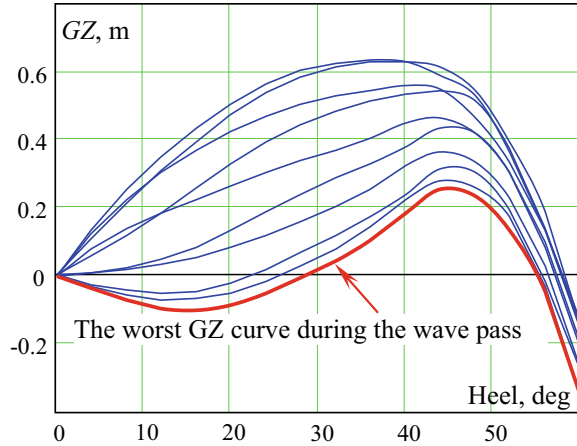
### 3.2 Physical Consistency

The second reason for the inconsistency between the levels of the pure loss of stability vulnerability criteria is actually the oversimplification of stability used in the level 1 criteria. The reason is that the  $GM$  alone does not characterize stability at large heel angles (a fact that is well known among naval architects). Thus, in order to avoid inconsistency with the level 2 criterion, the level 1 criterion should include enough information to characterize stability at large heel angles. At the same time, it should be more conservative while, perhaps, less accurate than the level 2 criterion.

This idea can be implemented by formulating the level 1 criterion for the  $GZ$  curve in the worst possible position of ship on a wave (which is not necessarily when the midship section is located at exactly at the wave crest). Then, the level 2 criterion can be defined based on the stability variation throughout a wave pass (see Fig. 11). The conservatism of the level 1 criterion is ensured by the simple fact that the worst  $GZ$  curve is not experienced for a long duration during a wave pass.

Indeed, the level 1 criterion becomes more complex compared to a  $GM$  based-formulation that has been in consideration since 2011, including the one contained in MSC.1/Circ.1627 [13]. The proposed level 1 criterion requires a computation of the  $GZ$  curve during the wave pass. One should note that a computer program suited for this purpose is normally needed for these calculations. This approach, however, seems to be inconsistent with the original intention [13] to limit level 1 efforts to spreadsheet-type calculations. However:

**Fig. 11** The  $GZ$  Curve during a wave pass, C11-class containership, with a wave steepness = 0.012,  $KG = 19.92$  m (maximum  $KG$  permitted for compliance with the 2008 IS Code [3])



- $GZ$  curves in longitudinal waves can be computed with most standard ship hydrostatic software. The level 1 criterion without any simplification can still be applied using a spreadsheet if the worst-case  $GZ$  curve during wave pass can be produced by the standard ship hydrostatic software; and
- It may be possible to approximate the worst  $GZ$  curve during pass with the worst  $GM$  during the wave pass. If this will be found to be possible, then the level of complexity of the proposed level 1 criterion will be on the same level as originally envisioned.

## 4 Consistent Criteria

Following the concept of the weather criterion, a dynamic angle can be considered as a level 1 criterion. The  $GZ$  curve is selected as the worst  $GZ$  curve during the wave pass (see Fig. 11). The  $GZ$  curves in waves are computed for the effective wave height, which correspond to the agreed safety level that must be below the standard accepted for the level 2 criterion. Currently, the value of the level 2 standard is 0.06 [paragraph 2.4.3.1, 2]. If the safety level for the level 1 criterion is taken as 0.02, then the steepness of the effective wave for a 260 m long ship becomes 0.0328, which is slightly lower than the current value of 0.0334 [paragraph 2.4.2.2, 2].

The mean wind pressure, which corresponds to the safety level of 0.02 is  $p_A = 0.407$  kPa (see Fig. 10). A few more assumptions are needed to compute the heeling lever:

- The pure loss of stability failure mode occurs in stern quartering and in following waves in which a beam wind will be too conservative to consider. Hence, the wave encounter angle  $\beta$  is assumed to be  $20^\circ$  with the ship heading.
- Since the roll motion is expected to be small in following and stern quartering seas, the roll back angle may be assumed to be zero.

- No developed wind drift is assumed because the relative wind angle is small (20°), which means that the hydrodynamic resistance to wind drift is also small. The effect of this is to cause the lever of the wind force to be the distance from the waterline to the center of wind pressure, which, of course, is different from the assumption made in the weather criterion.
- Following the weather criterion assumption [paragraph 2.3.2, part A, 3], the sudden increase of the wind force (the sustained gust) above the mean value is taken as 1.5.

As a result of these assumptions, the lever of the heeling moment in the considered loading condition is computed as follows:

$$l_w = 1.5 \cdot \frac{p_A \cdot A \cdot Z}{g \cdot \Delta} \cdot \sin(\beta) \tag{32}$$

where  $A$  is the projected lateral area of the ship and deck cargo above the waterline,  $Z$  is the vertical distance from the center of  $A$  to the waterline,  $\Delta$  is mass displacement in metric tons, and  $g$  is the acceleration due to gravity.

The level 1 criterion can be formulated as follows:

$$\varphi_d \leq K_{PL2} \tag{33}$$

where  $\varphi_d$  is a dynamic angle of heel calculated by equalizing area  $a$  and area  $b$ , as shown in Fig. 12, and  $K_{PL2} = 15^\circ$  for passenger vessels and  $25^\circ$  otherwise.

To be consistent, the level 2 criterion is formulated for the same scenario, but takes into account time: that is, that the GZ curve changes during the wave pass and does not remain at the worst case throughout duration of the wave pass. Thus, the computation of the dynamic angle is carried out by numerical integration of the

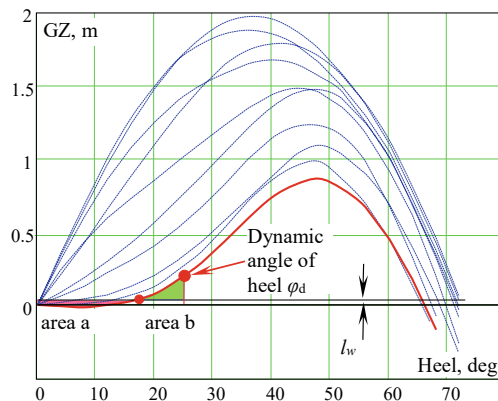


**Fig. 12** The GZ Curve during a wave pass, C11-class containership, with a wave steepness of 0.0328 and a  $KG = 18.55$  m



equations of motions that describe both surging  $x$  and rolling  $\varphi$ :

$$\begin{cases} (\Delta + A_{11})\ddot{x} + R_x(\dot{x}) - T(\dot{x}, n) = F_x(x, t) \\ (I_x + A_{44})\ddot{\varphi} + R_\phi(\dot{\varphi}) + \Delta g GZ(\varphi, x) = \Delta g l_w \end{cases} \quad (34)$$

where,  $I_x$  is the moment of inertia in roll;  $A_{11}$  and  $A_{44}$  are the added mass in surge and roll, respectively;  $R_x$  is the ship resistance in calm water;  $T$  is the ship thrust, achieved with a set propulsion point (i.e., a commanded number of propeller revolutions,  $n$ );  $F_x$  is the Froude-Krylov wave force in direction of surge [14], and  $R_\phi$  is the roll damping. A numerical integration is performed for the duration of one wave pass and largest encountered roll angle for that single wave pass is recorded, see the example in Fig. 13.

The equations of motion (34) includes the influence of the surging that may have affect the timing of the period of decreased stability [15] as well as the influence of surf-riding equilibria that can be manifested in asymmetric surging [16]. The equations of motion that constitute the model (34) does not include a hydrodynamic heeling moment of the vortex nature that arises from the asymmetry of the submerged portion of the hull [17]. Instead, the heeling moment is created by wind. This may be a reasonable simplification since the model (34) does not require hydrodynamic derivatives, which are needed for sway and yaw motions. The elements the model (34) require are the GZ curve variation in regular waves, roll damping, resistance and thrust approximations. The latter two elements should be already available from assessment of level 2 surf-riding/broaching vulnerability criteria [paragraph 2.6.3, 2].

The potential criterion is the maximum roll angle, which is observed over a single wave encounter as shown in Fig. 13b. This criterion is expected to be automatically consistent with the considered level 1 criterion, since the consideration of the worst GZ curve over the wave pass is certainly more conservative when compared to varying stability curve.

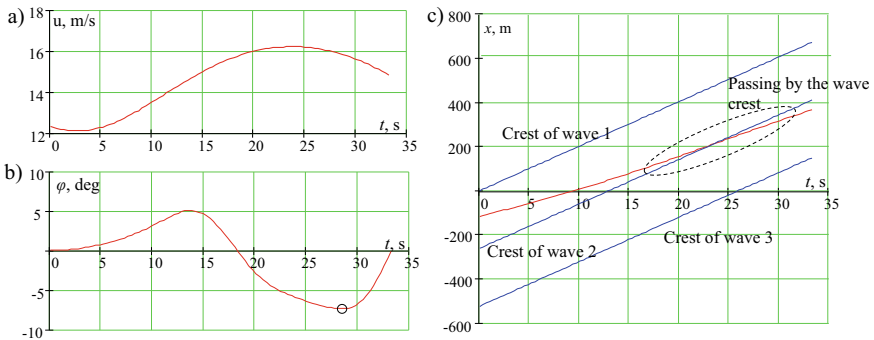


**Fig. 13** Display of elements of motions during the wave pass, C11-class containership with a wave steepness of 0.034 and  $KG = 18.55$  m: **a** surging velocity; **b** roll motion; **c** distance travelled;

## 5 Summary and Conclusions

The consistency of vulnerability assessments between levels 1 and 2 of the dead ship condition and the pure loss of stability failure modes have been considered.

The level 2 vulnerability criterion for the dead ship condition is a probabilistic long-term criterion, which assesses dynamic stability in waves with either an up-crossing rate or probability of up-crossing during a given exposure time. The level 1 vulnerability criterion replicates the weather criterion with an extended table for the natural roll period. Following other studies, it was found that consistency between the two levels cannot be guaranteed unless a certain probability of inconsistency is accepted.

As currently formulated, the level 2 criterion does not provide the roll back angle for the weather criterion, and, for this reason, it cannot be used to extend applicability of the weather criterion within the current stability regulatory framework. However, it can be used for independent assessment of the safety level in dead ship conditions.

The consistency of vulnerability assessments between levels 1 and 2 for the pure loss of stability failure mode can be achieved by satisfying two conditions:

- The level 1 and 2 criteria use same mathematical model (like a dynamical angle of heel) or the mathematical model for the level 2 criterion is less conservative compared to level 1 (e.g., the level 1 criterion is a dynamical angle computed for the worst GZ curve during the wave pass whereas the level 2 accounts for the variation of the GZ curve during the wave pass); and
- The safety level for the deterministic level 1 criterion is set below the standard for the probabilistic level 2 criterion.

The possibility of considering consistent vulnerability criteria for the pure loss of stability failure mode is suggested as a possible alternative for the future refinement of the second generation intact stability criteria.

**Acknowledgements** The work described in this paper has been funded by the Office of Design and Engineering Standards of the U.S. Coast Guard (CG-ENG) under the guidance of Mr. Jaideep Sirkar and by the US Navy Office of Naval Research under Dr. Woei-Min Lin. The authors are grateful to Mr. K. Weems (NSWCCD) for his help with calculations and to Prof. K. Spyrou for fruitful discussions on the methodology of calculations.

## References

1. Tompuri M, Rupponen P, Lindroth D (2017) On the consistency of the level 1 and 2 vulnerability criteria in the second generation intact stability. In: Proceedings of the 16th international ship stability workshop, Belgrade, Serbia, pp 3–8
2. IMO MSC.1/Circ.1627 Interim Guidelines on the Second Generation Intact Stability Criteria. London, December, 2020
3. IMO International Code on Intact Stability, 2008, IMO, London, 2009

4. IMO MSC.1/Circ.1200 Interim Guidelines for Alternative Assessment of the Weather Criterion. 24 May 2006
5. Dudziak J, Buczkowski A (1978) Probability of ship capsizing under the action of the beam wind and sea as a background of stability criteria. Polish Register of Ships, Prace Studialno-Roswojowe, Zeszyt Nr. 13, Gdansk
6. Belenky VL, Sevastianov NB (2007) Stability and safety of ships: risk of capsizing, 2nd edn. SNAME, Jersey City. ISBN 0-939773-61-9
7. IMO SDC 7/INF.3 Continued research into stability failure modes in support of the second generation intact stability criteria. Submitted by the United States, 20 November 2019
8. IACS Recommendation No. 34 Standard Wave Data, November 2001
9. Bickel PJ, Doksum KA (2015) Mathematical statistics: basic ideas and selected topics, vol I, 2nd edn. Chapman and Hall/CRC Texts in Statistical Science. ISBN 978-1498723800
10. Belenky VL (1995) Analysis of probabilistic balance of IMO stability regulation by piece-wise linear method. Marine Technology Trans. Polish Academy of Sciences, Branch in Gdansk 6:5-55
11. Thanou AA (2010) Probabilistic consideration of the weather criterion of ship stability. Diploma thesis, supervised by K.J. Spyrou, National Technical Institute of Athens (in Greek)
12. IMO SDC 5/6/5 Proposal on Improving Consistency of Pure Loss of Stability Vulnerability Criteria. Submitted by China, 17 November 2017
13. Peters W, Belenky V, Bassler C, Spyrou K, Umeda N, Bulian G, Altmayer B (2011) The second generation of intact stability criteria, an overview of development. SNAME Trans 119:225-264
14. Belenky V, Spyrou K, Weems K (2019) Modeling of surf-riding in irregular seas. In: Belenky V, Spyrou K, van Walree F, Neves MAS, Umeda N (eds) Contemporary ideas on ship stability. Risk of capsizing, Chapter 20. Springer, Berlin, pp 347-358. ISBN 978-3-030-00514-6
15. Umeda N, Yamakoshi Y (1994) Probability of ship capsizing due to pure loss of stability in quartering seas. Naval Architecture and Ocean Engineering, The Society of Naval Architects of Japan 30:73-85
16. Spyrou K (1996) Dynamic instability in quartering seas: the behavior of a ship during broaching. J Ship Res 40(1):46-59
17. Kubo H, Umeda N, Yamane K, Matsuda A (2012) Pure loss of stability in Astern Seas—is it really pure? In: Proceedings of 6th Asia-Pacific workshop on marine hydrodynamics, Johor, pp 307-312

# Simplifications in Direct Stability Assessment



V. Shigunov

**Abstract** Direct stability assessment requires a significant computational time since stability failures, which are very rare in practically relevant cases, should be encountered in numerical simulations. The problem can be simplified if stability failures can be assumed independent and thus described as a Poisson process, which requires neutralization of self-repetition, transient effects and autocorrelation of big roll motions, solutions for which are proposed in the paper. Two other simplifications considered here are the extrapolation of the stability failure rate over significant wave height and reduction of the assessment to few design situations. In the former method, the failure rate is defined from numerical simulations at large significant wave heights, where the failure rate is large, and extrapolated to lower significant wave heights. In the design situations method, the assessment is performed for few selected combinations of the significant wave height, mean wave period, wave direction and ship speed. Both methods are applied to five ships (a cruise and a RoPax vessels and three container ships), each in six loading conditions, and demonstrate a significant reduction in the required simulation time. Recommendations for practical application of these methods are provided.

**Keywords** Direct assessment · Numerical simulation · Statistical extrapolation

## 1 Introduction

Direct stability assessment means here an assessment which uses the probability of stability failure as the criterion and numerical simulations of ship motions in seaway to calculate this probability. Direct stability assessment implies that stability failures are encountered in numerical simulations, however, stability failures are very rare in practically relevant cases: according to [3],  $6.7 \times 10^{-4}$  capsizes happen on the average per ship per year due to heavy weather, i.e. the mean time to capsize is about 1500 years per ship. Moreover, estimate of stability failure probability obtained

---

V. Shigunov (✉)  
DNV Maritime, Hamburg, Germany  
e-mail: [vladimir.shigunov@dnv.com](mailto:vladimir.shigunov@dnv.com)

**Table 1** Main particulars of ships and loading conditions used in study

Ship	$L_{pp}$ , m	$B_{wl}$ , m	$d$ , m ( $GM$ , m)
Cruise vessel	230	32	6.9 (1.5, 2.0, 2.5, 3.25, 3.75, 4.0)
1700 TEU CV	160	28	9.5 (0.5, 1.2, 1.9), 5.5 (5.75, 6.75, 7.75)
8400 TEU CV	317	43	13.93 (0.89), 14.44 (1.26), 14.48 (2.01), 11.36 (5.0, 6.93, 9.0)
14,000 TEU CV	350	51	8.5 (1.0, 2.0, 3.0), 14.5 (9.0, 12.0, 15.0)
RoPax	175	30	5.5 (3.7, 4.5, 5.2, 5.9, 6.6)

from numerical simulations is a random variable, subject to statistical uncertainty. This uncertainty reduces with increasing number of simulated stability failures: e.g. reducing the width of the 95% two-sided confidence interval (interval containing the true value with probability 95%) to the level 10% of the stability failure probability (i.e. achieving 5% accuracy) requires simulation time of about  $2.3 \times 10^6$  years, which means tremendous computational time even using quick numerical simulation methods. One simplification is to assume that stability failures are independent, and thus can be described as a sum of stationary Poisson processes (see the next section), which reduces the problem to the definition of a single parameter, the stability failure rate (i.e. the number of stability failures per time unit) in multiple stationary situations (combinations of sea state and ship speed and course with respect to the mean wave direction). Two other approximations considered here are the *extrapolation of stability failure rate over wave height* and the reduction of the number of situations considered in the assessment to few *design situations*.

In the examples in this paper, exceedance of  $40^\circ$  roll angle was used as stability failure. Nonlinear simulations of ship motions in waves were performed with the method *rolls*, which was proposed in Söding [18, 19] and further developed for intact ships in [5] and ships with tanks and damaged compartments in [7, 8], comparison of simulation results with model tests for intact ships can be found in [2, 12] and [17]. Five ships were used in the examples here (a cruise and a RoPax vessels and three container ships of 1700, 8400 and 14,000 TEU capacity), each in six loading conditions, Table 1.

## 2 Poisson Process Assumption

The assumption that stability failures can be approximated as a Poisson process significantly simplifies assessment and is frequently used (one of the earliest examples can be found in [10], available in English in [11]), although its validity is not obvious, [16]. This assumption requires independence of stability failures, based on two heuristics: first, although big roll motions tend to appear in groups and are, therefore, not independent, independence can be assumed for the occurrence of such groups (note that this agrees with the approach used presently in rules, according to which only the triggering event is considered but not the further development of an

accident); second, such groups can be assumed independent if they are sufficiently rare since rare events tend to be independent. How rare should occur stability failures to be considered independent is studied below.

Especially simple is the model of a stationary Poisson process, although stationarity seems especially questionable: ships are sailing in situations that may change quicker than the time required for roll motion to become stationary; in some cases (e.g. transient flooding) also the hydrodynamic characteristics of the ship change too quickly for the stationarity assumption to be valid. If, however, ship hydrodynamic characteristics change slowly, stationarity assumption is applicable since we do not consider one ship operating in changing situations but average over many ships, each of which operates in a stationary situation. Then, using the splitting property of a stationary Poisson process, such “long-term” operation can be modelled as a stationary Poisson process with constant mean rate, which consists of an infinite number of stationary Poisson processes, each of which happens in a stationary situation.

The Poisson process model is also very useful for evaluation of simulations in such stationary “short-term” conditions, [16]: the probability density function of the Poisson distribution is equal to the probability that the number of stability failures  $N(t)$  during a time interval  $t$  is equal to  $k$ ,

$$f(k) = p\{N(t) = k\} = (rt)^k \times e^{-rt} / k! \quad \text{for } k = 0, 1, \dots \quad (1)$$

where constant  $r > 0$  is the *rate*.

Then, the probability that *no failures* occur from time 0 to time  $t$  can be calculated with  $k = 0$ , i.e. as

$$p\{N(t) = 0\} = e^{-rt} \quad (2)$$

and the probability that *at least one failure* occurs during time  $t$ , i.e. that  $k > 0$  (note the difference from the probability that *exactly one failure* occurs during time  $t$ , i.e. that  $k = 1$ ) can be calculated as the probability of the complementary event to the event that no failures occur, i.e. as

$$p\{N(t) > 0\} = 1 - p\{N(t) = 0\} = 1 - e^{-rt} \quad (3)$$

Equation (2) means that the probability that the time until the first failure  $T$  exceeds  $t$ , i.e.  $p\{T > t\}$ , is the same as  $p\{N(t) = 0\} = e^{-rt}$ , i.e.  $T$  is exponentially distributed (similarly for all time intervals  $T_i$  between stability failures), i.e. time intervals between failures for a Poisson process are independent random variables, exponentially distributed with rate  $r$  (the opposite is also true: if the time intervals between failures are not exponential, the process is not a Poisson process) with the probability density function

$$f(t) = r \times \exp(-rt) \quad \text{for } t \geq 0 \text{ and } 0 \text{ otherwise} \quad (4)$$

and cumulative density function

$$\begin{aligned} F(t) &= p\{0 < T < t\} = 1 - p\{T > t\} \\ &= 1 - \exp(-rt) \quad \text{for } t > 0 \quad \text{and } 0 \text{ otherwise} \end{aligned} \quad (5)$$

The mean  $\mu_T$  of exponentially distributed time between failures is  $\mu_T = 1/r$ , variance  $\sigma_T^2 = 1/r^2$  and standard deviation  $\sigma_T = 1/r = \mu_T$ , i.e. the rate (or mean time to stability failure) define all characteristics of a Poisson process.

To define distribution parameters from numerical simulations, measure time intervals to each failure  $T_i$ ,  $i = 1, 2, \dots, N$ , and define the total simulation time  $t_t = \sum_{i=1}^N T_i$ , then the *sample mean time to failure* is

$$\bar{T} = t_t/N \quad (6)$$

and the *maximum likelihood estimate of the failure rate* is

$$\hat{r} = 1/\bar{T} = N/t_t \quad (7)$$

Since rate estimates vary between series of simulations, the criterion should consider statistical uncertainty, hence the guidelines [4] use the upper boundary of the 95%-confidence interval of the stability failure rate. For its definition, Shigunov [14, 15] applies the central limit theorem: for a sufficiently big sample, sample mean time to failure is normally distributed with standard deviation  $\sigma_{\bar{T}} = \sigma_T N^{-0.5} = \bar{T} N^{-0.5}$ . As a normally distributed variable  $\bar{T}$  falls between  $\bar{T} - 1.96\sigma_{\bar{T}}$  and  $\bar{T} + 1.96\sigma_{\bar{T}}$  with a probability 0.95, the 95%-confidence interval for  $\bar{T}$  is  $\bar{T} - 1.96\sigma_{\bar{T}} < \bar{T} < \bar{T} + 1.96\sigma_{\bar{T}}$ , then the upper and lower boundaries of the 95%-confidence interval of the failure rate can be defined using Eq. (7) as

$$\hat{r}(1 - 1.96N^{-0.5}) = r_L < r < r_U = \hat{r}(1 + 1.96N^{-0.5}); \quad (8)$$

$r_L$  and  $r_U$  are respectively the lower and upper boundaries of the 95%-confidence interval of failure rate.

Shigunov [16] defines the  $C\%$  two-sided confidence interval of failure rate as the confidence interval of the rate parameter of exponential distribution, [9]. The parameter  $C\%$ , called the *confidence level*, denotes the probability that the true value of the rate parameter will be within the confidence interval (note that this means that there is a  $0.5(100 - C)\%$  probability that the true value of the rate parameter will be less than the left boundary of the confidence interval and  $0.5(100 - C)\%$  probability that it will be greater than the right boundary). The confidence level can be written in the form  $C\% = (1 - \alpha) \cdot 100\%$ , where  $\alpha$  is a small non-negative number,  $\alpha = 1 - C\%/100\%$  (e.g.  $\alpha = 0.05$  for 95%-confidence level), then the  $C\%$ -two sided confidence interval of failure rate can be written as

$$0.5\hat{r}\chi_{\alpha/2, 2N}^2/N = r_L < r < r_U = 0.5\hat{r}\chi_{1-\alpha/2, 2N}^2/N \quad (9)$$

where  $\chi_{p,f}^2$  denotes the  $p \cdot 100\%$ -quantile, corresponding to a lower tail area of the  $\chi^2$ -distribution with  $f$  degrees of freedom. For large  $N$ ,  $\chi_{p,2N}^2 \approx 2N + 2\sqrt{N} \cdot \mathfrak{K}_{0,1}(p)$ , where  $\mathfrak{K}_{0,1}(p)$  is the  $p \cdot 100\%$ -percentile of the standard normal distribution; for  $p = 0.95$ , this leads to Eq. (8).

Independence of stability failures in simulations can be ensured using ensemble statistics, at a fixed time instant, over numerical simulations in multiple independent realisations of the same sea state. If the sea state is modelled as a finite sum of harmonic components, [6], such independent realisations can be generated by random variation of phases and, possibly, frequencies, directions and amplitudes of components for each realisation (in the examples here, seaway with JONSWAP wave energy spectrum with the peak parameter 3.3 and  $\cos^2$ -wave energy spreading was used, discretised by 19 wave directions with  $10^3$  components of equal amplitudes per direction).

If time history statistics is used instead of ensemble statistics (assuming *ergodicity* of the process, i.e. that time averages are the same for any initial conditions: then time averages are equal to ensemble averages), three problems should be addressed: first, if sea state is modelled as a finite sum of components, collecting sufficient statistics in one run is impossible because of self-repetition effects; a solution is to generate multiple independent realisations of the sea state and simulate ship motions in each such realisation for a limited time (see below). Second, transient effects after the start of simulations violate the stationarity requirement; to address this, transient periods after the start of each simulation were not considered, i.e. this simulation time was not included in  $t_t$  and failures during this time were not counted in  $N$ . Third, independence of stability failures is violated by autocorrelation of big roll motions; to neutralize this, a simulation was stopped after the first encountered stability failure. Remaining pieces of roll motion time histories can be treated as a single stationary Poisson process. Thus, it is required to run simulations following the three described techniques and updating, after each simulation, the number of failures  $N$ , total simulation time  $t_t$  and estimates  $\hat{r} = N/t_t$ ,  $r_L$  and  $r_U$ , Eq. (9).

Shigunov [13, 14] checks whether this procedure ensures that  $\sigma_T = \mu_T$  by comparing the sample estimate of standard deviation  $\sigma_T$  with the sample mean time to failure  $\bar{T}$ , Fig. 1. To verify whether this procedure ensures exponentially distributed time to failure, [13] analyses distributions of  $-\ln[1 - F(T_i)]$  versus  $T_i/\bar{T}$  (quantile diagrams). Shigunov [16] uses such quantile diagrams to investigate self-repetition effects for parametric and synchronous resonance in irregular short-crested head and beam, respectively, waves at varied significant wave height. Two types of simulations are compared, both using  $1.9 \times 10^4$  components to discretise the wave energy spectrum: in one, denoted ‘limited’, the maximum duration of simulations is 3 h, while simulations are stopped after the first failure, and in the other (‘unlimited’), simulations are always run until the first failure. Examples in Fig. 2 show that whereas the results of ‘limited’ simulations agree with the exponential distribution, the results from the ‘unlimited’ simulations over-estimate (sometimes very significantly) time to failure compared to the exponential distribution, and that this over-estimation



increases with the increasing mean time to failure. Since the exponential distribution of time to failure is equivalent to the independence of failures, this deviation from exponential distribution means some dependence; moreover, since such deviation from the exponential distribution does not happen in ‘limited’ simulations but happens in ‘unlimited’ ones and increases with increasing duration of simulations, the reason of this dependence is the increasing duration of simulations. Since independence requires absence of self-repetition, such dependence that occurs due to increasing simulation time can be explained by self-repetition. Physically, this means that whereas for stability failures occurring early in the simulations, the self-repetition does not influence the result, stability failures occurring later are influenced by self-repetition effects, since the same ‘uncritical’ realisation repeats itself (note that since self-repetition is not exact, failures eventually happen but much later than they should). This explanation agrees with the fact that the deviations from the exponential distribution in ‘unlimited’ simulations in general over-estimate the time to failure.

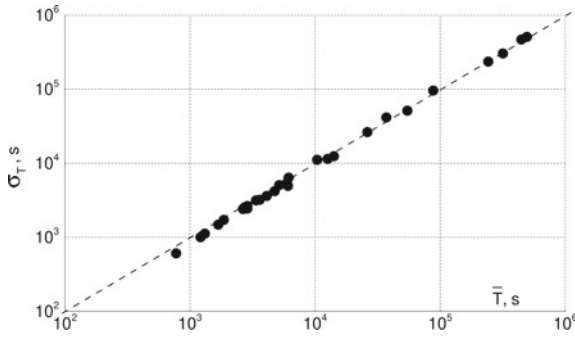


**Fig. 1** Sample estimate of standard deviation of time to failure versus sample mean time to failure after 200 simulated failures, [14]

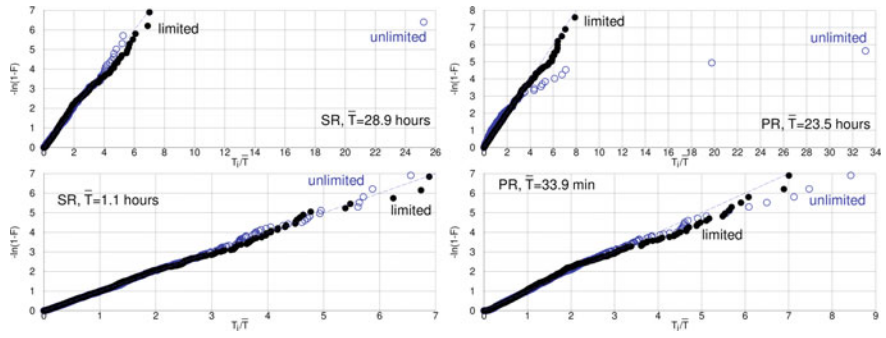


**Fig. 2** Quantile diagrams from ‘limited’ (•) and ‘unlimited’ (◦) simulations for synchronous (left) and parametric (right) resonance cases; dashed bisect line corresponds to exponential distribution;  $\bar{T}$  indicated in plots is sample mean time to stability failure

Self-repetition of ordinates of modelled irregular waves is known to occur when the discretisation of the wave energy spectrum is not sufficient for the intended duration of numerical simulations, see e.g. [1]. The above results show that the absence of the self-repetition of roll motion seems more demanding with respect to the necessary discretisation of the wave energy spectrum, i.e. absence of the self-repetition of wave ordinates does not guarantee the absence of self-repetition of roll motion. A possible explanation is the narrow-banded nature of roll excitation: whereas the discretisation of the wave energy spectrum may be sufficient for wave reconstruction, the narrow frequency range relevant for the excitation of excessive roll motion may contain too few components, which leads to self-repetition of roll (imagine a hypothetical case where roll motion reacts on only one wave component).

Note that self-repetition of roll always leads to the over-estimation of time to failure, i.e. a non-conservative error, which is undesirable in the assessment for regulatory approval.

To check whether the proposed measures ensure a Poisson process, [16] applies the  $\chi^2$  goodness-of-fit test to several cases of parametric and synchronous resonance in head and beam waves, respectively, at systematically varied significant wave height, using simulations of 3-h duration (or until stability failure), repeated until encountering about  $10^3$  failures in each sea state. Observed times to failure are compared with exponential distribution using the maximum likelihood estimate  $\hat{r}$  of the failure rate. Full range  $t \geq 0$  of time to failure is divided into  $k$  intervals of equal probability; the number of intervals is systematically increased up to  $k = 200$ . The number  $O_i$  of the observed times to failure within each interval  $i$  is compared with the expected number  $E_i = N / k$  using the test statistic  $x = \sum_{i=1}^k (O_i - E_i)^2 / E_i$ . The critical value of the test statistic at the significance level  $\alpha = 0.05$  is defined as  $c_{5\%} = \chi^2_{1-\alpha, f}$  with the number of degrees of freedom  $f = k - p - 1$ , where  $p = 1$  is the number of parameters of the assumed distribution estimated from the sample. Figure 3 shows the ratio  $x/c_{5\%}$  at  $k = 200$  versus sample mean time to failure: for synchronous resonance, the Poisson process model is acceptable in all studied cases, whereas for parametric resonance, the results disagree with the Poisson process assumption: marginally at  $\bar{T} \approx 2$  h and increasingly for  $\bar{T}$  decreasing below 2 h.

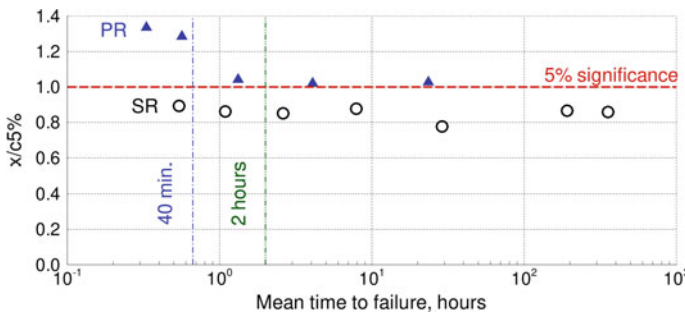


Fig. 3  $x/c_{5\%}$  for synchronous ( $\circ$ ) and parametric ( $\blacktriangle$ ) resonance versus sample mean time to failure

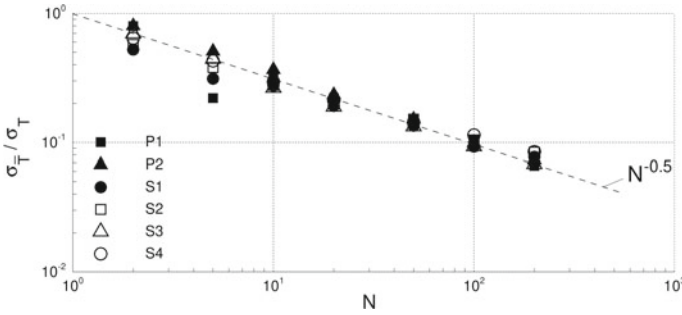


Fig. 4 Estimated standard deviation of mean time to failure versus number of failures, [14, 15]

Shigunov [14, 15] verifies that  $\sigma_{\bar{T}}/\sigma_T$  decreases as  $N^{-0.5}$  for several cases of parametric (P1, P2) and synchronous (S1–S4) resonance, Fig. 4. This dependency follows from the central limit theorem for ‘sufficiently big’ sample sizes; these results show that it is valid already for small sample sizes  $N$ .

### 3 Extrapolation Over Wave Height

Extrapolation of failure rate over significant wave height, Tonguč and Söding [20], employs the idea that rare events happen, with some unknown probability  $p$ , when a wave or a wave group consisting of a certain (unknown) number  $n$  of waves is encountered, which exceeds a certain (also unknown) height  $h$ . The rate of such events is proportional to  $p \cdot f(h, n \sim h_s)$ , where  $f$  is the frequency of encountering wave groups with the required characteristics. Such wave groups are approximately Rayleigh-distributed,  $f \sim \exp(-2nh^2/h_s^2)$ , then

$$\ln r = A + B/h_s^2 \tag{10}$$

where  $r$  is the failure rate and parameters  $A$  and  $B$  do not depend on  $h_s$  but depend on the forward speed and wave period and direction (similarly for  $\ln \mu_T = -\ln r$ ). Instead of defining parameters  $A$  and  $B$  explicitly in terms of unknown  $p$ ,  $n$  and  $h$ , the idea is to define them empirically at greater significant wave heights; note, however, that at greater significant wave heights, the events must remain sufficiently rare for this formulation to remain valid. It is also important to note that this method does not assume any relation between exceedance rates of different ship reaction levels (here different roll amplitudes).

Such extrapolation significantly reduces simulation time since numerical simulations are conducted at large significant wave heights and greater failure rate, and results at lower significant wave heights are obtained by extrapolation.

Extrapolation (10) over-estimates the mean time to failure, i.e. is non-conservative, when the dependency of  $\ln \bar{T}$  on  $1/h_s^2$  is concave. From numerical simulations for

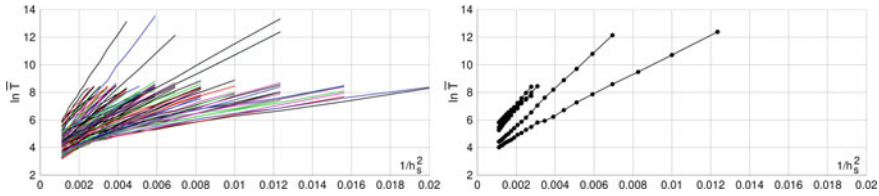


**Fig. 5** All cases with concave dependency of  $\ln \bar{T}$  on  $1/h_s^2$  taking (left) and not taking (right) into account results with  $\ln \bar{T} < 6$

ships and loading conditions in Table 1 for various forward speeds and sea states, [13] observes that the dependencies of  $\ln \bar{T}$  on  $1/h_s^2$  are rarely concave for  $\ln \bar{T} > 5$  and proposes to perform extrapolation (10) using only such simulation results for which  $\ln \bar{T} > 6$ . Shigunov [14, 15] verifies this conclusion: Fig. 5 shows all identified cases with concave dependencies of  $\ln \bar{T}$  on  $1/h_s^2$  (left) and those which are concave for  $\ln \bar{T} > 6$  (right): excluding cases with  $\ln \bar{T} < 6$  drastically reduces the possibility of non-conservative extrapolation; for remaining cases, accurate extrapolation is possible using ranges of sufficiently large values of  $1/h_s^2$ .

Shigunov [14, 15] validates extrapolation (10) by comparison with numerical simulations in irregular short-crested beam waves. Ships and loading conditions in Table 1 are used, each at six forward speeds, at the mean wave periods from 7 to 20 s every 1 s; significant wave height is varied with a step 1 m. For each ship and loading condition and each combination of ship forward speed and mean wave period, 4, 5 and 6 significant wave heights (“points”) are selected, starting from the minimal significant wave height for which simulation results are available. The simulation results for the minimal significant wave height were used to evaluate the deviation between the extrapolated and directly computed mean time to failure, whereas the remaining 3, 4 or 5 points, respectively, were used for extrapolation (10) using the least-squares method. Figure 6 shows the results as the number of cases (combinations of ship, loading condition, forward speed and mean wave period), normalized on 1, versus the ratio of the extrapolated mean time to failure  $T_e$  to the directly computed estimate  $\bar{T}$  for each of these cases. This study was conducted using  $N = 200$  and 20 simulated stability failures to compute the mean time to failure. Using  $N = 200$  simulated failures (Fig. 6, left) leads to accurate results (over 77% of extrapolated values are within the 95%-confidence interval of the directly computed estimate of the mean time to failure when 3 points are used for extrapolation, and about 80% when 4 or 5 points are used), whereas using  $N = 20$  simulated failures leads to a big spreading of the extrapolated results.

Here, such validation is conducted for roll, including parametric, in bow and stern waves and, including synchronous, in beam waves; 200 stability failures are simulated in each sea state. For validation, 4, 5, ..., 11 significant wave heights are used, starting from minimal for which simulation results are available and for which  $\ln \bar{T} > 6$ . Simulation results at the minimum significant wave height are used to evaluate the deviation between the extrapolated and directly computed estimate of the mean time to failure, whereas the remaining 3, 4, ..., 10 points, respectively, are

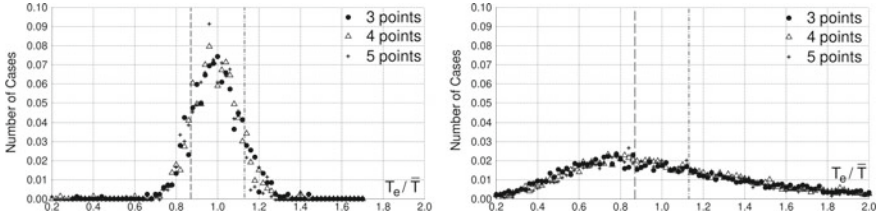


**Fig. 6** Number of cases normalized on 1 of ratio  $T_e/\bar{T}$  (symbols) and 95%-confidence interval of directly computed  $\bar{T}$  (vertical lines) using  $N = 200$  (left) and 20 (right) simulated stability failures

used for extrapolation (10) using the least-squares method. Figure 7 shows results in the same format as Fig. 6; Table 2 shows the percentage of extrapolated values within the 95%-confidence interval of the directly computed estimate, indicating that the extrapolation provides sufficiently accurate results.

To define the upper boundary  $r_{e,U}$  of the 95%-confidence interval of extrapolated failure rate, take  $K \geq 3$  maximum likelihood estimates  $\hat{r}_k$  of stability failure rate,  $k = 1, \dots, K$ , obtained after  $N_k$  simulated failures ( $N_k$  may differ) at significant wave heights  $h_{s,k}$ . The upper boundaries of the 95%-confidence interval of failure rate  $r_{U,k}$  are obtained with Eq. (9) with  $\alpha = 0.05$ . Linear extrapolation of  $\ln \hat{r}_k$  over  $1/h_{s,k}^2$  provides extrapolated failure rate  $r_e$  at some significant wave height  $h_s$  as  $\ln r_e = \sum_{k=1}^K b_k \ln \hat{r}_k$ , where coefficients  $b_k$ ,  $\sum_{k=1}^K b_k = 1$ , are obtained by e.g. least-squares method. To define the upper boundary of the 95%-confidence interval of the extrapolated failure rate, assume that confidence intervals are narrow compared to the maximum likelihood estimates (i.e. that  $N$  is sufficiently big) and use normal distribution approximation of  $\chi^2$ -distribution at big  $N$ ; linear combination of normal distributions gives.

$$r_{e,U} = r_e \cdot 0.5 \chi_{1-\alpha/2, 2N_e}^2 / N_e \quad (11)$$

where  $\alpha = 0.05$  and  $N_e$  is defined from  $1/N_e = \sum_{k=1}^K b_k^2 / N_k$ ; if all  $N_k$  are equal  $N$ , then  $N_e = N / \sum_{k=1}^K b_k^2$ .

To apply Eq. (11),  $N_e$  and all  $N_k$  should be sufficiently big (greater than 20). Note that  $\sum_{k=1}^K b_k^2$  is always greater than 1, therefore spreading of extrapolated values is always greater than spreading of the values used for extrapolation (which explains extreme spreading of extrapolated mean time to failure in Fig. 7 when  $N = 20$ :  $N_e$  for these cases is very small).

In examples in Fig. 8 for loading condition LC01 of the 14,000 TEU container ship in irregular short-crested beam and head waves, Eq. (10) used estimates  $\hat{r}_k$  obtained after 200 simulated failures at 1.0 m step of significant wave heights  $h_{s,k}$ ; extrapolated failure rate  $r_e$  was obtained with least-squares method. The figure shows maximum likelihood estimates  $\hat{r}_k$  obtained by simulations, extrapolated (over three or four points) failure rate  $r_e$  and the upper boundary of the 95%-confidence interval of failure rate versus  $1/h_s^2$ ; note widening of the confidence interval of extrapolated

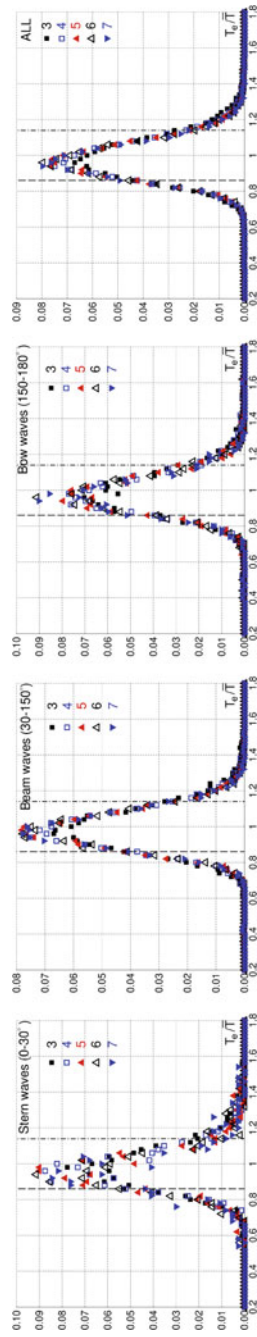


**Fig. 7** Number of cases normalized on 1 of ratio  $T_c/\bar{T}$  in (from left to right) stern, beam, bow and all wave directions; symbols differentiate number of points used for extrapolation

**Table 2** Percentage of extrapolated values of mean time to stability failure within 95%-confidence interval of its directly computed estimate

Number of significant wave heights used in extrapolation	3	4	5	6	7	8	9	10
Wave directions 0°–30°	79	82	81	79	76	78	76	68
Wave directions 30°–150°	77	82	83	84	84	84	82	78
Wave directions 150°–180°	79	83	85	84	83	81	78	81
All wave directions	77	81	82	83	82	81	79	75

failure rate with decreasing  $h_s$ . Example in Fig. 9 shows distribution of stability failure rate in head waves. Above the dashed black line, simulation time  $3.4 \times 10^6$  h was enough to encounter 200 stability failures, and the maximum likelihood estimate of stability failure rate and the upper boundary of its 95%-confidence interval were directly calculated using Eqs. (7) and (8), respectively; below this line extrapolation over significant wave height (10) was used.

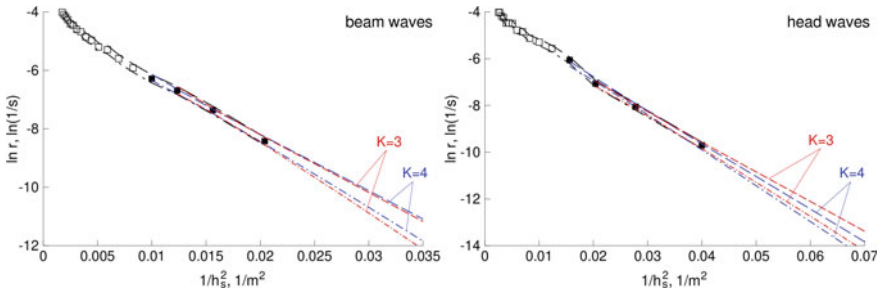


**Fig. 8** Examples of extrapolation of stability failure rate over significant wave height in beam (left) and head (right) waves: maximum likelihood estimate of failure rate suitable (■) and not suitable (□) for extrapolation and upper (dashed) and lower (dash-dot) boundaries of 95%-confidence interval

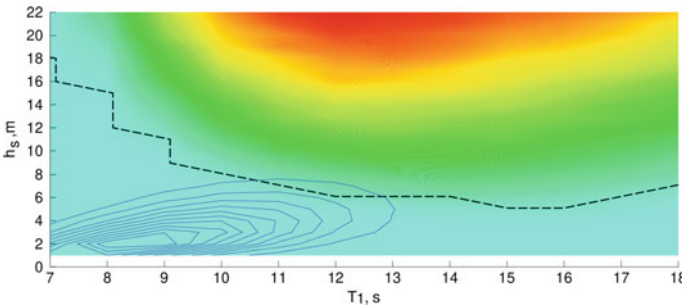


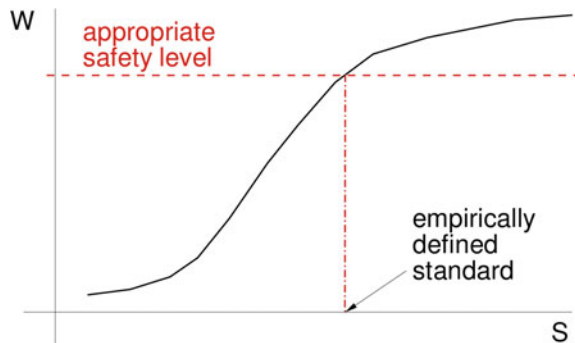
**Fig. 9** Stability failure rate (colours) and probability density of sea states (contours) versus mean wave period (x axis) and significant wave height (y axis)

## 4 Design Situations

Definition of the average “long-term” stability failure rate requires summation of “short-term” failure rates over all contributing sea states, wave directions and ship speeds. For 6 forward speeds and a  $10^0$ -step of mean seaway directions, the number of “short-term” conditions is about  $10^4$ , which means significant simulation time. [13] proposes to reduce assessment to few selected combinations of sea state (wave height and period) and sailing (ship speed and relative mean wave direction) parameters, called *design situations*. The idea is that any criterion  $s$ , Fig. 10, e.g. a criterion based on the assessment in few design situations, can be used if its relation to the true “long-term” probability of stability failure  $w$  (a) is monotonic and (b) shows insignificant scatter between ships, loading conditions and forward speeds. If it is proven that conditions (a) and (b) are satisfied, both the long-term probability of stability failure  $w$  and the dependency  $w(s)$  are not required in the practical approval since the criterion  $s$  can be used directly; the acceptance standard can be defined directly for the criterion  $s$  using a sufficient number of representative case studies, accident investigations etc.

As design situations, [13] proposes sea states covering full range of wave periods, one significant wave height per wave period (per steepness table of MSC.1/Circ.1200) and three wave directions (head, beam and following); failure rates are summed with weights equal to the occurrence frequencies of wave periods. The resulting dependencies  $w(s)$  are approximately monotonic but show significant scatter between ships, loading conditions and forward speeds, thus it is proposed to use different design situations for different stability failure modes. Shigunov [14, 15] applies this idea to roll in beam sea for the ships and loading conditions in Table 1. Different forward speeds are evaluated separately to check whether dependency  $w(s)$  shows scatter between cases with different roll damping. A range of wave periods is used and one significant wave height per wave period, selected according to (1) steepness table from MSC.1/Circ.1200, (2) constant steepness lines  $h_s T_z^2$ , (3) lines of constant density  $f_s$  of seaway occurrence probability, (4) lines of constant normed quantiles  $p_s^*$ , defined, for each  $T_z$ , as cumulative probability of sea states with  $h_s$  above

**Fig. 10** Idea of criterion  $s$  ( $w$  is “true” safety measure, e.g. long-term probability of stability failure)





considered, and (5) lines of constant quantiles  $p_s^{**}$ , defined as  $p_s^*$  values divided by the probability of occurrence of wave period  $T_z$ . As criterion, product  $r \cdot f_s$  is used in sea states (1) and (2) and  $r$  in sea states (3), (4) and (5), where  $r$  is the “short-term” stability failure rate. Sum and maximum of the criterion over design sea states are compared. The best correlation of criterion  $s$  with the average “long-term” failure rate in beam waves  $w$  is achieved using lines of constant probability density of sea state occurrence; using lines of constant quantiles leads to a poorer correlation; yet poorer correlation is achieved using the steepness line of MSC.1/Circ.1200, and the worst correlation corresponds to lines of constant wave steepness. The accuracy of all criteria  $s$  improves with increasing steepness of design sea states. In all cases, criteria defined as a sum over design sea states perform very similar to those defined as the maximum over design sea states.

Here, this idea is extended on all wave directions;  $180^\circ$ ,  $0^\circ$  and  $90^\circ$  are proposed for design situations to address parametric roll in bow and stern waves and synchronous roll in beam waves, respectively. The same approaches to selection of sea states for design situations as in Shigunov [14, 15] are compared; the results confirm that sea states selected along the lines of constant probability density of sea state occurrence provide the best correlation between  $w$  and  $s$  (here only these results are shown). Following the results of Shigunov [14, 15], maximum stability failure rate over design sea states is used as the criterion  $s$ . In the first step, assessment is done separately for each forward speed. To verify conditions (a) and (b), the average “long-term” stability failure rate  $w$  is computed separately for wave directions from  $150$  to  $180$ ,  $0$  to  $30$  and  $60$  to  $120^\circ$  to include dominating contributions from parametric resonance in bow and stern waves and synchronous resonance in beam waves, respectively. For each sea state, mean wave direction and ship speed, the failure rate was defined after encountering 200 failures.

Figure 11 shows the average “long-term” stability failure rate  $w$  versus maximum over design sea states failure rate  $s$  in design sea states with probability density  $10^{-6}$ ,  $10^{-5}$  and  $10^{-4}$   $(\text{m s})^{-1}$ ; each point corresponds to one ship, loading condition and forward speed. Sharp monotonic dependencies indicate that the accuracy of the criterion  $s$  is satisfactory and improves with increasing wave steepness.

Further reduction can be achieved by minimising the number of speeds used in design situations. For dead ship condition and excessive accelerations, only zero forward speed is used anyway; to select speed for design situations addressing parametric roll in bow waves, Fig. 12 (left) shows failure rate (maximum over wave periods) in head waves in sea states with probability density  $10^{-5}$   $(\text{m s})^{-1}$  versus Froude number.

For loading conditions with high failure rate, it decreases with increasing speed due to, first, broadening of the encounter wave energy spectrum and, second, increasing roll damping with increasing forward speed. For RoPax vessel in all loading conditions and cruise vessel in two loading conditions with the largest  $GM$ , failure rate increases with increasing forward speed, but it is very small for these cases. Thus, it is possible to use only zero (or as low as practicable) forward speed in design situations addressing parametric roll in bow waves. For parametric roll in stern waves, Fig. 12 (right) shows a more complex dependency of failure rate

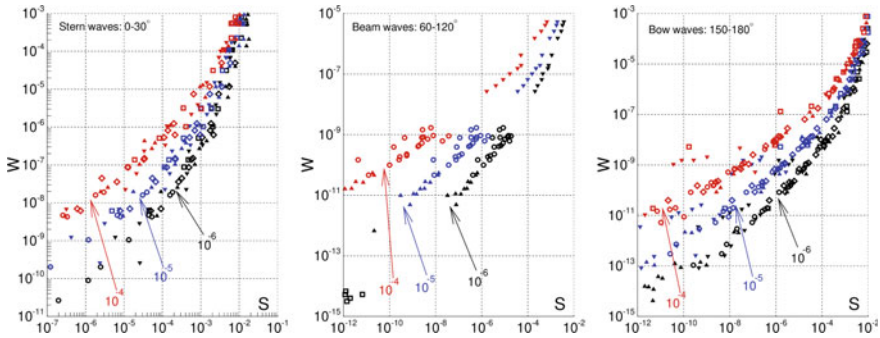


**Fig. 11** Average “long-term” stability failure rate  $w$ , 1/s, y axis, in wave directions from 0 to 30 (left), 60 to 120 (middle) and 150 to 180 (right) degrees versus criterion  $s$ , 1/s, x axis—“short-term” stability failure rate in following (left), beam (middle) and head (right) waves, maximum over design sea states with probability density  $f_s = 10^{-6}, 10^{-5}$  and  $10^{-4} \text{ (m s)}^{-1}$

on Froude number in design sea states in following waves, due to more complex behaviour of the encounter wave spectrum in stern waves. However, in all cases with big failure rate, assessment at zero speed will either be conservative or not introduce non-conservative error, i.e. zero (or as low as practicable) forward speed is appropriate also to address parametric roll in stern waves.

Although zero forward speed is impossible in high head or following waves for ships with usual steering system because of their inability to keep course, this assumption seems acceptable as a practical conservative simplification for the assessment of roll motion.

The acceptance standard for the average “long-term” stability failure rate is  $2.6 \times 10^{-8} \text{ 1/s}$ , [4]. From Fig. 11 and not shown results for design sea states with  $f_s = 10^{-7} \text{ (m s)}^{-1}$ , the corresponding threshold for the failure rate  $s$  in design situations is one failure in 20 h, 2 h, 40 min and 15 min in design sea states with  $f_s = 10^{-4}, 10^{-5}, 10^{-6}$  and  $10^{-7} \text{ (m s)}^{-1}$ , respectively. However, failure rate exceeding one failure in 2 h leads to violation of Poisson process assumption for parametric roll, which excludes design sea states with  $f_s \leq 10^{-6} \text{ (m s)}^{-1}$ ; besides, such sea states may be too steep to realise. Since required simulation time quickly reduces with increasing wave height, a logical choice is to use design sea states with the occurrence probability density  $10^{-5} \text{ (m s)}^{-1}$  and corresponding threshold of one failure in 2 h, as implemented in [4].

The assessment consists of running simulations in multiple independent realisations of design sea states, updating number of failures  $N$ , total simulation time  $t_t$ , estimate  $\hat{r} = N/t_t$  and estimate  $r_U$ , Eq. (9), after each simulation; once  $r_U$  is below acceptance threshold, simulations are stopped and loading condition is accepted in the considered design situation. Similarly, once the lower boundary  $r_L$  of the 95%-confidence interval of the failure rate exceeds the threshold in at least one design situation, simulations are stopped and loading condition is considered as unacceptable. In examples for the 1700 TEU container ship in loading conditions with  $GM =$

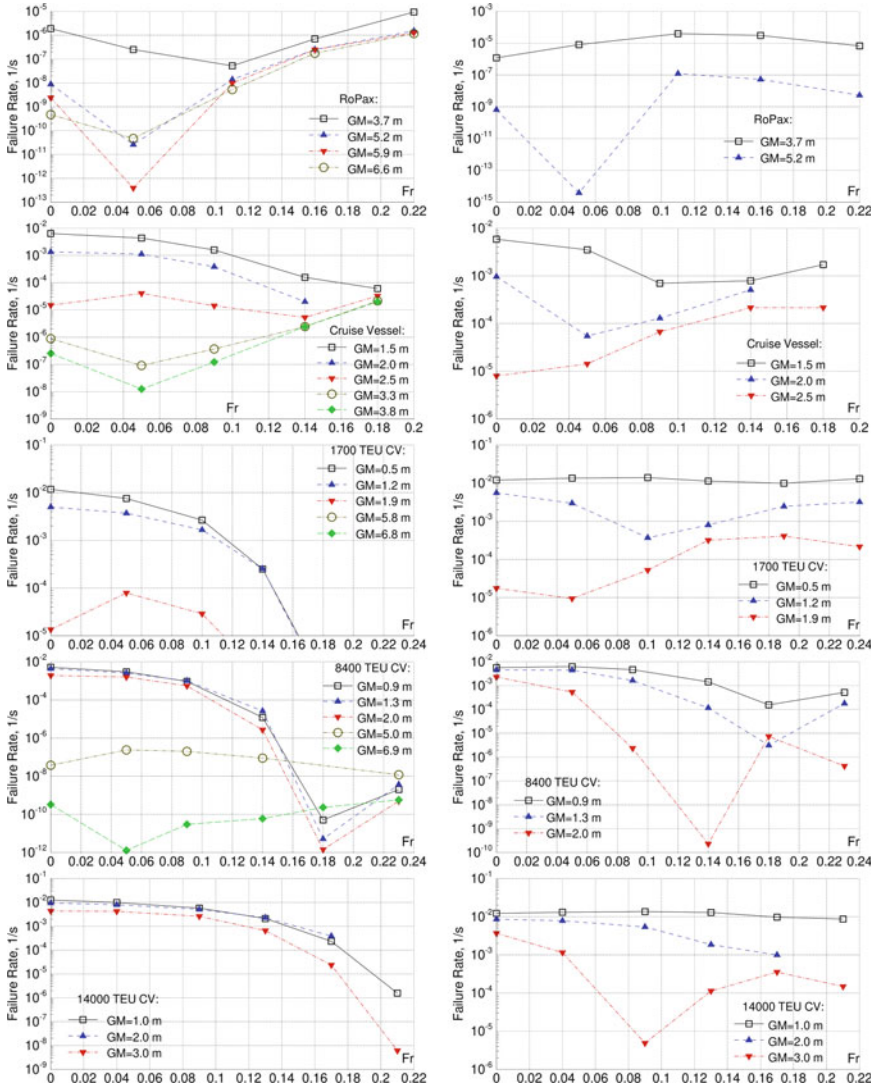


**Fig. 12** Maximum over wave period stability failure rate  $\hat{r}$ , 1/s, at wave height corresponding to sea state probability density  $10^{-5} \text{ (m s)}^{-1}$  (y axis) versus Froude number (x axis) in head (left) and following (right) waves for (from top to bottom) RoPax, cruise vessel and 1700, 8400 and 14,000 TEU container ships (one line per loading condition)

1.7, 1.8, ..., 2.2 m, Fig. 13, acceptance  $r_U < \lambda$  and unacceptance  $r_L > \lambda$  conditions are written as  $\hat{r} < 2N\lambda/\chi_{1-0.05/2,2N}^2$  and  $\hat{r} > 2N\lambda/\chi_{0.05/2,2N}^2$ , respectively, Eq. (9);  $\lambda = 1.389 \times 10^{-4} \text{ 1/s}$  (1 failure in 2 h) is the acceptance threshold. For each loading condition, results for only one  $T_z$  are shown, corresponding to maximum  $\hat{r}$ . Many simulations are required only in one case (following waves at  $GM = 1.9 \text{ m}$ ). Note

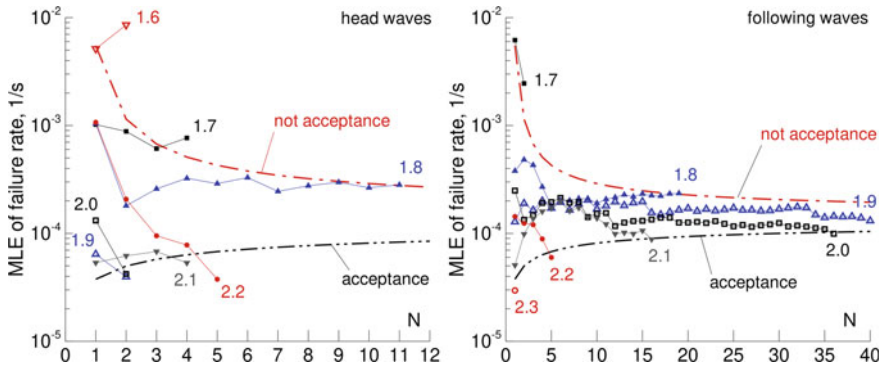


**Fig. 13** Maximum likelihood estimate  $\hat{r}$  of failure rate versus number of simulated failures together with acceptance  $2N\lambda/\chi^2_{1-0.05/2,2N}$  and not acceptance  $2N\lambda/\chi^2_{0.05/2,2N}$  boundaries in head (left) and following (right) waves; values at ends of lines indicate  $GM$

that it is not always necessary to wait until the end of a simulation: rewriting Eq. (6) as  $\bar{T} = \bar{T}_{N-1}(1 - 1/N) + T_N/N$ , where  $\bar{T}_{N-1}$  is the sample mean time to failure after  $N - 1$  failures and assuming, conservatively,  $T_N = t$  yields that a simulation can be stopped with acceptance before failure  $N$  when simulation time achieves  $0.5\chi^2_{1-\alpha/2,2N}/\lambda - (N - 1)\bar{T}_{N-1}$ .

## 5 Conclusions

Direct stability assessment requires that stability failures are encountered in numerical simulations, which requires significant computational time since stability failures are very rare in practically relevant cases. Assuming that stability failures are independent and thus can be described as a Poisson processes reduces the problem to the definition of one parameter, stability failure rate, in all situations (combinations of sea state, ship speed and relative wave direction) encountered in operation; since the estimate of stability failure rate obtained from numerical simulations is a random variable subject to statistical uncertainty, the upper boundary of the 95%-confidence interval of the stability failure rate is used as the criterion. For sufficiently big number of simulated stability failures, central limit theorem can be used to define this upper boundary; another possibility, applicable at any number of encountered stability failures, is to use the confidence interval of the rate parameter of exponential distribution.

To ensure independence of stability failures in numerical simulations, care is required to neutralize self-repetition effects, transient effects after the start of simulations and autocorrelation of big roll motions. A solution against self-repetition effects is to generate multiple independent realisations of the sea state and simulate ship motions in each such realisation for a limited time. Maximum duration

of simulations (for a given discretisation of the wave energy spectrum), possible without self-repetition of modelled irregular waves have been well studied so far; here the self-repetition of roll motion was studied. The results show that the absence of self-repetition of waves does not guarantee the absence of self-repetition of roll motion due to the narrow-banded nature of roll excitation: the discretisation of the wave energy spectrum may be sufficient for the reconstruction of irregular waves, but the narrow frequency range relevant for the excitation of excessive roll motion may still contain too few components, which leads to self-repetition of roll. Since self-repetition leads to over-estimation of the time to failure (i.e. a non-conservative error), this effect is critical in assessment for regulatory approval.

If self-repetition, transient effects and autocorrelation of big roll motions are neutralized, a Poisson process can be assumed, however, only if the stability failure rate is not too high: for parametric resonance, the results marginally disagree with the Poisson process assumption when the mean time to failure is about 2 h and increasingly with this time decreasing below 2 h.

The Poisson process approximation significantly simplifies assessment but still requires that stability failures are encountered in numerical simulations; two other simplifications are the *extrapolation of stability failure rate over wave height* and the reduction of the number of situations in the assessment to few *design situations*. The extrapolation of failure rate over wave height is based on the approximation of the logarithm of the failure rate as a linear function of the inverse significant wave height squared, so that the failure rate can be defined in numerical simulations at large significant wave heights (when it is large) and extrapolated to lower significant wave heights; however, only such results can be used for extrapolation for which the logarithm of the mean time to failure exceeds 6, otherwise the extrapolation can lead to over-estimation of the mean time to failure, i.e. non-conservative results. Besides, the estimates of the failure rate used for extrapolation should be based on a sufficiently big number of simulated failures since the extrapolation increases random spreading of extrapolated values compared to the spreading of the values used for extrapolation. The results prove the extrapolation of stability failure rate over significant wave height as a useful and sufficiently accurate method to estimate the failure rate in cases where it cannot be computed otherwise. Besides, it provides, at acceptable computational time, failure rate for all sea states encountered in operation, thus results can be directly used as operational guidance.

In the design situations method, assessment is performed in few selected *design situations*. As sea states for the design situations, full range of the wave periods and one significant wave height per wave period are proposed. Sea states along lines of constant probability density of sea state occurrence lead to the best correlation of assessment results with the long-term safety level, and the accuracy improves with increasing steepness of design sea states (however, since failure rate exceeding one failure in 2 h leads to violation of Poisson process assumption for parametric roll, too steep design sea states cannot be used, therefore, design sea states with the probability density  $10^{-5} \text{ (m s)}^{-1}$  are selected).

Regarding wave directions, the results show that it is sufficiently to use  $180^\circ$ ,  $0^\circ$  and  $90^\circ$  to address parametric roll in bow and stern waves and synchronous roll in beam waves, respectively.

Further reduction can be achieved by minimising the number of speeds used in design situations. For dead ship condition and excessive accelerations, only zero forward speed is used anyway; for parametric roll in bow waves, maximum over wave periods failure rate decreases with increasing speed for loading conditions with high failure rate, i.e. it is possible to use only zero (or as low as practicable) forward speed in design situations. For parametric roll in stern waves, the dependency of failure rate on forward speed is more complex, however, in all cases with big failure rate, assessment at zero speed will either be conservative or not introduce non-conservative error, i.e. zero (or as low as practicable) forward speed is also appropriate (note that although zero forward speed is impossible in high head or following waves for ships with usual steering system because of their inability to keep course, this assumption is acceptable as a practical conservative simplification for the assessment of roll motion).

Assessment examples for a container ship in 6 loading conditions (with  $GM$  varied every 0.1 m) show that apart from one (close to the acceptance boundary) loading condition, acceptance or unacceptance requires few simulations. Thus, the design situations method significantly reduces required simulation time (by an order of magnitude compared to the extrapolation method). Although results cannot be used as operational guidance, such assessment efficiently identifies those loading conditions which may require development of the operational guidance.

## References

1. Belenky VL (2011) On self-repeating effect in reconstruction of irregular waves, Chap. 33. In: Neves MAS, Belenky V, de Kat JO, Spyrou K, Umeda N (eds) Contemporary ideas on ship stability. Springer, Berlin, pp 589–598
2. Brunswig J, Pereira R, Kim D (2006) Validation of parametric roll motion predictions for a modern containership design. In: 9th international conference on stability of ships and ocean vehicles, Sao Paolo
3. IMO (2003) Information on a proposal of making the intact stability criteria mandatory, Paper SLF 46/INF.13 submitted by Germany
4. IMO (2020) Interim guidelines on the second-generation intact stability criteria, MSC.1/Circ.1627
5. Kröger H-P (1986) Rollsimulation von Schiffen im Seegang. Ship Technol Research Schiffstechnik 33(4):187–216
6. Longuet-Higgins MS (1952) On the statistical distribution of the heights of sea waves. J Marine Research
7. Petey F (1986) Forces and moments due to fluid motions in tanks and damaged compartments. In: Proceedings of STAB'86, pp 77–82
8. Petey F (1988) Ermittlung der Ketersicherheit lecker Schiffe im Seegang. Ship Technol Research Schiffstechnik 35(4):155–172
9. Ross SM (2009) Introduction to probability and statistics for engineers and scientists, 4th edn. Associated Press, p 267

10. Sevastianov NB (1963) On probabilistic approach to stability standards. Transactions of Kaliningrad Institute of Technology, vol. 18, Kaliningrad, pp 3–12 (in Russian)
11. Sevastianov NB (1994) An algorithm of probabilistic stability assessment and standards. In: Proceedings of 5th international conference on stability of ships and ocean vehicles, vol 5, Melbourne, Florida
12. Shigunov V, Moctar O, Rathje H (2009) On conditions of parametric rolling. In: 10th international conference on stability of ships and ocean vehicles, St.-Petersburg
13. Shigunov V (2016) Probabilistic direct stability assessment. In: 15th international ship stability workshop, 13–15 June, Stockholm, Sweden
14. Shigunov V (2017) Possible simplifications of direct stability assessment. In: 16th international ship stability workshop, 5–7 June, Belgrade, Serbia
15. Shigunov V (2017) Direct stability assessment: pragmatic solutions. Ship Technol Research Schiffstechnik 64(3):144–162
16. Shigunov V (2019) Direct counting method and its validation. In: 17th international ship stability workshop, 10–12 June, Helsinki, Finland, pp 119–128
17. Söding H, Shigunov V, Zorn T, Soukup P (2013) Method rolls for simulating roll motions of ships. Ship Technol Research Schiffstechnik 60(2)
18. Söding H (1982) Leckstabilität im Seegang, Report No. 429, Institut für Schiffbau, Hamburg
19. Söding H (1982) Gutachten über die Belastungen des Schiffes E.L.M.A. Tres durch Seegang am Vormittag des 26.11.1981, Note No. 2327, Institut für Schiffbau, Hamburg
20. Tonguč E, Söding H (1986) Computing capsizing frequencies of ships in seaway. In: 3rd international conference on stability of ships and ocean vehicles

# Regulatory Use of Nonlinear Dynamics: An Overview



William S. Peters, Vadim Belenky, and Kostas J. Spyrou

**Abstract** This chapter is focused on the physical background of the second level vulnerability criterion for surf-riding /broaching-to as a part of the IMO second generation intact stability criteria. The criterion is based on Nonlinear Dynamics, homoclinic bifurcation, in particular, and uses the Melnikov method for calculations. While well understood in the scientific community, these concepts may present a challenge for regulatory use since most practicing naval architects are not familiar with these concepts. The paper presents an explanation of the criterion background using conventional Naval Architecture physical concepts, and gives an overview of the dynamical aspects of the calculation procedure.

**Keywords** Surf-riding · Dynamical system · Equilibrium attraction

## 1 Introduction

Current development of the IMO second generation intact stability criteria brought a number of new problems and solutions that are not familiar to a practicing Naval Architect [6]. The reason is not as due to new physical phenomena of stability failures, but rather related to the fact that the new criteria are based on first principles. Thus, the new criteria have to rely on a mathematical model of the stability failure, the only input is hull geometry, propulsion and environment characteristics. Development experience has shown that one of the least familiar mathematical techniques is the Melnikov method [2, 5, 9] which is used in the second level vulnerability criteria for

---

W. S. Peters

US Coast Guard Office of Design and Engineering Standards, Washington, DC, USA  
e-mail: [william.s.peters@uscg.mil](mailto:william.s.peters@uscg.mil)

V. Belenky (✉)

David Taylor Model Basin (NSWCCD), West Bethesda, MD, USA  
e-mail: [vadim.belenky@navy.mil](mailto:vadim.belenky@navy.mil)

K. J. Spyrou

School of Naval Architecture, National Technical University of Athens, Athens, Greece  
e-mail: [spyrou@deslab.ntua.gr](mailto:spyrou@deslab.ntua.gr)



surf-riding and broaching-to [1, 3]. The objective of this text is to bring this subject to the attention of the expert community, as the regulatory use of this technique requires an explanation accessible for the practicing naval architect.

## 2 The Description of the Failure Model

### 2.1 General

Broaching-to is a violent uncontrollable turn, which occurs despite the application of a maximum effort to steer in the opposite direction. As with any other sharp turn event, broaching-to is frequently accompanied with a large heel angle, which may lead to partial or total stability failure. Broaching-to occurs in following and stern-quartering seas and it is usually preceded by surf-riding. Surf-riding occurs when a wave, which approaches from the stern of a ship, captures that ship and accelerates it to the speed of the wave profile, which is also referred to as the wave celerity. While surf-riding, the wave profile does not move in relation to the ship. Most ships are directionally unstable in a surf-riding scenario. This leads to the uncontrollable turn, which is defined as broaching-to (or often, just “broaching”). Therefore, the likelihood of surf-riding can be used to formulate the vulnerability criteria for broaching-to.

### 2.2 Surf-Riding Equilibria

When a ship sails in longitudinal waves, three main forces act in the longitudinal direction: thrust, resistance and a surging wave force. Since the surf-riding occurs when the ship speed is equal to the wave celerity, locating the frame of reference on the wave crest is appropriate. As the frame of reference moves with the wave, the ship remains unmovable in this frame of reference while the ship surf-rides.

For most practical cases, the surf-riding phenomenon is associated with the acceleration of a ship to the wave celerity. Thus, the thrust is not sufficient to provide a ship speed equal to the wave celerity in calm water. Consider the difference between the thrust and ship resistance in calm water within the accepted frame of reference; since the resistance is greater than the thrust, this difference is negative.

The value of the wave force depends on the location of the ship on the wave. The front slope of the wave pushes a ship forward and the back slope of the wave pushes in the opposite direction. As a result, there are neutral points around the wave crest and wave trough. If the wave is sufficiently long and steep, the pushing action of the wave force is sufficient to compensate the negative balance between thrust and resistance and create two equilibria. See Fig. 1 in which the wave force, with opposite sign, is shown for different positions of a ship on a wave.

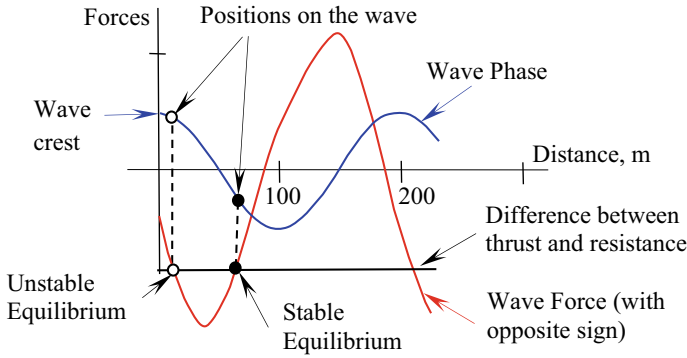


**Fig. 1** Wave forces and balance between thrust and resistance shown for different positions of a ship on a wave

Superimposed with the difference between thrust and resistance, the crossings with the wave force mark the position of two equilibria along the wave. It is noted that the difference between thrust and resistance is referred to as “balance between thrust and resistance” in some literature, e.g. [1], however, this term is not used here.

### 3 Mathematical Model of Ship Motions

#### 3.1 Mathematical Model of Resistance and Propulsion

Given the wave parameters (length and height), calculating the position of these equilibria does not extend beyond conventional naval architecture calculations. The first element needed is the approximation of the calm water resistance, which can be accomplished using a cubic polynomial:

$$R(V_S) = r_1 V_S + r_2 V_S^2 + r_3 V_S^3, \tag{1}$$

where  $V_S$  is ship speed in m/s, while  $r_1$ ,  $r_2$  and  $r_3$  are curve-fitting coefficients. Curve fitting is a standard operation, which is readily available from a number of software packages, including Microsoft Excel. This approximation of the calm water resistance is sufficient for a surf-riding assessment to get approximate fit around the self-propulsion point, such starting from around one-half of the service speed, see Fig. 2.

The second element needed is the effective thrust in calm water as a function of the thrust commanded of the propulsor, which is typically given in reference to propeller revolution rate  $n$  and  $V_S$  is ship speed in m/s:

$$T_e(V_S, n) = \tau_0 n^2 + \tau_1 V_S n + \tau_2 V_S^2. \tag{2}$$

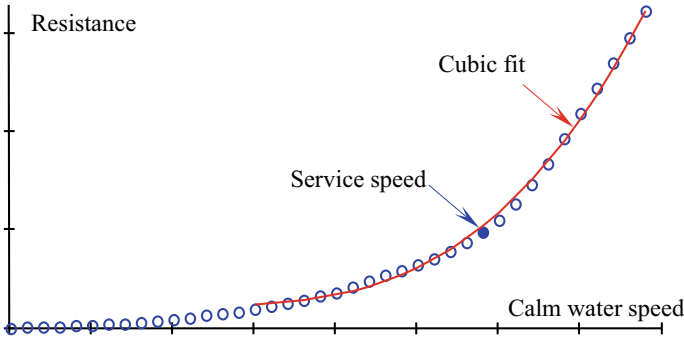


**Fig. 2** Cubic approximation of resistance

The coefficients  $\tau_0$ ,  $\tau_1$ ,  $\tau_2$  for thrust are defined as:

$$\tau_0 = c_0(1 - t_p)\rho D_p^4, \quad (3)$$

$$\tau_1 = c_1(1 - t_p)(1 - w_p)\rho D_p^3, \quad (4)$$

$$\tau_2 = c_2(1 - t_p)(1 - w_p)^2\rho D_p^2, \quad (5)$$

where,  $t_p$  is the coefficient for thrust deduction, while  $w_p$  is the wake fraction. Both coefficients are evaluated for calm water.  $D_p$  is the propeller diameter and  $\rho$  is mass density of water. The coefficients  $c_0$ ,  $c_1$ ,  $c_2$  are obtained from the polynomial presentation of the coefficient of thrust  $K_T$ :

$$K_T = c_0 + c_1J + c_2J^2, \quad (6)$$

where  $J$  is the advance ratio:

$$J = \frac{V_S(1 - w_p)}{nD_p}. \quad (7)$$

Thrust and resistance are plotted in Fig. 3. As expected, the curves cross at the self-propulsion point in calm water corresponding to the commanded thrust—i.e., the set speed. Figure 3 also shows the difference between thrust and resistance at the speed corresponding to the wave celerity.

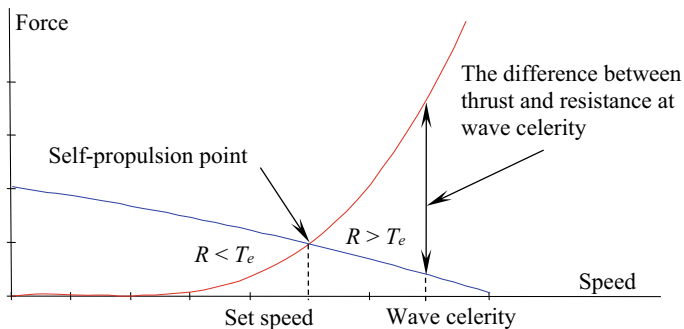


**Fig. 3** Resistance and propulsion showing the self-propulsion point and the thrust-resistance difference at the speed corresponding to the wave celerity

### 3.2 Mathematical Model of Wave Surging Force

The surging wave force is a result of the projection of the wave pressure on the longitudinal axis. When a ship is moving in waves, the wave pressure is usually influenced by the presence of the ship. The ship generates waves because of its motions and these waves radiate from the ship and interfere with incoming waves. Also, the waves that reach the ship, will be reflected from the ship as from any other obstacle (diffraction). These reflected (or diffracted) waves will also interfere with incoming waves which change the wave pressure on the hull.

However, when considering surf-riding, the ship speed is assumed to be close to wave celerity. Thus, the encounter frequency is close to zero, and no significant ship motions can be expected. Hence, the influence of radiated waves cannot be significant either. If an obstacle moves with a wave, the reflection is going to be weak. Thus, both diffraction and radiation wave forces can be assumed to be negligibly small, and, can be excluded from consideration.

This simplifies the problem for assessing the forces acting in surf-riding. An integration of the pressures along the hull when the ship is on a longitudinal wave leads to the following formula for the wave surging force:

$$F_w(\xi_G) = -\rho g k_W \zeta_{WA} (A_S \sin(k_W \xi_G) - A_C \cos(k_W \xi_G)), \quad (8)$$

where  $\rho$  is the density of water;  $g$  is gravity acceleration;  $\zeta_{WA}$  is the amplitude of the wave,  $\xi_G$  is the position of a ship on the wave; and  $k_W$  is the wave number, also known as the spatial frequency of a wave of length  $\lambda_W$ :

$$\lambda_W = \frac{2\pi}{k_W}, \quad (9)$$

$A_S$  and  $A_C$  are sine and cosine amplitudes of the wave force, respectively

$$A_S = \int_{-0.5L}^{0.5L} S_{St}(x) \exp(-0.5k_W d(x)) \cos(k_W x) dx, \tag{10}$$

$$A_C = \int_{-0.5L}^{0.5L} S_{St}(x) \exp(-0.5k_W d(x)) \sin(k_W x) dx, \tag{11}$$

where  $S_{St}(x)$  is the area of submerged part of a station at a distance  $x$  from midship section, while  $d(x)$  is a draft of that station.

The amplitude of the surging wave force shown in Fig. 1 is calculated as:

$$A_F = \rho g k_W \zeta_{WA} \sqrt{A_S^2 + A_C^2}. \tag{12}$$

Usually, the value  $A_S$  is about 10 times larger than  $A_C$  and, thus,  $A_C$  can be excluded from consideration of Eqs. (8) and (12).

## 4 The Physics Behind the Criterion

### 4.1 The Mechanics of Surging

The mechanics of surging can be illustrated using the curves of thrust and resistance. For this purpose, the consideration of a relatively small surging motion can be diagrammed as shown in Fig. 4. Here, the curves of thrust and resistance are not very different from the tangent lines plotted at the self-propulsion point in calm water.

In the case where the wave force pushes the ship forward, the ship continues motion in the same direction even when the wave force changes sign. Now both wave force and the difference between thrust and resistance pull the ship backwards relative to the wave. Eventually, the ship reverses direction and surges backward.

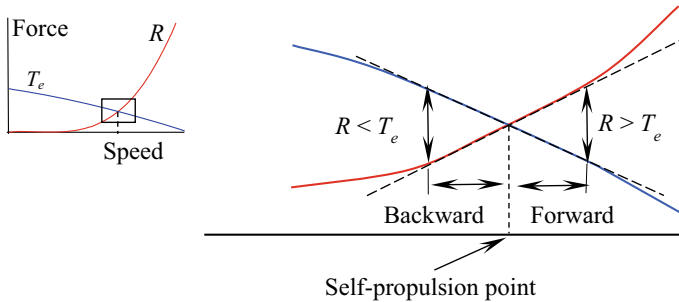


Fig. 4 Small surging motions around self-propulsion point

Once the self-propulsion point is passed the difference between the thrust and resistance changes sign and the surge starts to slow down. Then the surging force also changes direction and starts pushing the ship forward.

We now need to consider how the surging motion is stabilized, i.e. how the steady state amplitude is established.

One can consider the energy balance: the wave transfers to the ship some kinetic energy through the application of the wave force. The difference between thrust and resistance disperses this energy and the balance between the work of these forces establishes the amplitude of surge.

### 4.2 Stability of Surf-Riding Equilibrium

Surf-riding equilibria are referred to as stable and unstable in Fig. 1. The following is a description of these equilibria.

Consider a ship in a surf-riding mode and midship is located around 70 m forward of the wave crest (labeled as stable equilibria near the wave trough in Fig. 1). In addition, the ship has a speed that is equal to the wave celerity.

Let the ship be perturbed from this location forward, towards the wave trough. The surge force becomes smaller than the difference between thrust and resistance. The resistance pushes the ship back to the equilibrium, which is shown in Fig. 5.

Now, let the ship be perturbed from the equilibrium backwards, i.e. towards the wave crest. The wave force becomes larger than the difference between thrust and resistance. Thus, the ship will be pushed back to the surf-riding equilibrium (trough), see Fig. 6.

These simple considerations show that if a ship is perturbed from the equilibrium near the wave trough, a resultant force pushes it back to the equilibrium. Thus, the equilibrium near the wave trough is stable.

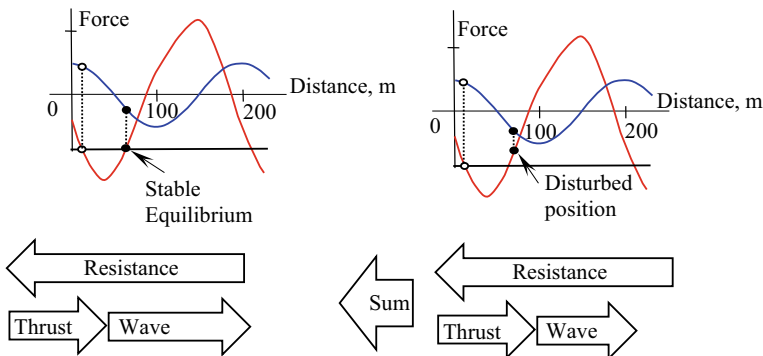
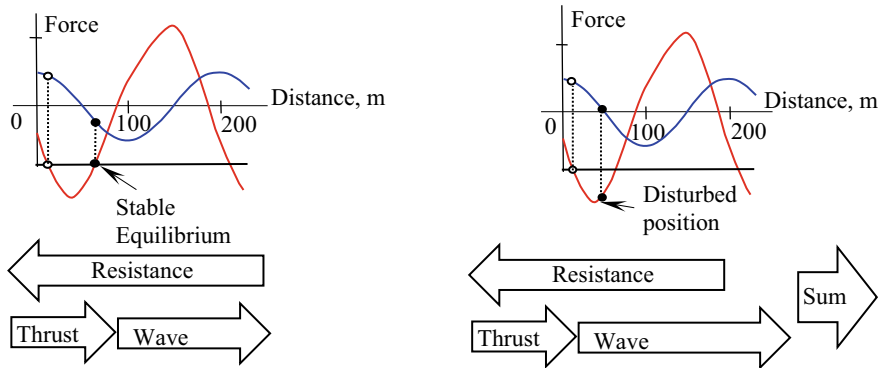


Fig. 5 Disturbance forward from the stable equilibrium



**Fig. 6** Disturbance backwards from the stable equilibrium

Consider a ship in a surf-riding mode that is located around 30 m forward of the wave crest (labeled as unstable equilibria near wave crest in Fig. 1) and has a speed equal to wave celerity.

If the ship is perturbed from this location forward, towards the wave trough, then the wave surging force increases. The ship will be pushed further forward until it ends up at the stable equilibrium near the wave trough, as shown in Fig. 7.

If the ship is perturbed from this location backward, towards the wave crest, then the wave force is decreased and the instantaneous speed also starts to decrease. The difference between thrust and resistance pulls the ship back and nothing keeps the wave from overtaking the ship. There are several scenarios that consider what may happen next (to be considered in the next subsection), but, the ship does not return back to the equilibrium, see Fig. 8.

These examples that if the ship is perturbed from the equilibrium near wave crest, a resultant force moves it away from that equilibrium. Thus, the equilibrium near the wave crest is unstable.

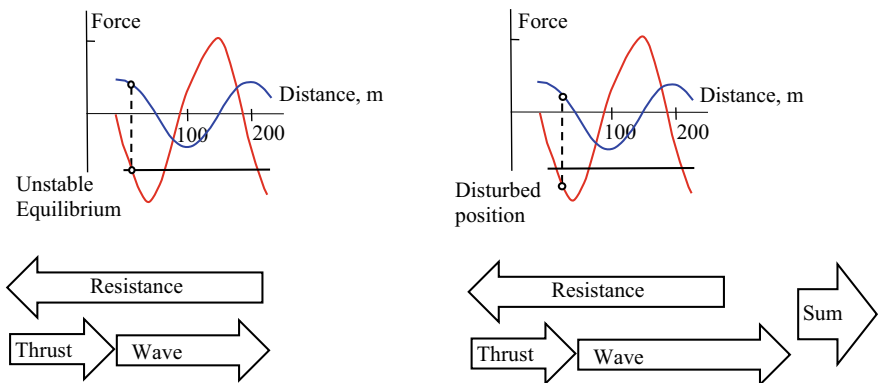


**Fig. 7** Disturbance forward from the unstable equilibrium

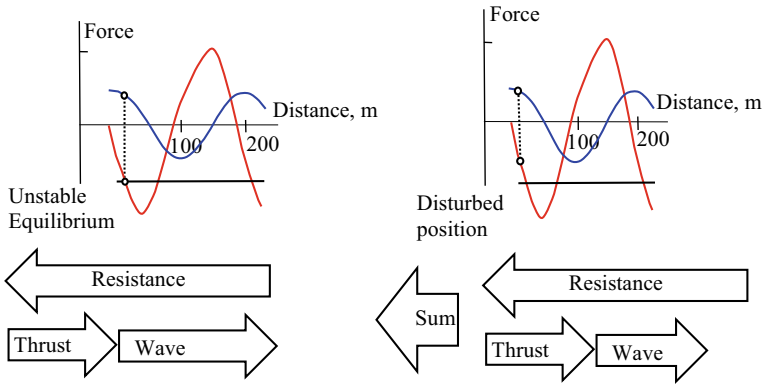


Fig. 8 Disturbance backwards from the unstable equilibrium

### 4.3 Attraction to Surf-Riding Equilibrium

If surf-riding equilibria do not exist, surf-riding is not possible and the ship will simply surge. That means that all the combinations of instantaneous speed and position on the wave lead to the same outcome i.e. it does not matter from where the motion has started.

However, once the equilibria points appear at certain positions on the wave, not all the combinations of the wave position and instantaneous speed lead to the same response.

If a ship is “placed” exactly at the location of the stable equilibrium near wave trough and accelerated to the wave celerity, then, the ship will stay there indefinitely. Any small perturbation from this position will return the ship back to equilibrium (see the discussion in the subsection 4.2). If a ship is in the unstable equilibrium near wave crest, accelerated to wave celerity, and perturbed towards the wave trough, then the ship will end up at the stable surf-riding equilibrium as well.

Thus, there is a set of combinations of wave positions and instantaneous speeds that will lead to surf-riding. These combinations form a “domain of attraction to surf-riding equilibrium.” Considering what happens to a ship when it is outside of this domain of interest.

For translating ship motions in the longitudinal direction, two options are possible: surging or surf-riding. Once the motions are outside of the attraction domain, the ship either continues to surge or is attracted to surf-riding equilibrium on another wave. How these options are determined is important.

Consider again the energy/work balance of the wave surging force and the difference between thrust and resistance. As discussed in the subsection 4.1, the latter disperses the kinetic energy obtained from wave. Once the balance between these two works is established, the ship’s response is surging. However, if a wave provides the ship with more kinetic energy than the difference between thrust and resistance can disperse, and then something other than surging occurs.



Eventually, this excessive kinetic energy leads to the acceleration of the ship and to an attraction to the surf-riding equilibrium. Surf-riding becomes a new energy balance between the works of wave surging force and the difference between thrust and resistance. In this sense, the ship is captured by the wave. Once the surf-riding equilibria appear, does surf-riding become inevitable and occur on one of the succeeding waves?

As was discussed in the beginning of this section, not all the combinations of position on the wave and instantaneous speed lead to the same result. The front slope of the wave provides more opportunities for surf-riding because the wave surging force is directed forward. If started on the back slope of the wave, the wave surging force is directed backward and the surging energy balance still may be achieved. Consequently, surging and surf-riding may co-exist for the same speed setting and wave parameters. How this can be explained?

If the initial energy level can be dispersed by the difference between thrust and resistance, surging will occur. If the initial energy level is too high (such as on front slope of the wave and/or high instantaneous speed) to be dispersed, surf-riding will occur.

If the wave adds too much kinetic energy (such as case of steep wave) to ship motions that it cannot be dispersed by the difference between thrust and resistance (when the commanded speed is too large), then surging motions are no longer possible. Even when starting with low initial energy level on the back slope of the wave and commanded speed, each sequential wave will add a bit of kinetic energy that cannot be dispersed. Subsequently, surf-riding will occur as the ship moves towards stable equilibrium.

#### ***4.4 Influence of the Commanded Speed***

The discussion in the subsection 4.3 led to the conclusion that if a ship cannot disperse kinetic energy by the difference between thrust and resistance, then surf-riding becomes inevitable. Thus, the commanded speed defines the surf-riding likelihood for the given wave parameters.

If the commanded speed is low, the difference between thrust and resistance (at the speed of wave celerity) is larger than the amplitude of the wave surging force, the intersection (in Fig. 1) does not exist, and surf-riding is impossible.

Increase of commanded speed leads to appearance of surf-riding equilibria (seen as the intersection in Fig. 1). Surf-riding may be possible for some combinations of wave position and instantaneous speed. Other combinations with lower initial energy levels can lead to surging as the difference between thrust and resistance is still capable of dispersing the additional energy. This is the case of co-existence of surging and surf-riding. The minimal commanded speed corresponding to appearance of the equilibria (i.e. leading to the difference between thrust and resistance equal to the amplitude of the wave surging force) is commonly referred as “the first threshold.”

Further increase of the commanded speed will eliminate the surging mode of motions, because the difference between the thrust and resistance becomes too small

to disperse the additional kinetic energy obtained from the wave surging force. Consequently, surf-riding becomes inevitable. The lowest commanded speed leading to inevitable surf-riding is commonly referred as “the second threshold.”

## 5 The Reasoning Behind the Criterion

### 5.1 Choice of the Criterion

Two thresholds described at the end of the Sect. 4 seem to be natural candidates for the criterion. Given the wave parameters, one can find the commanded speed corresponding to one of these thresholds. If a ship cannot attain this speed, there is no vulnerability for surf-riding and broaching-to. Therefore, a discussion of which threshold should be used for the criterion is appropriate.

Use of the first threshold seems to be more conservative as surf-riding is impossible for the commanded speed below it. However, a simple calculation with formulae (1), (2) and (12) show that the surf-riding equilibria may exist even for ships that have never been observed to surf-ride, such as bulk-carriers. Thus, the criterion based on the first threshold would lack the discriminating power to identify the ships vulnerable for broaching. Why?

Appearance of the surf-riding equilibria makes broaching possible, but requires a ship be placed into the domain of attraction to the stable surf-riding equilibrium. This domain is defined for combinations of wave positions and instantaneous speeds. So it is not enough for the ship to be on the front slope of the wave, but also needs to obtain an instantaneous speed close to the wave celerity. For example, for a ship of 180 m length and wave of the same length, the speed close to the wave celerity will be just above 30 knots. There is no real reason for a ship with the service speed of, say 18 knots, to be spontaneously accelerated up to 30 knots.

In contrast, the second threshold guarantees surf-riding for any ship that can achieve the speed above this threshold for a given wave. This gives the criterion its discriminatory power and this is the reason the second level vulnerability criterion is based on the second threshold.

### 5.2 Evaluation of the Criterion

Use of the criterion requires a way to calculate the commanded speed (setting of number of propeller revolutions or throttle setting) that corresponds to the second threshold. In principle, it can be performed by numerical simulations [1]. The Melnikov analysis provides a process that can be done quickly and easily [9].

Consider two or three sequential waves. Let's assume, one has found the boundaries of the domain of attraction to stable surf-riding equilibrium. If the commanded

speed is below the second threshold and allows co-existence of surging and surf-riding, the boundary of the attraction domains of sequential waves, must have some separation between them to lead to surging for certain combinations of position on a wave and instantaneous speed.

There is a class of mathematical models, known as Hamiltonians that provide analytical solutions for these boundaries. Unfortunately, they cannot be applied directly because they do not include any energy dispersion.

The Melnikov analysis is an asymptotic expansion, (similar to Taylor series) where the Hamiltonian is used as the first term. The influence of the energy dispersion terms is included in the higher order terms. This approach allows expressing the distance between the boundaries (Melnikov function, see [9] for its derivation) for a given commanded number of revolutions  $n$ :

$$M(n) = -2\pi \left( \frac{r(n)}{q} + \frac{4}{\pi} p_1(n) - 2p_2 + \frac{32}{3\pi} p_3 \right) \quad (13)$$

The terms in this equation have the following meaning:

$$r(n) = \frac{k_W(T_e(c_W, n) - R(c_W))}{m + A_{11}} \quad (14)$$

Here  $T_e(c_W, n)$  is the thrust at the speed equal to wave celerity  $c_W$ ,  $k_W$  is the wave number (spatial frequency, see formula 9),  $R(c_W)$  is the resistance at the speed equal to wave celerity  $c_W$ ,  $m$  is mass of the ship and  $A_{11}$  is the added mass of the ship computed for zero-frequency.

$$q = \frac{k_W A_F}{m + A_{11}} \quad (15)$$

The amplitude of the wave surging force,  $A_F$ , is defined by formula (12).

$$p_1(n) = \frac{3r_3 c_W^2 + 2(r_2 - \tau_2)c_W + r_1 - \tau_1 n}{\sqrt{k_w A_F (m + A_{11})}} \quad (16)$$

$$p_2 = \frac{3r_3 c_W + r_2 - \tau_2}{k_w (m + A_{11})} \quad (17)$$

$$p_3 = \frac{r_3 \sqrt{A_F}}{\sqrt{k_w^3 (m + A_{11})^3}} \quad (18)$$

The coefficient  $r$  and  $\tau$  are defined by formulae (1) through (5). The zero value of the Melnikov function approximately corresponds to a zero distance between the boundaries of the domains of attraction to stable surf-riding equilibrium for the sequential waves. The number of commanded revolutions is an approximation for the second threshold that was chosen as a criterion. To find the number of revolutions

corresponding to the second threshold, the Melnikov function (13) is presented as a quadratic equation. It always can be done because the modal of thrust (2) is the quadratic parabola relative to the number of revolutions:

$$an^2 + bn + c = 0 \tag{19}$$

$$a = \frac{\tau_0}{A_F} \tag{20}$$

$$b = \frac{\tau_1 c_W}{A_F} - \frac{4\tau_1}{\pi \sqrt{k_w A_F (m + A_{11})}} \tag{21}$$

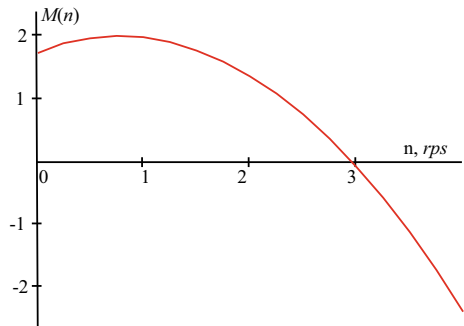
$$c = \frac{\tau_2 c_W^2 - R(c_W)}{A_F} - 4 \frac{3r_3 c_W^2 + 2(r_2 - \tau_2)c_W + r_1}{\pi \sqrt{k_w A_F (m + A_{11})}} - 2p_2 + \frac{32}{3\pi} p_3 \tag{22}$$

Sakai et al. [7] have shown that the Eq. (19) has two real solutions, one of them is always positive:

$$n = \frac{-b + \sqrt{b^2 - 4ac}}{2a}; b^2 \geq 4ac \tag{23}$$

The appearance of the Melnikov function (13) is given in Fig. 9. [4] have extended the Melnikov function for a general case of polynomial representation of resistance. Wu et al. [14] have generalized the method beyond a small damping assumption and theoretically validated the applicability of a small damping assumption for the criterion.

**Fig. 9** Appearance of Melnikov function



### 5.3 *Wave Parameters*

The calculation described in the subsection 5.2 is performed for a given set of wave parameters. A process by which these parameters should be chosen to reflect a realistic seaway is needed.

The idea is to approximate a realistic seaway as a series of regular waves with random lengths and heights. Then, the parameters of each wave become random numbers and can be obtained from known probability distributions. In principle, the final form of the criterion is probabilistic and is based on a critical wave/ wave group approach; see [11] and [12], whereas a model test to verify applicability was carried out by Umeda et al. [13].

## 6 Summary and Concluding Comments

This chapter is focused on dynamical aspects of the second level vulnerability criterion for surf-riding/broaching-to. The criterion is based on the commanded speed corresponding to the second threshold, exceedance of which makes surf-riding inevitable on a given wave. The appearance of such a threshold is associated with a phenomenon known in nonlinear dynamics as “homoclinic bifurcation” [8], see also [10]. However, the physical background can be explained without the vocabulary of nonlinear dynamics using physical concepts available in naval architecture.

The phenomenon of surf-riding is essentially the attraction to the surf-riding equilibrium created when the wave surging force is large enough to compensate for the difference of thrust at the commanded speed and resistance at the speed of the wave profile (wave celerity).

While surging, the difference between thrust and resistance disperses the additional kinetic energy obtained from the wave surging force. When the kinetic energy is too large or the difference between thrust and resistance is too small, the additional kinetic energy cannot be dispersed and the attraction to the surf-riding equilibrium becomes inevitable.

Calculation of the criterion, i.e. the commanded speed that leads to inevitable surf-riding on a given wave, can be calculated using the Melnikov method, which is an asymptotic expansion of an analytical solution of this problem. These calculations involve a numerical solution of an algebraic equation, which requires approximate resistance, propulsion and hull geometry data.

**Acknowledgements** The work described in this chapter has been funded by the Office of Design and Engineering Standards of the US Coast Guard (CG-ENG) under the guidance of Mr. Jaideep Sirkar and by the US Navy Office of Naval Research under Dr. Woei-Min Lin. The authors are also grateful to Dr. Arthur Reed of the David Taylor Model Basin and Prof. Naoya Umeda of Osaka University for fruitful discussions.

## References

1. Belenky V, Bassler CC, Spyrou KJ (2011) Development of Second generation intact stability criteria, Hydromechanics Department Report, Naval Surface Warfare Center Carderock Division, West Bethesda, Maryland, USA, NSWCCD-50-TR-2011/065
2. Guckenheimer J, Holmes PJ (1983) Nonlinear oscillations, dynamical systems and bifurcations of vector fields. Springer, Berlin
3. IMO SLF 54/3/3 (2011) Summary of research into stability failures modes and associated criteria development, London
4. Maki A, Umeda N, Renilson M, Ueta T (2010) Analytical formulae for predicting the surf-riding threshold for a ship in following seas. *J Mar Sci Technol* 15(3):218–229
5. Melnikov VK (1963) On the stability of a center for time-periodic perturbations. *Trans Moscow Math Soc* 12:3–52 (in Russian)
6. Peters WV, Bassler BC, Spyrou K, Umeda N, Bulian G, Altmayer B (2011) The second generation of intact stability criteria an overview of development. *Trans SNAME* 119:225–264
7. Sakai M, Maki A, Murakami T, Umeda N (2017) Analytical solution of critical speed for surf-riding in the light of melnikov analysis. *Proc Conf Jpn Soc Naval Architects Ocean Eng* 24:311–314
8. Spyrou KJ (1995) Dynamic instability in quartering seas: the behavior of a ship during broaching. *J Ship Res* 40(1):46–59
9. Spyrou KJ (2006) Asymmetric surging of ships in following seas and its repercussions for safety. *Nonlinear Dyn* 43:149–172
10. Spyrou KJ (2017) Homoclinic phenomena in ship motions. *J Ship Res* 61(3):107–130
11. Themelis N, Spyrou KJ (2007) Probabilistic assessment of ship stability. *SNAME Trans* 115:181–206
12. Umeda N, Shuto M, Maki A (2007) Theoretical prediction of broaching probability for a ship in irregular astern seas. In: *Proceedings of the 9th international ship stability workshop, Hamburg, Germany*, pp 1.5.1–1.5.7
13. Umeda N, Usada S, Mizumoto K, Matsuda A (2016) Broaching probability for a ship in irregular stern-quartering waves: theoretical prediction and experimental validation. *J Mar Sci Technol* 21:23–37
14. Wu W, Spyrou KJ, McCue L (2010) Improved prediction of the threshold of surf-riding of a ship in steep following seas. *Ocean Eng* 37:1103–1110

# **History of Stability Criteria**

# Rahola Criterion and the Development of the Intact Stability Code



Alberto Francescutto

**Abstract** The Criterion for Intact Ship Stability proposed by Rahola (The judging of the stability of ships and the determination of the minimum amount of stability—especially considering the vessels navigating Finnish waters, Doctoral thesis 1939) spread around different countries after the World War. It constituted the basis for the first international provision on intact stability adopted in 1968 in the frame of the recently created International Maritime Organization. This Criterion, although heavily criticized since the beginning for its semi-empirical nature, was included in both the Intact Stability Code, IMO Res. A. 749 and, with some modifications, got mandatory status in the International Intact Stability Code 2008. It is quite easy to foresee that it will survive in the near future too, at least until the Second Generation Intact Stability Criteria, recently approved as Interim Guidelines, will undergo thorough testing and tuning.

**Keywords** Ship stability · Stability criteria · IMCO · IMO · Jaakko Rahola

## 1 Introduction

Considering the last two millennia, from Archimedes [7], or more realistically the last two hundred years, from [3], it is clear that Ship Stability is an extremely complex and at the same time controversial subject.

Historical summaries of the developments at scientific, practical and regulatory levels have been provided by several Authors [1, 9, 25, 26, 32, 37] and, more recently reviewed by Francescutto [6] in the frame of the development of the Second Generation Intact Stability Criteria in progress at IMO. There is a clear progress in terms of comprehension of the dangerous phenomena; this, however for long time was not accompanied by a parallel progress at regulatory level. This is particularly true for what concerns Intact Stability, the issue discussed in this paper. The different role played by the different parties and the request to be “simple”, indeed, delayed the

---

A. Francescutto (✉)  
University of Trieste, Trieste, Italy  
e-mail: [francesc@units.it](mailto:francesc@units.it)



practical application [4]. If this was justified when calculations were made “by hand”, it is becoming less and less justified now, especially if we think that the developed regulations should guarantee the safety of ships carrying the population of a small town or substances able to heavily contaminate the environment. The length of time required to pass from formulation of a stability problem to adoption of a measure to avoid it has been highlighted in [6]. To quote recent developments in progress, it is interesting to remind the history of parametric rolling. The first scientific developments in this field, are typically connected with the names of Kerwin, Paulling, Grim and Wendel, all active on this phenomenon about 60 years ago. Bird and Odabashi [1], however, remind us that parametric rolling was already mentioned in 1892 [30], 20 years after [27], studying the vibrations of an elliptic membrane, introduced the well known equation suitable for its description. Partial stability failures have been reported attributable to this phenomenon, and yet in 2019 there is still some doubt concerning the adoption of criteria against parametric rolling!

As known, the development of provisions for Intact Stability at international level was started by IMCO, later IMO, triggered by the conclusions of SOLAS1960 [34], and of SOLAS1974 [35], this latter asking for explicit consideration of the effects of meteo-marine environment. After some post-processing this led to the Code of intact stability for all ships covered by IMO instruments [16].

In the following we will analyze the origins of this document, mainly consisting of two Stability Criteria, applicable to all ship types, which are based in two studies published in the 1930s of past century [31, 32], i.e. around 80 years ago.

There is no doubt that the Code of Intact Stability, although issued as a “recommendation” improved substantially the safety of navigation and the protection of the environment. A number of critical points, however, were raised since the beginning to these Criteria, based on the statistical nature of the first one and on the many empirical data and formulas used in the second one.

Situation changed with the adoption at IMO of the Formal Safety Assessment [20] changing the point of view for the development of regulations from “what went wrong” to “what could go wrong”, i.e. from a “reactive” approach to a “proactive” one.

The combination of criticism and FSA led, in recent times, to the revision of the Code of intact stability for all ships covered by IMO instruments, producing the new International Intact Stability Code 2008 [23] which to a large extent consists in a reorganization of the previous Code and is still in force, and to the studies aimed at the development of the Second Generation Intact Stability Criteria, which is still in progress.

In the following of this paper, we will consider in some detail the developments leading to the Code of intact stability for all ships covered by IMO instruments as contained in IMO Res. A.749 [16], to identify the reasons of the fortune of the approaches contained in the two above mentioned papers.

## **2 The Situation of Intact Stability Provisions at the Beginning of the 1960s and the Solas'60 Conference**

The situation of Intact Stability provisions in the period between Great War and WW II, with few exceptions related to individual designers, shipyards or shipping companies, was often more dominated by comfort [40], i.e. indications of maximum values of metacentric height, than by stability safety, i.e. by minimum values of metacentric height. These latter were quite generic, with some notable exceptions.

After WW II, perhaps along with the needs connected with the large scale reconstruction, requiring new fleets, and the slow restructuring of shipping lines due to the competition with the airplane, a new sensibility concerning stability safety spread-out.

At the beginning of the 1960s, several countries had adopted provisions:

- based on discriminatory analyses on the statical and dynamical elements of righting arm, conducted on databases of accidents of the type of that proposed by Rahola [32], and/or
- provisions based on physical modelling of the external forces acting on the ship, based on statical balance or on energy balance. Noteworthy of the first type, was the Russian standard (see [14], developed on the basis of the proposal contained in [2], while the Japanese standard [41], based on the proposal contained in [31], is of the second type.

Consideration of the effects of wind was also part of the criteria developed by US Coast Guard and Germany.

The 1960 SOLAS Conference was held in London from 17th May 1960 to 17th June. The Conference was attended by delegates from 55 countries. It was the first Conference to be held by IMCO. During the Conference both Damage and Intact Stability were discussed in detail. Here a short summary of the discussion concerning the Intact Stability is reported following [36]. In the meetings of the Subcommittee for the compartmentation and stability studies, the delegate of the URSS stressed the fact that the provisions of the SOLAS Convention relating to stability in the event of damage do not ensure sufficient intact stability of the ship, so it is essential to establish special rules on the intact stability of the ship to be applied to all types of ships, so that it is possible to count on sufficient safety of the ship during normal navigation. These rules should take into account the ability of the ship to resist external forces such as the actions of wind and sea and the agglomeration of passengers on one side of the ship.

Almost all the delegations agreed on the need to study norms regarding intact stability, rules that should be imposed especially for small ships, but at the same time it was pointed out that the problem was so important and so complex, that an in-depth study of it would have been impossible during the few days available for the work of the Conference. It was therefore unanimously decided to refer the matter to IMCO so that it could organize, with a matter of urgency, the study of intact

stability provisions, which was the subject of recommendation n. 7 (“Intact Stability of Passenger Ships, Cargo Ships and Fishing Vessels”) to the 1960 Convention [34]:

The Conference, having considered proposals made by certain Governments to adopt as part of the present Convention Regulations for intact stability, concluded that further study should be given to these proposals and to any other relevant material which may be submitted by interested Governments.

The Conference therefore recommended that “the Organization should, at a convenient opportunity initiate studies, on the basis of the information referred to above of:

- (a) intact stability of passenger ships,
- (b) intact stability of cargo ships,
- (c) intact stability of fishing vessels, and
- (d) standards of stability information,

taking into account the decisions of the present Conference on requirements for damage stability and the results of any further studies which may be carried out by the Organization on the subdivision and damage stability of cargo ships in pursuance of Recommendation 8 of the Conference, the object being the formulation of such international standards as may appear necessary.”

The Conference further recommended that “in such studies the Organization should take into account studies already undertaken by the Food and Agriculture Organization of the United Nations on the stability of fishing vessels and should co-operate with that Organization on that aspect of the matter.”

### **3 The Statistical Approach and the Development of the General Stability Criterion**

As well reported in [1, 9] several Authors developed Intact Stability provisions based on empirical formulas, with consideration of samples of ships, by discriminating some parameters, mostly consisting in the initial metacentric height and in characteristics of the statical righting arm. None of these had fortune, i.e. none became at least the basis for a national regulation.

Different consideration had the analysis done by Rahola [32]. While general details about this work are contained in the companion paper by Ruponen [33], we consider here some strong points. It is a too important contribution to be summarized here, but it is important to consider at least the following couple of sentences from the Introduction: “The object of the present investigation is to find a procedure by means of which it may be possible to judge with adequate certainty the amount of the stability of a certain vessel which may come to navigate under the conditions prevailing on the lakes and the waters adjacent to our country, and to decide whether it is sufficient or not.” ... “With regard to stability circumstances we must clearly make a distinction between the determining and the judging of stability.”. As reported

by Kuo and Welaya [26]: “Rahola’s thesis raised great interest throughout the world because it was the first comprehensive study of its kind and because the method is fairly simple to apply as it does not require any computations so long as the statical stability curve in still water is known. That is the reason why many national stability regulations or recommendations still rely on this approach in judging the stability of their fleets.”

The situation regarding the current status of national stability requirement in various countries was analyzed in 1964 by the IMO Working Group on Intact Stability as a background for the development of international standards.

As reported by Kobylinski [25], commencing its work on intact stability criteria the STAB Sub-Committee stated that when developing international criteria, it is necessary to take into account the heeling moments from external forces at sea. It realized, however, that such an approach would not enable the development of stability criteria in a short time. Therefore, the SubCommittee decided to base future criteria, as a first step, on statistics of casualties, and in particular, analyzing stability parameters for ships which capsized and for those which were considered safe in operation. It decided also to analyze the contents of existing national stability requirements. As a result of this decision, the Intact Stability Working Group (IS) as well as the Panel of Experts on Stability of Fishing Vessels (PFV) began to collect data on ships and fishing vessels that capsized and on ships that were considered safe in operation.

Rahola’s work [32], which at the time was already the base of several national regulations on Intact Stability, was considered the more systematic attempt to develop stability standards by applying an original method of analysis of stability parameters of ships that capsized and of ships considered safe in operation. This method, with modifications, was applied by IMO when developing the stability standards included in Resolutions A.167 [10] and A.168 [11], hence the nickname of “Rahola Criterion” often used to indicate these regulations.

Details on the development of IMO Res. A.167, regarding the extended sample of ships used in the statistics and the probability methods employed are contained in [25] and in Part C of International Intact Stability Code 2008). See also [29] and [38].

In their critical analysis, Bird and Odabashi [1] discuss the cases of two ships in order to show the desirability of improved criteria with respect to Res. A.167 and A.168. Those ships more than fulfilled the minimum stability requirements of IMCO but yet capsized,

They concluded: “These examples show that IMCO recommendations, by themselves, are not sufficient to provide acceptable safety of ships, and as in both the cases the weather conditions were not too severe, we must look for some other basic reasons causing the capsizes.”. We note that this is presently under discussion at IMO.

## 4 The Energy Balance and the Development of the Weather Criterion

Moseley [28] introduced the concept of “dynamic stability” as the work done in inclining a ship and consequently stored as potential energy. The dynamic stability arm was used since long time to supplement the information contained in the initial metacentric height and in the statical stability arm. This allowed to obtain the series of semi-empirical stability criteria, progressively including analyses of accident at sea, culminating in the Rahola proposal in 1939 [32]. We had, however to arrive at 1935 [31] to have the first complete formulation of an “energy balance” criterion. It is interesting to follow the debate following Pierrottet presentation at Royal Institution of Naval Architects; following the Chairman, “I do not wish in the least to detract from the good work that Professor Pierrottet has done. I think the Paper will be very useful to us, but I do hope it will be a long time before it is made the basis for new Board of Trade regulations by the Classification Societies. The number of losses from Capsizing is so exceedingly small, even more tiny than he says, that it would be a very stiff to impose these regulations.”

We had to wait 15 years and the tragedy of Toya Maru to have a national regulation based on a weather criterion, and additional 35 years to have an international one.

The discussion above referred is cyclical in this field. The warnings of Reed became clear only after the painful sinking of the monitor Captain 150 years ago; unfortunately, it looks that this spirit was not completely absent in recent discussions at IMO.

As mentioned in Sect. 2 above, at the beginning of the 60s, several countries had developed and adopted Criteria on Intact Stability based on physics, i.e. on the calculation of the heeling effect produced by external factors, like wind and waves, or internal factors, like passenger aggregation on side or manoeuvring. Two of them, although different as far as the “dynamic effects” were considered, i.e. if the maximum heeling was the result of a static balance or of the energy balance, were completely developed as Weather Criteria and applied since several years. In 1962 [8], laid the basis for what soon became the US Navy Weather Criterion.

It is interesting to note (as reported, for instance, in [36] that during the Conference SOLAS’60, there was a wide discussion on Intact Stability, almost entirely based on a document submitted by the Russian delegation describing their intact stability criterion. The ensuing discussion was focused on the effect on stability of external forces. No conclusion could be reached, however, due to the important differences between the different criteria already existing, notably between the Russian and the Japanese criteria. Hence the above mentioned Recommendation n. 7. As we have seen in previous paragraph, the working group at IMO decided differently, converging on the modification of Rahola’s work, which could guarantee an acceptable outcome in the short term available.

The following SOLAS Conference, while acknowledging the progress made, thus recommended that “steps be taken to formulate improved international standards on

intact stability of ships taking into account, inter alia, external forces affecting ships in a seaway which may lead to capsizing or to unacceptable angles of heel.” [35].

The result was the adoption of the “Weather Criterion” in 1985 [13] for passenger and cargo ships, and in 1991 for fishing vessels [15], mainly as effect of merging the Japanese Criterion [41] with elements of the Russian Criterion [see also 2, 14].

Actually, the first proposal of a criterion for “Severe Wind and Rolling” at an International level was done in Regulation 31 in the frame of the Torremolinos International Convention on Safety of Fishing Vessels [12]. The original text of the Conference quoted: “Vessels shall be able to withstand, to the satisfaction of the Administration, the effect of severe wind and rolling in associated sea conditions taking account of the seasonal weather conditions, the sea states in which the vessel will operate, the type of vessel and its mode of operation”. The Guidance on a Method of Calculation of the Effect of Severe Wind and Rolling in Associated Sea Conditions was contained in Recommendation I of Attachment 3 to the Final Act of the Conference. The Criterion contained in the Guidance was extremely close to what later on became the IMO Weather Criterion for passenger and cargo ships other than fishing vessels. The fast progress leading to this proposal was certainly due to the strict collaboration between IMO, FAO and ILO, in view of the extremely high risk for human life associated with this occupation. Unfortunately, the completion of the Weather Criterion for fishing vessels came only in 1991 [15] and all the matter never became mandatory [see 5].

## **5 The Code of Intact Stability for All Ships Covered by IMO Instruments, the International Intact Stability Code 2008 and Beyond**

The provisions contained in the mentioned IMO Resolutions [10, 11, 13], with the addition of all other provisions developed for other ship types, were finally included in the Resolution A.749—Code of intact stability for all ships covered by IMO instruments [16]. This Code was amended in several points by Res. MSC.75 [17].

In 2001 [18], following a submission from Italian delegation [19] criticizing the methodology adopted to calculate several parameters of Weather Criterion, the SLF Sub-Committee was tasked to start the revision of the Intact Stability Code as contained in Res. A.749. At the beginning the activity of the working group operating in the frame of the SLF Sub-Committee was concentrated on the development of “rational” intact stability criteria. Soon, however, priority was given to polishing and restructuring Res. A.749 to make Part A of the Code mandatory, under SOLAS and ILLC Conventions, as requested by German delegation who provided an FSA analysis supporting this decision [21]. This part was completed in 2007 with adoption of the new International Intact Stability Code 2008 [23]. This transformation, from “recommended” to “mandatory” of both the General Criterion (ex Res. A.167) and the Weather Criterion (ex Res. A.562), made it necessary to provide alternative

ways [22], Part C of ISC2008) to comply with Weather Criterion for ship typologies which previously could be managed at national level.

We note, in particular, that, in view of the difficulty for some ship typologies to fulfill the requirement regarding the position of the maximum of the righting arm curve the Res. A. 167 was modified by setting the angle to  $25^\circ$  and allowing to go down to  $15^\circ$  with a compensation in dynamic stability (see [23], Part C). It is interesting to note that Rahola originally proposed  $35^\circ$ . This standard, in fact, was ambiguous since the very beginning, since the regulation stated: “The maximum righting arm should occur at an angle of heel *preferably exceeding 30 deg but not less than 25 deg.*”.

The working group could at this point restart the activity on development of “rational” intact stability criteria, finally changing the title in “Second Generation Intact Stability Criteria”. The situation up to 2015 was summarized in [6]; an updating of the progress of this item is contained in [39].

It is noteworthy that the two pillars of the Intact Stability Code, i.e.:

- Criteria regarding righting lever curve properties, present evolution of “Rahola Criterion”;
- Severe wind and rolling criterion (weather criterion),

already survived 50 years, with reasonably small changes, and in addition reached the mandatory status. The statement “Criteria included in the Code are based on the best state-of-the-art concepts, available at the time they were developed, taking into account sound design and engineering principles and experience gained from operating ships.” was reiterated in the Preamble to ISC 2008.

It is at this point very likely that the Maritime Safety Committee of IMO will approve the Interim Guidelines on the second generation intact stability criteria as contained in [24]. Member States will be invited to use the annexed Interim guidelines as complementary measures when applying the requirements of the mandatory criteria of part A of the Code and to bring them to the attention of all parties concerned, in particular shipbuilders, shipmasters, shipowners, ship operators and shipping companies, and recount their experience gained through the trial use of these Interim guidelines to the IMO.

## 6 Conclusions

The Criterion proposed by Rahola [32] was the last before WW II, it included an extremely detailed critical analysis of all the research and regulations existing at the time and was the result of an innovative discriminatory analysis conducted on a sample of ships. After the war, it spread around in different countries and, also due to its simplicity, constituted the basis for the first international provision on intact stability in the frame of the recently created International Maritime Organization. This Criterion, although heavily criticized since the beginning for its semi-empirical

nature, was included in both the Intact Stability Code, Res. A. 749, and, with some modifications, got mandatory status in the International Intact Stability Code 2008.

It will survive in the near future too, as mandatory Criterion, at least until the Interim Guidelines on the Second Generation Intact Stability Criteria, approved to be used as complementary measures when applying the requirements of the mandatory criteria of part A of the Code, will undergo thorough testing and tuning.

## References

1. Bird H, Odabasi AY (1975) State of art: past, present and future. In: Proceedings international conference on stability of ships and ocean vehicles, Glasgow, pp 312–317
2. Blagoveshchensky SN (1932) On a method of stability standardization. Transactions of Scientific Research Institute of Shipbuilding USSR 12
3. Bouguer P (1746) “Traité du Navire, de sa Construction et de ses Mouvements (Treatise of the Ship, its Construction and Movements)”, Jombert, Paris
4. Francescutto A (1993) Is it really impossible to design safe ships? Transactions of the Royal Institution of Naval Architects 135:163–173
5. Francescutto A (2013) The evolution of the regulatory stability regime for fishing vessels. In: Proceedings of the international conference IDS2013, Iquitos, Peru, 17–19 July 2013, Iquitos, Peru, pp 14.1–14.18
6. Francescutto A (2016) Intact stability criteria of ships—past, present and future. Ocean Eng 120:312–317
7. Francescutto A, Papanikolaou AD (2011) Buoyancy, stability and subdivision: from Archimedes to SOLAS2009 and the way ahead. International Journal of Engineering for the Maritime Environment (Proceedings of the Institution of Mechanical Engineers Part M) 225:17–32
8. Goldberg LL, Sarchin TH (1962) Stability and buoyancy criteria for U.S. naval surface ships. Transactions of the American Society of Naval Architects and Marine Engineers 70:418–458
9. Herd RJ (1979) Rahola criterion—40 years on. Royal Institution of Naval Architects, Australian Branch, Sydney 17 August 1979
10. IMO (1968a) Resolution A.167—recommendation on intact stability for passenger and cargo ships under 100 metres in length, 28 Nov
11. IMO (1968b) Resolution A.168—recommendation on intact stability of fishing vessels, 28 Nov
12. IMO (1977) International conference on safety of fishing vessels 1977—final act of the conference, with attachments, including the torremolinos international convention for the safety of fishing vessels, 1977
13. IMO (1985) Resolution A.562—recommendation on a severe wind and rolling criterion (weather criterion) for the intact stability of passenger and cargo ships of 24 metres in length and over, 20 Nov
14. IMO (1988) SLF 33/INF.4—development of intact stability requirements for all types of ships covered by IMO instruments, submitted by the USSR, 6 May
15. IMO (1991) Resolution A.685(17)—weather criterion for fishing vessels of 24 metres in length and over, 6 Nov
16. IMO (1993) Resolution A.749—code of intact stability for all ships covered by IMO instruments, 4 Nov
17. IMO (1998) Resolution MSC.75(69)—adoption of amendments to the code on intact stability for all types of ships covered by IMO instruments (resolution A. 749(18)), 14 May
18. IMO (2001a) SLF 44/18—report to the maritime safety committee, 18 Oct
19. IMO (2001b) SLF 44/INF.6—weather criterion for large passenger ships, submitted by Italy, 12 July



20. IMO (2002) MSC/Circ.1023—MEPC/Circ.392—guidelines for formal safety assessment (FSA) for use in the IMO rule-making process, 5 April
21. IMO (2003) MSC 78/24/1—revision of the code on intact stability, submitted by Germany, 15 Dec
22. IMO (2006) MSC.1/Circ.1200—Interim guidelines for alternative assessment of the weather criterion, 24 May
23. IMO (2008) International code on intact stability. IMO, 2018, International intact stability code 2008
24. IMO (2020) SDC 7/16—report to the maritime safety committee, 9 March
25. Kobylinski LK, Kastner S (2003) Stability and safety of ships—volume 1: regulation and operation. Elsevier
26. Kuo C, Welaya Y (1981) A review of intact ship stability research and criteria. *Ocean Eng* 8:65–84
27. Mathieu E (1868) Mémoire sur le Mouvement Vibratoire d'une Membrane de Forme Elliptique. *Journal de Mathématiques Pures et Appliquées* 2(13):137–203
28. Moseley H (1850) On the dynamical stability and on the oscillations of floating bodies. *Philos Trans R Soc Lond* 140:609–643
29. Nadeinski VP, Jens JE (1968) The stability of fishing vessels. *Transactions of the Royal Institution of Naval Architects* 110:1–27
30. Pollard J, Dudebout A (1892) *Théorie du Navire, Vol. III - Dynamique du Navire: Mouvement de Roulis sur Houle, Mouvement Rectiligne Horizontal Direct (Résistance des Carènes)*, Gauthier-Villars, Paris
31. Pierrottet E (1935) Standards of stability for ships. *Transactions of the Royal Institution of Naval Architects* 77:208–222
32. Rahola J (1939) The judging of the stability of ships and the determination of the minimum amount of stability—especially considering the vessels navigating Finnish waters. Doctoral thesis, Helsinki, <https://aaltodoc.aalto.fi/handle/123456789/15149>
33. Ruponen P (2019) Rahola criterion revisited: an overview of Jaakko Rahola's research and career. In: *Proceedings of the 17th international ship stability workshop ISSW2019, Helsinki*, pp 15–20
34. SOLAS (1960) International convention for the safety of life at sea, 1960, London
35. SOLAS (1974) International conference on safety of life at sea 1974—final act of the conference, with attachments, including the international convention for the safety of life at sea, 1974, London
36. Spinelli F (1961) La Compartimentazione e la Stabilità delle Navi Mercantili dopo la Conferenza di Londra 1960 sulla Salvaguardia della Vita Umana in Mare (Compartmentation and Stability of Merchant Ships after London Conference of 1960 on Safety of Human Life at Sea). *Tec Ital* 26:1–17
37. Steel HE (1956) The practical approach to stability of ships. *Transactions of the Royal Institution of Naval Architects* 98:381–409
38. Thompson G, Tope JE (1970) International consideration of intact stability standards. *Transactions of the Royal Institution of Naval Architects* 112:43–67
39. Umeda N, Francescutto A (2023) The second generation intact stability criteria—achievements and remaining issues. In: Spyrou K, Belenky V, Katayama T, Bačkalov I, Francescutto A (eds) *Contemporary ideas on ship stability—from dynamics to criteria*, Chapt. 2, Springer, ISBN 978-3-031-16328-9, pp 21–34
40. Vincent SA (1939) Transverse stability. In: Rossell HE, Chapman LB (eds) *Principles of naval architecture—written by a group of authorities, vol I*. SNAME, New York, pp 99–137
41. Yamagata M (1959) The standard of stability adopted in Japan. *Transactions of the Institution of Naval Architects* 101:417–443

# **Improvements on Current Methods of Probabilistic Assessment of Ship Stability**

# Study on Short-Term Prediction of Roll in Beam Sea



Toru Katayama, Mai Kankaku, Atsuo Maki, Kei Sugimoto,  
and Yusuke Fukumoto

**Abstract** The formula to determine the roll angle for structural strength assessment in ClassNK's Technical Rule and Guidance gives a value based upon maximum roll amplitude at probability of exceedance  $Q = 10^{-8}$  within the design life of ship on long-term prediction of roll amplitude. The long-term prediction is obtained from combining short-term prediction of roll amplitude and a probability of occurrence of short-term irregular sea in long term (design life of ship). In the current rule, non-linearity of roll is included as some correction coefficients obtained from model experiments and empirical knowledge at the time of development. However, the ships have considerably changed since then, and the coefficients are not always suitable for the novel vessels. The purpose of this study is to propose a rational short-term prediction method considering nonlinearity of roll. In this paper, applicability of a non-Gaussian PDF (Probability Density Function) for PDF of roll angle is investigated.

**Keywords** Short-term prediction · Roll · Non-Gaussian distribution

---

T. Katayama (✉) · M. Kankaku  
Osaka Prefecture University, Osaka, Japan  
e-mail: [katayama@marine.osakafu-u.ac.jp](mailto:katayama@marine.osakafu-u.ac.jp)

M. Kankaku  
e-mail: [szb03054@edu.osakafu-u.ac.jp](mailto:szb03054@edu.osakafu-u.ac.jp)

A. Maki  
Osaka University, Osaka, Japan  
e-mail: [maki@naoe.eng.osaka-u.ac.jp](mailto:maki@naoe.eng.osaka-u.ac.jp)

K. Sugimoto · Y. Fukumoto  
Class NK, Tokyo, Japan  
e-mail: [sugimoto@classnk.or.jp](mailto:sugimoto@classnk.or.jp)

Y. Fukumoto  
e-mail: [y-fukumoto@classnk.or.jp](mailto:y-fukumoto@classnk.or.jp)

## 1 Introduction

The current formula to determine the roll angle for structural strength assessment in ClassNK's Technical Rule and Guidance gives a value based upon maximum roll amplitude at probability of exceedance  $Q = 10^{-8}$  within the design life of ship on long term prediction of roll amplitude. The long-term prediction is obtained from combining short-term prediction of roll amplitude and a probability of occurrence of short-term irregular sea within long term (design life of ship). And the short-term prediction of roll amplitude is obtained with the energy spectrum method [10] based on the assumption of linear superposition which uses frequency response function of roll for small wave height and wave spectrum of short-term irregular sea. Additionally, non-linearity of roll is included using correction coefficients obtained from model experiments and empirical knowledge at the time of development. However, the ships have considerably changed since then, and the coefficients are not always suitable for the novel vessels.

Therefore, the fundamental revision is required, which is not only revision of correction coefficients to apply the present formula to all type vessels in recent years, but also proposal of rational new method which could be successfully applied to the future vessels as well.

The purpose of this study is to propose a rational short-term prediction method including non-linearity of roll. If short term and life of ship are assumed 3 h and 25 years, accuracy of PDF (Probability Density Function) of roll angle to around probability  $7 \times 10^{-4}$  is significant. In this paper, it is considered to apply a non-Gaussian PDF to PDF of roll angle. Roll measurement tests in irregular beam waves for scale models of PCC and LNG carrier are carried out to obtain probability density of roll, and the measured results are compared with Gaussian PDF and a non-Gaussian PDF to investigate its applicability.

## 2 Probability Density Function of Roll

### 2.1 Gaussian Distribution

Gaussian PDF is given as

$$p_1(\phi) = \frac{1}{\sqrt{2\pi}\sigma} \exp\left\{-\frac{\phi^2}{2\sigma^2}\right\} \quad (1)$$

where  $\phi$  is roll angle (:time history data) [rad] and  $\sigma$  is standard deviation of roll angle. The standard deviation of roll angle  $\sigma$  is obtained from time history data of roll angle in irregular waves. If roll is linear, standard deviation can be obtained using Eq. (2) according to energy spectrum method based on the assumption of linear superposition [10].

$$\sigma^2 = \int_0^{\infty} S_{wave}(\omega)[A(\omega)]^2 d\omega \quad (2)$$

where  $S_{wave}(\omega)$  is wave spectrum and  $A(\omega)$  is frequency response function of roll for small wave height.

## 2.2 Non-Gaussian Distribution

If roll can be expressed by a one degree of freedom motion equation, a non-linear roll equation can be given as

$$\ddot{\phi} + \alpha\dot{\phi} + \beta\phi|\dot{\phi}| + \frac{W}{I_{xx}}GZ(\phi) = M_{wave}(t) \quad (3)$$

$$GZ(\phi) = GM\phi + GZ_2\phi^2 + GZ_3\phi^3 + GZ_4\phi^4 + GZ_5\phi^5$$

where  $t$  is time,  $\alpha$  is linear damping coefficient,  $\beta$  is quadratic damping coefficient,  $W$  is ship weight,  $I_{xx}$  is moment of inertia of roll (including added inertia component),  $GM$  is metacentric height,  $GZ_i$  is  $i$ th component of  $GZ$  polynomial fit and  $M_{wave}(t)$  is time history of wave excitation moment.

Maki [6] and Maki et al. [7] apply the method which is proposed by Sakata et al. [8, 9] and Kimura et al. [2, 3, 4, 5] to roll motion problems in irregular waves. Hereafter, the authors shortly explain its methodology. Kimura et al. [3] report that the form of PDF is strongly affected by the potential of the system even for the case of non-white excitation. It means the form of the PDF for the white noise can be used for the PDF for the colored noise. Kimura et al. [3] approximated the PDF for the colored noise by introduced the adjustable parameter  $d$  into the PDF for the white noise. Therefore, the key is to obtain the PDF for the white noise. As [1] shown, for the linear damping case, the stationary PDF for the white noise can be easily obtained by solving FPK (Fokker–Planck–Kolmogorov) equation [6]. On the other hand, the nonlinear damping factor is not negligible in the problem of ship roll motion. In order to overcome this point, by following the work of [5], the PDF [7] was obtained by the nonlinearization technique proposed by [11]. The obtained non-Gaussian PDF of roll angle and roll angular velocity is described as

$$p_2(\phi, \dot{\phi}) = C \exp \left[ -d \left\{ \alpha H(\phi, \dot{\phi}) + \frac{8\beta}{9\pi} (2H(\phi, \dot{\phi}))^{\frac{3}{2}} \right\} \right] \quad (4)$$

The coefficients  $C$  and  $d$  included in Eq. (4) are determined by Eqs. (5) and (6). Equation (5) represents the normalization condition of the PDF whereas Eq. (6) does the condition for variance.

$$\int_{-\infty}^{\infty} d\dot{\phi} \int_{\phi_{VN}}^{\phi_{VP}} p_2(\phi, \dot{\phi}; d) d\phi = 1 \quad (5)$$

$$\int_{-\infty}^{\infty} d\dot{\phi} \int_{\phi_{VN}}^{\phi_{VP}} \phi^2 p_2(\phi, \dot{\phi}; d) d\phi = E[\phi^2] \quad (6)$$

$$H(\phi, \dot{\phi}) = \frac{1}{2} \dot{\phi}^2 + \int_0^{\phi} GZ(\phi) d\phi \quad (7)$$

where  $\phi_{VP}$  and  $\phi_{VN}$  indicate two vanishing angles of roll restoring moment.  $H$  in Eq. (7) is the potential energy at instantaneous roll angle and roll angular velocity. In order to keep the numerical accuracy, the integral in Eqs. (5)–(6) are conducted by using the double exponential formula (DE formula). In this case, the DE formula is used for both integrations, that is roll directional integral and roll rate directional integral.

In order to obtain the PDF of Eq. (4), variance of roll angle, damping coefficients and restoring coefficients are necessary. In this study, the following three approaches are considered, however, only first one of them is adopted. First one is that variance of roll angle and damping coefficients are obtained from model tests, and restoring coefficients are calculated. Second one is that coefficients of roll motion equation Eq. (3) are obtained theoretically (e.g. a strip method, Ikeda's roll damping prediction method and calculation of the coefficients of the restoring moment) and variance of roll angle is obtained from solving Eq. (4) with MSC (Monte-Carlo Simulation). Third one is that all coefficients of Eq. (4) are obtained from the least square fit for measured probability density of roll angle.

### 3 Subject Ships

#### 3.1 Principal Particulars of Model Ships

Subject ships are typical large PCC and LNG carrier in recent years. Figure 1 shows the body plans of the ships, and Table 1 shows their principle particulars of the subject ships. Height of the center of gravity  $KG$  and natural roll period  $T_n$  are obtained from an inclining test and a free roll decay test, respectively.

#### 3.2 Characteristics of Roll Restoring

Figure 2 shows calculated  $GZ$ -curves of the models. In the calculation,  $GZ$  is obtained under the condition of equilibrium of vertical forces and trim moments for each heel angle. This figure also shows the linear restoring lever  $GM$  of the  $GZ$ -curve. This

**Fig. 1** Body plan of models of PCC and LNG carrier

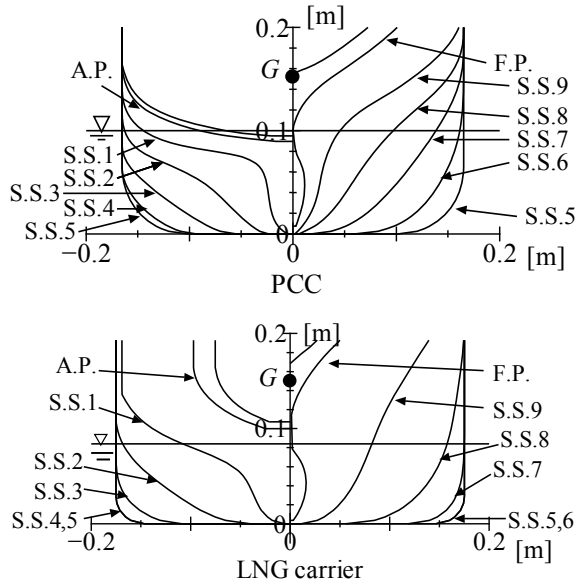


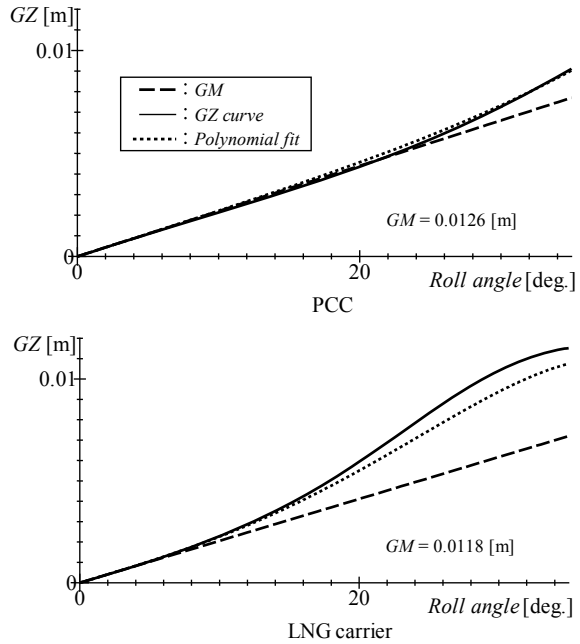
**Table 1** Principal particulars of the models

Name of ship	PCC	LNG carrier
Scale	1/97.5	1/140
Overall length: $L_{OA}$ [m]	2.054	2.095
Breadth: $B$ [m]	0.330	0.35
Depth: $D$ [m]	0.351	0.193
Draught: $d$ [m]	0.100	0.084
Ship weight: $W$ [kgf]	36.68	41.22
Height of the center of gravity: $KG$ [m]	0.152	0.150
Metacentric height $GM$ [m]	0.0126	0.0118
Natural roll period: $T_n$ [s]	1.96	2.19
Position of bilge keels	s.s.3.4–s.s.5.6	s.s.3.65–s.s.6.45
Initial trim [m]: $d_a - d_f$	0	0
$LCG$ [m] from midship (+ aft)	0.0615	-0.0193

figure shows that  $GZ$ -curve of PCC is linear up to 22 degree of heel angle and  $GZ$ -curve of LNG carrier is linear up to 10° of heel angle.

Equations (8) and (9) show the fifth order polynomials for  $GZ$ -curves ( $-30 < \varphi < 30$ ) of PCC and LNG carrier whose coefficients are decided by the least squares

**Fig. 2** Calculated GZ-curve of these models



method.

$$GZ(\phi) = 0.0126\phi + 0.00310\phi^3 + 0.00727\phi^5 \tag{8}$$

$$GZ(\phi) = 0.0118\phi + 0.04099\phi^3 - 0.06807\phi^5 \tag{9}$$

### 3.3 Characteristics of Roll Damping

In order to obtain roll damping coefficients, free decay tests were conducted. The models were free to roll, heave, pitch, and sway. Measurement device is shown in Fig. 7.

By constraining only rotation of the roll axis of the measurement device, four initial heel angles (5°, 10°, 15° and 20°) are given. After releasing the constrain instantly, roll decay motion is measured with a potentiometer.

The measured results are given in Fig. 3, where vertical axis shows the roll peak angle and the time of its occurrence is shown in horizontal axis. The curve in Fig. 3 is fitted by a polynomial using the least squares method. From the polynomial,  $\varphi_n$  at  $t_n$  is re-obtained, and  $\Delta\varphi_n$  and  $\varphi'_n$  of extinction curves shown Fig. 4 are obtained by Eq. (10).



$$\varphi'_n = \frac{\varphi_n + \varphi_{n+1}}{2}, \quad \Delta\varphi = \varphi_n - \varphi_{n+1} \tag{10}$$

where  $\varphi$  is expressed in degree. In order to obtain roll damping coefficients of Eq. (3), extinction curve is express as the Froude's expression of Eq. (11).

$$\Delta\varphi = a\varphi'_n + b\varphi_n'^2 \tag{11}$$

The relation between extinction coefficients and roll damping coefficients is Eq. (12).

$$\alpha = \frac{4a}{T_\phi}, \quad \beta = \frac{3b}{4} \cdot \frac{180}{\pi} \tag{12}$$

**Fig. 3** Peak angle of roll obtained by free decay test measured by potentiometer with 4 degrees of freedom ( $\varphi_0 = 5^\circ$ )

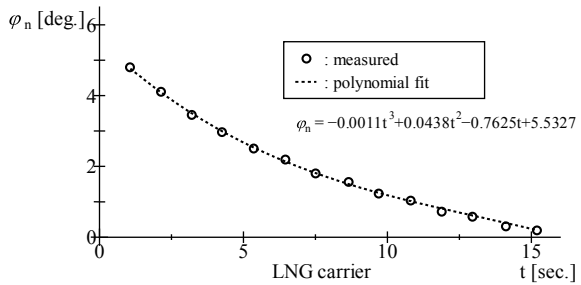
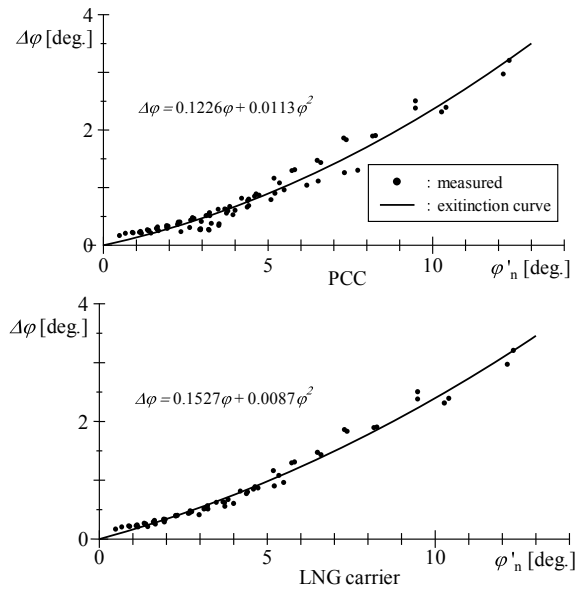


**Fig. 4** Extinction curves obtained by the data on Fig. 3



where,  $T_\phi$  is natural roll period, the units of  $\alpha$  and  $\beta$  are 1/s and 1/rad.

Roll damping coefficients of PCC and LNG carrier are obtained from Fig. 4 as  $\alpha = 0.254, \beta = 0.486$  for PCC and  $\alpha = 0.281, \beta = 0.374$  for LNG carrier.

### 3.4 Validation of Non-Gaussian PDF for Subject Ships

Before comparing with non-Gaussian PDF and measured results, non-Gaussian PDF is compared with the results of solved Eq. (3) with MCS.

In order to solve Eq. (3) with MCS, wave spectrum of incident wave is necessary, and the adopted wave spectrum in MCS is shown in Fig. 5. The spectrum is expressed by Eq. (13) in Sect. 4.2 with the significant wave height and average wave period, which are obtained by zero up-crossing analysis of time histories of measured irregular waves.

Figure 6 shows the comparisons with the non-Gaussian PDF and the results of Eq. (3) with MCS. Variance of roll angle of the non-Gaussian PDF is obtained from the results of Eq. (3) with MCS.

From the comparisons with the results of Eq. (3) with MCS and the non-Gaussian PDF, it is clear that the difference of them is negligible regardless type of ship. This result agrees with finding of [7] that non-Gaussian PDF coincides with results of MCS when their motion equation are same.

**Fig. 5** Wave spectrum of incident wave

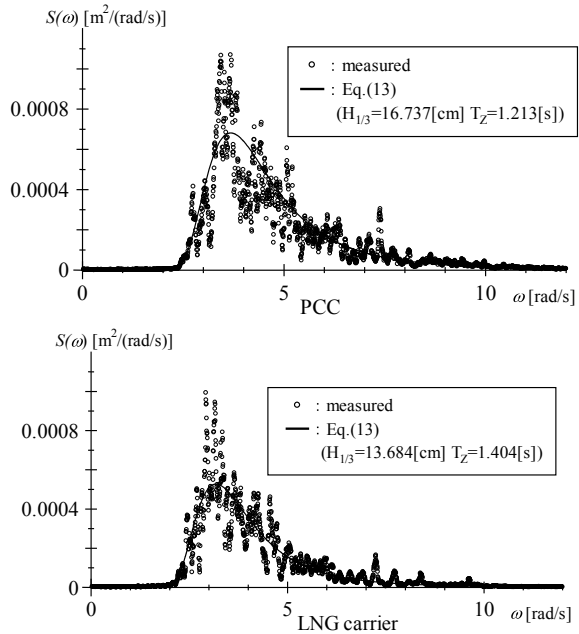


**Fig. 6** Comparison of probability density of roll angle obtained by results of Eq. (3) with MCS and non-Gaussian PDF. Variance of roll angle of non-Gaussian PDF is obtained from the results of Eq. (3) with MCS

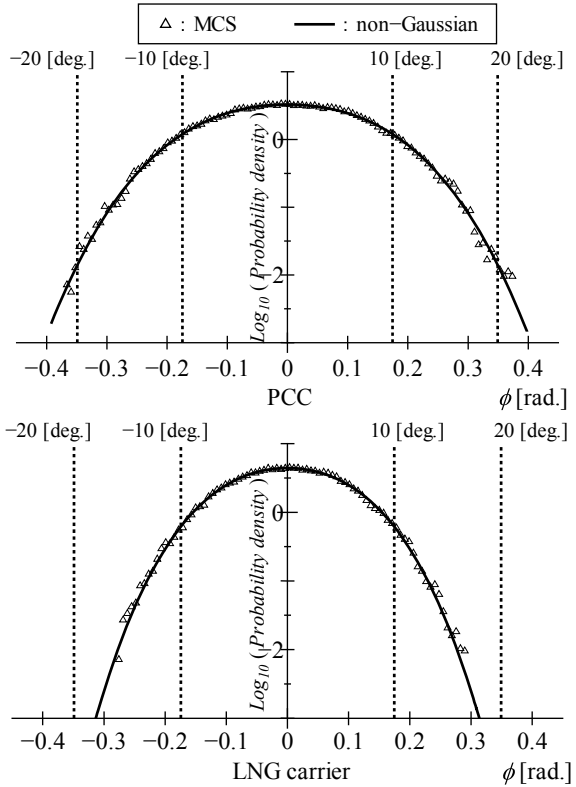
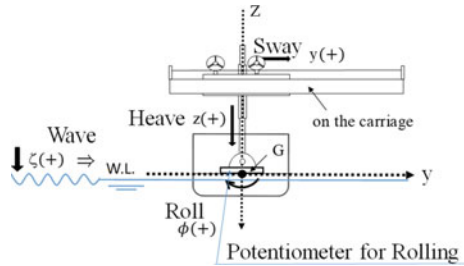


**Fig. 7** Schematic view of the motion measurement with fixed surge and yaw from the behind of hull



## 4 Roll Measurement in Beam Waves

### 4.1 Measuring Device and Coordinate System

Figure 7 shows a schematic view of experiment and its coordinate system. In this model experiment, surge and yaw are fixed whereas roll, sway (and drift), heave and pitch are free. Wave height is measured with a servo type wave height meter attached

to model basin. Data is collected with 100 Hz of sampling frequency. The carriage is pushed according to the drifting speed in order to avoid the sub-carriage hit both ends.

## 4.2 Roll Measurement in Irregular Beam Waves

The wave spectrum of long-crested irregular waves of IACSRec.34 (ISSC spectrum) shown as Eq. (13) is used.

$$S_{wave}(\omega) = \frac{H_{1/3}^2}{4\pi} \left(\frac{2\pi}{T_z}\right)^4 \omega^{-5} \exp\left[-\frac{1}{\pi} \left(\frac{2\pi}{T_z}\right)^4 \omega^{-4}\right] \quad (13)$$

where  $H_{1/3}$  is significant wave height and  $T_z$  is average zero up-crossing wave period. In this paper, it is adopted that peak period of the wave spectrum  $T_p$  is natural roll period  $T_n$  to cause large roll amplitude. The relation between peak period  $T_p$  and  $T_z$  is given as Eq. (14).

$$T_z = T_p \left(\frac{4}{5\pi}\right)^{0.25} \quad (14)$$

Therefore,  $T_z$  of PCC and LNG carrier are 1.392s and 1.561s, respectively.

The formulas of significant wave height for strength assessment in ClassNK's Technical Rule and Guidance is given as

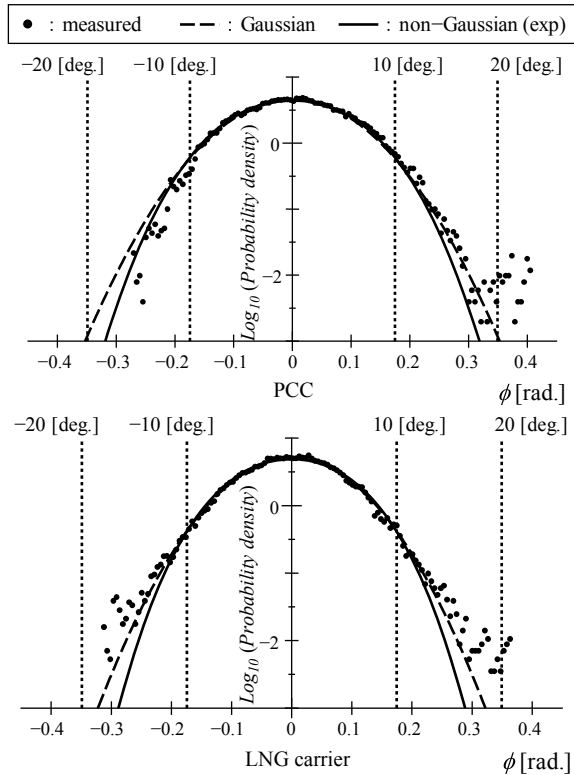
$$H_{1/3} = 0.85 \times \left\{ 10.75 - \left(\frac{300 - L}{100}\right)^{1.5} \right\} \times \sqrt{\frac{L + \lambda - 25}{L}} \quad (15)$$

where  $L$  is overall length of ship and  $\lambda$  is wavelength obtained by using natural roll period. From Eq. (15), the measuring conditions of the significant wave height of PCC and LNG carrier are 16.089 and 13.996 cm. The number of encounter waves is at least 700 waves each case. (The effects of the number of encounter waves on the variance of roll angle are shown in Appendix.)

## 4.3 Results

Figure 8 shows the PDF of roll angle. In this figure, measured result, Gaussian PDF of Eq. (1) and non-Gaussian PDF of Eq. (4) are shown. It is noted that non-Gaussian PDF having the form of Eq. (4) is the joint PDF of instantaneous roll angle and roll angular velocity. Therefore the PDF of instantaneous roll angle shown in Fig. 8 is the integrated properties for roll angular velocity at each roll angle.

**Fig. 8** Comparison of probability density of roll angle obtained by motion measurement, Gaussian PDF and non-Gaussian PDF. Variance of roll angle of PDF is obtained from the results of motion measurement

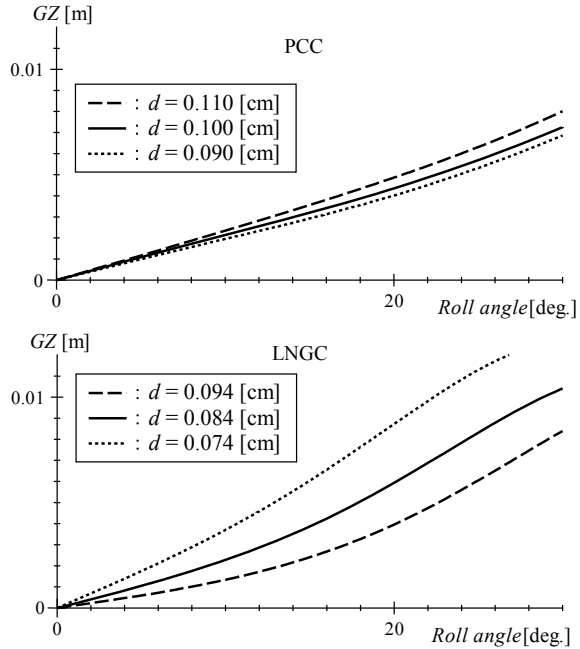


From the comparisons of these results, it is clear that the difference of them is negligible up to about  $\phi = 10^\circ$  for both ships, because the non-linearity of roll damping and restoring moments are small in the range. On the other hand, in the range over  $10^\circ$ , the non-Gaussian PDF includes the non-linearity of roll damping and restoring moments, therefore it is smaller than the Gaussian PDF. However, the non-Gaussian PDFs for both are different from the measured results.

The measured result for PCC shows asymmetry and it becomes larger according to increase of roll angle. However, in this study, non-Gaussian PDF as shown Eq. (4) does not include asymmetry. The non-Gaussian PDF can include asymmetry of  $GZ$ -curve shown Eq. (3), therefore, it should be considered to include second or fourth order terms of restoring coefficients.

The measured result for LNG carrier becomes larger than the Gaussian PDF around  $\phi = 20^\circ$ . The  $GZ$ -curve shown Fig. 2 indicates the tendency that the  $GZ$ -curve becomes larger than the linear component of restoring coefficient  $GM\phi$ . However, the tendency cannot be observed on the measured result of the PDF of roll angle, and the measured result is closer the Gaussian PDF than the non-Gaussian PDF. In the calculation of the non-Gaussian PDF, the calculated  $GZ$ -curve in the calm water as shown Fig. 2. However, the roll restoring moment in the extreme waves which cause

**Fig. 9** Calculated GZ-curve of models with different draught



large amplitude motions can be affected by the heaving and pitching. From Fig. 9 which shows the calculated  $GZ$ -curves in calm water for both ships with various draughts, it can be confirmed that the  $GZ$ -curve of LNG carrier has larger effects of the change of draught than that of PCC. For PCC, the  $GZ$ -curve including the above-mentioned effects may close to the linear component of restoring coefficient  $GM\phi$ . Therefore, it should be considered to include the above-mentioned effects in the calculation of non-Gaussian PDF.

## 5 Conclusions

In order to propose a rational short-term prediction method including non-linearity of roll, a non-Gaussian PDF is investigated and compared with measured results, Gaussian PDF and MCS result, and the following conclusions are obtained.

1. The non-Gaussian PDF coincides with results of MCS when their motion equations are same.
2. The non-Gaussian PDF can express the non-linear effects of roll equation by comparing with the Gaussian PDF.
3. The measured PDF for PCC shows asymmetry and it becomes larger according to increase of roll angle. In this study, non-Gaussian PDF does not include asymmetry, but the non-Gaussian PDF is able to include asymmetry of  $GZ$ -curve. Therefore, it should be considered to include the asymmetry.

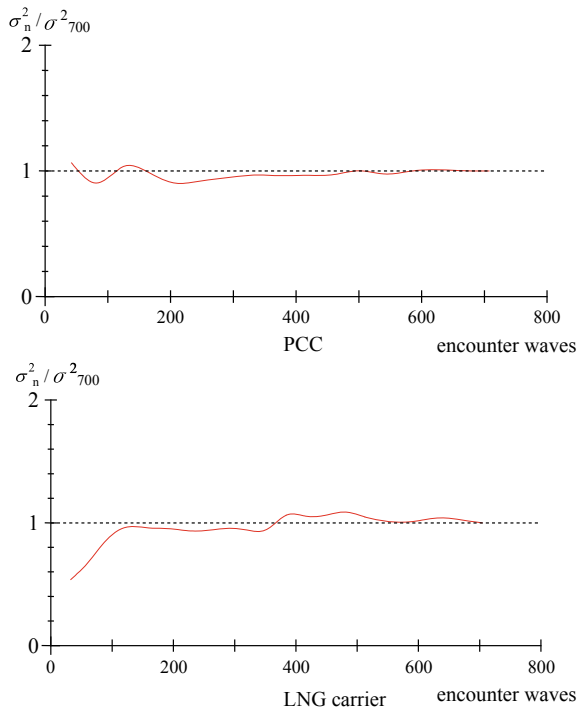
- 4. The measured PDF for LNG carrier becomes larger than the Gaussian PDF at the range over  $\phi = 10^\circ$ . This tendency caused by the difference between GZ-curve in calm water and that in the extreme waves which cause large amplitude heaving and pitching. Therefore, it should be considered how to include the above-mentioned effects in the calculation of non-Gaussian PDF.

**Acknowledgements** Part of this research was supported by ClassNK.

## Appendix

Figure 10 shows a sample results of calculated variance of roll angle using time series roll motion data in various number of encounter waves. Concretely, a long time series data of roll angle was used in order from the first.  $\sigma_n$  and  $\sigma_{700}$  means the standard deviation calculated by the roll angle data for  $n$  and 700 encounter waves. This figure shows that the variance over  $n = 500$  is almost converged.

**Fig. 10** Effects of number of encounter waves on variance of roll angle



## References

1. Caughey TK (1963) Derivation and application of the Fokker-Planck equation to discrete nonlinear dynamic systems subjected to white noise random excitation. *The Journal of the Acoustical Society of America* 35(2):1683–1692
2. Kimura K, Sakata M (1980) Non-stationary responses of a non-symmetric non-linear system subjected to a wide class of random excitation. *J Sound Vib* 76(2):261–272
3. Kimura K (1995) Non-Gaussian equivalent linearization for estimation of stochastic response distribution of nonlinear systems (in Japanese). *Transactions of the Japan Society of Mechanical Engineers Series C* 61(583):831–835
4. Kimura K, Morimoto T (1998) Estimation of non-Gaussian response distribution of a nonlinear system subjected to random excitation (application to nonwhite excitation with nonrational spectrum (in Japanese)). *Journal of the Japan Society of Mechanical Engineers* 64(617):1–6
5. Kimura K, Takahara K, Yamamoto S (2000) Estimation of non-Gaussian response distribution of a system with nonlinear damping (in Japanese). *Dynamics and Design Conference*
6. Maki A (2017) Estimation method of the capsizing probability in irregular beam seas using non-Gaussian probability density function. *J Mar Sci Technol* 22(2):351–360
7. Maki A, Sakai M, Umeda N (2018) Estimating a non-Gaussian probability density of the rolling motion in irregular beam seas. *J Mar Sci Technol* 24(4):1071–1077
8. Sakata K, Kimura K (1979) The use of moment equations for calculating the mean square response of a linear system to non-stationary random excitation. *J Sound Vib* 67(3):383–393
9. Sakata K, Kimura K (1980) Calculation of the non-stationary mean square response of a non-linear system subjected to non-white excitation. *J Sound Vib* 73(3):333–343
10. St. Denis M, Pierson WJ (1953) On the motions of ships in confused seas. *Transactions SNAME* 61:280–357
11. To CWS (2017) *Nonlinear random vibration: analytical techniques and applications*, 2nd edn. CRC Press



# An Efficient Formulation of the Critical Wave Groups Method for the Assessment of Ship Stability in Beam Seas



Panayiotis A. Anastopoulos and Kostas J. Spyrou

**Abstract** The paper presents a simplified setup of the “critical wave groups” method, suitable for swift probabilistic evaluations of ship capsize tendency due to beam-sea resonance. The simplifications proposed herein are twofold and aim at reducing the computational cost associated with the identification of the critical, for ship stability, wave episodes when these are represented by the “expected” wave groups for the ambient sea state. The first simplification concerns the initial conditions of the vessel at the moment of a wave group encounter which, according to the exact “critical wave groups” formulation, should be probabilistically treated. Instead, the simplified approach pursues reliable estimates by examining only the upright equilibrium state. Moreover, by focusing on sea states being highly probable to provoke resonance, fewer simulations need to be performed since, among all critical wave group candidates, the main probability contribution essentially comes from those having periods close to the natural period of the vessel in question. Considering these wave groups only constitutes the second simplification. Within this framework, regular wave trains are also tried to investigate the possibility of eliminating the computational burden due to the generation of the “expected” wave groups. The accuracy of both schemes in calculating the probability of extreme responses is assessed through comparisons with Monte Carlo simulations of roll motion.

**Keywords** Critical wave groups · Probability · Instability · Roll · Dynamics · Resonance · Extreme events

---

P. A. Anastopoulos (✉) · K. J. Spyrou  
School of Naval Architecture and Marine Engineering, National Technical University of Athens,  
Athens, Greece  
e-mail: [panasto@central.ntua.gr](mailto:panasto@central.ntua.gr)

K. J. Spyrou  
e-mail: [k.spyrou@central.ntua.gr](mailto:k.spyrou@central.ntua.gr)

## 1 Introduction

The study of large amplitude ship roll motions in stochastic beam seas is a non-trivial task expanding in both the fields of nonlinear dynamics and probability. As known, roll statistics deviate from Gaussianity with increasing level of nonlinearity, leading to probability distributions with heavy-tailed structure [6]. However, calculating the probability of extreme roll events by employing “brute force” methods suffers from a number of deficiencies. First, the accuracy of a “direct counting” definition of probability becomes questionable when dealing with rare events. At the same time, the fact that ship response is not essentially an ergodic random process for nonlinear systems calls for the use of ensemble averages in the direct counting procedure [4]. This, however, requires additional effort (comparing to an ergodic system) for generating a statistically meaningful amount of extremes since many short realizations need to be generated while their largest part, reflecting the “statistical” transients, will eventually be discarded (e.g. [3]). More so, even if temporal averages are to be used, one has to set-up the simulations carefully to sample throughout a relevant response sample space in the correct proportions without idly expending computational resources. Clearly, this type of sampling is not as straightforward as it would be for an ergodic dynamical system and thus, it may further deteriorate the efficacy of massive simulations in tracing the complex shape of the tails.

Various methods have been proposed to treat the so called “problem of rarity”, described in the above. Extrapolation methods employ statistics based on a limited number of realizations to predict the probability of an event that is too rare to be observed. The concept derives from extreme value theory (EVT) which is built upon two main theorems providing asymptotic expressions for the distributions of the maximum (first theorem) and of the excesses over a threshold (second theorem) of a sample of independent and identically distributed random variables. Thus, the objective is the estimation of the parameters of an extreme value distribution through fitting to a set of experimental or simulation data. The effectiveness of the approach has been investigated in several studies and much effort has been put into addressing practical issues regarding its application for ship stability assessment (e.g. [5, 23]).

On the other hand, wave group methods offer an alternative solution to the problem by focusing on specific time intervals when dangerous wave events occur. One of them is the “critical wave groups” method which quantifies instability tendency through the probability of encountering any wave group that could have provoked the instability [20]. In the deterministic part of the method, regular wave trains are employed to identify critical, for ship stability, height thresholds. Then, in the probabilistic part, the probability of encountering any wave sequence higher than the specified thresholds is calculated using distributions of wave heights and periods derived either empirically, from simulations of the wave field, or theoretically, directly from the spectrum. A first attempt to validate the concept was presented by Shigunov et al. [15] who selected a modern 8000 TEU containership to calculate the probability of exceeding a  $40^\circ$  roll angle threshold. The results were tested against Monte Carlo simulations and fair coincidence was noted in the case of beam seas excitation.

Recently, Anastopoulos and Spyrou [3] demonstrated that the performance of the method in predicting extreme roll responses in beam seas is improved if critical thresholds are defined in terms of realistic wave group shapes being, in fact, the “most expected” representatives of the ambient sea state. In assessing the accuracy of the approach, it was concluded that treating the initial state of the vessel in a probabilistic context is essential when dealing with sea conditions causing very few extremes.

In this paper, a simplified setup of the most contemporary version of the “critical wave groups” method, presented in [3], is developed. The simplifications address the problem of exhaustively generating wave group environments in the process of determining the critical ones and expand in two directions. In the first, the idea is to focus our attention on identifying instability-causing wave groups for only one set of initial conditions of the ship at the beginning of the simulations. To determine the most relevant, for ship stability evaluation, initial state, well-established concepts of dynamical systems theory are invoked. In the second direction, the intention is to reduce the number of possible critical wave group shapes by exploiting the features of the “expected” wave groups derived for a given sea state. The method is applied to two ship models operating in qualitatively different, with respect to the frequency that extreme responses are realized, sea states in order to calculate the probability of exceedance for a number of roll angle thresholds. In this context, the conditions under which the simplified “critical wave groups” scheme produces comparable results with those obtained from Monte Carlo simulations of roll motion are investigated and the focus is set on the region of extreme responses where the accuracy of the latter is disputable.

## 2 A Simplified “Critical Wave Groups” Method

In the literature of ocean and coastal engineering, wave groups are traditionally defined as sequences of waves with heights exceeding a certain preset level and periods varying within a potentially narrow range [11, 13]. No doubt, such a definition can only rely on subjective criteria regarding the selection of an “appropriate”, for the identification of wave grouping phenomena, height threshold. To overcome this issue in analyzing ship dynamics, wave groups are considered herein as sequences of waves which, given the variability of their periods, are sufficiently high to provoke instabilities.

### 2.1 *Mathematical Formulation*

Let us assume that we are interested in estimating the probability that a vessel exceeds a limiting, from ship stability point of view, roll angle threshold  $\varphi_{cr}$ . The key idea of the “critical wave groups” method is to first identify the wave events that cause

the exceedance and then, calculate the probability of encountering them. This is expressed by Eq. (1), presented below:

$$\Pr[\varphi > \varphi_{cr}] = \sum_k \underbrace{\Pr\left[\varphi > \varphi_{cr} \mid \left(\bigcup_q w g_{k,q}, i c_k\right)\right]}_{=1} \times \Pr\left[\bigcup_q w g_{k,q}, i c_k\right] \quad (1)$$

where  $w g_{k,q}$  is a wave group event with characteristics  $q$ , determined for the  $k$ -th set of initial conditions  $\{\varphi_0, \dot{\varphi}_0\}$  of the vessel at the moment of the encounter. Nonetheless, evaluating stability by considering a large number of initial states  $\{\varphi_0, \dot{\varphi}_0\}$  can be time-consuming and eventually may become impractical in early design stages when decision-making requires swift calculations. In assessing the influence of initial conditions on transient ship dynamics, Thompson and co-workers discovered that capsizing tendency is associated with a specific excitation level which is immensely independent of  $\{\varphi_0, \dot{\varphi}_0\}$  for a given ship hull (e.g. [22]). This is due to the fact that, at this critical level, the erosion of the safe basin is sudden, rapid and, most importantly, starts “from within”, i.e. in the vicinity of  $\{\varphi_0, \dot{\varphi}_0\} = \{0, 0\}$ . It can be argued, therefore, that examining only the upright equilibrium position of the vessel, corresponding to  $k = 0$  in Eq. (1), can be somehow acceptable. Moreover, from a preliminary investigation on the sensitivity of the estimates of the “critical wave groups” method to the initial conditions, Themelis and Spyrou [21] concluded that retaining only  $k = 0$  in Eq. (1) may be sufficient for sea states being highly probable to provoke resonance. Based on the above, the probability of exceeding  $\varphi_{cr}$  is approximated here through the following equation:

$$\begin{aligned} \Pr[\varphi > \varphi_{cr}] &= \sum_k \Pr\left[\bigcup_q w g_{k,q} \mid i c_k\right] \times \Pr[i c_k] \\ &\approx \Pr\left[\bigcup_q w g_{0,q} \mid i c_0\right] := \Pr\left[\bigcup_q w g_q^{(0)}\right] \end{aligned} \quad (2)$$

where the symbol “:=” is used to indicate the introduction of a new (more compact) notation (right-hand side) for the probability object appearing in the left-hand side. The superscript (0) implies that the probability calculations are performed over the set of instability-causing wave groups ( $w g_q$ ) determined for  $\{\varphi_0, \dot{\varphi}_0\} = \{0, 0\}$  only. Equation (2) describes the essence of a swift “critical wave groups” approach being, in fact, a reduced order version of the method presented in [3] which duly accounts for the probabilistic nature of the initial state  $\{\varphi_0, \dot{\varphi}_0\}$  of a vessel when hit by a wave group.

For large  $\varphi_{cr}$  one may assume that individual wave group occurrences are sufficiently rare to be treated as statistically independent. In the light of this, Eq. (2) is reformulated as [3]:

$$\begin{aligned} \Pr \left[ \bigcup_q w g_q^{(0)} \right] &= 1 - \Pr \left[ \overline{\bigcup_q w g_q^{(0)}} \right] \\ &= 1 - \Pr \left[ \bigcap_q \overline{w g_q^{(0)}} \right] = 1 - \prod_q (1 - \Pr[w g_q^{(0)}]) \end{aligned} \quad (3)$$

where the overbar denotes the complement of an event. A significant challenge in Eq. (3) is to ensure that wave groups causing  $\varphi > \varphi_{cr}$  form a set of mutually exclusive and collectively exhaustive events. To avoid possible overlaps in the calculations, wave groups are classified with respect to their characteristics  $q$  being: (a) the run length  $j$ , i.e. the number of consecutive heights exceeding a critical threshold and (b) the range within which the periods of participating waves are considered to vary  $T_{cr,m}$ :

$$\Pr[w g_q^{(0)}] = \Pr[w g_{m,j}^{(0)}] = \Pr[\mathbf{H}_j > \mathbf{h}_{cr,j}, \mathbf{T}_j \in T_{cr,m}] \quad (4)$$

where  $\mathbf{H}_j = \{H_1, \dots, H_j\}$  and  $\mathbf{T}_j = \{T_1, \dots, T_j\}$  are vectors of random variables referring respectively to the heights  $H_n$  and periods  $T_n$  of an individual wave group event with run length  $j$  ( $1 \leq n \leq j$ ),  $\mathbf{h}_{cr,j} = \{h_{cr,1}, \dots, h_{cr,j}\}$  is a deterministic vector containing the heights of a critical wave group with run length  $j$ . It is remarked that, in (4), the vectorial inequality denotes comparisons between the corresponding components of the two vectors.

Eventually, the calculation of the right-hand side of Eq. (4) is performed in two parts: a deterministic one, focused on the identification of the so called “critical” wave groups, i.e. those wave successions leading to only slight exceedance of  $\varphi_{cr}$ ; and a probabilistic part for calculating the probability of encountering any wave group higher than the determined critical. The implementation of the former is, in general, straightforward and requires a ship motion model and a method for systematically generating wave group excitations. Then, for a given set of wave group parameters  $\{T_{cr,m}, j\}$ , the associated  $\mathbf{h}_{cr,j}$  vector can be determined through successive simulations, each of them testing a different, in terms of the heights of participating waves, group scenario, until the critical height sequence is detected [3]. As realized, the impact of the deterministic part on the effectiveness of the overall approach is explicitly related to the shape of the waveforms employed for representing critical wave groups. As for the probabilistic part of the approach, we follow the work of [10] who introduced the idea of modeling wave successions as Markov chains.<sup>1</sup> Nowadays, the concept enjoys wide acceptance by the scientific community since it has been successfully validated several times by both numerical simulations and real wave field measurements (e.g. [17]). Within the Markovian framework, the probability of encountering dangerous wave groups with certain specifications, as in Eq. (4), can be expressed as:

<sup>1</sup> In very simple terms, a Markov chain is a sequence of random events in which a future outcome depends solely on the event realized at the previous step.

$$\begin{aligned}
& \Pr[\mathbf{H}_j > \mathbf{h}_{cr,j}, \mathbf{T}_j \in T_{cr,m}] \\
&= p_0 \times \prod_{n=2}^j \int_{h_{cr,n}}^{+\infty} \int_{T_{cr,m}} f_{H_n, T_n | H_{n-1}, T_{n-1}}(h_n, t_n | h_{n-1}, t_{n-1}) dt_n dh_n
\end{aligned} \tag{5}$$

where  $m = 1, 2, \dots, M$  denotes different cases of critical period segments and:

$$p_0 = \int_{h_{cr,1}}^{+\infty} \int_{T_{cr,m}} f_{H_1, T_1}(h_1, t_1) dt_1 dh_1 \tag{6}$$

In the above,  $f_{H_n, T_n | H_{n-1}, T_{n-1}}$  is the conditional probability density function (PDF) of wave height and period at time-step  $n$  given the values of these variables at the previous time step ( $n - 1$ ), while  $f_{H_n, T_n}$  is the joint height-period PDF of a single wave. Hence, the product term in Eq. (5) gives the probability of encountering a critical (or worse) sequence of  $j - 1$  waves given that an initial wave with height  $h_1 > h_{cr,1}$  and period  $t_1 \in T_{cr,m}$  is realized, while  $p_0$  is the probability of actually experiencing an initial wave with these characteristics.

## 2.2 Wave Groups Construction Method

Based on the Markovian property of sea waves, [1] developed a method for predicting the shape of the “expected” wave groups for a given sea state. In its original version, the method requires as input the run length  $j$  and the characteristics (height  $h_c$  and period  $t_c$ ) of the highest wave in order to generate the particular “expected” wave group for these specifications. In [3], a modified version of this method was discussed where the wave group construction algorithm could also allow for tuning the periods of individual waves to vary within a desired range  $T_{cr,m}$ . This, on the one hand, extends the capabilities of the “critical wave groups” method itself since the original construction process basically produces wave groups with periods varying only in the vicinity of the mean period of the assumed sea state. Therefore, when the natural period of the vessel in question is far from this regime, very few critical wave groups can be generated and eventually, the probability of stability failure is underestimated. On the other hand, having an additional design parameter ( $T_{cr,m}$ ) entails a larger number of possible wave group formations which, in turn, have to be tested in the deterministic part of the method. Here, aiming at formulating a relatively simpler “critical wave groups” setup, requiring fewer simulations, we resort to the original construction algorithm of [1], yet knowing that the effectiveness of the current (more efficient) approach will presumably be challenged when the examined sea conditions are very unlikely to provoke instabilities due to resonance. The algorithm is implemented in two steps described, in brief, next.

Given the wave group specifications  $\{j, h_c, t_c\}$ , the first step is to predict the “expected” values (in time) of the heights and periods of the participating waves. To this end, the height  $h_c$  and period  $t_c$  of the highest wave, assumed to occupy the  $n$ -th position ( $1 \leq n \leq j$ ) in the wave sequence, are used for initiating the following iterative scheme:

$$\bar{h}_n = \int_0^\infty h_n f_{H_n|H_{n-1}, T_{n-1}}(h_n|h_{n-1}, t_{n-1})dh_n \tag{7}$$

$$\bar{t}_n = \int_0^\infty t_n f_{T_n|H_n, H_{n-1}, T_{n-1}}(t_n|h_n, h_{n-1}, t_{n-1})dt_n \tag{8}$$

where the overbar is used to denote the expected value of the corresponding random variable. The integral kernels  $f_{H_n|H_{n-1}, T_{n-1}}$  and  $f_{T_n|H_n, H_{n-1}, T_{n-1}}$  are the transition PDFs of the Markov chain and can be obtained either from spectral methods [1] or by “direct counting” procedures based on Monte Carlo simulations of the wave field [2]. Provided the time reversibility property of this particular Markov chain, and since the characteristics of the highest wave are a priori known, at most  $j - 1$  iterations of Eqs. (7) and (8) are required for predicting the “expected” characteristics of the surrounding waves. If, for example, the objective is to construct a wave group with  $j = 5$  and highest wave encountered in the 4th position, then it is sufficient to predict the heights and periods  $\{h_n, t_n\}$  of the 3 preceding waves ( $n = 1, \dots, 3$ ) and eventually set  $\{h_5, t_5\} = \{h_3, t_3\}$  due to time reversibility. The concept applies to all wave group configurations, unless the highest wave occupies either the first or the last ( $j$ -th) position and thus, all  $j - 1$  iterations need to be performed. Finally, to avoid any confusion due to the notation used herein, we emphasize that Eqs. (7) and (8) naturally differ from Eqs. (6) and (8) in [3] due to the absence of the  $T_{cr,m}$  parameter from the current approach, as discussed in the above. Moreover, Eq. (8) improves Eq. (4) of [1] since it takes into account the correlation between the height and the period of a predicted wave.

The final step of the construction process deals with the generation of the wave group time-history at a fixed location  $x_0$ , given the height and period sequences obtained from the previous step. This can be formulated as an identification problem with respect to the  $b_i$  parameters appearing in the following expression for the water surface elevation  $\eta$ :

$$\eta(t) = \sum_{i=0}^{5j} b_i \sin(k_i x_0 - \omega_i t) \tag{9}$$

where  $j$  is the run length of the wave group under construction. The idea here is to consider Eq. (9) as an interpolating function passing through a number of key points (i.e. crests, troughs and zero-crossings) describing the wave group shape in the time domain. The coordinates of these points can be inferred from the “expected” height and period values derived from Eqs. (7) and (8) (more details on this part can be

found elsewhere, e.g. in [2]). To ensure the uniqueness of the solution, the number of terms kept in the series expansion (i.e.  $5j + 1$ ) is set equal to the number of imposed geometrical constraints and thus, it becomes a function of the run length  $j$ . The above constitute a well-defined (Hermite-type) interpolation problem for which closed-form expressions for the  $b_i$  parameters are available in the existing literature (e.g. [12]).

### 2.3 Equation of Roll Motion

In principle, “the critical wave groups” method is not biased towards any specific type of mathematical model (in fact, it can handle equally a simple ODE and a CFD model). However, since our intention is to evaluate the performance of the approach, massive Monte Carlo simulations will have to be carried out using the very same model of ship motion. Aiming at enhancing the reliability of Monte Carlo estimates (particularly in the tail region) through a large (and computationally inexpensive) simulation campaign, we adopt the following uncoupled equation, written in terms of the relative roll angle  $\varphi$ :

$$(I_{44} + A_{44})\ddot{\varphi} + D(\dot{\varphi}) + g\Delta GZ(\varphi) = M(t) \quad (10)$$

with  $I_{44}$  and  $A_{44}$  being the roll moment of inertia and the added moment of inertia, respectively,  $\Delta$  is the ship displacement,  $g$  is the gravitational acceleration and  $D$  is the damping moment:

$$D(\dot{\varphi}) = B_1\dot{\varphi} + B_2\dot{\varphi}|\dot{\varphi}| \quad (11)$$

The restoring arm in still water is given as:

$$GZ(\varphi) = \sum_k C_k \varphi^k \quad (12)$$

When information about the roll moment amplitude operator  $F_{roll}(\omega)$  is available, the wave group induced moment can be expressed, via Eq. (9), as:

$$M(t) = \sum_{i=0}^{5j} F_{roll}(\omega_i) b_i \sin(k_i x_0 - \omega_i t) \quad (13)$$

Alternatively, in the presence of long incident waves, the concept of instantaneous wave slope at the middle of the ship  $\alpha(t) = \partial\eta(x, t)/\partial x|_{x=x_0}$  can be employed [24]:

$$M(t) = -I_{44}\ddot{\alpha}(t) \quad (14)$$



### 3 Results and Discussion

In this section, the simplified “critical wave groups” scheme is applied to two different ship models in order to compute the probability of exceedance  $P_e = \Pr[\varphi > \varphi_{cr}]$  for several roll angle thresholds  $\varphi_{cr}$ . These are implied as possible limits of unacceptable behaviour given that Eq. (10) is a very simple roll model and it does not contain design information about deck submergence, downflooding angles etc. As a result, derived  $P_e$  values are considered to be referring to a parameterized limit for stability failure. Regarding the construction of the “expected” wave groups, the transition PDFs in Eqs. (7) and (8) are determined according to the copula-based methodology described in [1], yet the necessary correlation parameters are estimated from datasets produced from extensive simulations of the water surface displacement. In this way, the effectiveness of the Markov model in predicting the “expected” wave height and period sequences is enhanced. For calculating the probability in Eq. (5), the associated PDF  $f_{H_n, T_n | H_{n-1}, T_{n-1}}$  is also obtained by direct counting procedures based on the generated wave data. To investigate the possibility of eliminating the computational cost due to the generation of the “expected” wave groups, regular wave trains are also tried for representing critical group encounters. In both the regular and the “expected” wave group implementations of the approach the results are tested against Monte Carlo simulations of roll motion.

#### 3.1 Ship Model 1

An ocean surveillance ship, referred in the study of [19], was selected as the first ship model. Main parameters of the vessel are given in Table 1 and the roll moment amplitude operator  $F_{roll}(\omega)$  is presented in Fig. 1.

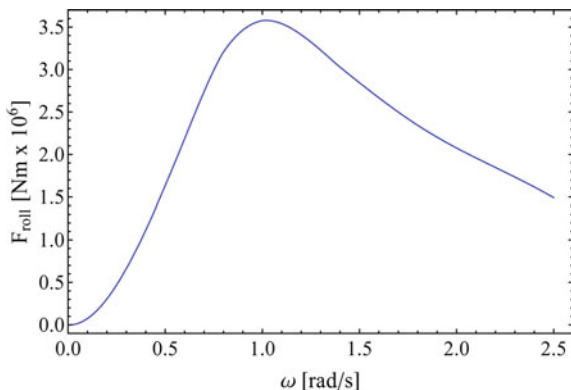
The ship is assumed to operate in conditions described by the Bretschneider spectrum with significant wave height  $H_s = 4\text{m}$  and peak period  $T_p = 6\text{s}$  (e.g. [13]):

$$S_{\eta\eta}(\omega) = \frac{1.25}{4} \frac{\omega_p^4}{\omega^5} H_s^2 \exp\left[-\frac{5}{4} \cdot \left(\frac{\omega_p}{\omega}\right)^4\right] \tag{15}$$

**Table 1** Main parameters of ship model 1

Parameter	Dimensional value	Dimensions
$I_{44} + A_{44}$	$5.540 \times 10^7$	kg m <sup>2</sup>
$\Delta$	$2.056 \times 10^6$	kg
$B_1$	$5.263 \times 10^6$	kg m <sup>2</sup> /s
$B_2$	$2.875 \times 10^6$	kg m <sup>2</sup>
$C_1$	3.167	m
$C_3$	-2.513	m

**Fig. 1** Roll moment amplitude operator  $F_{roll}(\omega)$  for ship model 1



were  $\omega_p = 2\pi/T_p$  is the peak frequency. For the simulations of the wave field, the spectral representation method is adopted [18]:

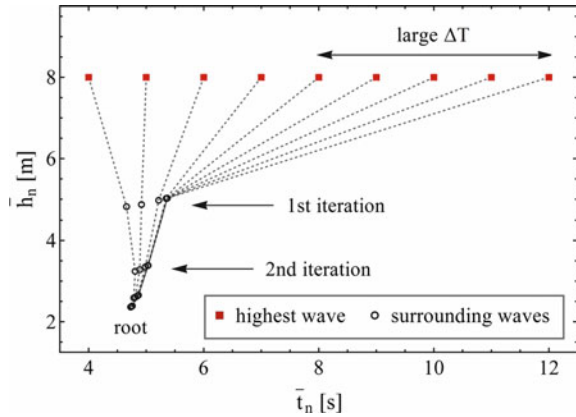
$$\eta(t) = \sum_i \sqrt{2S_{\eta\eta}(\omega_i)\delta\omega_i} \cos(\omega_i t + \varepsilon_i) \quad (16)$$

were  $\varepsilon_i$  are random variables uniformly distributed over  $[0, 2\pi)$ ,  $\omega_i$  are the frequencies of the wave components and  $\delta\omega_i$  is the frequency resolution. In total, 18,853 waves were analyzed from a set of 24 records of 1h produced within 7min on a modern laptop using the Fast Fourier Transform (FFT) approach [16].

Furthermore, Monte Carlo simulations of roll motion were set-up accordingly so as to estimate desired probabilities using ensemble averages, i.e. without assuming the ergodic property for the response [4]. The idea was to explore the roll probability space at a fixed time instant  $t_s$  beyond which the statistical properties of the response process remain practically constant. Specifically, a collection of approximately  $15 \times 10^5$  short-duration realizations was simulated and the roll angle value sampled at  $t_s = 150s$  was kept from each realization for further analysis (details for duly selecting  $t_s$  are given in [3]). Then, exceedance probabilities for various roll angle thresholds  $\varphi_{cr}$  were computed through the number of observed exceedances over  $\varphi_{cr}$  divided by the sample size ( $15 \times 10^5$ ). To quantify the uncertainty of these direct counting estimates, the Wilson score confidence interval was preferred knowing that it is the most consistent with the nominal coverage probability among a number of binomial proportion-based intervals described in the literature [7]. At this point, it is important to distinguish Eq. (9) from Eq. (16) since the latter is a well-known model for representing stochastic processes, while the former is only a Fourier-based interpolation function, essentially not designed for Monte Carlo simulations. Therefore, for massively generating roll response time-histories through Eq. (10), the wave induced moment was obtained by multiplying each individual wave component in Eq. (16) by the corresponding  $F_{roll}(\omega_i)$  amplitude.

Figure 2 illustrates the pattern of the predictions of Eqs. (7) and (8) for the examined sea conditions when various  $\{h_c, t_c\}$  values (squares) are considered. The

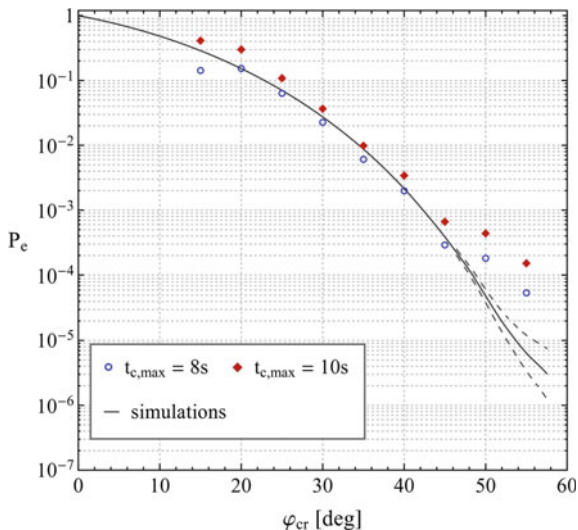
**Fig. 2** Map of the “expected” height and period sequences generated for the Bretschneider spectrum



“expected” heights  $\bar{h}_n$  and corresponding periods  $\bar{t}_n$ , as derived from successive iterations, are shown on the vertical and horizontal axes, respectively. The evolution of the procedure for a given set of  $\{h_c, t_c\}$  parameters is denoted by circles along the dashed lines. The root of this tree-shaped diagram is the stationary state of the Markovian system and the structure of the “expected” wave groups is largely affected by the distance of  $\{h_c, t_c\}$  from it. Since the width  $\Delta T$  of a critical period range  $T_{cr,m}$  is the difference of the shortest from the longest period in a generated sequence, it naturally coincides with this characteristic distance for wave groups with large  $j$  (i.e. when more iterations are applied). In this regard, the maximum period  $t_{c,max}$  used in the calculations should exhibit an interesting relationship with the deduced probability values. Finally, as anticipated, there is a large concentration of points close to the mean period of the sea state, indicated by the abscissa of the root.

Figure 3 presents the results of the Monte Carlo simulations (solid line) and the associated 95% confidence intervals (dashed lines) in the tail region. The estimates of the “critical wave groups” method, obtained by employing the “expected” wave group forms for the ambient sea state with run lengths  $j \leq 6$ , have been superimposed on the same plot. For the latter method, two implementations (denoted by circles and diamonds) are presented corresponding to different values of the maximum period  $t_{c,max}$  considered for initiating the iterations in Eqs. (7) and (8). As demonstrated in Fig. 2, for increasing  $t_c$  the highest wave progressively deviates from the periods of the surrounding waves leading to larger  $\Delta T$ . Therefore, the tolerance for the detection of resonant phenomena is relaxed and the probability in Eq. (5) increases. However, including very distant, with respect to the root,  $t_c$  values may be irrelevant, and more importantly inaccurate, since the period of the highest wave distorts the grouping character of the rest period sequence. To avoid this issue, Fig. 2 could be utilized for identifying the region where the Markov chain predictions are insensitive to  $t_{c,max}$ . For the sea state in question, this happens beyond  $t_c = 7s$  and thus, for  $t_{c,max} = 10s$  the proposed method consistently overestimates the probability of exceedance  $P_e$ . On the contrary, more reliable estimates are provided for  $t_{c,max} = 8s$ . Interestingly, for practical instability limits  $\varphi_{cr} \in [30 \text{ deg}, 40 \text{ deg}]$ , the selection of

**Fig. 3** Probability of exceedance for ship model 1 using irregular wave groups (circles and diamonds). Dashed lines indicate the 95% confidence intervals of the simulation-based estimates (solid line)



$t_{c,max}$  does not seem to be that important, given that in both the examined scenarios the method performs satisfactorily. In the tail region, though, both schemes predict more exceedances than the Monte Carlo approach; this, however, could be due to the very rarity of the extremes. The current method was not applied for  $\phi_{cr} < 15$  deg since in this regime ship response is, in principle, Gaussian [3]. In producing results for all 9 thresholds, the elapsed time per  $t_{c,max}$  case was less than an hour on a modern desktop, including the most time-consuming part of the procedure being the construction of the “expected” wave groups.

On the other hand, the effectiveness of the “critical wave groups” method deteriorates when regular wave trains with  $j \leq 6$  are employed, as shown in Fig. 4. In the same spirit, two different cases of critical period range widths  $\Delta T$  were studied and both were found to consistently underestimate the probability of exceedance below  $40^\circ$ . For larger angles, though, the accuracy of the method is improved, particularly for  $\Delta T = 2s$ . This is in accordance with the work of [22] who concluded that in analyzing capsizing tendency,<sup>2</sup> it is sufficient to consider only the upright equilibrium initial state of the vessel when hit by a regular wave train. In the context of the “critical wave groups” method, this was verified by Themelis and Spyrou [21] who observed that the effect of the initial state becomes weaker (in terms of probability) for sea conditions associated with resonant phenomena. Another important aspect of the regular-wave implementation of the current approach is that, in contrast to the “expected” wave groups-based scheme, there is no guidance (at the moment at least) for selecting  $\Delta T$  accordingly. Only in retrospect it can be deduced that setting  $\Delta T = 1s$  is too strict. Finally, although here calculations were performed for 11 thresholds, the associated computational cost per  $\Delta T$  scenario was only few minutes

<sup>2</sup> Defined as the escape from the potential energy well; thus, implying the exceedance of a large roll threshold.

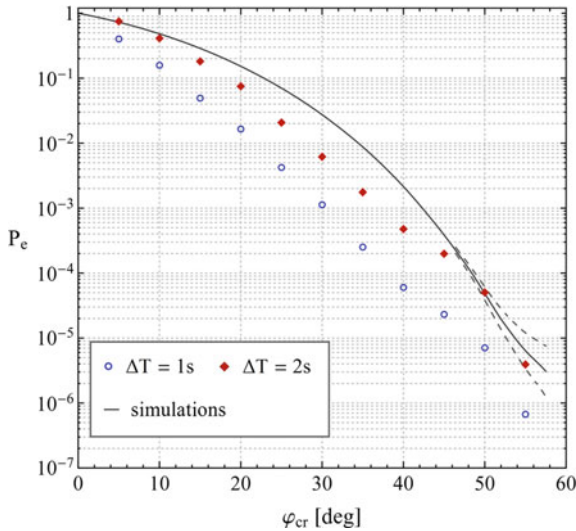


**Fig. 4** Probability of exceedance for ship model 1 using regular wave groups (circles and diamonds). Dashed lines indicate the 95% confidence intervals of the simulation-based estimates (solid line)

on a modern desktop. The dramatic speed-up comes from the time spent in generating wave group environments given that for regular waves it is practically negligible.

In the deterministic part of the method, critical wave group parameters, identified for  $\varphi_{crit} = 45\text{deg}$ , are summarized in Fig. 5 in the form “transient capsizing diagrams” [14]. These are plots of the wave steepness  $H/\lambda$  of a critical wave group against its period  $T$ , here normalized with the natural period of the vessel  $T_o = 5.9\text{s}$ . In the case of regular wave trains, the boundary between the “stable” and “unstable” regions is shown by solid lines, while for the “expected” wave groups, short and long dashed lines are utilized for indicating the boundary location when defined in terms of the mean and maximum steepness, respectively, of the participating waves. As one obtains two boundary lines for this case, shading has been applied to enhance the contrast against the regular-waves curve. For  $j = 2$ , height thresholds produced by regular and the “expected” wave trains are, in the mean sense, relatively close. For  $j = 3$ , however, the dangerous zone is enlarged when considering irregular wave groups. The shift of instability region towards the area of long waves has already been reported in [2].

### 3.2 Ship Model 2

A modern 4800 TEU Panamax containership with main parameters listed in Table 2 and natural period  $T_o = 15.2\text{s}$  was considered for a second case study. The restoring

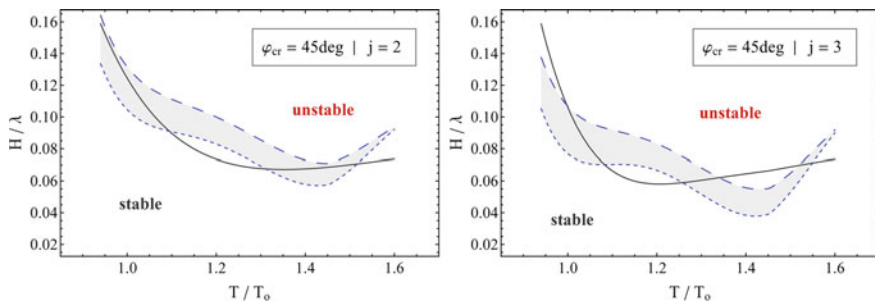


**Fig. 5** Transient capsizing diagrams for ship model 1 corresponding to run lengths  $j = 2$  (left panel) and  $j = 3$  (right panel); in both cases instability is defined as the exceedance of  $\varphi_{crit} = 45\text{deg}$

arm coefficients in Eq. (12) were provided directly from the loading manual of the vessel, while roll damping estimates were obtained by applying Ikeda’s method [9]. Since no information was available about the  $F_{roll}$  function, wave forcing was approximated by Eq. (14). In this application, the JONSWAP spectrum with  $H_s = 10\text{m}$ ,  $T_p = 14\text{s}$  and  $\gamma = 1.932$  was selected to describe the sea state of operation (e.g. [8]):

$$S_{\eta\eta}(\omega) = (1 - 0.287 \ln \gamma) S_B(\omega) \gamma^{\exp\left[-\frac{1}{2} \left(\frac{\omega - \omega_p}{0.08\omega_p}\right)^2\right]} \quad (17)$$

where  $S_B(\omega)$  is the Bretschneider spectrum. Again, wave group statistics were extracted by simulating 24 records of 1h length using Eq. (16). These produced a total population of 7,875 waves within only few minutes on a modern desktop. Roll motion time-histories were generated using the same setup as for ship model 1, yet sampled at  $t_s = 200\text{s}$ .

The results obtained from the implementation of the “critical wave groups” method when ship model 2 is excited by the “expected” wave groups for the given sea state and by regular wave trains are presented in Figs. 6 and 7, respectively. Regarding the accuracy of the approach for roll angle thresholds up to  $40^\circ$ , again it is enhanced when irregular waveforms are employed. Beyond  $43^\circ$ , the Monte Carlo simulations did not predict any extremes due to the problem of rarity; while in the same regime both schemes of the current method seem to reliably extrapolate the

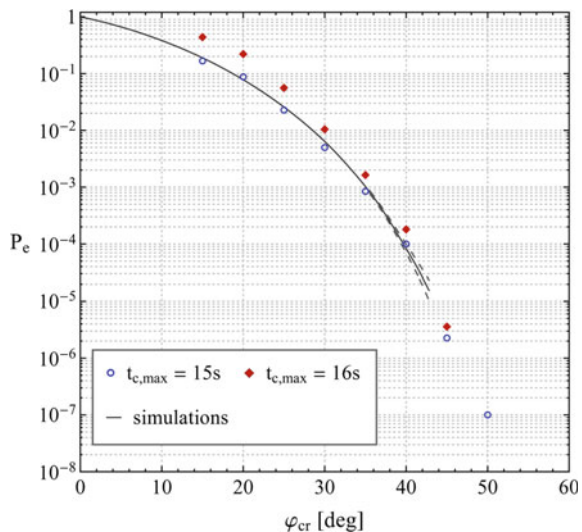
**Table 2** Main parameters of ship model 2

Parameter	Dimensional value	Dimensions	Parameter	Dimensional value	Dimensions
$I_{44}$	$1.020 \times 10^{10}$	kg m <sup>2</sup>	$C_1$	2.851	m
$A_{44}$	$1.021 \times 10^9$	kg m <sup>2</sup>	$C_3$	5.407	m
$\Delta$	$6.820 \times 10^7$	kg	$C_5$	-18.169	m
$B_1$	$4.829 \times 10^8$	kg m <sup>2</sup> /s	$C_7$	14.278	m
$B_2$	$6.316 \times 10^8$	kg m <sup>2</sup>	$C_9$	-3.677	m

trend of the direct counting estimates. As for the selection of  $t_{c,max}$ , it was based on the same methodology described for ship model 1. Specifically,  $t_{c,max} = 15s$  was anticipated to perform better since beyond this value the “expected” height and period sequences were found practically independent of the assumed  $\{h_c, t_c\}$ . In the regular-wave version of the approach, it can be argued that setting  $\Delta T = 2s$  is more suitable for calculating exceedance probabilities  $P_e$  associated with intermediate roll angle thresholds, while  $\Delta T = 1s$  appears more suitable for extrapolation, as documented also in [3]. The specific sea state was consciously selected for demonstrating the extrapolation character of the proposed method since although it is very likely to provoke resonance,  $H_s$  is not high enough for inducing many extremes. More so, [21] have observed that, for such sea states, considering various initial conditions within the “critical wave groups” framework is rather unnecessary.

Finally, Fig. 8 compares regular and irregular critical wave trains with  $j = 2$  and  $j = 3$  in terms of their contribution to the total probability of exceedance  $P_e$ . The calculations were made for the critical period parameters that provided the best agreement with the simulation results in Figs. 6 and 7. Thus,  $\Delta T = 2s$  and  $t_{c,max} = 15s$  were selected for the regular and the irregular case, respectively. The contribution of run lengths with  $j > 6$  to the total probability of exceedance was found negligible.

**Fig. 6** Probability of exceedance for ship model 2 using irregular wave groups (circles and diamonds). Dashed lines indicate the 95% confidence intervals of the simulation-based estimates (solid line)



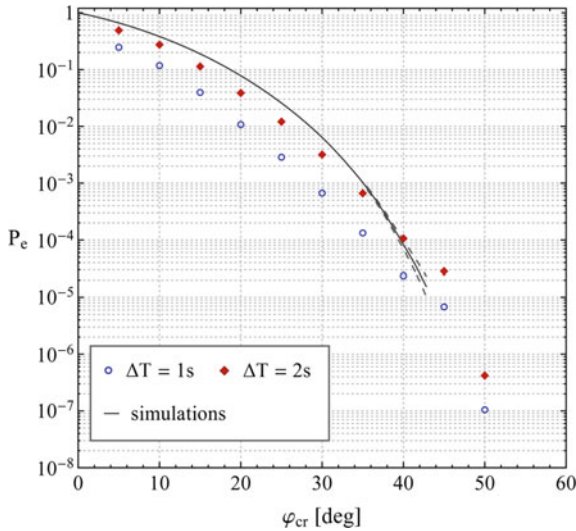


**Fig. 7** Probability of exceedance for ship model 2 using regular wave groups (circles and diamonds). Dashed lines indicate the 95% confidence intervals of the simulation-based estimates (solid line)

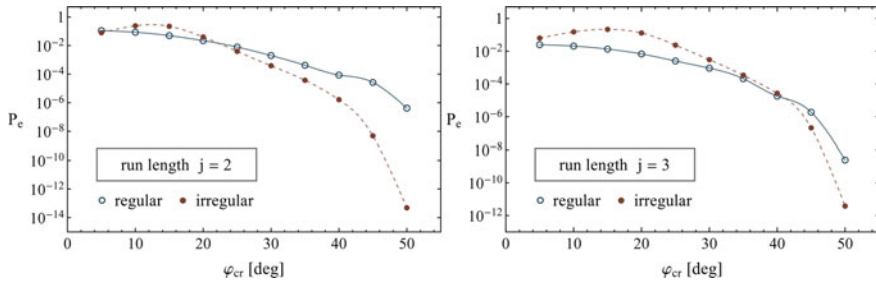


**Fig. 8** Contribution of individual run lengths  $j$  to the probability of exceedance for ship model 2

### 4 Concluding Remarks

In this study, a simple and computationally efficient “critical wave groups” method was developed for calculating the probability of large-amplitude ship motions in beam seas. The method is focused on providing swift estimates by examining only one scenario of initial conditions of the vessel when approached by the “expected” wave groups for the ambient state. To investigate the possibility of further simplification, since the generation of realistic wave environments is time-consuming, the method was applied also using regular wave trains. The effectiveness of both the regular and the “expected” wave group-based schemes was assessed through comparisons with the predictions of Monte Carlo simulations of roll motion. The results indicate that



the proposed method performs better when the “expected” wave groups are utilized for representing critical, for ship stability, wave episodes, particularly because period successions are modeled in a realistic manner. Since the degree of variability allowed in the wave period groupings is crucial for the accuracy of the method, guidelines were formulated for duly selecting it. This contributed not only in obtaining reliable estimates for practical limiting angles (e.g.  $40^\circ$ ), but also in extrapolating in the tail region where the efficiency of Monte Carlo simulations is generally low.

Most importantly, given that only few minutes were needed for completing the calculations with respect to a single roll angle threshold, the current approach appears very suitable for preliminary ship stability evaluations. At the same time, however, it is designed specifically for sea states being highly probable to provoke resonance since otherwise most critical wave encounters will presumably remain unidentified due to the very nature of the “expected” wave groups. More so, in non-resonant sea states the effect of initial conditions becomes quite important [21] and thus, the more detailed version of the “critical wave groups” method, discussed in [3], should be invoked. As a final remark, methods for quantifying the uncertainty of the estimates obtained via the “critical wave groups” approach are currently investigated and results will hopefully be presented in future studies.

**Acknowledgements** The work of Mr. Anastopoulos was supported by NTUA’s Special Account for Research Grants (ELKE). The final year thesis work of Mr. Georgios Papageorgiou, who graduated in 2017 from our School, has motivated partly the current study.

## References

1. Anastopoulos PA, Spyrou KJ, Bassler CC, Belenky VL (2016) Towards an improved critical wave groups method for the probabilistic assessment of large ship motions in irregular seas. *Probab Eng Mech* 44:18–27
2. Anastopoulos PA, Spyrou KJ (2016) Ship dynamic stability assessment based on realistic wave group excitations. *Ocean Eng* 120:256–263
3. Anastopoulos PA, Spyrou KJ (2019) Evaluation of the critical wave groups method in calculating the probability of ship capsize in beam seas. *Ocean Eng* 187:106213
4. Belenky VL, Degtyarev AB, Boukhanovsky AV (1998) Probabilistic qualities of nonlinear stochastic rolling. *Ocean Eng* 25(1):1–25
5. Belenky VL, Weems K, Pipiras V, Glotzer D, Sapsis TP (2018) Tail structure of roll and metric of capsizing in irregular waves. In: *Proceedings of the 32nd symposium on naval hydrodynamics*, Hamburg, Germany
6. Belenky VL, Glotzer D, Pipiras V, Sapsis TP (2019) Distribution tail structure and extreme value analysis of constrained piecewise linear oscillators. *Probab Eng Mech* 57:1–13
7. Brown LD, Cai TT, DasGupta A (2001) Interval estimation for a binomial proportion. *Stat Sci* 16(2):101–117
8. Det Norske Veritas (DNV) (2011) Modelling and analysis of marine operations. Report No. H103
9. Ikeda Y, Himeno Y, Tanaka N (1978) A prediction method for ship roll damping. Report No. 00405 of the Department of Naval Architecture, University of Osaka Prefecture
10. Kimura A (1980) Statistical properties of random wave groups. In: *Proceedings of the 17th international coastal engineering conference*, Sydney, Australia, pp 2955–2973

11. Masson D, Chandler P (1993) Wave groups: a closer look at spectral methods. *Coast Eng* 20:249–275
12. Nathan A (1975) Trigonometric interpolation of function and derivative data. *Inf Control* 28(3):192–203
13. Ochi M (1998) *Ocean waves: the stochastic approach*. Cambridge University Press, Cambridge. ISBN: 978-0-521-01767-1
14. Rainey RCT, Thompson JMT (1991) The transient capsizing diagram—a new method of quantifying stability in waves. *J Ship Res* 35(1):58–62
15. Shigunov V, Themelis N, Spyrou KJ (2019) Critical wave groups vs. direct Monte-Carlo simulations for typical stability failure modes of a container ship. In: Belenky V, Spyrou K, van Walree F, Almeida Santos Neves M, Umeda N (eds) *Contemporary ideas on ship stability*. Fluid mechanics and its applications vol 119, Springer, pp 407–421. ISBN: 978-3-030-00514-6
16. Shinozuka M, Deodatis G (1991) Simulation of stochastic processes by spectral representation. *Appl Mech Rev* 44(4):191–204
17. Stansell P, Wolfram J, Linfoot B (2002) Statistics of wave groups measured in the northern North Sea: comparisons between time series and spectral predictions. *Appl Ocean Res* 24:91–106
18. St Denis M, Pierson WJ (1953) On the motions of ships in confused seas. *Transactions of SNAME* 61:280–332
19. Su Z (2012) *Nonlinear response and stability analysis of vessel rolling motion in random waves using stochastic dynamical systems*. Ph.D. Thesis, Texas A&M University, United States
20. Themelis N, Spyrou KJ (2007) Probabilistic assessment of ship stability. *Transactions of SNAME* 115:181–206
21. Themelis N, Spyrou KJ (2008) Probabilistic assessment of ship stability based on the concept of critical wave groups. In: *Proceedings of the 10th international ship stability workshop*, Daejeon, Korea, pp 115–125
22. Thompson JMT, Rainey RCT, Soliman MS (1990) Ship stability criteria based on chaotic transients from incursive fractals. *Phil Trans R Soc A* 332(1624):149–167
23. Campbell B, Weems K, Belenky VL, Pipiras V, Sapsis TP (2023) Envelope peaks over threshold (EPO) application and verification. Chapter 16 in: Spyrou K, Belenky VL, Katayama T, Bačkalov I, Francescutto A (eds) *Contemporary ideas on ship stability—from dynamics to criteria*. Fluid mechanics and its applications vol 134, Springer, pp 265–289. ISBN: 978-3-031-16328-9
24. Wright JHG, Marshfield WB (1980) Ship roll response and capsizing behavior in beam seas. *RINA Transactions* 122:129–148

# On Extending Multifidelity Uncertainty Quantification Methods from Non-rare to Rare Problems



Brendan Brown and Vlasdas Pipiras

**Abstract** When modeling a random phenomenon (e.g. ship motions in irregular seas), data are often available from multiple sources, or models, of varying fidelity, those with higher fidelity carrying higher costs. Multifidelity uncertainty quantification (UQ) offers tools that allow using lower-fidelity and lower-cost models to inform decisions being made about high-fidelity models. With a few exceptions though, much of the focus of the multifidelity UQ literature has been on characterizing uncertainty related to averages, in the context of non-rare problems where data are available to estimate these averages directly. In this work, we extend some multifidelity UQ methods to estimation of probabilities of rare events, possibly those that have not been observed in high-fidelity data. The suggested approach is based on bivariate extreme value theory, applied to simultaneously large observations from low-fidelity and high-fidelity models. The ideas are illustrated on simulated data associated with ship motions. It is not assumed that the reader is familiar with multifidelity UQ, with the discussion focusing on the most basic setting and building naturally from the recalled methods for non-rare problems.

**Keywords** Uncertainty quantification · Multifidelity estimators · Bivariate extremes · Sampling variability · Probability of rare event · Nonlinear random oscillator · Ship motions

## 1 Introduction

When studying random phenomena of interest, it is common to examine data from multiple sources or models. For example, ship motions or loads data can be collected from a model basin or sea trials, or generated from various computer programs, e.g. SimpleCode [12], LAMP [6, 11]. LAMP is a potential-flow code with a body nonlinear formulation for hydrostatic and Froude-Krylov forces, while diffraction and radiation forces are computed over mean waterplane. SimpleCode

---

B. Brown · V. Pipiras (✉)  
University of North Carolina, Chapel Hill, USA  
e-mail: [pipiras@email.unc.edu](mailto:pipiras@email.unc.edu)

is a volume-based body-nonlinear numerical simulation, capturing radiation forces through constant added mass and damping coefficients. LAMP alone has myriad options for calculations (various ways to account for water on deck, inclusion of different terms for disturbance forces, and so on). With data at hand, a common goal is to estimate some quantities of interest, for example, mean, single significance amplitude (SSA), etc. In this case, how should different estimates of the same quantities of interest obtained across multiple models be interpreted? If one of the models is less “expensive” to run but less accurate, how can it be used in conjunction with the more expensive and more accurate models in order to estimate better the quantities of interest? What does this say about differences among the models?

These questions have been studied from various angles as part of the Uncertainty Quantification (UQ) literature in the direction of the so-called multifidelity (MF) methods. See, for example, a recent survey paper [8]. As above, at the most basic level, the underlying assumption of these methods is the availability of two sets of data, one associated with the variable  $X_e$  and the other with the variable  $X_s$ , referring to expensive (true, high-fidelity, etc.) model and simple (low-fidelity, surrogate, etc.) model, respectively. (We shall use the terms and subscripts for “expensive” and “simple” throughout this work, in lieu of perhaps more sophisticated “high-fidelity” and “low-fidelity.”) For example,  $X_e$  could refer to CFD and  $X_s$  to LAMP calculations. The interest is in estimating the mean (or the expected value)  $\mathbb{E}(X_e)$  of the expensive response, or some function thereof, having the data from both expensive and simple models. Construction and calibration of simple models also make an important part of MF methods, but these will not be our focus here. That is, we suppose that data on  $X_e$  and  $X_s$  are given and ask questions about implications of this setting.

Estimation of the mean through available MF methods concerns non-rare behavior of the studied random phenomenon in that there is enough variability in collected data to make an informed decision about behavior of the mean. In this work, we are interested in analogous MF methods but for rare problems. A working example throughout this paper is that of estimating an exceedance probability  $\mathbb{P}(X_e > x)$  for some large threshold  $x$ , so that  $X_e > x$  is a rare event. The latter event might be so rare that it is not even observed in the data from the expensive model. It should be noted nevertheless that in the latter case, the rare probability could, in principle, still be estimated through the approach of the statistical Extreme Value Theory (EVT); see e.g. [2]. This approach for extreme ship motions, capsizing and other rare phenomena has been studied quite extensively by the second author of this work and collaborators over the past number of years (e.g. [1, 3, 4]).

In the context of estimating a rare exceedance probability  $\mathbb{P}(X_e > x)$ , we are thus interested in whether and how the data for the variable  $X_s$  from the simple model might be useful. For example, since the simple model is thought to be inexpensive to run, the events  $X_s > x$  could, in principle, be observed in long records of the model. Then, could one use the direct estimate of the probability  $\mathbb{P}(X_s > x)$  for that of  $\mathbb{P}(X_e > x)$ ? These are the kind of questions that will be discussed in this work, within an introduced mathematically justified framework.

We are not aware of other works pursuing this exact line of investigation. The closest are perhaps MF methods for failure probabilities as in e.g. [7]. These failure

probabilities though are still estimated directly, perhaps in conjunction with importance sampling, whereas in this work, we do so indirectly through EVT. For this reason, the reader should also expect our approach to appear more complex, especially to those unfamiliar with EVT. Another work to mention is [10] who suggests using extremes from a reduced-order model to guide the study of those for a higher-fidelity model, in lieu of the more traditional extrapolation methods.

The MF methods discussed in this work will be illustrated on synthetic data generated from a non-linear random oscillator mimicking ship rolling. It should be noted that the synthetic data framework is for illustration purposes only; there is nothing more expensive or simpler about either model in the synthesis.

The rest of this work is organized as follows. Section 2 sets some notation and introduces the more probabilistic notions used throughout this work. In Sects. 3 and 4, we discuss and illustrate the most basic available MF estimator when making inference about the expected value (mean) in non-rare problems. Sections 5 and 6 extend this MF approach to estimating probabilities of rare events. Basic bivariate EVT is recalled and employed in developing the approach in Sect. 5. Section 7 concludes.

## 2 Basic Setting and Notation

At the most basic level, we assume the following setting. We observe two signals:  $X_e(t)$ ,  $t \in [0, T_e]$ , from an expensive, true, high- (or maybe engineering-level) fidelity model, and  $X_s(t)$ ,  $t \in [0, T_s]$ , from simple, surrogate, low-fidelity model. Again, the terms “expensive” and “simple” will be used exclusively below. The observation window sizes  $T_e$  and  $T_s$  are such that  $T_e \ll T_s$ , reflecting the idea that the simple model can be run for a much longer time period at low cost, though the exact costs will be mostly ignored here. More importantly, we assume that the expensive and simple models are run under the same “conditions” in that the error process

$$\epsilon(t) = X_e(t) - X_s(t), t \in [0, T_e], \quad (1)$$

is meaningful over the smaller observation window  $[0, T_e]$ .

Furthermore, the following notation will be used:  $\mu(Z)$ ,  $\sigma^2(Z) = \text{Var}(Z)$  will stand for a theoretical mean and variance, respectively, of a variable  $Z$  or a stationary process  $Z(t)$ ;  $\hat{\mu}(Z)$ ,  $\hat{\sigma}^2(Z)$  will denote statistical estimators of the latter quantities from data;  $\bar{Z}_T$  will refer to the sample average of  $Z(t)$  over time interval  $[0, T]$ . The hats used for other quantities will also refer to estimators. For example,  $\hat{\mathbb{P}}$  will refer to a probability estimate.

### 3 Methods for Non-rare Problems

In the setting described in Sect. 2, suppose that one is interested in estimating the mean  $\mu(X_e)$  of  $X_e$ . A multifidelity (MF) estimator of the mean is defined as

$$\hat{\mu}_{mf}(X_e) = \bar{X}_{s,T_s} + \bar{\epsilon}_{T_e} \quad (2)$$

or, equivalently, as

$$\hat{\mu}_{mf}(X_e) = \bar{X}_{s,T_s} + (\bar{X}_{e,T_e} - \bar{X}_{s,T_e}) = \bar{X}_{e,T_e} + (\bar{X}_{s,T_s} - \bar{X}_{s,T_e}), \quad (3)$$

where the last expression is a simple rearrangement of the previous one. For comparison, let also

$$\hat{\mu}_0(X_e) = \bar{X}_{e,T_e} \quad (4)$$

We make several observations that might be useful to readers unfamiliar with MF estimators. Note that  $\hat{\mu}_{mf}(X_e)$  is unbiased for  $\mu(X_e)$  even if  $\mu(X_e) \neq \mu(X_s)$ . This follows from Eq. (3) since

$$\mathbb{E}\hat{\mu}_{mf}(X_e) = \mathbb{E}\bar{X}_{s,T_s} + (\mathbb{E}\bar{X}_{e,T_e} - \mathbb{E}\bar{X}_{s,T_e}) = \mu(X_s) + (\mu(X_e) - \mu(X_s)) = \mu(X_e). \quad (5)$$

Another key observation and the crux of MF methods is that  $\hat{\mu}_{mf}(X_e)$  can potentially do better in estimating the mean than the baseline estimator  $\hat{\mu}_0(X_e)$ , in the sense that

$$\text{Var}(\hat{\mu}_{mf}(X_e)) < \text{Var}(\hat{\mu}_0(X_e)). \quad (6)$$

Indeed, suppose for simplicity that the two terms in Eq. (2) are independent so that the variance of their sum is the sum of the variances. The variance of the sample average  $\bar{Z}_T$  of a stationary process  $Z(t)$  behaves for large  $T$  as

$$\text{Var}(\bar{Z}_T) \approx \frac{\Pi(Z)}{T}, \quad (7)$$

where the so-called long-run variance  $\Pi(Z) = \int_{-\infty}^{\infty} \gamma_Z(u) du$  accounts for temporal dependence in the process  $Z(t)$  having the auto-covariance function  $\gamma_Z(u) = \text{Cov}(Z(t+u), Z(t))$  at lag  $u$ . Then, Eq. (5) is equivalent (for large  $T_e$  and  $T_s$ ) to

$$\frac{\Pi(X_s)}{T_s} + \frac{\Pi(\epsilon)}{T_e} < \frac{\Pi(X_e)}{T_e}, \quad (8)$$

which provides a verifiable condition for the MF estimator to outperform the baseline. As seen from Eq. (8), this will happen if

$$T_e \ll T_s \quad \text{and} \quad \Pi(\epsilon) < \Pi(X_e). \quad (9)$$

The first relation of Eq. (9) is natural in the scenario of low costs for the simple model. The second relation in Eq. (9) states effectively that the error between the signals of the simple and expensive models must be small compared to the original expensive signal. This is also intuitive as the simple model should be useful only if it approximates the expensive model well. The same will be true in our extension to rare problems. We should also note that the key consequence of Eqs. (6) and (8) is that a normal confidence interval for the mean  $\mu(X_e)$  would be smaller when using  $\hat{\mu}_{mf}(X_e)$  as its length is determined by  $Var(\hat{\mu}_{mf}(X_e))$ .

In practice, the above discussion also suggests how to proceed in estimating the mean with the simple and expensive model data. First, estimate the long-run variances  $\Pi(\epsilon)$  and  $\Pi(X_e)$ . Estimation of these quantities is discussed in detail in e.g. [9]. Second, compare the resulting estimates  $\hat{\Pi}(\epsilon)$  and  $\hat{\Pi}(X_e)$ . If  $\hat{\Pi}(\epsilon)$  is smaller than  $\hat{\Pi}(X_e)$ , then the MF estimator should be preferred to for sufficiently large  $T_s$ . Again, this would translate into smaller confidence intervals for  $\mu(X_e)$ .

It should also be stressed that though the case of the mean seems simplistic, it is at the core of estimation of many quantities. For example, the variance  $Var(X_e) = \mu(X_e^2) - (\mu(X_e))^2$  is expressed through the means of a process and its square and can be dealt with similarly.

**Remark** More generally, the MF estimator in Eqs. (2)–(3) is defined as

$$\hat{\mu}_{mf}(X_e) = \bar{X}_{e,T_e} + \alpha(\bar{X}_{s,T_s} - \bar{X}_{s,T_e})$$

for some real  $\alpha$ . The parameter  $\alpha$  plays at least two roles. Note that when  $\alpha = 0$ , one recovers the baseline estimator in Eq. (4). Other values of  $\alpha$  allow for potentially different scales of  $X_e$  and  $X_s$ . The value of  $\alpha$  is chosen by minimizing  $Var(\hat{\mu}_{mf}(X_e))$

## 4 Illustration for Non-rare Problems

To illustrate the procedure of Sect. 3, we use synthetic data from a non-linear random oscillator model describing qualitatively ship rolling. More specifically, suppose the dynamics of a stationary process  $X(t)$  is governed by the equation

$$\ddot{X}(t) + 2\delta\dot{X}(t) + r(X(t)) = Z(t), \quad (10)$$

where  $\delta > 0$  is a damping parameter,  $r(x)$  is a restoring force and  $Z(t)$  is a zero-mean random excitation. The excitation  $Z(t)$  is commonly assumed to be a Gaussian

stationary process, with the spectral density suggested by e.g. the Bretschneider spectrum for wave elevations. We further assume a piecewise linear restoring force  $r(x)$ , given by

$$r(x) = \begin{cases} \omega_0^2 x, & \text{if } |x| \leq x_m, \\ -k\omega_0^2(x - x_m) + \omega_0^2 x_m, & \text{if } |x| > x_m, \end{cases} \quad (11)$$

where  $\omega_0$  is a natural frequency of the system,  $x_m$  is referred to as a knuckle point (separating the linear and nonlinear regimes) and  $k > 0$  enters the negative slope of the nonlinear part. The restoring force has a softening shape for  $|x| > x_m$ , typical in modeling ship motions.

Figure 1, left plot, presents time plots of two realizations of the random oscillator model in Eq. (10), labeled expensive and simple. For the expensive signal  $X_e$ , the values  $w_0 = 0.6$ ,  $\delta = 0.15w_0$ ,  $k = 1$ ,  $x_m = 30\pi/180$  are taken. The same values were used for the simple signal  $X_s$ , except that  $k = 0.3$  and the variance for the excitation is smaller. We emphasize again that these expensive and simple signals are called so for illustration purposes only; there is nothing more expensive or simpler, or high- or low-fidelity about either of the signals. The signals were generated for  $T_e = 3600$  s (1 h) and  $T_s = 36,000$  s (10 h). Figure 1, right plot, depicts the time plot of the error process  $\epsilon(t)$  between the two signals for the first 360 s. Note that the vertical scale in Fig. 1, right plot, is much smaller compared to that in Fig. 1, left plot, suggesting that the simple model might be a good approximation for the expensive model.

For the two signals, the long-run variances estimated through triangular kernel and “decorrelation time” bandwidth (see [9]) were  $\hat{\Pi}(\epsilon) = 0.0001$  and  $\hat{\Pi}(X_e) = 0.0051$ . Clearly,  $\hat{\Pi}(\epsilon)$  is smaller than  $\hat{\Pi}(X_e)$  by an order of magnitude. In this case, the MF estimator is preferred for  $T_s$  larger than  $T_e$ . The confidence interval for the mean resulting from the MF estimator is depicted in Fig. 2 (the right vertical segment) in comparison to the confidence interval if the baseline estimator is used (the left vertical

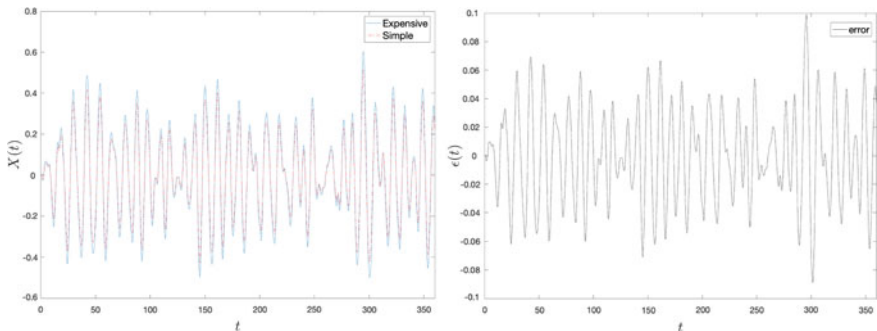
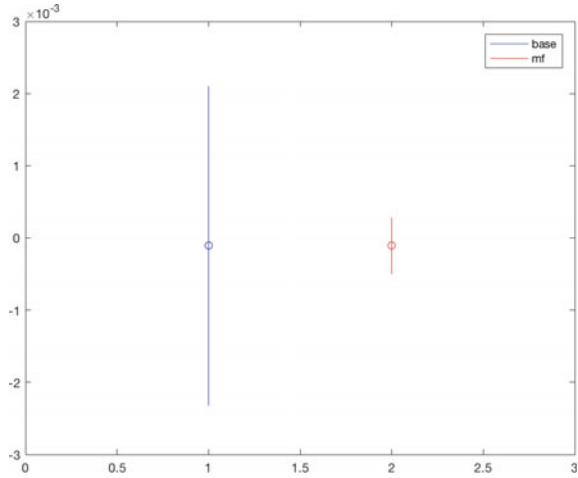


**Fig. 1** Left: Two realizations of random oscillator model. Right: The error process for the two realizations



**Fig. 2** Confidence intervals for the mean based on the baseline and the MF estimator



segment). The two mean estimates are indicated as circles on the two confidence intervals.

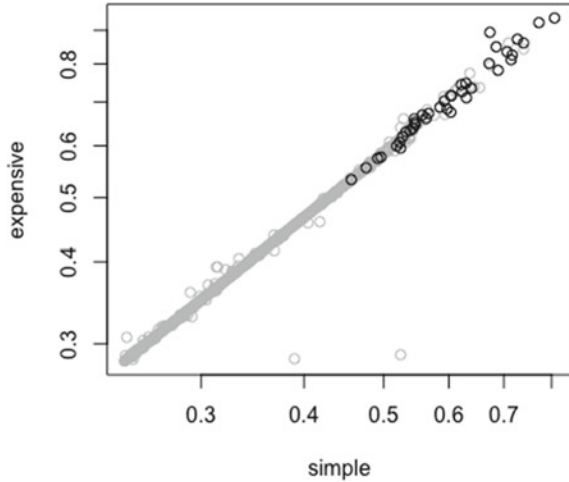
Figure 2 shows a clear benefit of the MF estimator and the simple signal in this case. Again, what makes this possible is a relatively small variance of the error process for the two signals and the fact that  $T_s > T_e$ . This should not be taken for granted in each situation and might require proper calibration of the simple and expensive models.

## 5 Methods for Rare Problems

We would like to extend the methods described in Sects. 3 and 4 to estimation of an exceedance probability  $\mathbb{P}(X_e > x)$  for large target  $x$ . For oscillating signals related to ship dynamics,  $X_e$  in the exceedance probability typically represents suitable peaks of the signal, perhaps even peaks of an envelope (e.g. [1]). To simplify the discussion and for technical reasons, we shall further assume that  $X_e$  represents block maxima of the peaks. If needed, block maxima exceeding a critical value could be translated to peak exceedances per unit time.

Figure 3 illustrates the notions of peaks and block maxima on the same synthetic data as in Sect. 3, where 10 h of data are used with both expensive and simple models. The figure depicts a scatterplot of peaks from the expensive and simple signals, and in a darker shade, the respective block maxima are marked for 39 blocks of size 30. In this setting, for example, one might be interested to estimate  $\mathbb{P}(X_e > 1.5)$ , with no occurrences of the event  $X_e > 1.5$  in the data as can be seen from Fig. 3. Would having potentially larger simple model data for  $X_s$  help in this case, and through what method?

**Fig. 3** Scatterplot of peaks and block maxima for the simple and expensive models



Before addressing these questions, it is instructive to discuss what the baseline estimator for  $\mathbb{P}(X_e > x)$  is, without the availability of  $X_s$  from the simple model. It is known from the statistical Extreme Value Theory (EVT) that the distribution of the block maxima follows approximately that of a generalized extreme value (GEV) distribution as

$$\mathbb{P}(X_e \leq z_1) = e^{-y_1}, \tag{12}$$

where

$$y_1 = y_1(z_1) = \left( 1 + \xi_1 \frac{z_1 - \mu_1}{\sigma_1} \right)_+^{-1/\xi_1} \tag{13}$$

with location, scale and shape parameters  $\mu_1$ ,  $\sigma_1$  and  $\xi_1$ , respectively, and the subscript  $+$  indicating the positive part of the function. After fitting these parameters to the data, the GEV distribution in Eq. (12) would be used to “extrapolate” into the tail  $X_e > x$ . A confidence interval for  $\mathbb{P}(X_e > x)$  could also be provided.

Suppose now that the block maxima  $X_s$  are available for the simple model as well. To see how they could be used together with  $X_e$ , we need an analogue of Eq. (5). At the population (theoretical) level, consider

$$\mathbb{P}(X_e > x) = \mathbb{P}(X_s > y) + (\mathbb{P}(X_e > x) - \mathbb{P}(X_s > y))$$

and, after rewriting the difference in the parentheses,

$$\mathbb{P}(X_e > x) = \mathbb{P}(X_s > y) + \mathbb{P}(\epsilon), \tag{14}$$

where

$$\mathbb{P}(\epsilon) = \mathbb{P}(X_e > x, X_s \leq y) - \mathbb{P}(X_e \leq x, X_s > y). \tag{15}$$

We view Eqs. (14) and (15) as analogues of Eq. (5). That is,  $\mathbb{P}(X_e > x)$  for the expensive model is being replaced by  $\mathbb{P}(X_s > y)$  for the simple model, with the error probability  $\mathbb{P}(\epsilon)$ . The error probability in Eq. (15) is expressed in terms of the joint behavior of  $X_e$  and  $X_s$ , and could be expected small if the simple model is a good approximation to the expensive model at the extremes. The value  $y$  could but does not have to be equal to  $x$ ; in fact, in analogy to Eq. (5) where  $\mu(X_e)$  and  $\mu(X_s)$  can be different, having different  $y$  and  $x$  can be critical. As in the remark at the end of Sect. 3,  $X_e$  and  $X_s$  can also have different scales.

Turning to estimation, the probability  $\mathbb{P}(X_s > y)$  in Eq. (14) could, in principle, be estimated directly if needed, by taking a large enough  $T_s$ . The probabilities in Eq. (15), however, need to be estimated from the data on  $X_e$  and  $X_s$  gathered under the same conditions over the smaller observation window of size  $T_e$ . This is where bivariate GEV distributions come in, as those modeling the joint behavior of  $X_e$  and  $X_s$ . As in Eqs. (12) and (13), let

$$\mathbb{P}(X_s \leq z_2) = e^{-y_2}, \tag{16}$$

where

$$y_2 = y_2(z_2) = \left( 1 + \xi_2 \frac{z_2 - \mu_2}{\sigma_2} \right)_+^{-1/\xi_2} \tag{17}$$

with a similar set of parameters. The cross-dependence between the two variables  $X_e$  and  $X_s$  of a bivariate GEV is described through a dependence function  $A$ , for example, as in

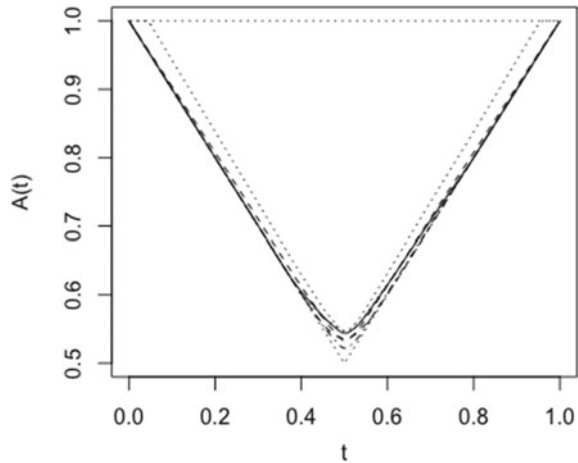
$$\mathbb{P}(X_e \leq z_1, X_s \leq z_2) = e^{-(y_1+y_2)A\left(\frac{y_1}{y_1+y_2}\right)}, \tag{18}$$

where  $y_1$  and  $y_2$  are given in Eqs. (13) and (17). The function  $A(t)$  is defined for  $t \in [0, 1]$ , is convex and satisfies  $\max(t, 1 - t) \leq A(t) \leq 1$ ,  $A(0) = A(1) = 1$ . (See Fig. 4 for a plot of such functions.) The case of  $A(t) = 1$  for all  $t \in [0, 1]$  corresponds to independence of  $X_e$  and  $X_s$ , since in this case  $\mathbb{P}(X_e \leq z_1, X_s \leq z_2) = e^{-(y_1+y_2)}$  is the product of the marginals in Eqs. (12) and (16), and that of  $A(0.5) = 0.5$  to their complete dependence. There are parametric models for  $A(t)$  that can be fitted in practice.

After a bivariate model is fitted to  $X_e$  and  $X_s$ , one could obtain an estimate  $\hat{\mathbb{P}}(\epsilon)$  of the error probability, and also the estimate  $\hat{\mathbb{P}}(X_s > y)$  of the error probability (in the same way as the baseline estimator  $\hat{\mathbb{P}}(X_e > x)$ ), leading to the MF estimator

$$\hat{\mathbb{P}}(X_e > x) = \hat{\mathbb{P}}(X_s > y) + \hat{\mathbb{P}}(\epsilon). \tag{19}$$

**Fig. 4** Estimation of  $A(t)$  through four parametric models



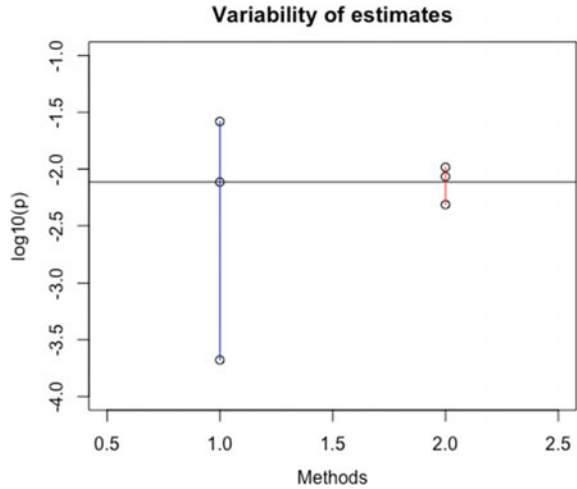
A confidence interval can be constructed to go with  $\hat{\mathbb{P}}(\epsilon)$ . For large enough  $T_s$ , the variability of  $\hat{\mathbb{P}}(X_s > y)$  can be thought negligible in comparison. If the variability expressed through a confidence interval on  $\hat{\mathbb{P}}(\epsilon)$  is smaller than that of the baseline estimate  $\hat{\mathbb{P}}(X_e > x)$ , then the MF estimate in Eq. (19) should be preferred. In practice,  $y$  can be chosen as the point minimizing the resulting uncertainty for  $\hat{\mathbb{P}}(\epsilon)$ .

## 6 Illustration for Rare Problems

We illustrate the ideas of Sect. 5 on the same synthetic data used in Sect. 4 and also in Fig. 3. For this example, the estimated marginal parameters (and their standard errors in parentheses) are:  $\hat{\mu}_1 = 0.5475(0.0083)$ ,  $\hat{\sigma}_1 = 0.0471(0.0060)$ ,  $\hat{\xi}_1 = 0.3876(0.1118)$  and  $\hat{\mu}_2 = 0.6431(0.0102)$ ,  $\hat{\sigma}_2 = 0.0577(0.0075)$ ,  $\hat{\xi}_2 = 0.3963(0.1128)$ . Figure 4 presents estimation of the function  $A(t)$  entering Eq. (18) and modeling dependence through four parametric models. (For reference, the function  $\max(t, 1-t)$  is also plotted in Fig. 4.) Since  $A(0.5)$  are close to 0.5 [see the discussion following Eq. (18)], the resulting plot suggests that the bivariate block maxima of  $X_e$  and  $X_s$  are quite strongly correlated. This is also consistent with the scatterplot of the block maxima (in a darker shade) in Fig. 3.

Figure 5 depicts the resulting baseline and MF probability estimates and their variability in vertical segments for the target  $x = 1.5$ . In producing the plot, we treated the fitted bivariate GEV model as the truth, with the horizontal line and the middle circle in the first vertical segment as the baseline estimator representing the true GEV probability  $\mathbb{P}(X_e > 1.5)$ . Variability is measured by generating data from the bivariate GEV model, re-estimating the probability  $\mathbb{P}(X_e > 1.5)$ , either through the baseline or the MF estimator, and taking the 0.025th and 0.975th quantiles of

**Fig. 5** The baseline (left) and MF (right) probability estimates with confidence intervals



the obtained estimates as the endpoints of the vertical segments. In the statistical literature, this method is known as a parametric bootstrap (e.g. [5], Sect. 3.3.4).

Since the variability of the MF estimator is smaller than that of the baseline, the MF estimator is preferred. It should also be stressed that this is very much a result of strong extremal dependence in the simple and expensive models. Were the dependence not as strong (as expressed through the function  $A(t)$  and which can be checked easily), the effect seen in Fig. 5 would not be present.

## 7 Conclusions

In this work, we showed how a basic MF estimator for low-fidelity and high-fidelity models for non-rare problems could be adapted to estimate probabilities of rare events, especially those that are not observed in high-fidelity data. At a technical level, our approach was rooted in bivariate EVT, that allows modeling simultaneously extremes from the low-fidelity and high-fidelity models. The ideas were illustrated on synthetic data mimicking ship roll motion.

Several directions related to this work could be pursued in the future. First, the methodology should be applied to more realistic models of ship dynamics. Our first attempt in this direction was to compare roll extremes from SimpleCode and LAMP, but their dependence was not strong enough to warrant the use of MF methods. This could partly be a result of the lack of calibration and consistency between the two models, which is an important topic of its own interest. Second, an even more mathematical treatment of the issues presented in Sects. 5 and 6 should also be undertaken, for example, with the introduction of costs, a more careful construction of confidence intervals, and the use of bivariate peaks-over-threshold methods instead of block maxima, etc.

**Acknowledgements** This work has been funded by the Office of Naval Research grant N00014-19-1-2092 under Dr. Woei-Min Lin. The authors also thank Drs. Vadim Belenky and Kenneth Weems at NSWC Carderock Division, as well as two anonymous Reviewers, for their comments on this work.

## References

1. Campbell B, Belenky V, Pipiras V (2016) Application of the envelope peaks over threshold (EPOT) method for probabilistic assessment of dynamic stability. *Ocean Eng* 120:298–304
2. Coles S (2001) An introduction to statistical modeling of extreme values. Springer, London
3. Belenky V, Weems K, Pipiras V, Glotzer D, Sapsis T (2018) Tail structure of roll and metric of capsizing in irregular waves. In: Proceedings of the 32nd symposium of naval hydrodynamics, Hamburg, Germany
4. Belenky V, Glotzer D, Pipiras V, Sapsis T (2019) Distribution tail structure and extreme value analysis of constrained piecewise linear oscillators. *Probab Eng Mech* 57:1–13
5. Good P (2005) Permutations, parametric, and bootstrap tests of hypotheses. Springer, New York
6. Lin WM, Yue DKP (1991) Numerical solutions for large amplitude ship motions in the time-domain. In: Proceedings of the 18th symposium on naval hydrodynamics, Ann Arbor
7. Peherstorfer B, Kramer B, Willcox K (2017) Combining multiple surrogate models to accelerate failure probability estimation with expensive high-fidelity models. *J Comput Phys* 341:61–75
8. Peherstorfer B, Willcox K, Gunzburger M (2018) Survey of multifidelity methods in uncertainty propagation, inference, and optimization. *SIAM Rev* 60:550–591
9. Pipiras V, Glotzer D, Belenky V, Levine M, Weems K (2018) On confidence intervals of mean and variance estimates of ship motions. In: Proceedings of the 13th international conference on the stability of ships and ocean vehicles, Kobe, Japan
10. Reed AM (2021) Predicting extreme loads and the processes for predicting them efficiently and with confidence. In: Proceedings of the 1st international conference on the stability and safety of ships and ocean vehicles, Glasgow, Scotland, UK
11. Shin YS, Belenky V, Lin WM, Weems K, Engle AH (2003) Nonlinear time domain simulation technology for seakeeping and wave-load analysis for modern ship design. *SNAME Transactions* 111:557–578
12. Weems K, Wundrow D (2013) Hybrid models for fast time-domain simulation of stability failures in irregular waves with volume-based calculations for Froude-Krylov and hydrostatic forces. Proceedings of the 13th international ship stability workshop, Brest

# **Evaluation of Probabilistic Methods and Interpretation of Results**

# Review of Probabilistic Methods for Direct Dynamic Stability of Ships in Random Seaway



Clève Wandji

**Abstract** This paper focused on reviewing some statistical methods based on large-sample-size time-domain simulations to characterize dynamic stability failure (for example large roll angle or large acceleration). In order to analyze the assumptions behind these methods and to identify the link between them, these statistical methodologies have been tested in two datasets obtained by numerical simulations. The first dataset represents a nonlinear process obtained for a ship in parametric roll condition and the second dataset represents a linear process. Both processes are obtained from a very long simulation 3000 h ( $3 \text{ h} \times 1000$ ) in order to insure a better statistical convergence of the sampling. In addition, when possible, a Pearson chi-square test goodness of fit is performed to determine whether there is a significant difference between the predictions of the discussed methodologies and the observed data.

**Keywords** Probabilistic methods · Nonlinear process · Direct stability assessment · Independence of events · Chi-square test

## 1 Introduction

Predicting the stability of a ship in waves is quite an important and challenging problem as recognized by the International Maritime Organization (IMO). The generalized problem of stability in waves has been subdivided into five stability failure modes, which are: parametric rolling, pure loss of stability, surf-riding/broaching, loss of stability under dead ship condition and excessive accelerations [26]. Note that the IMO Sub-Committee on Ship Design and Construction (SDC) has developed the Second Generation Intact Stability Criteria (SGISC) for these five stability failure modes. These SGISC are based on a multi-tiered assessment approach. The third level also referred as direct stability assessment uses probabilistic approach for the definition of the criteria.

---

C. Wandji (✉)  
Bureau Veritas (BV), Paris, France  
e-mail: [cleve.wandji@bureauveritas.com](mailto:cleve.wandji@bureauveritas.com)



Difficulties to evaluate probability of stability failure (large roll angles and excessive accelerations) are related to both the rarity of the failure and the nonlinearities of the dynamical system describing ship behavior of a ship in rough seas. These nonlinearities are introduced by stiffness, roll damping and excitation. These nonlinearities are essential for proper modeling of these phenomena, while alternatives for accurate assessment may be limited to numerical simulations (e.g. potential-flow code for parametric roll) and a model test. Dynamic stability failures, considered in SGISC, are caused by irregular waves and/or gusty wind. The inherent randomness of the environmental conditions makes the probability of stability failure a very useful tool for both design and operation.

Direct counting methods are perhaps the most used and the best known amongst the currently applied techniques for calculating the exceedance probability. As the name suggests, these methods are based on counting of the failure events, observed from numerical simulations or model tests. Beyond the direct counting, there are other methods such as the “path integration” and the “stochastic averaging” (e.g. [8]) as well as extrapolation based on the critical wave groups [1] which can be used to estimate the rate of events (probability of an event per unit of time). The current paper is focused on direct counting methods based on large-sample-volume simulations.

In order to test and understand the assumptions behind the direct counting methodologies based on “large-sample-volume”, an example has been generated with numerical simulations to be used for different statistical techniques. The text is subdivided in the following parts: first of all, an example case is described; secondly, definitions of different estimates are presented; and finally, the relationships between these estimates are discussed.

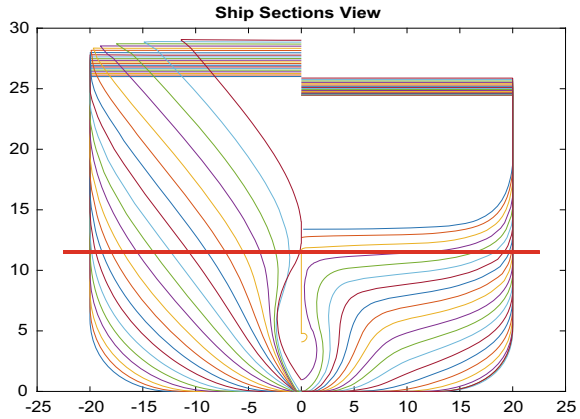
## 2 Example Case

The roll motion time series has been obtained by performing time domain simulation on C11-class containership. The main characteristics of this vessel are contained in Table 1 and a body plan is shown in Fig. 1.

**Table 1** Main characteristics of C11 containership

Parameter	Value	Unit
Length between perpendiculars	262.0	m
Breath	40.0	m
Speed	0.0	m/s
Natural roll period	25.1	s
Metacentric height	2.75	m
Bilge keel length	76.28	m
Bilge keel breath	0.4	m

**Fig. 1** Body plan of C11 containership



### 2.1 Simulations Conditions

Nonlinear time domain computations using HydroStar++ (see [25] for more details on this tool) have been performed in following, irregular and short crested seas having  $H_s = 6.0$  m and  $T_p = 12.5$  s. For this sea state, 1000 realizations of 3 h each have been computed. For each realization, a different set of random phases, frequencies of the wave component composing the sea state is used, as described in [24]. To ensure that this discretization does not lead to self-repeating effect, the autocorrelation function has been checked using Eq. (1):

$$R(\tau) = \int_0^\infty S_{wave}(\omega) \cos(\omega\tau) d\omega; \quad \tau \in [0, 10800s] \tag{1}$$

where  $S_{wave}(\omega)$  is the spectral density of waves and  $\tau$  the time lag. The same discretization of frequencies has been used for the wave reconstruction and in autocorrelation function. Figure 2 shows a zoom-in of a couple (over the 1000 wave records) of the non-dimensional autocorrelation function. It can be seen from Fig. 2 that, there is no self-repeating effects.

The ship experiences large roll motions in almost all realizations. These roll motions may be caused by parametric resonance, as the natural roll period is about twice the encounter period. An example of roll time series is shown in Fig. 3 (blue line). Note that this signal can be considered as a nonlinear process since parametric rolling is a highly nonlinear phenomenon as observed by [12] and by [4].

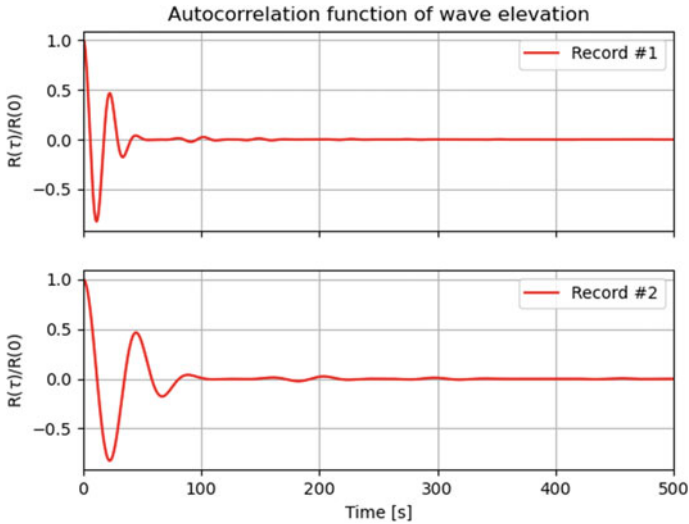


Fig. 2 Zoom-in of Autocorrelation of wave elevation

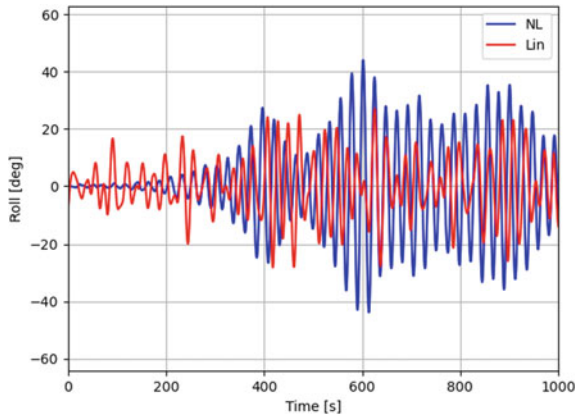
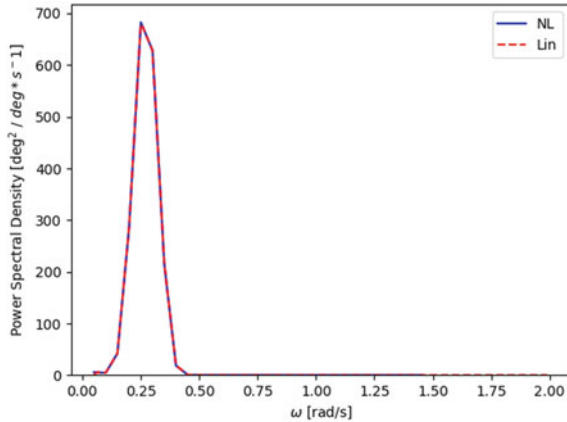


Fig. 3 Time series for nonlinear (parametric roll, blue line) and linear processes (red line)

## 2.2 Construction of the Linear Process

Spectral density was estimated over the sample of parametric roll motions and then used to generate a linear stochastic process. The linear process was generated for 1000 records, 3 h each. Thus, the parametric roll and the linear processes have the same energy content. Figure 4 shows the two spectrums derived from the two processes, they are identical. Figure 3 shows an example of time series for one realization of 3 h for both processes.

**Fig. 4** Power spectral density for parametric resonance (blue) and linear (red) processes



Using the two processes (linear and parametric roll) defined above; we will review, and test some available formulations for relating the probability of occurrence (large roll angle or accelerations for example) and the time of exposure. In this paper, all results for the linear process will be shown in red (associated to the legend Lin) and those for the parametric resonance process will be shown in blue (associated to the legend NL).

### 3 Distribution of Instantaneous Values

Distribution of instantaneous values of the process is estimated for each time instant. It is interpreted as the distribution of the process at any instant of time. The linear process  $x$  (for example roll angle), with standard deviation  $\sigma_x$ , follows a Gaussian or Normal distribution with zero mean:

$$F_i = \phi\left(\frac{x}{\sigma_x}\right) \tag{2}$$

where  $\phi$  is a standard normal distribution (with zero mean and unity variance). The distributions of instantaneous values are shown in Fig. 5 (histograms—probability density function) and Fig. 6 (estimated exceedance probability). As expected, the linear process follows very well the theoretical distribution (named Gauss in Figs. 5 and 6), while the parametric resonance process has a leptokurtic distribution as observed by Belenky and Weems [5]; and by Mohamad and Sapsis [20].

**Fig. 5** Probability density function of the instantaneous value distribution

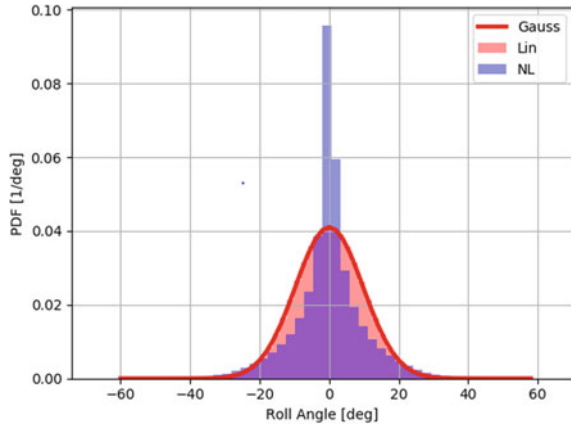
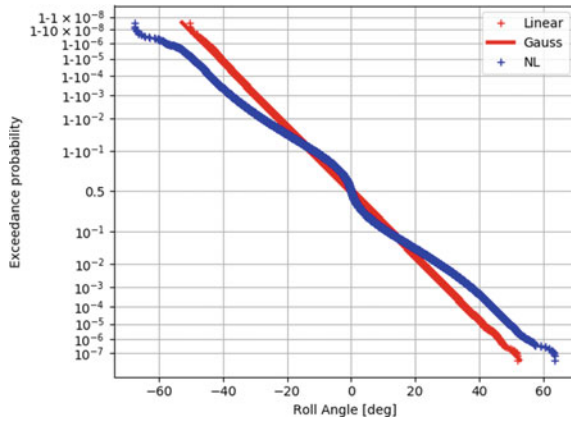


**Fig. 6** Instantaneous value distribution for linear and parametric resonance processes



### 4 Mean Upcrossing Rate

An upcrossing rate  $\nu$  of a differentiable process  $x$  can be expressed as (e.g. [11, 22])

$$\nu(x(t)) = \int_0^{\infty} f(x, \dot{x}) \dot{x} dx \tag{3}$$

A dot above a symbol means a temporal derivative.

The integral in formula (3) has also the meaning of a derivative of the instantaneous probability of event  $p$  with respect to time e.g. [11]. If the process is stationary, its PDF does not depend on time and the rate of events is constant. If the process and its derivative can be assumed independent, Eq. (3) can be simplified. This is an assumption while the first derivative of a stationary process is uncorrelated of the process itself, it does not constitute independence, except if the process is normal

where the process and its derivative are independent. The formula (3) becomes:

$$v(x) = f(x) \int_0^\infty f(\dot{x}) \dot{x} d\dot{x} \tag{4}$$

The theoretical rate of events for a normal process can be found as:

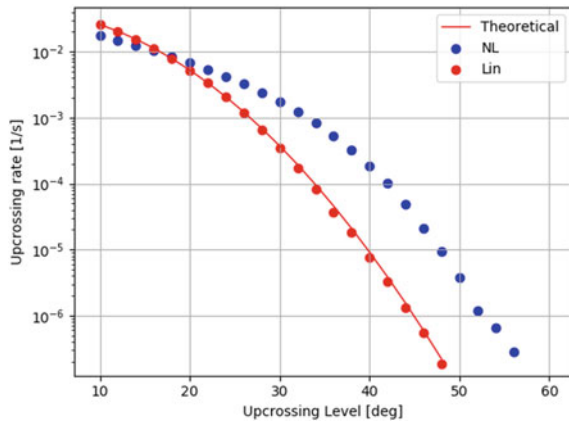
$$v(x) = \frac{1}{2\pi} \left( \frac{\sigma_{\dot{x}}}{\sigma_x} \right) \exp\left(-\frac{x^2}{2\sigma_x^2}\right) = \frac{1}{T_Z} \exp\left(-\frac{x^2}{2\sigma_x^2}\right) \tag{5}$$

where  $\sigma_{\dot{x}}$  is the standard deviation of the time derivative of the process and  $T_Z$  is the average zero-upcrossing period of the process. In a general case, the derivative of the process may not be independent on the process. In particular, for nonlinear ship roll motions, the derivative was found to be independent from the process in beam seas, whereas significant dependence was found for the cases with apparent stability variation as discussed in [6].

Using the linear and parametric resonance processes of the example case, upcrossing rate has been estimated for different levels by counting of upcrossing events, see Fig. 7.

The estimate of upcrossing rate for the linear process is very close to the theoretical formula (5). This result was expected, since we have seen in Sect. 3 that the linear process follows a normal distribution. Note that the objective of the following sections is a review of statistical methodologies i.e. to understand a tendency. To keep the focus, confidence interval of the estimates is not considered in this work.

**Fig. 7** Estimate of upcrossing rate for linear and parametric resonance processes



## 5 Time to First Event Distribution

Since an upcrossing is a random event and may occur at any instant of time, the time to first event is a random variable.

An exponential distribution for this random variable is used in reliability engineering (e.g. [19]).

The exponential distribution is derived under the assumption of the independence of events. The exponential distribution for an exposure time  $T$  and failure rate  $\lambda_x$  related to an upcrossing level  $x$  is presented as:

$$f_x(T) = \lambda_x \exp(-\lambda_x T) \quad (6)$$

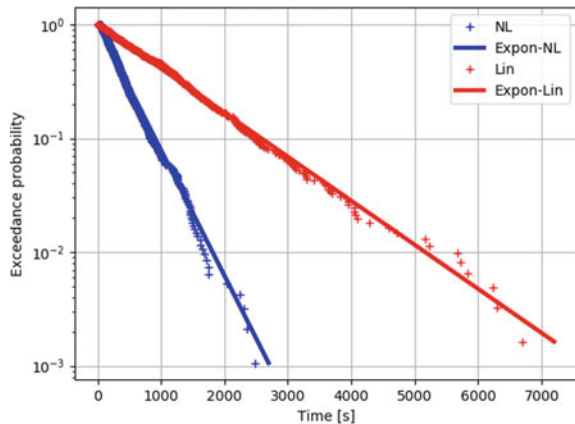
A sample of intervals before the first upcrossing has been populated for both processes described in Sect. 2. To ensure the independence of events, the time to upcrossing event was measured from the beginning of the simulation. After the event occurs, the simulation was stopped and restarted from the beginning for another seed in the same sea conditions.

For a given level, the time to first event (also referred as time to failure) was determined by averaging 1000 samples obtained from simulation. There were some cases where the process did not cross the failure level. As a result, the estimate of the mean time to failure may be biased.

To correct the bias a censoring procedure was used. If a failure was not observed, it was assume to be occurred at the end of the record (see Meeker and Escobar [19] for more details about censoring procedure). The inverse of mean time to first event provides the failure rate  $\lambda_x$ . CFD for time-to-first event distribution can be computed using the formula (6). Then the exceedance is computed. Results for a failure level of  $20^\circ$  are shown in Fig. 8 as an exceedance probability plot.

Observed distributions of time-to-event for both linear and parametric resonance processes are very close to the exponential. In addition, a Pearson chi-square

**Fig. 8** Time before first event distribution for linear and parametric resonance processes— $20^\circ$  failure level



goodness-of-fit test was performed. The results of the tests are 0.93 for the linear process and 0.92 for the parametric resonance process. The test does not reject exponential distributions for both processes since the probabilities are well above the accepted significance level of 0.05. These results confirm the independence of the observed events and the time-to-first-event follows exponential distribution. The time to first event is used in SGISC Level 3 (also called direct stability assessment see [21]).

## 6 Time Between Events Distribution

The rate of event can also be estimated from statistics of time intervals between the events. The exponential distribution (6) is assumed for these intervals.

Using the dataset described in Sect. 2, samples of time interval between crossings have been populated for the linear and parametric resonance processes. Estimates for probability of exceedance for a failure level of 20° are shown in Fig. 9. The linear process shows a good agreement with the theoretical distribution; a Pearson chi-square goodness of-fit-test yields the probability 0.62 > 0.05. Significant difference between the estimated and the theoretical distributions is observed for parametric resonance process; the Pearson chi-square goodness of fit test, shows the probability below the accepted significant level: 0.00156 < 0.05. The hypothesis of exponential distribution is not supported by observed data. The apparent reason is that the condition of the independence of upcrossing events was not met, while it is required for the exponential distribution of time-between-events (e.g. [3]).

Looking into the time series of the parametric resonance process for the crossing level of 20° as presented in Fig. 20, it's observed that most of upcrossings are clustered and there are many cases where neighboring periods have upcrossings.

**Fig. 9** Time between events distribution for linear and parametric resonance processes—20° failure level

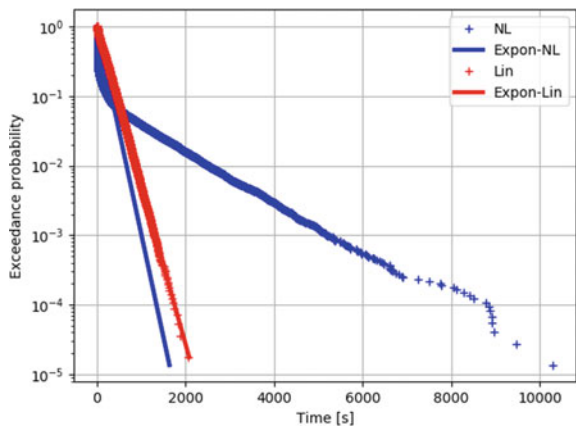
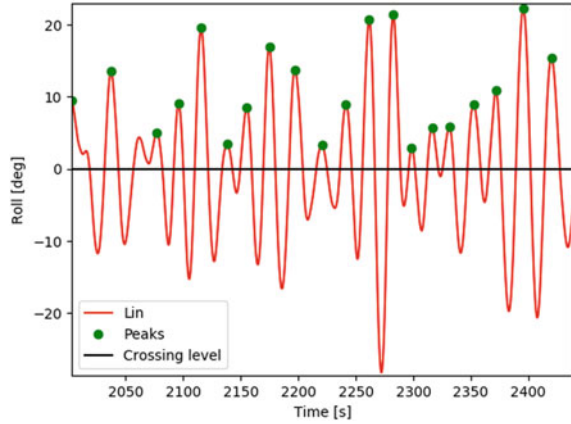




**Fig. 10** Example of identified peaks to build cycle amplitudes distribution for the linear process



## 7 Cycle Amplitudes Distribution

A cycle amplitude is defined as the greatest positive peak in each cycle. Secondary peaks are not taken into account. Figure 10 illustrates this definition for the linear process.

It's known that an envelope (and cycle amplitudes) of a normal process follows Rayleigh distribution. The probability density function  $f_a$  of a Rayleigh distribution is given by:

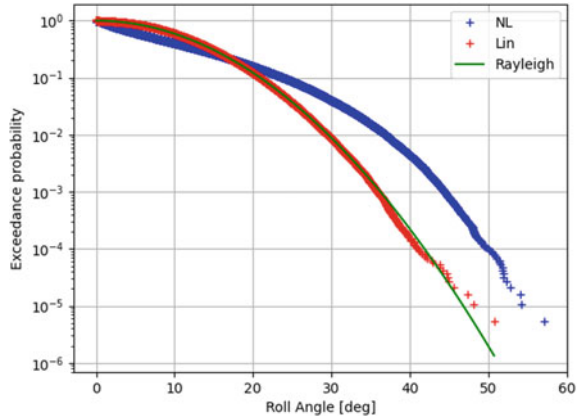
$$f_a(x) = \frac{x}{\sigma_x^2} * \exp\left(-\frac{1}{2}\left(\frac{x}{\sigma_x}\right)^2\right) \quad (7)$$

The cycle amplitude distribution estimated for both processes are shown in Fig. 11. As expected, the distribution of cycle amplitudes of the linear process follows Rayleigh distribution, with Pearson chi-square goodness-of-fit test probability  $0.94 > 0.05$ . We can also observe that distribution of cycle amplitudes of the parametric resonance process does not follow Rayleigh distribution.

## 8 Maximum Value Over an Interval

A distribution of the maximum value over an interval or block maxima method is estimated by dividing the observation period into non-overlapping independent blocks of equal duration and uses the maximum observation in each block. For a normal process, the theoretical distribution for the maximum over a duration is (e.g. [10])

**Fig. 11** Cycle amplitudes distribution for linear and parametric resonance processes



$$F_T(x) = \left[ 1 - \exp\left(-\frac{1}{2}\left(\frac{x}{\sigma_x}\right)^2\right) \right]^{\frac{T}{T_Z}} \tag{8}$$

In Eq. (8),  $T/T_Z$  represents the number of upcrossing cycles contained in the period T (block length). When the number of cycles is large enough (that means mathematically tends to infinity) the Eq. (9) becomes:

$$F_T(x) = \exp\left[-\frac{T}{T_Z} \exp\left(-\frac{1}{2}\left(\frac{x}{\sigma_x}\right)^2\right)\right] \tag{9}$$

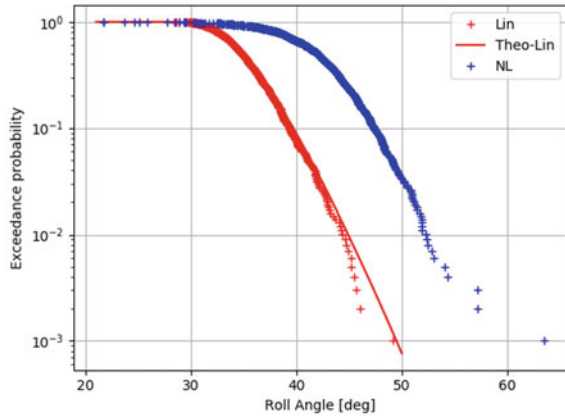
Maximum roll values for 3-h records were determined for linear and parametric resonance processes. Exceedance probability estimates are shown in Fig. 12. As expected, the results for the linear process are very close to theoretical distribution. A Pearson chi-square goodness-of-fit test shows that the fitted distribution is supported by the data ( $0.54 > 0.05$ ).

The distribution of block maxima can be considered as the most comprehensive measure with regards to design criteria. The final objective of short-term probabilistic approach is to estimate this distribution.

## 9 Relation Between Distributions

This section describes relations between the different distributions discussed in Sect. 3 through 8. The derivation of these distributions was not free of assumptions. Additional assumptions may include stationarity of the process (meaning that the conditions during the exposure time under assessment can be considered unchanged), the process is differentiable (meaning that the derivative of the process exists), and the events are independent and identically distributed.

**Fig. 12** 3 h maxima block exceedance probability for linear and parametric resonance processes



### 9.1 Upcrossing Rate Versus Maximum Over an Interval

Using the upcrossing rate  $\nu$ , and assuming independent upcrossings and applicability of the Poisson process, the exceedance probability of the maximum over an interval can be computed using the formula (10):

$$F_T(x) = 1 - \exp(-\nu(x) \cdot T) \tag{10}$$

Using the results from Sect. 4, the exceedance probability estimate over an interval of 3 h has been computed using upcrossing rate for both linear and parametric resonance processes. The results compared to those of Sect. 8 and the comparison is shown in Fig. 13.

From Fig. 13, one can observe that the linear process results are very close to block maxima distribution (Max-Lin in Fig. 13) computed in Sect. 8 for almost all values

**Fig. 13** Maximum over a duration (3 h) using upcrossing rate for linear and parametric resonance processes

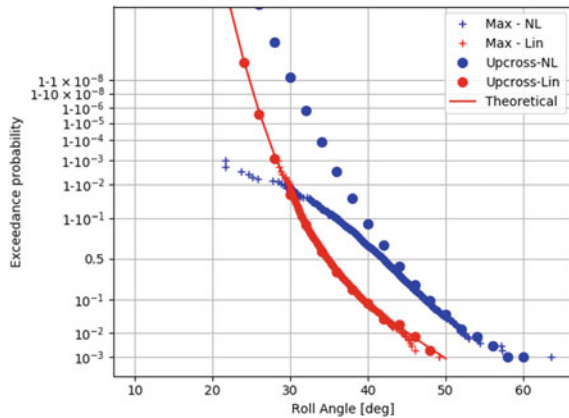
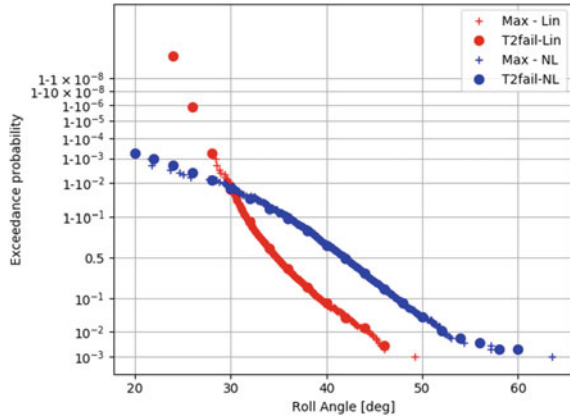


**Fig. 14** Maximum over a duration (3 h) using time to first event for linear and parametric resonance processes



of roll angles., There are some differences below 44° for the parametric resonance process between the block maxima distribution (Max-NL) and the results obtained from upcrossing rate. These differences can be explained by the used assumptions of independence of upcrossing events that may not be applicable below 44°.

### 9.2 Time to First Event Versus Maximum Over an Interval

Using failure rate  $\lambda$  based on the time to first event, and assuming independent upcrossing events and applicability of Poisson process, the exceedance probability for the block maxima is computed as:

$$F_T(x) = 1 - \exp(-\lambda(x) \cdot T) \tag{11}$$

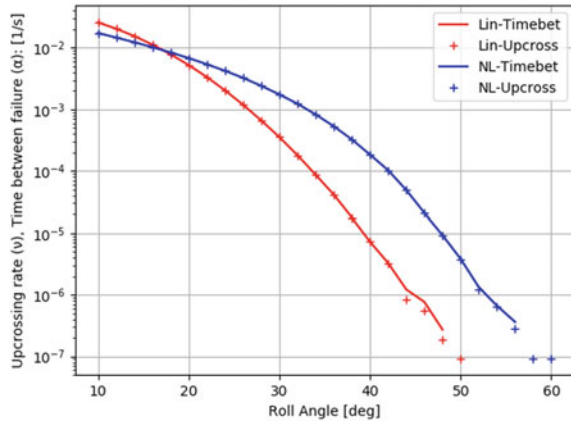
Using the results from Sect. 5, the exceedance probability of 3 h block maxima has been computed using the failure rate, based on time-to-first event The results are shown in Fig. 14.

From results in Fig. 14, one can observe that the results based on time-to-first-event are in agreement with the block maxima results computed in Sect. 8 (Max-Lin and Max-NL). These results are not surprising since independence of events is ensured for a measure based on the time-to-first-event.

### 9.3 Time Between Events Versus Upcrossing Rate

Upcrossing rate (average number of upcrossings per unit of time) is estimated by counting the number of upcrossings of a given threshold, while failure rate based on time between events (inverse of the average time between upcrossings) is obtained

**Fig. 15** Comparison between upcrossing rate and time between events rate for linear and parametric resonance processes



by counting directly the time between upcrossings. Using the results from Sect. 4 (mean upcrossing rate) and Sect. 6 (time between events distribution), the rate of events estimated from upcrossing counting and time-between-events counting are compared in Fig. 15.

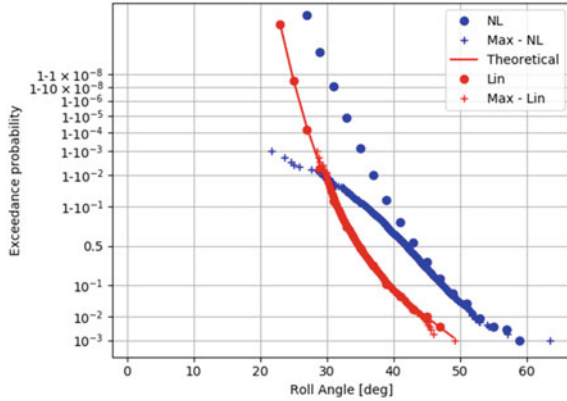
One can observe that the failure rate estimated from counting upcrossing events and time-between-events are almost identical especially when the number of events is large. Therefore, a similar conclusion can be made on the estimates based on time-between-events and block maxima.

### 9.4 Cycle Amplitudes Distribution Versus Maximum Over an Interval

Using distribution of cycle amplitudes described in Sect. 7, and assuming independence of peaks, the CFD for the block maxima can be computed using the formula (8). Then the exceedance is computed and compared to the results in Sect. 8, see Fig. 16.

Figure 16 shows that the exceedance probability for the linear process estimated using cycle amplitudes distribution (identified as “Lin” in Fig. 16) follows very well the block maxima results computed in Sect. 8 for the linear process (Max-Lin in Fig. 16). There are some discrepancies between the results obtained from cycle amplitudes distribution (identified as “NL” in Fig. 16) and block maxima result for parametric (Max-NL in Fig. 16) for the parametric resonance process when the roll angle is less than 44°. These discrepancies are caused by inapplicability of the independence assumptions below 44°.

**Fig. 16** Maximum over a duration (3 h) using cycle amplitudes distribution for linear and parametric resonance processes



### 9.5 Instantaneous Roll Angle Distribution Versus Upcrossing Rate

The relation between the distribution of instantaneous roll angles and upcrossing rate estimate is given by First Order Reliability Method (FORM). A distribution of nonlinear roll response can be estimated using FORM method originally developed for structural reliability problems.

Using FORM approach, the mean upcrossing rate of roll motion and the most probable wave scenarios leading to the specified maximum roll angle are assessed.

The FORM approach [17] starts with the transformation of the non-normal variables to standard normal i.e. zero mean and unit variance (see [18]) using Rosenblatt transformation (see also [2]). The objective is to find the most probable failure point, also referred as failure locus. It is defined as the minimum distance between the limit state surface and the origin in the space of the reduced variables [23]. It is referred as the reliability index  $\beta_{FORM}$ . This point can be found with the method of Lagrange multipliers [2], following an iterative procedure. The failure probability of the system can be approximated by Eq. (13), which is exact for linear system.

Within the FORM approach, the mean upcrossing rate can be written according to [14] using the reliability index  $\beta_{FORM}$  as:

$$v(x) = \frac{1}{T_Z} \exp\left(-\frac{1}{2}\beta_{FORM}^2\right) \tag{12}$$

The instantaneous roll angle distribution is related to the FORM reliability index ( $\beta_{FORM}$ ) by the following approximated relation [14]:

$$F_i \approx \phi(\beta_{FORM}) \tag{13}$$

Since computing the reliability index,  $\beta_{FORM}$  is time consuming, values of  $\beta_{FORM}$  have been selected directly from the instantaneous roll angle distribution computed in Sect. 3 for both linear and parametric resonance see Fig. 17.

Figure 18 shows upcrossing rates, estimated with FORM approach. From Fig. 18, one can see that the upcrossing rate computed for the linear process using FORM approach are very close to those obtained using the theoretical formula (12).

A comparison between the upcrossing rates estimated from FORM approach and counting of upcrossing events (see Sect. 3) are shown in Fig. 19. From Fig. 19 we can see that the results are identical for the linear process. There are some differences for the parametric resonance process at lower roll angles.

**Fig. 17** Instantaneous values distribution in FORM approach for linear and parametric resonance processes

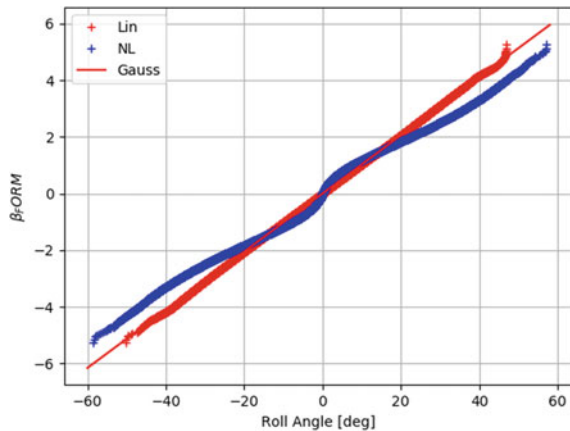


**Fig. 18** Upcrossing rate distribution using FORM approach for linear and parametric resonance processes

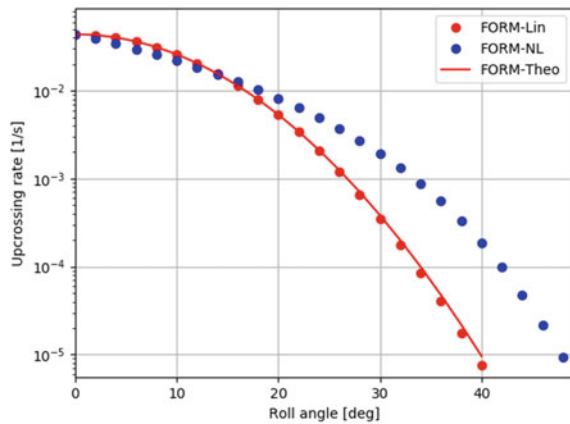


**Fig. 19** Comparison between upcrossing rates obtained from upcrossing counting and those from FORM approach for linear and parametric resonances processes

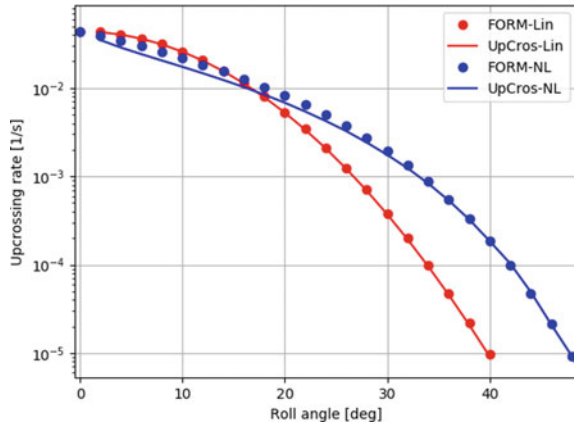
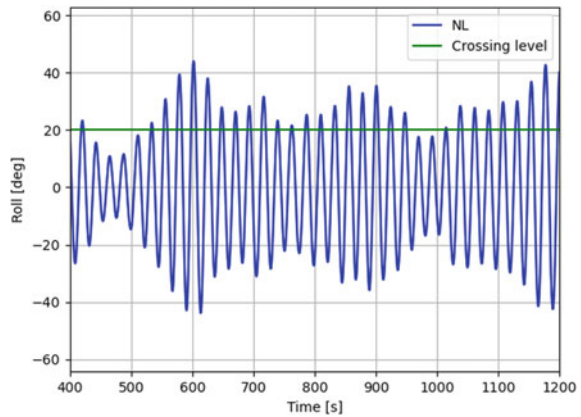


**Fig. 20** Time series of parametric resonance process; 20° upcrossing level



## 10 Assumption of Independence of Events

We have seen that independence of events is one of the most important condition to satisfy when using statistics related to Poisson process.

### 10.1 Case of Parametric Resonance Process

Most of upcrossings of 20° level (for example for upcrossings counting, time between events, and cycle amplitudes) are clustered (i.e. encountered in groups). There are many neighboring periods with upcrossings see Fig. 20.



De-clustering the data could be a potential way to overcome this issue and a technique for de-clustering could be the use of the envelope approach as described in [7] and [16].

## 10.2 Linear Process Case

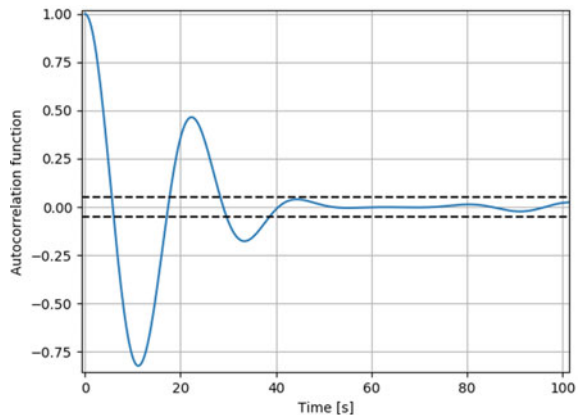
For linear process which is normal, the autocorrelation function provides all information about dependence. This dependence is significant for a limited time; it is the time it takes for the autocorrelation function to drop below a given level (usually 0.05). The autocorrelation is computed using formula (1), where the spectral density of waves is replaced by the spectral density of roll motion.

The autocorrelation function for the linear process result is shown in Fig. 21. If the level is set to 0.05, it takes about 50 s for this autocorrelation to die out.

To confirm that the violation of independence assumption is the key reason for observed discrepancies, a probability of exceedance of  $5^\circ$  level has been estimated from statistics of time between events, see Fig. 22. From Fig. 22, one can observe that estimated distributions of both linear and parametric resonance processes do not agree with the theoretical distribution. Pearson chi-square goodness-of-fit-test shows 0.0012 for the linear process and 0.00068 for the parametric resonance process. Thus, the exponential distribution hypothesis is rejected for the upcrossing level of  $5^\circ$ . As the observed data are obviously clustered for the upcrossing level of  $5^\circ$ , so there is no the independence of upcrossing events.

This conclusion can be confirmed also with autocorrelation function. The mean time between events for  $5^\circ$  upcrossing level is  $38.6 \text{ s} < 50 \text{ s}$ .

**Fig. 21** Autocorrelation function for the linear process



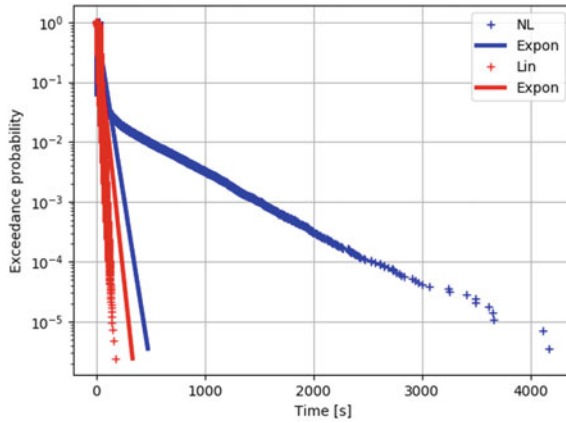


Fig. 22 Probability of exceedance, based on time between events. Upcrossing level is  $5^\circ$

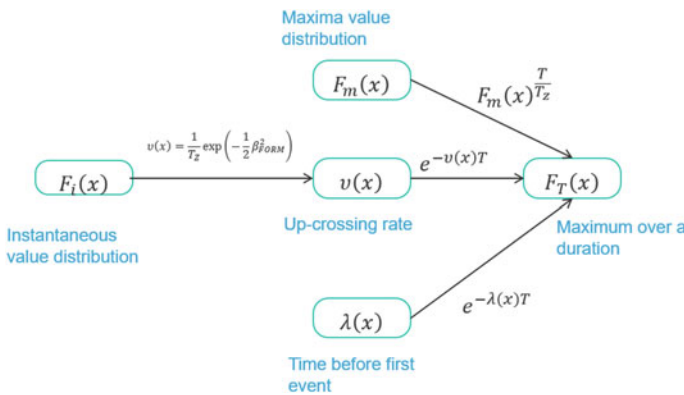


Fig. 23 Relation between different of statistical estimates

## 11 Conclusions

The difficulties to evaluate the probability of large roll angles are related to both the rarity of the event and the nonlinearity of the dynamical system describing the motion of a ship. One solution to overcome these difficulties is to use probabilistic or statistical techniques.

In summary, this work focused on the review of existing statistical methods of evaluating dynamic stability using a dataset originated from numerical simulation. Different statistical estimates have been reviewed and tested on two datasets represented by a linear process and a parametric resonance process. These estimates are related and Fig. 23 shows these relationships.

The middle branch in Fig. 23 represents the FORM approach, a method widely used in structure reliability problems. This approach has been applied on dynamic stability problems, e.g. [15] used FORM for statistical characterization of parametric roll. [9] applied the FORM to analyze stability under dead ship condition. Jensen [13] applied FORM to estimate characteristics of extreme roll motions.

One of the most important assumption behind the different statistical approaches is the independence of the stability failure events, understood as an exceedance or upcrossing of a certain level. The independence assumption is not always justified for upcrossing events of general stochastic process. Stochastic processes, such as roll angles or wave elevations do have some memory. Therefore, the instantaneous value of the process cannot change abruptly.

Direct counting based on time-to-first event is one method included in SGISC for direct stability assessment. We have seen that, the results are the same for other statistical approaches if the formulated assumptions behind these methodologies are satisfied.

**Acknowledgements** The author wish to thank Quentin Derbanne and Guillaume De Hauteclouque of Bureau Veritas for their guidance and their support for the investigation and compilation of these approaches. The present study was partly supported by the Cooperative Research Ships (CRS) under the Direct Dynamic Stability Assessment (DYNASTY) Working Group.

## References

1. Anastopoulos PA, Spyrou KJ (2019) Evaluation of the critical wave groups method in calculating the probability of ship capsizing in beam seas. *Ocean Eng* 187:106203
2. Ang AH-S, Tang WH (1984) Probability concepts in engineering planning and design volume II: decision, risk and reliability. Wiley, New York
3. Belenky VL, Sevastianov NB (2007) Stability and safety of ships: risk of capsizing. SNAME, 2nd edn
4. Belenky VL, Weems WM, Lin WM, Paulling JR (2011) Probabilistic analysis of roll parametric resonance in head seas, Chapter 31. In: Neves MAS, Belenky V, de Kat JO, Spyrou K, Umeda N (eds) Contemporary ideas on ship stability. Springer, pp 555–572. ISBN 978-94-007-1481-6
5. Belenky, V. and Weems, K., M., 2012, “Probabilistic Properties of Parametric Roll”, Chapter 7 of Parametric Resonance in Dynamical Systems, Fossen, T. I. and H. Nijmeijer, eds., Springer, pp 129–146. ISBN 978-1-4614-10423-0
6. Belenky V, Weems KM (2019) Dependence of roll and roll rate in nonlinear ship motions in following and stern quartering seas, Chapter 27. In: Belenky V, Spyrou K, van Walree F, Neves MAS, Umeda N (eds) Cotemporary ideas on ship stability. Risk of capsizing. Springer, pp 445–473. ISBN 978-3-030-00514-6
7. Campbell B, Weems K, Belenky V, Pipiras V, Sapsis T (2023) Envelope peaks over threshold (EPOT) application and verification, Chapter 16. In: Spyrou K, Belenky V, Katayama T, Backalov I, Francescutto A (eds) Contemporary ideas on ship stability—from dynamics to criteria, Springer, Berlin, pp 265–289. ISBN 978-3-031-16328-9
8. Chai W, Dostal L, Naess A, Leira BJ (2018) A comparative study of the stochastic averaging method and the path integration method for nonlinear ship roll motion in random beam seas. *J Mar Sci Technol* 23(4):854–865

9. Choi J, Jensen JJ, Kristensen HO, Nielsen UD, Erichsen H (2017) Intact stability analysis of dead ship conditions using FORM. *J Ship Res* 61(3):167–176
10. Coles S (2001) An introduction to statistical modelling of extreme values. Springer series in statistics
11. Cramér H, Leadbetter MR (1967) Stationary and related stochastic processes. Sample function properties and their applications. Wiley, New York
12. Hashimoto H, Umeda N, Matsuda A (2011) Experimental study on parametric roll of a post-panamax containership in short-crested irregular waves, Chapter 14. In: Neves MAS, Belenky V, de Kat JO, Spyrou K, Umeda N (eds) Contemporary on ship stability. Springer, Berlin, pp 267–276. ISBN 978-94-007-1486-6S
13. Jensen JJ (2007) Efficient estimation of extreme non-linear roll motions using the first-order reliability method (FORM). *J Mar Sci Technol* 12(4):191–202
14. Jensen JJ, Capul J (2006) Extreme response predictions for jack-up units in second order stochastic waves by FORM. *Probabilistic Engineering Mechanics* 21(4)
15. Jensen JJ, Choi J, Nielsen UD (2017) Statistical prediction of parametric roll using FORM. *Ocean Eng* 144:235–242
16. Kim DH, Belenky V, Campbell BL, Troesch AW (2014) Statistical estimation of extreme roll in head seas. In: Proceedings of the 33rd international conference on ocean, offshore and arctic engineering OMAE 2014, San Francisco, USA
17. Lekou DJ (2013) Probabilistic design of wind turbine blades. Woodhead Publishing Series in Energy, 325–359
18. Madsen HO, Krenk S, Lind NC (1986) Methods of structural safety. Dover Publication, Mineola
19. Meeker WQ, Escobar LA (1998) Statistical methods for reliability data. Wiley Interscience Publication, New York, p 680p
20. Mohamad MA, Sapsis TS (2016) Probabilistic response and rare events in Mathieu's equation under correlated parametric excitation. *Ocean Eng* 120:289–297
21. MSC.1-Circ 1627 (2020) Interim guidelines on the second generation intact stability criteria
22. Rychlik I (2000) On some reliability applications of rice's formula for the intensity of level crossings. *Extremes* 3(4):331–348
23. Shinozuka M (1983) Basic analysis of structural safety. *J Struct Eng* 109(3):721–740
24. St Denis M, Pierson Jr. WJ (1953) On the motions of ships in confused seas. New York University Bronx School of Engineering and Science
25. Wandji C (2018) Investigation on IMO second level vulnerability criteria of parametric rolling. In: Proceedings of 13th international conference on the stability of ships and ocean vehicles, pp 202–212
26. Wandji C, Corrigan P (2012) Test application of second generation IMO intact stability criteria on a large sample of ships. In: Proceedings of 11th international conference on the stability of ships and ocean vehicles, pp 129–139

# Verification, Validation and Accreditation in the Context of the IMO Second Generation Intact Stability Criteria and the Role of Specific Intended Uses in This Process



Arthur M. Reed

**Abstract** Verification, Validation and Accreditation (VV&A) are introduced in the context of IMO's Second Generation Intact Stability Criteria (SGISC). IMO's implementation of the SGISC has put in place a multitiered process by which the adequacy of a vessel's stability can be assessed. The application of Verification and Validation (V&V) to the Level 1, Level 2 and Direct Assessment stages of the SGISC are discussed. From the perspective of Level 1 and Level 2 V&V, the user's only responsibility is to verify that the algorithms for assessing vulnerability to stability failure contained in IMO documentation are implemented correctly. The developers of the algorithms for the Level 1 and Level 2 vulnerability assessments need to validate that their algorithms are consistent across a large range of vessel types and sizes. The most stringent criteria of SGISC is Direct Assessment where a vessel is assessed using a physics-based simulation tool. For direct assessment using ship dynamics software for predicting motions in extreme seas, existing well established and documented VV&A processes apply. To be applied to stability assessment, these tools should undergo a formal VV&A to assure that they perform adequately. Before the VV&A can be performed, the problem for which the simulation tool is to be assessed must be defined. This use—the *objectives* of the simulation are defined by the establishment of Specific Intended Uses (SIUs). SIUs are characterized and the way in which they are used are defined.

**Keywords** Second generation intact stability criteria · Verification, Validation and Accreditation (VV&A) · Specific intended uses (SIU)

## 1 Introduction

For most vessels, the general intact stability criteria is based on the work of [21]. Today, the intact stability criteria for commercial vessels is provided by the Inter-

---

A. M. Reed (✉)

David Taylor Model Basin, Carderock Division, Naval Surface Warfare Center,  
Bethesda, MA, USA

e-mail: [arthur.m.reed.civ@us.navy.mil](mailto:arthur.m.reed.civ@us.navy.mil)

national Code on Intact Stability, the 2008 IS Code (MSC 85/26/Add.1<sup>1</sup>). Similar criteria for naval vessels are provided by [26] and codified in the NATO Naval Ship Code [18, 19] and by a US Navy Design Data Sheet [25]. These criteria are prescriptive—that is they are a set of criteria, based on empirical data, which are assumed to ensure that a vessel meeting the criteria will have adequate intact stability (static and to a limited extent dynamic stability). The criteria are also binary, in that a vessel either meets the criteria or it does not. The history of development and the background of the IMO criteria are described by [16]; a summary of the origin of these criteria is also available in Chap. 3 of the Explanatory Notes to the International Code on Intact Stability (MSC.1/Circ.1281).

Beginning in the early 2000s efforts were initiated to develop performance based stability criteria for commercial vessels with the re-establishment of the intact-stability working group by IMO’s Subcommittee on Stability and Load Lines and on Fishing Vessels Safety (SLF) (cf. [9, 10]).<sup>2</sup> Over time, the terminology to describe the new intact stability criteria evolved from “Performance Based” to “Next Generation” to “Second Generation”—the terminology in use today. This entire evolution is described in the introduction to [20].

The SLF Working Group on intact Stability decided that the Second Generation Intact Stability Criteria (SGISC) should be performance-based and address three modes of stability failure (SLF 48/21, paragraph 4.18):

- *Restoring arm variation* problems, such as parametric roll and pure loss of stability;
- *Stability under dead ship condition*, as defined by SOLAS regulation II-1/3-8; and
- *Maneuvering related problems in waves*, such as surf-riding and broaching-to.

Ultimately, a fourth mode of stability failure was added:

- *Excessive accelerations*.

The criteria and processes were first discussed in [4]. The state-of-the-art in the assessment of vulnerability is presented in detail in [20] and further summarized in [23]

The deliberations of the Working Group on intact Stability led to the formulation of the framework for the SGSIC, which is described in SLF 50/4/4 and was discussed at the 50th session of SLF in May 2007. The key elements of this framework were the distinction between parametric criteria (the 2008 IS Code) and performance-based criteria, and between probabilistic and deterministic criteria. Special attention was paid to probabilistic criteria; the existence of the *problem of rarity* was recognized for the first time and a definition was offered. Also, due to the rarity of stability failures, the evaluation of the probability of failure with numerical tools was recognized as a significant challenge.

---

<sup>1</sup> References to IMO documents such as “MSC 85/26/Add.1” appear in the list of references with an “IMO” prefix, i.e., as: IMO MSC 85/26/Add.1. As there is no ambiguity in the names of the IMO citations, the year will be omitted from the citations.

<sup>2</sup> Due to a reorganization of IMO in the early 2010s,s, functions of SLF were transferred to the Subcommittee on Design and Construction (SDC); since 2013 SDC has been developing the second-generation intact stability criteria.

The SGISC are based on a three-tiered assessment approach: for a given ship design, each stability-failure mode is evaluated using two levels of vulnerability assessment in the first and second tiers, respectively. A vessel that fails to comply with the criteria of the first and second tiers must progress to the third tier where it is examined by means of a direct assessment procedure based on tools and methodologies corresponding to the best state-of-the-art physics-based prediction methods in the field of ship-stability failure prediction.

If decisions regarding the adequacy of a vessel stability-wise, are going to be made based on the predictions of a Modeling and Simulation (M&S) tool, there must be a reasonable assurance that the tool provides acceptably accurate results. The process by which a tool may be determined to be sufficiently accurate is known as Verification, Validation and Accreditation (VV&A).

As the SGISC are more extensive (deal with multiple stability failure modes) and more complex than the older prescriptive approach to stability, it will be necessary to ensure that the algorithms supporting the assessment are consistent and implemented correctly. It is the objective of this paper to provide some insights on these latter two issues.

In the process leading to accreditation by a Flag Administration, VV&A must be a formal process with structure that is prescribed. This structure includes the identification of an Accreditation Authority and the establishment of accreditation panels; and is described in [23]. Additionally, the process of accreditation requires Specific Intended Uses (SIUs)—the objectives against which accreditation occurs.

## 2 IMO Second Generation Intact Stability Criteria

The SGISC are based on a three-tiered assessment approach: for a given ship design and loading condition, each stability-failure mode is evaluated using the first two tiers of vulnerability assessment, as necessary. The criteria for the first tier is the Level 1 criteria and that of the second tier, the Level 2 criteria—these two tiers of vulnerability assessment criteria are characterized by different levels of accuracy and computational effort, with Level 1 being simpler and more conservative than Level 2.

A ship, which fails to comply with the Level 1 criteria is assessed using the Level 2 criteria. In a case of unacceptable results at the second tier, the vessel must then proceed to the third tier, and be examined by means of a direct assessment procedure based on tools and methodologies corresponding to the best state-of-the-art prediction methods in the field of ship-capsizing prediction. This third-tier methodology should capture the physics of capsizing as practically possible.

If a design does not meet the stability requirements after direct assessment, then the only choices are: abandoning that specific loading condition, changing the design, operational measures or operational guidance. In reality, at any stage of the assessment the designer, the builder or the owner may choose to proceed to the application of any one of these four options if he wishes. This process is illustrated in Fig. 1.

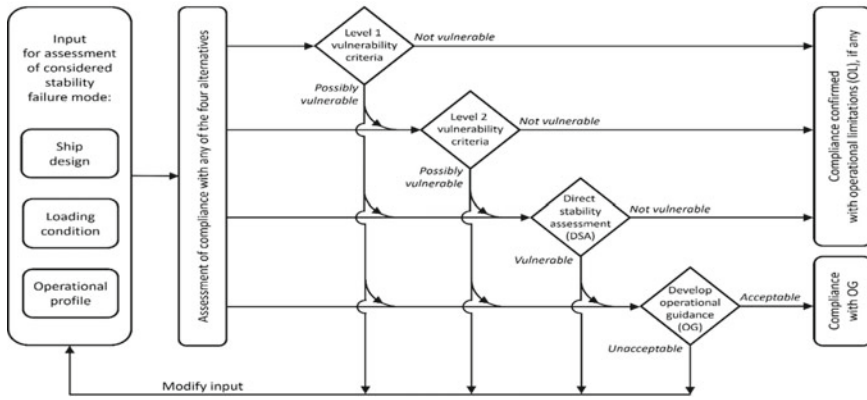


**Fig. 1** High-level flow chart for the IMO 2nd generation intact stability criteria (from: MSC.1/Circ.1627)

The three levels of assessment are intended to be of increasing complexity with the Level 1 assessment being a simple “back of the envelope” calculation that should be simple enough that it can be completed for all stability failure modes in a day. The Level 2 assessment is more complex and might require as much as a week’s effort to assess all stability failure modes, and require the use of computational algorithm implemented in a program such as Excel or MathCad—here after referred to as a spreadsheet. The third level direct assessment will require the use of serious computing resources and could take a month or more’s effort.

The specific formulations for the SGISC were released for the trial use in December 2020 as MSC.1/Circ.1627, Interim Guidelines on The Second Generation Intact Stability Criteria. MSC.1/Circ.1627 consists of four main sections: General, Guidelines on vulnerability criteria, Guidelines for direct stability failure assessment and Guidelines for operational measures. The Guidelines on vulnerability criteria section defines the Level 1 and Level 2 vulnerability criteria. The explanatory notes for MSC.1/Circ.1627 are still under development by the Intact Stability Correspondence Group (ISCG)<sup>3</sup>.

### 3 Verification, Validation and Accreditation

Software that is being used for engineering computations, upon which design decisions will be based needs to be correct. The processes by which software is assessed as to its correctness and being adequate for the job is called verification, validation and accreditation (VV&A)—verification assesses correctness and validation assesses the degree to which it is adequate for the task, accreditation assures that the software

<sup>3</sup> MSC.1/Circ.1652, to be published in 2023.



is adequate for the specific use that is specified. As stated by [24], verification is “solving the equations right” and validation is “solving the right equations.” People have said that accreditation is simply “validation with criteria.”

Papers and reports by [1–3, 5–8, 11, 17, 22, 23] provide different, although consistent, formal definitions of VV&A. The U.S. DoD definitions for these terms are provided below, each followed by a practical commentary relevant to computational tools for predicting dynamic stability.

1. *Verification*—the process of determining that a model or simulation implementation accurately represents the developer’s conceptual description and specification, *i.e.*, does the code accurately implement the theory that is proposed to model the problem at hand?
2. *Validation*—the process of determining the degree to which a model or simulation is an accurate representation of the real world from the perspective of the intended uses of the model or simulation, *i.e.*, does the theory and the code that implements the theory accurately model the relevant physical problem of interest?
3. *Accreditation*—the official determination that an model or simulation, ...is acceptable for use for a specific purpose, *i.e.*, is the theory and the code that implements it adequate for modeling the physics relevant to a specific platform? In other words, are the theory and code relevant to the type of vessel and failure mode for which it is being accredited?

As the Level 1 and Level 2 vulnerability criteria are specified by IMO, the code for these assessments only need to go through the verification and validation (V&V) processes to ensure that the code is correct. The direct assessment software, not being specified in any detail needs to undergo the entire VV&A process.

## 4 V&V from the User’s Perspective

For the SGISC, the question of V&V has to cover a broad range of computations/computational tools—from the “back of an envelope” assessment to sophisticated ship dynamics computational tools. As each of the levels of assessment has its own issues, they will be discussed separately, beginning with Direct Assessment, where the computational tools that are traditionally put through the V&V process would be employed.

### 4.1 Direct Assessment

As just stated, the hydrodynamic computational tools for predicting ship dynamics are the types of software for which the V&V processes have been developed. So while these are the most complex software tools that must be put through the V&V

process, and the tools for which the most effort will have to be expended, they are the tools for which the process is the most mature. As stated previously, there is an abundance of literature on the subject of formal V&V of software (cf. [1, 2, 5–8]). [23] provide a survey of the formal V&V process tailored for the ship stability community.

From the users perspective, it is unlikely that a user will be developing a computational tool for assessing dynamic stability performance in extreme seas; the user will most likely be employing software developed by a third party. Thus, the user will not be responsible for verification of the software, he will have to assume that the software vender has performed that function, and the user will only be responsible for performing validation to assure that the software tool is adequate for predicting the stability failure mode(s) of concern. The Flag Administration, responsible for the vessel being assessed, should have defined the process for formal validation.

## ***4.2 Level 2 Criteria***

For Level 2, the SGISC will explicitly provide the user with the algorithm for use in assessing the vulnerability of a ship to each particular stability failure mode. Thus, there should be no requirement for the user to perform validation of a spreadsheet that is used to perform the vulnerability calculations. However, it will be necessary to perform verification to insure that the calculations are performed correctly.

The issue then becomes one of how best to perform this verification. It would appear that the ideal situation would be to have a series of benchmark cases for each stability failure mode. For each failure mode there would be pairs of cases, one of the pairs being a case that passes the vulnerability test for that mode and one that fails the vulnerability test. For Level 2 algorithms where there are binary decision points within the algorithm, there should be a pair of benchmark cases that will test each branch of the decision tree.

Under these conditions, the user would be required to enter each pair of benchmark data into his spreadsheet and show that the results of each case agree with the expected answer within a specified accuracy, say 2-percent. When a user has performed and passed this level of validation for all five stability failure modes, he could be “certified” by a Flag Administration to use his spreadsheet to assess the vulnerability of his design to stability failure.

## ***4.3 Level 1 Criteria***

In principle, the Level 1 V&V should be similar in complexity to the Level 2 problem and have the same approach. However, there is one complication at Level 1. Level 1 vulnerability assessment has been characterized as an assessment that can be carried out on the “back of an envelope” using a hand calculator, but this opens the Level 1

assessment up to a lack of repeatability due to simple calculation errors—the *details* of the Level 1 calculations need to be recorded. Therefore, it is proposed that, even at Level 1, it be required that the vulnerability assessment for each mode of stability failure be implemented in a spreadsheet. This will vastly reduce the possibility of inadvertent errors due to “hitting the wrong key” on a calculator, and will greatly facilitate verification using the same benchmarking process proposed for Level 2.

## 5 V&V from the Criteria Developer’s Perspective

The developers of the Level 1 and Level 2 intact stability vulnerability criteria are not developing software, so they do not have any responsibility for V&V in the traditional sense. However, they do have responsibility for ensuring that the algorithms that they are developing are consistent—this is a validation function.

What is meant by consistency of algorithms? If the Level 1 and Level 2 algorithms are developed from the same theoretical basis, then the validation can be performed largely at the theory/algorithm basis, but if not, then extensive computational testing is required. A hypothetical example of a theoretically consistent Level 1 and Level 2 vulnerability assessment would be where the Mathieu equation is used to evaluate the sensitivity to parametric roll, with the Level 1 algorithm using the Mathieu equation without the roll damping term and the Level 2 algorithm using the Mathieu equation with a roll damping term.

In the absence of such a consistent theoretical basis, the validation of the Level 1 and Level 2 algorithms consists of two steps. First, the algorithms must be rational, that is they should not be based on the use of logically inconsistent information; and second, they must undergo an extensive computational consistency check. To give a ludicrous example of a rationality check, a stability failure algorithm based, among other things, on the distance from the earth to the moon would be highly suspect. Someone other than the developer of the algorithm should conduct the *rationality* step of the validation.

The second step, the computational validation, will involve evaluating a large number of vessels of various types and sizes using both the Level 1 and Level 2 algorithms for each mode of stability failure. The metric here is two-fold, first that a vessel in a given loading condition that passes the Level 2 vulnerability test should not fail the Level 1 vulnerability check. And secondly, for those vessels that pass both the Level 1 and Level 2 vulnerability check, the margin at Level 2 should not be smaller than the margin at Level 1—if a vessel passes the Level 1 check by a large margin, it should not pass the Level 2 check by only a small margin, this is admittedly somewhat subjective.

## 6 Role of SIUs in Accreditation

As described above, accreditation is the process by which a computational tool is certified as being sufficiently accurate and thus acceptable for use in a particular case for a particular vessel or class of vessels. In the IMO SGISC context, this would be a vessel of a particular size and proportions, which will have a particular mode of operation. In practice this would also be tied to a particular mode of stability failure and would be defined as a particular SIU.

Specific Intended Uses (SIUs) are the statements that define the scope of the problem or simulation that is to be modeled, and for which the M&S will be accredited. In the context of direct assessment under SGISC, this will need to include a definition of the type of vessel for which the M&S tool is to be accredited—accreditation for small fishing vessels may well not apply to a container carrier; as well as the mode of stability failure that is anticipated to be an issue. There can, and in fact would likely be multiple SIUs for the same VV&A activity.

### 6.1 Example of an SIU

As stated earlier, the SIU effectively defines the objective of the accreditation. As such, the SIU needs to answer the questions “what” and “why.” The “what” part of the answer will in the case of accreditation have two parts, one part pertaining to the type of vessel, and the other pertaining to the mode of stability failure. An example of this would be the accreditation of a code for predicting parametric roll of a container carrier—container carrier would be the type of vessel and parametric roll would be the mode of stability failure.

The “why” question relates to the way in which the predictions from the code will be used. Will the code be used to determine whether a vessel is susceptible to parametric roll in head seas at 24 kt in a particular sea state, or will it be used to derive a speed polar plots for susceptibility to parametric roll in a series of sea states. The answer to the “why” question serves to define the scope of the effort required in the accreditation process.

To clarify, an example of a SIU is: “The XYZ simulation tool will be used to generate operator guidance polar plots for all applicable speeds and headings against pure loss of stability for RO/PAX vessels in the 11,000–13,000 t displacement range, lengths of 130–150 m, and with beam-to-draft ratios of 4.5 to 5.5. These polar plots will enable the vessel operators to avoid situations where pure loss of stability could be an intact stability issue. The information used to generate the operational guidance polar plots will be developed using numerical data generated by the XYZ simulation tool.”

In the example SIU, the answers to the “what” question are RO/PAX vessels in a particular size range with the stability failure mode being pure loss of stability. The answer to the “why” question is to generate operational guidance polar plots for all applicable speeds and headings.

## 6.2 Requirements Flow-Down Table

The answers to the “what” and “why” questions within the SIU are used to determine what needs to be characterized and analyzed from the perspective of the V&V process. This is accomplished by the development of a Requirements Flow-Down Table. In the Requirements Flow-Down Table, each SIU is decomposed into several high level requirements (HLRs), which characterize important aspects of the SIU. The HLRs are each further mapped into several detailed-functional requirements (DFRs). A comparison metric and an acceptance criterion are identified for each DFR. Additional clarification is provided by the definition of the comparison metrics and their associated acceptance criteria. HLRs reflect the technical specifications provided by SME-opinion. DFRs provide additional specifications as necessary to more fully-describe each HLR. Requirements Flow-Down Tables are useful tools in high-level assessment of the appropriateness of the proposed accreditation criteria as well as required components of the Accreditation Plan [8].

An example of a Requirements Flow-Down Table, Table 1, is provided for the example SIU given above.

## 7 Summary

With the advent of the Second Generation Intact Stability Criteria, IMO has initiated a three-tier performance-based stability assessment process for unconventional hulls with a risk of intact stability failure. If the design fails the first and second level tests, it then progresses to the third tier and direct assessment, which requires an accredited physics-based simulation tool.

From the perspective of Level 1 and Level 2 verification and validation, the user’s only responsibility is to verify that the algorithms for assessing vulnerability to stability failure contained in IMO documentation are implemented correctly. To facilitate this, there needs to be a comprehensive set of benchmark cases that both meet and fail to meet the vulnerability criteria, covering each of the stability failure modes. For direct assessment using ship dynamics software for predicting motions in extreme seas, the well-established and documented V&V process of [1, 2, 5–8, 11], *etc.* apply. The developer of the algorithms for the Level 1 and Level 2 vulnerability assessments need to validate that their algorithms are consistent across a large range of vessel types and sizes.

The one significant note is that even though, in general, the Level 1 vulnerability assessment can be performed “on the back of an envelope” using a hand calculator, those calculations need to be performed using a spreadsheet program on a personal computer or reliable and consistent verification will be virtually impossible.

Accreditation requires that a set of Specific Intended Uses (SIUs) defining the objectives of the accreditation, be defined. These SIUs must define what the M&S is to be accredited for (type of vessel and mode of stability failure) and why (the product to be produced by the M&S).

**Table 1** Example requirements flow-down table

High level requirements	Detailed functional requirement	Comparison metric	Acceptance criteria
<p>HLR 1.a Simulation must demonstrate good correlation to model data for ship responses to elemental tests to suggest that underlying physics are sound.</p>	<p>DFR 1.a.1 Simulation must demonstrate the ability to successfully predict critical motion values in a large number of Quantitative Accreditation conditions for which model test data is available for comparison</p> <p>DFR 1.a.2 Collective SME judgment shall ultimately decide whether or not this requirement is met (regardless of the code's ability to meet the suggested quantifiable metrics).</p>	<p>CM 1.a.1 Check-list of quantifiable metrics defining "reasonable" correlation for elemental tests used to inform SME opinion</p> <p>CM 1.a.2 SME opinion/judgment</p>	<p>AC 1.a ARP will vote using SME opinion informed by elemental test comparisons whether to assess subsequent acceptance criteria</p>
<p>HLR 1.b The simulation and model-scale data must show consistently good correlation ranging from the more simple conditions to the more complex conditions. Good correlation must be demonstrated for the range of operational, environmental, and loading conditions defined in the Quantitative Accreditation scope for which comparison model data are available.</p>	<p>DFR 1.b.1 Parameters which characterize the ship's operating condition relative to the seaway, and identify the corresponding critical motion, must be assessed.</p> <p>DFR 1.b.2 All comparisons must take into account all known sources of uncertainty (sampling, instrument, condition, etc.)</p> <p>DFR 1.b.3 Parameters that are used to define Quantitative Accreditation polar plots risk values and lifetime risk calculation must be assessed. If direct validation of these quantities is not achievable, a sufficient substitute quantity shall instead be assessed. (rare motion metrics)</p> <p>DFR 1.b.4 Parameters that are used to evaluate the quantitative accreditation system health must be assessed. (non-rare motion metrics)</p>	<p>CM 1.b.1 Mean values, <math>\mu</math>, of achieved speed and heading</p> <p>CM 1.b.2 90% uncertainty intervals on the each parameter (model and simulation)</p> <p>CM 1.b.3 The 90th percentile of peak amplitudes, A90%, of motions (in lieu of exceedance rates of physical limit thresholds which are not expected to be available for validation)</p> <p>CM 1.b.4 Mean standard deviation, <math>\sigma</math>, of motions</p>	<p>AC 1.b.1 Differences between mean achieved speed and mean achieved heading for each validation condition must be less than specified amounts</p> <p>AC 1.b.2 The 90% confidence intervals on each parameter value (<math>\sigma</math> and A90%) for a given motion and condition must overlap in order to suggest that the underlying populations (model and simulation) may be the same</p>

(continued)

**Table 1** (continued)

High level requirements	Detailed functional requirement	Comparison metric	Acceptance criteria
<b>High level requirements</b>	<b>Detailed functional requirement</b>	<b>Comparison metric</b>	<b>Acceptance criteria</b>
HLR 1.c Necessary accuracy of the simulation shall be influenced by an appropriate balance between technical excellence and judiciousness	DFR 1.c Thoughtful engineering judgment shall be applied in the determination of permissible differences between simulation and model test results	CM 1.c Margin applied to observed sample parameter values (defined in CM 1.b.2 and CM 1.b.3)	AC 1.c The observed values of compared sampled parameters may be deemed acceptable if the difference between the values is less than a specified amount (margin)
HLR 1.d The safety of the ship and sailor must be prioritized and reflected in the criteria established for validation	<p>DFR 1.d.1 Reasonable conservatism on the part of the simulation solution should be endorsed to promote the overall safety of the sailor.</p> <p>DFR 1.d.2 Determination of simulation tool success must only be reached using reasonably high-fidelity validation data sets</p>	<p>CM 1.d.1 Margin applied to observed sample parameter values (defined in CM 1.b.2 and CM 1.b.3)</p> <p>CM 1.d.2 Combined uncertainty in the comparison, calculated as a function of the 90% uncertainty intervals (CM 1.b.2) on both data sets, model and simulation</p>	<p>AC 1.d.1 The margin allowed by AC 1.c shall be increased by 50% in the case of over-prediction on the part of the simulation to allow for additional conservatism on the part of the simulation. (additional conservative margin)</p> <p>AC 1.d.2 Successful validation comparisons for both rare and non-rare motions (<math>\sigma</math> and A90%) may only be accepted if the combined uncertainty in both data sets is sufficiently small</p>
HLR 1.e Simulation must be deemed usable for conditions within the current scope of the quantitative accreditation for which comparison model test data is not available	DFR 1.e.1 Simulation must demonstrate the ability to successfully produce critical motion values in a large number of quantitative accreditation conditions for which model test data is available for comparison	CM 1.e.1 Number of conditions which successfully pass the following criteria: AC.1.b.1 through AC 1.d	AC 1.e 70% of quantitative accreditation conditions for which model data are available for comparison must pass criteria (AC 1.a through AC 1.d) for 100% of critical motion parameter values. (rare and non-rare motion assessments calculated independently)

Additionally, the Requirements Flow-Down Table which is used to define comparison metrics and acceptance criteria based on the SIUs are described, and an example is provided.

## References

1. AIAA (1998) Guide for the verification and validation of computational fluid dynamics simulations. AIAA Guide AIAA G-077-1998 Guide. American Institute of Aeronautics and Astronautics, viii+19. Reston
2. ASME (2009) Standard for verification and validation in computational fluid dynamics and heat transfer. Standard V&V 20-2009. American Society of Mechanical Engineers, New York, NY, x+87
3. Beck RF, Reed AM, Rood EP (1996) Application of modern numerical methods in marine hydrodynamics. *Trans SNAME* 104:519–537
4. Belenky V, de Kat JO, Umeda N (2008) Toward performance-based criteria for intact stability'. *Mar Technol* 45(2):101–123
5. DoD (1998) DoD modeling and simulation (M&S) glossary. DoD 5000.59-M. U. S. Department of Defense. U. S. Department of Defense, Washington, DC, 175 pp
6. DoD (2003) DoD modeling and simulation (M&S) verification, validation and accreditation (VV&A). DoD Instruction 5000.61. DoD Instruction. U. S. Department of Defense. U. S. Department of Defense, 10 pp
7. DoD (2007) DoD modeling and simulation (M&S) management. DoD Directive 5000.59. DoD Directive. U. S. Department of Defense. U. S. Department of Defense, 7 pp
8. DoD (2012) Department of defense standard practice: documentation of verification, validation and accreditation (VV&A) for models and simulations. MIL-STD-3022 w/Change 1. Department of Defense, USD (AT&L), 55 pp
9. Francescutto A (2004) Intact ship stability-the way ahead. *Mar Technol* 41:31–37
10. Francescutto A (2007) Intact stability of ships—recent developments and trends. In: Basu RI, Belenky V, Wang G, Yu Q (eds) *Proceedings 10th international symposium on practical design in shipbuilding & other floating structures (PRADS'07)*, vol 1. Houston, TX, pp 487–496
11. IEEE (2005) IEEE standard for software verification and validation, viii+110. Revision of IEEE Std 1012-1998. IEEE Std 1012TM-2004. American National Standard (ANSI). Software Engineering Standards Committee of the IEEE Computer Society. Institute of Electrical and Electronics Engineers, New York, NY
12. IMO MSC 85/26/Add.1 (2008) International code on intact stability, 2008 (2008 IS Code). London, UK, 96 pp
13. IMO MSC.1/Circ.1281 (2008) Explanatory notes to the international code on intact stability, 2008. London, UK, 30 pp
14. IMO SLF 48/21 (2005) Report to maritime safety committee. London, UK, 65 pp
15. IMO SLF 50/4/4 (2007) Framework for the Development of New Generation Criteria for Intact Stability, submitted by Japan, the Netherlands and the United States. London, UK, 6 pp
16. Kobylinski LK, Kastner S (2003) Stability and safety of ships. Volume I, Regulation and operation. Elsevier ocean engineering book series 9. Elsevier, Amsterdam, The Netherlands, xviii+412
17. McCue LS, Story WR, Reed AM (2008) Nonlinear dynamics applied to the validation of computational methods. In: *Proceedings 27th symposium on naval hydrodynamics* (Seoul, South Korea)
18. NATO (2007a) Buoyancy, stability and controllability. Chapter III of naval ship code. Allied Naval Engineering Publication ANEP-77. NATO Naval Armaments Group, Maritime Capability Group 6, Specialist Team on Naval Ship Safety and Classification. Chap. 3. vii+121
19. NATO (2007b) Guidance on NSC Chapter III buoyancy and stability, Part B: application. Chapter 3, guide to the naval ship code. NATO Naval Armaments Group, Maritime Capability Group 6, Specialist Team on Naval Ship Safety and Classification, 91 pp
20. Peters W, Belenky V, Bassler C, Spyrou KJ, Umeda N, Bulian G et al (2011) The second generation intact stability criteria: an overview of development. *Trans SNAME* 119:225–264
21. Rahola J (1939) The judging of the stability of ships and the determination of the minimum amount of stability especially considering the vessel navigating finnish waters. Ph.D. Thesis. Technical University of Finland, Helsinki, Finland, viii+232



22. Reed AM (2009) A naval perspective on ship stability. In: Proceedings 10th international conference on the stability of ships and ocean vehicles (STAB'09) (St. Petersburg, Russia), pp 21–44
23. Reed AM, Zuzick AV (2015) Direct assessment will require accreditation—what this means. In: Proceedings 12th international conference on the stability of ships and ocean vehicles (STAB'15). Ed. by STAB2015 Secretariat. Glasgow, UK, pp 49–78
24. Roache PJ (1998) Verification and validation in computational science and engineering. Hermosa Publishers, Albuquerque, NM, p 446
25. Rosborough JM (2007) Stability and buoyancy of U.S. Naval surface ships. Design Data Sheet DDS 079-1, Version: 2.01, 30 Jan 2008. NSWCCD-20-TR-2007/05. Carderock Division, Naval Surface Warfare Center. 107 pp
26. Sarchin TH, Goldberg LL (1962) Stability and buoyancy criteria for U. S. Naval surface ships. Trans SNAME 72:418–458

# Statistical Validation of the Split-Time Method with Volume-Based Numerical Simulation



Kenneth Weems, Vadim Belenky, Bradley Campbell, and Vlasdas Pipiras

**Abstract** The application of a statistical validation procedure for estimating the probability of capsizing with the split-time method is described. The method is a numerical-extrapolation scheme incorporating motion perturbation simulations to evaluate a critical roll rate leading to capsizing following an up-crossing event. Fast volume-based numerical simulations create a sample of capsizing events in realistic irregular wave conditions that serves as a “true” value. Subsets of this data are used with the split-time method to estimate the capsizing probability. The split-time estimates are compared to the “true” value to judge the validity of the estimate. A short description of volume-based numerical simulation, review of the essence of the split-time methods, and the statistical validation and performance assessment of the estimation of the probability of capsizing is contained in the chapter.

**Keywords** Probability of capsizing · Validation · Split-time method

## 1 Introduction

The application of advanced hydrodynamic codes in the probabilistic assessment of capsizing in irregular waves inevitably leads to the solution of an extrapolation problem. The Monte-Carlo application cannot be applied effectively with advanced numerical methods, as capsizing in realistic sea conditions is too rare to be directly observed within a limited simulation time and the computation cost of such codes

---

K. Weems · V. Belenky (✉) · B. Campbell  
David Taylor Model Basin (NSWCCD), West Bethesda, Maryland, USA  
e-mail: [vadim.belenky@navy.mil](mailto:vadim.belenky@navy.mil)

K. Weems  
e-mail: [kenneth.weems@navy.mil](mailto:kenneth.weems@navy.mil)

B. Campbell  
e-mail: [bradley.campbell@navy.mil](mailto:bradley.campbell@navy.mil)

V. Pipiras  
University of North Carolina, Chapel Hill, NC, USA  
e-mail: [pipiras@email.unc.edu](mailto:pipiras@email.unc.edu)

prohibits the time and cost of obtaining a sufficiently large sample size. At the same time, the complexity of the problem's physics precludes the application of overly simplified simulations. This conundrum has led to development of extrapolation methods that attempt to characterize the probability of rare events from limited simulation data (for example, [1, 3, 6, 11, 16, 25, 34]). These methods are typically performed with hybrid numerical seakeeping codes such as LAMP [23, 27] and TEMPEST [12], which can practically generate hundreds or even thousands of hours of quantitatively relevant responses in random irregular wave fields.

The validation of the extrapolation methods, however, presents a challenge, as the data set must be extremely large in order to be able to observe the "true" extreme value and yet capture the principal physics of the large amplitude motion in order to be relevant [28]. Moreover, the result of simulation-based extrapolation is a random number that is estimated with uncertainty quantified as a confidence interval. If the "true" value is known, the extrapolation can be regarded as successful if this "true" value falls within the confidence interval. However, due to the very same random nature, a single successful extrapolation result is hardly convincing. How would one know if this was not just a coincidence?

To ensure that the result is representative relative to the environmental conditions, [28] introduced a multi-tier concept of statistical validation. The first tier is elemental: it is successful if the extrapolation result contains a "true" value within its confidence interval (the methodology of obtaining the true value is considered in the next section). The extrapolation procedure is then repeated several times for exactly the same condition but with independent data sets, this is second tier. A successful validation for a given condition produces a certain percentage of successes, referred to as a "passing rate"; [28] proposed 90% as a level for acceptance for 100 extrapolations. The third tier of statistical validation includes consideration of several conditions reflecting the expected operational conditions. How many of those conditions need to be successful for an extrapolation method to pass is not clear. Examples of the application of the procedure for the EPOT (Envelope Peak over Threshold) method [15] are considered in [28] as well as in [16]. This chapter describes the application of this multi-tiered procedure to the evaluation of the probability of capsizing in irregular waves with the split-time method.

## 2 Estimation of "True Value"

The extrapolation validation procedure reviewed in the sect. 1 requires a priori knowledge of the probability of capsizing. Theoretical solutions for the probability of capsizing are available for piecewise linear models [5], but while these models do describe capsizing qualitatively, i.e. as a transition between two stable equilibria, they are too simplistic to be considered as quantitative ship motion models. In particular, they cannot describe the realistic change of stability in waves as well as the fact that the restoring is inseparable from wave excitation for large-amplitude ship motions.

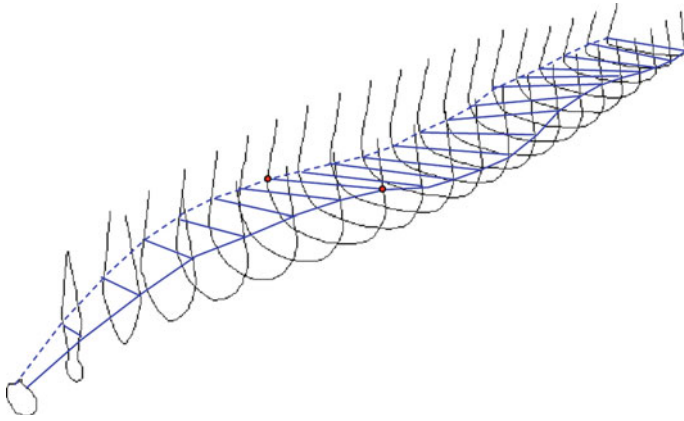


**Fig. 1** Station/incident wave intersection for volume based hydrostatic and Froude-Krylov forces for the ONR Tumblehome hull in stern oblique seas [30]

A solution was proposed by [30]. The main idea is to compute the inseparable nonlinear hydrostatic and Froude-Krylov forces from the distribution of the instantaneous submerged volume along the hull, implemented as a sectional-based calculation to preserve the variation of relative motion along the ship’s hull, as illustrated in Fig. 1.

In a typical hybrid numerical method, hydrostatic and Froude-Krylov forces are computed by pressure integration over the instantaneous wetted surface:

$$\vec{F}_{FK+HS}(t) = -\rho \iint_{S_B(t)} \left( \frac{\partial \varphi_0(x, y, z, t)}{\partial t} + gz \right) \vec{n} ds \tag{1}$$

where  $\rho$  is density,  $g$  is gravity acceleration  $t$  is time,  $x, y, z$  are spatial coordinates,  $\vec{n}$  is a unit vector, normal to a time-variant surface of submerged portion of ship hull  $S_B(t)$ , and  $\varphi_0(x, y, z, t)$  is the incident wave velocity potential, whose time derivative is the pressure distribution of the undisturbed wave field.

While straightforward to evaluate in a standard spectrum-based wave field, formula (1) can be very expensive to calculate for an irregular seaway with many components. If the incident wave pressure can be approximated by constant gradient over each section, Gauss theorem relates the integration of pressures to the instantaneously submerged volume, while the moment can be expressed through the coordinate of the centroid of this volume. This idea has evolved into a very fast algorithm, comparable in performance with calm-water  $GZ$  for restoring and effective slope for excitation, but with a much more complete model of nonlinear forcing and stability variation in waves. A known limitation of the volume-based technique is related to short wave lengths that are comparable to or shorter than the ship’s beam. Derivation of the formulae, a detailed description of the algorithm, and cross-validation with LAMP can be found in [33] and [32]. Additional hydrodynamic

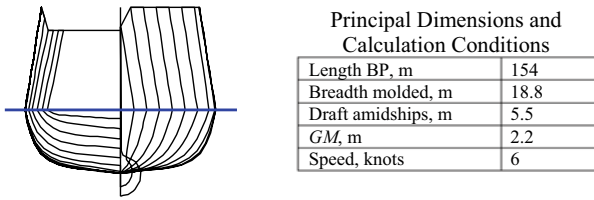


**Fig. 2** Lines, principal dimensions, and flotation of the ONR tumblehome topside configuration

forces including added mass, damping and maneuvering forces are approximated by ordinary differential equation (ODE) style models.

Weems and Belenky [31] reported that 10 h of data could be generated in 7 s on a single processor of a laptop computer, allowing millions of hours of simulation data to be computed practically on a standard workstation or modest sized cluster.

The subject ship for the validation exercise is the tumblehome configuration from the ONR topside series [14]. The ship lines, principal dimensions, and flotation are in Fig. 2. The statistical validation campaign included four different sea states and various relative wave headings, which are summarized in Table 1.

To avoid a self-repeating effect (e.g. [8]), the simulations for each sea state consisted of a large number of 30-min records. 240 frequency components provided

**Table 1** Summary of validation conditions and “true” value estimates

Significant wave height, m	Modal Period, s	Heading, degrees	Total simulation time, hours	Number of capsizes	Estimate of rate 1/s	Low boundary of rate	Upper boundary of rate
8.5	14	45	200,000	8	1.13 E-08	4.24 E-09	1.98 E-08
8.5	14	60	200,000	31	4.38 E-08	2.97 E-08	5.93 E-08
9	14	35	720,000	12	4.71 E-09	2.04 E-09	7.37 E-09
9	14	40	200,000	12	1.70 E-08	8.48 E-09	2.68 E-08
9	14	45	200,000	51	7.20 E-08	5.37 E-08	9.18 E-08
9	14	50	20,000	7	9.89 E-08	2.83 E-08	1.84 E-07
9	14	55	60,000	69	3.25 E-07	2.50 E-07	4.05 E-07
9	14	60	200,000	176	2.49 E-07	2.12 E-07	2.85 E-07
9	14	65	200,000	80	1.13 E-07	8.90 E-08	1.38 E-07
9	14	70	200,000	6	8.48 E-09	2.83 E-09	1.55 E-08
9	15	45	345,000	10	8.19 E-09	3.11 E-09	1.33 E-08
9	15	60	300,000	11	1.04 E-08	4.71 E-09	1.70 E-08
9.5	15	45	1,000,000	157	4.44 E-08	3.74 E-08	5.13 E-08
9.5	15	60	1,000,000	242	6.84 E-08	5.98 E-08	7.70 E-08

a statistically valid model of irregular waves for 30 min duration. The total simulation time and number of observed capsizes are reported in Table 1.

The rate of the capsizing events,  $\hat{\lambda}_T$ , based of these observations is estimated as

$$\hat{\lambda}_T = \frac{N_T}{T_T} = \frac{N_T}{N_R T_R - \sum_{i=1}^{N_T} (T_R - t_{Ci})} \tag{2}$$

where  $N_T$  is a number of capsizing events observed and  $T_T$  is the total simulation time,  $N_R$  total number of records in the simulation campaign,  $T_R$  duration of a record,  $t_{Ci}$  time of  $i$ th recorded capsizing. The observed number of capsizes  $N_T$  is assumed to follow a binomial distribution as capsizings are rare and can be treated as Bernoulli trials. The binomial distribution has two parameters: the total number of trials  $N_R$  (which is a total number independent records) and the probability  $p$  of an event's occurring during a particular record.

$$p \approx \hat{p} = N_T / N_R \tag{3}$$

Boundaries of the confidence interval for the estimate  $\hat{\lambda}_T$  are computed by a binomial distribution (e.g. [5])

$$\hat{\lambda}_T^{Up,Low} = \frac{1}{T_T} Q_B \left( \frac{1 \pm P_\beta}{2} \right); \tag{4}$$

where  $Q_B$  is a quantile (inverse cumulative distribution function) for the binomial distribution with parameters (3) and  $P_\beta$  is a confidence probability. The calculation of this quantile encounters numerical error for the total time of 720,000 h and above (too large to compute a factorial in double precision), so a normal approximation for the estimate distribution was employed for those cases, with the mean value and variance ( $\hat{p}$  is small compared to 1.0) equal to the estimate itself:

$$E(\hat{\lambda}_T) = \frac{1}{T_T} p N_S \approx \frac{\hat{p} N_S}{T_T} = \hat{\lambda}_T; \tag{5}$$

$$Var(\hat{\lambda}_T) = \frac{1}{T_T} p N_S (1 - p) \approx \frac{\hat{p} N_S}{T_T} (1 - \hat{p}) \approx \hat{\lambda}_T \tag{6}$$

The boundaries of the normal-approximation-based confidence interval are:

$$\hat{\lambda}_T^{Up,Low} = \hat{\lambda}_T \pm Q_N \left( \frac{1 + P_\beta}{2} \right) \sqrt{\hat{\lambda}_T} \tag{7}$$

$Q_N$  is the standard normal (with zero mean and unity variance) quantile. The boundaries of the confidence interval for the capsizing rate estimates, computed with a confidence probability of 0.95, are listed in Table 1.

### 3 Essence of the Split-Time Method

The objective of the split-time method is to provide a way to use an advanced numerical code for estimating the probability of a rare event without actually having to observe it in simulations. Its principal idea is to separate the estimation procedure into an observable or “non-rare” problem and a non-observable or “rare” problem. The “non-rare” problem is an estimation of the crossing rate of an intermediate roll threshold. The threshold roll angle must be low enough to observe a statistically significant number of up-crossing events in, say, 100 h, but high enough so that most of these up-crossings can be treated as independent events.

The “rare” problem is solved for each up-crossing with a motion perturbation scheme in Fig. 3. The roll rate is perturbed at the instant of up-crossing until capsizing is observed. The minimum value of roll rate perturbation leading to capsizing is computed by a metric of the danger of capsizing at the instant of up-crossing

$$y_i = c + \dot{\phi}_{U,i} - \dot{\phi}_{C,i}; c = 1 \text{ rad/s}; i = 1, \dots, N_U \tag{8}$$

$\dot{\phi}_{C,i}$  is the critical roll rate calculated for the  $i$ -th up-crossing defined as the minimum perturbed roll rate leading to capsizing (corresponds to capsizing time history in Fig. 3),  $\dot{\phi}_{U,i}$  is the roll rate observed at the  $i$ -th up-crossing, and  $N_U$  number of observed up-crossings. The constant  $c = 1 \text{ rad/s}$  is introduced for convenience in working with the metric.

A rate of capsizing events  $\lambda_C$  (a number of events per unit of time) is expressed as

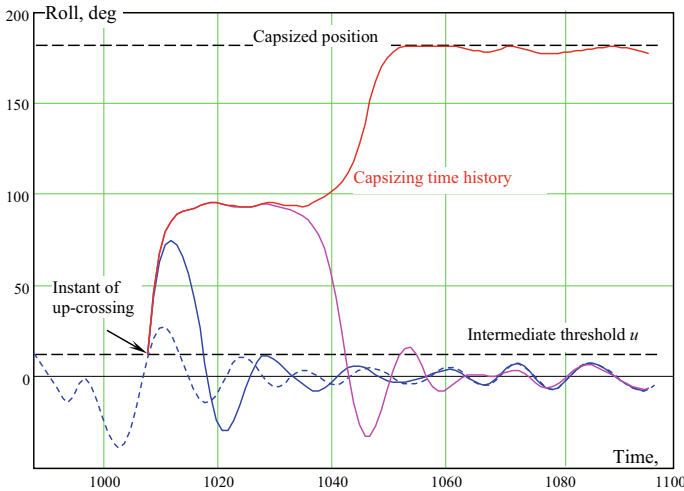


Fig. 3 Illustration of motion perturbations

$$\lambda_C = \lambda_U P(y \geq c | \phi = u \cap \dot{\phi} > 0) \tag{9}$$

where  $\lambda_U$  is a rate of up-crossings of the intermediate threshold  $u$ ;  $P(y \geq c | \phi = u \cap \dot{\phi} > 0)$  is a conditional probability that the capsizing occurs after an up-crossing of the intermediate threshold  $u$  (i.e. the capsizing metric  $y$  exceeds the constant  $c = 1$  rad/s). Following standard definition (e.g. [18]), an up-crossing event is defined when the roll angle crosses the intermediate threshold  $\phi = u$  with a positive roll rate ( $\dot{\phi} > 0$ ).

To find the conditional probability  $P(y \geq c | \phi = u \cap \dot{\phi} > 0)$ , modeling of the entire distribution of the capsizing metric  $y$  is not necessary (as was done by [9] for a time-variant piecewise linear model, Eq. 61 of the cited reference). As the capsizing event is rare, to fit the tail of the distribution of the capsizing metric is sufficient.

Following the second extreme value theorem (e.g. [17]), the tail of any distribution can be approximated with a Generalized Pareto Distribution (GPD), whose probability density function is described as

$$\text{pdf}(y) = \begin{cases} \frac{1}{\sigma} \exp\left(-\frac{y-w}{\sigma}\right) & \text{for } \xi = 0 \\ \frac{1}{\sigma} \left(1 + \xi \frac{y-w}{\sigma}\right)^{-(1+1/\xi)} & \text{for } \xi \neq 0 \text{ and } \xi \frac{y-w}{\sigma} > -1 \\ 0 & \text{otherwise} \end{cases} \tag{10}$$

where  $\xi$  is a shape parameter,  $\sigma$  is a scale parameters, and  $w$  is a threshold for the capsizing metric (secondary threshold, in angular velocity units), defining the beginning of the distribution tail. A brief overview on extreme value theorems is available from [7].

Fitting the GPD for the tail of a capsizing metric, which is described in detail in [10], consists of the following steps:

- Define a set of “candidate” secondary thresholds
- Estimate shape and scale parameters of GPD for each secondary threshold value
- Search for the secondary threshold
- Evaluate the confidence intervals for estimates of the conditional probability (with the distribution of the extrapolated estimate, derived from a bivariate normal distribution of  $\hat{\xi}$  and  $\ln \hat{\sigma}$ ) and capsizing rate in Eq. (9).

This fitting procedure is completely data-driven and does not account for any physical considerations that may be available for the problem at hand. Adding physical considerations to a data-driven model may reduce statistical uncertainty (for example, Fig. 8 of [20]).

Nonlinearity of roll rate is usually considered to be weak as it is related to roll damping, which is a weakly nonlinear function of roll rate. As a result, a roll rate process is assumed normal. The capsizing metric contains a value of roll rate at an instant of up-crossing  $\dot{\phi}_U$ . If both roll and roll rate are normal, the value  $\dot{\phi}_U$  follows a Rayleigh distribution (for example, p. 201 of [21]). Similar to the normal distribution, the Rayleigh distribution has an exponential tail (a proof is in Example 1.1.7 in [19]).



For the roll rate at the instance of up-crossing of an actual nonlinear roll process, the exponential tail is a plausible assumption.

The second random component of the capsizing metric (8) is the value of the critical roll rate  $\dot{\phi}_C$ . Its randomness reflects the variation of stability in waves. The variability of the roll rate at up-crossing is assumed larger than the variability due to the changing stability in waves. Finally, the assumption of exponential tail is adopted for the entire capsizing metric (8). The exponential tail is a particular case of GPD (Eq. 10) when the shape parameter  $\xi = 0$ .

Applying the exponential tail, the conditional probability of capsizing after up-crossing of the intermediate threshold  $u$  is expressed as

$$P(y \geq c | \phi = u \cap \dot{\phi} > 0) = P(y \geq w) \exp(-(c - w)/\gamma_w) \quad (11)$$

where  $\gamma_w$  is the parameter of the exponential tail and  $w$  is the secondary threshold.

Fitting the exponential tail follows the same steps as fitting the GPD. Given a sufficient number of up-crossings of the intermediate threshold  $u$ , the parameter for the tail of the distribution can be estimated as

$$\hat{\gamma}_w = \frac{1}{N_w} \sum_{i=1}^{N_w} (y_i - w) \quad (12)$$

where  $N_w$  is the number of data points remaining above the secondary threshold  $w$ .

The value of the secondary threshold  $w$  is found by testing a number of “threshold candidates” and finding one that provides the best fit for the tail. Two methods were selected in Belenky et al. [6]: a prediction error criterion developed by Mager [24] and a goodness-of-fit test, modified for exponential distribution by [29].

The rate of up-crossing of the intermediate threshold  $u$  and the probability of exceedance of the secondary threshold  $w$  are estimated as

$$\hat{\lambda}_U = \frac{N_U}{T}; \quad \hat{P}(y \geq w) = \frac{N_w}{N_U} \quad (13)$$

where  $T$  is the total simulation time. The final expression for the capsizing rate estimate is

$$\hat{\lambda}_C = \frac{N_w}{T} \exp(-(c - w)/\hat{\gamma}_w) = \hat{\lambda}_w \exp(-(c - w)/\hat{\gamma}_w) \quad (14)$$

where  $\hat{\lambda}_w = N_w/T$  is an estimate of exceedance rate of the secondary threshold  $w$ .

The estimate of the capsizing rate Eq. (14) is a function of two other estimates,  $\hat{\lambda}_w$  and  $\hat{\gamma}_w$ , which are random numbers. To evaluate a confidence interval for the capsizing rate estimate, distributions are needed for the estimates  $\hat{\lambda}_w$  and  $\hat{\gamma}_w$ .

Similarly to the capsizings, the exceedance events of the secondary threshold  $w$  can be considered rare enough to be treated as Bernoulli trials (independence assumed). The number of events observed within simulation time  $T$  then follows binomial

distribution. The binomial distribution has two parameters: number of trials  $N$  and probability  $\hat{p}$  of an exceedance event at any instant of time so that

$$N = \frac{T}{\Delta t}; \hat{p} = N_w/N \tag{15}$$

where  $\Delta t$  is the time increment in the simulations. The estimate of the exponential tail parameter (5) is essentially a mean value. Its distribution is approximately normal with the standard deviation

$$\hat{\sigma}_\gamma = \frac{1}{N_w} \sqrt{\widehat{\text{Var}}(y - w)} = \frac{1}{N_w} \sqrt{\frac{1}{N_w} \sum_{i=1}^{N_w} (y_i - w)^2 - \hat{\gamma}_w^2} \tag{16}$$

where  $\widehat{\text{Var}}(y - w)$  is an estimate of the variance of the capsizing metric values on the tail.

Boundaries of confidence interval for the estimates  $\hat{\lambda}_w$  and  $\hat{\gamma}_w$  can be found as follows:

$$\begin{aligned} \hat{\lambda}_w^{Up,Low} &= \frac{1}{T} Q_B \left( \frac{1 \pm P_{\beta 1}}{2} \right); \\ \hat{\gamma}_w^{Up,Low} &= \hat{\gamma}_w \pm Q_N \left( \frac{1 + P_{\beta 1}}{2} \right) \hat{\sigma}_\gamma \end{aligned} \tag{17}$$

where  $Q_B$  is a quantile (inverse cumulative distribution function) for binomial distribution with parameters (15),  $Q_N$  is standard normal (with zero mean and unity variance) quantile, and  $P_{\beta 1}$  is confidence probability for the estimates  $\hat{\lambda}_w$  and  $\hat{\gamma}_w$ .

The confidence probability of the estimates  $\hat{\lambda}_w$  and  $\hat{\gamma}_w$  is related to the confidence probability for the complete capsizing as estimate  $P_\beta$  as

$$P_\beta = \sqrt{P_{\beta 1}} \tag{18}$$

under an assumption of mutual independence of the estimates  $\hat{\lambda}_w$  and  $\hat{\gamma}_w$ . The boundaries of the confidence interval for capsizing rate estimate  $\hat{\lambda}_c^{Up,Low}$  can be obtained through the boundaries of the confidence intervals of the estimates  $\hat{\lambda}_w^{Up,Low}$  and  $\hat{\gamma}_w^{Up,Low}$ :

$$\hat{\lambda}_c^{Up,Low} = \hat{\lambda}_w^{Up,Low} \exp(-(c - w)/\hat{\gamma}_w^{Up,Low}) \tag{19}$$

Justification for Eq. (17), sometimes referred as “boundary method”, can be found in Sect. 4.4 of [13].

### 4 Results of Statistical Validation

Examples of the tier-two validation are in Fig. 4 (GPD tail fit) and Fig. 5 (exponential tail fit). A seaway derived from a Bretschneider wave spectrum [22] with a significant wave height of 9.0 m and a modal period of 14 s is used in both examples. The tier-two validation data set consists of 50 independent extrapolations. Each extrapolation estimate uses 100 h of volume-based simulations, with no capsizing cases observed during those times. The extrapolation result is presented with a confidence interval for the 0.95 confidence probability. Besides these boundaries, each extrapolation has the most probable value (identified by red x-marks in Fig. 4) and the mean value (indicated as circles in Fig. 4). The calculation of the mean and most probable values is discussed in detail in [10]. The tier-one validation is successful if the confidence interval contains the “true” value. The case in Fig. 4 has 45 individual extrapolations that contain the “true” value within their confidence interval. The tier-two validation is successful when a percentage of the underlining tier-one validation successes (“passing rate”) is close to the accepted confidence probability. This number is 0.90 for the case in Fig. 4, which would be considered a successful passing rate by [28].

The vertical scale of Fig. 4 is logarithmic. To indicate zero, a small value of  $10^{-15} \text{ s}^{-1}$  was applied. A total of 37 values of lower boundary of the confidence interval extends below  $10^{-15} \text{ s}^{-1}$ , and 11 most probable extrapolated estimates and even 1 value of upper boundary are also very small. The reason is an apparent light tail and associated right bound of the estimated distribution of the metric. It is one of the known issues of practical application of GPD [2, 4, 26].

Figure 5 has results for the exponential tail, inferred from weak nonlinearity of the roll rate and the assumption that the variability of roll rate at up-crossings is larger than the variability of critical roll rate caused by changing stability in waves see the sect. 3 of this chapter. This inference is essentially a choice of statistical model

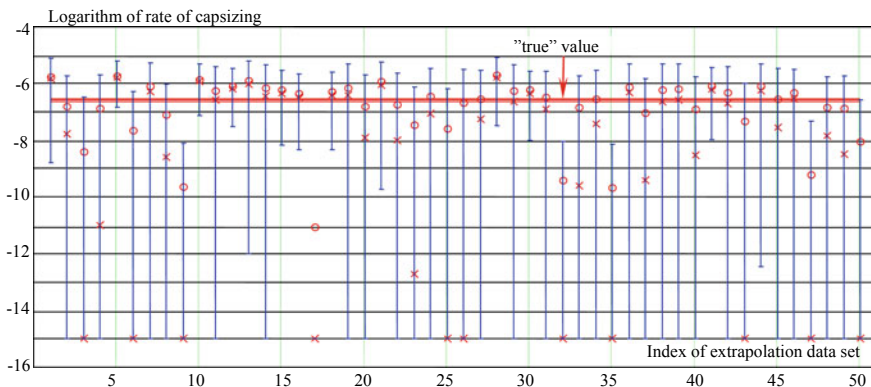


**Fig. 4** Example of tier-two validation with the GPD tail fit; significant wave height 9.0, modal period 14 s, heading 60°, passing rate 0.90; circles indicate mean value of extrapolated estimates, x-marks are most probable extrapolated estimates

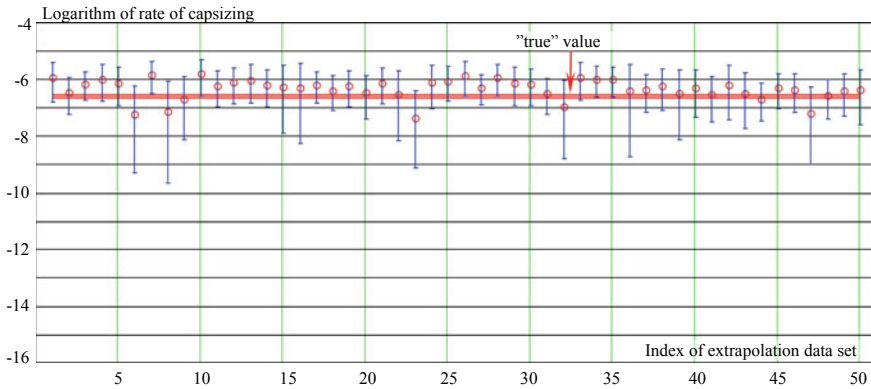


**Fig. 5** Example of tier-two validation with the exponential tail fit (prediction error criterion); significant wave height 9.0, modal period 14 s, heading 60°, passing rate 0.98

(exponential tail) based on physical considerations. Including physical information reduces uncertainty, which is reflected in the decreased width of the confidence intervals in Fig. 5 as compared to Fig. 4. Similar results were reported previously by [20]. A mathematical aspect of the decreased uncertainty is a transition from the GPD tail with two estimated parameters to the exponential tail with a single estimated parameter. Comparing Figs. 4 and 5, the difference in the upper boundary is not that dramatic. The practical advantage of this physics-informed approach is improved reliability of prediction.

Besides the passing rate, assessing the performance of the different approaches and elements of an extrapolation is done with two other indicators: “conservative distance” *CD* and “relative bias” *RB*. These are defined as:

$$CD = \log \left( \frac{E(\hat{\lambda}_c^{Up})}{\hat{\lambda}_T} \right); \quad RB = \frac{E(\hat{\lambda}_c) - \hat{\lambda}_T}{\hat{\lambda}_T} \tag{20}$$

where  $E(\hat{\lambda}_c^{Up})$  is the upper boundary of extrapolated estimates averaged over all the considered extrapolation data sets,  $E(\hat{\lambda}_c)$  is the extrapolated estimate (most probable estimate is used for GPD) averaged over all the considered data sets, and  $\hat{\lambda}_T$  is the true value estimated from capsizing observations with Eq. (2).

In a sense, the *CD*-value expresses the practicality of the extrapolation. The upper boundary of the extrapolated estimate is likely to be utilized for the final answer, to keep the whole procedure conservative. If the upper boundary is too far from the “true” value, the result may be too conservative to be practical. The *CD*-value shows, on average, by how many orders of magnitude the upper boundary exceeds the true value. The *RB*-value may be helpful for comparing the accuracy of the fit, including most probable estimate vs. mean value estimate of GPD and two different techniques

of the exponential fit. It also indicates if a method is conservative (when its sign is positive).

As mentioned above, the third tier of the [28] validation procedure is carried out over a number of environmental conditions. Table 1 lists the conditions considered in the present validation campaign. Table 2 summarizes the results with the GPD fit (meaning of different font colors are explained in the next section). The tier-two validation procedure was repeated three times on independent data to check the variability of the results. Each data set included 50 records with a duration of 100 h. The passing rate for each individual data set is indicated as  $PR_1$ ,  $PR_2$ , and  $PR_3$ , while  $PR_A$  stands for the passing rate averaged over all three data sets. Conservative distance and relative bias were also averaged over all three data sets. The symbol  $RB_M$  is for the relative bias, computed over the mean value of the extrapolated estimate, while  $RB_{MP}$  means relative bias of the most probable value of the extrapolated estimate. Two more values were included in Table 2 to indicate the ability to complete the extrapolation with a given data set. The value  $NF_{MP}$  shows how many times the calculations did not yield the most probable extrapolated value over 150 data sets, e.g. data set #3 in Fig. 4. The value  $NF_U$  indicates how many times over 150 data sets the upper boundary of the extrapolated estimate was not provided, e.g. data set #17 in Fig. 4. Finally, averaged quantities for all performance indicators are included in Table 2.

**Table 2** Summary of validation results with GPD tail

$H_s$ , m	$T_m$ , s	$\beta$ deg	$PR_1$	$PR_2$	$PR_3$	$PR_A$	$CD$	$RB_M$	$RB_{MP}$	$NF_{MP}$	$NF_{UB}$	
8.5	14	45	1.00	0.98	0.90	0.96	2.31	32.21	21.77	10	0	
8.5	14	60	0.92	0.96	0.94	0.94	1.85	10.96	8.43	25	4	
9	14	35	1.00	0.98	0.98	0.99	2.53	45.39	25.15	7	0	
9	14	40	1.00	0.98	1.00	0.99	2.20	22.61	13.15	6	0	
9	14	45	0.98	0.98	0.96	0.97	1.68	7.62	5.66	18	1	
9	14	50	0.98	0.92	0.94	0.95	1.55	5.32	4.31	30	2	
9	14	55	0.90	0.80	0.92	0.87	0.89	0.38	0.20	42	3	
9	14	60	0.90	0.86	0.94	0.90	1.02	0.81	0.57	42	3	
9	14	65	0.94	0.92	0.94	0.93	1.33	2.47	1.75	35	3	
9	14	70	0.92	1.00	0.90	0.94	2.20	16.89	9.01	46	3	
9	15	45	0.98	0.96	0.96	0.97	2.53	50.58	32.68	14	1	
9	15	60	0.96	0.98	0.98	0.97	2.40	40.27	27.94	13	0	
9.5	15	45	0.96	0.94	0.96	0.95	1.80	8.71	5.35	14	1	
9.5	15	60	0.98	0.94	0.96	0.96	1.64	6.70	5.25	25	1	
Averaged quantities							0.95	1.85	17.92	11.52	23.36	1.57

Table 3 summarizes the results of the extrapolations with the exponential tail fit. Both methods of fit are included: prediction error criterion and goodness-of-fit test. Any justification for setting a level of significance  $\alpha$  for the goodness-of-fit test is not apparent, the level of significance was varied from 0.1 to 0.5. Averaged quantities for all performance indicators are also included in Table 3.

Passing rate is the main criterion in tier-two validation. [28] considers the tier-two validation successful if the passing rate does not fall below a standard value that depends on the number of extrapolation data sets, and it equals to 0.9 for 100

**Table 3** Summary of validation result with exponential tail fit

Hs, m	Tm, s	$\beta$ deg	Prediction error criterion			Goodness-of-fit $\alpha = 0.1$			Goodness-of-fit $\alpha = 0.2$		
			PR	CD	RB	PR	CD	RB	PR	CD	RB
8.5	14	45	0.94	1.54	2.53	0.94	1.32	0.99	0.94	1.50	1.78
8.5	14	60	0.96	1.56	5.96	0.94	1.43	4.28	0.96	1.64	6.11
9	14	35	0.94	1.41	1.20	1.00	1.42	0.32	1.00	1.75	1.03
9	14	40	0.98	1.71	5.64	0.92	1.33	2.88	0.98	1.65	3.93
9	14	45	0.98	1.35	3.20	0.98	0.95	0.66	0.98	1.19	1.12
9	14	50	1.00	1.23	2.64	0.98	1.14	1.79	1.00	1.27	1.63
9	14	55	1.00	0.75	0.77	0.98	0.76	0.61	0.98	0.84	0.30
9	14	60	0.98	0.88	1.31	0.92	0.89	1.11	0.98	0.97	0.69
9	14	65	0.90	1.12	2.82	0.92	0.99	1.54	0.98	1.16	1.56
9	14	70	0.98	1.75	7.96	0.86	1.67	7.81	0.96	1.82	7.07
9	15	45	0.92	2.01	13.55	0.74	1.82	8.09	0.90	1.97	7.32
9	15	60	0.98	1.76	6.76	0.96	1.54	3.31	1.00	1.79	4.76
9.5	15	45	0.98	1.26	1.73	0.94	1.06	0.71	0.96	1.22	0.56
9.5	15	60	0.92	1.32	3.41	0.84	1.05	1.72	0.96	1.28	2.06
Averaged quantities			0.96	1.40	4.25	0.92	1.24	2.56	0.97	1.43	2.85

Hs, m	Tm, s	$\beta$ deg	Goodness-of-fit $\alpha = 0.3$			Goodness-of-fit $\alpha = 0.4$			Goodness-of-fit $\alpha = 0.5$		
			PR	CD	RB	PR	CD	RB	PR	CD	RB
8.5	14	45	0.98	1.65	2.77	0.98	1.75	3.49	0.96	1.78	4.10
8.5	14	60	0.96	1.69	6.35	0.96	1.71	5.96	0.96	1.71	5.55
9	14	35	1.00	1.84	1.58	1.00	1.90	1.87	1.00	1.98	2.92
9	14	40	1.00	1.75	4.16	1.00	1.80	4.68	0.98	1.81	5.11
9	14	45	0.96	1.28	1.47	0.98	1.34	1.57	0.98	1.36	1.87
9	14	50	1.00	1.32	1.78	1.00	1.36	1.73	1.00	1.38	1.76
9	14	55	0.98	0.88	0.31	0.98	0.90	0.30	0.98	0.91	0.29
9	14	60	0.96	1.01	0.72	0.96	1.03	0.70	0.96	1.04	0.69
9	14	65	1.00	1.21	1.38	0.96	1.22	1.46	0.96	1.24	1.26
9	14	70	0.98	1.85	5.45	1.00	1.88	5.37	0.98	1.89	4.52
9	15	45	1.00	2.07	8.09	1.00	2.13	9.76	1.00	2.19	11.61
9	15	60	1.00	1.79	3.34	1.00	1.88	4.20	1.00	1.96	5.73
9.5	15	45	0.96	1.32	0.71	0.96	1.39	1.02	0.96	1.45	1.37
9.5	15	60	1.00	1.39	2.30	1.00	1.43	2.32	1.00	1.44	2.25
Averaged quantities			0.98	1.50	2.89	0.98	1.55	3.17	0.98	1.58	3.50

**Table 4** Upper and lower acceptable passing rates

$N_e$	50	100	150	700	2100
Lower	0.88	0.90	0.91	0.93	0.94
Upper	1.00	0.99	0.98	0.97	0.96

extrapolations. The standard should be lower for 50 extrapolations in this validation campaign, as the random variability is expected to be larger. To adjudicate a tier-two validation with an arbitrary number of data sets, consider each extrapolation (*i.e.* tier-one validation) as a Bernoulli trial. If an extrapolation procedure works perfectly, the probability of covering a true value with the confidence interval is equal to the accepted confidence probability  $P_\beta$ . Then the number of successful extrapolations  $N_S$  of a total of  $N_e$  extrapolations is a random number following binomial distribution with parameters  $N_e$  and  $P_\beta$ .

Using the same confidence probability  $P_\beta$ , the expected boundaries of the passing rate can be computed as

$$PT^{Up,Low} = \frac{1}{N_e} Q_B \left( \frac{1 \pm P_\beta}{2}; N_e, P_\beta \right) \quad (22)$$

The upper and lower acceptable passing rates for different number of extrapolations are listed in Table 4.

## 5 Discussion

Only the lower boundary for the passing rate (Table 4) is proposed for validation use by [28]. An apparent reason is that exceeding the upper boundary of the passing rate indicates that the width of the confidence interval was likely overestimated. The results are likely to be conservative, but the extrapolation method is still usable.

If the passing rate falls below the lower boundary from Table 4, the extrapolation result may be questionable. A likelihood that its confidence interval does not contain a true value may be too high and cannot be explained by natural variability. These cases were encountered during the described validation study for both GPD and exponential tail fits. They are indicated by the red font in Tables 2 and 3.

Two tier-two validation failures were observed for GPD tail fit: in date set 2 for the heading 55 and 60° at significant wave height of 9 m and modal period 14 s. Two other data sets for these conditions did not indicate a failure. The reason for failure is likely that the shape parameter was significantly underestimated, leading to a very light tail and to one of the “pitfalls” of GPD tail fitting described by [26]. Table 2 also contains the passing rate averaged over three data sets in the column marked  $PR_A$ . As the total number of “trials” for this column is 150, the acceptable passing rate is between 0.91 and 0.98 (Table 4). The cases when the passing rate exceeded the upper boundary of 0.98 are in the blue font. The observed number of failures for

the most probable estimate and upper boundary are given for 150 data sets as well as values of the conservative distance and relative bias.

Two failures were observed with the exponential tail: for a heading of  $70^\circ$  with a modal period 14 s and at  $45^\circ$  with a model period 15 s and significant wave 9 m. Both failures were observed when applying goodness-of-fit with the level of significance 0.1. As no failures were recorded for a level of significance exceeding 0.1, the reason is likely to be the fitting method. Based on these observations, the significance level must be 0.2 or more for successful use of the goodness-of-fit test. No failures were observed for the prediction error criterion.

As mentioned above, the requirements for tier three are not yet clear. One approach described by [28] is to fail a validation if one of the conditions at tier two did not pass. Following this approach, the GPD tail fit and exponential tail fit with the goodness-of-fit and significance level of 0.1 should be limited in application to those conditions that passed tier two.

Alternatively, the passing rates averaged over all the considered conditions could be reviewed. That would correspond to 2100 extrapolation data sets for the GPD tail and 700 for the exponential tail. Acceptable boundaries for the passing rates are available in Table 4. This approach finds the GPD tail acceptable with a perfect passing rate of 0.95, indicating that the light tail “pitfall” still can be overcome by a large-volume sample. This is also a possible indication of slow convergence of GPD. The “averaged” approach still fails the exponential tail with a significance level goodness-of-fit of 0.1. Significance levels of 0.3 and above may be seen as too conservative with a passing rate of 0.98, exceeding an acceptable level of 0.97 from Table 4. The exponential tail estimated with 0.2 significance level for goodness-of-fit and prediction error criterion are found acceptable by both tier-three approaches.

The conservative distance,  $CD$ , as follows from its name and definition in Eq. (20), is an indicator of how conservative the extrapolated estimate could be, expressed as an order of magnitude. The  $CD$  values are evaluated for all the extrapolation data sets individually and averaged over all conditions. The latter is a convenient metric to compare the performance of different tail fits. The exponential tail reduces the  $CD$  value to 1.4–1.5 from the 1.85 evaluated for GPD. This conclusion is consistent with the visual observation in Figs. 4 and 5, showing a more significant decrease for the lower boundary of the confidence interval.

The relative bias,  $RB$ , is defined in Eq. (20) and is similar to the  $CD$ -value. It measures the conservativeness of the extrapolated estimate but uses the most probable value (and mean value for the GPD tail) rather than the upper boundary of the confidence interval. Since the upper boundary is expected to be of practical use, the  $RB$  value can be observed as an auxiliary performance indicator. Similar to the conservative distance,  $RB$  values are evaluated for all the extrapolation data sets individually and averaged over all the conditions. The  $RB$  value is formulated as a factor rather than an order of magnitude, so the most probable value can be expected to converge to the true value if the extrapolation is perfect.

The relative bias values reveals that for the GPD tail, the most probable value is a better estimate, as  $RB_{MP} < RB_M$  in Table 2. However, the estimation of the most probable extrapolated value fails on average in about 15% (22.36/150, the column



identified  $NF_{MP}$  in Table 2) of extrapolation attempts, while the mean value estimate always can be computed (Eq. 27 in [10]). The difference between  $RB$  values for GPD and exponential tail is also a good illustration of improvement made by the physics-informed approach: on average 11 for GPD in Table 2 versus 2.9–4.25 for the exponential tail in Table 3. This difference is believed to be caused by slower convergence of GPD vs. exponential tail.

The last column in Table 2 (identified as  $NF_U$ ) is the number of failures for the calculation of the upper boundary of the confidence interval for the GPD extrapolated estimate. The percentage of failures is about 1% (1.57/150), which is smaller than the percentage of failures for the most probable estimate,  $NF_U < NF_{MP}$ ; therefore, so even if the calculation of the most probable GPD value fails, the upper boundary of the confidence interval still may be available.

Concluding the overall performance assessment, the best method was found to be an exponential fitted with goodness-of-fit test with significance level of 0.2 with  $CD = 1.43$  and  $RB = 2.85$ , while the fitting with the error prediction criterion having a similar  $CD = 1.4$  but  $RB = 4.25$ . However, since no theoretical background exists for the choice of the significance level in the goodness-of-fit test, the recommendation is to use the extrapolation with exponential tail fitted with the error prediction criterion.

## 6 Summary and Conclusions

This chapter describes the statistical validation of the split-time method for estimating the probability of capsizing in irregular waves. The main feature of the split-time method is to compute a metric of the likelihood of capsizing as a difference between the observed roll rate at a roll threshold up-crossing and a critical roll rate leading to capsizing at a particular instant of time. Statistics for the metric values can be collected without actual observation of capsizing and extrapolated to estimate the probability of capsizing.

Extrapolation is performed with Generalized Pareto distribution (GPD) following the second extreme value theorem. Accounting for weak nonlinearity of roll rate and assuming lesser influence of stability variation in waves, an exponential tail can be applied instead of GPD. Including physical information into extrapolation scheme (i.e. the physics-informed approach) allows a significant decrease in the statistical uncertainty and improvement of the reliability of the prediction.

Validation of extrapolation is determined with a fast numerical simulation algorithm, capable of qualitatively reproducing the most principle nonlinearity of roll motion by computing the instantaneous submerged volume and its centroid. These calculations were carried out for sufficiently long times to observe capsizing in realistic conditions. The validation is considered to be successful if a small subset of this data can predict the capsizing probability without observing capsizing.

The statistical validation considered 14 conditions for the ONR tumblehome top configuration. A three-tiered validation procedure was employed for GPD and exponential tail extrapolation. Two tail fitting techniques were applied for the exponential tail: prediction error criterion and goodness-of-fit test, with the series level of significance varying from 0.1 to 0.5.

If the successful multi-condition validation requires that all the conditions to be validated individually, only extrapolation with exponential tail fitted with error prediction criterion or goodness-of-fit test with the significance level 0.2 and above can pass. If adjudication of success is based on the averaged outcomes, GPD extrapolation also passes.

In addition to validation, performance of the extrapolation methods was assessed with criteria for conservativeness and accuracy. The best performing methods were extrapolations by exponential tail fitted with error prediction criterion and goodness-of-fit test with a significance level of 0.2. The final recommendation is application of the split-time method with exponential tail fitted with the error prediction criterion.

**Acknowledgements** The work described in this chapter has been funded by the Office of Naval Research (ONR) under Dr. Woei-Min Lin. This work was also supported by the NSWCCD Independent Applied Research (IAR) program under Dr. Jack Price. The participation of Prof. Pipiras was facilitated by the NSWCCD Summer Faculty and Sabbatical Programs, both of which were also managed by Dr. Jack Price. The authors are very grateful for the support that made this work possible.

## References

1. Anastopoulos PA, Spyrou KJ (2019) Evaluation of the critical wave groups method in calculating the probability of ship capsizing in beam seas. *Ocean Eng* 187:106213
2. Anastopoulos P, Spyrou KJ (2019) Can the generalized Pareto distribution be useful towards developing ship stability criteria? In: *Proceedings of the 17th international ship stability workshop (ISSW 2019)*, 10–12 June, Helsinki
3. Anastopoulos PA, Spyrou KJ (2023) An efficient formulation of the critical wave groups method for the assessment of ship stability in beam seas. In: Spyrou K, Belenky V, Katayama T, Bačkalov I, Francescutto A (eds) *Contemporary ideas on ship stability—from dynamics to criteria*, Chapter 10. Springer, Berlin, pp 157–174. ISBN 978-3-031-16328-9
4. Anastopoulos PA, Spyrou KJ (2023) Effectiveness of the generalized Pareto distribution for characterizing ship tendency for capsizing. In: Spyrou K, Belenky V, Katayama T, Bačkalov I, Francescutto A (eds) *Contemporary ideas on ship stability—from dynamics to criteria*, Chapter 15. Springer, Berlin, pp 245–263. ISBN 978-3-031-16328-9
5. Belenky V, Weems K, Lin WM (2016) Split-time method for estimation of probability of capsizing caused by pure loss of stability. *Ocean Eng* 122:333–343
6. Belenky V, Weems K, Pipiras V, Glotzer D (2018) Extreme-value properties of the split-time metric. In: *Proceedings of 13th international conference on stability of ships and ocean vehicles (STAB 2018)*, Kobe, Japan
7. Belenky V, Weems KM, Spyrou K, Pipiras V, Sapsis T (2023) Modeling broaching-to and capsizing with extreme value theory. In: Spyrou K, Belenky V, Katayama T, Bačkalov I, Francescutto A (eds) *Contemporary ideas on ship stability—from dynamics to criteria*, Springer, Chapter 26. Berlin, pp 435–457. ISBN 978-3-031-16328-9

8. Belenky V (2011) On self-repeating effect in reconstruction of irregular waves. In: Neves MAS, Belenky V, de Kat JO, Spyrou K, Umeda N (eds) *Contemporary ideas on ship stability*, Chapter 33. Springer, Berlin, pp 589–598. ISBN 978-94-007-1481-6
9. Belenky V, Reed AM, Weems KM (2011) Probability of capsizing in beam seas with piecewise linear stochastic GZ curve. In: Neves MAS, Belenky V, de Kat JO, Spyrou K, Umeda N (eds) *Contemporary ideas on ship stability*, Chapter 30. Springer, Berlin, pp 531–554. ISBN 978-94-007-1481-6
10. Belenky V, Weems K, Campbell B, Pipiras V (2014) Extrapolation and validation aspects of the split-time method. In: *Proceedings of 30th symposium on naval hydrodynamics*, Hobart, Tasmania, Australia
11. Belenky V, Weems K, Pipiras V, Glotzer D, Sapsis T (2018) Tail structure of roll and metric of capsizing in irregular waves. In: *Proceedings of 32nd symposium on naval hydrodynamics*, Hamburg, Germany
12. Belknap WF, Reed AM (2019) TEMPEST: a new computationally efficient dynamic stability prediction tool. In: Belenky V, Spyrou K, van Walree F, Neves MAS, Umeda N (eds) *Contemporary ideas on ship stability*. Risk of capsizing, Chapter 1. Springer, Berlin, pp 3–21. ISBN 978-3-030-00514-6
13. Bickel PJ, Doksum KA (2001) *Mathematical statistics: basic ideas and selected topics*, vol 1, Prentice Hall. ISBN 978-0138503635
14. Bishop RC, Belknap W, Turner C, Simon B, Kim JH (2005) Parametric investigation on the influence of GM, roll damping, and above-water form on the roll response of model 5613, hydromechanics department report, Naval Surface Warfare Center Carderock Division, West Bethesda, Maryland, USA, NSWCCD-50-TR-2005/027
15. Campbell B, Belenky V, Pipiras V (2016) Application of the envelope peaks over threshold (EPOT) method for probabilistic assessment of dynamic stability. *Ocean Eng* 120:298–304
16. Campbell B, Weems KM, Belenky V, Pipiras V, Sapsis T (2023) Envelope peaks over threshold (EPOT) application and verification. In: Spyrou K, Belenky V, Katayama T, Bačkalov I, Francescutto A (eds) *Contemporary ideas on ship stability—from dynamics to criteria*, Springer, Chapter 16. Berlin, ISBN 978-3-031-16328-9
17. Coles S (2001) *An introduction to statistical modeling of extreme values*. Springer, London. ISBN 978-1849968744
18. Cramér H, Leadbetter MR (2004) *Stationary and related processes*. Dover, Sample function properties and their application
19. De Haan L, Ferreira A (2007) *Extreme value theory: an introduction*. Springer Science & Business Media. ISBN 978-0387239460
20. Glotzer D, Pipiras V, Belenky V, Campbell B, Smith T (2017) Confidence interval for exceedance probabilities with application to extreme ship motions. *REVSTAT Statistical Journal* 15(4):537–563
21. Leadbetter MR, Lindgren G, Rootzen H (1983) *Extremes and related properties of random sequences and processes*, Springer series in statistics. Springer, Berlin. ISBN 978-1461254492
22. Lewis EV (ed) (1989) *Principles of naval architecture*. Vol. 3: motions in waves and controllability. SNAME, Jersey City, 429 p. ISBN 0-939773-02-3
23. Lin WM, Yue DKP (1990) Numerical solutions for large amplitude ship motions in the time-domain. In: *Proceedings of the 18th symposium on naval hydrodynamics*, Ann Arbor, Michigan, USA, pp. 41–66
24. Mager J (2015) Automatic threshold selection of the peaks over threshold method. Master's thesis, Technische Universität München
25. Mohamad MA, Sapsis T (2018) Sequential sampling strategy for extreme event statistics in nonlinear dynamical systems. *Proceedings of the national academic of sciences of United States of America (PNAS)* 115:11138–11143
26. Pipiras V (2020) Pitfalls of data-driven peaks-over-threshold analysis: perspectives from extreme ship motions. *Probab Eng Mech* 60:103053
27. Shin YS, Belenky VL, Lin WM, Weems KM, Engle AH (2003) Nonlinear time domain simulation technology for seakeeping and wave-load analysis for modern ship design. *SNAME Trans* 111:557–578

28. Smith TC (2019) Validation approach for statistical extrapolation. In: Belenky V, Neves M, Spyrou K, Umeda N, van Walree F (eds) *Contemporary ideas on ship stability. Risk of capsizing*, Chapter 33. Springer, Berlin, pp 573–589. ISBN 978-3-030-00514-6
29. Stephens MA (1974) EDF statistics for goodness of fit and some comparisons. *J Am Stat Assoc* 69(347):730–737
30. Weems K, Wundrow D (2013) Hybrid models for fast time-domain simulation of stability failures in irregular waves with volume-based calculations for Froude Krylov and hydrostatic forces. In: *Proceedings of 13th international ship stability workshop*, Brest, France
31. Weems K, Belenky V (2015) Fast time-domain simulation in irregular waves with volume-based calculations for Froude-Krylov and hydrostatic force. In: *Proceedings of 12th international conference on stability of ships and ocean vehicles (STAB 2015)*, Glasgow, UK
32. Weems K, Belenky V (2018) Extended fast ship motion simulations for stability failures in irregular seas. In: *Proceedings of 13th international conference on stability of ships and ocean vehicles (STAB 2018)*, Kobe, Japan
33. Weems K, Belenky V, Spyrou K (2018) Numerical simulations for validating models of extreme ship motions in irregular waves. In: *Proceedings of 32nd symposium on naval hydrodynamics*, Hamburg, Germany
34. Weems K, Belenky V, Campbell B, Pipiras V, Sapsis T (2019) Envelope peaks over threshold (EPOT) application and verification. In: *Proceedings of 17th international ship stability workshop*, Helsinki, Finland, pp 71–79

# Effectiveness of the Generalized Pareto Distribution for Characterizing Ship Tendency for Capsize



Panayiotis A. Anastopoulos and Kostas J. Spyrou

**Abstract** The paper investigates the effectiveness of the generalized Pareto distribution (GPD) for modelling the tail of the distribution of ship rolling motions, and particularly for calculating the probability of capsizes in beam seas. To this end, large-scale Monte Carlo numerical experiments were performed for an ocean surveillance ship assumed to operate in two qualitatively different, in terms of the observed frequency of stability failures, sea states; one where capsizes are realized quite often and another where they are extremely rare. For both sea conditions, GPD models were fitted to datasets containing roll angle exceedances above a pre-defined threshold and their reliability is tested herein against the rough Monte Carlo estimates, obtained by direct counting. Aiming at establishing links between dynamics and probability, in this study, the roll angle distribution is parametrized through successive GPDs and the idea of associating threshold selection with the shape of the GZ curve is developed. In this setting, a new framework is proposed for addressing the problem of ship capsizes which, formally, is outside the scope of the classical GPD implementations. To evaluate the rumoured “extrapolation” character of the GPD beyond the largest observation used in the fitting procedure, a comparison with the predictions of the “critical wave groups” method is presented for the second (mild) sea state.

**Keywords** Probability · Capsize · Generalized Pareto distribution · Statistical extrapolation · Extreme events · Critical wave groups

---

P. A. Anastopoulos (✉) · K. J. Spyrou  
School of Naval Architecture and Marine Engineering, National Technical University of Athens,  
Athens, Greece  
e-mail: [panasto@central.ntua.gr](mailto:panasto@central.ntua.gr)

K. J. Spyrou  
e-mail: [k.spyrou@central.ntua.gr](mailto:k.spyrou@central.ntua.gr)

## 1 Introduction

Several techniques can be employed for obtaining the distribution of the responses of a dynamical system subjected to random excitation (e.g. [8]). However, their application in the problem of ship capsizing is hindered by their large computational requirements and/or deficiencies in dealing with the complexity of ship dynamics at large angles. Brute-force Monte Carlo simulations, despite being very attractive due to their accuracy, can easily turn into a computationally intensive exercise when a large number of extremely rare events, like capsizing, must be produced.

One possibility to alleviate the problem could be the tools provided by extreme value theory (EVT), a branch of statistics focused on making inferences about the extreme values in a random process. Specifically, the second extreme value theorem [2, 18] states that, under certain conditions, the generalized Pareto distribution (GPD) is a limiting distribution for excesses over thresholds. This has motivated the development of a number of threshold-based methods seeking a solution to the problem of rarity of extreme ship responses through fitting the GPD to data obtained from pertinent time-domain simulations (e.g. [5, 24]). Nonetheless, it is the strong data-driven character of such methods that may eventually deteriorate their effectiveness and therefore, their application for direct ship stability assessment remains an open question. Aiming at highlighting the causes of problematic behaviour in this context, recently, Pipiras [17] demonstrated that the efficacy of standard EVT tools cannot be asserted unless key physical aspects of the examined dynamical system are considered.

As is well known, the main issue, arising rather naturally in practical implementations of the theorem, is the selection of an appropriate threshold for fitting the GPD. Despite the model being mathematically exact at infinitely high levels, it is believed that it could still be reliable if determined with respect to a sufficiently high threshold. This runs the danger, on the one hand, of idly expending computational resources if an exceptionally high threshold is set, resulting in datasets with only few (if not any at all) extremes. On the other hand, a lower threshold may not be able to produce reliably the tail. In practical ship stability, normally we do not need very large roll angles for judging safety since, beyond some moderate to high angle, the flooding of closed spaces is inevitable. Hence, another question is raised on whether the GPD could be meaningfully applied towards developing a stability criterion. In view of these concerns, much of effort has been put over the last years in efficiently fitting the GPD using reasonably-sized datasets generated by fast, yet qualitatively realistic, hydrodynamic codes (e.g. [23]).

As a next step, in the current work, the possibility of parametrizing the response distribution through successive GPD fits is discussed for the problem of ship rolling in beam seas. Based on this strategy, an attempt is made to associate threshold selection with the underlying physics, and particularly with the shape of the GZ curve of a vessel. The idea is to first identify regimes where, due to the changes in the restoring, the response is expected to exhibit different probabilistic qualities and then, utilize the limits of these regimes for thresholding. Moreover, a novel setup is described for

applying the GPD to the problem of capsizing, which hitherto has not been addressed by the literature, and its performance is tested in severe sea conditions against the rough Monte Carlo estimates, obtained by direct counting. Finally, to evaluate the reliability of the GPD for “statistical extrapolation” (i.e. for predicting events beyond the largest observation used in the fitting procedure), a comparison with the results of the “critical wave groups” method [1] is presented for a sea state characterized by very rare extremes.

## 2 Mathematical Background

In this section, the second extreme value theorem is formulated and the basic properties of the GPD are outlined. The potential of the model for treating the problem of rarity, described in the above, is discussed in the context of a more general framework commonly known as the “principle of separation” (e.g. [4, 15]).

### 2.1 The Principle of Separation

The term is often utilized to express the idea of decomposing the ship response problem into sub-problems with the aim of analysing the rare extremes separately from a background state, mostly associated with the conventional (non-rare) outcomes. Thence, the “non-rare” part deals with the distribution of the conditions that can lead to the occurrence of extreme events, while the “rare” one targets the conditional probability of extremes given that specific conditions are met:

$$\Pr[X > x] = \underbrace{\Pr[X > x | X > u^*]}_{\text{rare}} \times \underbrace{\Pr[X > u^*]}_{\text{non-rare}} \quad (1)$$

where  $X$  is the response process,  $x$  is the associated state variable and  $u^*$  is a threshold introduced for distinguishing rare/extreme from non-rare/non-extreme regimes.

As realized, ship motions have, thus far, been classified with respect to their relative frequency of occurrence (rare/non-rare) rather than according to the corresponding level of nonlinearity which is more informative about the dynamics governing each sub-problem. In the “rare” part, however, one is confronted with phenomena that are not only very unlikely, but also strongly nonlinear. On the contrary, non-rare ship responses are not necessarily linear, particularly in heavier seas where extremes are experienced more often. To explicitly account for the effect of nonlinearity also on the solution of the “non-rare” part, the last term in Eq. (1) is further decomposed as:

$$\Pr[X > u^*] = \underbrace{\Pr[X > u^* | X > u_L]}_{\text{nonlinear}} \times \underbrace{\Pr[X > u_L]}_{\text{linear}} \tag{2}$$

where  $u_L$  is an intermediate threshold indicating the limit between linear and nonlinear ship responses within the “non-rare” sub-region. Definitely, through this concept, one could go even deeper by disassembling both the “rare” and “non-rare” sub-problems of Eq. (1) in more parts; yet this would require a rational procedure for selecting those additional intermediate thresholds  $u_i, i = 1, \dots, n$  which would separate regimes with different levels of nonlinearity.

In this setting, mathematical justification for the solution of the “rare” sub-problem in Eq. (1) will be provided by the second extreme value theorem, presented in the following section. Moreover, the “linear” term in Eq. (2) can naturally be determined by fitting a Gaussian distribution to the available ship response data.<sup>1</sup> As for the probability of “nonlinear” events in Eq. (2), this also can be approximated using a fitting method. In this case, however, one has to decide which statistical model should be selected for the fitting since this cannot be inferred from neither the dynamics, as done for the linear sub-problem in Eq. (2), nor the EVT, which is designed for the rare extremes in Eq. (1). Although there are numerous models to try, in this study, the GPD is employed once again knowing that it embodies a large class of distribution functions covering a continuous range of possible shapes. This allows for the data to decide the most suitable amongst the various models integrated into the GPD.

It is worth emphasizing here that the standard approach in the implementation of EVT-based techniques in conjunction with the concept of separation is to rely solely on Eq. (1), without proceeding to further decomposition via Eq. (2). In that case, the “rare” probability can still be described by the GPD, but the “non-rare” term is usually estimated by direct counting (e.g. [17]). From this perspective, introducing Eq. (2) may seem unnecessary considering that it is not expected to deliver substantially different predictions from those produced by the direct counting method. However, the true benefit from the coupling of Eqs. (1) and (2) is that one can associate ship dynamics with well-known statistical models throughout the stability range rather than only in the tail. This, apart from contributing towards understanding the probabilistic qualities of ship motion in general, opens the way for formulating stability criteria since the entire response distribution is expressed in a fully parametric form.

## 2.2 The Generalized Pareto Distribution (GPD)

In the literature, the GPD is specified by three parameters  $(u, \sigma, \xi)$  and below it is defined through its complementary distribution function  $F_X(x) = 1 - F_X(x)$ :

---

<sup>1</sup> Provided that, in sufficiently deep waters, waves are adequately described by Gaussian statistics (e.g. [16]).



$$\bar{F}_X(x) = \begin{cases} \left(1 + \frac{\xi(x-u)}{\sigma}\right)^{-1/\xi}, & \text{if } \xi \neq 0 \\ \exp\left(-\frac{x-u}{\sigma}\right), & \text{if } \xi = 0 \end{cases} \quad (3)$$

where  $x \geq u$ , if  $\xi \geq 0$  and  $u \leq x \leq u - \sigma/\xi$ , if  $\xi < 0$ . In Eq. (3),  $u$  is the location parameter representing the minimum value that the associated random variable  $X$  can attain (thus,  $u$  plays the role of the reference threshold). In this sense, whenever the GPD is employed for modelling the tail of another distribution,  $u$  determines the point where the two distributions merge. Regarding the scale parameter  $\sigma$ , it is a “spread” factor controlling the dispersion of  $X$  above  $u$ . Finally,  $\xi$  affects the shape of the GPD in a more qualitative way. For distributions with exponentially decreasing tails, such as the Normal, the GPD leads to  $\xi = 0$ . For heavy-tailed distributions, often encountered in the case of unbounded systems,  $\xi > 0$ . The opposite ( $\xi < 0$ ) implies a light-tailed distribution and consequently, the existence of an upper bound at  $x = u - \sigma/\xi$ .

The theoretical importance of Eq. (3) was proved by Balkema and de Haan [2] and Pickands [18] who showed that the distribution of independent and identically-distributed (i.i.d.) excesses over  $u$  asymptotically tends towards the GPD, as  $u \rightarrow \infty$ . The statement holds if and only if the parent distribution belongs to the so called “domain of attraction” of one of the extreme value distributions (i.e. Gumbel, Fréchet and reverse Weibull), all incorporated into a single model known as the generalized extreme value distribution (GEVD). Moreover, it can be verified that if times until exceedance constitute a Poisson random process with GPD excesses, then the GEVD is obtained as the distribution of the corresponding extremes. Another interesting property of the GPD is its “threshold stability”, meaning that if  $X$  is a GP-distributed random variable for some  $u^* > 0$ , then it is also generalized Pareto for any  $u > u^*$  retaining the same shape parameter. It is worth noting that the GPD is uniquely characterized through the last two properties since no other family of distributions exhibits such qualities [10]. For additional background on the GPD, the reader may refer to Coles [9].

### 2.3 Threshold Selection

On these terms, it is rather natural to assume that local stabilization of the shape parameter could be the key for detecting the minimum threshold value above which the distribution of excesses has practically converged to the GPD. The idea has been discussed in several studies (e.g. [24]), often in comparison with alternative identification procedures, such as those described in e.g. [19, 14]. From a different perspective, though, the threshold stability property itself could be the source of inherent limitations in pinning down the threshold. Specifically, if a dataset obeys the GPD at one threshold, then, the model, in order to preserve its validity at all higher thresholds, should be free to adapt through its only left unconstrained parameter, i.e.

the scale parameter  $\sigma$ . Equally, restricting the threshold to a fixed value in an attempt to extrapolate a trend into the tail region could entail the possibility of overfitting.

Knowing that there are various ways for setting the threshold, we cannot be certain about whether the chosen one is also the optimal, meaning that it exploits the maximum amount of the available data without sacrificing from the mathematical consistency of the resulting GPD. As such, there may be a multitude of other GPDs, determined with respect to lower thresholds than ours, which could be useful in making predictions even below  $u^*$ . This was an additional motivation for approximating the ship response distribution in the nonlinear regime by employing successive GPDs in Eqs. (1) and (2). Although  $u_L$  may not be sufficiently high for satisfying the second extreme value theorem, the GPD, due to its very flexibility as a statistical model, will probably succeed in providing reliable estimates locally, i.e. within the intermediate range  $[u_L, u^*]$ . The crucial step, however, remains the selection of  $u^*$ . To avoid the issues arising from the use of “data-driven thresholds”, discussed in the foregoing, in the current study the fitting of the GPD in the tail region will be based on the notion of “physical thresholds” (i.e. thresholds having close connection with the physics of the system under examination). Within this context, the angle  $\varphi_{\max}$  corresponding to the maximum of the GZ curve could be tried since rolling beyond this limit is quite likely to result in capsizing or, at least, in an extreme (and most presumably rare) dynamic event. More so, the fact that  $u_L$  is by definition a physical threshold supplies the whole decomposition, i.e. Equations (1) and (2), with a meaningful interpretation stemming directly from the dynamics of ship rolling.

### 3 Results and Discussion

Massive Monte Carlo simulations were performed for an ocean surveillance ship, with main parameters listed in Table 1, to evaluate the accuracy of the GPD-based approach presented in the above. The concept of separation, as expressed through Eqs. (1) and (2), is illustrated in Fig. 1 where the GZ curve of the vessel is divided into three sub-regions with limits indicated by vertical lines: (I)  $\varphi \in [0, u_L]$ , with  $u_L = 20^\circ$ , (II)  $\varphi \in [u_L, u^*]$ , with  $u^* = \varphi_{\max} = 37^\circ$  and (III)  $\varphi > u^*$ .

**Table 1** Main parameters of the vessel

Parameter	Dimensional value	Dimensions
$I + A_{44}$	$5.540 \times 10^7$	$\text{kg} \cdot \text{m}^2$
$\Delta$	$2.056 \times 10^6$	kg
$B_1$	$5.263 \times 10^6$	$\text{kg} \cdot \text{m}^2/\text{s}$
$B_2$	$2.875 \times 10^6$	$\text{kg} \cdot \text{m}^2$
$C_1$	3.167	m
$C_3$	-2.513	m

**Fig. 1** The restoring arm of the vessel divided into sub-regions: (I) non-rare/linear, (II) mildly rare/nonlinear and (III) rare/nonlinear

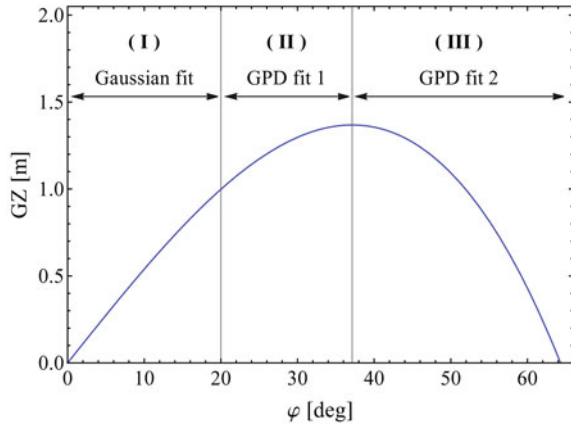


**Table 2** Sea state characteristics

	$H_s$ (m)	$T_p$ (s)
Sea state A	4	11
Sea state B	3	11

The ship is assumed to operate in sea conditions described by the Bretschneider spectrum (e.g. [16]):

$$S_{\eta\eta}(\omega) = \frac{1.25}{4} \frac{\omega_p^4}{\omega^5} H_s^2 \exp\left[-\frac{5}{4} \cdot \left(\frac{\omega_p}{\omega}\right)^4\right] \quad (4)$$

where  $H_s$  is the significant wave height and  $\omega_p = 2\pi/T_p$  is the modal frequency of the spectrum. Two sea states of slightly different severity were duly selected for demonstrating certain capabilities and limitations of the proposed method. Their characteristics are given in Table 2.

Time histories of roll motion  $\varphi(t)$  were generated using a simple 1DOF roll equation:

$$(I + A_{44})\ddot{\varphi} + B_1\dot{\varphi} + B_2\dot{\varphi}|\dot{\varphi}| + g\Delta(C_1\varphi + C_3\varphi^3) = M(t) \quad (5)$$

with  $I + A_{44}$  being the total roll moment of inertia (including the added mass effect),  $g$  is the gravitational acceleration,  $\Delta$  is the ship displacement and  $B_1$ ,  $B_2$  and  $C_1$ ,  $C_3$  are the damping and restoring coefficients, respectively. The wave-induced moment was modelled using the standard spectral representation method [20]:

$$M(t) = \sum_n \sqrt{2S_{\eta\eta}(\omega_n)F_{roll}(\omega_n)\delta\omega_n} \cos(\omega_n t + \varepsilon_n) \quad (6)$$

In Eq. (6),  $\varepsilon_n$  are random variables uniformly distributed over  $[0, 2\pi)$ ,  $\delta\omega_n$  is the frequency resolution and  $\omega_n$  are the frequencies of the elementary wave components. Details for the roll moment amplitude operator  $F_{roll}$  of the vessel can be found in Su [21].

Regarding the calculation of exceedance probabilities by direct counting, it was based on the notion of “ensemble statistics”, i.e. statistics derived by repeating the same random experiment a large number of times. Specifically, 6,000,000 short-duration response time histories were produced using Eqs. (5) and (6) and the roll angle value observed at  $t_s = 150$  s was kept from each realization for statistical analysis (guidelines for selecting a suitable  $t_s$  have been formulated in Anastopoulos and Spyrou [1]). The great benefit from this setup is that collected roll data are statistically independent, as required by the second extreme value theorem. At the same time, and in contrast to the case when time averages are employed, no assumptions on the ergodicity of ship response need to be made (for an extensive discussion on the problem of “practical non-ergodicity” of ship rolling the reader may refer to Belenky et al. [3]).

Knowing that simulating massively ship responses via Eq. (5) is computationally tractable due to the very simplicity of this roll model, it may be unrealistic to apply the described GPD-based methodology using the entire sample (6,000,000 observations). Instead, it would be more relevant to evaluate the performance of the approach as if smaller datasets were available (which is typically the case when high fidelity hydrodynamic codes are used for simulation). On this basis, the total sample was partitioned in 15 datasets, each containing 400,000 roll angle records. Then, for each dataset, three fittings were implemented using the maximum likelihood estimation (MLE) method: one using a Gaussian distribution (for all 400,000 data) and two using the GPD (one for excesses over  $u_L = 20^\circ$  and one for excesses over  $u^* = 37^\circ$ ). Through this procedure, 15 pairs of parameters were obtained for each of the aforementioned fitting models. To be able to conclude on the overall behaviour of these models (i.e. with respect to all 15 datasets), the mean value of each parameter was selected as the most representative. Eventually, the mean values of all six parameters (two per fitting model) were inserted into Eqs. (1) and (2) for synthesising the roll angle distribution.

To quantify the uncertainty in the fitting results, a similar procedure was followed. In detail, 15 pairs of confidence intervals were constructed for the (two) parameters of each statistical model using a bivariate Normal distribution expressed in terms of the observed information matrix of the corresponding dataset (e.g. [9]). Subsequently, confidence intervals for the associated “mean” distribution parameters were formulated by averaging respectively the upper and lower limits of the intervals derived from all 15 datasets. Finally, the averaged limits were employed for inferring the uncertainty in the exceedance probabilities predicted by Eqs. (1) and (2) through the “boundary method” [12]. Thus, in the following, a “95% confidence interval” of a GPD-related quantity (being either a parameter or a probability) will actually denote the average of the individual 95% confidence intervals computed for this particular quantity. In this way, one is provided with the best estimate about the precision of the

current method in view of the findings of the 15 smaller-scale numerical experiments assumed to have been carried out independently.

### 3.1 Sea State Scenario A

In this case study, the objective is to evaluate the reliability of the GPD for calculating the probability of capsize when data are available in the entire range of stability  $[0, \varphi_v]$ , where  $\varphi_v = 64^\circ$  is the angle of vanishing stability of the vessel in question. The selection of the capsize limit was based on the well-known feature of Eq. (5) concerning the time-depending shifting of the unstable equilibrium in the presence of wave excitation (e.g. [11]). In this regard, response trajectories that exceeded (in absolute sense) the limiting value  $1.2\varphi_v$  before reaching  $t_s = 150$  s were marked as corresponding to capsize, resulting in a total number of 393 capsizes for the specific sea state. No doubt, considering stability failure at an exceptionally high roll angle is unreasonable since flooding is very likely to occur at lower angles. As a matter of fact, it is sufficient to confirm accuracy in GPD predictions only up to intermediate roll angles representing practical capsize limits (e.g.  $40^\circ$ – $50^\circ$ ). For scientific curiosity reasons however, and since a similar model could be the subject of investigation in a different (non-marine) context, the tail region  $[\varphi_{\max}, \varphi_v]$  is examined in its entirety just for highlighting particular features of the ship rolling process that may not be so evident at lower levels.

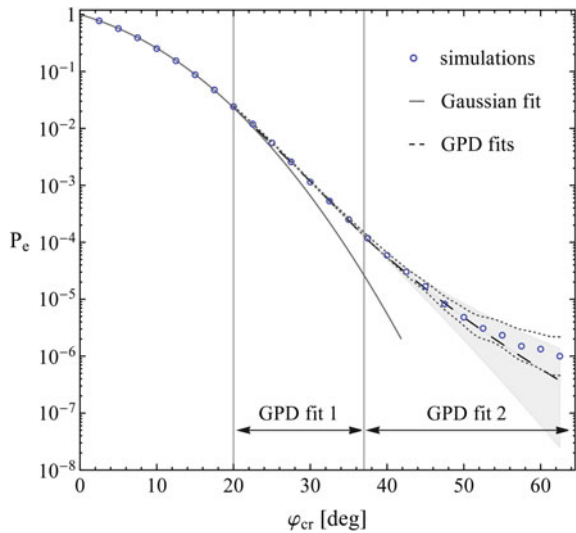
Next, results are first presented for the case of “bounded” ship motions, meaning that desired statistics were computed after filtering out the 393 capsize cases. As realized, eliminating the possibility of capsize may conceal valuable information for our analysis. It is, nevertheless, interesting to investigate the effectiveness of traditional techniques of EVT, such as the POT/EPOT (peaks or envelope peaks over threshold) methods, which rely solely on the peak excesses of a random process for fitting the GPD. Since a “peak” by definition implies the return of a response trajectory towards the upright state, it is clear that these methods deal with a qualitatively different problem in which the underlying system remains always bounded. On the contrary, in our approach the GPD is fitted to all the exceedances recorded at the selected sampling instant  $t_s$ , regardless of being peaks.

Figure 2 shows the probability of exceedance  $P_e = \Pr[\varphi > \varphi_{cr}]$  of various roll angle thresholds  $\varphi_{cr} \in [0, \varphi_v]$  derived from the Monte Carlo (MC) simulations through direct counting (circles) for the bounded system (i.e. without capsizes). For constructing the associated 95% confidence bands (dotted lines), the “Wilson score” interval was utilized since it was found to be the most consistent, in terms of coverage probability, among a number of binomial-type arguments discussed in the literature [7]. The solution of the linear “non-rare” sub-problem, being the “Gaussian fit” curve (solid line), is extended up to region (III) for comparison purposes. Dashed lines indicate the solution of the combined nonlinear sub-problem (“non-rare” + “rare”), obtained by two individual GPD fits; namely, the “GPD fit 1” using data above  $u_L = 20^\circ$  and the “GPD fit 2” using data above  $u^* = 37^\circ$ . Although formally the domain

of the “GPD fit 1” includes also region (III), in Fig. 2, only the part of the curve lying within region (II) is presented. Instead, the “GPD fit 2” is used for extending the solution of the nonlinear sub-problem in region (III). The merging of the two GPDs was based on Eq. (1) in which the “rare” probability term was multiplied by the “GPD fit 1” value at  $u^* = 37^\circ$ , while Eq. (2) was applied for attaching the “GPD fit 1” to the “Gaussian fit” at  $u_L = 20^\circ$ . The same operations were performed for connecting the upper and lower bounds (respectively) of the confidence bands constructed for each fitting model according to the averaging procedure described in the foregoing. In Fig. 2, the synthesised 95% confidence intervals (CI) are illustrated by the shaded area. In analogy to Fig. 1, vertical lines denoting the limits of regions (I–III) are drawn to facilitate the interpretation of the results. Details for the estimated GPD parameters are provided in Table 3.

As observed, there is good coincidence between the proposed calculation scheme and the MC results in the entire range of stability of the vessel. The largest deviation

**Fig. 2** GPD fits (dashed lines) versus rough Monte Carlo estimates (circles) for the bounded system



**Table 3** GPD fitting results (bounded system)

GPD fit 1—region II: $[20^\circ, \varphi_{\max}]$			
Scale parameter		Shape parameter	
Mean value	95% CI	Mean value	95% CI
3.471	[3.443, 3.499]	-0.024	[-0.029, -0.018]
GPD fit 2—region III: $[\varphi_{\max}, 64^\circ]$			
Scale parameter		Shape parameter	
Mean value	95% CI	Mean value	95% CI
3.550	[3.240, 3.860]	0.071	[-0.019, 0.161]

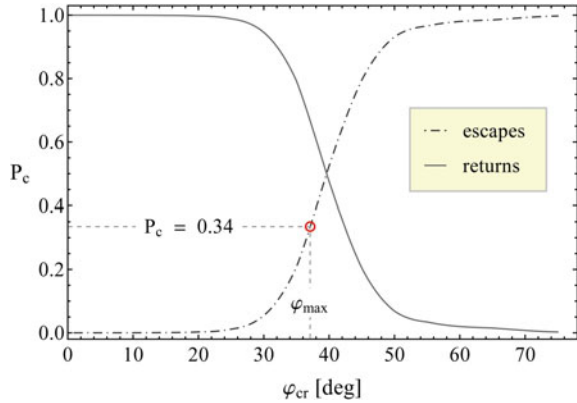
is noticed very close to the angle of vanishing stability  $\varphi_v = 64^\circ$  where the probability of exceedance is slightly underestimated, yet it is still within an acceptable confidence band. Moreover, the negative shape parameter in region (II) manifests the existence of a right boundary, as possibly anticipated in this investigation because of the constraints imposed on the magnitude of ship responses. By contrast, a positive shape parameter was recorded in region (III) implying that the “GPD fit 2” turns into a heavy tail; although it is remarkable that the associated confidence interval includes also negative values. Finally, there is less discrepancy in the computation of the scale parameter, given that its value is practically the same in both regimes.

Considering that we have restricted the analysis to ship responses below  $1.2\varphi_v$ , one may superficially expect that the “GPD fit 2” should maintain the light tail trend in region (III). Yet, it seems that deducing the existence of a physical boundary is more difficult when being at higher levels since, due to the thresholding, the softening effect of the restoring in Eq. (5) becomes more pronounced. If this effect could somehow be mitigated, a statistically significant proportion of roll data would be in the vicinity of the boundary  $1.2\varphi_v$  and the fitting would have been influenced towards predicting a light-tailed GPD [6]. In reality, however, this is hardly feasible given that when rolling close to  $1.2\varphi_v$  it is more likely to capsize rather than to return to the upright state. Since capsizes have been excluded, most of the rest of the extremes are far from the boundary and thus, they cannot feel its presence. Meanwhile, the softening part of the GZ curve is still governing the dynamics above  $u^* = 37^\circ$ , inducing the heavy tail shown in Fig. 2. On the other hand, the “GPD fit 1” does not appear to suffer from this issue because the main volume of the corresponding excesses is concentrated in region (II) where, albeit the GZ is nonlinear, the impact of the softening part is weaker. So, eventually, neither an exponential tail ( $\xi = 0$ ) nor a heavy tail ( $\xi > 0$ ) is realized.

Below, the assumption of bounded motions is removed to assess the validity of the treatment presented so far. To this end, direct counting statistics were derived separately for threshold exceedances that led to capsize (“escapes”) and for short-time exceedances that remained bounded in the long run (“returns”). In Fig. 3,  $P_c$  is the conditional probability of a return/escape, given that a roll angle threshold  $\varphi_{cr}$ , displayed on the horizontal axis, has already been exceeded. Since  $P_c$  is, in fact, the ratio of the observed escapes/returns to the total number of exceedances over a threshold  $\varphi_{cr} \in [0, \varphi_v]$ , this plot essentially reflects the contribution of each outcome to the overall probability of exceedance  $P_e$ . A circle has been placed on the curve of the escapes at  $u^* = \varphi_{\max}$  to highlight that in region (III) extremes are, at least, 34% underpredicted with respect to their “true” values which would be obtained if capsizes had been included in the calculations. This demonstrates the necessity of developing methods free of POT/EPOT-like assumptions, often introduced in the light of “wide-sense stationarity” of ship response [13].

At the same time, Fig. 3 reveals new locations for potential thresholding, other than those used in this study. Even more, one may be tempted to analyse individual sub-problems into more parts than those proposed here. For instance, one could perform the decomposition over both/either the point where the two curves intersect (e.g. at  $40^\circ$ ) and/or the angle where the maximum curvature on the escapes curve is observed

**Fig. 3** Contribution of escapes and returns to the total probability of a threshold exceedance



(e.g. at 50°). However, proceeding to exhaustive decompositions is not recommended because information could be lost due to the separation principle itself. The concept assumes that the excesses have negligible influence on the statistical characteristics of the response process below the threshold. In this sense, it may be more difficult to capture the whole picture when approximating the solution through a large number of conditionals, considering that extremes may eventually be inconsistent with the mechanism that generates the main body of the data.

In Fig. 4, the probability of exceedance  $P_e$  was derived by analysing the entire sample, including the 393 capsizes cases. The notation is the same as in Fig. 2. The results of the corresponding GPD fitting procedure are summarized in Table 4. As noticed, the MC trend (circles) implies a heavy tail which, in region (III), becomes almost parallel to the  $\varphi_{cr}$ -axis. However, this cannot be inferred from the synthesised GPDs of the current method (dashed lines). Evidence for the tail structure has already been given in Fig. 3 where it was shown that above 40° exceedance probabilities are mostly determined by the escaping trajectories. With returns gradually vanishing in the very extreme region (above 50°), the probability of exceedance  $P_e$  naturally tends to the probability of capsizes (393 capsizes/6,000,000 samples). In Fig. 4, this resulted in almost two orders of magnitude greater probabilities than those presented in Fig. 2 for the bounded system.

Although having a “rich”, in terms of capsizes occurrences, sample enhances the reliability of the MC predictions in the tail region (III), the coexistence of escapes and returns within a dataset entails technical difficulties in their joint statistical description in the form of exceedance probabilities. These difficulties emerge from the fact that capsizing refers more to a phenomenon rather than to a physically realizable position of a vessel. Specifically for Eq. (5), capsizing equals to a response trajectory diverging constantly towards infinity and thus, special treatment is required for integrating the contribution of this type of exceedances into the direct counting (MC) estimates. The same numerical concerns limit the applicability of the current method since neither the Gaussian distribution nor the GPDs in Eqs. (1) and (2) can be fitted to datasets containing ill-defined values. To overcome these issues, clearly one has to assume



**Fig. 4** GPD fits (dashed lines) versus rough Monte Carlo estimates (circles) for the unbounded system

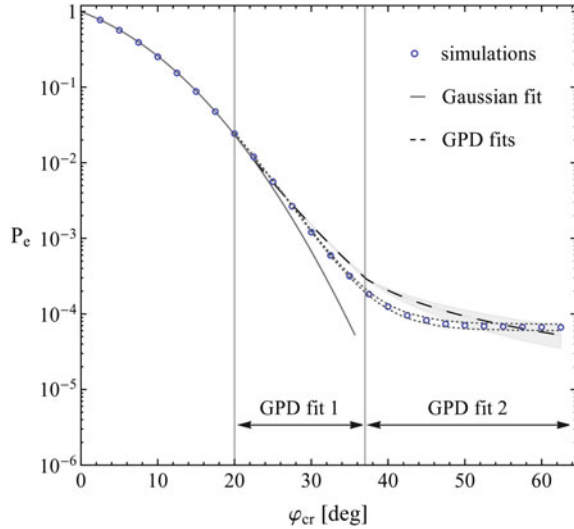


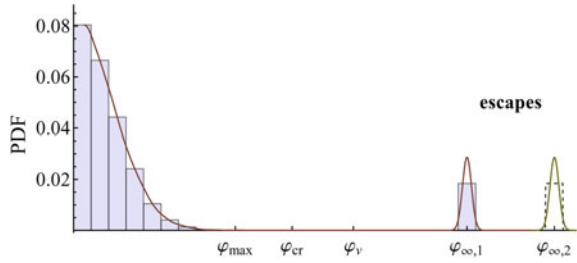
**Table 4** GPD fitting results (unbounded system)

GPD fit 1—region II: [20°, φ <sub>max</sub> ]			
Scale parameter		Shape parameter	
Mean value	95% CI	Mean value	95% CI
3.221	[3.200, 3.243]	0.085	[0.080, 0.090]
GPD fit 2—region III: [φ <sub>max</sub> , 64°]			
Scale parameter		Shape parameter	
Mean value	95% CI	Mean value	95% CI
7.038	[5.526, 8.551]	0.781	[0.657, 0.904]

a finite analogue for the “capsize state” (noted here as  $\varphi_\infty$ ). In our MC setup, if a response trajectory exceeded the capsizes limit  $1.2\varphi_v$  at some time instant  $t < t_s$ , the integration of Eq. (5) was terminated and a fixed value  $\varphi_\infty = 1.2\varphi_v$  was kept for further analysis.

In this setting, Fig. 4 demonstrates that our GPD can provide estimates for the probability of capsizes with fair accuracy. Nevertheless, its suitability for approximating the roll angle tail remains questionable provided that the model exhibits a quite different shape from that indicated by the direct counting probabilities in region (III). Again, the uncertainty in the calculation of the associated parameters is not negligible despite that proportionally more extremes were analysed than in the case of bounded motions. It is encouraging, though, that the “GPD fit 2” is now characterized by a large positive shape parameter  $\xi$  (cf. Table 4) implying that by introducing  $\varphi_\infty$ , one succeeds in inducing the desirable qualitative changes in the statistics of the extremes. Interestingly,  $\xi$  was found greater than 0.5, being the critical value above which the GPD has infinite variance. Judging from the almost horizontal

**Fig. 5** Sensitivity of GPD estimates to the statistical description of escapes (schematically)



tail in Fig. 4, manifesting the softening effect of the restoring in Eq. (5), one could argue that the “true” roll angle distribution possesses the same property; yet formally this is only a conjecture based on intuition.

Albeit very practical, the idea of treating the escapes as finite-value extremes does not resolve the mathematical intricacies in the application of the GPD to the problem of capsizes. The reason is that by assigning the exact same value  $\varphi_\infty = 1.2\varphi_v$  to all capsized cases (i.e. escapes), an artificial “mass” concentration will inevitably appear in the corresponding probability density function (PDF), as qualitatively illustrated in Fig. 5. In fact, depending on the number of the observed escapes, this mass may grow excessively resulting in a distribution with very special shape. Since it is not clear if this type of distribution belongs to the domain of attraction of the GEVD, the validity of the GPD may not be asserted by the second extreme value theorem. Yet even if this could be overcome, due to the nature of the fitting procedures, the computation of the GPD parameters would still be affected by the assumed  $\varphi_\infty$  value. As an example, in Fig. 5,  $\varphi_{\infty,1}$  and  $\varphi_{\infty,2}$  denote two (out of the infinitely many) alternatives from which one has to select before fitting the GPD.

The sensitivity of the approach to the selection of  $\varphi_\infty$  was investigated by calculating the probability of exceeding  $50^\circ$  for four  $\varphi_\infty$  scenarios ( $1.2\varphi_v$ ,  $80^\circ$ ,  $90^\circ$  and  $180^\circ$ ). The results revealed that by increasing the relative distance between  $\varphi_\infty$  and the main probability mass, the “GPD fit 2” monotonically overestimates (from 1.2 up to 2.4 times) the corresponding probabilities derived by direct counting. Hence, in Fig. 4, the current method was shown in its utmost performance since setting  $\varphi_\infty > 1.2\varphi_v$  would certainly deteriorate its accuracy. This is because the sample variance in region (III) varies through  $\varphi_\infty$  and thus, the GPD adapts, although not very successfully, to the data. This sensitivity justifies why the scale parameter is larger in Table 4 than in Table 3, where the  $\varphi_\infty$  parameter is not involved.

### 3.2 Sea State Scenario B

Lowering  $H_s$  by only 1 m leads to substantial changes in ship behaviour, given that for the specific sea conditions all roll angle records were below  $\varphi_{\max} = 37^\circ$  (no capsizes observed). Therefore, the interest here lies in utilizing the GPD for

predicting events that are considerably more extreme than those found in the generated datasets. However, evaluating the “extrapolation” quality of the model having only few extremes is a non-trivial task since the uncertainty in the produced estimates becomes too large for the confidence intervals to maintain meaningful sizes [17, 23]. To avoid this problem in the current study, the GPD trends are compared with the predictions of the “critical wave groups” method [22]. Unlike the method presented here, the “critical wave groups” scheme does not make any assumptions regarding the shape of the distribution of extreme responses. Instead, it quantifies instability tendency implicitly, through the probability of encountering any wave group that could provoke the instability using distributions describing statistical properties of the wave field. Recently, the potential of the method in handling the rarity of extreme ship rolling events was demonstrated by Anastopoulos and Spyrou [1].

Regarding the implementation of the proposed GPD-based methodology, the only change with respect to the previous sea state scenario is that Eq. (1) could not be employed due to absence of data above  $u^* = \varphi_{\max}$ . Consequently, the separation was applied with respect to  $u_L = 20^\circ$ , as prescribed by Eq. (2), but this time the “GPD fit 1” was exploited for extrapolating in region (III). In Fig. 6, the results (dashed line) are tested against the MC direct counting probabilities (circles), while details for the associated GPD parameters are given in Table 5. As before, the corresponding 95% confidence intervals (CI) are represented by the shaded area and the dotted lines, respectively. Information about the “critical wave groups” (CWG) probabilities is directly available from the work of [1] who applied the method to the vessel examined here and for the same sea conditions. Although their results cover the entire nonlinear part  $[u_L, \varphi_v]$ , in this investigation, staying below  $40^\circ$  seems to be sufficient for reaching conclusions since from very early ( $25^\circ$ – $30^\circ$ ) the “GPD fit 1” and the “critical wave groups” curves exhibit different trends. Besides, it was found that, due to sparsity of data above  $40^\circ$ , the GPD confidence band becomes excessively large. Finally, in this plot, the “Gaussian fit” (solid line) is not extended beyond region (I) because it was noticed that it would practically coincide with the “GPD fit 1” curve. This is explained by the large confidence interval of the shape parameter in Table 5, indicating that nonlinear data are very few (specifically, only 0.2% of the 6,000,000 roll angle records exceeded  $u_L$  at  $t_s = 150$  s). The GPD captures this feature but without further guidance it cannot do more than to extrapolate Gaussianity also in region (II). A similar behaviour has been reported in Pipiras [17], yet in the context of the POT method.

Despite the unambiguous linear character of the GPD in Fig. 6, the negative shape parameter in Table 5 suggests that the model eventually turns into a light tail. Since the probability of capsizing is, in general, non-zero (even for this seemingly innocuous sea state), a heavy tail should be expected. Here, though, it is masked by the problem of rarity, leading the GPD to assume the existence of a physical boundary. This is the reason for the deviation between the GPD and the “critical wave groups” curves. The latter succeeds in tracing the unobserved heavy tail and because of its consistency with the MC values from lower levels ( $20^\circ$ – $25^\circ$ ) one could argue that it is more appropriate for extrapolation in the specific sea conditions. However, in view of the inherent uncertainties in the interpretation of direct counting estimates when data

**Fig. 6** GPD fit (dashed line) versus rough Monte Carlo estimates (circles) and comparison with the “critical wave groups” (CWG) predictions (dot-dashed line)

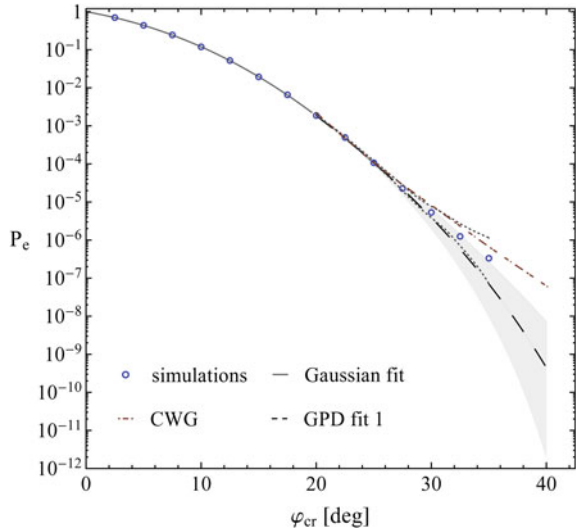


**Table 5** GPD fitting results (no escapes observed)

GPD fit 1—region II: [20°, φ <sub>max</sub> ]			
Scale parameter		Shape parameter	
Mean value	95% CI	Mean value	95% CI
1.893	[1.836, 1.951]	-0.051	[-0.071, -0.032]

in the range of interest are very few, comparing results obtained from techniques originating from different principles would, at least, contribute towards their mutual development, if not achieving the ultimate validation goal.

## 4 Summary and Conclusions

A method based on extreme value theory (EVT) was proposed for calculating the probability of exceeding exceptionally high roll angles in beam seas. The method analyses the ship response problem into three parts (sub-problems), each associated with a different level of rarity and/or nonlinearity. For the first part, targeting statistical description of small-amplitude (linear) motions, a Gaussian distribution was utilized. In the nonlinear part, the solution was composed by fitting the generalized Pareto distribution (GPD) to roll exceedances over two levels: (a) a “non-rare” intermediate threshold and (b) a “rare” extreme threshold. The selection of these thresholds was based on the shape of the GZ curve which provides indications for the limits of regimes where the response process exhibits distinct characteristics.

The performance of the approach was tested against the rough estimates of Monte Carlo simulations, obtained by direct counting. Several aspects regarding the implementation of the approach were discussed and particular attention was given to the problem of capsizing. The results reveal that, given “sufficient” data, the method can accurately determine the probability of extreme dynamic events, yet if the possibility of system escape is practically zero. However, information is essentially lost due to this assumption since escaping induces qualitative changes in the shape of the response distribution. In the case of unbounded motions, though, the GPD-tail produced by our method could not fit the data very successfully. In our opinion, this is not just a consequence of the well-known limitations of the EVT, but an indication of a broader problem relating to the fitting techniques themselves. The reason is that the latter can handle only finite-type exceedances which ensure that the necessary, for the fitting, regularity conditions are satisfied. On the contrary, capsizing is not a regular exceedance in the sense that there is no obvious value to which it can be directly assigned. Hence, incorporating a number of such “disturbances” into a sample of well-defined records (i.e. with bounded extremes only) imposes to assume some value for representing the capsizing state. Although practical, such an ad-hoc solution may not be very physically relevant and this could be the source of the deficiencies discussed in this paper.

Finally, regarding the “statistical extrapolation” character of the GPD, this was evaluated through a comparison with the predictions of the “critical wave groups” method. In this context, evidence was provided that, for the examined sea conditions, the latter may be more suitable for making inferences beyond the largest observation. However, further investigation is definitely needed for reaching more general conclusions. In this direction, assessing methods with different backgrounds against each other seems the only option for their mutual validation in regimes where extremes cannot be directly “seen” through straightforward Monte Carlo procedures. It should be noted, though, that the desire of controlling the probability of stability failures directly through the ship design parameters requires, in fact, knowledge of the GPD form at the time when data are not available. Therefore, even if the effectiveness of the GPD idea is eventually proven, this very desire will presumably remain unsatisfied due to the data-driven nature of the concept itself.

**Acknowledgements** The work of Mr. Anastopoulos was partly supported by NTUA’s Special Account for Research Grants (ELKE). The idea of performing multiple GPD fits came up during a discussion with Dr. Vadim Belenky. Both Dr. Vadim Belenky and Mr. Kenneth Weems (David Taylor Model Basin, NSWCCD) are thanked for providing valuable feedback during this study.

## References

1. Anastopoulos PA, Spyrou KJ (2019) Evaluation of the critical wave groups method in calculating the probability of ship capsizing in beam seas. *Ocean Eng* 187:106213
2. Balkema A, de Haan L (1974) Residual life time at great age. *Ann Probab* 2:792–804
3. Belenky VL, Degtyarev AB, Boukhanovsky AV (1998) Probabilistic qualities of nonlinear stochastic rolling. *Ocean Eng* 25(1):1–25
4. Belenky V, Weems KM, Bassler CC, Dipper MJ, Campbell BL, Spyrou KJ (2012) Approaches to rare events in stochastic dynamics of ships. *Probab Eng Mech* 28:30–38
5. Belenky VL, Weems K, Pipiras V, Glotzer D, Sapsis TP (2018) Tail structure of roll and metric of capsizing in irregular waves. In: *Proceedings of the 32nd symposium on naval hydrodynamics, Hamburg, Germany*
6. Belenky V, Glotzer D, Pipiras V, Sapsis TP (2019) Distribution tail structure and extreme value analysis of constrained piecewise linear oscillators. *Probab Eng Mech* 57:1–13
7. Brown LD, Cai TT, DasGupta A (2001) Interval estimation for a binomial proportion. *Stat Sci* 16(2):101–117
8. Chai W, Dostal L, Naess A, Leira BJ (2017) Comparative study of the path integration method and the stochastic averaging method for nonlinear roll motion in random beam seas. *Procedia Eng* 199:1110–1121
9. Coles S (2001) *An introduction to statistical modeling of extreme values*. Springer-Verlag, London, ISBN: 978-1-4471-3675-0
10. Davison AC, Smith RL (1990) Models for exceedances over high thresholds. *J Royal Statist Soc Series B (Methodol)* 52:393–442
11. Falzarano JM, Shaw SW, Troesch AW (1992) Application of global methods for analyzing dynamical systems to ship rolling motion and capsizing. *Int J Bifurcation Chaos* 2:101–115
12. Glotzer D, Pipiras V, Belenky V, Campbell B, Smith T (2017) Confidence intervals for exceedance probabilities with application to extreme ship motions. *REVSTAT-Statist J* 15(4):537–563
13. Kougioumtzoglou IA, Spanos PD (2014) Stochastic response analysis of the softening duffing oscillator and ship capsizing probability determination via a numerical path integral approach. *Probab Eng Mech* 35:67–74
14. Mager J (2015) *Automatic threshold selection of the peaks over threshold method*. Master's thesis, Technische Universitat Munchen, Germany
15. Mohamad MA, Sapsis TP (2016) Probabilistic response and rare events in Mathieu's equation under correlated parametric excitation. *Ocean Eng* 120:289–297
16. Ochi M (1998) *Ocean waves: the stochastic approach*. Cambridge University Press, Cambridge, England, ISBN: 978-0-521-01767-1
17. Pipiras V (2020) Pitfalls of data-driven peaks-over-threshold analysis: perspectives from extreme ship motions. *Probab Eng Mech* 60:103053
18. Pickands J (1975) Statistical inference using extreme order statistics. *Ann Stat* 3:119–131
19. Reiss R-D, Thomas M (2007) *Statistical analysis of extreme values with applications to insurance, finance, hydrology and other fields*, 3rd Edn. Birkhäuser Verlag, Basel, Switzerland, ISBN: 978-3-7643-7399-3
20. St. Denis M, Pierson WJ (1953) On the motions of ships in confused seas. *SNAME Trans* 61:280–332
21. Su Z (2012) *Nonlinear response and stability analysis of vessel rolling motion in random waves using stochastic dynamical systems*. PhD thesis, Texas A&M University, United States

22. Themelis N, Spyrou KJ (2007) Probabilistic assessment of ship stability. *SNAME Trans* 115:181–206
23. Weems K, Belenky V, Campbell B (2016) Validation of split-time method with volume-based numerical simulation. In: *Proceedings of the 15th international ship stability workshop (ISSW2016)*, Stockholm, Sweden, pp 103–108
24. Campbell B, Weems K, Belenky VL, Pipiras V, Sapsis TP (2023) Envelope peaks over threshold (EPOt) application and verification. Chapter 16 in: Spyrou K, Belenky VL, Katayama T, Bačkalov I, Francescutto A (eds) *Contemporary ideas on ship stability—from dynamics to criteria. Fluid mechanics and its applications vol 134*, Springer, pp 265–289. ISBN: 978-3-031-16328-9

# Envelope Peaks Over Threshold (EPOT) Application and Verification



**Bradley Campbell, Kenneth Weems, Vadim Belenky, Vladas Pipiras,  
and Themis Sapsis**

**Abstract** A statistical validation of the EPOT method for estimating the probability of large roll angle for a ship in irregular ocean waves is described in this chapter. EPOT is a numerical extrapolation scheme based on modelling the tail of the roll distribution while accounting for the nonlinearity of the roll response. Fast volume-based numerical simulations create a very large sample of roll events in realistic random irregular wave conditions, which establish a “true” value of the frequency of large-roll events. The EPOT method is applied to a number of small subsets of this data to estimate the probability of a large roll angle encounter. The EPOT estimates are compared to the “true” value in order to judge the validity of the estimate. This chapter describes a set of “true” value simulations, reviews the essence of the EPOT method, and presents the statistical validation and performance assessment of EPOT with two models for the tail of roll distribution.

**Keywords** Probability of exceedance · Validation · Extrapolation · Peak-over-threshold

---

B. Campbell · K. Weems · V. Belenky (✉)  
David Taylor Model Basin (NSWCCD), West Bethesda, Maryland, USA  
e-mail: [vadim.belenky@navy.mil](mailto:vadim.belenky@navy.mil)

B. Campbell  
e-mail: [bradley.campbell@navy.mil](mailto:bradley.campbell@navy.mil)

K. Weems  
e-mail: [kenneth.weems@navy.mil](mailto:kenneth.weems@navy.mil)

V. Pipiras  
University of North Carolina at Chapel Hill, Chapel Hill, NC, USA  
e-mail: [pipiras@email.unc.edu](mailto:pipiras@email.unc.edu)

T. Sapsis  
Massachusetts Institute of Technology, Cambridge, MA, USA  
e-mail: [sapsis@mit.edu](mailto:sapsis@mit.edu)



## 1 Introduction

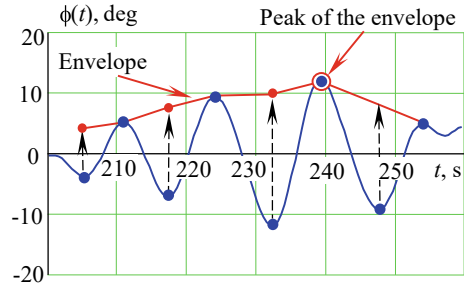
The development of advanced numerical codes for the time-domain simulation of large-amplitude ship motions [4, 28] has provided new capabilities for assessing the dynamic stability of a ship in waves. The procedures for performing this type of simulation-based assessment, which is referred to as Direct Stability Assessment (DSA), have become a part of the Interim Guidelines on the Second Generation Intact Stability Criteria (referred further as the Interim Guidelines), published by the International Maritime Organization (IMO) in Chap. 3 of the Annex to MCS.1/Circ. 1627 [19].

Unless deterministic criteria are employed (paragraph 3.5.3.3 of the Annex to MCS.1/Circ.1627), the stochastic nature of ocean waves forces DSA to incorporate a statistical characterization of the ship's response in irregular waves. If a response sample of sufficient volume (i.e. simulated motion histories of sufficient duration) is available, a direct counting procedure can be applied (section 3.5.4 of the Interim Guidelines). However, large amplitude roll is generally rare in conditions of practical importance. To obtain a sample of sufficient volume via time domain simulation is frequently impractical or impossible. Consequently, extrapolation methods will need to be applied to the obtainable data.

A number of extrapolation methods have been and are being investigated. Extrapolation over significant wave height was proposed by Tongu  and S ding [32] and further developed by Shigunov [30]. The application of the extreme value distribution to numerical simulation results were studied by McTaggart and de Kat [23, 24]. The critical wave group approach was developed by Themelis and Spyrou [31], and the current state of the art is summarized in Anastopoulos and Spyrou (Chap. 10) [2]. Mohamad and Sapsis [25] proposed a sequential sampling strategy facilitating the application of high-fidelity simulations. Umeda et al. [33] developed a single-critical-wave method for the estimation of the probability of broaching. Weems et al. [35] contains a brief description of the split-time method for assessment of capsizing probability.

Envelope peaks over threshold (EPOT) is one of the extrapolation methods mentioned in paragraph 3.5.5.4 of the Annex to MCS.1/Circ. 1627. The EPOT method belongs to the family of Peak-over-Threshold (POT) methods. The basic idea of POT methods is to fit a Generalized Pareto Distribution (GPD) to the observed data above a particular threshold value of the response. The mathematical background of the method is the second extreme value theorem, which states that the tail of an extreme value distribution can be approximated with GPD above a "large enough" value [26]. A brief overview of extreme value theorems is available from Chap. 26 [9]. A key feature of the POT extrapolation is that it can capture the nonlinearity of the large amplitude response, such as that caused by changes in the restoring moment at large roll angles and in waves. Physical considerations can further improve the estimate by explicitly accounting for nonlinearity by applying a Pareto distribution for the tail of distribution of roll peaks [7, 8].

**Fig. 1** De-clustering with an envelope



The POT method is only applicable to independent data points, (due to restrictions in the application of the 2nd extreme value theorem, in particular, in confidence interval construction) while the roll motions of a ship are correlated because of the ship’s inertia, correlation of the wave excitation, and “memory” in the hydrodynamic forces. The application of POT, therefore, requires an extraction of independent points from the time history, a process known as “de-clustering.” Fitting an envelope to the time history of the roll motion, as illustrated in Fig. 1, is a convenient way to de-cluster the data, as the peaks of the envelope of the roll response are sufficiently far from each other to provide the necessary independence. The use of an envelope to de-cluster the roll motion provides the additional letter in the name of the method, so POT becomes EPOT—Envelope Peaks Over Threshold.

The confident application of any extrapolation method is possible only when supported by a statistical validation. The idea of statistical validation is as follows. First, generate a large data set that contains enough large values or other rare events to estimate their rate of occurrence (i.e. with direct counting); this estimate will further serve as a “true” value. Then, the extrapolation is performed with many small subsets of these data. If the extrapolation method is valid, the extrapolated estimates will recover the “true value” in a statistical sense; therefore a confidence interval of extrapolated estimate will contain the “true” value with a probability close to the confidence probability used in computing the confidence interval. The validation procedure is carried out for several speeds, headings, and wave conditions representative for ship operation. This validation procedure was formulated by Smith [29], and its application to the split-time method is described in Chap. 14 [35]. The Interim Guidelines contain requirements for statistical validation in section 3.5.6. A brief description of the statistical validation of EPOT can be found in subsection 5.4.4 of Appendix 4 to the Explanatory Notes for the Interim Guidelines (MSC.1/Circ.1652).

## 2 Estimation of “True” Value

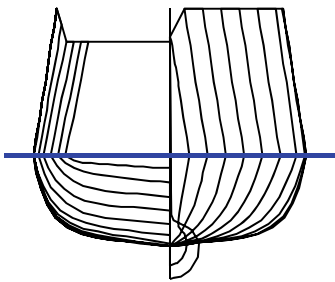
The motion data for both determining the “true” value and exercising the extrapolation method is computed using a rapid time-domain seakeeping simulation based on a volume-based algorithm described by Weems and Wundrow [34]. The idea is

to compute the inseparable nonlinear hydrostatic and Froude-Krylov forces, which are critical contributors to non-linear roll motion, from the distribution of the instantaneous submerged volume along the hull. A brief description of this algorithm is available from chap. 14 of this book [35].

The subject ship for the validation exercise is the Tumblehome configuration from the ONR Topsides series [12]. The ship lines, principal dimensions, and flotation are shown in Fig. 2. The statistical validation campaign was carried out for sea condition with a significant wave height of 9 m and modal period of 15 s, which was modeled using a Bretschneider spectrum [21]. These conditions correspond to a high Sea State 7 or low Sea State 8 (Table 7 of [21]).

The calculations were performed for various relative wave headings and a number of target roll angles, which are summarized in Table 1. The heading convention is such that 45° is quartering seas, 90° is beam seas, and 135° is bow seas.

Simulations were performed with 3 degrees of freedom: heave, roll, and pitch. Besides generating the time history of ship motions, the calculations included fitting an envelope to the peaks of roll time histories in Fig. 1. The peaks of the envelope were recorded. The events when the envelope peaks exceeded each predetermined target



Principal Dimensions and Calculation Conditions

Length BP, m	154
Breadth molded, m	18.8
Drafta midships, m	5.5
GM, m	2.2
Speed, knots	6

Fig. 2 Lines, principal dimensions, and flotation of the ONR tumblehome topside configuration

Table 1 Summary of validation conditions

Headings deg	Total time, hrs	Number of targets	Largest target	Number of exceedances of largest target, deg	Number of capsizings
15	285,000	5	20	14	0
22.5	100,000	7	27.5	16	0
30	100,000	13	45	9	0
37.5	100,000	15	60	7	0
45	345,000	15	70	8	10
60	300,000	15	70	12	11
90	345,000	9	37.5	12	0
135	345,000	3	20	6	0

level were also recorded. Table 1 lists the number of exceedances of the largest target for every heading angle, while Table 2 in the Appendix lists all available targets.

To avoid a self-repeating effect in the incident wave model (e.g. [6]), the simulations for each sea state consisted of a large number of 30-min records. The total simulation time and number of observed capsizes are reported in Table 1. Table 2 reports the recorded number of exceedance events of each target level. The rate of exceedances  $\hat{\lambda}_T$  is estimated from the observations as

$$\hat{\lambda}_T = \frac{N_T}{T_T} = \frac{N_T}{N_R T_R - \sum_{i=1}^{N_R} (T_R - t_{Ci})} \quad (1)$$

where  $N_T$  is a number of exceedance events observed and  $T_T$  is the total simulation time,  $N_R$  is the total number of records in the simulation campaign,  $T_R$  is the duration of each record, and  $t_{Ci}$  is time of capsizing if it occurred during  $i$ -th record. Evaluation of the confidence interval for estimate (1) is described in chap. 14 of this book [35].

Table 2 includes data on larger targets than those indicated in Table 1, for which the number of observations were insufficient to use for validation. The data on these targets is given for reference and is shown in red in Table 2. As expected, the confidence intervals of the rate of exceedance are small for cases with a large number of observed target values but large for cases with few observed values.

### 3 Essence of the EPOT Method

Two extreme-value theorems provide the mathematical background for statistical extrapolations including the POT family of methods. The first extreme value theorem (a.k.a. Fisher-Tippett-Gnedenko theorem, e.g. [16]) proves that a distribution of the largest value in a sample has a limit in the form of a Generalized Extreme Value (GEV) distribution. The second extreme-value theorem (a.k.a. Pickands-Balkema-de Haan theorem) shows that the GEV distribution can be approximated by GPD above a threshold [16]. The tail ( $y > u$ ) of *any* distribution can be approximated with GPD above a sufficiently large threshold. The GPD is defined by three numbers—a shape parameter  $\xi$ , a scale parameter  $\sigma$ , and threshold value  $u$ —and has the following form:

$$\text{pdf}(y) = \begin{cases} \frac{1}{\sigma} \exp\left(-\frac{y-u}{\sigma}\right) & \text{for } \xi = 0 \\ \frac{1}{\sigma} \left(1 + \xi \frac{y-u}{\sigma}\right)^{-(1+1/\xi)} & \text{for } \xi \neq 0 \text{ and } \xi \frac{y-u}{\sigma} > -1, \\ 0 & \text{otherwise} \end{cases} \quad (2)$$

$$\text{cdf}(y) = \begin{cases} 1 - \exp\left(-\frac{y-u}{\sigma}\right) & \text{for } \xi = 0 \\ 1 - \left(1 + \xi \frac{y-u}{\sigma}\right)^{-(1+1/\xi)} & \text{for } \xi \neq 0 \text{ and } \xi \frac{y-u}{\sigma} > -1. \\ 0 & \text{otherwise} \end{cases} \quad (3)$$

The objective of the present application is to estimate a rate of exceedance  $\hat{\lambda}(c)$  of a target value  $c$  above the threshold  $u$ :

$$\hat{\lambda}(c) = \hat{\lambda}(u) \left( 1 - \widehat{\text{cdf}}(c|y)u \right) \tag{4}$$

where  $\hat{\lambda}(u)$  is the rate of upcrossing of the threshold  $u$  estimated by Eq. (1) with available data. The scale parameter  $\sigma$  in Eqs. (2) and (3) is positive, while the shape parameter  $\xi$  can be either positive or negative. A negative shape parameter imposes a limitation on the expressions in parenthesis of Eqs. (2) and (3) and formally introduces a right bound to the distribution:

$$\text{pdf}(y) = 0, \quad \text{if } y > u - \frac{\sigma}{\xi} \text{ and } \xi < 0. \tag{5}$$

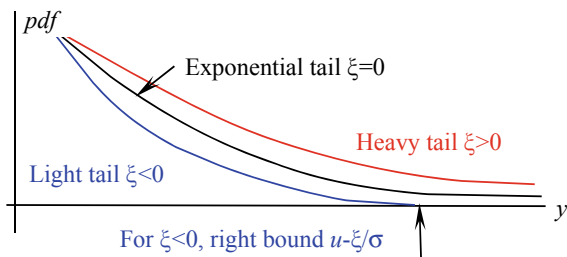
The shape parameter defines the type of tail—heavy, exponential, or light—in Fig. 3. The exponential tail ( $\xi = 0$ ) describes the extreme values of a normal distribution. The heavy tail ( $\xi > 0$ ) is above the exponential tail, while the light tail ( $\xi < 0$ ) is below. As the exponential tail is the lowest among the infinite tails, the light tail has a limit, which is its right bound. The heavy tail is unbounded. No universally accepted definitions of heavy and light tails exist, so other sources may use heavy/light tail in a different context.

For the application of GPD, two parameters must be estimated—shape  $\xi$  and scale  $\sigma$ —and threshold  $u$  must be found. The details of fitting the GPD tail for the EPOT method is described by Campbell et al. [15] and consists of the following steps:

- Define a set of “candidate” thresholds
- Estimate shape and scale parameters of GPD for each threshold value
- Find “the best” value for the threshold
- Evaluate the confidence intervals for estimates of the conditional probability and rate of exceedance in Eq. (4).

The shape and scale parameters are estimated by the maximum likelihood method. The threshold is found from by stabilizing the shape parameter estimate and minimizing the deviation between the observed and modeled distributions. The confidence interval for the conditional probability  $\widehat{\text{cdf}}(c)$  is evaluated in two steps:

Fig. 3 Types of tails [7]



- Characterization of the uncertainty of shape  $\xi$  and scale  $\sigma$  estimates: as the maximum likelihood method involves the summation of observed data points (which are random), to assume a joint normal distribution is logical for the estimates of  $\xi$  and  $\sigma$  (Central Limit Theorem). A formula for the covariance matrix for the joint distribution of  $\hat{\xi}$  and  $\hat{\sigma}$  is available (e.g. [13]), while their mean values equal to the estimates themselves. Practical application of the joint normal distribution of  $\hat{\xi}$  and  $\hat{\sigma}$  may cause difficulties, because  $\sigma > 0$  while normal distribution supports negative values for  $\hat{\sigma}$ . A conventional method to resolve these difficulties is to consider  $\ln \hat{\sigma}$  instead of  $\hat{\sigma}$  itself [14].
- Characterization of the uncertainty of the conditional probability  $1 - \widehat{\text{cdf}}(c)$ : given a joint normal distribution of  $\xi$  and  $\ln \sigma$  estimates, the conditional probability  $1 - \widehat{\text{cdf}}(c)$  can be considered as a deterministic function of random arguments of  $\hat{\xi}$  and  $\ln \hat{\sigma}$ . As the joint distribution of  $\hat{\xi}$  and  $\ln \hat{\sigma}$  is assumed, the distribution of  $\widehat{\text{cdf}}(c)$ , can be computed, see Campbell et al. [14] or Glotzer et al. [18]. Alternatively, the boundaries of the confidence interval for  $\hat{\xi}$  and  $\ln \hat{\sigma}$  can be substituted into formula for  $\widehat{\text{cdf}}(c)$ , and the results can be interpreted as boundaries of confidence interval for  $\widehat{\text{cdf}}(c)$ , the so-called “boundary method”, cf. section 4.4 of Bickel and Doksum [11].

Glotzer et al. [18] compared several methods for computing the confidence interval of extrapolated estimates, including the direct computation of distribution of  $\widehat{\text{cdf}}(c)$  and the boundary method. These two techniques will be further used for statistical validation of EPOT.

To complete the characterization of the uncertainty of the extrapolated estimate  $\hat{\lambda}(c)$ , its confidence interval is evaluated by the “boundary method”:

$$\hat{\lambda}_{Up,Low}(c) = \hat{\lambda}_{Up,Low}(u) \left( 1 - \widehat{\text{cdf}}_{Up,Low}(c) \right). \quad (6)$$

The expression  $\widehat{\text{cdf}}_{Up,Low}(c)$  means the boundaries of confidence interval for  $\widehat{\text{cdf}}(c)$ , while  $\hat{\lambda}_{Up,Low}(u)$  expresses the confidence interval for the upcrossing rate of threshold  $u$ . The latter has been addressed in the previous section, while details are available from chap. 14 of this book [35].

The confidence interval for the individual estimates  $\widehat{\text{cdf}}(c)$  and  $\hat{\lambda}(u)$  is computed for the confidence probability  $P_{\beta 1}$ , related to the confidence probability  $P_{\beta}$  of the complete estimate  $\hat{\lambda}(c)$ , as:

$$P_{\beta} = \sqrt{P_{\beta 1}}, \quad (7)$$

assuming independence of the estimates  $\widehat{\text{cdf}}(c)$  and  $\hat{\lambda}(u)$ .

The GPD fitting procedure outlined above is completely data-driven and does not account for any physical considerations that may be available for the problem at hand. Adding physical considerations to a data-driven model may reduce the statistical uncertainty: for example, Fig. 8 of [35] or Figs. 4 and 5 as a comparison in

chap. 14 of this book [35]. The reduction of uncertainty in both cases was achieved by assuming a certain tail type of distribution, based on physical considerations. Glotzer et al. [18] assumed light tail and a certain value of the upper bound, leading to a relation between shape and scale parameters in Eq. (5). Weems et al. [35] assumed an exponential tail, i.e. the shape parameter equals zero.

Belenky et al. [8] argues that the distribution of large roll peaks should have a combination of heavy and light tails. The instantaneous  $GM$  decreases near the maximum of  $GZ$  curve and becomes negative for roll angles beyond the maximum. As the restoring decreases, a ship may attain larger roll amplitudes as compared to a case with linear restoring. A dynamical system with piecewise linear restoring

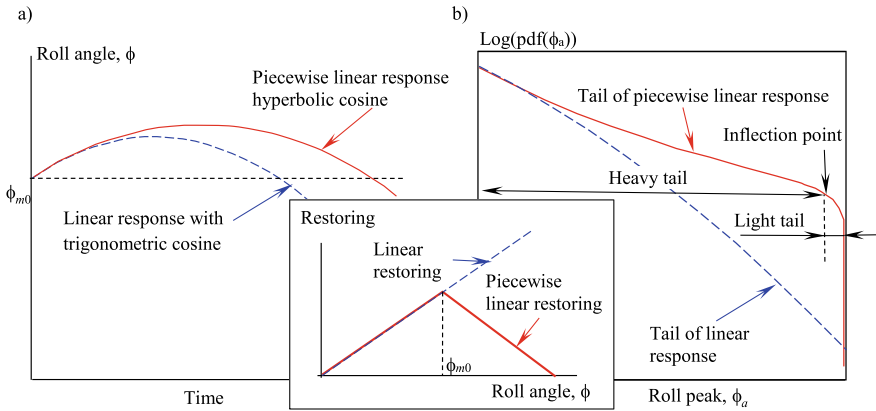


**Fig. 4** On a structure of tail of roll peak distribution **a** free linear and piecewise linear response; **b** tails of peak distribution of linear and piecewise linear response

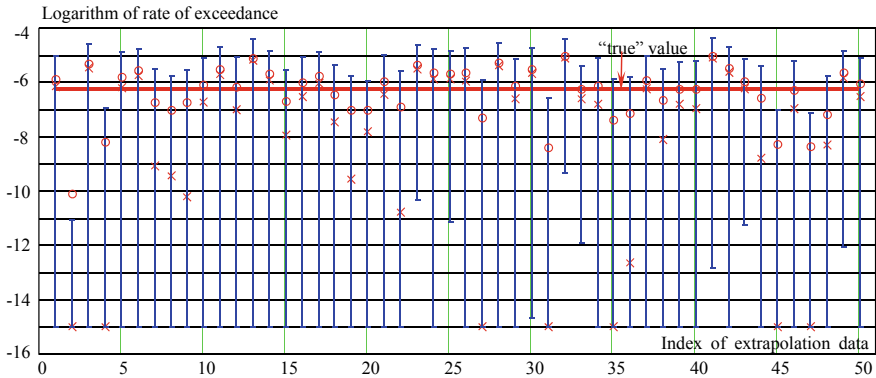


**Fig. 5** Example of Tier 1 validation with the GPD tail fit for target  $40^\circ$  roll angle at a heading of  $45^\circ$  (quarterming seas); confidence interval for conditional probability computed with distribution of  $\widehat{\text{cdf}}(c)$ ;  $PR = 0.9$ ,  $CD = 1.22$ ,  $RB = 0.81$ ; circles are the mean values of the extrapolated estimates; x-marks the most probable extrapolated estimates

provides a good illustration in Fig. 4. This dynamical system retains most of the known qualitative properties of nonlinear roll motion [5] and allows a closed-form solution for a number of associated problems. The peak of the free piecewise response is described by a hyperbolic cosine, and exceeds the peak of a linear response started from the same initial conditions in Fig. 4a. As a result, the peaks of stochastic piecewise linear response are, on average, larger compared to the peaks of linear response. As a result, the tail of the piecewise linear response is heavy, while the tail of linear response is known to be exponential (linear response is normal), Fig. 4b.

When the roll peak becomes too large (i.e. close to the angle of vanishing stability), the possibility of capsizing becomes significant. As a result, the population of very large roll peaks decreases (no roll peak will occur in capsizing) and the tail becomes light in Fig. 4b. A more formal consideration is available in [8].

The above considerations justify the assumption that the tail of distribution of roll peaks can be approximated with a heavy tail. The heavy tail can be modeled with a Pareto distribution that has a power law tail. When the shape parameter  $\xi > 0$  (heavy tail) and threshold value  $u = \sigma/\xi$ , the GPD is equivalent to a Pareto distribution with scale  $y_m = \sigma/\xi$  and shape  $\alpha = 1/\xi$ :

$$\text{pdf}(y) = \frac{\alpha y_m^\alpha}{y^{\alpha+1}} \quad (8)$$

The conditional probability of exceedance of a target value  $y$  associated with dynamic stability failure is expressed as:

$$P(Y > y | Y > u) = \left(\frac{u}{y}\right)^\alpha = \left(\frac{y}{u}\right)^{-\frac{1}{\xi}} \quad (9)$$

where the threshold  $u$  does not have to be the same as in the GPD case. A method for finding the threshold and estimating the shape parameter is proposed in Belenky et al. [7], which is based on [10, 17, 22].

## 4 Results of Statistical Validation

Following the multi-tier framework for statistical validation of extrapolation methods laid out by [29], the following three tiers are defined:

- Tier 1: all extrapolations for a single target value (50 sets, each 25 h/50 records)
- Tier 2: extrapolations for all available target values
- Tier 3: extrapolations for all available operational and environmental conditions.

This definition is different from one by Weems et al. [35], described in chap. 14 of this book, where Tier 1 was represented by a single extrapolation. The success of the single extrapolation was counted when the “true” value was contained in the confidence interval. In this chapter, Tier 1 consists of 50 single extrapolations, similar



to Tier 2 in [35]. This “shift” of tiers accommodates the assessment of several targets, while in the case of [35], extrapolations were aimed only on capsizing events.

The success of the Tier 1 validation is defined through a “passing rate”, which is a fraction of successful individual extrapolations after  $N_e$  attempts:

$$PR(c) = \frac{1}{N_e} \sum_{i=1}^{N_e} \begin{cases} 1; \hat{\lambda}_T \in [\hat{\lambda}_{low}(c); \hat{\lambda}_{up}(c)] \\ 0; \hat{\lambda}_T \notin [\hat{\lambda}_{low}(c); \hat{\lambda}_{up}(c)] \end{cases} \quad (10)$$

where  $\hat{\lambda}_T$  is the “true” value defined above with Eq. (1), while  $[\hat{\lambda}_{low}(c); \hat{\lambda}_{up}(c)]$  is a confidence interval of extrapolated estimate for the target value  $c$ .

The Tier 1 validation is successful if the passing rate (10) falls within a certain interval around accepted confidence probabilities. The boundaries of this interval depend on the number of individual extrapolations and can be derived by considering a success of an individual extrapolation as a Bernoulli trial. For  $N_e = 50$ , the passing rate should be between 0.88 and 1.0. Details are available in [35]. Besides the passing rate, the performance of an extrapolation method is assessed with two other indicators: “conservative distance”  $CD$  and “relative bias”  $RB$ . These are defined as:

$$CD(c) = \log\left(\frac{E(\hat{\lambda}_{up}(c))}{\hat{\lambda}_T}\right); \quad RB(c) = \frac{E(\hat{\lambda}(c)) - \hat{\lambda}_T}{\hat{\lambda}_T} \quad (11)$$

where  $E(\hat{\lambda}_{up}(c))$  is the upper boundary of the confidence interval of the extrapolated estimates for target  $c$ , averaged over all the considered extrapolation data sets.  $E(\hat{\lambda}(c))$  is the extrapolated estimate averaged over all the considered data sets; and  $\hat{\lambda}_T$  is the true value estimated from all the observations with Eq. (1). The  $CD$ -value expresses the practicality of the extrapolation: the upper boundary of the extrapolated estimate is an expected outcome and does not have to be too conservative to be practical. The  $CD$ -value indicates, on average, by how many orders of magnitude the upper boundary exceeds the true value. The  $RB$ -value is intended to measure the accuracy of the fit, comparing the most probable estimate vs. the “true” value.

Examples of the Tier 1 validation for the GPD tail fit are in Figs. 5 and 6. Besides the boundaries of the confidence interval, each extrapolation shows the most probable values, identified by red x-marks, and the mean values as circles. Calculation details are described by Campbell et al. [14].

The vertical scale of Figs. 5 and 6 is logarithmic. To indicate zero, a small value of  $10^{-15}$  1/s was applied. A total of 44 and 50 lower boundaries extend below this value in Figs. 5 and 6, respectively. The seven most-probable extrapolated estimates below  $10^{-15}$  1/s appear in Figs. 5 and 6. The reason is an apparent light tail and associated right bound of the estimated distribution. This apparent light tail should not be confused with the light tail caused by the angle of vanishing stability in Fig. 4b. The former is a result of a relatively small number of large peaks and relatively large

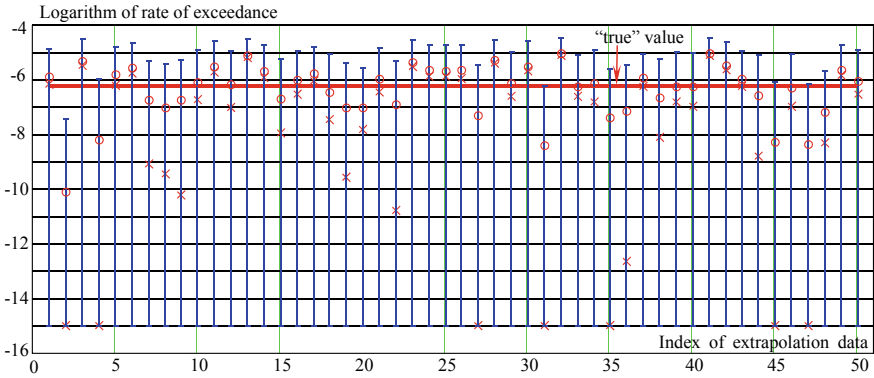


**Fig. 6** Example of Tier 1 validation with the GPD tail fit for a target 40° roll angle at a heading of 45° (quartering seas); confidence interval for conditional probability computed with boundary method.  $PR = 0.98$ ,  $CD = 1.32$ ,  $RB = 0.81$ ; circles are the mean values of the extrapolated estimates, x-marks the most probable extrapolated estimates

number of moderate peaks leading to a significantly negative shape parameter. It is one of the known issues of the application of GPD [1, 3, 27]. Five unsuccessful extrapolations are in Fig. 5, resulting in a passing rate of 0.90, which is between 0.88 and 1.0, which means a successful Tier 1 validation. Only one unsuccessful extrapolations is in Fig. 6, resulting in a passing rate of 0.98, which similarly indicates a successful Tier 1 validation for the boundary method as well.

The example with physics-informed extrapolation by a heavy tail fit with Pareto distribution [7] is in Fig. 7.

Physical information on the nature of large roll motions has dictated the choice of Pareto distribution as a statistical model for the tail. Including this physical information reduces uncertainty, which is reflected in the decreased width of the confidence

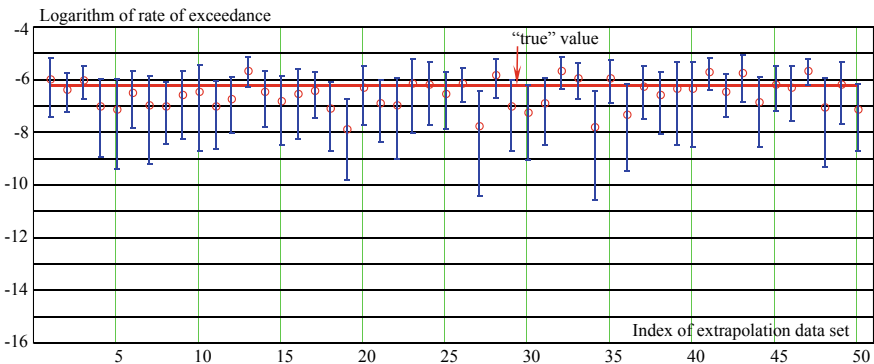


**Fig. 7** Example of Tier 1 validation with the Pareto tail fit for target 40° at wave heading 45°;  $PR = 0.94$ .  $CD = 0.566$ ,  $RB = -0.079$

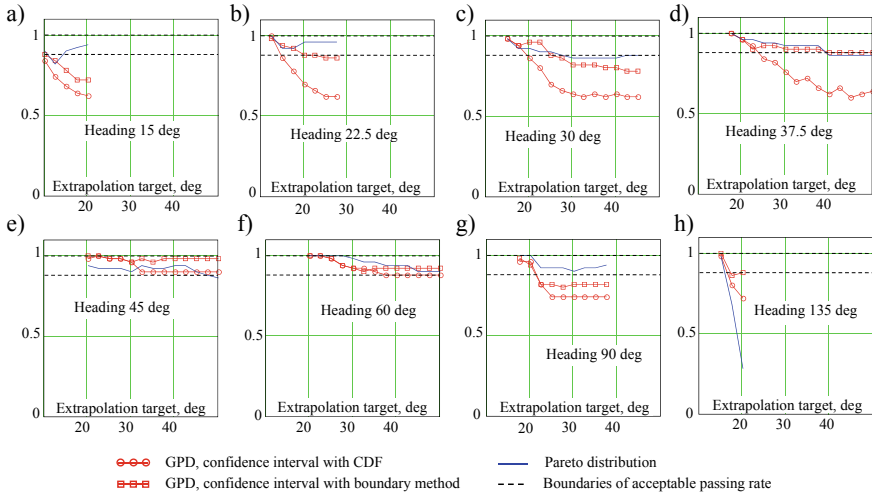


**Fig. 8** Passing rate as function of extrapolation target for different wave heading angles: **a** 15°; **b** 22.5°; **c** 30°; **d** 37.5°; **e** 45°; **f** 60°; **g** 90°; **h** 135°

intervals in Fig. 7 as compared to Figs. 5 and 6. The most apparent difference between the GPD (Figs. 5 and 6) and Pareto (Fig. 7) extrapolations is in the lower boundary, which does not have a significant practical influence—the upper boundary is meant to be in practical assessment. However, the decrease of the “conservative distance” (11), from 1.2 to 1.3 for GPD-tail to 0.57 for Pareto-tail, indicates the expected decrease of statistical uncertainty. A decrease of the relative bias (11) from 0.81 for GPD-tail to  $-0.079$  for Pareto-tail also indicates improvement in statistical uncertainty for the considered sample heading and target.

Tables 3 and 4 in the Appendix contain all the statistical validation data for the conditions described in Table 2. “Head” indicates the relative heading angle of the relative to the waves, with 45 for quartering seas, etc. “Trg.” is the target roll angle, in degrees, for the extrapolation. “CDF” in the “Passing Rate” column means extrapolation by the GPD-tail, with the confidence interval of the extrapolated estimate computed with distribution of  $\widehat{cdf}(c)$  estimate. “Bnd.” stands for boundary method of confidence interval calculations of a GPD extrapolated estimate. “CD” and “RB” are conservative distance and relative bias, respectively, Eq. (11).

Values of acceptable passing rate (above 0.88) are in Tables 3 and 4 in black. The passing rate values that are a little short of acceptable (say, 0.8) are in blue. Finally, the cases of obvious failures are in red. Passing rate values for most of the extrapolation targets and all headings is depicted in Fig. 8. Conservative distances are presented in Fig. 9, while relative bias data are placed in Fig. 10. Finally, the described validation effort is summarized in Fig. 11 showing the minimum passing rate, average conservative distance (to serve as a typical value) and maximum relative bias as functions of heading.

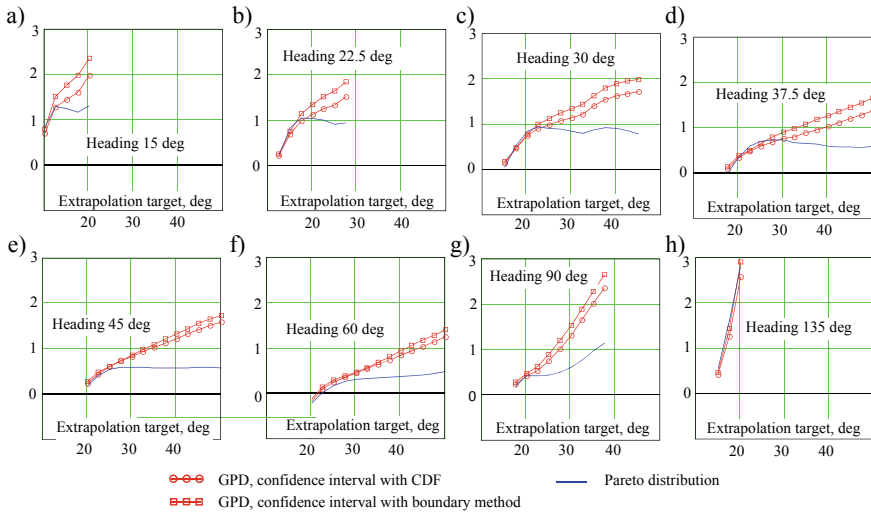


**Fig. 9** Conservative distance as functions of extrapolation target for different wave heading angles: **a** 15°; **b** 22.5°; **c** 30°; **d** 37.5°; **e** 45°; **f** 60°; **g** 90°; **h** 135°

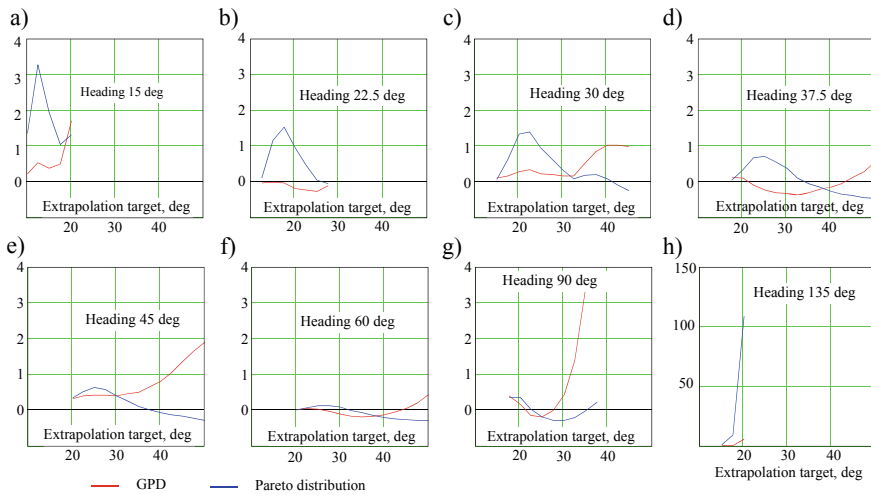


**Fig. 10** Relative bias as a function of extrapolation target for different wave heading angles: **a** 15°; **b** 22.5°; **c** 30°; **d** 37.5°; **e** 45°; **f** 60°; **g** 90°; **h** 135°

## 5 Discussion

For all headings except 135° (bow seas), the Pareto-tail extrapolation demonstrates superior results in comparison to the GPD-tail extrapolation. In Fig. 8, the passing rate of Pareto-tail extrapolation stays within acceptable interval for almost all targets

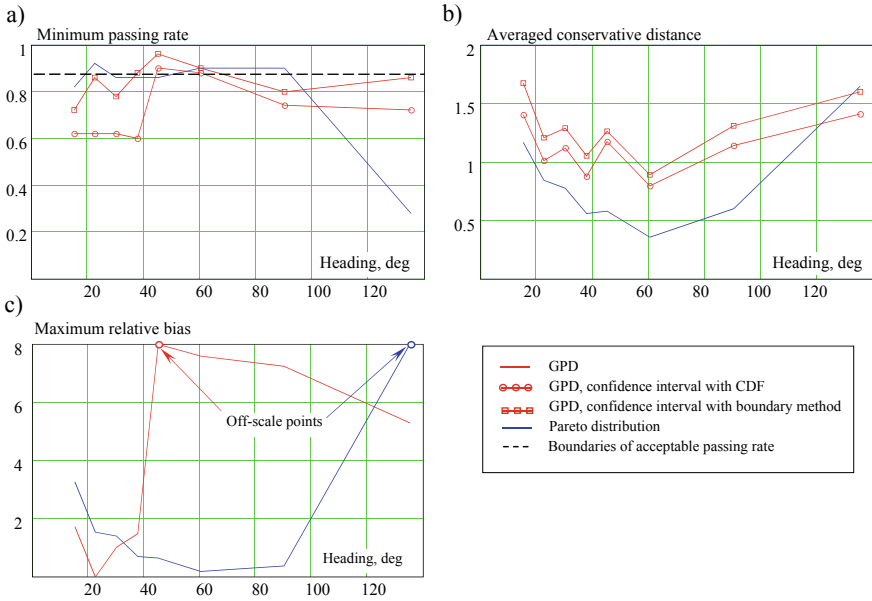


**Fig. 11** Minimum passing rates (a), averaged conservative distance (b) and maximum relative bias (c) for all headings

at heading 15 through 90°. Even when it drops out of the range, it does not fall below 0.86 (headings 30 and 37.5°, Fig. 8e, h). The only exception is heading 15° (Fig. 8a), where the passing rate falls to 0.82 for the 12.5° target value, while passing rates for all other targets stay well above the minimum.

The Pareto-tail extrapolation obviously does not work for 135° heading. This is indicated by the very large value of relative bias, reaching a value of 108 (the last line in Table 4). This means that the Pareto-tail extrapolation overestimates the actual probability of exceedance, which is illustrated in Fig. 12. GPD-tail extrapolation does better with  $RB = 5.29$  (the last line in Table 3). The  $RB$  for this case is not small compared to other cases in Table 3 but is still better than the Pareto-tail extrapolation result. The passing rate for the boundary method of confidence interval is actually 0.88, which is right at the minimum acceptable level.

These results are consistent with the conclusion from Belenky et al. [7] that the case of 135° heading does not have sufficient nonlinear data to justify the assumption of the heavy tail. The roll motions around 20° are essentially in the linear range, for which an exponential tail is expected. That is why the heavy tail overestimates the probability (Fig. 1), while GPD is capable of recovering the exponential tail and gets a correct extrapolation even with the relatively large statistical uncertainty ( $CD = 2.89$  in Table 3).

A logical question arises: why did the Pareto-tail work for the same extrapolation target of 20° for a heading of 15°? The most plausible reason is that the variation of stability in stern seas has added nonlinearity to the roll motions, making the heavy

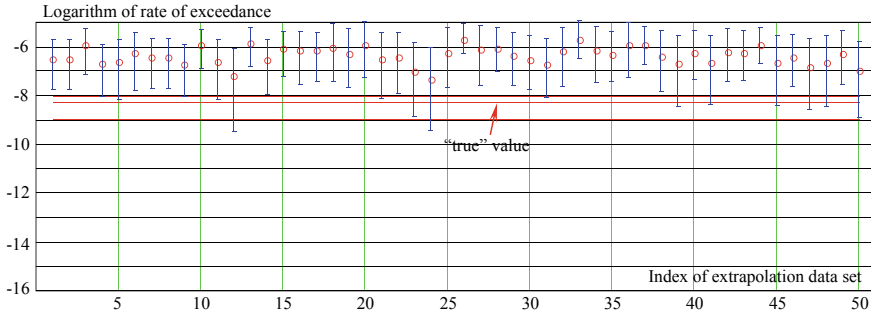


**Fig. 12** Example of Tier 1 validation with the Pareto tail fit for target  $20^\circ$  at heading of  $135^\circ$   $PR = 0.28$ .  $CD = 2.8$ ,  $RB = 108.57$

tail applicable. The variation of stability occurs in oblique waves as well, but it is too brief to cause a large roll unless parametric resonance is involved.

From Fig. 8, the Pareto-tail extrapolation outperformed the GPD in terms of conservative distance (except for the  $135^\circ$  heading where the heavy tail is not applicable). The  $CD$  values consistently remain below 1, except for the  $15^\circ$  heading where it is slightly above one (Fig. 8b). The conservative distance is an important indicator of the practical applicability of the extrapolation: if  $CD$  is too large, the extrapolation becomes too conservative to have practical value.

The relative bias,  $RB$ , defined by Eq. (11) also measures conservativeness of the extrapolated estimate but uses the most probable value rather than the upper boundary and can be considered as an auxiliary indicator. In principle, the  $RB$ -value for the GPD tail can be estimated from the mean value estimate. However, as demonstrated in [35], the  $RB$ -estimate based on the most probable value is better, despite the fact that the most probable GPD estimate can sometimes fail if the shape parameter is too small. For example, the seven most-probable estimates fell below  $10^{-15}$  1/s in Fig. 5.

The relative bias is a useful indicator of a reason why Pareto may be inapplicable for the  $135^\circ$  heading. The relative bias may also be interpreted as an indicator of the convergence of the most probable extrapolated estimate towards the “true” value. The absolute value of the  $RB$  may indicate how fast the extrapolated estimate converges. Most of the observed absolute values of  $RB$  were well below 1.0. Fifteen values are above 1.0 for GPD-tailed extrapolation, and eleven for Pareto-tailed distribution, which are in blue font in Tables 3 and 4.

The large absolute values of  $RB$  for the GPD-tailed distribution are associated with large extrapolation targets. This may indicate that the convergence of GPD is worse when extrapolating far from the available data, which seems to be logical for the data-driven approach. Large absolute values of  $RB$  for the Pareto-tail extrapolation behave differently. Except for the bow waves, where Pareto is not applicable, the large absolute values of  $RB$  are observed for  $15^\circ$ ,  $22.5^\circ$  and  $30^\circ$  headings and are associated with the mid-range targets. Perhaps these values indicate how well the Pareto distribution describes the actual tail of the data distribution.

The results for all available conditions are in Fig. 11, i.e. the Tier 3 validation. Minimum passing rate over all of the targets is plotted in Fig. 11a. The Pareto-tail distribution may be recognized as valid for all the headings except  $135^\circ$ . The blue curve is oscillating around the acceptable level of 0.88, but its deviations seems to be not too significant. The GPD-tail extrapolation with boundary method for confidence interval is the second-best, but is the only method that is valid for  $135^\circ$  heading.

A value conservative distance averaged for all extrapolation targets is in Fig. 11b. It is meant to represent the typical performance of the considered methods. Again, for the range of its validity, Pareto-tail extrapolation comes out as the best, keeping the “representative” conservative distance under 1.0, except for the  $15^\circ$  heading where it is slightly above 1.0. Another interesting observation can be made from Fig. 11b. The boundary method for the confidence interval of GPD extrapolation is not that much more conservative, when compared to the CDF-based method. The depicted conservative distances are quite similar. Since the performance of the former is better in terms of passing rate, the boundary method seems to be preferable if GPD-tail extrapolation must be used for EPOT. Finally, the relative bias is in Fig. 11c.

## 6 Summary and Conclusions

The statistical validation of the Envelope Peak over Threshold (EPOT) method for the extrapolation of larger roll motions from time domain ship motion in random irregular seas was described in this chapter. The EPOT method is one of the options mentioned for the Direct Stability Assessment within the framework of the second generation IMO intact stability criteria.

As its name suggests, the EPOT method belongs to a family of peak-over-the-threshold methods. It is based on the second extreme value theorem that states that a tail of any distribution can be approximated by Generalized Pareto Distribution (GPD) above a large-enough threshold. As this theorem is applicable to independent data only, envelope peaks create independent data points.

GPD-tail distribution is a data-driven approach. The statistical uncertainty of GPD-tail extrapolation can be decreased by including physical information in the statistical model. Large roll angles are associated with the proximity of angle of maximum of  $GZ$  curve. This leads to a decrease of instantaneous  $GM$  and an increase of natural roll period—physical changes that are reflected in a heavy tail to the distribution of roll motion. Pareto distribution models this heavy tail. The mere fact of modeling heavy tail (vs. any type of tail) makes the statistical model “physically informed”. However, use of the Pareto distribution requires the presence of a significantly nonlinear response that leads to the heavy tail.

A validation of the extrapolation was performed by a fast numerical simulation algorithm, capable of qualitatively reproducing the most principal nonlinearity of roll motion by computing the body-nonlinear wave forcing and restoring from the instantaneous submerged volume and its centroid. These calculations were executed for sufficiently long times to observe a statistically significant number of large roll

angles in random ocean waves. The validation is considered successful if a small subset of these data predict the probability of large roll without necessarily observing such angles in the data subset.

The statistical validation considered eight conditions for the ONR Tumblehome top configuration. A three-tiered validation procedure was applied for EPOT with both GPD and Pareto tail extrapolation. Two methods for calculating the confidence interval were used for the GPD tail. The Pareto-tail extrapolation was found to be inapplicable for one condition (bow seas), while the GPD-tail extrapolation is applicable at this condition; for all other conditions, Pareto-tail extrapolation outperforms the GPD tail extrapolation.

**Acknowledgements** The work described in this chapter has been funded by the Office of Naval Research (ONR) under Dr. Woei-Min Lin. This work was also supported by the NSWCCD Independent Applied Research (IAR) program under Dr. Jack Price. The participation of Prof. Sapsis was facilitated by the NSWCCD Summer Faculty Program, while the participation of Prof. Pipiras was facilitated by NSWCCD Summer Faculty and Sabbatical Programs, both of which are also managed by Dr. Jack Price. The authors are very grateful for the support that made this work possible.

## Appendix

This appendix contains tables of numerical values for “true” value estimates (Table 2), level 2 and 3 statistical validation for the GPD (Table 3) and Pareto distributions (Table 4).



**Table 2** Observed “true” value estimates

Target, Deg.	Observations	Est. of rate 1/s	Low boundary	Upper boundary	Target, deg	Observations	Est. of rate 1/s	Low boundary	Upper boundary
Heading 15 degrees									
10.0	4790	4.7 E-06	4.6 E-06	4.9 E-06	17.5	46	4.6 E-08	3.3 E-08	5.9 E-08
12.5	361	3.6 E-07	3.2 E-07	4.0 E-07	20.0	14	1.4 E-08	6.9 E-09	2.2 E-08
15.0	112	1.1 E-07	9.1 E-08	1.3 E-07	22.5	5	5.0 E-09	9.9 E-10	9.9 E-09
Heading 22.5 degrees									
10.0	151836	4.3 E-04	4.3 E-04	4.3 E-04	25.0	32	9.0 E-08	5.9 E-08	1.2 E-07
12.5	15455	4.4 E-05	4.3 E-05	4.4 E-05	27.5	16	4.5 E-08	2.5 E-08	6.8 E-08
15.0	1388	3.9 E-06	3.7 E-06	4.1 E-06	30.0	4	1.1 E-08	2.8 E-09	2.3 E-08
17.5	288	8.1 E-07	7.2 E-07	9.1 E-07	32.5	2	5.6 E-09	0.0	1.4 E-08
20.0	115	3.2 E-07	2.7 E-07	3.8 E-07	35.0	1	2.8 E-09	0.0	8.5 E-09
22.5	55	1.6 E-07	1.2 E-07	2.0 E-07					
Heading 30 degrees									
10.0	741643	2.1 E-03	2.1 E-03	2.1 E-03	32.5	61	1.7 E-07	1.3 E-07	2.2 E-07
12.5	182749	5.2 E-04	5.1 E-04	5.2 E-04	35.0	33	9.3 E-08	6.2 E-08	1.3 E-07
15.0	33278	9.4 E-05	9.3 E-05	9.5 E-05	37.5	20	5.6 E-08	3.4 E-08	8.2 E-08
17.5	5443	1.5 E-05	1.5 E-05	1.6 E-05	40.0	14	4.0 E-08	2.0 E-08	6.2 E-08
20.0	1220	3.4 E-06	3.3 E-06	3.6 E-06	42.5	11	3.1 E-08	1.4 E-08	5.1 E-08
22.5	458	1.3 E-06	1.2 E-06	1.4 E-06	45.0	9	2.5 E-08	1.1 E-08	4.2 E-08
25.0	245	6.9 E-07	6.1 E-07	7.8 E-07	47.5	5	1.4 E-08	2.8 E-09	2.8 E-08
27.5	141	4.0 E-07	3.3 E-07	4.7 E-07	50.0	5	1.4 E-08	2.8 E-09	2.8 E-08
30.0	90	2.5 E-07	2.0 E-07	3.1 E-07					
Heading 37.5 degrees									
10.0	1592360	4.5 E-03	4.5 E-03	4.5 E-03	32.5	246	6.9 E-07	6.1 E-07	7.8 E-07
12.5	576395	1.6 E-03	1.6 E-03	1.6 E-03	35.0	159	4.5 E-07	3.8 E-07	5.2 E-07
15.0	165777	4.7 E-04	4.7 E-04	4.7 E-04	37.5	104	2.9 E-07	2.4 E-07	3.5 E-07
17.5	41487	1.2 E-04	1.2 E-04	1.2 E-04	40.0	75	2.1 E-07	1.7 E-07	2.6 E-07
20.0	10289	2.9 E-05	2.9 E-05	3.0 E-05	42.5	53	1.5 E-07	1.1 E-07	1.9 E-07
22.5	3077	8.7 E-06	8.4 E-06	9.0 E-06	45.0	37	1.0 E-07	7.3 E-08	1.4 E-07
25.0	1270	3.6 E-06	3.4 E-06	3.8 E-06	47.5	27	7.6 E-08	4.8 E-08	1.1 E-07
27.5	645	1.8 E-06	1.7 E-06	2.0 E-06	50.0	19	5.4 E-08	3.1 E-08	7.9 E-08
30.0	366	1.0 E-06	9.3 E-07	1.1 E-06	60.0	7	2.0 E-08	5.6 E-09	3.7 E-08
Heading 45 degrees									
10.0	6922060	5.7 E-03	5.7 E-03	5.7 E-03	35.0	1569	1.3 E-06	1.2 E-06	1.3 E-06
12.5	3005060	2.5 E-03	2.5 E-03	2.5 E-03	37.5	1020	8.4 E-07	7.8 E-07	8.9 E-07
15.0	1067330	8.7 E-04	8.7 E-04	8.8 E-04	40.0	699	5.7 E-07	5.3 E-07	6.1 E-07
17.5	339789	2.8 E-04	2.8 E-04	2.8 E-04	42.5	481	3.9 E-07	3.6 E-07	4.3 E-07
20.0	105381	8.6 E-05	8.6 E-05	8.7 E-05	45.0	332	2.7 E-07	2.4 E-07	3.0 E-07
22.5	35235	2.9 E-05	2.9 E-05	2.9 E-05	47.5	240	2.0 E-07	1.7 E-07	2.2 E-07
25.0	14082	1.2 E-05	1.1 E-05	1.2 E-05	50.0	182	1.5 E-07	1.3 E-07	1.7 E-07
27.5	6886	5.6 E-06	5.5 E-06	5.8 E-06	60.0	53	4.3 E-08	3.2 E-08	5.5 E-08
30.0	3955	3.2 E-06	3.1 E-06	3.3 E-06	70.0	8	6.6 E-09	2.0 E-09	1.1 E-08
32.5	2395	2.0 E-06	1.9 E-06	2.0 E-06	80.0	1	8.2 E-10	0.0	2.4 E-09

(continued)

**Table 2** (continued)

Target, deg	Observations	Est. of rate 1/s	Low boundary	Upper boundary	Target, deg	Observations	Est. of rate 1/s	Low boundary	Upper boundary
Heading 60 degrees									
10.0	12479700	1.2 E-02	1.2 E-02	1.2 E-02	35.0	3915	3.7 E-06	3.6 E-06	3.8 E-06
12.5	6077780	5.7 E-03	5.7 E-03	5.7 E-03	37.5	2521	2.4 E-06	2.3 E-06	2.5 E-06
15.0	2296420	2.2 E-03	2.2 E-03	2.2 E-03	40.0	1663	1.6 E-06	1.5 E-06	1.6 E-06
17.5	780867	7.4 E-04	7.3 E-04	7.4 E-04	42.5	1103	1.0 E-06	9.8 E-07	1.1 E-06
20.0	271082	2.6 E-04	2.5 E-04	2.6 E-04	45.0	763	7.2 E-07	6.7 E-07	7.7 E-07
22.5	100142	9.4 E-05	9.4 E-05	9.5 E-05	47.5	525	4.9 E-07	4.5 E-07	5.4 E-07
25.0	41660	3.9 E-05	3.9 E-05	4.0 E-05	50.0	353	3.3 E-07	3.0 E-07	3.7 E-07
27.5	19934	1.9 E-05	1.9 E-05	1.9 E-05	60.0	77	7.3 E-08	5.6 E-08	8.9 E-08
30.0	10748	1.0 E-05	9.9 E-06	1.0 E-05	70.0	18	1.7 E-08	9.4 E-09	2.5 E-08
32.5	6343	6.0 E-06	5.8 E-06	6.1 E-06	80.0	2	1.9 E-09	0.0	4.7 E-09
Heading 90 degrees									
10.0	9860070	8.1 E-03	8.1 E-03	8.1 E-03	27.5	788	6.5 E-07	6.0 E-07	6.9 E-07
12.5	3822120	3.1 E-03	3.1 E-03	3.1 E-03	30.0	279	2.3 E-07	2.0 E-07	2.6 E-07
15.0	869572	7.1 E-04	7.1 E-04	7.1 E-04	32.5	98	8.0 E-08	6.4 E-08	9.6 E-08
17.5	117329	9.6 E-05	9.6 E-05	9.7 E-05	35.0	33	2.7 E-08	1.8 E-08	3.6 E-08
20.0	20912	1.7 E-05	1.7 E-05	1.7 E-05	37.5	12	9.8 E-09	4.3 E-09	1.5 E-08
22.5	6376	5.2 E-06	5.1 E-06	5.3 E-06	40.0	3	2.5 E-09	0.0	5.2 E-09
25.0	2198	1.8 E-06	1.7 E-06	1.9 E-06	42.5	1	8.2 E-10	0.0	2.4 E-09
Heading 135 degrees									
10.0	3823600	3.1 E-03	3.1 E-03	3.1 E-03	17.5	444	3.6 E-07	3.3 E-07	4.0 E-07
12.5	597021	4.9 E-04	4.9 E-04	4.9 E-04	20.0	6	4.9 E-09	9.8 E-10	8.8 E-09
15.0	25444	2.1 E-05	2.1 E-05	2.1 E-05					

**Table 3** Tier-two and three validation of EPOT with GPD-tail

Target, deg.	Passing Rate		CD		RB	Target, deg.	Passing Rate		CD		RB
	CDF	Bnd.	CDF	Bnd.			CDF	Bnd.	CDF	Bnd.	
Heading 15 degrees											
10.0	0.84	0.88	0.70	0.78	0.22	17.5	0.64	0.72	1.61	1.97	0.49
12.5	0.74	0.84	1.28	1.51	0.53	20.0	0.62	0.72	1.97	2.35	1.71
15.0	0.68	0.78	1.45	1.76	0.38						
Heading 22.5 degrees											
12.5	1.00	0.98	0.21	0.25	-0.02	22.5	0.66	0.88	1.24	1.51	-0.22
15.0	0.86	0.94	0.68	0.74	-0.01	25.0	0.62	0.86	1.33	1.63	-0.27
17.5	0.78	0.92	0.98	1.14	-0.03	27.5	0.62	0.86	1.51	1.83	-0.11
20.0	0.70	0.88	1.12	1.34	-0.18						
Heading 30 degrees											
15.0	0.98	0.98	0.13	0.17	0.11	32.5	0.62	0.82	1.21	1.42	0.16
17.5	0.94	0.94	0.46	0.48	0.16	35.0	0.64	0.82	1.40	1.62	0.52
20.0	0.86	0.96	0.74	0.78	0.27	37.5	0.62	0.80	1.53	1.78	0.85
22.5	0.80	0.96	0.90	0.99	0.33	40.0	0.64	0.80	1.62	1.88	1.02
25.0	0.70	0.88	0.98	1.11	0.22	42.5	0.62	0.78	1.67	1.94	1.02
27.5	0.66	0.86	1.07	1.24	0.20	45.0	0.62	0.78	1.71	1.98	0.98
30.0	0.64	0.82	1.14	1.34	0.17						
Heading 37.5 degrees											
17.5	1.00	1.00	0.09	0.14	0.12	37.5	0.66	0.90	0.95	1.18	-0.22
20.0	0.96	0.96	0.34	0.38	0.11	40.0	0.62	0.88	1.02	1.26	-0.16
22.5	0.92	0.90	0.48	0.49	-0.09	42.5	0.66	0.88	1.09	1.35	-0.05
25.0	0.84	0.92	0.59	0.65	-0.24	45.0	0.60	0.88	1.20	1.45	0.12
27.5	0.82	0.92	0.67	0.78	-0.31	47.5	0.62	0.88	1.27	1.54	0.28
30.0	0.76	0.90	0.75	0.90	-0.32	50.0	0.64	0.88	1.37	1.65	0.55
32.5	0.70	0.90	0.78	0.97	-0.36	60.0	0.62	0.88	1.63	1.94	1.46
35.0	0.72	0.90	0.88	1.07	-0.31						
Heading 45 degrees											
20.0	0.98	1.00	0.23	0.28	0.31	40.0	0.90	0.98	1.22	1.32	0.81
22.5	1.00	1.00	0.43	0.48	0.40	42.5	0.90	0.98	1.31	1.43	1.04
25.0	0.98	0.98	0.60	0.60	0.42	45.0	0.90	0.98	1.42	1.55	1.35
27.5	0.98	0.98	0.73	0.73	0.42	47.5	0.90	0.98	1.51	1.65	1.65
30.0	0.96	0.96	0.83	0.86	0.40	50.0	0.90	0.98	1.58	1.73	1.89
32.5	0.90	0.98	0.93	0.98	0.45	60.0	0.90	0.98	1.97	2.14	4.34
35.0	0.90	0.96	1.02	1.09	0.50	70.0	0.90	0.98	2.66	2.87	20.82
37.5	0.90	0.98	1.12	1.21	0.66						

(continued)

**Table 3** (continued)

Target, deg.	Passing Rate		CD		RB	Target, deg.	Passing Rate		CD		RB
	CDF	Bnd.	CDF	Bnd.			CDF	Bnd.	CDF	Bnd.	
Heading 60 degrees											
20.0	1.00	1.00	-0.17	-0.13	0.01	40.0	0.88	0.92	0.83	0.92	-0.13
22.5	1.00	1.00	0.08	0.13	0.05	42.5	0.88	0.92	0.93	1.05	-0.04
25.0	0.98	0.98	0.24	0.28	0.03	45.0	0.88	0.92	1.03	1.16	0.05
27.5	0.94	0.94	0.35	0.38	-0.03	47.5	0.88	0.92	1.14	1.28	0.21
30.0	0.92	0.92	0.44	0.46	-0.10	50.0	0.88	0.92	1.25	1.41	0.43
32.5	0.92	0.90	0.54	0.56	-0.17	60.0	0.90	0.92	1.72	1.91	2.27
35.0	0.90	0.92	0.64	0.68	-0.18	70.0	0.90	0.94	2.21	2.43	7.59
37.5	0.88	0.92	0.73	0.80	-0.18						
Heading 90 degrees											
17.5	0.96	0.98	0.22	0.27	0.39	30.0	0.74	0.82	1.31	1.53	0.44
20.0	0.96	0.94	0.42	0.45	0.16	32.5	0.74	0.82	1.64	1.89	1.39
22.5	0.82	0.82	0.53	0.61	-0.16	35.0	0.74	0.82	2.00	2.28	3.47
25.0	0.74	0.82	0.74	0.89	-0.19	37.5	0.74	0.82	2.36	2.64	7.23
27.5	0.74	0.80	1.00	1.19	-0.02						
Heading 135 degrees											
15.0	0.98	1.00	0.42	0.45	0.21	20.0	0.72	0.88	2.56	2.89	5.29
17.5	0.80	0.86	1.25	1.44	0.32						

**Table 4** Tier-two and three validation of EPOT with Pareto-tail

Trg.	Passing Rate	CD	RB	Trg.	Passing Rate	CD	RB
Heading 15 degrees							
10.0	0.90	0.82	1.36	17.5	0.92	1.17	1.03
12.5	0.82	1.29	3.26	20.0	0.94	1.30	1.30
15.0	0.90	1.24	1.94				
Heading 22.5 degrees							
12.5	1.00	0.20	0.10	22.5	0.96	0.99	0.48
15.0	0.92	0.81	1.15	25.0	0.96	0.90	0.05
17.5	0.92	1.04	1.54	27.5	0.96	0.92	-0.05
20.0	0.96	1.03	0.95				
Heading 30 degrees							
15.0	0.98	0.04	0.06	32.5	0.86	0.78	0.09
17.5	0.92	0.52	0.63	35.0	0.86	0.87	0.18
20.0	0.92	0.83	1.34	37.5	0.86	0.91	0.20
22.5	0.90	0.93	1.39	40.0	0.86	0.90	0.09
25.0	0.90	0.91	0.94	42.5	0.88	0.84	-0.09
27.5	0.88	0.88	0.62	45.0	0.88	0.78	-0.24
30.0	0.86	0.84	0.33				
Heading 37.5 degrees							
17.5	1.00	-0.01	0.05	37.5	0.92	0.64	-0.14
20.0	0.96	0.34	0.33	40.0	0.86	0.59	-0.27
22.5	0.96	0.59	0.66	42.5	0.86	0.57	-0.35
25.0	0.94	0.69	0.70	45.0	0.86	0.57	-0.39
27.5	0.94	0.72	0.56	47.5	0.86	0.56	-0.45
30.0	0.92	0.72	0.38	50.0	0.86	0.58	-0.46
32.5	0.92	0.66	0.09	60.0	0.86	0.50	-0.62
35.0	0.92	0.64	-0.05				
Heading 45 degrees							
20.0	0.94	0.19	0.34	40.0	0.94	0.57	-0.08
22.5	0.92	0.40	0.52	42.5	0.94	0.57	-0.14
25.0	0.92	0.53	0.63	45.0	0.90	0.58	-0.17
27.5	0.92	0.59	0.57	47.5	0.88	0.58	-0.22
30.0	0.90	0.59	0.40	50.0	0.86	0.57	-0.29
32.5	0.94	0.59	0.25	60.0	0.86	0.65	-0.32
35.0	0.92	0.57	0.10	70.0	0.98	1.13	0.54
37.5	0.92	0.58	0.01				

(continued)

**Table 4** (continued)

Trg.	Passing Rate	CD	RB	Trg.	Passing Rate	CD	RB
Heading 60 degrees							
20.0	1.00	-0.23	0.00	40.0	0.94	0.36	-0.21
22.5	1.00	0.01	0.06	42.5	0.94	0.39	-0.24
25.0	1.00	0.17	0.12	45.0	0.90	0.40	-0.28
27.5	1.00	0.26	0.13	47.5	0.90	0.43	-0.29
30.0	0.98	0.31	0.08	50.0	0.90	0.48	-0.28
32.5	0.96	0.33	-0.01	60.0	0.94	0.70	-0.16
35.0	0.96	0.34	-0.08	70.0	0.98	0.97	0.17
37.5	0.94	0.35	-0.16				
Heading 90 degrees							
17.5	1.00	0.18	0.36	30.0	0.90	0.60	-0.28
20.0	1.00	0.41	0.36	32.5	0.92	0.76	-0.21
22.5	0.92	0.41	0.02	35.0	0.92	0.95	-0.01
25.0	0.92	0.43	-0.19	37.5	0.94	1.13	0.23
27.5	0.92	0.49	-0.28				
Heading 135 degrees							
15.0	0.98	0.53	0.82	20.0	0.28	2.80	108.57
17.5	0.68	1.60	9.37				

## References

1. Anastopoulos P, Spyrou KJ (2019) Can the generalized Pareto distribution be useful towards developing ship stability criteria? In: Proceedings of the 17th international ship stability workshop (ISSW 2019), 10–12 June, Helsinki, Finland
2. Anastopoulos PA, Spyrou K (2023) An efficient formulation of the critical wave groups method for the assessment of ship stability in beam seas. In: Spyrou K, Belenky V, Katayama T, Bačkalov I, Francescutto A (eds) Contemporary ideas on ship stability—from dynamics to criteria, Chapter 10. Springer, pp 157–174. ISBN 978-3-031-16328-9
3. Anastopoulos PA, Spyrou K (2023) Effectiveness of the generalized Pareto distribution for characterizing ship tendency for capsizing. In: Spyrou K, Belenky V, Katayama T, Bačkalov I, Francescutto A (eds) Contemporary ideas on ship stability—from dynamics to criteria, Chapter 15. Springer, pp 245–263. ISBN 978-3-031-16328-9
4. Beck RF, Reed AM (2001) Modern computational methods for ships in a seaway. *SNAME Trans* 109:1–51
5. Belenky VL (2000) Piecewise linear approach to nonlinear ship dynamics. In: Vassalos D, Hamamoto M, Papanikolaou A, Molyneux D (eds) Contemporary ideas on ship stability, Elsevier, ISBN 0-08-043652-8, pp149–160
6. Belenky V (2011) On self-repeating effect in reconstruction of irregular waves. In: Neves MAS, Belenky V, de Kat JO, Spyrou K, Umeda N (eds) Chapter 33 of contemporary ideas on ship stability, Springer, ISBN 978-94-007-1481-6, pp 589–598
7. Belenky V, Weems K, Pipiras V, Glotzer D, Sapsis T (2018) Tail structure of roll and metric of capsizing in irregular waves. In: Proceedings of 32nd symposium naval hydrodynamics, Hamburg, Germany
8. Belenky V, Glotzer D, Pipiras V, Sapsis T (2019) Distribution tail structure and extreme value analysis of constrained piecewise linear oscillators. *Probab Eng Mech* 57:1–13
9. Belenky V, Weems KM, Spyrou K, Pipiras V, Sapsis T (2023) Modeling broaching-to and capsizing with extreme value theory. In: Spyrou K, Belenky V, Katayama T, Bačkalov I, Francescutto A (eds) Contemporary ideas on ship stability—from dynamics to criteria, Chapter 26. Springer, pp 435–457. ISBN 978-3-031-16328-9
10. Beirlant J, Goegebeur Y, Teugels J, Segers J (2004) Statistics of extremes, Wiley Series in Probability and Statistics. John Wiley & Sons, Ltd., Chichester, UK, ISBN: 978-0-471-97647-9
11. Bickel PJ, Doksum KA (2001) Mathematical statistics: basic ideas and selected topics, vol 1. Prentice Hall, ISBN 978-0138503635
12. Bishop RC, Belknap W, Turner C, Simon B, Kim JH (2005) Parametric Investigation on the influence of GM, roll damping, and above-water form on the roll response of model 5613. Hydromechanics Department Report, Naval Surface Warfare Center Carderock Division, West Bethesda, Maryland, USA, NSWCCD-50-TR-2005/027
13. Boos DD, Stefanski LD (2013) Essential statistical inference: theory and method. Springer, ISBN: 978-1461448174
14. Campbell B, Belenky V, Pipiras V (2015) Properties of the tail of envelope peaks and their use for the prediction of the probability of exceedance for ship motions in irregular waves. In: Deodatis G, Spanos PD (eds) Proceedings of 7th international conference computational stochastic mechanics (CSM 7), ISBN: 978-981-09-5347-8. [https://doi.org/10.3850/978-981-09-5348-5\\_012](https://doi.org/10.3850/978-981-09-5348-5_012)
15. Campbell B, Belenky V, Pipiras V (2016) Application of the envelope peaks over threshold (EPOT) method for probabilistic assessment of dynamic stability. *Ocean Eng* 120:298–304
16. Coles S (2001) An introduction to statistical modeling of extreme values. Springer-Verlag, London, ISBN 978-1849968744
17. Dupuis DJ, Victoria-Feser M-P (2006) A robust prediction error criterion for Pareto modelling of upper tails. *Canadian J Statist* 34(2006):639–658
18. Glotzer D, Pipiras V, Belenky V, Campbell B, Smith T (2017) Confidence interval for exceedance probabilities with application to extreme ship motions. *REVSTAT Statist J* 15(4):537–563

19. International Maritime Organization, MCS.1/Circ.1627 Interim guidelines on the second generation intact stability criteria. London, 2020
20. International Maritime Organization, MSC.1/Circ.1652 Explanatory notes to the Interim Guidelines on second generation intact stability criteria. London, 2022
21. Lewis EV (ed) (1989) Principles of naval architecture, vol 3. Motions in waves and controllability. SNAME, Jersey City, p 429. ISBN 0-939773-02-3
22. Mager J (2015) Automatic threshold selection of the peaks over threshold method. Master's Thesis, Technische Universität München
23. McTaggart KA (2000) Ongoing work examining capsizes of intact frigates using time domain simulation. In: Vassalos D, Hamamoto M, Papanikolaou A, Molyneux D (eds) Contemporary ideas of ship stability, Elsevier, ISBN 978-0080436524, pp 587–595
24. McTaggart KA, de Kat JO (2000) Capsizes of intact frigates in irregular seas. *Trans SNAME* 108:147–177
25. Mohamad MA, Sapsis T (2018) Sequential sampling strategy for extreme event statistics in nonlinear dynamical systems. *Proc Nat Acad Sci USA (PNAS)* 115(44):11138–11143
26. Pickands J (1975) Statistical Inference using extreme order statistics. *Ann Stat* 3(1):119–131
27. Pipiras V (2020) Pitfalls of data-driven peaks-over-threshold analysis: perspectives from extreme ship motions. *Probabilistic Eng Mech* 60:103053
28. Reed AM, Beck RF (2016) Advances in the predictive capability for ship dynamics in extreme waves. *SNAME Trans* 124
29. Smith TC (2019) Validation approach for statistical extrapolation. In: Belenky V, Neves M, Spyrou K, Umeda N, van Walree F (eds) Contemporary ideas on ship stability — risk of capsizing, Chapter 34. Springer, ISBN 978-3-030-00514-6, pp 573–589
30. Shigunov V (2017) Direct stability assessment: pragmatic solutions. *Ship Technol Res (Schiffstechnik)* 64(3):144–162
31. Themelis N, Spyrou KJ (2007) Probabilistic assessment of ship stability. *Tr. SNAME* 115:181–206
32. Tonguç E, Söding H (1986) Computing capsizing frequencies of ships in seaway. In: Proceedings of 3rd international conference on stability of ships and ocean vehicles, Gdansk, Poland, vol. 2, Add. 1, pp 51–60
33. Umeda N, Usada S, Mizumoto K, Matsuda A (2016) Broaching probability for a ship in irregular stern-quartering waves: theoretical prediction and experimental validation. *J Marine Sci Technol* 21:23–37
34. Weems K, Wundrow D (2013) Hybrid models for fast time-domain simulation of stability failures in irregular waves with volume-based calculations for Froude Krylov and hydrostatic forces. In: Proceedings of 13th international ship stability workshop, Brest, France
35. Weems K, Belenky V, Campbell B, Pipiras V (2023) Statistical validation of the split-time method with volume-based numerical simulation. In: Spyrou K, Belenky V, Katayama T, Bačkalov I, Francescutto A (eds) Contemporary ideas on ship stability—from dynamics to criteria, Chapter 14. Springer, pp 225–243. ISBN 978-3-031-16328-9



# Interpretation of Results of Numerical Simulation



Arthur M. Reed

**Abstract** Running a numerical simulation of motions in waves is in and of itself of little significance. The results of the simulation—the motion time histories—must be processed to produce statistical quantities if they are to be of any practical use. Techniques for dealing with time histories of non-rare and rare events are presented. In the realm of non-rare statistics, the techniques are further divided into statistics for the linear and nonlinear motion regimes. The focus of this paper is on non-rare events but predicting rare event statistics is discussed.

**Keywords** Simulation · Rare events · Single significant amplitude · Confidence interval

## 1 Introduction

The raw output from a time-domain simulation of motions in random seas is of little use, unless the simulation is lucky enough to encounter a rare event—a stability failure that results in the termination of the run. Thus, the simulations must be planned based on the expected outcomes from the simulations. This planning needs to establish objectives as to what will be achieved by performing the simulations.

Without belaboring the planning process, which is worthy of a paper of its own, it is assumed that the interest is in knowing the “average” motion amplitudes, the maximum motions that a vessel would be expected to experience, whether a vessel will have exceeded a particular motion threshold in given operational period in a given sea state or if it could be expected to suffer a stability failure over its lifetime. These are different questions, which are approached using different statistical techniques.

The first of these questions requires statistical analysis to determine an estimate of the single significant amplitude (SSA) motion amplitude and the confidence intervals on the SSA motion—the non-rare problem. The other questions, relating to

---

A. M. Reed (✉)

David Taylor Model Basin, Carderock Division, Naval Surface Warfare Center,  
Bethesda, MD, USA

e-mail: [arthur.m.reed.civ@us.navy.mil](mailto:arthur.m.reed.civ@us.navy.mil)

maximum motions and rare problem, will require either an extremely long computer simulation resulting, with a bit of luck, in a stability failure, or reliance on statistical extrapolation.

This paper will discuss the methods by which answers to both the non-rare and rare problems of seakeeping and ship stability are derived from the results of a time-domain simulation of motions in a random seaway. The problem of setting objectives and further planning will not be discussed.

## 2 The Non-rare Problem

In the case of simulations associated with a non-rare problem, either the “average” motions that a vessel will experience under a certain operational condition (loading condition, speed and heading) in a given sea state are computed, or the maximum motions that a vessel will experience in a given loading and operational condition in a specific sea state are determined. Either way, it is necessary to determine the “average” motions—the single significant amplitude (SSA) motions, so that further decisions can be made regarding the statistical approaches that will be employed.

The characterization of a vessel’s expected maximum motions in a given sea state and condition takes further statistical analysis—relatively simple or quite complex, depending on whether the motions are in the linear or nonlinear regime.

The process begins with the computation of the vessel’s motions for a minimal period of time, typically 3 h.<sup>1</sup> The length of time necessary to characterize the motions with a reasonable certainty is discussed in Reed [21]. Reed [21] shows that at least 1000–1200 motion responses are necessary—many more responses than

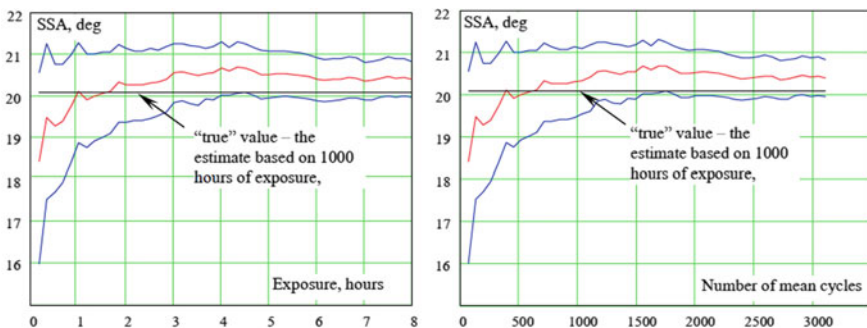


**Fig. 1** SSA convergence of predicted roll motion as a function of run length based on synthetic data generated by LS3DoF; left-hand figure as function of time, right-hand figure as a function of cycles. Courtesy of Vadim Belenky

<sup>1</sup> Unless otherwise noted, all times will be full-scale durations.

recommended in some other references that state that as few as 50 wave encounters are adequate.

For a seaway with a modal period of around 10 s, 1000 wave encounters requires around 3 h of data. However, it should be noted that a vessel does not respond to every wave encounter in every mode of motion, so that in fact it could require 25–30% longer than the 3 h to achieve the ideal 1000–1200 cycles of motion response. Figure 1 shows the convergence of the SSA for roll as both a function of time and number of wave encounters, using synthetic data generated using the volume-based computational tool, LS6DoF [26]. Based on this data, it might even be concluded that 6 h of data and 2500 wave encounters are required for convergence.

The motion computations can be a single run of 3 h duration, or could be an ensemble of several shorter runs totaling 3 h, say 9 20 min runs. If a single run is employed, then care must be taken to ensure that the autocovariance function of the incident wave train remains well behaved throughout the entire length of the simulation, without any repeats—this requires a great number of Fourier series terms if the seaway is represented by a series with random phases, which is the most common way of generating a seaway for simulations. On the other hand, if a number of shorter runs is used, to ensure that the runs are statistically independent, unique wave seeds must be used to initialize the seaway for each run.

To compute the SSA motions and confidence intervals for the motions of interest, the estimate of variance and estimate of variance of the variance of the motion time histories are computed [5, 15, 20]. Given the variance and the variance of the variance, the standard deviations of the motions are calculated as the square root of the variance and the SSA is twice the standard deviation. The confidence intervals follow in a similar manner, based on the confidence intervals of the variance. (See ITTC [15], for the details of computing the confidence intervals.)

If the only requirement is to predict the “average” motions, the SSA of the motions, that a vessel will experience while operating at a condition in a given sea state, this completes the process. This process must be repeated for every speed, heading to the seas, loading condition and seaway—significant wave height and modal period.

When it is necessary to predict the maximum motions that a vessel will experience in a given condition in a particular seaway or to determine whether a vessel will exceed a particular motion limit or criteria, then additional statistical analysis is required. Computationally and statistically both of these questions are answered in a similar manner. Assuring, with a reasonable confidence, that the vessel does not exceed an operational limit only requires comparing the expected maximum motions against the requirement to see if that limit will be exceeded.

The statistics used to predict the maximum expected motions depend on the magnitude of the motions that are expected and the vessel’s hull form. The magnitude of the motions and the hull form determines whether the statistics are being analyzed in the linear motion regime or the nonlinear motions regime, and thus the statistical models that are required.

## 2.1 The Process in the Linear Regime

If the motions are in the linear region, then the problem is simple, while if the motions are in the nonlinear regime, then statistical extrapolation must be employed. Significantly greater simulated time is required for predictions in the nonlinear regime. For roll, the motion which this paper will focus on, linearity depends on the GZ curve, linearity applies as long as the initial range of the GZ curve relatively constant slope—for virtually all vessels, it can be reasonably assumed that the motions are linear through 25° or 30°. <sup>2</sup> This is where the expected motion amplitude comes into play, if the vessel's motions will not exceed the linear response regime then it should not be necessary to simulate more than the 3 h of motions used to determine the SSA motions.

For motions in the linear regime the maximum expected motions are purely a function of the standard deviation ( $\sigma$ ) of the motions, and the only decision is whether to use  $\sigma$  or to be conservative and use a “ $\sigma$ ” based on the upper confidence limit for the motions. The key here is that linear ship motions are assumed to be Gaussian and for narrow banded seas, the motions are equally or even more narrow banded due to the ship being a well-tuned filter for those modes of motion for which there is a restoring force. Thus the extremes of the process are Rayleigh, and for linear statistics the extremes of the Rayleigh distribution are directly related to the standard deviation of the motions [17, 18].

For a given number of responses, there are available tables that give the expected extreme motions with a 95% confidence limit, i.e., 95% of the responses will be less than this limit ([25], p. 91). The 95% non-exceedance maximum amplitudes,  $\hat{y}_n$ , are:

$$\begin{aligned} n = 100 \quad \hat{y}_n &= 3.90\sqrt{m_0} \\ n = 1000 \quad \hat{y}_n &= 4.45\sqrt{m_0} \end{aligned}$$

where  $n$  is the number of cycles over which the limit is to apply and  $m_0$  is the variance of the motions ( $\sqrt{m_0}$  is the standard deviation). For motion limits,  $n = 1000$  is a good choice, as most storms only last about 3 h, which corresponds to approximately 1000 wave encounters. SNAME [25] provides no source for the above  $\hat{y}_n$  limits, but Eq. (6.19) of Ochi [17] provides a generalized formula for computing the limit:

$$\hat{y}_n = \sqrt{2 \ln(n/\alpha)} \sqrt{m_0} \quad (1)$$

where  $\alpha$  is the fraction of cycles that are to exceed the limit, and  $m_0$  is as before. In the table above  $\alpha$  is 0.05 ( $= 1 - 0.95$ ).

Equation (1) is sufficient to assess the expected motions of a vessel based on its motion time history. However, it can also be used to determine whether the vessel meets a limiting criteria, and to determine the acceptable SSA motions for a vessel to satisfy a criteria.

---

<sup>2</sup> Some vessels with high freeboard may have “s-shaped” GZ curves, and thus, experience nonlinear effects for smaller roll angles.

As a *totally fictitious* example, if there were a requirement that a cruise ship not exceed  $25^\circ$  of roll in a storm, the formula  $\hat{y}_n = 4.45\sqrt{m_0}$  could be inverted to determine that the SSA based on the computed motions should not exceed  $11.2^\circ$  ( $11.2^\circ = 25^\circ/2.225$ , where  $2.225 = 4.45/2$ ).

Based on the above, it is obvious that it is easy to assess and interpret the results of a simulation when the motions are in the linear regime. However, when the motions are extreme, and thus outside the linear regime, the interpretation becomes more complex and requires the simulation of longer time histories.

## 2.2 *The Process in the Nonlinear Regime*

In the event of needing to characterize non-rare motions in the nonlinear regime, requires the development of the statistical distribution of the motions that have been predicted so that the tail of the distribution can be evaluated to determine the probability of a certain motion level being exceeded. This is accomplished by fitting an appropriate statistical distribution to a histogram of the predicted motions, which in turn requires enough data for the histogram to represent the tail with sufficient fidelity.

There is not a good definition of what is enough data to determine the histogram fit for the tail of the distribution. The American Petroleum Institute (API) [1] in their guidance for model testing states that to characterize ship motions, 3 h of data should be collected, and that to characterize extremes that at least five times more data is required. Extending the API guidance for model testing to simulations and assuming that motions in the nonlinear regime are extreme motions, that would say that a minimum of 15 h of motion data is required. Weems et al. [28] have used 50 h of data for their studies on statistical extrapolation (obtained as 100 1/2 h data sets). However, they have not performed any convergence studies to determine minimum data requirements—they obtain satisfactory results with 50 h of data for their cases. So it appears that somewhere between 15 and 50 h of motions must be simulated for statistical extrapolation, *for each condition that includes nonlinear motions*. Yet other researchers have used 100 h of data [14].

As stated above, the statistical extrapolation process requires fitting a statistical distribution to a histogram of the time-history data from the simulation. Knowledge of the appropriate statistical distribution affects the amount of data required, as it influences the number of parameters that need to be determined to define the distribution for extrapolation. If the motions are in the linear range, then the normal distribution is appropriate and only one parameter needs to be determined, the standard deviation (as has been described above, statistical extrapolation is not required if the data is Gaussian). Figure 2 shows a histogram with a distribution fit and illustrates statistical extrapolation.

When the motions data is from the nonlinear range, then usually the most general of distributions, the generalized Pareto distribution (GPD) [19, 22] must be employed. The probability density function (*pdf*) of the GPD is:

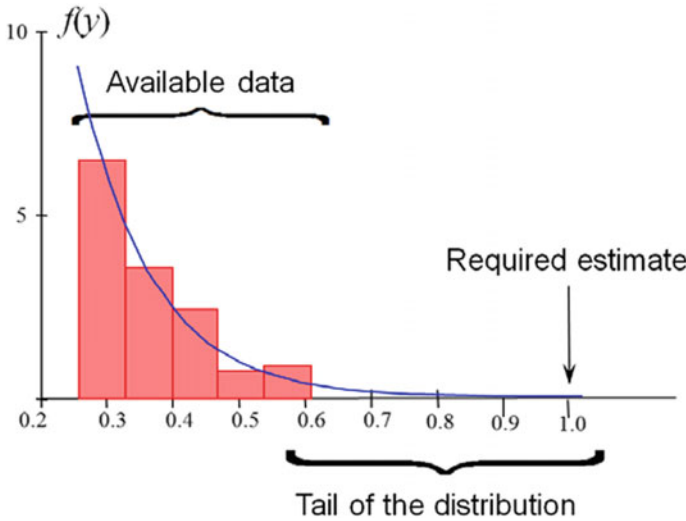


Fig. 2 Tail of histogram fit with a GPD, showing extrapolation [12]

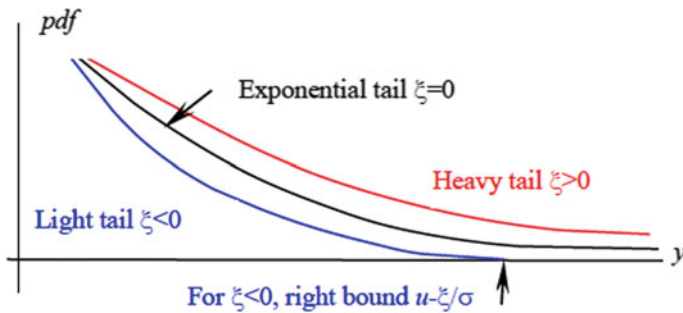


Fig. 3 Heavy and light tails of a distribution relative to an exponential distribution [10]

$$f_{(\xi, \mu, \sigma)}(x) = \frac{1}{\sigma} \left( 1 + \frac{\xi(x - \mu)}{\sigma} \right)^{\left( -\frac{1}{\xi} - 1 \right)}$$

for  $x \geq \mu$  when  $\xi \geq 0$ , and  $\mu \leq x \leq \mu - \sigma/\xi$  when  $\xi < 0$ ; where  $\xi$  is the shape,  $\mu$  is the threshold (also called the location in the literature) where GPD starts to be applicable and  $\sigma$  is the scale. For  $\xi = 0$  the GPD is the exponential distribution. If the tail of the distribution is above the exponential distribution the distribution has a “heavy” tail;  $\xi > 0$  and is defined for all  $x \geq 0$ . However, if the tail of the distribution lies below the exponential distribution the distribution has a “light” tail;  $\xi < 0$  and  $0 \leq x \leq -1/\xi$ . Figure 3 illustrates heavy and light tails relative to the exponential distribution.

The threshold is more of a parameter for the GPD, than a value defining the character of the distribution. The GPD is used to fit the tail of a distribution and is not appropriate for approximating an entire distribution over its whole range of support. Therefore, the choice of the threshold is not particularly critical to the fit of the distribution. If the threshold is chosen too small, portions of the underlying distribution that are inappropriate for defining the tail of the distribution will be included, and if too large a threshold is chosen, useful data for defining the tail will be excluded. Thus, several choices for the threshold should be tested and the smallest one that does not appear to affect the details of the tail chosen, as this should minimize uncertainty.

The scale and shape parameters are the ones that need to be fitted to define the tail of the GPD distribution. The need to accurately determine these parameters will have a significant influence on the length of the simulation that must be run—the amount of data required to fit these parameters with reasonable accuracy.

There are a number of papers that describe fitting a GPD to ship motions time history data. As it is necessary to only fit the tail of the histogram, these papers apply either one of two methods to exclude the majority of the data, the data that makes up the peak of the histogram. These methods are peaks over threshold (POT) and envelop peaks over threshold (EPOT).<sup>3</sup> In the EPOT approach, an envelope is constructed connecting the peaks and reflected troughs motion time history. The envelope can be determined by taking the Hilbert transform of the time history, or by brute force connecting the peaks and reflected troughs with straight lines—either is satisfactory for the purpose of determining the peaks above the threshold. Figure 4 shows an example of a POT using  $\pm 10^\circ$  as the threshold, and Fig. 5 shows an EPOT, for a heave time history. Either the POT or EPOT approach is acceptable, though one must use a statistically independent set of peaks, so the clustering that results from the POT is less ideal than the EPOT approach, as one must eliminate clustered (adjacent) peaks, selecting only the maximum from the cluster, when using the POT approach. All the papers mentioned in the following discussion use EPOT.

The earliest of the papers fitting a GPD to the data is Campbell et al. [12]. Smith and Zuzick [24] (and [23]) perform a formal validation of statistical extrapolation methods for predicting the tail of the distributions for roll, pitch, and vertical and lateral acceleration. They employ two methods to determine the confidence intervals of their fit distribution, one that assumes a normal distribution for the distribution of the scale and shape parameters, and the other follows the method used by Campbell et al. [12], except that they use the logarithm of the scale parameter to ensure that it remains positive. More recently Belenky et al. [3] have used the GPD to study the nature of the tail of the extreme roll distribution.

As the tail of the roll distribution is heavy [10], it is possible to make use of that fact to simplify the statistical extrapolation of roll by using a power law—Pareto distribution (PD) to fit the tail rather than the GPD. The *pdf* of the PD is defined as:

---

<sup>3</sup> A threshold selected for POT may not necessarily be the same as that chosen if an envelope is used as de-clusterization method, as in EPOT—although they will be similar.

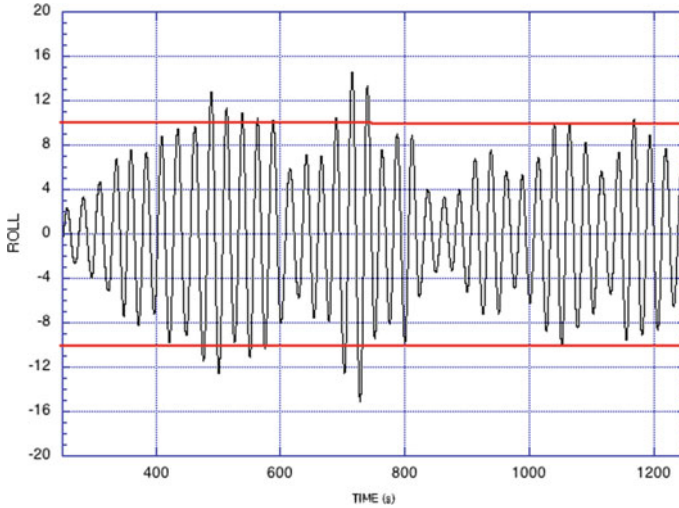


Fig. 4 Peaks over threshold (POT) for a roll time history, heavy horizontal lines are the threshold

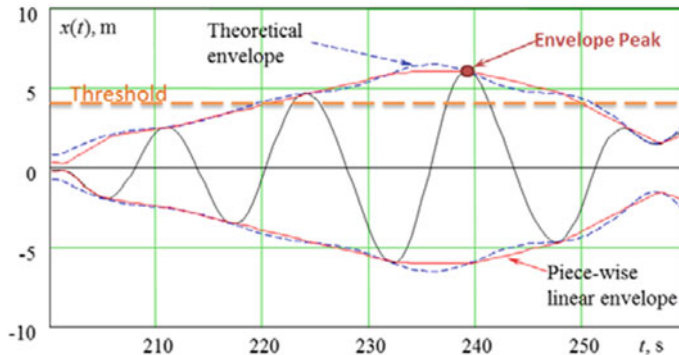


Fig. 5 Envelope peaks over threshold (EPOT) for a heave time history [12]

$$f_{(x_m, \alpha)}(x) = \frac{\alpha(x_m^\alpha)}{x^{1+\alpha}}$$

for  $x \geq x_m$ , where  $x_m$  is the threshold and  $\alpha$  is the exponent (equivalent to  $1/\xi$  in the GPD). The threshold of the PD serves the same function as the threshold of the GPD, so the PD only has one parameter, the exponent, that defines the tail, reducing the length of record (amount of data) needed to define the distribution, and there are rigorous methods for determining the exponent [2, 13, 16].

Glotzer et al. [14] have evaluated a number of methods for fitting the confidence interval (particularly the upper bound) for the exceedance probability in the GPD framework: the normal method, the lognormal method, the boundary method, the bootstrap method, the profile (likelihood) method, and the quantile method. Glotzer



et al. [14] use the maxim likelihood method for estimators  $\xi$  and  $\sigma$ , employing both direct and quantile methods. They conclude that the quantile method based on profile likelihood works best, and the bootstrap method the poorest. They also find that the normal and lognormal methods are slightly nonconservative.

In an effort to reduce uncertainty, Glotzer et al. [14] examine using knowledge of the expected motion responses to further refine the fit. In particular, they take advantage of the fact that if the roll exceeds a certain limit, then capsize will result, and the fact that pitch is typically limited to  $12^\circ$ – $15^\circ$ , based on the shape of the longitudinal GZ curve. These limits dictate that the shape parameter of the GPD will be negative and determine its value. Resulting in the need to fit only a single parameter, the scale parameter,  $\sigma$ .

### 3 The Rare Problem

It should be recognized that the simulation of a single stability failure is of little statistical significance—what if the vessel were to experience the 1-in-100,000 wave in the first few minutes of the simulation? And, in the case of predicting stability failures such as capsize in the dead-ship condition, one is seldom lucky enough to predict a failure in a reasonable length simulation. Proving that this is a truly rare stability failure in a random seaway, would require the simulation of many thousands of additional hours of motion histories. Therefore, another approach to predicting the occurrence of actual rare events is required.

The split-time method appears to be the most feasible way of assessing stability failure. However, it must be noted that the split-time method does not rely on a single time history of motions, but rather relies on repeated perturbations of a motion time history to identify upcrossings at high enough rates to result in a stability failure. This requires a custom modification of a motion simulation code and thus is beyond the scope of the effort defined by the title of this paper—interpretation of the results of a numerical simulation.

The split-time method was first reported in Belenky et al. [7, 11], where roll at zero speed in beam seas was analyzed. The essential idea behind the split-time method is that of breaking the motion responses into non-rare and rare portions. The motions are predicted in the usual manner until the predicted motion amplitude exceeds a preestablished threshold.<sup>4</sup> At this point the simulation is halted and the state recorded. Then the motion predictions are continued for a few cycles to see if the vessel returns to oscillating about its upright equilibrium position or proceeds to a stability failure. The motion predictions are then repeated from the state where the threshold was exceeded with the roll rate at the moment of exceedance perturbed upward or downward to identify the critical roll rate at up-crossing that defines the boundary between stable motion equilibrium and stability failure. Figure 6 illustrates this process.

---

<sup>4</sup> This threshold is *not* the same as the POT and EPOT methods' threshold, where the threshold is chosen based on different considerations.

**Fig. 6** Split-time method at zero speed in beam seas, showing extrapolations with different roll rates at the threshold—threshold is constant [6]

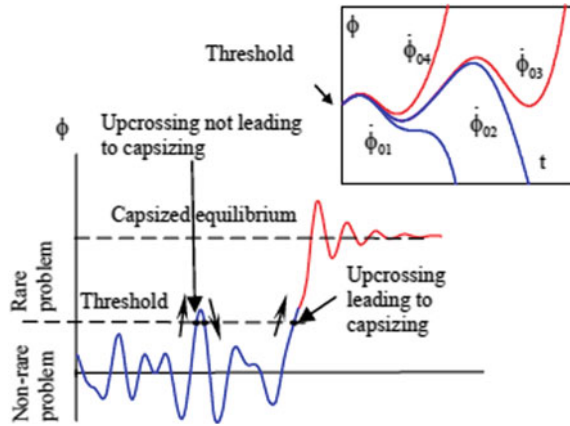
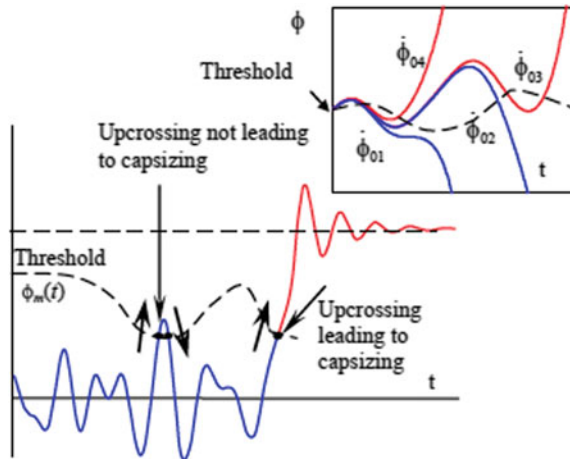


**Fig. 7** Split-time method at speed in bow quartering seas, showing extrapolations with different roll rates at the threshold—threshold varies with time (as a function of attitude on waves) [6]



A series of the “distances” of the roll rate from that dividing rate is used as a *metric* to define the exceedance rate, accumulated over an extended period of time 50–100 h, is fitted with a GPD to determine the exceedance rate. This process must be repeated multiple times to assure that the results are statistically consistent.

The problem described above is idealized, in that the righting-arm curve of a vessel in beam seas is essentially constant—like that of a vessel in calm water. In bow or stern quartering seas, the righting-arm curve becomes time varying, complicating the problem even further. The extension of the split-time method to an unsteady righting arm curve is illustrated in Fig. 7.

Belenky et al. [9] extended their split-time method model to forward speed in bow quartering seas to deal with this more complicated problem, of a time varying righting-arm curve and began to discuss the application of the split-time method to surf riding and broaching, Belenky et al. [6] further extended their bow quartering

seas and surf-riding analyses. Belenky et al. [4] extended split-time method to pure loss of stability in waves, which requires a rigorous assessment of the instantaneous roll restoring force in waves. All of the above work is summarized in Belenky et al. [8].

Weems et al. [27, 28] present a validation of the split-time method using a simplified model for predicting the motions, this simplified model allows the simulation of hundreds of thousands to millions of full-scale hours of motions in extreme seas in a few days. Each of these extended runs produces a few hundred stability failures, allowing the calculation of the “true” exceedance rates against which the results of the split-time method exceedance rates can be compared. Belenky et al. [10] use this data to study the tail of the distributions of the metric used to determine the critical roll rate.

## 4 Summary

The characterization of ship motions in the linear and nonlinear regimes is described. In the linear regime, the extremes can be easily characterized using the standard deviation of the motions. In the nonlinear regime, an extended simulation length is required for a reasonable prediction of the tail of the statistical distribution to be determined—this tail in turn can be evaluated to provide estimates of the probability of extreme motions. The Generalized Pareto Distribution and Pareto Distribution are used for these fits. To facilitate the fitting of the tail to a histogram of the motion data a peaks over threshold (POT) or preferably an envelope peaks over threshold (EPOT) technique is employed to eliminate the smaller motions from the histogram.

It is not reasonable to directly observe stability failures using a time-domain ship motion simulation tool. Therefore, advanced techniques such as the split-time method must be utilized. A high-level overview of the split-time method is provided with many references to the implementation of the method. Even with the use of the split-time method, the prediction of exceedance rates for stability failures is not trivial.

## References

1. API (2005) Design and analysis of stationkeeping systems for floating structures. Upstream segment. Recommended practice RP 2SK, 3rd edn. American Petroleum Institute, Washington, DC, pp vii+181
2. Beirlant J, Goegebeur Y, Segers J, Teugels JL (2004) Statistics of extremes: theory and applications. Contributions by De Waal D, Ferro C. Wiley Interscience, New York, pp xi+520
3. Belenky V, Glozter D, Pipiras V, Sapsis TP (2016) On the tail of nonlinear roll motions, chap 4. In: Proceedings of 15th international ship stability workshop, Stockholm, Sweden. STAB International Organizing Committee. Chalmers University of Technology and KTH Royal Institute of Technology, pp 109–114

4. Belenky V, Pipiras V, Weems KM (2013) Split-time method for calculation of probability of capsizing due to pure loss of stability. In: Proceedings of 13th international ship stability workshop, Brest, France, p 9
5. Belenky V, Pipiras V, Weems KM (2015) Statistical uncertainty of ship motion data. In: STAB2015 Secretariat (ed) Proceedings of 12th international conference on the stability of ships and ocean vehicles (STAB-15), Glasgow, UK, p 12
6. Belenky V, Spyrou KJ, Weems KM, Lin W-M (2012) Split time method for the probabilistic characterization of stability failures in quartering seas. In: Proceedings of 29th symposium on naval hydrodynamics, Gothenburg, Sweden, p 20
7. Belenky V, Weems KM, Lin W-M (2008) Numerical procedure for evaluation of capsizing probability with split time method. In: Proceedings of 27th symposium on naval hydrodynamics, Seoul, South Korea, p 25
8. Belenky V, Weems KM, Lin W-M (2016) Split-time method for estimation of probability of capsizing caused by pure loss of stability. *Ocean Eng* 122:333–343
9. Belenky V, Weems KM, Lin W-M, Spyrou KJ (2010) Numerical evaluation of capsizing probability in quartering seas with split time method. In: Proceedings of 28th symposium on naval hydrodynamics, Pasadena, CA, p 17
10. Belenky V, Weems KM, Pipiras V, Glotzer D, Sapsis TP (2018) Tail structure of roll and metric of capsizing in irregular waves. In: Kim K-H, Abdel-Maksoud M (eds) Proceedings of 32nd symposium on naval hydrodynamics, Hamburg, Germany. Office of Naval Research and the Hamburg University of Technology, Arlington, VA and Hamburg, Germany, p 18
11. Belenky V, Weems KM, Lin W-M (2007) A probabilistic procedure for evaluating the dynamic stability and capsizing of naval vessels, phase 1: technology demonstration. SAIC technical report ASTD 08-017. Science Applications International Corp., 211 pp
12. Campbell BL, Belenky V, Pipiras V (2014) On the application of the generalized Pareto distribution for statistical extrapolation in the assessment of dynamic stability in irregular waves. In: Proceedings of 14th international ship stability workshop, Kuala Lumpur, Malaysia, p 8
13. Dupuis DJ, Victoria-Feser M-P (2006) A robust prediction error criterion for Pareto modelling of upper tails. *Can J Stat* 34(4):639–658
14. Glotzer D, Pipiras V, Belenky V, Campbell B, Smith T (2017) Confidence intervals for exceedance probabilities with application to extreme ship motions. *REVSTAT Stat J* 15(4):537–563
15. ITTC (2017) Single significant amplitude and confidence intervals for stochastic processes. Recommended procedures and guidelines 7.5-02-01-08. Procedure. Version 1. In: International towing tank conference, 28 pp
16. Mager J (2015) Automatic threshold selection of the peaks over threshold method. Master's thesis, Technische Universität München, Munich, Germany, pp viii+106
17. Ochi MK (1998) Ocean waves: the stochastic approach. In: Dyer I, Eatock Taylor R, Newman JN, Price WG (eds) Cambridge ocean technology series 6. Cambridge University Press, Cambridge, UK, pp xii+319
18. Ochi MK, Motter L (1973) Prediction of slamming characteristics and hull responses for ship design. *Trans SNAME* 81:144–173
19. Pickands III J (1975) Statistical inference using extreme order statistics. *Ann Stat* 3(1):119–131
20. Pipiras V, Glotzer D, Belenky V, Levine M, Weems KM (2018) On confidence intervals of mean and variance estimates of ship motions. In: Umeda N, Katayama T, Maki A (eds) Proceedings of 13th international conference on the stability of ships and ocean vehicles (STAB'18), Kobe, Japan, pp 575–586
21. Reed AM (2020) Practical aspects of validating a six-degrees-of-freedom maneuvering in irregular waves code for extreme conditions. In: Spanos PD (ed) Probabilistic engineering mechanics 62, pp 103050-1–103050-11
22. Smith RL (1987) Estimating tails of probability distributions. *Ann Stat* 15(3):1174–1207
23. Smith TC (2019) Validation approach for statistical extrapolation, chap 49. In: Belenky VL, Spyrou KJ, van Walree F, Santos Neves MA, Umeda N (eds) Contemporary ideas on ship stability and capsizing in waves, 2018. Springer Nature Switzerland AG, Cham, Switzerland, pp 573–589

24. Smith TC, Zuzick A (2015) Approaches to ship motion simulation acceptance criteria. In: STAB2015 Secretariat (ed) Proceedings of 12th international conference on the stability of ships and ocean vehicles (STAB'15), Glasgow, UK, pp 1157–1170
25. SNAME (1989) Motions in waves, chap 8. In: Lewis EV (ed) Principles of naval architecture. Volume III. Motions in waves and controllability, vol 3. Society of Naval Architects and Marine Engineers, Jersey City, NJ, pp 1–190
26. Weems KM, Belenky V (2015) Rapid ship motion simulations for investigating rare stability failures in irregular seas. In: STAB2015 Secretariat (ed) Proceedings of 12th international conference on the stability of ships and ocean vehicles (STAB'15), vol 2. STAB2015 Secretariat, Department of Naval Architecture and Marine Engineering, University of Strathclyde, Glasgow, UK, pp 911–921
27. Weems KM, Belenky V (2018) Extended fast ship motion simulations for stability failures in irregular seas. In: Umeda N, Katayama T, Maki A (eds) Proceedings of 13th international conference on the stability of ships and ocean vehicles (STAB'18), Kobe, Japan, pp 587–597
28. Weems KM, Belenky V, Spyrou KJ (2018) Numerical simulations for validating models of extreme ship motions in irregular waves. In: Kim K-H, Abdel-Maksoud M (eds) Proceedings of 32nd symposium on naval hydrodynamics, Hamburg, Germany. Office of Naval Research and the Hamburg University of Technology, Arlington, VA and Hamburg, Germany, p 14

# **Parametric Roll, Operational Measures and Stability Monitoring**

# A Case Study on Operational Measures for Avoiding Parametric Rolling



Hirotsada Hashimoto, Yuuki Taniguchi, and Michio Fujii

**Abstract** Within the framework of the second-generation intact stability criteria finalised at the International Maritime Organization in 2020, ships that fail to pass either vulnerability criteria or direct stability assessment can still be operated by taking operational measures as a risk control option. The introduction of such operational measures is a new attempt to secure the safety of the ships at sea. Therefore, careful examinations and discussions based on various case studies are indispensable for their implementation in actual use. Therefore, a case study was conducted on the operational measures to avoid parametric rolling, which is one of five stability failure modes. In addition, an example of operational limitations related to significant wave height and simplified operational guidance for a C11 class container ship are presented. Finally, the voyage simulation was performed considering the operational limitations using a rather small maximum significant wave height. Consequently, the practicality of operational measures in terms of their influence on the navigation route and time is discussed.

**Keywords** Operational measures · Second-generation intact stability criteria · Ocean-going voyage simulation · Parametric rolling · Container ship

---

H. Hashimoto (✉)

Graduate School of Engineering, Osaka Metropolitan University, Sakai, Osaka, Japan

e-mail: [hashimoto.marine@omu.ac.jp](mailto:hashimoto.marine@omu.ac.jp)

Y. Taniguchi

Graduate School of Maritime Sciences, Kobe University, Kobe, Hyogo, Japan

M. Fujii

Agency of Maritime Education and Training for Seafarers, Marine Technical College, Ashiya, Hyogo, Japan

## 1 Introduction

The second-generation intact stability criteria (SGISc) were finalised at the 7th session of the International Maritime Organization (IMO) sub-committee on ship design and construction (SDC) [8]. In the SGISc, the risks of a ship's stability failure are evaluated at three levels for five stability failure modes: pure loss of stability, parametric rolling, surf-riding/broaching, dead ship, and excessive acceleration. Level 1 vulnerability criteria are quite simple in application and have the maximum safety margin among the three levels. The assessment complexity increases, while the safety margin decreases in the level 2 vulnerability criteria. The third level criteria are the so-called direct stability assessment (DSA), that requires highly complex calculations to assess the safety level of ships. Furthermore, the numerical simulation tools used for DSA must be validated quantitatively through comparisons with model experiments. Thus, the safety margin is minimal, and it can be applied to new types/concepts of ships.

If a ship fails to pass level 1 vulnerability criteria, it must pass level 2 or DSA criteria to guarantee the safety at sea. However, ships can be operated without passing any level criteria by taking operational measures (OM) as a risk control option [8]. OM consists of operational limitations (OL) and operational guidance (OG). The SGISc will temporarily be distributed as the maritime safety committee (MSC) circular, but it will be in Part B of the intact stability (IS) code after trial use to collect examples of its application.

Guaranteeing the safety of ships using a combination of passive design criteria and active operational measures is a new challenge [1]. Although there exist several studies on this problem, such as Hashimoto et al. [6], Liwång and Rosén [12], and Manderbacka [13], they have been rather limited in their scope. Therefore, the implementation of OM in actual operations and the extent to which operational efforts are needed to apply OM in a seaway requires further studies. To make OM useful and practically executable as a risk control option, a numerical investigation was conducted using a verified voyage simulation. This was done to provide application examples for the practical use of OL related to the maximum significant wave height and simplified OG.

In this study, a C11 class container ship was selected as the subject ship. Parametric rolling is one of the major stability problems for modern container ships. Therefore, OL related to significant wave height and simplified OG for avoiding parametric rolling are discussed based on application examples for the subject ship engaged in the trans-in Pacific Ocean. Subsequently, a voyage simulation with OL using a small maximum significant wave height as the operational limit is presented. Finally, the practicality of the operational measures is discussed, from various viewpoints such as the proportion of violations, changes in ship routes, and delays in navigation time.



## 2 Operational Measures

### 2.1 *Operational Limitations Related to Significant Wave Height*

Operational limitations related to the maximum significant wave height, permit operation in conditions up to a maximum significant wave height at which the ship can operate [8]. Here, a specified environment condition to be used for vulnerability assessment is that the wave occurrence over a specific significant wave height is neglected. To prepare operational limitations for operating to the maximum significant wave height, the environmental conditions applied in preparing the operational limitations should be consistent with the corresponding vulnerability criteria. If level 2 vulnerability criteria for parametric rolling are applied for preparing the operational limitations, the corresponding procedure of the vulnerability assessment, and the same standard value should be used. Operational limitations related to the maximum significant wave height can be developed with a limited wave scatter table, prepared by removing all the wave occurrence probabilities beyond a specific significant wave height from the original wave scatter table [7].

### 2.2 *Simplified Operational Guidance*

It is quite complicated to prepare an OG because DSA is required. Furthermore, OG is difficult to implement in actual operation because depending on the sea state, it is recommended to avoid a specified combination of ship speed and wave direction. Therefore, a simplified OG based on the vulnerability assessment has been made available [8], and it will be more practical in actual implementation. In the simplified OG, the dangerous conditions to be avoided can be determined from the numerical results of the vulnerability assessment and not from the DSA. Hence, the specified dangerous condition is rather simple. In this sense, the simplified OG seems to have an aspect of route selection in navigation rather than detailed ship handling at sea. In the simplified OG for the parametric rolling stability failure mode, it is recommended to avoid the forward speed at which severe parametric rolling could occur, i.e.  $C_{S,i} = 1$  in the level 2 vulnerability assessment, in all wave directions. Although the simplified OG is easier to prepare than OG, significant wave height and wave period are needed for route selection through weather forecasting.

### 2.3 *Level 2 Vulnerability Criteria for Parametric Rolling*

In the level 2 vulnerability criteria for parametric rolling, the vulnerability to the parametric rolling failure mode is determined using long-term stability failure indices

$C1$  and  $C2$ . A ship is considered not to be vulnerable to the parametric rolling failure mode if  $C1 \leq 0.06$  or  $C2 \leq 0.025$ . In this study, vulnerability checks using  $C1$  and  $C2$  criteria are referred to as “check 1” and “check 2”, respectively. A ship can be regarded as not vulnerable to the parametric rolling stability failure mode if one of the two checks passes. In the following sections, check 2 of the level 2 vulnerability criteria with the full wave scatter table are used for the vulnerability check. To evaluate the maximum roll angle due to parametric rolling in the head and following waves, a time-domain simulation method with a GZ curve calculated in the waves needs to be used. The short-term parametric rolling failure index for the respective wave cases,  $C_{S,i}(F_{ni}, \beta_i)$ , takes a value of 1 if the calculated maximum roll angle exceeds  $25^\circ$ .

## 2.4 Subject Ship

In this study, a C11 class container ship was selected as the subject ship because container ships are major players in international seaborne trade. Because modern container ships have a slender body, an exaggerated bow flare, and a transom stern; severe parametric rolling can occur in the longitudinal seas owing to the significant variation in transverse stability [14]. The principal particulars of the subject ship in the full-load condition are shown in Table 1. The hull form is similar to that of an actual ship that experienced parametric rolling at  $40^\circ$  in the North Pacific in 1998 [11]. The subject ship fails to pass check 1 and check 2 of the level 2 vulnerability criteria for parametric rolling, as shown in Table 2. Here, the roll damping is calculated using the simplified Ikeda’s method. This result is reasonable because the required value was set to reject the accident ship. Therefore, a ship master must decide whether the loading condition is to be changed, or whether operational measures are to be applied to avoid parametric rolling stability failure before departure.

**Table 1** Principal particulars of a C11 class container ship

Length between perpendiculars: $L_{pp}$	262.0 m
Breadth: $B$	40.0 m
Draught: $d$	11.5 m
Depth: $D$	24.45 m
Total projected area of bilge keels: $A_{BK}$	30.6 m <sup>2</sup>
Ship service speed: $V$	20.0 kt
Metacentric height: $GM$	1.965 m
Designed natural roll period: $T_\phi$	25.1 s

**Table 2** Level 2 vulnerability checks for the sample ship for parametric rolling

Index	Required value	Remark
C1 = 0.4368	$R_{PR1} = 0.06$	Fail
C2 = 0.02592	$R_{PR2} = 0.025$	Fail

### 3 Ocean-Going Voyage Simulation

#### 3.1 Simulation Model

In this study, a ship voyage simulation model was used to examine the effectiveness of OM and its influence on actual navigation. The voyage simulation is based on a simulation model originally developed for weather routing [10]. A ship horizontal manoeuvring motion was calculated by solving a 3 degrees of freedom (DOF) mathematical model based on the so-called Manoeuvrings Modelling Group (MMG) model [16] which considers the hydrodynamic forces with respect to the ship hull, propeller, rudder, and their interaction components. The ship arrival point was calculated by Mercator’s sailing from the moving distance and course, which were obtained by solving the equations of manoeuvring motion. Hydrodynamic forces from ocean currents, winds, and added resistance in waves were considered to be external forces acting on the ship hull. The wind pressure was calculated using an empirical formula [3], and the added wave resistance was calculated using the enhanced unified theory [9]. With respect to ocean currents, 5 d average data with a longitude interval of  $1.0^\circ$  and a latitude interval of  $1.0^\circ$  were used, which were supplied by the American National Oceanic and Atmospheric Administration (NOAA). With respect to winds and waves, 6 h of data supplied by the American National Centers for Environmental Prediction (NCEP) were used. The obtained longitude interval was  $1.25^\circ$  and the latitude interval was  $1.0^\circ$ . The Powell method, which is an unconstrained nonlinear optimisation method [15], was used to search for the optimum route that minimises an evaluation function, such as the amount of fuel consumption. Bezier curve was used to conveniently express complicated route curves with a small number of control points. In a voyage simulation taking OM into account, a large penalty fee was given each time a ship stays in a specified dangerous condition. The penalty fee is set at 280,000 USD/minute which could be regarded as the economic loss of containers due to damage or loss as a consequence of severe parametric rolling. The value was estimated by dividing the total worth of damaged or lost containers, 50 million USD [5] in case of the actual accident of the C11 class container ship in 1998 [4], by the duration of short-term sea state, 3 h. In this study, the optimum route was pursued to minimise the objective function, that is, the total operational cost (fuel cost + penalty fee). It was found that the most economical route could be derived by considering OM. Obviously, the voyage route with OM does not change from that without OM if the ship never meets a specified condition to be avoided throughout the navigation.

### 3.2 Level 2 Vulnerability Assessment and Operability

To prepare a simplified OG, dangerous conditions in which parametric rolling exceeding  $25^\circ$  occur were determined based on check 2 of level 2 vulnerability assessment using the standard wave scatter table. The specified dangerous conditions  $C_{s,i} = 1$  for the subject ship are shown in Fig. 1. Here,  $F_n$  denotes the Froude number corresponding to ship speed,  $H_s$  is the significant wave height, and  $T_z$  is the average zero-crossing wave period. The heading angle of  $0^\circ$  indicates that a ship sails in the following waves, while  $180^\circ$  indicates a direction in head waves. To accept operational measures, the ratio of the total duration of situations to be avoided to the total operation time, should be less than 0.2 [8]. In the case of the simplified OG for the subject ship, the probability of danger could be obtained by dividing the sum of  $CR$  in Table 3 by the number of divisions of ship speed, that is, 25 in the level 2 vulnerability assessment. By dividing the sum of  $CR$  by 25, the probability of situations to be avoided was calculated as 0.03695, which is less than 0.2. Therefore, the ship could navigate by following a simplified OG for the tested loading conditions.

### 3.3 Condition for Voyage Simulation

A case study using voyage simulation was performed for the subject ship engaged in trans-Pacific services between Yokohama and San Francisco in winter. The ship speed in calm water was set as 20 knots,  $F_n=0.203$ , and it varied depending on disturbances such as waves, currents, and winds. In the voyage simulation, a navigation route that minimises the operational cost, including the penalty fee for violation, was obtained such that the simulated result represented a possible ocean-going voyage taking the OM, which was a recommendation to avoid the specified dangerous conditions for parametric rolling.

### 3.4 Validation of Voyage Simulation

For the numerical investigation of OM, the validity of the voyage simulation should first be demonstrated. Therefore, the simulation results were compared with actual navigation records, which were derived from automatic identification system (AIS) data collected by satellites from 2015 to 2016. Satellite AIS data were purchased from ExactEarth (<https://www.exactearth.com>). The ship length was obtained from the static data of the AIS data and was used to estimate its performance by converting the performance of a reference ship using a scale ratio. The average navigation speed was obtained from the dynamic data of the AIS data. To obtain numerical results for comparison with the actual navigation data, environmental data such as ocean currents, winds, and waves were prepared for the period corresponding to the AIS

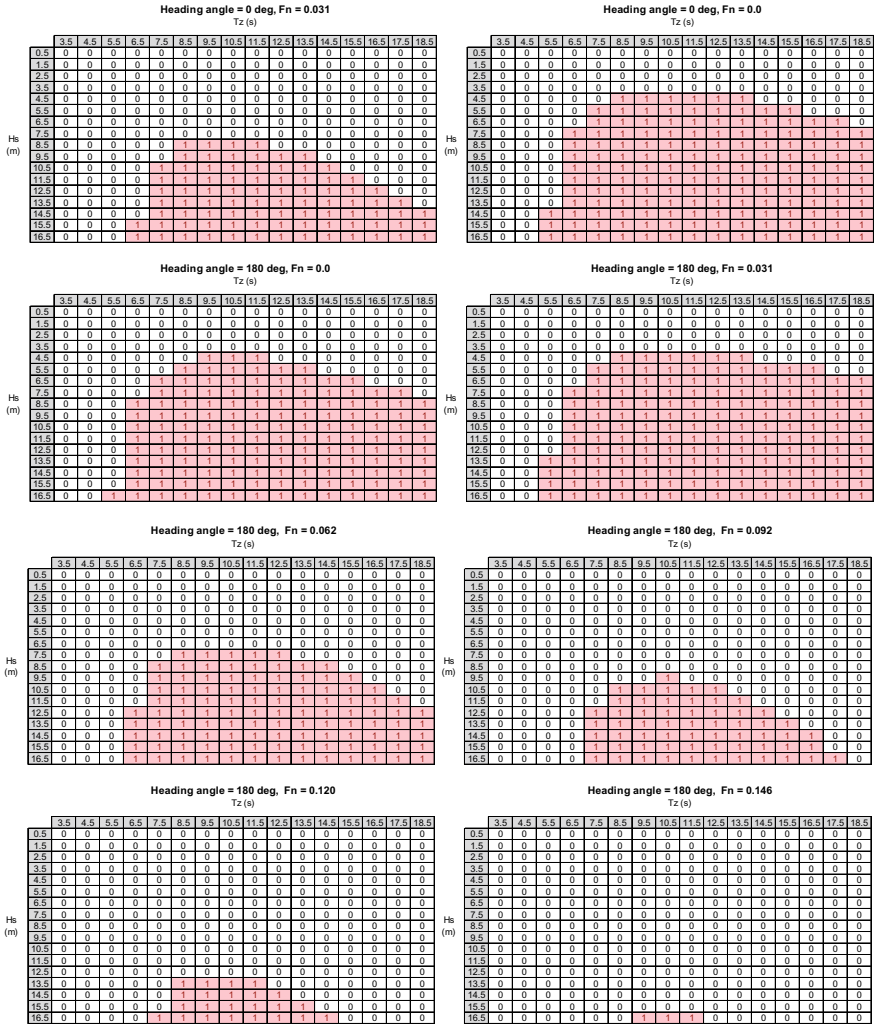


Fig. 1  $C_{S_i}$  value in level 2 vulnerability assessment

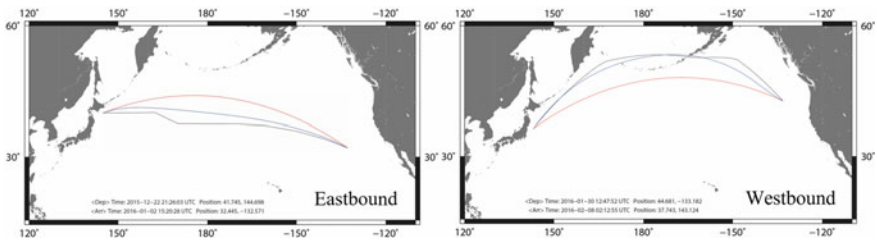
data. Navigation simulations were performed with the same departure time, departure place, and destination.

Figure 2 shows an example of the comparison results of a randomly selected container ship in the North Pacific route in winter. In the figure, the great circle shows the route with the shortest navigation distance. If there was no disturbance, a voyage route matches the great circle in general, but the actual and simulated voyage routes were different from the great circle. Because the present simulation took the route that minimised the operational cost and the safety margin for the uncertainty of weather forecast is not considered, the voyage simulation avoided the harsh areas

**Table 3** Weighted criteria at each ship’s speed

Heading angle (deg)	$F_n$	$CR = W_i C_{S,i}$
0	0.031	0.02081
0	0.0	0.29772
180	0.0	0.25342
180	0.031	0.29774
180	0.062	0.04781
180	0.092	0.00594
180	0.120	0.00019
180	0.146	0.00000
Sum of CR		0.92363

$W_i$ : weighting factor for the respective wave cases  
 $W_i C_{S,i} = 0$  in other conditions



**Fig. 2** Comparison of navigation routes between AIS data and voyage simulation (Red: great circle, black: AIS data, blue: simulation)

with minimum safety margins. However, in general, the present voyage simulation could reproduce the actual navigation qualitatively in severe weather. Therefore, it is used for the discussion on OM in the latter sections. Detailed information and statistical validation of the voyage simulation can be found in the literature [2].

## 4 Results and Discussions

### 4.1 Preparation of Operational Limitations Related to Significant Wave Height

To begin with, the cumulative probability with respect to the significant wave height was calculated, as shown in Table 4. The wave occurrence probability was derived from the standard wave scatter table referred to in check 2 of the level 2 vulnerability criteria for parametric rolling. From the viewpoint of operability, the ratio of the

**Table 4** Cumulative probability of wave up to a specified significant wave height

$H_{1/3}$ (m)	Probability of wave occurrence	Cumulative probability
0.5	0.030504	0.03050
1.5	0.225754	0.25626
2.5	0.238104	0.49436
3.5	0.191277	0.68564
4.5	0.132894	<b>0.81853 &gt; 0.8</b>
5.5	0.083281	0.90181
6.5	0.048063	0.94988
7.5	0.025862	0.97574
8.5	0.013087	0.98883
9.5	0.006262	0.99509
10.5	0.002848	0.99794
11.5	0.001236	0.99917
12.5	0.000511	0.99968
13.5	0.000205	0.99989
14.5	0.000077	0.99997
15.5	0.000028	0.99999
16.5	0.000009	1.00000

total duration of situations to be avoided to the total operational time needs to be smaller than 0.2 when applying operational measures for navigation. To satisfy this requirement in the operational limitations related to significant wave height, the cut-off significant wave height must be equal to or greater than 5.0 m as long as the check 2 of level 2 vulnerability criteria with the standard wave scatter table are used. When the specified significant wave height for cutting-off is 5.0 m, the allowable maximum significant wave height for operation is 5.0 m.

Secondly, check 2 of the level 2 vulnerability criteria for parametric rolling was applied to the preparation of operational limitations. The results of the vulnerability check presented in Table 5 indicate that the maximum navigable significant wave height is 10.0 m for the subject ship/condition. The significant wave height for cutting-off was obtained as 10.0 m, which was greater than 5.0 m, as shown in Table 5. Therefore, operational limitations with a maximum significant wave height of 10.0 m could be applied for operation. It should be noted that the allowable maximum significant wave height becomes smaller if the probability of wave occurrence is renormalized after neglecting the probability above the specified value in order to satisfy the total probability of 1.0. The same procedure is also applicable for a specific wave scatter table approved by the administration.

**Table 5** Level 2 vulnerability check with limited wave scatter diagrams

Cut-off $H_{1/3}$ (m)	Maximum operable $H_{1/3}$ (m)	C2	Remark
5.0	5.0	0.00858	Pass
6.0	6.0	0.01509	Pass
7.0	7.0	0.01892	Pass
8.0	8.0	0.02194	Pass
9.0	9.0	0.02391	Pass
10.0	10.0	0.02496	Pass
11.0	11.0	0.02551	Fail
12.0	12.0	0.02575	Fail
13.0	13.0	0.02585	Fail
14.0	14.0	0.02590	Fail
15.0	15.0	0.02591	Fail
16.0	16.0	0.02592	Fail
None	–	0.02592	Fail

### 4.2 Voyage Simulation with Simplified Operational Guidance

Voyage simulation was performed using a simplified OG to avoid parametric rolling. As a sample case engaged in the trans-Pacific during winter, three departure dates, 6 December 2008 and 10 and 17 January 2009, were selected. Table 6 shows the maximum and average of the significant wave height and mean wave period encountered in a voyage sailing along the great circle. When the departure date is 10 January the average significant wave height was 5.24 m in eastbound, which was a very severe condition in the top 3% of the North Pacific during the specified winter season.

Figures 3 and 4 show the numerical results of the eastbound and westbound navigations with the simplified operational guidance. The voyage time along the simulated route changed depending on the weather. The numerical results were the

**Table 6** Sea state in voyage simulation

Eastbound			
Date of departure	Max. $H_{1/3}$ (m)	Ave. $H_{1/3}$ (m)	Ave. $T_z$ (s)
6/12/2008	5.41	3.62	7.38
10/1/2009	9.60	5.24	10.10
17/1/2009	5.68	3.50	9.29
Westbound			
6/12/2008	7.41	3.54	8.91
10/1/2009	8.32	4.53	9.40
17/1/2009	6.15	3.66	9.42



optimum voyage routes in terms of total operational cost (fuel cost + penalty fee), while they were exactly the same with the results only in terms of fuel oil consumption for all departure dates. This meant that the voyage route with a simplified OG does not change operations for the subject ship, even in winter. As presented in Fig. 1, parametric rolling exceeding 25° occurred mostly at a low Froude number, less than 0.1. The minimum Froude number derived along the simulated route was 0.183 in the eastbound cases and 0.173 in the westbound cases; thus, the ship could navigate without any restrictions from the simplified OG. This is because the optimum route in terms of fuel consumption tended to avoid severe head sea conditions trying not to reduce the ship speed due to added wave resistance.

The simulated result was quite interesting because the risk of stability failure due to parametric rolling could be effectively controlled by operational efforts, while it was difficult to do so with only the design criteria. However, a ship may suffer severe parametric rolling if intentional reduction of the ship’s speed is commanded in the seaway for other reasons. In summary, the voyage simulation results demonstrated the potential of operational measures to secure safety in actual navigation, but a concern about intentional speed reduction should be addressed in some cases. Further research and discussion on the OG, as well as developing an advanced on-board or land support system dedicated to OM are needed for future applications.

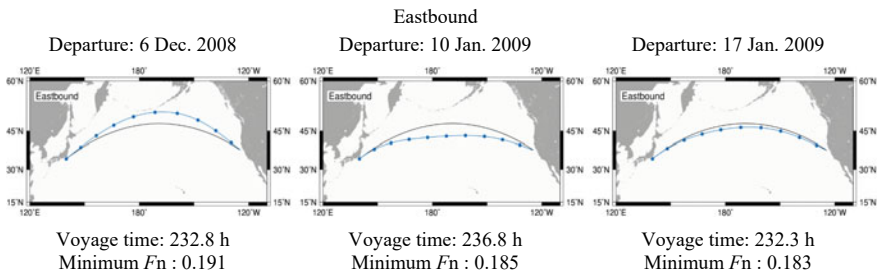


**Fig. 3** Voyage route with simplified operational guidance (Eastbound) (Black: great circle, blue: voyage simulation)

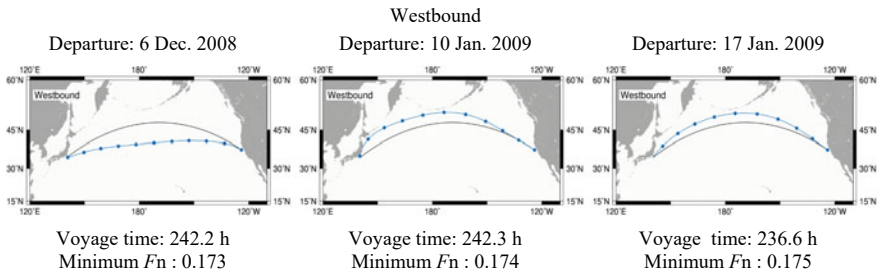


**Fig. 4** Voyage route with simplified operational guidance (Westbound) (Black: great circle, blue: voyage simulation)

### ***4.3 Voyage Simulation with Operational Limitations Related to Maximum Significant Wave Height***

For the full load condition of the subject container ship, the maximum operable significant wave height was 10 m, as shown in Table 5. A ship master does not have any operational restrictions unless the ship enters the sea area with a significant wave height of 10 m or more. A voyage simulation with this limit value was executed, but the simulated voyages were the same as those with the simplified OG as shown in Figs. 3 and 4. This was because the probability of significant wave height over 10.0 m was rare and the optimal route in terms of fuel consumption avoided such stormy areas. However, this is only a result for the full load condition, and a more critical situation was studied for further discussion.

As a case study, the maximum significant wave height for operation was assumed to be 6.0 m because this was the threshold value at which ship masters try to avoid the head sea in the North Pacific [2]. In this case, the significant wave height for cutting-off was 6.0 m, which was greater than 5.0 m, as discussed in Table 4, so that the ship can navigate with OL. The numerical results of the voyage simulation with OL using 6.0 m as the operable limit are shown in Figs. 5 and 6. As described in Sect. 3.1, a large penalty fee was given if the ship stays in the specified dangerous condition, so that a voyage route with OL could be obtained as the optimal route to minimise the operational cost, including the penalty fee. In the figures, GC denotes the great circle, FOC denotes the optimal route without penalty fee, and OL represents the route with a penalty fee due to violation of OL. The OL voyage route differs from that of FOC for three cases, and the most significant changes appear in the case at the departure date of 10 January 2009. This meant that a ship master had to give significant attention during navigation to ensure safety against parametric rolling. Figure 7 shows the simulated results of voyage time and the proportion of situations in danger. From this figure, it was confirmed that the optimum route in terms of FOC resulted in less voyage time than that of GC. It might be expected that the proportion of situations in danger naturally decreases in FOC routes, but this is not true, and the departures on 10 January 2009 in eastbound and 17 January 2009 in westbound stand as testimonials. This signified that a ship master needs special attention to satisfy the OL when the maximum operable wave height is rather small. For the departure on 10 January 2009 the proportion of violations was about 25% in GC and over 30% in FOC, but it became 2.5% in OL by operational efforts. Accordingly, the arrival time was delayed by 10 h or more, but this might be an acceptable delay to avoid stability failure leading to container damage or loss. In westbound at the same departure date, the voyage with OL could reduce the proportion of situations in danger to almost zero with only 2.5 h delay. These results suggested that OL with a rather small limit of significant wave height could still be executable, but dedicated attention/efforts to avoid danger are necessary in severe sea states.

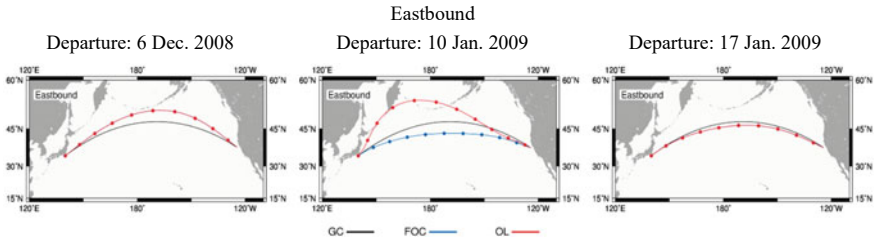


**Fig. 5** Voyage route with operational limitations related to maximum significant wave height using 6.0 m as the operable limit (Eastbound)

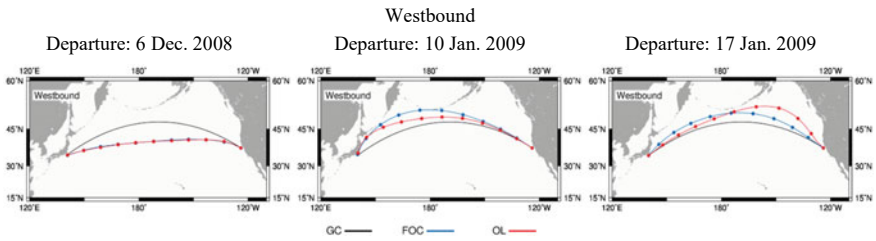


**Fig. 6** Voyage route with operational limitations related to maximum significant wave height using 6.0 m as the operable limit (Westbound)

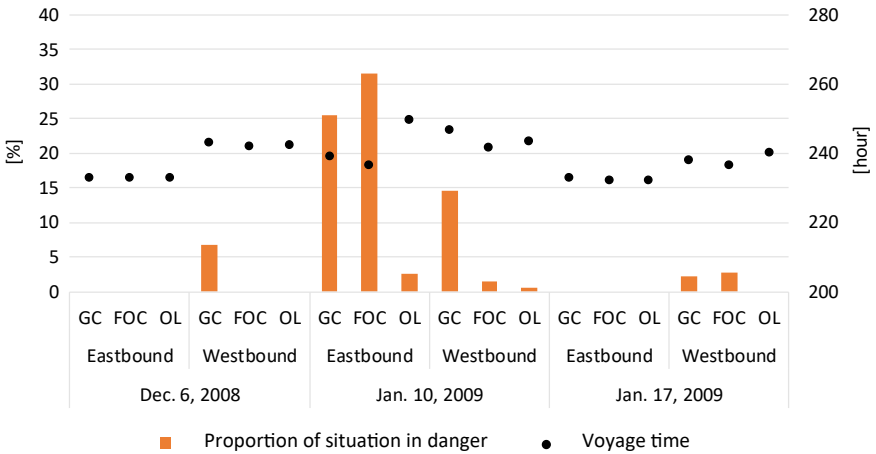


**Fig. 7** Voyage result with operational limitations related to maximum significant wave height using 6.0 m as the operable limit

## 5 Conclusions

A case study on operational measures in the second-generation intact stability criteria was conducted, and application examples of operational limitations related to maximum significant wave height and simplified operational guidance for avoiding parametric rolling were demonstrated for a C11 class container ship.

For the operational limitations related to the maximum significant wave height, the tolerance limit of the significant wave height for cutting-off was derived to satisfy the operability requirement. The operable maximum significant wave height was 10.0 m for the subject ship/condition. For simplified operational guidance, voyage simulation in the North Pacific demonstrated good potential for operational measures to secure safety against parametric rolling. However, concerns regarding the intentional speed reduction should be addressed. Operational limitations with a rather small maximum significant wave height was also investigated using voyage simulation. The simulation results, including the voyage route, voyage time, and the violation rate of OL, suggested that OL with 6.0 m of significant wave height for the operable limit could still be executable, but dedicated attention/efforts to avoid danger are necessary.

A similar study needs to be conducted for different types of ships and other stability failure modes for further discussion of actual applications. It is also important to develop an advanced on-board/on-land support system in future applications for ship masters to make appropriate decisions on-board.

**Acknowledgements** This work was carried out as a research activity of the Goal-Based Stability Criteria Project of Japan Ship Technology Research Association in the fiscal years from 2016 to 2020, funded by the Nippon Foundation. This study was partially supported by JSPS KAKENHI Grant Numbers 15H02327 and 17H03493. The authors sincerely thank Prof. Naoya Umeda from Osaka University for useful discussions and technical advice.

## References

1. Bačkalov I, Bulian G, Rosén A, Shigunov V, Themelis N et al (2016) Improvement of ship stability and safety in intact condition through operational measures: challenges and opportunities. *Ocean Eng* 120:353–361
2. Fujii M, Hashimoto H, Taniguchi Y, Kobayashi E (2019) Statistical validation of a voyage simulation model for ocean-going ships using satellite AIS data. *J Mar Sci Technol* 24:1297–1307
3. Fujiwara T, Ueno M, Nimura T (1998) Estimation of wind forces and moments acting on ships. *J Soc Naval Architects Japan* 183:77–90 (in Japanese)
4. France WN, Levadou M, Treacle TW et al, An investigation of head-sea parametric rolling and its influence on container lashing systems. *Marine Technol* 40(1):1–19
5. Ginsberg S (1998) Lawsuits rock APL's boat—Cargo goes overboard; insurance lawyers surface
6. Hashimoto H, Taniguchi Y, Fujii M (2017) A case study on operational limitations by means of navigation simulation. In: *Proceedings of the 16th international ship stability workshop, Belgrade*, pp 41–48

7. International Association of Classification Societies (IACS) (2001) Recommendation No. 34, Standard Wave Data. IACS Rec. 2000/Corr
8. IMO (2020) Interim guidelines on the second generation intact stability criteria. MSC.1/Circ.1627, London
9. Kashiwagi M (1992) Added resistance, wave-induced steady sway force and yaw moment on an advancing ship. *Ship Technol Res* 39(1)
10. Kobayashi H, Hashimoto H, Taniguchi Y, Yoneda S (2015) Advanced optimized weather routing for an ocean-going vessel. In: Proceedings of the 2015 international association of institutes of navigation world congress, Prague
11. Levadou M, van't Veer R (2006) Parametric roll and ship design. In: Proceedings of the 9th international conference of ships and ocean vehicles, Hamburg, 1, pp191–206
12. Liwång H, Rosén A (2018) A framework for investigating the potential for operational measures in relation to intact stability. In: Proceedings of the 13th international conference on stability of ships and ocean vehicles, pp 488–499, Kobe
13. Manderbacka T (2019) On the uncertainties of the weather routing and support system against dangerous conditions. In: Proceedings of the 17th international ship stability workshop, Helsinki, pp 97–101
14. Paulling JR (2011) Parametric rolling of ships—then and now. *Fluid Mech Appl* 97:347–360
15. Powell MJD (1964) An efficient method for finding the minimum of a function of several variables without calculating derivatives. *Comput J* 7(2):155–162
16. Yasukawa H, Yoshimura Y (2015) Introduction of MMG standard method for ship maneuvering predictions. *J Mar Sci Technol* 20:37–52

# Wave Radar Application to the Simplified Parametric Roll Operational Guidance at Actual Sea



Takehiro Yano, Naoya Umeda, Keiichi Hirayama, Mitsunori Baba,  
and Masahiro Sakai

**Abstract** The authors executed measurements of the encounter waves by an X band wave radar and the roll angles by a gyro sensor onboard for a Ropax ship. By using the measured wave spectrum, the roll amplitude is estimated by using the simplified method for parametric rolling, which is used for the draft IMO vulnerability criteria. The estimated roll angle shows reasonably good agreement with the measured roll angle. Therefore, the wave-radar-assisted simplified operational guidance could be promising for practical uses onboard.

**Keywords** IMO second generation intact stability criteria · RoPax ship · Parametric rolling · Wave radar · Operational guidance

## 1 Introduction

Current stability safety of ships is realised not only with good ship design but also with the appropriate operation. Based on this understanding, the International Maritime Organization (IMO) has approved guidelines for the operational guidance [1] other than the stability design criteria as a part of the second generation intact stability criteria. The criteria deal with the five failure modes, i.e., pure loss of stability, parametric rolling, dead ship stability, broaching and excessive acceleration. Both design criteria and operational guidance are based on physics, reflecting the state-of-the-art methodology [1].

---

T. Yano · N. Umeda (✉) · M. Sakai  
Osaka University, Suita, Japan  
e-mail: [umeda@naoe.eng.osaka-u.ac.jp](mailto:umeda@naoe.eng.osaka-u.ac.jp)

M. Sakai  
e-mail: [sakai@naoe.eng.osaka-u.ac.jp](mailto:sakai@naoe.eng.osaka-u.ac.jp)

K. Hirayama · M. Baba  
Japan Radio Co. Ltd, Tokyo, Japan  
e-mail: [hirayama.keiichi@jrc.co.jp](mailto:hirayama.keiichi@jrc.co.jp)

M. Baba  
e-mail: [baba.mitsunori@jrc.co.jp](mailto:baba.mitsunori@jrc.co.jp)

IMO developed guidance to the master for avoiding dangerous situations in following and quartering seas as MSC/Circ. 707 [2], which was superseded by MSC.1/Circ.1228 [3] for covering all wave directions. By using the wave information, including the wave height, wave period and wave direction, the master can select appropriate ship course and speed. This guidance is also based on physics but does not utilise the ship dependent data, such as hull forms and loading conditions. As a result, the dangerous zones specified by this guidance could often be too broad for ships having sufficient intact stability.

For overcoming such drawback, the new operational guidance could be developed to fully utilise the ship conditions, which are used for the direct stability assessment as well [1]. In the direct stability assessment, safety level against the specified failure mode is evaluated by using a numerical tool for simulating ship behaviours in irregular waves in the time domain. Here, the numerical tool should be validated with model experiments based on the ITTC recommended procedure. While the ship stability failure probabilities under different sea states are summed up in the direct stability assessment, the operational guidance requests the shipmaster to utilise only the ship stability failure probabilities under the sea state that he or she meets. Even so, for providing the operational guidance, the same computational efforts are required for the ship designers because the guidance should cover all possible encounter sea states during the life of ships.

However, for accurately evaluating such safety level, required computational efforts are not so small, hence the operational guidance is not always a feasible solution for most smaller ships. Ironically such smaller ships are more relevant to intact stability failure. Thus, the IMO also agreed to provide a way for the simplified operational guidance, which uses simplified methodologies for the simplified design criteria named as the vulnerability criteria. In the simplified methodologies for parametric rolling, as an example, the safety level is calculated as the probability of encountering dangerous sea states and the dangerous sea states is judged by a comparison of the roll amplitude with the acceptable value. The roll amplitude is calculated by using an uncoupled but nonlinear roll model in representative regular waves determined from the wave spectrum. Thus, the method still involves nonlinearity of ship dynamics and randomness of the wave environment. However, the coupling effect from heave and pitch is ignored so that the final judgement could be conservative to some extent. This nature is suitable for a regulatory purpose, and the computation could be made even with spreadsheet software.

The use of operational guidance, even in case of its simplified one, is relatively new for mariners. In particular, wave information, such as the significant wave height, the mean wave period and the main wave direction, is not easily determined by visual observation on board. In the simplified method, often the shape of the wave spectrum is assumed, but it could be different from actual ones. On the other hand, nowadays the wave radars are available for obtaining the wave information by using reflection of electromagnetic waves at the inclined wave surface (e.g. [4–7]). In the case of the wave radar, firstly the directional wave spectrum is determined from the spatial distribution of water elevation and then the significant wave height and so on are straightforwardly determined. If this approach is feasible, the use of operational

guidance can be promising by relaxing the limitation of the capability of mariners on board. Furthermore, the directional wave spectrum data could be directly used for simplified operational guidance.

Based on this understanding, the authors attempt to apply the simplified method to a Ropax ship at seas. Here the wave information is determined from the directional wave spectrum obtained by the wave radar on the Ropax ship, and her ship roll motion simultaneously is recorded by a gyro sensor. By comparing these two data, the feasibility of the simplified operational guidance using the wave radar is investigated. In this paper, we focus on parametric rolling as its first step. Similar researches were reported as follows: Bruns et al. [8] considered relationship between occurrence of parametric rolling and wave encountering period derived from measured wave and ship data, and Suzuki et al. [9] concentrated on synchronous rolling.

## 2 Subject Ship and Used Wave Radar

The subject ship used by the authors is a Ropax ship operated in the coastal area around the Japanese archipelago. Its principal particulars and the restoring arm curve are shown in Table 1 and Fig. 1, respectively. Because of high freeboard, there is almost no possibility of capsizing, but the danger of cargo shift on the vehicle deck may exist if the roll motion is significant.

The ship is equipped with a wave radar system, which consists of an X band antenna, a radar display and a computer. An example of the obtained wave image is shown in Fig. 2. Its measuring range is 3.8 km and measuring direction range is about 190°. In order to obtain spectrum of waves with wavelength of around 40 m or more, Hirayama et al. [10] used the square region of 1920 m on a side (the area surrounded by the red square in Fig. 2) and divided into squares of 7.5 m on a side (256 s in one side) for spectrum analysis according to actual wave measurements. Every one rotation of the radar antenna, 2–3 s, the raw sea clutter image is recorded. Then the two dimensional Fourier transformation is applied to the images, and their cross spectra are calculated for determining the wave spectrum removing noise spectrum by using a wave dispersion relationship. The average of 50 cross spectra is used for

**Table 1** Principal particulars of the Ropax ship under the designed full load condition

Items	Values	Units
Length	208.0	m
Breadth	26.0	m
Depth	20.4	m
Draft	7.4	m
Metacentric height	1.49	m
Natural roll period	15.5	s
Projected area of both bilge keels	41.6	m <sup>2</sup>



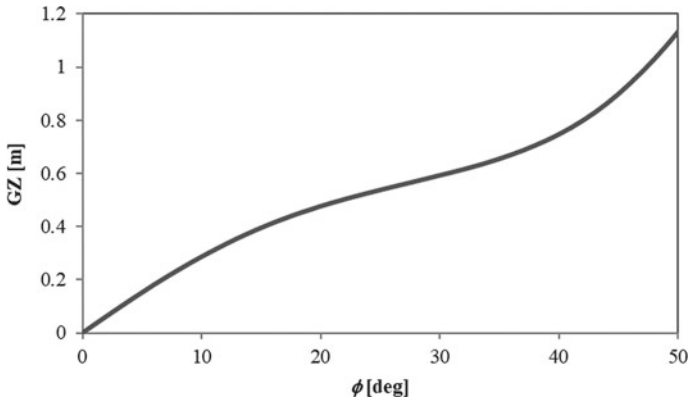


**Fig. 1** GZ curve of the Ropax ship in still water

the output having a sufficient signal–noise ratio. The wave height itself is calibrated by comparisons with direct wave measurement using a wave buoy. An example of a comparison between the visual wave height and radar-measured significant wave height is shown in Fig. 3 [10]. The accuracy of the wave radar is not perfect but could be used for practical purpose.

The second check of the level 2 vulnerability criteria for parametric rolling was applied to this subject ship as shown in Table 2. Here the probability of encountering dangerous sea states in the North Atlantic is required to be calculated as the C2 index. Since this work was done before SDC 6 in 2019, the details used here is based on older version: the number of ship speeds is seven and the averaging method is used so that the standard is 0.06 [11]. The results indicate that the limited number of loading

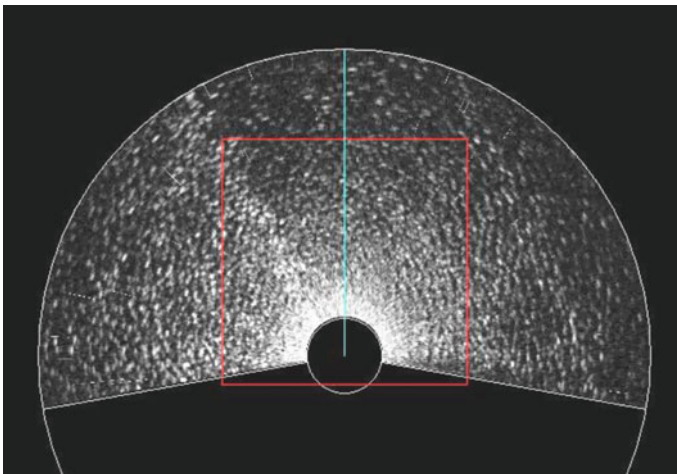
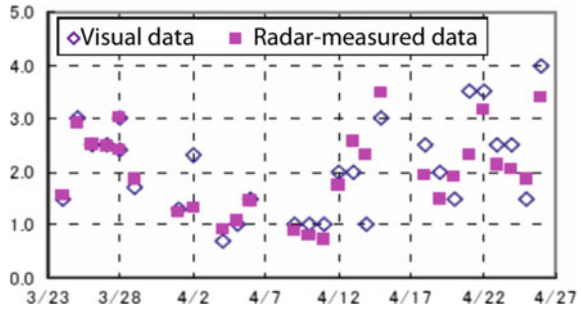


**Fig. 2** An example of sea clutter [10]

**Fig. 3** Comparison in wave height (m) between the visual and the radar-measured data on a containership in the North Atlantic and North Pacific for several weeks [10]



conditions, i.e. those having deeper drafts with medium metacentric heights, slightly exceed the standard. The criteria are requested to use the wave scatter table for the operational water area. Since the water area around the Japanese archipelago is not so severe as that in the North Atlantic, the identified vulnerability could be removed [12]. Thus, we can say that no real danger exists for this Ropax ship in the Japanese water area, but tendency of parametric rolling may exist.

**Table 2** C2 index of the second check of the draft level 2 vulnerability criteria for parametric rolling applied to the RoPax ship

d(m)	GM(m)						
	1.49	1.50	1.60	1.70	1.80	1.90	1.93
6.2	0.0129	0.0129	0.0188	0.0193	0.0188	0.0002	0.0002
6.3	0.0188	0.0188	0.0222	0.0230	0.0223	0.0004	0.0004
6.4	0.0193	0.0193	0.0230	0.0247	0.0232	0.0004	0.0007
6.5	0.0229	0.0230	0.0248	0.0249	0.0251	0.0009	0.0010
6.6	0.0246	0.0248	0.0249	0.0359	0.0255	0.0010	0.0018
6.7	0.0248	0.0248	0.0359	0.0399	0.0360	0.0018	0.0018
6.8	0.0248	0.0249	0.0397	0.0422	0.0425	0.0018	0.0024
6.9	0.0357	0.0357	0.0419	0.0442	0.0447	0.0023	0.0024
7.0	0.0396	0.0397	0.0438	0.0444	0.0454	0.0024	0.0026
7.1	0.0416	0.0416	0.0439	0.0453	0.0454	0.0026	0.0043
7.2	0.0415	0.0418	0.0439	0.0607	0.0461	0.0049	0.0042
7.3	0.0396	0.0415	0.0438	0.0604	0.0615	0.0462	0.0059
7.4	0.0415	0.0415	0.0444	0.0603	0.0658	0.0247	0.0067

Here d and GM indicate draft (m) and metacentric height (m), respectively

### 3 Simplified Estimation Method for Parametric Rolling for a Short-Term Sea State

In this work, a simplified estimation method is used, which is based on an averaging method applied to an uncoupled roll equation with time-dependent roll restoring variation in regular oblique waves [13]. The used wave is determined from the directional wave spectrum [14] by using Grim's effective wave concept [15]. Grim's effective wave spectrum,  $S\eta_{eff}$ , is

$$S\eta_{eff}(\omega, L_{pp}, \alpha) = \left[ \frac{\frac{\omega^2}{g} L_{pp} \cos(\chi) \sin\left(\frac{\omega^2}{2g} L_{pp} \cos(\chi)\right)}{\pi^2 - \left(\frac{\omega^2}{2g} L_{pp} \cos(\chi)\right)^2} \right]^2 S(\omega, \alpha) \quad (1)$$

$$H_{eff} = 4.0043 \sqrt{\int_{\alpha=-\pi/2}^{\alpha=\pi/2} \int_{\omega=0}^{\omega=\infty} S\eta_{eff}(\omega, L_{pp}, \alpha) d\omega d\alpha} \quad (2)$$

where

$$\chi = \bar{\chi} - \alpha \quad (3)$$

$\omega$  is wave frequency,  $L_{pp}$  is the ship length,  $\alpha$  is the propagating direction of each individual wave,  $g$  is the gravitational acceleration,  $\chi$  is the angle formed by the ship course with respect to the wave propagating direction,  $\bar{\chi}$  is the ship course,  $S$  is the incident wave spectrum, and  $H_{eff}$  is the significant height of Grim's effective waves. This calculation method, although the wave short-crestedness and oblique wave heading are ignored, was adopted for the second check of the vulnerability level 2 criteria for parametric rolling [1]. While the IMO criteria deal with the longitudinal waves only, the current method takes account of waves from all possible directions as well. The IMO decided to use time-domain simulation by using the Runge–Kutta method, but the current method uses the averaging method. It was already confirmed that these two provide the same solution for most of the cases if we pay sufficient attention to the initial value dependence of the time-domain simulation.

### 4 Results and Discussion

By using the wave radar and the gyro sensor onboard, we automatically recorded the wave spectra and the roll angles for about five years. During the measurement, one of the largest roll cases is selected for validating the wave-radar-based simplified operational guidance. The selected case is the 9th February 2015 at 10:25 am JST. At this time, the subject ship was heading southward off Akita in the Sea of Japan with the Froude number of 0.33. The weather map indicated a wind velocity of about

20 m/s from the south to the low-pressure system, which was situated in Sakhalin. The onboard wave radar outputted the wave spectrum, as shown in Fig. 4, which results in the significant wave height of 2.15 m and the mean wavelength of 177 m. Under this situation, the maximum roll angle that she experienced was  $12.7^\circ$ , which is half the critical roll angle that the Japanese administration requested for RoPax ships for avoiding cargo shift. Thus, no actual danger existed for this ship.

The ship was almost fully loaded so that the ship draft is about 7.4 m, but the metacentric height was not recorded. Thus, the simplified method for calculating the representative roll amplitude is applied for different metacentric heights, as shown in Figs. 5, 6, 7, 8, 9 and 10. Here,  $0^\circ$  indicates head waves, and  $180^\circ$  does following waves. It covers the possible metacentric height range, i.e. from 1.49 to 1.9 m. Here, the metacentric height was assumed to be higher than that of the full load condition of 1.49 m at least. The natural roll period is estimated by Morita’s formula, which is used in the IMO weather criterion [16] using the relevant metacentric height.

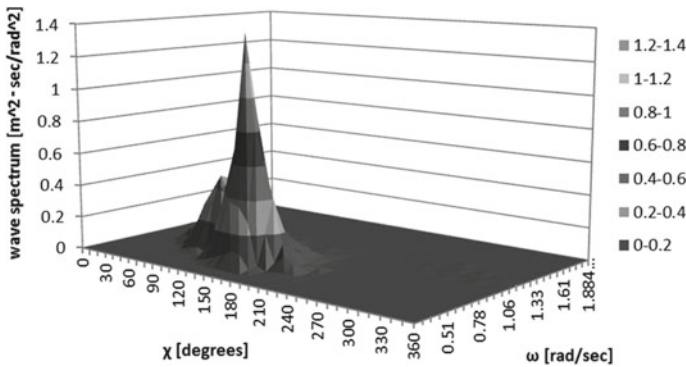


Fig. 4 Wave spectrum measured by the wave radar as a function of the wave frequency,  $\omega$  (rad/s), and directional angle,  $\chi$  (deg)

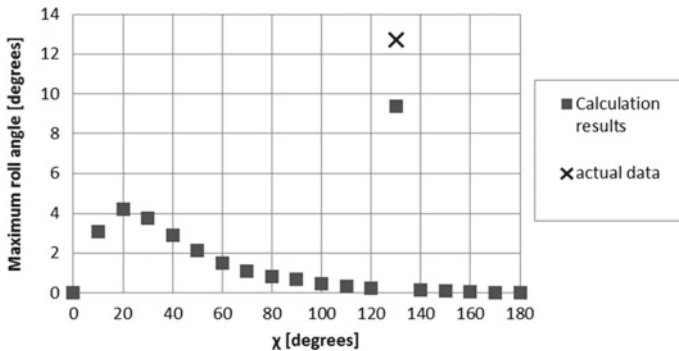


Fig. 5 Roll angles estimated by the wave radar-assisted simplified operational guidance and the measured roll angle with the metacentric height is 1.49 m

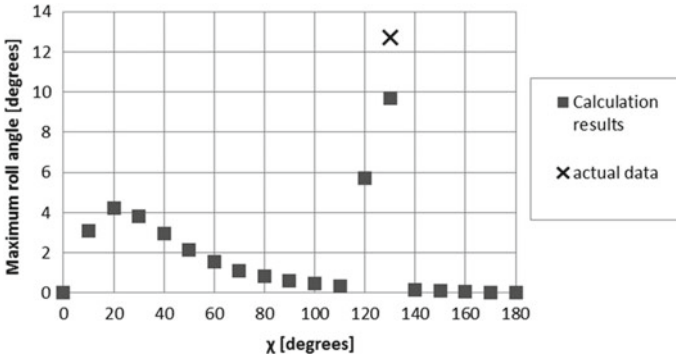


Fig. 6 Roll angles estimated by the wave radar-assisted simplified operational guidance and the measured roll angle with the metacentric height is 1.50 m

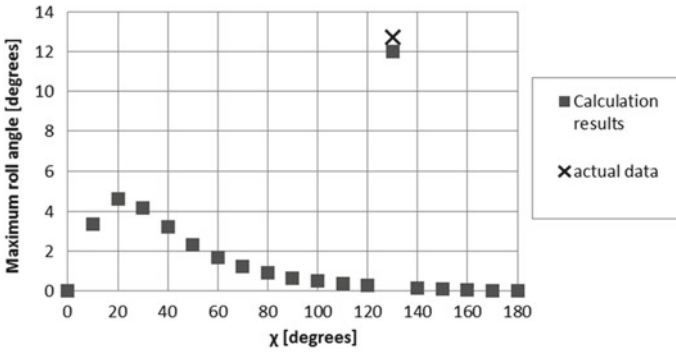


Fig. 7 Roll angles estimated by the wave radar-assisted simplified operational guidance and the measured roll angle with the metacentric height is 1.60 m

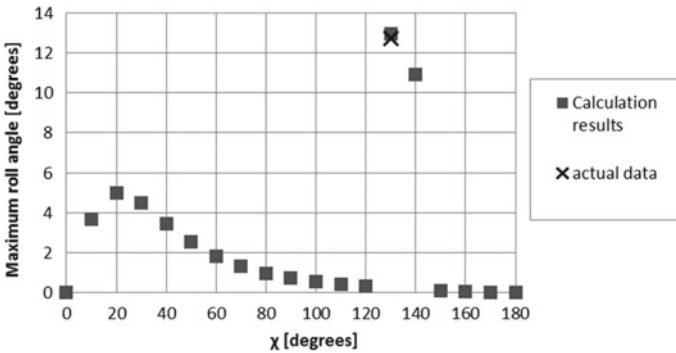
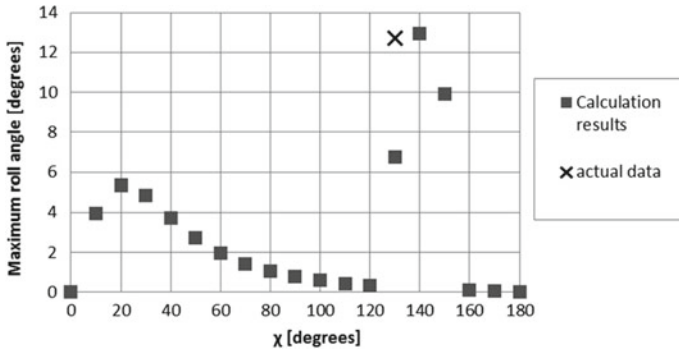
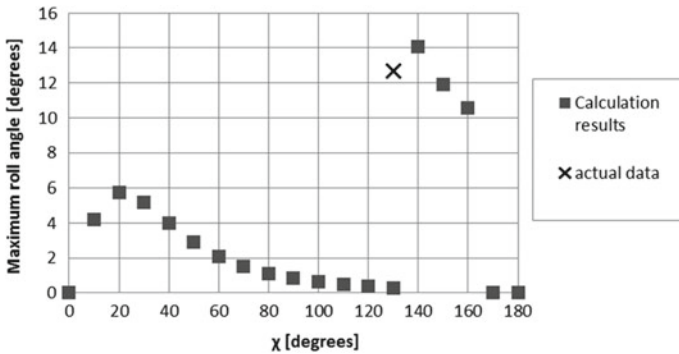


Fig. 8 Roll angles estimated by the wave radar-assisted simplified operational guidance and the measured roll angle with the metacentric height is 1.70 m



**Fig. 9** Roll angles estimated by the wave radar-assisted simplified operational guidance and the measured roll angle with the metacentric height is 1.80 m



**Fig. 10** Roll angles estimated by the wave radar-assisted simplified operational guidance and the measured roll angle with the metacentric height is 1.90 m

A single measured roll angle is also plotted in Figs. 5, 6, 7, 8, 9 and 10. Besides the uncertainty in the metacentric height, these comparisons show reasonable agreement between the wave radar-assisted simplified operational guidance and the measured roll angle. Therefore, we cannot say that the wave radar-assisted simplified operational guidance does not have practical importance. Here, the simplified method estimates steady-state roll angle in equivalent regular waves, while the measured roll is the maximum roll angle in irregular waves. Appendix 5 of the draft IMO explanatory notes [17] shows that numerical simulation using methodologies of the second check of the level 2 criterion normally provides conservative estimation of parametric roll measured in the model experiment in irregular waves. Hence, it is confirmed that the relationship between the estimated roll and the measured roll is consistent with the this investigation at seas.

Besides, this guidance suggests that the roll motion could be significantly reduced if the ship course is changed by just  $15^\circ$ . This information is not relevant to ship capsizing or cargo shift very much but is useful for passengers' comfort.

The reason why parametric rolling occurs here is that the mean wavelength is comparable to the ship length, and the mean encounter period can be almost half the natural roll period. Whether the fin stabiliser was used under this situation was not recorded so that this is another uncertainty. However, the good agreement with the estimation excluding the fin stabiliser effect suggests that the fin stabiliser was not used during the measurement.

## 5 Concluding Remarks

The authors executed measurements of the encounter waves by the wave radar and the roll angles by the gyro sensor onboard for a Ropax ship. By using the measured wave spectrum, the roll amplitude is estimated by using the simplified method, which is equivalent to the method used for the draft IMO vulnerability criteria. The comparison between the two suggests that this simplified methodology was able to identify the conditions with large measured roll angles. Therefore, we may conclude that the roll angle of  $13^\circ$  that the ship experienced seem to be parametric rolling and the wave-radar-assisted simplified operational guidance could be promising for practical uses onboard. In any case, this Ropax ship does not have any danger due to parametric rolling if the ship is operated in the water areas around the Japanese archipelago. In addition, the guidance suggests that the parametric roll motion can be significantly reduced if only the ship course is changed by only  $15^\circ$ . Further validation study should be encouraged.

**Acknowledgements** This work was supported by a Grant-in-Aid for Scientific Research from the Japan Society for Promotion of Science (JSPS KAKENHI Grant Number 19H02360). The authors are grateful to the shipbuilder and operator of the subject ship, allowing the publishing the obtained data. This paper is an updated version of the paper read at the 17th International Ship Stability Workshop [18] with more details.

## References

1. IMO (2020) Interim Guidelines on the Second Generation Intact Stability Criteria, MSC.1/Circ.1627
2. IMO (1995) Guidance to the master for avoiding dangerous situations in following and quartering seas, MSC/Circ. 707, IMO
3. IMO (2007) Revised guidance to the master for avoiding dangerous situations in adverse weather and sea conditions, MSC.1/Circ. 1228, IMO
4. Borge JCN, Reichert K, Dittmer J (1999) Use of nautical radar as a wave monitoring instrument. *Coast Eng* 37(3–4):331–342

5. Hirayama K, Oka K, Baba M (2010) Marine wave observation system with radar. Technical Report of Japan Radio 10:229–234 (in Japanese)
6. Young IR, Rosenthal W, Ziemer F (1985) A three-dimensional analysis of marine radar images for the determination of ocean wave direction and surface currents. *J Geophys Res Oceans* 90(C1):1049–1059
7. Suzaki H, Hirakawa Y, Takayama T, Hirayama T (2017) Acquisition and prediction of wave surface by marine radar for the safety of small ships. In: Proceedings of the 16th international ship stability workshop, Belgrade, pp 49–56
8. Bruns T, Lehner S, Li XM, Hessner K, Rosenthal W (2011) Analysis of an event of “parametric rolling” onboard RV “polarstern” based on shipborne wave radar and satellite data. *IEEE J Oceanic Eng* 36(2):364–372
9. Suzuki K, Nihei Y, Ikeda Y, Suzumura R (2014) A study on onboard navigation assistant systems to advise risk of dangerous rolling to navigators using motion and wave monitoring systems. *J Academ Soc Cruise Ferry, Japan*, 4:15–22, (in Japanese)
10. Hirayama K, Baba M, Iseki T (2015) Wave monitoring on board. In: Proceedings of marine dynamics symposium on ship performance monitoring in actual seas. The Japan Society of Naval Architects and Ocean Engineers, pp 229–234, (in Japanese)
11. IMO (2015) Report of the Working Group (Part 1), SDC 2/WP.4, Annex 2, pp 1–7
12. Usada S, Umeda N (2016) Safety assessment of broaching for a large domestic RoPax Ship. *J Academ Soc Cruise Ferry, Japan* 6:1–8, (in Japanese)
13. Sakai M, Umeda N, Yano T, Maki A, Yamashita N, Matsuda A, Terada D (2017) Averaging methods for estimating parametric roll in longitudinal and oblique waves. *J Mar Sci Technol* 23:413–424
14. Umeda N, Yamakoshi Y (1992) Probability of ship capsizing due to pure loss of stability in quartering seas. *Naval Architect Ocean Eng* 30:73–85
15. Grim O (1961) Beitrag zu dem Problem der Sicherheit des Schiffes in Seeegang. *Schiff und Hafen Heft* 6:490–497
16. IMO (2008) Explanatory notes to the international code on intact stability, 2008, MSC.1/Circ. 1281, IMO
17. IMO (2022) Report of the drafting group, SDC 8/WP.4/Add.5, pp.37–40
18. Yano T, Umeda N, Hirayama K, Baba M, Sakai M (2019) Wave radar application to the simplified parametric roll operational guidance at actual sea. In: Proceedings of the 17th International ship stability workshop, Helsinki, pp 91–96



# On the Application of Artificial Neural Networks for the Real Time Prediction of Parametric Roll Resonance



Marcos Míguez González, Vicente Díaz Casás, Fernando López Peña, and Luis Pérez Rojas

**Abstract** In this paper, the practical implementation methodology of an artificial neural network (ANN) based parametric roll prediction system, is studied. In order to avoid expensive scale tests, an uncoupled nonlinear roll model is applied to tune the system. The capability of this model to accurately simulate the phenomenon of parametric roll resonance is validated using towing tank tests. Finally, the behavior of the ANN system for forecasting roll motion in a realistic sailing condition has been investigated, obtaining very promising results.

**Keywords** Parametric rolling · Neural networks · Time series forecasting · Ship stability

## 1 Introduction

Fishing represents one of the industrial sectors where occupational accidents are more frequent. In fact, fishing is considered as one of the most dangerous activities worldwide. Data from several sources indicate that it is among the first ranked activities in fatal injury rates, including different European countries or the US [1–3].

Most of the human losses occur due to ship related events, such as stability issues, grounding, falling objects, etc. Among them, incidents due to stability failures (i.e. capsizes or large heel) account for the majority of the casualties, especially in small

---

M. Míguez González (✉) · V. Díaz Casás · F. López Peña  
Integrated Group for Engineering Research, Ferrol Industrial Campus,  
University of A Coruña, A Coruña, Spain  
e-mail: [marcos.miguez@udc.es](mailto:marcos.miguez@udc.es)

V. Díaz Casás  
e-mail: [vicente.diaz.casas@udc.es](mailto:vicente.diaz.casas@udc.es)

F. López Peña  
e-mail: [fernando.lopez.pena@udc.es](mailto:fernando.lopez.pena@udc.es)

L. Pérez Rojas  
Model Basín, ETSIN, Technical University of Madrid, Madrid, Spain  
e-mail: [luis.perezrojas@upm.es](mailto:luis.perezrojas@upm.es)

ships. This could be explained by the fact that very often these accidents develop very fast and because they usually imply the complete loss of the vessel [4].

Small and medium length vessel skippers base their capability for evaluating the stability of their ships mainly on previous experience, which usually does not include important incidents. In addition, they lack training for adequately understanding the information contained in the stability booklets, which are, if available, the only help they have for evaluating the intact static stability of the ship in a given sailing condition. An even more dramatic situation shows up when talking about dynamic stability issues. Considering that in most cases these phenomena are completely unknown to the skippers, it is impossible that they could face them correctly in order to avoid their consequences. All these issues, together with the fact that they need to fish even under very rough weather conditions and other circumstantial factors, are the main causes of such accidents.

Stability guidance systems were developed to try to mitigate this situation, providing the crew with stability-related information. Traditionally, they have ranged from stability posters to computer approaches, which considered only a limited set of conditions or relied in subjective data provided by the crew [5]. However, in recent years these systems started pointing towards the so called “second generation guidance systems”, which in addition to the characteristics of the previous ones, also use real time data acquisition and analysis to determine the stability characteristics of the vessel and to provide objective and more precise information to the crew.

In this last group, some of the authors of this work have proposed their own alternative (Fig. 1). This system provides the minimum essential information related to the stability of the vessel in the current loading condition, in a very clear and understandable way, even for users with no specific training in the use of computer software [5, 6]. Although it was initially based only on the computation of static stability criteria from loading condition data introduced in the system by the crew, in the last years the authors have been working on implementing additional real-time capabilities. These included the automatic estimation of the stability parameters of the vessel during operation [7] and the detection of the onset of parametric roll resonance. And is in this last functionality where this work is focused.

As it is well known, parametric roll is a phenomenon which affects fishing vessels, among other types of ships, and that may generate very large amplitude roll motions in a very sudden way, leading to heavy damage or even capsizing [8].

The main objective of the proposed prediction system is to alert the crew about the immediate appearance of an episode of parametric rolling and to allow them to take preventive actions. This approach is based on the use of artificial neural networks (ANN). These are biologically inspired algorithms, which after a training process with a set of samples, are capable of reproducing the behavior of nonlinear systems [9]. ANN have been widely used as forecasters in different fields, including ship roll motions (e.g. [10]). In previous works, the authors have tested the performance of this approach with some success, both using as training and testing cases roll motion data obtained from a three degrees of freedom mathematical model [11] and from a more realistic approach using towing tank tests in head seas [12].

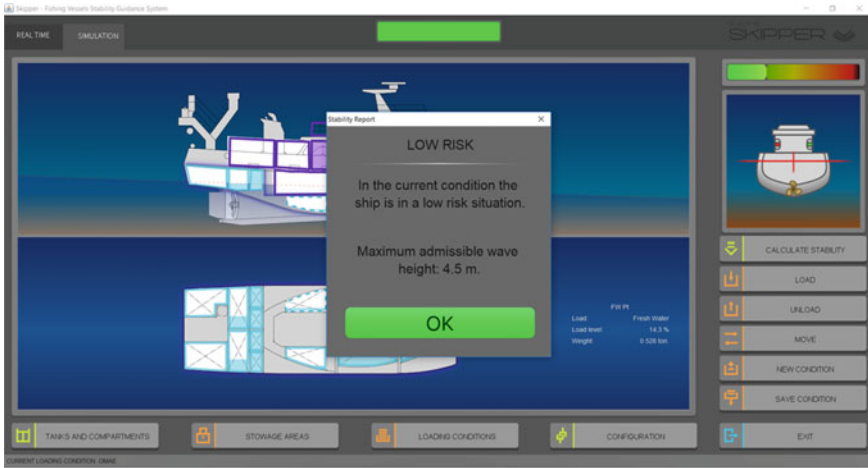


**Fig. 1** Fishing vessel stability guidance system screenshot

However, when it comes to the practical implementation of such a system in a fishing vessel, there are some economic constraints that have to be taken into account. Carrying out a large campaign of towing tank tests for obtaining the training data, needed to accurately set up the ANN detector, implies a large cost and complicates the adaptation of the system to each ship, especially in the case of a small or mid-sized fishing vessels. So, in order to overcome this issue, an alternative approximation is presented in this work. In order to reduce the cost of fitting the system to each ship, a simple 1.5 degrees of freedom nonlinear mathematical model has been proposed as the source of training data, instead of using more expensive towing tank tests data or more complex mathematical codes. The performance of this model itself to accurately reproduce the roll motion of a medium sized trawler has been validated by using data from towing tank tests. And finally, the performance of the mathematical model-tuned ANN forecasting system to predict the appearance of parametric roll in a realistic seaway is evaluated. In order to do this, some results from the application of the ANN forecaster to a set of roll motion time series obtained from towing tank tests, are presented. This work updates and complements the findings previously described by Míguez González et al. [13].

## 2 Model Tests

The ship under analysis is a medium sized stern trawler having an acute tendency towards developing parametric roll resonance even in not very heavy seas. This trend is caused, in part, by its transom stern hull forms and bow flare. This ship has also been studied by de Juana Gamo et al. [14], and a very similar one by Míguez González and Bulian [15]. Its main characteristics are described in Table 1, and its bodyplan

is included in Fig. 2. A 1/18.75th scale model has been used for the towing tank experiments, which arrangement is also shown in Fig. 2. It is important to note that, although this type of vessels are usually equipped with bilge keels, in this case the vessel under consideration has no bilge keels installed.

These scale model tests have been carried out in the ETSIN test basin (Technical University of Madrid). The scale model has been restrained as to ensure that surge, sway and yaw are limited, while leaving the model to heave, roll and pitch freely. All tests have been done in longitudinal head regular waves. Considering that the main parameter affecting the appearance of parametric roll resonance is the wave encounter frequency to natural roll frequency ratio ( $\omega_e/\omega_0$ ), and the fact that parametric roll resonance could be expected for ratios between 1.9 and 2.2 and even more, tests included ratios ranging between 1.7 and 2.3. Regarding wave height ( $H_w$ ), tests included values between 0.5 m and 3 m. Finally, four ship speeds, corresponding to Froude numbers ( $Fn$ ) 0, 0.1, 0.2 and 0.3, have been considered. The complete test matrix is composed of 24 different combinations for the zero speed case, 16 for  $Fn$  0.1, 15 for  $Fn$  0.2 and 13 for the  $Fn$  0.3. These conditions include cases where parametric roll resonance develops and others where it does not. Wave length

**Table 1** Test vessel main characteristics

Overall length	34.50 m
Length between perpendiculars	29.00 m
Beam	8.00 m
Depth	3.65 m
Draft	3.290 m
Displacement	448 t
Metacentric height ( $GM$ )	0.350 m
Natural roll frequency ( $\omega_0$ )	0.563 rad/s
Dry roll gyradius w.r.t. CoG ( $k_{xx}$ )	3.128 m (39.1% B)

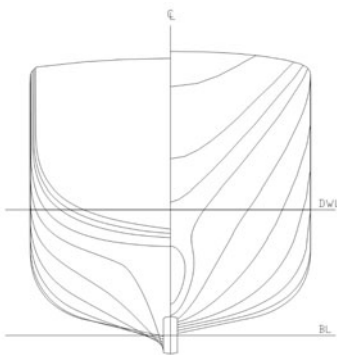


**Fig. 2** Hull bodyplan (left) and scale model towing tank tests arrangement (right)

$(\lambda_w)$  is determined as a function of wave frequency ( $\omega_w$ ), under the deep water approximation. In addition, still water roll decay tests have also been accomplished at four different forward speeds (corresponding to Froude numbers 0, 0.1, 0.2 and 0.3) and different initial roll angles. These decay tests were also used to estimate the dry roll gyradius of the vessel with respect to the centre of gravity, included in Table 1. In order to obtain this value, the added inertia in roll at the natural roll frequency was estimated by using a potential theory code. A complete description of this campaign, including detailed procedures, results and their analysis, could be found in Míguez González [16].

### 3 Mathematical Model

In order to tune the prediction system in a simple and inexpensive way, it was necessary to define a mathematical model able to adequately reproduce the behaviour of the ship in parametric roll conditions, but minimizing the number of parameters that have to be computed to fit the model to other different vessels.

In this work, the 1 degree of freedom (d.o.f.) nonlinear uncoupled roll model proposed by Bulian [17] has been adopted. On it, the time varying nonlinear roll restoring term needed for triggering parametric roll is computed taking into account the quasi-static effects of heave and pitch motions in roll. This leads to considering this model as a 1.5 degrees of freedom approach, having the following structure:

$$(I_{xx} + A_{44}) \cdot \ddot{\phi} + B_{44,T}(\dot{\phi}) \cdot \dot{\phi} + C_{44}(\phi, t) = 0 \quad (1)$$

where  $I_{xx}$  and  $A_{44}$  are respectively the mass and added mass moments of inertia in roll,  $B_{44,T}(\dot{\phi})$  represents the nonlinear damping term and  $C_{44}(\phi, t)$  is the time varying nonlinear restoring coefficient ( $C_{44}(\phi, t) = \Delta \cdot GZ(\phi, t)$ ). As it is generally accepted, the added mass term  $A_{44}$  has been obtained by potential theory methods. The computation of restoring and damping terms is described in the following subsections.

#### 3.1 Restoring Arm

As mentioned above, the influence of pitch and heave motions, together with wave passing along the hull, has to be taken into account for an accurate simulation of parametric roll. Considering that the proposed model doesn't explicitly include the coupling between roll and heave and pitch, both effects have been taken into account in a quasi-static way within the restoring term.

In order to do this, the "look up table" approach, described by Bulian [17] and applied by many authors to different types of ships [18], recommended by class societies for modelling the variation of the ship restoring capabilities in longitudinal

waves [19] and included within the Second Generation Intact Stability Criteria Level 2 vulnerability assessment for parametric roll [20], was applied for computing the restoring term  $C_{44}(\phi, t)$ .

Under this approach, for each wave crest position and roll angle, trim and sinkage are statically balanced. This method has demonstrated to perform well in following seas and in head seas with wavelengths longer than ship length (where heave and pitch motions are supposed to be quasi-static). Additionally, in Bulian [17], its application to the head seas case in wavelengths similar to ship length, was also successful.

For each set of wave parameters (height and wavelength) and for the different positions of wave crest along the hull, the  $GZ$  curves were computed applying classical hydrostatics under free trim conditions. In order to obtain the time dependant restoring coefficient  $C_{44}(\phi, t)$ , the aforementioned wave crest domain  $GZ$  curves, were transformed to the time domain by considering the wave encounter frequency.

An example of the results of these  $GZ$  computations are displayed and compared to the still water case in Fig. 3. Additionally, the interpolated  $GZ$  surface for this same case and the different wave crest positions is also presented.

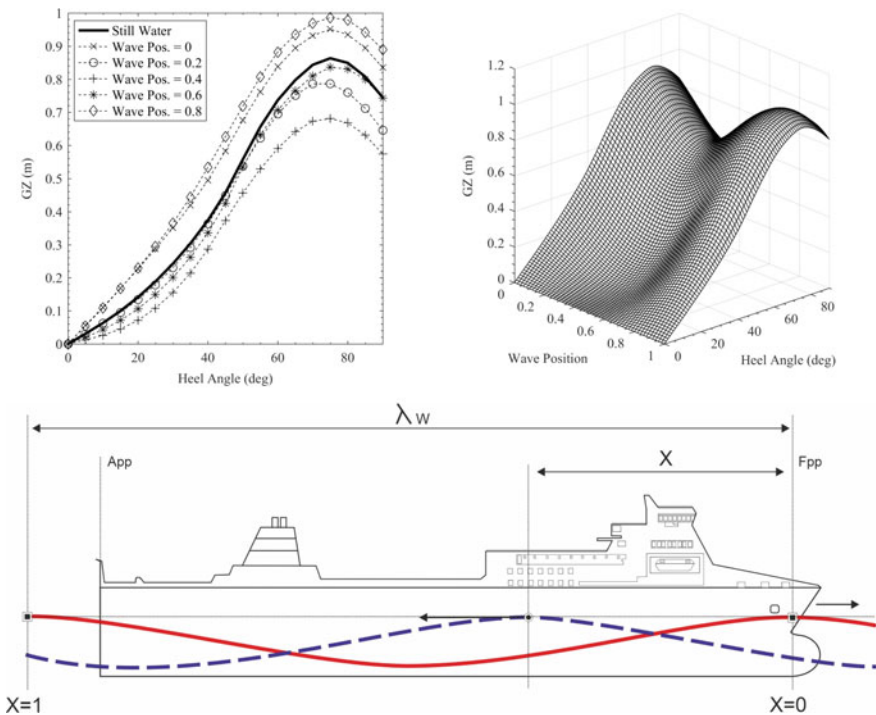


**Fig. 3** Top Left:  $GZ$  curves as a function of wave position. Top Right:  $GZ$  variation due to wave passing.  $\lambda_w = 40$  m.  $H_w = 2$  m. Bottom: Wave position ( $X$ ) along the hull.  $X = 0$ , wave crest at the forward perpendicular.  $X = 1$ , wave crest  $\lambda_w$  m away from the forward perpendicular

### 3.2 Roll Damping

One of the most critical elements for ensuring a good simulation of parametric roll resonance is the modelling of roll damping, as it is highly nonlinear in the large roll amplitudes present during parametric resonance. In order to account for these nonlinearities, a nonlinear quadratic approach has been adopted, decomposing roll damping in a linear and a quadratic term. This same approach has been broadly applied in other works dealing with parametric roll modeling, (e.g. [21]). According to this structure, the ship roll damping would read:

$$B_{44,T}(\dot{\phi}) \cdot \dot{\phi} = B_{44a} \cdot \dot{\phi} + B_{44b} \cdot \dot{\phi} \cdot |\dot{\phi}| \tag{2}$$

In order to obtain the linear ( $B_{44,a}$ ) and quadratic ( $B_{44,b}$ ) coefficients, still water roll decay tests for different forward speeds and initial roll angles have been carried out. The procedure followed for determining the damping coefficients from these tests, is the one described in Himeno [22]. In Fig. 4, the results of roll decrement (obtained between subsequent full cycles) as a function of mean roll angle are presented, together with a quadratic fitting for the whole set of data points obtained in the roll decay tests at the four tested forward speeds.

In addition, in Table 2, the obtained damping coefficients at the four Froude numbers are shown in the form of non-dimensional damping coefficients, defined by:

$$2 \cdot v \cdot \omega_{\phi} = \frac{B_{44a}}{(I_{xx} + A_{44})}; \beta = \frac{B_{44b}}{(I_{xx} + A_{44})} \tag{3}$$

The validation of the damping coefficient results has been done by comparing the towing tank results of the roll decay tests to those obtained by using the mathematical model. Results presented in Fig. 5, corresponding to forward speeds of Fn

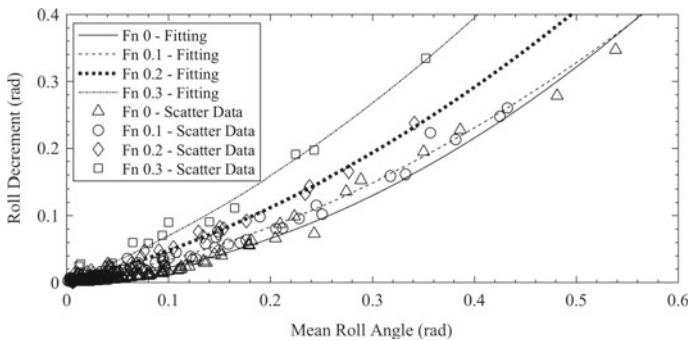


**Fig. 4** Roll decrement data (scatter points) and fitting quadratic polynomial (lines) from roll decay tests

**Table 2** Non-dimensional damping coefficients

Froude number ( $F_n$ )	$\nu$ [-]	$\beta$ [ $\text{rad}^{-1}$ ]
0	0.0187	0.3932
0.1	0.0404	0.3008
0.2	0.0620	0.3158
0.3	0.0953	0.3631

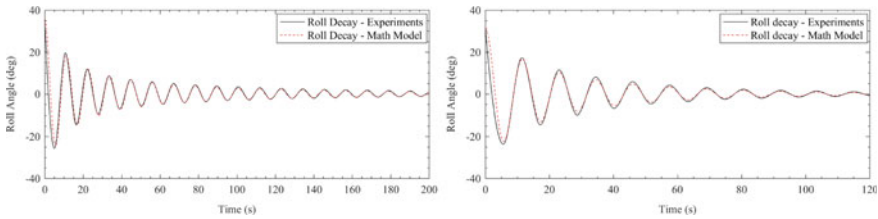


**Fig. 5** Roll decay tests.  $F_n = 0$  (left) and  $F_n = 0.1$  (right)

0 and 0.1, show that the roll damping model is adequate, accurately reproducing the experimental roll decay tests.

### 3.3 Model Validation

In this section, the performance of the model for accurately simulating the roll motion of the studied vessel in the different sailing conditions, including those where parametric rolling is present, is analyzed. The data used for the validation process are those obtained from the towing test campaign that has been already described, including runs at different forward speeds, wave frequencies and wave heights.

In Fig. 6, two sample comparisons between the simulations and the towing tank tests, are presented. On them, the roll motion time series obtained with the proposed mathematical model, for conditions likely to induce parametric roll, are compared to the corresponding results from the towing tank experiments. These conditions include  $\omega_e/\omega_0 = 2$ , wave height  $H_w$  of 1.491 m and forward speeds corresponding to  $F_n$  0 and 0.1. A full description of the results from the whole test matrix is available in Míguez González [16].

Observing these results, it can be concluded that the correspondence between simulated and towing tank test data is quite good, both in the initial transient stage and in the steady state motion; however, a slight underestimation of the roll amplitude has been observed, not only in the two presented cases, but also in the rest of the compared time series at these two speed values.

This issue is more noticeable as speed increases, as could be appreciated in the right side of Fig. 6; in fact, the model is unable to reproduce any of the parametric



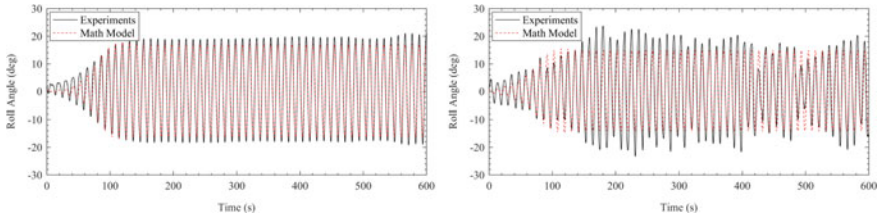


**Fig. 6** Comparison between experimental roll motion and 1.5 d.o.f. model simulations. Left:  $F_n = 0$ .  $\omega_e/\omega_0 = 2.0$ .  $H_w = 1.491$  m.  $\lambda_w = 48.640$  m. Right:  $F_n = 0.1$ .  $\omega_e/\omega_0 = 2.0$ .  $H_w = 1.491$  m.  $\lambda = 66.145$  m

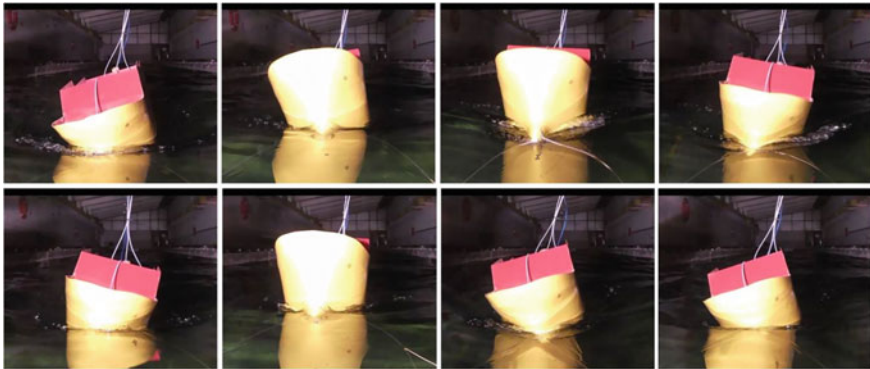


**Fig. 7** Detail of pitch motions during one roll cycle under the effect of parametric roll.  $F_n = 0.2$ .  $\omega_e/\omega_0 = 2.0$ .  $H_w = 1.988$  m.  $\lambda_w = 81.965$  m

roll events which occur for the higher speeds of  $F_n$  0.2 and  $F_n$  0.3, where lower wave frequencies imply much longer wavelengths [16].

This behavior may be related with the quasi static approach adopted for the computation of the time varying restoring term. From the towing tank tests experiments, it has been observed that heave and pitch motions were of quite large amplitude in these conditions (see Fig. 7), and that their influence in the developing of parametric roll was much higher than that predicted by the quasi static approach. However, and in order to illustrate the performance of the parametric roll prediction system, only conditions of up to  $F_n$  0.1, where the mathematical model has demonstrated to work fine, have been used.

## 4 Parametric Roll Forecasting System

Developing a system which could alert the crew and allow them to take corrective actions before a parametric roll event takes place, is a task which has gained a lot

of attention in the last years, due to the increase in size and number of ships likely to suffer from the phenomenon, especially containerships. Among the published alternatives, the one by Galeazzi et al. [23, 24] is the only under real scale testing nowadays.

On the other hand, the authors of the present work have been working on the development of a roll forecasting system, based on the application of Artificial Neural Networks (ANN). The main objective of this approach is to predict, some time in advance, the roll motion time series of the vessel, including possible episodes of parametric roll resonance. In comparison to the single detection provided by the proposal by Galeazzi et al. [23], the availability of the roll motion time series forecast which provides the ANN approach, has the main advantage of increasing the performance of possible corrective actions [12].

The structure of an ANN consists of an input layer, which receives the data, a series of hidden layers, where the so-called neurons are included, and an output layer. Neurons are in charge of processing the data by weighing, biasing and summing up the input data they receive, processing them with an activation function and sending them to the following neuron. The process of training consists of feeding the network with known data of the behavior of the system to be modeled, and selecting the weights and biases which minimize the errors between real and predicted outputs [25], modifications which are done relying in the so called learning algorithm. In this work, a multilayer perceptron architecture (MPNN) has been selected, which is shown in Fig. 8. MPNN are also called feedforward or backpropagation networks, as they use the error backpropagation algorithm for the update of weights and biases [9].

The process for obtaining the outputs of this network from the corresponding inputs, is summarized in Eqs. 4 and 5. Basically, in each neuron  $k$ , each input  $x_j$  is weighted by a synaptic weight  $w_{kj}$  and all the weighed inputs of the neuron are added, together with a bias  $b_k$ . The obtained result  $v_k$ , known as activation potential, is processed by an activation function  $f()$ , obtaining the neuron output  $y_k$ . This activation function is selected depending on the type of problem and data under consideration, and it keeps the output of the neuron under some desired limits. Finally, and regarding the number of hidden layers and neurons of an ANN, it has to be said that it determines the degree of complexity of the problems which could be tackled by the network, but only up to a specific threshold. From that point onwards, the capabilities of the system are not improved although the number of neurons or hidden layers is increased.

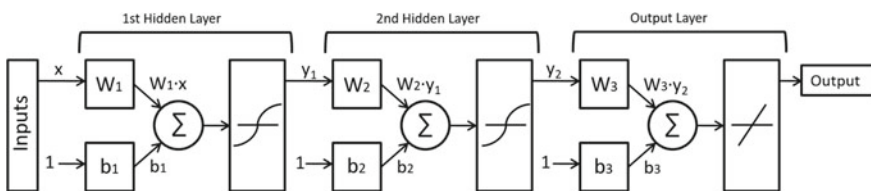


Fig. 8 Multilayer perceptron artificial neural network architecture

$$v_k = \sum_{j=1}^m w_{kj}x_j + b_k \quad (4)$$

$$y_k = f(v_k) \quad (5)$$

As it has been already described, the objective of this work is to evaluate the performance of a roll motion forecaster based on the use of ANN, which have been trained using a simplified nonlinear mathematical model of roll motion. This would reduce the cost of adapting the system to each vessel, as the setting up of the mathematical model is a simpler task than developing a whole scale model test campaign. This way, the only need when setting up the system on a ship will be to compute the mathematical model parameters and then use it to train the networks, with no need for complex towing tank testing. This approach would represent the practical way of implementing the system in a real case.

After some previous testing, which is described in detail in Míguez González [16], it was concluded that the structure with a better compromise between simplicity and performance, is that of a multilayer perceptron network with three hidden layers, 30 neurons per layer, and one output layer. The input vector is composed by 40 elements, representing 20 s of the roll motion time series. The output is composed by only one element, being it the prediction one step ahead. Substituting the output value within the input vector and recursively executing the algorithm, predictions in different degrees of advance can be obtained. Tan sigmoid-functions have been used as activation functions in the hidden layers and a piecewise linear function has been selected for the output layer.

Regarding the training algorithm, its objective is to modify the different weights and biases in order to optimize a given performance (loss) function. In this case, the error between the network's prediction and the target value, measured using the Mean Squared Error, has been selected as performance function. In the case of the training algorithm, the Levenberg–Marquardt (L–M) algorithm [26] has been used. In Fig. 9, the evolution of the MSE during the subsequent training epochs for the best performing network is shown. In this case, training was stopped when the obtained MSE value was below the goal value of  $1 \times 10^{-8}$ .

The training data was obtained from 56 time series of roll motion, obtained with the 1.5 d.o.f. nonlinear mathematical roll model previously described, at different combinations of wave frequency and height and for a forward speed of  $Fn$  0.1. The selected parameters are included in Table 3. This data set not only includes cases where resonance is most likely, but also combinations of parameters where resonance does not develop.

Regarding training, it has to be taken into account that the first set of weights and biases are randomly generated at the beginning of the process; so, the same set of training cases could lead to trained networks with different performance. In order to improve the obtained results, the training process has been repeated 50 times, and the best network structure out of the 50 cases was selected based upon the network performance index.

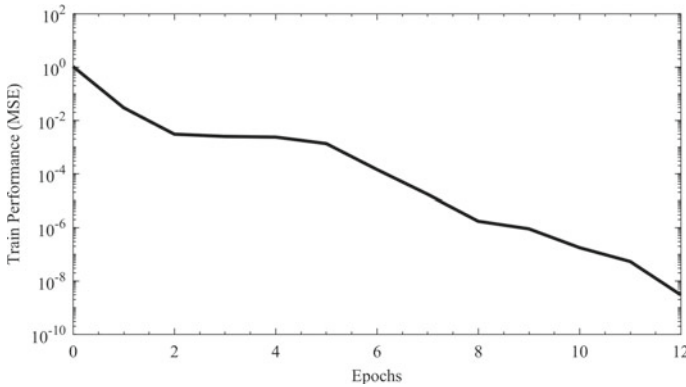


**Fig. 9** Evolution of MSE with epochs during the training process. Best performing network

**Table 3** Training data parameters

Froude number $F_n$	0.1
$\omega_e/\omega_0$ range	1.6–2.6
$H_w$ range	0.5–2.5 m

In order to test the system, two time series, where parametric roll takes place, have been selected from the towing tank tests described in preceding sections. The parameters of these time series are included in Table 4. In both cases, the forecasting system has been executed to obtain predictions 10 s ahead, which approximately represent one whole roll period. The obtained results are presented in Fig. 10. The Mean Squared Error (MSE) of the predictions is included also in Table 4.

Analyzing the obtained results, it can be observed that the forecasting system correctly tracks the onset of the phenomenon in both test cases. However, as roll motion amplitude increases, some overpredictions are observed, which are especially relevant in Test Case 1. If the system is applied only for detecting the appearance of the phenomenon, these overpredictions won't be very relevant, as they won't imply a misdetection or false alarm. Nevertheless, if forecasted roll motion is needed for establishing preventive measures, it is necessary to improve the performance of the system in order to avoid these peaks in the predicted roll motion.

**Table 4** Test data parameters and MSE results

	Test case 1	Test case 2
Froude number $F_n$	0.1	
$\omega_e/\omega_0$	2.0	
$H_w$ (m)	1.491	1.988
$MSE \times 10^{-4}$	442.00	504.14

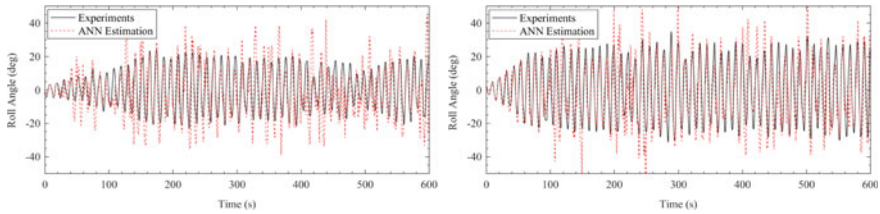


Fig. 10 Prediction results. Test Case 1 (left) and Test Case 2 (right)

## 5 Conclusions

This work presents some of the activities carried out by the authors for implementing a parametric roll prevention system based on the use of Artificial Neural Networks within an onboard stability guidance software. This system is primarily focused on providing stability information to the skipper of small and medium sized fishing vessels. The main requirements of such a system are ease of use and installation, and low cost. These requirements make the use of towing tank test campaigns not a feasible option for training the forecaster. The presented approach relies on the use of a mathematical model to train the ANNs for forecasting roll motion in realistic sailing conditions.

In order to do this, a one degree of freedom nonlinear roll model of a medium sized trawler, where pitch and heave effects on roll are taken into account in a quasi-static way has been developed. Moreover, a nonlinear quadratic approximation of roll damping term has been selected. The capacity of this model to accurately reproduce parametric roll resonance in different conditions of wave frequency, wave height and ship forward speed, has been analyzed by comparing the results obtained with the model against those obtained from a towing tank test campaign. In addition, roll decay tests in still water have been carried out to define the components of the quadratic damping.

The proposed model has shown a good performance for simulating parametric rolling at small forward speeds (up to  $F_n$  0.1). However, at higher speeds the model is unable to simulate the large coupling between heave, roll and pitch observed in the tank tests and the parametric rolling events that were observed in them.

Once the model behaviour has been analyzed, it has been applied for computing the ANN training data, including different combinations of wave parameters. The selected speed corresponds to a  $F_n$  0.1, at which the proposed forecasting model showed to be accurate.

With the objective of testing the system in a realistic situation, two time series where parametric roll is completely developed, have been selected from the  $F_n$  0.1 tank test results and the forecaster was executed in order to obtain 10 s in advance predictions. The obtained forecasts are quite accurate in both test cases, especially during the transient period in which resonance develops, although some overpredictions were observed during the steady state phase.

Regarding the prediction horizon, it is necessary to improve this value because 10 s (1 roll period) could be enough for triggering automatic corrective actions in the type of vessels analyzed in this work; but they seem to be too short if these corrective actions have to be undertaken by the crew.

In any case, the obtained results empower the idea of applying mathematical model trained artificial neural networks, for parametric roll prediction, with no need of expensive and time consuming towing tank tests. Nevertheless, further research is needed to improve the performance of the forecaster during the steady state phase, and also to increase the prediction time horizon.

**Acknowledgements** The present work was supported by the Spanish Ministry of Education under the FPU program, grant AP2006-03211, by MICIIN project TRA2009-13805 with EDF FEDER funding, and by Xunta de Galicia under project 08DPI011CT.

## References

1. Bureau of Labor Statistics (BLS) (2014) National census of fatal occupational injuries in 2013. Bureau of Labor Statistics, U.S. Department of Labor
2. Jensen OC, Petursdottir G, Holmen IM, Abrahamsen A, Lincoln J (2014) A review of fatal accident incidence rate trends in fishing. *Int Marit Health* 65(2):47–52
3. MESS (2014) Estadística de Accidentes de Trabajo. Ministerio de Empleo y Seguridad Social. Subdirección General de Estadísticas, Gobierno de España, Madrid, Spain
4. Mata-Alvarez-Santullano F, Souto-Iglesias A (2014) Stability, safety and operability of small fishing vessels. *Ocean Eng* 79:81–91
5. Santiago Caamaño L, Míguez González M, Díaz Casás V (2018) Improving the safety of fishing vessels through roll motion analysis. In: Proceedings of the 37th ASME international conference on ocean, offshore and arctic engineering (OMAE 2018), Madrid, Spain
6. Míguez González M, Caamaño Sobrino P, Tedín Álvarez R, Díaz Casás V, Martínez López A, López Peña F (2012) Fishing vessel stability assessment system. *Ocean Eng* 41:67–78
7. Santiago Caamaño L, Galeazzi R, Nielsen UD, Míguez González M, Díaz Casás V (2019) Real time detection of transverse stability changes in fishing vessels. *Ocean Eng* 189:106369
8. Ghamari I, Greco M, Faltinsen OM, Lugni C (2020) Numerical and experimental study on the parametric roll resonance for a fishing vessel with and without forward speed. *Appl Ocean Res* 101:102272
9. Golden R (1996) Mathematical methods for neural network analysis and design. The MIT Press
10. Yin JC, Zou ZJ, Xu F (2013) On-line prediction of ship roll motion during maneuvering using sequential learning RBF neural networks. *Ocean Eng* 61:139–147
11. Míguez González M, López Peña F, Díaz Casás V, Galeazzi R, Blanke M (2011) Prediction of parametric roll resonance by multilayer perceptron neural network. In: Proceedings of the 21st international offshore (ocean) and polar engineering conference (ISOPE 2011), Maui, EEUU
12. Míguez González M, Díaz Casás V, López Peña F, Pérez Rojas L (2012b) Experimental parametric roll resonance characterization of a stern trawler in head seas. In: Proceedings of the 11th international conference on the stability of ships and ocean vehicles, Athens, Greece
13. Míguez González M, Díaz Casás V, López Peña F, Pérez Rojas L (2013) Experimental analysis of roll damping in small fishing vessels for large amplitude roll forecasting. In: Proceedings of the 13th International Ship Stability Workshop, Brest, France

14. De Juana Gamo J, Arias Rodrigo C, Pérez Rojas L (2005) On the parametric rolling of fishing vessels. In: Proceedings of the 1st international conference on marine research and transportation
15. Míguez González M, Bulian G (2018) Influence of ship dynamics modelling on the prediction of fishing vessels roll response in beam and longitudinal waves. *Ocean Eng* 148:312–330
16. Míguez González M (2012) A study of ship parametric roll resonance for the evaluation of preventive strategies. PhD Thesis, University of A Coruña, A Coruña, Spain
17. Bulian G (2006) Development of analytical nonlinear models for parametric roll and hydrostatic restoring variations in regular and irregular waves. PhD Thesis, Università Degli Studi di Trieste, Trieste, Italy
18. Bačkalov I, Bulian G, Cichowicz J, Eliopoulou E, Konovessis D, Leguen JF, Rosen A, Themelis N (2016) Ship stability, dynamics and safety: status and perspectives from a review of recent STAB conferences and ISSW events. *Ocean Eng* 116:312–349
19. American Bureau of Shipping (ABS) (2004) Guide for the assessment of parametric roll resonance in the design of container carriers
20. IMO (2019) SDC 7/WP.6. Finalization of second generation intact stability criteria; report of the drafting group on intact stability. International Maritime Organization, London, UK
21. Neves MAS, Rodríguez CA (2006) On unstable ship motions resulting from strong non-linear coupling. *Ocean Eng* 33:1853–1883
22. Himeno Y (1981) Prediction of ship roll damping. A state of the art. The University of Michigan College of Engineering, Michigan, USA, Department of Naval Architecture and Marine Engineering
23. Galeazzi R, Blanke M, Poulsen NK (2012) Early detection of parametric roll resonance on container ships. *IEEE Trans Control Syst Technol* 21(2):489–503
24. Galeazzi R, Blanke M, Falkenberg T, Poulsen NK, Violaris N, Storhaug G, Huss M (2015) Parametric roll resonance monitoring using signal-based detection. *Ocean Eng* 109:355–371
25. Haykin S (1999) *Neural networks: a comprehensive foundation*. Prentice Hall
26. Demuth H, Beale M, Hagan M (2011) *Neural network toolbox™ 6. user's guide*. The MathWorks Inc., Natick, MA, USA

# Application of Real-Time Estimation Techniques for Stability Monitoring of Fishing Vessels



Lucía Santiago Caamaño, Marcos Míguez González, Roberto Galeazzi, Ulrik D. Nielsen, and Vicente Díaz Casás

**Abstract** This work presents a comparative study of two signal processing methods for the estimation of the roll natural frequency towards the real-time transverse stability monitoring of fishing vessels. The first method is based on sequential application of the Fast Fourier Transform (FFT); the second method combines the Empirical Mode Decomposition (EMD) and the Hilbert-Huang Transform (HHT). The performance of the two methods is analysed using roll motion data of a stern trawler. Simulated time series from a one degree-of-freedom nonlinear model, and experimental time series obtained from towing tank tests are utilized for the evaluation. In both cases, beam waves are considered but, while irregular waves are adopted in the simulated data, the towing tank tests are made in regular waves. Based on the available data the performance of both estimation methods is comparable, but the EMD-HHT method turns out slightly better than the sequential FFT. Finally, the use of a statistical change detector, together with the EMD-HHT methodology, is proposed as a possible approach for the practical implementation of an onboard stability monitoring system.

---

L. Santiago Caamaño (✉) · M. Míguez González · V. Díaz Casás  
Integrated Group for Engineering Research, Ferrol Industrial Campus, University of A Coruña,  
Ferrol, Spain  
e-mail: [lucia.santiago.caamano@udc.es](mailto:lucia.santiago.caamano@udc.es)

M. Míguez González  
e-mail: [marcos.miguez@udc.es](mailto:marcos.miguez@udc.es)

V. Díaz Casás  
e-mail: [vicente.diaz.casas@udc.es](mailto:vicente.diaz.casas@udc.es)

R. Galeazzi  
Department of Electrical Engineering, Technical University of Denmark, DTU Electrical  
Engineering, Kgs. Lyngby, Denmark  
e-mail: [roga@dtu.dk](mailto:roga@dtu.dk)

U. D. Nielsen  
Department of Mechanical Engineering, Technical University of Denmark, Kgs. Lyngby, Denmark  
and for Autonomous Marine Operations and Systems, NTNU AMOS, Trondheim, Norway  
e-mail: [udni@dtu.dk](mailto:udni@dtu.dk)



**Keywords** Ship stability monitoring · Generalized likelihood ratio test · Hilbert-Huang transform · Empirical mode decomposition

## 1 Introduction

Small and medium fishing vessels have historically suffered a large amount of stability-related accidents, which led to one of the highest fatality rates among all industrial sectors. It has been acknowledged by administrations and the research community, that this very high accident rate could be related not only to the lack of a (common) regulatory framework, but also to the lack of crew training programs or formation in vessel stability. In the last two decades, the use of simplified stability guidance systems has been proposed as a possible solution to try reducing the number of accidents by providing the crew with simple, easy to understand information regarding the stability situation of their vessel. These approaches include the use of simplified stability posters [18, 19], the analysis of residual freeboard [14], or the real-time estimation of stability parameters [3, 15–17].

The main objective of this work is to evaluate and compare the performance of two frequency estimation methods. The first method was introduced in [9], and it is based on sequential application of the Fast Fourier Transform (FFT) for estimation of the vessel's roll natural frequency, which in turn can be used to estimate the metacentric height and initial stability. The second method [11, 12] also estimates the natural roll frequency, achieved through the combined use of Empirical Mode Decomposition (EMD) and the Hilbert-Huang Transform (HHT).

The investigation utilizes two sets of roll motion data from a stern trawler. The first data set consists of simulated roll time series generated in irregular beam waves applying a one degree of freedom nonlinear model [1]. The second data set consists of experimental roll time series obtained from towing tank tests in regular beam waves.

It is noteworthy that, although two techniques are introduced for the estimation of the roll natural frequency of the vessel, the current chapter presents the theory of just the method based on EMD-HHT. The FFT-based approach is presented and analyzed in detail in another Chap. 22 of this book.

Potentially, both methods can be part of a computer based stability guidance system for small and medium sized fishing vessels. This is demonstrated by briefly presenting the condition monitoring system built atop the EMD-HHT estimator. Here a statistical change detector based on the Generalized Log-likelihood Ratio Test (GLRT) for Weibull stochastic processes is shown to trail changes in the vessel transverse stability and differentiate between safe and non-safe navigation situations.

This work updates and complements the findings previously described in [13].

## 2 Estimation of Roll Natural Frequency Through EMD-HHT

Vessel rolling in waves is nonlinear thanks to the nonlinearities in the restoring moment and damping. Therefore the extraction of frequency information from roll time series, such as the estimation of the roll natural frequency, should be performed by relying on signal processing methods developed for nonlinear (and non-stationary) signals.

Míguez González et al. [9] proposed to estimate the roll natural frequency by applying a sliding window FFT to bypass the lack of signal stationarity and attempt a quasi real-time estimation. Due to the time-frequency constraint, the window length played an important role in the trade-off between estimation accuracy and real-time processing.

To overcome the drawbacks of the sliding-window FFT, Santiago Caamaño et al. [12] proposed to use the Empirical Mode Decomposition and the Hilbert-Huang Transform to develop a roll natural frequency estimator that processes the roll motion signal directly in the time domain. The EMD-HHT method does not require stationarity and linearity of the signal to be processed.

The EMD is applied to decompose the measured roll motion signal into its main oscillatory components, the IMFs (Intrinsic Mode Functions) [2, 4, 5]. For a vessel sailing in waves, the IMFs will include components oscillating at frequencies included in the wave encounter spectrum, which are not naturally filtered out by the ship's roll dynamics; a component oscillating at or nearby the roll natural frequency; and additional components oscillating at very low frequencies corresponding to e.g. wind, swell. Once the IMFs have been obtained from the original signal, the Hilbert-Huang Transform (HHT) [2, 5] is applied to them for computing an estimate of the instantaneous frequency of each IMF. From these values the mean instantaneous frequency is computed according to [20] for each IMF, and stored in the vector  $\Omega_{IMF}$

$$\Omega_{IMF} = [\hat{\omega}_1, \hat{\omega}_2, \dots, \hat{\omega}_{N_{IMF}}] \quad (1)$$

where  $\hat{\omega}_1 > \hat{\omega}_2 > \dots > \hat{\omega}_{N_{IMF}}$ . The vector  $\Omega_{IMF}$  is naturally ordered since the EMD decomposes the signal from high to low frequencies.

Values of  $\Omega_{IMF}$  being above and below a maximum and minimum expected value for the vessel's roll natural frequency (related with the maximum and minimum expected level of stability) are discarded, and the vessel estimated natural roll frequency is selected as the maximum value from the remaining mean instantaneous frequencies (which is usually that one associated with the highest energy content).

The whole process is iterated to consecutive and partly overlapping batches of measured roll motion, in order to obtain a real-time estimate of the actual roll natural frequency and quickly capture changes due to variation in metacentric height.

To reduce the sensitivity of the estimation process to the wave conditions in specific sailing conditions the measured roll motion is filtered prior to being

processed by the EMD-HHT. The description of the filter and the conditions for its application, as well as the detailed description of this methodology can be found in [11, 12].

### 3 Test Cases

In order to evaluate the performance of the proposed methodologies, roll motion time series have been obtained both from a nonlinear mathematical model of roll motion and from towing tank tests.

The mathematical model is described in detail in [1] and has been already applied to the same vessel used in this work [9]. In this case, zero forward speed and irregular beam waves with no wind have been considered.

Regarding the scale model experiments, they have been carried out at the University of A Coruña towing tank. In this case, tests have been carried out under regular beam waves and zero speed. Further description of the experiments can be found in [11].

#### 3.1 Test Vessel

The vessel under consideration is a mid-sized stern trawler, which has been studied by the authors in previous works [8, 9, 11, 12].

In order to evaluate the performance of both methodologies, even when changes in the loading of the vessel take place during operation (which is very common in fishing vessels), two conditions have been analysed. The first one represents a realistic sailing situation with a  $GM$  over the minimum required value [6]. This one could be considered, for the sake of demonstration, as a safe loading condition. The second loading condition corresponds to the critical situation, i.e., the one with the minimum mandatory  $GM$  value and which has been defined as the limit between a safe (acceptable) and a non-safe (non-acceptable) situation.

The main characteristic of the vessel and the parameters of these two loading conditions are included in Table 1.

**Table 1** Test vessel: main characteristics and loading conditions

Vessel main characteristics		Loading condition parameters		LC 1	LC 2
Overall length (m)	34.50	Displacement (t)		489	448
Beam (m)	8.00	Metacentric height (m)		0.501	0.350
Depth (m)	3.65	Natural roll frequency (rad/s)		0.701	0.563
Linear roll damping coefficient ( $\nu$ )	0.0187	Natural roll period (s)		8.963	11.160
Quadratic roll damping coefficient ( $\beta$ ) ( $\text{rad}^{-1}$ )	0.393	Draft (m)		3.484	3.294

**Table 2** Wave condition parameters

Mathematical model: irregular waves			Towing tank tests: regular waves			
Wave condition	$H_s$ (m)	$\omega_{wp}$ (rad/s)	Wave condition	$H$ (m)	$\omega_w$ (rad/s)	$S_w$
1	1.95	0.563	1	1.95	0.563	0.01
2	3.03	1.008	2	3.03	1.008	0.05

### 3.2 Test Conditions

Regarding the wave conditions under analysis, they have been selected in order to consider the possible impact of the wave encounter frequency on the performance of the methodologies [12]. For this reason two different wave conditions have been tested, using both the mathematical model (irregular beam waves) and the towing tank experiments (regular beam waves). The first wave condition under consideration corresponds to a wave which frequency (or peak frequency in the irregular wave case) matches the natural roll frequency of the vessel in the loading condition LC 2. The second wave condition represents a situation where the wave encounter frequency is far from the roll natural frequency of the vessel in any of the considered loading conditions.

The wave parameters of both the mathematical model tests and the towing tank experiments, are included in Table 2.

## 4 Comparative Analysis

In order to analyse the performance of the EMD-HHT method and to compare it with results obtained by using the FFT-based one, both have been applied to the roll motion time series described in the previous section.

### 4.1 Mathematical Model Tests

Regarding the results obtained from the time series computed with the mathematical model, Fig. 1 shows from top to bottom the roll motion time series, the results of the EMD-HHT and the results of FFT-based method for Wave condition 1. It has to be mentioned that the EMD-HHT provides an estimate every 45 s while the FFT every 10 s. This is due to the fact that overlapping in each analysed roll motion batch has been considered in both methodologies: a 75% in the first method and a 94% in the second one. In this case, the peak wave encounter frequency matches the roll natural frequency of LC 2. As it can be seen, the roll natural frequency estimates are very close to the target value in both loading conditions and both methodologies. It has to be mentioned that the output of the FFT shows a slightly larger dispersion of the frequency estimates than the one from the EMD-HHT.

For Wave condition 2, in which the wave encounter frequency is far from the roll natural frequency of the vessel, the performance of the EMD-HHT remains satisfactory (Fig. 2). However, a slight overprediction of the frequency in LC 1 and an underprediction in LC 2 can be appreciated. Furthermore, the dispersion of the results is larger if compared to that observed in Wave condition 1. Regarding the FFT,

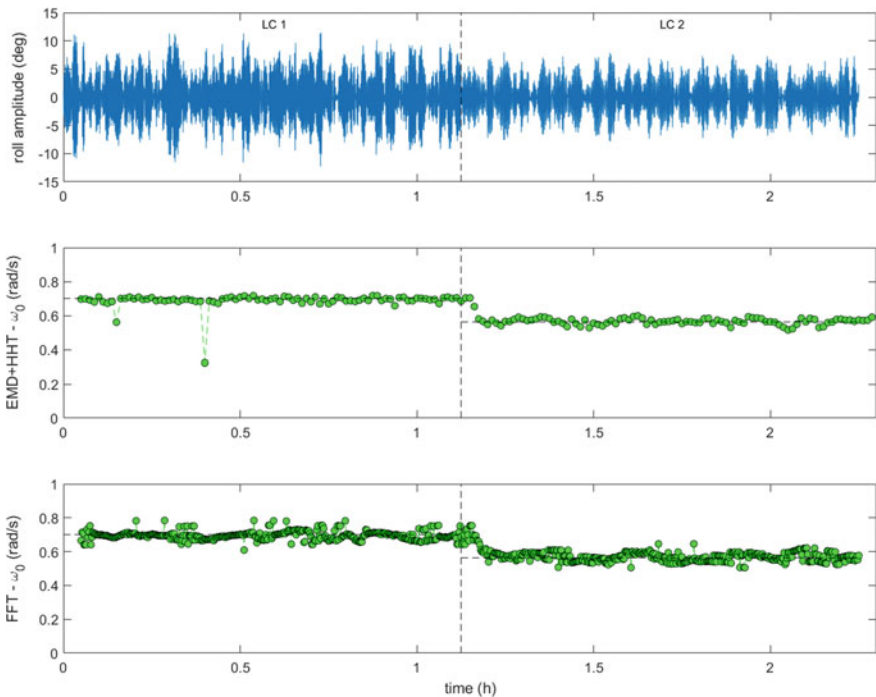


**Fig. 1** Results of EMD-HHT and FFT-based methods for simulated roll motion and wave condition 1

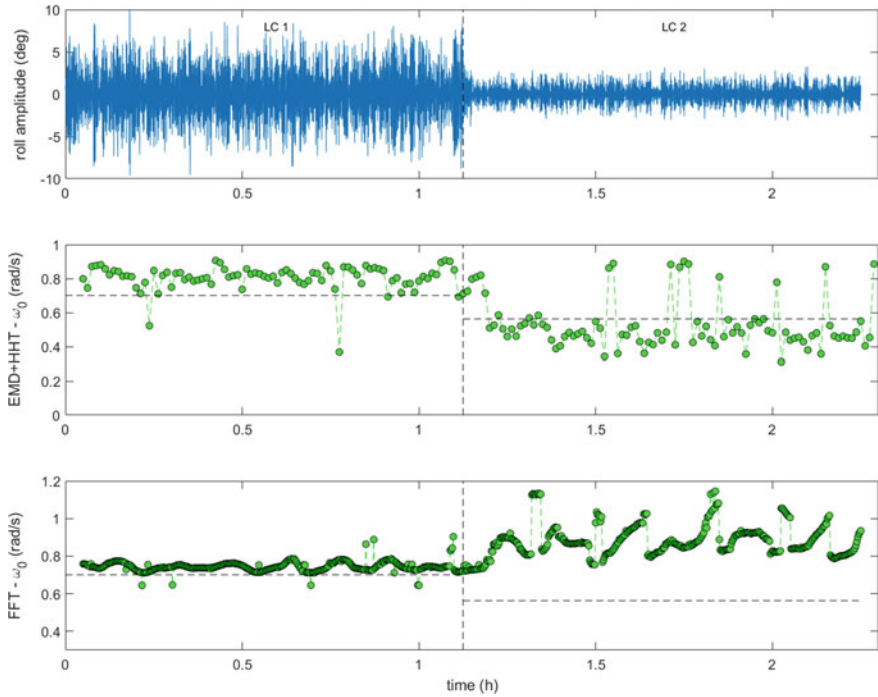


**Fig. 2** Results of EMD-HHT and FFT-based methods for simulated roll motion and wave condition 2

In LC 1 the estimates are quite close to the target value, although there is a perceptible overestimation. In LC 2 the estimated roll natural frequency is wrong, and it oscillates around the peak wave encounter frequency. This fact suggests, as expected, that this methodology could be more affected by the wave encounter frequency than the EMD-HHT.

Figure 3 summarises the results of the two wave conditions for the simulated roll motion time series. As it can be seen for Wave condition 1 (Fig. 3left) both methods behave well, although the results from the EMD-HHT present less dispersion than those from the FFT. In Wave condition 2 (Fig. 3right), the performance of the two methods decreases in comparison to the previous case. Although the EMD-HHT still performs relatively well in estimating the roll natural frequency of both loading conditions, the FFT is only able to obtain the roll natural frequency in one of them. This fact suggests, as it has been already mentioned, that the FFT is more vulnerable than the EMD-HHT to the effect of the wave encounter frequency.

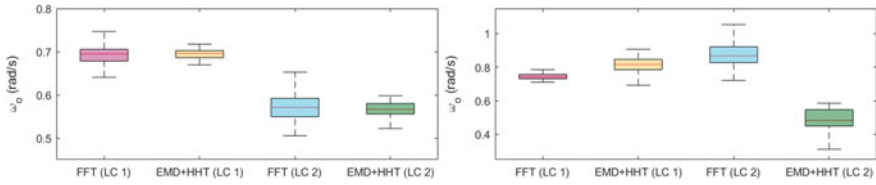


Fig. 3 Summary of results for simulated roll for wave condition 1 (left) and 2 (right)

### 4.2 Towing Tank Tests

In this section, the results of applying the estimation methods to roll motion time series from towing tank test are presented. In this case, a low-pass filter with a cut-off frequency of 1.75 rad/s has been applied to the time series to mitigate signal content related to possible wave reflection in the tank, wall effects, etc.

Figure 4 shows the roll motion time series corresponding to Wave condition 1, the output of the EMD-HHT and the output of the FFT. In this case, again, the EMD-HHT seems to work much better. The roll natural frequency estimates are quite

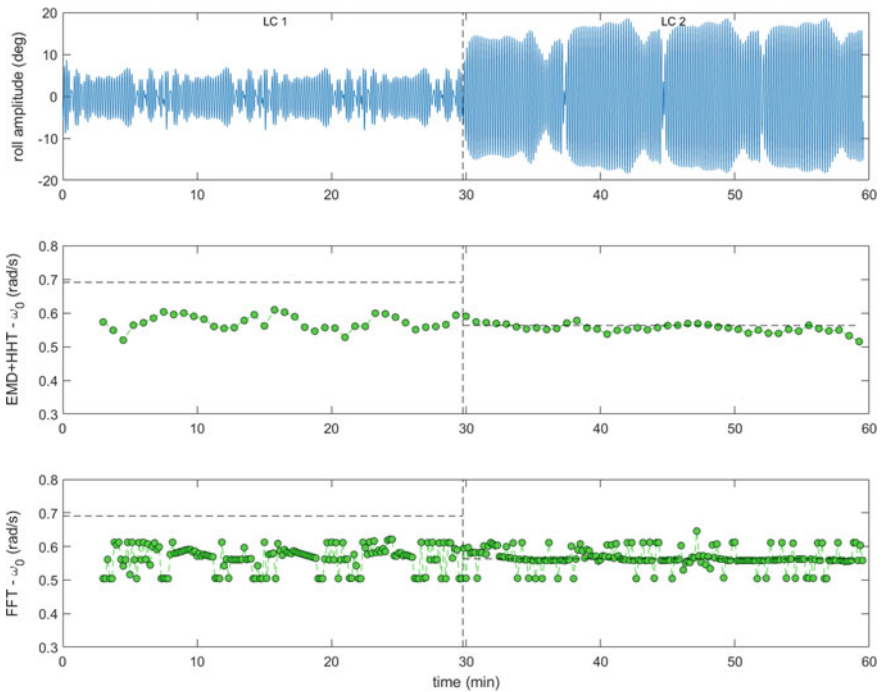
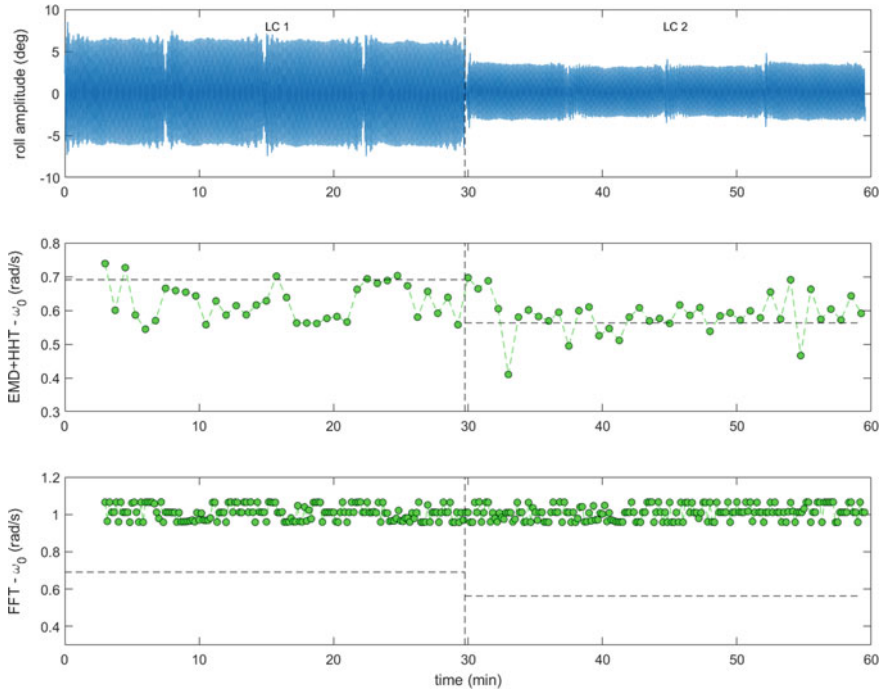


Fig. 4 Results of EMD-HHT and FFT-based methodologies for experimental roll motion and wave condition 1



**Fig. 5** Results of EMD-HHT and FFT-based methodologies for experimental roll motion and wave condition 2

accurate for LC 2, showing little dispersion. Nevertheless, there is a considerable underestimation in LC 1. Regarding the output of the FFT, some dispersion could be appreciated in the estimates obtained in both loading conditions. In addition, the method is not able to distinguish between the wave encounter frequency and the roll natural frequency of the vessel in LC 1, as the obtained values are very close to the former one.

Regarding Wave condition 2 (Fig. 5), on the one hand, the EMD-HHT presents again some underestimation in LC 1, and some dispersion of the results could be observed in both loading conditions. On the other hand, the performance of the FFT-based methodology is not satisfactory. As it can be seen, the obtained estimates of the roll natural frequency of the vessel are again very close to the wave encounter frequency in both loading conditions.

Figure 6 summarises the results of both methodologies in both wave conditions (Wave condition 1 in Fig. 6 left, and Wave condition 2 in Fig. 6 right). As it can be appreciated, in the case of the towing tank experiments, the FFT is highly influenced by the wave encounter frequency and it is not able to accurately identify the roll natural frequency of the vessel in some of time series. On the other hand, the EMD-HHT results seem to be better, and although especially some underpredictions take place, the general performance of the method is acceptable.



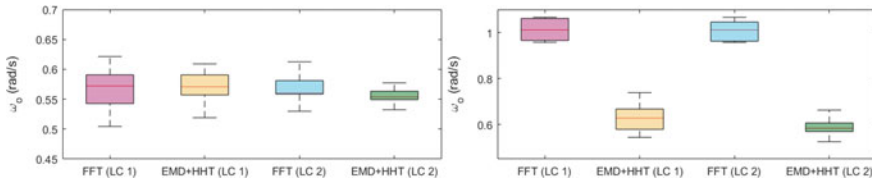


Fig. 6 Summary of results for experimental roll for wave condition 1 (left) and 2 (right)

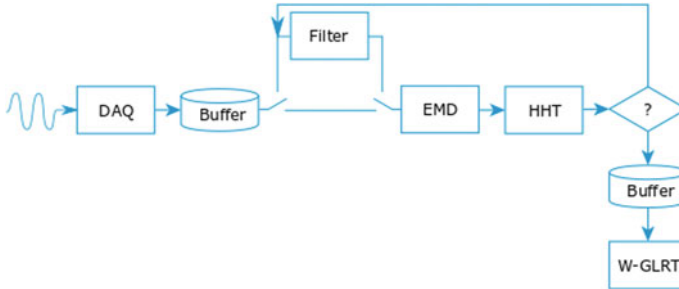


Fig. 7 Structure of the stability monitoring system

### 5 Change Detection-Based Stability Monitoring System

With a view in the practical implementation of an onboard stability guidance system, and in order to reduce its dependency on the accuracy of the roll frequency estimates, a monitoring system, based on the use of change-detection tools, has been implemented.

The objective of this statistical change detector is to determine, from the analysis of the roll natural frequency estimates obtained by the best performing method from the two previously analyzed (EMD-HHT), if a change between an acceptable and a non-acceptable sailing situation is taking place.

In Fig. 7, a block diagram describing the structure of the proposed stability monitoring system has been included, where W-GLRT represents the proposed statistical change detector.

In order to take into consideration that there is some level of uncertainty in the estimation of the natural roll frequency done by the EMD-HHT, these values have been statistically characterized using the Weibull distribution. The probabilistic median of this distribution is taken as the estimator of the natural roll frequency ( $\hat{\omega}_0$ ).

$$\hat{\omega}_0 = \lambda(\ln 2)^{\frac{1}{\kappa}} \tag{2}$$

Being ( $\kappa$ ) the shape parameter and ( $\lambda$ ) the scale parameter.

Considering that both scale and shape parameters change with the vessel loading condition, the proposed detector has been designed to track their variations and subsequently, the variations in the vessel roll natural frequency. The detection problem

under consideration is then to decide between two hypotheses; the null one ( $\mathcal{H}_0$ ), which corresponds to a safe condition, and the alternative one ( $\mathcal{H}_1$ ), which is related to a non-safe condition,

$$\begin{aligned} \mathcal{H}_0 &: \lambda_0 (\ln 2)^{\frac{1}{\kappa_0}} \geq \omega_0, \\ \mathcal{H}_1 &: \hat{\lambda}_1 (\ln 2)^{\frac{1}{\kappa_1}} < \omega_0, \end{aligned} \tag{3}$$

where  $\omega_0$  is defined as the critical natural roll frequency, and is the one corresponding to a GM equal to the minimum required by IMO for this type of ships ( $GM = 0.350$  m).

Taking into consideration that it depends on the Weibull parameters, the detection problem above could be reduced to a standard parameter test, where the decision between the two different hypotheses is done using the Generalized Likelihood Ratio Test (GLRT) [7]. This statistical test, based on the Neyman-Pearson theorem, maximizes the probability of detection for a desired probability of false alarms ( $\gamma$ ). The GLRT would decide that the hypotheses is fulfilled if:

$$L_G(\mathbf{\Omega}_0) = \frac{\mathcal{W}(\mathbf{\Omega}_0; \hat{\theta}_1, \mathcal{H}_1)}{\mathcal{W}(\mathbf{\Omega}_0; \theta_0, \mathcal{H}_0)} > \gamma \tag{4}$$

where  $\mathbf{\Omega}_0$  is the vector containing the estimations of natural roll frequency under analysis,  $\theta = [\lambda, \kappa]^T$  is the vector containing the characteristic parameters of the Weibull distribution,  $\theta_0$  is its realization for the null hypotheses and  $\hat{\theta}_1$  is the maximum likelihood estimate of the parameter vector for the hypotheses, which is obtained by maximizing the Weibull probability density function  $\mathcal{W}(\mathbf{\Omega}_0; \theta)$  under  $\mathcal{H}_1$ .

In addition to the above, a situation awareness system has been also included, with the objective of informing the crew about the stability level of their vessel following a colour coded pattern, in a similar way as it has been done in previous works by the authors [10]. This information is obtained by comparing  $\hat{\omega}_0$  with  $\omega_0$ .

Finally, the performance of the monitoring system for two of the previous test cases is analysed. Figure 8 shows, from top to bottom, the simulated roll motion time series for Wave condition 1, the results of the EMD-HHT, the results of the detector and the results of the awareness indicator. As it can be seen, the performance of the detector is very good. In the detector output graph, the upper continuous line represents the limit between safe and non-safe situation, which triggers the alarm, and the lower one represents the level in which this alarm is deactivated [11].

It adequately classifies the loading conditions and no false alarms or miss detections took place. Also the awareness indicator appropriately distinguish both loading conditions, providing the crew with a perception of the risk.

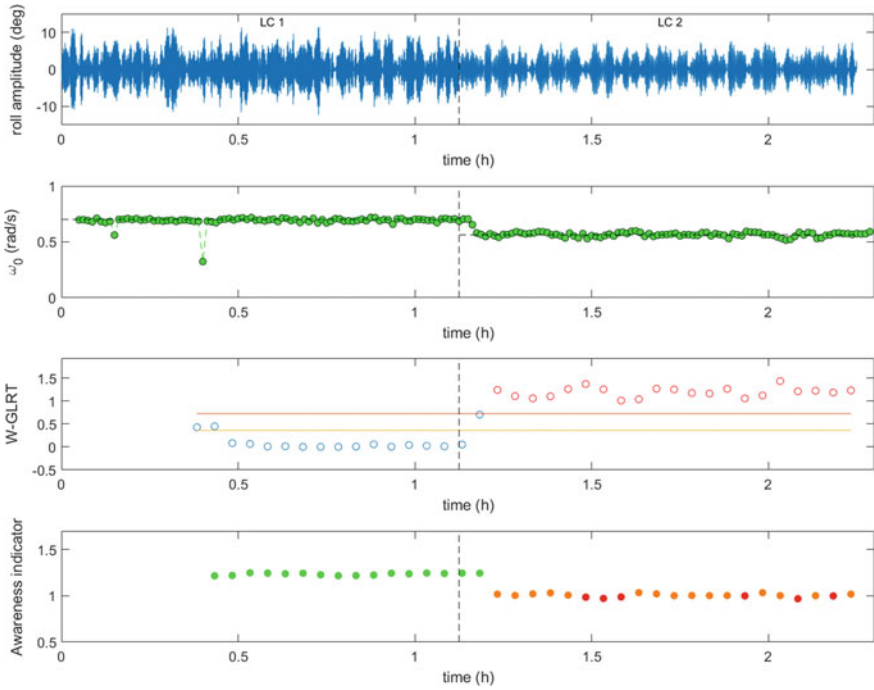


**Fig. 8** Results of EMD-HHT and change detection methodology for simulated roll motion and wave condition 1

Figure 9 illustrates, from top to bottom, the roll motion time series, the output of the EMD-HHT, the output of the detector and the output of the awareness indicator for Wave Condition 2 of the towing tank tests. Despite of the fact that the roll natural frequency is underestimated in LC 1, the performance of the detector remains satisfactory. It correctly identifies the loading conditions, triggering the alarm in the risky situation. Only one false alarm appeared and two miss detections took place. Regarding the awareness indicator, its behaviour seems to be also acceptable.

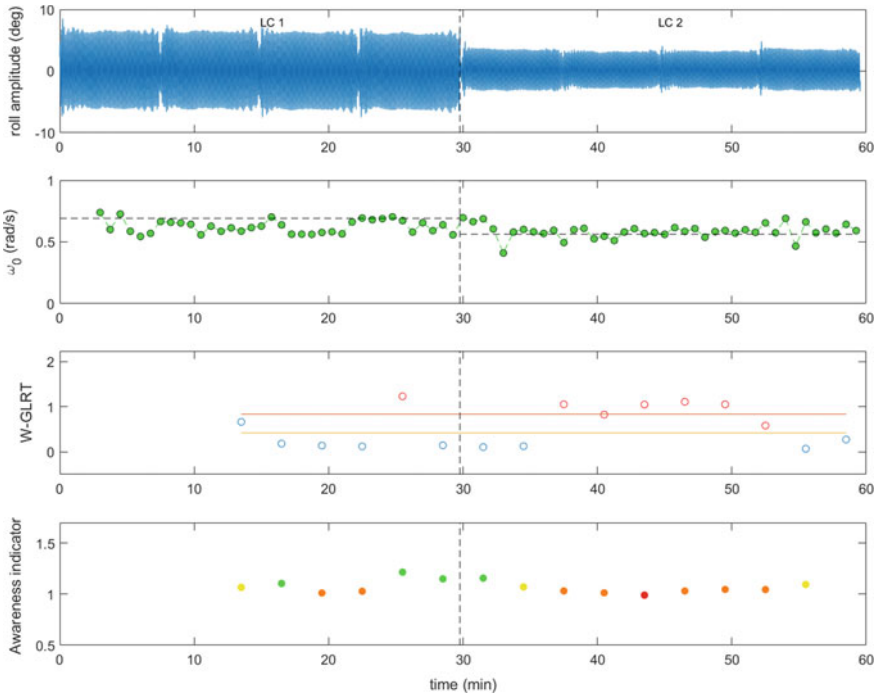


**Fig. 9** Results of EMD-HHT and change detection methodology for experimental roll motion and wave condition 2

## 6 Conclusions

In this work, a comparison between two methods for real-time evaluation of the stability of the ship has been presented. The first method is based on the application of the EMD-HHT to estimate the natural roll frequency of the vessel. The second one is based on the recursive application of the FFT to obtain the same parameter.

In order to evaluate and compare the performance of both methods, a nonlinear mathematical roll model of a stern trawler in irregular beam waves has been used to simulate the vessel roll motion sailing in two different loading conditions, a safe one and another which is supposed to be non-safe from an initial stability point of view. Also, roll motion time series for the same loading conditions from towing tank tests in regular waves have been used.

The estimations of the natural roll frequency of the vessel obtained by the EMD-HHT method have shown to be quite accurate, performing better than the FFT-based estimator previously proposed in [9], at least in the wave conditions under analysis. In particular, in the case of the experiments, this method is strongly affected by the wave encounter frequency.

With the intention of implementing the EMD-HHT estimation method in an on board stability guidance system, and also to mitigate its dependency on the accuracy of the roll frequency estimates, a monitoring system that integrates change-detection tools has been presented. It is based on a probabilistic detector which analyzes if the current loading condition is safe or not from a stability point of view (W-GLRT).

The performance of this monitoring system has been very satisfactory in the tested wave conditions, accurately differentiating between safe and non-safe conditions, and timely detecting the changes in the vessel loading condition. Even in situations where the roll natural frequency estimates are not too accurate, robustifying the methodology.

Although the results are very promising, and could represent a step forward compared to the previous developments of some of the authors of this work, additional testing is needed to verify this behaviour in more wave conditions and vessel speeds and headings.

## References

1. Bulian G, Francescutto A (2004) A simplified modular approach for the prediction of the roll motion due to the combined action of wind and waves. *Proc Inst Mech Eng Part M J Eng Marit Environ* 218:189–212. <https://doi.org/10.1243/1475090041737958>
2. Dätig M, Schlurmann T (2004) Performance and limitations of the Hilbert-Huang transformation (HHT) with an application to irregular water waves. *Ocean Eng* 31:1783–1834. <https://doi.org/10.1016/j.oceaneng.2004.03.007>
3. Galeazzi R, Perez T (2011) A nonlinear observer for estimating transverse stability parameters of Marine surface vessels. *IFAC* 44. <https://doi.org/10.3182/20110828-6-IT-1002.01474>
4. Gupta R, Kumar A, Bahl R (2014) Estimation of instantaneous frequencies using iterative empirical mode decomposition. *Signal Image Video Process* 8:799–812. <https://doi.org/10.1007/s11760-012-0305-5>
5. Huang N, Shen Z, Long S, Wu M, Shih H, Zheng Q, Yen N, Tung C, Liu H (1998) The empirical mode decomposition and the Hilbert spectrum for nonlinear and non-stationary time series analysis. *Proc R Soc A Math Phys Eng Sci* 454:903–995. <https://doi.org/10.1098/rspa.1998.0193>
6. International Maritime Organization (2012) Cape town agreement of 2012 on the implementation of the provisions of the Torremolinos Protocol of 1993 relating to the Torremolinos International Convention for the safety of fishing vessels, 1977
7. Kay SM (1998) *Fundamentals of statistical signal processing: detection theory*. Prentice-Hall Inc, Englewood Cliffs
8. Míguez González M, Bulian G (2018) Influence of ship dynamics modelling on the prediction of fishing vessels roll response in beam and longitudinal waves. *Ocean Eng* 148:312–330. <https://doi.org/10.1016/j.oceaneng.2017.11.032>
9. Míguez González M, Bulian G, Santiago Caamaño L, Díaz Casás V (2017) Towards real-time identification of initial stability from ship roll motion analysis. In: *Proceedings of the 16th international ship stability workshop*. Belgrade, Serbia
10. Míguez González M, Caamaño Sobrino P, Tedín Álvarez R, Díaz Casás V, Martínez López A, López Peña F (2012) Fishing vessel stability assessment system. *Ocean Eng* 41:67–78
11. Santiago Caamaño L, Galeazzi R, Míguez González M, Díaz Casás V, Nielsen UD (2019) Experimental validation of transverse stability monitoring system for fishing vessels. *IFAC-PapersOnLine* 52(21):57–63. <https://doi.org/10.1016/j.ifacol.2019.12.283>

12. Santiago Caamaño L, Galeazzi R, Nielsen UD, Míguez González M, Díaz Casás V (2019) Real-time detection of transverse stability changes in fishing vessels. *Ocean Eng* 189. <https://doi.org/10.1016/j.oceaneng.2019.106369>
13. Santiago Caamaño L, Míguez González M, Galeazzi R, Nielsen UD, Díaz Casás V (2019) On the application of change detection techniques for the stability monitoring of fishing vessels. In: *Proceedings of the 17th international ship stability workshop*. Helsinki, Finland
14. Scarponi M (2017) Use of the Wolfson stability guidance for appraising the operational stability of small fishing vessels. In: *Proceedings of the 16th international ship stability workshop*. Belgrade, Serbia
15. Terada D, Hashimoto H, Matsuda A, Umeda N (2018) Direct estimation of natural roll frequency using onboard data based on a Bayesian modeling procedure. In: *Proceedings of the 13th international conference on the stability of ships and ocean vehicles*. Kobe, Japan
16. Terada D, Tamashima M, Nakao I, Matsuda A (2019) Estimation of metacentric height using onboard monitoring roll data based on time series analysis. *J Mar Sci Technol* 24(1):285–296
17. Wawrzynski W, Krata P (2016) Method for ship's rolling period prediction with regard to non-linearity of GZ curve. *J Theoret Appl Mech* 1329–1343. <https://doi.org/10.15632/jtam-pl.54.4.1329>
18. Wolfson Unit (2004) Research project 530. Simplified presentation of FV stability information—phase 1. Final report. Tech Rep 4, Univeristy of Southampton
19. Womack J (2003) Small commercial fishing vessel stability analysis: where are we now? Where are we going? *Mar Technol* 40(4):296–302
20. Xie H, Wang Z (2006) Mean frequency derived via Hilbert-Huang transform with application to fatigue EMG signal analysis. *Comput Methods Programs Biomed* 82:114–120. <https://doi.org/10.1016/j.cmpb.2006.02.009>

# Real-Time Estimation of Natural Roll Frequency for the Stability Guidance of Fishing Vessels



Marcos Míguez González, Gabriele Bulian, Lucía Santiago Caamaño, Sandra Allegue García, and Vicente Díaz Casás

**Abstract** Stability failures are known to be one of the major causes of accidents involving fishing vessels. The use of guidance systems, focused on complementing the capabilities of the crews for dealing with the assessment of their vessel stability, have been proposed by many authors as a possible way for reducing the frequency of this type of incidents. Initially, these systems were basically color-coded posters or were relying on subjective data introduced by the crew. However, the use of approaches which operate in real time with no need of interaction could overcome the problems identified for these “first generation” methods. This work presents a methodology based on the analysis of roll spectrum for estimating in real time the metacentric height of the vessel. The integration of the presented methodology within a first generation guidance system could increase its capabilities for providing stability guidance. The performance of the proposed methodology is analysed using the simulated roll motion of a mid-sized fishing vessel in irregular beam waves and lateral gusty wind, computed by a one degree of freedom nonlinear model. Obtained results are promising in most of the analysed conditions, although some open issues regarding the implementation of the methodology still require further analysis.

---

M. Míguez González (✉) · L. Santiago Caamaño · V. Díaz Casás  
Integrated Group for Engineering Research, Ferrol Industrial Campus, University of A Coruña, A Coruña, Spain  
e-mail: [marcos.miguez@udc.es](mailto:marcos.miguez@udc.es)

L. Santiago Caamaño  
e-mail: [lucia.santiago.caamano@udc.es](mailto:lucia.santiago.caamano@udc.es)

V. Díaz Casás  
e-mail: [vicente.diaz.casas@udc.es](mailto:vicente.diaz.casas@udc.es)

G. Bulian  
Department of Engineering and Architecture, University of Trieste, Trieste, Italy  
e-mail: [gbulian@units.it](mailto:gbulian@units.it)

S. Allegue García  
Navantia S.A, Ferrol, Spain  
e-mail: [sallegue@navantia.es](mailto:sallegue@navantia.es)

**Keywords** Fishing vessels · Intact stability · Stability monitoring · Guidance systems

## 1 Introduction

Operational guidance systems are common and broadly used today among the commercial fleet, and include loading and intact stability guidance systems, weather routing systems, damage stability analysis software and dynamic stability evaluation software [22]. The use of these systems has helped crews to increase the safety of their vessels and their economic performance. Although their operation is usually non-straightforward and their working principles require a more-than-average knowledge of naval architecture, dedicate crew training programs can be put in place among shipping companies to familiarize crews with such systems [10]. In fact, the importance of guidance to masters has been already highlighted by the IMO and the Classification Societies, as could be seen, for instance, in the MSC.1/Circ.1228 [11]. In addition to this, the development of regulations based on direct stability assessment has also been embedded in the IMO second generation intact stability criteria [12, 27]. In Bačkalov et al. [1] and references therein, a discussion on the importance, potentialities and open issues related to operational guidance can be found.

The case of fishing vessels is largely different to that described above. Crews of fishing vessels are not usually trained in risk and stability analysis, especially in the smallest vessels. Guidance systems are not common at all onboard those vessels and most regulators have not tackled the problem of guidance in fishing vessels [16]. This issue is particularly relevant if the number of casualties which occur within the fishing sector is taken into account [9]. A relevant amount of corresponding fatalities is due to stability issues, and one of the main causes is the crew lack of objective capability for determining the risk level of the vessel [14].

However, some national authorities and institutions proposed in the last years their own alternatives of simplified stability guidance systems, with different degrees of success and levels of implementation among the corresponding fleets [28–30]. Some of the authors of this work have also proposed a tool based on a naval architecture software that, together with an IMU module and a simplified user interface, analyses the ship motions and the ship loading condition, and provides the master with real-time information of the safety level of the ship in the current sailing situation [16, 24]. Within the mentioned tool, this safety level is presently obtained by using the intact stability characteristics of the vessel and the maximum wave to capsize approach proposed by Deakin [7]. Most of the nowadays available proposals fulfil a given set of basic requirements, including ease of use, simplicity of implementation and reduced cost of implementation and maintenance. However, all of them rely, up to some extent, on subjective interaction with the crew. Such interaction can occur, for instance, through the comparison of the current condition of the vessel to those provided by a suitable stability poster [7, 30], or through the inputting of information within a stability guidance software [16].



This work presents a sample application of a methodology aiming at providing the crew with realistic stability data of their vessel in real time, minimizing the need for user interaction and the influence of subjective analysis. This approach is based on the estimation of the vessel natural roll frequency in real time from the analysis of roll motion spectrum. The underlying idea is that this information can then be used for the estimation of the initial metacentric height of the vessel and it could then be eventually embedded in a guidance system such as the one described above [16, 24]. Information regarding the metacentric height of the vessel is in fact fundamental for any guidance system relying on ship motions prediction, irrespective of whether such approach is based on short-term deterministic assessment (e.g. [15]), more classical linear-seakeeping-based forecasting systems [19], or more advanced approaches intended to address also potentially dangerous dynamic stability phenomena in waves [21]. In order to test the proposed methodology, a nonlinear model of a medium sized stern trawler, under the excitation of beam irregular waves and lateral gusty wind, has been applied. This work updates and complements the findings previously described by Míguez González et al. [17].

## 2 Real Time Estimation of Natural Roll Frequency

As it has been already mentioned, the proposed methodology relies on the estimation of natural roll frequency in real time, as a basis for obtaining an estimation of the vessel metacentric height ( $\overline{GM}$ ), which is of major importance if the stability condition of the ship is to be monitored. From the well-known roll natural frequency formula, obtained under the simplifying assumption of 1-DOF uncoupled linear roll model,

$$\omega_0 = \sqrt{\frac{\Delta \cdot \overline{GM}}{I_{xx} + I_{add}}} = \sqrt{\frac{g \cdot \overline{GM}}{k_{xx}^2}} \quad (1)$$

it can be observed that, apart from the natural roll frequency, the vessel displacement ( $\Delta$ ), the dry inertia ( $I_{xx}$ ) and the hydrodynamic added inertia term ( $I_{add}$ ) (or the wet roll gyradius  $k_{xx}$ ) are unknown parameters that are also necessary for obtaining the vessel  $\overline{GM}$ . In case the vessel could be equipped with draft sensing devices, it could be possible to determine the displacement and to estimate the dry inertia (using a weight breakdown method) and added inertia (using, for example, some potential theory code) with no need for crew interaction. However, in the case of small and medium sized fishing vessels, using these systems is not feasible due to cost limitations. In Santiago Caamaño et al. [23], an analysis of the influence of these parameters in the estimation of  $\omega_0$  is done, concluding that reasonably good results could be obtained by obtaining the wet roll gyradius using typical approximate values ( $k_{xx} \approx 0.4 \cdot B$ ) and disregarding the effects of the variation of the other parameters, which is the approach followed in this work.

The method proposed herein for the estimation of natural roll frequency is based on the analysis of the roll spectrum, obtained in real time from the analysis of the vessel roll motion time series. A different approach was proposed in the past by Terada et al. [26], based on an autoregressive procedure and a general state space modelling.

Santiago Caamaño et al. [23], reported some results applying an approach similar to that presented herein to a set of towing tank tests of a medium sized stern trawler in longitudinal regular waves, under parametric roll resonance conditions. In that work, *Fast Fourier Transform* (FFT) analysis was directly applied to a single chunk (180 s) of each of the analysed roll motion time series, with the goal of obtaining the roll spectrum for that given chunk. The length of these chunks was defined considering that, under operational conditions, the stability characteristics of such a vessel could be assumed to be invariant within that time window. Once the spectrum was obtained, the natural roll frequency of the ship could be estimated from the location of the spectrum maximum value, taking as a basic assumption that most of the energy would be concentrated around the roll natural frequency. In addition to this, the performance of the system if windowing was applied to the spectra computation was also investigated, concluding that no significant improvement was obtained with these techniques.

Although the obtained results were satisfactory, there were some points which remained open for discussion. On the one hand, the tested cases were limited to the case of head waves. Under these conditions, roll motion was just limited to that due to small misalignments of the model in the tank or, in the proper conditions, to parametric excitation in roll (and so, approximately at the vessel roll natural frequency). Roll energy was then mainly concentrated around natural roll frequency, which lead to clear single-peaked spectra. On the other hand, the studied conditions, under regular waves, represented an idealized scenario. Both issues lead to the fact that the tested conditions were far from realistic operational situations.

## **2.1 Proposed Methodology**

In this work, some of the aforementioned drawbacks are tackled, proposing a refined and improved methodology, and more realistic test conditions. This approach is, as the previously described one, based on the fundamental assumption that the peak frequency of the roll spectrum corresponds, at least approximately, to the roll natural frequency. Such assumption is herein made as a consequence of the peculiar dynamical characteristics of roll, which tends to cut the effect of those excitations which are not leading to roll oscillations close to the roll natural frequency. However, it is clear that this is an approximation and this assumption requires further analysis.

Although, similarly to Santiago Caamaño et al. [23], also the proposed methodology relies on the estimation of the vessel roll spectrum using FFT analysis, the present approach is more onboard-implementation oriented and three main aspects have been taken into account, which have not been previously considered, namely:

the limitations induced by FFT frequency resolution, the variation of the roll spectrum in time, and the use of overlapped analysis in real time.

Regarding the FFT frequency resolution, it is well known that the frequency resolution which a FFT analysis can provide and that determines the accuracy of the spectrum shape, is only related to the length of the time series under analysis ( $T$  (s)) [20]. This resolution can be obtained as:

$$\delta\omega = \frac{2 \cdot \pi}{T} = \frac{2 \cdot \pi \cdot f_s}{N} \tag{2}$$

where  $\delta\omega$  is the FFT frequency resolution (rad/s),  $f_s$  is the sampling frequency (Hz),  $T$  is the analysis time (s), and  $N$  is the number of samples analysed by the FFT. As it can be appreciated, if the aforementioned 180 s analysis time is applied, it will result in a frequency resolution  $\delta\omega = 0.035$  (rad/s). This is not a negligible magnitude and, for the fishing vessel described later in this work, it amounts to more than a 6% of the natural roll frequency. This fact makes it difficult to accurately estimate the natural roll frequency from the location of the peak of a roll spectrum which is so scarcely discretized.

Taking into account that roll motion data will be available in real time and that the roll spectrum shape of each analysed time chunk could be different from each other, a strategy based on overlapped measures and averaging of spectra has been adopted in order to obtain a more robust estimation of the spectrum. Based on this methodology, instead of relying on the spectrum given by a single time chunk, the analysed spectrum is the one obtained from averaging a number of spectra, obtained from a set of partially overlapped measures each one having the same “Analysis Time” length, and separated each other by a constant “Sample Time”. The resulting spectrum is an average spectrum within a given “Averaging Time”, which will be representative of the roll spectrum of the vessel during that time. The proposed methodology is represented in Fig. 1.

However, the resulting averaged spectrum is still affected by the aforementioned lack of frequency resolution, which is of course independent of the averaging process. In order to try to increase the frequency resolution of the intended results, a fitting process of the averaged spectrum with a simple parametric model based on the

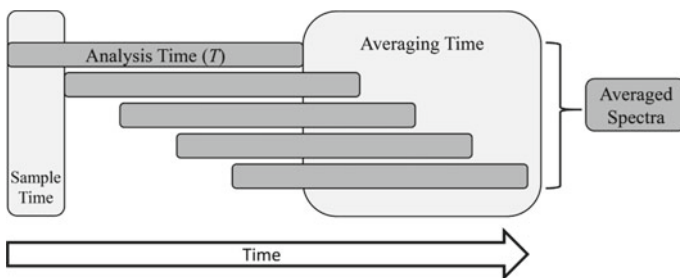


Fig. 1 Proposed methodology

superposition of three Gaussian functions has been implemented. The parametric model has 9 parameters; three parameters for each of the three Gaussian functions. The number of Gaussian functions has been selected as to allow the fitting of up to three superimposed spectra, which could correspond with the roll motion at the principal wind and wave excitation frequencies, and the roll motion of the vessel at its natural frequency. The simplified parametric model for the roll spectrum takes the following form:

$$S_{roll}(\omega) = a_1 \cdot e^{-\left(\frac{\omega-b_1}{c_1}\right)^2} + a_2 \cdot e^{-\left(\frac{\omega-b_2}{c_2}\right)^2} + a_3 \cdot e^{-\left(\frac{\omega-b_3}{c_3}\right)^2} \quad (3)$$

It is important to note that the main purpose of the model is not to provide a very accurate fitting of the roll spectrum, but to be a robust model for the identification of the most prominent peak, which is assumed herein to be associated to the roll frequency.

The fitting process has been divided into two steps; the first one is done by a minimization process by applying a genetic algorithm, which provides a first set of fitting parameters  $a_i$ ,  $b_i$  and  $c_i$  for  $i = 1, 2, 3$ . In the second step, this set of parameters is used as starting guess point for a Nonlinear Least Squares Fitting process, which is used to determine the final parameters of the fitting function. Once the fitting is completed, the analytical expression (3) is used for the identification of the maximum peak which is assumed to be associated with the vessel natural roll frequency. This latter step is no longer bound by the frequency resolution associated from the Fourier analysis. In order to improve the performance of this process, a preliminary smoothing of the average spectrum is carried out by applying a 5-point moving average technique. Thus, the previously described fitting process is applied to this smoothed spectrum.

Regarding the selection of the Analysis, Sample and Averaging Times, the typical operational profile of the tested vessel (a medium sized stern trawler, which will be later described), has been taken into account. Regarding the Analysis Time, it has to fulfil two main requirements. On the one hand, it has to be sufficiently long as to provide a minimum basic frequency resolution. On the other hand, it has to be short enough to allow the detection of changes on the vessel stability characteristics, which is in fact the main objective of the proposed methodology. From these considerations, and taking into account also the comments by Santiago Caamaño et al. [23], an Analysis Time of 180 s has been considered. Regarding the Sample Time, its selection is only determined by the speed of the analysis algorithm and the possibility of being able to track any possible variation on ship natural frequency in real time. In this case, a 10 s Sample Time has been selected. Finally, the Averaging Time is the period in which the spectral information of the roll motion is averaged, and so “stored” by the system. A too long averaging time will lead to hiding possible changes in the vessel condition, while a too short averaging time will not be long enough for sufficiently reducing the variability of the short term estimations. In this case, Averaging Time has been taken as 120 s. However, it has to be highlighted that these values are

applicable only to this specific vessel, and that further refinement should be needed after some time of operation in a real scale scenario.

### 3 Test Environment

#### 3.1 Fishing Vessel Model

In order to test the proposed methodology under realistic conditions, the ship roll motion in irregular beam seas has been simulated by applying a one degree of freedom nonlinear model, where the excitation due to waves, mean wind and wind gustiness, has been taken into account. The details of this model are given by Bulian and Francescutto [3], who also applied the model to the case of a small fishing vessel. The structure of this model is the following,

$$\ddot{\phi} + 2 \cdot \nu \cdot \omega_0 \cdot \dot{\phi} + \beta \cdot \dot{\phi} \cdot |\dot{\phi}| + \omega_0^2 \cdot \frac{\overline{GZ}(\phi)}{GM} = \omega_0^2 \cdot (m_{wave}(t) + m_{wind}(t)) \quad (4)$$

where  $\nu$  and  $\beta$  are, respectively, the linear and nonlinear quadratic damping coefficients,  $\omega_0$  is the natural roll frequency of the ship,  $GM$  is the still water metacentric height and  $\overline{GZ}(\phi)$  is the nonlinear righting lever as a function of the absolute roll angle.  $m_{wave}(t)$  and  $m_{wind}(t)$  represent the time dependant nondimensional moments due to the effect of beam waves and lateral wind.

Regarding wave excitation, it has been modelled through the “Absolute Angle Approach” [4]. The effective wave slope coefficient ( $r(\omega)$ ) has been obtained from linear hydrodynamic analysis of the proposed vessel according to Bulian and Francescutto [5]. Finally, a Bretschneider spectrum has been selected to model irregular waves [13].

Wind speed excitation has been divided into a steady component (mean wind speed) and a fluctuating one (wind gustiness), which reflect in a time dependent, non-zero-mean heeling moment. In order to obtain the total wind moment, aerodynamic coefficients have been obtained using experimental data from Blendermann [2]. The mean wind speed is obtained as a function of the significant wave height by applying the relationship used in the Pierson-Moskowitz spectrum [13]. Finally, wind gustiness has been modelled by applying a Davenport spectrum [6].

The selected test vessel is a medium sized stern trawler, which details are reported in Table 1, hull sections and 3D view are shown in Fig. 2, and  $\overline{GZ}$  curve in calm water and effective wave slope coefficient in Fig. 3. The same vessel has been studied also by Míguez González and Bulian [18].

**Table 1** Test vessel: main characteristics

Length overall	34.50 m
Beam	8.00 m
Depth	3.65 m
Draft	3.340 m
Hull volume	448 m <sup>3</sup>
Metacentric height ( $\overline{GM}$ )	0.350 m
Natural roll frequency ( $\omega_0$ )	0.563 rad/s
Natural roll period ( $T_0$ )	11.16 s
Wet roll gyradius ( $k_{xx}$ )	3.291 m
Linear roll damping coefficient ( $\nu$ )	0.0187
Quadratic roll damping coefficient ( $\beta$ )	0.393 rad <sup>-1</sup>
Lateral windage area ( $A_{lat}$ )	163.19 m <sup>2</sup>
Height of center of $A_{lat}$ above the waterline ( $H_{ip}$ )	2.670 m

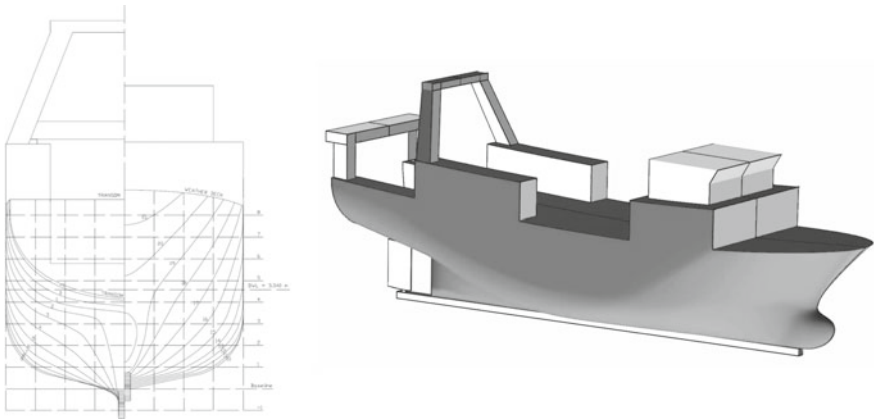


**Fig. 2** Hull bodyplan (left) and 3D view (right)

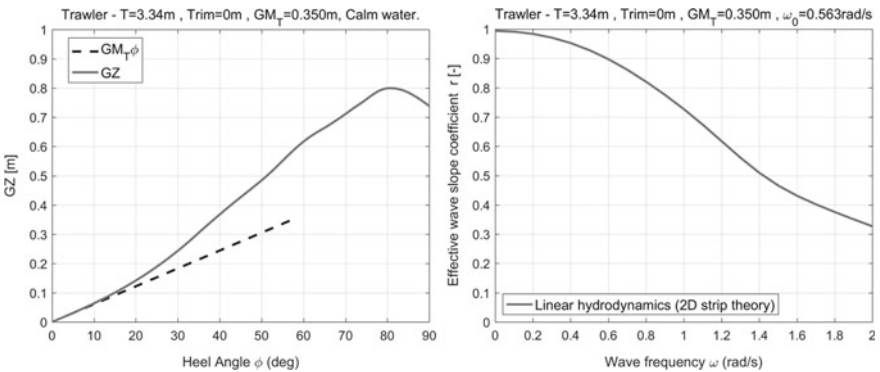


**Fig. 3** Test vessel:  $\overline{GZ}$  curve in calm water (left) and effective wave slope coefficient (right)

### 3.2 Test Condition

The vessel under study sails in coastal waters off Galicia, Spain. In order to obtain the typical meteorological conditions for this area, historical data from four Puertos del Estado wave buoys (Silleiro, Vilán, Bares and Peñas SeaWatch buoys) have been used [8]. Wave data from these buoys for the period between 1997 and 2015 were used to generate one scatter diagram for each of the locations. An approximate scatter diagram for the entire Galician Coast area was eventually determined by averaging them. From this average scatter diagram, a series of wave conditions have been selected for being used in this study. For each value of the 9 considered spectral peak periods ( $T_p$ ), the conditional average significant wave height ( $H_{SAve}$ ) has been determined and taken as reference. This leads to a corresponding limited set of reference wave scenarios ( $T_p, H_{SAve}$ ).

The conditional average significant wave height  $H_{SAvej}$  for the considered  $j$ -th peak period is calculated as:

$$H_{SAvej} = \sum_{i=1}^N \frac{H_{Si} \cdot p_{ji}}{P_j} \text{ with } P_j = \sum_{i=1}^N p_{ji} \tag{5}$$

where  $H_{Si}$  is the centre-cell significant wave height for the  $i$ -th interval in the wave scatter diagram,  $p_{ji}$  is the probability associated to each combination of significant wave height and peak period, and  $P_j$  is the probability for the  $j$ -th peak period. The resulting wave conditions (peak period and corresponding significant wave height), which are those used in this work, are included in Table 2, together with a map showing the location of the four considered SeaWatch buoys.

In order to test the performance of the system, the aforementioned model has been used to generate 3600 s roll motion time series for each of the reference sea conditions of Table 2, to which the proposed methodology has been applied. 1000 harmonic components were used for generating irregular wave and wind moments, and a 20 Hz sampling rate has been selected. Results including standard deviation of roll motion ( $\sigma_{roll}$ ) and maximum ( $\phi_{max}$ ) and mean ( $\phi_{mean}$ ) roll values for each of the nine tested sea conditions, are shown in Table 3.

The behaviour of the vessel roll motion under the studied wave and wind conditions is illustrated using as sample case the roll time series corresponding to the case with the characteristic period with maximum marginal probability of occurrence (reference sea condition 4), and which is shown in Fig. 4. As it can be appreciated, the ship roll motion shows an asymmetric behaviour due to the effect of mean wind. The wave spectrum peak period in this case is relatively close the vessel natural roll period, thus some relatively large amplitude motions due to harmonic resonance were expected, and in fact, can be observed in the roll time series (this phenomenon can also be appreciated in reference sea conditions from 5 to 8). Since the gustiness spectrum is linked to the mean wind speed, wind effects on roll motion overall increase as the mean wind speed increases.

**Table 2** Location of SeaWatch buoys (left) and tested wave and wind conditions (right)

Reference sea condition	Peak period ( $T_P$ ) (s)	Significant wave height ( $H_{S,Ave}$ ) (m)	Mean wind speed ( $\bar{V}_W$ ) (m/s)
1	4	0.932	6.448
2	6	1.481	8.126
3	8	1.772	8.890
4	10	1.971	9.375
5	12	2.671	10.912
6	14	3.499	12.492
7	16	4.297	13.843
8	18	4.715	14.499
9	20	5.028	14.973



**Table 3** Roll motion characteristics

	Reference sea condition								
	1	2	3	4	5	6	7	8	9
$\sigma_{roll}$ (deg)	0.424	0.848	1.621	3.661	5.202	5.861	5.976	6.165	5.363
$\phi_{max}$ (deg)	2.120	4.091	6.835	13.275	17.332	21.675	19.36	20.455	20.323
$\phi_{mean}$ (deg)	0.725	1.148	1.368	1.480	1.975	2.561	3.126	3.406	3.678

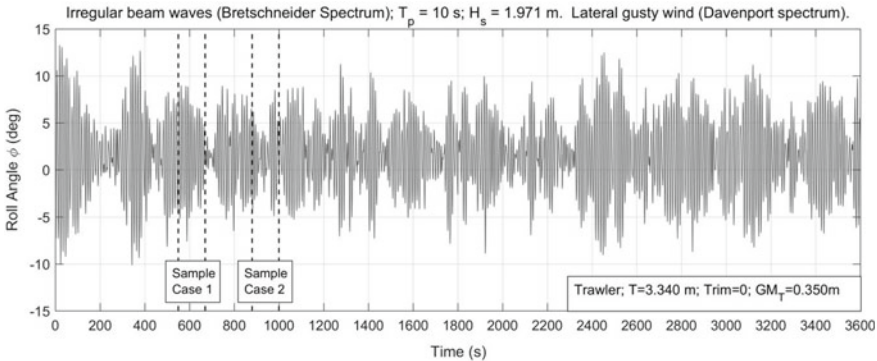


**Fig. 4** Roll motion time series. Irregular beam waves and lateral gusty wind. Reference sea condition 4

## 4 Results

In order to test its performance, the described methodology has been applied to the test time series which have been already described. The spectrum analysis algorithms have been executed in a continuous way, following the same procedure as it would have been done in a real case on board.

In Fig. 5, results from the reference sea condition 4, which is used as sample case, are shown. The large grey circular markers in this figure represent the estimated natural roll frequency, obtained every 10 s (Sample Time). These values are obtained from the averaging of the previous spectra (120 s of Averaging Time), which were estimated from the analysis of 180 s time chunks (Analysis Time). In addition to the above, and for a better understanding of the proposed strategy, two sample cases are shown in Fig. 6 (marked using a grey rectangle and diamond in Fig. 5). These two spectra correspond to the time instants 670 s and 1000 s respectively. The dashed grey lines in Fig. 6 represent the raw averaged spectrum for the time intervals shown in Fig. 4 by the vertical black dashed lines. As it can be appreciated, the frequency resolution, in the range of interest, is quite low. Dotted black lines represent the smoothed spectrum, aimed at reducing the secondary peaks that could appear in the raw estimated spectra. Finally, the grey continuous line represents the spectra obtained after the fitting process of the smoothed spectra using Gaussian functions.

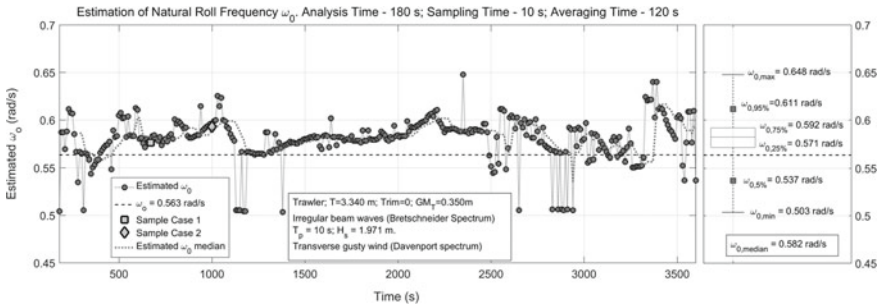


**Fig. 5** Left: Natural roll frequency estimation results. Right: representation of estimated natural roll frequency distribution through minimum observed value, 5%, 25%, 50% (median), 75% and 95% estimated percentiles, and maximum observed value. Reference sea condition 4

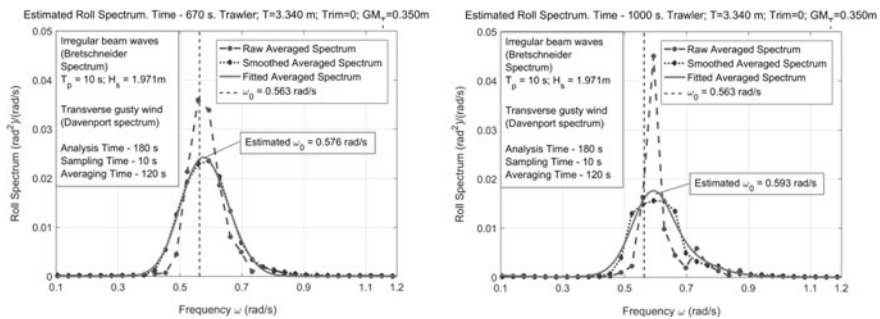


**Fig. 6** Estimated roll spectrum. Sample Case 1 (left) and Sample Case 2 (right)

Regarding the general results shown in Fig. 5 for the reference condition 4, it can be appreciated that, although the obtained estimations do not exactly match the real natural frequency, they remain continuously in the vicinity of the target value  $\omega_0 = 0.563$  rad/s, with the exception of some outlier values, as those present around 1100 s and 2900 s. Even though these outliers are taken into account, the 90% of the estimated roll frequency samples remains in the range [0.537, 0.611] rad/s (corresponding to estimated 5% and 95% percentiles). This range corresponds to a percentage difference with respect to the target value in the range [−4.62%, +8.58%]. Regarding the aforementioned outliers, and as it can be appreciated from Fig. 5, they do not last in time, as the situation only lasts for a single Sample Time (10 s in this case). This fact makes it relatively easy to discard such points, always verifying that these values do not extend in time. In this case, the repetition in time of such points could indicate a true change in stability, and not taking them into consideration (by inappropriate filtering or removing) could lead to missing a possible low stability dangerous situation. One option for robustifying the approach is to use, at each Sample Time, a moving median, where the reference estimated frequency value is determined as the median of the estimated natural roll frequencies from a group

of past local estimations. Such an approach, which is based on the assumption of slowly varying ship stability characteristics, allows to disregard the outliers of short duration. The use of the median has been preferred compared to the use of the mean, because of the sensitivity of mean to outliers. An example result from the application of this approach is shown as the dotted line in Fig. 5, where the median is calculated from the group of past 12 local estimations.

Regarding the systematic average over prediction of  $\omega_0$  observed along the whole time series in Fig. 5, and in other reference conditions as it will be described later, could be partially explained by the fact that, under the relatively large roll motions present in the simulated condition, nonlinear effects in restoring (which is of the hardening type, see Fig. 3) become more noticeable, and thus the observed dominant roll oscillation frequency tends to be slightly increased compared to the linear (small amplitude) roll natural frequency. This is a quite classic phenomenon in nonlinear ship dynamics, and it is also described in Míguez González and Bulian [18] for a very similar vessel to the one analyzed in this work in case of regular waves.

The obtained results corresponding to all the tested sea conditions are reported in Table 4.

With reference to the results in Table 4, the considerations done for the reference condition 4 could be extended to sea conditions from 4 to 9, where 90% of the natural roll frequency samples remain in a similar range  $[-5.49\%, +11.62\%]$  and again some over prediction of  $\omega_0$  is observed. However, results from reference sea conditions 1–3 display larger errors, and that over prediction appears not to be so noticeable (as roll amplitude is much smaller in these cases). These three reference conditions are those corresponding to wave peak periods smaller than the vessel natural roll period, with the smallest wave excitations and also with the smallest amplitudes of vessel roll motions. This behaviour could be explained by the larger dispersion of the roll spectrum, which leads to a multi-peaked shape, which reduces the performance of the methodology. In fact, as it could be appreciated in reference conditions 2 and 3, the value of  $\omega_{0,95\%}$  is very close to the wave peak frequency of those cases. This fact is analysed more in detail by Santiago Caamaño et al. [25] where it is shown that, in these conditions, the roll spectrum display several peaks of similar amplitude, where the different wave and wind frequency components mask that corresponding to the vessel natural roll frequency. On the contrary, in those cases with wave peak periods in the vicinity of the natural roll period or higher, the obtained roll spectra show a clear peak close to the vessel natural roll frequency, which explains the better performance of the methodology in these conditions.

## 5 Discussion

It is worth mentioning that, although the obtained estimation ranges in natural frequency could seem to be relatively accurate in many of the reference sea conditions, the main final target of this methodology is the estimation of the vessel meta-centric height ( $\overline{GM}$ ). Considering the results of reference conditions from 4 to 9 and if

**Table 4** Full results. Estimated natural roll frequency ( $\omega_{0,5\%}$ : 5% percentile;  $\omega_{0,median}$ : median;  $\omega_{0,95\%}$ : 95% percentile), with correspondingly estimated GM ( $GM_{5\%}$ ,  $GM_{median}$ ,  $GM_{95\%}$ ). Deviations to target values for 5% and 95% percentiles for estimated natural roll frequency ( $\varepsilon_{\omega_{0,5\%}}$ ,  $\varepsilon_{\omega_{0,95\%}}$ ) and GM ( $\varepsilon_{GM_{5\%}}$ ,  $\varepsilon_{GM_{95\%}}$ )

	Reference sea condition								
	1	2	3	4	5	6	7	8	9
$\omega_{0,median}$ (rad/s)	0.551	0.555	0.629	0.582	0.582	0.577	0.568	0.572	0.568
$\omega_{0,5\%}$ (rad/s)	0.035	0.519	0.579	0.537	0.541	0.541	0.532	0.539	0.541
$\omega_{0,95\%}$ (rad/s)	0.582	1.032	0.741	0.611	0.619	0.628	0.613	0.617	0.599
$\varepsilon_{\omega_{0,5\%}}$ (%)	-93.80	-7.87	2.82	-4.62	-3.87	-3.85	-5.49	-4.21	-3.98
$\varepsilon_{\omega_{0,95\%}}$ (%)	3.41	83.29	31.67	8.58	9.98	11.62	8.83	9.64	6.32
$GM_{median}$ (m)	0.334	0.340	0.436	0.373	0.373	0.367	0.356	0.361	0.356
$GM_{5\%}$ (m)	0.001	0.297	0.369	0.318	0.323	0.323	0.312	0.321	0.322
$GM_{95\%}$ (m)	0.374	1.173	0.606	0.412	0.423	0.435	0.414	0.420	0.395
$\varepsilon_{GM_{5\%}}$ (%)	-99.62	-15.29	5.52	-9.20	-7.78	-7.74	-10.85	-8.42	-7.98
$\varepsilon_{GM_{95\%}}$ (%)	6.73	235.28	73.03	17.66	20.72	24.34	18.20	19.98	12.82

only the error in the estimation of the natural roll frequency is taken into account (i.e.  $k_{xx}$  in Eq. (1) is taken as a constant known value), the [5%, 95%] percentiles range of estimated natural frequency is ( $\omega_0 \cdot (1 + [-5.49\%, 11.62\%])$ ). This leads to a range in the error of  $\overline{GM}$  estimation corresponding to  $[-10.85\%, 24.34\%]$ . Although these errors in the estimation of  $\overline{GM}$  could seem to be acceptable if adequate safety margins are applied, the situation is different if results from reference conditions 1–3 are taken into consideration. In these cases, errors in the estimation of natural roll frequency and  $\overline{GM}$  are much larger. Combined with the unavoidable uncertainties in the estimation of the other relevant parameters, they could lead to underestimations and especially overestimations of  $\overline{GM}$ . This latter are of particular importance, as they are of course non-conservative from a safety perspective and are therefore not acceptable.

In addition to this, it is also important to remark that the performance of the proposed methodology is largely dependent on the selected Analysis and Averaging times. A detailed analysis of the real operation of these vessels would be needed to determine, in a more accurate way, which is the maximum length of time series chunk which could track loading condition changes.

From the above results and considerations, it may be concluded that, although good results are obtained in those situations where wave peak periods are larger than the expected vessel natural roll period, further work is needed to improve the methodology capabilities in the rest of reference conditions. Moreover, an analysis of the performance of the method including the exclusion of outlier points is also needed before a conclusion regarding the practical applicability of this methodology could be achieved.

## 6 Conclusions

In this contribution, a methodology based on the spectral analysis of medium sized fishing vessels roll motion, for the estimation of the vessel roll natural frequency while in operation, has been described. This methodology represents one step towards the development of a technique for the on-board real-time identification of  $\overline{GM}$ .

A demonstration case of the aforementioned methodology has been presented, taking as a test case the roll motion of a mid-sized stern trawler under the effect of different combinations of beam irregular waves and gusty lateral wind, which has been simulated by means of a one degree of freedom nonlinear roll model.

Although the obtained results seem to be promising in most of the tested conditions, further work is needed to reduce the level of error in the estimation of natural roll frequency, especially when such errors can potentially lead to unacceptable non-conservative overestimations of the metacentric height of the vessel.

Finally, some points remain open for discussion, including the level of error in the estimation of  $\overline{GM}$  which can be considered to be acceptable if such a system is

installed onboard a ship, and the maximum analysis time which would be acceptable for accurately tracking the possible variations in the vessel initial stability and, consequently, its risk level.

**Acknowledgements** Part of the present work was carried out during a research visit at University of Trieste, supported by the Spanish Ministry of Education, Culture and Sport (<http://www.mecd.gob.es>) under the “José Castillejo” program, grant CAS16/00013.

## References

1. Bačkalov I, Bulian G, Rosén A, Shigunov V, Themelis N (2016) Improvement of ship stability and safety in intact condition through operational measures: challenges and opportunities. *Ocean Eng* 120:353–361
2. Blendermann W (1996) Wind loading of ships: collected data from wind tunnel tests in uniform flow, IFS Bericht 574. Universität Hamburg, Hamburg, Germany, Institut für Schiffbau
3. Bulian G, Francescutto A (2004) A simplified modular approach for the prediction of the roll motion due to the combined action of wind and waves. *Proc Instit Mech Engin Part M: J Eng Maritime Environ* 218:189–212
4. Bulian G, Francescutto A (2006) Safety and operability of fishing vessels in beam and longitudinal waves. *Trans Royal Instit Naval Archit Part B, Int J Small Craft Technol* 148:1–16
5. Bulian G, Francescutto A (2009) Experimental results and numerical simulations on strongly nonlinear rolling of multihulls in moderate beam seas. *Proc Instit Mech Engin Part M J Eng Maritime Environ* 223:189–210
6. Davenport AG (1961) The spectrum of horizontal gustiness near the ground in high winds. *Q J R Meteorol Soc* 87:194–211
7. Deakin B (2006) Developing simple safety guidance for fishermen. In: *Proceedings of 9th international conference on stability of ships and ocean vehicles, (STAB 2006)*, Rio de Janeiro, Brazil
8. FOM (2017) Predicción de oleaje, nivel del mar; Boyas y mareógrafos. Ministerio de Fomento, Government of Spain, Madrid, Spain. Retrieved from [www.puertos.es/es-es/oceanografia/Paginas/portus.aspx](http://www.puertos.es/es-es/oceanografia/Paginas/portus.aspx). Accessed on the 1/03/17
9. Gudmundsson A (2013) The FAO/ILO/IMO safety recommendations for decked fishing vessels of less than 12 metres in length and undecked fishing vessels—a major milestone to improve safety for small fishing vessels. In: *Proceedings of 13th international ship stability workshop (ISSW 2013)*, Brest, France, pp 112–120
10. Huss M (2016) Operational stability beyond rule compliance. In: *15th International ship stability workshop, (ISSW 2016)*, Stockholm, Sweden, pp 193–200
11. IMO (2007) MSC.1/Circ.1228—Revised guidance to the master for avoiding dangerous situations in adverse weather and sea conditions. 11 January, London, UK
12. IMO (2020) Interim guidelines on the second generation intact stability criteria. MSC.1/Circ.1627
13. ITTC (2002) The specialist committee on waves. Final report and recommendations to the 23rd ITTC. In: *Proceedings of the 23rd international towing tank conference, (ITTC 2002)*, Venice, Italy, pp 505–736
14. Jensen OC, Petursdottir G, Holmen IM, Abrahamsen A, Lincoln J (2014) A review of fatal accident incidence rate trends in fishing. *Int Marit Health* 65(2):47–52
15. Míguez González M, López Peña F, Díaz Casás V, Neves MAS (2011) Large amplitude roll motion forecasting through an artificial neural network system. In: *Proceedings of 12th international ship stability workshop, (ISSW 2011)*, Washington D.C., U.S., pp 219–224

16. Míguez González M, Caamaño Sobrino P, Tedín Álvarez R, Díaz Casás V, Martínez López A, López Peña F (2012) Fishing vessel stability assessment system. *Ocean Eng* 41:67–78
17. Míguez González M, Bulian G, Santiago Caamaño L, Díaz Casás V (2017) Towards real-time identification of initial stability from ship roll motion analysis. In: Proceedings of the 16th international ship stability workshop (ISSW 2017), Belgrade, Serbia, pp 221–230
18. Míguez González M, Bulian G (2018) Influence of ship dynamics modelling on the prediction of fishing vessels roll response in beam and longitudinal waves. *Ocean Eng* 148:312–330
19. Nielsen JK, Pedersen NH, Michelsen J, Nielsen UD, Bastrup J, Jensen JJ, Petersen ES (2006) SeaSense—real-time onboard decision support. In: Proceedings world maritime technology conference, London, UK
20. Oppenheim AB, Schaffer RW, Buck JR (1999) Discrete time-signal processing. Prentice-Hall Inc., New Jersey, U.S.
21. Ovegård E, Rosén A, Palmquist M, Huss M (2012) Operational guidance with respect to pure loss of stability and parametric rolling. In: Proceedings of 11th international conference on the stability of ships and ocean vehicles, (STAB2012), Athens, Greece
22. Palmquist M, Nygren C (2004) Recordings of head-sea parametric rolling on a PCTC. Annex to IMO Document SLF47/INF.5 (see also SFL47/6/6) submitted by Sweden, 10 June
23. Santiago Caamaño L, Míguez González M, Díaz Casás V (2018a) On the feasibility of a real time stability assessment for fishing vessels. *Ocean Eng* 159:76–87
24. Santiago Caamaño L, Míguez González M, Díaz Casás V (2018b) Improving the safety of fishing vessels through roll motion analysis. In: Proceedings of the 37th ASME international conference on ocean, offshore and arctic engineering (OMAE 2018), Madrid, Spain
25. Santiago Caamaño L, Galeazzi R, Nielsen UD, Míguez González M, Díaz Casás V (2019) Real-time detection of transverse stability changes in fishing vessels. *Ocean Eng* 189:106369
26. Terada D, Tamashima M, Nakao I, Matsuda A (2016) Estimation of the metacentric height by using onboard monitoring roll data based on time series analysis. In: Proceedings of 15th international ship stability workshop, (ISSW 2016), Stockholm, Sweden, pp 209–215
27. Umeda N, Francescutto A (2016) Current state of the second generation intact stability criteria-achievements and remaining issues. In: Proceedings of 15th international ship stability workshop, (ISSW 2016), Stockholm, Sweden, pp 13–15
28. Viggosson G (2009) The icelandic information system on weather and sea state. Seminar on Fishing Vessels' Crews and Stability, World Fishing Exhibition, Vigo, Spain
29. Wolfson Unit (2004) MCA research project 530. Simplified presentation of fishing vessels stability information. Phase 1. Final Report", Wolfson Unit, University of Southampton, U.K
30. Womack J (2002) Small commercial fishing vessel stability analysis. Where are we now? Where are we going? In: Proceedings of 6th international ship stability workshop, (ISSW 2002), Webb Institute, U.S

# **Surf-Riding and Broaching-to**



# Estimates of the Probability of Surf-Riding in Irregular Seas



Kostas J. Spyrou, Nikos Themelis, and Ioannis Kontolefas

**Abstract** The concept of surf-riding in irregular seas is investigated and two calculation schemes are implemented in order to establish upper and lower bounds of the probability of surf-riding. The first scheme extrapolates from the concept of surf-riding in regular seas and is product of analysis of system dynamics. Points of the phase-space that could be considered as the counterparts, for irregular sea, of the conventional surf-riding equilibria are targeted. Due to the time-varying nature of the considered phase-space however, these points exist only temporarily, emerging and later vanishing at random time instants. The second scheme is more empirical, targeting time intervals of ship motion where the speed remains above the expected range. We call such behavior a “high run”. The probability values obtained by the two schemes are compared against each other and conclusions are drawn.

**Keywords** Surf-riding · High-run · Irregular waves · Instantaneous celerity

## 1 Introduction

Phenomenologically, as “surf-riding” can be characterized a ship’s capture by a steep following/quartering wave and its push forward with a speed that is equal to the wave celerity [3]. As is well-known, for regular seas such behavior is owed to the generation of an equilibrium condition in the surge dynamics which gives rise to the capture of the ship at the down-slope of a steep wave [5]. For irregular seas however, as the wave field is continually changing in time and in space, such equilibrium conditions can be considered only in an approximate sense and only if the variation of the wave

---

K. J. Spyrou · N. Themelis (✉) · I. Kontolefas  
School of Naval Architecture and Marine Engineering, National Technical University of Athens, 9  
Iroon Polytechniou, 15780 Zographos, Athens, Greece  
e-mail: [nthemelis@naval.ntua.gr](mailto:nthemelis@naval.ntua.gr)

K. J. Spyrou  
e-mail: [k.spyrou@central.ntua.gr](mailto:k.spyrou@central.ntua.gr)

I. Kontolefas  
e-mail: [ikon@central.ntua.gr](mailto:ikon@central.ntua.gr)

field, in the vicinity of the ship, is very slow. In a more general context, any plausible notion that could be invented for an irregular sea in order to play the role of surge equilibria, it would be relevant only within finite time intervals of a ship run.

One wonders therefore if what is established for regular seas could reasonably be extended to the irregular seas; since new phenomena, distinctively identified with the time-varying nature of the system may also emerge.

In the first part of the current chapter, the concept of surf-riding in a multi-frequency wave field is enquired and a suitable scheme for the identification of surf-riding conditions is developed, involving calculation of the value of celerity at the instantaneous position of the ship. In the second part we are dealing with prolonged runs of a ship with a speed that is higher than the speed corresponding to her propulsive thrust. We call such runs as “high-runs” and they can be regarded as representing the generalization of surf-riding for irregular seas. A high run can involve not only phenomena of capture by a wave, but also, other complex oscillatory phenomena where the mean speed is maintained, for a time interval, at a level higher than her nominal speed. A numerical scheme was implemented for identifying such time intervals. Moreover, a massive campaign of simulations was performed for contrasting high-run occurrences against the existence of “equilibrium-like” objects, in the phase space, corresponding to the conventional definition of surf-riding.

## 2 Notion of Surf-Riding in Irregular Sea

As is well known, a simple condition for the realization of surf-riding in steep and regular following/quartering seas is whether the projection of the ship’s velocity to the direction of wave propagation matches the celerity value. Extending this condition for the irregular sea would entail, in the first place, to calculate the instantaneous celerity in the ship’s neighborhood. Approaches for such calculation have already been developed; see Spyrou et al. [11–12].

Extensive simulations have revealed that, for irregular seas, finite time intervals exist over which the instantaneous celerity (calculated at the ship’s center of axes for the incident wave) and the surge velocity, strongly correlate with each other [9]. For an observer moving with the instantaneous wave celerity, such correlation can be attributed to the generation of “equilibrium-like” points in the phase space. It is possible to identify computationally these points and assess whether they truly affect substantially the dynamics of a ship travelling nearby. They have finite life-spans and, as our simulations revealed, they invoke acceleration of the ship when the ship is found in their basin of attraction. The percentage of the total simulation time that the computational scheme returns “positives” for the existence of such points close to the ship, can be used as an upper bound estimate of the “probability of surf-riding” in irregular seas.

### 3 Mathematical Model

Consider the mathematical model of surge motion in following seas, written with respect to an earth- fixed observer, see for example Spyrou et al. [9].

$$\begin{aligned}
 \dot{\xi} &= u \\
 &\underbrace{(m - X_{\dot{u}})\dot{u}}_{\text{Inertia}M(\dot{u})} + \underbrace{(r_1u + r_2u^2 + r_3u^3)}_{\text{Resistance}R(u)} - \underbrace{(\tau_0n^2 + \tau_1nu + \tau_2u^2)}_{\text{Thrust}T(u;n)} \\
 &= \underbrace{\sum_{i=1}^N f_i \sin(k_i\xi - \omega_i t + \varepsilon_i^{(r)} + \varepsilon_{fi})}_{\text{Waveforce}F(\xi;t)} \tag{1}
 \end{aligned}$$

where  $\xi$  is the longitudinal position of the ship;  $m$  and  $-X_{\dot{u}}$  are the mass and the “added mass” respectively. By  $n$  is indicated the propeller rate. In the wave excitation term,  $k_i$ ,  $\omega_i$  and  $\varepsilon_i^{(r)}$  denote, respectively, the wave number, the wave frequency and the random phase of the  $\omega$ -harmonic wave component of the spectrum. By  $f_i$  is denoted the amplitude and by  $\varepsilon_{fi}$  the phase of the  $\omega$ -harmonic wave force component with respect to the corresponding incident wave elevation at the ship center.

Let us conceive a transformation that, in analogy to the one used for the harmonic case, would allow us to identify stationary points with respect to an accelerating observer. This could be feasible if a new, non-inertial system of axes was introduced moving with the instantaneous celerity  $c[\xi(t); t]$  of the incident wave at ship center’s position. Let us suppose that instantaneous celerity satisfies some appropriate smoothness conditions over some finite time interval (despite knowing that, the more the sea becomes “broad-banded”, the more difficult will be to satisfy these conditions over such an interval). The location of the ship with respect to the new origin can be expressed by a new distance variable  $\chi$  as follows,

$$\chi = \xi - z \tag{2}$$

The variable  $z$  is the abscissa of the moving origin with respect to the earth-fixed frame, expressed as,

$$z = z_0 + \int_{t_0}^t c[\xi(s); s]ds \tag{3}$$

The dynamical system can be expressed for the non-inertial origin that moves with the wave celerity, as follows:

$$\begin{aligned}
 \dot{\chi} &= \sigma (= \dot{\xi} - c) \\
 \dot{c} &= a
 \end{aligned}$$

$$\dot{\sigma} = -\frac{1}{(m - X_{\ddot{u}})} \left\{ \underbrace{[3r_3c^2 + 2(r_2 - \tau_2)c + r_1 - \tau_1n]}_{A_1(c;n)} \sigma + \underbrace{[3r_3c + (r_2 - \tau_2)]}_{A_2(c;n)} \sigma^2 + r_3\sigma^3 + \underbrace{\sum_{i=1}^N f_i \cos \left[ k_i \left( \chi + \int_0^t c(s) ds \right) - \omega_i t + \varepsilon_i^{(r)} + \varepsilon_{f_i} \right]}_{F(\chi,c;t)} - \underbrace{(\tau_0n^2 + \tau_1cn + \tau_2c^2)}_{T(c;n)} + \underbrace{(r_1c + r_2c^2 + r_3c^3)}_{R(c)} \right\} - a \tag{4}$$

In comparison to the canonical form of the surge equation that was written earlier for earth-fixed axes origin (Eq. 1), the difference is in the acceleration term  $a$  that is a function of time and it arises due to the time variability of the celerity.

In an irregular sea there is continuous variation of the wave field in space–time and true force equilibrium conditions basically cannot be sustained. Thereafter, setting zero values in ship velocity and acceleration with respect to the non-inertial system of axes, that is  $\sigma = \dot{\sigma} = 0$ , yields only a theoretical destination of trajectories since these cannot be reached in finite time. We have called such points, which are not true solutions of the dynamical system’s equations, “pseudo-equilibria”. For  $\sigma = 0$ , the condition  $\dot{\sigma} = 0$  yields according to (4) the following sufficient condition for their existence in the phase space:

$$\sum_{i=1}^N f_i \cos \left[ k_i \left( \chi + \int_0^t c(s) ds \right) - \omega_i t + \varepsilon_i^{(r)} + \varepsilon_{f_i} \right] = (\tau_0n^2 + \tau_1cn + \tau_2c^2) - (r_1c + r_2c^2 + r_3c^3) - (m - X_{\ddot{u}})\dot{c} \tag{5}$$

Once surf-riding pseudo-equilibria are located, their paths are traced, under the condition however of remaining always within the close vicinity of the ship (since only nearby equilibria can pose a threat).

### 4 Identification Scheme

The ship selected for applying the above method is the ONR “tumblehome topside” that has been used in several previous studies ( $L_{WL} = 159$  m,  $L_{BP} = 154$  m,  $B_{WL} = 18.802$  m,  $T_{max} = 7.605$  m, and the draft at midship section is  $T = 5.5$  m), (see for example [1, 14, 11]). A JONSWAP spectrum is assumed. It is discretized by applying a fixed frequency increment  $\delta\omega = 2\pi/t_{sim}$  where  $t_{sim} = 300$  s. To assess the effect of band-width, four scenarios are investigated in terms of the considered range around spectrum’s peak. Several simulations were carried out, for the parameters’ values shown in Table 1. It is noted that the mathematical model described previously

**Table 1** Parameters of the simulations carried out

Parameter	Value
$u_{nom}$ (m/s)	12, 13
$u_0$ (m/s)	10
$H_s$ (m)	3, 6
$T_p$ (s)	9.5, 10
Considered range around $\omega_p$ ( $\% \omega_p$ )	10, 20, 30, 40
Total simulation time $T_{sim}$ (s)	1200

was used by employing the standard numerical solvers of the Wolfram Mathematica software.

The detection scheme involves the finding of the real roots of Eq. (5), at every time step of the simulation time, for a discretized moving spatial window that is always centered amidships. The size of this window is pre-specified and it is used as a parameter of the investigation. When a real root is detected, starting from a time instant let's say  $t_i$  and existing for  $n_i$  consecutive time steps, then  $(t_i, t_i + (n_i - 1)\delta t)$  represents a time interval of existence of a potentially dangerous pseudo-equilibrium in ship's neighborhood. Nonetheless, it is not necessary the attraction to be felt by the ship and her motion to be affected. The time ratio  $a$  of existence of these pseudo-equilibria can then be expressed as follows,

$$a = \frac{1}{T_{sim}} \sum_{i=1}^N (n_i - 1) \delta t \tag{6}$$

The results obtained can be visualized as animated series. Actually, the identification scheme can yield a number of pseudo-equilibria for the vicinity of the ship, some behaving like stable and others like unstable. In Fig. 1 are shown snapshots of ship behavior with the locations of pseudo-equilibria and the forces. Red circles correspond to pseudo-equilibria identified using condition (5). Black circles correspond to roots of (5) when the celerity acceleration term is neglected. On the bottom part of these figures one can observe the time history of surge velocity (black line) versus that of instantaneous celerity calculated at the ship position (gray line).

From multiple similar observations we were able to recognize two different scenarios of “engagement to” and “disengagement from” surf-riding:

1. The ship is initially attracted by the attracting inset of an unstable pseudo-equilibrium. Likewise regular sea scenarios, the trajectories in the neighborhood seem to be organized in such a way that the ship is engaged to a chase with the coexisting stable pseudo-equilibrium.
2. A stable equilibrium appears suddenly in the close vicinity of the ship immediately capturing her in the surf-riding condition.

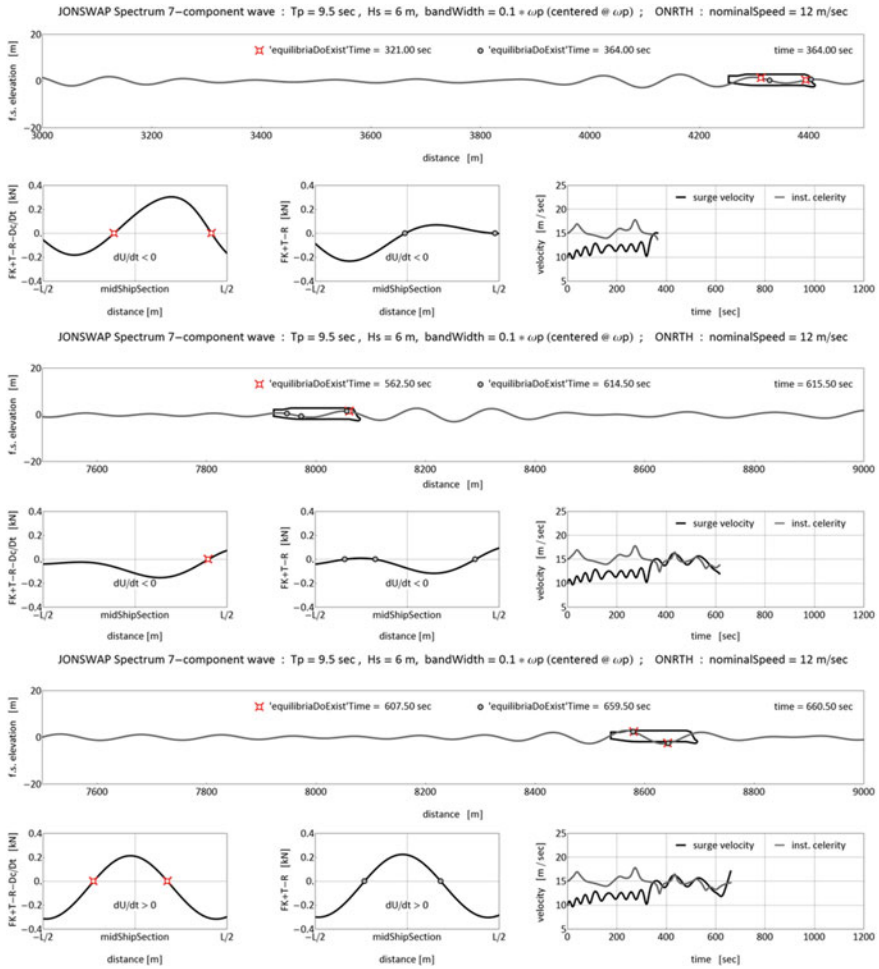


**Fig. 1** Three time instants from a simulation with  $H_s = 6$  m,  $T_p = 9.5$  s, frequency range  $10\% \omega_p$  (one side),  $u_{nom} = 12$  m/s. The detection scheme was applied on a spatial window of one ship length

## 5 Identification of High-Runs

### 5.1 Definitions

At this stage we considered, through simulation, high speed incidents according to the high-run pattern explained in the introduction. Such events are evidenced by the up-crossing of a certain high velocity threshold and the later down-crossing of the same (or another selected) velocity threshold. In general, these two thresholds need not be identical, and a subjective element is inevitable. The individual time durations

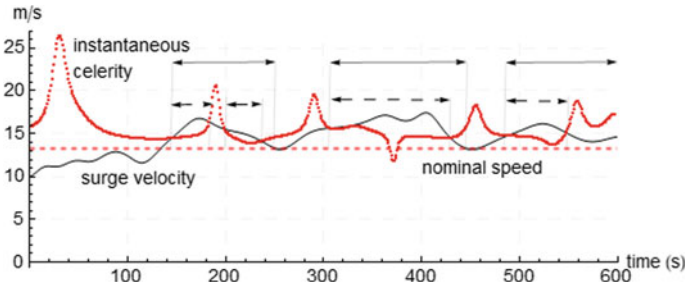


**Fig. 2** Schematic explanation of the two definitions of high-run

of such events are summed up, then they are divided by the total time of the run in order to obtain the “time ratio of high-run”.

$$\tilde{P}_{surf-riding} = \frac{\sum_i t_{(i)high-run}}{T_{sim}} \tag{7}$$

Two different specifications of a high run have been evaluated:

**Definition 1** The two thresholds are identical, and they are defined by the instantaneous celerity. In Fig. 2, such “high runs” are indicated by the dashed line arrows.

**Definition 2** The threshold of up-crossing is the instantaneous celerity, and the threshold of down-crossing is the nominal speed. This allows dealing with the fluctuations of the motion during surf-riding. This definition includes surge velocity fluctuations that may be below the instantaneous celerity but higher than nominal speed. Such time intervals are indicated in Fig. 2 with continuous line arrows. The condition the surge velocity to be higher than nominal speed is still invoked to exclude cases that qualitatively, should not qualify as high runs.

### 5.2 Simulation Settings

The simulation time was varied from  $t_{sim}$  to  $40 \times t_{sim}$ , where  $t_{sim} = 300$  s. Four ranges around spectrum’s peak have been considered. Table 2 presents the considered ranges of the simulation parameters. Sensitivity studies related to the sea state, narrowness of the spectrum and simulation time were carried out. The number of wave components that participate in the simulation depends on the frequency range (Table 3). We run 100 wave realizations per scenario. The nominal and the initial speed of the ship in each scenario were unchanged.

**Table 2** Ranges of values of parameters

Parameter	Value
Nominal speed, $u_{nom}$ (m/s)	12
Nominal Froude number, $Fn_n$	0.308
Initial speed, $u_0$ (m/s)	10
Wave realizations per scenario	100
Significant wave height, $H_s$ (m)	$3 \div 6$
Peak period of spectrum, $T_p$ (s)	$8.5 \div 13$
Frequency range, $\% \omega_p$	$5 \div 30\%$
Total simulation time, $T_{sim}$ (s)	$300 \div 40 \times 300$

**Table 3** Number of wave components per scenario for  $t_{sim} = 300$  s

$T_p$ (s)	$5\% \omega_p$	$10\% \omega_p$	$20\% \omega_p$	$30\% \omega_p$
8.5	4	8	15	22
9	4	7	14	21
9.5	4	7	13	19
10	4	7	13	19
10.5	3	6	12	18
11	3	6	11	17
11.5	3	6	11	16
12	3	6	11	16
12.5	3	5	10	15
13	3	5	10	14

### 5.3 Results

In Fig. 3 are shown time histories of surge velocity and instantaneous celerity for a high-run occurrence according to the 2nd definition. The lower diagram of Fig. 3 shows the calculated time segments of high-run. It is noted that the convergence of the statistics was examined and the simulation time per run was selected appropriately (see Fig. 4).

#### *Effect of the high-run threshold*

In Fig. 5 are shown the obtained time ratios (which can be regarded as probability estimates) by varying the peak period and keeping constant the significant wave height. As expected, the first definition produces lower probabilities than the second. However, there is significant influence on the probability by a 10% increase of the down-crossing threshold.



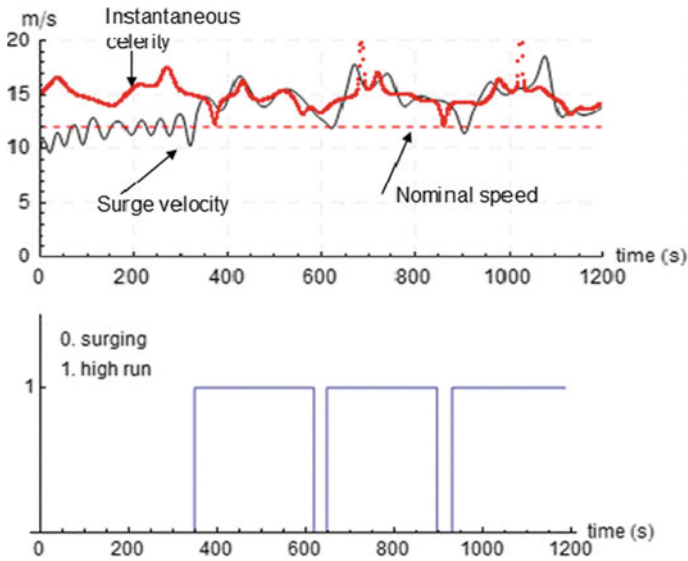


**Fig. 3** Sample simulation of a “high-run” and the respective time segments (low diagram) [ $H_S = 6$  m,  $T_P = 6$  s,  $u_{nom} = 12$  m/s, frequency range  $10\% \omega_p$  (one side)]

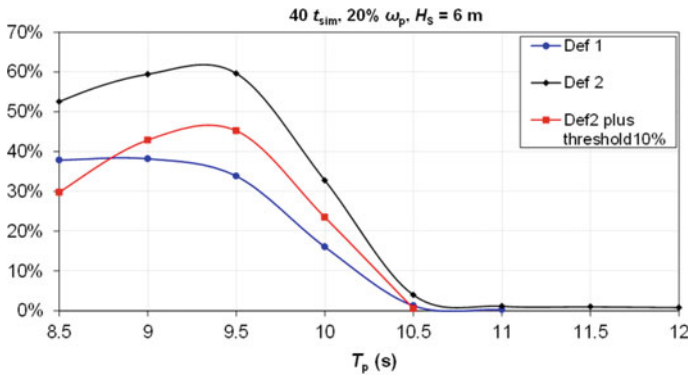


**Fig. 4** Probability estimates of high-run according to the two definitions, as function of the peak period  $T_P$ . The duration of the simulations was  $40 \cdot t_{sim} = 12 \times 10^3$  s, the frequency range (one-side) was  $20\% \omega_p$  and the significant wave height was  $H_S = 6$  m

*Effect of the frequency range*

We have varied the peak period by keeping constant the significant wave height (Fig. 6). It was derived that in all cases, there is a peak period value below which there is sharp increase of the probability. By increasing the considered frequency range, high probabilities of surf-riding appear for a broader range.

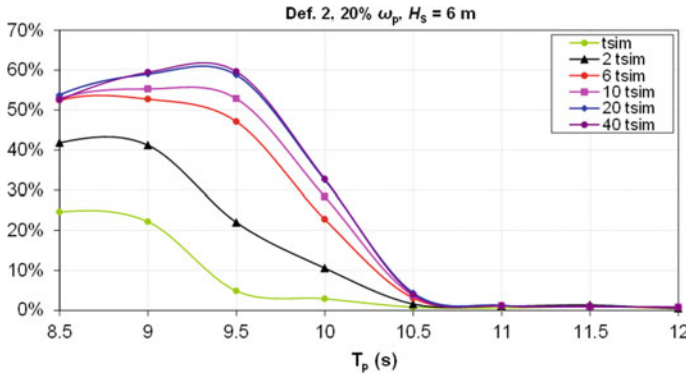


**Fig. 5** Convergence of statistics per simulation time and varying  $T_P$  for  $20\% \omega_p$  (one side),  $H_S = 6$  m

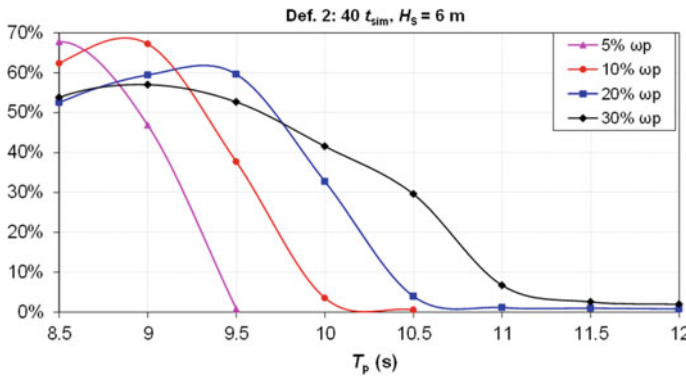


**Fig. 6** Probability estimate of high-run (2nd definition) per  $\% \omega_p$  and varying  $T_P$  for  $40 \cdot t_{sim} = 12 \times 10^3$  s,  $H_S = 6$  m

## 6 Cross-Comparison of Calculated Time Ratios

A comparative study on the calculated time segments based on the method of pseudo-equilibria and the method of high-run thresholds was carried out. Both results correspond to the same wave realizations, while a range of spatial window lengths (from  $L/32$  up to  $L$ , where  $L$  is the ship length: taken as the  $L_{BP}$ ) has been considered. Furthermore, four sea states and three frequency ranges were studied and the simulation time was fixed to  $4 \times t_{sim}$ .

The results with the comparison are summarized in Fig. 7. At first, one should note alike trends regarding the effect of the spatial window in the time ratios. However, larger differences exist for the higher sea states.

Additionally, in Fig. 7 are included the time ratios according to the 2nd definition, but with a 10% increase of the down-crossing velocity threshold. As the time

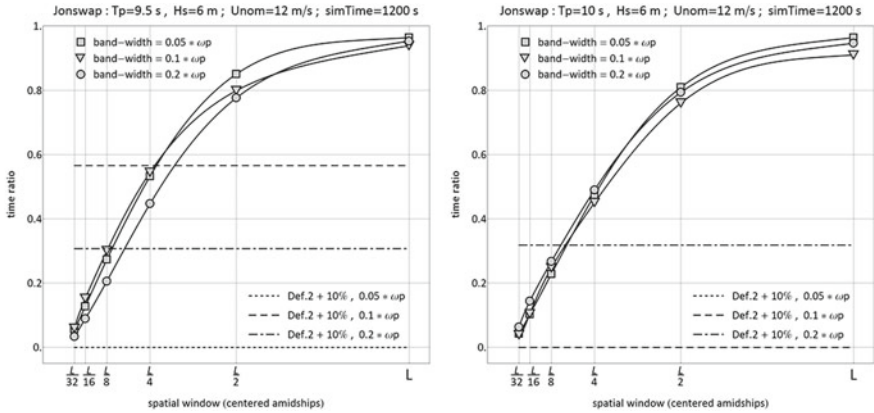


**Fig. 7** Effect of the different size of spatial windows on the upper bound of the time ratio of attraction to surf-riding and comparison with similar ratios corresponding to high runs

segments of equilibrium existence are not always felt by the ship, the two methods are not expected to produce directly comparable time-ratio results, a fact reflected by the diagrams.

## 7 Concluding Remarks

The notion of surf-riding equilibrium was extended from the regular to a multi-chromatic sea where such “features” can exist for a finite time interval. A numerical scheme that is based on the concept of instantaneous celerity was developed to determine the time-ratio upper bound regarding the exposure to the danger of surf-riding. A more empirical approach for surf-riding prediction was subsequently applied, based on a campaign of numerical simulations, in order to calculate time intervals of ‘high run’.

Various up-crossing and down-crossing velocity thresholds that can determine a “high run” have been investigated. Statistical measures such as the mean time ratio and mean time duration of “high runs” were obtained. Moreover, sensitivity studies related to the sea state, narrowness of the spectrum and simulation time duration were carried out. Lastly, a preliminary comparison study on the time ratio of equilibrium existence and “high run” duration was performed, seeking a relation between these two quantities which, whilst related, they produce quantitatively very different time ratios of exposure to danger.

Recently, alternative approaches have emerged for the prediction and assessment of a ship’s tendency for surf-riding in irregular seas. In Kontolefas and Spyrou [6] Lagrangian coherent structures of the surge equation of motion are identified in the phase-space via finite-time Lyapunov exponent fields [4, 8]. These structures provide insights into the dynamical mechanisms that lead to surf-riding in irregular

seas, by highlighting the location of transport barriers as well as the final destinations of particle trajectories (see [13]). Furthermore, in Kontolefas & Spyrou [7] a clustering scheme is applied for capturing qualitatively different ship motion patterns in following irregular seas. This scheme is built upon the concepts of Lagrangian coherent structures and finite-time coherent sets [2] and permits the identification of two distinguished dynamic regimes with respect to longitudinal ship motions. The ordinary behavior, where the ship approximately advances with the commanded speed and the not ordinary; where she deviates upwardly from that speed. Consequently, in that approach, the problem of assessing the ship's tendency for surf-riding can be treated as a problem of determining whether the state of the ship belongs to the coherent set corresponding to ordinary/not-ordinary behavior. More research is required on comparing all these alternative approaches.

**Acknowledgements** This work has been funded by the Office of Naval Research under Dr. Ki-Han Kim and by the Office of Naval Research Global (grant number N62909-13-1-7) under Dr. Woei-Min Lin. The project was administered at the University of Strathclyde. This support is gratefully acknowledged. The authors acknowledge also the contribution of Dr. Vadim Belenky of David Taylor Model Basin with whom there had been continuous scientific interaction in this research work.

## References

1. Bishop RC, Belknap W, Turner C, Simon B, Kim JH (2005) Parametric investigation on the influence of GM, roll damping, and above-water form on the roll response of model 5613. Report NSWCCD-50-TR-2005/027
2. Froyland G, Padberg-Gehle K (2015) A rough-and-ready cluster-based approach for extracting finite-time coherent sets from sparse and incomplete trajectory data. *Chaos* 25(9):097617
3. Grim O (1951) Das Schiff in von achtern auflaufender See. *Jahrbuch der Schiffbautechnischen Gesellschaft (STG)* 45:264–287
4. Haller G (2011) A variational theory of hyperbolic Lagrangian coherent structures. *Physica D* 240:574–598
5. Kan M (1990) Surging of large amplitude and surf-riding of ships in following seas. Selected papers in naval architecture and ocean engineering, The Society of Naval Architects of Japan 28
6. Kontolefas I, Spyrou KJ (2016) Coherent structures in phase space, governing the nonlinear surge motions of ships in steep waves. *Ocean Eng* 120:339–345
7. Kontolefas I, Spyrou KJ (2020) Probability of ship high-runs from phase space data. *J Ship Res* 64(1):81–97
8. Shadden SC (2011) Lagrangian coherent structures. In: Grigoriev R (ed) *Transport and mixing in laminar flows: from microfluidics to oceanic currents*, Wiley-VCH
9. Spyrou KJ, Belenky V, Themelis N, Weems K (2014) Detection of surf-riding behavior of ships in irregular seas. *Nonlinear Dyn* 78(1):649–667. <https://doi.org/10.1007/s11071-014-1466-2>
10. Spyrou KJ, Themelis N, Kontolefas I (2016) Numerical statistical estimates of ship broaching-to. *J Ship Res* 60(4):219–238. <https://doi.org/10.5957/JOSR.60.4.160027>
11. Spyrou KJ, Themelis N (2013) Wave celerity in a multi-chromatic sea: a comparative study. In: *Proceedings, 13th international ship stability workshop, Brest, France*, pp 88–94
12. Spyrou KJ, Belenky V, Themelis N, Weems K (2019) Definitions of celerity for investigating surf-riding in an irregular seaway. In: Belenky V, Spyrou K, van Walree F, Neves MAS, Umeda

- N (eds) Chapter 21 of contemporary ideas on ship stability. Risk of capsizing, Springer, ISBN 978-3-030-00514-6, pp 359–377
13. Spyrou KJ, Themelis N, Kontolefas I (2023) Abnormal high speed ship motions in two-frequency and multi-frequency following waves. In: Spyrou KJ, Belenky V, Katayama T, Backalov I, Francescutto A (eds) Chapter 24 of contemporary ideas on ship stability. From dynamics to criteria, Springer, pp 400–412. ISBN 978-3-031-16328-9
  14. Spyrou KJ, Belenky V, Themelis N, Weems K (2012) Conditions of surf-riding in an irregular seaway. In: Proceedings, 11th international conference on stability of ships and ocean vehicles, Athens, Greece, pp 323–336

# Abnormal High Speed Ship Motions in Two-Frequency and Multi-Frequency Following Waves



Kostas J. Spyrou, Ioannis Kontolefas, and Nikos Themelis

**Abstract** Steps are taken towards extending the theory of surf-riding in order to deal with multi-chromatic waves. New bifurcation phenomena are identified and classified which are intrinsic to the presence of extra frequencies in the excitation. Alternative types of surf-riding are discovered. Chaotic transients seem to be quite a common feature of ship surge motion in extreme following seas.

**Keywords** Ship motions · Surf-riding · Lagrangian coherent structures · Basin erosion · Chaos

## 1 Introduction

The theory explaining the nonlinear surging and surf-riding of ships in steep following waves has been built upon the assumption of monochromatic waves [8]. It is tacitly taken for granted that these phenomena endure, in almost identical form, in irregular seas too. Nevertheless, the multi-chromatic sea renders the phase space flow of the underlying dynamical system time-dependent, a fact apparently bearing many new possibilities of dynamic behavior [2, 9, 12]. For example, a ship can appear to shift randomly, in finite time intervals, between ordinary surging and irregular high speed motions. Then, the concept of surf-riding equilibrium that had been the basis for explaining involuntary high speed runs in following waves becomes less relevant and only for specific scenarios.

---

K. J. Spyrou · I. Kontolefas (✉) · N. Themelis  
School of Naval Architecture and Marine Engineering, National Technical University of Athens, 9  
Iroon Polytechniou, 15780 Zographos, Athens, Greece  
e-mail: [ikon@central.ntua.gr](mailto:ikon@central.ntua.gr)

K. J. Spyrou  
e-mail: [k.spyrou@central.ntua.gr](mailto:k.spyrou@central.ntua.gr)

N. Themelis  
e-mail: [nthemelis@naval.ntua.gr](mailto:nthemelis@naval.ntua.gr)

It appears as greatly desirable all yet undocumented motions types that can be realized in irregular seas to be systematically identified, evaluated and classified. However, towards this, conventional computational techniques that have been successfully applied for studying the effect of monochromatic seas are no longer sufficient. A novel set of state-of-art computational tools will be required.

Driven by these remarks, in this paper are presented results from an exploration into the unsteady phase space of ship surging under bi-chromatic and multi-chromatic excitation, using novel techniques. The purpose is, on the one hand to demonstrate the potential of these new approaches; and on the other, to identify and to analyze new extreme types of ship behavior, in relation to the frequency content and intensity of the wave excitation.

## 2 Description of the Approach

Unidirectional waves are considered. They are created by the superposition of two or more wave components propagating in the direction of ship's surge motion. A standard mathematical model that can reproduce asymmetric surging and surf-riding has been employed, incorporating multi-frequency excitation (see [11]). Once more, the examined ship was the tumblehome topside vessel, from the ONR series, with length  $L = 154$  m, beam  $B = 18.8$  m and mean draft  $T = 5.5$  m [1].

The investigation is focused on the identification of hyperbolic *Lagrangian coherent structures* (LCS) in the system's phase space. LCS are phase space objects of separatrix nature, that can be considered as analogous to the stable and unstable manifolds of hyperbolic fixed points of autonomous dynamical systems. Hence, they indicate basins of attraction and, in general, they expose the skeleton of the flow. The LCS concept came about from the interbreeding of nonlinear dynamics and fluid mechanics [3, 7]. LCS appear as cores of trajectory patterns, identified as being, locally, the strongest attracting/repelling material surfaces advected with the flow. A few approaches have been proposed for their identification, which vary in their robustness, potential for handling multi-dimensional phase space, in terms of computational cost, etc. Here we have implemented a scheme based on the calculation of the largest finite-time Lyapunov exponent (FTLE) field [4, 6]. Alternative approaches are also under evaluation (see [10]).

For the bi-chromatic sea in particular, a supplementary massive campaign of time-domain simulations was performed. The goal was to capture the mean and the amplitude of surge velocity's oscillations, in order to evaluate how these relate with characteristic reference velocities, such as the nominal speed and the celerities of the participating wave components.

### 3 Principal Features of the Unsteady Phase Flow for Bi-Chromatic Waves

The ship is excited by two harmonic waves, defined as follows: the first (identified from now on as the “primary”), has fixed length  $\lambda_1$  equal to the ship length  $L$  and its steepness is set at  $s_1 = 0.035$ . The other (“secondary”), can be regarded as a perturbation effect, although its height will be allowed sometimes to become large. It will have a comparable frequency, while its steepness will be varied according to the scenario.

The arrangement of system’s LCS right upon the inception of global surf-riding is revealed through the two snapshots of Fig. 1. Some differences from the monochromatic case are noticed: firstly, tangling of LCS appears, i.e., tangling of the “effective” manifolds associated with influential hyperbolic trajectories. These trajectories (marked with black crosses, Fig. 1) are counterparts of the saddle points appearing in the monochromatic case. The tangling of LCS is accompanied by the usual, in these cases, stretching and folding process. Secondly, as evidenced from Fig. 2, surf-riding is oscillatory (the power spectrum of the motion is also shown). In fact, this is a universal feature of surf-riding in bi-chromatic waves. It will be revealed later that the celerity of the primary wave dictates the mean value of ship velocity during surf-riding. The perturbing wave on the other hand, is responsible for velocity’s oscillation around the celerity of the primary wave.

The crossing of LCS brings along the fractalization of basin boundaries and subsequently, basin’s erosion. In the series of graphs of Fig. 3 the steepness of the secondary wave is raised from a very low value, in order to observe the successive transformations of phase space as the effect of the secondary wave is intensified. However, the steepness of the primary wave is set lower than previously in order to ensure that, in

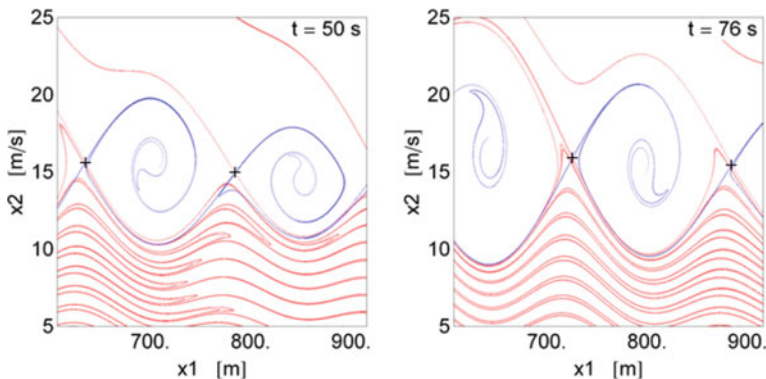


**Fig. 1** Phase-space portraits at different time instants for bi-chromatic wave excitation. Variables  $x_1$  and  $x_2$  correspond to the longitudinal position and surge velocity of the ship (respectively). Black crosses mark locations of hyperbolic trajectories that strongly affect the surrounding phase flow. Blue and red curves correspond to attracting and repelling (respectively) LCS



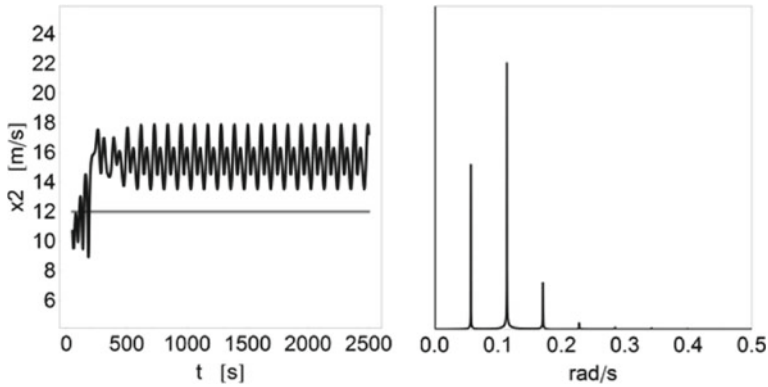


**Fig. 2** Character of surf-riding in bi-chromatic waves. (Left) Time history of surge velocity (black curve) contrasted to the nominal speed (grey line). (Right) The discrete Fourier transform of the time history of surge velocity

the absence of the secondary wave, coexistence of surging and surf-riding will exist (this fact is basically confirmed by the first graph of Fig. 3).

The fact that basin boundaries become fractal is verified by zooming successively onto a small area enclosing a basin boundary segment, revealing the well-known self-similarity pattern (see Fig. 4). The erosion of surf-riding’s basins bears an important consequence: surging becomes motion destination from areas deep into surf-riding’s domain, in a rather unpredictable manner. Two time-domain simulation

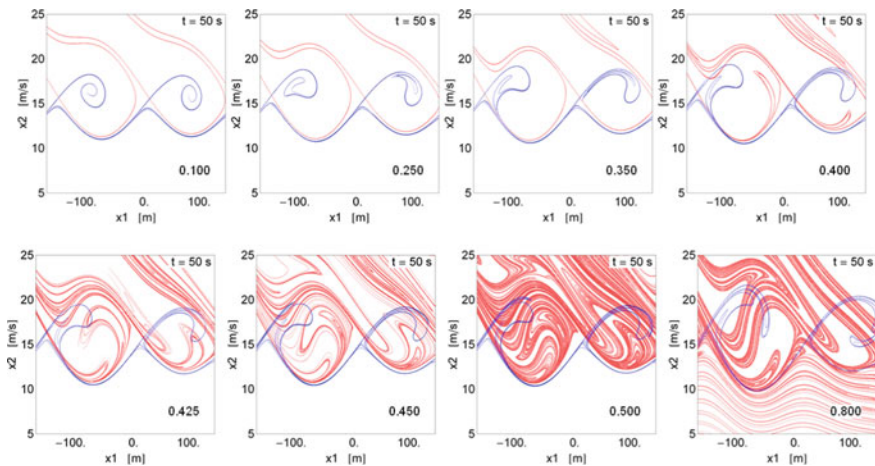


**Fig. 3** Transformation of the phase space as the steepness of the secondary wave is increased, due to tangling of the attracting and the repelling LCS (blue and red curves respectively). The steepness ratio (secondary to primary wave) can be seen on the bottom-right corner of each graph. All graphs refer to the same time instant

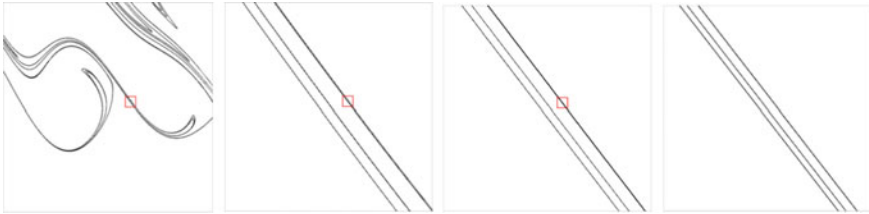


**Fig. 4** Self-similarity is revealed by successive enlargements of small rectangles placed on a surf-riding basin boundary

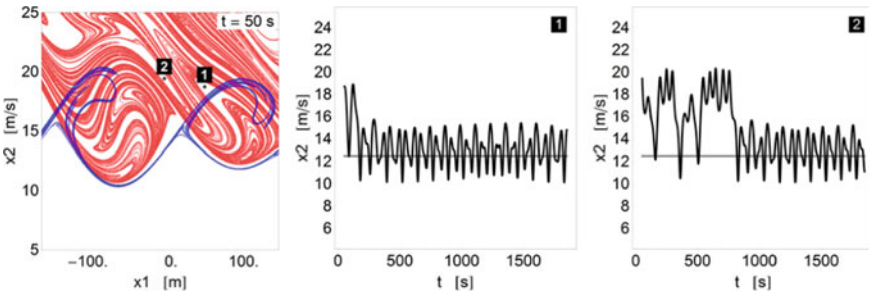


**Fig. 5** The erosion of surf-riding basins creates possibility of initiating surging from deep within the surf-riding area

examples, shown in Fig. 5, verify this behavior. The particularly long, seemingly chaotic, transient of case 2 should be noticed.

A strong hint about the arrangement of surf-riding and surging domains is offered from the graphs of Fig. 6. These graphs represent the field produced by the integration of the squared velocity of the phase-space-particles along trajectories. The process of fractal destruction of the surf-riding domain (as the steepness of the secondary wave is increased, Fig. 6 from left to right) is confirmed. Although the ship was very close to global surf-riding when the secondary wave excitation was established, this extra forcing did not lead to global surf-riding but to the fractal erosion of the surf-riding domain.

### 4 Behavior for Irregular Wave Excitation

The time-changing LCS for wave excitation deriving from a JONSWAP spectrum are shown in Fig. 7. We considered a frequency band with width  $0.5\omega_p$ , centered on spectrum's peak  $\omega_p = 0.598$  rad/s. The significant wave height was  $H_S = 5.5$  m. The spectrum was discretized through 48 components. Ship's nominal speed was 12 m/s. Substantial time variation of phase space flow can be noticed and, at first reading, the flow shows less coherence. In Fig. 7 is illustrated, in addition, the evolution of

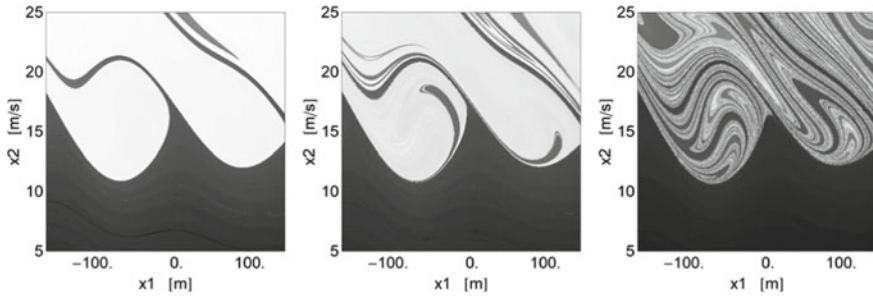


**Fig. 6** (Left, middle) Areas of surging (dark) and surf-riding (pale). (Right) Surging has dominated the entire phase space (pale regions indicate high-velocity transients)

two groups of initial conditions (the green and the red) separated by a repelling LCS segment. Their initial placement is shown in Fig. 7a. The green points are found directed towards lower velocities (they should be identified as engaged in surging) compared to the red points that seem like being trapped at a higher velocity region. As a result, eventually, the green points lag behind the red points. This is evident from the two snapshots at 410 s; red points (Fig. 7d) have covered greater distance when compared to the green ones (Fig. 7c).

In the final investigation targeting the phase space, an irregular perturbation (calculated from a spectrum) was superimposed to a harmonic excitation, in such a way that, the wave energy content (based on the amplitudes of the participating discrete harmonics including the primary one) was maintained constant. The excitation was computed by applying a filter that had one of its parameters working as a control knob, gradually raising the amplitudes of the perturbation harmonics while lowering primary's. This filter has been described in [5]. The effect of the filter on the JONSWAP spectrum (with  $T_p = 9.93$  s and  $H_s = 7$  m) is shown in Fig. 8. The number of participating harmonics was  $n = 74$  and ship's speed was set again at 12 m/s.

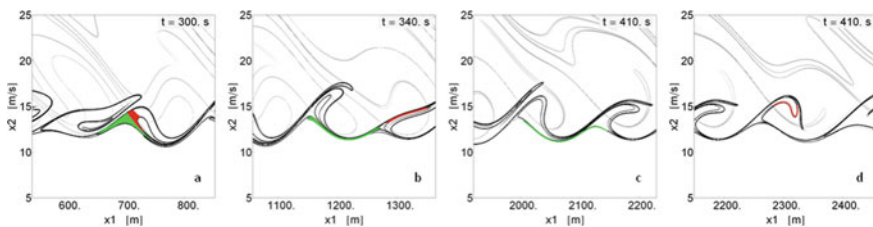


**Fig. 7** Portrait of phase space flow for JONSWAP spectrum. Two selected sets of initial conditions (appearing as green and red areas) evolve into different velocity ranges. Black and gray curves correspond to attracting and repelling (respectively) LCS

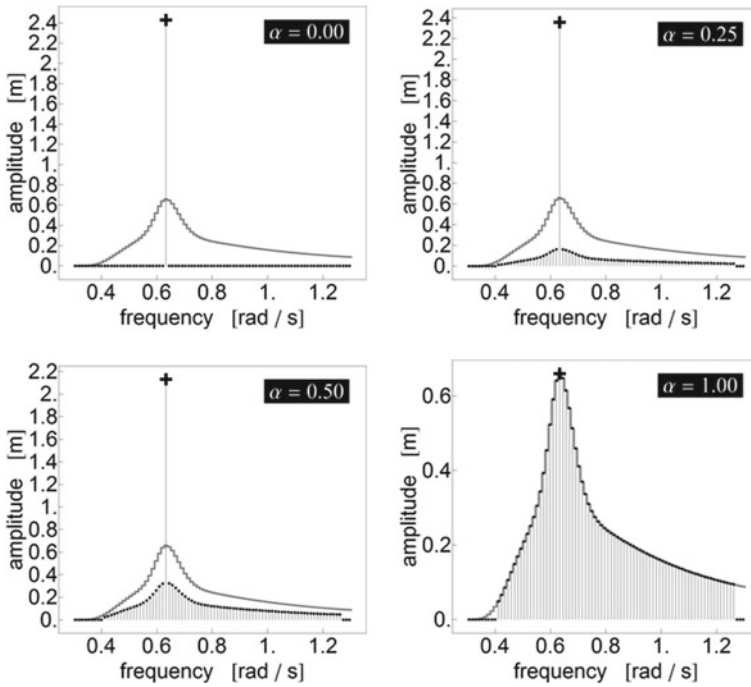


**Fig. 8** Wave amplitudes (black dots) obtained from a JONSWAP spectrum on the basis of energy equivalence, compared to the amplitude of the primary harmonic (black cross). The control parameter varies from zero to one, as one moves gradually from regular waves to waves corresponding to the intact spectrum. The intact spectrum (defining the energy level) is shown in grey

In Fig. 9 are illustrated successive transformations of the phase space, which are provoked by the gradual turning of the excitation from mainly regular to mainly irregular. We have started, again, from a condition very close to the beginning of global surf-riding. Whilst, this time, global surf-riding did truly happen, it was followed by an erosion process of the surf-riding basins, provoked by LCS tangling corresponding to neighboring surf-riding basins.

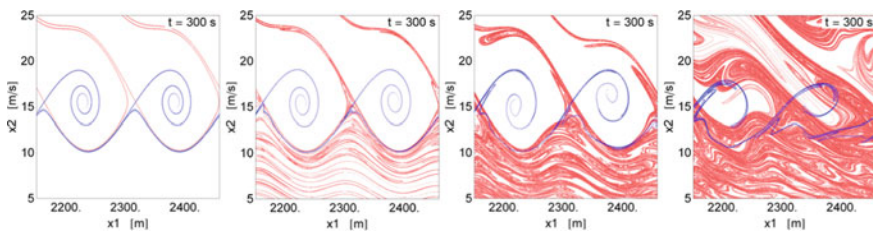


**Fig. 9** Transformations of phase space layout as moving from regular to irregular excitation

This is a new event where a surf-riding basin intrudes into another basin of the same kind. This makes uncertain the destination where the ship will settle, although surf-riding remains as the certain outcome.

It is evident therefore that, several new phenomena of behavior become possible when one looks beyond the monochromatic sea; implying that, the probabilistic evaluation of a ship's tendency for surf-riding in irregular seas becomes an even more daring task.

## 5 Characterization of High-Runs

The final aspect considered was the characterization of the encountered types of high-speed motion. Consider once more the idea of having a steep primary wave, perturbed by a secondary harmonic that is kept initially at a very low height. Naturally, one would expect to see a perturbed version of surf-riding, ruled by the celerity of the first wave. When the two wave components start having comparable magnitudes however, the outcome becomes difficult to predict. Three examples, corresponding to frequency ratios 0.8, 0.9 and 1.05, are shown, respectively, in Figs. 10, 11 and 12. For frequency ratio 0.8, and as the steepness ratio is raised, the mean surge velocity falls initially perfectly on the celerity of the primary wave. Later however there is a jump to the celerity of the secondary wave, returning shortly to intermediate values (in-between the two celerities). Further increase of the steepness leads to domination of the celerity of the secondary wave. A look into the fluctuating surge velocity reveals period doublings and chaos. Some surf-riding oscillations are extremely large, driving the ship, in repeating short spells, to very high-speed values. Similar patterns are noticed for the other two frequency ratios. Apparently, these do not resemble surf-riding as we have known it and for this reason, we invented the term "high-run" for all these abnormal high-speed motions encountered in irregular seas. It should also be noticed that the reference system is moving with the wave celerity  $c_1$  of the prime wave ( $\lambda = L$ ), as a matter of fact the horizontal axis of the figures of the mean surge velocity corresponds to  $c_1$ .

## 6 Conclusions

Several new phenomena of ship surge dynamics were observed when two or more frequencies were included in the excitation. In bi-chromatic waves, different types of oscillatory surf-riding exist, governed either by the first or by the second wave component. However, no coexistence of these two types was noticed as stable motions. Moreover, chaotic motions were identified in the intermediate range, sometimes extending to very high surge velocity values. They are preceded by homoclinic/heteroclinic tangling of LCS found, creating fractalization of the surf-riding

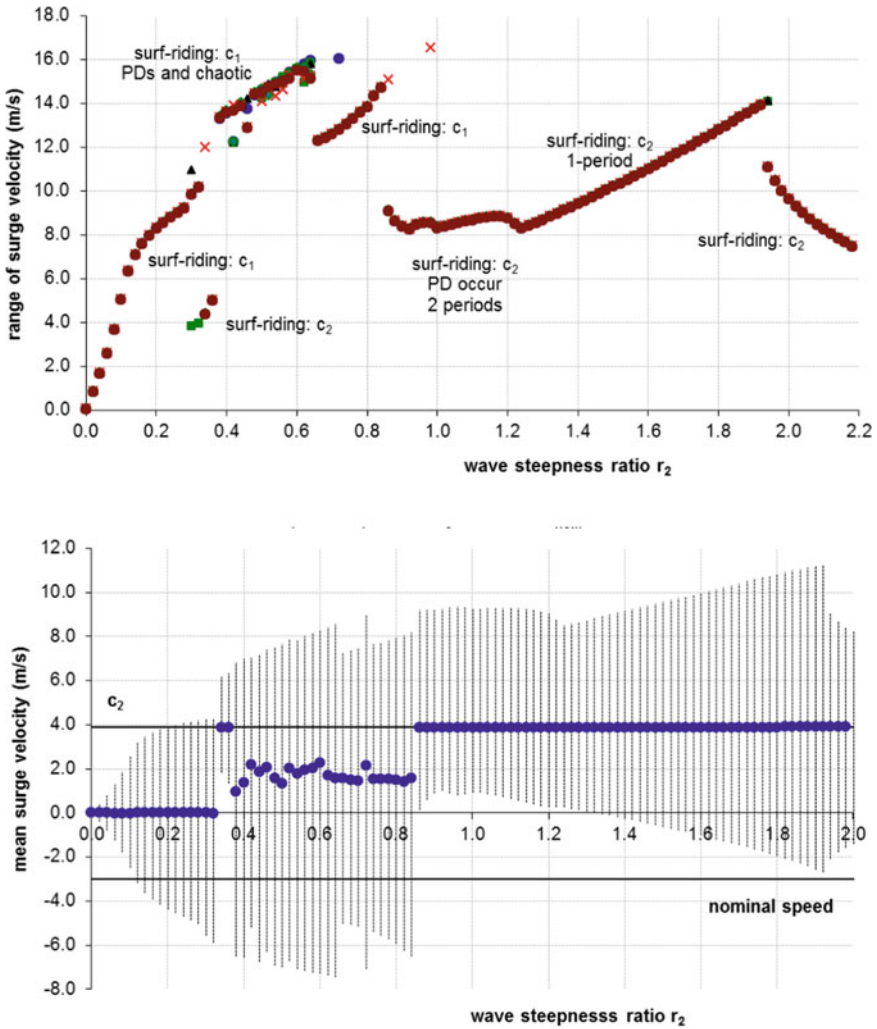


**Fig. 10** Range of surge velocity (upper) and mean value of surge velocity (down), for frequency ratio (of secondary to primary wave) 0.8, steepness of primary wave 1/30, nominal speed 12.5 m/s and initial surge velocity 10.5 m/s. Different colours of the points in the upper graph correspond to different initial conditions for surge velocity

basin boundaries. Such phenomena were noticed in bi-chromatic as well as in multi-chromatic waves and seem to be quite common. In general, the exhibited dynamic behavior is very rich.

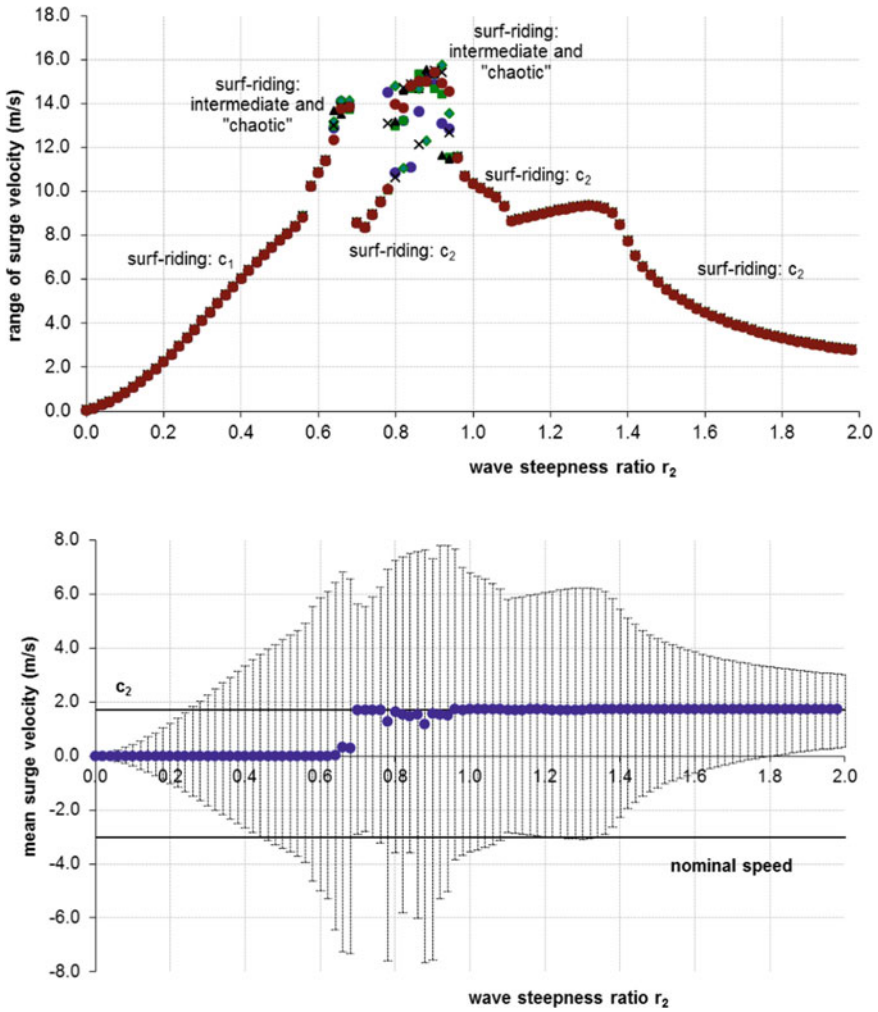


Fig. 11 As Fig. 10, with frequency ratio 0.9

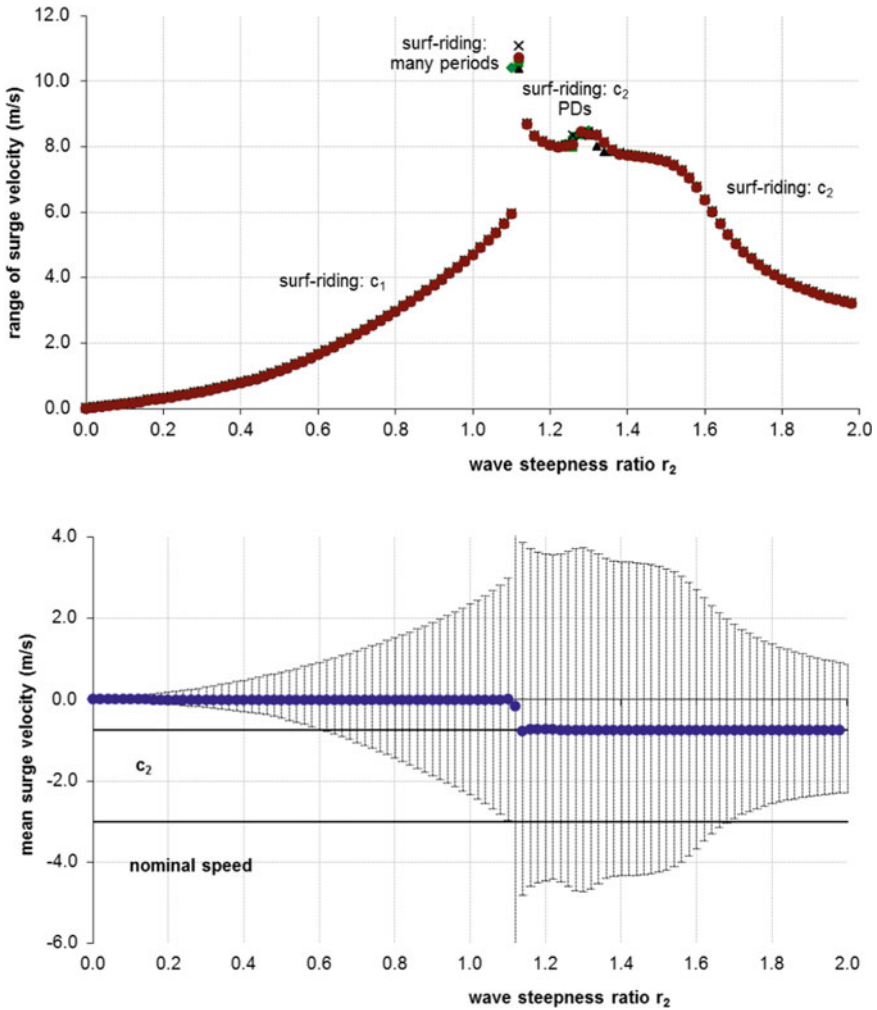


Fig. 12 As Fig. 10, with frequency ratio 1.05

**Acknowledgements** The following sources are acknowledged for sponsoring parts of the investigations reported in this paper:

The Greek General Secretariat of Research and Technology, in the framework of the General Program "ARISTEIA I", with contract reference number GSRT-252.

The Office of Naval Research under Dr. Thomas Fu and the Office of Naval Research Global under Dr. Woei-Min Lin (grant number N62909-13-1-7).

Useful discussions with Dr. Vadim Belenky and Mr. Kenneth Weems are acknowledged.



## References

1. Bishop RC, Belknap W, Turner C, Simon B, Kim JH (2005) Parametric investigation on the influence of GM, roll damping, and above-water form on the roll response of model 5613. Report NSWCCD-50-TR-2005/027
2. Belenky V, Weems K, Spyrou K (2016) On probability of surf-riding in irregular seas with a split-time formulation. *Ocean Eng.* <https://doi.org/10.1016/j.oceaneng.2016.04.003>
3. Haller G, Yuan G (2000) Lagrangian coherent structures and mixing in two-dimensional turbulence. *Physica D* 147:352–370
4. Kontolefas I, Spyrou KJ (2016) Coherent structures in phase space, governing the nonlinear surge motions of ships in steep waves. *Ocean Eng.* <https://doi.org/10.1016/j.oceaneng.2016.02.013>
5. Kontolefas I, Spyrou KJ (2020) Probability of ship high-runs from phase-space data. *J Ship Res* 64:81–97. <https://doi.org/10.5957/jsr.2020.64.1.81>
6. Shadden SC, Lekien F, Marsden JE (2005) Definition and properties of Lagrangian coherent structures from finite-time Lyapunov exponents in two-dimensional aperiodic flows. *Physica D* 212(3–4):271–304
7. Shadden SC (2011) Lagrangian coherent structures. In: Grigoriev R (ed) *Transport and mixing in laminar flows: from microfluids to oceanic currents*. Wiley-VCH
8. Spyrou KJ (1996) Dynamic instability in quartering seas: the behaviour of a ship during broaching. *J Ship Res, SNAME* 40(1):46–59
9. Spyrou K, Belenky V, Themelis N, Weems K (2014) Detection of surf-riding behavior of ships in irregular seas. *Nonlinear Dyn* 78(1):647–649
10. Spyrou KJ, Kontolefas I, Themelis N (2016) Dynamics of the surf-riding behavior of a ship in a multi-chromatic sea environment. In: *Proceedings of 31st symposium of naval hydrodynamics, Monterey, California, USA*
11. Spyrou K, Kontolefas I, Themelis N (2023) Estimates of the probability of surf-riding in irregular seas. In: Spyrou KJ, Belenky V, Katayama T, Backalov I, Francescutto A (eds) *Chapter 23 of contemporary ideas on ship stability. From dynamics to criteria*, Springer, pp 387–399. ISBN 978-3-031-16328-9
12. Themelis N, Spyrou KJ, Belenky V (2016) “High runs” of a ship in multi-chromatic seas. *Ocean Eng.* <https://doi.org/10.1016/j.oceaneng.2016.04.024>

# Critical Distance on a Phase Plane as a Metric for the Likelihood of Surf-Riding in Irregular Waves



Vadim Belenky, Kostas Spyrou, and Kenneth Weems

**Abstract** The formulation of a metric for the likelihood of surf-riding in irregular waves is addressed in this chapter. This metric measures how close a ship is to surf-riding at a given time and is computed through a series of perturbation simulations. This approach allows the physics of severe ship motions to be included in the statistical extrapolation of the response by the split-time method. The candidate metric is the distance, in the surge phase plane, between the ship's position (location and velocity) at an instant of a random seas simulation and the instantaneous boundary between surging and surf-riding (if the latter exists). The distance is measured along the line connecting the position of the dynamical system and the stable surf-riding pseudo-equilibrium at that time. The instance of surf-riding is defined when the surging velocity exceeds the value of the instantaneous celerity, computed at the position of a stable pseudo-equilibrium just behind the ship.

**Keywords** Surf-riding · Dynamical system · Pseudo-equilibrium · Attraction

## 1 Introduction

Surf-riding is observed as an extended acceleration of a ship in following or stern-quartering seas beyond that associated with propulsion, resistance and oscillatory surging in waves. The physical mechanism of surf-riding in regular waves includes the appearance of dynamical equilibria and a ship's attraction to the stable equilibrium. The equilibria appear when the wave surging force becomes large enough to offset the difference between the ship's thrust and its resistance at wave celerity. The

---

V. Belenky (✉) · K. Weems  
David Taylor Model Basin (NSWCCD), West Bethesda, Maryland, USA  
e-mail: [vadim.belenky@navy.mil](mailto:vadim.belenky@navy.mil)

K. Weems  
e-mail: [kenneth.weems@navy.mil](mailto:kenneth.weems@navy.mil)

K. Spyrou  
School of Naval Architecture, National Technical University of Athens, Athens, Greece  
e-mail: [spyrou@deslab.ntua.gr](mailto:spyrou@deslab.ntua.gr)

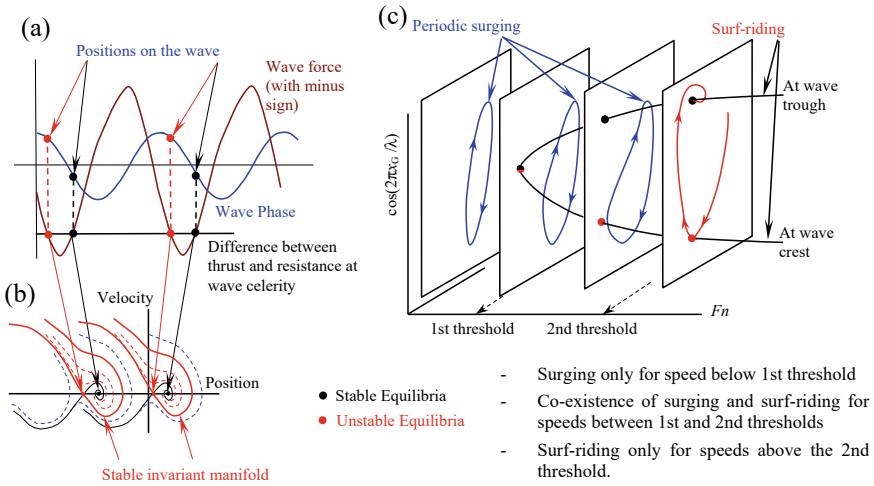


**Fig. 1** Overview of surf-riding in regular waves: **a** spatial snapshot for forces and equilibria, **b** phase portrait and saddle-node bifurcation, **c** global homoclinic bifurcation

equilibrium points are the positions of the ship in the wave field where the forces balance exactly (Fig. 1a).

The nature of surf-riding in regular waves has been well understood since the 1990s, when local and global surf-riding are the result, respectively, of a local (“saddle-node”, Fig. 1b) and a global (“homoclinic saddle connection”, Fig. 1c) bifurcation in phase space (e.g. [24]). Two transformations (global bifurcations) in phase space when surf-riding occurs had been stated by Makov [21] (available in English from [5]) and by Kan [17]: first when surf-riding equilibrium appears and then when surf-riding becomes the only option. The second transformation is a homoclinic bifurcation as it involves collision of a saddle point at the unstable equilibrium and a limit cycle representing surging. A high-level description of surf-riding within the context of other homoclinic events is available from Spyrou [25].

Surf-riding in irregular waves has been a challenging subject to study, and no universally accepted approach has been established. The first published approach was a semi-analytical one by Grim [14], which has recently been evaluated from a numerical perspective by Themelis et al. [32]. Umeda [33] attempted to calculate the probability of surf-riding, assuming a narrow-band wave spectrum that allowed some probabilistic interpretation to the conditions of surf-riding. Direct time-domain simulation approaches have been investigated by de Kat et al. [12], de Kat and Thomas [13], Ayyub et al. [4], and others.

Even in the simplest case of a single-degree of freedom system, which considers only surging and surf-riding in long-crested irregular waves, the wave elevation is a random function of two arguments: time and a spatial coordinate. As a result, the Froude-Krylov incident wave force is also a random function of the same two arguments: time and position. Thus, periodicity in space cannot be assumed, and a

spatial snapshot for forces and equilibria, such as in Fig. 1a, is no longer sufficient. The problem must be considered both in time and space, leading to the formulation of a spatial–temporal framework (e.g. [7]). It is essentially a set of spatial snapshots, computed for sequential instants of time.

Wave celerity is an important quantity for the surf-riding phenomenon. As it defines the speed at which a ship will remain at the same position on a propagating wave, it is the ship speed at which the difference between thrust and resistance needs to be “compensated” by the Froude-Krylov wave force in order to accelerate a ship to surf-riding. The definition of wave celerity for irregular waves is not trivial, but it can be formulated with either the velocity of certain elements (e.g. position of maximum slope) of a wave profile or through the instantaneous frequency. Details of these definitions and a demonstration of their adequacy is available in Spyrou et al. [26], while a comprehensive summary can be found in the previous issue of this book, Spyrou et al. [28]. A particular feature of random wave celerity is that it is not just another stochastic process, like wave amplitudes. It can experience “jumps to infinity” when one wave overtakes another.

As both the Froude-Krylov force and wave celerity are random quantities in irregular waves, the points where the sum of the wave force, thrust, and resistance equals zero also behave randomly. These points appear, disappear, and move in an unsteady fashion relative to the wave profile and, therefore, move with an acceleration. The acceleration causes inertial forces that prevent a dynamical system from remaining at that point. As a result, the term “equilibria” is intentionally not used for these points. At the same time, these points are still special in the phase plane, so they will be referred to as “pseudo-equilibria”.

The phase portrait, in Fig. 1b for regular waves, becomes time-dependent for irregular waves. The invariant manifold, as a solid red curve in Fig. 1b, separating surging and surf-riding in regular waves, becomes a surface that can be identified as a Lagrangian Coherent Structure (LCS) often found to be formed in physical flows. Results of a study of LCS for surf-riding in irregular waves are available from Kontolefas and Spyrou [18] and are summarized in Spyrou et al. [30].

The introduction of realistic (irregular) waves into the consideration of surf-riding changes its physics dramatically. This change of physics makes the estimation of probability of surf-riding even more challenging. The first logical step is to build an estimate from observations. It is clear that instances of surf-riding should be observed as episodes of abnormally high forward speeds that are close to the instantaneous values of celerity at the ship’s location. Additionally, a surf-riding equilibrium should be nearby. These episodes have been named “high runs” and were studied by Themelis et al. [32]. The evaluation of the LCS in the ship vicinity makes the “high-run” definition more robust [19]. The current status of this research is described in Spyrou et al. [29].

While the high-run approach allows the estimation and analysis of the statistics of a surf-riding response, a direct observation of the phenomenon is required. For moderate sea states, the high-run approach application may incur significant computation cost as such occurrences are likely to be rare. The critical wave group approach is a viable alternative for estimation, if an extrapolation is required. The idea of the

critical wave group approach is that ship behaviors of interest in moderate seas are caused by relatively rare groups of steep waves. The first practical application of this approach is described by Themelis and Spyrou [31], while this approach was further developed by Anastopoulos and Spyrou [1, 2]. Sequential sampling [22] allows the employment of high-fidelity simulation to evaluate a ship response within the critical group approach. While not addressing surf-riding in particular, the wave group approach provides a promising framework for the application of extrapolation to surf-riding. A description of the current status of the wave group approach is available from Anastopoulos and Spyrou [3].

The split-time method is another possible approach for statistical extrapolation, when complex physics are involved. The method separates the estimation procedure into an observable or “non-rare” problem and a non-observable or “rare” problem. The “non-rare” problem is associated with an up-crossing of an intermediate threshold, which should be frequent enough to collect a statistically representative sample of values associated with the crossing within a practical simulation time. For the application of the split-time method to surf-riding, the intermediate threshold may be set for the surging velocity.

The “rare” problem is the estimation of the probability of surf-riding if the intermediate threshold has been crossed. It is solved by perturbing a dynamical system at the point of up-crossing until surf-riding is observed. The value of the required perturbation is a “metric of likelihood”. The calculation of the metric for each crossing creates a sample that can fit a distribution tail and complete the extrapolation. The phase-plane distance to a stable pseudo-equilibrium has been proposed as a surf-riding metric by Belenky et al. [7]. This metric is the main focus of this chapter. Further descriptions of the split-time method to capsizing and broaching-to can be found in Weems et al. [34] and Belenky et al. [9].

## 2 Mathematical Model of Surf-Riding in Irregular Waves

A single degree-of-freedom mathematical model for surging and surf-riding in irregular waves, described by Belenky et al. [10], will explore the metric of the likelihood of surf-riding. Three coordinate systems are as follows: an Earth-fixed system, a ship-fixed system, and a moving coordinate system that is located at a wave crest and is translating with the constant velocity equal to wave celerity at the crest at the start of the perturbation analysis. These coordinate systems are illustrated in Fig. 2.

The dynamical system is expressed with the following equation of motion:

$$(M + A_{11})\ddot{\xi}_G + R(\dot{\xi}_G) - T_e(\dot{\xi}_G; n) + F_X(t, \xi_G) = 0 \quad (1)$$

where  $M$  is the mass of the ship,  $A_{11}$  is the added mass in surge,  $\xi_G$  is the position of the center of gravity of the ship in the Earth-fixed coordinate system,  $R$  is a resistance in calm water,  $T_e$  is effective thrust produced by the propulsor with shaft speed  $n$ , and  $F_X$  is the Froude-Krylov wave force in surge.

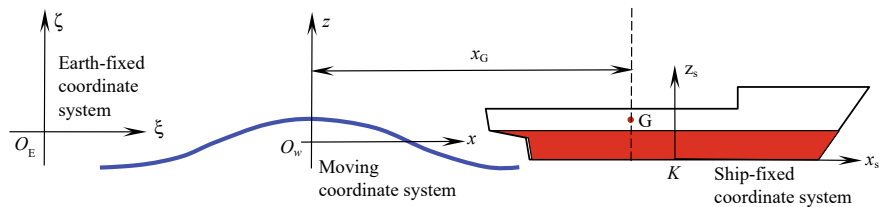


**Fig. 2** Coordinate systems: earth-fixed ( $\xi O_E \zeta$ ); moving ( $z O_w x$ ; moves with constant velocity); ship fixed ( $x_s K z_s$ )

The calm water resistance and effective thrust are modeled with polynomials:

$$R(U) = r_1 U + r_2 U^2 + r_3 U^3 \tag{2}$$

$$T_e(U; n) = \tau_0 n^2 + \tau_1 n U + \tau_2 U^2 \tag{3}$$

where  $U$  is a nominal forward speed and the coefficients  $r$  and  $\tau$  can be fitted to resistance and propulsion data by a least square method.

The Froude-Krylov wave force in surge is formulated as a body linear problem and is expressed as:

$$F_X(t, \xi_G) = \sum_{i=1}^N A_{X_i} \sin(k_i \xi_G - \omega_i t + \varphi_i + \gamma_i) \tag{4}$$

where  $k_i$  is the wave number (spatial frequency),  $\omega_i$  is the temporal frequency, and  $\varphi_i$  is a random phase shift for the  $i$ th wave component of the standard Longuet-Higgins model of irregular waves.  $A_{X_i}$  and  $\gamma_i$  are the force amplitude and phase shift, expressed in the frequency domain as:

$$A_{X_i} = \rho g k_i a_i \sqrt{a_{si}^2 + a_{ci}^2}; \quad \gamma_i = -\text{atan}\left(\frac{a_{si}}{a_{ci}}\right) \tag{5}$$

where  $a_i$  is the amplitude of the  $i$ th wave component,  $\rho$  is the density of water, and  $g$  is the gravitational acceleration. The components of the amplitude of the surge force are computed with the integrals:

$$\begin{aligned} a_{si} &= \int_{-0.5L}^{0.5L} \cos(k_i x_s \cos \psi) \int_{-d}^0 e^{-k_i z} C(x_s, z) dz dx_s \\ a_{ci} &= \int_{-0.5L}^{0.5L} \sin(k_i x_s \cos \psi) \int_{-d}^0 e^{-k_i z} C(x_s, z) dz dx_s \end{aligned} \tag{6}$$

where  $L$  is the ship length,  $d$  is the draft at the station with coordinate  $x_s$  and  $C(x_s, z)$  is a result of integration by  $y$ -coordinate, expressed as:

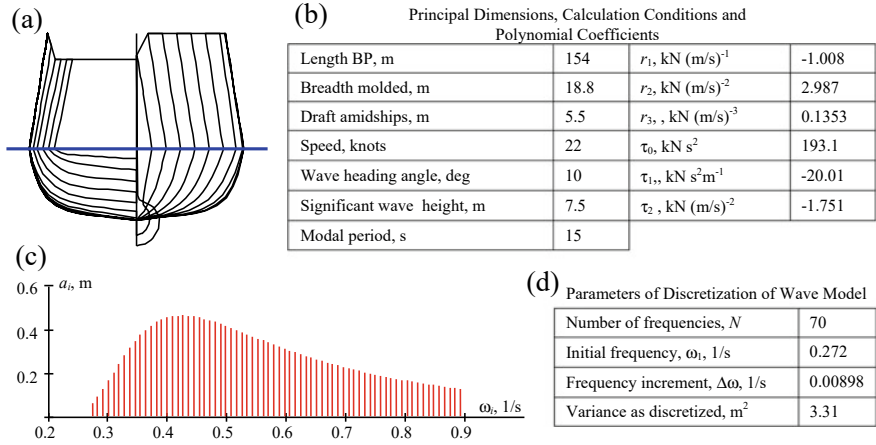


**Fig. 3** Computation setup: **a** hull lines, **b** principal dimensions, calculation conditions, and polynomial coefficients for approximation of resistance and propulsion, **c** amplitudes of wave components, **d** parameters of spectral discretization

$$C(x_s, z) = 2 \begin{cases} \frac{\sin(k_t b(x_s, z) \sin \psi)}{k_t \sin \psi}, & \psi \neq 0 \\ b(x_s, z), & \psi = 0 \end{cases} \quad (7)$$

In this equation,  $\psi$  is a wave heading angle,  $z$  is measured in the ship-fixed coordinate system (positive upward from the base line), and  $b$  is the molded local half-breadth located at  $z + d$  above the base line.

The tumblehome configuration from the ONR topside series [11] was selected for numerical study. The ship lines, principal dimensions, and flotation are shown in Fig. 3. Calm water resistance was estimated with regression formulae by Holtrop and Mennen [15] and Holtrop [16], while the propulsor was modeled with the Wageningen B-series propeller data [23]. The polynomial coefficients  $r$  and  $\tau$  fitted to the results of these calculations can be found in Fig. 3b.

Calculations were performed for regular (as a test case), bi-chromatic, tri-chromatic, and full-band irregular waves. To keep the energy equivalence between all four cases, a filtering scheme described in Belenky et al. [10] was applied. Full-band irregular waves corresponded to sea state 7 (see Table 7 of [20]) with details in Fig. 3d.

### 3 Definition of Critical Distance in Phase Plane

The metric of the likelihood of surf-riding is first formulated for regular waves and then extended for irregular waves. The metric is formulated for the situation of coexistence of surging and surf-riding [7]. The coexistence situation in regular

waves can be a primitive imitation of surf-riding in moderate irregular waves, where pseudo-equilibria do not move and the boundary between surging and surf-riding does not depend on time.

The idea of critical distance as a metric of likelihood of surf-riding is illustrated in Fig. 4. The metric is defined as a distance from the initial ship position to the intersection with the stable invariant manifold, measured along the line connecting the initial position in the phase plane with the nearest stable equilibrium behind the ship.

The moving coordinate system is used for formulating the metric (Fig. 2). The initial position of the ship on the phase plane is defined as the vector:

$$\vec{X}_0 = (x_{G0}, \dot{x}_{G0})^T = (\xi_{G0} - \xi_{C0}, \dot{\xi}_{G0} - c_{w0})^T \tag{8}$$

where  $x_{G0}$  is the distance from a wave crest (origin of the moving coordinate system) to the ship’s center of gravity at the initial moment,  $\dot{x}_{G0}$  is the velocity in the moving coordinate system at the initial moment,  $\xi_{G0}$  is the ship’s initial position in the Earth-fixed coordinate system,  $\xi_{C0}$  is a position of the nearest wave crest behind the ship in the Earth-fixed coordinate system,  $\dot{\xi}_{G0}$  is a ship velocity in the Earth-fixed coordinate system at the initial moment, and  $c_{w0}$  is the wave celerity at the nearest stable equilibrium behind the ship at the initial moment.

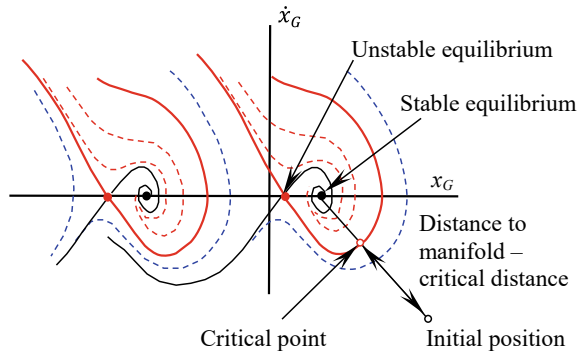
Similarly, the position of the nearest stable equilibrium behind the ship is defined by the vector:

$$\vec{X}_s = (x_{s0}, 0)^T = (\xi_{s0} - \xi_{C0}, c_{w0} - c_{w0})^T \tag{9}$$

where  $x_{s0}$  is the distance from a wave crest (origin of the moving coordinate system), and  $\xi_{C0}$  is the coordinate of the stable equilibrium in the Earth-fixed coordinate system at the initial moment.

The surging and surf-riding responses is illustrated in Fig. 5, where time histories were computed by a numerical integration of the equation of motion (1) with different initial conditions. The wave length was 225 m (frequency 0.52 1/s, period 12 s),

**Fig. 4** Illustrating the definition of critical distance, as a measure of likelihood of surf-riding





which was chosen to be close to the modal period but short enough to be sufficiently steep for surf-riding. Wave celerity was 18.73 m/s. The initial position of the surging time history was  $x_{G0} = 133$  m ahead of the wave crest with an initial speed of  $\dot{x}_{G0} = 22$  kt = 11.3 m/s. The closest stable equilibrium was located 83 m from the wave crest, so the initial conditions for the surf riding response were  $x_{s0} = 83$  m and  $c_{w0} = 18.73$  m/s.

The object is to find the “boundary” between surging and surf-riding responses located on the line connecting the initial position with the stable equilibria. A scalar-valued function of vector argument is introduced as:

$$S(\vec{X}) = \max(\dot{x}_G(t)); t \in [0; T_s] \tag{10}$$

where  $\vec{X}$  is a vector of arbitrary initial conditions similar to the one defined by Eq. (8), and  $T_s$  is a simulation time slightly exceeding the duration of a typical “high-run” (e.g. 300 s). A case of surf-riding is associated with a condition

$$S(\vec{X}) > c_{w0} \tag{11}$$

To reflect that the critical point is searched along the line between  $\vec{X}_0$  and  $\vec{X}_s$ , consider the following vector-valued function of a scalar argument:

$$\vec{F}(\varepsilon) = \vec{X}_0 - \varepsilon(\vec{X}_s - \vec{X}_0); \varepsilon \in [0; 1] \tag{12}$$

where

$$\vec{F}(0) = \vec{X}_0; \vec{F}(1) = \vec{X}_s \tag{13}$$

Time histories for different values of  $\varepsilon$  are in Fig. 6, while the phase trajectories corresponding to these time histories are presented in Fig. 7. The critical point can

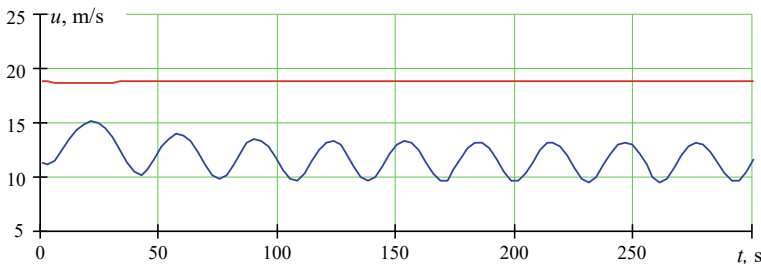


**Fig. 5** Co-existence of surging (blue) and surf-riding (red) for regular wave, height 5.14 m, frequency 0.52 1/s, length 225 m, celerity 18.7 m/s, initial position 133 m from the wave crest, distance to stable equilibrium from the wave crest is 83 m

be found with a dichotomic search. The phase trajectories originating from above and below the critical point are in red and blue, respectively. Finally the distance between the initial position and critical point is defined as a critical distance and a metric of likelihood of surf-riding.

This definition of critical distance is slightly different from the one given by Belenky et al. [7]. The current definition has a formal criterion for surf-riding (11) that was absent in the cited reference. The criterion, expressed as Eq. (11), relates the surf-riding phenomenon with the crossing of a threshold by the velocity. A similar criterion is specified in the high-run approach (e.g. [30]).

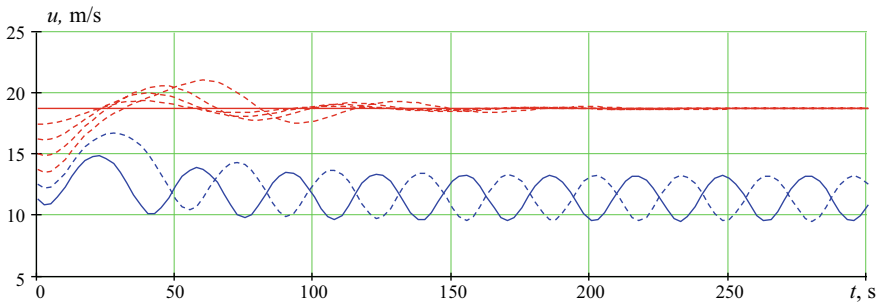


**Fig. 6** Time histories of iterations to find a critical distance by varying  $\epsilon$  in Eq. (12); values of  $\epsilon$  below the critical distance return to surging (dashed blue curves), while values at or above the critical distance result in surf-riding (dashed red curves)

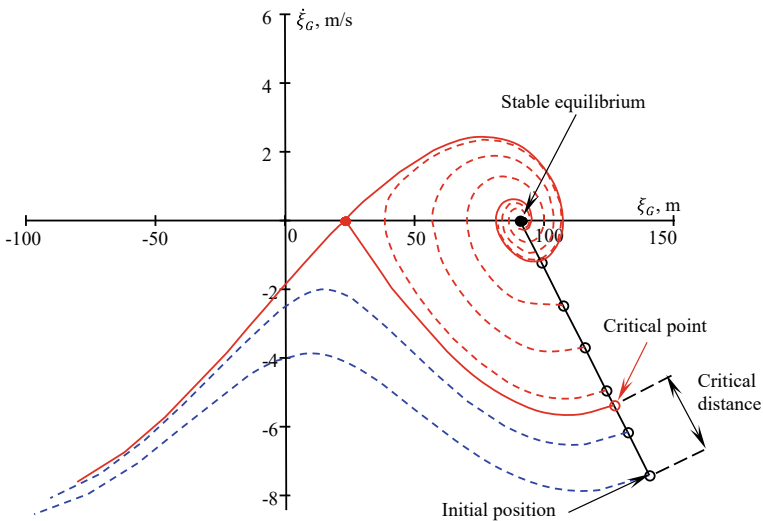


**Fig. 7** Phase trajectories of iterations to find a critical distance, the solid red curves are an approximation of branches of the invariant manifold separating surging and surf-riding responses, dashed curves correspond to values of  $\epsilon$  above (red) and below (blue) the critical distance

## 4 Critical Distance in Bi-Chromatic Waves

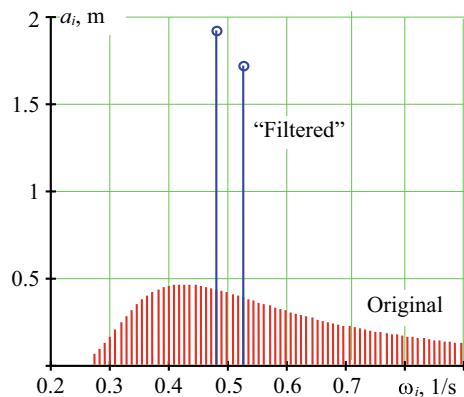
Starting from a limited the number of frequencies in a wave model, as a first step towards full-band irregular waves, seems to be a natural way to study the effect of irregularity on the surf-riding phenomenon. The reasonableness (no controversy to existing knowledge) of the surging and surf-riding model (Eqs. 1 through 7) was demonstrated with a three-component or tri-chromatic wave by Belenky et al. [10]. Spyrou et al. [27] applied two-component or bi-chromatic waves to study the effect of irregularity on the physics of surf-riding. Dynamics of surf-riding under the action of multi-components wave is quite rich. In particular, chaotic attractors were discovered. These results were summarized in Spyrou et al. [29].

A spectral representation of the bi-chromatic wave is in Fig. 8. The frequencies were chosen to be  $\omega_1 = 0.48$  1/s,  $\omega_2 = 0.52$  1/s, corresponding to wave lengths  $\lambda_1 = 269$  m and  $\lambda_2 = 225$  m between one and three ship lengths, i.e. in the range of wave length where surf-riding may be expected. The justification is similar to that in the previous section, as these waves are long enough to be relevant for surf-riding. The heights of these waves were computed to keep the variance of wave elevations equal to the full-band value from Fig. 3d.

A series of spatial snapshots of wave celerity computed by the instantaneous frequency method (e.g. [28]) is illustrated in Fig. 9a. The celerity remains almost constant through the space domain, with the exception of two spots around  $\xi = 2$  km and  $\xi = 3.5$  km, where it goes to infinity as the first wave overtakes the second. These spots slowly move forward. For these plots, the upper limit of celerity was capped at 35 m/s.

The balance of forces is depicted in Fig. 9b, where the difference between thrust and resistance at the instantaneous wave celerity (brown curve) and Froude-Krylov wave surging force (indicated by the minus sign in Fig. 9b as a blue curve). The intersection of these two curves defines pseudo-equilibria; stable pseudo-equilibria are marked with black dots, while unstable pseudo-equilibria are marked with red dots. These spatial snapshots are similar to the one in Fig. 1a for a regular wave;

**Fig. 8** Spectral representation of bi-chromatic waves



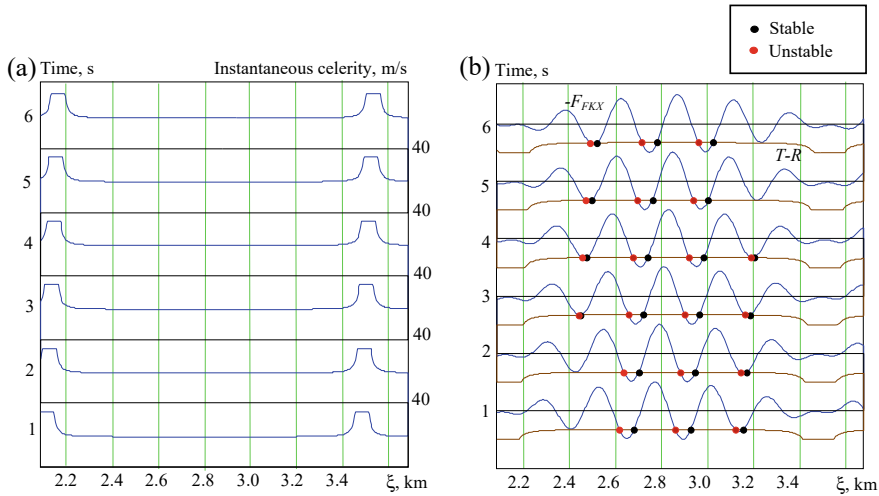


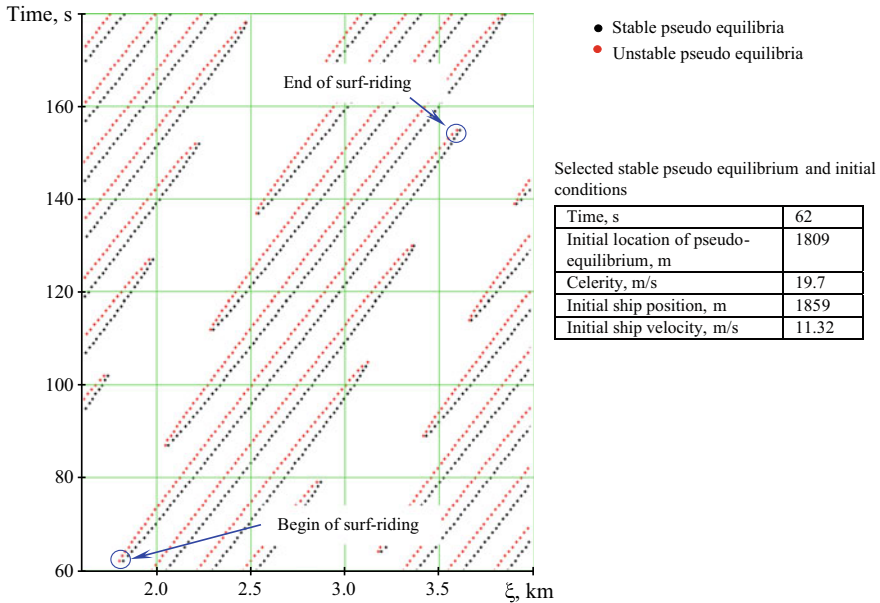
**Fig. 9** Spatial–temporal snapshots for bi-chromatic case: **a** wave celerity and **b** balance of forces and the surf-riding equilibria (blue curves are surging wave force, brown curves are balances between commanded thrust and resistance at the wave celerity)

however, the difference between thrust and resistance is changing in space due to the variation of wave celerity. Increases of celerity toward the “jumps to infinity” lead to increased resistance at this celerity and essentially lower the balance between thrust and resistance, requiring a larger wave surging force for surf-riding; as a result, the surf-riding equilibria will cease to exist near these jumps.

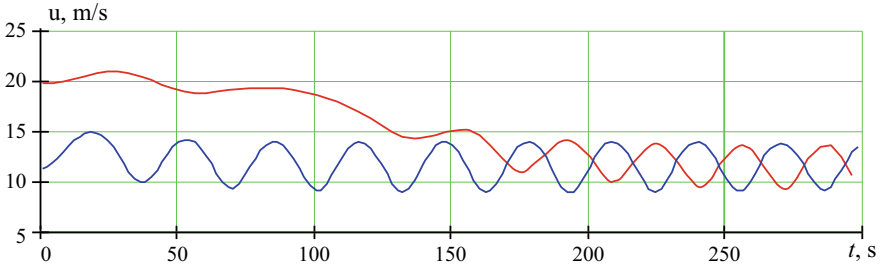
The Froude-Krylov wave surging force follows a beating pattern made by two wave components of similar frequency. The decrease of wave height as the two waves go out of phase leads to a decreased wave surge force, providing yet another reason for the pseudo-equilibria to cease to exist (details in [10]). The latter scenario is also in Fig. 9b. The pair of equilibria near 3150 m disappears between 4 and 5 s.

Figure 10 is a “big picture” view of the pseudo-equilibria locations and movements in the form of loci (traces) of these points in a spatial–temporal snapshot. The pseudo-equilibria form a pattern that is regular and apparently related to the beating pattern formed by the two wave components.

A stable surf-riding pseudo-equilibrium is chosen at the beginning of the strip (marked by a blue circle in Fig. 10) and subsequently exists for over a minute. Time histories of surging velocity for two calculations are in Fig. 11: (1) starting from the stable surf-riding pseudo-equilibria point with the wave celerity and (2) starting from a point 50 m in front of the selected stable pseudo-equilibrium, while sailing with calm water self-propulsion speed of 11.32 m/s (22 kt). The red curve in Fig. 11 is the time history originating from the stable surf-riding pseudo-equilibrium, which rides the wave until about  $t = 150$  s before slowing to unsteady surging. As can be seen from Fig. 10, the stable pseudo-equilibrium ceases to exist somewhere around  $t = 150$  s, and the dynamical system is “released from captivity”.



**Fig. 10** Loci of surf-riding pseudo-equilibria; initial conditions for sample calculations and location of selected stable pseudo-equilibrium is given in table



**Fig. 11** Co-existence of surging and surf-riding for bi-chromatic wave

The procedure for calculating critical distance is similar to the regular wave case. Time histories for different values of  $\varepsilon$ , Eq. (12), are shown in Fig. 12, while the phase trajectories corresponding to these time histories are presented in Fig. 13. The critical point can be found with a dichotomic search. The phase trajectories originating from above and below the critical point are in red in Fig. 13. The distance between the initial position and critical point is defined as a critical distance and is a metric of the likelihood of surf-riding.

The appearances of the time histories in Figs. 11 and 12 and the phase portrait in Fig. 13 change dramatically as compared to the regular wave case. The moving of the pseudo-equilibria in Fig. 13 is actually quite substantial, so the assumption of

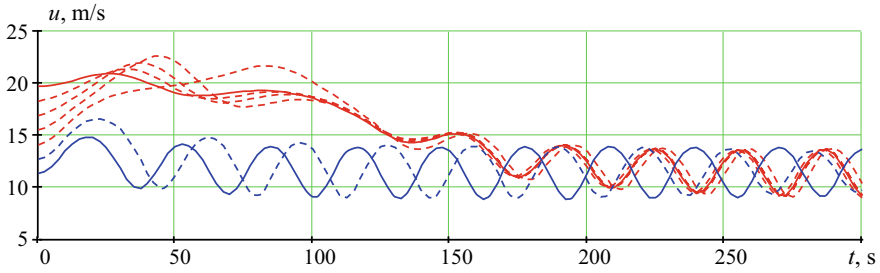


**Fig. 12** Time histories of iterations to find a critical distance for bi-chromatic wave

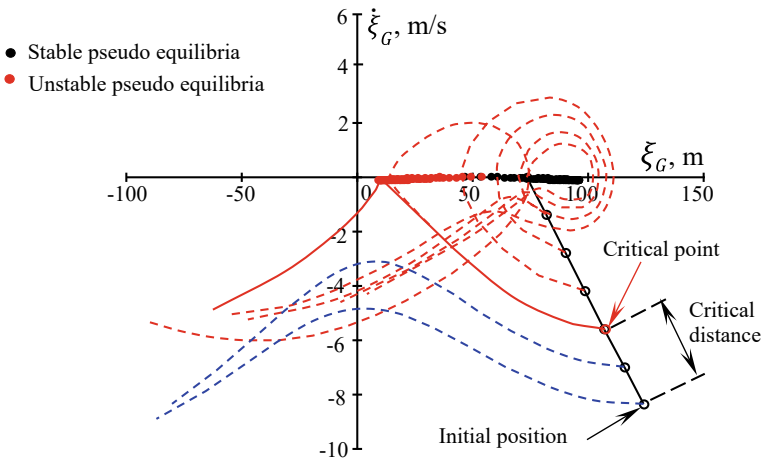


**Fig. 13** Phase trajectories of iterations to find a critical distance for bi-chromatic waves: solid red curves are approximations of LCS projection, separating surging and surf-riding responses

slowly changing parameters is not applicable even in a “benign” case of bi-chromatic waves. The disappearance of the pseudo-equilibria and subsequent transition from surf-riding to surging is seen as a loop in the phase plane in Fig. 13. These loops cross the zero, exceeding the value of the wave celerity at the initial moment and computed at the point of stable pseudo-equilibrium just behind the initial ship position. In other words, these trajectories are classified as instances of surf-riding according to Eq. (11).

### 5 Critical Distance in Tri-Chromatic Waves

The next case uses a three-component (tri-chromatic) wave is presented in Fig. 14c. The wave components have lengths of 191 m, 225 m, and 269 m and heights of 3.3 m,

3.0 m, and 2.6 m. The loci of pseudo-equilibria for the tri-chromatic case and the point used for the metric calculations are shown in Fig. 14a with the point selected for the surf-riding metric calculation marked with a blue circle, while Fig. 14b depicts the numerical characteristics of selected stable pseudo-equilibrium.

The picture of pseudo-equilibria is similar to the bi-chromatic case in Fig. 10, but the existence and non-existence of the pseudo-equilibria is not as regular. Shorter durations also can be observed (e.g. around 40 s and 100 m), although most of the pseudo-equilibria exist for longer times.

A different distribution of the pseudo-equilibria may lead to a longer duration of surf-riding as compared to the bi-chromatic case. The solid red curve in Fig. 15 shows surf-riding originating from the stable pseudo-equilibrium (Fig. 14b) and lasting for about 400 s. This stable pseudo-equilibrium only lasts for about 120 s and ceases to exist around 135 s and 3 km, as marked with a triangle in Figs. 14a and 15. As the surf-riding continues, another wave must be providing energy and creating another stable pseudo-equilibrium to attract the dynamical system. A possible candidate is marked with a blue square in Fig. 14a. This indicates, in principle, a possibility of multi-wave surf-riding.

Time histories in Fig. 15 are computed with initial conditions corresponding to different values of  $\varepsilon$ , Eq. (12). The distinction is quite clear between time histories of surf-riding (red curves) and of surging (blue curves). This response in phase plane together with the loci of pseudo-equilibria and the trajectory, originated from the critical point, is in Fig. 16.

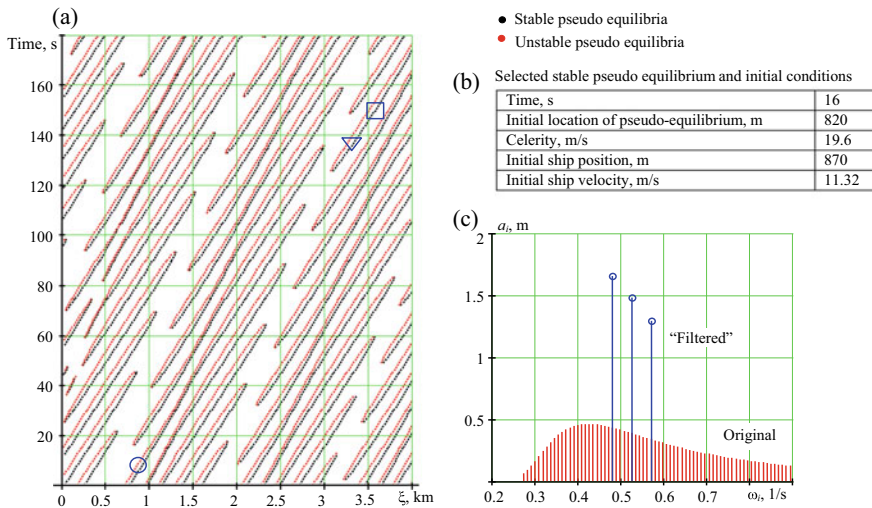


**Fig. 14** Pseudo-equilibria in tri-chromatic waves: **a** loci of pseudo-equilibria (blue circle is an initial point for calculation of the surf-riding metric), **b** selected pseudo-equilibrium and initial conditions, **c** amplitudes and frequencies of tri-chromatic waves

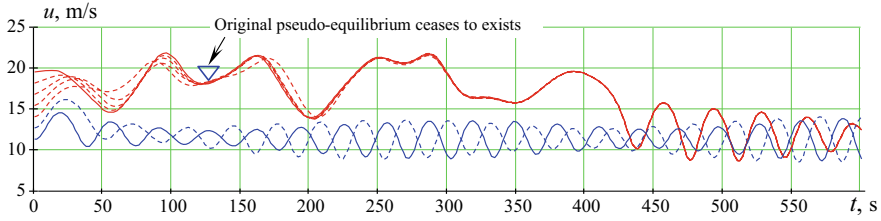


**Fig. 15** Co-existence of surging and surf-riding for tri-chromatic wave (solid curves) and time histories of iterations to find a critical distance for tri-chromatic wave (dashed curves)

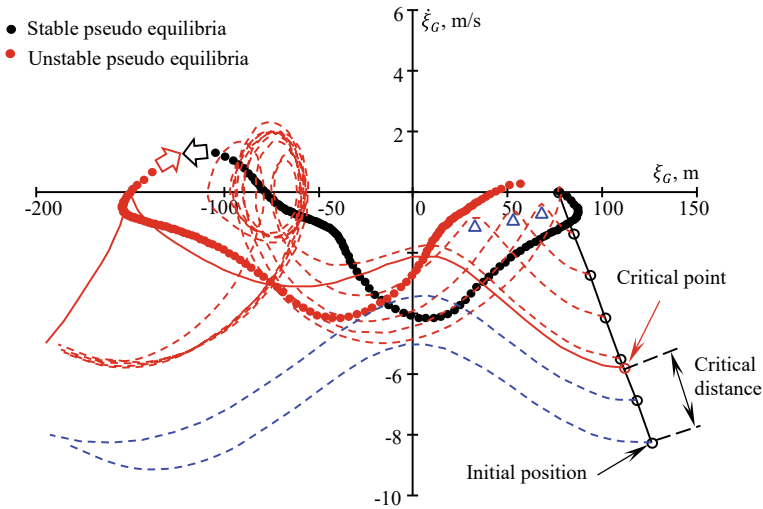


**Fig. 16** Phase trajectories of iterations to find a critical distance for tri-chromatic waves: the solid red curves approximate branches of the invariant manifold separating surging and surf-riding responses

Compared to the bi-chromatic case (Fig. 13), the range of movement of pseudo-equilibria in Fig. 17 is significantly larger. As in the bi-chromatic case, the surf-riding phase trajectories exhibit loops, which are probably related to local minima of the time histories in Fig. 15 at around 60 s. Notable features are saddle-point-like trajectories in the vicinity of the unstable pseudo-equilibria, which are marked in Fig. 16 with triangles. Also, the phase portrait only covers the motion until the pseudo-equilibria cease to exist for the first time around 120 s in Fig. 15 (The stable and unstable pseudo-equilibria move toward each other before they disappear. The disappearance is marked with arrows). The metric of surf-riding defined with criterion (11) seems to work for the tri-chromatic case, as it successfully identifies initial conditions associated with surf-riding.



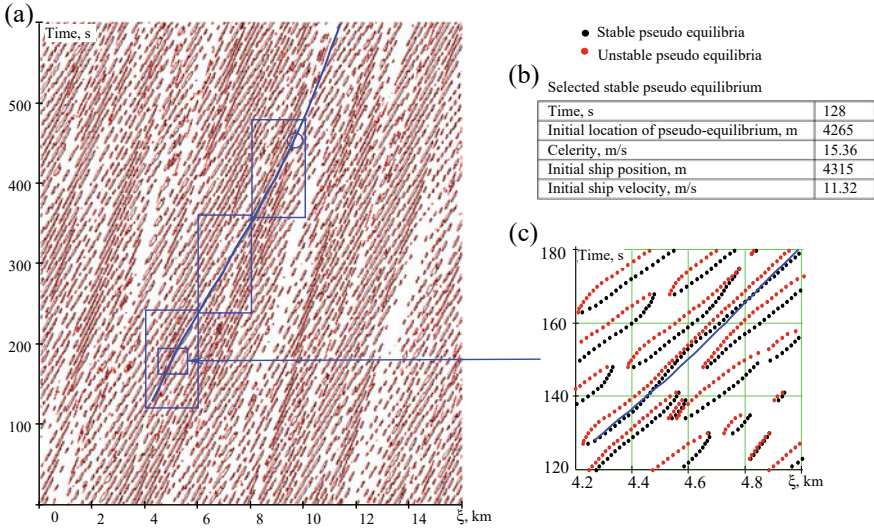


**Fig. 17** Pseudo-equilibria in the “full-band” irregular waves: **a** loci of pseudo-equilibria (blue curve is a ship response trace originating from the selected stable surf-riding pseudo-equilibrium, blue rectangles are zoomed areas, and blue circle shows approximate termination of surf-riding), **b** selected pseudo-equilibrium and initial conditions, **c** zoomed-in loci

## 6 Critical Distance in Full-Band Irregular Waves

Pseudo-equilibria for “full-band” irregular waves is illustrated in Fig. 17. Spectra and parameters of the wave discretization are given in Fig. 3. The loci of pseudo-equilibria appear more complex compared to the cases with bi- and tri-chromatic waves. Long episodes of pseudo-equilibria (100 s and more) are complemented with relatively brief episodes lasting only for few seconds. Parameters for a stable pseudo-equilibrium are in Fig. 17b. The initial point was located 50 m forward of the stable pseudo-equilibrium, and speed was taken to be a nominal 22 kt = 11.32 m/s. A time history originated from the initial point is a solid blue curve in Fig. 18, while the solid red curve depicts a motion time history started from the stable pseudo-equilibrium.

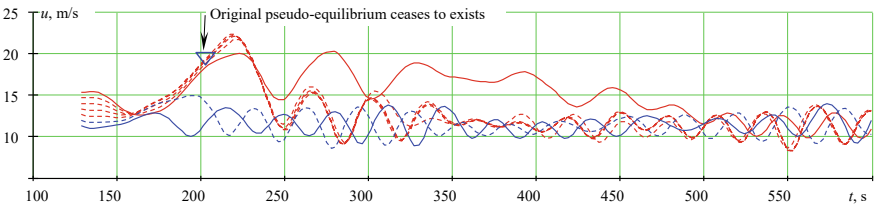


**Fig. 18** Co-existence of surging and surf-riding for full-band irregular waves (solid curves) and time histories of iterations to find a critical distance for full-band irregular waves (dashed curves)

The solid red curve in Fig. 18, depicting surf-riding, experiences a local minimum around 170 s. This minimum may be related to a particular pattern of pseudo-equilibria. A zoomed-in view of the loci in Fig. 17c indicates decreasing distance between stable and unstable pseudo-equilibria occurring from 145 to 160 s. A plausible explanation is that the dynamical system was “released” and then “picked-up” again. Interestingly, the speed dropped to the “unperturbed” level, as the solid red and solid blue curves touch at around 160 s in Fig. 18.

The original pseudo-equilibrium ceases to exist at about 200 s, marked with a triangle in Fig. 19a, where zoomed-in loci are shown for the time range 120–240 s. The velocity continues to increase as another pseudo-equilibria appears that exists for another 22 s. Then, no pseudo-equilibrium occurs until 250 s (Fig. 19b), and the solid red curve in Fig. 18 experiences another minimum around that time.

A zoomed-in view of the loci of pseudo-equilibria is depicted in Fig. 19b for the interval from 240 to 360 s. A series of brief episodes are encountered that, while being short, are close enough to each other to continue surf-riding. A very brief episode occurs around 290 s, which is marked with an arrow in Fig. 19b. Stable and unstable pseudo-equilibria are located very close to each other, repeating the situation encountered round 145–160 s in Fig. 17c—another local minimum of a solid red curve in Fig. 18 around 300 s. The next noticeable local minimum of that curve occurs around 425 s in Fig. 18. This corresponds to another short “void” between the episodes in Fig. 19c. Finally, the dynamical system encounters a longer “void” around 450 s, and the ship loses speed and drops to surging, and the solid red curve joins with other time histories in Fig. 18.

Time histories are computed for Fig. 18 with initial conditions corresponding to different values of  $\varepsilon$ , Eq. (12). While the distinction is quite clear between time histories of surf-riding (red curves) and of surging (blue curves), the values of  $\varepsilon < 1$  lead to a shorter surf-riding response, transiting back to surging around 240 s. Probably, the dynamical system could not “overcome the void” from 220 to 245 s. The local

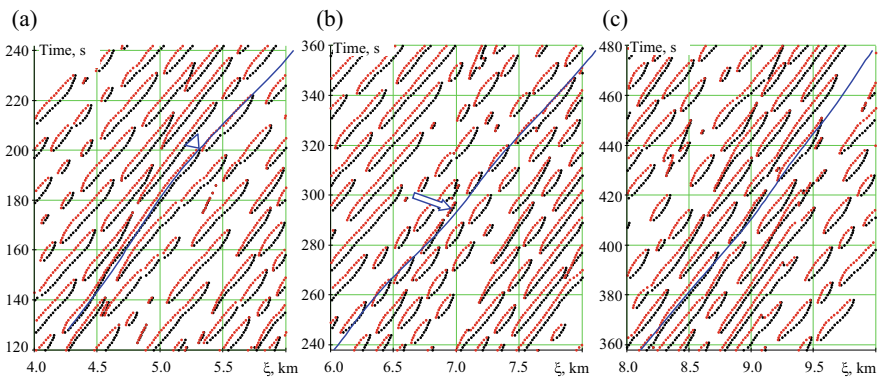


**Fig. 19** Zoomed-in areas of loci of pseudo-equilibria with ship response trace superimposed with ship response trace

maxima at 215 s of dashed red curves are larger than the local maximum of solid red curve around 225 s in Fig. 18. Most probably, the higher speed made the system go too far ahead and missed the series of short episodes in Fig. 19b. Also, a group of dashed red phase trajectories crosses the horizontal axis around 150–170 m in Fig. 20.

The response in Fig. 20 is in phase plane together with loci of pseudo-equilibria, and the trajectory originates from the critical point. Loci of pseudo-equilibria are only for the first episode from 128 s until 200 s. The appearance and disappearance of the pseudo-equilibria are indicated with arrows. To keep the phase portrait compact, however, phase trajectories are only within 300 m of the origin of the moving frame of reference.

The phase portrait in Fig. 20 is not simple. The complex motion of the pseudo-equilibrium causes the phase trajectories to loop several times. Nevertheless, a dichotomic search for a value of  $\epsilon$  in Eq. (12) to satisfy criterion (11) yields a critical point that separates initial conditions leading to surf-riding from those that lead to surging. Thus, the critical distance can be considered as a possible metric of likelihood of surf-riding in irregular wave.

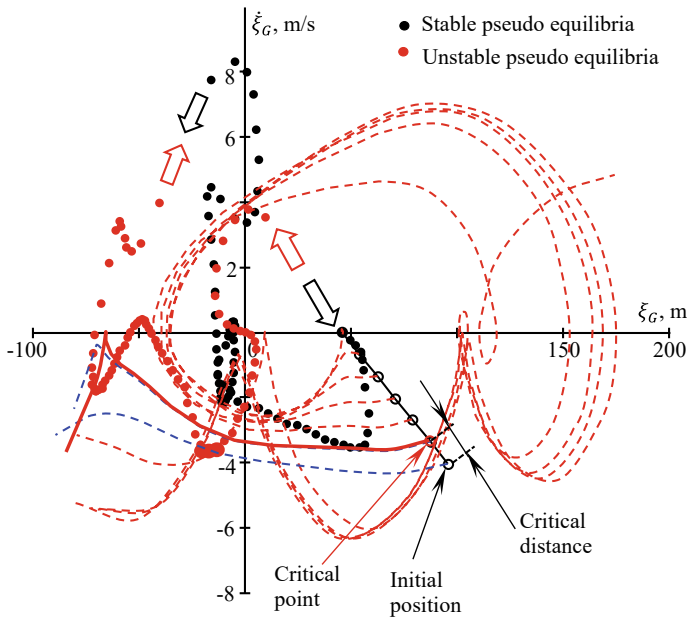


**Fig. 20** Phase trajectories of iterations to find a critical distance for full-band irregular waves: red curves approximate branches of invariant manifold separating surging and surf-riding responses

## 7 Discussion

A distance in a phase plane as a metric of the likelihood of surf-riding was first formulated in Belenky et al. [6]. It was tested by slowly varying wave parameters in an attempt to emulate the motion of the pseudo-equilibria. The outcome appeared not so different from the regular wave case, and the surf-riding was still perceived as an attraction to a slowly moving point in a phase plane. However, an attempt to apply this formulation for actual irregular waves, reported by Belenky et al. [7], turned out to be inconclusive, as the pseudo-equilibria do not move slowly. As a result, surf-riding in irregular waves does not look like a focus point in a phase plane.

At the same time, an attempt to use the phase plane distance as a metric of likelihood for broaching-to was conclusive [8]. The broaching event can be clearly defined as a substantial deviation from a commanded heading  $-10^\circ$  was used in the cited reference. As broaching is essentially a directional instability phenomenon, the particular threshold for heading deviation is not that important. It just has to be large enough in order not to be distinguished from “normal” yaw motions.

Thus, in order to make the surf-riding metric conclusive, a definition of surf-riding in irregular waves is needed such that can be used in a search for a critical point. As surf-riding is a phenomenon of acceleration beyond the commanded speed, to look for a forward speed threshold to cross would be natural. This threshold must be large enough to distinguish surf-riding from “normal” surging in irregular waves.

A value of 10% above the commanded speed was within time-domain numerical simulation approach from the nineties (e.g. [12, 13]). Looking at Fig. 18 and taking into account that a single-degree of freedom solution may exaggerate the response, this 10% threshold does not look unreasonable. The “high-run” approach adds essential physics such as the presence of stable pseudo-equilibrium in the vicinity of a ship. Knowledge of the instantaneous wave celerity is also quite helpful (e.g. [30]).

The discussed metric also uses the position of a stable pseudo-equilibrium and instants wave celerity. The value of the latter, computed at the position of the stable pseudo-equilibrium at the initial moment, is a threshold to define the instance of surf-riding in irregular waves. The problem is that the wave celerity is random and the evolutions of pseudo-equilibria are also random. Therefore, the crossing of this threshold does not mean that the surf-riding will continue long enough to generate directional instability or cause other navigational problem (like colliding with a ship in front). In order to account for the duration of the surf-riding, Spyrou et al. [30] considers “prolonged high-run”, including the surf-riding time, as a part of the definition.

Thus, including duration into the metric definition makes sense. Further study is needed, however, to see if getting closer to the position of the stable pseudo-equilibrium always means a longer duration of surf-riding. A dangerous surf-riding event may be defined in terms of duration, additional distance travelled, and so on. Depending on what event is considered a hazard, a point in the phase plane may exist that is more dangerous than a stable pseudo-equilibrium. This point, however, is likely

to be in vicinity of the stable pseudo-equilibrium, as was observed for broaching-to in Belenky et al. [8].

Making the metric consistent with the “high-run” approach is also sensible, enabling extrapolation with the split-time method, while “high-run” approach plays the role of direct counting. This creates a possibility of statistical validation of extrapolation. Physical validation of the metric can be conceivably be performed with LCS (e.g. [29]), which provides a complete description of surf-riding in irregular waves.

## 8 Summary and Conclusions

The formulation of a metric for the likelihood of surf-riding that could be applied to the case of irregular waves was described in this chapter. The irregularity of waves changes the physics of surf-riding, as the wave celerity becomes random as does the Froude-Krylov wave force in surge. As a result, the dynamic equilibria characterizing surf-riding in regular waves no longer exist. Instead, special points occur where all forces are equal, but these points move with acceleration, so they are not solutions of the equation of motions. They still define the topology of the phase plane and are referred as pseudo-equilibria.

The metric of likelihood is intended to be used within the split-time framework for extrapolation, estimating a probability of surf-riding when it cannot be directly observed, so a physical description must be included. The metric is formulated as a distance to the boundary between surging and surf-riding from an initial position in the phase plane. The distance is measured along a line connecting the initial position, corresponding to an up-crossing of the non-rare problem in the split-time method, and stable pseudo-equilibrium, located just behind the ship.

A critical point on the boundary between surf-riding and surging is computed with a series of short time-domain simulations starting from a point located on the line between the initial position and stable pseudo-equilibrium. If the velocity exceeds a threshold, the response is classified as surf-riding. The value of the instantaneous celerity, computed at the stable pseudo-equilibrium at the initial moment, is taken as the threshold. Other thresholds could also be used, while additional conditions (such as duration of surf-riding) can be considered in the future.

The chapter describes the formulation of the metric with regular wave, while the testing has been performed with bi-chromatic, tri-chromatic, and “full-band” irregular waves. The proposed metric was successful for the considered examples. Cases with multi-wave surf-riding were observed for tri-chromatic and “full-band” irregular waves. Future development may be envisioned to make the metric consistent with the “high-run” approach and validate it with Lagrangian Coherent Structures, providing a complete description of boundary between surging and surf-riding in irregular waves.

**Acknowledgements** The work described in this chapter has been funded by the Office of Naval Research (ONR) and ONR Global under Dr. Thomas Fu, Dr. Woei-Min Lin, and Dr. Salahuddin

Ahmed, and by a David Taylor Model Basin /NSWCCD Independent Applied Research (IAR) program under Dr. Jack Price. The authors are grateful to Dr. Art Reed, Tim Smith, and Brad Campbell of David Taylor Model Basin and to Nikos Themelis and Ioannis Kontolefas of the National Technical University of Athens for fruitful discussion of this work.

## References

1. Anastopoulos PA, Spyrou KJ (2016) Ship dynamic stability assessment based on realistic wave group excitations. *Ocean Eng* 120:256–263
2. Anastopoulos PA, Spyrou KJ (2019) Evaluation of the critical wave groups method in calculating the probability of ship capsize in beam seas. *Ocean Eng* 187:106–213
3. Anastopoulos PA, Spyrou KJ (2023) An efficient formulation of the critical wave groups method for the assessment of ship stability in beam seas. In: Spyrou K, Belenky V, Katayama T, Bačkalov I, Francescutto A (eds) *Contemporary ideas on ship stability—from dynamics to criteria*, Chapter 10. Springer, pp 157–174. ISBN 978-3-031-16328-9
4. Ayyub BM, Kaminsky M, Alman PR, Engle A, Campbell BL, Thomas WL III (2006) Assessing the probability of the dynamic capsizing of vessels. *J Ship Res* 50(4):289–310
5. Belenky VL, Sevastianov NB (2007) *Stability and safety of ships: risk of capsizing*, 2nd edn, ISBN 978-0939773619
6. Belenky V, Spyrou K, Weems KM (2014) Critical distance on a phase plane as a metric for the likelihood of surf-riding in irregular waves. In: *Proceedings of 14th international ship stability workshop*, Kuala Lumpur, Malaysia, pp 144–148
7. Belenky V, Weems K, Spyrou K (2016) Towards a split-time method for estimation of probability of surf-riding in irregular seas. *Ocean Eng* 120:264–273
8. Belenky V, Spyrou KJ, Weems KM (2016) On probabilistic properties of surf-riding and broaching-to in irregular waves. In: *Proceedings 31st symposium naval hydrodynamics*, Monterey, California, USA
9. Belenky V, Weems K, Spyrou K, Pipiras V, Sapsis T (2023) Modeling broaching-to and capsizing with extreme value theory. In: Spyrou K, Belenky V, Katayama T, Bačkalov I, Francescutto A (eds) *Contemporary ideas on ship stability—from dynamics to criteria* Chapter 26. Springer, pp 435–457. ISBN 978-3-031-16328-9
10. Belenky V, Spyrou K, Weems KM (2019) Modeling of surf-riding in irregular waves. In: Belenky V, Spyrou K, van Walree F, Neves MAS, Umeda N (eds) *Contemporary ideas on ship stability. risk of capsizing*, Chapter 20. Springer, ISBN 978-3-030-00514-6, pp 347–358
11. Bishop RC, Belknap W, Turner C, Simon B, Kim JH (2005) *Parametric Investigation on the influence of GM, roll damping, and above-water form on the roll response of model 5613*. Hydromechanics Department Report, Naval Surface Warfare Center Carderock Division, West Bethesda, Maryland, USA, NSWCCD-50-TR-2005/027
12. de Kat JO, Brouwer R, McTaggart KA, Thomas WL (1994) Intact ship survivability in extreme waves: new criteria from a research and navy perspective. In: *Proceedings of 5th international conference on stability of ships and ocean vehicles (STAB '94)*, Melbourne, Florida, USA
13. de Kat JO, Thomas WL (1998) Extreme rolling, broaching, and capsizing-model tests and simulations of a steered ship in waves. In: *Proceedings of 22nd symposium Naval Hydrodynamics*, Washington, DC, USA
14. Grim O (1963) Surging motion and broaching tendencies in a severe irregular sea. *Ocean Dyn* 16(5):201–231
15. Holtrop J, Mennen GGJ (1982) An approximate power predication method. *Int Shipbuilding Progress* 29(334):166–170
16. Holtrop J (1994) A statistical re-analysis of resistance and propulsion data. *Int Shipbuilding Progress* 31(363):272–276

17. Kan M (1990) Surging of large amplitude and surf-riding of ships in following seas. *Naval Architecture Ocean Eng* 28:49–62
18. Kontolefas I, Spyrou KJ (2016) Coherent structures in phase space, governing the nonlinear surge motions of ships in steep waves. *Ocean Eng* 120:339–345
19. Kontolefas I, Spyrou KJ (2020) Probability of ship high-runs from phase space data. *J Ship Res* 64(1):81–97
20. Lewis EV (ed) (1989) Principles of naval architecture, vol 3: motions in waves and controllability. SNAME, Jersey City, p 429. ISBN 0-939773-02-3
21. Makov Y (1969) Some results of theoretical analysis of surf-riding in following seas. *Trans Krylov Society, "Maneuverability and Seakeeping of Ships. Sudostroenie, Leningrad*, 126:124–128 (in Russian; review in English is available in Belenky & Sevastianov (2007), Chapter 6.3.5)
22. Mohamad MA, Sapsis T (2018) Sequential sampling strategy for extreme event statistics in nonlinear dynamical systems. In: *Proceedings of the national academy of sciences of United States of America (PNAS)*, vol 115, pp 11138–11143
23. Oosterveld MWC, van Oossanen P (1975) Further computer-analyzed data of the Wageningen B-screw series. *Int Shipbuilding Progress* 22(251):251–262
24. Spyrou KJ (1996) Dynamic instability in quartering seas: the behavior of a ship during broaching. *J Ship Res* 40(1):46–59
25. Spyrou KJ (2017) Homoclinic phenomena in ship motions. *J Ship Res* 61(3):107–130
26. Spyrou KJ, Belenky V, Themelis N, Weems K (2014) Detection of surf-riding behavior of ships in irregular seas. *Nonlinear Dyn* 78(1):649–667
27. Spyrou KJ, Kontolefas I, Themelis N (2016) Dynamics of the surf-riding behavior of a ship in a multi-chromatic sea environment. In: *Proceedings of 31st symposium of naval hydrodynamics, Monterey, California, USA*
28. Spyrou K, Belenky V, Themelis N, Weems KM (2019) Definitions of celerity for investigating surf-riding in an irregular seaway. In: Belenky V, Spyrou K, van Walree F, Neves MAS, Umeda N (eds) *Contemporary ideas on ship stability. Risk of capsizing*, Chapter 21. Springer, ISBN 978-3-030-00514-6, pp 359–377
29. Spyrou KJ, Kontolefas I, Themelis N (2023) Abnormal high speed ship motions in two-frequency and multi-frequency following waves. In: Spyrou K, Belenky V, Katayama T, Bačkalov I, Francescutto A (eds), *Contemporary ideas on ship stability—from dynamics to criteria*, Chapter 24. Springer, pp 400–412. ISBN 978-3-031-16328-9
30. Spyrou KJ, Themelis N, Kontolefas I (2023) Estimates of the probability of surf-riding in irregular seas. In: Spyrou K, Belenky V, Katayama T, Bačkalov I, Francescutto A (eds) *Contemporary ideas on ship stability—from dynamics to criteria*, Chapter 23. Springer, pp 387–399. ISBN 978-3-031-16328-9
31. Themelis N, Spyrou KJ (2007) Probabilistic assessment of ship stability. *Tr SNAME* 115:181–206
32. Themelis N, Spyrou K, Belenky V (2016) High runs of a ship in multi-chromatic seas. *Ocean Eng* 120:216–230
33. Umeda N (1990) Probabilistic study on surf-riding of a ship in irregular following seas. In: *Proceedings of 4th international conference stability of ships and ocean vehicles (STAB 1990)*, vol 1, pp 336–343
34. Weems K, Belenky V, Campbell B, Pipiras V (2023) Statistical validation of the split-time method with volume-based numerical simulation. In: Spyrou K, Belenky V, Katayama T, Bačkalov I, Francescutto A (eds) *Contemporary ideas on ship stability—from dynamics to criteria*, Chapter 14 Springer, pp 225–243. ISBN 978-3-031-16328-9

# Modeling Broaching-to and Capsizing with Extreme Value Theory



Vadim Belenky, Kenneth Weems, Kostas Spyrou, Vladas Pipiras,  
and Themistocles Sapsis

**Abstract** Recent research on the application of extreme value theory is reviewed for stability failures associated with qualitative physical changes in the dynamic system: broaching-to and capsizing associated with the change of stability in large waves. As these events are very rare, evaluating their occurrence in ocean waves through direct numerical simulation is not practical with a code of reasonable fidelity. Probability must, therefore, be assessed without direct observation. This is done in the split-time framework, which introduces a metric of the likelihood of failure at selected times of an irregular wave response. The metric is computed by perturbing the dynamical system, in phase space, towards the failure state, and computing the perturbed response by numerical simulations that account for the changing physics of the extreme motions. Extreme value theory is applied to this metric in order to extrapolate a rate of failure.

**Keywords** Broaching-to · Capsizing in waves · Extreme values

---

V. Belenky (✉) · K. Weems  
David Taylor Model Basin (NSWCCD), West Bethesda, Maryland, USA  
e-mail: [vadim.belenky@navy.mil](mailto:vadim.belenky@navy.mil)

K. Weems  
e-mail: [kenneth.weems@navy.mil](mailto:kenneth.weems@navy.mil)

K. Spyrou  
School of Naval Architecture, National Technical University of Athens, Athens, Greece  
e-mail: [spyrou@deslab.ntua.gr](mailto:spyrou@deslab.ntua.gr)

V. Pipiras  
University of North Carolina, Chapel Hill, NC, USA  
e-mail: [pipiras@email.unc.edu](mailto:pipiras@email.unc.edu)

T. Sapsis  
Massachusetts Institute of Technology, Cambridge, MA, USA  
e-mail: [sapsis@mit.edu](mailto:sapsis@mit.edu)



# 1 Theory of Extreme Values

In recent times, any intact stability failure is an extreme event—in the sense that its probability is very small—so the value of the response associated with the failure, which might be a roll angle for capsizing or a yaw deviation for broaching-to, is quite far down the tail of its distribution. Extreme value theory is a part of mathematical statistics that studies such distribution tails.

The essence of extreme value theory is that the maxima of independent and identically distributed random variables have a limiting distribution, which is known as a Generalized Extreme Value (GEV) distribution. This is stated by the 1st extreme value or Fisher-Tippett-Gnedenko theorem. Figure 1 demonstrates the convergence of the largest values of a sample toward the GEV distribution for standard normal (Gaussian) and Rayleigh underlining distributions.

The probability density function (PDF) of GEV distribution is expressed as follows:

$$pdf_{GEV}(y) = \begin{cases} \exp\left(-\frac{y-\mu}{\sigma}\right) \cdot \exp\left(-\exp\left(-\frac{y-\mu}{\sigma}\right)\right) & \text{for } \xi = 0 \\ \left(1 + \xi \frac{y-\mu}{\sigma}\right)^{-(1+1/\xi)} \cdot \exp\left(-\left(1 + \xi \frac{y-\mu}{\sigma}\right)^{-1/\xi}\right) & \text{for } \xi \neq 0 \text{ and } \xi \frac{y-\mu}{\sigma} > -1 \\ 0 & \text{otherwise} \end{cases} \quad (1)$$

where  $\xi$  is shape parameter,  $\sigma$  is a scale parameter, and  $\mu$  is a location parameter.

The other important distribution is the Generalized Pareto Distribution (GPD), which is derived from GEV as a conditional distribution above a “large-enough” threshold. The ability of GPD to approximate any tail above a certain threshold is stated by the 2nd extreme value or Pickands-Balkema-de Haan theorem. The PDF of the GPD is expressed as:

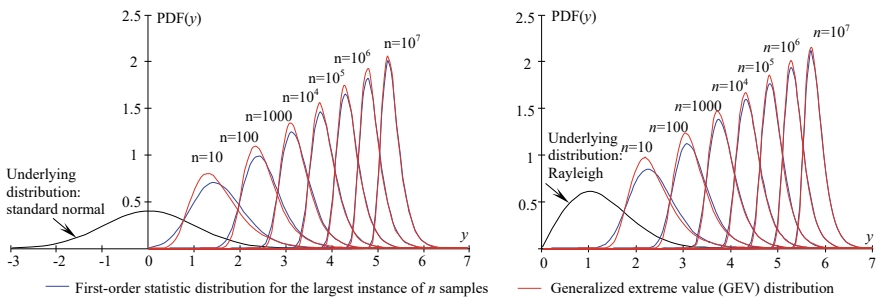


**Fig. 1** Convergence of the distribution of the largest values in a sample to the GEV distribution with an increasing number of samples  $n$  (Explanatory notes to the interim guidelines on the second generation intact stability criteria, MSC.1/Circ.1652 [14])

$$\text{pdf}_{GPD}(y) = \begin{cases} \frac{1}{\sigma} \exp\left(-\frac{y-u}{\sigma}\right) & \text{for } \xi = 0 \\ \frac{1}{\sigma} \left(1 + \xi \frac{y-u}{\sigma}\right)^{-(1+1/\xi)} & \text{for } \xi \neq 0 \text{ and } \xi \frac{y-u}{\sigma} > -1 \\ 0 & \text{otherwise} \end{cases} \quad (2)$$

A tail with a shape parameter of zero is defined as an “exponential” tail, positive shape parameters are associated with “heavy” tail, and negative shape parameters make the tail “light”. A negative shape parameter leads to the appearance of an upper bound, above which the PDF is zero. The different types of tails are depicted in Fig. 3 of Campbell et al. [9].

These theorems present a possibility of modeling the behavior of the tail without having to model the entire distribution. This is a very attractive way to address many safety-related engineering problems because the safety hazards are associated with large and rare excursions. The probabilistic assessment of ship stability would not then require the modeling of roll distribution over its full range—to model the tail would be enough. Both GEV and GPD have three parameters, counting location threshold. Therefore, to determine only those three parameters from simulated or measured data is necessary, and the entire problem of probabilistic stability assessment is solved.

Unfortunately, the simplicity of this approach is quite superficial. Available procedures for estimating those parameters merely find the values that best fit the data. However, a ship as a dynamical system is nonlinear, and the nature of those nonlinearities manifests itself at large roll angles. Both GEV and GPD are limit distributions so the applicability of extreme value theory is related to the context of the problem and the specific physical mechanisms of stability failure.

A review and principal derivation of both extreme value theorems is available from Coles [10]. Limiting extreme value distributions are also known for dependent data (e.g. [16]). However, practical application of these distributions may require more complex methods of confidence interval construction. The first application of extreme value theory to the problem of ship stability has been attributed to McTaggart [17] and McTaggart and de Kat [18].

## 2 Nonlinearity and Statistics

The nonlinearity of a dynamical system refers to its equations of motions and reflects the relationship of motions and velocities with forces and moments. The nonlinearity of ship dynamics manifests itself in the difference of the physics for small and large-amplitude motions. Whereas forces (and moments) can be considered linear for small-amplitude motions and velocities, they cannot for large-amplitude motions and velocities. The degree of nonlinearity, however, varies for forces associated with different physical phenomena, and the importance of different phenomena strongly depends on the type of motion or stability failure being examined.

The nonlinearity of hydrostatic moments is essential for ship stability and can be expressed in the form of the roll restoring arm ( $GZ$ ) curve. Strictly speaking, the concept of separate hydrostatic forces and moments for large-amplitude motions is only applicable to calm water. Once waves are introduced, the hydrostatic forces and moments can no longer be separated from Froude-Krylov forces and moments, unless small-amplitude motions are assumed. Including a nonlinear restoring term based on the calm-water  $GZ$  curve into roll equation may be reasonable for qualitative study, but this is questionable for practical application. The inseparability of hydrostatic and Froude-Krylov forces (and moments) leads to a simultaneous consideration of heave, roll, and pitch in order to avoid unphysical imbalance of forces and unrealistic attitude of a ship.

For hydrodynamic forces of a vortical nature, “maneuvering” forces associated with hull and appendage lift can be modeled as linear functions for small drift angles and rates (i.e. at the inception of turn). A nonlinear representation is needed for a developed turn or extended maneuver. Roll damping can also be assumed as linear for small roll rates, while “linear plus quadratic” models are common for large-amplitude roll motions.

The nonlinearity of ship motion data presents a challenge for the statistics of extremes because the small-amplitude motions dominate a sample. To address this challenge, the problem is separated into two parts: a “non-rare” problem and a “rare” problem, where the latter emphasizes large-amplitude motion data and accounts for nonlinearity. Using Poisson flow to relate stability failures (large roll angle or capsizing) with time, the probability of at least one failure during exposure time  $T$  is expressed as:

$$P(T) = 1 - \exp(-\hat{\lambda}_f T) \quad (3)$$

where  $\hat{\lambda}_f$  is an estimate of the rate of stability failures in a given environmental (sea state) and operational (commanded speed and heading) conditions. The separation between the non-rare and rare problems is associated with an up-crossing of an intermediate threshold. The value of the threshold depends on the method for the solution of rare problem:

$$\hat{\lambda}_f = \hat{\lambda}_U \hat{P}_r = \hat{\lambda}_U \hat{P}(f|U) \quad (4)$$

where  $\hat{\lambda}_U$  is an estimate of up-crossing rate of the intermediate threshold—a solution of the non-rare problem;  $\hat{P}_r = \hat{P}(f|U)$  is an estimate of conditional probability that stability failure will occur after an up-crossing of the intermediate threshold—a solution of the rare problem.

One way to apply this separation is a critical wave group approach, where the seaway is represented as a sequence of dangerous wave groups that can cause stability failure within otherwise benign waves that are considered safe [26]. The rare problem is the ship’s response to the dangerous wave groups, while the non-rare problem is an estimation of the rate at which such groups are encountered. The current state of the

art on such approaches is reflected in Anastopoulos and Spyrou [1–3], Mohammad and Sapsis [19], and others.

Peak-over-threshold (POT) is a relatively simple application of the extreme value theory to data exceeding a certain threshold, and fits well into the paradigm of separation into non-rare and rare problems. The threshold is set where extreme value properties can be applied to the available data. In other words, POT requires finding the beginning of the tail of distribution:

$$\hat{P}_r = \hat{P}(f|U) = \int_c^\infty \widehat{\text{pdf}}_{GPD}(y) dy \tag{5}$$

where  $c$  is the extrapolation target, which might be a roll angle associated with stability failure.

The method seems to work well even for a target angle beyond the maximum of the roll restoring ( $GZ$ ) curve (Fig. 8 of Campbell et al. [9]), however, the confidence interval becomes rather large (like in Fig. 6 of the cited reference). Other problems are associated with solely data-driven GPD application, such as light tail, leaving the target being beyond the right bound, described in Pipiras [21] or inability to handle escapes, Anastopoulos and Spyrou [4].

In principle, a reduction of the confidence interval may be achieved without increasing the sample size by introducing a deterministic relationship between the GPD parameters based on physical considerations. If the shape parameter of a GPD is negative, it has an upper limit beyond which the probability will be zero. Glotzer et al. [11] described how the uncertainty of the pitch extrapolation could be decreased by introducing a pitch angle limit of about 12 degrees. The longitudinal  $GZ$  becomes flat at that angle of 12 degrees, the ship can no longer receive significant energy from wave excitation.

The peaks of roll motions can have a complex structure of the distribution tail. The possibility of capsizing implies an upper limit to the roll peaks as a peak stipulates return. However, statistics of roll peaks typically show a positive shape parameter, suggesting that no limit exists. This problem was considered in Belenky et al. [6]. The softening nonlinearity of the  $GZ$  curve around its maximum value leads to a positive shape parameter through stretching in the phase plane (Fig. 2a). The peaks that are close to the unstable equilibrium are rare as their population drastically decreases due to capsizing. As a result, the tail of roll angle peaks has a complex structure including both heavy and light regions in Fig. 2b. A more detailed description of this tail structure is available from Campbell et al. [9].

Since the tail is expected to be heavy for the angles associated with stability failure, a Pareto distribution describes the tail. This results in a significant decrease in uncertainty, demonstrating a power of physics-informed statistical model (choice of heavy tail was made based on physical considerations). This is described in Campbell et al. [9], which also describes a validation of the POT method following the procedure of Smith [22].

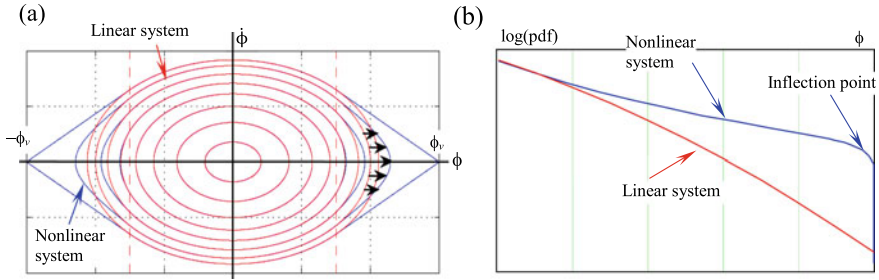
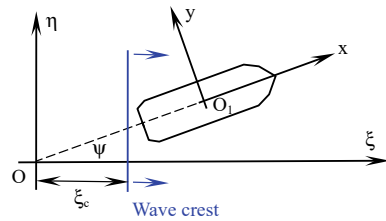


**Fig. 2** Stretching in the phase plane **a** due to softening nonlinearity leads to a distribution tail of roll angle peaks **b** that include a heavy tail before the inflection point and a light tail after the inflection point

**Fig. 3** Coordinate systems



### 3 Capsizing in Waves

Capsizing is a transition out of the safe domain to the motions around another stable equilibrium that is dangerous from a practical point of view, i.e. “mast down”. During this transition, the dynamical system passes the unstable equilibrium at the point of vanishing stability. The presence of the unstable equilibrium defines the topology of the phase plane in its vicinity and serves as a “separator” between the domains of attraction to the motion around the upright and capsized equilibria. This influence in a statistical sense can be detected when the system is passing relatively close to the unstable equilibria (“inflection point” in Fig. 2 above, and also in Fig. 4 of Campbell et al. [9]). However, this information is absent in a roll motion data set that does not contain a statistically significant number of capsizes or “near-misses”.

When the capsizing data are absent from the sample, to compute a value is still possible reflecting how likely the capsizing is at any given instant of time by the split-time/motion perturbation method (MPM). An intermediate motion threshold is considered, which is set low enough to observe a statistically significant number of crossings but high enough for these crossings to be independent. The rate of up-crossing through the intermediate threshold,  $\hat{\lambda}_U$ , is estimated from a series of random wave simulations that comprise the non-rare problem. At the instant of each crossing, the roll rate is perturbed until the capsizing is observed (Fig. 3 of Weems et al. [27]) and the minimum perturbed roll rate that leads to capsizing is recorded.

The difference between this critical roll rate and the observed roll rate provides a metric for the likelihood of capsizing at this instant of time.

This metric is a random variable, as it depends on the value of the roll rate at up-crossing. The metric values can be considered independent if they are computed at instances that are far enough from each other—such as beyond the de-correlation duration. The independence of the data points in the sample allows extreme value theory to be applied straightforwardly to the metric values. With the motion perturbation method, the metric sample set reflects the change of physics, as all of the effects of the transition are explicitly included in the metric’s calculation. Once a model is fitted to the metric data, the probability of capsizing can be found as the probability that the observed roll rate reaches the critical roll rate. This is the solution for the rare problem  $\hat{P}_r$ :

$$\hat{P}_r = \hat{P}(f|U) = \int_{c=1}^{\infty} \widehat{\text{pdf}}_{GPD}(y) dy. \quad (6)$$

The capsizing metric mostly depends on the roll rate at the instant of up-crossing. Roll damping is a function of roll rate, but it is not strongly nonlinear. In a linear case, roll rate at the instant of up-crossing follows Raleigh distribution and has the exponential tail. Thus, to use exponential distribution is appropriate to model extreme behavior of the metric of capsizing. Application of exponential tail rather than GPD is another example of physics-informed statistical modeling, demonstrating how physical consideration can reduce statistical uncertainty. Weems et al. [27] contains a brief description of the split-time/MPM method with a statistical validation for 14 combinations of sea state, heading, and speed.

## 4 Broaching-to in Irregular Waves

Broaching-to is a violent uncontrolled turn, occurring in following or stern-quartering waves despite full control effort applied on the opposite side. The most frequent mechanism of broaching-to begins with surf-riding, after which the ship becomes directionally unstable. This directional instability leads to repelling in the yaw direction. A sharp turn resulting from this repelling may cause a large roll angle or even capsize.

The probabilistic assessment of a stability failure caused by broaching-to in irregular waves presents an extreme challenge. Being rare in a moderate-to-high sea condition, estimating its probability may require a very expensive set of calculations. Capsizing is not the only risk. Even if the roll angle remains tolerable, the loss of control is a hazard by itself.

The complexity of the physics involved in surf-riding and broaching-to has motivated the development of split-time/MPM formulation for this type of stability failure. As the most common type of broaching-to is a direct consequence of surf-riding, the

non-rare problem is formulated as an up-crossing of an intermediate level of forward speed.

The rare problem, in particular, the formulation of the likelihood metric is the focus of the remainder of the chapter. The development of the broaching metric is based upon a very similar development of the likelihood metric for surf-riding in irregular waves in Belenky et al. [7].

Surf-riding in regular waves is driven by a dynamic equilibrium that appears when the surging component of the incident wave (Froude-Krylov) force compensates for the difference between the available thrust and the ship's resistance at a speed equal to wave celerity. A similar force balance can occur at instantaneous wave celerity in irregular waves, but such points are not strictly equilibria. The irregularity of the waves and wave forces make both celerity and force change with time so those balance points move unsteadily in the phase plane. The "acceleration" creates additional inertial forces that prevent the ship from staying at such balance points, so these points are not a solution of the equation of motion. To reflect this fact, those points are further referred to as "pseudo-equilibria."

These pseudo-equilibria define the topology of the phase space and create an attraction subset of initial conditions, known in literature as Lagrangian Coherent Structure (LCS), which is described in Kontolefas and Spyrou [15] as well as Spyrou et al. [24]. The appearance of the pseudo-equilibrium near the current position of a ship (within the coherent structure containing the ship position) will accelerate the ship toward the instantaneous wave celerity. If this specific coherent structure makes the ship directionally unstable and if this directional instability lasts long enough, broaching-to must follow.

A basic model of horizontal motion was developed as a "test bed" for a metric of the likelihood of broaching-to. This model extended a standard single degree-of-freedom (1-DOF) surf-riding model by adding sway and yaw equations. In an effort to keep the model basic, the maneuvering forces as well as the incident wave (Froude-Krylov) forces are assumed to be linear, which should be sufficient for the onset of broaching-to. Two coordinate systems are illustrated in Fig. 3. A global (Earth-fixed)  $\xi O\eta$  and a ship-fixed  $xO_1y$ . Direction of wave propagation coincides with the axis  $\xi$ . A detailed description of the model can be found in Belenky et al. [5].

## 5 Formulation of the Metric

The metric of the likelihood of broaching-to is a scalar value that indicates how close the ship is to broaching-to at any given time. To calculate this metric, function  $S$  is introduced that maps a vector of the state variables  $\vec{X}$ , at a given time  $t_0$ , to the maximum deviation from the commanded heading observed over a subsequent duration of time  $T_S$ :

$$\Delta\psi_{\max} = S(\vec{X}, t_0, T_S, Q) \tag{7}$$

where  $Q$  is an array of parameters that define the condition of interest, including the seaway, commanded heading, propeller rate, autopilot settings, and all other input data needed for the model [5]. This function is evaluated by simply running the model in the conditions defined by  $Q$  from time  $t_0$  for the duration  $T_S$  with initial conditions  $\vec{X}$ .

Consider two vectors of initial conditions,  $\vec{X}_0$  and  $\vec{X}_d$ , such that:

$$\begin{aligned} S(\vec{X}_0; t_0, T_S, Q) &< \Delta\psi_b \\ S(\vec{X}_d; t_0, T_S, Q) &> \Delta\psi_b \end{aligned} \tag{8}$$

where  $\Delta\psi_b$  is the deviation from the commanded heading that is qualified as broach. For this study, it is set equal to 10 degrees, to account for the fact that the linear maneuvering model cannot accurately model large yaw angles.

The vector of initial conditions  $\vec{X}_0$  is associated with the absence of broaching-to, while the vector  $\vec{X}_d$  leads to broaching-to. Introduce a vector-valued function:

$$\vec{X}_S(\varepsilon) = \vec{X}_0 - \varepsilon(\vec{X}_d - \vec{X}_0); \quad \varepsilon \in [0; 1] \tag{9}$$

where

$$\vec{X}_S(0) = \vec{X}_0; \quad \vec{X}_S(1) = \vec{X}_d \tag{10}$$

The critical value of the parameter  $\varepsilon$  is defined by the condition:

$$S(\vec{X}_S(\varepsilon_{cr}); t_0, T_S, Q) = \Delta\psi_b \tag{11}$$

This critical value, which defines the boundary of broaching-to between the two sets of conditions defined in (9), can be calculated with any method for a numerical solution of algebraic equations. The bisection iteration method was applied in the present work.

The critical value  $\varepsilon_{cr}$  therefore measures the distance of the non-broaching condition  $\vec{X}_0$  from the boundary of broaching. If the condition  $\vec{X}_0$  were the state variables at any time in a simulation of ship motions, then  $\varepsilon_{cr}$  is a measurement of how close the ship was to broaching-to at that time and can be employed for the metric.

The study of surf-riding in irregular waves and its metric of likelihood has demonstrated that stable surf-riding pseudo-equilibrium is not necessarily the most dangerous point [7]. As a result, additional steps may be needed for the metric calculation procedure, as the locations of such dangerous points must be found.



### 6 Numerical Examples: Regular Wave Case

The tumblehome configuration from the ONR topside series [8] was engaged for a set of numerical studies. The ship lines, principal dimensions, and flotation are in Fig. 3 of Belenky et al. [7]. Calm water resistance was estimated with regression formulae by Holtrop and Mennen [12] and Holtrop [13], while the propulsor was modeled with the Wageningen B-series data [20]. Polynomial coefficients  $r$  and  $\tau$ , fitted with the results of these calculations, can be found in a table in Fig. 3 of Belenky et al. [7].

Calculations were performed for regular waves (as a test case) and for bi-chromatic, tri-chromatic, full, and irregular waves. Details are in Figs. 3, 8, 14c of Belenky et al. [7]. The rudders have a total planform area of 25 m<sup>2</sup> and the PD autopilot is set up with a proportional gain of 0.002 and differential gain of 0.

The simplest test of the metric is a regular wave case in which modes coexist for stable surging and surf-riding, so whether a ship will be surging or surf-riding

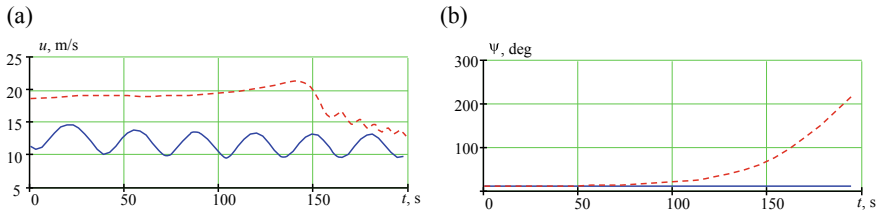


**Fig. 4** Time histories of **a** forward speed and **b** heading showing a situation of the coexistence of surf-riding leading to broaching-to (red) and unsteady surging that does not (blue)

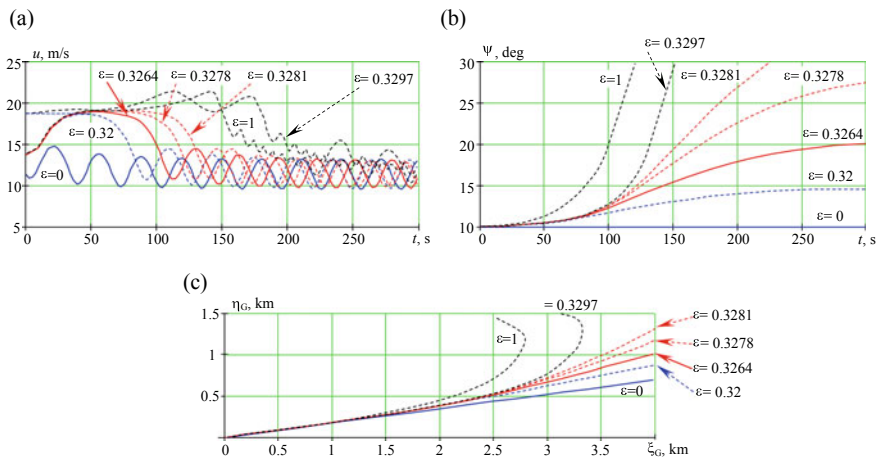


**Fig. 5** Elements of solution corresponding to boundary of broaching-to: **a** surging velocity, **b** heading angle, **c** trajectories in global coordinate system

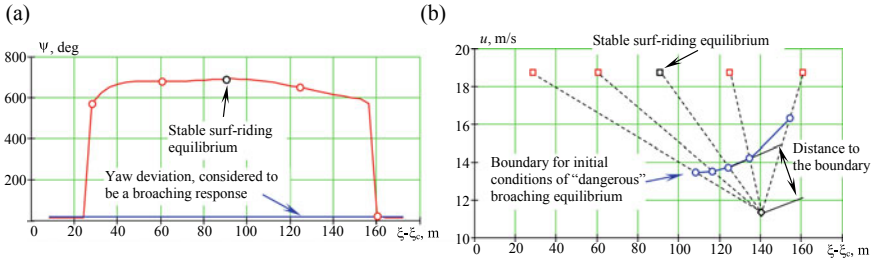


**Fig. 6** **a** Selection of “dangerous” points, with circles identifying locations toward which the metric of broaching likelihood was computed, **b** boundary for initial condition of “dangerous” broaching-to, computed for selected “dangerous” points

depends only on the initial conditions. The wave length was 225 m (frequency 0.52 1/s, period 12 s), which was chosen to be close to the modal period, but short enough to be sufficiently steep for surf-riding. Wave celerity was 18.73 m/s. Results of two simulations are in Fig. 4 that are free to surge, sway, and yaw with rudder control. The initial sway velocity, yaw rate, and rudder angle are set to zero for both simulations. The initial conditions for the first simulation have been chosen to be “safe”, with an initial longitudinal position 140 m ahead of the wave crest and an initial velocity of 11.32 m/s (22 knots). This “safe” simulation, which is plotted as blue curves in Fig. 4, indicates periodic surging and sailing with constant heading. The second simulation starts from the stable surf-riding equilibrium, which is 90 m ahead of the wave crest, and the initial velocity was set equal to wave celerity of 18.73 m/s. Time histories of this second simulation are the red curves in Fig. 4. A surf-riding response is observed for about 150 s, after which the speed drops dramatically. The yaw angle steadily increases after ~ 50 s, until the heading deviation exceeds 200 degrees and broaching-to is observed.

Figure 4 shows the existence of two vectors of initial conditions satisfying condition (8)—one of which leads to broaching-to while the other does not. An iterative numerical solution of Eq. (11) for the boundary of broaching required 14 iterations and yielded  $\epsilon_{cr} = 0.3264$ , corresponding to an initial position 123.8 m ahead of the wave crest and an initial surging velocity of  $u_0 = 13.74$  m/s.

The process of finding the broaching boundary is illustrated in Fig. 5, which identifies time histories and trajectories corresponding to different values of  $\epsilon$  from Eq. (9). The cases marked  $\epsilon = 0$  corresponds to selected initial condition and are blue curves. The cases  $\epsilon = 1$  are the dashed black curves. Four other cases show time histories and trajectories for  $\epsilon$ -values below the solution (dashed blue curves) and above the solution (dashed red or black curves). These intermediate curves were grouped around the solution, being 0.98, 1.004, 1.005 and 1.01 of  $\epsilon_{cr}$ . These numbers were chosen to achieve roughly equal spread of curves for yaw angles (Fig. 5b) and trajectories (Fig. 5c). The case with the critical  $\epsilon_{cr} = 0.3264$  is the solid red curve and, as expected, has deviated from the command heading of exactly 10 degrees.

A notable difference in the duration of surf-riding is apparent, compared to the 1-DOF surf-riding sample in Belenky et al. [7], Figs. 5 and 6 of the cited reference. In the 1-DOF regular wave case, the surf-riding continues indefinitely. With the addition of sway and yaw motions, the duration of surf-riding is finite, as the instability in yaw takes the system out of surf-riding conditions. If the yaw instability is very strong, as in the  $\varepsilon = 1$  case, broaching-to occurs faster and surf-riding terminates earlier, as compared to the case with  $\varepsilon = 0.3297$ .

Results from the iterative process are in Fig. 6 to find “dangerous” points, i.e. initial conditions other than the stable surf-riding equilibrium that can cause broaching-to. The initial search for “dangerous” points was done along the wave profile in front of and behind the stable surf-riding equilibrium, with the initial velocity equal to the wave celerity. The maximum yaw angle versus the distance from the wave crest is plotted in Fig. 6a. A broaching response (i.e. large deviation in yaw) was observed from 25 to 160 m ahead of the wave crest.

Four “dangerous” points were selected for the metric calculations. These points, with stable surf-riding equilibrium, are marked by circles in Fig. 6a. Two of these points were placed on the boundary of the broaching response interval, with the other two at intermediate locations. These four points in a surging phase plane with the stable surf-riding equilibrium are shown in Fig. 6b. The metric of broaching likelihood was computed for all five points, resulting in the boundary for initial condition leading to “dangerous” broaching-to (i.e. yaw deviation more than  $\Delta\psi_b = 10$  degrees). The shortest distance to the boundary was found to be the line, in phase space, connecting the initial point to the stable surf-riding equilibrium.

## 7 Bi-Chromatic Wave Case

The broaching metric was then calculated for the bi-chromatic wave case from the surf-riding study described in Belenky et al. [7]. The two wave components have wave lengths  $\lambda_1 = 269$  m and  $\lambda_2 = 225$  m. The amplitudes were 1.918 m and 1.716 m, respectively. As in the surf-riding study, the initial position was selected to be 123 m forward of the wave crest at the initial time. The stable surf-riding pseudo-equilibrium was located 73 m forward of the wave crest at the initial moment.

Figure 7 illustrates the process of finding the broaching boundary point on a line connecting the initial ship position with the stable surf-riding pseudo-equilibrium, showing time histories and trajectories corresponding to different values of  $\varepsilon$  from Eq. (9). The case  $\varepsilon = 0$  corresponds to the selected initial conditions (123 m forward of the crest and a speed of 11.32 m/s), and is plotted as solid blue curves. The solution for the boundary point was found to be  $\varepsilon_{cr} = 0.389$ , and is plotted as solid red curves. The time histories and trajectory starting from stable surf-riding pseudo-equilibrium and wave celerity (19.7 m/s) corresponds to  $\varepsilon = 1.0$  and is plotted with dashed black curves. Four other cases show time histories and trajectories for  $\varepsilon$ -values below (dashed blue curves) and above (dashed red or black curves) the critical value. As for the regular wave case, these intermediate curves were grouped around the solution,

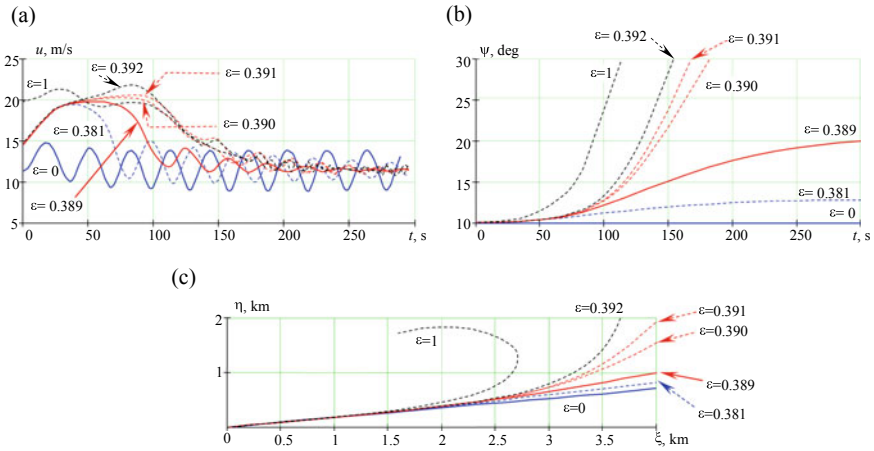


**Fig. 7** Elements of solution corresponding to boundary of broaching-to in bi-chromatic waves: **a** surging velocity, **b** heading angle, **c** trajectories in global coordinate system

being 0.98, 1.004, 1.005, and 1.01 of  $\epsilon_{cr}$ . A half a percent of  $\epsilon$  makes a difference to the yaw angle histories (Fig. 7b) and trajectories (Fig. 7c).

Figure 8 contains results from the iterative process to find “dangerous” points, i.e. initial conditions other than the stable surf-riding equilibrium that can cause broaching-to. The initial search for “dangerous” points was done along the wave profile in front of and behind the stable surf-riding pseudo-equilibrium, with the initial velocity equal to the instantaneous wave celerity. The maximum yaw angle versus the initial distance from the wave crest are plotted in Fig. 8a. A broaching response (i.e. large deviation in yaw) was observed from 25 to 180 m ahead of the wave crest. The range of initial conditions leading to broaching-to has slightly increased as compared to the regular wave case in Fig. 6a, while the maximum yaw values have decreased.

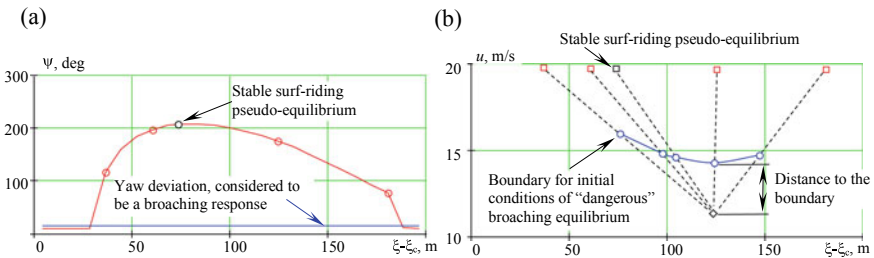


**Fig. 8** Bi-chromatic wave case: **a** selection of “dangerous” points, circles identify locations toward with the metric of broaching likelihood was computed, **b** boundary for initial condition of “dangerous” broaching-to, computed for selected “dangerous” points

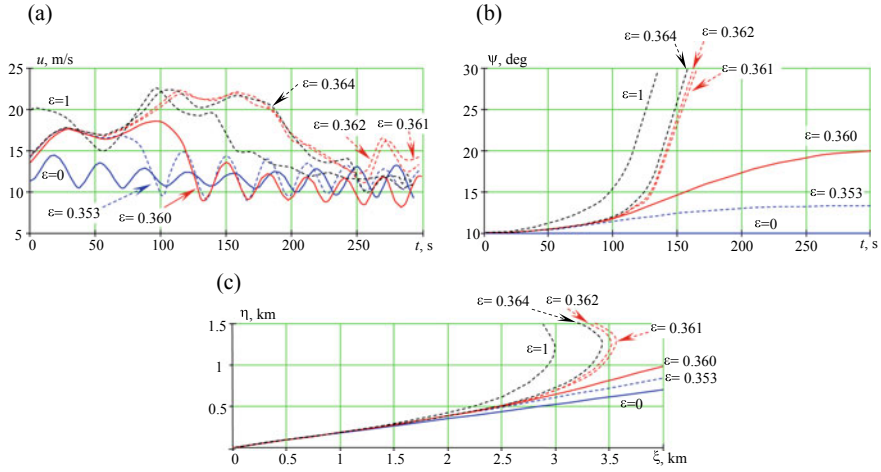
The most notable difference between the bi-chromatic and regular wave cases is the distance between the initial ship position and the boundary curve. In the regular wave case, the shortest distance was in the direction of stable surf-riding equilibrium (Fig. 6b). While in the case of the bi-chromatic wave, the shortest distance was measured toward a different “dangerous” point (Fig. 8b).

## 8 Tri-Chromatic Wave Case

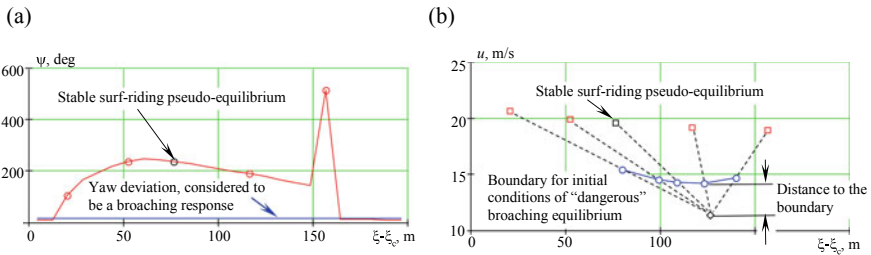
The broaching metric is applied for the tri-chromatic wave case from Belenky et al. [7]. The wave components have wave lengths of 191 m, 225 m, and 269 m and amplitudes of 1.66 m, 1.48 m, and 1.3 m. As in the surf-riding study, the initial position in global coordinates was selected to be at 870 m at the initial time, which is 126 m forward of a wave crest. The stable surf-riding pseudo-equilibrium was located at 820 m, which is 76 m ahead of the wave crest at the initial moment.

Figure 9 illustrates the process of finding the broaching boundary point on a line connecting the initial ship position with the stable surf-riding pseudo-equilibrium, showing time histories and trajectories corresponding to different values of  $\varepsilon$  from Eq. (9). The cases  $\varepsilon = 0$  correspond to the selected initial conditions ( $\xi_{G0} = 870$  m and  $u_0 = 11.32$  m/s) and are the solid blue curves. The solution for the boundary point was found with  $\varepsilon_{cr} = 0.360$  and is the solid red curves. The time histories and trajectory starting from the stable surf-riding pseudo-equilibrium ( $\xi_{G0} = 820$  m and  $u_0 = 19.6$  m/s) corresponds to  $\varepsilon = 1.0$  and are the dashed black curves. Dashed curves show four other cases for  $\varepsilon$ -values below (dashed blue curves) and above (dashed red or black curves) the critical value. These intermediate curves were grouped around the solution, being 0.98, 1.004, 1.005, and 1.01 of  $\varepsilon_{cr}$ . Half of a percent difference in  $\varepsilon$  makes an even larger difference to the histories of yaw angle and trajectories than for the bi-chromatic wave case plotted in Fig. 7.

As with the previous cases, the initial search for “dangerous” points was done along the wave profile in front of and behind the stable surf-riding pseudo-equilibrium, with the initial velocity equal to the instantaneous wave celerity. The maximum yaw angle versus the initial distance from the wave crest is plotted in Fig. 10a. A broaching response (i.e. large deviation in yaw) was observed from 10 to 160 m ahead of the wave crest. The interval of initial conditions leading to broaching-to has moved slightly forward compared to the regular wave case in Fig. 6a. The maximum yaw values are similar to the bi-chromatic case except for one point. The nearest boundary point was found for the dangerous point just forward of the pseudo-equilibrium.



**Fig. 9** Elements of solution corresponding to boundary of broaching in tri-chromatic waves: **a** surging velocity, **b** heading angle, **c** trajectories in global coordinate system



**Fig. 10** Tri-chromatic wave case: **a** selection of “dangerous” points, circles identify locations toward which the metric of broaching likelihood was computed, **b** boundary for initial condition of “dangerous” broaching-to, computed for selected “dangerous” points

### 9 Full-Band Irregular Wave Case

Finally, the broaching metric is tested on the full-band irregular wave case from Belenky et al. [7]. As in the surf-riding study, the initial position in global coordinates was selected to be at 4.315 m, which is 95 m in front of a wave crest at the initial time. The stable surf-riding pseudo-equilibrium was located at 4265 m, or 45 m ahead of the wave crest at the initial moment.

Figure 11 illustrates the process of finding the broaching boundary point on a line connecting the initial ship position to the stable surf-riding pseudo-equilibrium, showing time histories and trajectories corresponding to different values of  $\epsilon$  from Eq. (9). The case  $\epsilon = 0$  corresponds to selected initial conditions ( $\xi_{G0} = 4.315$  m and  $u_0 = 11.32$  m/s) and is plotted as solid blue curves. The solution for the boundary

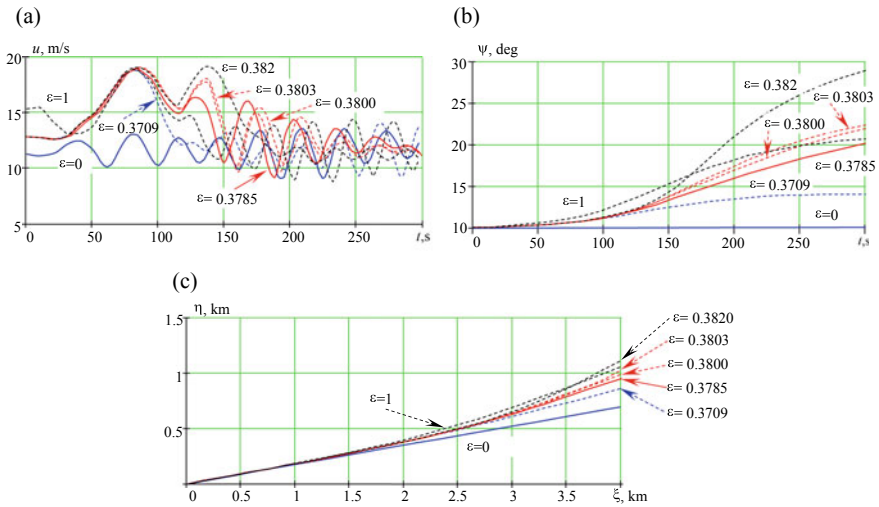


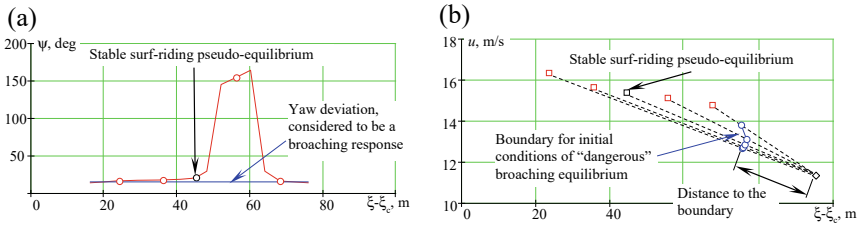
**Fig. 11** Elements of solution corresponding to boundary of broaching-to in full-band irregular waves: **a** surging velocity, **b** heading angle, **c** trajectories in global coordinate system

point was found with  $\varepsilon_{cr} = 0.3785$ , and is plotted as solid red curves. The time histories and trajectory starting from the stable surf-riding pseudo-equilibrium ( $\xi_{G0} = 4.265$  m and  $u_0 = 15.36$  m/s) is plotted as a dashed black curve marked as  $\varepsilon = 1$ .

The yaw response originating from the stable pseudo-equilibrium ( $\varepsilon = 1$  in Fig. 11b) appears to be weak, as the maximum deviation barely exceeded 10 degrees. Moreover, the intermediate yaw time histories, corresponding to  $\varepsilon$ -values of 0.38, 0.3803, and 0.382, yielded larger maximum yaw angle during the 300 s perturbation simulation time. The latter observation is consistent with the forward speed time history: the time history originating from the stable pseudo-equilibrium ( $\varepsilon = 1$  in Fig. 11a) shows an end to surf-riding after about 140 s, while the intermediate time histories with  $\varepsilon$ -values of 0.38, 0.3803, and 0.382 experienced slightly longer surf-riding of 150–160 s. As the surf-riding regime may be characterized by yaw instability (especially for the small autopilot gains chosen for this example), a larger maximum yaw would be expected for the longer period of surf-riding.

Belenky et al. [7] observed a longer duration of surf-riding—about 340 s—in the 1-DOF simulation with the same initial condition (Fig. 18 in that reference). The small increase of yaw angle and sway motion has terminated surf-riding in this case much earlier by taking the dynamical system outside of the attraction domain of the pseudo-equilibrium.

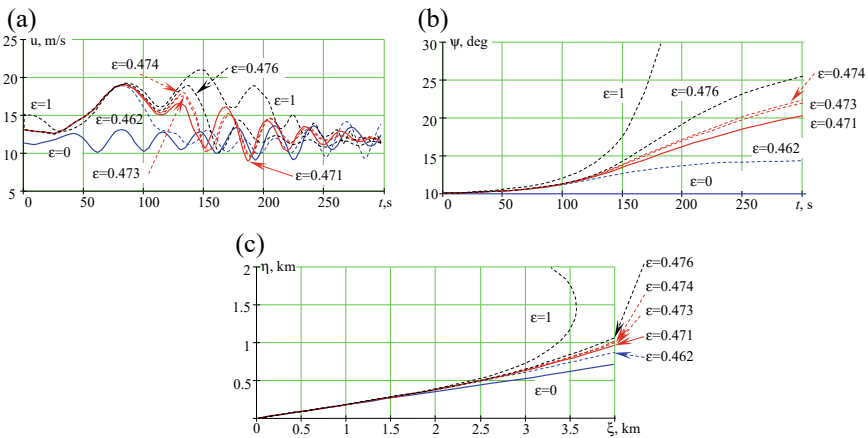
Figure 12 illustrates the search for “dangerous” points to see if a stronger broaching response may be encountered from alternate initial conditions. Figure 12a plots the maximum yaw response as a function of the initial position along the wave and shows an interval of larger broaching response from 50 to 65 m forward of the wave crest. As with the previous cases, five points—marked by circles in Fig. 12b—were selected for calculation of the boundary. As the yaw deviation indicating a



**Fig. 12** Full band irregular wave case: **a** selection of “dangerous” points, circles identify locations toward which the metric of broaching likelihood was computed, **b** boundary for initial condition of “dangerous” broaching-to, computed for selected “dangerous” points

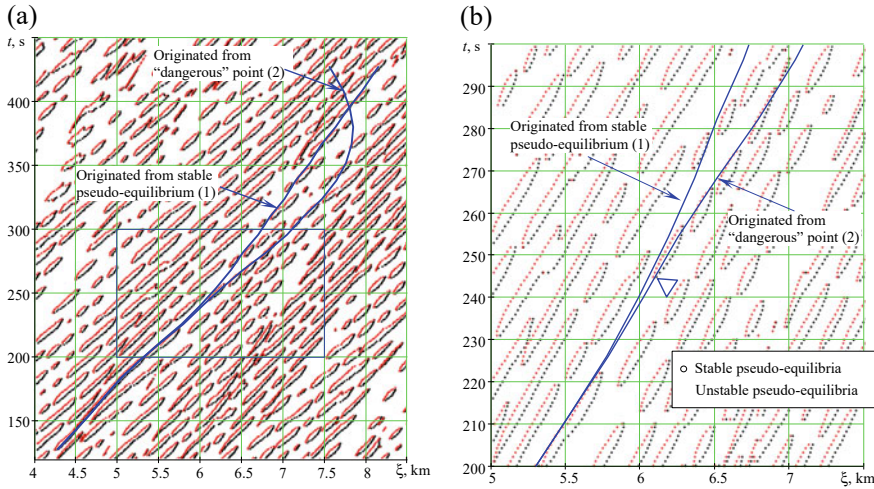
broaching response is set to 10 degrees, the boundary shown in Fig. 12b does not differentiate between a “weak” and “significant” broaching response. This “significant” broaching response needs to be considered rather as an indicator, as the model for maneuvering forces is linear and not expected to be accurate for a complete broach.

Figure 13 shows time histories computed for initial conditions between the initial and the “dangerous” points; the latter is located at  $\xi = 4276$  m (56 m ahead of the wave crest) with wave celerity equal to 15.09 m/s. The forward speed time history originated from this “dangerous” point ( $\epsilon = 1$  at Fig. 13a) has longer surf-riding for about 210 s. This duration was sufficient for a stronger broaching response, as shown in the yaw time history (Fig. 13b) and trajectory (Fig. 13c). As with the boundary value calculation toward the stable pseudo-equilibrium in Fig. 11, and in a contrast with the boundary calculations for the bi-chromatic and tri-chromatic waves in Figs. 7 and 9, the intermediate time histories are close to the boundary calculation at  $\epsilon_{cr}$ .



**Fig. 13** Elements of solution corresponding to boundary of broaching in full-band irregular waves, using a “dangerous point” at  $\xi = 4276$  m with wave celerity of 15.09 m/s: **a** surging velocity, **b** heading angle, **c** trajectories in global coordinate system





**Fig. 14** Pseudo-equilibria in “full-band” irregular waves: blue curves are ship response traces originating from the selected stable surf-riding pseudo-equilibrium and “dangerous” point; blue rectangle in (a) indicates enlarged area in (b)

The reason for the difference in response may be revealed by examining the pseudo-equilibrium loci in the temporal-spatial plot in Fig. 14. Two time histories are presented: one originated from the pseudo-equilibrium (identified as curve 1) and the other one originated at a “dangerous” point (identified as curve 2). The curves are almost identical until 230 s (the zoomed-in plot in Fig. 14b). While the difference in initial condition is not large (11 m in position and 0.27 m/s in velocity), that was apparently enough to place curve 2 close to the stable surf-riding pseudo-equilibrium at around 245 s (marked with a triangle in Fig. 14b). That stable pseudo-equilibrium, which existed for only about 12 s, was able to keep the speed high enough to “catch a ride” around 260 s with a series of four pseudo-equilibria. Curve 1 misses that “opportunity” and starts to lose speed, so when the next stable pseudo-equilibrium is encounter at 270 s, the forward speed is not sufficient to initiate surf-riding again.

## 10 Discussion

Broaching-to is a complex physical phenomenon. The most common type of broaching-to is preceded by surf-riding, creating a chain of events: encounter a stable surf-riding equilibrium, attraction to that equilibrium, actual surf-riding, development of yaw instability, and finally an uncontrollable turn that is the broaching-to. The introduction of irregular waves makes this problem even more complex. Surf-riding equilibria appears and disappears randomly, and as they move with acceleration they

are no longer a solution of the equations of motion. To emphasize that a dynamical system cannot stay in those points, they are referred to as “pseudo-equilibria”.

Appearing and disappearing equilibria make the duration of surf-riding finite and random. If the duration of surf-riding is too short, the deviation in heading may be not large or fast enough to qualify for broaching-to. Nevertheless, it is still a manifestation of directional instability of a ship that is directionally stable in calm water.

The split-time framework is well suited for the probabilistic characterization of broaching-to for moderate seas when those phenomena are too rare to be observed in a numerical simulation of reasonable length. Within this framework, two problems are considered: a non-rare problem that can be resolved by observing random wave simulations and a rare problem that requires additional perturbation simulations. As the broaching-to is preceded by surf-riding and surf-riding involves acceleration, the non-rare problem is formulated as an exceedance of an intermediate threshold of forward speed. The rare problem is focused on a metric of likelihood of broaching-to after the threshold was crossed. The metric is calculated with a series of perturbations of initial conditions until broaching-to is observed.

The broaching metric is an extension of a similar metric for surf-riding [7]. The calculation of the surf-riding metric requires the existence of a pseudo-equilibrium near the initial point, which is provided by the solution of the non-rare problem. Following the high-run approach of Spyrou et al. [23, 25], surf-riding in irregular waves is defined as an exceedance of the instantaneous wave celerity evaluated at the initial moment at the nearest stable surf-riding pseudo-equilibrium located behind the ship. The surf-riding metric is computed as the shortest distance to conditions that lead to the surf-riding response. The distance is measured along the line, in the surging phase plane, between the initial point and the stable surf-riding pseudo-equilibrium.

The most obvious difference between surf-riding and broaching-to is the dimensionality. Surf-riding can be considered as a single-degree-of-freedom problem. Its phase space is a plane. The consideration of broaching-to requires a minimum of three degrees of freedom, resulting in six-dimensional phase space. However, solving the high-dimensional problem can be avoided, as the type of broaching-to under consideration is preceded by surf-riding. The broaching metric can thus be formulated by conditioning the surf-riding metric by the yaw deviation instead of exceedance of the instantaneous wave celerity. As the current model applies a linear representation of maneuvering forces, the yaw deviation has been set equal to 10 degrees.

One of the main conclusions of the study described in Belenky et al. [7] was that surf-riding in irregular waves may go through several episodes involving the appearance and disappearance of the pseudo-equilibria, and the initial conditions leading to the longest surf-riding do not necessarily coincide with the stable pseudo-equilibrium.

The broaching metric has been computed for a series of test cases, including a regular wave, bi- and tri-chromatic waves, and full-band irregular waves. Besides the stable pseudo-equilibria, the metric was computed for several other “dangerous” points along the wave profile (Figs. 6a, 8a, 10a, and 12a). The instantaneous wave

celerities computed at these “dangerous” points are the initial velocities. The calculation of several points not only allows the worst one (leading to the largest yaw deviation) to be found, but also identifies an approximate boundary separating the broaching domain in surging phase plane (Figs. 6b, 8b, 10b, and 12b).

As could be expected, the stable surf-riding equilibrium is in the middle of the “broaching” domain for the regular wave case. However, as the number of components increases, the domain was observed to shift right, toward the initial point. The tri-chromatic wave case demonstrates that the pseudo-equilibrium is not the “worst” in term of yaw deviation (Fig. 10a). Finally, the pseudo-equilibrium in the full-band irregular wave case leads to a very modest yaw deviation, barely above 10 degrees (Fig. 12a). The actual broaching domain is still nearby, but the limitation of the linear maneuvering model does not allow its quantitative consideration in the present study.

As with surf-riding in irregular waves, the realization of broaching-to may involve the encounter of a series of episodes of pseudo-equilibria, during which the forward speed remains high enough to stay in the domain of attraction (i.e. inside the Lagrangian Coherent Structure). The initial conditions that lead to a dangerous response are expected to be located near the stable surf-riding pseudo-equilibrium, so to use it as an initial point for the search makes sense.

## 11 Summary and Conclusions

A general framework for the application of general extreme value theory is first described for the characterization of ship capsizing in irregular waves, and then broaching-to as one of the most physically complex scenarios of capsizing is discussed.

Extreme value theory is based on the observed motion response or other data. A capsize event is not observable under normal conditions, so a “proxy” to use the statistical apparatus is needed. An obvious way to create a “proxy” is to relate capsizing with exceedance of a large roll angle. A split-time framework provides an alternative, separating the task into non-rare (observable) and rare (non-observable) problems. The non-rare problem is associated with crossing an intermediate threshold, low enough for the crossing to be observed at a statistically significant rate. The non-rare problem is the computation of a metric of the likelihood of the random event under the condition that the intermediate threshold has been crossed.

The metric is computed by perturbing the initial conditions at the point of crossing until the event in question is observed. That value of the perturbation becomes a data point, and extreme value theory is then applied to a sample of these metric data points. As a mathematical model of the event is applied for the metric, physical information is present in the sample. An additional step can propagate this physical information to extreme statistics, typically in the form of a distribution tail type, e.g. application of a heavy tail for the extremes of roll peaks.

The metric of likelihood of broaching-to following surf-riding in irregular waves is discussed. In regular waves, this type of broaching-to is a result of yaw instability that

develops during surf-riding, when a ship has been “captured” by a wave and moves with wave celerity. The physical mechanism of broaching-to is significantly different in irregular waves, where wave celerity is a stochastic process and surf-riding is finite, random, and governed by pseudo-equilibria rather than equilibria.

A simple 3-DOF mathematical model of broaching-to (surge-sway-yaw) has been developed with body-linear Froude-Krylov forces and a linear formulation for maneuvering forces. The metric of broaching-to is formulated by conditioning the previously developed surf-riding metric with an unintended 10-degree deviation of yaw. The metric is a distance, in the surging phase plane, from an initial position (corresponding to a crossing in the non-rare problem) and a stable surf-riding pseudo-equilibrium at that time.

While testing this metric in regular waves, bi- and tri-chromatic waves, and full-band irregular waves, it was found that the stable surf-riding pseudo-equilibrium may not be the worst case scenario. Similar to surf-riding, broaching-to in irregular waves may depend on a series of episodes of appearance/disappearance of surf-riding pseudo-equilibria. So the worst case scenario positions the ship to surf-ride in a series of successive waves, providing time for yaw instability to build up.

The next steps in the study of broaching-to and capsizing caused by broaching-to in irregular waves are envisioned as follows. First, the broaching metric should be tested with a nonlinear model of the maneuvering forces. The nonlinear model will allow the simulation of the entire broaching-induced turn, rather than just its inception, to allow the characterization of how dangerous broaching-to may be in terms of loss of controllability. Second, the body-nonlinear formulation of the incident wave (Froude-Krylov) and hydrostatic forces need to be implemented for the metric to consider capsizing. The nonlinearity of Froude-Krylov and hydrostatic forces will require the consideration of all six degrees of freedom, as roll cannot be properly computed without heave and pitch within the body-nonlinear formulation.

**Acknowledgements** The work described in this chapter has been funded by the Office of Naval Research (ONR) and ONR Global under Dr. Thomas Fu, Dr. Woei-Min Lin, and Dr. Salahuddin Ahmed, and by a David Taylor Model Basin/NSWCCD Independent Applied Research (IAR) program under Dr. Jack Price.

The participation of Prof. Sapsis was facilitated by the NSWCCD Summer Faculty Program, while the participation of Prof. Pipiras was facilitated by NSWCCD Summer Faculty and Sabbatical Programs, both of which are also managed by Dr. Jack Price. The authors are very grateful for the support that made this work possible.

## References

1. Anastopoulos PA, Spyrou KJ (2016) Ship dynamic stability assessment based on realistic wave group excitations. *Ocean Eng* 120:256–263. <https://doi.org/10.1016/j.oceaneng.2016.04.018>
2. Anastopoulos PA, Spyrou KJ (2019) Evaluation of the critical wave groups method in calculating the probability of ship capsize in beam seas. *Ocean Eng* 187(1). <https://doi.org/10.1016/j.oceaneng.2019.106213>

3. Anastopoulos PA, Spyrou K (2023) An efficient formulation of the critical wave groups method for the assessment of ship stability in beam seas. In: Spyrou K, Belenky V, Katayama T, Bačkalov I, Francescutto A (eds), *Contemporary ideas on ship stability—from dynamics to criteria*, Chapter 10. Springer, ISBN 978-3-031-16328-9, pp 157–174
4. Anastopoulos PA, Spyrou K (2023) Effectiveness of the generalized pareto distribution for characterizing ship tendency for capsizes. In: Spyrou K, Belenky V, Katayama T, Bačkalov I, Francescutto A (eds), *Contemporary ideas on ship stability—from dynamics to criteria*, Chapter 15. Springer, ISBN 978-3-031-16328-9, pp 245–263
5. Belenky V, Spyrou KJ, Weems KM (2016) On probabilistic properties of surf-riding and broaching-to in irregular waves. In *Proceedings of 31st symposium naval hydrodynamics*, Monterey, California, USA
6. Belenky V, Glotzer D, Pipiras V, Sapsis T (2019) Distribution tail structure and extreme value analysis of constrained piecewise linear oscillators. *Probab Eng Mech* 57:1–13
7. Belenky V, Spyrou K, Weems KM (2023) Critical distance on a phase plane as a metric for the likelihood of surf-riding in irregular waves. In: Spyrou K, Belenky V, Katayama T, Bačkalov I, Francescutto A (eds), *Contemporary ideas on ship stability—from dynamics to criteria*, Chapter 25. Springer, ISBN 978-3-031-16328-9, pp 413–434
8. Bishop RC, Belknap W, Turner C, Simon B, Kim JH (2005) Parametric investigation on the influence of GM, roll damping, and above-water form on the roll response of model 5613. In: *Hydromechanics department report, naval surface warfare center carderock division*, West Bethesda, Maryland, USA, NSWCCD-50-TR-2005/027
9. Campbell B, Weems K, Belenky V, Pipiras V, Sapsis T (2023) Envelope peaks over threshold (EPOT) application and verification. In: Spyrou K, Belenky V, Katayama T, Bačkalov I, Francescutto A (eds), *Contemporary ideas on ship stability—from dynamics to criteria*, Chapter 16. Springer, ISBN 978-3-031-16328-9, pp 265–289
10. Coles S (2001) *An introduction to statistical modeling of extreme values*. Springer-Verlag, London. ISBN 978-1849968744
11. Glotzer D, Pipiras V, Belenky V, Campbell B, Smith T (2017) Confidence Interval for exceedance probabilities with application to extreme ship motions. *REVSTAT Statist J* 15(4):537–563
12. Holtrop J, Mennen GGJ (1982) An approximate power predication method. *Int Shipbuilding Progress* 29(334):166–170
13. Holtrop J (1994) A statistical re-analysis of resistance and propulsion data. *Int Shipbuilding Progress* 31(363):272–276
14. International Maritime Organization, MSC.1/Circ.1652 Explanatory notes to the Interim Guidelines on second generation intact stability criteria. London, 2022
15. Kontolefas I, Spyrou KJ (2016) Coherent structures in phase space, governing the nonlinear surge motions of ships in steep waves. *Ocean Eng* 120:339–345. <https://doi.org/10.1016/j.oceaneng.2016.02.013>
16. Leadbetter MR, Lindgren G, Rootzen H (1983) *Extremes and related properties of random sequences and processes*. Springer Series in Statistics, Springer-Verlag, New York–Berlin, ISBN 978-0-387-90731-4
17. McTaggart KA (2000) Ongoing work examining capsizes risk of intact frigates using time domain simulation. In: Vassalos D, Hamamoto M, Papanikolaou A, Molyneux D (eds), *Contemporary ideas of ship stability*, Elsevier, ISBN 978-0080436524, pp 587–595
18. McTaggart KA, de Kat JO (2000) Capsizes risk of intact frigates in irregular seas. *Trans SNAME* 108:147–177
19. Mohamad MA, Sapsis T (2018) Sequential sampling strategy for extreme event statistics in nonlinear dynamical systems. In: *Proceedings of the national academy of sciences of United States of America (PNAS)*, vol 115, Issue 44, pp 11138–11143
20. Oosterveld MWC, van Oossanen P (1975) Further computer-analyzed data of the wageningen B-screw series. *Int Shipbuilding Progress* 22(251):251–262
21. Pipiras V (2020) Pitfalls of data-driven peaks-over-threshold analysis: Perspectives from extreme ship motions. *Probabilistic Eng Mech* 60, 103053

22. Smith TC (2019) Validation approach for statistical extrapolation. In: Belenky V, Neves M, Spyrou K, Umeda N, van Walree F (eds), *Contemporary ideas on ship stability. Risk of capsizing*, Chapter 34. Springer, ISBN 978-3-030-00514-6, pp 573–589
23. Spyrou KJ, Themelis N, Kontolefas I (2016) Numerical statistical estimates of ship broaching-to. *J Ship Res* 60(4):219–238. <https://doi.org/10.5957/jsr.2016.60.4.219>
24. Spyrou KJ, Kontolefas I, Themelis N (2023) Abnormal high speed ship motions in two-frequency and multi-frequency following waves. In: Spyrou K, Belenky V, Katayama T, Bačkalov I, Francescutto A (eds), *Contemporary ideas on ship stability—from dynamics to criteria*, Chapter 24. Springer, ISBN 978-3-031-16328-9, pp. 400–412
25. Spyrou KJ, Themelis N, Kontolefas I (2023) Estimates of the probability of surf-riding in irregular seas. In: Spyrou K, Belenky V, Katayama T, Bačkalov I, Francescutto A (eds) *Contemporary ideas on ship stability—from dynamics to criteria*. Chapter 23. Springer, ISBN 978-3-031-16328-9, pp 387–399
26. Themelis N, Spyrou KJ (2007) Probabilistic assessment of ship stability. *Tr SNAME* 115:181–206
27. Weems K, Belenky V, Campbell B, Pipiras V (2023) Statistical validation of the split-time method with volume-based numerical simulation. In: Spyrou K, Belenky V, Katayama T, Bačkalov I, Francescutto A, eds, *Contemporary ideas on ship stability—from dynamics to criteria*, Chapter 14. Springer, ISBN 978-3-031-16328-9, pp 225–243

# Roll Damping

# Estimation of Force Coefficients for Bilge Keel and Skin Friction Roll Damping of Ships by CFD Simulations



Sven Wassermann and Moustafa Abdel-Maksoud

**Abstract** A finite-volume method (FVM) is used to simulate the roll motion of an ellipsoid equipped with wall-bounded flat plates with and without forward speed. Due to the circular form and a fixed roll axis of the simulated ellipsoid, only normal forces act on the plates. The normal force component in phase with the roll velocity over a harmonic roll period is estimated. The roll period, amplitude and the plate dimension are varied. The simulation results are compared with results of different model test techniques. The focus is set on modeling a simple definition for the normal force coefficient based on the Keulegan-Carpenter number ( $KC$ ). To transfer roll damping results from model scale into full scale, the frictional roll damping component of different ships is investigated. FVM simulations of the roll motion for full and model scale are carried out. A simple extrapolation procedure based on Kato's approach is developed.

**Keywords** Roll damping · Force coefficient method · Bilge keels · Skin friction roll damping · Scale effects

## 1 Introduction

### 1.1 Normal Forces on Bilge Keels

The roll motion of ships in waves is weakly damped by wave radiation. Simple roll damping devices such as bilge keels (BK) improve ship roll damping with and without forward speed in all weather conditions. Bilge keel constructions of a width up to 450 mm with shipbuilding profiles were the industry practice in the last decades. In the mean time, the ship breadth grew which led to large ratio of roll radius ( $r_{BK}$ ) to bilge keel width ( $b_{BK}$ ), see Table 1.

---

S. Wassermann (✉) · M. Abdel-Maksoud  
Hamburg University of Technology, Hamburg, Germany  
e-mail: [sven.wassermann@tuhh.de](mailto:sven.wassermann@tuhh.de)

M. Abdel-Maksoud  
e-mail: [m.abdel-maksoud@tuhh.de](mailto:m.abdel-maksoud@tuhh.de)



**Table 1** Examples of wall bounded flat plates, e.g. bilge keels, for low and high  $KC$ -numbers ( $r_{BK}$ -roll radius,  $b_{BK}$ -plate width,  $\varphi_a$ -roll amplitude)

$KC$	Examples	$r_{BK}/b_{BK}$	$\varphi_a$ [deg]
200	plate in a tank	121.5	30
100	BK on ULCC	72.75	25
25	BK on RoPax	45.5	10
2	keel on lifeboat	7.4	5
0.3	plate at a buoy	1.2	5

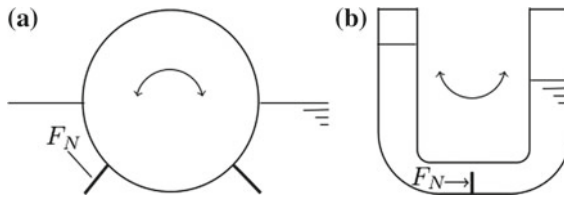


**Fig. 1** Techniques to measure the normal force on flat plates  $F_N$ : **a**—periodical rolling ellipsoid body in towing tank, **b** U-Tank with periodical flow

Two different common techniques can be found in the literature which are used to measure normal forces on wall bounded plates: (A) measurement of ellipsoid models in towing tanks and (B) force measurements in U-Tanks, see Fig. 1. Ikeda et al. [7] and Fujino et al. [3] used an ellipsoid, respectively a spindle-like body to determine the drag force coefficient  $c_E$ . Sarpkaya and O’Keefe [11] measured the force coefficient  $c_E$  for different plate dimensions in a U-Tank. The force coefficients for different  $KC$  numbers estimated by the mentioned experimental techniques are compared in Fig. 2. Additionally, the approximation function which is used in Ikeda’s method and Ikeda’s given range of validity,

$$c_{E,Ikeda} = \frac{22.5}{KC} + 2.4 \text{ for } 4 < KC < 20 \tag{1}$$

with

$$KC = \pi \frac{r_{BK} \varphi_a}{b_{BK}}, \tag{2}$$

is plotted in this Figure. It can be clearly seen that

1. no results exist for  $KC > 20$  and
2. Eq. (1) does not fit for  $KC < 3$ .

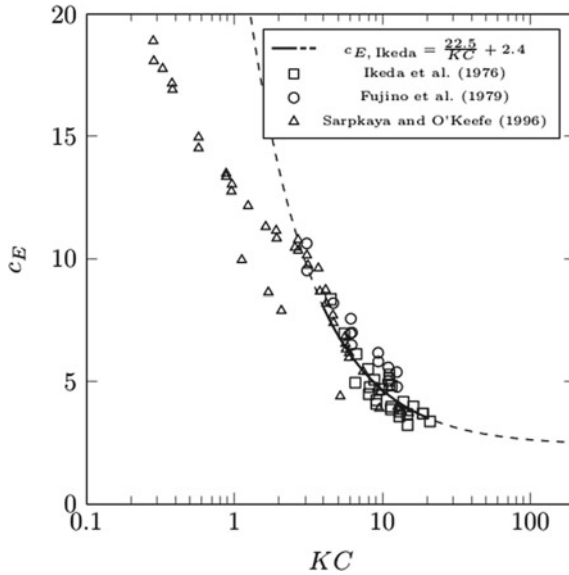


**Fig. 2** Force coefficients of normal forces on BK—comparison of experimental measurement values and Eq. 1 (Ikeda’s Method)

The paper presents a FVM simulation approach to estimate force coefficients  $c_E$  for  $KC$ -values between 0.5 and 100. Based on these simulation results, an equation for the force coefficient  $c_E$  is given.

### 1.2 Skin Friction Roll Damping

The skin friction roll damping is the smallest damping component and is mainly influenced by flow phenomena which depend on Reynolds number. Nevertheless, if Froude similarity is used to extrapolate the damping moment to full scale, a large scale factor can overestimate the total roll damping. An extrapolation error of around 5% can be typical for larger scale factors, see ITTC [1]. Figure 3 shows the influence of skin friction damping on total roll damping for the benchmarking Duisburg Test Case (DTC, [2]) container ship. The result given in Fig. 3 is based on the later presented extrapolation approach.

The skin friction roll damping moment  $M_F(\dot{\varphi})$  was focused on in previous studies. Especially the estimation approach of Ikeda [8], based on results of Kato [9] for  $M_{F0e}$ , Komura and Tamiya [10] for forward speed correction, became common practice and is recommended by the ITTC [1]. For a harmonic full roll cycle, it will be assumed that the roll damping moment can be approximated by a linear coefficient:  $M_F(\dot{\varphi}) = M_{Fe}\dot{\varphi}$ . The approach is based on the forward velocity  $U$  of the ship, the ship length  $L_{WL}$  at waterline, the roll frequency  $\omega$ , the kinematic viscosity  $\nu$  and the

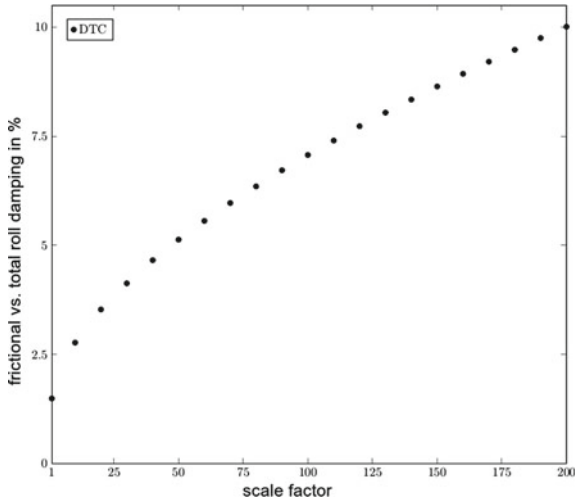


**Fig. 3** Influence of skin friction damping on total roll damping for Duisburg Test Case (DTC) based on the later presented extrapolation approach

wetted surface of the ship  $S$ :

$$\frac{M_{Fe,Ikeda}}{M_{F0e}} = 1 + 0.653 K C_L = 1 + 4.1 \frac{U}{\omega L_{WL}}, \tag{3}$$

$$M_{F0e} = 0.787 \rho S \bar{r}^2 \sqrt{\omega \nu} \left[ 1 + 0.00814 \left( \frac{\bar{r}^2 \varphi_a^2 \omega}{\nu} \right)^{0.386} \right]. \tag{4}$$

To estimate an equivalent roll radius  $\bar{r}$ , Kato [9] used the following empirical method ( $\overline{OG}$ -distance from origin at waterline to center of gravity, coordinate system positive downwards):

$$\bar{r} = \frac{1}{\pi} \left( [0.887 + 0.145 C_B] \frac{S}{L_{WL}} - 2 \overline{OG} \right). \tag{5}$$

Based on FVM simulations of several test cases for three modern monohull ship forms, a small database of skin friction coefficients was generated. Based on the analysis of these results, Ikeda’s approach was slightly modified. A comparison of the original and the modified approach was carried out for a container ship simulated in model scale.

## 2 FVM Simulations

The simulation procedure is described in detail in Handschel et al. [4, 6]. The solver STAR-CCM+ is used to simulate the incompressible flow around the rolling ship. The FVM solves the governing equations in integral form for mass and momentum, as well as for the volume fraction of water and air and equations for the turbulence modeling. The segregated iterative solution method is based on the SIMPLE-algorithm.

The computational domain is divided into two regions, see Fig. 4. An inner cylinder (rotor) is rolling around a fixed roll axis. A sliding interface boundary condition is applied between the stationary (stator) and the rotating part of the grid. The grid is unstructured and trimmed hexahedral. A prism layer on the wall region exists. Local refinements are applied near the hull, the appendages and the free water surface. A volume of fluid (VOF) method is used to calculate the free water surface flow. In all RANS computations, the turbulence model  $k - \omega - SST$  is used. The dimensionless wall distance  $y^+$  for the first layer reaches values between 30 and 90.

Simulation results were compared with experimental results of an ellipsoid body, see Fig. 4, measured by Ikeda [7] (Fig. 5) and with results of the container ship Duisburg Test Case (DTC), see Handschel et al. [6]. The CFD results seem to be in good agreement with the presented but limited number of available experiments.

To reduce simulation time, calculations with the ellipsoid body to estimate the normal forces on bilge keels were optimized. Instead of the previous described domain discretization, an ellipsoid with only one bilge keel is simulated. The rotor–stator motion model is replaced by general mesh motion model. The multi-phase flow is reduced to a single-flow simulation. For  $KC = 11.2$  a comparison was carried out. A deviation of 2% was observed. The simulation time was further reduced by a splitting of the ellipsoid. Only half of the ellipsoid with the bilge keel was discretized. Results of the optimized CFD discretization have a good comparability to experimental results, see Fig. 6.

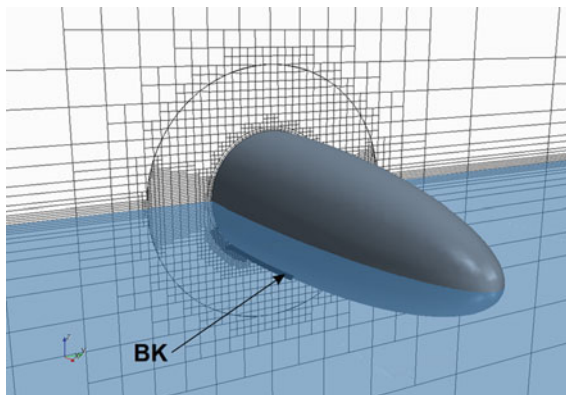


**Fig. 4** Non-optimized simulation domain discretization for an ellipsoid body with free surface

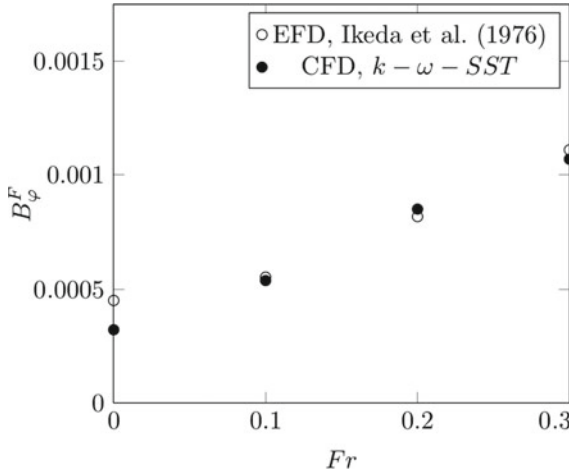


**Fig. 5** Frictional roll damping—comparison of experimental [7] and numerical results—rolling ellipsoid for various Froude numbers, grid resolution 1.3 Mio. cells, time step  $\Delta t = \pi/100\omega$

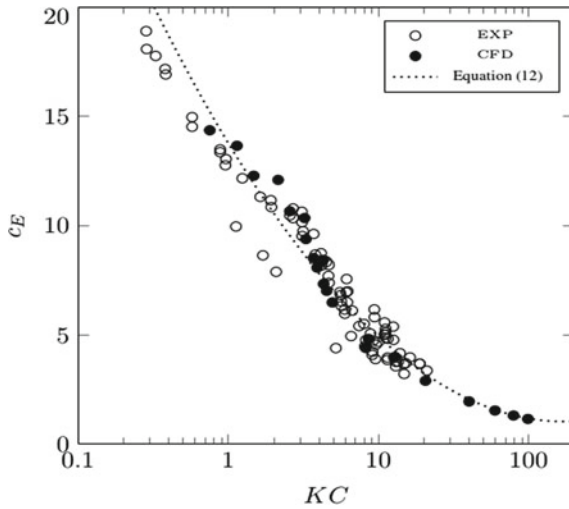


**Fig. 6** Force coefficients of normal forces on BK—comparison of experimental values and CFD

### 3 Normal Forces on Bilge Keels

To estimate normal forces on bilges keels, the moment  $M_{BK}$  around the longitudinal axis of the ellipsoid is determined by pressure integration. The moment can be formulated as Fourier polynomial:

$$M_{BK} = \sum_{j=1}^{\infty} [C_{A,j} \sin(j\omega t) + C_{B,j} \cos(j\omega t)], \tag{6}$$

$C_{A,j}$  are coefficients in phase with the roll angle,  $C_{B,j}$  coefficients in phase with the roll velocity. Assuming harmonic roll motion behavior,

$$\varphi = \varphi_a \cdot \sin(\omega t), \tag{7}$$

the equivalent damping energy  $E_{BK_e}$  can be expressed by the conservation of energy approach:

$$E_{BK_e} = \pi \varphi_a C_{B,1}. \tag{8}$$

Details of this approach can be found in Wassermann et al. [12]. The moment  $M_{BK}$  can also be approximated by a force coefficient  $c_E$  approach with

$$M_{BK} = \frac{\rho}{2} c_E \omega^2 \varphi_a^2 \cos^2(\omega t) \int b_{BK} r_{BK}^3 dl \tag{9}$$

which leads to the energy over a roll cycle of

$$E_{BK} = \frac{4}{3} \rho c_E \omega^2 \varphi_a^3 \int b_{BK} r_{BK}^3 dl. \tag{10}$$

The relation  $E_{BK_e} = E_{BK}$  results into an estimation approach for the force coefficient  $c_E$  of one bilge keel:

$$c_E = \frac{3\pi C_{B,1}}{4\rho\omega^2\varphi_a^2 \int b_{BK} r_{BK}^3 dl}. \tag{11}$$

The Fourier coefficient  $C_{B,1}$  is determined with a Fast Fourier Transformation (FFT) algorithm.

In Fig. 6, results of CFD simulations and the presented experiments of Fig. 2 are compared. Simulation and experimental results are in good agreement. The experimental and the simulation results can be approximated by:

$$c_E = 0.47 \cdot \ln(KC)^2 - 4.94 \cdot \ln(KC) + 13.75$$

for  $0.3 < KC < 100$ . (12)

Compared to Eq. (1), the range of validity is extended by Eq. (12). Nevertheless, Eq. (12) should be applied with care because a detailed validation study for the range of  $KC$ -numbers larger 20 is still missing. Simulations to estimate results for large  $KC$ -numbers are very sensitive to small changes in simulation setups. As a precaution, it was decided to choose simulation setups for the approximation which

achieve the smallest force coefficients. A recent study, Wassermann et al. [13], seems to show that the presented results in the range  $KC > 20$  should be further investigated. In the referenced paper, a slightly modified approach is compared with model tests of a container ship equipped with different bilge keel sizes.

### 4 Skin Friction Roll Damping

Roll simulations with different roll setups for two ships in full scale, a RoPax (*m1413z006*, [5]) and a Pax (*m1399z001*) vessel, and simulations in model scale for the containership DTC (*m1398s001*, [6]) were carried out to study total ship roll damping. Furthermore, the skin friction roll damping was determined. The main dimensions of the ship are listed in Table 2. The results were compared to those of Ikeda’s method. Based on the analysis of the simulations, the following could be observed:

1. The skin friction roll moment based on the analysis of the calculated shear stress is not completely in phase with roll velocity. Based on measured phase angles  $\varepsilon_F$ , an averaged phase shift was approximated:

$$\varepsilon_F = (-0.206 - \varepsilon_{F,BK}) \exp\left(\frac{U}{\sqrt{gL_{WL}}}\right) [\text{rad}]. \tag{13}$$

$\varepsilon_{F,BK} = 0$  for ships without,  $\varepsilon_{F,BK} = 0.18$  for ships with bilge keels.

2. The influence of forward speed on the skin friction roll moment is modeled by the ratio of the moment at forward speed to this at zero speed, see Eq. (3). A comparison of this approach relative to simulation results is presented in Fig. 7 (upper Figure). In the lower Figure, it can be clearly seen that the forward speed effect can be described more exactly for the simulation results by a formulation based on the ratio  $KC_L/\varphi_a$ . A correction of Tamiya’s Eq. (3) to

$$\frac{M_{Fe}}{M_{F0e}} = 1 + 0.79 \frac{KC_L}{\varphi_a} - 0.022 \left(\frac{KC_L}{\varphi_a}\right)^2 \tag{14}$$

is done.

**Table 2** Main dimensions of the ships,  $L$ -ship length,  $B$ -ship breadth,  $D$ -ship draft,  $C_B$ -block coefficient

Dim	m1398s001	m1399z001	m1413z006
$L/B$	6.979	8.176	6.525
$B/D$	4.246	4.456	4.304
$L/D$	29.631	36.433	28.087
$C_B$	0.632	0.647	0.542

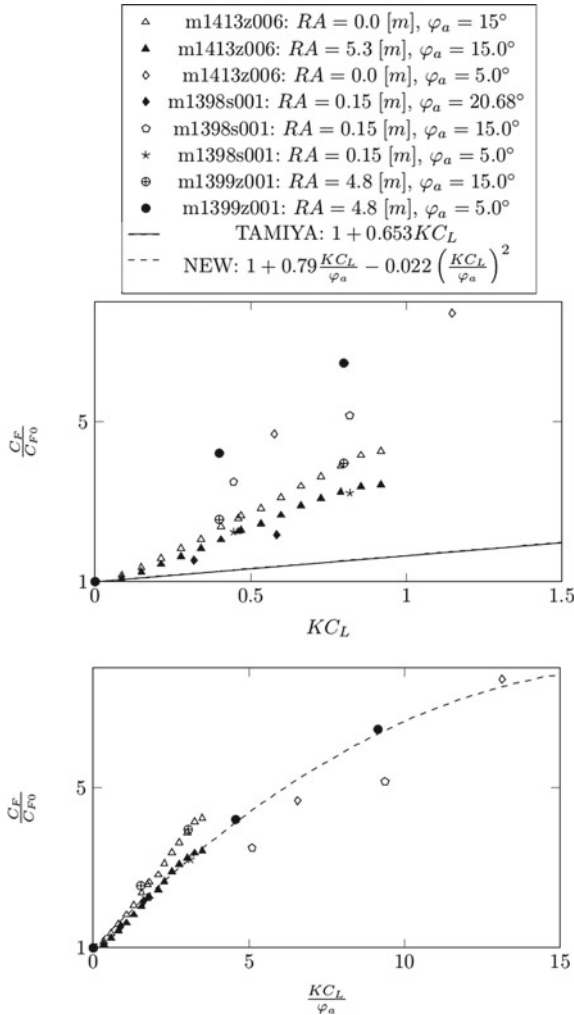


**Fig. 7** Skin friction forward speed correction—comparison Tamiya’s Eq. (3) and new Eq. (14)—RA—different roll axis heights

- Kato used Hughes skin friction line as formulation for the skin friction force coefficient. To consider the oscillating roll motion, the Reynolds number definition is modified. Based on experiments with small rolling cylinders, Kato estimated a correction factor  $k = 0.51$ . Here, factor  $k$  was calibrated on 31 simulations of the container ship DTC with a scale factor of 1:59.467. After several iterations, a factor of  $k = \frac{1}{\varphi_a}$  was determined which seems to be a good compromise between exactness and ease of use. Table 3 given in the Appendix presents the results for the test cases. Besides the roll setups, the ratio of frictional damping and total damping estimated with CFD, the difference between CFD and the extrapolation



method (EM) presented in Eqs. (16)–(20) and the difference between CFD and Ikeda (IK) are listed.

The focus of carrying out the simulations was set on the estimation of total ship roll damping. The frictional roll damping component is small compared to the other components. Verifying that the frictional moment is approximately correctly is difficult without the availability of suitable EFD data. Only a comparison between Ikeda's experiments and CFD could be carried out. Compared to CFD, Ikeda's method gives larger damping values for  $Fr = 0.0$  and smaller values for higher Froude numbers. This explains the necessity of using the new forward speed correction. The reason for these differences has to be investigated further. In particular, the influence of different turbulence models should be deeply investigated.

For a conversion approach of total roll damping (based on the simulations results),  $M(\dot{\varphi}) = M_e \dot{\varphi}$ , from model ( $m$ ) to full scale ( $FS$ ) with scale factor  $\lambda$ , the method could be applied as follows:

$$M_{e,FS} = \frac{\rho_{FS}}{\rho_m} M_{e,m} \lambda^{\frac{9}{2}} - \left[ \frac{1}{3\pi} \bar{r}_m^3 \varphi_a \omega_m S_m \lambda^{\frac{9}{2}} (\rho_m C_{F,m} - \rho_{FS} C_{F,FS}) \cdot (-2 \sin(2\varepsilon_F) + \cos(2\varepsilon_F) + 3) \right] \quad (16)$$

$$C_F = C_{F0} \left[ 1 + 0.79 \frac{KC_L}{\varphi_a} - 0.022 \left( \frac{KC_L}{\varphi_a} \right)^2 \right] \quad (17)$$

$$KC_L = 2\pi \frac{U}{\omega L_{WL}} \text{ for } 0 < \frac{KC_L}{\varphi_a} < 20 \quad (18)$$

$$C_{F0} = 1.328 Re_{F,x}^{-0.5} + 0.016 Re_{F,x}^{-0.114} \quad (19)$$

$$Re_{F,m} = k \frac{\bar{r}_m^2 \varphi_a^2 \omega_m}{v_m} \text{ or } Re_{F,FS} = k \frac{\bar{r}_{FS}^2 \varphi_a^2 \omega_{FS}}{v_{FS}} \cdot \lambda^{\frac{3}{2}} \quad (20)$$

with  $k = \frac{1}{\varphi_a}$ .

## 5 Conclusion

The investigation shows that the calculation of force coefficients based on Ikeda's method for normal forces on bilge keels and skin friction damping can be slightly improved for today's application. Based on finite-volume method simulation results, a new formulation for the force coefficient of normal forces on bilge keels over a wider range of  $KC$  numbers could be determined, see Eq. (12). To transfer the skin friction roll damping depending on the Reynolds number from model scale into full scale, an extrapolation method based on Kato's approach was formulated. Especially for model tests with large scale factors, a best-practice conversion approach has advantages. However, further investigations should be performed to verify the presented results.

The discussed method, Eqs. (16–20), was calibrated on only 31 simulations with one scale factor. For the development of the forward speed correction additional simulations in full scale were used.

Before the presented approaches can be applied for industrial applications, further test cases need to be analyzed to have a reliable adjustment of the used parameters. It should be also noted that the presented simple parameter methods do not replace experiments or more exact simulation methods which should be preferred if possible. The authors' opinion is that appropriate experiments and high-quality numerical CFD simulations should be applied in particular for decisions related to ship safety.

**Acknowledgements** The presented approximation methods were developed based on simulations which were carried out as part of a project which was funded by the German Federal Ministry of Economics and Technology under the aegis of the BMWi-project "Best-Rolldämpfung" within the framework program "Schifffahrt und Meerestechnik für das 21. Jahrhundert". The authors would like to thank Mr. Krambs for carrying out some of the CFD simulations and the cooperation partners in the project: University Duisburg-Essen, SVA Potsdam and the DNV-GL.

## Appendix

See the Table 3.

**Table 3** Results for coefficient  $k = \frac{1}{\varphi}$ , container ship DTC with bilge keels, model scale 1:59.467

Case	1	2	3	4	5	6	7	8	9	10	11
$U$ [m/s]	1.47	1.47	1.47	1.47	0.80	0.80	0.80	0.00	0.00	0.00	1.47
$\varphi_a$ [deg]	4.90	8.80	12.80	20.40	5.00	9.00	20.68	5.00	13.00	20.68	5.00
$T$ (s)	2.49	2.49	2.49	2.49	2.49	2.49	2.49	2.49	2.49	2.49	2.22
$\frac{N^F_{\varphi,a,stim}}{N_{\varphi,a,stim}}$ [%]	11.31	9.47	7.88	5.80	17.43	10.83	4.81	13.07	5.31	3.45	10.28
Diff. $\frac{N^F_{EM}}{EM}$ [%]	1.12	-1.31	-4.05	-11.68	-5.25	-8.63	-16.93	32.96	0.76	-6.80	1.92
Diff. $\frac{N^F_{IK}}{IK}$ [%]	55.19	41.44	30.74	14.18	12.03	2.49	-8.02	-48.79	-36.70	-27.41	51.59
Case	12	13	14	15	16	17	18	19	20	21	22
$U$ [m/s]	1.47	1.47	0.80	0.80	0.80	0.80	0.80	0.00	0.00	0.00	1.47
$\varphi_a$ [deg]	15.00	20.00	5.00	10.00	15.00	17.50	20.00	4.90	14.80	19.80	4.90
$T$ (s)	2.22	2.22	2.22	2.22	2.22	2.22	2.22	2.22	2.22	2.22	3.49
$\frac{N^F_{\varphi,a,stim}}{N_{\varphi,a,stim}}$ [%]	7.11	5.94	16.17	9.08	6.45	5.57	4.96	10.51	4.06	3.36	12.06
Diff. $\frac{N^F_{EM}}{EM}$ [%]	-5.14	-9.03	-3.21	-7.16	-11.01	-12.54	-14.51	40.71	2.44	0.09	1.16
Diff. $\frac{N^F_{IK}}{IK}$ [%]	23.43	15.34	9.66	0.12	-4.38	-5.63	-7.18	-45.81	-30.92	-22.93	64.09

(continued)

**Table 3** (continued)

Case	23	24	25	26	27	28	29	30	31
$U$ [m/s]	1.47	1.47	0.80	0.80	0.80	0.80	0.00	0.00	0.00
$\varphi_a$ [deg]	14.70	19.60	5.00	10.00	15.00	20.00	4.90	14.70	19.60
$T$ (s)	3.49	3.49	3.49	3.49	3.49	3.49	3.49	3.49	3.49
$\frac{N_{\varphi,a,stim}^F}{N_{\varphi,a,stim}}$ [%]	7.95	6.59	23.97	13.39	8.34	6.14	16.71	6.40	4.15
Diff. $\frac{N_{EM}^F}{N_{EM}^F}$ [%]	-9.66	-12.24	-2.41	-6.14	-10.94	-13.77	34.48	12.07	-7.03
Diff. $\frac{N_{IK}^F}{N_{IK}^F}$ [%]	30.18	21.12	29.84	15.55	5.96	1.19	-50.25	-27.21	-30.90

## References

1. 26th ITTC, Specialist Committee on Stability in Waves (2011) Recommended procedures—numerical estimation of roll damping. In: International towing tank conference, URL April 2016: <http://ittc.info>
2. El Moctar B, Shigunov V, Zorn T (2012) Duisburg test case: post-panamax containership for benchmarking. *Ship Technol Res Schiffstechnik* 59(3)
3. Fujino M, Ida T, Maeto T, Numata T (1979) A consideration on the hydrodynamic normal forces acting on bilge keel. *J Kansai SNA* 144 (in Japanese)
4. Handschel S, Köllisch N, Soproni JP, Abdel-Maksoud M (2012a) A numerical method for estimation of ship roll damping for large amplitudes. In: 29th Symposium on naval hydrodynamics. Gothenburg, Sweden
5. Handschel S, Köllisch N, Abdel-Maksoud M (2012b) Roll damping of twin-screw vessels: comparison of RANSE with established methods. In: Proceedings of the 11th international conference on the stability of ships and ocean vehicles, Athens, Greece
6. Handschel S, Fröhlich M, Abdel-Maksoud M (2014) Experimental and numerical investigation of ship roll damping by applying the harmonic forced roll motion technique. In: 30th Symposium on naval hydrodynamics, Hobart, Tasmania, Australia
7. Ikeda Y, Himeno Y, Tanaka N (1976) Ship roll damping—frictional component and normal pressure on bilge keel. *J Kansai SNA* 161(in Japanese)
8. Ikeda Y, Himeno Y, Tanaka N (1978) A prediction method for ship roll damping. Report of the Department of Naval Architecture, University of Osaka Prefecture, No. 00405
9. Kato H (1958) On the frictional resistance to the rolling ships. *J Kansai SNA* 102 (in Japanese)
10. Komura T, Tamiya S (1972) Topics on ship rolling characteristics with advance speed. *J Kansai SNA* 132 (in Japanese)
11. Sarpkaya T, O'Keefe JL (1996) Oscillating flow about two and three-dimensional bilge keels. *J Offshore Mech Artic* 1
12. Wassermann S, Feder D-F, Abdel-Maksoud M (2016) Estimation of ship roll damping—a comparison of the decay and the harmonic excited roll motion technique. *Ocean Eng J Special Issues Dedicated Stability Saf Ships Ocean Vehicles*
13. Wassermann S, Schumacher A, Langer G, Sumislawski P, Valanto P, Abdel-Maksoud M (2018) Effective Improvements in ship roll damping estimation. In: 32th Symposium on naval hydrodynamics. Hamburg, Germany

# Study on Bilge Keel Component of Roll Damping for Non-periodic Motion



Jun Umeda, Toru Katayama, Hirotada Hashimoto, and Burak Yıldız

**Abstract** Accurate prediction of roll damping moments of ships is important to predict roll responses accurately. A method for estimating the roll damping moment in the time domain is necessary for estimating parametric rolling and other phenomena in irregular waves. In this paper, we investigate the characteristics of the roll damping moments acting on bilge-keels by utilizing CFD computation to propose a time-domain prediction method for the bilge-keel component. The roll damping moment acting on the bilge keel depends on the current and previous rolling of the hull. The reason for this is that the vortices generated at the bilge keel are rapidly strengthened by the vortices generated by the previous rolling. A method for predicting the roll damping moment of the bilge keel is proposed considering this effect.

**Keywords** Roll damping · Bilge keel · Keulegan-Carpenter number · Transitional and non-periodic motion

## 1 Introduction

Predicting roll responses of ships is essential for ship stability. Accurate prediction of roll moments of ships is required to predict roll responses accurately. It is not easy to predict the roll moments theoretically because roll damping moments strongly depend on viscous effects.

---

J. Umeda (✉)

National Maritime Research Institute, Tokyo, Japan

e-mail: [umeda@m.mpat.go.jp](mailto:umeda@m.mpat.go.jp)

T. Katayama · H. Hashimoto

Graduate School of Engineering, Osaka Metropolitan University, Sakai, Japan

e-mail: [katayama@marine.osakafu-u.ac.jp](mailto:katayama@marine.osakafu-u.ac.jp)

H. Hashimoto

e-mail: [hashimoto@marine.osakafu-u.ac.jp](mailto:hashimoto@marine.osakafu-u.ac.jp)

B. Yıldız

Faculty of Naval Architecture and Maritime, Yıldız Technical University, İstanbul, Turkey

e-mail: [buraky@yildiz.edu.tr](mailto:buraky@yildiz.edu.tr)

There are several methods for predicting the roll moments such as experiments in model basins and computational fluid dynamics (CFD). In addition to these methods, the prediction method proposed by Ikeda et al. has been widely used from a practical perspective [3]. Ikeda's prediction method is based on theoretical and experimental backgrounds. In Ikeda's method, a linear roll damping coefficient for periodic rolling can be obtained in the frequency domain.

When time-domain simulations predicting non-periodic and transient rolling such as parametric rolling in irregular waves are carried out, applying Ikeda's method to the numerical simulations requires modifying Ikeda's method on basis of some assumptions. In previous research, the linear roll damping coefficients were calculated for various rolling amplitudes using Ikeda's method to create the database of the roll damping coefficients, and the roll damping coefficients in the simulations were calculated by interpolating the values in the database [1].

Rolling amplitudes in irregular motions are required to interpolate roll damping coefficients corresponding to roll amplitudes. In the parametric rolling in irregular waves, the roll amplitudes were determined by Eq. (1) with the rolling angle and the rolling angular velocity.

$$\phi_a = \sqrt{\phi^2 + \left(\frac{2\dot{\phi}}{\omega_e}\right)^2} \quad (1)$$

where,  $\phi$  is the rolling angle,  $\omega_e$  is the angular frequency at the natural roll period.

Regarding roll damping moments due to bilge-keels, which are dominant damping moments in the total roll damping, previous research implied that there was a problem in the modification. Previous research showed the drag coefficients of a flat plate under transition motions and irregular oscillating motions to investigate the drag coefficient of the bilge-keel [4, 6]. Previous research reported the drag coefficient of the flat plate under the transient motion varied continuously [6]. In addition, the drag coefficients of the flat plate under the irregular oscillation varied corresponding to the amplitude of the previous motion [4]. These effects were named the flow memory effect in this study.

Roll damping moments due to the normal force of bilge-keels may be affected on the flow memory-effect as well as flat plates. Predicting roll damping moments acting on bilge-keels requires considering the flow memory effect [6, 8]. The flow memory effect on roll damping moments acting on bilge-keels, however, has not been discussed significantly at present.

In this paper, we investigate the flow memory effect on roll damping moments acting on bilge-keels by utilizing CFD computation. Furthermore, we propose a prediction method considering the flow memory effect for the bilge-keel component.

First, roll damping moment coefficients were in the sinusoidal roll motion to validate the CFD computation.

Second, roll moments in irregular rolling were computed by CFD computation to obtain damping coefficients in irregular rolling. Moreover, the computed flow fields were visualized to reveal flow physics around bilge-keels in detail. Based

**Table 1** Principal particulars of two-dimensional model

Hull		Bilge-keel	
Breadth: $B$ , Draft: $d$ , Depth: $D$	0.237 m, 0.096 m, 0.145 m	Breadth	0.01 m
Section coefficient	0.966	Thickness	0.001 m
Height of roll axis	0.096 m	Lever from the rotation center	0.138 m

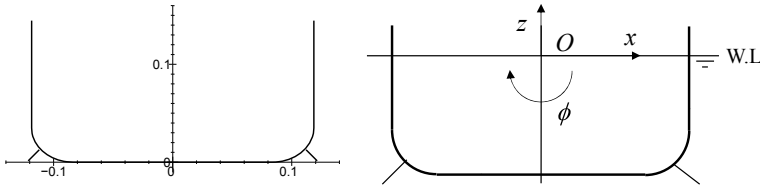


**Fig. 1** Hull section of the two-dimensional model and coordinate system

on the obtained damping coefficients and the visualization of the flow, the method considering the flow memory effect for the bilge-keel component is proposed. Finally, numerical simulations for parametric rolling in irregular head waves were carried out by using the proposed method as an application example.

## 2 Methodology

### 2.1 Geometry of Hull Section with Bilge-Keels

Since Ikeda’s prediction method dealt with the two-dimensional flow as well as the strip method, roll damping moment acting on the two-dimensional hull section similarly was discussed in this study. Table 1 shows the principal particulars, and Fig. 1 shows the hull section and coordinate system. The hull section has two bilge-keels at starboard and port sides. Positive  $x$ -direction and positive  $z$ -direction in the coordinate system correspond to the starboard side and upward, respectively.  $\phi$  describes the roll angle.

### 2.2 Experimental Method

Roll moments acting on a two-dimensional tank model were measured to validate the CFD results and Ikeda’s method. The length of the tank model is 0.8 m. Endplates were mounted on the tank model to remove three-dimensional effects. Figure 2 shows



the schematic view of the experimental setting. The forced motion device gave the tank model the sinusoidal rolling. The rolling angles and the roll moments of the hull were measured by a potentiometer and strain gages. In the experiments, the rolling moments with sinusoidal rolling were measured because the forced motion device can generate only mechanical periodical sinusoidal rolling.

Table 2 shows the experimental conditions. The previous research showed that the linearized roll damping coefficient of the bilge-keel component significantly depends on the following parameter [3].

$$KC_a = \frac{\pi r \phi_a}{b_{bk}} \tag{2}$$

where  $\phi_a$  is the rolling amplitude,  $r$  is the distance from the roll axis to the tip of the bilge-keel, and  $b_{bk}$  is the breadth of the bilge-keel. The parameter is equivalent to the Keulegan-Carpenter number. The Reynolds number ( $R_n$ ) in Table 2 is based on the following definition:

$$R_n = \frac{3.22r^2 \phi_a}{T \nu} \tag{3}$$

where,  $T$  is the rolling period, and  $\nu$  is the kinematic viscous of the water [9].

**Fig. 2** Schematic view of the experimental settings

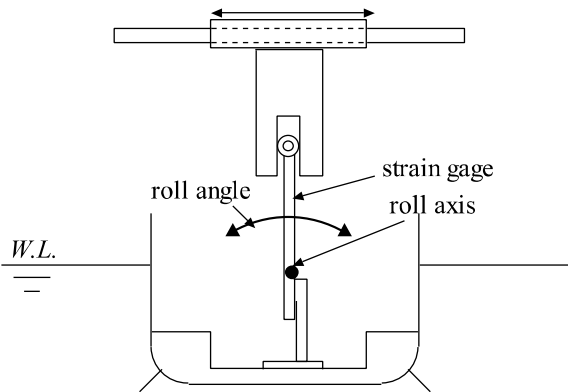


**Table 2** Experimental conditions for sinusoidal rolling

Rolling period	1.0 s
Rolling amplitude	5.0–15 deg
Reynolds number	458–3800
KC number	3.78–11

### 2.3 Computational Method

The viscous CFD code, ‘NAGISA’, was used. The NAGISA is the in-house code developed at the National Maritime Research Institute (NMRI) in Japan [11]. The code can solve the mass-conservation equation and the Reynolds-averaged Navier–Stokes equation by structured overset grids based on the finite-volume method. The computational grids for the CFD computation were generated by the ‘Point-wise’, commercial software. Domain connectivity information for the overset grids was computed by the in-house overset grid-assembler developed at the NMRI, ‘UP\_GRID’ [10].

Figure 3 shows the computational grids and boundary conditions. The computational grids are composed of the block around the hull with two bilge-keels and the block of the external zone. The shape of the bilge keel was modified from a rectangular to a triangular shape to improve the mesh quality. Minimum spacing next to the body surface was set to the non-dimensional wall distance,  $y^+$ , was smaller than 1.0 according to the criteria suggested by the ITTC [5].

The Share Stress Transport (SST)  $k$ – $\omega$  model was selected in this study. The single-phase localized level-set method was applied to capture the free surface around the hull. The NAGISA can handle the moving and deforming grid approach and dynamic overset-grid approach to deal with the calculation around moving bodies. The moving and deforming grid approach was selected because the dynamic overset-grid approach requires a high computational cost.

The  $x$ -axis is positive from the port side to the starboard side with  $z$  pointing upward. The  $y$ -axis is positive from the stern to the bow. The free surface at rest was set to  $z = 0$ . The size of the external zone in  $x$ ,  $y$ , and  $z$  directions are  $-50.0 \leq x/(0.5B) \leq 50.0$ ,  $-0.05 \leq y/(0.5B) \leq 0.05$ , and  $-7.5 \leq z/(0.5B) \leq 7.5$ ,

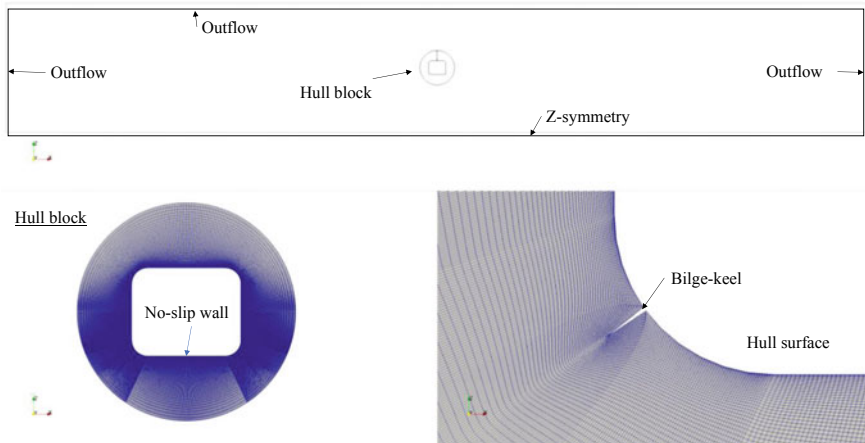


Fig. 3 Computational grids

respectively. The hull was located in the center of the computational zone when the hull was at initial rest.

For the boundary conditions of the CFD, the no-slip condition was applied on the surface of the hull and the bilge-keels. The y-symmetry condition was imposed on the forward and afterward surface of the external zone. Although the vessel's longitudinal direction was very short, the velocity of the y-direction can be suppressed due to the y-symmetry condition. The outflow was imposed on the starboard, port, and top surfaces of the external zone. The z-symmetry condition was applied on the bottom surface. The total number of the computational grids was approximately 0.6 million.

In the CFD computation, the roll moments were divided into roll moments acting on the hull and roll moments acting on the two bilge-keels in the sinusoidal and irregular rolling to focus on the damping moment acting on the two bilge-keel.

The sinusoidal rolling angle slowly increased from zero to the target rolling amplitude to improve convergence at the earlier time-steps of the CFD computation. Figure 4 and Table 3 show the generated sinusoidal rolling and some parameters for explaining conditions of the CFD computation.

Irregular rolling was generated by summing a couple of sinusoidal rolling because simple rolling is convenient for clarifying the flow physics of the vortex flow around the bilge-keel. Figure 5 shows the generated irregular rolling angle of the hull. In the CFD computation, the rolling moments were acquired when the hull rotated according to these irregular rolling.

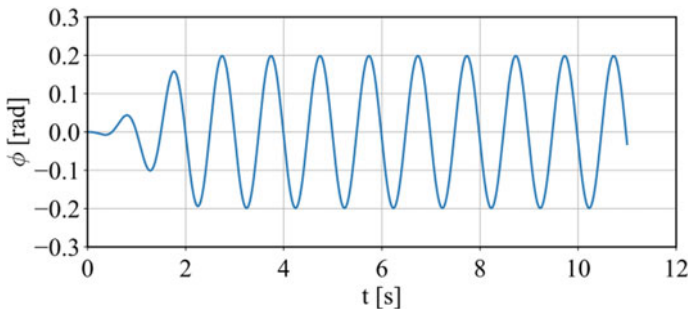


**Fig. 4** Generated sinusoidal rolling angle (Period: 1.0 s, Amplitude: 11.39 deg)

**Table 3** Conditions of the CFD computation in sinusoidal rolling

Rolling period	1.0 s
Rolling amplitudes	5.0–15 deg
Reynolds numbers	458–3800
KC numbers	3.78–11

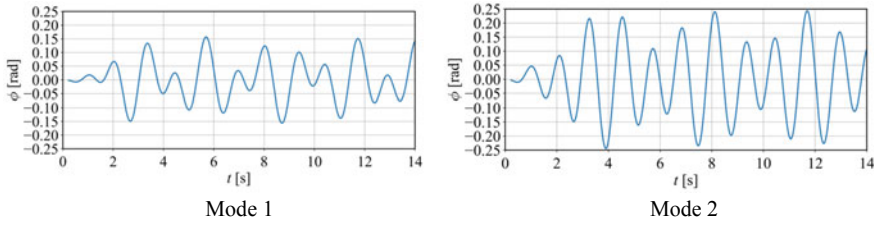


Fig. 5 Irregular rolling generated in the CFD computations

### 2.4 Rolling Damping Analysis for Sinusoidal and Irregular Rolling

In the sinusoidal rolling, the linear roll damping coefficients derived from the CFD computation were compared to the linear damping coefficients obtained via the experiments to validate the CFD computation.

First, time-series data of the rolling and the roll moment acting on the hull with the bilge-keels were acquired via the experiments and the CFD computation. The amplitudes of the roll moment and phase shifts between the rolling angle and the roll moment were calculated by applying time-series data to the Fourier series analysis. Finally, the roll damping coefficient can be expressed as follows:

$$B_{44} = \frac{M_a \sin \varepsilon}{\omega \phi_a} \tag{4}$$

where,  $M_a$  is the amplitude of the roll moment,  $\varepsilon$  is the phase shift between the rolling angle and the roll moment,  $\omega$  is the circular frequency of the rolling.

The non-dimensional form of the linearized roll damping coefficient was transformed to compare with results in other studies. The non-dimensional linearized roll damping coefficient,  $\hat{B}_{44}$ , are defined by

$$\hat{B}_{44} = \frac{B_{44}}{\rho \nabla B^2} \sqrt{\frac{B}{2g}} \tag{5}$$

where,  $\rho$  is the water density,  $\nabla$  is the displacement volume of the hull,  $g$  is the gravitational acceleration, and  $B$  is the breadth of the hull.

In the CFD computation, since the roll moment acting on the bilge-keels can be acquired, the damping coefficient of the normal force component of the bilge-keel was obtained by applying the roll moment acting on the bilge-keels to the analysis method.

The analysis method for the sinusoidal rolling cannot be applied to the analysis for irregular motions because the damping coefficient in the irregular rolling varies continuously. Therefore, we applied the roll moment for irregular rolling to the method based on previous research [4].

Assuming that the force on the bilge-keel is equivalent to the force on the flat plate, the normal force component of the bilge-keel expressed by Morison's equation as the sum of the quadratic damping and the added moment of inertia as follows:

$$M_{BKN} = A_N \ddot{\phi} + B_{N2} \dot{\phi} |\dot{\phi}| \quad (6)$$

where,  $M_{BKN}$ ,  $A_N$ , and  $B_{N2}$  are the roll moment acting on the bilge-keel, the added inertial moment, and the quadratic damping coefficient.  $A_N$ , and  $B_{N2}$  can be obtained by fitting Eq. (6) to time-series data between the peaks and valleys of the rolling by the least-squares method (LSM). However, the added inertial moment and the quadratic damping coefficient obtained by this method are constant between the peaks and the valleys of the rolling. Therefore, the coefficients varying continuously were obtained by fitting Eq. (6) to the data while increasing the number of the data used for fitting Eq. (6) one by one.

## 2.5 Prediction Method for Normal Force Component of the Bilge-Keel

In Ikeda's method, the linearized damping coefficient of the normal force component ( $B_N$ ) is calculated by Eqs. (7)–(9). Ikeda's method applies to motions in the frequency domain [3].

$$B_N = \frac{8}{3\pi} \rho r l_{bk} b_{bk} \phi_a \omega C_{Dperiod} \quad (7)$$

$$C_{Dperiod} = \frac{22.5}{f K C_a} + 2.40 \quad (8)$$

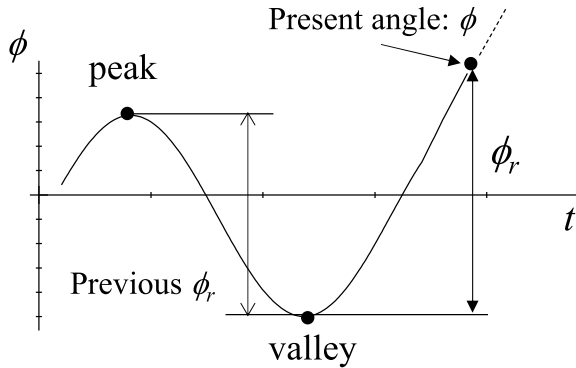
$$f = 1 + 0.3 \exp(-160[1 - \sigma]) \quad (9)$$

where,  $l_{bk}$  is the length of the bilge-keels,  $f$  is the correction factor considering the increment of the flow velocity at the bilge of the hull,  $\sigma$  is the section coefficient of the hull, and  $\omega$  is the circler frequency of the rolling.

Katayama's method is extended to time-domain prediction based on Ikeda's method by using the drag force of a flat plate under the transient motion to calculate the rolling damping moment during irregular motion [6, 8]. The roll damping moment for the normal force component of the bilge-keel is predicted in the time domain as follows:

$$B_{N2} \dot{\phi} |\dot{\phi}| = \rho l_{bk} b_{bk} C_{Dacc} r^3 f^2 \dot{\phi} |\dot{\phi}| \quad (10)$$

**Fig. 6** Illustration of relative rolling angle



The instantaneous drag coefficient ( $C_{Dacc}$ ) is calculated by the empirical formula (Eq. (12)) based on the drag coefficient of the flat plate under one direction accelerating [6, 8]. The equivalent KC number in the irregular rolling is defined by a parameter involved in the relative rolling angle.

$$KC_d = \frac{\pi r \phi_r}{b_{BK}} \tag{11}$$

$$C_{Dacc} = (14.3e^{-1.80KC_d} + 4.41e^{-0.37KC_d} - 10.4e^{-1.03KC_d} - 0.30e^{-0.17KC_d} + 1) \left( 0.908 + \frac{1.2}{1 + 1.01KC_d} \right) C_{D0} \tag{12}$$

where,  $\phi_r$  is the relative rolling angle starting from the previous peaks or valleys of the rolling as shown in Fig. 6.  $C_{D0}$  is the drag coefficients of the flat plate in the uniform flow, and was set to 2.0 in this study.

### 3 Results

#### 3.1 Roll Damping Moment in Sinusoidal Roll Motions

Figure 7 summarizes the total linearized damping coefficients and the normal component in the experiments, CFD computation, and Ikeda’s method. The 95% confidence intervals for the amplitude and phase difference were calculated. Since the confidence intervals were within the 1% range, we concluded that there was no problem with the accuracy.

The total damping coefficients derived from the experiments and the CFD computation agreed with the coefficients predicted by Ikeda’s method. On the other hand, the damping coefficients due to the bilge-keels of the CFD computations were larger than the ones predicted by Ikeda’s method.

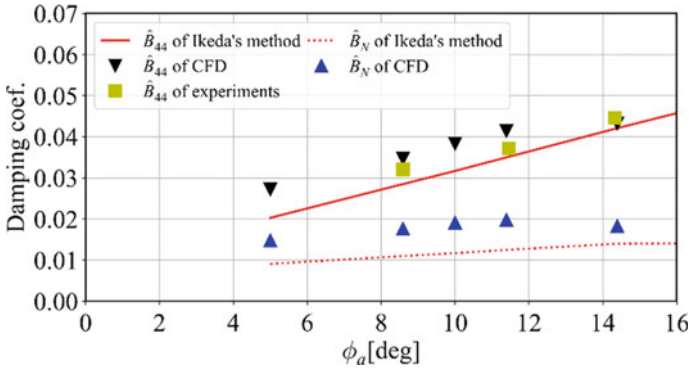


**Fig. 7** Comparisons of non-dimensional linearized coefficients of the total damping and the normal force components among the three methods

The cause of this difference is unknown. For the damping moment acting on the bilge-keels, the assumptions based on the experiments in the estimation method may be different from the flow field calculated by CFD. Although this difference needs to be discussed in the future, the CFD calculation results are reasonable because the total rolling damping coefficients agreed with the experimental results.

### 3.2 Roll Moments Acting the Bilge-Keels in Irregular Roll Motions

Figure 8 shows the time-series data acquired by the CFD computation. The blue dot line and red dash line in Fig. 8 indicate the results using Katayama’s method and the fitting curve of the LSM. Spikes can be seen in the curve of  $B_{N2}$  in Fig. 8. This is due to the small amount of data to which the least-squares method is applied. However, this does not affect the results because the rolling angular velocity is almost zero at this time and thus no damping moments are generated.

Katayama’s method using the damping coefficient during each motion is not suitable to estimate the rolling moment. On the other hand, the fitting curve using the instantaneous damping coefficients agreed with the moment computed by the CFD. The present analysis allows obtaining the instantaneous damping coefficients. Instantaneous damping coefficients decreased with increasing  $KC_d$ . These coefficients converged to the steady values simultaneously while roll motion went toward the next peaks/valleys from previous peaks/valleys. The results showed that damping coefficients of bilge-keels also varied continuously depending on  $KC_d$  as pointed out by Katayama et al. [6]

Figure 9 shows the converged values of damping coefficients at the peaks/valleys. The color map indicates the difference between  $KC_d$  derived from the present relative rolling angle and  $KC_d$  derived from the previous relative rolling angle. The

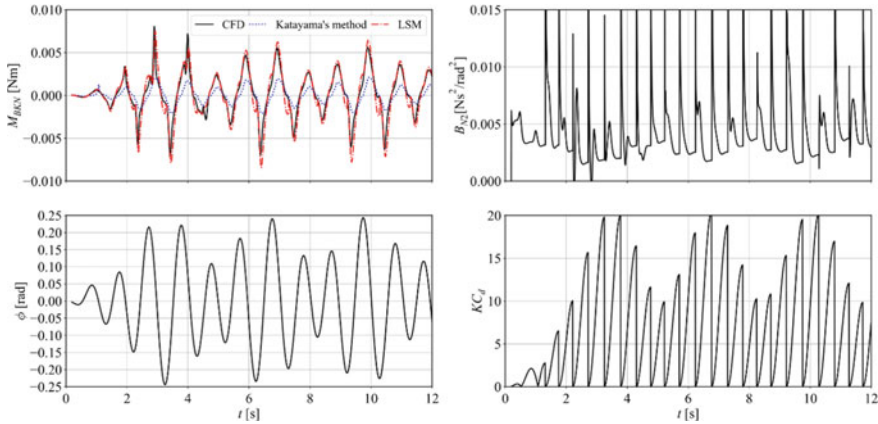


Fig. 8 Examples of the time-series data in mode 2

positive values mean that previous  $KC_d$  is larger than present  $KC_d$ . The black solid line in Fig. 9 shows results predicted by Katayama’s method. The blue dot line in Fig. 9 denotes the results using Ikeda’s method for the normal force component.  $B_{N2}$  increased with increasing the difference of  $KC_d$  although the results have variances. This trend is an agreement with the trend observed in experiments about flat plates [4]. The results using Katayama’s method and Ikeda’s method were smaller than converged values. The reason is that these methods do not consider the flow memory effect. The modification of Katayama’s method is required to take into the flow memory effect.

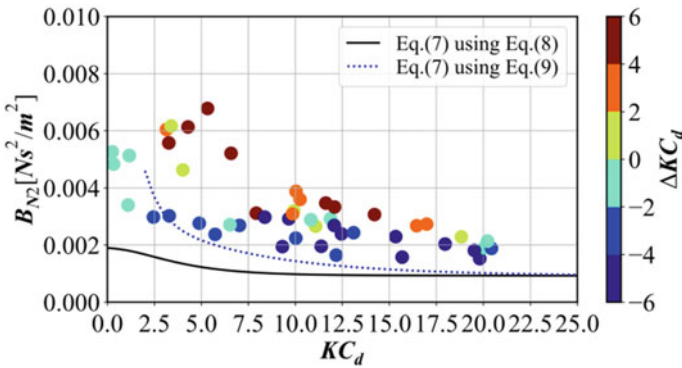


Fig. 9 Converged values of damping coefficients in irregular roll motion



### 3.3 Flow Physics Around the Hull and Bilge-Keels

Computed flow fields were visualized to clarify flow physics around the hull and bilge-keels. Figure 10 shows limiting streamlines and velocity magnitude distributions in two cases. Arrows and white lines in Fig. 10 illustrate the direction of roll velocity and the lengths of vortices based on the limiting streamlines. Two cases illustrate the development of new vortices in the motion from  $KC_d = 20.2$  to  $KC_d = 17.0$  and the motion from  $KC_d = 10.3$  to  $KC_d = 15.3$ .

Figure 10a, b, vortices generated by the previous rolling remained in front of the bilge-keels. In Fig. 10a, the bilge keel generated vortex. On the other hand, in

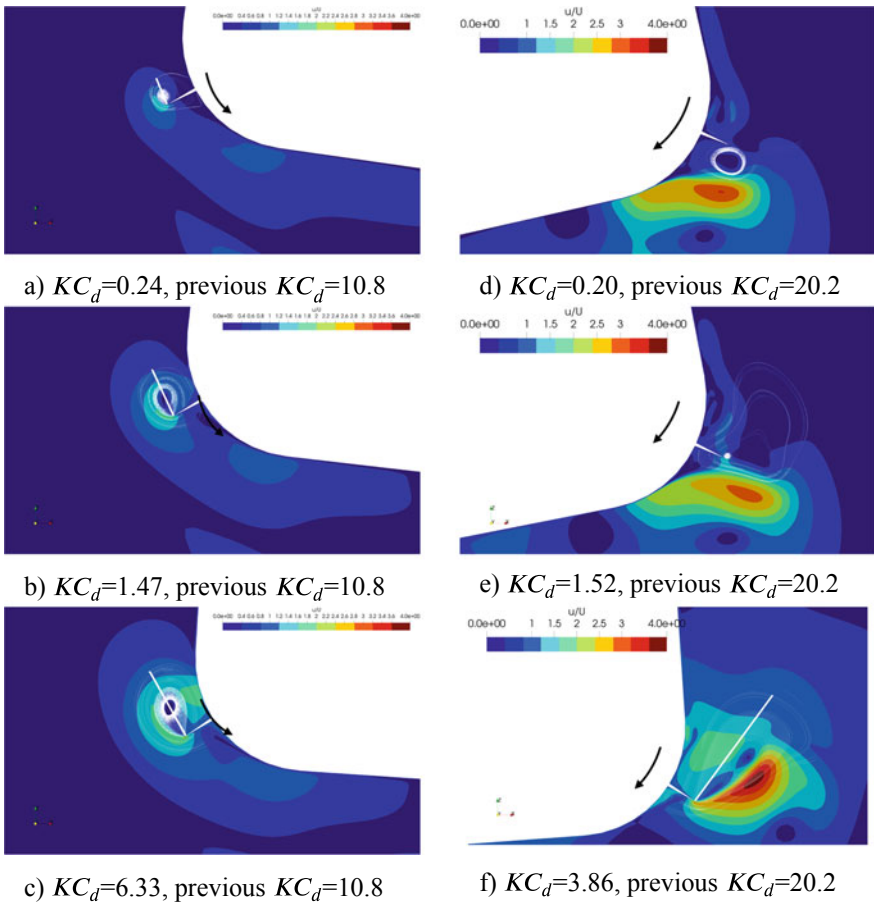


**Fig. 10** Flow fields visualized around the hull under the irregular rolling. **a–c** show the flow fields from  $t = 8.75$  s to 8.875 s in the rolling of mode 2. **d–f** show the flow fields from  $t = 10.31$  s to 10.43 s in the rolling of mode 2

Fig. 10d, vortices are not generated from the bilge keel yet because the vortices remaining in front of the bilge keel are strong.

$K C_d$  at Fig. 10b, e were 1.47 and 1.52. In Fig. 10b, the length of the vortex increased with increasing of  $K C_d$ . In Fig. 10e, the bilge keel started to generate the vortex, and the fluid velocity in front of the bilge keel was larger because of the remaining vortices.

The length of the vortex in Fig. 10f was longer than that in Fig. 10c although the  $K C_d$  at Fig. 10f was smaller than  $K C_d$  at Fig. 10c. In addition to the length of the vortex, fluid velocities in Fig. 10f were higher than those in Fig. 10c. The result shows that when previous  $K C_d$  is large, new vortices develop rapidly and strongly because of the vortices generated in the previous rolling.

### 3.4 Modification Factor Considering the Flow Memory Effect

The flow memory effect was investigated in Sects. 3.2 and 3.3. In this section, we proposed the prediction method considering the flow memory effect. Modification factor was introduced to Eq. (10). The modification factor fills the gap between Eq. (10) and the damping coefficients under irregular rolling.

$$B_{N2}\dot{\phi}|\dot{\phi}| = \rho l_{BK} b_{BK} m C_D (K C_d) r^2 f^2 \dot{\phi}|\dot{\phi}| r \quad (13)$$

$$m = 1 + \alpha K C'_d \exp(-\beta K C_d) \quad (14)$$

where,  $K C'_d$  is the previous  $K C_d$  derived from the previous  $\phi_r$ . To identify the modification factor, the ratio of the results using Katayama's method to the plot markers in Fig. 9 was calculated. Figure 11 shows the relation between the obtained modification factor and the  $K C'_d$ . The color map indicates the  $K C_d$ . The modification factor was in proportion to  $K C'_d$ . On the other hand, the gradient of proportionality decreased with increasing  $K C_d$ . The modification factor is expressed by Eq. (14) to consider the trend. The coefficients,  $\alpha$ ,  $\beta$  in Eq. (14) were obtained by fitting the curve. The obtained  $\alpha$ , and  $\beta$  were 0.517 and 0.103. The results by curve fitting are shown in Fig. 11. The trend was approximately expressed by the Eqs. (13) and (14).

The flow visualization showed previous vortices develop new vortices rapidly. Because  $K C_d$  is correlative with developments of vortices, we proposed correcting  $K C_d$  by the Eq. (13) to consider the flow memory-effect although how to correct  $K C_d$  requires further discussions.  $K C_d^*$  is substituted for  $K C_d$  in Eq. (11).  $\gamma$  in Eq. (15) was set to 0.30 in the case. In this research,  $K C_d$  was modified by the Eq. (15), where gamma was assumed to be 0.3. However, the method of modifying  $K C_d$  requires further discussion through experiments and calculations under various conditions.

$$K C_d^* = K C_d + \gamma K C'_d \quad (15)$$

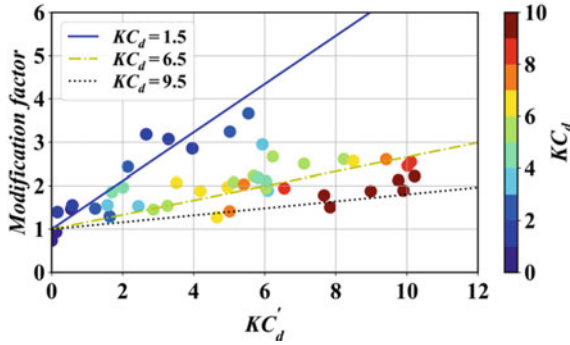


Fig. 11 Modification factor of the prediction method to the normal force component

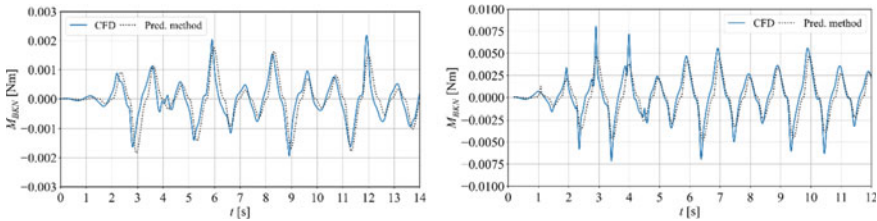


Fig. 12 Comparison between CFD and prediction method (left: mode1, right: mode2)

The prediction method considering the flow memory effect was compared with the normal component computed by the CFD. Figure 12 shows the time-series data of CFD and the proposed method. The results predicted by the proposed method agreed with the CFD results. The result confirmed that considering the flow memory effect enables the calculation of roll damping moment in the time domain (Fig. 12).

## 4 Time-Domain Simulation of Irregular Roll Motion

### 4.1 The Sample Calculation in the Irregular Motions

The numerical simulation for parametric rolling in irregular head waves was carried out to reveal the effects of the proposed prediction method. Three degrees of freedom coupled models of heaving, rolling, and pitching was utilized for the numerical simulations of ship motion [8].

$$\begin{aligned}
 (m + A_{33}(\phi))\ddot{\zeta} + B_{33}(\phi)\dot{\zeta} + A_{34}(\phi)\ddot{\phi} + B_{34}(\phi)\dot{\phi} + A_{35}(\phi)\ddot{\theta} \\
 + B_{35}(\phi)\dot{\theta} = F_3^{FK+B}(t, \zeta, \phi, \theta) + F_3^{DF}(\varphi)
 \end{aligned}
 \tag{16}$$

$$\begin{aligned}
 (I_r + A_{44}(\phi))\ddot{\phi} + B_{44}(\phi)\dot{\phi} + B_{N2}\dot{\phi}|\dot{\phi}| + A_{43}(\phi)\dot{\zeta} + B_{43}(\phi)\dot{\zeta} \\
 + A_{45}(\phi)\ddot{\theta} + B_{45}(\phi)\dot{\theta} = F_4^{FK+B}(t, \zeta, \phi, \theta) + F_4^{DF}(\phi)
 \end{aligned}
 \tag{17}$$

$$\begin{aligned}
 (I_p + A_{55}(\phi))\ddot{\theta} + B_{55}(\phi)\dot{\theta} + A_{53}(\phi)\dot{\zeta} + B_{53}(\phi)\dot{\zeta} + A_{54}(\phi)\ddot{\phi} \\
 + B_{54}(\phi)\dot{\phi} = F_5^{FK+B}(t, \zeta, \phi, \theta) + F_5^{DF}(\phi)
 \end{aligned}
 \tag{18}$$

where,  $m$  is the mass of the ship,  $I_r$  is the inertial moment on rolling,  $I_p$  is the inertial moment on pitching,  $A_{ij}$  is the added mass and moment,  $B_{ij}$  is damping coefficient,  $\zeta$  is heaving,  $\theta$  is pitching angle,  $F_i^{DF}$  is diffraction force, and  $F_4^{FK+B}$  is the sum of Froude-Krylov and buoyancy forces. Froude-Krylov forces are directly calculated by integrating wave pressure up to an irregular wave surface profile. The 2D hydrodynamic forces used for the radiation and diffraction forces are calculated for the submerged hull by the integral equation method with considering an instantaneous rolling angle. The modeling of the roll damping acting on the bilge-keel was modified to the proposed method considering the flow memory effect. When the modeling of the roll damping was not modified, the roll damping moment was determined by interpolating results based on Ikeda’s method.

Figure 13 and Table 4 show the body plan and principal particulars of the subject ship [7]. The spectrum of irregular waves was based on the ITTC spectrum expressed by Eq. (19). Here,  $\omega$  is the frequency of each wave,  $H_{1/3}$  is significant wave height. The significant wave heights were 5.0 and 6.0 m. Froude number was set to 0.083. Maximum angles and probability density functions of roll motions were compared between the simulations without and with modification for the bilge-keel component.

$$S(\omega) = \frac{8.1 \times 10^{-3} g^2}{\omega^2} \exp\left(-\frac{3.11 H_{1/3}^{-2}}{\omega^4}\right)
 \tag{19}$$

**Fig. 13** Body plan of the subject ship

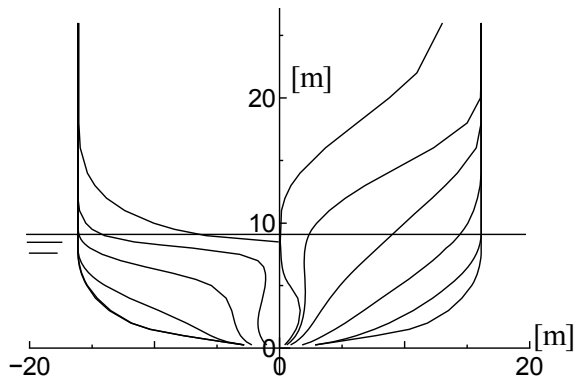


**Table 4** Principal particulars of the subject ship

Length	192.0 m
Breadth	32.26 m
Draught	9.0 m
Height of gravity: <i>KG</i>	17.0 m
Metacentric height: <i>GM</i>	1.89 m
Natural roll period	18.42 s
Displacement	27,205 ton
Breadth of bilge-keels	0.7 m
Position of bilge-keels	Station number 3.34–5.59

### 4.2 Simulated Results

Figure 14 shows the probability density functions of instantaneous roll angles. The results were compared with the normal distributions. The variances of the normal distribution compared were the variances of the simulated rolling angles. Both probability density functions were large around zero degrees and did not follow the normal distributions. The reason is that parametric rolling is a strongly nonlinear phenomenon. The proposed method gave the narrow distribution which is similar to a result of a free-running model experiment [2]. The method proposed in this research can be useful for predicting the occurrence of the parametric rolling.

The maximum roll angles with the proposed method were 11.2 degrees and 14.2 degrees in  $H_{1/3} = 5.0$  m and  $H_{1/3} = 6.0$  m. The maximum roll angles with the conventional method were 22.7 degrees and 32.6 degrees in  $H_{1/3} = 5.0$  m and  $H_{1/3} = 6.0$  m. The maximum values with the proposed method also were smaller than those with the conventional method. The damping coefficients using Ikeda’s method were smaller than the coefficients including the flow memory effect as shown in Fig. 9. The results with the proposed method were smaller than that with the conventional method because the damping using Ikeda’s method was underestimated.

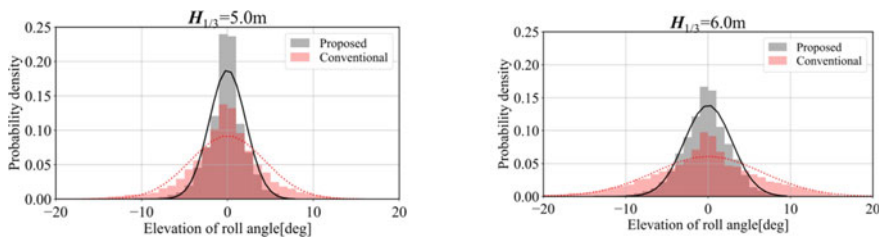


**Fig. 14** Probability density functions of instantaneous roll angles

## 5 Conclusions

In this study, the flow memory effect on the normal force component of bilge keels was investigated by CFD computations. The results are summarized as follows:

- The method used for calculating roll damping for regular motion is not suitable for calculating roll damping for irregular roll motion. Damping coefficients of bilge-keels vary continuously depending on  $K C_d$ .
- In addition to the current motion of the hull, new vortices are generated strongly and rapidly by the vortices generated by the previous motion. Consequently, the roll damping coefficient will be larger than the coefficient without flow memory effect, depending on the previous  $K C_d$ .
- Roll damping moments due to the normal force of bilge-keels can be predicted in the time domain by using the proposed method considering the flow memory effect.
- Regarding the normal force component, roll damping moments are underestimated when the conventional method using Ikeda's method is applied. Ignoring the flow memory effect leads to large maximum roll angles predicted in numerical simulations parametric rolling in irregular head waves.

## References

1. Hashimoto H, Umeda N (2019) Prediction of parametric rolling in irregular head waves. In: Belenky VL et al (eds) Contemporary ideas on ship stability. Fluid mechanics and its applications 119, 275–290
2. Hashimoto H, Umeda N, Matsuda A. (2011) Experimental study on parametric roll of a post-panamax containership in short-crested irregular waves. In: Neves MAS et al (eds) Contemporary ideas on ship stability and capsizing in waves. Fluid mechanics and its applications 96, 267–276
3. Ikeda Y, Himeno Y, Tanaka N (1978) Components of roll damping of ship at forward speed. Report of Department of Naval Architecture University of Osaka Prefecture
4. Ikeda Y, Osa K, Tanaka N (1998) Viscous forces acting on irregular oscillating circular cylinders and flat plates. Trans ASME 110(140):140–147
5. ITTC (2014) Practical guidelines for ship CFD applications. 7.5-03-02-03, rev01
6. Katayama T, Yoshioka Y, Kakinoki T, Ikeda Y (2010) Some topics for estimation of bilge-keel component of roll damping. In: Proceedings of the 11th international ship stability workshop, pp 225–230
7. Katayama T, Miyamoto S, Hashimoto H, Tai Y (2019) An experimental study on characteristics of rolling in head wave for a vessel with non-linear GZ-curve. In: Belenky VL et al (eds) Contemporary ideas on ship stability. Fluid Mechanics And Its Applications 119, pp 491–505
8. Katayama T, Umeda J, Hashimoto H, Yildiz B (2013) A study on roll damping estimation for non periodic motion. In: Proceedings of 13rd international ship stability workshop, Brest, France, pp 44–49

9. Kato H (1958) On the frictional resistance to the rolling of ships. *J Zosen Kyokai* 102:105–119 (in Japanese)
10. Kobayashi H, Kodama Y (2016) Developing spline based overset grid assembling approach and application to unsteady flow around a moving body. *J Math Syst Sci* 6:339–347
11. Ohashi K, Hino T, Kobayashi H, Onodera N, Sakamoto N (2019) Development of a structured overset Navier-Stokes solver with a moving grid and full multigrid method. *J Mar Sci Technol* 24:884–901

# On Application of Standard Methods for Roll Damping Prediction to Ships with High Block Coefficient



Stefan Rudaković and Igor Bačkalov

**Abstract** Proper estimation of roll damping moment is of paramount importance for adequate assessment of dynamic stability of ships. However, experimental data on roll damping of inland vessels are scarce and unreliable. Thus, the applicability of the classic Ikeda's method and its simplified version on typical European inland vessels is investigated, with specific focus on eddy making component. It is found that the simplified Ikeda's method, in comparison to the classic method, may considerably underestimate the eddy making component of damping of full hull forms, or even return negative values, although the block coefficient is within the limits of method applicability. This deficiency of the simplified Ikeda's method does not affect inland vessels only, but it is equally relevant for seagoing ships with high block coefficients. Hence, the paper explores the possibilities of adjusting the simplified Ikeda's method in order to improve the observed shortcoming, as well as to extend its application to stability analysis of inland ships.

**Keywords** High block coefficient · Inland vessels · Roll damping · Ikeda's method · Simplified Ikeda's method · Eddy damping

## 1 Introduction

Proper mathematical modeling of ship dynamics was indicated by Bačkalov et al. [2] as one of the most important tasks of the future research on stability of inland vessels. In this respect, it is well-known that the outcome of the analysis of roll motion and, consequently, assessment of ship stability, considerably depend on roll damping. However, experimental data on roll damping of inland vessels are scarce and unreliable. In such a case, a possible solution could be to use some of the existing semi-empirical methods in order to estimate roll damping coefficients.

---

S. Rudaković · I. Bačkalov (✉)  
Development Centre for Ship Technology and Transport Systems, Duisburg, Germany  
e-mail: [backalov@dst-org.de](mailto:backalov@dst-org.de)

S. Rudaković  
e-mail: [srudakovic@mas.bg.ac.rs](mailto:srudakovic@mas.bg.ac.rs)



Nevertheless, the viability of such approach is questionable knowing that the available methods are primarily intended for conventional seagoing ships. This concerns the well-established Ikeda's method [4] and its "simplified" version [7] which is based on regression analysis of data generated by applying the classic method on a series of ships developed from the Taylor series. The question of applicability of the simplified method is particularly relevant as it is considered as a "common method of calculations recommended for assessment of vulnerability" within the Second Generation Intact Stability Criteria framework (see [5]) and it is suggested for use in absence of either experimental data or another, more suitable method (see [6]). In fact, the doubts regarding the applicability of the simplified Ikeda's method were expressed in several studies. Kawahara et al [7] found considerable discrepancies between the experimentally derived roll damping coefficients and those predicted by either the original or the simplified Ikeda's method in case of the so-called buttock-flow stern hull forms. Oliva-Remola and Pérez-Rojas [8] argued that it would be necessary to examine the consequences of application of the simplified Ikeda's method when one or more ship parameters fall outside of the designated range of method's applicability. Oliveira et al. [9] carried out roll damping estimations for a very large crude carrier (VLCC) based on both the physical experiments and the semi-empirical methods (classic and simplified Ikeda's method) and found that the simplified Ikeda's method failed to properly predict the roll damping coefficients in several examined conditions. Moreover, Oliveira et al. [9] proposed to consider the use of classic Ikeda's method (instead of its simplified version) particularly in direct stability assessment.

In order to examine the relevance of the simplified Ikeda's method for inland vessels, roll damping coefficients were calculated for several sample ships. The preliminary results were quite unexpected: for some inland vessels, featuring remarkably high block coefficients, estimated roll damping coefficients were found to be negative. Such results triggered a further investigation which included several seagoing ships and confirmed, somewhat surprisingly, that simplified Ikeda's method generally fails to accurately predict the roll damping of ships with full hull forms. Thus, even though the original intention of the study was to examine the possibility of applying the simplified Ikeda's method to inland vessels, it became obvious that the use of the method could affect safety assessment of seagoing ships as well. It is therefore believed that the outcome of the study herein presented is not relevant for inland vessels only but could have an impact on ship stability analysis in general.

## 2 Application of the Simplified Ikeda's Method to Sample Ships

Inland vessel hulls often have high breadth-to-draught ratios (i.e.  $B/d > 4$ ), while geometry of some of the aft cross sections may yield as much as  $B/d \approx 10$ . In

**Table 1** Sample inland vessels

Vessel	$L$ [m]	$B$ [m]	$d$ [m]	$C_B$	$C_M$	$B/d$	$GM$
T1	66.00	10.50	3.45	0.8212	0.9959	3.043	1.355
T2	84.28	9.56	3.60	0.9226	0.9987	2.656	0.321
T3	81.821	9.40	3.07	0.8497	0.9967	3.062	0.574
T4	85.95	10.95	2.80	0.8535	0.9982	3.911	1.293
T5	85.95	11.40	4.30	0.8514	0.9969	2.651	1.278
T6	105.76	11.40	2.80	0.8806	0.9964	4.071	1.850
C7	110.00	11.45	2.60	0.8783	0.9986	4.634	3.272
C8	109.70	11.40	2.46	0.8664	0.9964	4.404	3.333
C9	111.25	14.50	3.30	0.8336	0.9886	4.390	1.575
T10	121.10	11.40	4.30	0.8976	0.9965	2.651	0.823
T11	125.00	11.40	4.50	0.8992	0.9988	2.533	1.498
C12	134.26	14.50	3.60	0.9031	0.9957	4.028	3.443
C13	135.00	14.50	4.00	0.9123	0.9978	3.625	2.014
C14	135.00	11.45	2.68	0.9088	0.9974	4.272	3.249
C15	135.00	11.45	3.33	0.9101	0.9974	3.438	1.778

addition, block coefficients of these vessels are typically  $C_B = 0.82 - 0.94$  and mid-ship section coefficients are  $C_M \geq 0.99$ . The geometric properties of inland cargo ships used in the present investigation are given in Table 1.

According to Kawahara et al. [7], the simplified Ikeda’s method may be applied to ships having:

$$0.5 \leq C_B \leq 0.85, \quad 2.5 \leq B/d \leq 4.5, \quad \hat{\omega} \leq 1, \\ -1.5 \leq OG/d \leq 0.2, \quad 0.9 \leq C_M \leq 0.99.$$

Symbol  $\hat{\omega}$  stands for non-dimensional frequency:

$$\hat{\omega} = \omega \cdot \sqrt{\frac{B}{2g}},$$

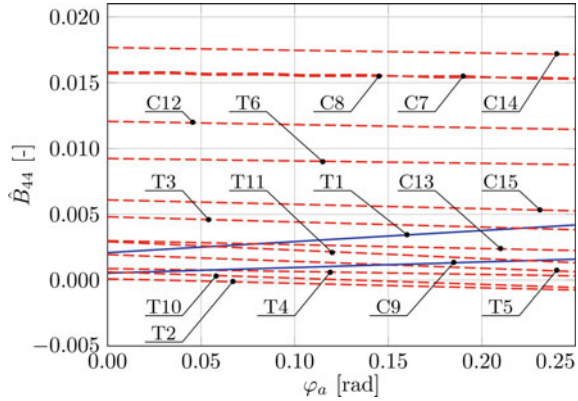
while the distance  $OG$  of the center of gravity from the calm water level is downwards positive.

Due to the aforementioned specific features, most of the vessels in Table 1 are clearly out of range of applicability of the simplified Ikeda’s method.

Despite this, the roll damping coefficients were calculated for all sample inland ships, whereby the total roll damping was considered to consist of:

$$B_{44} = B_F + B_W + B_E, \tag{1}$$

**Fig. 1** Total roll damping of examined inland vessels as a function of roll amplitude  $\varphi_a$ , according to the simplified Ikeda's method



where  $B_F$  is friction damping,  $B_W$  is wave damping and  $B_E$  is eddy damping. Bilge keel damping  $B_{BK}$  is omitted from the calculations since inland vessels normally do not have bilge keels. Lift damping component  $B_L$  is also excluded, since it is considered that the vessel speed is  $v = 0$ . It should be noted that whenever the limits of applicability range were exceeded, maximal values of  $B/d$ ,  $C_B$  and  $C_M$  were used in the calculations. Consequently, since the use of the simplified method does not require knowledge of any details of hull geometry that would distinguish an inland vessel from a seagoing one, the calculated  $B_{44}$  coefficients could formally correspond to a Taylor standard series ship of the same characteristics.

Figure 1 shows the non-dimensional equivalent linear total roll damping:

$$\hat{B}_{44} = \frac{B_{44}}{\rho \nabla B^2} \cdot \sqrt{\frac{B}{2g}}, \tag{2}$$

as a function of roll amplitude for all inland vessels examined. The damping was calculated for typical values of metacentric heights at design draught, given in Table 1. It can be noticed that, except for the sample vessels T1 and C9, the total roll damping of the examined ships decreases with the increase of roll amplitude. Surprisingly, some ships (T2 and T10) may even reach negative roll damping at large enough rolling amplitudes.

A closer examination of components revealed that in all the cases analyzed (again, except for sample vessels T1 and C9), eddy making component was negative. The focus of investigation thus turned to the eddy damping.

Eddy damping is calculated as follows:

$$\hat{B}_E = \frac{4\hat{\omega} \cdot \varphi_a}{3\pi \cdot x_2 \cdot x_1^3} \cdot C_R, \tag{3}$$

where:

$$C_R = A_E \cdot \exp(B_{E1} + B_{E2} \cdot x_3^{B_{E3}}), \tag{4}$$

and

$A_E = f(x_1, x_2)$ ,  $B_{E1} = f(x_1, x_2, x_4)$ ,  $B_{E2} = f(x_2, x_4)$ ,  $B_{E3} = f(x_1, x_2)$ , while  $x_1 = B/d$ ,  $x_2 = C_B$ ,  $x_3 = C_M$ ,  $x_4 = OG/d$ .

From formula (3) it may be concluded that eddy damping could be negative only if  $C_R$  becomes negative. Furthermore,  $C_R$  given by formula (4) could be negative only if  $A_E$  becomes negative. Therefore, it would be interesting to examine the structure of the formula for the computation of  $A_E$ :

$$A_E = A_{E1} + A_{E2} = \underbrace{(-0.0182 \cdot x_2 + 0.0155) \cdot (x_1 - 1.8)^3}_{A_{E1}} - \underbrace{79.414 \cdot x_2^4 + 215.695 \cdot x_2^3 - 215.883 \cdot x_2^2 + 93.894 \cdot x_2 - 14.848}_{A_{E2}} \tag{5}$$

If the geometric properties of an examined ship i.e.  $B/d$  and  $C_B$  remain within the boundaries of method applicability,  $A_{E1}$  cannot become negative. However,  $A_{E2}$  may become both negative and larger than  $A_{E1}$  in case  $C_B > 0.84$ , whereby the exact value of this “critical” block coefficient depends on  $B/d$  ratio.  $A_E$  as a function of  $B/d$  and  $C_B$  is given in Fig. 2. The value of the block coefficient which would result in negative  $A_E$  is given in Fig. 3 as a function of  $B/d$ . Now it is possible to explain the principal difference in eddy making component (and, consequently, the total roll damping) between ships T1 and C9 and the rest of the sample vessels: T1 and C9 are the only ships with block coefficients below the critical value of  $C_B$ .

It was already pointed out that the simplified Ikeda’s method does not take into account hull geometry specifics that distinguish typical inland vessels from seagoing ships. This could mean that the findings obtained so far may apply to seagoing ships as well. To test this hypothesis, the total roll damping consisting of friction damping, wave damping and eddy damping, as in Eq. (1), was calculated for eight seagoing ships whose properties are given in Table 2. The non-dimensional equivalent linear

**Fig. 2**  $A_E$  as a function of  $B/d$  and  $C_B$

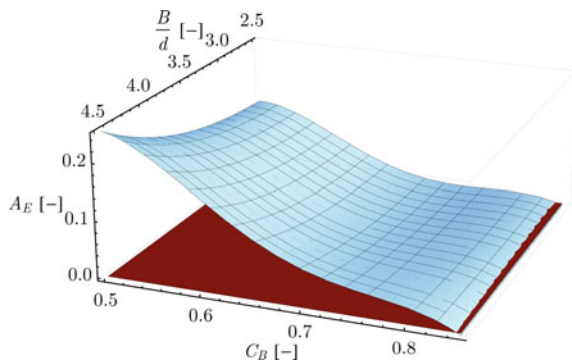


**Fig. 3** The position of examined inland vessels with respect to the critical value of  $C_B = f(B/d)$  (full line) whose exceedance leads to negative  $A_E$  values

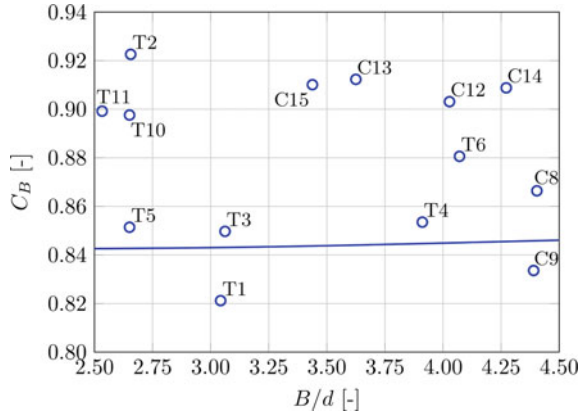


**Table 2** Sample seagoing ships<sup>1</sup>

Vessel	$L$ [m]	$B$ [m]	$d$ [m]	$C_B$	$C_M$	$B/d$	$GM$
Small feeder	95.77	15.85	4.87	0.7295	0.9903	3.255	0.770
Bulk carrier G	183.13	33	11.6	0.8475	0.9982	2.845	1.886
Bulk carrier 03	190.03	29	10.95	0.7731	0.9917	2.648	1.906
Panamax tanker	230.7	32.2	11	0.8430	0.9959	2.927	2.491
JBC	285.05	45	16.5	0.8423	0.9981	2.727	1.376
Suezmax tanker	287.78	45.5	16.6	0.7982	0.9872	2.741	3.296
KVLCC2	325.52	58	20.8	0.7960	0.9979	2.788	5.710
VLCC	327.49	54.5	21	0.8097	0.9962	2.595	7.900

total roll damping defined by Eq. (2), obtained for sample seagoing ships is given in Fig. 4. Indeed, the same anomaly which was observed in roll damping estimation of inland vessels (Fig. 1) appears in roll damping calculations for seagoing ships as well: the roll damping decreases as the roll amplitude increases if ships have block coefficients above the “critical”  $C_B$  (Fig. 5). It may be also noticed that one of the sample ships (JBC) whose block coefficient is barely below the corresponding critical value also exhibits a peculiar behavior, as her roll damping is almost independent of the roll amplitude.

<sup>1</sup> Some of the sample seagoing ships used in this analysis were a subject of other reports and benchmark studies: Boonstra, H., de Jongh, MP., 2003, “Initial safety assessment of small container feeders: a study into the ‘Dongedijk’ accident and stability sensitivity of low freeboard ships”, Delft University of Technology (Small feeder); Vantorre, M., Journée, JMJ., 2003, “Validation of the strip theory code SEAWAY by model tests in very shallow water”, Colloquium on Numerical Modelling (Bulk carrier G); Workshop on CFD in Ship Hydrodynamics, 2015, <https://t2015.nmri.go.jp/> (JBC); Workshop on Verification and Validation of Ship Manoeuvring Simulation Methods, 2008, <http://www.simman2008.dk/> (KVLCC2). Hull forms of the sample ships Bulk carrier 03, Panamax tanker, and Suezmax tanker were retrieved from the publicly available database of DELFTShip software.

**Fig. 4** Total roll damping of examined seagoing ships as a function of roll amplitude  $\varphi_a$ , according to the simplified Ikeda's method

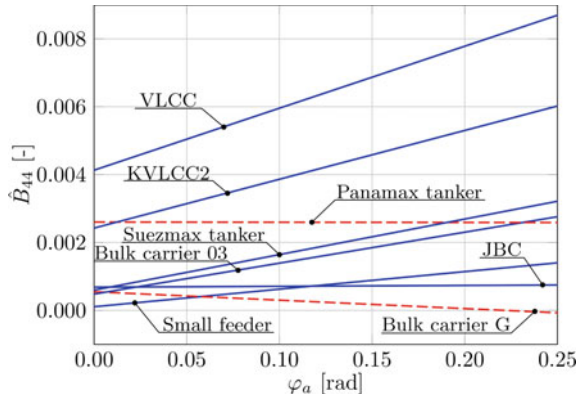
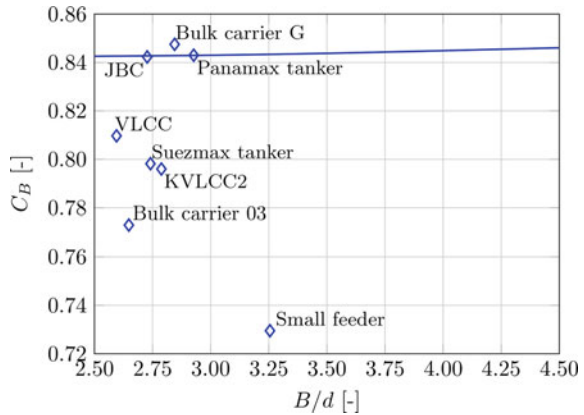


**Fig. 5** The position of examined seagoing ships with respect to the critical value of  $C_B = f(B/d)$  (full line) whose exceedance leads to negative  $A_E$  values



The factor  $C_R$  computed over the complete domain of applicability of the simplified Ikeda's method is given in Fig. 6. In line with the analysis of formulas (4) and (5),  $C_R$  is negative for high values of  $C_B$  regardless of  $OG/d$  and  $C_M$ . Another interesting feature is noticeable: the sign of the partial derivative of the function (4) with respect to  $C_B$  changes when block coefficient attains sufficiently high value. This happens at  $C_B = 0.74 - 0.81$  (depending on  $OG/d$  and  $C_M$  values) and becomes particularly evident for high mid-ship coefficients  $C_M$ .

Therefore, while the eddy making component of damping and, consequently, the total roll damping corresponding to high block coefficients above the critical value of  $C_B$  given in Fig. 2 are obviously incorrect, it is also questionable whether  $B_{44}$  calculated with simplified Ikeda's method could be considered reliable in a much wider range of block coefficients, i.e. within  $0.74 < C_B < 0.84$ . Thus, the issue of accuracy of the simplified method is not limited to inland vessels and seagoing ships with high values of  $C_B$  but may also concern seagoing ships with moderate-to-high block coefficients, otherwise believed to be covered by the method.

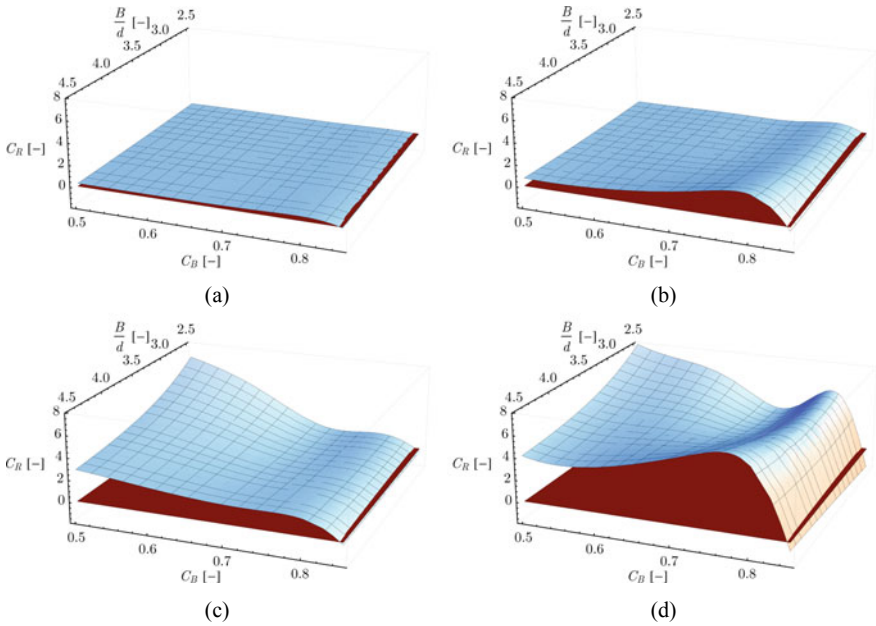


**Fig. 6**  $C_R$  computed over the applicability domain of simplified Ikeda’s method: **a)**  $OG/d = 0.2$ ,  $C_M = 0.9$ , **b)**  $OG/d = 0.2$ ,  $C_M = 0.99$ , **c)**  $OG/d = -1.5$ ,  $C_M = 0.9$ , **d)**  $OG/d = -1.5$ ,  $C_M = 0.99$

### 3 A Possible Adjustment of Simplified Formula for Eddy Making Component of Damping

It would be interesting to examine the possibility to amend the simplified Ikeda’s method, so as to get a more reliable prediction of eddy making component of damping for ships with high  $C_B$ , and ultimately for inland vessels. In absence of experimental data, the appropriate modification of function  $A_{E2}$ , given by formula (5), could be sought by calculating eddy making damping component with the classic Ikeda’s method and using the calculated data to fix the observed deficiency of the simplified method.

Consequently, the following procedure is proposed. Assuming that, for each ship, it may be established:

$$B_{E(s)} \approx B_{E(c)}, \tag{6}$$

(where “s” stands for the simplified and “c” stands for the classic method) it would be possible to extract the “correct” value of  $A_{E2}$  corresponding to a given (high) block coefficient, provided that  $B_{E(c)}$  is calculated beforehand.

$B_{E(c)}$  is obtained by numerical integration of sectional eddy damping over the ship length:

$$B_{E(c)} = \int_L B'_{E(c)} dx, \quad (7)$$

where

$$B'_{E(c)} = \frac{4 \cdot \omega \cdot \varphi_a}{3\pi} \cdot \rho d_s^4 \cdot C_{R(c)}. \quad (8)$$

Unlike its simplified version, the classic Ikeda's method requires the knowledge of detailed hull geometry, that is, the geometric particulars of cross-sections. The sectional  $C_{R(c)}$  depends on the sectional breadth  $B_s$  and the draught  $d_s$ , the sectional area coefficient  $\sigma$ , the bilge radius  $r_b$ , and the local maximal distance between the roll axis and hull surface  $r_{\max}$ ,  $OG$  as well as the pressure coefficient  $C_P$ . More precisely:

$$C_{R(c)} = \left( \frac{r_{\max}}{d_s} \right)^2 \cdot f \left( \frac{r_b}{d_s}, \frac{B_s}{2d_s}, \sigma, \frac{OG}{d_s} \right) \cdot C_P. \quad (9)$$

Given the complexity of the procedure for the calculation of  $r_b$ ,  $r_{\max}$  and  $C_P$ , the respective expressions are omitted from this study, but may be found in e.g. Falzarano et al. [3], who presented the consolidated formulas of the classic method. On the other hand, eddy damping of a ship, according to the simplified method, is:

$$B_{E(s)} = \frac{4 \cdot \omega \cdot \varphi_a}{3\pi} \cdot \rho d^4 \cdot L \cdot C_{R(s)}, \quad (10)$$

where  $C_{R(s)}$  is defined by Eq. (4). From Eqs. (6)–(8) and (10) it follows:

$$C_{R(s)} = \frac{1}{d^4 L} \int_L d_s^4 \cdot C_{R(c)} dx. \quad (11)$$

Then, using the formulas (4), (5) and (11), an estimate of  $A_{E2}$  may be obtained for a given ship.

For this purpose, four inland vessels, whose block coefficients are in the range  $C_B = 0.798 - 0.851$ , were selected from Table 1. Eight seagoing ships given in Table 2 were included as well. The body plans of selected ships are given in Figs. 7 and 8. In each case, eddy making component computations were performed using 51 equidistant cross sections.

It should be noted that in the classic method, the pressure distribution on the hull surface is obtained assuming the cross sections are approximated by Lewis forms. Clearly, this is not a proper approximation for a number of aft cross sections of examined inland vessels or e.g. for the cross sections of seagoing ships with bulbous bow. Therefore, although the proposed procedure seems to be simple, it is not free from challenges.



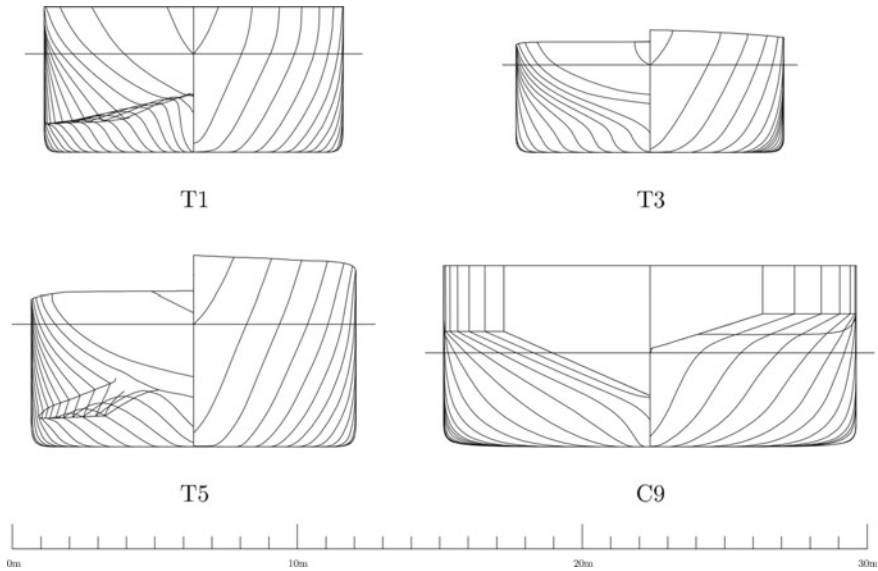


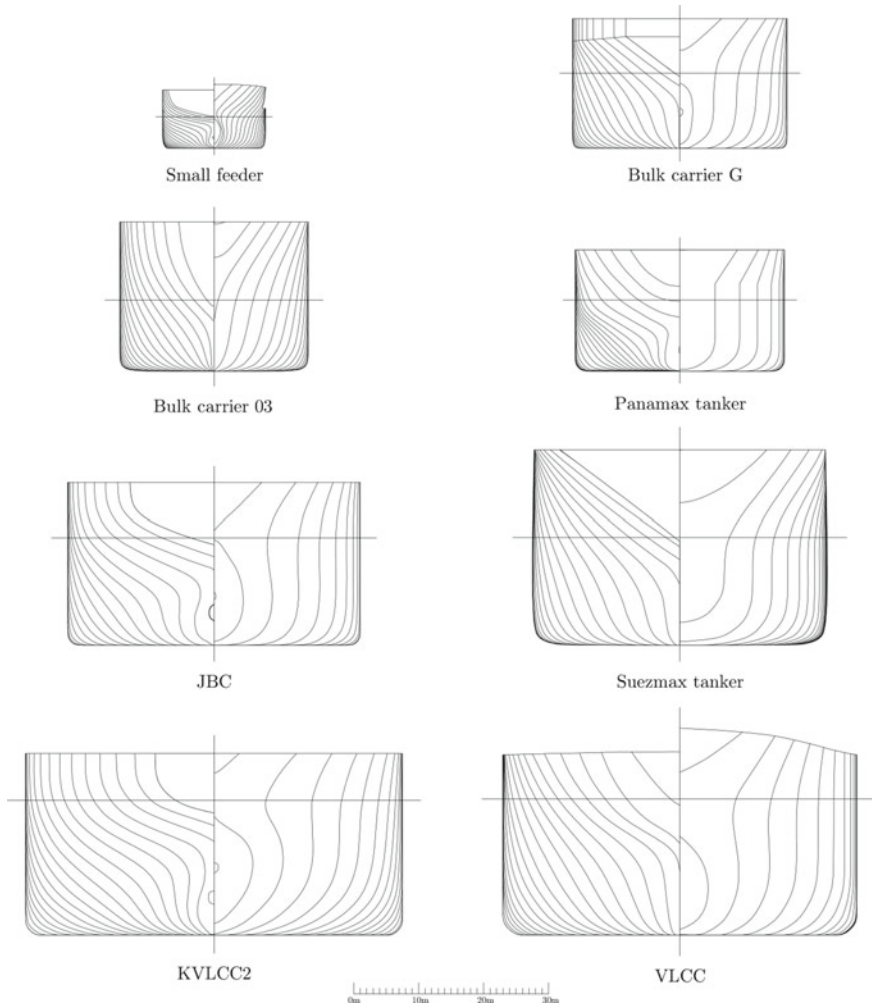
**Fig. 7** Inland vessels used in computation of eddy making component according to the classic Ikeda’s method

Furthermore, for cross sections of certain geometric characteristics, (typically for combinations of high beam-to-draught ratios and relatively low area coefficients) sectional eddy damping calculated by the classic Ikeda’s method could also be negative. This is often the case with forward- and aft-most cross sections of inland vessels. A trivial solution (and it seems, the usual remedy, see Kawahara et al. [7]) for this deficiency is to take the damping of a “problematic” cross section as zero. Having no possibility to estimate the correct value of eddy making damping corresponding to such cross sections, the same approach was used in this analysis.

Finally, using the described procedure,  $A_{E2}$  values were calculated for the selected inland vessels and seagoing ships (see Fig. 9). As the results to some extent depend on the  $OG/d_s$  ratio, average values of  $OG$  corresponding to realistic loading conditions of each ship were adopted in the calculations. Table 3 provides information on realistic metacentric heights which can be attained within the  $OG/d$  range of applicability of Ikeda’s method.

Based on these results, a new expression for  $A_E$ , valid in the whole range of applicability of the simplified Ikeda’s method, is proposed:

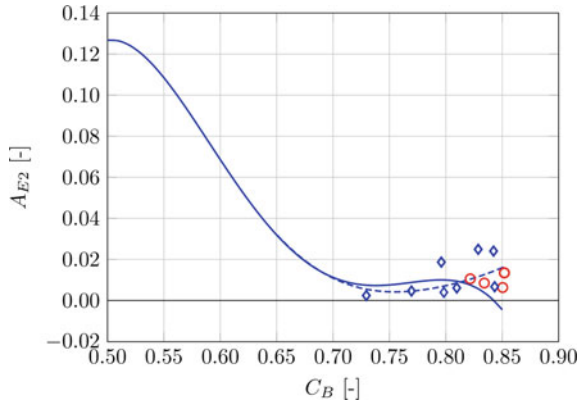
$$\begin{aligned}
 A_{E-new} = A_{E1} + A_{E2-new} = & \underbrace{(-0.0182 \cdot x_2 + 0.0155) \cdot (x_1 - 1.8)^3}_{A_{E1}} \\
 & + \underbrace{148.223 \cdot x_2^5 - 549.619 \cdot x_2^4 + 807.464 \cdot x_2^3 - 585.231 \cdot x_2^2 + 208.221 \cdot x_2 - 28.8891}_{A_{E2-new}}
 \end{aligned}
 \tag{12}$$



**Fig. 8** Seagoing ships used in computation of eddy making component according to the classic Ikeda's method

$A_{E-new}$  as a function of  $B/d$  and  $C_B$  is given in Fig. 10. The factor  $C_R$  adjusted by formula (12) is computed within the range of applicability of the simplified Ikeda's method and given in Fig. 11. Finally, the non-dimensional equivalent linear total roll damping of the sample ships given in Tables 1 and 2 is computed using the adjusted simplified formula for eddy making damping component, see Fig. 12. Whenever the block coefficient exceeded the applicability range, the calculations were carried out with  $C_B = 0.85$ . As it can be seen in Fig. 12, the total roll damping now has an increasing trend with respect to the roll amplitude, as it should be normally expected.

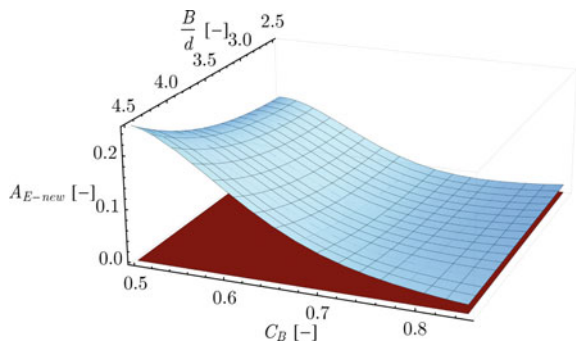
**Fig. 9**  $A_{E2}$  calculated by formula (5) (full line) and the proposed correction given by formula (12) (dashed line). Circles represent the values calculated for inland vessels, while diamonds correspond to seagoing ships



**Table 3** The ranges of  $OG/d$  values used in calculation of  $A_{E2}$  values for the selected inland vessels and seagoing ships (see Fig. 9) and the corresponding metacentric heights

Vessel	$OG/d$	$GM$
T1	-0.2 - 0.2	0.520 - 1.900
T3	-0.2 - 0.2	0.443 - 1.671
T5	0.0 - 0.2	0.571 - 1.431
C9	-1.0 - 0.2	0.475 - 4.435
Small feeder	-0.2 - 0.2	1.140 - 3.088
Bulk carrier G	0.0 - 0.2	1.886 - 4.206
Bulk carrier 03	0.0 - 0.2	0.956 - 3.146
Panamax tanker	0.0 - 0.2	1.691 - 5.011
JBC	0.0 - 0.2	2.076 - 5.376
Suezmax tanker	-0.2 - 0.2	0.496 - 4.896
KVLCC2	0.0 - 0.2	3.515 - 7.675
VLCC	0.0 - 0.2	1.210 - 5.410

**Fig. 10**  $A_{E-new}$  as a function of  $B/d$  and  $C_B$



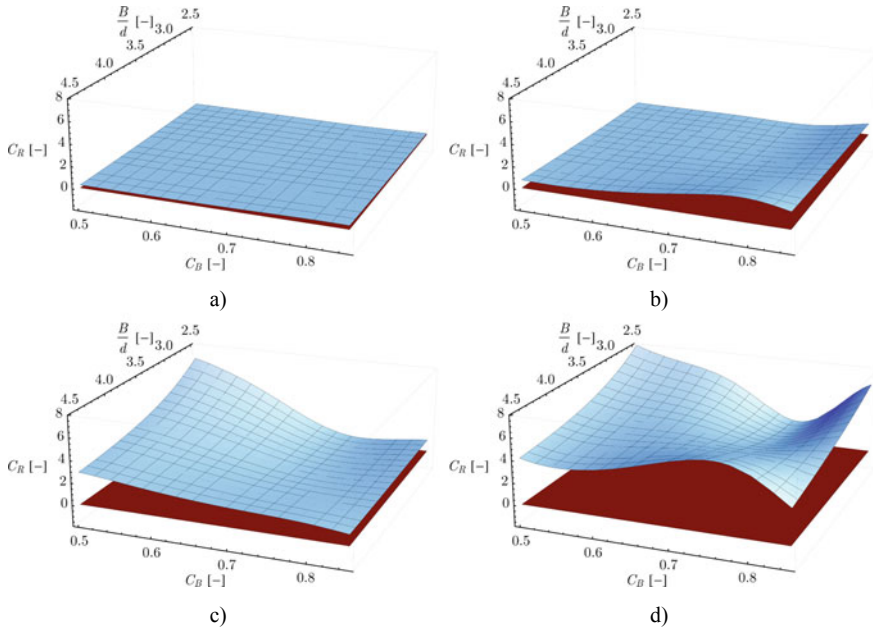


**Fig. 11** Factor  $C_R$  adjusted by formula (12) computed over the applicability domain of simplified Ikeda’s method: **a)**  $OG/d = 0.2, C_M = 0.9$ , **b)**  $OG/d = 0.2, C_M = 0.99$ , **c)**  $OG/d = -1.5, C_M = 0.9$ , **d)**  $OG/d = -1.5, C_M = 0.99$

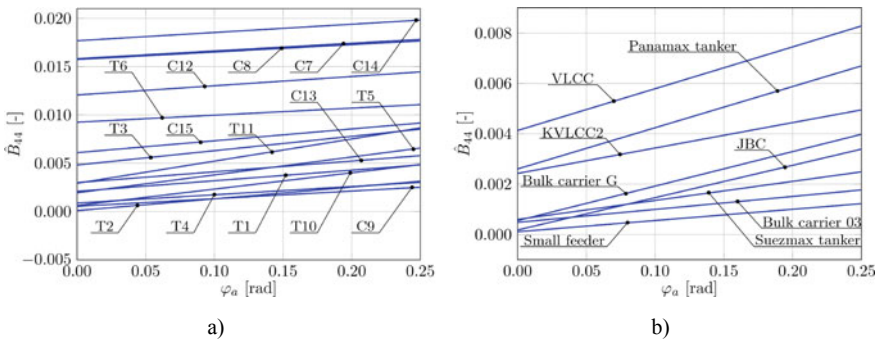
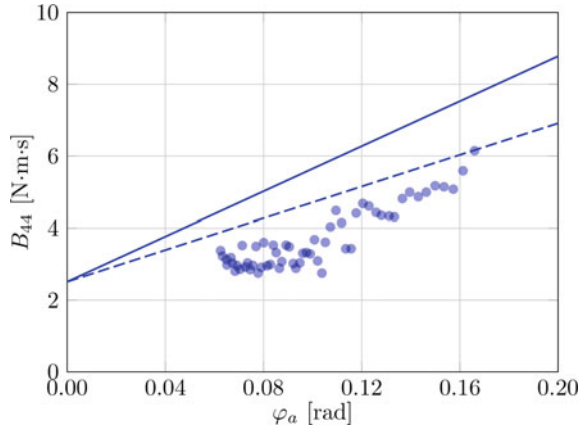


**Fig. 12** Total roll damping of examined ships as a function of roll amplitude  $\varphi_a$ , according to the simplified Ikeda’s method, taking into account the proposed adjustment of eddy making damping component: **a)** inland vessels, **b)** seagoing ships

To get an insight into the effects of the proposed modification of simplified Ikeda’s method on accuracy of prediction of roll damping of ships with high block coefficients, the use was made of available experimental data. The data were published by Alexandersson et al. [1] who performed roll decay tests on a model of KVLCC2, one

**Fig. 13** Total roll damping of a scaled model of KVLCC2 according to Eq. (1) calculated by the simplified Ikeda's method using the current eddy damping expression (full line) and using the proposed modification of eddy damping (dashed line). Dots represent the model test data published by Alexandersson et al. [1]



of the sample ships used in this study. The comparison of the total roll damping of the scaled model (comprising friction damping, wave damping and eddy damping) calculated using the simplified Ikeda's method (both with and without the proposed modification of eddy damping component) and experimentally derived data is given in Fig. 13. It may be observed that the proposed modification considerably reduces the difference between the predicted and the experimentally derived data.

#### 4 Further Extension of Simplified Formula for Eddy Damping to Inland Vessels

It was already pointed out that most of the sample vessels given in Table 1, and most of inland vessels in general, fall out of the range of applicability of the simplified Ikeda's method with respect to  $B/d$  and  $C_B$ . For instance, beam-to-draught ratios of typical European river cruisers are in the range of 5.5 – 8.5. Therefore, without model tests, it appears difficult to adjust the simplified Ikeda's method so as to extend its applicability to just any inland vessel.

For the sake of comparison, for some sample inland vessels having  $C_B > 0.85$  (see Table 4),  $C_{R(s)}$  was calculated using formula (11), based on classic Ikeda's method, taking into account actual hull form geometry (corresponding to real  $C_B$ ) in the computation of  $C_{R(c)}$ . These figures are subsequently compared to data obtained by applying the simplified formula (4) using both the current expression (5) for  $A_E$  and the proposed adjustment of  $A_E$  given by (12); in these two latter cases,  $C_B = 0.85$  is always used, instead of actual block coefficients.

Significant discrepancies (both qualitative and quantitative) between the values of  $C_R$  obtained using different approaches indicate that an accurate estimation of eddy making component of such full-bodied vessels remains a task for the future. For the time being, however, if the simplified Ikeda's method is employed, the negative

**Table 4** Discrepancies in estimation of eddy making component of roll damping for inland vessels with very high block coefficient, using different formulas and limitations

Vessel	$C_B$	$C_{R(s)}$		
		(4) using (5)	(4) using (12)	(11)
T2	0.9226	-0.3773	1.3516	4.6228
T4	0.8535	-0.3876	1.4997	6.3669
C8	0.8664	-0.3744	1.5933	3.5575
C12	0.9031	-0.3862	1.5168	2.6430
C15	0.9101	-0.3884	1.4374	3.5152

All calculations were carried out for  $OG = 0$  m

values of eddy damping could be avoided by using the adjusted eddy damping formula (proposed in this analysis and based on (12)) whilst applying the method limitations whenever the geometric properties of the analyzed hull exceed the applicability range.

## 5 Conclusions

In course of investigation of applicability of the simplified Ikeda’s method for roll damping prediction to European inland vessels, it was found that the eddy damping formula fails to properly predict the corresponding damping component if the block coefficient of the vessel is sufficiently large, i.e.  $C_B > 0.8$ . This deficiency is particularly striking for  $C_B > 0.84$ , when eddy making component of damping becomes negative. The roll damping calculations performed on seagoing ships confirmed that this anomaly of the simplified Ikeda’s method is not limited to inland vessels only.

Therefore, an adjustment of the simplified formula for eddy making component prediction is proposed, based on calculations performed using the classic Ikeda’s method. The method was applied to several typical inland hulls with high block coefficients ( $C_B = 0.82 - 0.85$ ) and high mid-ship coefficients ( $C_M \geq 0.99$ ), covering a complete range of applicability of the simplified method with respect to beam-to-draught ratios ( $B/d = 2.6 - 4.4$ ). Eight seagoing ships having  $C_B = 0.73 - 0.85$  were included in the calculations as well. It is expected that the derived expression could extend the applicability of the simplified Ikeda’s method to inland ships, in absence of adequate experimental data.

Furthermore, it is believed that the adapted formula provides a better estimation of eddy making damping component not only for inland vessels but also for seagoing ships with high block coefficients.

**Acknowledgements** The research herein presented was supported by Ministry of Education, Science and Technology Development of Republic of Serbia, Contract No. 451-03-68/2020-14/200105 and Contract No. 451-03-9/2021-14/200105.

The authors would like to thank Prof. Milan Hofman (University of Belgrade) and Prof. Gabriele Bulian (University of Trieste) for valuable suggestions and comments in course of the study.

## References

1. Alexandersson M, Kjellberg M, Wengang Mao W, Ringsberg JW (2021) Prediction of roll motion using fully nonlinear potential flow and Ikeda's method. In: Proceedings of the 31st international ocean and polar engineering conference (ISOPE-2021), Rhodes, Greece
2. Bačkalov I, Bulian G, Cichowicz J, Eliopoulou E, Konovessis D, Leguen JF, Rosén A, Themelis N (2016) Ship stability, dynamics and safety: Status and perspectives from a review of recent STAB conferences and ISSW events. *Ocean Eng* 116:312–349
3. Falzarano J, Somayajula A, Seah R (2015) An overview of the prediction methods for roll damping of ships. *Ocean Syst Eng* 5(2):55–76
4. Himeno Y (1981) Prediction of ship roll damping—state of the art. Report No. 239, College of Engineering, University of Michigan
5. IMO (2019) SDC 7/INF. 2, Annex: draft consolidated explanatory notes of interim guidelines on second generation intact stability criteria. Submitted by Japan, 26 November
6. IMO (2016) SDC 4/5/1/Add.3-Annex 4: draft explanatory notes on the vulnerability of ships to the dead ship stability failure mode. Submitted by Japan, 11 November
7. Kawahara Y, Maekawa K, Ikeda Y (2009) A simple prediction formula of roll damping of conventional cargo ships on the basis of Ikeda's method and its limitation. In: Proceedings of the 10th international conference on stability of ships and ocean vehicles, (STAB2009), St. Petersburg, Russia, pp 387–398
8. Oliva-Remola A, Pérez-Rojas L (2017) Contributions on roll damping coefficient for fishing vessels. In: Proceedings of the 16th international ship stability workshop, (ISSW2017), Belgrade, Serbia, pp 207–212
9. Oliveira MCd, de Barros Mendes Kassar B, Gomes Coelho LC, Vieira Monteiro F, Torres de Santis R, Rodriguez Castillo CA, de Almeida Santos Neves M, Polo JCF, Themistocles Esperança PdT (2019) Empirical and experimental roll damping estimates for an oil tanker in the context of the 2nd generation intact stability criteria. *Ocean Eng* 189, 106291

# A Pragmatic Approach to Roll Damping



Jakub Cichowicz and Dracos Vassalos

**Abstract** Roll damping is probably the most intriguing of the components of hydrodynamic reaction in ship dynamics. It is also a problematic one—small, nonlinear, difficult to measure or predict and crucially, a key determinant of ship stability. Undoubtedly, some of the problems in computing or predicting roll damping are intrinsic. It can be argued, however, that most of the difficulties do not originate from physical anomalies of energy dissipation in roll but are due to fundamental flaws in the approach to roll damping estimation or measurement. It appears that the root causes of these flaws stem from three concepts central to analysis of hydrodynamic reaction in roll: decomposition of the hydrodynamic reaction moment to added moment of inertia and roll damping moment, the assumption of small-amplitude motions, and the inevitable coupling of roll with other modes of motion. In this paper, the authors present a pragmatic approach to these fundamental concepts and discuss the implication of incorrect assumptions, pertaining to definition, measurement, calculation and use of roll damping in intact and damaged ship dynamics.

**Keywords** Roll motion · Damping · Hydrodynamics

## Abbreviations

$A$	A point on the natural axis of rotation
$a_{ij}$	Added mass/inertia coefficient in $j$ -th into $i$ -th mode of motion
$B$	Centre of buoyancy
$B$	Beam of the cylinder
$B$	Damping matrix

---

J. Cichowicz (✉)  
DNV AS, Høvik, Norway  
e-mail: [jakub.cichowicz@dnv.com](mailto:jakub.cichowicz@dnv.com)

D. Vassalos  
University of Strathclyde, Glasgow, Scotland  
e-mail: [d.vassalos@strath.ac.uk](mailto:d.vassalos@strath.ac.uk)

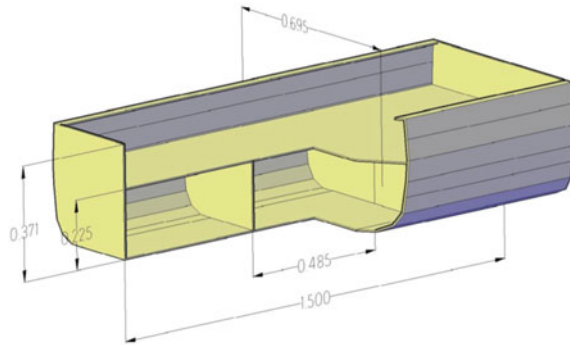


$C$	Stiffness matrix
$b_{ij}$	Damping coefficient in j-th into i-th mode of motion
$c_{ij}$	Stiffness (restoring) coefficient in j-th into i-th mode of motion
$F_i$	Lateral component of the rigid body's inertia force
$F_{hy}$	Lateral component of the hydrodynamic reaction force
$F_{hz}$	Vertical component of the hydrodynamic reaction force
$G$	Centre of gravity of the rigid body
$I$	Identity matrix
$I_{44}$	Moment of inertia of the rigid body (about centre of gravity)
$m$	Mass of the rigid body
$M$	Metacentre
$M_A$	Added inertia matrix
$\mathbf{M}_h$	Moment of the hydrodynamic reaction (variables in bold typeface denote vectors)
$\mathbf{M}_{44}$	Moment to sustain motion
$M_{RB}$	Tensor of inertia of the rigid body
$O$	Origin of the inertial coordinate system and the origin of the body-fixed coordinate system
$P$	Pivoting point of the forcing apparatus
$P$	Power function of the dissipative forces
$\mathbf{Q}$	Vector of the external excitation
$\mathbf{q}, \dot{\mathbf{q}}, \ddot{\mathbf{q}}$	Vector of generalised coordinates, generalised velocity and acceleration
$R$	Kinematic constraint
$T$	Total kinetic energy of the system
$T_A$	Kinetic energy of the fluid domain
$T_{RB}$	Kinetic energy of the rigid body
$V$	Potential energy of the rigid body
$\mathbf{v}$	Velocity of the rigid body
$\mathbf{x}$	Vector of unknown hydrodynamic coefficients
$y$	Lateral displacement of the origin of the body-fixed coordinate system
$y_G$	Lateral displacement of the rigid body's centre of gravity
$z$	Vertical displacement of the origin of the body-fixed coordinate system
$z_G$	Vertical displacement of the rigid body's centre of gravity
$\lambda$	Lagrange multiplier
$\phi$	Roll angle
$\nabla$	Displacement of the cylinder

## 1 Motivation

The motivation for and content of this paper derives from some of the journal and conference articles on roll damping published in recent years. Considering the STAB

**Fig. 1** Section and main particulars of the tested cylinder



Conference<sup>1</sup> papers and the most recent research projects alone, it is apparent that as a research topic roll damping attracts considerable attention. The problems addressed by researchers vary from uncertainty assessment in deriving critical damping from roll decay tests, estimation of damping from roll decay or forced roll. Both numerical and physical experiments are often conducted to the highest of standards with the help of sophisticated equipment and the most advanced analytical techniques. Unfortunately, it appears that many of the experiments in hydrodynamics of roll motion put emphasis on technicalities rather than the actual physics of the problem. Consequently, in spite of the perfect execution, the experiments per se are ill conditioned. Hence, whilst numbers are produced with remarkable efficiency and accuracy, understanding of the nature of the problem is not being advanced. It appears that in the pursuit of finding a perfect solution the effort is being expended on solving the wrong problem. In this respect, it is a good opportunity to have a more pragmatic view at the problem in hand.

## 2 The Experiment

The following discussion is based on the physical experiments conducted in 2009/2010 at the hydrodynamic laboratory<sup>2</sup> of the Department of Naval Architecture, Ocean and Marine Engineering of the University of Strathclyde. The main objective of the experiments involved determining the hydrodynamic reaction in harmonic roll motion of an unconstrained cylindrical body (Fig. 1) forced to oscillate in calm water (Fig. 2) by an internal gyroscopic apparatus. The measurements, conducted in intact and damaged (flooded) conditions were reported in Ref. [2]

<sup>1</sup> This refers to the proceedings of both, the International Conference on Stability of ships and Ocean Vehicles (STAB conference) and the International Ship Stability Workshops (ISSW).

<sup>2</sup> Kelvin Hydrodynamic Laboratory.

**Fig. 2** A photograph of the model taken during the test in intact condition



### 3 Mathematical Modelling

Figure 4 shows a free-body diagram of the system under consideration. Given the cylindrical shape of the body (symmetric with respect to the centre-plane and the midship-section) the system is represented as a 3 DoF (degrees of freedom) harmonic oscillator with the sway and heave resulting from the coupling with roll motion (i.e. sway and heave are roll-induced). It is noteworthy, however, that due to the shape of the body and relatively small amplitudes of motions, the contributions from heave can be considered insignificant and for that reason the system can be reduced to 2 DoF oscillator.

The most common way of describing the dynamics of such a system is to follow the vectorial formalism of Newton and d'Alembert. On the other hand, although the system formally has three (and practically two) degrees of freedom these degrees of

**Fig. 3** Schematic of the model configuration

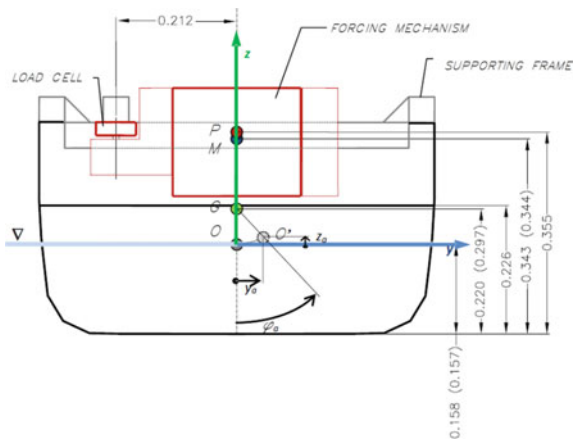
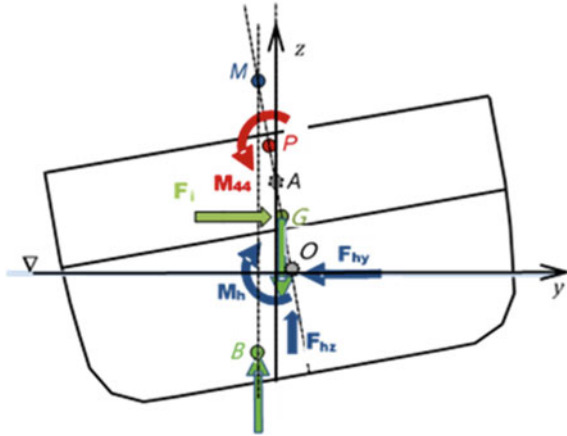


**Fig. 4** Free body diagram of the system under consideration. The moment  $M_{44}$  is a moment to sustain motion



freedom are not independent. Hence, the system under consideration is a single DoF oscillator with roll angle being the sole independent coordinate. This is because both sway and heave are resultant modes of motion, related to the roll motion by means of strict relationships (i.e. kinematic constraints). Furthermore, the system consists of two entirely distinct sub-systems, namely the fluid domain (represented in the free-body diagram by the forces and moment of hydrodynamic reaction  $F_{hy}$ ,  $F_{hz}$  and  $M_h$ ) and the rigid body (all other forces in the free-body diagram). For these reasons, it is more convenient to adopt the Lagrange method which allows for deriving the equations of motions of the compound system from scalar quantities and handling the kinematic constraints by the simple and elegant multipliers method.

It is convenient to commence the derivation by looking at the unconstrained system first, and noting that the motion of the rigid body can be described as translations of its centre of gravity (CG) and the rotation about an axis, passing through its centre of gravity (CG) and parallel to the  $Ox$  axis of the inertial coordinate systems (perpendicular to the cross-section of the rigid body). In the inertial frame of reference the translations of the body are given as  $y_G = y - \overline{OG} \sin \phi$  and  $z_G = z + \overline{OG} \cos \phi$ . The  $y$  and  $z$  are coordinates the origin of the body-fixed coordinate system which at rest coincides with the origin  $O$  of the inertial coordinate system,  $\overline{OG}$  is the vertical distance between centre of gravity of the body (CG) and the origin  $O$  while  $\phi$  is the angle of roll. The vector of generalised coordinates is thus given as  $\mathbf{q} = [y \ z \ \phi]^T$ . Considering small to moderate roll angles the trigonometric identities can be reduced by assuming that  $\sin \phi \cong \phi$  and  $\cos \phi \cong 1$  hence the vector  $\mathbf{v}$  representing the velocity of the rigid body can be expressed in terms of the generalised velocities  $\dot{\mathbf{q}}$ :

$$\mathbf{v} = \begin{bmatrix} \dot{y}_G \\ \dot{z}_G \\ \dot{\phi} \end{bmatrix} = \begin{bmatrix} \dot{y} - \overline{OG} \dot{\phi} \cos \phi \\ \dot{z} - \overline{OG} \dot{\phi} \sin \phi \\ \dot{\phi} \end{bmatrix} \cong \begin{bmatrix} \dot{y} - \overline{OG} \dot{\phi} \\ \dot{z} - \overline{OG} \dot{\phi} \phi \\ \dot{\phi} \end{bmatrix} \quad (1)$$

Furthermore, as the axes of the inertial coordinate system coincide with the body's principal axes of inertia the rigid body's tensor of inertia is given as  $\mathbf{M}_{RB} = \mathbf{I} \cdot [m \ m \ I_{44}]^T$ , where  $\mathbf{I}$  is a  $3 \times 3$  identity matrix,  $m$  is the body's mass and  $I_{44}$  is the body's moment of inertia about the axis passing through CG and parallel to the axis  $Ox$  of the inertial frame of reference. Thus, kinetic energy of the rigid body,  $T_{RB}$ , is given as:

$$T_{RB} = \frac{1}{2} \mathbf{v}^T \mathbf{M}_{RB} \mathbf{v} = \frac{1}{2} \left( m (\dot{y} - \overline{OG} \dot{\phi})^2 + m (\dot{z} - \overline{OG} \dot{\phi})^2 + I_{44} \dot{\phi}^2 \right) \quad (2)$$

Potential energy  $V$  of the rigid body has an implicit form  $\frac{\partial V}{\partial \mathbf{q}} = \mathbf{C} \mathbf{q}$  where  $\mathbf{C}$  is a stiffness (restoring) matrix:

$$\frac{\partial V}{\partial \mathbf{q}} = \mathbf{C} \mathbf{q} = \begin{bmatrix} 0 & 0 & 0 \\ 0 & c_{33} & 0 \\ 0 & 0 & c_{44} \end{bmatrix} \begin{bmatrix} y \\ z \\ \phi \end{bmatrix} = \begin{bmatrix} 0 \\ c_{33} z \\ c_{44} \phi \end{bmatrix} \quad (3)$$

Kinetic energy of the fluid domain is represented as  $T_A = \frac{1}{2} \dot{\mathbf{q}}^T \mathbf{M}_A \dot{\mathbf{q}}$  where  $\mathbf{M}_A$  is a  $3 \times 3$  added inertia matrix with coefficients  $a_{ij}$  corresponding to the added mass and inertia in the  $i$ th direction due to motions in  $j$ th direction (i.e.  $a_{34}$  is the added mass of roll into heave while  $a_{43}$  is the added inertia of heave into roll, etc.). Physically, the added mass and inertia correspond to the components of pressure-induced forces and moments due to harmonic oscillations of the body. These added (virtual) forces and moments are in phase with the body's acceleration [4]. The added mass and inertia coefficients are symmetrical (i.e.  $a_{ij} = a_{ji}$ ) thus in general case of 3 DoF oscillations the added inertia matrix  $\mathbf{M}_A$  has nine distinct coefficients. In the case reported herein, due to the symmetry of the body and the nature of the excitation (i.e. the pure moment about an axis parallel to the axis  $Ox$  of the inertial frame of reference) some of the coefficients will vanish. Specifically, pure heave cannot induce any sway (i.e.  $a_{23} = 0$ ) or roll (i.e.  $a_{43} = 0$ ) and furthermore, pure sway cannot introduce any heave (i.e.  $a_{32} = 0$ ). Thus, following this reasoning kinetic energy of the fluid domain is represented as

$$\begin{aligned} T_A &= \frac{1}{2} \dot{\mathbf{q}}^T \mathbf{M}_A \dot{\mathbf{q}} = \frac{1}{2} [\dot{y} \ \dot{z} \ \dot{\phi}] \begin{bmatrix} a_{22} & 0 & a_{24} \\ 0 & a_{33} & a_{34} \\ a_{42} & 0 & a_{44} \end{bmatrix} \begin{bmatrix} \dot{y} \\ \dot{z} \\ \dot{\phi} \end{bmatrix} \\ &= \frac{1}{2} (a_{22} \dot{y}^2 + a_{33} \dot{z}^2 + a_{44} \dot{\phi}^2 + (a_{42} + a_{24}) \dot{y} \dot{\phi} + a_{34} \dot{z} \dot{\phi}) \end{aligned} \quad (4)$$

The non-conservative forces (i.e. damping) are derived from a power function  $P$  given as  $P = \frac{1}{2} \dot{\mathbf{q}}^T \mathbf{B} \dot{\mathbf{q}}$  where  $\mathbf{B}$  is a  $3 \times 3$  matrix of damping coefficients  $b_{ij}$ . The damping matrix shares certain properties with the added inertia matrix  $\mathbf{M}_A$ —it is symmetrical (i.e.  $b_{ij} = b_{ji}$ ) and some of its components can be reduced following the reasoning in relation to the geometry of the body and the nature of the excitation.

This allows to express the power function  $P$  in the following way:

$$\begin{aligned}
 P &= \frac{1}{2} \dot{\mathbf{q}}^T \mathbf{B} \dot{\mathbf{q}} = \frac{1}{2} [\dot{y} \quad \dot{z} \quad \dot{\phi}] \begin{bmatrix} b_{22} & 0 & b_{24} \\ 0 & b_{33} & b_{34} \\ b_{42} & 0 & b_{44} \end{bmatrix} \begin{bmatrix} \dot{y} \\ \dot{z} \\ \dot{\phi} \end{bmatrix} \\
 &= \frac{1}{2} (b_{22} \dot{y}^2 + b_{33} \dot{z}^2 + b_{44} \dot{\phi}^2 + (b_{24} + b_{42}) \dot{y} \dot{\phi} + b_{34} \dot{z} \dot{\phi}) \quad (5)
 \end{aligned}$$

The three scalar quantities—kinetic energy of the compound system  $T = T_{RB} + T_A$ , potential energy  $V$  and the power function of dissipative forces allow to formulate the Euler–Lagrange equation for the unconstrained and non-conservative system where the external excitation is represented by the vector  $\mathbf{Q} = [0 \ 0 \ M_{44}]^T$ :

$$\frac{d}{dt} \left( \frac{\partial T}{\partial \dot{\mathbf{q}}} \right) + \frac{\partial V}{\partial \mathbf{q}} + \frac{\partial P}{\partial \dot{\mathbf{q}}} = \mathbf{Q} \quad (6)$$

The above equation represents an unconstrained system where all the generalised coordinates are independent. However, the system examined herein has only one independent coordinate—roll angle  $\phi$ —and the other two coordinates, i.e. sway and heave can be expressed as functions of roll angle. Such relationships between the coordinates represent constraints for the motion. During the particular experiments reported here it was noted that the cylinder oscillated about an axis passing through a point  $A$  whose coordinates remained virtually constant throughout the motion, i.e.  $y_A(t) = \text{const}$  and  $z_A(t) = \text{const}$ . In literature such instantaneous axis of rotation is known as *natural axis of rotation*.

The fact that the coordinates of point  $A$  remain unchanged during the motion allows formulating the following relationships between the coordinates:

$$y - z_A \cos \phi = y - \overline{OA} \sin \phi = 0 \quad (7)$$

and

$$z + z_A \cos \phi - z_A = z + \overline{OA} (\cos \phi - 1) = 0 \quad (8)$$

It follows immediately from the latter relationship that for the small angles of roll the heave amplitude,  $z$ , is small and therefore the heave motion can be neglected and the former relationship can be simplified:

$$y - \overline{OA} \phi = 0 \quad (9)$$

The Euler–Lagrange equation given by Eq. (6) represents an over-determined system of equations with three scalar equilibrium conditions (sway, heave and roll equations) and just a single independent variable (roll angle). The method of Lagrange multipliers allows for the including the forces maintain the constraints directly, by

augmenting the Euler–Lagrange equation with an additional term  $\sum \lambda_k \frac{\partial R_k}{\partial \mathbf{q}}$  where  $R_k$  represent all the constraints ( $k = 1 \dots n$ ) and  $\lambda_k$  are unknown multipliers.<sup>3</sup> In the present case the constraints are  $R_1 = y - \overline{OA} \sin \phi$  and  $R_2 = z + \overline{OA}(\cos \phi - 1)$  thus the additional terms in the Euler–Lagrange equations are

$$\lambda_1 \frac{\partial R_1}{\partial \mathbf{q}} + \lambda_2 \frac{\partial R_2}{\partial \mathbf{q}} \quad (10)$$

Algebraically, the augmented Euler–Lagrange equation corresponds to a determined set of three equations with three unknowns (independent variables):  $\phi$ ,  $\lambda_1$  and  $\lambda_2$ .

However, since the second constraint is trivial for the small angles of roll the sway-roll system of equations require single constrain  $R = y - \overline{OA}\phi$  and the single multiplier  $\lambda$ :

$$\frac{d}{dt} \left( \frac{\partial T}{\partial \dot{\mathbf{q}}} \right) + \frac{\partial V}{\partial \mathbf{q}} + \frac{\partial P}{\partial \dot{\mathbf{q}}} + \lambda \frac{\partial R}{\partial \mathbf{q}} = \mathbf{Q} \quad (11)$$

In scalar form, the augmented Euler–Lagrange equations of motion take the following form:

$$\begin{aligned} m(\ddot{y} - \overline{OG}\ddot{\phi}) + a_{22}\ddot{y} + \frac{1}{2}(a_{24} + a_{42})\ddot{\phi} + b_{22}\dot{y} + \frac{1}{2}(b_{24} + b_{42})\dot{\phi} - \lambda = 0 \\ I_{44}\ddot{\phi} - m(\ddot{y} - \overline{OG}\ddot{\phi})\overline{OG} + a_{44}\ddot{\phi} + \frac{1}{2}(a_{24} + a_{42})\ddot{y} + b_{44}\dot{\phi} \\ + \frac{1}{2}(b_{24} + b_{42})\dot{y} + c_{44}\phi + \lambda \overline{OA} = M_{44} \end{aligned} \quad (12)$$

These equations can be simplified by accounting for the symmetry of the hydrodynamic coefficients  $a_{ij}$  and  $b_{ij}$  and by maintaining consistent notation (i.e. with  $a_{i2}$  and  $b_{i2}$  coefficients standing by the sway derivatives and  $a_{i4}$  and  $b_{i4}$  with the respective roll angle derivatives):

$$\begin{aligned} m(\ddot{y} - \overline{OG}\ddot{\phi}) + a_{22}\ddot{y} + a_{24}\ddot{\phi} + b_{22}\dot{y} + b_{24}\dot{\phi} = \lambda \\ I_{44}\ddot{\phi} - m(\ddot{y} - \overline{OG}\ddot{\phi})\overline{OG} + a_{44}\ddot{\phi} + a_{42}\ddot{y} + b_{44}\dot{\phi} + b_{42}\dot{y} \\ + c_{44}\phi + \lambda \overline{OA} = M_{44} \end{aligned} \quad (13)$$

---

<sup>3</sup> In variational mechanics the method of Lagrangian multipliers allows for replacing the given kinematical conditions by forces maintaining those constraints. As explained in [5] “these forces are exerted through a microscopic violation of the constraints, and the factor  $\lambda$  can be interpreted as a measure of this violation”.

The first of the above equations describes the lateral force balance (sway equilibrium) with the first term corresponding to the inertia of the rigid body followed by the force of hydrodynamic reaction  $F_{hy}$ . The force preventing the lateral displacement of the natural axis of rotation is given by  $\lambda$  (in this particular case it is that  $\lambda \frac{\partial R}{\partial y} = \lambda$ ).

The second of the above equations represents the force equilibrium in roll with the last term on LHS ( $\lambda \frac{\partial R}{\partial \phi} = \lambda \overline{OA}$ ) corresponding to the moment necessary to maintaining the constant elevation of the natural axis of rotation ( $\overline{OA}$ ).

## 4 Analysis

### 4.1 Hydrodynamic Coefficients

Algebraically the system of equations given by (13) is determined because it consists of two equations and two independent variables ( $\phi$  and  $\lambda$ ). However, the purpose of the experiment is to derive the forces and moments of hydrodynamic reaction (i.e.  $F_{hy}$  and  $M_{hy}$  for the case of the 2 DoF system) while measuring the moment to sustain motion and the motion itself. The hydrodynamic reaction is a function of unknown coefficients  $a_{ij}$  and  $b_{ij}$  which results in eight unknowns. The additional unknown comes in the form of the Lagrangian multiplier  $\lambda$  and therefore the system of equations has nine unknowns:  $a_{22}, a_{24}, a_{42}, a_{44}, b_{22}, b_{24}, b_{42}, b_{44}$  and  $\lambda$ . On the other hand, in harmonic oscillations the force and moment equilibria conditions can be expanded into two orthogonal terms each, which results in the system of four linearly independent equations with nine unknowns.

The undetermined system of equations has infinite number of solutions, it is possible however to select one solution which meets certain auxiliary conditions. A common strategy is to select the solution that is closest to the null vector, i.e. the solution that minimises the norm (length) of the vector  $\mathbf{x}$  whose components are the unknown variables. However, the problem at hand can be further restricted by noting that the experiment was conducted on the *unconstrained* system. This implies that the force to maintain the constraint should vanish, i.e.  $\lambda = 0$ . It is an intuitive condition for the system oscillating about the *natural* axis of rotation, i.e. axis not imposed by some *external* constraint but resulting from the natural equilibrium. The condition requiring the force maintaining the constraint to vanish allows to re-write the system (13) into the following form:

$$\begin{aligned}
 a_{22}\ddot{y} + a_{24}\ddot{\phi} + b_{22}\dot{y} + b_{24}\dot{\phi} &= -m(\ddot{y} - \overline{OG}\ddot{\phi}) \\
 a_{22}\overline{OA}\ddot{y} + a_{24}\overline{OA}\ddot{\phi} + a_{42}\ddot{y} + a_{44}\ddot{\phi} + b_{22}\overline{OA}\dot{y} + b_{24}\overline{OA}\dot{\phi} + b_{42}\dot{y} \\
 + b_{44}\dot{\phi} &= M_{44} - I_{44}\ddot{\phi} - c_{44}\phi - m(\ddot{y} - \overline{OG}\ddot{\phi})(\overline{OA} - \overline{OG})
 \end{aligned} \tag{14}$$



The first of the above equation is the auxiliary requirement, i.e. the condition under which the force to maintain the constraint vanishes (i.e.  $\lambda = 0$ ) while the second equation is the formulation of the actual problem. Furthermore, it is noteworthy that the second of the above equations is augmented with the term  $\lambda \overline{OA}$  but since the first equation is a condition under which  $\lambda$  vanishes the additional terms augmenting the second equation must sum up to zero. The solution to the above system of equations is a vector  $\mathbf{x}$  such that  $\|\mathbf{x}\| = \min$  (where  $\mathbf{x} = [a_{22} \ a_{24} \ a_{42} \ a_{44} \ b_{22} \ b_{24} \ b_{42} \ b_{44}]^T$ ) and for which  $\lambda = 0$ .

Most interestingly, the minimum norm solution under the condition of the self-maintaining constraint is a solution in which the sway and sway into-roll terms vanish (i.e. with  $a_{i2} \cong b_{i2} \cong 0$ ). This solution may be surprising at first, but it is an outcome which should have been anticipated since the investigated system is a single degree of freedom oscillator. In the absence of any external sway or heave excitation the dynamic equilibrium cannot depend on sway and heave coefficients (neither the direct sway/heave nor the coupling sway/heave into roll coefficients). The system of equations (14) has a single solution (i.e. it is fully determined) and all non-zero hydrodynamic coefficients can be derived directly from the simplified equations:

$$\begin{aligned}
 a_{24}\ddot{\phi} + b_{24}\dot{\phi} &= -m(\ddot{y} - \overline{OG}\ddot{\phi}) \\
 a_{44}\ddot{\phi} + b_{44}\dot{\phi} &= M_{44} - I_{44}\ddot{\phi} - c_{44}\phi + m(\ddot{y} - \overline{OG}\ddot{\phi})\overline{OG}
 \end{aligned}
 \tag{15}$$

It is important to note that these simple equations hold for both intact and flooded cylinder measurements although in the latter case, at frequencies very close to the sloshing resonance, the dynamics of the system becomes a little more complex and the simplified kinematic constraint  $y = \overline{OA}\phi$  needs to account for the phase difference between roll and sway.<sup>4</sup>

Figures 5 and 6 present the results of the estimation of the hydrodynamic coefficients.

It is important to note that the damping coefficient obtained for flooded body becomes negative for the frequencies near and beyond the sloshing resonance. This obviously cannot be correct as damping, being a form of energy dissipation cannot be negative. The authors are unable to offer a convincing explanation of these results. Nevertheless, the significant shift in the behaviour of the system was observed at that range of frequencies, which clearly manifested itself in a change in the roll phase lag as reported in [2]. Therefore, it can be assumed that in the presence of significant

---

<sup>4</sup> It is noteworthy, that during the oscillations within the range of frequencies close to the sloshing resonance the action of floodwater causes the damaged cylinder to drift with constant (albeit varying with the frequency) velocity. In flooded condition part of the cylinder's shell is removed on one side which allows for free-flooding of the internal compartment located at the mid-length of the cylinder. The weight of the model was reduced in comparison with the "intact case" to maintain the same draught in both conditions. In the present analysis the effect of the drift could be neglected on the account the constant drift velocity (i.e. the inertial system of reference was also moving with the drifting body) but the significant force generated by the floodwater and causing such an effect should be studied in details.

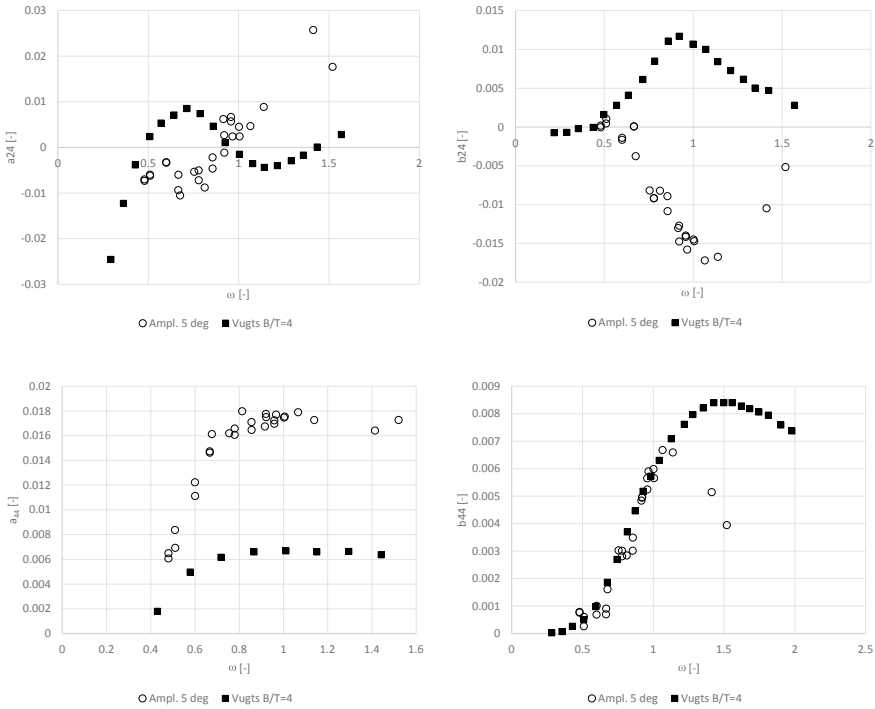


**Fig. 5** Hydrodynamic coefficients for the intact cylinder. The experimental results by Vugts’ (for the rectangular cylinder with the aspect ratio  $B/T = 4$ ) are shown for reference [6]. Non-dimensional forms:  $\omega(0.5Bg^{-1})^{0.5}$ ,  $a_{24}(mB)^{-1}$ ,  $a_{44}(mB^2)^{-1}$ ,  $b_{24}(mB)^{-1}(0.5Bg)^{0.5}$  and  $b_{44}(mB^2)^{-1}(0.5Bg)^{-0.5}$

sloshing the simplified model discussed herein ceases to capture the dynamics of the system accurately.

### 4.2 Phase Difference Between Roll and Roll-induced Sway

The results of measurements in both intact and damaged conditions, show a considerable phase difference between roll and roll-into-sway motions (i.e. difference in phase angles measured with respect to moment  $M_{44}$ ). The phase difference is particularly large in the flooded case at the sloshing resonance frequency (i.e. at about 6.5 rad/s in the experiment presented here) where it indicates strong damping in the roll-into-sway coupled mode of motion (Fig. 8).

It will be shown in the following section that the phase difference between sway and roll play influences all the important parameters behind the dynamic equilibrium.

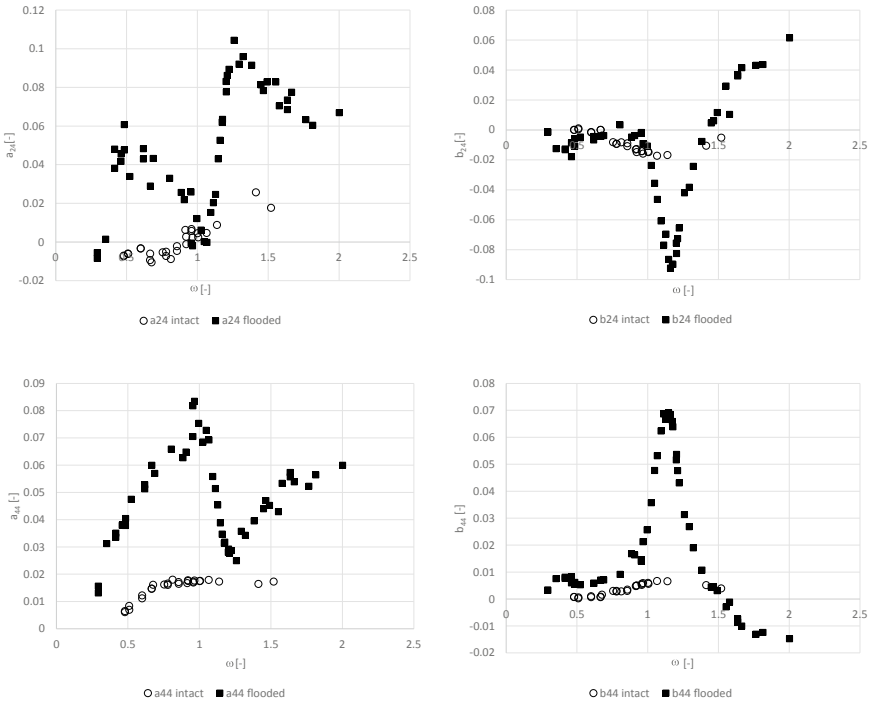


Fig. 6 Hydrodynamic coefficients for the flooded cylinder

### 4.3 Axis of Rotation

An analysis presented in [1] shows that the natural axis of rotation passes through the centre of mass of the compound system comprising the rigid body and the fluid domain. Hence, the elevation of the axis of rotation above the calm water plane is given as:

$$\overline{OA} = \frac{m\overline{OG} - a_{24}}{m + a_{22}} \tag{16}$$

It is noteworthy that the above formula can be derived directly from the first equation of the system (13), i.e. the lateral force balance, when  $\lambda = 0$ . Furthermore, in pure roll  $a_{22} = 0$ , hence the above equation assumes a simpler form:

$$\overline{OA} = \frac{m\overline{OG} - a_{24}}{m} = \overline{OG} - \frac{a_{24}}{m} \tag{17}$$

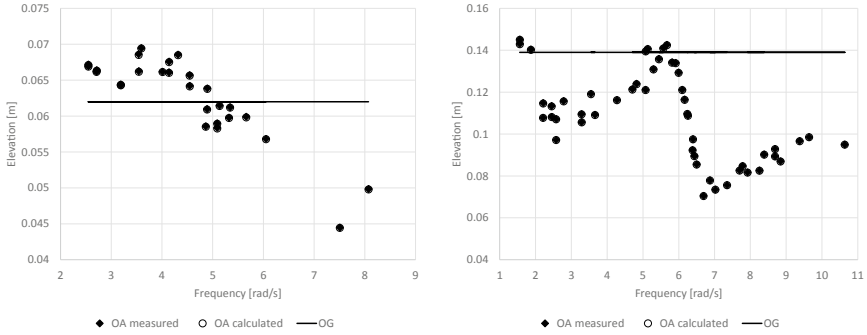


**Fig. 7** Calculated and measured elevation of the natural axis of rotation for intact (left) and damaged cylinder

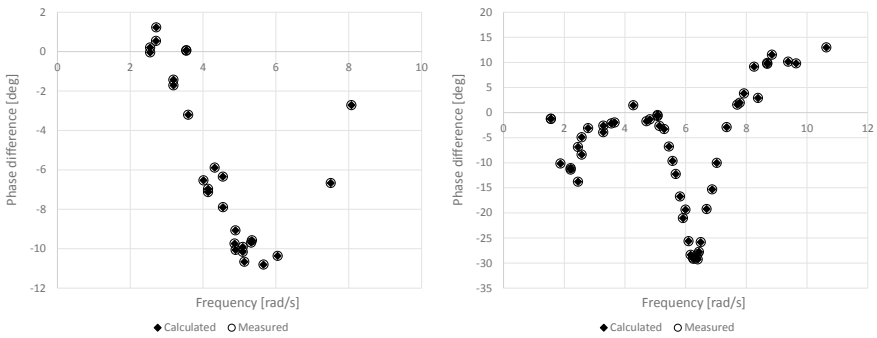


**Fig. 8** Calculated and measured phase difference between sway and roll

The above equation gives an approximated elevation of the axis of rotation assuming the perfectly in-phase roll and sway motions. Accounting the phase difference between sway and roll resulting from damping in coupled motion of roll into sway,  $b_{24}$  allows incorporating of the additional terms in the lateral force balance and the elevation of the axis of rotation can be calculated exactly:

$$\overline{OA} = \frac{m\overline{OG} - a_{24}}{m} \cdot \frac{1}{\cos(\varepsilon_y - \varepsilon_\phi)} \tag{18}$$

where  $\varepsilon_y$  and  $\varepsilon_\phi$  are the phase angles of sway and roll, respectively. Comparison of the measured<sup>5</sup> and calculated elevation of the axis of rotation is presented in Fig. 7.

<sup>5</sup> The elevation of the axis of rotation was measured indirectly during the experiments by determining the point in the model’s centreplane for which the amplitude of lateral oscillations would vanish.

It is noteworthy that for a hypothetical hull form for which the coupling added mass and damping would vanish (i.e.  $a_{24} = b_{24} = 0$ ) the natural axis of rotation would pass through the centre of gravity of the rigid body (i.e. it would be that  $\overline{OA} = \overline{OG}$ ).

## 5 Synthesis

The discussion thus far has been centred on rather fragmented observations, which clearly showed that

- The simple roll equation together with the auxiliary condition representing the lateral force balance and given by (15) holds for intact and flooded cylinder.
- Roll-induced sway is not exactly in phase with roll because of the presence of damping in the coupling of roll-into-sway. As a result, the body is undergoing sideways motions even if the external excitation has a form of pure moment.
- Elevation of the natural axis of rotation is determined by the mass of the body, its centre of gravity as well as the added mass and damping of roll-into-sway. Consequently, the elevation is a function of frequency of the oscillation.

To synthesise these findings, it is convenient to commence with the kinematic constraint  $y - \overline{OA}\phi = 0$  and note that it holds exactly only in the case of roll and sway perfectly in phase. The occurrence of phase difference between these modes of motion causes violation of the constraint. To avoid the violation, the constraint should be formulated as follows

$$y - \overline{OA}\phi \cos(\varepsilon_y - \varepsilon_\phi) - \frac{\overline{OA}}{\omega} \dot{\phi} \sin(\varepsilon_y - \varepsilon_\phi) = 0 \quad (19)$$

Furthermore, it can be shown that  $b_{24} = m\omega\overline{OA} \sin(\varepsilon_y - \varepsilon_\phi)$  which together with (18) allows the following reformulation of the constraint:

$$y - \left( \overline{OG} - \frac{a_{24}}{m} \right) \phi - \frac{b_{24}}{m\omega^2} \dot{\phi} = 0 \quad (20)$$

Similar manipulations allow to formulate the expression describing the relationship between the phase angles of roll and sway. This relationship takes the following form

$$\varepsilon_y - \varepsilon_\phi = \text{atan} \frac{b_{24}}{\omega(m\overline{OG} - a_{24})} \quad (21)$$

Furthermore, it can be shown that the roll damping coefficient  $b_{44}$  is a function of the added mass of roll into sway,  $a_{24}$ :

$$b_{44} = -\frac{M_a \sin \varepsilon_\phi}{\phi_a \omega} - \omega(m\overline{OG} - a_{24})\overline{OG} \tag{22}$$

where  $M_a$  is the amplitude of the moment to sustain motion and  $\phi_a$  stands for the amplitude of roll motion.

The above equation highlights the intimate relationship between the pressure-induced component of the hydrodynamic reaction (i.e. proportional to  $a_{24}$ ) and the dissipative component of the hydrodynamic moment. This relationship would cease to exist should the roll-induced sway were perfectly in phase with roll.

All the formulae presented thus far aimed at formulating the relationships between various components of the motion and forces. However, what is more important from the global perspective is the comparison between the results for the intact and flooded cylinder. To this point, it was shown that both cases can be accurately described by the same mathematical model. Nevertheless, quantitatively the impact of floodwater on the dynamics of the tested system was profound. Firstly, the results show that the relative contribution from added inertia  $a_{44}$  in the flooded case is much higher than in intact case, and at frequencies approaching sloshing resonance it nearly matches the inertia of the rigid body. Secondly, sloshing and floodwater ingress/egress cause an immense increase in damping with the maximum magnitude of roll damping in flooded case being about tenfold the magnitude in the intact case. Similarly, the magnitude of damping in the coupled mode of motion is about five-fold the magnitude in the intact case.

Furthermore, the much larger variations in the elevation of the natural axis of rotation show clearly that any restraint forcing the motion about an arbitrary axis of rotation would introduce significant changes to the dynamics of the oscillating system. This would result in significant errors in predicting the roll damping (Fig. 9).

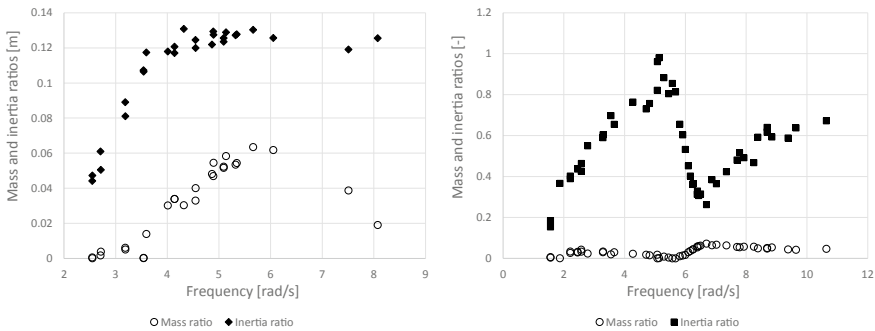


Fig. 9 Relative contributions from added mass and added inertia in intact and flooded case

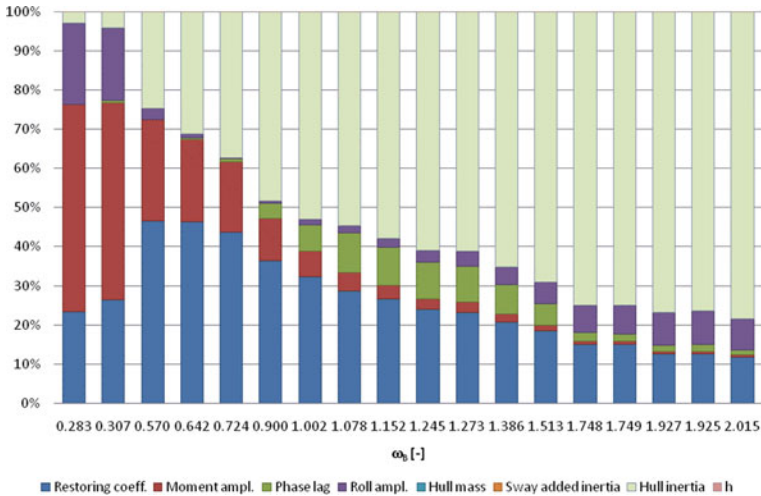


Fig. 10 Relative contributions to the total error in  $a_{44}$  coefficient

## 6 Errors and Uncertainty

With roll damping being such a small quantity and of such complex composition, any inaccuracies in measurements in model experiments, particularly linked to the restoring/inertia moments will have a large impact on the value of the hydrodynamic coefficient being derived. Specifically, the uncertainty study reported in [3] and elaborated further in [2] shows clearly that restoring coefficient, amplitude of external moment and hull inertia are dominant contributors to the uncertainty in estimates of roll added inertia, as shown in Figs. 10 and 11. In the case of roll damping coefficient, the key contribution comes from the phase lag between the excitation and response with some measurable influence from the magnitude of the forcing moment.

Some of the parameters derived in the foregoing exhibited noticeable scatter which resulted from the uncertainty in measured values, particularly near the resonance frequencies (of the cylinder and the sloshing). However, it should be noted that the scatter is a consequence of the measurement errors and not the mathematical models employed to derive the sought quantities. The experimental errors could be significantly reduced by measurements conducted on a bigger and stiffer model.

## 7 Concluding Remarks

The analysis presented in the foregoing can be summarised as follows

- All roll and roll-into-sway coefficients can be derived from the forced-roll experiments on a floating body through the system of equations (13).

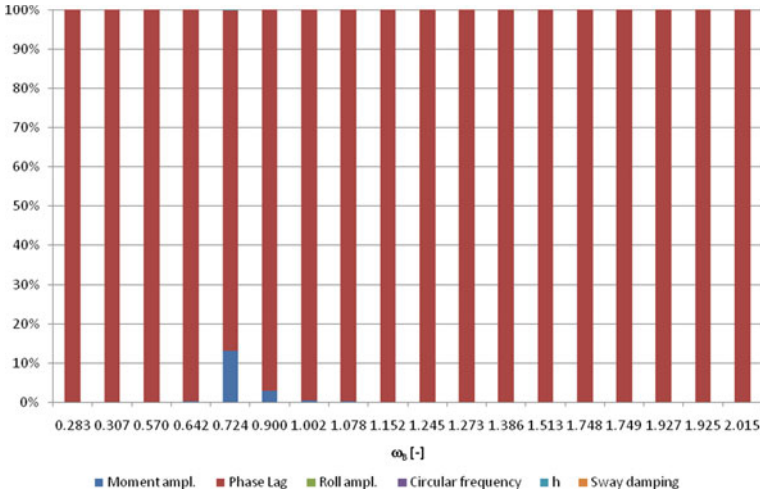


Fig. 11 Relative contributions to the total error in  $b_{44}$  coefficient

- Roll motion of an unconstrained cylinder oscillating in a free surface can be accurately described by a single degree of freedom model even in the flooded case. The right choice of coordinates and the robust method for handling constraints and auxiliary conditions allow for significant simplification of the mathematical model whilst maintaining its physical comprehensiveness.
- The oscillations about the natural axis of rotation maintain the kinematic relationship between sway and roll without any additional force necessary to maintain the constraint. In the natural configuration the dynamic equilibrium is maintained by the inertia of the rigid body and the roll-into-sway coupling component of the hydrodynamic reaction.
- The elevation of axis of rotation depends on the added mass coefficient  $a_{24}$  thus any hull fitting changing substantially the pressure distribution around the hull (i.e. added moment of inertia) such as bilge keels, will change the elevation of natural axis of rotation.
- Forcing the roll motion about an arbitrary axis will have a strong impact on the dynamic equilibrium of the system. The additional forces necessary will be needed to maintain the constraints  $\overline{OR} \neq \overline{OA}$  and  $\varepsilon_y = \varepsilon_\phi$  and unless these extra forces are properly accounted for they will lead to erroneous prediction of the hydrodynamic reaction and its components.

Last but not least, while working on this paper the authors were engaged in many rewarding discussions, which often focused on the discrepancies between the results reported herein and the works of Vugts. Undisputedly, there is a merit in such observation, however, the authors feel that the evident discrepancies overcast the heart of the argument. This is because the only similarity of this experiment to that of Vugts is that the authors tested a cylindrical body of a B/T ratio similar



to Vugts' rectangular cylinders ( $B/4 = 4$ ). This is where the similarities end. In previous papers, the authors indicated that the results show very weak (or virtually) no nonlinearities in damping and added inertia estimations based on the measurements on the unconstrained cylinder. This was in contrast with the Vugts results showing very strong nonlinearities even at relatively small roll angles (2 and 5°). In this paper, the authors focus on the relationship between the roll motion, roll-induced sway and the axis of rotation. The intention is to demonstrate that dynamic equilibrium is maintained by the moment to sustain motion, the rigid body inertia and the forces of hydrodynamic reaction. The equilibrium does not require any sway or sway into roll coupling as suggested by Vugts nor does it require any other external force to maintain the kinematic constraint (i.e. the coupling of roll into sway). On the other hand, the authors show how exactly changing the added mass coefficient of roll into sway,  $a_{24}$ , (e.g. by adding bilge keels) will change the roll damping coefficient and how that change would impact the centre of rotation. This becomes of particular significance if in our physical or numerical experiments we chose to force the rotations about an arbitrary axis which will introduce a force to maintain the new (and, in a way, artificial) constraint. In this context, the authors find the use of Lagrangian approach, allowing for the intricacies of dynamic equilibrium to unfold by their own without the need of any arbitrary assumptions, truly pragmatic.

## References

1. Balcer L (2004) Location of ship rolling axis. Polish Maritime Research, pp 3–7
2. Cichowicz J (2012) Hydrodynamics of an unconstrained cylinder in forced roll. University of Strathclyde, Glasgow
3. Cichowicz J, Jasionowski A, Vassalos D (2011) Uncertainty assessment in experiments on a floating body in forced roll. International Ship Stability Workshop, Washington DC
4. Fossen TI (1994) Guidance and control of ocean vehicles. John Wiley and Sons, New York
5. Lanczos C (1970) The variational principles of mechanics. Dover Publications Inc., New York
6. Vugts JH (1968) The hydrodynamic coefficients for swaying, heaving and rolling cylinders in a free surface. Delft Technological University, Delft

# **Damaged Stability**

# Regulatory, Design, Operational and Emergency Response Measures for Improving the Damage Survivability of Existing RoPax



Dracos Vassalos, Evangelos Boulougouris, Luis Guarin,  
and Andrzej Jasionowski

**Abstract** This paper describes the background and provides the rationale and the framework to embrace the whole spectrum of measures (regulatory, design, operational and emergency response) for improving the damage survivability of existing RoRo passenger vessels. The damage stability workshop elaborated here is the first step of a process initiated by INTERFERRY Europe to assess impact on/options for existing ships of increasing the required subdivision index R should IMO decide to apply new damage stability requirements retrospectively. This, in turn, would provide the motivation for instigating and establishing a framework and propose an approach for alternative compliance to account for the contribution made to damage survivability by operational and active damage control measures that could be undertaken in case of a flooding accident. This represents a step change both in the mind-set of naval architects and in safety legislation but the impact will be immense and mostly positive.

**Keywords** RoPax damage stability · Alternative means of compliance · Vulnerability management

---

D. Vassalos (✉) · E. Boulougouris  
Maritime Safety Research Centre (MSRC), University of Strathclyde, Glasgow, UK  
e-mail: [d.vassalos@strath.ac.uk](mailto:d.vassalos@strath.ac.uk)

E. Boulougouris  
e-mail: [evangelos.boulougouris@strath.ac.uk](mailto:evangelos.boulougouris@strath.ac.uk)

L. Guarin  
Brookes Bell, Liverpool, UK  
e-mail: [luis.guarin@brookesbell.com](mailto:luis.guarin@brookesbell.com)

A. Jasionowski  
SophusQuorum, Singapore, Singapore  
e-mail: [andrzej.jasionowski@sophusquorum.com](mailto:andrzej.jasionowski@sophusquorum.com)

## 1 Introduction

Recent discussions at IMO on the safety of passenger ships include a potential increase in the required subdivision index for all passenger ships. An initiative, started by INTERFERRY Europe, seeks to assess the impact of the above on existing vessels (if such changes were applied retrospectively) and propose an approach for alternative compliance based on a fair recognition and credit of the contribution to risk reduction afforded by operational and active damage control measures that would be undertaken in case of a flooding accident. This should be accounted for, in addition to the contribution made by traditional design measures. This approach was first presented in the 13th ISSW in BREST 2013 [1]. To this end, a tentative plan of action was prepared to carry out a study aimed at quantifying and validating the risk-reduction effectiveness potential of such measures. The proposal included a one-day workshop to discuss the context and the relevant issues on the subject as a first step in the process. This took place in London on 22 January 2014 with a participation of 19 persons representing 5 ferry operators, 1 class society, 1 yard, 2 Flag Administrations and a number of damage stability experts.

Following a brief description of the rationale in support of adopting an alternative compliance approach that accounts for all meritorious contributions to enhancing damage survivability, the paper focuses on the objectives of and the key outcomes from the damage stability workshop.

## 2 Background

Every time there is an accident with passenger ships, exposing their vulnerability to flooding as a result of collision/grounding accidents, societal outcry follows and industry and academia “buckle up”, delving for design improvements to address the Achilles heel of this ship type, namely inadequate damage stability. However, any such improvements are targeting mainly newbuildings, which comprise a small minority of the existing fleet. Therefore, state-of-the-art knowledge on damage stability is all but wasted, scratching only the surface of the problem and leaving thousands of ships with severe vulnerability, that is likely to lead to further (unacceptably high) loss of life. This problem is exacerbated still further, today more rapidly, as the pace of scientific and technological developments is unrelenting, raising understanding and capability to address damage stability improvements of newbuildings cost-effectively, in ways not previously considered. As a result, SOLAS is becoming progressively less relevant and unable to keep up with this pace of development. This has led to gaps and pitfalls, which not only undermine safety but inhibit progress.

However, lack of retrospectively applied legislation (supported by what is commonly known as the Grandfather Clause) is not the only reason for damage stability problems with passenger ships. Tradition should share the blame here. In

the quest for damage stability improvement, design (passive) measures have traditionally been the only means to achieve it in a measurable/auditable way (SOLAS 2009, Ch. II-1). However, in principle, the consequences from inadequate damage stability can also be reduced by operational (active) measures, which may be very effective in reducing loss of life (the residual risk). There are two reasons for this. The first relates to the traditional understanding that operational measures safeguard against erosion of the design safety envelop (possible increase of residual risk over time). The second derives from lack of measurement and verification of the risk reduction potential of any active measures. In simple terms, what is needed is the means to account for risk reduction by operational measures as well as measures that may be taken during emergencies. Such risk reduction may then be considered alongside risk reduction deriving from design measures.

Therefore, new measures for risk reduction (operational and in emergencies) should be considered in addition to design measures. What needs to be demonstrated and justified is the level of risk reduction and a way to account for it, the latter by adopting a formal process and taking requisite steps to institutionalise it.

### 3 Life-Cycle Risk Management

Traditionally regulations, as a risk control measure for damage stability improvement, always focus on design solutions, normally referred to as passive measures (**category 1 measures**), Fig. 1 [1]. Operational/active measures (**category 2 measures**) whilst abundant in SOLAS Ch. II-2 (e.g. damage control), have not been validated to the same level of rigour as category 1 measures. Finally, measures/systems focusing on emergency response (**category 3 measures**), such as Decision Support Systems for Crisis Management, Evacuation, LSA, Escape and Rescue, whilst fuelling debates on being effective risk control measures or not, the cost-effectiveness of their risk reduction potential has never been measured nor verified. One of the reasons for this, arguably, derives from the fact that because these measures are there to address 'residual' risk and residual risk is by definition small, therefore risk reduction is also perceived to be small. However, this could not be further from the truth. The second is again lack of measurement and verification of such risk reduction.

Considering the above, a life-cycle perspective offers a framework for a holistic approach to damage stability, focusing on life cycle and encompassing all 3 categories of risk control options, accounting for these based on IMO cost-effectiveness criteria. This assumes that the risk reduction potential of all measures in the three categories is known and this is where there is a big gap in this approach that needs to be overcome before such a process can be formalised and adopted. This constitutes the kernel of the work to be undertaken, with the workshop described in the following constituting and facilitating the first step.

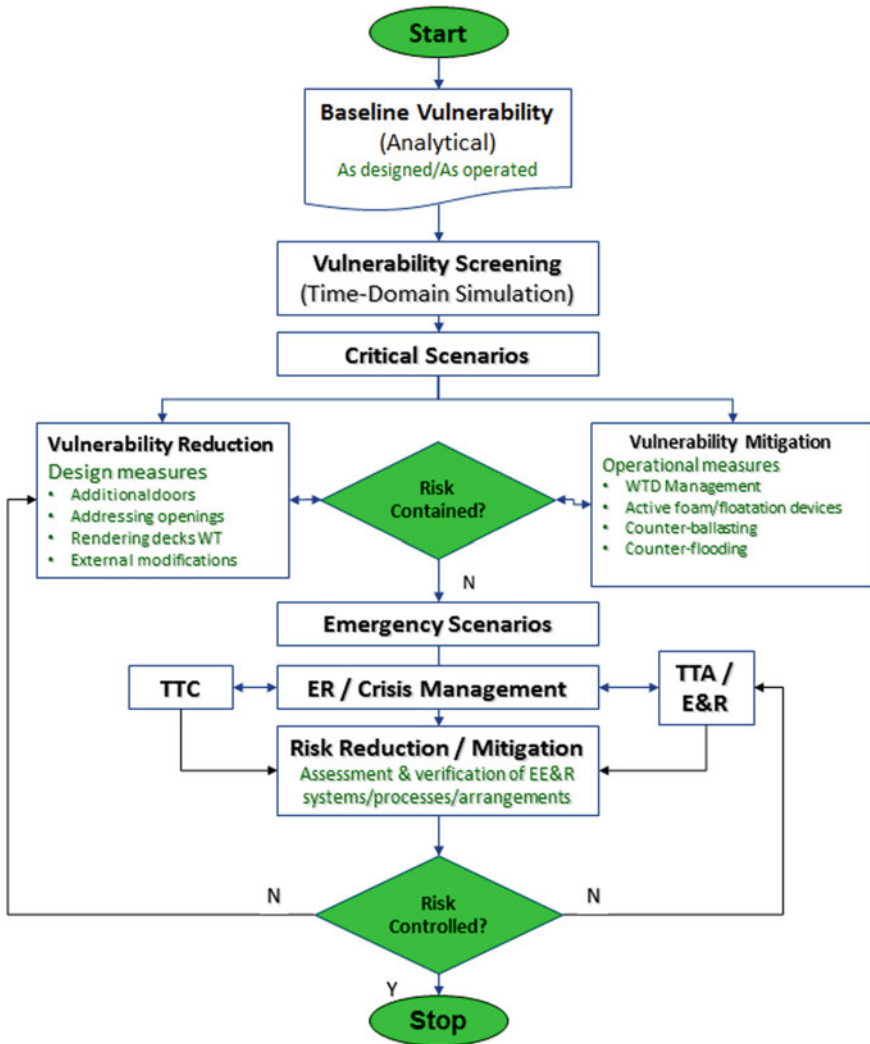


Fig. 1 Vulnerability management [1]

#### 4 Workshop—Brainstorming Session

The brainstorming session was conducted on the basis of a number of basic premises related to risk as defined below. Mind maps were used to record the views of the participants. Whilst this method is relatively unstructured, it allows recording of high-level discussions of hazards, influencing factors and risk control measures.

## Risk

- Risk can be quantified by the likelihood of undesirable consequences (e.g. fatalities per ship year, total losses per year, etc.)
- The range of undesirable consequences includes: impact on human life (fatalities and injuries) and impact on property (loss of and/or damage to the ship).
- For the purposes of this workshop, the accidental event that may lead to undesirable consequences is “flooding”.

## Accidental flooding events

- Water ingress and flooding may be the result of casualty incidents or systems failure including—but not limited to the following:
  1. Collision
  2. Contact (e.g. with quay)
  3. Bottom/side raking damage
  4. Failure (e.g. crack) of hull envelope
  5. Failure of overboard valve
- Incidents resulting in internal flooding (ballast water, fuel oils, etc.) may be the result of the following types of systems failures
  6. Internal structural failure (e.g. ballast tank, manhole, structural degradation, etc.)
  7. Failure of fire mains valve.

## Risk Reduction

In order to reduce the risk associated with flooding, the likelihood of occurrence and/or the severity of the consequences need to be reduced.

### *Reducing the likelihood of a flooding event*

- Although, it was agreed that this is an important element of the risk associated with flooding, this is out with the scope of the workshop. However, some of the factors affect both likelihood and consequences (e.g. crew competence).

### *Reducing the severity of the consequences of a flooding event*

- The internal watertight subdivision is a passive barrier or risk control measure, the objective of which is to reduce the severity of the consequences should a flooding event occurred.
- However, as indicated in the foregoing, there are other measures that may reduce the severity of the consequences (mitigation) of a flooding event. Those measures are of operational and/or active nature and as such less amenable to statutory verification unless an alternative method is applied.

**Table 1** Generic sequence of events that may occur after a flooding event (typical muster list)

Stage 1	Stage 2	Stage 3
<b>INCIDENT</b> (1) Detection & Alarm	(2) Damage control	(5) Abandon Ship (6) Rescue
	(3) Muster of Passengers	
	(4) Preparation of LSA	

**Risk Contributing Factors**

- There are also other factors that can influence the severity of the consequence of flooding. These factors influence the sequence of events that occur after the accidental event. This sequence can be generalised in terms of the following activities, see Table 1:
  1. Flooding detection and alarm
  2. Damage control
  3. Muster of passengers
  4. Preparation of LSA
  5. Abandon ship
  6. Rescue to a place of safety
- *Identification of the factors that influence the outcome of each of the above stages, is one of the key objectives of the brainstorming session.* These factors can be of the following types:
  1. Human (crew, passengers)
  2. Hardware (e.g. ship, systems, equipment)
  3. Organisational (e.g. procedures)
  4. External (e.g. weather-related, SAR assets)
- In addition, human and organisational factors are significant in terms of Damage Control and Emergency Response performance.

**5 Identification of Hazards**

Risk contributing factors and potential hazards were identified as listed below. These lists only reflect the scope of the discussions and therefore are not exhaustive; they can however be regarded to be representative.

**Stage 1: Detection and Alarm**

Relevant hazards identified during the brainstorming session include:

1. Flooding in space not fitted with water alarms
2. No/difficult access for validation of alarm



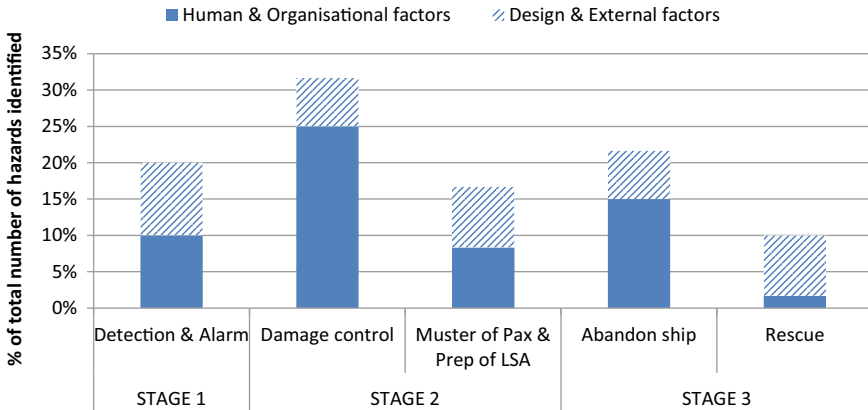


**Fig. 2** Breakdown of identified hazards (60 hazards in total)

3. Failure or impairment of automatic means of detection
4. Not effective (slow) means of detection
5. Trips, falls, exposure to flood water when trying to validate an alarm
6. Crew not familiar with layout of the ship
7. No information or uncertainty about the location and the extent of the damage
8. Unclear, ineffective procedures (reference to muster list)
9. Poor competence of crew—lack of training in flooding detection
10. Lack of crew preparedness in searching for water
11. Poor/ineffective internal and/or external communications
12. Initiation of mustering (general alarm) too soon—this will create MUSTERING hazards unnecessarily (Fig. 2).

### Stage 2: Damage Control

Relevant hazards identified during the brainstorming session include:

1. High vulnerability of watertight subdivision & arrangements to flooding
2. Impairment of watertight subdivision & arrangements (due to accidental event)
3. Ineffective/blocked scuppers in car deck
4. No/difficult access for effective damage control (e.g. vehicles on car deck, voids)
5. No/difficult access to damage control equipment
6. Additional hydrostatic pressure on internal structures, doors and bulkhead penetrations
7. No redundancy of essential ship systems after flooding
8. Crew not prepared/not able to reconfigure systems for damage control
9. Trips, falls, exposure to flood water when trying to deploy damage control measures
10. Ship systems not dimensioned for dealing with damage control (e.g. pumps)
11. No information or uncertainty about the location and the extent of the damage, especially if flooding is escalating

12. Crew not able to effectively assess the criticality of the damage
13. Poor competence of crew—not trained in damage control
14. Lack of crew preparedness in damage control
15. Crew not familiar with layout of the ship
16. Crew not available for damage control (low crew redundancy)
17. Lack of effective leadership in an emergency situation
18. Breakdown of internal communication (due to language barriers, inappropriate use or failure of communications equipment)
19. Ineffective/unhelpful external support
20. Rough weather, cold climates.

### **Stage 2: Muster of Passengers & Preparation of LSA**

Relevant hazards identified during the brainstorming session include:

1. False alarm—muster initiation too soon, creating unnecessary hazards for passengers
2. Impairment of escape routes, muster areas and/or LSA systems (due to accidental event)
3. Impairment or failure of lighting along escape routes and/or muster areas (e.g. due to blackout as a result of the flooding)
4. Impairment or failure of internal communication systems (e.g. due to blackout as a result of flooding)
5. Ship motions, heel, trim—making moving to muster areas difficult and hazardous
6. Trips and falls when moving to muster area
7. Exposure to weather (to passengers if mustering externally; to crew when preparing LSA)
8. Inefficient internal communication (with passengers)
9. Difficult in managing passenger behaviour—crew not prepared in crowd control
10. Not sufficient crew numbers available to assist passengers (e.g. due to damage control efforts) and control of mustering.

### **Stage 3: Abandon Ship**

Relevant hazards identified during the brainstorming session include:

1. Fast ship capsize
2. Poor/delayed decision by the Master
3. Impairment of embarkation areas and/or LSA (due to accidental event)
4. Failure of deployment of LSA systems
5. Impairment or failure of emergency abandonment systems (e.g. due to blackout as a result of flooding)
6. MOB situation
7. Lack of key crew redundancy
8. Rough weather
9. Large heel and trim angles (in excess of LSA design criteria)

10. Poor competence of crew—not trained in deployment and use of all LSA on-board
11. Lack of crew preparedness in LSA deployment and embarkation
12. Not sufficient competent crew numbers available to deploy and control LSA units
13. Poor/ineffective passage planning (with SAR in mind).

#### **Stage 4: Rescue to Place of Safety**

Relevant hazards identified during the brainstorming session include:

1. Ineffective/no SAR planning
2. Safe place (to transfer people) not available
3. Unavailability of adequate SAR assets (for the number of persons)
4. Lack of crew preparedness
5. Poor/ineffective communication with external stakeholders (safe port, class, Coastal and Flag State)
6. Rough weather.

## **6 Flooding Risk Mitigation Options**

Although it was acknowledged that it is always preferable to have passive or semi-automatic measures in place, the discussion was focused on active and operational damage mitigation options including the following (see Fig. 1):

### **Design Modifications (Category 1)**

The following observations are made:

- Passive measures providing additional buoyancy (sponsons, ducktails, buoyancy tanks, etc.)
- The performance of design modifications is related to the effectiveness of flooding mitigation
- The effectiveness of design modifications does not depend explicitly on crew performance
- Design modifications reducing the inherent vulnerability to flooding; from all mitigation measures, these may have the highest potential for improving the value of the A-index (Fig. 3).
- Well known solutions and their implications—relating to the following
  - Double hull machinery room → may introduce flooding asymmetry and maintenance/rust problems
  - Rendering decks watertight → not always possible
  - Relocation of openings → not always possible or effective
  - SWT/Splash-tight doors (Fire doors); not always possible or effective

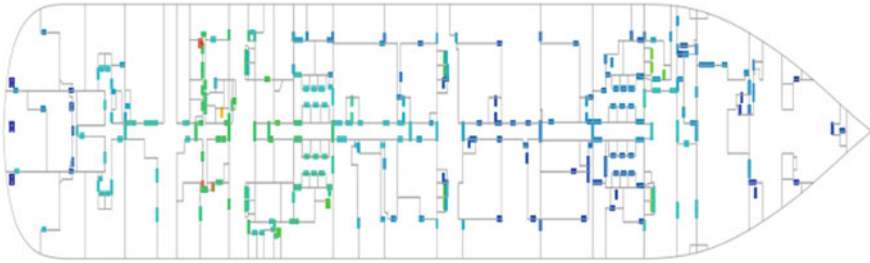


**Fig. 3** Vulnerability screening in a passenger ship (identification of focal areas for improved survivability; in this case deck openings with high frequency and high volume of floodwater during progressive flooding scenarios)

- Buoyancy tanks

### Operational Measures (Category 2)

In relation to containment actions, the following observations are made:

- Containment actions limit the severity of the consequences of a flooding accident by preventing progressive flooding
- Limited experience on merchant ships—better experience on naval vessels
- Simple tools and equipment available on-board
- Crew competence and preparedness is a significant influencing factor in ensuring containment actions are effective
- However, in terms of statutory A index calculations or flooding simulations, it is assumed that the existing watertight integrity performs as expected, e.g. watertight doors do not leak, penetrations in watertight bulkheads do not leak, etc.

In relation to *active damage* control, the following observations are made:

- Counter ballasting and/or counter flooding measures limit the severity of the consequences of a flooding accident by preventing excessive heel/trim of the ship (Fig. 4). However, timing of this action might be an issue.
- Damage-specific measures not possible in all cases
- Depends on tank and internal arrangements
- Relies on the *availability of relevant ship systems* (bilge, ballast, power, among others)
- Large number of possibilities—difficult to assess and execute by the crew without support
- Hazard of significant hydrostatic loads on internal structures
- Potential for using new materials/technologies (e.g. foams, inflatable devices):
  - Fast semi-automatic deployment, essential
  - To be effective in critical damages where time to capsize less than say 20 min
  - Requires type approval and additional maintenance and training

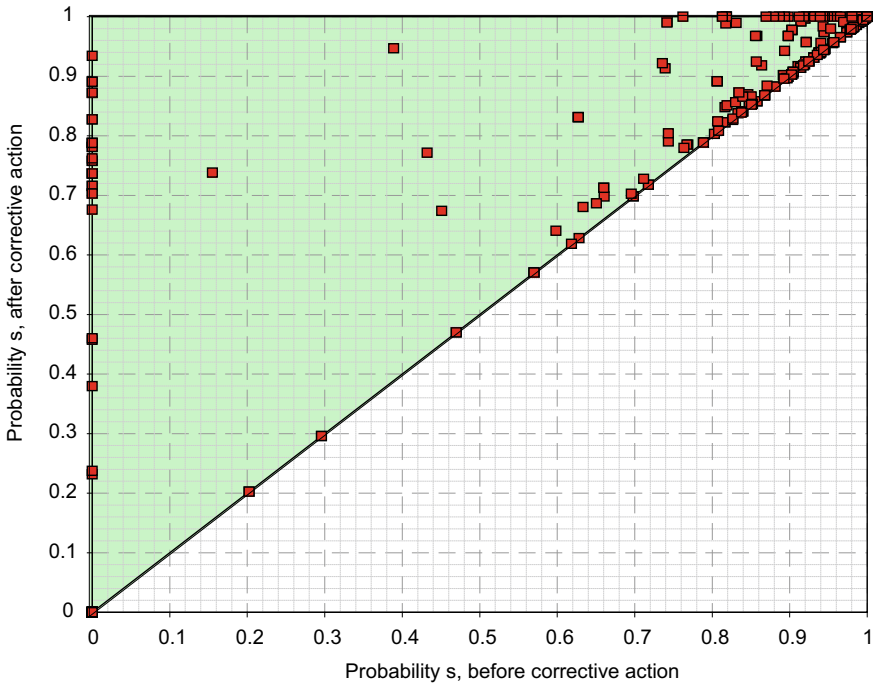


Fig. 4 Counter-ballasting capacity post-casualty (typical example)

- Crew competence and preparedness as well as availability of relevant ship systems are significant influencing factors for ensuring that active damage control actions are effective
- The contribution to A-index can be assessed by means of flooding simulations (not by statutory calculations). However, in order to ensure that the actions can be accomplished effectively, crew performance and availability of relevant ship systems needs to be demonstrated.

Some *radical* actions were identified, for which the following observations are made:

- Running the ship aground when/if possible
- Unloading cargo overboard when/if necessary
- Such actions will require additional planning and crew preparedness.

### Emergency Response Measures (Category 3)

These relate mainly to escape, evacuation and rescue arrangements; for which the following comments are made:

- Measures reducing the severity of the consequences of a flooding accident by allowing the persons on-board to abandon the vessel

- Effective evacuation requires the vessel to remain afloat and upright—to the limits of LSA systems
- Crew competence and preparedness as well as availability of relevant ship systems are significant influencing factors for ensuring that people on-board can be evacuated effectively.

## 7 Workshop Outcome

The outcome of the workshop discussions and subsequent analysis is presented under the following headings:

- Long-terms goals
- Ship vulnerability to flooding
- Active flooding mitigation
- Risk reduction.

### Long-term Goals

Although in the short to medium term, the goal of the initiative started by INTER-FERRY EUROPE is related to the potential retrospective application of increased R-Index requirements, the participants of the workshop agreed that the long-term goals and implications of the issues addressed in the workshop need to be established.

Key items that will be affected include:

1. Alternative arrangements and means for assigning credit to operations/emergency response measures
2. Definition and interpretation of required subdivision index R, SOLAS Ch.II-1 Regulation 6
3. Alternative methodology for the calculation of the A index value—in accordance with SOLAS Ch.II-1 Regulation 4
4. Verification of essential ship systems redundancy for existing ships. This is in line with SOLAS Ch.II-2 Safe return to Port requirements for ship systems
5. Evacuation and LSA arrangements—considering that SOLAS Ch.III is under revision
6. Verification and validation of crew preparedness and performance. ISM Code implementation is the minimum level or performance expected
7. Contribution from INTERFERRY on potential changes to SOLAS and the ISM Code.

### Ship Vulnerability to Flooding

In terms of the subdivision index, used for design verification of ship damage stability, the following observations are made:

1. The required index of subdivision R expressed the accepted probability of a ship surviving a collision incident for 30 min or more. Consequently, the attained

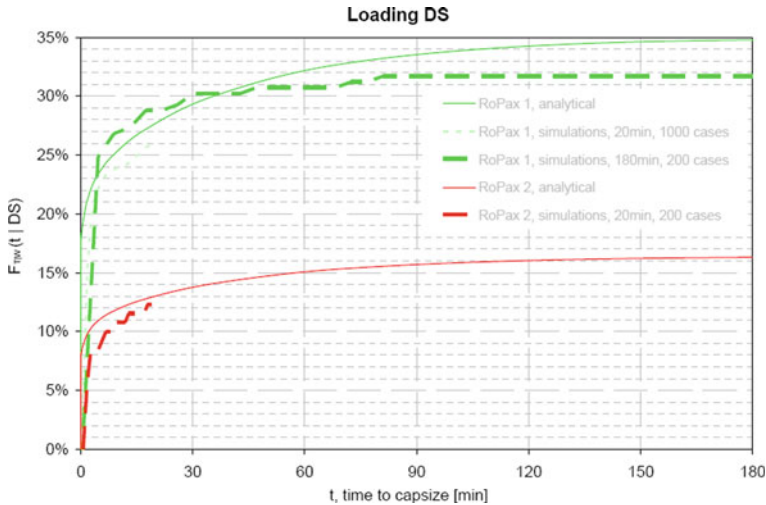


**Fig. 5** SOLAS versus numerical simulations (Reg. 4, Part B)—simple internal architecture

index A reflects the average probability of a ship surviving 30 min or more, such average deriving from consideration of damage statistics as described in SOLAS 2009.

2. On this basis, a ship attaining a value of  $A = 0.8$ , implies that the ship has a 20% average probability of capsizing within 30 min, following flooding of ship spaces as a result of collision damage.
3. The statutory calculation<sup>1</sup> of A-index encompasses many empirical approximations (e.g. s-factor, p-factor) and conservative assumptions, some of which are not justified in practice (e.g. loading conditions, damage statistics).

Moreover, there is extensive knowledge and evidence to make the following assertions:

4. A method based on numerical (flooding) simulations and Monte-Carlo sampling techniques can be used reliably as an alternative approach to the statutory calculation of the A-index, in accordance with SOLAS Ch.II-1 Regulation 4.2.
5. Previous studies have shown that by using this alternative method, the simplicity and conservatism implicit in the statutory calculations may, in some cases lead to underestimation, while in other cases lead to overestimation of the attained index A (Figs. 5 and 6).
6. Furthermore, regarding these flooding cases in which a ship is likely to capsize within 30 min, it has been shown that in some cases, (i) the ship will have no damage stability at all: i.e. the ship will capsize fast, whilst in other cases (ii) the ship may be recovered with effective active damage control: i.e. the ship can be saved or the time to capsize can be extended to allow for safe evacuation of passengers and crew (Fig. 4).

<sup>1</sup> Referred to as 'SOLAS2009' calculation.

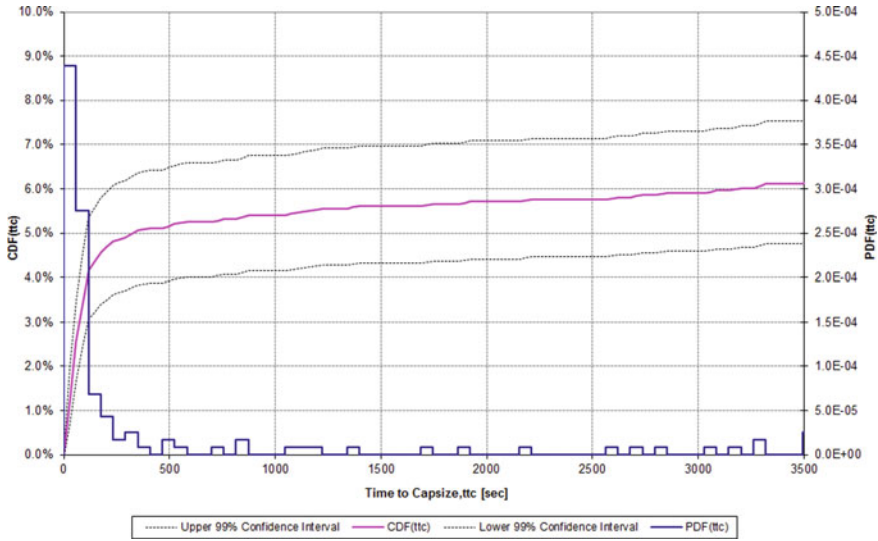


**Fig. 6** SOLAS versus numerical simulations (Reg. 4, Part B)—medium complexity internal architecture

7. The alternative approach is a better method for assessing the vulnerability of a ship to flooding, regardless of the type of accident (collision, grounding, raking damage, etc.).
8. The use of the alternative approach to assess ship vulnerability has many benefits; it allows the incorporation of realistic operating conditions and it allows for verification of active damage control actions such as counter-ballasting and counter-flooding. Moreover, by providing information on the time line of events, it allows assessing the effectiveness of the evacuation arrangements.

**Active Flooding Mitigation**

Assuming that an alternative method for assessing ship vulnerability to flooding is adopted, active flooding mitigation options for which credit can be obtained in terms of the attained A-index (by simulation), include the following:

1. Design modifications—although not the preferred option for existing ships unless they are easy to implement and are cost-effective
2. Active, counter-ballasting, counter-flooding measures—these are damage-specific therefore, verification may be extensive. In order to realise the potential gains, additional verification is required:
  - (a) Relevant ship systems must be demonstrated to be available (Safe Return to Port concept of SOLAS Ch.II-2)—note that 16% of the hazards related to damage control relate to ship systems redundancy in case of flooding
  - (b) Crew competence and preparedness must be demonstrated (objective evidence as per or beyond SOLAS and ISM Code requirements). Note that



32% of the hazards identified relate to damage control. Of those, the majority (78%) can be controlled by effective crew performance and/or effective operating procedures.

### **Risk Reduction**

Effective evacuation and rescue (EER) arrangements also reduce the risk to people. These measures can be successful only if the ship remained afloat and upright for as long as necessary to complete the ship abandonment process. Therefore, the following is required to demonstrate risk reduction:

1. Time line of key events in the flooding process—e.g. time to reach a heel angle of, say 20°. This can be provided by the numerical flooding simulations (alternative approach)
2. A verification of the time required to carry out ship abandonment as per the ship's muster list. This includes quantification of the time for general alarm, response and mustering, embarkation of LSA, deployment of LSA and sail away from vessel
3. Crew competence and preparedness must be demonstrated (objective evidence as per or beyond SOLAS and ISM Code requirements)—Note that 32% of the hazards identified relate to ship abandon and rescue. Of those, the large majority (86%) can be controlled by effective crew performance and/or effective operating procedures.

## **8 Concluding Remarks**

1. Building on the knowledge and understanding of damage stability fundamentals, a process has been elucidated to address the vulnerability to flooding of passenger ships from a life-cycle perspective and with focus on operational and emergency response measures alongside the more traditional design measures, with emphasis of application on existing ships.
2. An initiative undertaken by INTERFERRY Europe is putting this concept to test, starting with a workshop to assess the impact of possible changes in the required subdivision index R and the potential implications for existing vessels should IMO decided to apply the new requirements retrospectively.

**Acknowledgements** The authors would like to express their gratitude to INTERFERRY for sponsoring this work and for their invaluable contribution to identifying and targeting cost-effective solutions to improving the damage survivability of Ro-Ro passenger ships. The contribution made by Dr Jasionowski was during his stay with Safety at Sea Brookes Bell Ltd.

## Reference

1. Vassalos D (2013) Emergency response in flooding casualties. In: 13th International ship stability workshop, Brest, France, 21–26 September 2013

# The Inertia Contributions Due to Floodwater Mass



Gyeong Joong Lee, Arthur M. Reed, Frans van Walree, Andrew Peters, Paola Gualeni, Toru Katayama, and WenYang Duan

**Abstract** The Stability in Waves committee of the 27th ITTC investigated how to deal with the inertia due to floodwater mass from three points of view: (1) floodwater domain, (2) floodwater inertia itself, (3) floodwater entering ship. The committee suggested three criteria indicating the concept of how to deal with floodwater and providing clues on what to consider as floodwater when examining damage ships: (1) whether the water is moving with the ship or not, and amount of that water, (2) whether there is a significant pressure jump across the compartment boundary or not, (3) whether the dynamics of water can be solved separately or not. For floodwater inertia, the committee divided this into the partially flooded case and fully flooded case, and investigated the properties and showed how to deal with floodwater inertia for each case. For the case of the floodwater entering ship, the treatment of inertia

---

G. J. Lee (✉)  
KRISO, Daejeon, Korea  
e-mail: [gjee@kriso.re.kr](mailto:gjee@kriso.re.kr)

A. M. Reed  
NSWC, Bethesda, USA  
e-mail: [arthur.reed@navy.mil](mailto:arthur.reed@navy.mil)

F. van Walree  
MARIN, Wageningen, Netherlands  
e-mail: [F.v.Walree@marin.nl](mailto:F.v.Walree@marin.nl)

A. Peters  
QinetiQ, Gosport, UK  
e-mail: [ajpeters@qinetiq.com](mailto:ajpeters@qinetiq.com)

P. Gualeni  
University of Genoa, Genoa, Italy  
e-mail: [paola.gualeni@unige.it](mailto:paola.gualeni@unige.it)

T. Katayama  
Osaka Prefecture University, Osaka, Japan  
e-mail: [katayama@marine.osakafu-u.ac.jp](mailto:katayama@marine.osakafu-u.ac.jp)

W. Duan  
Harbin Engineering University, Harbin, China  
e-mail: [duanwenyang@hrbeu.edu.cn](mailto:duanwenyang@hrbeu.edu.cn)

change due to floodwater was made clear using the momentum change principle. The related procedure was updated reflecting this work.

**Keywords** Floodwater · Inertia of floodwater · Domain of floodwater

## 1 Introduction

In the literatures on flooding simulations, Spouge [1] opened the simulation method to investigate the sinking accident of a damaged ship. In the earlier period, the free surface of a damaged compartment was treated as horizontal by many studies. The movement of flood water became more realistic, as the concept of ‘lump mass’ was introduced (see [2, 3]). Valanto [4, 5] treated the flood water as point mass when the water height is higher than the breadth of damaged compartment, and if the water height is lower the flood water would be calculated by the shallow water equation. And CFD was also used in flooding calculations in many studies like van’t Veer [6], Cho [7]. Recently SPH method was also tried. Nowadays, a study on the damaged ship uses one or two methods above mentioned, according to the dynamic characteristics of a damaged ship and the computational power provided.

One of the tasks of the committee on Stability in Waves of the 27th ITTC is to investigate how to deal with the inertia due to the flood water mass [8, 9], and update the relevant procedure [10]. The committee investigated this task from three points of view: (1) floodwater domain, (2) floodwater inertia itself, (3) floodwater entering ship.

The boundary of floodwater domain is hard to determine for a large damage opening. The committee suggested three criteria indicating the concept of how to deal with floodwater and providing clues on what to consider as floodwater when examining damage ships: (1) whether the water is moving with the ship or not, and amount of that water, (2) whether there is a significant pressure jump across the compartment boundary or not, (3) whether the dynamics of water can be solved separately or not.

For the partially flooded compartment, the motion of floodwater is usually analysed by three analysing techniques, namely quasi-static, quasi-dynamic, full dynamic analysis. In quasi-static and quasi-dynamic analysis, because it considers only the centre of gravity of the flood water, the mass of flood water should be included in the ship’s mass. However in full dynamic analysis, the pressure includes all the static and dynamic pressure, the force derived from the pressure integration on the surface of the compartment includes all the effects of floodwater inertia and flow properties. This is subject to the condition that the body force includes the actual acceleration, that is, the gravitational acceleration and the acceleration of the flood water. In this case, the mass of flood water should not be included in the ship’s mass.

In the case of fully flooded compartment, the floodwater is often treated as solid and is included in the ship’s mass in many studies for the motion dynamics of ships. In order to clarify this problem, the committee reviewed the work of [11]. In his

study, the inertial properties of fully filled liquid in a tank were studied based on the potential theory. The analytic solution was obtained for the rectangular tank, and the numerical solutions using Green's 2nd identity were obtained for other shapes. The inertia of liquid behaves like solid in recti-linear acceleration. But under rotational acceleration, the moment of inertia of liquid becomes small compared to that of solid. The shapes of tank investigated in his study were ellipse, rectangle, hexagon, and octagon with various aspect ratios. The numerical solutions were compared with analytic solution, and an ad hoc semi-analytical approximate formula is proposed herein and this formula gives very good predictions for the moment of inertia of the liquid in a tank of several different geometrical shapes. The results of his study will be useful in analysing of the motion of LNG/LPG tanker, liquid cargo ship, and damaged ship.

For the case of the floodwater entering ship, the treatment of inertia change due to floodwater was made clear using the momentum change principle. The related procedure was updated reflecting this work.

## 2 Floodwater Domain

There is the problem of which region should be treated as floodwater if the damage opening is large enough. So we first need a more reasonable and clear definition of floodwater in the analysis of a damaged ship. If we focus on the inertia properties, the floodwater can be determined by looking at whether the water is moving together with the ship or not. If we focus on the hydrodynamics, floodwater may be determined by investigating whether the pressure of it is strongly related with outside water level or not, and whether the hydrodynamic problem of floodwater can be analysed separately or not, provided that the boundary condition is given for the matching of inner and outer flow domains.

Therefore the followings may be criteria that will be used to determine the floodwater.

- Whether the water is moving with the ship or not, and amount of that water.
- Whether there is a significant pressure jump across the compartment boundary or not.
- Whether the dynamics of water can be solved separately or not.

The above three criteria indicate the concept of how to deal with floodwater and provide clues on what to consider as floodwater when examining damage ships.

### 3 Inertia of Floodwater

#### 3.1 Partially Flooded Compartments

The hydrodynamics and its force on the compartment partially filled with flood water can be calculated by theory or numerical scheme, such as resonant mode analysis, potential theory, CFD with free surface etc. In these methods, the force originated from flood water is treated as external forces, and the motion of a ship is affected by it. However in this case, there is a problem to consider i.e. whether the mass of flood water should be included in the ship’s mass or not.

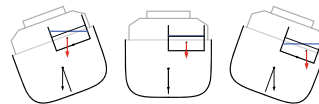
The forces due to floodwater can be divided into three parts by considering their origins. The first is the one due to gravitational acceleration, the second one is due to the acceleration by a ship’s motion, and the last one is due to the dynamic pressure of the flow of floodwater. The interactions of floodwater and ship motion were summarised in 26th ITTC report by Stability in Waves committee. The interaction concept was given as Table 1, and the concept of these three models was drawn as in Fig. 1.

The quasi-static model (like [1]) represents one in which the free surface remains horizontal and the floodwater mass is included in ship’s mass. In the quasi-dynamic

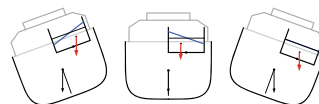
**Table 1** Three models of interactions (from 26th ITTC report)

	Floodwater treatment	Interaction concept
Quasi-static	Static	Added weight
Quasi-dynamic	Dynamic	Added weight
Dynamic	Dynamic	Added force

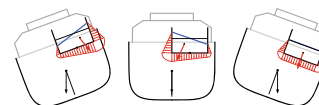
**Fig. 1** Concept of floodwater and ship motion interaction (from 26th ITTC report)



(a) quasi-static(free surface horizontal)



(b) quasi-dynamic(dynamic free surface)



(c) dynamic(dynamic free surface, fluid pressure force)

model (like [2–5]), the free surface and the center of gravity of floodwater could be calculated as mass-damper-spring dynamic system or the equivalent dynamic system, and the floodwater mass is treated as in the quasi-static model. The dynamic model (like [6, 7]) usually use CFD method, so the pressure forces acting on the compartment can be directly calculated and would be acting as the external forces in the equation of motion of a damaged ship.

In quasi-static or quasi-dynamic analysis, because it considers only the centre of gravity of the flood water and only the gravitational force, the mass of flood water should be included in the ship’s mass in order to represent the inertia force, that is, the force due to the acceleration by the ship’ motion. However in fully dynamic analysis, the pressure includes all the static and dynamic pressure, the force derived from the pressure integration on the surface of the compartment includes all the effects of floodwater inertia and flow properties. This is subject to the condition that the body force includes the actual acceleration, that is, the gravitational acceleration and the acceleration of the flood water due to the ship’s motion. In this case, the mass of flood water should not be included in the ship’s mass. The following conceptual equations of motion show in which side of the equation the floodwater inertia should be included.

*Quasi-static, quasi-dynamic analysis,*

$$(m + m_F)\ddot{x} + b\dot{x} + cx = F_{ext} + F_G \quad (1)$$

*Fully dynamic analysis,*

$$m\ddot{x} + b\dot{x} + cx = F_{ext} + F_{FL} \quad (2)$$

As explained above, in quasi-static or quasi-dynamic analysis, the force due to the floodwater is gravitational force, this is included in the right side as external force. In this case, the mass of floodwater,  $m_F$  should be included into the ship’s mass, as in Eq. (1). And in fully dynamic analysis, if the floodwater force,  $F_{FL}$  includes all the forces due to gravitational acceleration, the acceleration by a ship’s motion, and dynamic pressure of the flow, the mass of floodwater should not be included into the ship’s mass.

### 3.2 Fully Flooded Compartments

The flood water in a fully filled compartment is often treated as a part of the ship and treated as a solid. In rectilinear acceleration, the flood water acts like a solid. In rotational acceleration, the moment of inertia is smaller than that of a solid, because there is a part of water that does not rotate with the ship. Lee [11] shows the ratio of the moment of inertia of flood water and that of solids for various shapes of compartments.

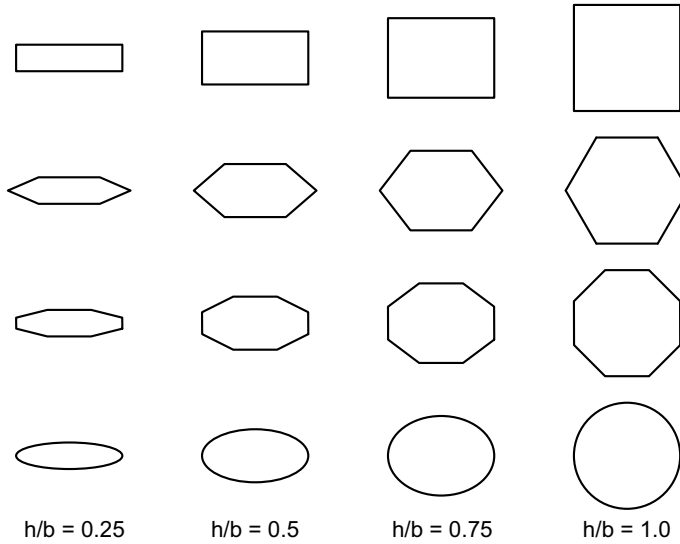


Fig. 2 Various shapes of tanks useful for application from Lee [11]

$$C_R = I_{Liquid}/I_{Solid} \tag{3}$$

where  $I_{Liquid}$  and  $I_{Solid}$  are the moment of inertias of the flood water when treated as liquid and solid respectively.

The following, Fig. 2 shows the shapes of compartment treated in his study.

The inertias of the fluid in tanks of different aspect ratios and shapes, Fig. 3, become small as the aspect ratio goes to unity.

The solid lines in Fig. 3 are analytical or numerical results while the dashed lines are an estimation formula that provides accurate results. His estimation formula is as follows,

$$I_{Liquid} = I_{Solid} - I_e = I_{Solid} - \rho k_e \frac{A^2}{\pi} \left( \frac{hb}{h^2 + b^2} \right) \tag{4}$$

where the shape correlation factor  $k_e$  is

$$k_e = \left( \frac{A_{ellipse}}{A} \right)^{2/n} = \left( \frac{\pi hb}{4A} \right)^{2/n} \tag{5}$$

If we put the area  $A$  from Table 2, the factor  $k_e$  turns out the coefficient dependant only on the type of the shape as follows,



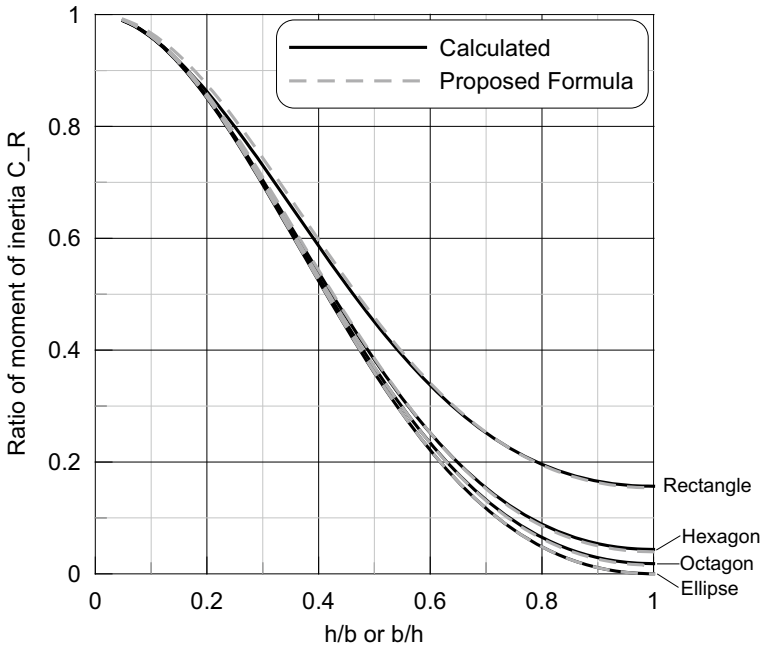


**Fig. 3** Moment of Inertia prediction of fully filled liquid for various shaped tanks; calculated and estimated from Lee [11]

$$k_e = \begin{cases} (\pi/4)^{1/2} & \text{for rectangle} \\ (\pi/2\sqrt{3})^{1/3} & \text{for hexagon} \\ \left(\frac{\pi}{8(\sqrt{2}-1)}\right)^{1/4} & \text{for octagon} \\ 1 & \text{for ellipse} \end{cases} \quad (6)$$

The experimental validation of the above has not been performed yet, and expected.

**Table 2** Area and moment of inertia of solid for various shapes from Lee [11]

Shape	Number of edge ( <i>n</i> )	Area	Moment of inertia for roll
Rectangle	<i>n</i> = 4	<i>A</i> = <i>hb</i>	$\frac{I_{Solid}}{\rho} = \frac{1}{12} A(h^2 + b^2)$
Hexagon	<i>n</i> = 6	$A = \frac{\sqrt{3}}{2} hb'$	$\frac{I_{Solid}}{\rho} = \frac{5}{72} A(h^2 + b^2)$
Octagon	<i>n</i> = 8	$A = 2(\sqrt{2} - 1)hb$	$\frac{I_{Solid}}{\rho} = \frac{3-\sqrt{2}}{24} A(h^2 + b^2)$
Ellipse	<i>n</i> = ∞	$A = \frac{\pi}{4} hb$	$\frac{I_{Solid}}{\rho} = \frac{1}{16} A(h^2 + b^2)$

## 4 Inertia of Floodwater Entering Ship

Newton's Second Law states that the force (moment) on a body is equal to its time rate-of-change of momentum (angular momentum). For a body of constant mass (moment of inertia) this translates to  $F = ma$  ( $M = I d\omega/dt$ ). However, for a body such as a rocket which is burning fuel and ejecting gas or a damaged ship in a seaway taking on and possibly discharging water, the  $F = ma$  analogy is not correct, but in fact the time-rate-of-change of mass must be taken into account. As the force must remain independent of the coordinate system, a simple application of the rule for differentiation of the product of two functions is not correct. The contribution from the time-rate-of-change of mass term belongs on the left-hand side of the equation with the force. In the context of rocket propulsion, the time-rate-of-change of mass contribution is the equivalent of the thrust of the rocket motor. Similar analogies apply to the time-rate-of-change of moment of inertia.

If we represent the momentum of the vessel as  $p$  and the angular momentum as  $L$ , where  $p = mv$  and  $L = I\omega$ , with  $m$  the mass of the ship,  $v$  the velocity,  $I$  the moment of inertial tensor and  $\omega$  the angular velocity, then Newton's second law can be written as:

$$\begin{aligned} F &= m \frac{dv}{dt}, \\ M &= I \frac{d\omega}{dt}. \end{aligned} \quad (7)$$

When the mass and hence the moment of inertia are constant, then these equations reduce to the traditional  $F = ma$  form. However, in the damaged condition, the vessel's mass and moment of inertia vary with time and the equations of motion must be written in the above form. Rewriting Eq. (7) to account for the intake or discharge of floodwater as for a closed system yields:

$$\begin{aligned} F - v' \frac{dm}{dt} &= m \frac{dv}{dt}, \\ M - \omega' \frac{dI}{dt} &= I \frac{d\omega}{dt}, \end{aligned} \quad (8)$$

where  $v'$  and  $\omega'$  are the relative velocity and angular velocity of the flooding (discharging) water relative to the vessel, respectively. All of the quantities  $v'$ ,  $dm/dt$ , and  $\omega'$  can be determined from analysis of the flow at the damaged opening (if there is flow between flooded compartments, then the flow between the compartments must be incorporated in a similar manner). The evaluation of  $dI/dt$  is somewhat more complex as it involves the actual shape of the compartment.

The above material dealing with the inertia change due to floodwater was included in the procedure ITTC 7.5-02-07-04.4 [10].

## 5 Conclusions

The committee investigated how to deal with the inertia due to floodwater mass from three points of view: (1) floodwater domain, (2) floodwater inertia itself, (3) floodwater entering ship.

For the floodwater domain, the committee proposed the criteria that will be used to determine the floodwater. For floodwater inertia, the committee divided this into the partially flooded case and fully flooded case, and investigated the properties and showed how to deal with floodwater inertia for each case. For the case of the floodwater entering ship, the treatment of inertia change due to floodwater was made clear using the momentum change principle. The related procedure was updated reflecting this work.

**Acknowledgements** The aim of this paper is to introduce the work of ITTC Stability in Waves committee on the damage model test. The large part of this material is come from the report of ITTC and rearranged.

## References

1. Spouge JR (1986) The technical investigation of the sinking of the Ro-Ro ferry european gateway. *Trans Royal Inst Naval Architect RINA* 128:49–72
2. Papanikolaou A, Zaraphonitis G, Spanos D, Boulougouris E, Eliopoulou E (2000) Investigation into the capsizing of damaged Ro-Ro passenger ships in waves, In: Proceedings of the 7th international conference on stability of ships and ocean vehicles, Launceston, Tasmania, Australia, 7–11 Feb 2000, pp 351–362
3. Papanikolaou A, Spanos D (2002) On the modelling of floodwater dynamics and its effects on ship motion. In: Proceedings of the 6th international ship stability workshop, New York, USA, 13–16 Oct 2002
4. Valanto P (2002) Time-dependent survival probability of a damaged passenger ship, vol 1 (Capsizing). HSVA Report No. CFD 05/2002, published as the IMO document SLF 45/INF.3, 28 Feb 2002
5. Valanto P (2006) Time dependent survival probability of a damaged passenger ship II—evacuation in seaway and capsizing. HSVA Report No. 1661, Hamburg, 31 May 2006, 101 p, published in internet at [http://www.hsva.de/10\\_downloads\\_content/Valanto.pdf](http://www.hsva.de/10_downloads_content/Valanto.pdf) (cited 18.12.2006)
6. van't Veer R, de Kat O, Cojeen P (2002) Large passenger ship safety: time to sink. In: Proceedings of the 6th international ship stability workshop, New York, USA, 13–16 Oct 2002
7. Cho SK, Hong SY, Kim YH, Lee KJ (2005) Investigation of dynamic characteristics of the flooding water of the damaged compartment of an ITTC RORO Passenger Ship. In: Proceedings of the 8th international ship stability workshop, Istanbul, Turkey, 6–7 Oct 2005
8. Committee on Stability in Waves (2014) Final report and recommendations to 27th ITTC, 27th ITTC.
9. Committee on Stability in Waves (2011) Final report and recommendations to 26th ITTC, 26th ITTC

10. ITTC (2014) Recommended procedures and guidelines—numerical simulation of capsize behaviour of damaged ships in irregular beam seas, 7.5-02-07-04.4, Effective Date:2014, Revision:01
11. Lee GJ (2014) Moment of inertia of liquid in a tank. *Int J Naval Architect Ocean Eng* 6(1):132–150

# Air Pressure Scale Effects During Damage Model Tests



Gyeong Joong Lee, Arthur M. Reed, Frans van Walree, Andrew Peters, Paola Gualeni, Toru Katayama, and WenYang Duan

**Abstract** The Stability in Waves committee of the 27th ITTC has investigated the significance of scale effects in air pressure on flooding model tests under atmospheric conditions. For this purpose, the committee classified the flooding cases into the trapped air case and vented air case and investigated the flooding process for a simple geometry, using the state equation of air and orifice equation. As a result, the committee concluded that the scale effect is large for the case of trapped air and small vent area. For the other cases, the effect is small and can therefore be neglected in the model test of a damaged ship. In addition, the committee proposed some directions that can be used to reduce the scale effect of air pressure.

**Keywords** Scale effect of air · Damage model test · Depressurised wave basin

---

G. J. Lee (✉)  
KRISO, Daejeon, Korea  
e-mail: [gjee@kriso.re.kr](mailto:gjee@kriso.re.kr)

A. M. Reed  
MARIN, Wageningen, Netherlands  
e-mail: [athur.reed@navy.mil](mailto:athur.reed@navy.mil)

F. van Walree  
NSWC, Bethesda, USA  
e-mail: [F.v.Walree@marin.nl](mailto:F.v.Walree@marin.nl)

A. Peters  
QinetiQ, Gosport, UK  
e-mail: [ajpeters@qinetiq.com](mailto:ajpeters@qinetiq.com)

P. Gualeni  
University of Genoa, Genoa, Italy  
e-mail: [paola.gualeni@unige.it](mailto:paola.gualeni@unige.it)

T. Katayama  
Osaka Prefecture University, Osaka, Japan  
e-mail: [katayama@marine.osakafu-u.ac.jp](mailto:katayama@marine.osakafu-u.ac.jp)

W. Duan  
Harbin Engineering University, Harbin, China  
e-mail: [duanwenyang@hrbeu.edu.cn](mailto:duanwenyang@hrbeu.edu.cn)

## 1 Introduction

One of the tasks of the committee on Stability in Waves of 27th ITTC is to investigate the scale effect of air pressure on damage model test and update the ITTC Recommended Procedure 7.5-02-07-04.2 “Model Tests on Damage Stability in Waves” [1, 2]. The guideline provides the test procedure for carrying out model tests on a damaged ship in irregular waves to determine the probability of capsizing or the significant wave height that will cause the model to capsize in a fixed time period. If there is a compartment of the model, which is not vented, and this compartment has a large effect on the model test, the scale effect of air pressure arises. However, most tests on damaged ship models are carried out in atmospheric conditions, and the model test in vacuum condition is very limited, there is only one facility suitable for the damage model test among many ITTC member facilities [3]. Ypma [4] reported the comparisons of the model test in atmospheric and vacuum conditions, including the difficulties of model test in the latter.

The effect of air compression on the cross-flooding process was taken into account in Refs. [5, 6]. Peters et al. [7] carried out rigorous calculations with air-flow to find the design alternatives of cross-flooding duct, and Ruponen et al. [8] calculated cross-flooding time with complex duct. Besides cross-flooding, Palazzi and deKat [9] studied the air flow/compression effects by model experiments; Ruponen et al. [10] provided the results of full-scale experiments with various air pipes. Most researchers knew there is a scale effect on the air compression, but the study on these air scale effects has not published yet.

The Stability in Waves committee has investigated the significance of scale effects in air pressure on flooding model tests under atmospheric conditions. For this purpose, the committee classified the flooding cases into the trapped air case and vented air case and investigated the flooding process for a simple geometry using the state equation of air and orifice equation.

In the case of trapped air, the scale effect of air is significant regardless of the damage size. In the case of vented air, the scale effect of air is dependent of the size of vent area. The ratio of the vent area to the damage area plays an important role in the flooding process. When this ratio is large, i.e. a large vent area (the ratio is greater than circa 0.1), the scale effect turns out to be small. For the small vent area, the scale effect is large during the initial stage, and as time passes the scale effect becomes small. In order to reflect the damage model test procedure, in which the model is initially set in equilibrium condition, the effects of assuming the air compression process to be isothermal or adiabatic were investigated after setting the inner air pressure to be equal to the outside water pressure at the position of damage opening in calm water. The scale effect is small in this case for both isothermal and adiabatic process.

As a result, the committee concluded that the scale effect is large for the case of trapped air and small vent area. For the other cases, the effect is small and can therefore be neglected in the model test of a damaged ship. In addition, the committee proposed some directions that can be used to reduce the scale effect of air pressure.

## 2 Model Test and Scale Factor

Damage model test is carried out under the Froude hypothesis. If the Froude number is set to be the same in full scale and model test, there is a dynamic similitude in both. The Froude number,

$$F_n = \frac{V}{\sqrt{gL}} \quad (1)$$

is the ratio of inertia force and gravitational force. Let the scale factor  $\lambda$  be the ratio of ship length to model length. Then the physical quantities follow the scale rules below.

$$\frac{L_s}{L_m} = \lambda, \quad \frac{V_s}{V_m} = \sqrt{\lambda}, \quad \frac{t_s}{t_m} = \sqrt{\lambda}, \quad \frac{\omega_s}{\omega_m} = \frac{1}{\sqrt{\lambda}}, \quad \frac{p_s}{p_m} = \lambda, \quad (2)$$

where  $L$  is length,  $V$  velocity,  $t$  time,  $\omega$  frequency,  $p$  pressure, and the subscript ‘s’ means full scale ship and ‘m’ means model scale. In order to follow the scale rule, the pressure head of the model and the atmospheric pressure should be reduced to the ratio of  $1/\lambda$ .

The water flow through an opening is usually represented by the orifice equation

$$q = C_D \rho_w A \sqrt{2(g\Delta h + \Delta p_a / \rho_w)}, \quad (3)$$

where  $C_D$  is the discharge coefficient of opening,  $\rho_w$  the density of water,  $A$  the area of opening,  $\Delta h$  the difference of water pressure head,  $p_a$  the difference of air pressure in and out. Using water with the same density and gravity, the flow rate obeys the scale rule provided that the air pressure, namely, it follows the scale rule of  $1/\lambda$ .

The model scale pressure should be  $1/\lambda$  in order to maintain dynamic similitude. That is, if the model is small, then the pressure of the air should be reduced proportionally. This is possible only in a depressurised tank facility. Most model basins can only test in atmospheric air conditions, not scaled air pressure. Figure 1 reveals conceptually the difference in pressure head between the scaled air pressure model test and atmospheric model test.

## 3 Scale Effects in Air Pressure

There are some cases in which the flooding of a ship is affected by the air pressure inside the vessel. The main contribution of air pressure takes place in trapped air cases and in vented air cases with small vent area (the area ratio of vent to damage is less than approximately 0.1). In a model test of a damaged ship, if the air pressure is maintained at atmospheric pressure, then scale effects in air pressure occur.

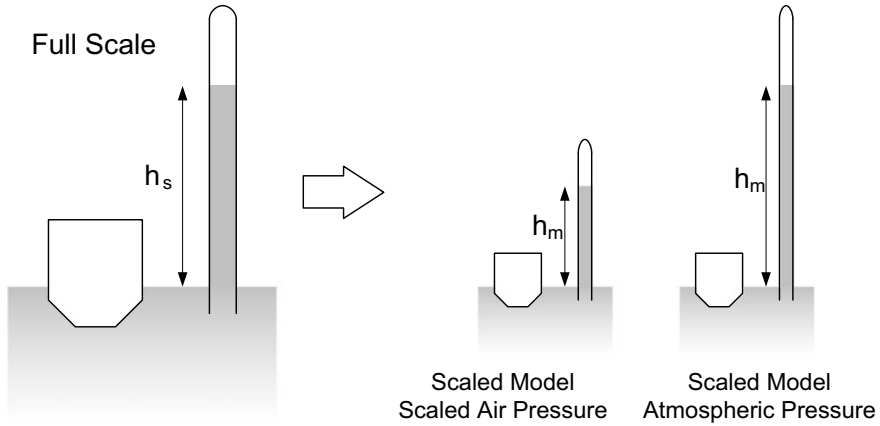


Fig. 1 Concept of scaled model test

For the trapped air case, the pressure of the model in atmospheric conditions is higher than in scaled pressure. Therefore, the flooding to that compartment is restricted as shown in the Fig. 2.

For the vented air case, the air will be compressed and the internal pressure increases. The pressure in atmospheric conditions is higher than in scaled air pressure, so the flooding speed will be slower than in scaled air pressure. Therefore, the following situation will occur, Fig. 3.

We can simulate the above situation by using the state equation of air.

$$PV^\gamma = const., \tag{4}$$

where  $P$  is absolute pressure of the air,  $V$  is the volume under consideration, and  $\gamma$  is the ratio of specific heat, in the case of air it is 1.0 for an isothermal process and 7/5 for an adiabatic process. The flow through an opening can be estimated by the orifice equation.

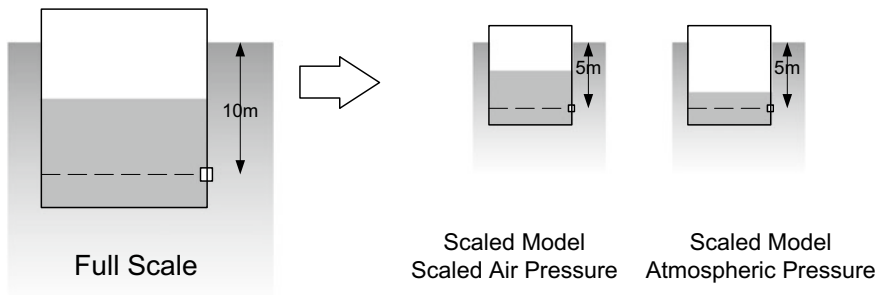
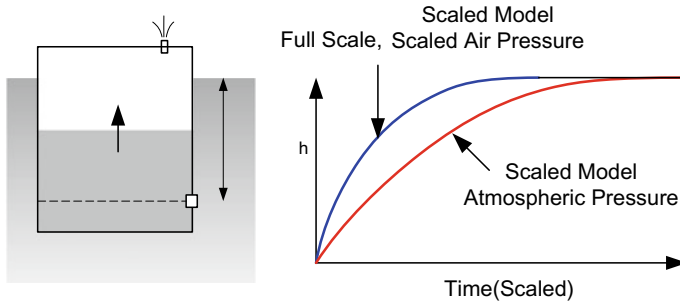


Fig. 2 Flooding in trapped air case





**Fig. 3** Flooding in vented air case

Figures 4, 5 and 6 show the water height behaviour along with scaled time in the case of trapped air case for small opening and large opening in the compartment bottom.

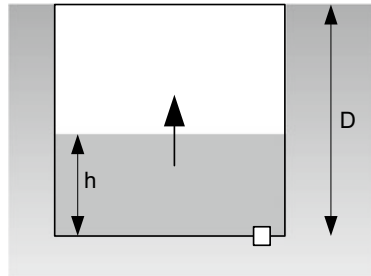


**Fig. 4** Schematic drawing for flooding in non-vented air case

The above two figures are exactly the same except for the time scale. This time scale difference comes from the opening area ratio. As one over the scale ratio becomes small, the final water height reduces also. In this case, the scale effect of air pressure is significant regardless of damage size.

For the vented case, Figs. 7, 8, 9 and 10 show the density ratio of air and water height during the flooding process.

The ratio of the vent area to the damage area plays an important role in the flooding process. When this ratio is large (tentatively over 0.1), i.e. a large vent area, the scale effect turns out to be small. For the small vent area, the scale effect is large during the initial stage, and as time passes the scale effect becomes small.

In order to reflect the damage model test procedure in which the model is initially set in equilibrium condition, the effects of assuming the air compression process to be isothermal or adiabatic can be simulated after setting the inner air pressure to be equal to the outside water pressure at the position of damage opening. For this purpose, the pressure of the compartment is set to the outside water pressure initially

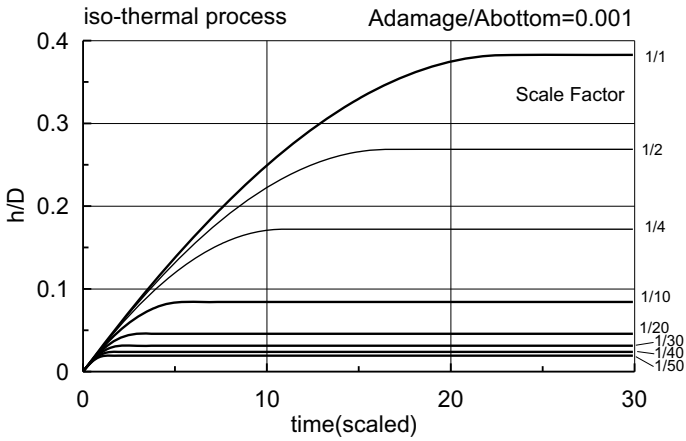


Fig. 5 Flooding in non-vented air case for a small opening

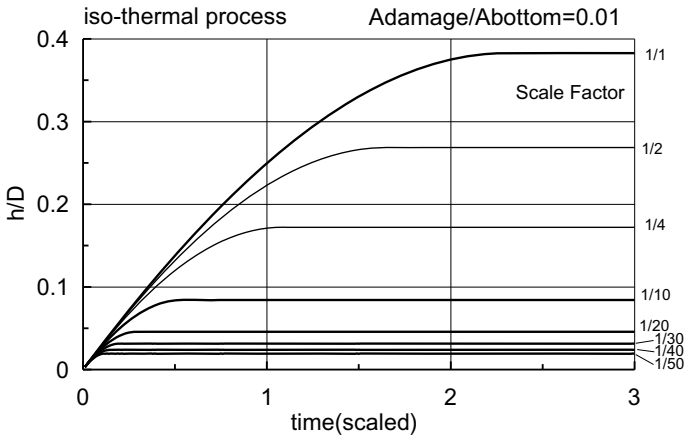


Fig. 6 Flooding in non-vented air case for a large opening

for the vented case. Figures 11 and 12 show the flooding process of the isothermal and adiabatic processes, respectively.

If the flooding speed is slow, the air compression process will be isothermal and if the speed is high the adiabatic process can be applied. When a damaged ship with a large damage opening floats in waves, the flooding due to waves and ship motion is relatively fast, so an adiabatic process takes place in the air compression process. Figures 11 and 12 show that the scale effect is not large.

In line with the above discussion, it can be concluded that the scale effect is large for the case of trapped air and small vent area. For the other cases, the effect is small and can, therefore, be neglected in model tests of a damaged ship.

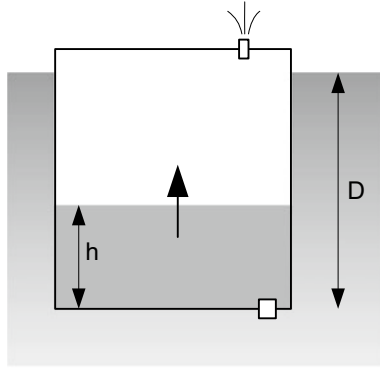


Fig. 7 Schematic drawing for flooding in vented air case

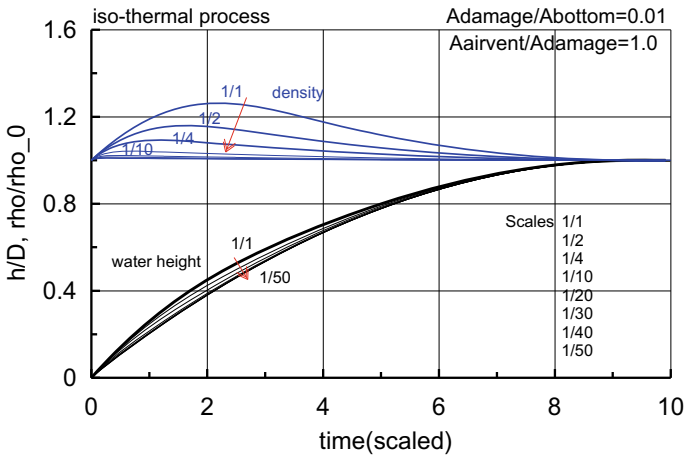


Fig. 8 Flooding in vented air case for a large air vent area

In atmospheric conditions, it is possible to use alternative methods to reduce the scale effect of the air pressure. For the case of a small vent area, the vent opening can be enlarged to an appropriate size in order to reflect the inflow and outflow of the full scale situation. For the case of trapped air, a simple solution would be to attach a balloon to the compartment in order to lessen the scale effect of air pressure and to obtain realistic flooding results in the test condition.

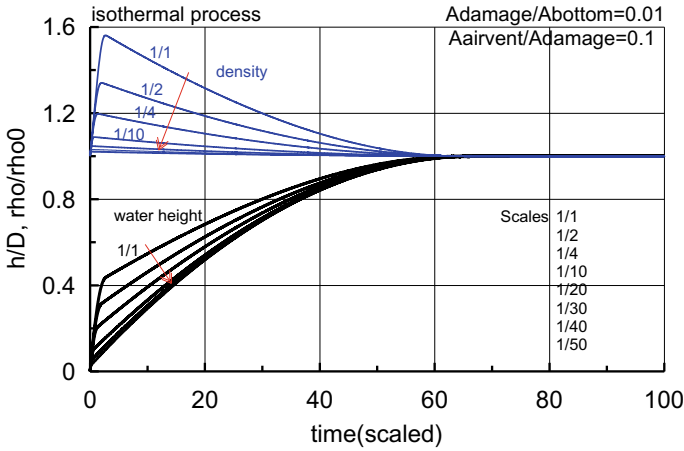


Fig. 9 Flooding in vented air case for a medium air vent area

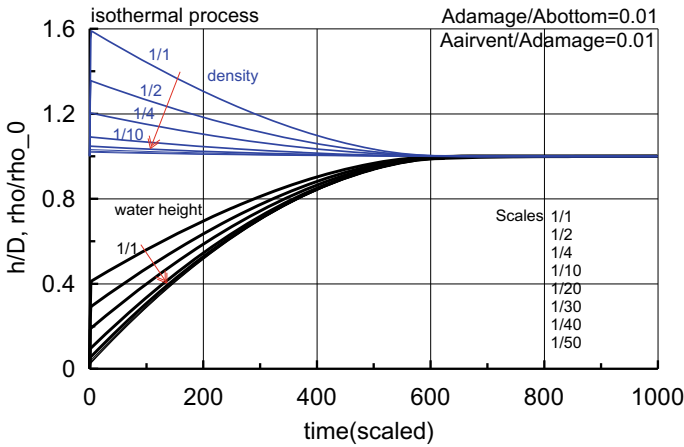


Fig. 10 Flooding in vented air case for a small air vent area

### 4 Conclusions

In summary, if the damage opening is large and the compartment is well vented the scale effect of air pressure will be small and model tests in atmospheric conditions are suitable. The scale effect will be large in the trapped air case and small vent area case. In that situation, if precise and accurate test results are required, the use of pressure regulation values on the compartments to control the internal pressure or model tests in a depressurised model basin are necessary. As a minimum, in the case of model tests in atmospheric conditions, modifications are recommended to reduce scale effects.

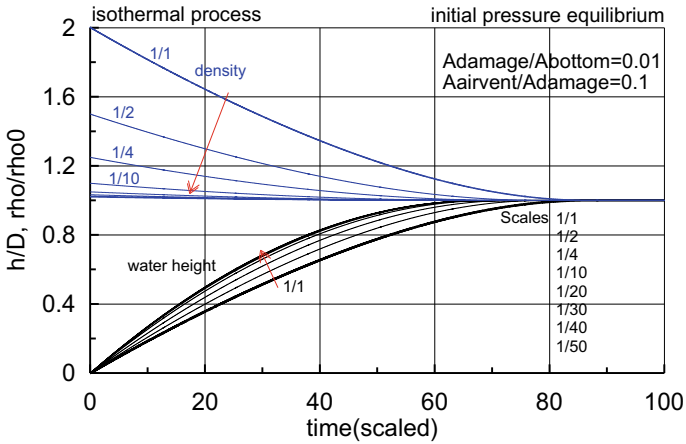


Fig. 11 Flooding for the isothermal process; when the air pressure was initially balanced

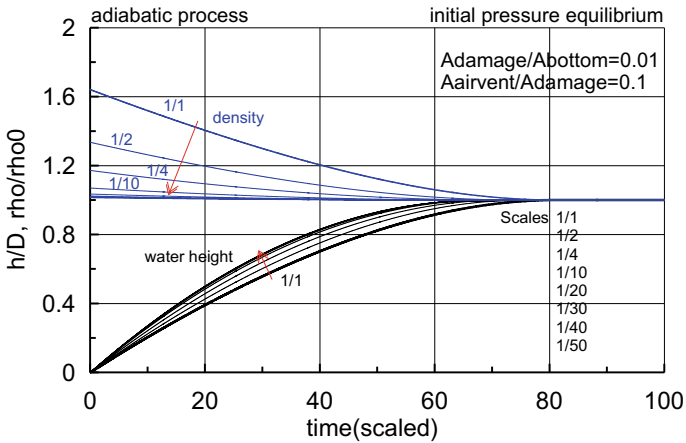


Fig. 12 Flooding for the adiabatic process; when the air pressure was initially balanced

The model test guideline for damage stability experiments (ITTC 7.5-02-07-04.2) was updated to reflect the above discussion.

**Acknowledgements** The aim of this paper is to introduce the work of ITTC Stability in Waves committee on the damage model test. A large part of this material comes from the report of ITTC with some rearrangements.

## References

1. Committee on Stability in Waves (2014) Final Report and Recommendations to 27th ITTC, 27th ITTC
2. ITTC (2014) Recommended procedures and guidelines—model tests on damage stability in waves, 7.5-02-07-04.2, Effective Date:2014, Revision:02
3. MARIN (2013) Depressurised wave basin, Leaflet V2013/05/29, MARIN
4. Ypma E (2010) Model tests in atmospheric and vacuum conditions. FLOODSTAND Report D2.5b
5. Journee J, Vermeer H, Vredeveldt A (1997) Systematic model experiments on flooding of two RO/RO vessels. In: Proceedings of the 6-th international conference on stability of ships and ocean vehicles, 22–27 Sept 1997, Varna, Bulgaria, vol II, pp 81–98
6. Vredeveldt AW, Journee MJ (1991) Roll motion of ships due to sudden water ingress, calculations and experiments. In: RINA'91, International conference on Ro-Ro safety and vulnerability the way ahead, London, UK, 17–19 April 1991, vol 1, paper no 12
7. Peters AJ, Galloway M, Minnick PV (2003) Cross-flooding design using simulations. In: Proceedings of the 8th international conference on stability of ships and ocean vehicles, Madrid, Spain, vol 2, paper no 58, pp 743–755
8. Ruponen P, Queutey P, Kraskowski M, Jalonen R, Guilmineau E (2012) On the calculation of cross-flooding time. *Ocean Eng* 40:27–39
9. Palazzi L, de Kat J (2004) Model experiments and simulations of a damaged ship with air flow taken into account. *Mar Technol* 41(1):38–44
10. Ruponen P, Kurvinen P, Saisto I, Harras J (2013) Air compression in a flooded tank of a damaged ship. *Ocean Eng* 57:64–71

# A Framework for Probabilistic Damage Stability Assessment of Passenger Ships Considering Collision, Grounding and Contact Accidents



**Gabriele Bulian, Mike Cardinale, George Dafermos, Eleftheria Eliopoulou, Alberto Francescutto, Rainer Hamann, Daniel Lindroth, Henning Luhmann, Pekka Ruponen, and George Zaraphonitis**

**Abstract** This contribution provides an overview of the framework implemented in the joint industry project “eSAFE—enhanced Stability After a Flooding Event” for probabilistic damage stability assessment of passenger ships. The framework takes into account collision, bottom grounding and side grounding/contact accidents, by providing specific corresponding attained subdivision indices. Damage

---

G. Bulian (✉) · A. Francescutto  
Department of Engineering and Architecture, University of Trieste, Trieste, Italy  
e-mail: [gbulian@units.it](mailto:gbulian@units.it)

A. Francescutto  
e-mail: [francesc@units.it](mailto:francesc@units.it)

M. Cardinale  
Fincantieri S.p.A., Merchant Ship Business Unit—Basic Design, Trieste, Italy  
e-mail: [mike.cardinale@fincantieri.it](mailto:mike.cardinale@fincantieri.it)

G. Dafermos · E. Eliopoulou · G. Zaraphonitis  
School of Naval Architecture and Marine Engineering, National Technical University of Athens, Athens, Greece  
e-mail: [dafermos@deslab.ntua.gr](mailto:dafermos@deslab.ntua.gr)

E. Eliopoulou  
e-mail: [eli@deslab.ntua.gr](mailto:eli@deslab.ntua.gr)

G. Zaraphonitis  
e-mail: [zar@deslab.ntua.gr](mailto:zar@deslab.ntua.gr)

R. Hamann  
DNV, Regulatory Affairs, Hamburg, Germany  
e-mail: [rainer.hamann@dnv.com](mailto:rainer.hamann@dnv.com)

D. Lindroth · P. Ruponen  
NAPA, Helsinki, Finland  
e-mail: [daniel.lindroth@napa.fi](mailto:daniel.lindroth@napa.fi)

P. Ruponen  
e-mail: [pekka.ruponen@napa.fi](mailto:pekka.ruponen@napa.fi)

H. Luhmann  
Meyer Werft GmbH and Co. KG, Papenburg, Germany  
e-mail: [henning.luhmann@meyerwerft.de](mailto:henning.luhmann@meyerwerft.de)

cases and associated flooding probabilities are determined through a common automatic non-zonal approach, while the post-damage survivability metric is based on the SOLAS “s-factor”. The framework is intended for practical application and is generally consistent with existing SOLAS probabilistic damage stability regulations. To support designers in the application of the framework, a specific software functionality has been developed, tested and applied. Some example applications of the framework are reported.

**Keywords** eSAFE · Damage stability · Non-zonal approach · Collision · Grounding · Contact · SOLAS

## 1 Introduction

The joint industry project “eSAFE—enhanced Stability After a Flooding Event” [28, 29] ran between 2017 and 2018, with the aim of investigating the survivability of cruise ships in damaged conditions, taking into account the specific design features of such complex type of vessels. As described by Luhmann et al. [28, 29], the project investigated a series of aspects related to the assessment of cruise ships survivability in damaged condition, with a view towards practical implementation of the findings from the project in the actual ship design process. Overall, eSAFE represented a significant step forward to achieve survivability standards beyond current statutory SOLAS damage stability regulations.

One of the key objectives of the eSAFE project was the development of a holistic probabilistic methodology, together with an associated NAPA software functionality to be used in actual design, for assessing post-damage ship survivability combining collision, bottom grounding and side grounding/contact damages, through a sound and consistent generalised approach.

To achieve this target, the activities carried out in eSAFE leveraged on, further developed and expanded relevant outcomes from the preceding EMSA 3 project [11], for which a summary of overall final results and corresponding recommendations for decision making have been provided by Vassalos et al. [44]. The results from EMSA 3 and the applied methodology have also been evaluated by the IMO FSA Experts Group [17].

During the EMSA 3 study, a probabilistic method was developed, implemented in a software tool and tested on real designs, for addressing survivability following bottom grounding and side grounding/contact in case of passenger vessels [4, 46]. The method was based on a non-zonal approach where: (a) breaches are directly generated on the basis of a geometrical and probabilistic model for the damage extent through a Monte Carlo approach; (b) “damage cases” are automatically created based on the identification of breached compartments; (c) associated probabilities of flooding are estimated by collecting the probability contribution from breaches leading to the same “damage case”. Survivability for each damage case can then be determined through the usual s-factor, and attained indices are eventually obtained for each



calculation draught and corresponding loading condition. Recently, Bulian et al. [8] have provided a comprehensive description, together with example applications, of the EMSA 3 non-zonal approach, embedding also some improvements stemming from the eSAFE project.

The non-zonal method developed in EMSA 3 for bottom grounding and side grounding/contact has been extended in eSAFE in order to address also collision damages, keeping consistency with present SOLAS [19]. In this context, it was necessary to develop a probabilistic model for the position of the lower edge of damage, as this is missing in the present SOLAS framework [5, 6]. This development, combined with a clear geometrical description of the breach, allowed to develop a non-zonal approach for collision, which could be used alongside those for grounding/contact.

Then, approaches were explored in eSAFE for defining safety metrics in order to combine survivability in case of collision, bottom grounding, and side grounding/contact [47]. To this end, reference has been made to statistical analysis of accidents data and to existing risk-models [23, 46]. In this respect, it is worth noting that, in general, risk-based approaches for damage stability are, of course, not new, and have been developed and used already in the past. This can be appreciated, for instance, from the content in Vassalos et al. [43], Papanikolaou [36], Neves et al. [35] and Belenky et al. [2], and from the relevant papers in the review by Bačkalov et al. [1].

Based on the findings from the mentioned eSAFE activities, a new functionality for practical implementation of the non-zonal approach has been made available in NAPA [27], and the tool has been tested within eSAFE to gain experience and provide feedback.

A procedure for calculation and reporting of results was also envisaged which takes into account the presence of random sampling uncertainty in the application of the non-zonal approach [47].

It is noted that the outcomes from the eSAFE project also represented input for further advancement and development activities within the subsequent FLARE project [12].

Some brief discussion is also worth at this stage regarding the methodological approach used in eSAFE for the results presented herein. In fact, as it will be evident in the following, the reported eSAFE developments are essentially based on a combination of use of historical data and implementation of expert judgement for the risk modelling, when necessary, and on the use of simplified models for the specification of the post-damage survivability metric, essentially the *s*-factor. The use of historical data is the most common approach, and it has the benefits of being based on evidence and to inherently embed information on design and operation of existing ships. At the same time, historical accident data tend to be generally scarce (in terms of total numbers and details), and this eventually leads to statistical uncertainty in the estimation of frequencies/probabilities. Further uncertainty is introduced when, in absence of sufficient historical data, it is necessary to resort to expert judgement. The analysis by Hamann et al. [13] recognises the benefits as well as the shortcomings of exploiting historical data for the development of risk models, and outlines a framework where the analysis of historical data is combined with first-principle

simulation approaches. Such a combined approach has valuable potential, although it should be recognised that the use of first-principle approaches is not free from shortcomings itself. In fact, when first-principle approaches are used, uncertainty may be shifted from the analysis of historical data to the inevitable assumptions implemented in the usage of simulation tools. Nevertheless, the use of first-principle approaches is definitely more flexible, and it allows to carry out more thorough analyses taking into account in more detail ship-specific characteristics. Sensitivity with respect to the used assumptions can also be properly assessed, as deemed necessary. Furthermore, while modelling based on historical data, by its very nature, focuses on “what has happened in the past”, the use of first-principle simulation approaches has the potential for trying to foresee what “may happen in the future”. A typical, well-known, example of first-principle approach for damage stability assessment is the use of numerical time domain flooding simulation tools (e.g. [22, 40, 41, 45]), that may have the potential for, at least, complementing the use of the SOLAS simplified s-factor. As another interesting example, recently, Conti et al. [9] have shown how first-principle approaches for crashworthiness could be quantitatively embedded into a SOLAS-like flooding assessment framework, in order to give proper credit to differences in the ship structural design. Earlier work on this topic can also be linked to the HARDER project [30]. The approach of Conti et al. [9] clearly shows its potential, but it also shows the necessity of introducing simplifying assumptions. Another example in the direction of a more extensive use of first-principle approaches is provided by Zhang et al. [48], who combined AIS traffic data analysis (see also, e.g., [33]), structural analysis and s-factor-based damage stability analysis, to determine the attained subdivision index. Also the work by Zhang et al. [48] clearly shows the potential of first-principle approaches, but, at the same time, it also shows the associated complexity and the need to introduce working/simplifying assumptions. Therefore, while the use of first-principle approaches shall definitely be pursued for future advancement, still the approach based on historical data, expert judgement and simplified survivability metric as used in eSAFE can be considered fully justified.

This contribution is based on Bulian et al. [7] and provides an updated summary overview of the main outcomes of the mentioned activity (see also [28, 29]). In the following, Sect. 2 provides a summary regarding the development of the non-zonal approach for collision. Afterwards, Sect. 3 summarises the different approaches that have been considered for addressing collision, bottom grounding, and side grounding/contacts in a common framework. Section 4 then provides an overview of the software implementation. Section 5 shows some examples from the testing and application. Finally, Sect. 6 reports some summarising conclusions.

## 2 Non-zonal Approach for Collision

The present damage stability framework in SOLAS Ch.II-1 [19] allows determining the probabilities of flooding of a (group of) compartment(s) by using p-, r- and v-factors (SOLAS/II-1/B-1/7-1, SOLAS/II-1/B-1/7-2). In particular, p-factor

accounts for transversal subdivision defining so-called “zones”, and this is why the SOLAS approach can be shortly referred to as “zonal”. The analytical formulae for such factors embed the assumed probability distributions of collision damage characteristics (position, length, penetration and vertical extent above waterline).

It is well known that the basic ideas leading to the present SOLAS originated from the HARDER project (see [30, 31]). Subsequently, some modifications regarding damage distributions have been introduced during the discussion at IMO, leading to the final formulation, as embedded in SOLAS 2009 and eventually in the present SOLAS 2020 regulations.

In the EMSA 3 project a different methodology was proposed for addressing bottom grounding and side grounding/contact [4, 8, 46], which was referred to as “non-zonal”. In the “non-zonal” approach, single breaches are generated using a Monte Carlo procedure based on the distributions of damage characteristics. Each individual breach will lead to the flooding of a certain (set of) room(s), which represents what is usually called a “damage case”. Summing up the probabilities associated to all breaches leading to the same damage case, it is possible to estimate the probability of occurrence of each damage case. This can then be directly used in the calculation of A-indices. The idea of exploiting Monte Carlo generation of breaches for determining damage cases and associated probability of flooding was used also by Kehren and Krüger [24], Krüger and Dankowski [25, 26], Valanto and Friesch [42] and Dankowski and Krüger [10] considering ship performance in terms of regulatory damaged ship stability and/or oil outflow following MARPOL [14, 21, 46]. Given the ship model for damage stability calculations, the application logic of the non-zonal approach is illustrated in Fig. 1.

During eSAFE, the EMSA 3 non-zonal approach was extended to cover also collision damages, keeping, as main target, the highest possible consistency with existing SOLAS framework [5]. To this end, an explicit definition of the geometrical model for collision damages was provided, and the generation of breaches due to collision damages was based on the distributions for damage characteristics according to SOLAS background.

SOLAS, however, does not provide a distribution for the lower limit of vertical extent of damage. Instead, SOLAS uses a “worst-case approach” (often referred to as “damages of lesser extent”), where a systematic variation of the lower limit of damage is carried out in the calculations to find the damage case giving the least s-factor when there are horizontal subdivision boundaries below the waterline (SOLAS/II-1/B-1/7-2/6.2). This approach, by its very nature, is conservative, as it leads to a systematic conservative estimation of the attained subdivision indices [6, 47]. Shortcomings of the use of “damages of lesser extent” have also been highlighted by Krüger and Dankowski [25]. In order to allow a consistent generation of breaches in the eSAFE non-zonal framework for collision, it was therefore necessary to specifically develop and embed a probabilistic model for the lower limit of vertical extent of damage.

The geometrical model for collision damage (conventionally referred to as damage of type “C00” in eSAFE) was defined according to the following characteristics:

- The damage penetration is measured orthogonally to the ship’s centre plane;

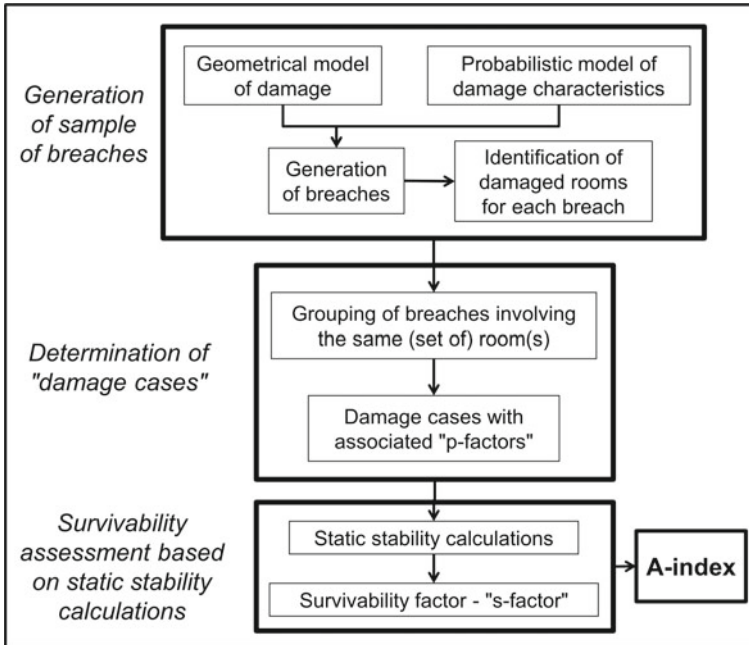


**Fig. 1** Application logic of non-zonal approach

- The longitudinal extent of damage (damage length) is measured parallel to the ship's longitudinal axis;
- The vertical damage extent is measured along the vertical direction;
- The horizontal section (profile) of the damage follows the waterline at the actual calculation draught. As a result, the damage, in general, is not box-shaped.

In addition, for consistency with SOLAS [15, 18], collision damages have been defined to be always crossing the calculation waterline, i.e. the upper limit of damage is always above the waterline and the lower limit of damage is always below the waterline, for each calculation draught.

The damage is defined as a potential damage, this meaning that it can also partially extend outside the vessel. The distributions of all relevant damage characteristics were taken from the analysis of the SOLAS background, with the exception of the distribution for the lower limit of damage that has been newly introduced in eSAFE. In particular [5]:

- Damage side: 50% probability on each side, unless the damage side is specified in the calculations.
- Longitudinal position of centre of the extent of damage within the limits of the ship length,  $X_C$ : uniformly distributed along the ship length.

- Longitudinal extent of damage (potential damage length),  $L_{x,p}$ : bilinear probability density function, with characterising coefficients  $b_{11}$ ,  $b_{12}$ ,  $b_{21}$  and  $b_{22}$  (see [30, 31]) from SOLAS/II-1/B-1/7-1/1.1.
- Transversal extent of damage (potential damage penetration),  $L_{y,p}$ : truncated trapezoidal distribution depending on potential damage length. The cumulative distribution function, before truncation, corresponds to the function  $C(\bar{z})$  reported by Lützen [30, 31].
- Vertical position of upper limit of damage above the waterline,  $z_{UL,p} - d$ : the cumulative distribution function corresponds to the SOLAS v-factor.

For consistency reasons, the “ship length” to be considered in the calculations has been taken as the subdivision length of the ship according to SOLAS.

Furthermore, in order to be consistent with the analytical and theoretical formulation of zonal SOLAS p-factors for compartments at the extremities of the ship length [30, 31, 39], it was necessary to pay particular attention to the proper positioning of the damage, given  $X_C$  and  $L_{x,p}$ . When the damage is fully contained within the ship length, the longitudinal coordinate  $X_C$  corresponds to the centre of damage. However, if the potential damage partially extends outside the vessel, this is no longer the case and the longitudinal coordinate of the midpoint of the potential damage differs from  $X_C$  [3, 16]. The procedure for the longitudinal positioning of the damage is reported in Fig. 2, where, for simplicity of notation, the aft and the forward end of the ship length are assumed to correspond to  $x = 0$  and  $x = L_{ship}$ , respectively. In the figure,  $L_{x,max}$  is the maximum damage length with centre in  $X_C$  that can be within the ship length  $L_{ship}$ , while  $x_{min,p}$  and  $x_{max,p}$  are the longitudinal coordinates for the aft end and forward end of potential damage, respectively.

A further point of attention concerned the proper generation of the potential damage penetration  $L_{y,p}$ , in order to be consistent with the zonal SOLAS r-factor. The absolute maximum damage penetration according to SOLAS is  $B/2$ , where  $B$  is the ship breadth, and this limit is directly embedded in the function  $C(\bar{z})$  reported by Lützen [30, 31], and already mentioned before. However, in addition, the SOLAS framework also implicitly assumes that the ratio between the dimensionless damage penetration and the dimensionless damage length cannot exceed 15 [3, 16, 30, 31, 39]. One possibility to generate damage penetrations consistently with the maximum limit embedded in SOLAS, is to initially generate a potential damage penetration according to the distribution associated with  $C(\bar{z})$ , then, in case the generated penetration exceeds the maximum value  $L_{y,p,max} = (15 \cdot B/L_S) \cdot L_{x,p}$ , the penetration is limited to  $L_{y,p,max}$ , otherwise the generated penetration is kept. It is noted that, since  $L_{y,p,max}$  depends on  $L_{x,p}$ , in this generation approach  $L_{x,p}$  has to be generated before  $L_{y,p}$ .

It is worth mentioning that Krüger and Dankowski [25, 26] addressed SOLAS probabilistic damage stability assessment using a Monte Carlo approach sharing the fundamental logic of the non-zonal approach, and they highlighted some implementation problems related to the treatment of extremities and the treatment of penetration consistently with SOLAS. Such consistency problems are actually resolved by the

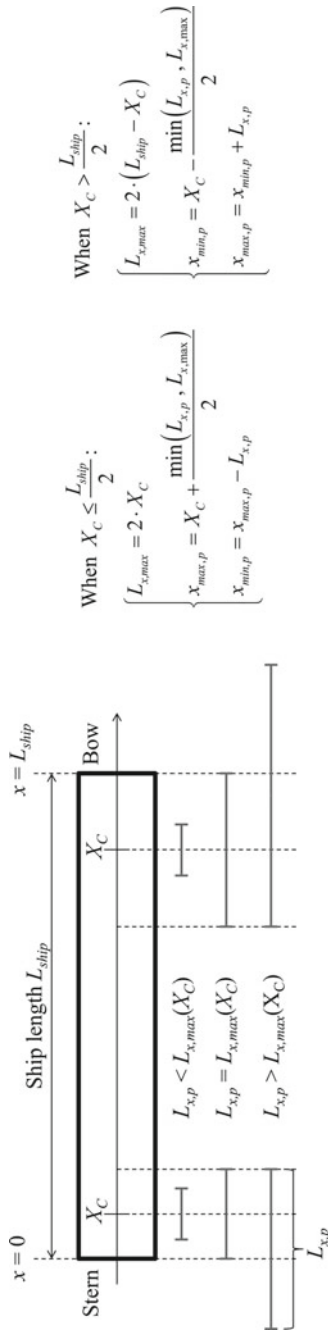


**Fig. 2** Graphical representation of longitudinal positioning of collision damage with corresponding analytical formulae for the determination of longitudinal coordinates for aft end ( $x_{min,p}$ ) and forward end ( $x_{max,p}$ ) of potential damage

damage positioning procedure reported in Fig. 2 and by the described procedure for the generation of penetration, as used in eSAFE.

As SOLAS does not provide a probabilistic model for the extent of damage below the waterline, it was necessary to specifically develop one to be embedded in the non-zonal approach. The development was based on the analysis of historical accident data, using data from the HARDER accidents database as updated in the GOALDS project [3, 16, 32]. Collision damages were considered to be always crossing the waterline, i.e. with upper limit above the waterline and lower limit below the waterline. Two probabilistic models for the lower limit of damage below waterline, with different levels of complexity, were developed, discussed, implemented in the non-zonal approach, and compared [5, 27]. Eventually, one of the two models was selected for describing the vertical position of lower limit of potential damage from the ship bottom,  $z_{LL,p}$ . This model considers  $z_{LL,p}$  to be statistically independent of the other damage characteristics, and to have the following cumulative distribution [5, 6]:

$$\begin{cases} CDF(z_{LL,p}) = 1.4 \cdot \frac{z_{LL,p}}{d} - 0.4 \cdot \left(\frac{z_{LL,p}}{d}\right)^2 \\ z_{LL,p} \in [0, d] \end{cases} \quad (1)$$

where  $d$  is the actual calculation draught. This model is used for describing, and hence generating,  $z_{LL,p}$  in the non-zonal approach. Details of the derivation of this model are given by Bulian et al. [5, 6].

It is noted that the finally selected probabilistic model for the lower limit of damage also allows to easily define a “u-factor” which can be directly embedded in the existing SOLAS zonal framework (see [5, 6] for details).

### 3 Safety Metrics for the Combined Impact of Collision, Grounding and Contact Accidents

For each type of accident (collision, bottom grounding, side grounding/contact), a corresponding attained subdivision index (A-index) can be obtained from damage stability calculations, namely  $A_{CL}$  for collision,  $A_{GR-B}$  for bottom grounding, and  $A_{GR-S}$  for side grounding/contact.

The three mentioned A-indices represent ship survivability, separately, for each type of accident. Depending on the application, these indices are either partial indices, i.e. indices associated with a specific loading condition, or global indices, i.e. indices obtained after averaging across different draughts as in SOLAS.

However, a measure is needed in order to provide a combined quantification of the ship safety. To this end, two different methods to derive a measure of ship survivability, covering all three accident types, have been considered in eSAFE:

- A risk-based safety metric, directly related to societal risk;

- A probability/survivability-based safety metric, based on the relative frequencies of different types of accidents.

The metrics defined by the two approaches are both represented by weighted combinations of individual A-indices corresponding to different types of accidents. Relevant detailed information, in the framework of eSAFE, have been provided by Zaraphonitis et al. [47] and Luhmann et al. [28, 29].

### 3.1 Risk-Based Safety Metric—SM

The risk-based safety metric  $SM$  is directly related to societal risk from collision, bottom grounding and side grounding/contact damages. The fundamental ideas and assumptions behind the developed risk-based safety metric have been anticipated in the EMSA 3 project [23, 44, 46], and can be summarised as follows:

- With reference to consequences from flooding accidents, the total societal risk which is accounted for is given by the sum of the risk due to collision, the risk due to bottom grounding, and the risk due to side grounding/contact;
- The risk is measured through the “Potential Loss of Life ( $PLL$ )”, i.e. the expected number of fatalities per ship-year (which, if needed, can be transformed to ship-life);
- The reference risk models which have been used are those developed in the EMSA 3 study and which are relevant for cruise ships.

The approach has then been applied within eSAFE [28, 29, 47], as described in the following.

The analysis started from existing risk models. Specifically, the reference risk models that have been used in the derivation are those developed in the EMSA 3 study [23, 46] that are relevant for cruise ships. In particular, see Sect. 10.2.5 and Figs. 10–22 in Konolessis et al. [23] for the collision risk model, and Sect. 8.9.2 and Fig. 52 in Zaraphonitis et al. [46] for the grounding and contact risk model.

On the basis of the available risk models, the potential loss of life ( $PLL$ ) associated with each type of accident can be determined, in general, as follows:

$$\begin{cases} PLL_j = POB \cdot c_j \cdot (1 - A_j) \\ j = CL, GR - B, GR - S \end{cases} \quad (2)$$

where  $POB$  is the number of persons on board (crew and passengers, considering assumptions with respect to occupancy). The coefficients  $c_{CL}$ ,  $c_{GR-B}$  and  $c_{GR-S}$  depend on, and can be directly calculated from, the assumed reference risk models. In fact, following the branches of the event tree of the relevant risk model (collision, bottom grounding, side grounding/contact),  $PLL$  can be expressed explicitly as a function of products of initial frequency, conditional probabilities, assumed percentages of fatalities,  $1 - A$ , and  $POB$ . Therefore, each coefficient  $c_{CL}$ ,  $c_{GR-B}$  and  $c_{GR-S}$ ,



can be determined as the proportionality factor between  $PLL$  and  $POB \cdot (1 - A)$  for each type of accident, and each coefficient reflects the whole underlying relevant risk model.

It is noted that, according to Eq. (2), the same value of the attained index  $A$  leads, in general, to different  $PLL$  for given  $POB$ , because coefficients  $c_{CL}$ ,  $c_{GR-B}$  and  $c_{GR-S}$  are, in general, different. This is a direct consequence of the differences among the relevant risk models, in terms of structure of the model, initial frequencies, conditional probabilities and modelling of consequences.

The total  $PLL$  can then be determined by summing up the contribution to risk from the three accidents, which provides the means for defining the safety metric  $SM$ , as follows:

$$\begin{cases} PLL_{TOT} = PLL_{CL} + PLL_{GR-B} + PLL_{GR-S} = POB \cdot c_T \cdot (1 - SM) \\ \text{with } c_T = c_{CL} + c_{GR-B} + c_{GR-S} \end{cases} \quad (3)$$

The safety metric  $SM$  can then be obtained, in general, from its definition in Eq. (3) and from the relations in Eq. (2), as follows:

$$\begin{cases} SM = k_{CL} \cdot A_{CL} + k_{GR-B} \cdot A_{GR-B} + k_{GR-S} \cdot A_{GR-S} \\ k_j = c_j / c_T \quad \text{with } j = CL, GR - B, GR - S \end{cases} \quad (4)$$

and the following result has been obtained in eSAFE, on the basis of the background information:

$$SM = 0.11 \cdot A_{CL} + 0.17 \cdot A_{GR-B} + 0.72 \cdot A_{GR-S} \quad (5)$$

The weighting coefficients of the attained indices in Eq. (5) represent the relative contribution to societal risk stemming from the different types of accidents on the basis of the risk models from EMSA 3, in a hypothetical condition where the attained index is the same for all types of accidents.

It can be noted that the weighting coefficient for side grounding/contact in Eq. (5) is significantly larger than the other two coefficients, and this makes the attained index  $A_{GR-S}$  playing a dominant role in the quantification of the safety metric  $SM$ . This is a direct natural consequence of the background information used in the development. At the same time, this outcome raised a discussion within the eSAFE project, and some relevant considerations are reported hereinafter in Sect. 3.3.

### 3.2 Combined Attained Subdivision Index—A

An alternative way for the derivation of a safety metric considering all three types of accidents is through the definition of a Combined Attained Subdivision Index, using appropriate weighting factors for the three individual A-indices, based on the relative

frequencies (conditional probabilities) of the corresponding accidents, as follows:

$$A = Pr_{CL} \cdot A_{CL} + Pr_{GR-B} \cdot A_{GR-B} + Pr_{GR-S} \cdot A_{GR-S} \quad (6)$$

The combined A-index, therefore, represents a measure of the probability of survival conditional to the occurrence of a flooding accident, hence not considering differences in the consequences for the different accident categories. The relative frequencies (conditional probabilities)  $Pr_{CL}$ ,  $Pr_{GR-B}$  and  $Pr_{GR-S}$  can be determined from the analysis of historical data. To this end, the accidents data analysis in eSAFE relied on the accidents database developed in the EMSA 3 project [23].

Also this approach has been followed in eSAFE [28, 29, 47]. It is noted that the size of available accidents sample, after the filtering, was rather limited, corresponding to 16 accidents in total (collisions: 4, bottom grounding: 3, side grounding/contact: 9). Although this is a good outcome from a safety perspective, it leads to a large uncertainty in the estimated relative fractions of different types of accidents, i.e. in the weighting coefficients of different A-indices. In fact, according to the available data, the conditional probabilities with associated 95% confidence intervals have been estimated as  $Pr_{CL} = 25\%$  [7% , 52% ],  $Pr_{GR-B} = 19\%$  [4% , 46% ] and  $Pr_{GR-S} = 56\%$  [30% , 80% ]. Therefore, from the analysis of data, the following Combined Attained Subdivision Index,  $A$ , was eventually derived (see also [28, 29, 47]):

$$A = 0.25 \cdot A_{CL} + 0.19 \cdot A_{GR-B} + 0.56 \cdot A_{GR-S} \quad (7)$$

It can be noted from Eq. (7) that also in case of the combined A-index, the side grounding/contact accidents are associated with the largest weighting coefficient, which reflects the highest relative fraction of observed accidents. The outcomes from the analysis have been subject to extensive discussion within the eSAFE project, and some relevant considerations are reported in the following Sect. 3.3.

### 3.3 Discussion on Selection and Use of the Safety Metric

Two safety metrics have been defined in eSAFE which share the characteristic that they can both be represented by weighted combinations of individual A-indices corresponding to different types of accidents, namely the risk-based safety metric  $SM$  (see Eq. (5)) and the Combined Attained Subdivision Index  $A$  (see Eq. (7)).

Both options for a combined measure of survivability after a flooding event have been thoroughly discussed during the eSAFE project, and it was concluded that the risk-based approach is to be the preferred one.

Comparing Eqs. (5) and (7), it can be seen that the weighting coefficients for the three attained indices in the two metrics are different. This is a consequence of the fact that the two metrics provide measures associated with two different quantities: societal risk on the basis of the assumed risk models in case of  $SM$ , and probability

of ship survival conditional to the occurrence of a flooding accident in case of the combined A-index. Accordingly, on the one hand, the weighting coefficients in the combined A-index only accounts for relative frequencies of different types of accidents. On the other hand, the weighting coefficients in  $SM$  also embed the relative effect of consequences from different types of accidents, on the basis of the assumed risk models.

The estimated weighting coefficients for both metrics are affected by uncertainty due to the limited sample size coming from accidents data. In addition, the risk-based safety metric  $SM$  also embeds a certain level of uncertainty coming from the subjective expert judgement related to the structure of the underlying risk models and to the specification of probabilities of some events. The topic of quantification of uncertainty was discussed, but not fully explored during eSAFE. This is due to complexity of the matter combined with the limited time frame. As a result, this topic has been left as an important topic to be addressed in future research activities.

Considering the main characteristics and inherent limitations of the two alternatives, it was agreed within eSAFE to use the risk-based safety metric  $SM$ .

However, as shown by the sensitivity analysis in EMSA 3 [23] and by the details of the underlying accident statistics, the number of accidents in the various branches of the event trees of the risk models is small. This, as already highlighted, increases the uncertainty in the weighting coefficients of  $SM$ . In addition, the calculated weighting coefficients show that side grounding/contact seems to be the dominating risk for flooding. This result raised some concerns during the discussions, because it is based on past casualty reports, and it may not reflect the actual situation of cruise ships. Modern technical features and improved operational procedures may have changed the probability for grounding and contact events, and respectively the consequences. Hence, the application of the safety metric  $SM$  in its current form, which to a great degree is based on historical accident data, may not lead to the proper focus during the design of cruise ships. Thus, even if the combined evaluation of different types of damages is regarded as favourable, these aspects require further investigations.

Therefore, it has been decided to use the attained indices separately for collision, bottom grounding and side grounding/contact, for the time being.

In addition, a regular review and update of the risk models has been recommended, in order to achieve a more reliable measure for the risk due to flooding [28, 29, 47].

## 4 Software Implementation for Practical Application

In industrially oriented projects like eSAFE, the implementation of scientific and technical advances into practically applicable tools is of utmost importance in order to quantify and maximize the impact and benefit of the fundamental developments.

By utilizing and extending the technology and a tool developed in the EMSA 3 project [46], a new functionality was originally developed in eSAFE for generating bottom grounding, side grounding/contact and also collision damages, on the basis of the non-zonal approach stemming from eSAFE. This functionality was initially

made available in a modified test version of NAPA software, for evaluation use in the project.

The tool in NAPA was first extended to cover collision damages which, as described in Sect. 2, are consistent with current SOLAS with the addition of a probabilistic model for the extent of damage below the waterline. In addition, the tool embedded an update of the EMSA 3 approach for addressing bottom grounding and side grounding/contact damages, with the aim of harmonizing some aspects of the calculation methods among different types of damages.

The tool was then tested through pilot applications by the developers of the methodology and by the designers [27]. Results from the pilot usage were eventually used to provide insight to the newly developed approach and to guide subsequent calculations within the project. Systematic tests have also shown the usability and robustness of the tool.

The successful pilot testing led to the interest in continuing exploring the potentials and benefits of the developed approach and associated tool. As a result, the original eSAFE test tool has recently been further refined and implemented as a new feature in NAPA software [34]. This recent evolution basically brings the eSAFE approach from the research and development stage, to a new level with potential for generalised practical application.

The tool allows the application of the non-zonal approach considering bottom grounding (B00 damages) and side grounding/contact (S00 damages) according to EMSA 3 modelling [8, 46] and collision (C00 damages) according to the approach developed in eSAFE, which is in line with, and extends, SOLAS (see Sect. 2).

It is also noted that breaches for each damage type are generated separately for each calculation draught. As a result, the calculation of flooding probability for each damage case is also draught dependent for each type of accident. This represents an improvement of the EMSA 3 approach, where, for reasons related to computational time, damage cases and corresponding flooding probabilities were calculated only at the deepest draught and then were kept the same for the other calculation draughts [4, 46]. This updated capability is used in the application examples in the following Sect. 5, and it has also been used by Bulian et al. [8].

## 5 Application Examples

The developed non-zonal approach has been extensively applied throughout the eSAFE project. At first, a series of calculations were carried out to verify the correct implementation of the non-zonal approach for collision [5, 27]. In this context, among other checks, an example verification was carried out for a barge [27] with and without double bottom, and without any additional horizontal subdivision boundary below the waterline.

The barge configuration with double bottom is depicted in Fig. 3. The subdivision of the configuration without double bottom is exactly the same as that shown in Fig. 3, but without the inner bottom. The overall length of the barge, which corresponds to the

subdivision length [19], is 170.25 m, while the length between perpendicular, which is taken as ICLL length [20], is 165 m. The breadth of the barge is 28 m and its total height is 16 m, with a double bottom height of 2 m and a bulkhead deck positioned at 10 m above the bottom. The barge does not have any longitudinal bulkhead, all compartments extend from side to side, and Fig. 3 reports the longitudinal coordinates of the transversal bulkheads.

The loading conditions used in the calculations correspond to a light service draught  $d_l$  of 6.2 m, a partial subdivision draught  $d_p$  of 6.8 m and a deepest subdivision draught  $d_s$  of 7.2 m, all with zero trim. The same metacentric height,  $\overline{GM} = 2$  m, was used for all calculation draughts.

Since the focus of this analysis was the relative comparison between non-zonal and zonal approach, and not the assessment of A-indices in absolute sense, all calculations have been carried out using a permeability  $\mu = 1.00$  for all compartments, without considering any connection between rooms, without considering any opening, without considering any applied moment, and considering only  $s_{final}$ . The s-factor was calculated following SOLAS 2009 according to SOLAS/II-1/B-1/7-2, assuming that the vessel is a passenger ship.

For the case of the barge without double bottom, the SOLAS zonal approach provides exact results in terms of A-indices, because, for that configuration, the “worst-case approach” adopted by SOLAS to deal with horizontal subdivision boundaries below the waterline has no impact on the results. Therefore, the non-zonal approach could be directly compared with SOLAS for such configuration [27]. Instead, in case of the barge with double bottom, the standard SOLAS zonal approach cannot be directly compared with the non-zonal approach due to the use of the “worst-case approach” in SOLAS/II-1/B-1/7-2/6.2 [6]. Therefore, for the barge configuration with double bottom, the outcomes from the non-zonal approach have been compared with those from the SOLAS zonal approach supplemented by the use of the “u-factor” [6]. The verification was successful in both cases, confirming the proper implementation of the non-zonal approach for collision in a way which is consistent with SOLAS.

As an example, a comparison of A-indices for the barge with double bottom is shown in Fig. 4. The figure reports partial and global A-indices from standard SOLAS zonal approach, from SOLAS zonal approach supplemented by “u-factor”, and from non-zonal approach for collision. To increase the accuracy of non-zonal calculations, a total of 12 repetitions with  $10^5$  breaches for each repetition were carried out, and non-zonal data in Fig. 4 correspond to the average A-indices across repetitions, together with 95% confidence interval (which are so small that they are hardly visible). The observed very small differences in Fig. 4 between SOLAS+“u-factor” and non-zonal results are associated with random sampling uncertainty. Instead, the differences with respect to standard SOLAS are due to the use of the “worst-case approach” in the standard SOLAS zonal approach.

A number of practical design-oriented applications have then been carried out throughout the project to assess the developed approach. Among them, a series of calculations have been carried out, as a pilot application, for a cruise ship with overall

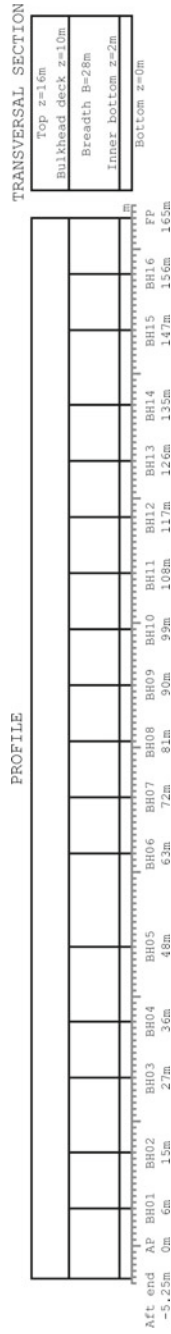
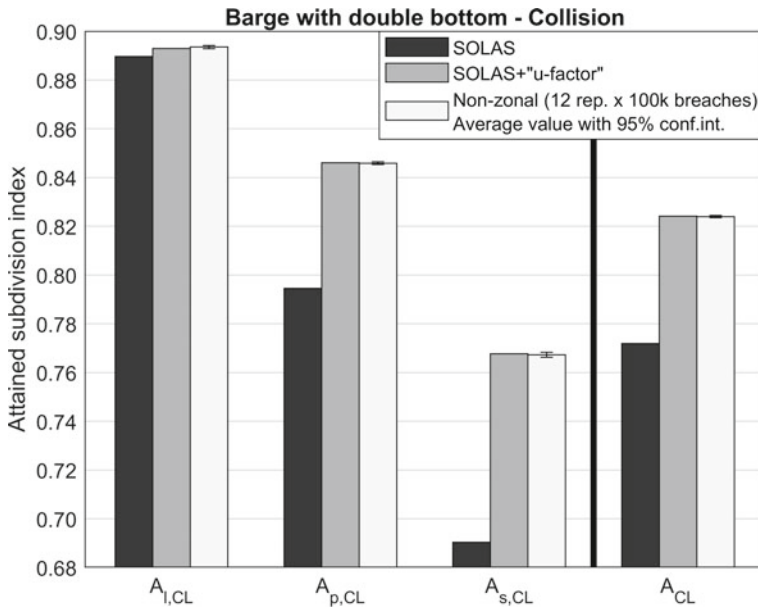


Fig. 3 Barge used for testing. Configuration with double bottom



**Fig. 4** Barge with double bottom. Comparison of partial and global A-indices obtained by standard SOLAS zonal approach, SOLAS zonal approach supplemented by “u-factor”, and non-zonal approach (average values with 95% confidence interval)

length of about 240 m carrying more than 2000 persons onboard, using loading conditions providing marginal compliance with SOLAS 2009 damage stability requirements [27]. An example result of this application of the non-zonal approach for collision is shown in Fig. 5. This figure compares the attained subdivision indices calculated according to standard SOLAS zonal approach, SOLAS zonal approach supplemented by the “u-factor”, and non-zonal approach for collision (average index across repetitions, with 95% confidence interval).

Differently from the case of the barge (see Fig. 4), for the cruise ship (see Fig. 5) the zonal SOLAS+“u-factor” approach is an approximate one, because the cruise ship is not box-shaped and the compartments are, in general, not box-shaped as well. Therefore, in this case, results from the non-zonal approach are to be considered as the “exact” ones, bearing in mind the random sampling uncertainty which is reflected by the confidence intervals shown in Fig. 5. It is therefore expected that results from the non-zonal approach and the SOLAS+“u-factor” approach do not perfectly match. Nevertheless, it can be seen that the zonal SOLAS+“u-factor” provides a very good approximation of the results obtained from the non-zonal approach. Further investigations would be useful to better understand the general level of discrepancy between the application of the approximate SOLAS+“u-factor” approach and the non-zonal approach. It can also be noticed that the introduction of a probabilistic model for the lower limit of damage below the waterline (SOLAS+“u-factor” approach and

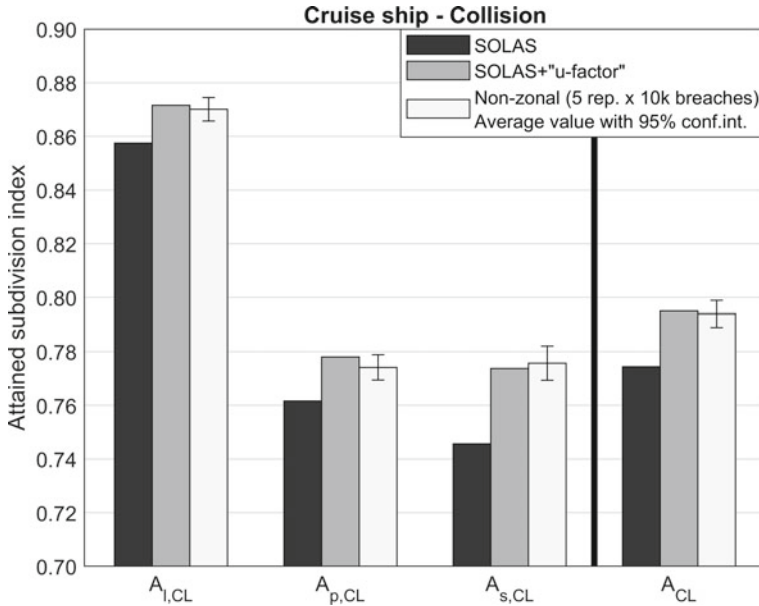


**Fig. 5** Example cruise ship. Comparison of partial and global A-indices obtained by standard SOLAS zonal approach, SOLAS zonal approach supplemented by “u-factor”, and non-zonal approach (average values with 95% confidence interval)

non-zonal approach) provides, as expected, an increase of the calculated attained subdivision indices (see Bulian et al. [6] for more details on this topic).

Further example outcomes from practical application on the same cruise ship are reported in Fig. 6, which shows partial and global A-indices obtained from the non-zonal approach for the three considered types of accidents: collision (CL), bottom grounding (GR-B), side grounding/contact (GR-S). In all cases, the global indices are obtained by averaging the partial indices for the three calculation draughts using standard SOLAS weighting factors, i.e. 0.2 for light service draught  $d_l$ , 0.4 for partial subdivision draught  $d_p$ , and 0.4 for deepest subdivision draught  $d_s$ . In this respect, it is worth noting that the eSAFE project also investigated the suitability of SOLAS assumptions regarding the relative frequency of different draughts in the specific case of cruise vessels, showing that the actual operational profile of cruise vessels would call for the use of weighting factors different from the standard ones [37, 38].

## 6 Conclusions

This contribution has provided an overview of the development and implementation of a common framework for probabilistic damage ship stability assessment of



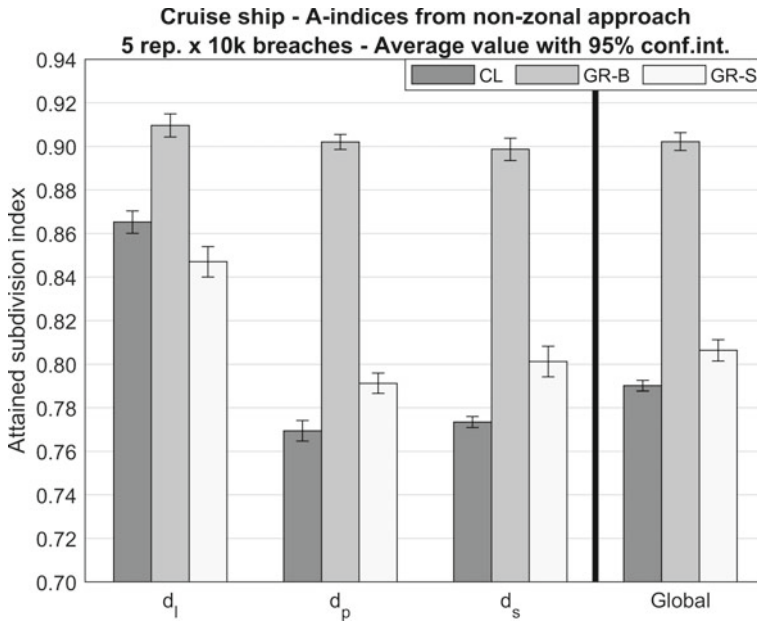


**Fig. 6** Example cruise ship. Partial and global A-indices from non-zonal approach for collision (CL), bottom grounding (GR-B) and side grounding/contact (GR-S). Average values with 95% confidence interval

passenger ships, considering damages due to collision, bottom grounding and side grounding/contact accidents, as carried out during the eSAFE project.

In this respect, the non-zonal approach, originally developed in the EMSA 3 project for bottom grounding and side grounding/contact has been extended in eSAFE to the case of collision.

Consistency with present SOLAS has been taken as a key objective, and it has been demonstrated. Moreover, the lack of a probabilistic description for the lower limit of collision damage in the present SOLAS zonal approach has also been overcome with the development of a specific model based on historical accidents data. This allows a more consistent assessment of the effect of horizontal subdivision boundaries below the waterline and, eventually, of the ship survivability in case of collision accidents.

A software functionality has been developed in NAPA software for the application of the common non-zonal methodology for collision, bottom grounding and side grounding/contact. A number of systematic tests have shown the usability and robustness of the tool, so that it can be used in daily design work. Consequently, the developed approach has a potential generalised practical applicability beyond the research and development level.

Different alternatives have been considered in eSAFE for dealing with the attained subdivision indices from different types of damages: a risk-based safety metric, a combined attained subdivision index, and the separate use of attained indices from

different types of damages. An extensive analysis and associated discussion were carried out within eSAFE regarding the different alternatives. Eventually, it has been recommended by eSAFE to actively use the new tools and first gain experience on the impact of design changes on the survivability following a collision, bottom grounding and side grounding/contact accident, by using the respective attained subdivision indices separately, for the time being. In addition, a regular review and update of the risk models has been recommended, to achieve a more reliable measure for the risk due to flooding. In this respect, it can also be added that a more complete collection of accident details, resulting in additional and higher quality data, would definitely be important to achieve the goal of improving the risk models through the review and update process. It is noted that advances with respect to revision and update of the risk models are being pursued by the recent FLARE project.

The eSAFE non-zonal framework provides now the basis for a holistic assessment of survivability after flooding considering collision, bottom grounding and side grounding/contact. The experience gained during eSAFE also shows that the approach can be of practical application in the actual design activity.

**Acknowledgements** This work was carried out in the framework of the project “eSAFE—enhanced Stability After a Flooding Event—A joint industry project on Damage Stability for Cruise Ships”. The funding partners of eSAFE are: Carnival Corporation Plc, DNV GL, Fincantieri, Lloyd’s Register, Meyer Werft, RINA Services, Royal Caribbean Cruises Ltd. and STX France. The financial support from the eSAFE funding partners is acknowledged.

A number of the achievements from eSAFE reported in this paper build upon and extend some of the outcomes from the EMSA 3 project “Study assessing the acceptable and practicable risk level of passenger ships related to damage stability” (EMSA/OP/10/2013—[www.emsa.europa.eu/damage-stability-study.html](http://www.emsa.europa.eu/damage-stability-study.html)). The original funding of EMSA 3 project from the European Maritime Safety Agency (EMSA), as well as the encouragement to continue the research & development activity in the framework of the eSAFE project, are highly acknowledged.

**Disclaimer** The information and views as reported in this paper are those from the authors and do not necessarily reflect the views of the eSAFE Consortium.

The views as reported in this paper are those of the authors and do not necessarily reflect the views of the respective organizations.

## References

1. Bačkalov I, Bulian G, Cichowicz J, Eliopoulou E, Konovessis D, Leguen J-F, Rosén A, Themelis N (2016) Ship stability, dynamics and safety: Status and perspectives from a review of recent STAB conferences and ISSW events. *Ocean Eng* 116:312–349. <https://doi.org/10.1016/j.oceaneng.2016.02.016>
2. Belenky VL, Spyrou KJ, van Walree F, Neves MAS, Umeda N (eds) (2019) Contemporary ideas on ship stability—risk of capsizing. Springer. <https://doi.org/10.1007/978-3-030-00516-0>
3. Bulian G, Francescutto A (2010) Exploratory data analysis of ship-ship collision data from the updated GOALDS database. Project GOALDS (GOAL based Damage Stability), 30 August
4. Bulian G, Lindroth D, Ruponen P, Zaraphonitis G (2016) Probabilistic assessment of damaged ship survivability in case of grounding: development and testing of a direct non-zonal approach. *Ocean Eng* 120:331–338. <https://doi.org/10.1016/j.oceaneng.2016.02.018>

5. Bulian G, Zaraphonitis G, Francescutto A, Ruponen P (2017) eSAFE-D2.1.1—Description of geometrical and probabilistic model for collision damage. Joint Industry Project “eSAFE—enhanced Stability After a Flooding Event—A joint industry project on Damage Stability for Cruise Ships”, 03 May (Rev.1)
6. Bulian G, Cardinale M, Francescutto A, Zaraphonitis G (2019) Complementing SOLAS damage ship stability framework with a probabilistic description for the extent of collision damage below the waterline. *Ocean Eng* 186(106073):1–11. <https://doi.org/10.1016/j.oceaneng.2019.05.055>
7. Bulian G, Cardinale M, Dafermos G, Eliopoulou E, Francescutto A, Hamann R, Lindroth D, Luhmann H, Ruponen R, Zaraphonitis G (2019) Considering collision, bottom grounding and side grounding/contact in a common non-zonal framework. In: *Proceedings of 7th international ship stability workshop (ISSW2019)*, 10–12 June, Helsinki, Finland, pp 245–257
8. Bulian G, Cardinale M, Dafermos G, Lindroth D, Ruponen P, Zaraphonitis G (2020) Probabilistic assessment of damaged survivability of passenger ships in case of grounding or contact. *Ocean Eng* 218(107396):1–27. <https://doi.org/10.1016/j.oceaneng.2020.107396>
9. Conti F, Le Sourne H, Vassalos D, Kujala P, Lindroth D, Kim SJ, Hirdaris S (2021) A comparative method for scaling SOLAS collision damage distributions based on ship crashworthiness—application to probabilistic damage stability analysis of a passenger ship. *Ships Offshore Struct.* <https://doi.org/10.1080/17445302.2021.1932023>
10. Dankowski H, Krüger S (2011) On the safety level of the SOLAS 2009 damage stability rules for RoPax vessels. *Marine Syst Ocean Technol* 6:87–96. <https://doi.org/10.1007/BF03449296>
11. EMSA (2020) Study assessing the acceptable and practicable risk level of passenger ships related to damage stability. <http://www.emsa.europa.eu/damage-stability-study.html>. Last accessed 14 Aug 2020
12. FLARE (2021) Flooding Accident REsponse (FLARE) Project. <https://flare-project.eu/>
13. Hamann R, Eliopoulou E, Zaraphonitis G (2019) Deliverable 2.5—Revised event tree and recommendations for improvements. Project “Flooding Accident REsponse (FLARE)”, 30 November (V01). Available from <https://flare-project.eu/>
14. IMO (2003) Resolution MEPC.110(49)—Revised interim guidelines for the approval of alternative methods of design and construction of oil tankers under regulation 13F(5) of Annex I of MARPOL 73/78. 18 July (see also corrigenda issued through IMO Document MEPC 49/22/Add.2/Corr.1 on 3 February 2006)
15. IMO (2008) Resolution MSC.281(85)—Explanatory notes to the SOLAS Chapter II-1 Subdivision and damage stability regulations, 4 Dec
16. IMO (2012) SLF 55/INF.7—The GOAL based Damage Stability project (GOALDS)—Derivation of updated probability distributions of collision and grounding damage characteristics for passenger ships. Submitted by Denmark and the United Kingdom, 14 Dec
17. IMO (2015) SDC 3/3/4—Report of the intersessional meeting of the Experts Group on Formal Safety Assessment (FSA). Submitted by the Chairman of the FSA Experts Group, 12 Nov
18. IMO (2017) Resolution MSC.429(98)—Revised explanatory notes to the SOLAS Chapter II-1 Subdivision and damage stability regulations, 9 June
19. IMO (2020) International Convention for the Safety of Life at Sea (SOLAS). Consolidated edition
20. IMO (2020) International Convention on Load Lines, 1966, as amended by the 1988 Protocol by Res. MSC.143(77) in 2003. Consolidated edition
21. IMO (2020) International Convention for the Prevention of Pollution from Ships. Consolidated edition
22. Jasionowski A (2001) An integrated approach to damage ship survivability assessment. PhD Thesis, University of Strathclyde
23. Konovessis D, Hamann R, Eliopoulou E, Luhmann H, Cardinale M, Routi A-L, Kujanpaa J, Bertin R, Harper G, Pang E, Papanikolaou A (2015) Risk acceptance criteria and risk based damage stability, Final Report, part 2: Formal Safety Assessment. DNVGL Report No.: 2015-0166 Rev.3, Project EMSA/OP/10/2013, European Maritime Safety Agency, 29 June. Available from <http://www.emsa.europa.eu/damage-stability-study.html>

24. Kehren F-I, Krüger S (2007) Development of a probabilistic methodology for damage stability regarding bottom damages. In: Proceedings of 10th international symposium on practical design of ships and other floating structures (PRADS2007), Houston, Texas, USA
25. Krüger S, Dankowski H (2009) On the evaluation of the safety level of the Stockholm Agreement. In: Proceedings of 10th International Marine Design Conference (IMDC2009), Trondheim, Norway, 26–29 May
26. Krüger S, Dankowski H (2019) A Monte Carlo based simulation method for damage stability problems. In: Proceedings of ASME 2019 38th International Conference on Ocean, Offshore and Arctic Engineering (OMAE2019), June 9–14, Glasgow, Scotland, UK
27. Lindroth D, Bulian G, Dafermos G, Zaraphonitis G, Cardinale M, Luhmann H, Ruponen P (2017) eSAFE-D2.3.1—Final report of “WP2.3—Development of a software tool for the application of the combined methodology”. Joint Industry Project “eSAFE—enhanced Stability After a Flooding Event—A joint industry project on Damage Stability for Cruise Ships”, 09 Aug (Rev.1)
28. Luhmann H, Olufsen O, Atzampos G, Bulian G (2018) eSAFE-D4.3.1—Summary report. Joint Industry Project “eSAFE—enhanced Stability After a Flooding Event—A joint industry project on Damage Stability for Cruise Ships”, 24 Oct (Rev.4)
29. Luhmann H, Bulian G, Vassalos D, Olufsen O, Seglem I, Pöttgen J (2018) eSAFE-D4.3.2—Executive summary. Joint Industry Project “eSAFE - enhanced Stability After a Flooding Event—A joint industry project on Damage Stability for Cruise Ships”, 24 October (Rev.3). Available from <https://cssf.cruising.org/projects>
30. Lützen M (2001) Ship collision damages. PhD Thesis, Department of Mechanical Engineering, Technical University of Denmark, Lyngby, Denmark, December
31. Lützen M (2002) Damage distributions. Document 2-22-D-2001-01-4, Project HARDER (Harmonisation of Rules and Design Rationale), 29 Jul
32. Mains C (2010) WP3 Database of damage characteristics—File: GOALDS-database-rev3.xls. Project GOALDS (GOAL based Damage Stability)
33. Montewka J, Hinz T, Kujala P, Matusiak J (2010) Probability modelling of vessel collisions. *Reliab Eng Syst Saf* 95:573–589. <https://doi.org/10.1016/j.res.2010.01.009>
34. NAPA (2020) NAPA for Design Manuals 2020.1—Damage Stability (DAM)—Non-Zonal Analysis (DAM)
35. Neves MAS, Belenky VL, de Kat JO, Spyrou K, Umeda N (eds) (2011) Contemporary ideas on ship stability and capsizing in waves. Springer. <https://doi.org/10.1007/978-94-007-1482-3>
36. Papanikolaou A (ed) (2009) Risk-based ship design—Methods, tools and applications. Springer. <https://doi.org/10.1007/978-3-540-89042-3>
37. Paterson D, Atzampos G, Vassalos D, Boulougouris E (2017) eSAFE-D1.2.1—Analysis of onboard data with regards to probabilities of initial draughts. Joint Industry Project “eSAFE—enhanced Stability After a Flooding Event—A joint industry project on Damage Stability for Cruise Ships”, 01 Mar (Rev.5)
38. Paterson D, Vassalos D, Atzampos G, Boulougouris E, Luhmann H (2019) Impact of drafts on the damage survivability of cruise ships. *Ocean Eng* 187(106136):1–8. <https://doi.org/10.1016/j.oceaneng.2019.106136>
39. Pawłowski M (2004) Subdivision and damage stability of ships. Euro-MTEC book series, Foundation for the Promotion of Maritime Industry, Gdansk, Poland, Poland, ISBN 83-919488-6-2, 311p
40. Ruponen P, Lindroth D, Routi A-L, Aartovaara M (2019) Simulation-based analysis method for damage survivability of passenger ships. *Ship Technology Research* 66:180–192. <https://doi.org/10.1080/09377255.2019.1598629>
41. Spanos D, Papanikolaou A (2014) On the time for the abandonment of flooded passenger ships due to collision damages. *J Mar Sci Technol* 19:327–337. <https://doi.org/10.1007/s00773-013-0251-0>
42. Valanto P, Friesch J (2009) HSVA Report No. 1669—Research for the parameters of the damage stability rules including the calculation of water on deck of Ro-Ro passenger vessels, for the amendment of the directives 2003/25/EC and 98/18/EC—Final report Part I. 22 Jul

43. Vassalos D, Hamamoto M, Papanikolaou A, Molyneux D (eds), Spyrou K, Umeda N, de Kat JO (co-eds) (2000) Contemporary ideas on ship stability. Elsevier
44. Vassalos D, Hamann R, Zaraphonitis G, Luhmann H, Kuusisto T, Lietzen J (2016) Combined assessment of cost-effectiveness of previous parts, FSA compilation and recommendations for decision making. DNVGL Report No.: 2015-0404 Rev.1, Project EMSA/OP/10/2013, European Maritime Safety Agency, 12 Jan. Available from <http://www.emsa.europa.eu/damage-stability-study.html>
45. Vassalos D (2022) The role of damaged ship dynamics in addressing the risk of flooding. *Ships Offshore Struct* 17(2):279-303. <https://doi.org/10.1080/17445302.2020.1827639>
46. Zaraphonitis G, Bulian G, Lindroth D, Hamann R, Luhmann H, Cardinale M, Routi A-L, Bertin R, Harper G, Papanikolaou A, Francescutto A, Ruponen P (2015) Evaluation of risk from raking damages due to grounding, Final report. DNV GL Report No.: 2015-0168 Rev.2, Project EMSA/OP/10/2013, European Maritime Safety Agency, 17 Jun. Available from <http://www.emsa.europa.eu/damage-stability-study.html>
47. Zaraphonitis G, Bulian G, Hamman R, Eliopoulou E, Cardinale M, Luhmann H (2017) eSAFE-D2.2.1—Description of methodology. Joint Industry Project “eSAFE—enhanced Stability After a Flooding Event—A joint industry project on Damage Stability for Cruise Ships”, 29 Mar (Rev.2)
48. Zhang M, Conti F, Le Sourne H, Vassalos D, Kujala P, Lindroth D, Hirdaris S (2021) A method for the direct assessment of ship collision damage and flooding risk in real conditions. *Ocean Eng* 237(109605):1–20. <https://doi.org/10.1016/j.oceaneng.2021.109605>

# Cruise Ship Survivability in Waves



**Georgios Atzamos, Dracos Vassalos, Jakub Cichowicz, Donald Paterson,  
and Evangelos Boulougouris**

**Abstract** Recent developments in damage stability legislation have drawn from ships with simple internal architecture such as RoPax and cargo ships. However, ships with complex internal architecture, such as cruise ships, have been rather neglected. In a regulatory context, cruise ships are currently grouped with RoPax and other passenger ships and this can be misleading. Moreover, it is well known that cruise ships vary significantly in their behaviour post-flooding incidents in comparison to RoPax ships. This problem has been acknowledged by the Cruise Ship Safety Forum Steering Committee who consequently funded the Joint Industry Project eSAFE to undertake cruise ship-focused research on damage stability. This entails analysis of pertinent simplifications embedded in SOLAS, the development of a methodology to combine consequences from collision and grounding accidents, the establishment of new survival criteria for cruise ships and finally the development of guidelines to use numerical flooding simulation in seaways as an alternative approach to assessing ship damage survivability. The findings of this research are presented in this paper, based on a full set of time-domain numerical simulations along with static calculations for a number of cruise ships. A new s-factor is derived catering specifically for cruise ships that accounts more accurately for survivability in a wave environment. A number of simulations are undertaken on varying size cruise ships with the view to deriving a relationship between the critical significant wave height and the residual stability

---

G. Atzamos (✉)

Royal Caribbean Group, Miami, FL, USA

e-mail: [gatzamos@rccl.com](mailto:gatzamos@rccl.com)

D. Vassalos · D. Paterson · E. Boulougouris

Maritime Safety Research Centre, Glasgow, Scotland

e-mail: [d.vassalos@strath.ac.uk](mailto:d.vassalos@strath.ac.uk)

D. Paterson

e-mail: [d.paterson@strath.ac.uk](mailto:d.paterson@strath.ac.uk)

E. Boulougouris

e-mail: [evangelos.boulougouris@strath.ac.uk](mailto:evangelos.boulougouris@strath.ac.uk)

J. Cichowicz

DNV, Oslo, Norway

e-mail: [jakub.cichowicz@dnv.com](mailto:jakub.cichowicz@dnv.com)

properties of such vessels. The results provide the requisite evidence for comparison between SOLAS 2009 A-Index and the ensuing Damage Survivability Index.

**Keywords** Damage stability · Survivability · s-factor · Safety · Time domain numerical simulations · Cruise ship · Flooding

## 1 Introduction

Damage stability has largely developed as a subject over the past 50 years with most of the scientific advances achieved over the latter half of this period. However, the focus concerning such developments and the ensuing legislation is clearly on ships with simple internal architecture such as RoPax and Cargo ships. Ships with complex internal architecture, on the other hand, such as cruise ships, have been treated as a side line; in essence seldom the focus of scientific research on damage stability. For example, the current SOLAS for probabilistic damage stability is based on cargo ships, irrespective of the fact that RoPax have spearheaded developments over the recent past, following a number of serious accidents. In the regulatory context, cruise ships are currently grouped with RoPax and other passenger ships and this is causing serious problems. Cruise ships have a significantly different behaviour after flooding incidents as opposed to RoPax ships. In particular, cruise ships are usually found not so vulnerable to rapid capsizes as RoPax vessels. Results from numerical time-domain simulations of damage scenarios for both ship types support this fact. More specifically, comparison between results from SOLAS2009 calculations and numerical simulations display a significant difference for cruise ships [19]. This problem has been acknowledged by the Cruise Ship Safety Forum, which has consequently initiated research on this subject in a Joint Industry Project, namely eSAFE. A key objective in this project is to identify and to the degree possible quantify the differences between known and/or expected safety levels as indicated by the results from time-domain flooding simulations of cruise ships and the simplified methodology defined in SOLAS II-1 [11].

This paper delves in this direction through the use of available methods to defining damage stability/survivability of passenger ships, namely the Statistical (SOLAS) and Direct (numerical time-domain simulation) approaches. In this respect, a new s-factor, specifically catering for cruise ships has been devised following the statistical approach based on four sample cruise ships. In addition, a number of numerical simulations in pertinent sea states are performed with the view to gauging survivability in waves, linked to collision and grounding damages for two large cruise ships. On this basis, a comparison is conducted between the statistical and direct approaches results leading to drawing specific conclusions.

## 2 Statistical Approach to Damage Stability (A-Index)

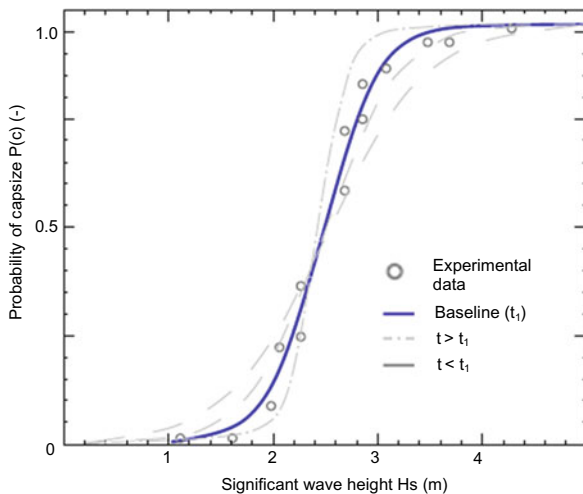
### *Critical significant wave height and capsize band*

The critical sea state for a specific damage extent and loading condition can be established either with the aid of model tests or by employing time-domain numerical simulations based on first principles. Traditionally, both approaches have been utilised in the past in the course of developing damage stability criteria, including comparisons between the two [7, 8]. Generally, both physical and numerical experiments refer to repeated trials (usually corresponding to 30 min full-scale) in a specific random sea with the view to deriving capsize rate at a specific significant wave height.

In this respect, one of the main elements, which can be derived from the characteristics of the damaged ship is the capsize band. This indicates the range of sea states within which a transition from unlikely ( $P_c = 0$ ;  $P_s = 1$ ) to certain capsize ( $P_c = 1$ ;  $P_s = 0$ ) can be observed, where  $P_c$  is probability of capsize  $P_s$  probability of survival. Another concept intrinsically linked to the capsize band is the capsize rate. The capsize rate follows always a sigmoid shape distribution. The rate of observed capsizes depends on the time of observation. In this respect, in case of a limiting case of infinite exposure time the capsize rate distribution will turn into a unit step function as indicated in Fig. 1 for increased simulation times. Indeed, for low capsize probability, the corresponding significant wave height will remain the same (minor difference) when the time of observation is increased [13]. Hence, a sea state corresponding to a low capsize rate can be established on the basis of relatively short simulations and would still remain valid for longer observations.

Following previous studies, the concept of the s-factor is linked to the critical significant wave height. Originally, during the EU project HARDER (Tuzcu, 2003b) the s-factor was linked to the critical significant wave height of the sea state at which

**Fig. 1** Indicative capsize rate transition from baseline curve with increase or decrease of observation time. Where  $t$  represents the simulation observation time and  $t_n$  stands for infinite time. When  $t = t_n$  the sigmoid becomes a vertical line





a ship exposed for half an hour (30 min) to the action of waves would have a 50% chance of capsizing. However, based on subsequent observations in project GOALDS [16], it was found that when the simulation time increases, the capsize band contracts towards its lower boundary, with the capsize probability becoming a step function of  $H_s$ .

***eSAFE—Cruise ship specific s-factor***

In order to account for the complex internal watertight architecture and loss mechanisms of modern passenger ships, a new s-factor derivation has been developed within project eSAFE, catering specifically for cruise ships. Such internal watertight detail can be sufficiently captured with the aid of numerical simulations. To this end, for the first time in the history of development of damage stability criteria, estimation of damage survivability is solely based on numerical time-domain simulation results for four varying size cruise ships using the dynamic numerical time-domain code PROTEUS3 [12].

The new s-factor, does not only account for the variations in cruise ship size but also has been proven robust for different compartment damages, namely (1, 2, 3 and 4-compartment equivalent). Based on regression of the numerical simulation results (94 points in total), a relationship has been derived between the critical significant wave height and residual stability properties, in line with previous work.

A new formula for predicting the critical significant wave height  $H_{s_{crit}}$  has been developed as shown by Eq. (1). Based on statistical analysis of the various data sets, the most accurate regression was achieved with reference to  $GZ_{max}$  and Range properties (as in Project HARDER) but with an additional scaling factor taken into account ( $\lambda$ ) namely EVR as explained further below (similar to Project GOALDS), [6]. The regression has been conducted with consideration of all data points, accounting for critical significant wave heights that span up to 7 m, using global wave statistics [14]. The deviation from SOLAS of using actual wave statistics, rather than wave statistics pertaining to sea states at the time of the incident, is based on the argument that it is essential to estimate the risk of exposing ships to all operating sea states (thus, calculating pertinent risk), and not just those wave characteristics at which accidents have taken place in the past (historical risk). The multiplier in Eq. (1) represents the 99th percentile of the cumulative probability.

$$H_{s_{crit}} = 7 \cdot \left[ \frac{\min(\lambda \cdot Range, T Range)}{T Range} \cdot \frac{\min(\lambda \cdot GZ_{max}, T GZ_{max})}{T GZ_{max}} \right]^{1.05} \quad (1)$$

where,

- $T G Z_{max}$  30 cm Target  $GZ_{max}$  value
- $T Range$  30° Target range value
- $\lambda$  Scaling factor accounting for damage and ship size.

The new s-factor addresses only progressive flooding and is derived on the basis of  $GZ_{max}$  and Range of the un-truncated residual stability curve. This implies that these

values have not been limited to the angle in which unprotected openings are immersed but instead only the angle at which the righting lever vanishes. Such characteristics (openings) relate to local details in ship geometry that cannot be easily captured by global parameters such as properties of the residual stability curve.

In light of the derived results, a disparity was observed, which was attributed to the difference in scale in both the size of each vessel and the volume of accumulated flood-water associated with each of the respective damage cases. To account for this, it was deemed necessary to find an appropriate scaling factor. In this effort, several parameters were investigated including residual freeboard and residual volume. However, the most suitable scaling parameter was found to be the “Effective Volume Ratio” denoted as  $\lambda$ ; a parameter which accounts for both the scale of the damage and that of the vessel. Therefore, the EVR is provided by Eq. (2) as follows,

$$\lambda = \text{Effective Volume Ratio} = \frac{V_{residual}}{V_{flooded}} \tag{2}$$

where, the residual volume  $V_{residual}$  is provided from Eq. (3) below,

$$V_{residual} = V_{WTE} - V_{Displacement} - V_{Flooded} \tag{3}$$

where specifically,

- $V_{WTE}$  Weathertight Envelope is the real weathertight extent and refers to the total volume of all rooms contained in the area spanning from the base line up to and including the deck at which weathertight structure spans vertically. This represents the physical properties of the vessel.
- $V_{Displacement}$  Volume displacement of a given vessel ( $m^3$ )
- $V_{Flooded}$  Volume of the water in the flooded compartments at the final stage of flooding, based on static calculations.

Thus, the scaling factor ( $\lambda$ ) is the ratio of Effective Volume Ratios for two cruise ships used as mentioned earlier. This is applied directly to residual stability properties of the GZcurve, namely Range and GZmax as shown in Eq. (1). Given this, a formulation to calculate the s-factor is given by the regressed CDF of wave heights from IACS Global wave statistics. The new s-factor is provided next:

$$s(H_{s_{crit}}) = e^{-e(1.1717-0.9042 \times H_s)} \tag{4}$$

where,

$H_{s_{crit}}$  critical significant wave height [Notably, when  $H_{s_{crit}} = 7$  m,  $s(H_{s_{crit}}) = 1$ ].

### 3 Direct Approach to Survivability Assessment of Cruise Ships

#### Background

The s-factor in SOLAS 2009 is estimated based on the assumption that the ship capsizes within half an hour exposure [17, 18]. This, however, is not applicable for cruise ships since they take minutes to hours due to their intricate internal architecture, hence the need to ascertain the impact of time on cruise ship survivability and to account for this. The Time To Capsize (TTC), is a random variable, thus only known as a distribution determined through probabilistic methods. Moreover, survivability depends on a number of governing parameters (e.g. loading condition, sea state, damage extent) all of which are also stochastic in nature. In this respect, accounting only for the damage case scenarios implicit in SOLAS 2009 (typically over 1000 for a typical passenger ship) and considering the 3 loading conditions, also implicit in these regulations, and some 10 sea states per damage case for estimating capsize rates, it becomes readily obvious that some form of simplification and reduction will be meritorious.

To this end, one of the most efficient ways, entails a process involving Monte Carlo sampling from distributions of pertinent random variables (damage extents, loading conditions, sea states, etc.) to generate damage scenarios and perform numerical time-domain simulations. The latter accounts accurately for the physical phenomena of ship-floodwater-wave interactions as function of time providing robust indication on which of these scenarios would lead to ship capsize/sinking and the TTC. In this manner, any assumptions and approximations inherent in the probabilistic elements of SOLAS 2009 damage stability regulations are diminished/minimised (Fig. 2).

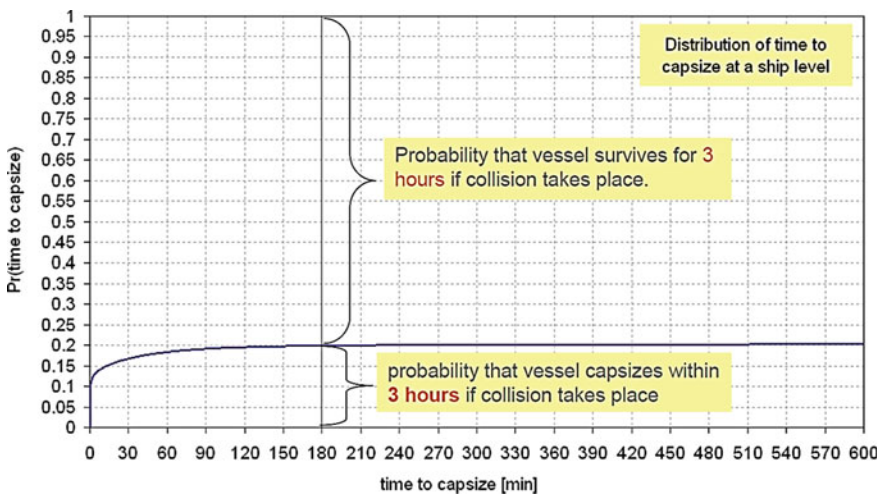


Fig. 2 Cumulative marginal probability for time to capsize [19]

In the comparison of the two sets of results between the direct and statistical approaches, it is to be noted that the Attained subdivision Index (Eq. 5) is an aggregate probability representing the average probability of survival for a set of generated damages. Hence, survivability is calculated for each damage scenario as the “expected” outcome averaged with respect to the distribution of wave heights. On the other hand, the survivability level obtained from numerical simulations (herein denoted as “Survivability Index” indicated by Eq. 6) uses a single significant wave height sampled from pertinent wave statistics and the random outcome (survival or capsized) is then averaged across all damages and loading conditions.

$$Attained\ Index\ (AI) = \sum p \cdot w \cdot \bar{s} \tag{5}$$

$$Survivability\ Index\ (SI) = \sum p \cdot w \cdot s \tag{6}$$

**Monte Carlo numerical simulation methodology**

Survivability can be assessed with use of time-domain simulations for a group of damages. This allows for derivation of an estimate of the expected probability of survival for a given group of damages characterised by random locations, damage extent and sea states. The Time To Capsize (TTC) can be defined through an automated process using Monte Carlo sampling (see Fig. 4) and dynamic flooding simulations with the time-domain numerical simulation code PROTEUS3 as shown in Fig. 3 for a 3 compartment damage [12].

Two large cruise ships ranging in overall length ( $290 \leq L_{OA} \leq 325$ ) have been subjected to a number of Monte Carlo simulations for a single loading condition, namely the deepest subdivision draft. Significant wave heights are randomly sampled from the distribution of global wave statistics as presented in [14], which is provided

**Fig. 3** 3-compartment aft damage in PROTEUS3

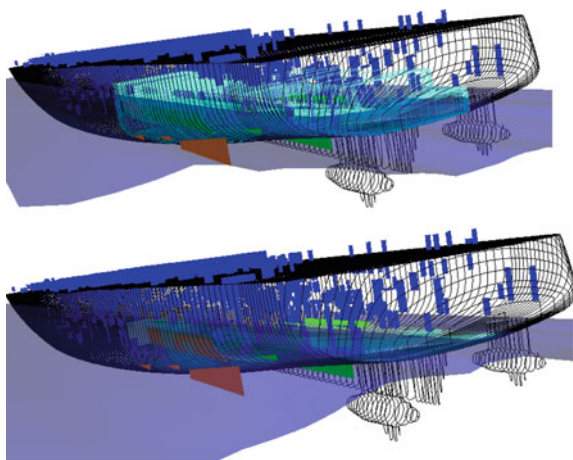
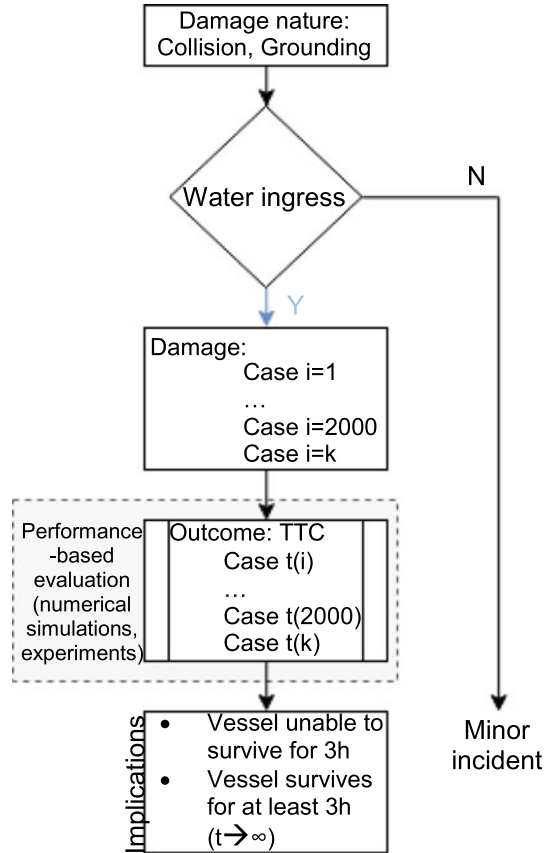


**Fig. 4** Monte Carlo simulation set-up



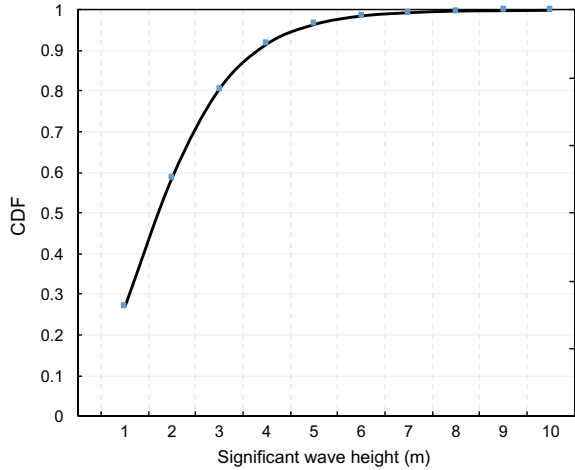
in Fig. 5. In the case of collision scenarios, time-domain simulations were also performed in calm water, in order to ascertain impact of waves and ship dynamics on survivability.

The total time for each simulation run is 1820s (30 min) and they are initiated after 20 s in order to allow for any transients to settle. This means that the damage openings are activated after 20 s of simulation time. Survivability is assessed not only on the basis of physical/actual capsizes (ship turns over,  $\theta_{\text{heel}} > 90$  deg) but also on the basis of the following three capsizes criteria:

- ITTC capsizes criteria [9] when the instantaneous roll angle exceeds 30 degrees or the 3-min average heel angle exceeds 20°.
- Criterion for insufficient capability of evacuation, assessing the effect of heeling angle when the angle of heel is higher or equal to 15° SOLAS CH. II-1 [10].

The maximum final flooding rate of mass per hour for each damage case. The three aforementioned criteria are applied in a parallel fashion during filtering process of the numerical simulation results.

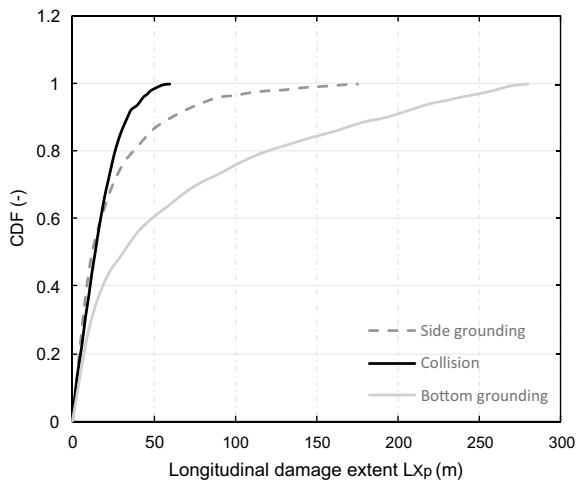
**Fig. 5** Cumulative distribution of the significant wave heights in the case of global wave statistics [15]



Figures 6, 7, 8 and 9 present the damage distributions with respect to their longitudinal and transverse damage extents for each of the two vessels. The damages are sampled based on distributions, which have been derived from work presented in Refs. [2–5, 20]. There, a probabilistic framework has been devised to account for bottom, side groundings and collisions. This overcomes the dichotomy present in SOLAS where survivability in case of collision is addressed in a probabilistic framework while the issue of grounding is addressed in a deterministic manner. The developed approach is compatible with the SOLAS2009 conceptual framework for collision.

A total of 6000 damages are investigated through the time domain simulations relating to 2000 breaches for collision, side and bottom grounding, respectively for

**Fig. 6** Cumulative distribution of the longitudinal damage extent (length)  $L_{x,p}$  for ship A



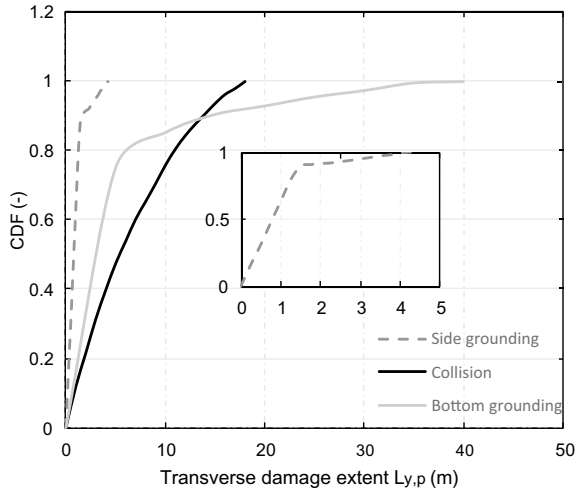


Fig. 7 Cumulative distribution of the transverse damage extent (length)  $L_{y,p}$  for ship A

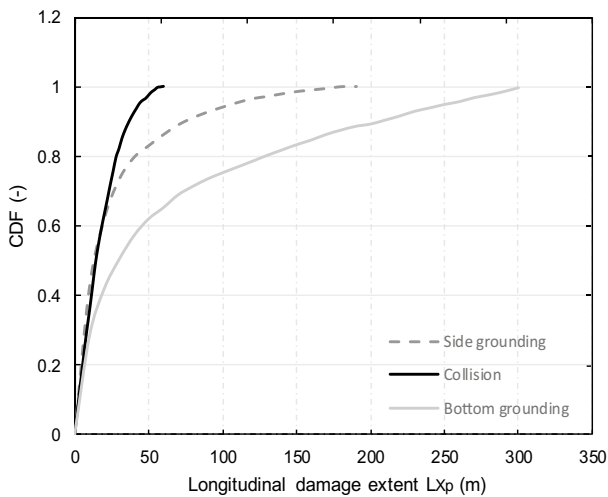
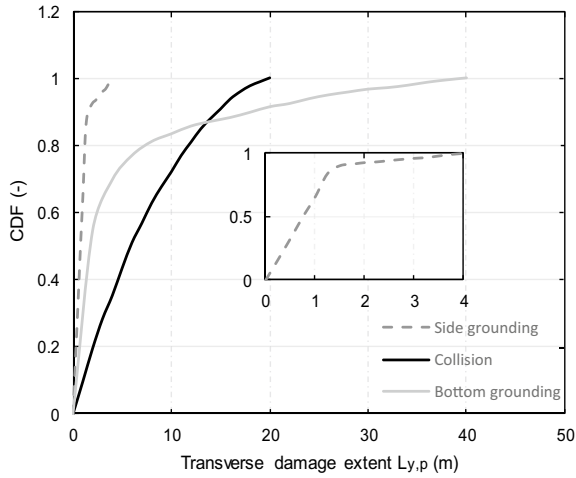


Fig. 8 Cumulative distribution of the longitudinal damage extent (length)  $L_{x,p}$  for ship C

each vessel. The calm-water runs for the case of collisions were repeated for all damage case scenarios.

**Numerical simulation results**

The numerical simulation results are presented with indications linking these to the aforementioned failure criteria for each ship in Fig. 10. In particular, ship A results in 72 capsizes due to collision damages, of which 19 cases are actual capsizes



**Fig. 9** Cumulative distribution of the transverse damage extent (length)  $L_{y,p}$  for ship C

(26%). The time required to perform the numerical simulations is depended on the significant wave height used and total size of damage which in turn defines the floodwater accumulation mass. Indicatively, on average, simulations varied between 30 min and 1.2 h.

The cumulative distribution function for Time To Capsize in case of collision damages, based on actual capsizes, shows that the majority of capsizes occurred

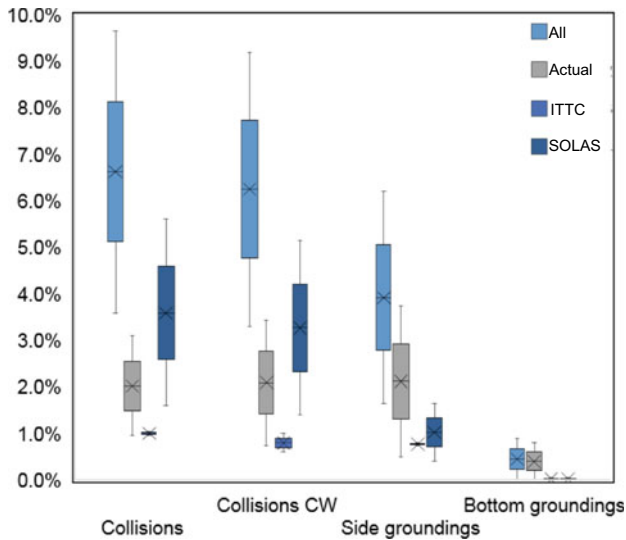


**Fig. 10** Quartiles of capsizes for both cruise ships



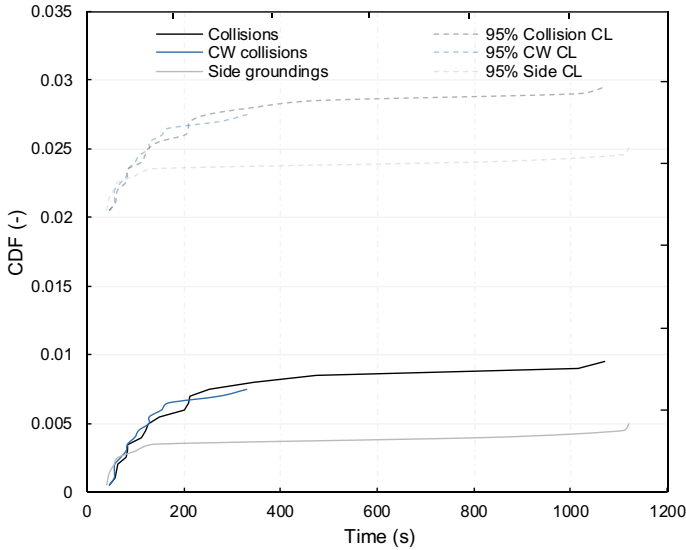


**Fig. 11** Cumulative probability distribution of Time To Capsize for collisions—actual capsizes (ship A) including Calm Water (CW) collisions

within the early stage of the simulations (under 5 min) with no cases beyond 18 min duration, as shown in Fig. 11.

Based on these findings [1], the expected probability of survival as expressed by the Survivability Index lies between 0.97 and 1 with 95% confidence. However, the CDF for TTC calculated for all capsizes (i.e., actual and those violating the ITTC and SOLAS maximum heel criteria) does not stagnate, indicating that some further capsizes would be observed for longer simulation times. Nevertheless, considering the estimates based on half-an-hour runs, the average probability of surviving at least 30 min can be estimated to fall between 0.94 and 0.98 with 95% confidence.

The calm-water runs (CW) resulted in fewer capsizes (63 cases) when compared to collisions in waves. Specifically, three of the calm-water capsizes represent a “shift” towards more conservative failure criteria (i.e. from actual capsizes to ITTC, and from ITTC to SOLAS max heel). This denotes the impact of waves on survivability assessment.

In the case of side groundings, the results indicate 2% of capsizes (33 capsizes) of which 30% represent actual capsizes. Hence, the expected probability of survival corresponds to an equivalent Attained-Index (Survivability Index) of 98.3%. The simulations of Ship A for bottom groundings did not result in any capsizes or violations of the aforementioned survivability criteria. This is likely to be the result of insufficient duration of the simulations, given the slow up-flooding process. In fact, analysis of the final 3-min of the simulations reveals that 52 cases show significant rate of change of heel (over 2 deg/h), 2 show a rate of change of trim in excess of 1 deg/h and 39 indicate sinking at a rate of 2 m/h. Finally, in 62 cases the net

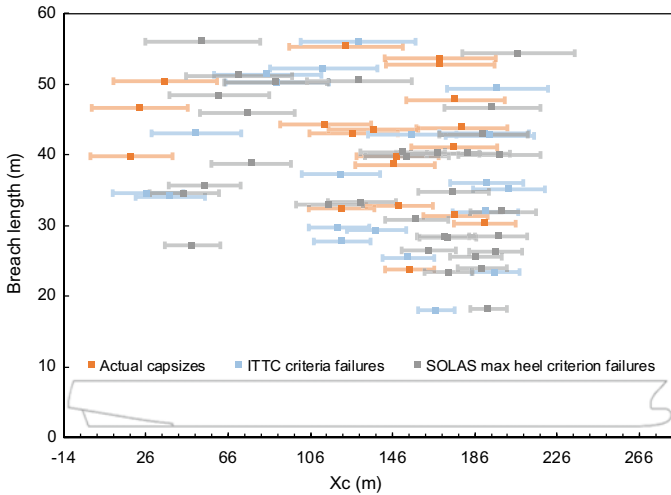


**Fig. 12** Distribution of critical collision damages along the length of ship A with indication of actual capsizes and cases that failed the ITTC and SOLAS criteria

floodwater inflow rate exceeded 1000 t/h. The damage extents and location of the highlighted cases are shown in Fig. 12.

For the second ship, the results demonstrate that the probability of survival (1-A) for collisions corresponds to a Survivability Index of 90.35%, as indicated in Fig. 13. Notably, the calm-water runs resulted in fewer capsizes (181 cases) when compared to in-waves simulations (193 cases). The damage extents and location of the highlighted cases are shown in Fig. 14.

Finally, the CDF of TTC for side groundings yields a Survivability Index of 93.7. In the case of bottom groundings, the simulations result in approximately 2% of capsizing cases, of which 89% represent actual capsizes. In this case the cumulative probability distribution of Time To Capsize provides an indication of Survivability Index as high as 99.1%.

The calm-water runs provide an interesting insight on the impact of waves showing that a significant number of capsizes were either missed in the calm water (herein denoted as CW) runs or would fail only the more conservative criteria. One of the main implications of this is that the impact of waves should be explored in more detail, which could be achieved by testing individual damages in a range of wave heights, preferably with multiple repetitions per wave height. Such approach would be an extension to the methodology employed for deriving the s-factor (based on capsizing band).

***Comparison between Direct and Statistical approaches***

In light of the numerical results, a comparison is conducted between the static calculations linked to the statistical approach and numerical simulations as shown in Figs. 15 and 16, respectively, linked to the Direct Method, for both cruise vessels.

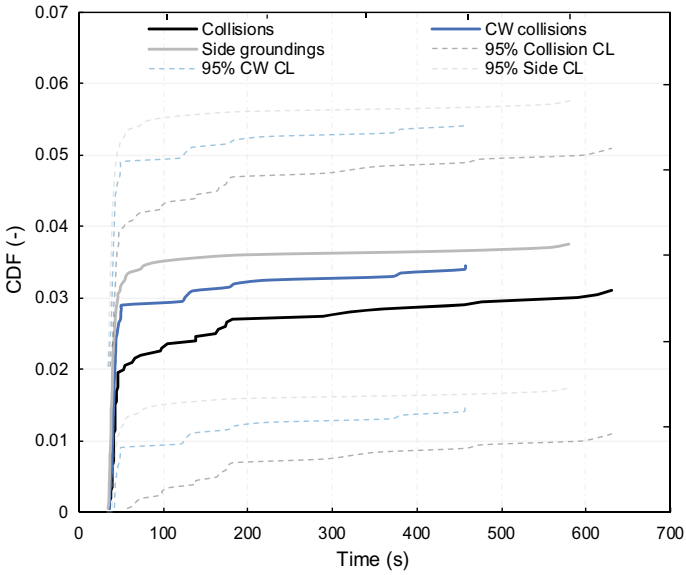


**Fig. 13** Cumulative distribution function of TTC—actual capsizes in collision damages (ship C)

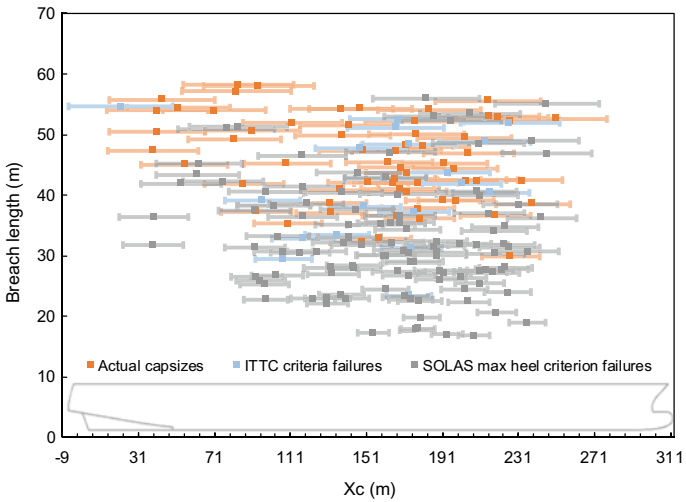


**Fig. 14** Distribution of critical collision damages along the length of ship C with indication of actual capsizes and cases that failed the ITTC and SOLAS criteria

Figure 15 demonstrates the impact on the Attained Subdivision Index using three different formulations namely, the current SOLAS s-factor, the non-zonal average survivability model with the current s-factor and finally the non-zonal average survivability model with the new eSAFE s-factor. In addition, Fig. 16 presents the obtained survivability levels through dynamic simulations in two ways; conditionally through employing all criteria and solely actual capsizes.

On the basis of the foregoing, the newly developed survivability factor is found to underestimate survivability of cruise ships in collision damages. Cruise ships have demonstrated resistance to capsize in waves higher than 5 m (Maximum 8 m) and the prevailing s-factor does not reflect this. Numerical simulation results are consistent with the static calculations. In particular, both methods identify the same vulnerable locations along the ship. However, the numerical simulation results indicate higher survivability than the static calculations. The discrepancies in expected survivability levels are particularly large in grounding scenarios. This is likely due

**Fig. 15** Comparison of survivability based on static calculations for: **a** Ship A, **b** Ship C

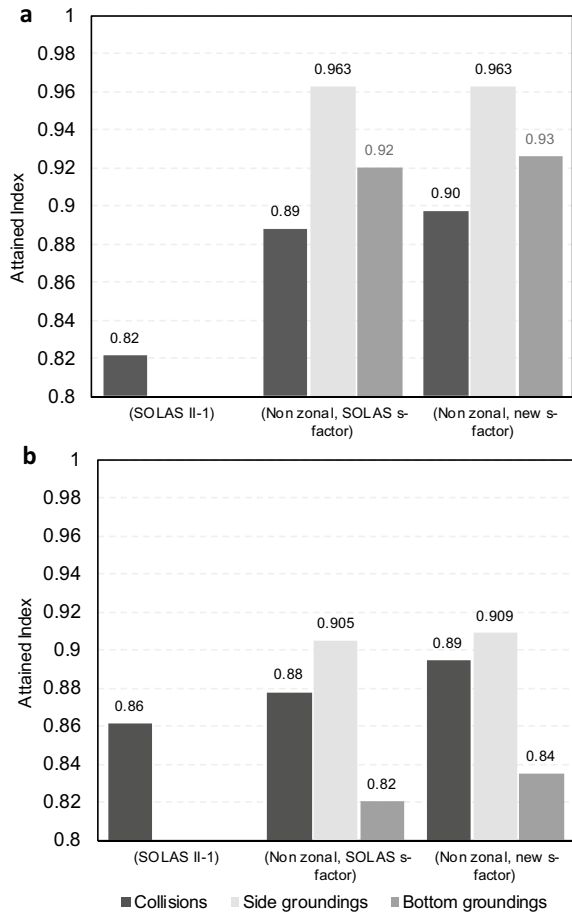
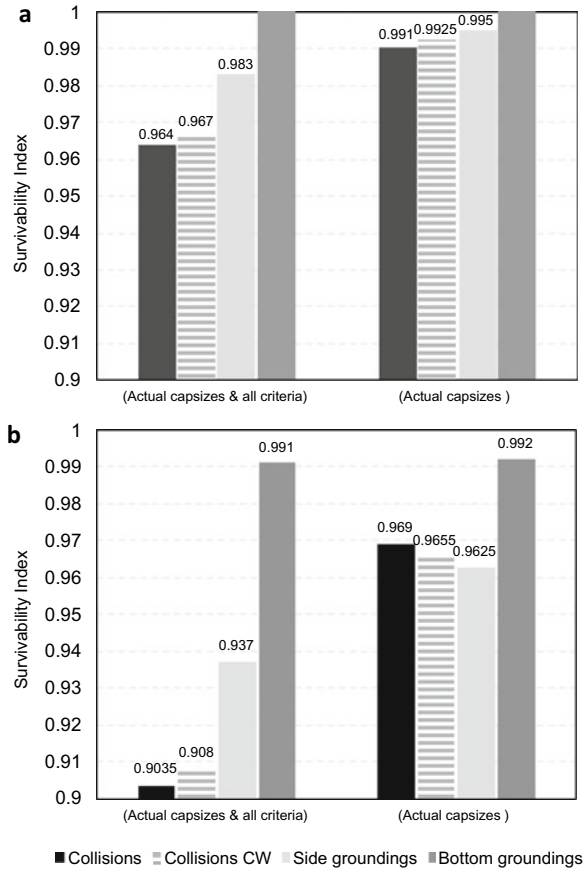


**Fig. 16** Comparison of survivability based on simulations for ship for: **a** Ship A, **b** Ship C



to relatively short simulation durations given the slowly developing up-flooding. In general, it is understood that the time-domain simulations of flooding within complex geometries require significantly longer simulation runs. Notwithstanding this, the gap between the simulation results and static calculations has been significantly reduced, in comparison to earlier results.

Generally, the results represent significant steps forward in understanding flooding events, although, the differences between SOLAS Attained subdivision Index and expected survivability levels (Survivability Index), based on simulations, cannot yet be fully explained and further work is needed in this direction.

## 4 Concluding Remarks

On the basis of the aforementioned work, a new  $s$ -factor is being proposed specifically for cruise ships and a critical  $H_s$  formulation applicable to ships in service worldwide. In addition, a comparison has been conducted between Statistical (SOLAS) and Direct (numerical time-domain simulations) approaches on survivability through time-domain numerical simulations, on the basis of which the following conclusions can be drawn:

- The results demonstrate that survivability does depend on sea state and a relationship that is cruise-ship specific has been derived, linking  $H_s$ -critical to characteristics of the residual GZ curve, namely Range and  $GZ_{\max}$ .
- Similarly to project GOALDS, where the residual intact volume following flooding was used as a parameter within the  $s$ -factor formulation, results also indicate that ship size and amount of floodwater are linked to survivability, meaning that survivability in cruise ships is affected by scale. As such, a suitable scaling factor depending on both floodwater volume and residual volume has been derived.
- A new  $s$ -factor that caters for pertinent geometry characteristics of cruise ships and captures their flooding mechanism has been devised which addresses progressive flooding and is derived on the basis of  $GZ_{\max}$  and Range of the un-truncated residual stability curve.
- Dynamic time-domain flooding simulations provide an effective means for screening flooding scenarios, likely to lead to vessel loss. At the same time, they offer additional information to address the ensuing potential risk at a forensic level not afforded by static calculations.
- The numerical simulation results indicate higher survivability than the static calculations. The discrepancies in expected survivability levels are particularly large in grounding scenarios. This is likely due to relatively short simulation durations given the slowly developing up-flooding.
- Overall, the gap between the simulation results and static calculations has been significantly reduced. In this respect, the results obtained in the eSAFE project represent significant steps forward in understanding flooding events.
- Through this work, it has been understood that the survivability level of cruise ships is considerably higher than that postulated by rules and there is now clearer understanding why this is the case.

**Acknowledgements** This work was carried out within the framework of the project “eSAFE—enhanced Stability After a Flooding Event—A joint industry project on Damage Stability for Cruise Ships” funded by the Cruise Ship Safety Forum. The authors would like to express their gratitude to all the partners in eSAFE project for their constructive criticism and help in the undertaking of this invaluable research.

**Disclaimer** The information and views as reported in this paper are those from the authors and do not necessarily reflect the views of the eSAFE Consortium.

## References

1. Atzampos, G. 2019. A holistic approach to damage survivability assessment of large passenger ships. PhD thesis, University of Strathclyde, Glasgow, UK.
2. Bulian, G., Cardinale, M., Francescutto, A. & Zaraphonitis, G. Complementing SOLAS framework with a probabilistic description for the damage extent below water. Proceedings of the 13th International Conference on the Stability of Ships and Ocean Vehicles, 2018 Kobe, Japan.
3. Bulian G, Lindroth D, Ruponen P, Zaraphonitis G (2016) Probabilistic assessment of damaged ships survivability in case of grounding: development and testing of a direct non-zonal approach. *Ocean Eng* 120:331–338
4. Bulian, G., Cardinale, M., Dafermos, G., Lindroth, D., Ruponen, P., Zaraphonitis, G. 2020. Probabilistic assessment of damage survivability of passenger ships in case of grounding or contact. *Ocean Engineering*, 218.
5. Bulian G., Cardinale, M., Francescutto, A., Zaraphonitis, G., 2019. Complementing SOLAS damage ship stability framework with a probabilistic description for the extent of collision damage below the waterline. *Ocean Engineering*, 186.
6. Cichowicz J, Tsakalakis N, Vassalos D, Jasionowski A (2016) Damage survivability of passenger ships - Re-engineering the safety factor. *Safety MDP I:2*
7. GOALDS 2009–2012. Goal-based Damage Stability”, Project funded by the European 13th Commission, FP7- DG Research, Grant Agreement 233876.
8. HARDER 1999–2003. Harmonization of Rules and Design Rational”. Project funded by the European Commission, DG XII-BRITE.
9. ITTC 2017. ITTC Quality System Manual, recommended procedures and guidelines. Procedures: Numerical simulation of capsizes behaviour of damaged ships in irregular seas 7.5–02–07–04.4, Specialist committee on stability in waves of the 28th ITTC.
10. IMO 2006. MSC 82/24 Adoption of amendments to the international convention for the safety of life at sea, Resolution MSC 216 (82). London.
11. IMO 2009. SOLAS (Safety of Live at Sea) consolidated edition 2009. London.
12. Jasionowski, A. 2001. An integrated approach to damage ship survivability assessment. PhD Thesis, University of Strathclyde.
13. Papanikolaou A, Hamann R, Lee B, Mains C, Olufsen O, Vassalos D, Zaraphonitis G (2013) GOALDS- GOAL Based damage ship stability and safety standards. *Accid Anal Prev* 60:353–365
14. Paterson, D., Atzampos, G., Vassalos, D. & Boulougouris, E. Impact of wave statistics on ship survivability. Proceeding of the 16th International Ship Stability Workshop, 2017 Belgrade, Serbia.
15. Paterson, D., Vassalos, D., Atzampos, G. & Boulougouris, E. Impact of drafts on the damage survivability of cruise ships. *Ocean Engineering Journal*, vol. 187, 2019.
16. Tsakalakis, N., Cichowicz, J. & Vassalos, D. The capsizes band concept revisited. Proceedings of the 11th International Ship Stability Workshop, ISSW, 2010 Wageningen, Netherlands. 262–271.
17. Tuzcu, C. Development of factor s: the damage survival probability. 8th International Conference on the Stability of Ships and Ocean Vehicles, STAB, 2003a Madrid.
18. Tuzcu, C. 2003b. A unified approach to determining the damage survival factor. PhD Thesis, University of Strathclyde.
19. Vassalos, D. Damage stability of cruise ships - evidence and conjecture. 12th International Conference on the Stability of Ships and Ocean Vehicles, STAB2015, 2015 Glasgow.
20. Zaraphonitis, G., Bulian, G., Lindroth, D., Luhmann, H., Cardinale, M., Routi, A.-I., Bertin, R. & Harper, G. 2013. Evaluation of risk form ranking damages due to grounding, EMSA/OP/10/2013 report 2015–0168. DNV-GL.

# Model Experiments



# Overview of Model Test Procedures for Stability Under Dead Ship Condition and Pure Loss of Stability in Astern Waves



Naoya Umeda, Daichi Kawaida, Yuto Ito, Yohei Tsutsumi, Akihiko Matsuda, and Daisuke Terada

**Abstract** For facilitating the development of the guidelines for direct stability assessment as a part of the second generation intact stability criteria at the International Maritime Organization (IMO), this paper provides examples of comparison between model experiments and numerical simulations for stability under dead ship condition and pure loss of stability in astern waves. As a result, some essential elements for proper validation were identified. For dead ship stability, a good selection of representative wind velocity generated by wind fans is crucial. For pure loss of stability, accurate Fourier transformation and reverse transformation of incident irregular waves are essential. These remarks were partly utilised in the interim guidelines as finalised in 2020.

**Keywords** Second generation intact stability criteria · Direct stability assessment · IMO · Dead ship condition · Pure loss of stability

## 1 Introduction

At the IMO, the second generation intact stability criteria, which consist of three-level criteria, are now under development. Here their highest level means direct stability assessment using time-domain numerical simulation tools, which should be validated with physical model experiments. For this purpose, the IMO started to develop the guidelines for direct stability assessment procedures under the initiative of the United States and Japan as SDC 1/INF. 8, annex 27 [8]. For finalising the

---

N. Umeda (✉) · D. Kawaida · Y. Ito · Y. Tsutsumi  
Osaka University, Suita, Japan  
e-mail: [umeda@naoe.eng.osaka-u.ac.jp](mailto:umeda@naoe.eng.osaka-u.ac.jp)

A. Matsuda  
Japan Fisheries Research and Education Agency, Kamisu, Japan  
e-mail: [amatsuda@fra.affrc.go.jp](mailto:amatsuda@fra.affrc.go.jp)

D. Terada  
National Defence Academy, Yokosuka, Japan  
e-mail: [dterada@nda.ac.jp](mailto:dterada@nda.ac.jp)

guidelines, particularly their quantitative acceptance criteria, it is indispensable to examine their feasibility by comparing model experiments with numerical simulations. Thus, it is important to collect comparisons between model experiments and numerical simulations for the relevant stability failure modes.

The second generation intact stability criteria deal with five failure modes, i.e., parametric rolling, pure loss of stability in astern waves, broaching, stability under dead ship condition and excessive acceleration. Among them, a relatively large number of validation reports for parametric rolling (e.g. [6]) and broaching (e.g. [5]) are available, but only the limited number of reports for stability under dead ship condition [14] and pure loss of stability [13]. Since few published experimental data are available, even the experimental procedures for stability under dead ship condition have not yet been established by the International Towing Tank Conference [12].

Therefore, the authors attempted to validate numerical simulation codes for stability under dead ship condition in irregular beam wind and waves and pure loss of stability in irregular astern waves and published its report at the International Ship Stability Workshop as [19]. Some part of this information was used for the development of the IMO interim guidelines for direct stability assessment, which was circulated in 2020 [9]. This means that this work was based on the draft guidelines available in 2013, which was slightly different from the current guidelines finalized in 2020. The authors presume that it could facilitate the revision of the ITTC recommended procedures for intact stability model test in future.

## **2 Draft Guidelines of Direct Stability Assessment Procedures in 2013**

The draft guidelines for direct stability assessment procedures drafted by the United States and Japan by 2013 consist of requirements for numerical modelling, qualitative and quantitative validation of software and extrapolation procedures. For the quantitative validation, numerically simulated results are requested to be compared with the model experiments based on the ITTC recommended procedures [12]. Its acceptance criteria are shown in Table 1. In this table, it was accepted in 2013 that all quantitative numbers that appeared as the acceptance standards here should be considered tentative unless sufficient evidence of their feasibility is submitted to the IMO. It is noteworthy here that these requirements do not refer to irregular wind at all. This is because it is not easy to find literature describing ship model experiments with artificial irregular wind and waves except for Kubo et al. [14]. It can also be remarked that no acceptance criteria for pure loss of stability in astern waves exist. This is because only recently the mechanism of “pure loss of stability” was discussed by Umeda et al. [18] and Kubo et al. [13]. They experimentally and numerically confirmed that large roll triggered by a loss of restoring moment due to longitudinal waves could usually induce lateral motions because of the asymmetric underwater hull due to

heel. Centrifugal force due to such lateral motions could induce further roll motion. Thus, the phenomenon known as “pure loss of stability” should be theoretically investigated with restoring reduction and centrifugal force due to lateral motions. These raised points have already been adopted by the IMO [9] for the vulnerability criteria as a part of the second generation intact stability criteria. Therefore, it is an urgent issue to provide examples of comparison in artificial irregular waves between model experiments and numerical simulation.

### 3 Stability Failure in Irregular Beam Wind and Waves

#### 3.1 *Experimental Procedures*

For examining the validation procedures for stability under dead ship condition experiments using a 1/70 scaled model of the 205.7 m-long CEHIPAR2792 vessel [16] were conducted at the Marine Dynamics basin, shown in Fig. 1, of the National Research Institute of Fisheries Engineering [15]. The ship model has a flat plate on the upper deck for realising the windage area and its area centre height of the superstructure but without additional buoyancy. It was not equipped with bilge keels, propellers, shaft brackets and rudders. An optical fibre gyroscope inside the model is used for detecting the roll, pitch and yaw angles. For sway and heave motions, the total station system, which is described in Chap. 4, was used.

The model was kept orthogonal to the wind and wave direction by a wired system, which softly restrains drift and yaw, as shown in Figs. 2 and 3. The wind blows in one direction, and the long-crested wave propagated in the same direction. Here the wired system was connected to the ship model at bow and stern, where the height was set to be equal to calm water surface based on measured hydrodynamic reaction force and moment in a captive model test of the subject ship. As shown in Fig. 3, the mean of the low-frequency sway motion due to mean wind velocity and the second-order wave force was cancelled out by the tension due to a counterweight. Thus, high-frequency sway motion was not prevented. Alternatively, an automatic tension adjustment system using a constant torque motor can be introduced to cancel it out.

Irregular water waves were generated by plunger-type wavemakers with the ITTC wave energy spectrum recommended in 1978 [11]. The wave elevation was measured by a servo-needle-type wave height meter equipped in the sub towing carriage. Figure 4 shows one example of the comparison of wave energy spectra. The straight blue line indicates the specified spectrum in this figure, and the green square symbols indicate the measured one. From this figure, it can be seen that the specified spectrum was satisfactorily realized.

The fluctuating wind was generated by a wind blower in the wave direction. The wind blower, as shown in Fig. 5, consists of 36 axial flow fans and is controlled by inverters with a v/f control law, by which the ratio of primary voltage for the induced motor and the inverter output frequency is controlled to be constant.

**Table 1** Quantitative validation requirements [8]

	Required for	Objective	Acceptance criteria
Response curve for parametric roll	Parametric roll and excessive accelerations	To demonstrate reasonable agreement between numerical simulation and the models test on both bandwidth of parametric resonance and the amplitude of the roll response	[1/10] of natural roll frequency for the bandwidth and [10%] of amplitude if below angle maximum of GZ curve in calm water and [20%] if above the angle of maximum of the GZ curve in calm water
Response curve for synchronous roll	All modes	To demonstrate reasonable agreement between numerical simulation and the models test on the amplitude of the roll response	[10%] of amplitude if below angle maximum of GZ curve in calm water and [20%] if above the angle of maximum of the GZ curve in calm water
[Turning circle maneuver	Software for numerical simulation of surf-riding and broaching	Demonstrate correct modeling of maneuvering forces and turn dynamics in calm water	[20%] difference in terms of diameter of turning circle between the model test and numerical simulation and the correct sign of drift angle
Zig-zag maneuver	Software for numerical simulation of surf-riding and broaching	Demonstrate correct modeling of maneuvering forces and turn dynamics in calm water	[10%] difference in terms of the 1st and second overshoot angles between the model test and numerical simulation]
Variance test/synchronous roll	Software for numerical simulation of dead ship condition and excessive accelerations	Demonstrate correct (in terms of statistics) modeling of roll response in irregular waves	Probability that the difference between the ensemble estimates of variance of roll is caused by the random reasons is above the significant level of [5%]
Variance test/parametric roll	Software for numerical simulation of dead ship condition and excessive accelerations	Demonstrate correct (in terms of statistics) modeling of roll response in irregular waves	Probability that difference between the ensemble estimates of variance of roll is caused by the random reasons is above the significant level of [1%]

(continued)

**Table 1** (continued)

	Required for	Objective	Acceptance criteria
Wave conditions for surf-riding and broaching	Software for numerical simulation of surf-riding and broaching	Demonstrate correct modeling of surf-riding broaching dynamics in regular waves	Wave steepness causing surf-riding and broaching at the wave length [0.75–1.5] of ship length is within [15%] of difference between model test and numerical simulation; speed settings are also within [15%] difference between model test and numerical simulation

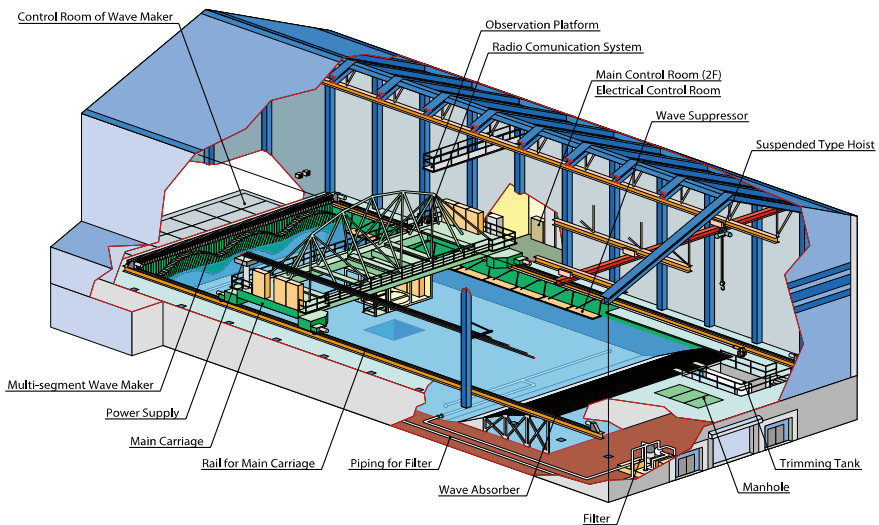
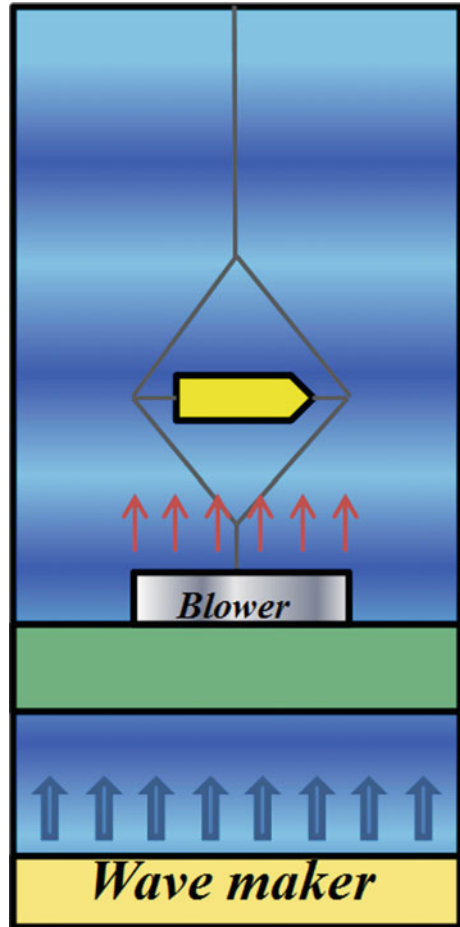


**Fig. 1** Marine Dynamics Basin of National Research Institute of Fisheries Engineering [15]

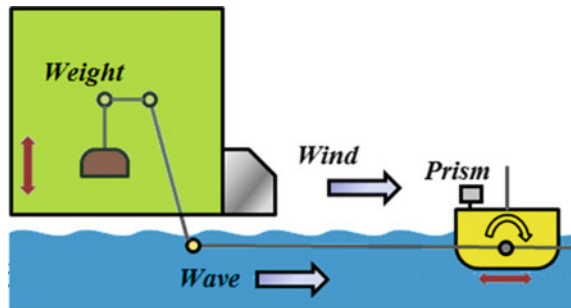
Although in our previous experiment [14], the relationship between the drive frequency for this control and the wind velocity was adjusted by measuring the steady heel angle of the ship model under the non-fluctuating wind, the wind velocity was directly measured with a hot wire anemometer in this experiment. This wind measurement was executed without the ship model, and 15 measured points were used, as shown in Fig. 6. Further, the distance between the wind blower and the ship position was changed with the shift of the position of the blower.

These measured data, as shown in Fig. 7, the wind velocity gradually decreases with the distance from the blower. In this study, the data where the ship model position

**Fig. 2** Overviews of the experimental set-up



**Fig. 3** Lateral views of the experimental set-up



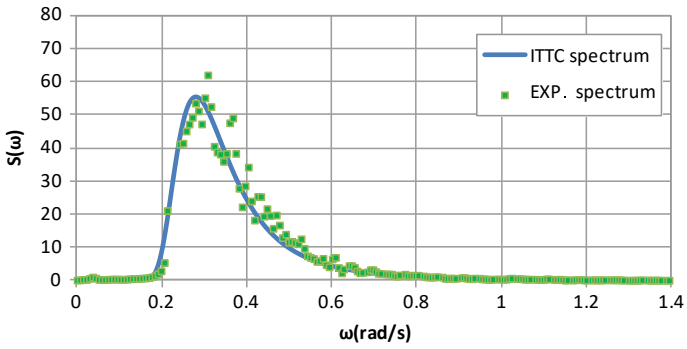


Fig. 4 Comparison of wave energy spectra

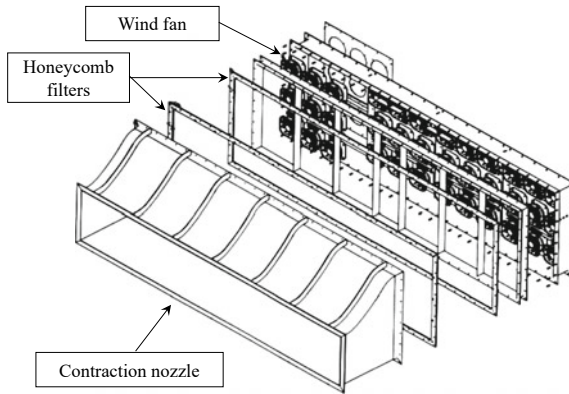


Fig. 5 Wind blower

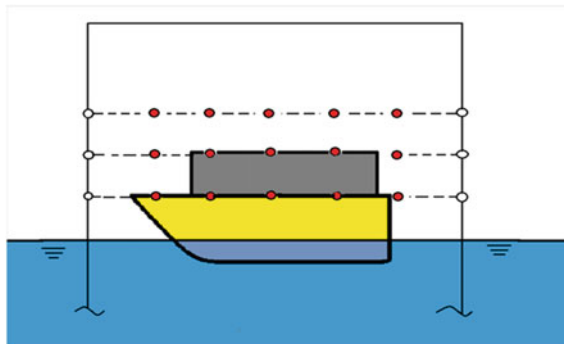


Fig. 6 Measurement points for wind velocity

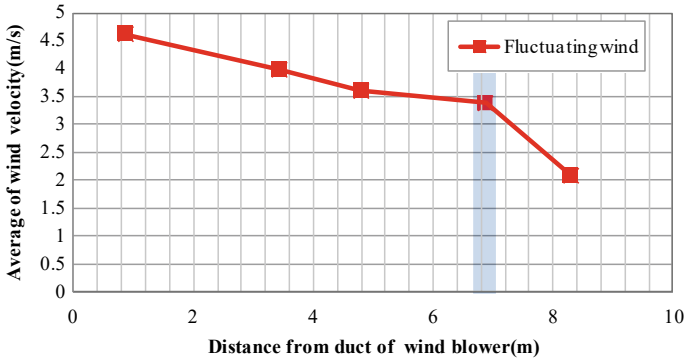


Fig. 7 Measured wind velocity as a function of distance from the blower. Here shaded zone indicates ship position during experiments in wind and waves

measured during the experiment is used so that the mean wind velocity used here is about 28 m/s in full scale.

The wind velocity has some spatial non-uniformness, as shown in Fig. 8, because the ratio of blower breadth to ship length of 1.327 is not so sufficiently large. The use of a wider blower or smaller ship model is preferable.

The wind velocity spectrum is designed with the Davenport spectrum [4] without the transfer function between the drive frequency and the wind velocity. Figure 9 shows one example of the comparison of wind velocity spectra. In this figure, the red line indicates the specified spectrum, and the blue diamond shape symbols indicate the measured one. From this figure, it can be seen that the measured spectrum was qualitatively similar to the specified one. In our previous experiment [14], a better agreement was obtained between the measured and specified spectra but with a mean

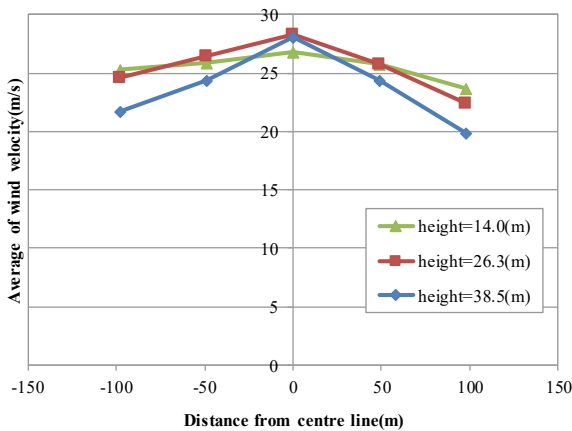
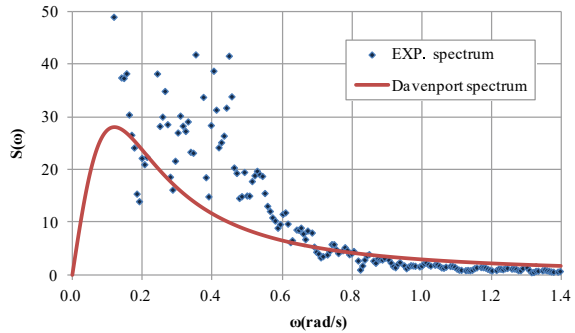


Fig. 8 Mean wind velocities measured at different positions



**Fig. 9** Comparison of wind velocity spectra



wind velocity of 22.5 m/s. In the case of high wind velocity, it seems appropriate to take account of the transfer function. As to this problem, in our other study [20] conducted after this study, more detailed consideration was provided, and it was confirmed that the approach mentioned above is valid.

At present, in the National Research Institute of Fisheries Engineering, two units were added to the wind blower, the problem of the spatial non-uniformness shown in Fig. 8 was reduced [20].

### 3.2 Numerical Modelling

For a comparison with the model experiment, the uncoupled roll model [14] was used in this study. As recommended by the IMO [7], the nonlinear roll damping coefficients in calm water and the effective wave slope coefficient were estimated with roll decay model tests and the roll response model tests in regular beam waves, respectively. The wind-induced moment was estimated with the relationship with wind drag coefficient and heeling angle, which were directly measured with constant beam wind velocities on their own using the cable tension and the gyroscope. As shown in Figs. 10 and 11, the estimated wind drag and heel angle reasonably agree with the measured data so that the estimation of wind velocity from these ship data, which was used in our previous work [14], can be judged as reliable.

### 3.3 Comparison of Experiment and Simulation

Following the draft guidelines in 2013 [8], the ensemble average of the variance of roll angle obtained by the model experiment was compared with that by the numerical simulation with the confidential intervals using the significant level of 5%, i.e., 95% confidence interval, assuming the Gaussian distribution as shown in Fig. 12. Here 20 realisations were used for both model experiment and numerical simulation, and the

**Fig. 10** Steady heel angle with constant wind velocity

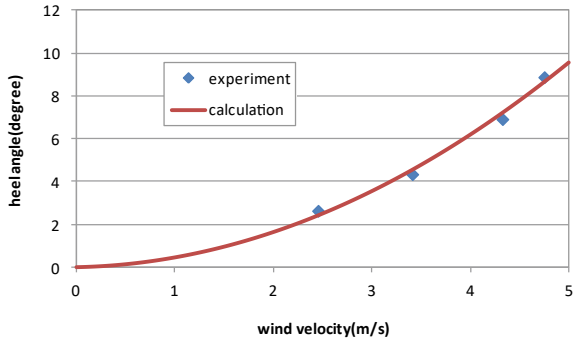
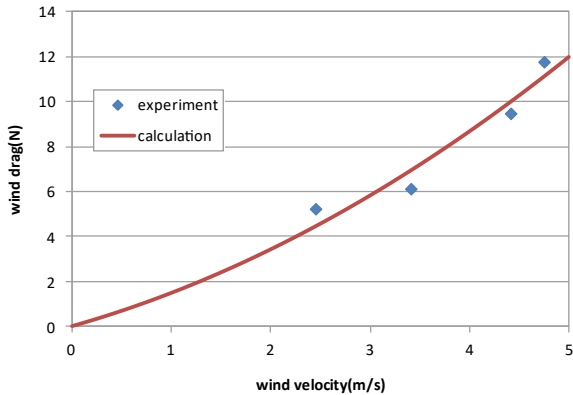


**Fig. 11** Wind drag with constant wind velocity



duration is 3600 s in full scale. The initial heel angle due to cargo shift was 6 degrees towards the lee side because capsizing was not likely to occur without the initial heel angle. In the numerical simulation, the mean wind velocity was set to that from the mean of central points for wind velocity measurement except for the highest one. In the numerical simulation here, the measured wind velocity spectrum is used. Since the two confidential intervals are overlapped, we could conclude that the numerical model was validated with the model experiment. As reported in a separate paper [17], the measured roll spectrum in the same experimental campaign has a single peak at the natural roll frequency inside the region of external excitation due to wind and waves. The draft guidelines in 2013 requested a significant level of 1% for a synchronous roll, but the above suggests that the significant level of 5% seems to be reasonable.

As a next step, the comparison of capsizing probability between the model experiment and numerical simulations is shown in Fig. 13 with 95% confidence intervals using a binomial distribution [3]. Here three different ways of determining the mean wind velocity are used. The “simulation 2” indicates the way that used in the comparison of the variance of roll angles. The “simulations 1 and 2” use the mean of three points at the middle height and that of the central point at the middle height,

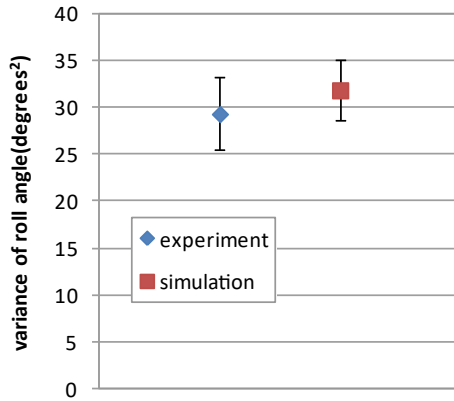


Fig. 12 Comparison of variance of roll angle between experiment and simulation

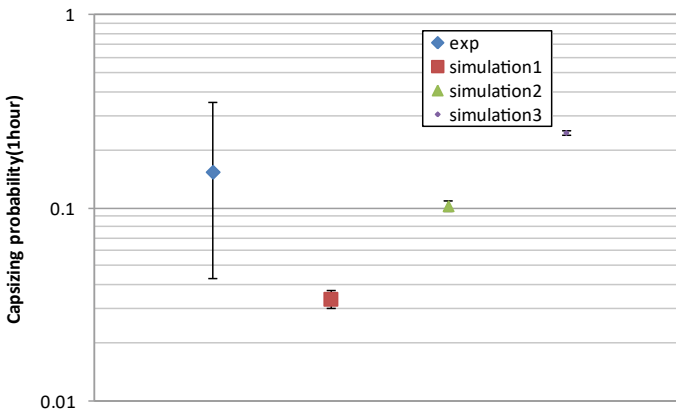
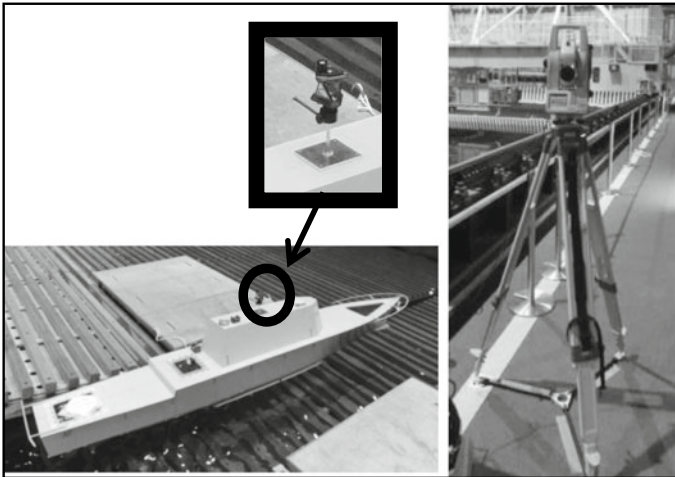


Fig. 13 Comparison of capsizing probability of experiment and simulation

respectively. The results indicate that both “simulation 2 and 3” shows acceptable agreement, and “simulation 1” provides a too low probability. Thus, the appropriate selection of measured points for wind velocity is crucial for validating numerical models with the width of the wind blower array taken into account.

#### 4 Stability Failure Due to Pure Loss of Stability

For validating a numerical model for pure loss of stability in irregular astern waves, experiments using a 1/48.8 scaled model of the 154 m-long ONR flared topside vessel [1] were executed at the Marine Dynamics basin, as shown in Fig. 1, of National



**Fig. 14** Total station system (left; prism right; theodolite) used in the model experiment

Research Institute of Fisheries Engineering [15], based on the ITTC recommended procedure on intact stability model test [12]. The position of the ship model was observed by a total station system. It consists of the theodolite, which is an optical distance and direction measuring device, and the prism which reflects light rays from the theodolite is on the ship model, as shown in Fig. 14. The size of the prism is much smaller than the lateral projection area of the above water hull. By synchronising data of the total station system and gyroscope on the vessel, the ship position in the inertial coordinate system was obtained. Ship velocity was calculated by differentiating the position of the centre of gravity of the ship.

For precise comparison in time series between the experiment and the simulation, estimation of wave height at each ship position is indispensable. The wave elevation was measured by a servo-needle-type wave height meter near the wave maker. It was synchronised, by the trigger in radio signal, with the ship position data and the ship motions. The Fourier spectrum from these measured wave data was converted with the ship position data. Then it was inversely transformed so that the wave elevation at the ship position was obtained. This converted Fourier spectrum was also used for numerical simulation as its input.

The wave elevation at the ship's centre of gravity was calculated by the above procedure, and is shown in Fig. 15 in model scale with measured roll and pitch data. Here positive wave elevation indicates the movement downwards, the positive roll results in downward movement of the starboard side and positive pitch means bow up. This measured result indicates that the roll angle becomes large whenever the ship meets a wave crest, which is defined as the minima of the wave elevation. The measured roll period of 3.55 s, which is equal to the encounter wave period, is longer than the natural roll period of 2.95 s. These facts suggest that the typical behaviour known as pure loss of stability was relevant [10]. Here the significant wave height is

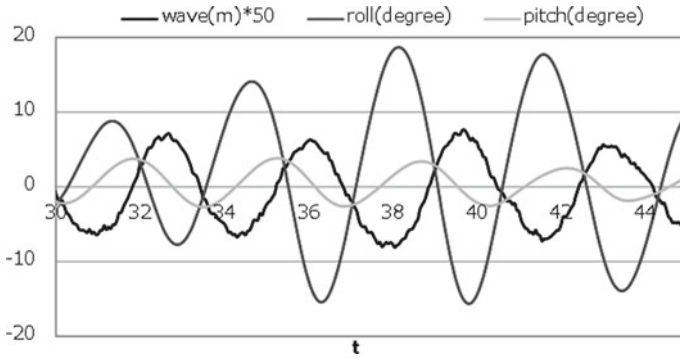


**Fig. 15** Wave elevation at ship’s centre of gravity and roll and pitch angle recorded in irregular waves shown in model scale

0.2066 m, the mean wave period is 1.627 s, the rudder gain is 1.0, the Froude number is 0.25, and the autopilot course from the wave direction is  $-15^\circ$ . Earlier and similar procedures and results were published by Clauss and Hennig [2].

The numerical model proposed by Kubo et al. [13] is based on a nonlinear manoeuvring model with linear wave forces and nonlinear restoring variation. The manoeuvring, roll damping and propulsion coefficients were obtained by conventional model tests such as Circular Motion Test (CMT). The linear wave forces were estimated with a slender body theory with very low encounter frequency, and nonlinear restoring variation was predicted with Grim’s effective concept and the Froude-Krylov assumption.

The numerical model mentioned above was applied to the experimental condition in Fig. 15. Figure 16 shows the comparison in time series between experiment and calculation in irregular waves. In this figure, the solid lines indicate the results of the model experiment, and the broken lines indicate the results of the calculation based on the numerical model, respectively. As shown in this figure, this numerical model well explains the present model experiment in irregular waves. This experimental procedure could be useful for developing guidelines for the validation of direct stability assessment once the acceptance standard is introduced for the failure modes of pure loss of stability at the IMO.

## 5 Concluding Remarks

The main remarks from this work are summarised as follows:

- (1) For the failure mode of stability under dead ship condition, the experiment was executed by generating irregular waves and the fluctuating wind for a softly moored ship model. The number of capsizing was counted, and the capsizing

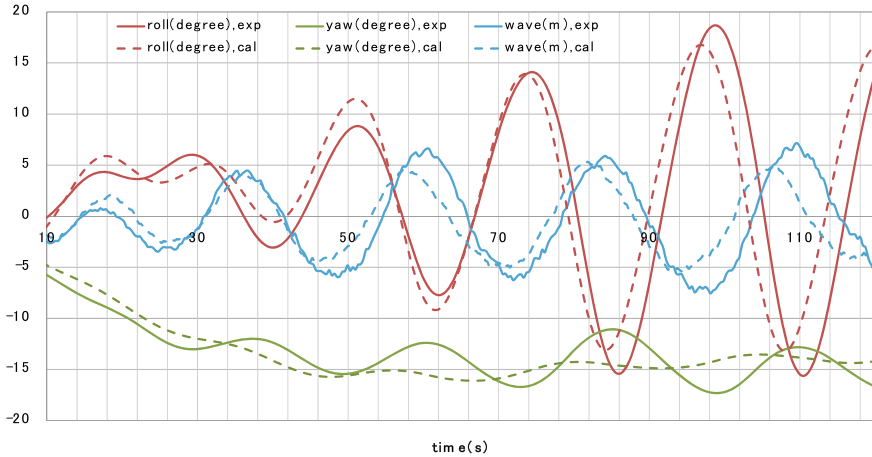


**Fig. 16** Comparison in time series between experiment and calculation in irregular waves shown in full scale

probability was estimated with its 95% confidence interval. Here the adequate selection of representative wind velocity generated by wind fans is crucial.

- (2) For the failure mode of pure loss of stability in stern quartering waves, the experiment was executed by generating irregular waves for the free-running ship model using autopilot. The ship angular motions and positions were measured by the gyroscope and the total station system, respectively. The incident wave elevation was measured by a wave probe fixed at a location of the model basin. Here the accurate Fourier transformation and reverse transformation of incident irregular waves are essential.

**Acknowledgements** This work was supported by a Grant-in-Aid for Scientific Research of the Japan Society for Promotion of Science (No. 24360355). It was partly carried out as a research activity of Goal-Based Stability Criterion Project of Japan Ship Technology Research Association in the fiscal year of 2013, funded by the Nippon Foundation.

This paper is an updated version of the paper read at the 14th International Ship Stability Workshop[19] with the latest information.

## References

1. Bishop B, Belknap W, Turner C, Simon B, Kim J (2005) Parametric investigation on the influence of GM, roll damping, and above-water form on the roll response of model 5613, Report NSWCCD-50-TR-2005/027, Naval Surface Warfare Center/Carderock Division, West Bethesda, Maryland
2. Clauss GF, Hennig J (2004) Deterministic analysis of extreme roll motions and subsequent evaluation of capsizing risk. *Int Shipbuild Prog* 51(2/3):135–155

3. Clopper CJ, Pearson ES (1934) The use of confidence or fiducial limits illustrated in the case of the binomial. *Biometrika* 26(4):404–413
4. Davenport AG (1961) The spectrum of horizontal gustiness near the ground in high winds. *Q J Metrol Soc* 87:194–211
5. Hashimoto H, Umeda N, Matsuda A (2012) Broaching prediction of a wave-piercing tumblehome vessel with twin screws and twin rudders. *J Mar Sci Technol* 448–461
6. Hashimoto H, Umeda N (2019) Prediction of parametric rolling in irregular head waves. In: Belenky V, Spyrou K, van Walree F, Almeida Santos Neves M, Umeda N (eds) *Contemporary ideas on ship stability. Fluid mechanics and its applications*, vol 119. Springer, Cham, pp. 275–290
7. IMO (2006) Interim guidelines for alternative weather criterion, MSC.1/Circ. 1200, IMO (London)
8. IMO (2013) Information collected by the correspondence group on intact stability, submitted by Japan, SDC 1/INF.8, IMO (London)
9. IMO (2020) Interim guidelines on the second generation intact stability criteria, MSC.1/Circ. 1627, IMO (London), pp 1–60
10. IMO (2021) Report of the correspondence group (part 3), submitted by Japan, SDC 8/5.Add.2, IMO (London)
11. ITTC (1978) Report of Seakeeping Committee, Proceedings of the 15th ITTC
12. ITTC (2008) Recommended procedures, model tests on intact stability, 7.5-02-07-04
13. Kubo H, Umeda N, Yamane K, Matsuda A (2012) Pure loss of stability in astern seas—is it really pure? In: Proceedings of the 6th Asia-Pacific workshop on marine hydrodynamics, Johor, pp 307–312
14. Kubo T, Umeda N, Izawa S, Matsuda A (2019) Total stability failure probability of a ship in beam wind and waves: model experiment and numerical simulation. In: Belenky V, Spyrou K, van Walree F, Almeida Santos Neves M, Umeda N (eds) *Contemporary ideas on ship stability. Fluid mechanics and its applications*, vol 119. Springer, Cham, pp 591–603
15. NRIFE (2020) [http://nrife.fra.affrc.go.jp/plant/kaiyou/kaiyou\\_e.html](http://nrife.fra.affrc.go.jp/plant/kaiyou/kaiyou_e.html) (Cited at 29 Sept 2020)
16. ShipStab (2021) <http://shipstab.org/index.php/data-access/13-benchmarkingdata/11-cehipa-r2792-units> (Cited at 22 Oct 2021)
17. Tsutsumi Y, Umeda N, Kawaida D, Matsuda A (2014) Probability of ship capsizing in beam wind and waves—comparison between model experiment and numerical simulation. In: Proceedings of the 7th Asia-Pacific workshop on marine hydrodynamics, pp 156–159
18. Umeda N, Izawa S, Sano H, Kubo H, Yamane K (2011) Validation attempts on draft new generation intact stability criteria. In: Proceedings of the 12th international ship stability workshop, pp 19–26
19. Umeda N, Kawaida D, Ito Y, Tsutsumi Y, Matsuda A, Terada D (2014) Remarks on experimental validation procedures for numerical intact stability assessment with latest examples. In: Proceedings of the 14th international ship stability workshop, pp 77–83
20. Umeda N, Matsuda A, Terada D (2015) Examination of guidelines for determining minimum propulsion power in the light of model experiment. In: Proceedings of international workshop on environmentally friendly ships, Yokohama National University

# Model Experiments of an Offshore Supply Vessel Running in Astern Waves



Naoya Umeda, Sreenath Subramaniam, Aqmil Alway, Akihiko Matsuda, Atsuo Maki, Satoshi Usada, and Daisuke Terada

**Abstract** At the IMO (International Maritime Organization), the second generation intact stability criteria for pure loss of stability was developed in 2020. In its interim guidelines (IMO in “Interim Guidelines on the Second Generation Intact Stability Criteria”, MSC.1/Circ. 1627, 2020 [2]), vessels with extended low weather deck such as offshore supply vessels (OSVs) are exempted from this application, but its background has not yet been explained other than a sample calculation resulting in inconsistencies between different criteria levels. To solve this problem, the authors executed model experiments for a typical OSV in astern waves. The test results demonstrated that the phenomenon assumed by the pure loss of stability criteria is not pertinent to the OSV. Instead, it is the phenomenon which occurs due to trapped water on deck which seems to be of greater relevance for the stability of the OSV in astern seas. The effect of low weather deck length was also investigated by systematically modifying hull forms with the help of CAD software. Further, the on-deck trapped water behaviour was also studied in a separate series of model experiments involving direct measurement of the changing deck water level. The tests confirmed that the

---

N. Umeda · S. Subramaniam (✉) · A. Maki · S. Usada  
Osaka University, Suita, Japan  
e-mail: [sreenath\\_subramaniam@naoe.eng.osaka-u.ac.jp](mailto:sreenath_subramaniam@naoe.eng.osaka-u.ac.jp)

N. Umeda  
e-mail: [umeda@naoe.eng.osaka-u.ac.jp](mailto:umeda@naoe.eng.osaka-u.ac.jp)

A. Maki  
e-mail: [maki@naoe.eng.osaka-u.ac.jp](mailto:maki@naoe.eng.osaka-u.ac.jp)

A. Alway  
NAPA Japan, Kobe, Japan  
e-mail: [Aqmil.Alway@napa.fi](mailto:Aqmil.Alway@napa.fi)

A. Matsuda  
Japan Fisheries Research and Education Agency, Kamisu, Japan  
e-mail: [amatsuda@fra.affrc.go.jp](mailto:amatsuda@fra.affrc.go.jp)

D. Terada  
National Defense Academy of Japan, Yokosuka, Japan  
e-mail: [dterada@nda.ac.jp](mailto:dterada@nda.ac.jp)



trapped water can induce both static and dynamic moments depending on the speed of the vessel and the wave conditions.

**Keywords** IMO · Second generation intact stability criteria · Pure loss of stability · Water on deck · Offshore Supply Vessel

## 1 Introduction

The second generation intact stability criteria developed by the IMO [2] are intended to cover stability failure due to pure loss of stability in following and stern quartering waves [7]. For this failure mode, the direct stability assessment and two-level vulnerability criteria should be applied. As a possible tool for the direct stability assessment, a coupled surge-sway-yaw-roll numerical model in irregular waves was developed and validated with model experiments using a containership [5].

Based on the knowledge obtained from this numerical model, the level 1 and 2 vulnerability criteria were developed [2]. Here the level 1 and 2 criteria utilise GM and GZ in longitudinal waves, respectively. The standards of these criteria were determined to avoid the “false negative” problem between the two levels utilising many sample calculation results which did not include offshore supply vessels [1]. The sample calculations executed by the delegations from Japan and China, [4] indicate that offshore supply vessels easily comply with the level 1 but do not comply with the level 2 criterion. This inconsistency is a so-called “false negative” problem, which should be avoided in regulatory applications. Thus, the interim vulnerability criteria [2] are not allowed to be applied to “a vessel with extended low weather deck due to increased likelihood of water on deck or deck-in-water”.

However, the definition of the extended low weather deck, based on a model experiment or equivalent, has not yet been established. Published free-running model experiments of OSVs in astern waves were also not available. Therefore, the authors executed the first set of model experiments in 2015, using a scaled model of typical offshore supply vessel in stern quartering waves and compared the measured results with the second generation intact stability criteria. As a result, the reasons why OSVs should be exempted from the application of the pure loss of stability criteria are revealed. In order to investigate the effect of weather deck length, calculations of the vulnerability criteria were conducted by systematically modifying the above-water hull forms of the offshore supply vessel using CAD software, i.e. the NAPA software.

Further, the assumptions regarding the behaviour of trapped water on deck from the model experiments conducted in 2015 were confirmed in a second set of model experiments carried out in 2019, short summary of these experiments are available in Subramaniam et al. [6]. This additional set of model runs involved the direct measurement of the changing deck water level using camera and pressure sensors. The second set of experiments was also separated into two stages. Stage 1 runs were carried out with the openings, i.e. aft end and freeing ports opened, similar to 2015

model experiments. Stage 2 runs were carried out with closed openings and deck filled in advance with a constant amount of water. These additional free running model test data confirmed that the trapped water can act as a kind of anti-rolling tank around the service speed of the vessel.

## 2 Subject Ship and Model Experiments

The first set of free-running model experiments of the 60 m long offshore supply vessel (OSV), as shown in Figs. 1 and 2, in stern quartering waves were conducted at a seakeeping and manoeuvring basin of the National Research Institute of Fisheries Engineering of Japan in 2015. The vessel has a deckhouse forward and a low weather deck situated from its midship to its stern with bulwarks and freeing ports. The length of the low weather deck is 40 m in full scale. The service Froude number of the vessel is 0.3 and the vessel is equipped with twin propellers and twin rudders. Its principal particulars and righting arm curve are shown in Table 1 and Fig. 3, respectively. The metacentric height is set to marginally comply with level 2 criteria for pure loss of stability, which is lower than the designed one. The vessel under the experimental condition is judged not to be vulnerable to pure loss of stability according to the level 1 criterion because the GM with the wave steepness of 0.0334 is 1.32 m, which is much larger than the standard of 0.05 m. However, the OSV is regarded as critical with the level 2 criterion having CR value of 0.06. Thus, an inconsistency between the two levels could appear if the calm-water GM is smaller than 1.45 m.

The vessel model ran with a constant propeller speed (revolutions per minute) and attempted to keep its specified course with a PD autopilot in stern quartering waves. The translational and rotational motions of the vessel model were measured with an optical tracking system, consisting of two theodolites and two prisms, and an optical-fibre gyroscope, respectively.

For the second set of free running model tests conducted in 2019, the same model as the 2015 model experiments was utilised. In this experiment, the vertical position

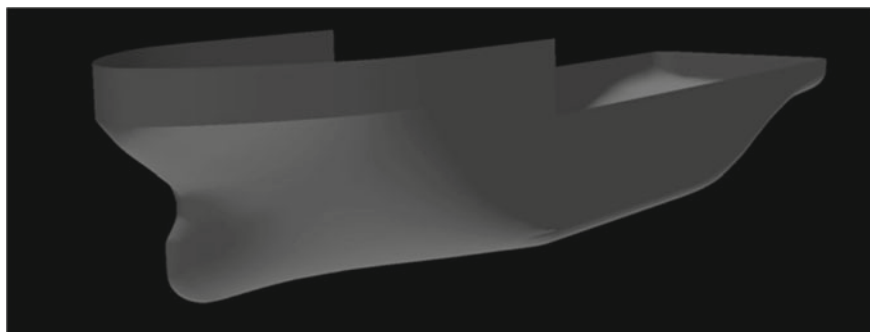


Fig. 1 3D view of the hull form of the used OSV



**Fig. 2** Free-running model experiment of the OSV in stern quartering waves executed in 2015

**Table 1** Principal particulars of the OSV

Items	Ship	Model
Length between perpendiculars ( $L_{pp}$ )	60.00 m	2.00 m
Moulded breadth	16.40 m	0.547 m
Moulded depth	7.20 m	0.24 m
Moulded draught	6.00 m	0.20 m
Metacentric height (GM)	1.45 m	0.0483 m
Natural roll period	11.50 s	2.10 s

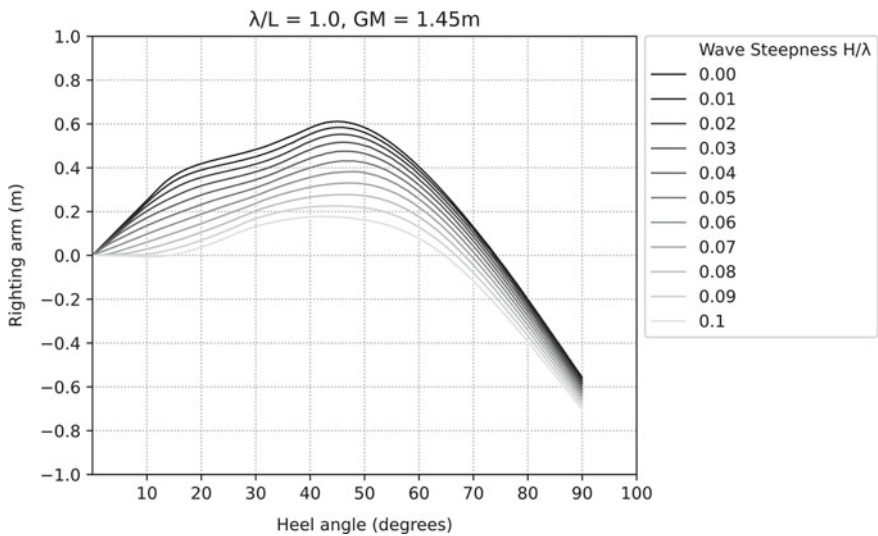


**Fig. 3** GZ curve of the OSV with a wave crest amidship in longitudinal waves. Here the wavelength is equal to the ship length, and the wave steepness ranges from 0 to 0.1

of the casing of the steering gears at the aft end was moved from the weather deck to the bulwark height, to allow more free movement of water on the deck, as shown in Figs. 2 and 4. Also, apart from the conventional system for free-running model experiments, additional systems were used to continuously monitor the changing deck water level. This additional system included a set of 5 cameras and 4 pressure sensors. Four cameras were positioned at the four corners of the weather deck, and one camera was placed at the forecabin with a clear view of the deck. Linear scales were placed opposite each camera placed on the weather deck to note the changing water level. The four pressure sensors were placed adjacent to the linear scale: the measured pressure was converted into the head of water. The arrangement can be seen in Figs. 4 and 5. The second set of experiments was also executed with closed openings trapping a constant amount of water on deck (Stage 2) to isolate the water on deck phenomenon, other than the approach of the experiment in 2015 (Stage 1).

The model was released when waves were sufficiently propagated in the water area of the basin. These experimental procedures are based on the ITTC (International Towing Tank Conference) recommended procedures for intact stability model test [3].

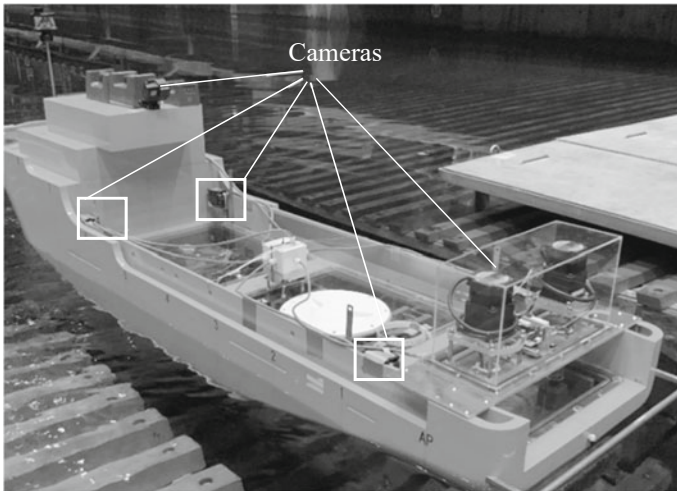
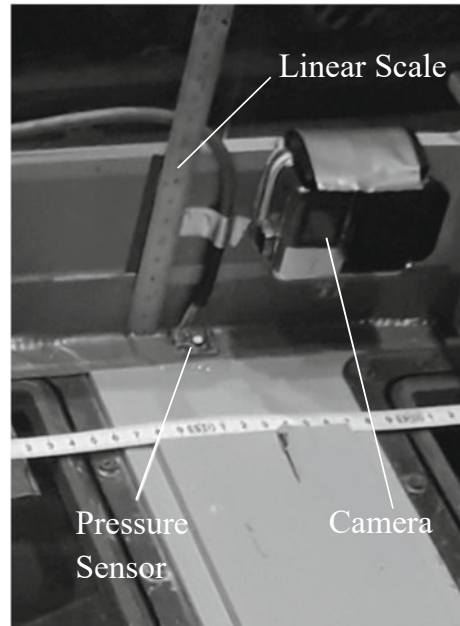


**Fig. 4** Model and camera arrangement of the model experiment in 2019

**Fig. 5** Camera and pressure sensor arrangement of the model experiment in 2019



### 3 Experimental Results and Discussions

#### 3.1 2015 Model Experiment

The maximum roll angles measured during each model run in astern waves are shown in Fig. 6. Here the wavelength is equal to the ship length, as the worst case assumed in the criteria for pure loss of stability and the nominal Froude number ranges from 0.24 to 0.37 as also specified by the criteria. The used wave steepness  $H/\lambda$ , are 0.03, 0.05 and 0.1. The results indicate that roll angles under these wave and operational conditions are smaller than  $15^\circ$  so that no real danger can be expected. While for a normal ship running in astern waves the roll response increases with the increasing ship speed (e.g. [2, 5]), this particular ship shows a different trend with respected to speed.

The reason presumed was that the trapped water-on-deck acted as a kind of anti-rolling tank, partly because the estimated natural period of possible trapped water on deck, which ranges between 1.8 s and 2.4 s in model scale as shown in Fig. 7, is comparable to the natural roll period of 2.1 s. The roll decay test of this model in calm water with large instantaneous initial roll angle (enabling water to ingress into the deck via the openings), was rapidly damped, as shown in Fig. 8. Thus, we can presume that this large roll damping is due to resonance of the ship roll motion and the trapped water on deck. It is similar to a mechanism of an anti-rolling tank.

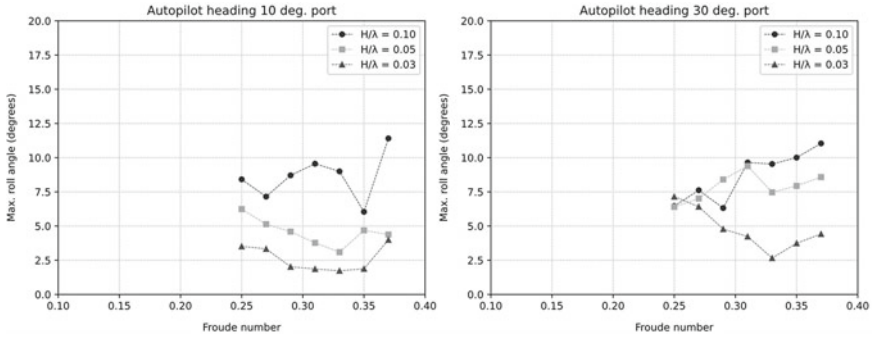


**Fig. 6** Maximum roll angles (in degrees) recorded in the experiment for the wavelength to ship length ratio ( $\lambda/L$ ) of 1.0 and the wave steepness ( $H/\lambda$ ) of 0.03, 0.05 and 0.1 with the autopilot headings of 10 and 30° port from the wave direction

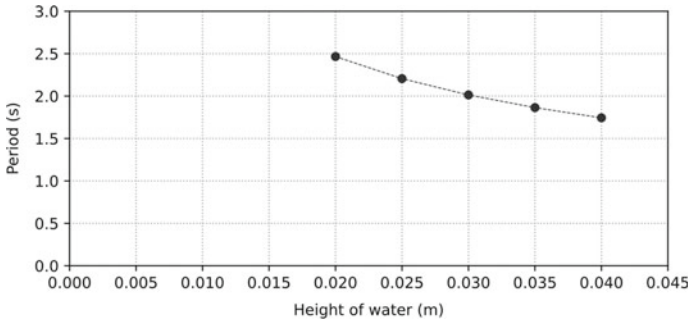


**Fig. 7** Estimated natural period of trapped water on deck as a function of water depth on deck

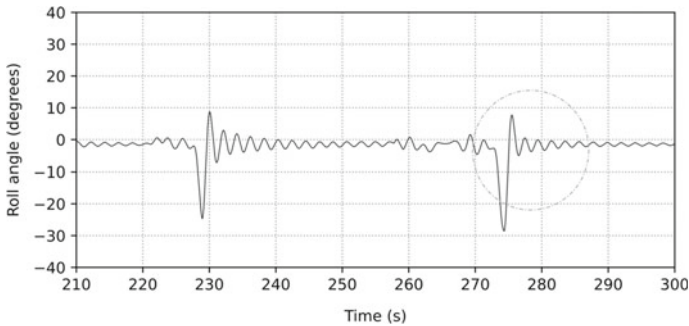
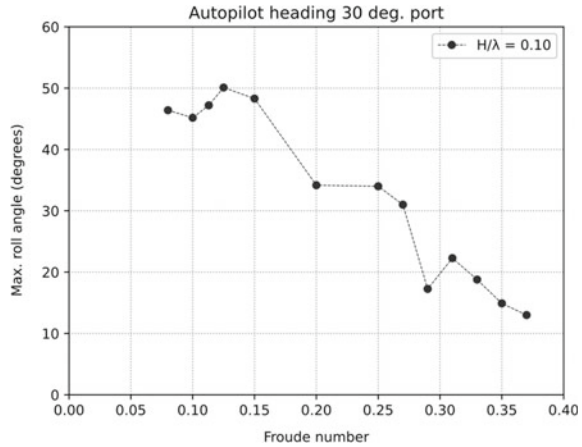


**Fig. 8** Time series of roll decay test with the large instantaneous initial roll angle in degrees

**Fig. 9** Maximum roll angles (in degrees) recorded during each free running test for the wavelength to ship length ratio ( $\lambda/L$ ) of 1.5 and wave steepness ( $H/\lambda$ ) of 0.1 with the autopilot heading of 30° port from the wave direction



As a next step, model runs were conducted with longer waves. Here the ratio of wavelength to ship length,  $\lambda/L$ , was 1.5, and the wave steepness was 0.1. In this case, larger water volume was trapped on deck because water ingress across the bulwarks exceeds egress through the freeing ports. The results shown in Fig. 9 indicate that larger roll angles, such as about 50°, were recorded. When the speed decreased, the roll angle increased. This tendency is entirely different from the pure loss of stability.

The reason for the larger roll could be the heeling moment of trapped water-on-deck, which could depend on the height of bulwarks. In the case of this OSV, if the roll angle exceeds about 21°, the relative water level exceeds the bulwark (bulwark submerged). From the GZ curve for this wavelength shown in Fig. 10, it can be observed that the loll angle is almost 20° and the angle of vanishing stability is slightly larger than 50°. Thus, the bulwark submergence cannot be avoided with wave crest amidship as the OSV will roll to the loll angle and submerge the bulwark. Then the maximum roll angle could be 50°. This suggests that the reason for large roll seems to be hydrostatic heel moment due to water on deck.

### 3.2 2019 Model Experiments

#### Maximum Roll angles

The maximum roll angles observed during the free runs carried out in Stage 1 are shown in Fig. 11. In Stage 1, the model run was executed with all the weather deck openings opened, and there was water ingress and egress, so the results include the complete water on deck phenomenon. The ratio of wavelength to ship length,  $\lambda/L$ , was set as 1.5. Figure 11 indicates that trends exist in the maximum roll angle when the larger wave steepness of  $H/\lambda = 0.1$  is used. It is the result of a significant amount of water getting trapped in the weather deck due to steep waves.

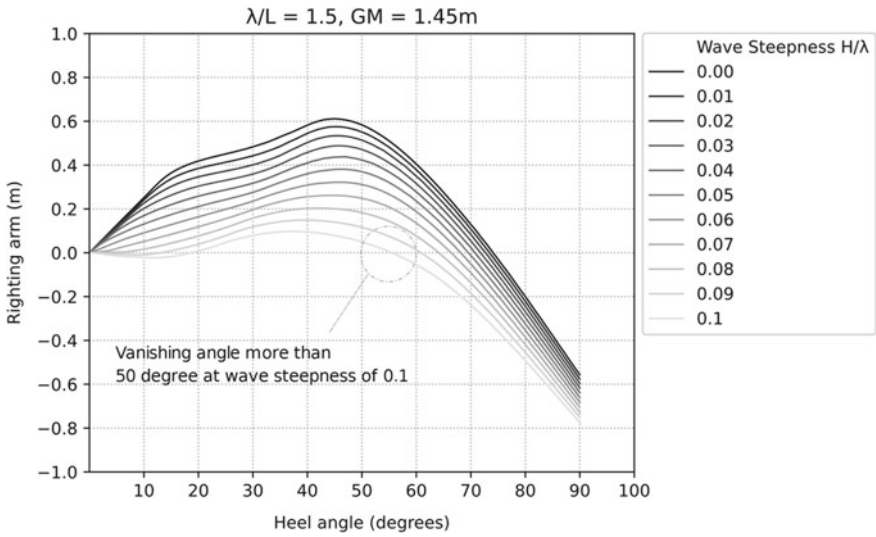


**Fig. 10** GZ curve of the OSV at a wave crest amidship in longitudinal waves for the wavelength to ship length ratio,  $\lambda/L$  of 1.5 and the wave steepness ranges from 0 to 0.1

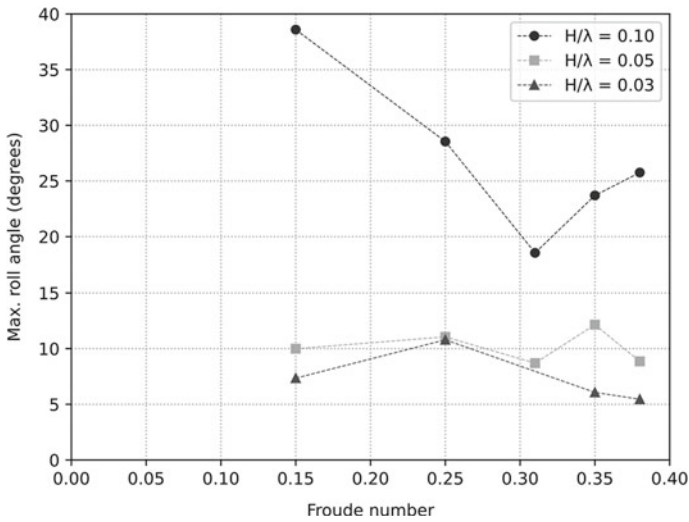


**Fig. 11** Maximum roll angle vs Froude number for  $\lambda/L = 1.5$  and autopilot heading relative to waves = 30° port (Stage 1, all openings open)



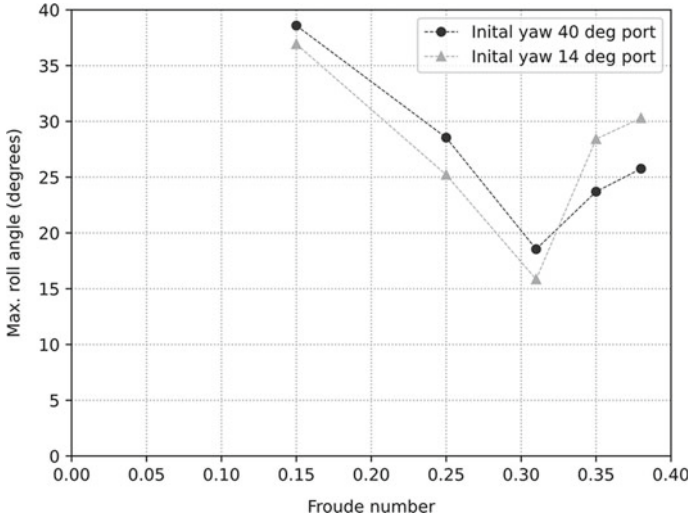
At low speed, the roll angle is very high since much water enters the ship from the stern opening and causes a large static heeling moment. When the speed of the vessel increases, the encounter frequency of the waves decreases and the average amount of trapped water decreases because of reduced ingress from the stern opening, so the maximum roll angle decreases. The increase in damping caused by the trapped water could be another reason for the decrease in roll angle. However, when the Froude number exceeds 0.31, the maximum roll angle again increases. The primary reason for this increase in roll angle is the near in-phase motion of the water with the low frequency ship roll. Roll restoring variation and yaw-roll coupling [5] could be secondary effects contributing to the increase in the roll angle for this vessel.

Comparison of the 2015 and 2019 model experiments for the same wave conditions of  $\lambda/L = 1.5$  and  $H/\lambda = 0.1$  (Figs. 9 and 11), shows both similarities and differences. For the case of lower Froude numbers, the maximum roll angle variation is similar for both Figs. 9 and 11, as the maximum roll angle is mainly governed by the amount of water entering over the bulwark from the sides. But for higher speeds (above  $F_n$  0.31) the variation of maximum roll angle is different in the two figures, this is because at higher speeds the entry of water from the stern becomes important. For the 2019 model experiments since the steering gear location was raised, water could more easily ingress from the aft. The motion of this trapped water nearly in phase with the low frequency ship roll motion, may have caused an increase in the roll angle at higher speeds for the 2019 model experiments.

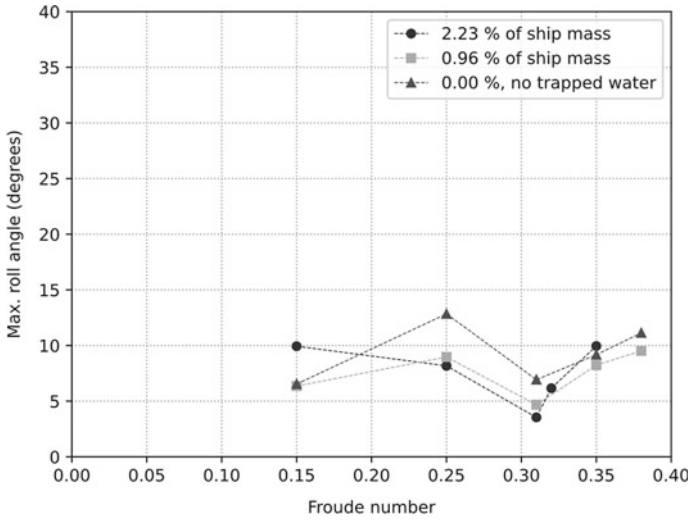
In order to investigate the effect of initial yaw on the maximum roll angles we carried out an additional set of free runs for the case of  $H/\lambda = 0.1$  and  $\lambda/L = 1.5$ , with a smaller initial yaw. The results are shown in Fig. 12. For lower Froude numbers maximum roll angle is almost the same irrespective of the initial yaw, as the deck is saturated with a large amount of water. At higher Froude numbers (above 0.31) the maximum roll angle is slightly larger with a smaller initial yaw. This could be due to the initial increased ingress of water from the stern compared to the case with larger initial yaw. The trends of variation of maximum roll angles is however similar for both cases.

Figure 13 shows the variation of maximum roll with Froude number during Stage 2 with closed openings. Free running model tests were executed with the deck both empty and pre-filled with a known amount of water. Result from the latter contains the ship motion along with the deck water motion behaviour; water inflow and outflow through the openings are absent. In these cases, the ratio of wavelength to ship length,  $\lambda/L$ , was set as 1.5 but a smaller wave steepness of  $H/\lambda = 0.03$  was used to avoid additional water shipping over the bulwarks.

For the case of amount of water filled on deck equal to 2.23% of ship mass, the initial drop in the maximum roll angle from the Froude number of 0.15–0.31 may be attributed to the increase in the roll damping and a further increase in the maximum roll beyond the Froude number of 0.31 may be attributed to the near in phase motion of water with ship roll and secondary effects of roll restoring variation or yaw-roll coupling.



**Fig. 12** Maximum roll angle versus Froude number for  $\lambda/L = 1.5$ ,  $H/\lambda = 0.1$ , autopilot heading relative to waves =  $30^\circ$  port and initial yaw angles of 14 and  $40^\circ$  port (Stage 1, all openings open)



**Fig. 13** Maximum roll angle versus Froude number for  $\lambda/L = 1.5$ ,  $H/\lambda = 0.03$  and autopilot heading relative to waves =  $30^\circ$  port (Stage 2, all openings closed and deck is filled in advance with a known amount of water as a percentage of ship mass)

### Damping caused by water trapped on the deck

The confirmation of the presence of damping was obtained by analysing the results of Stage 2 free-running data from the 2019 model experiments. The results with the larger amount of trapped water (2.23% of ship mass) were utilised. Here all the openings were closed, and the amount of water inside the deck was constant throughout the model run. Thus, the initial decrease in the maximum roll angle could be attributed to roll damping caused by the water on deck. Time histories of the varying deck water level and the ship roll motion were compared to check the phase difference between the two. The time difference between a peak of roll angle on starboard/port side and the corresponding water level peak of the same side was calculated and converted to the phase difference using the average frequency of ship roll and water motion. Figure 14 show the time histories of ship roll and water motion for the Froude number of 0.31 and the phase difference. Figure 15 shows the change of the phase difference between water motion and ship roll with ship speed. It can be seen that the phase difference is close to  $90^\circ$  between the Froude number 0.25 and 0.31. The damping effect due to deck water motion is highest in this region. The phase difference further decreases with increasing speed.

The reason why the damping effect is at the maximum when the phase difference between ship motion and water motion is  $90^\circ$  is explained in Fig. 16. In Fig. 16a the ship roll angle is the largest towards starboard and the water is moving towards starboard. It induces no roll moment due to the water on deck. In Fig. 16b the ship is rolling to port and the water trapped is on the starboard side, which induces a roll moment in the opposite direction to the roll velocity. Similar explanations can

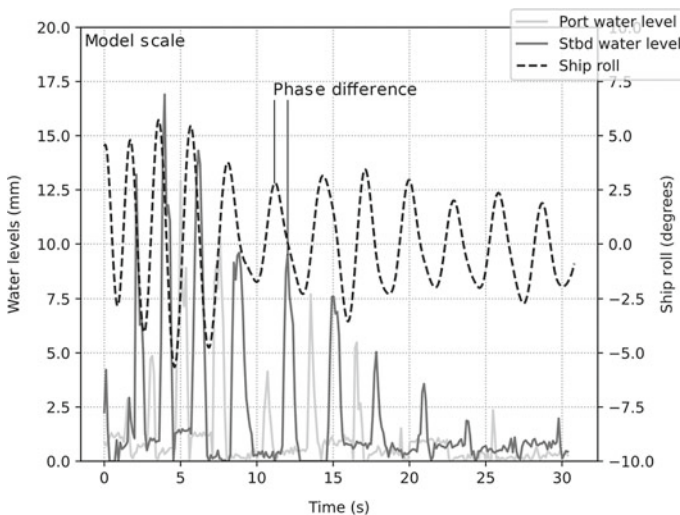


**Fig. 14** Time history of ship roll and water levels for  $F_n = 0.31$ ,  $\lambda/L = 1.5$ ,  $H/\lambda = 0.03$  and autopilot heading relative to waves =  $30^\circ$  port (Stage 2, all openings closed but the deck is filled in advance with a known amount of water, 2.23% of ship mass)

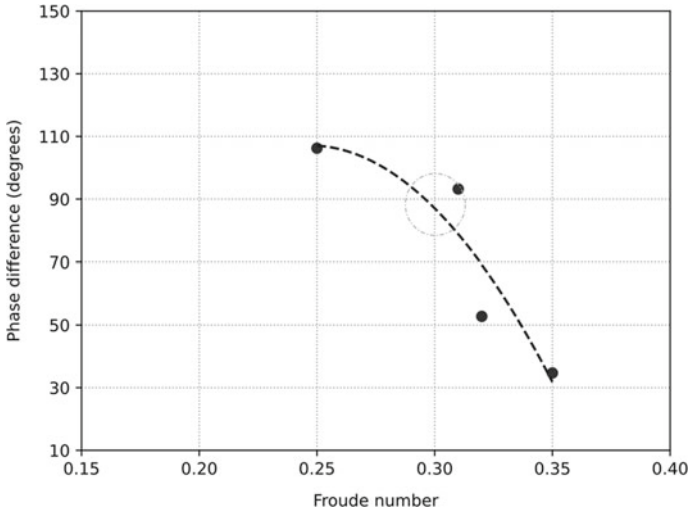


**Fig. 15** Phase difference between motion of trapped water on deck and ship roll angle versus Froude number

be provided for the Fig. 16c and d. The maximum roll moment due to water and maximum roll velocity are out of phase; in other words, the phase difference between the ship roll and the water motion is 90°.

## 4 Numerical Simulations

### 4.1 Free Running Simulations

Numerical simulations were carried out based on the data from the 2015 model experiments. For investigating the mechanism of this dangerous phenomenon, the coupled surge-sway-yaw-roll numerical model proposed by Kubo et al. [5] was used for simulating the dynamic behaviour under the wave conditions used in the experiment. This is a manoeuvring-type model with linear wave exciting forces and restoring variation focusing on low-frequency phenomena, but the effect of trapped water on the deck is not considered in the first attempt. All propulsion and manoeuvring coefficients input for the simulation model are estimated from conventional captive model experiments. The linear wave exciting forces and restoring variation were calculated by a slender body theory with low encounter frequency assumption and a direct pressure integral of incident wave pressure up to instantaneous water level, respectively.

The comparisons between the experiments and the simulations are shown in Figs. 17 and 18. For the case with the Froude number of 0.31 shown in Fig. 17, the measured and calculated roll periods are 14.80 s and 17.68 s respectively. The

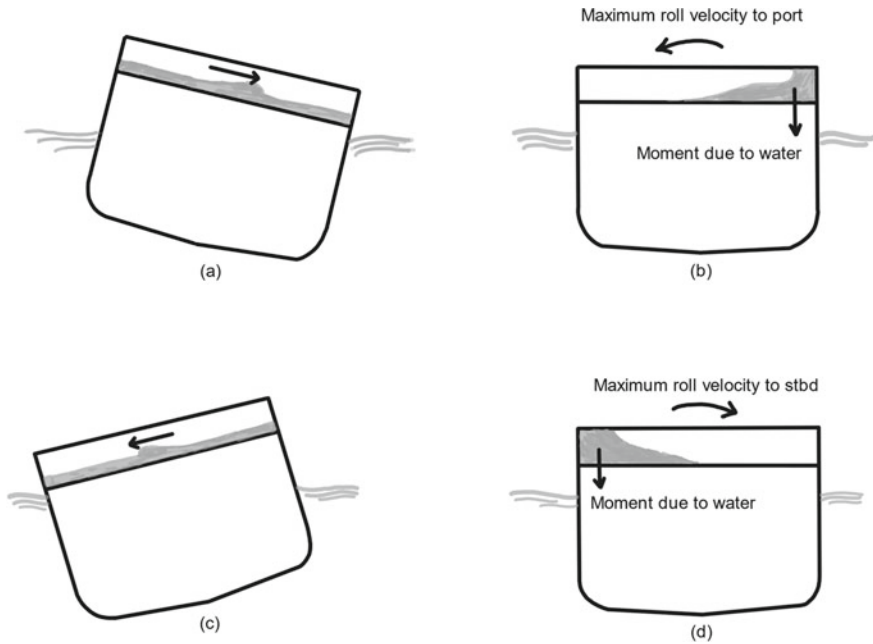


**Fig. 16** Phase difference between motion of trapped water on deck and ship motion

encounter wave period (calculated using the average yaw and average surge velocity) is 15.29 s. The natural roll period of the system without water is 11.5 s. The measured roll amplitude is much smaller than the calculated one so that the trapped water, which is not included in the numerical model, has a role to damp the roll motion as a kind of anti-rolling tank.

For the lower speed case of the Froude number of 0.125 shown in Fig. 18, the measured and calculated roll period are 20.80 s and 10.23 s respectively. The encounter wave period is 10.84 s so that the period doubling of roll motion was identified in the experiment. The measured roll amplitude is much larger than the simulated one. Furthermore, the mean of the measured roll angle is also larger than that of the calculated roll angle. This suggests that hydrostatic heel moment due to trapped water on deck, which is not included in the numerical model, has a crucial role for inducing the extremely large roll angle in the experiment. The large amount of water trapped on the deck could result not only in large mean roll angle but also in large roll amplitude due to the varying restoring moment due to the relative ship position to overtaking waves.

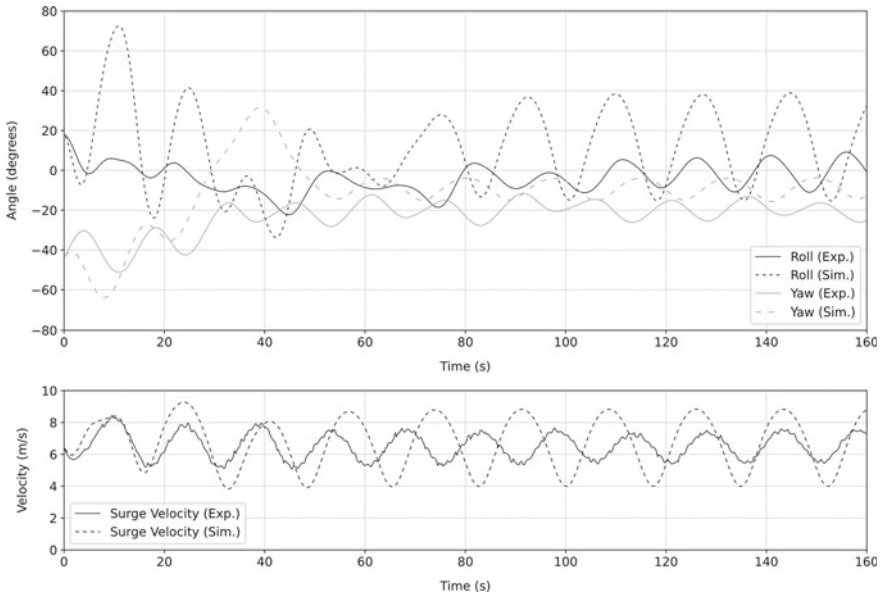


**Fig. 17** Comparison between the simulation and the experiment for the wave steepness ( $H/\lambda$ ) of 0.1, the wavelength to ship length ratio ( $\lambda/L$ ) of 1.5, the nominal Froude number is 0.31, the specific heading angle from the wave direction of  $30^\circ$  and the rudder gain of 3.0. Here the positive roll means starboard side down and the positive yaw does starboard turn

### 4.2 Effect of Weather Deck Length

For creating a proper definition of a vessel with extended low weather deck, the NAPA system was used to make systematically modified hulls of our offshore supply vessel (OSV) model.

The weather deck length, as defined in Fig. 19, was systematically modified by extending the forecastle deck towards the aft while keeping other dimensions constant. The displacement, draft and trim of the vessel was assumed to remain unchanged during the process. Then the level 1 and 2 criteria were applied to the generated hulls. All modified hulls comply with the level 1 criteria with directly calculated GM in waves exceeding the required value of 0.05 m. The level 2 criteria consist of two requirements: CR1 is based on the angle of vanishing stability, and CR2 is based on the angle of the heel under the action of the speed-dependent heeling lever. The standard for these values is 0.06. Here the Froude number is set to be 0.25. The results are shown in Fig. 20.

When the weather deck length is larger than half the length between perpendiculars, the CR2 value rapidly increases so that the vessel is judged as vulnerable to pure loss of stability. However, the vessel is not so relevant to the danger due to pure loss of stability as mentioned before. To avoid such “false negative” case, it can be

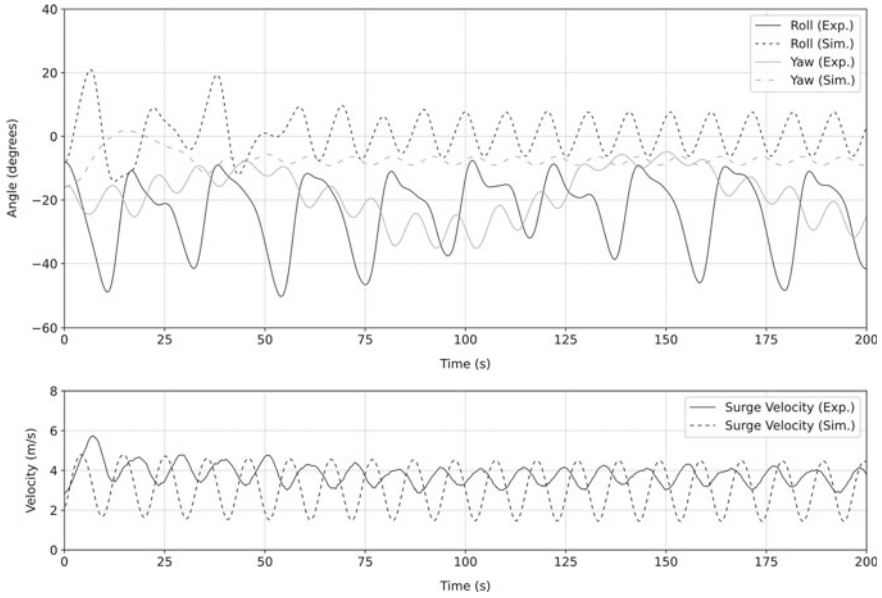


**Fig. 18** Comparison between the simulation and the experiment for the wave steepness ( $H/\lambda$ ) of 0.1, the wavelength to ship length ratio ( $\lambda/L$ ) of 1.5, the nominal Froude number is 0.125, the specific heading angle from the wave direction of  $30^\circ$  and the rudder gain of 3.0

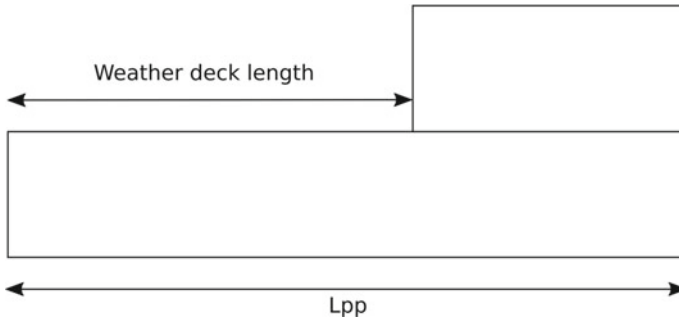


**Fig. 19** Simplified OSV with weather deck length definition

recommended to include the low weather deck length in the definition of a vessel with extended low weather deck.

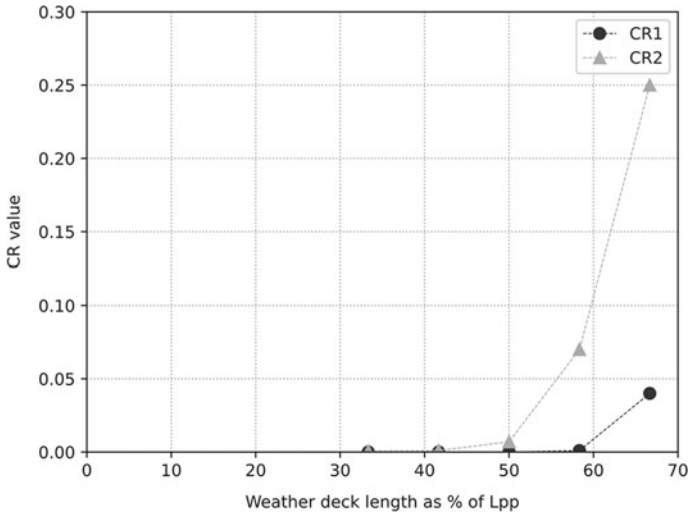


Fig. 20 Weather deck length and CR values from Level 2 criteria results

### 5 Conclusions

Two separate model experiments were carried out to study the behaviour of the OSV in astern waves, and from both the experiments it is clear that the water on deck effect plays a major role in the vessel’s roll motion. The following main conclusions can be drawn:

- When the wave conditions are such that the water ingress is significant ( $\lambda/L = 1.5$  and  $H/\lambda = 0.1$ ),
  - At lower Froude numbers, the maximum roll angle could be very high, close to the angle of vanishing stability. This is due to the large static heeling moment caused by the significant amount of water trapped on one side of the weather deck.
  - As the speed of the vessel increases, the maximum roll angle decreases due to the combined effect of reduced water ingress, and roll damping due to trapped water. This tendency is different from the pure loss of stability.
  - At very high Froude number (above 0.31), the maximum roll angle again starts to increase due to the near in-phase motion of water with the low frequency ship roll. Roll restoring variation and yaw-roll coupling could be secondary effects contributing to the increase in roll angle.
- When the wave conditions are such that the water ingress is less ( $\lambda/L = 1.0$  and  $H/\lambda = 0.1, 0.05, 0.03$ ;  $\lambda/L = 1.5$  and  $H/\lambda = 0.05, 0.03$ ),
  - The amount of water trapped inside is small and the ship can easily roll with reduced amounts of water. The roll frequency is high at low Froude number



and it reduces as the ship speed increases. Thus, the phase difference between ship motion and trapped water motion would be high at low Froude number and would decrease as the ship speed increases. The damping effect would be most effective when the phase difference approaches  $90^\circ$ .

- At very high Froude number, the near in phase motion of deck water and ship roll contributes to the increase in the maximum roll angle.
- Based on the systematic hull modification survey, it also can be concluded here that, if the length of low weather deck is greater than  $0.5L_{pp}$ , it is not appropriate to apply the level 2 pure loss criterion to this type of ships. As mentioned before, the vessel used here is not so relevant to the danger due to pure loss of stability.

**Acknowledgements** This work was supported by Grant-in Aids for Scientific Research from the Japan Society for Promotion of Science (JSPS KAKENHI Grant Numbers 15H02327 and 19H02360). It was partly carried out as a research activity of Goal-based Stability Criteria Project of Japan Ship Technology Research Association in the fiscal years of 2015 and 2019 funded by the Nippon Foundation. It was also a part of the collaborative research on intact stability between NAPA Japan and Osaka University. The authors sincerely thank these organisations. This is an updated version of the paper read at the 15th International Ship Stability Workshop [8] with additional research outcomes [6].

## References

1. IMO (2015) Report of the working group (Part 1), SDC 2/WP.4
2. IMO (2020) Interim guidelines on the second generation intact stability criteria. MSC.1/Circ. 1627
3. ITTC (2008) Recommended procedures and guidelines, model test on intact stability; 7.5-02-07-04.1 Revision 2
4. IMO (2018) Information collected by the correspondence group on intact stability, submitted by Japan, SDC 5/6/INF.4
5. Kubo H, Umeda N, Yamane K, Matsuda A (2012) Pure loss of stability in astern seas—is it really pure? In: Proceedings of the 6th Asia-Pacific workshop on marine hydrodynamics-APHydro2012, pp 307–312
6. Subramaniam S, Umeda N, Maki A, Matsuda A (2020) Systematic experimental study on water on deck effect of an offshore supply vessel in stern quartering waves. In: Conference proceedings of the Japan society of naval architects and ocean engineers, vol 30, pp 623–627
7. Umeda N, Francescutto A (2016) Current state of the second generation intact stability criteria—achievements and remaining issues. In: Proceedings of the 15th international ship stability workshop, pp 1–7
8. Umeda N, Alway A, Usada S, Matsuda A, Terada D (2016) Model experiment of an offshore supply vessel running in astern waves, In Proceedings of the 15th Ship Stability Workshop, pp 11–16

# Characteristics of Capsizing Phenomena of Fishing Vessels



Akihiko Matsuda, Daisuke Terada, and Hirotada Hashimoto

**Abstract** The second generation intact stability criteria have been finalized at International Maritime Organization. The criteria are developed for 5 stability failure modes, those are pure loss of stability, broaching-to, dead ship condition, parametric rolling and excessive acceleration. The authors have carried out free running capsizing model experiments in following and quartering seas for more than 18 fishing vessels. The series of experiments demonstrated pure loss of stability, broaching-to and bow-diving are major phenomena resulted in capsizing for fishing vessels while parametric rolling is not.

**Keywords** Fishing vessels · Broaching-to · Bow-diving · Pure loss of stability · Harmonic roll · Model experiments

## 1 Introduction

In 2008, a 135GT Japanese purse seiner capsized in anchored condition. It was reported by JTSB in M2010-4. In 2009, a 135GT Japanese purse seiner capsized in quartering heavy seas. It was reported M2011-4. In 2010, a Japanese trawler capsized in head seas. It was reported M2011-8. More than 30 fishermen's lives were lost in these accidents. To prevent capsizing accidents, the authors have been conducting free running capsizing model experiments for fishing vessels.

The second generation intact stability criteria finalized at the International Maritime Organization (IMO) are aimed at securing the safety against 5 stability

---

A. Matsuda (✉)

Fisheries Research and Education Agency, Kamisu, Japan  
e-mail: [matsuda\\_akihiro34@fra.go.jp](mailto:matsuda_akihiro34@fra.go.jp)

D. Terada

National Defence Academy, Yokosuka, Japan  
e-mail: [dterada@nda.ac.jp](mailto:dterada@nda.ac.jp)

H. Hashimoto

Osaka Metropolitan University, Sakai, Japan  
e-mail: [hashimoto.marine@omu.ac.jp](mailto:hashimoto.marine@omu.ac.jp)

failure modes, those are dead ship condition, pure loss of stability, broaching-to, parametric rolling and excessive acceleration. The Level 1 and Level 2 vulnerability criteria for these 5 stability failure modes can be calculated without any model experiments. Although ship-dependent characteristics of dangerous phenomena can be qualitatively assessed by the vulnerability criteria, detailed characteristics of capsizing phenomena cannot be evaluated without model experiments. In addition, the applicability of the current vulnerability criteria to a specific type or a new type of vessels is an important issue.

So far, we have conducted free running capsizing model experiments for more than 18 fishing vessels. In this study, the experimental results are summarized to highlight major failure modes for fishing vessels. Then, an example of time history of capsizing for each failure mode is presented. Finally, we discuss the cause of sub-harmonic roll observed for a European fishing vessel.

## 2 Model Experiments

### 2.1 Instrumentation and Procedures

In the experiments that had been carried out before 2009, the Tele-tele System of Osaka University (developed by Hamamoto et al. [1]) was used (see Fig. 1). For the experiments carried out after 2009, the Model Motion Tracking System of the National Research Institute of Fisheries Engineering (developed by Matsuda et al, [7]) was used (see Fig. 2). In both systems, ship models were controlled by autopilot for course keeping using proportional rudder gain of 1.0 and constant propeller revolution. All model experiments were conducted following the Recommended Procedure of ITTC [3]. Free-running model experiments were conducted at Marine Dynamics Basin of National Research Institute of Fisheries Engineering shown in Fig. 3. In the last 20 years, we have conducted free running model experiments using not only Japanese fishing vessels but also European fishing vessels and commercial vessels.

### 2.2 Subject Ships

Fishing vessels used for the experiments are shown in Table 1. The total number of vessels is 16. Ship A to Ship J are purse seiners, Ship K to Ship N are trawlers, Ship O is a fishing vessel for set net, ship P to ship R are fishing vessels for pacific saury and Ship S is a North European purse seiner. The general arrangements of 4 vessels are shown in Figs. 4, 5, 6 and 7. We have executed more than 2000 runs in total for capsizing model experiments.

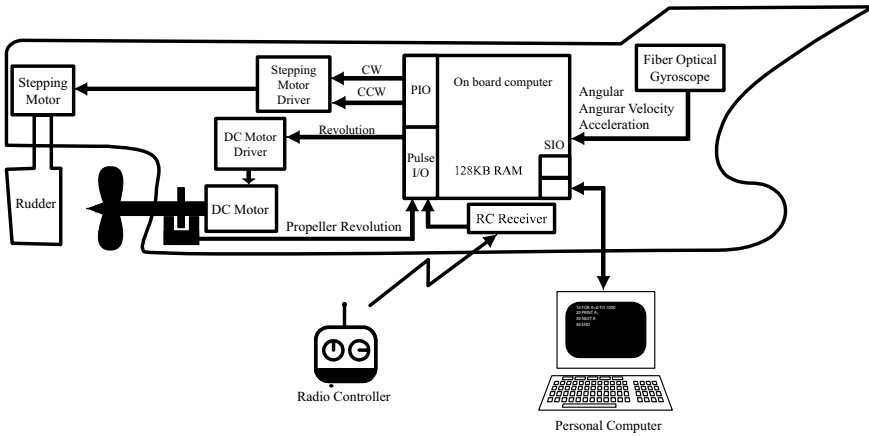


Fig. 1 Tele-tele system

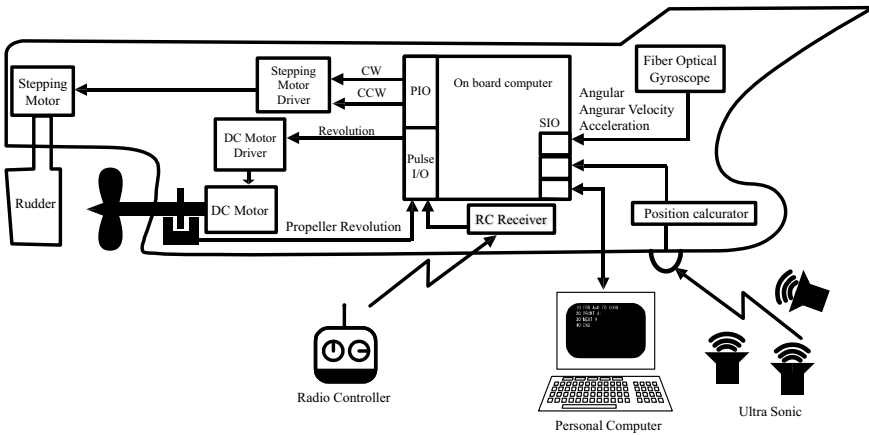
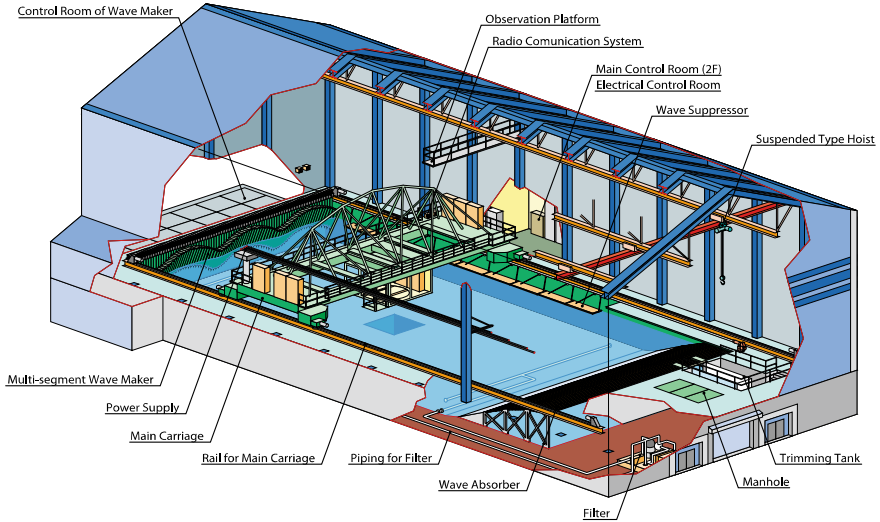


Fig. 2 Model motion tracking system

### 3 Experimental Results

#### 3.1 Capsizing Modes

Experimental results, including a past result by Umeda et al. [8], are summarized in Table 2. Here the check mark denotes the occurrence of capsizing in the experiment. For Japanese fishing vessels, capsizing due to pure loss of stability, broaching-to and bow-diving were observed. No capsizing due to parametric rolling/harmonic roll occurred. A European fishing vessel (Ship S) capsized due to harmonic roll



**Fig. 3** Marine dynamics basin

**Table 1** Subject ships

	Length (Lpp) (m)	Breadth (B) (m)	Depth (D) (m)	Max nominal Froude number (Fn)
Ship A	34.5	7.6	3.07	0.43
Ship B	29.0	6.8	2.6	0.46
Ship C	28.8	7.5	2.6	0.4
Ship D	30.0	7.9	2.78	0.33
Ship E	29.0	6.9	2.58	0.38
Ship F	23.0	5.9	2.15	0.43
Ship G	21.2	6.35	2.41	0.46
Ship H	20.35	5.83	1.76	0.43
Ship I	37.0	7.90	3.23	0.35
Ship J	46.0	10.6	5.57	0.34
Ship K	26.85	5.9	2.6	0.44
Ship L	26.85	6.6	2.85	0.38
Ship M	17.8	3.24	2.24	0.39
Ship N	11.35	5.1	2.1	0.49
Ship O	21.2	4.82	1.26	0.43
Ship P	21.35	5.21	1.22	0.5
Ship Q	19.8	4.80	1.99	0.41
Ship R	22.4	4.58	1.71	0.41
Ship S	55.0	12.0	7.6	0.24

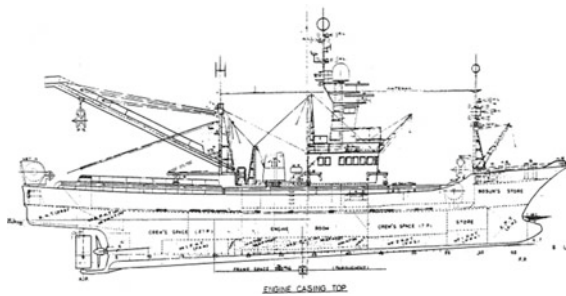


Fig. 4 Ship A (135GT Purse seiner)

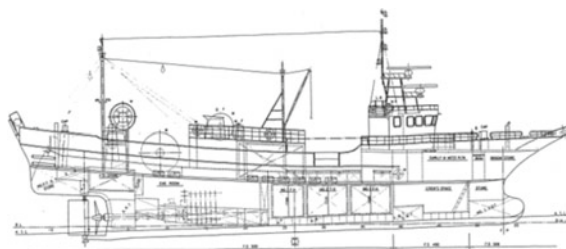


Fig. 5 Ship K (Trawler)

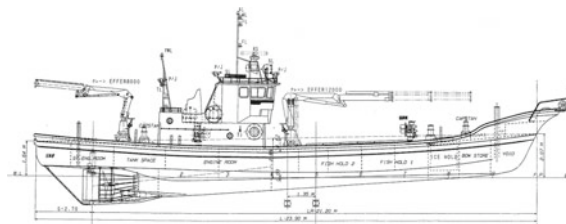


Fig. 6 Ship O (Fishing Vessel for Set net)

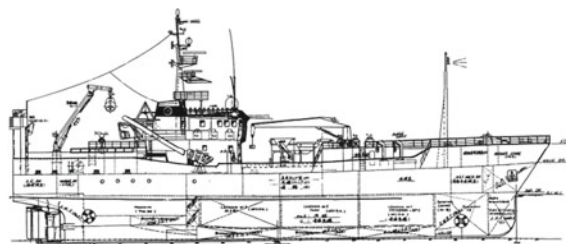


Fig. 7 Ship S (North European Purse Seiner)

**Table 2** Experimental results

	Pure loss of Stability	Broaching -to	Bow-diving	Parametric rolling/Sub-harmonic Roll
Ship A	✓	✓		
Ship B	✓	✓	✓	
Ship C	✓		✓	
Ship D	✓			
Ship E	✓		✓	
Ship F	✓	✓		
Ship G		✓		
Ship H				
Ship I	✓			
Ship J				
Ship K	✓		✓	
Ship L				
Ship M	✓	✓		
Ship N		✓		
Ship O	✓	✓	✓	
Ship P		✓	✓	
Ship Q		✓		
Ship R		✓		
Ship S				✓

while capsizing due to pure loss of stability, broaching-to and bow-diving were not observed.

### 3.2 *Pure Loss of Stability*

A time series of capsizing due to pure loss of stability is shown in Fig. 8 and sequence snapshots are done in Photo 1. In this case, the ship was running in quartering seas at a speed close to the wave celerity and stayed on a wave crest for a time and capsized after a while. Thus, it can be judged the ship capsized due to pure loss of stability.

### 3.3 *Broaching-to*

A time series of broaching-to is shown in Fig. 9 and sequence snapshots are done in Photo 2. In this case, the ship was accelerated by a following wave up to the

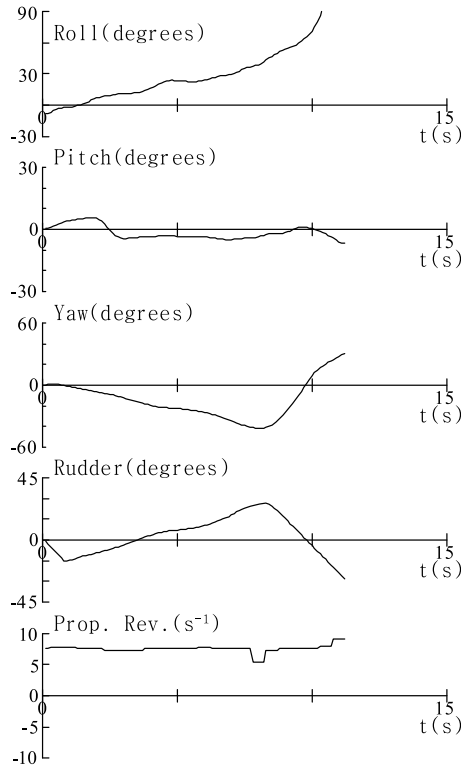


**Fig. 8** Pure loss of stability of Ship F (39GT purse seiner) ( $F_n = 0.43$ ,  $\chi = -15^\circ$ ,  $\lambda/L = 1.25$ ,  $h/\lambda = 1/9$ )

wave celerity, defined as surf-riding. During the surf-riding on a wave down slope, she could not keep the desired course despite the maximum effort of auto pilot and capsized in a short time due to the centrifugal force.

### 3.4 Bow-Diving

In case a ship has a sufficiently large propulsion force, stable surf-riding on a wave up slope occurs after a short surf-riding on a wave down slope. If the height of bow is not high enough, she dives into a front wave slope and takes massive water on deck. Finally, she could capsize due to water on deck as well as the reduction of transverse stability on a wave crest. A time series of bow-diving is shown in Fig. 10



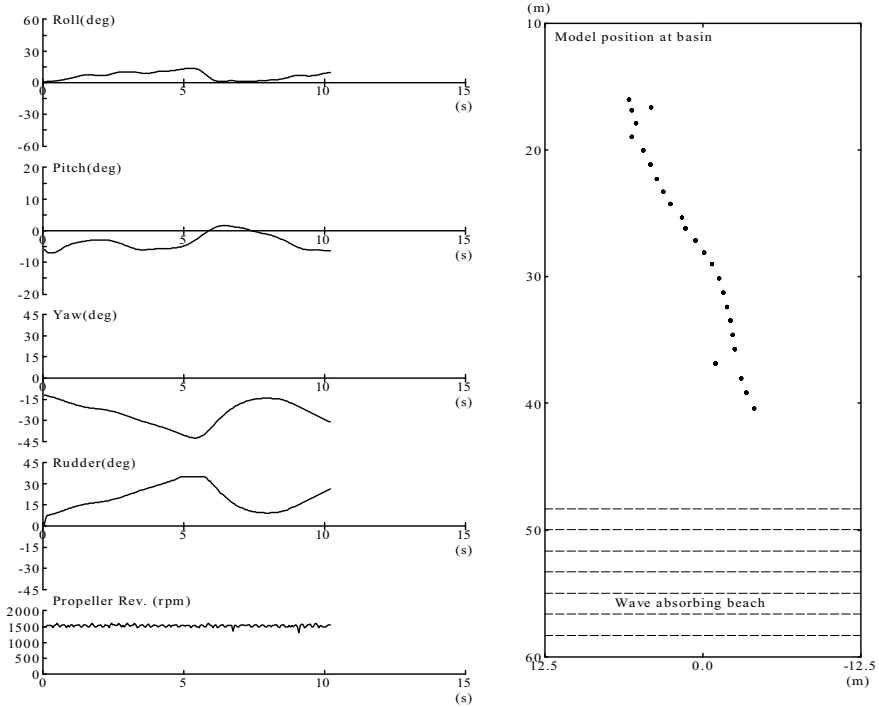


**Fig. 9** Broaching-to of Ship G (19GT purse seiner) ( $F_n = 0.43$ ,  $\chi = -5^\circ$ ,  $\lambda/L = 1.5$ ,  $h/\lambda = 1/9$ )

and snapshots are shown in Photo 3. For Ship P, she never capsized due to broaching-to but capsized due to bow-diving. From the experience of past experiments, bow-diving is more dangerous phenomena leading to capsizing than broaching-to for Japanese fishing vessels.

### 3.5 Sub-harmonic Roll

Sub-harmonic roll occurs when the roll frequency is about half of the wave encounter frequency. Ship S which is a European fishing vessels suffered severe sub-harmonic roll and capsized as shown in Fig. 11 and Photo 4. Parametric rolling is known as a sub-harmonic roll in which the wave encounter frequency is 2 times large as the natural roll frequency. However, the roll period in Fig. 10 is about 8 s and it is apart from the natural roll period of 3.54 s.

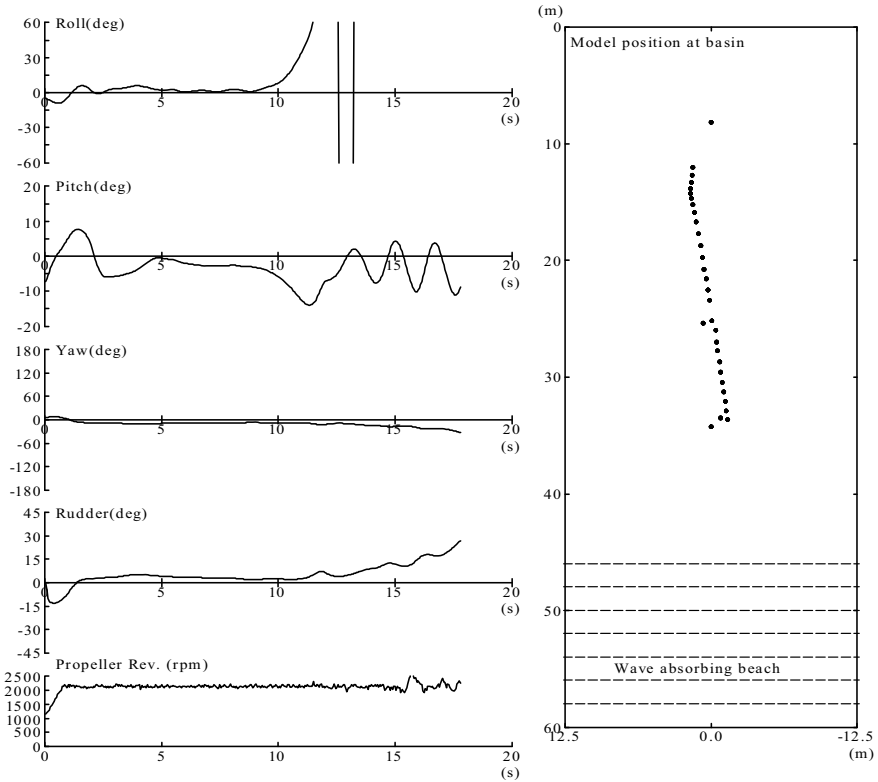


**Fig. 10** Bow-diving of Ship P (fishing vessel for pacific saury) ( $F_n = 0.50$ ,  $\chi = -5^\circ$ ,  $\lambda/L = 1.5$ ,  $h/\lambda = 1/9$ )

### 4 Characteristics of Sub-harmonic Roll

It was demonstrated that Japanese fishing vessels could capsizing due to pure loss of stability, broaching-to and bow-diving, but capsizing due to parametric rolling/sub-harmonic roll was not observed. For a European fishing vessel (Ship S), it could only capsizing due to sub-harmonic roll. Hamamoto et al. [2] suggested that a ship could suffer parametric rolling if it has a hard spring type GZ curve. The GZ curve of Ship S is shown in Fig. 12 and GZ curves of Japanese fishing vessels are shown in Fig. 13. Figure 12 shows that the GZ curve of Ship S is the hard spring type. Figure 13 shows that all GZ curves of Japanese fishing vessels are the soft spring type. The difference of the type of GZ curve would be a reason why sub-harmonic roll occurred only for the European fishing vessel.

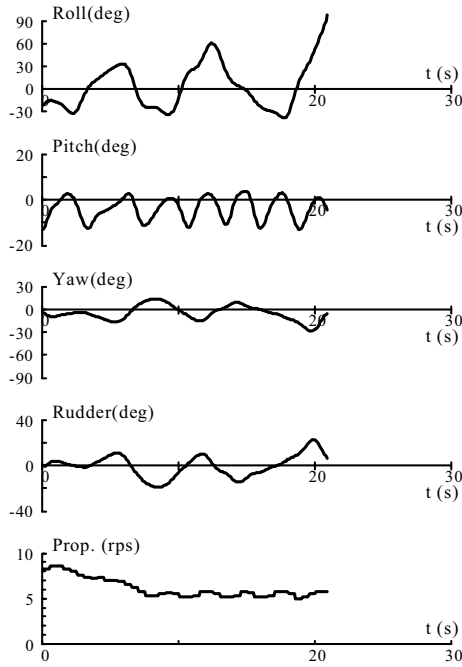


**Fig. 11** Sub-harmonic roll of Ship S (European fishing vessel) ( $F_n = 0.30$ ,  $\chi = -5^\circ$ ,  $\lambda/L = 1.5$ ,  $h/\lambda = 1/9$ )

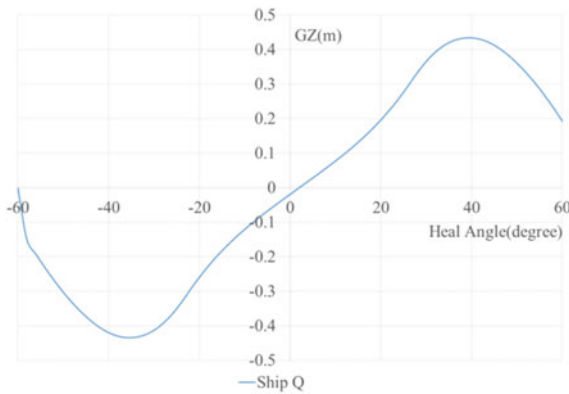
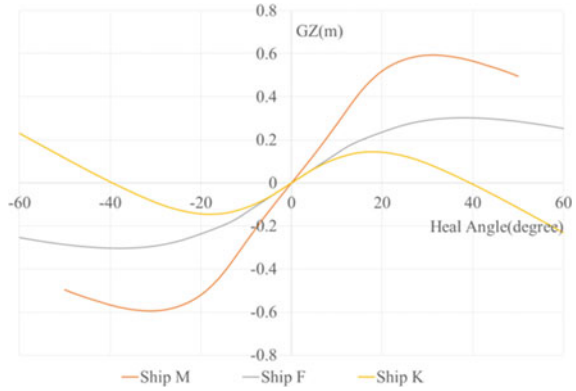


**Fig. 12** GZ curve of European fishing vessel

**Fig. 13** GZ curves of Japanese fishing vessels



## 5 Conclusions

In this study, we have described a series of free-running capsizing model experiments to clarify dangerous phenomena leading to capsizing for fishing vessels. The conclusions are summarized as follows.

1. Japanese fishing vessels could capsize due to broaching-to, pure loss of stability and bow-diving in following and stern quartering seas.
2. European fishing vessels could capsize due to sub-harmonic roll in following and stern quartering seas.
3. An example of time history of each dangerous phenomenon resulted in capsizing was presented.
4. European fishing vessels having a hard spring type GZ curve could suffer sub-harmonic roll while Japanese fishing vessels having a soft spring type GZ curve could not.

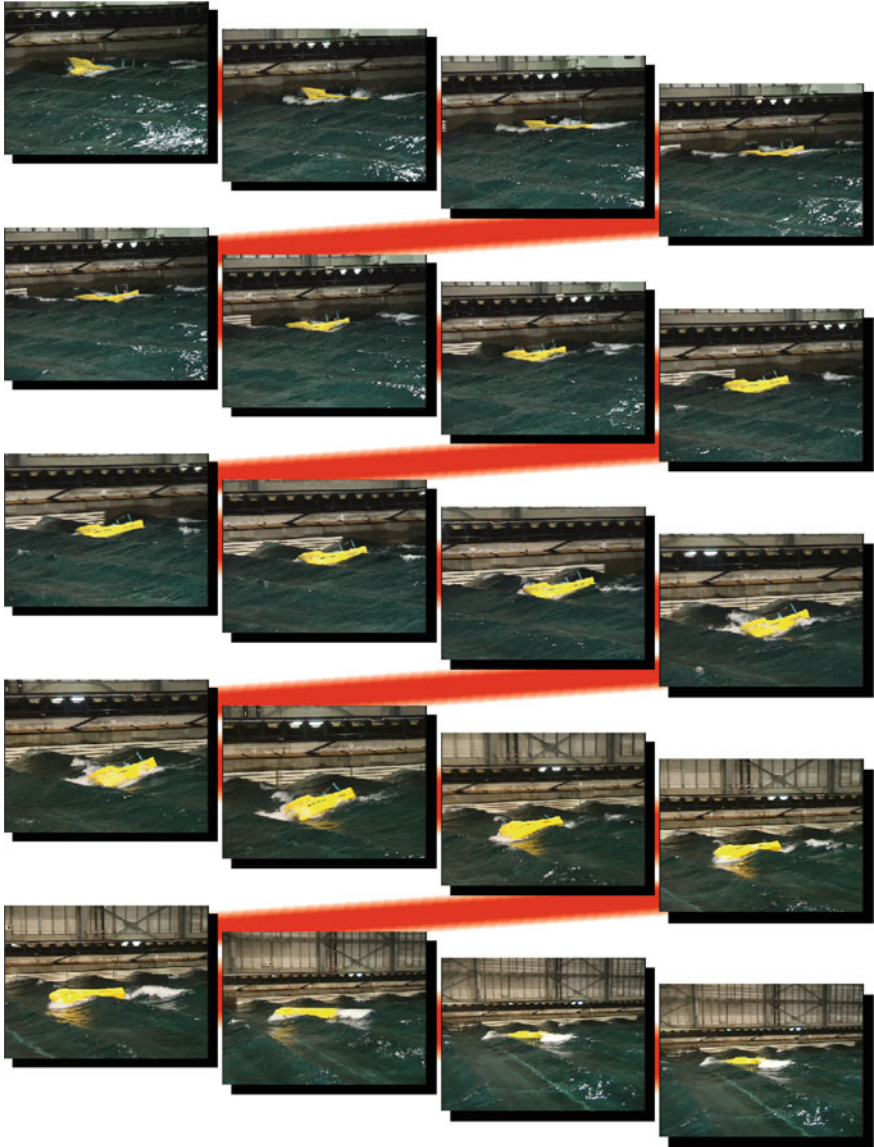


**Photo 1** Pure loss of stability



**Photo 2** Broaching-to



**Photo 3** Bow diving

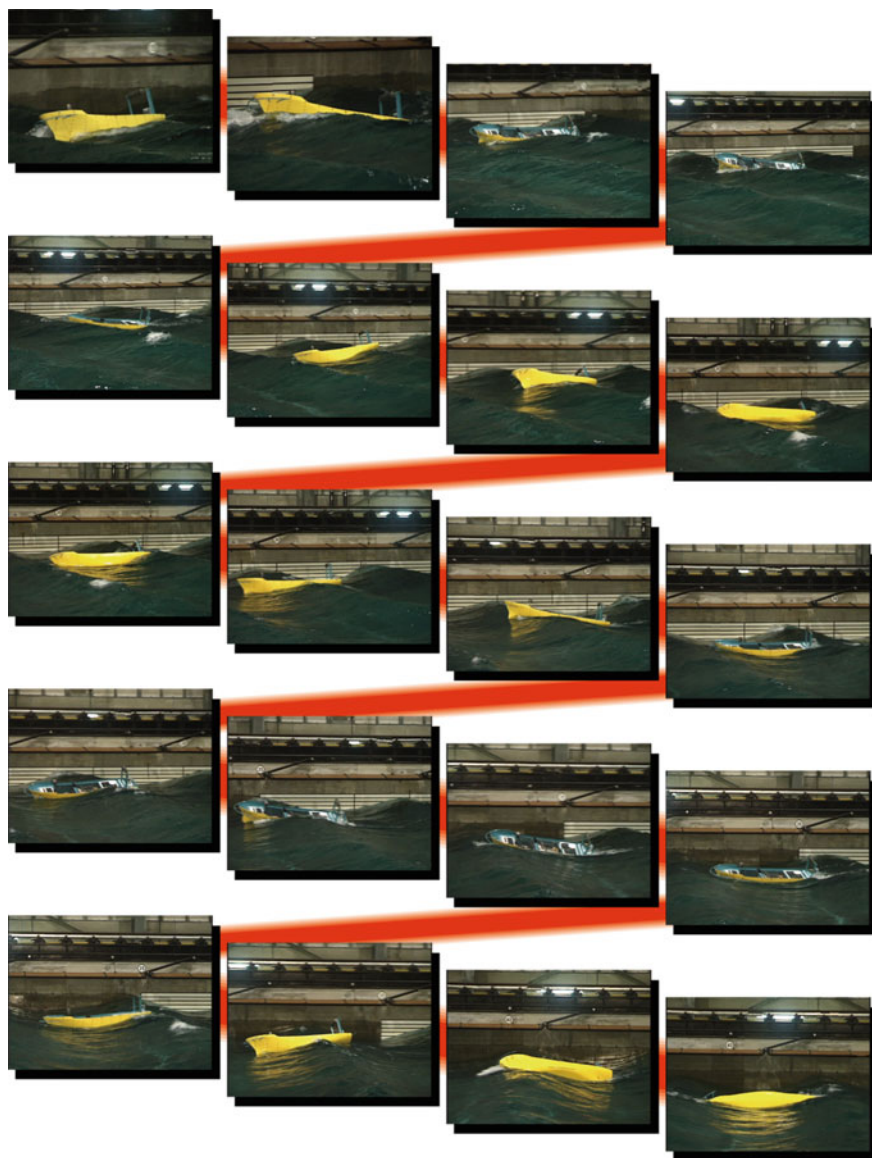


**Photo 4** Sub-harmonic roll



## References

1. Hamamoto M, Enomoto T, Sera W, Panjaitan JP, Ito H, Takaishi Y, Kan M, Haraguchi T, Fujiwara T (1996) Model experiments of ship capsizing in astern seas—second report. *J Soc Naval Archit Jpn* 77–87
2. Hamamoto M, Umeda N, Matsuda A, Sera W (1995) Analyses on low cycle resonance of ship in Astern Seas. *J Soc Naval Archit Jpn* 197–206
3. International Towing Tank Conference (2008) Recommended procedures, model tests on intact stability, 7.5-02-07-04.1
4. Japan Transport Safety Board (2010) The report of ship accident investigation, M2010-5
5. Japan Transport Safety Board (2011) The report of ship accident investigation, M2011-4
6. Japan Transport Safety Board (2011) The report of ship accident investigation, M2011-8
7. Matsuda A, Hashimoto H, Terada D, Taniguchi Y (2016) Validation of free running model experiments in heavy seas. In: Proceedings of 3rd international conference on violent flows, Osaka
8. Umeda N, Matsuda A, Hamamoto M, Suzuki S (1999) Stability assessment for intact ships in the light of model experiments. *J Mar Sci Technol* 4(2):45–57

# **Accident Investigation**

# Experimental Investigations into Accidents of Two Japanese Fishing Vessels



Harukuni Taguchi, Akihiko Matsuda, and Kuniaki Shoji

**Abstract** This paper outlines the experimental investigations into serious accidents of a purse seiner, which capsized and foundered during lying to with a parachute sea anchor in the North Pacific Ocean on 23 June 2008, and a stern trawler of pair trawling, which foundered on the way to a fishing ground in the East China Sea on 12 January 2010. In order to clarify the sequence and mechanism of each accident, model experiments in waves were carried out individually and further consideration with stability calculation so on were made.

**Keywords** Accident investigation · Purse seiner · Capsizing · Shipping water · Stern trawler · Foundering · Free water

## 1 Introduction

In one and half years from June 2008, three serious accidents of relatively large fishing vessels, which related to their stabilities, successively happened in Japan and total 39 lives of crews on board were lost. The Japan Transport Safety Board (JTSB) had investigated these accidents and identified the probable causes of each accident. The results of the investigations were compiled into investigation reports and submitted to the Minister of Land, Infrastructure, Transport and Tourism and publicized.

---

H. Taguchi (✉)  
National Maritime Research Institute (NMRI), Tokyo, Japan  
e-mail: [taguchi@m.mpat.go.jp](mailto:taguchi@m.mpat.go.jp)

A. Matsuda  
Fisheries Research and Education Agency (FRA), Kamisu, Japan  
e-mail: [matsuda\\_akihiko34@fra.go.jp](mailto:matsuda_akihiko34@fra.go.jp)

K. Shoji  
Japan Transport Safety Board (JTSB), Tokyo, Japan  
e-mail: [qqr467u29@comet.ocn.ne.jp](mailto:qqr467u29@comet.ocn.ne.jp)

For two of these three accidents, namely “Purse seiner Suwa-maru No.58 accident” [2] and “Stern trawler Yamada-maru No.2 accident” [3], as parts of the investigations model experiments along with stability calculation were carried out in NMRI and FRA respectively. Based on the experimental results and so on the JTSC concluded the probable causes of the accidents and issued remarks to parties relevant to the causes in order to prevent similar accidents.

In this paper the main points of experimental investigations are presented.

## 2 135GT Purse Seiner Accident

### 2.1 Outline of the Accident

A 135GT purse seiner “Suwa-maru No.58” (L = 48.28 m, B = 8.10 m and D = 3.35 m) capsized and foundered during lying to with a parachute sea anchor in the North Pacific Ocean on 23 June 2008. The accident claimed 17 lives out of 20 crews on board. According to survivors, who stayed in the crew space inside the hull at the initial stage of the accident, the vessel had impact twice on the starboard bow section and it started to heel to starboard side then capsized in about one minute after the second impact.

The supposed wind and sea conditions at the time of the accident are summarised in Table 1. Furthermore, the impacts on the bow section were presumed to be caused by isolated big waves, which might hit the side of the vessel.

Table 2 summarises the estimated conditions of the vessel at the accident. In this condition the vessel complied with the requirements of the Japanese stability criteria for fishing vessels. In addition, the vessel is presumed to be inclined to starboard side due to unintentional unbalanced loading of the fishing net and the fishing gears before the accident.

**Table 1** Wind and sea conditions at the accident

Average wind speed	14 m/s ~ 16 m/s
Wind direction	SW ~ S
Significant wave height	2.5 m ~ 3.6 m
Average wave period	6.8 s ~ 8.4 s
Wave direction	SW ~ S

**Table 2** Hull conditions at the accident

Displacement: W	430.70 t
Mean draft: dm	2.68 m
Freeboard: Fb	0.68 m
Height of C.G.: KG	3.16 m
Metacentric height: GM	1.81 m

## 2.2 Model Experiment

As all survivors stayed in the crew space inside the hull at the initial stage of the accident, the sequence and mechanism of the accident were not clear. In order to ascertain the capsizing process and factors related to the accident, a model experiment aiming to reproduce the situation at the accident was carried out in a wave tank (50 m in length, 8 m in width and 4.5 m in depth) at NMRI.

In the experiment a 1/23.9 scaled model ship was moored to the carriage with weak springs to simulate the situation of lying to with a parachute sea anchor and keep intended encounter angle in waves and ship motions were measured in starboard bow to beam waves (Fig. 1). In the experiment wave conditions (properties and encounter angle) and ship conditions (position of centre of gravity and function of freeing ports) were varied and their effects on capsizing were investigated.

Waves used in the experiment were regular waves with superimposition of a concentrating wave intending to simulate the isolated big waves, which were presumed to be a cause of the impact at bow section at the accident. The height ( $H_w$ ) and period ( $T_w$ ) of regular waves were varied,  $H_w = 0.10\text{--}0.25$  m,  $T_w = 0.80\text{--}1.55$  s, with referring to the supposed sea condition at the accident (Table 1). And the height of concentrating wave was set 1.6 times of superimposed regular wave. Encounter angle were varied from  $165^\circ$  (starboard bow wave) to  $90^\circ$  (starboard beam wave).

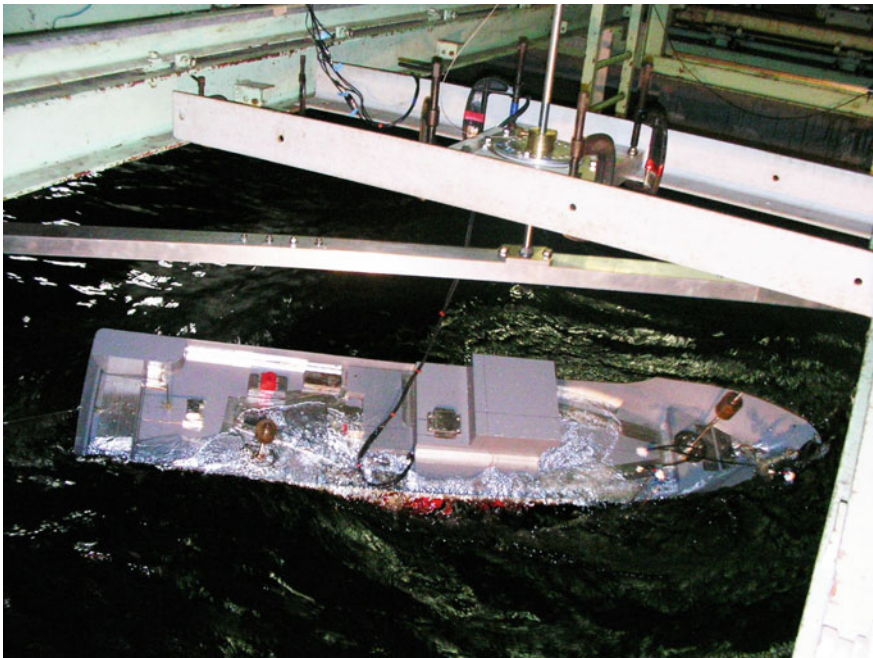


Fig. 1 Model Ship in Waves

**Table 3** Ship conditions in the experiment

Height of C.G	KGo, 1.05KGo or 1.10KGo; KGo means the estimated value at the accident shown in Table 2
Lateral deviation of C.G	0 m (on C.L.) or 1 m to starboard side in ship scale; 1 m deviation leads 3° heel of the vessel
Function of freeing ports	Opened or closed

With following possible situations at the accident considered, ship conditions were also varied in the experiment and the measured conditions were set in appropriate combination of parameters listed in Table 3.

- (1) Actual height of the loaded fishing net and fishing gear, ropes and other items loaded on the canopy of wheelhouse might increase the height of the centre of gravity than that in Table 2 which is estimated without above things considered.
- (2) Unintentional loading the fishing net and the fishing gears in unbalanced condition might lead lateral deviation of the centre of gravity and the vessel might exhibit steady heel or be in initial heel condition before the accident.
- (3) Inherent structure of the freeing ports and fittings around them might disturb shipped water drainage and reduce their function.

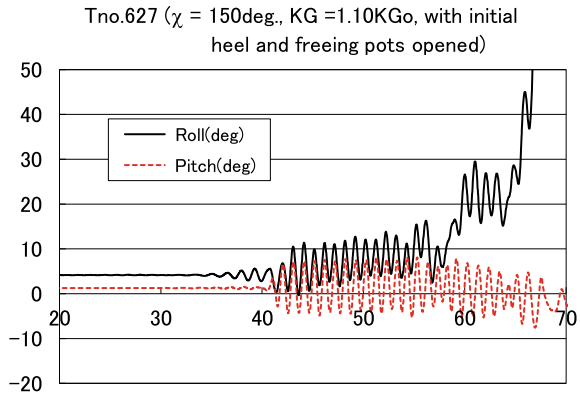
### 2.3 Experimental Results

In the experiment capsizing occurred in 30 cases out of all 133 measured cases. Table 4 summaries all the experimental results.

**Table 4** Occurrence of capsizing in the experiment

(a) Height of C.G KG = KGo		Function of freeing ports	
		Opened	Closed
Lateral deviation of C.G	0 m; w/o initial heel	-	No
	1 m; with initial heel	-	No
(b) Height of C.G KG = 1.05KGo		Function of freeing ports	
		Opened	Closed
Lateral deviation of C.G	0 m; w/o initial heel	No	Yes
	1 m; with initial heel	Yes	Yes
(c) Height of C.G KG = 1.10KGo		Function of freeing ports	
		Opened	Closed
Lateral deviation of C.G	0 m; w/o initial heel	No	Yes
	1 m; with initial heel	Yes	Yes

**Fig. 2** Measured roll angle and pitch angle in regular wave of  $T_w = 1.01$  s and  $H_w = 0.14$  m with a superimposed concentrating wave.  $\chi = 150^\circ$ ,  $KG = 1.10KGo$  and with initial heel and all freeing ports opened



As shown in Table 4, capsizing occurred under the conditions with the increased height of C.G. ( $KG = 1.05KGo$  or  $1.10KGo$ ) and initial heel and/or closed freeing ports. No capsizing occurred in the originally estimated C.G. ( $KG = KGo$ ) even with initial heel and closed freeing ports. And even in the increased height of C.G., hull conditions with no initial heel and opened freeing ports did not lead the model ship to capsize. In the experiment it was confirmed that as the height of C.G. is increased, the range of encounter angle leading to capsizing is extended, but capsizing with the encounter angle of  $150^\circ$  occurred only in the highest C.G. condition ( $KG = 1.10KGo$ ).

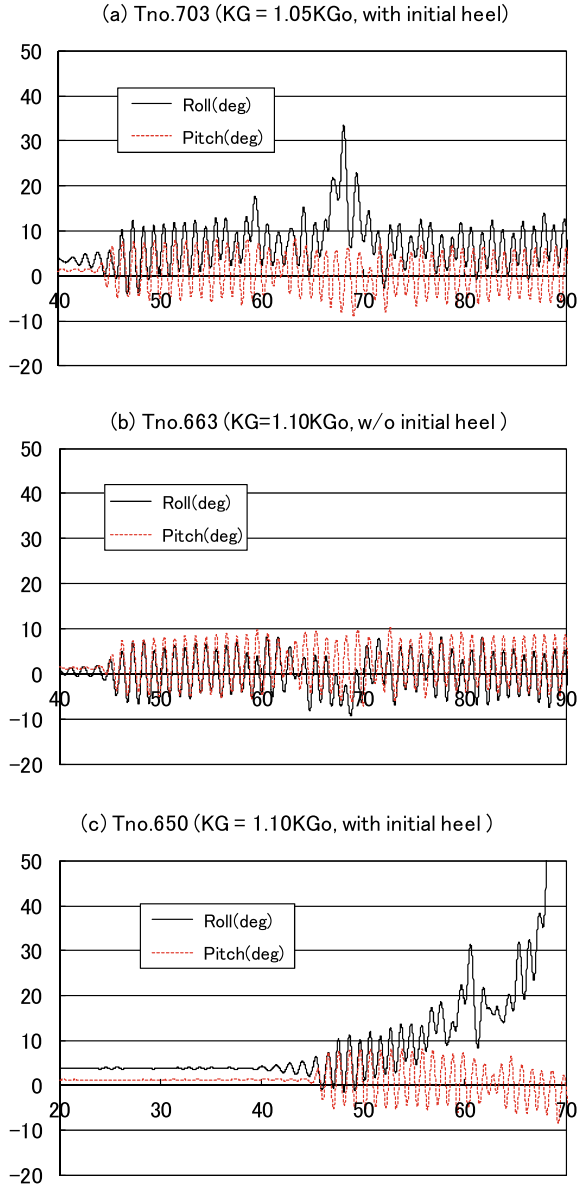
Figure 2 shows typical time histories of roll angle and pitch angle in capsized case. From the measured ship motion and the observation during the experiment the capsizing sequence in bow waves could be summarised as follows (refer to Fig. 2). At first shipping water around midship part occurs and water floods the fore deck. This increases the bow trim and the starboard heel and the resultant freeboard around the starboard bow section decreases. This change in the mean position of the ship stimulates further shipping water. At last successive shipping water occurs and the increased flooded water reduces the stability of the ship, then the wave action turns over the ship. In short, the mechanism of the capsizing in bow waves is that the increased flooded water on the fore deck reduces the freeboard of bow part and the reduced freeboard accelerates shipping water then with the increased flooded water stability of the ship reduces drastically and capsizing occurs.

### 2.4 Consideration on Factors Related to the Accident

Based on the conditions leading to capsizing and the capsizing sequence in bow waves, which have been clarified in the experiment, it is presumed that following factors, increased height and lateral deviation of C.G., poor function of freeing ports and improper encounter angle to waves played key roll to the capsizing of the purse seiner.

On the other hand, the experimental result shows that no capsizing occurred with the encounter angle of  $165^\circ$  and even in the highest C.G. condition capsizing did not occur with no lateral deviation of C.G. and all freeing ports opened (Table 4 and Fig. 3).

**Fig. 3** Effects of height and lateral deviation of C.G. on measured roll angle and pitch angle in regular wave of  $\lambda = 1.6$  m and  $H_w = 0.13$  m with a superimposed concentrating wave.  $\chi = 150^\circ$ . and with all freeing ports opened





These experimental results imply that careful operation and sufficient maintenance of vessels with the above things into consideration might prevent similar accident.

## ***2.5 Conclusions for Experimental Investigation into the Purse Seiner Accident***

With the model experiment the situation, which could lead a vessel during lying to in bow waves to capsizing was confirmed, and the key factors related to the purse seiner accident, namely increased height and lateral deviation of C.G., poor function of freeing ports and improper encounter angle to waves, were clarified. Moreover, it is pointed out that experimental results imply that as safety measure careful operation, e.g. restraining increase in the height of C.G., is important to prevent similar accident.

## **3 113GT Stern Trawler Accident**

### ***3.1 Outline of the Accidents***

A 113GT stern trawler “Yamada-maru No.2” of pair trawling foundered on the way to a fishing ground in the East China Sea on 12 January 2010. All 10 crews died at the accident.

The stern trawler was sailing with heading angle of  $310^\circ$ . At that time, the wind speed was 13.0 m/s, the mean wave height was 1.94 m and the mean wave period was 6.0 s. The wave and wind direction was  $338^\circ$ . The captain called to the captain of the consort trawler that “we cannot recover from heeling with water on deck!” And a few minutes later, she was lost from the radar of the consort trawler. The foundered trawler was salvaged to investigate conditions and damages. There was no serious damage of hull and some water tight doors were opened.

For the investigation of the accident, firstly we did free running model experiments in head seas. Secondly, we calculated for stability with flooded water in the engine room.

### ***3.2 Free Running Model Experiments***

The subject ship model used in this research is the 1/16 scaled. The principal particulars are shown in Table 5. According to the investigation of salvaged trawler, two watertight doors were opened. Opened doors are shown in Fig. 4. For recording shipping water and flowing point, the model ship was installed with 5 video cameras and

**Table 5** Principal particulars of the stern trawler

	Ship	Model
Length between perpendiculars: $L_{pp}$	26.50 m	1.656 m
Breadth: $B$	6.85 m	0.428 m
Depth: $D$	3.10 m	0.194 m
Displacement: $W$	350.17t	0.0835t
KG	2.61 m	0.056 m
Scale		1/16

360° video camera. The positions of cameras are shown in Fig. 5. The 360° camera recorded situation in the working room as shown in Fig. 6.

In this accident, the ship speed was 9 knots and the encounter angle between wave and ship was 5° or 28° in head seas to starboard. So, experimental conditions were set as shown in Table 6.

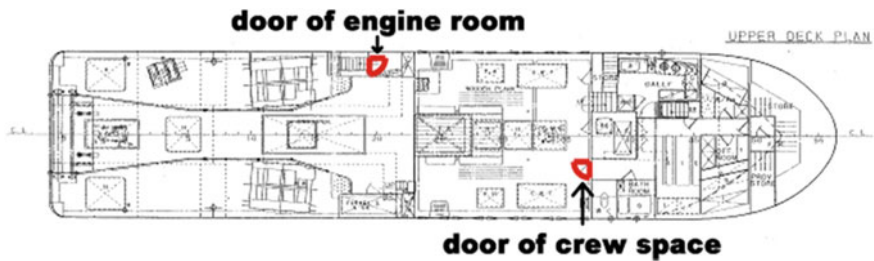


**Fig. 4** Opened watertight doors

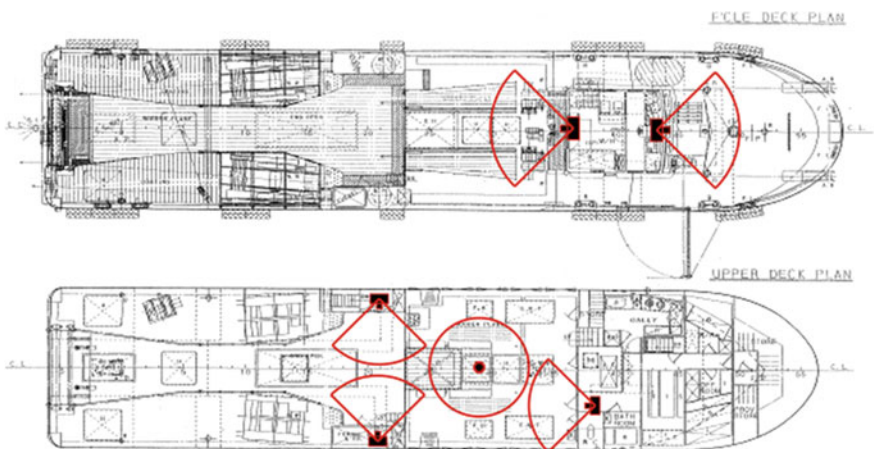


**Fig. 5** Positions of video cameras

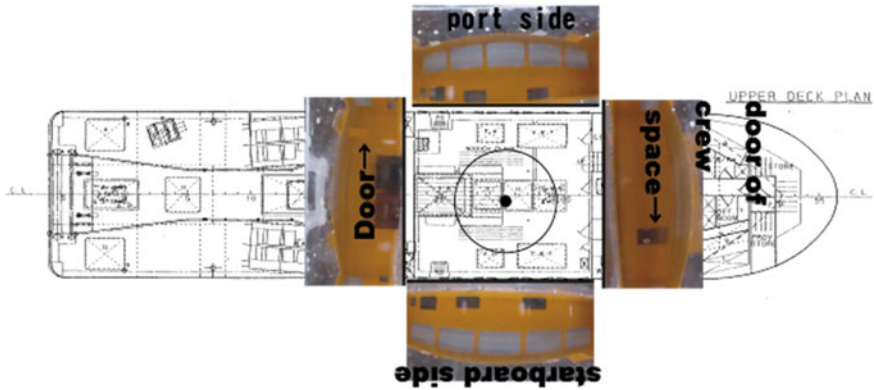


**Fig. 6** The recording area by 360° camera

**Table 6** Conditions of experiments

	Conditions
Heading angle	5°, 28°, 45°, 60°
Ship speed	9 knots
Wave period	4.5 s, 5.0 s, 5.5 s, 6.0 s
Wave heights	1.94 m, 2.91 m, 3.88 m, 4.85 m, 5.82 m

The results of shipping and flooded water are shown in Tables 7 and 8. In these tables, the results are shown with following abbreviations, “No”: no shipping water occurred, “Yes”: shipping water occurred, “FW”: flooded water on deck occurred, and “HFW”: huge flooded water on deck occurred. Shipping water occurred in the waves of more than 2.91 m height. And flooded water on deck occurred in waves of more than 3.88 m height.

An example of flooded water in the working room at “huge flooded water on deck” case is shown in Fig. 7 and the time series of ship motion and rudder angle in the same condition are shown in Fig. 8. The average heel angle of water on deck was

**Table 7** Results of experiments (heading angle: 5°)

Wave height	Wave period			
	4.5 s	5.0 s	5.5 s	6.0 s
5.82 m				HFW
4.85 m		HFW	FW	FW
3.88 m	Yes	FW	FW	Yes
2.91 m	No	Yes	Yes	No
1.94 m	No	No	No	No

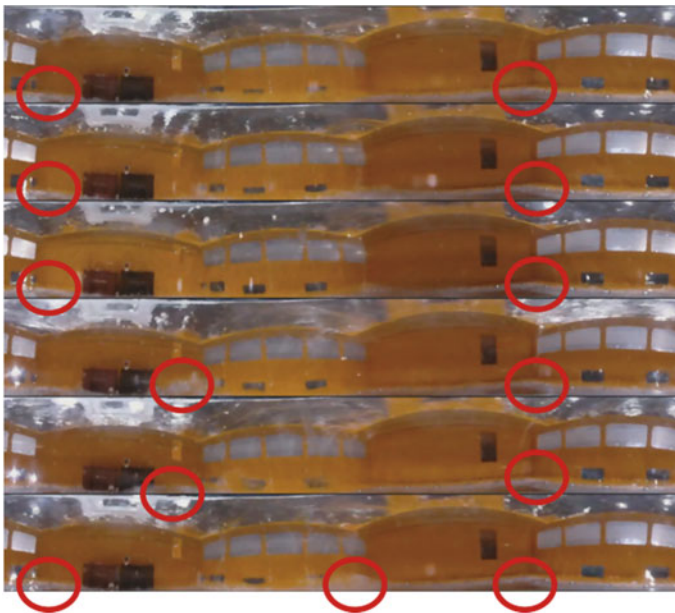
**Table 8** Results of experiments (heading angle: 28°)

Wave height	Wave period			
	4.5 s	5.0 s	5.5 s	6.0 s
5.82 m				HFW
4.85 m		HFW	FW	FW
3.88 m	Yes	FW	FW	No
2.91 m	Yes	Yes	No	No
1.94 m	No	No	No	No

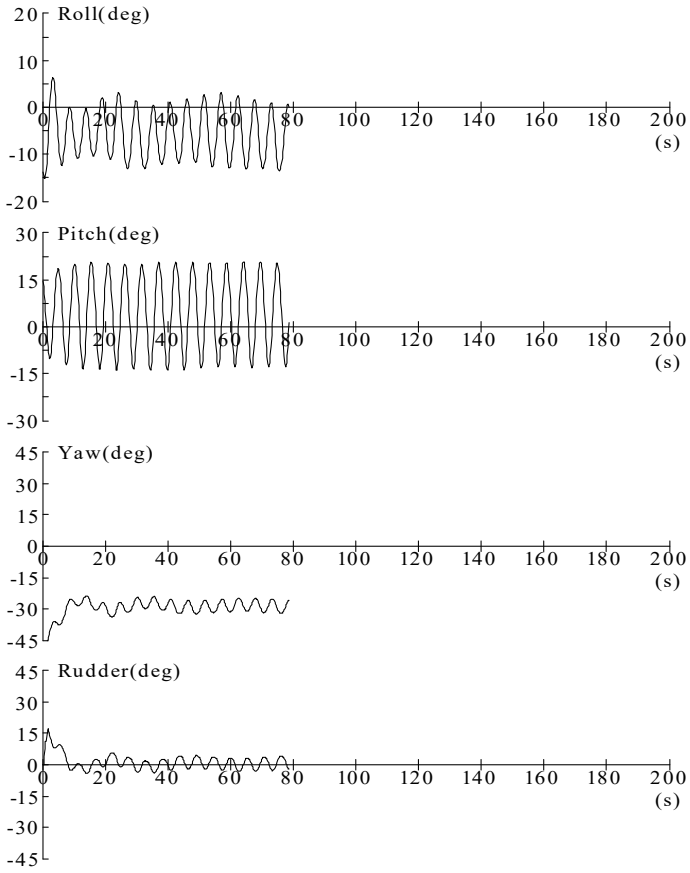
-7° in this case. But Fig. 7 shows that the flooded water in the working room had never reached to the door of crew space.

Figure 9 shows the shipping water on upper deck. It shows that the shipping water from bow went straight to the opening entrance of engine room.

In these watertight conditions, the model ship never capsized.



**Fig. 7** Flooding water in the working room (red circle) observed with wave period = 6 s, wave height = 5.88 m,  $\chi = 28^\circ$ . (interval = 0.8 s; time goes on from top to bottom)



**Fig. 8** Time series (wave period = 6 s, wave height = 5.88 m,  $\chi = 28^\circ$ )



**Fig. 9** Shipping water on upper deck

### 3.3 Flooded Water

According to the experiments, shipping water continues to flow into the entrance of engine room for 1 s per one time in model scale. Flowing water volume  $Q_1$  can be calculated using Eq. (1) [1].

$$Q_1 = C_1 \frac{2}{3} \sqrt{2gb} (h^{\frac{3}{2}} - h'^{\frac{3}{2}}) \quad (1)$$

Here  $C_1$ : flow coefficient,  $g$ : gravitational acceleration,  $b$ : width of opening,  $h$ : depth of bottom of opening,  $h'$ : depth of top of opening. Flooding water to the engine room was estimated about 2.56 t to 7.24 t one time.

### 3.4 Model Experiments with Flooding Water

Free running model experiments were implemented with hanging weight for simulating of flooded water into the engine room. The model is shown in Fig. 10.

Time series with 12t which are two times flooding water to the engine room is shown in Fig. 11. 1.94 m wave height is enough to make initial roll angle to the situation of water on deck.

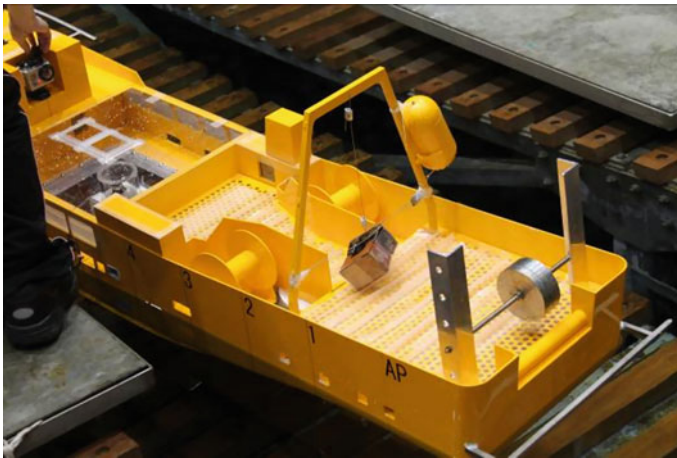


**Fig. 10** Model with hanging weight

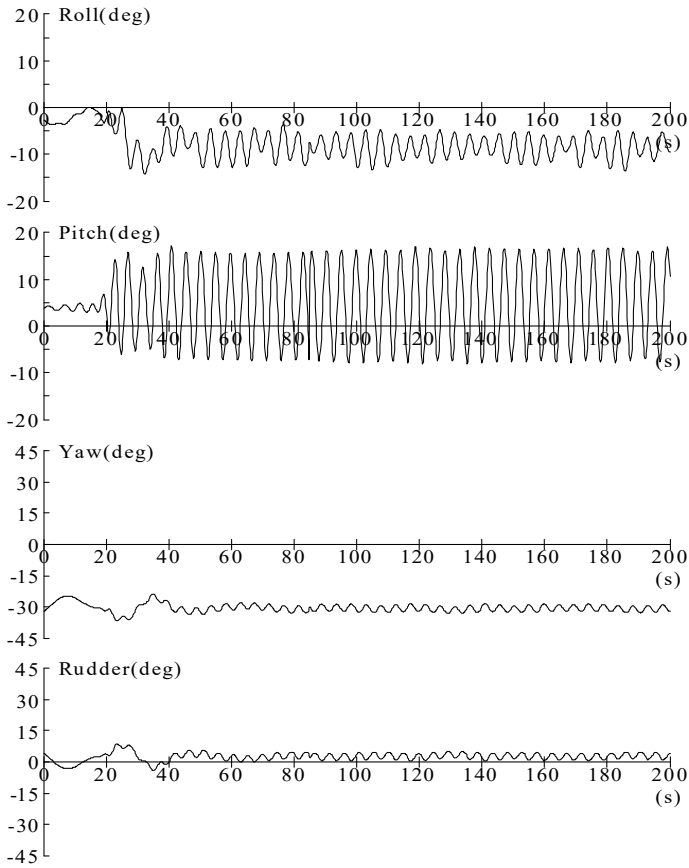


**Fig. 11** Time series (wave period = 5.5 s, wave height = 1.94 m,  $\chi = 28^\circ$ )

### 3.5 Stability Calculations

Stability curve with flooding water in engine room is shown in Fig. 12. It shows that maximum GZ is reduced by 30% with 12 t of flooded water and by 50% with 16 t of flooded water. And, there is no stability left with 70 t of flooded water.

Stability calculations show that more than 70 t of flooded water in the engine room makes total loss of stability. Based on the estimated flowing rate of water into the engine room, 2 min is enough time for flowing water of 70 t into the engine room. Reserve buoyancy of this trawler is about 202.7t. Less than 5 min is enough to sink it.

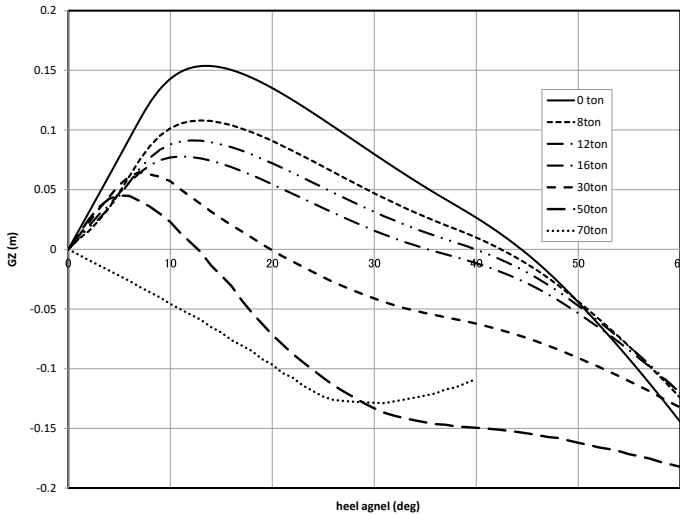


Fig. 12 GZ curve with flooded water

### 3.6 Conclusions for Experimental Investigation Along with Stability Calculation into the Stern Trawler Accident

The accident causation of stern trawler is inferred from this research.

- (1) The stern trawler met more than 2 times higher wave of average.
- (2) Shipping water flowed into the engine room from the opened watertight door.
- (3) Maximum of GZ was decreased by flooded water.
- (4) With the reduced stability the opening of engine room was easy to under the water level.
- (5) In less than 5 min, the trawler sank.

## 4 Conclusions

Model experiments and stability calculation were carried out as parts of the investigations into two serious accidents of Japanese fishing vessels. As a result, sequences and mechanisms of the accidents were inferred and supposed factors related to the accidents were also clarified.

Based on the results of these experimental investigations so on, the JTSC has concluded the probable causes of the accidents and issued remarks on safety measures to parties relevant to the causes in order to prevent similar accidents [2, 3]. Main points of remarks are as follows and some details are also available in “Japan Transport Safety Board Annual Report 2012” [4].



For “Purse seiner Suwa-maru No.58 accident”, the remarks require that during lying to with a sea anchor a seaman, such as the master, with plenty of navigation knowledge and experience, should stand on bridge to look out situation around and keep the main engine in its stand-by state so that prompt attitude adjustment is possible so as to prevent water from flooding in. And for “Stern trawler Yamadamaru No.2 accident”, the remarks require that during navigation, exit doors etc. on the deck should always be closed and whenever they are opened for access, they should be closed promptly.

**Acknowledgements** The model experiment at NMRI was carried out with help of Mr. H. Sawada and Mr. Y. Tsukada along with Dr. M. Ohnawa. And the model experiments and stability calculations at FRA were carried out with help of Dr. D. Terada from FRA, Dr. H. Hashimoto and Mr. S. Amano from Osaka University. The authors thank all of them for their efforts to carry out investigations stated in this paper.

## References

1. Katayama T, Takeuchi Y, Ikeda Y (2005) A study on model test method to assess safety of damaged ship with flooding from damaged opening. *J Jpn Soc Naval Archit Ocean Eng* 1:137–144 (in Japanese)
2. Japan Transport Safety Board (2011a) Fishing vessel SUWAMARU No.58 sinking. Marine Accident Investigation Report, MA2011-4, 2011 (in Japanese)
3. Japan Transport Safety Board (2011b) Fishing vessel YAMADAMARU No.2 sinking. Marine Accident Investigation Report, MA2011-11, 2011 (in Japanese)
4. Japan Transport Safety Board (2012) Appendix 28 Remarks made in 2011", Japan Transport Safety Board Annual Report 2012

# **Cargo Liquefaction**

# Liquefaction of Sand and Olive Pomace Cargo and Its Effect on the Stability of a Bulk-Carrier



I. A. Koromila, C. C. Spandonidis, and K. J. Spyrou

**Abstract** Liquefaction of granular materials in a rectangular container has been experimentally investigated using NTUA's School of Naval Architecture and Marine Engineering "shaking table" facility. Two different materials (sand and olive pomace) in several moisture content scenarios were tested. Harmonic forcing in a range of frequencies and amplitudes has been applied. The intention was to develop some qualitative understanding on how liquefaction comes about for materials of different properties; and also how the phenomenon relates with the duration and intensity of the excitation. The two materials presented substantially different behaviour, interpreted to be due to differences in moisture's diffusion in material's body and in their specific gravity. In a parallel study, was investigated the impact of liquefaction to a bulk carrier's stability by using commercial design software. Different cases of cargo stowage and distribution in the holds were examined. This study confirms that homogeneous cargo loading can lead to substantial loss of stability after cargo liquefaction and that alternating or suitable inhomogeneous loading is often preferable. The current paper is an updated and improved version of a paper presented in the International Ship Stability Workshop, held in Brest in 2013 [16].

**Keywords** Ship · Stability · Liquefaction · Experiments

---

I. A. Koromila (✉) · K. J. Spyrou  
School of Naval Architecture and Marine Engineering, National Technical University of Athens,  
Athens, Greece  
e-mail: [ikoromila@central.ntua.gr](mailto:ikoromila@central.ntua.gr)

K. J. Spyrou  
e-mail: [k.spyrou@central.ntua.gr](mailto:k.spyrou@central.ntua.gr)

C. C. Spandonidis  
Prisma Electronics SA, Alexandroupoli, Greece  
e-mail: [c.spandonidis@prismael.com](mailto:c.spandonidis@prismael.com)

## 1 Introduction

Cargo liquefaction is dangerous as it turns a dry cargo into an easily movable one, thus bearing a detrimental effect on the intact stability characteristics of the ship carrying it. Casualty data referring to bulk carriers, collected by the International Association of Dry Cargo Shipowners (INTERCARGO), indicate that cargo-related reasons stand as the dominant factor behind total loss accidents for this category of ships. Notwithstanding the significant decrease of the number of ship casualties due to cargo liquefaction in the last decade, as shown in Table 1 the human lives lost per accident were substantially increased [7, 8]. Actually, the number of lives lost in the last decade due to liquefaction were almost 50% more than those lost in the preceding decade.

Cargoes that are at risk of liquefaction are those constituted of fine particles and containing moisture [4]. Such cargoes, at the time of loading are typically in granular state and look like damp sand. In this state, the shear strength of the cargo is provided by the direct contact between the cargo particles. Nevertheless, sufficient interstitial spaces exist to accommodate the moisture of the transported particles and the interstitial air [1]. The oscillatory movement of the tank leads to resettling of the particles and compaction of the intra-particle spaces. This compaction raises the water pressure, forcing the particles apart, potentially leading to them losing direct contact with each other. The cargo loses shear strength and thus conditions are created for the cargo to behave like a liquid [10].

Recent casualties mostly involved unprocessed or minimally processed ore cargoes; such as nickel ore, iron ore fines, iron sand, and bauxite. According to The Swedish Club [23], the major problem is due to the storage place in the countries of origin. Unprocessed or minimally processed ore cargoes are often stored in open-air stockpiles, even next to the sea, meaning that they are subject to all weather conditions. Any wet weather will therefore cause the moisture content (MC) of the fines to increase, especially during the monsoon season. Furthermore, when it comes to Mediterranean countries, one of the most common material causing liquefaction-based accidents is olive pomace.

An early description and analysis of the problem from a soil mechanics perspective is found in Terzaghi and Peck [22]. Despite the great importance of liquefaction for ship safety, a coherent, science-based, framework for the transportation of wet bulk cargoes has not been fully set up yet. The industry is regulated of course by several national and international codes. As soon as 2008, the International Maritime Organisation (IMO) issued, by resolution MSC.268(85), the International Maritime Solid Bulk Cargoes (IMSBC) Code whereby incorporates provisions aimed at ensuring that

**Table 1** Bulk carrier casualties due to cargo liquefaction

Year	Lost vessels	Lost lives
2010–2019	8	106
2002–2009	48	158

only cargoes with sufficiently low inherent moisture content (based on measurement of Flow Moisture Point-FMP and Transportable Moisture Limit-TML) are loaded [10]. The code contains instructions for the safe handling (loading and unloading) and stowage of bulk cargoes which however are largely empirical. Yet, complexities can arise due to the coupled ship cargo responses to random environmental excitations, the variety of transported materials substantially differing in properties and sizes, the presence of humidity etc. With the experience gained over the years, further cargoes were recognized as prone to liquefaction and incorporated into the code, as well as further requirements were amended [12]. Besides, provisions are encompassed for specially constructed vessels hindering cargo shift and hence allowing the carriage of high-moisture cargoes. For these vessels, it is required to meet the IMO Grain code and Intact Stability code criteria [9, 11].

The primary research in the field of granular materials liquefaction was related to a few prominent problems, mostly of soil mechanics nature. Bjerrum et al. [2], Lee and Fitton [17], and Castro [3] were among the pioneers who paved the way for the development of methods for determining the possible liquefaction of a granular material. Typically, sand samples (both clear and mixed with fines or silts) were used for experimental investigation to determine shear strengths and deformations that cause excessive pore water pressure and lead to liquefaction [5, 24]. Research on the liquefaction phenomenon in marine cargoes is still at the stage of infancy [13, 14, 19]. Modelling approaches based on discrete particles behaviour have appeared, yet these mostly address the behaviour of particles with humidity on their surface, rather than the full liquefaction condition [20, 21]. A few efforts to address, via modeling, phenomena such as sloshing due to the movement of slurry cargoes in ship holds have also appeared [15, 25–27].

The initial version of the current paper presented during the 2013 International Ship Stability Workshop was perhaps the first documented experimental effort in the maritime field addressing the liquefaction process [16]. It referred specifically to sand and olive pomace cargoes. The current paper is an update of this work. Liquefaction of a medium weight material (sand) and a light one (olive pomace) have been investigated experimentally using the shaking table equipment installed at the School of Naval Architecture and Marine Engineering of the National Technical University of Athens. The interest was on identifying essential qualitative differences in the two materials' behaviour. Results were evaluated in the light of the requirements of the IMSBC code. Appropriate ways of cargo's distribution for avoiding capsizing in case of liquefaction, were also considered.

## 2 Investigation Through Experiments

### 2.1 Facility

The experimental facility is presented in Fig. 1. It is consisted of a 6-DOF table that is driven to move as desirable, at a low to medium range of frequencies. The motion of the table can reach up to  $\pm 30^\circ$  in rotation, and  $\pm 0.5$  m in translation.

For the current experiments, a rectangular tank was used and placed on the top of the shaking table. The tank is made from non-coloured Perspex of 20 mm thickness to permit direct observation. Its size was 0.23 m—0.31 m—0.15 m (width—length—height). The dimensions of the tank correspond to a Panamax bulk carrier with a beam of 32.2 m. It is considered that the ship (full scale) is excited in roll and sway with maximum frequency 0.29 Hz. The amplitude for sway ranges between 0.26 m and 17.7 m and for roll it ranges between 0 and  $30^\circ$ . By applying the dimensionless frequency, which is principally defined as  $\omega\sqrt{l/g}$  ( $\omega$  denotes the wave absolute frequency,  $l$  denotes the tank width, and  $g$  denotes the gravity acceleration), the model scale frequency for roll is 3.0 Hz. In addition, the amplitude for sway ranges between 0.25 cm and 17 cm (the relation  $a/l$  is applied;  $a$  denotes the excitation amplitude), while the roll angle remains the same as that of the full scale.



**Fig. 1** The shaking table equipment of NTUA's School of Naval Architecture and Marine Engineering



**Fig. 2** Visualisation of the samples of sand (left) and olive pomace (right) through optical microscope

## ***2.2 Used Materials and Procedure of Investigation***

Two materials of different composition, particle size and behaviour were selected, namely sand and olive pomace. Sand constitutes a large conglomeration of granules that are consisted at least of O, Si, Fe, Al, K, Mg, Ca and Na. However, the specific chemical composition of individual particles can be quite different (amount of Ti, S and C can be found in different granules). The specific gravity of the tested sample was  $1.386 \text{ t/m}^3$  and the average diameter, as found from analysis with an optical microscope, was 0.5 mm (Fig. 2). Olive pomace, on the other hand, is a by-product of olive processing. The specific gravity was  $0.52 \text{ t/m}^3$  and the average diameter of particles 4.5 mm.

## ***2.3 Results for Sand***

The initial moisture content of the sand was 0% and it was achieved by heating it in a furnace. The moisture level was later increased in steps, up to 40% of the total weight of the material. A wide range of excitation frequencies and amplitudes were applied to the model scale tank. Specifically, for roll: 0.1—3.0 Hz/2.09—22.2° (in full scale these correspond to 0.0098—0.29 Hz/2.09—22.2°), and for sway: 0.6—3.0 Hz/0.25—17 cm (in full scale these correspond to 0.058—0.29 Hz/0.26—17.7 m).

As it turned out, there is a critical moisture level (at about 27%) below which the material behaves almost like a solid; in the sense that it follows container's motion without flowing, no matter what the external frequency and or amplitude value is. Right after the critical moisture content is reached however, two phenomena emerge. For frequencies between 0.1 and 0.2 Hz (in roll as well as in sway) the material forms a small heap with its peak appearing at the centre of the free surface, while a

small amount of water appears at each side of the tank (Fig. 3, left). For frequencies between 0.4 and 0.8 Hz for roll and above 1.2 Hz for sway oscillations a shift of sand to the sides of the container is formed while water appears in a thin layer at the top of the free surface (Fig. 3, right). It is noted that these findings are in good agreement with simulation results presented by Ahmed [1].

Moreover, further increase of moisture means that the amount of water on the top increases too and, for low external frequency, it moves separately from the lower, solid like, material (Fig. 4, left). The frequency range in which shifting of the sand underneath the water occurs, appears now at relatively lower values (e.g. 0.7 Hz instead of 0.8 Hz for the roll motion, see Fig. 4, right). For higher excitation frequency the water layer enters a resonance area and moves following the corresponding natural mode (Fig. 5). At the same time, the material underneath the water layer rearranges itself.

Last but not least, the time duration of the experiment seems to be directly related to the appearance of liquefaction. Increase of the duration leads to lowering of the

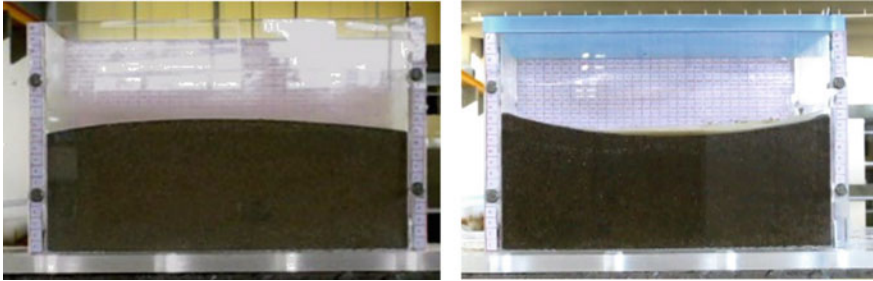


**Fig. 3** Sand with MC 27.5% after being excited in roll. Left:  $f = 0.15$  Hz,  $\varphi_{\max} = 4.2^\circ$ ; Right:  $f = 0.5$  Hz,  $\varphi_{\max} = 13.2^\circ$

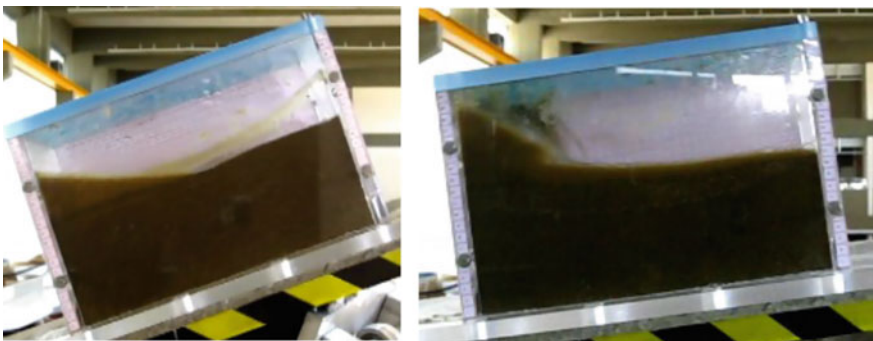


**Fig. 4** Sand with MC 40% excited in roll: Left:  $f = 0.1$  Hz,  $\varphi_{\max} = 22.2^\circ$ . The upper water layer is the only part that moves; Right:  $f = 0.8$  Hz,  $\varphi_{\max} = 9.05^\circ$ . At the higher frequency, the material below water moves too, albeit sluggishly



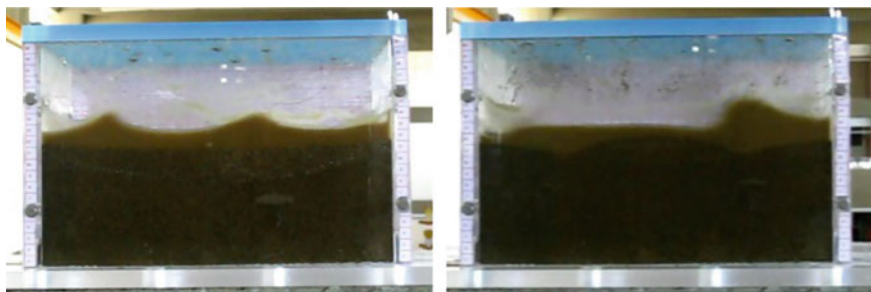


**Fig. 5** Sand with MC 40% excited in high frequency—small amplitude sway. Left:  $f = 2.5$  Hz,  $a = 2.37$  cm; Right:  $f = 1.4$  Hz,  $a = 4.3$  cm

frequencies where liquefaction first appears. The key findings are basically similar irrespectively of the direction of excitation (roll or sway).

## 2.4 Results for Olive Pomace

The olive pomace used for the experiments was supplied from two different olive mills in Greece (one in Corfu and one in Kalamata). Samples of “dry” and “wet” olive pomace, having moisture content that is commonly found when such a material is transported by sea, were examined. The focus of this work now turned from the identification of the critical moisture level, to the differences of material’s behaviour in realistic moisture scenarios for this material’s transportation. Similarly, to the dry sand, dry pomace behaves like a solid too, basically following container’s motion. Yet, for the wet olive pomace, two phenomena should be noted: (a) Moisture diffusion from specific areas of moisture concentration (black areas inside the material appearing in Fig. 6) towards the entire material body through the formation of moisture layers, leading to a jelly like motion of the material. This result is in good agreement with the findings of Jian-Ping [13] for a heavier material (wet nickel ore), and (b) Excitation at frequencies above 1.0 Hz leads to noticeable shift of a portion of material to the sides of the container.

For examining the change in the semi-static behaviour of the olive pomace before and after liquefaction occurrence, further comparative tilting tests were conducted. In accordance with the tilting box test method prescribed in IMSBC code [10], the tank was tilted with rate  $0.3^\circ/\text{s}$ . Due to physical limits (container’s height) the tilting stopped when  $30^\circ$  was reached. In the second test where the material had already been shaken and liquefaction had been established, the material started to move earlier (by about  $10^\circ$ ). However, due to the moisture (almost 60%), the angle observed is not the typical angle of repose. Here, the entire body of material has tended to move and not only some portion of it near to the free surface.

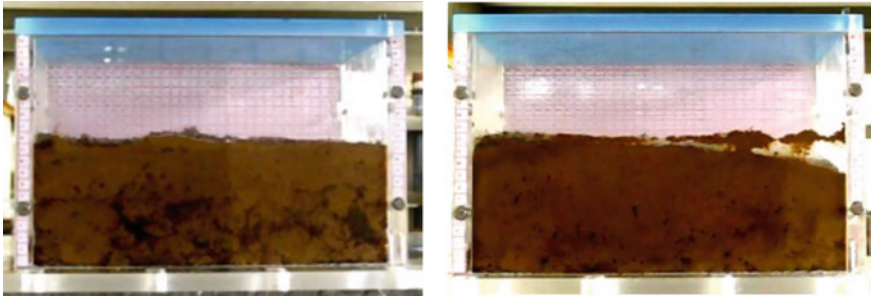


**Fig. 6** Wet olive pomace before (left) and after (right) the application of sway excitation ( $f = 2.2$  Hz,  $A = 4.3$  cm). Moisture's diffusion is apparent (the black spots in the first picture have become moisture layers in the second). Also, there is some shift of material after liquefaction occurred

### 3 Stability Analysis

The computer code “AVEVA Marine” was used to investigate how cargo liquefaction can affect the static stability of a bulk carrier. The bulk carrier used, was designed by the first author as part of the requirements of diploma course of NTUA's School of Naval Architecture and Marine Engineering. The main dimensions of the ship are presented in Table 2. Different cases of cargo's specific gravity, namely heavy and light cargoes, and cargo's distribution were examined.

As heavy cargoes were selected nickel ore ( $1.7\text{--}3.0$  t/m<sup>3</sup>), iron ore ( $1.2\text{--}3.5$  t/m<sup>3</sup>), sand ( $1.0\text{--}2.0$  t/m<sup>3</sup>) and bauxite ( $1.2\text{--}1.4$  t/m<sup>3</sup>). In the light cargo category ( $<1.0$  t/m<sup>3</sup>) were considered olive pomace and coal. It is common for large bulk carriers to stow high density cargo in odd numbered holds, with the remaining holds kept empty [6]. Nevertheless, heavy cargoes, such as iron ore, are sometimes loaded homogeneously. Hence, alternate and homogeneous loadings were considered.

#### 3.1 Heavy Cargoes

In case of alternate loading of heavy cargoes, with specific gravity 1.6 and 3.6 t/m<sup>3</sup>, as the cargo becomes heavier the loss of stability after liquefaction becomes greater,

**Table 2** Ship's main dimensions

Length Overall ( $L_{OA}$ )	290.049 m
Breadth Mld (B)	44.600 m
Depth Mld (D)	25.700 m
Design Draft (T)	18.000 m
Deadweight (DWT)	172,000 t

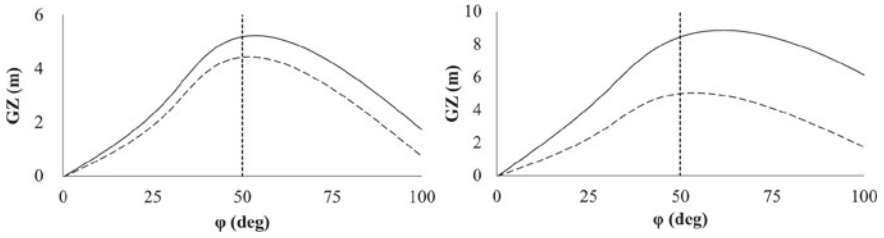


**Fig. 7** Effect on GZ of liquefaction for alternate loading of cargo having specific gravity  $1.6 \text{ t/m}^3$  (left) and  $3.6 \text{ t/m}^3$  (right). Solid line indicates the situation before liquefaction while dashed line indicates the situation after liquefaction

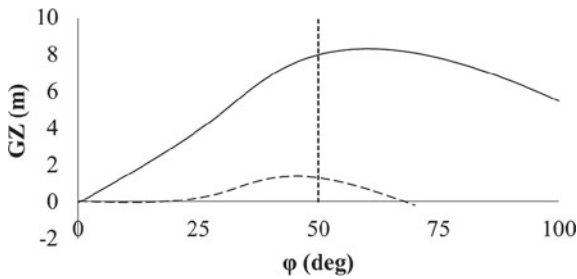


**Fig. 8** GZ curves for homogeneously loaded cargo of specific gravity  $1.6 \text{ t/m}^3$  before (solid) and after (dashed) liquefaction

as shown in Fig. 7. In the case of homogeneous cargo loading (all holds are filled to 50%) with specific gravity  $1.6 \text{ t/m}^3$ , it was found that, after liquefaction there can be a serious loss of stability (Fig. 8), despite the fact that the stability was initially better than that of alternate loading.

### 3.2 Light Cargoes

For light cargoes ( $0.77 \text{ t/m}^3$ ) homogeneously loaded, and after considering a range of filling ratios, it was found that, while prior to liquefaction the stability of the vessel improves as this ratio is raised (Fig. 9, left), after liquefaction stability significantly drops (Fig. 9, right). Greatest reduction occurs for 60–70% filling of the holds, producing a lolling phenomenon.

Several other cases of cargo quantity and distribution were investigated whose results are summarized in Fig. 10. Alternate loading cases corresponded to partial filling of the odd-numbered-holds with complete filling of all remaining holds. Inhomogeneous loading cases related to partial filling of the holds No. 4, 5, and 6 and complete filling of all others. When liquefaction occurred under inhomogeneous loading as described above, there was little reduction of stability. For the cases of

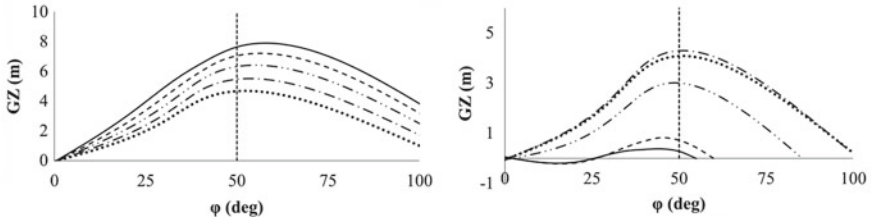


**Fig. 9** GZ curves for examined light cargoes before (left) and after (right) liquefaction. Five different holds filling are shown corresponding to homogeneous loading; Solid line: 60% filled holds. Dashed: 70% filled holds. Double dot - long dashed: 80% filled holds. Dot - dashed: 90% filled holds. Dotted: 100% filled holds

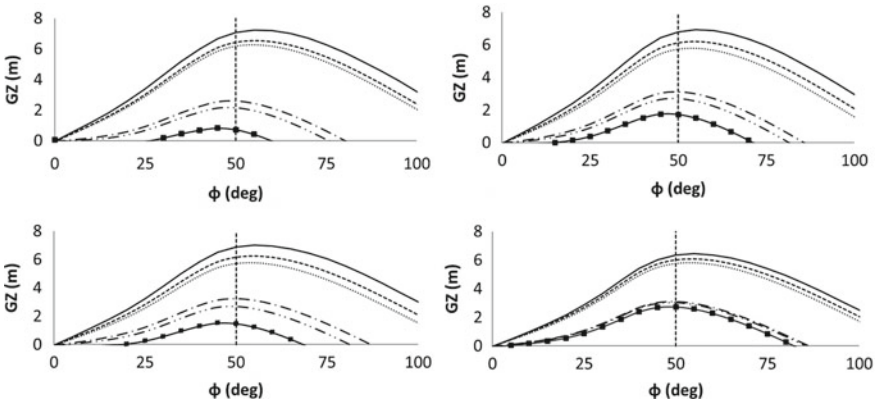


**Fig. 10** GZ curves for the examined light cargoes before and after liquefaction. Four different cargo distributions (for homogeneous, alternate and inhomogeneous loading) are shown, corresponding to 70% (up-left); 73% (down-left); 74% (up-right); and 80% (down-right) filled holds (in total). Curves are distinguished as follows; Solid line: Before liquefaction, for homogeneous loading. Solid - square: After liquefaction, for homogeneous loading. e Dashed: Before liquefaction, for inhomogeneous loading. Double dot - long dashed: After liquefaction, for inhomogeneous loading. Dotted: Before liquefaction, for alternate loading. Dot - dashed: After liquefaction, for alternate loading

homogeneous loading, there is a critical filling ratio (73% of hold volume) below which, whilst the vessel satisfied the intact stability criterion before liquefaction, after liquefaction substantial loss of stability occurred.

### 4 Concluding Remarks

A first step towards a systematic investigation of the liquefaction phenomenon, based on experimental procedures, was presented. Roll and sway oscillations were applied

on a scaled container containing two commonly transported materials (sand and olive pomace). Results indicated that, although the same liquefaction mechanism appears in both materials (oscillation of short duration under critical frequency led to a water layer formation at the top of the material) the difference in their size, shape and specific gravity give rise to qualitatively different behavior. The olive pomace seems to be more dangerous as the whole volume of material tends, after liquefaction, to behave like a fluid.

Stability calculations indicate that homogeneous loading of heavy cargoes can lead to a significant reduction in stability in case that liquefaction occurs. On the other hand, alternate loading produces a smaller reduction of stability. Similar behavior has noted for light cargoes: alternate and inhomogeneous loadings lead to less loss of stability. When cargo is converted to a liquid-like behaving mass due to liquefaction, having fewer free surfaces would definitely enhance the safety against capsizing.

The presented work was expanded recently to the experimental examination of heavier materials (nickel and iron ore) (see the NTUA diploma thesis of Pittara [18]). A step forward would be the computational investigation of liquefied-cargo shift based on Discrete Element Methods and comparison with the experimental results.

## References

1. Ahmed M (2012) The nautical institute seminar on cargo liquefaction—hazards and developments. The Nautical Institute London Branch, London, UK
2. Bjerrum L, Kringstad S, Kummeneje D (1961) The shear strength of a fine sand. In Proceedings of 5th international conference on soil mechanics and foundation engineering, Paris, FR, vol 1, pp 29–37
3. Castro G (1969) Liquefaction of Sands, Ph.D. Thesis, Harvard Soil Mechanics Series N81, Harvard University, Cambridge, MA
4. DNV GL (2015) Bulk Cargo Liquefaction—Guideline for design and operation of vessels with bulk cargo that may liquefy
5. Dorby R, Ladd RS, Yokel FY, Chung R, Powell D (1982) Prediction of pore water pressure buildup and liquefaction of sands during earthquakes by the cyclic strain method. Building science series, 138. National Bureau of Standards, US Department of Commerce, US Governmental Printing Office
6. International Association of Classification Societies (IACS) (1997) Bulk carriers, guidance and information on bulk cargo loading and discharging to reduce the likelihood of over—stressing the hull structure, IACS publishing
7. International Association of Dry Cargo Shipowners (INTERCARGO) (2011) Benchmarking bulk carriers
8. International Association of Dry Cargo Shipowners (INTERCARGO) (2019) Bulk carrier casualty report—Years 2010 to 2019 and trends, 2019
9. International Maritime Organization (IMO) (1991) The international code for the safe carriage of grain in Bulk (International Grain Code) [IC Code, MSC.23 (59)], IMO publishing, London, UK
10. International Maritime Organization (IMO) (2008a) International maritime solid bulk cargoes code [IMSBC Code, MSC. 268(85)]. IMO publishing, London, UK
11. International Maritime Organization (IMO) (2008b) International code on intact stability [IS Code, MSC. 267(85)]. IMO publishing, London, UK

12. International Maritime Organization (IMO) (2015) Amendments to the international maritime solid bulk cargoes (IMSBC) Code [IMSBC Code, MSC. 393(95)]. IMO publishing, London, UK
13. Jian-Ping W (2011) A study on safe operation of Nickel Ore. In: Proceedings of the international conference IMLA 19, Opatija, HR
14. Jonas M (2012) Liquefaction of mineral ores—IMSBC Code regulations and test methods. *Bulletin* 107(2):22–30
15. Ju L, Vassalos D, Wang Q, Wang Y, Liu Y (2018) Numerical investigation of solid bulk cargo liquefaction. *Ocean Eng* 159:333–347. <https://doi.org/10.1016/j.oceaneng.2018.04.030>
16. Koromila IA, Spandonidis CC, Spyrou KJ (2013) Experimental investigation of cargo liquefaction and impact on the stability of a bulk—Carrier. In: Proceedings of 13th international ship stability workshop, Brest, FR
17. Lee K, Fitton J (1968) Factors affecting the cyclic loading strength of soil. In: *Vibration effects of earthquakes on soils and foundation*, ASTM STP 450, American Society for Testing and Materials, pp 71–95
18. Pittara KA (2018) Investigation of nickel ore liquefaction in bulk carriers. Diploma thesis, National Technical University of Athens, Athens, GR
19. Popek M (2010) The influence of organic polymer on parameters determining ability to liquefaction of mineral concentrates. *Int J Mar Navig Saf Sea Transp* 4(4):435–440
20. Spandonidis CC, Spyrou KJ (2013) Micro-scale modeling of excited granular ship cargos: a numerical approach. *Ocean Eng* 74:22–36. <https://doi.org/10.1016/j.oceaneng.2013.09.015>
21. Spandonidis CC, Spyrou KJ (2016) Coupled vessel-dry-granular-cargo roll dynamics in regular beam seas. *Ocean Eng* 120:238–245. <https://doi.org/10.1016/j.oceaneng.2016.04.023>
22. Terzaghi K, Peck BR (1948) *Soil mechanics in engineering practice*. John Wiley and Sons, New York
23. The Swedish Club (2012) Carriage of nickel ore and iron ore fines, Detailed Bulletin
24. Xenaki VC, Athanasopoulos GA (2003) Liquefaction resistance of sand–silt mixtures: an experimental investigation of the effect of fines. *Soil Dyn Earthq Eng* 23:183–194
25. Zhang J, Wu W, Hu J (2017) Study on the sloshing of nickel ore slurries with three different moisture contents. *J Offshore Mech Arct Eng* 139(3):032001. <https://doi.org/10.1115/1.4035476>
26. Zhang J, Wu W, Zhao Z, Chen Y (2020) Numerical study on coupled effect of a vessel loaded with liquefied nickel ore. *J Mar Sci Technol* 25:520–535. <https://doi.org/10.1007/s00773-019-00658-9>
27. Zou Y, Shen C, Xi X (2013) Numerical simulations on the capsizing of bulk carriers with nickel ores. *J Navig* 66:919–930. <https://doi.org/10.1017/S0373463313000349>

# **Offshore Structures**

# Experimental and Numerical Investigation on Parametrically-Excited Motions of a Mono-Column Platform in Waves



Claudio A. Rodríguez, Julio C. F. Polo, and Marcelo A. S. Neves

**Abstract** The paper shows results from a comprehensive experimental investigation on a mono-column in regular and irregular waves. Focus is centered on improving the understanding on the occurrence of resonant motions associated with Mathieu instabilities for cylindrical floating platforms. Experimental results with the mono-column showed both roll and pitch parametric amplifications. It is concluded that the instabilities observed in the mono-column experiments were very much influenced by the mooring system configuration. A numerical algorithm is used as a relevant tool for discriminating the role of the different nonlinear contributions to parametric amplifications arising from hydrostatics, Froude-Krylov and mooring loads within the observed diverse patterns of roll and pitch responses.

**Keywords** Mathieu instability · Parametric resonance · Platform stability · Model tests · Waves

## 1 Introduction

Mathieu instabilities are nowadays a quite well understood phenomenon which may lead to parametric rolling in ships and literature on the topic is abundant. Recent compilations may be found in Neves et al. [8], Guedes Soares [2] and Fossen and Nijmeijer [1]. However, this may not be the case when reference is made to instabilities in waves of offshore floating platforms. Apparently, dramatic Mathieu instabilities in platforms are rare, an exceptional observation was reported in Haslum and Faltinsen [3], this has much to do with the tendency of these vessels to have vertical walls. Yet, it is noticed from the pertinent literature that there are numerous interpretations on the probable causes of such instabilities, revealing perhaps a gap in the understanding of their main causes. As this understanding may be quite relevant for

---

C. A. Rodríguez (✉) · J. C. F. Polo · M. A. S. Neves  
LabOceano, Federal University of Rio de Janeiro, Rio de Janeiro, Brazil  
e-mail: [claudiorc@oceanica.ufrj.br](mailto:claudiorc@oceanica.ufrj.br)

M. A. S. Neves  
e-mail: [masn@oceanica.ufrj.br](mailto:masn@oceanica.ufrj.br)



the best design of such floating structures, the Authors have focused on that topic in the present paper.

An investigation on the occurrence of parametric resonance of spar platforms has been made by Haslum and Faltinsen [3] in which the relevance of Mathieu amplifications has been assessed mainly centered on the heave/pitch coupled motions. They reported on some few test results with a 1:300 model scale, in which large angles were reached. Rho et al. [11, 12], Liu et al. [6] have also reported on numerical and experimental simulations on spar platforms, all papers focusing on the discussion of heave and pitch instabilities. In Rho et al. [11] a 1/400 model was tested. Hong et al. [4] tested a set of spar platforms, models built at 1/160 scale. This last one is one of the few reports encountered in the pertinent literature discussing (albeit on a limited way) the occurrence of heave-roll-pitch instabilities in the case of vertical cylinders.

Neves et al. [7] and Rodríguez and Neves [10] have discussed the mechanisms of heave-roll-pitch parametric excitation for spars, based on an analytical model. They argued that parametric resonance of vertical cylinders is not related to pure hydrostatic pressure variations, but instead to the variations of the nonlinear Froude-Krylov pressure induced by wave passage, vertical motions and the associated attenuation of wave pressure with depth (Smith effect). It was concluded that very deep structures such as spar platforms tend to be more prone to parametric resonance than small-draft platforms as is the case of the mono-column investigated in the present paper. In fact, the tests reported by Hong et al. [4] seem to indicate stronger parametric excitation than the mono-column herein investigated.

Yet, it is still a relevant engineering problem to well ascertain the expected level of parametric resonance in mono-columns in strong seas and to better understand the associated complexities of the coupled responses. Specifically, it will be interesting to understand when pitch and/or roll may find ways of manifesting themselves in high waves. Taking into account the experimental evidence reported in the present paper on the coexistence of roll and pitch parametric amplification and the associated exchange of energy between the two modes, a time domain numerical algorithm is used as a relevant tool for discriminating the different nonlinear contributions involved. Another aim of the paper is to verify whether the parametric amplifications experimentally encountered in regular waves may also occur in irregular waves, in which there is not the pure tuning and regularity that may be found in regular waves.

## 2 Mono-Column Particulars and Test Set-Up

Figure 1 illustrates the experimental model of the mono-column tested at LabOceano. The model was built to a 1:100 scale. Main dimensions and characteristics of the mono-column at the tested conditions are shown in Table 1 (prototype values).

As the focus of the tests was to investigate vertical motions in longitudinal waves, a simplified horizontal soft mooring system was prescribed. The nominal linear restoring coefficients of the mooring system in surge and sway directions were 750 kN/m and 950 kN/m, respectively. The corresponding expected natural periods in

**Fig. 1** Mono-column experimental model**Table 1** Mono-column main particulars

Parameter		Value
Diameter, $D$	[m]	110
Depth, $H$	[m]	70
Draught, $T$	[m]	43
Displacement, $\Delta$	[t]	418 858
Metacentric height, $\overline{GM}_0$	[m]	3.82

surge and sway were 180 s and 160 s. These periods were quite far from the specified wave periods and heave, roll and pitch natural periods so that the influence of the horizontal motions on the vertical motions (heave, roll and pitch) was expected to be minimized. However, during the roll and pitch decay tests, the roll and pitch natural periods showed significant differences compared to their expected free-floating values. These differences were associated to the influence of the mooring restoring system. To assess this influence, two additional mooring lines arrangements were considered in the test program. Under the original mooring configuration (configuration #1), the lines were almost symmetrical such that surge and sway natural periods were close. Under mooring configuration #2 the lines system was aligned with the incident wave direction, resulting in a surge natural period around 180 s and a sway natural period around 380 s, i.e., the mooring system was more compliant in the sway direction than in the surge direction. Under mooring configuration #3 the lines system was aligned normal to the incident wave direction, i.e., normal to configuration #2. The surge and sway natural periods were around 380 s and 180 s, respectively. Graphical sketches of the tested mooring arrangements are shown in Fig. 2.

For all the mooring configurations, decay tests were performed to obtain heave, roll, and pitch natural periods and their corresponding damping coefficients. Table 2 displays the measured natural periods, where Configuration #0 means free-floating body, i.e., without mooring system. Decay tests under this configuration were

**Fig. 2** Tested mooring configurations: #1 (upper), #2 (middle), #3 (lower)—values in model scale

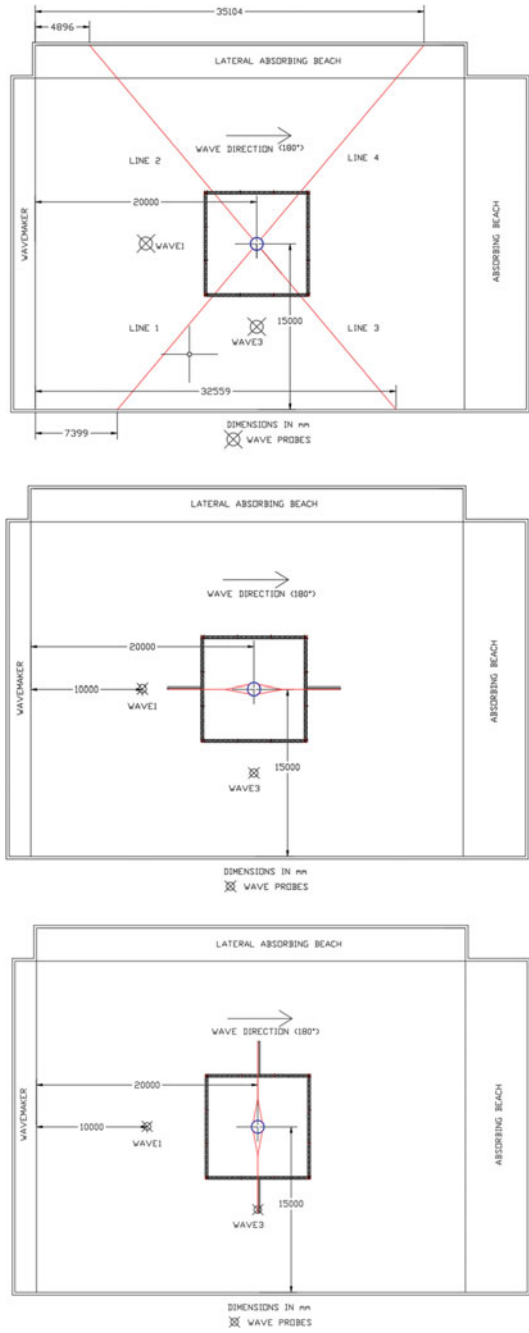


**Table 2** Heave, roll and pitch natural periods for different mooring configurations

Configuration #	Heave	Roll	Pitch
0	17.0	38.3	38.3
1	17.0	32.4	32.4
2	17.0	38.0	31.8
3	17.0	32.0	37.8

conducted to estimate the free-floating natural periods, so that the mooring influence on the mono-column dynamics could be assessed.

From Table 2 and Fig. 2, it can be concluded that depending on the mooring arrangement, the values of the roll and pitch natural periods are affected differently by the mooring system when compared to the corresponding free-floating values (configuration #0), i.e., approximately 38 s for both modes. In configuration #2 only the natural pitch period is affected reducing from ~38 s to ~32 s, while in configuration #3 only the roll natural period is affected reducing its value also from ~38 s to ~32 s. In summary, the mooring system introduced additional restoring to the roll and pitch modes.

## 2.1 Test Matrix

Table 3 summarizes the experimental tests discussed in the present paper. Nine regular and three irregular longitudinal head waves (180° incidence) have been used. Three levels of wave amplitudes ( $H = 5$  m, 10 m, and 15 m), and wave frequencies around half the roll and pitch natural periods were considered.

## 3 Experimental Results and Analyses

### 3.1 Regular Waves

#### Configuration #1

Figures 3, 4, 5 and 6 show results in the surge, sway, heave, roll and pitch modes for different wave conditions at configuration #1. Figure 3 shows the responses when the wave period was tuned to the pitch/roll natural period. In this case, since the wave period is far lower from the heave natural period, heave motions are quite low (with amplitudes of approximately 3.1 m). On the other hand, pitch motion is (directly) excited by the wave at its resonant period and reaches 4.3°, while roll motion displayed smaller amplitudes (~1.5°). Pitch responses are typical of first-order motions and occur at the wave period but roll responses (which according to linear

**Table 3** Experimental test matrix

Config.	Test code	T [s]	H [m]	Wave type
1	T18-01000	17.0	5.0	Regular
	T18-01300	32.4	5.0	
	T18-01400	16.5	10.0	
	T18-01500	16.5	15.0	
	T18-01700	16.5	5.0	Irregular
2	T18-02400	18.0	10.0	Regular
	T18-02500	18.9	10.0	
	T18-02700	16.5	10.0	
	T18-02800	16.5	10.0	Irregular
3	T18-02000	18.0	10.0	Regular
	T18-02100	18.9	10.0	
	T18-02200	18.9	10.0	Irregular

theory should not be excited by head waves) can be regarded as parametrically excited motions and occur at roll natural frequency). Surge and sway motions basically occurred at the wave frequency without significant drift and low-frequency motions. The surge motion (which is directly excited by the waves) display amplitudes of 2.3 m while the sway response reaches 0.70 m probably due to its coupling with roll.

To investigate the occurrence of parametric resonance, the platform should be excited at a wave period close to half the roll/pitch natural period (in this case, corresponds to approximately the heave natural period). Figures 4, 5 and 6 show

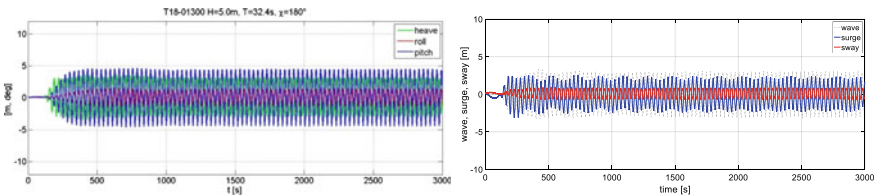


**Fig. 3** Config. #1, regular wave ( $T = 32.4$  s,  $H = 5.0$  m): linear pitch resonance

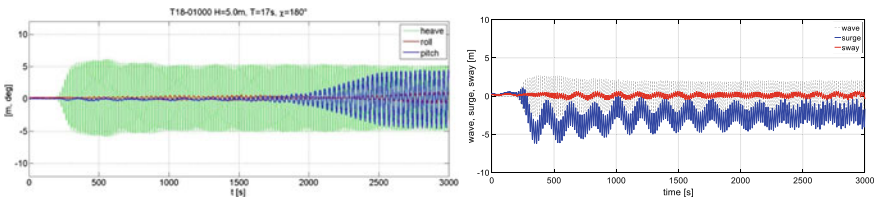


**Fig. 4** Config. #1, regular wave ( $T = 17.0$  s,  $H = 5.0$  m): parametric pitch

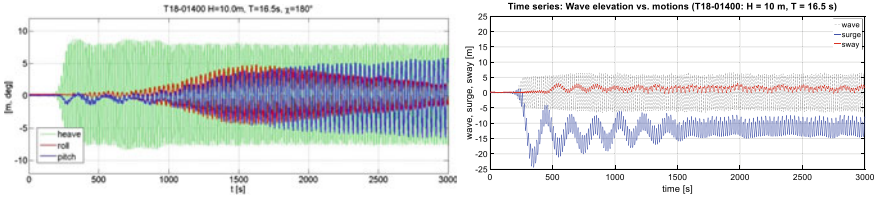


Fig. 5 Config. #1, regular wave ( $T = 16.5$  s,  $H = 10.0$  m): parametric roll and pitch

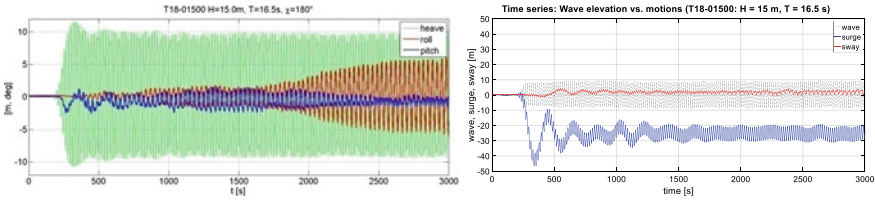


Fig. 6 Config. #1, regular wave ( $T = 16.5$  s,  $H = 15.0$  m): parametric roll and pitch

the surge, sway, heave, roll and pitch coupled responses for wave heights of 5, 10 and 15 m, respectively. Since the wave is tuned with the heave natural period, heave amplitudes rise to approximately 5.1 m (see Fig. 4). Pitch motions occurred at twice the exciting wave frequency, thus characterizing typical parametric resonance. Pitch amplification started around 1750s, reaching a steady state amplitude of  $4.2^\circ$  (same order of the linear resonant pitch—shown in Fig. 3). After 2400 s, roll amplifications also appeared with twice the wave frequency (thus, also characterizing parametric motions), but with very small amplitudes. In surge, the mono-column displayed, besides the wave-frequency motion, mean and low-frequency oscillations. In sway, both low- and wave-frequency motions are hardly perceptible.

For the wave height of  $H = 10$  m (Fig. 5) more energy is fed into the system and (parametric) roll motion amplification occurred earlier, initially stronger than the (parametric) pitch. Later, parametric roll decreases and pitch continues to increase above  $7^\circ$ , probably associated to an exchange of energy between these modes. In the horizontal plane, low-frequency surge motions increased with the larger wave height while no significant motions are observed in sway.

Figure 6 displays the responses for the highest wave height,  $H = 15$  m. Heave motion displayed its largest value, and initially both roll and pitch amplifications occur. Later, parametric roll became dominant achieving amplitudes above  $6^\circ$ , and parametric pitch started to decrease—probably associated to an exchange of energy from pitch to roll. Mean drift in surge further increased while the amplitudes of low-frequency oscillations decay with time.

This set of tests (configuration #1) evidenced that at lower levels of energy (lower wave heights), pitch motion, which can be excited either external or internally (parametrically), is more prone to absorb energy from the heave motion. Whereas, the roll motion, which can ONLY be internally (parametrically) excited, requires higher

levels of energy (higher waves) to develop. Thus, depending on the level of wave excitation, an interesting interchange of energy between pitch and roll may be postulated: at intermediate levels of wave excitation (Fig. 5), pitch motion is dominant, whereas at higher levels of wave excitation (Fig. 6) roll motion prevails. Regarding the horizontal motions, different from synchronous pitch resonance where only wave-frequency surge motions took place, strong mean and low-frequency oscillations in the surge direction have been observed when parametric pitch occurred. Sway motions were small, even when relatively large parametric roll occurred.

### Configuration #2

Under this configuration (see Fig. 2), the natural periods in heave, roll and pitch are, respectively, 17.0 s, 38.0 s and 31.8 s (Table 2). Tests for this configuration try to explore the pattern of responses when roll and pitch have slightly different natural periods. Figure 7 shows responses for  $H = 10$  m,  $T = 18.9$  s, where roll mode is parametrically excited. This situation may be explained by the fact that, the exciting period is close to half the roll natural period. On the other hand, Fig. 8 shows the responses for another test, where the same wave amplitude was used ( $H = 10$  m), but with a lower wave period,  $T = 16.5$  s. As observed, roll motion is insignificant, but pitch is parametrically excited (the exciting period is close to half the pitch natural period).

It is worth noting that, heave amplitudes were practically the same in the two tested conditions—around 7.0 m. However, parametric pitch reached amplitudes of  $6^\circ$  (see Fig. 8) and parametric roll achieved only  $2.5^\circ$ . The above feature confirms the experimental evidence observed in configuration #1 (Figs. 4, 5 and 6), i.e., parametric pitch motions are more likely to occur than parametric roll. This characteristic may be explained by the fact that, in longitudinal waves, pitch receives energy both

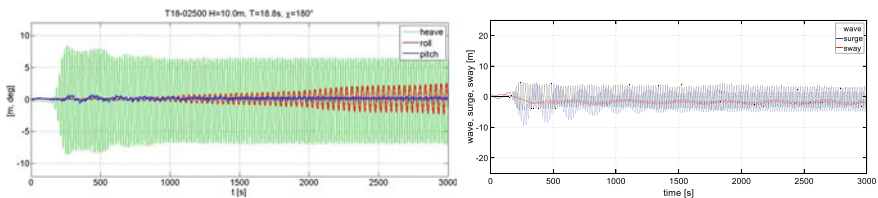


Fig. 7 Config. #2, regular wave ( $T = 18.8$  s,  $H = 10.0$  m): parametric roll

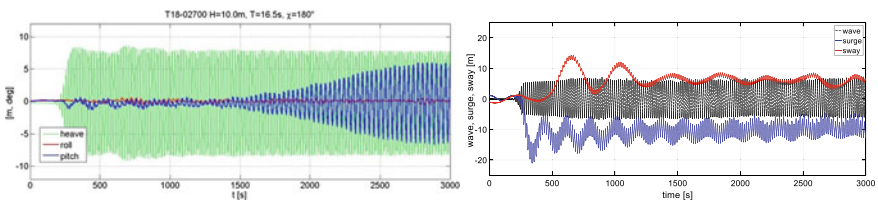
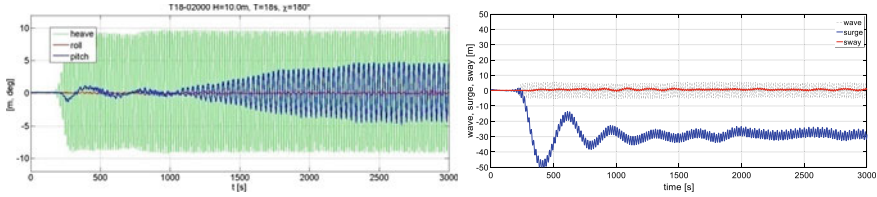


Fig. 8 Config. #2, regular wave ( $T = 16.5$  s,  $H = 10.0$  m): parametric pitch



**Fig. 9** Config. #3, regular wave ( $T = 18.0$  s,  $H = 10.0$  m): parametric pitch

from external and internal excitation, while roll only receives internal (parametric) excitation. The results evidence that mean drift in surge direction appears when parametric pitch is present as observed in Fig. 8 (and previously observed in Figs. 4, 5 and 6), however, that relationship is not observed between parametric roll and sway (Fig. 7). An interesting fact in Fig. 8 is the appearance of mean and slow oscillations in sway even with negligible roll motions (however, with significant surge and parametric pitch). Since this behavior has not been observed in the other tests, a possible explanation may be any asymmetric perturbation in the sway direction and the low restoring and damping of this mooring system in that direction.

**Configuration #3**

Under this mooring arrangement, the roll mode is affected by the mooring restoring, thus affecting the roll natural period. In this case natural periods in heave, roll and pitch were 17.0 s, 32.0 s and 37.8 s, respectively. Figure 9 shows the mono-column responses for a wave height of  $H = 10$  m and a wave period of  $T = 18$  s. Only parametric pitch was excited, reaching amplitudes of  $4.6^\circ$ . In surge, it is confirmed that when parametric pitch occurs, mean surge drift is also induced. No significant sway motions occurred.

**3.2 Irregular Waves**

**Configuration #1**

Tests in irregular waves (JONSWAP spectrum) were also prescribed for each of the mooring configurations of the mono-column. The aim was to verify whether the parametric amplifications observed in regular waves could also appear under irregular waves conditions. Figure 10 shows the heave-roll-pitch responses under a JONSWAP wave with significant wave height and peak period like those values defined for the regular wave in test T18-01,000 (Fig. 4). The same pattern observed for that regular wave test was also observed in the corresponding irregular wave, i.e., prevailing pitch parametric amplifications. Figure 11 shows the spectral densities for the incident wave and for heave, roll and pitch motions.



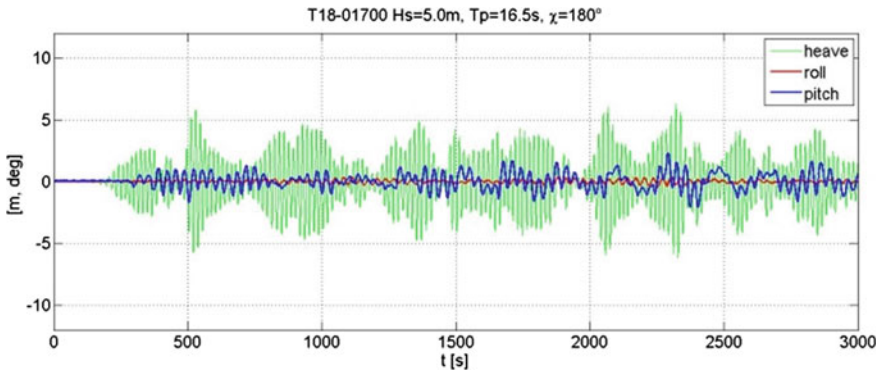


**Fig. 10** Config #1, irregular waves: dominant pitch

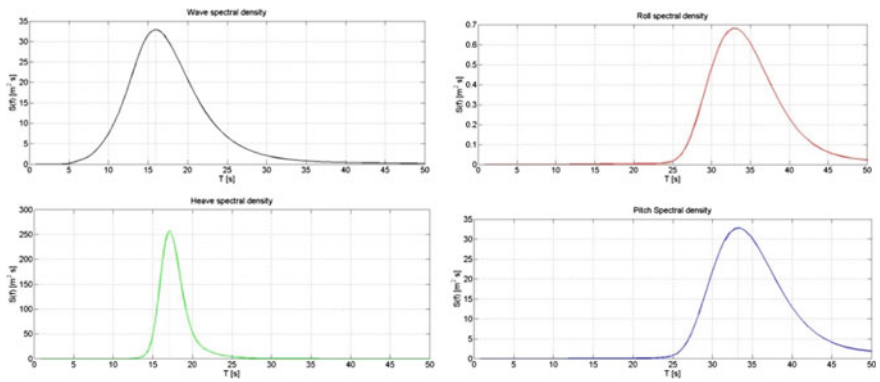


**Fig. 11** Config #1, irregular waves,  $T = 16.5$  s;  $H_s = 5$  m. Wave, heave, roll and pitch spectra

**Configuration #2**

Figure 12 shows the irregular seas responses under a JONSWAP sea with wave parameters similar to those of the regular wave condition reported in Fig. 8. Again, the same pattern of results observed in regular waves occurred in irregular waves—see response spectra in Fig. 13. Notice that the main energy content for roll and pitch (spectral peaks) do not occur at the same period, but at each mode’s natural period, which are different due to influence of the mooring arrangement—pitch natural period being smaller than the roll natural period.

**Configuration #3**

Figure 14 shows the response time series for a JONSWAP wave with  $H_s = 10$  m, and  $T_p = 18.9$  s, similar to the regular test condition shown in Fig. 9. Again, parametric pitch amplifications are displayed—like what was already observed for the regular test. The spectral densities for the irregular wave responses are shown in Fig. 15.

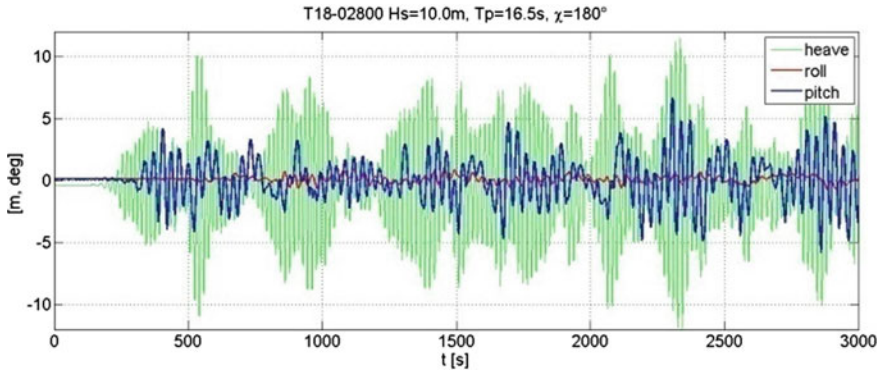


Fig. 12 Config #2, irregular waves: dominant pitch

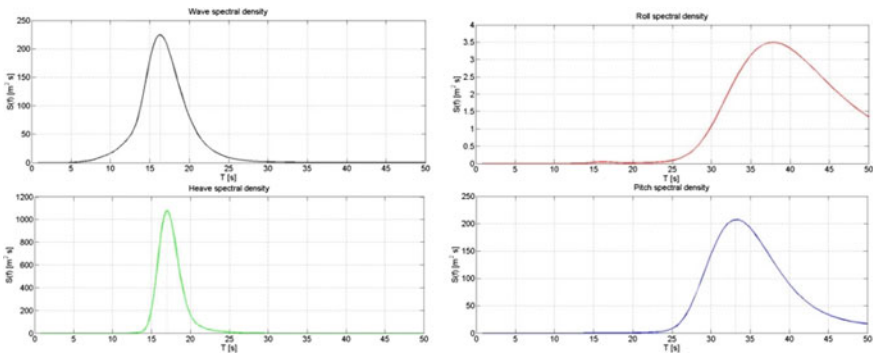


Fig. 13 Config #2, irregular waves,  $T = 16.5$  s;  $H = 10$  m. Wave, heave, roll and pitch spectra

Roll and pitch motions do not occur at the same period, but at each mode’s natural period—now, the roll natural period being smaller than the pitch natural period (due to the influence of the mooring arrangement).

### 4 Numerical Analysis

A nonlinear algorithm, called DSSTAB, has been used to verify the different parametric roll/pitch motions of the mono-column. DSSTAB is a suite of numerical algorithms for the prediction of the 6-degree-of-freedom rigid-body motions of floating structures in waves. Radiation and diffraction forces are considered linear and are computed based on potential theory using third-party software such as WAMIT®. For the computation of hydrostatic restoring forces and incident (not disturbed) wave forces, a panel method is adopted with direct pressure integration over the

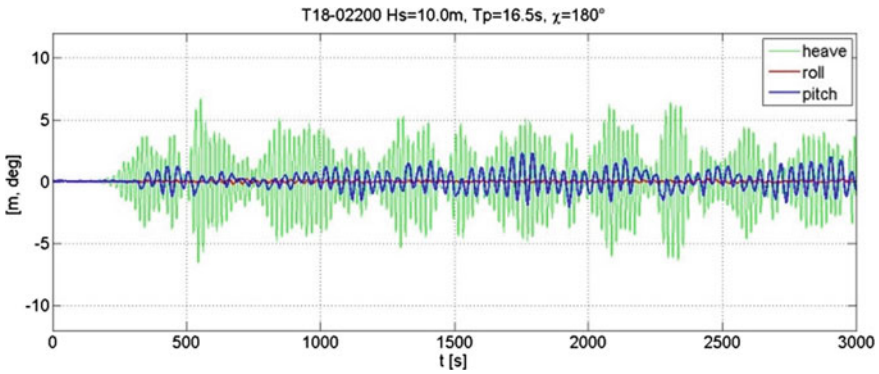


Fig. 14 Config #3, irregular waves: dominant pitch

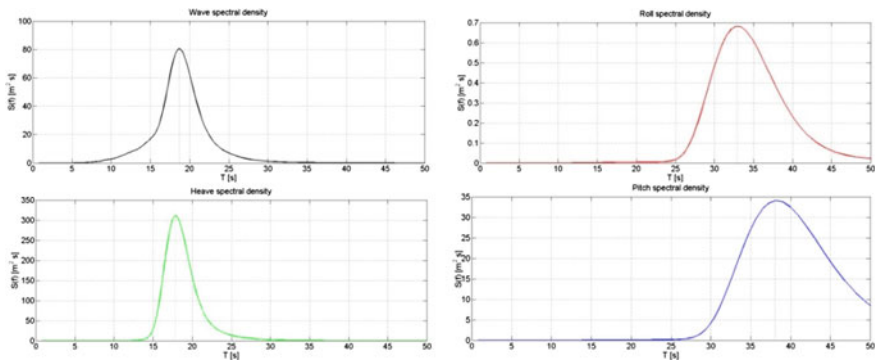


Fig. 15 Config #3, irregular waves, T = 18.9 s; H = 10 m. Wave, heave, roll and pitch spectra

instantaneous wet surface of the body. Besides the nonlinear restoring and Froude-Krylov wave forces, DSSTAB allows the introduction of external linear and nonlinear damping as well as mooring forces. For more details on the algorithm, see Pasquetti et al. [9]. Figure 16 shows the numerical model of the mono-column with mooring lines and incident wave.

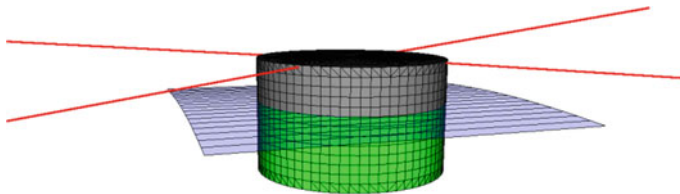


Fig. 16 Mono-column numerical model with mooring lines

The test case reported in Fig. 5 (Config. #1, regular wave:  $T = 16.5$  s and  $H = 10.0$  m) has been chosen for the present limited numerical analyses. Figure 17 indicates that, despite the decaying transients at the beginning of the experimental tests, the numerical simulation captures well the mean surge offset of the body by taking into account the coupling of mooring lines with body responses in waves. Prior to the numerical simulations in waves, calibration of damping coefficients in heave, roll and pitch was performed in the numerical model by comparison of decay tests results between experiments and simulations. After this calibration, the numerical code was capable of reproducing roll and pitch responses in waves very close to the observed ones during the experiments—see, for example, Fig. 18, which should be compared to Fig. 5. Since decay tests were not performed for the surge/sway motions, the calibration of damping coefficients has not been performed for these modes.

One of the main capabilities of the numerical model used here is that it allows the assessment of the different instantaneous contributions on forces and moments coming from: (a) hydrostatics; (b) incident wave field and (c) mooring lines. Typical spectra of these effects are shown in Figs. 19, 20, 21 and 22. Quadratic (2nd order) wave pressures have in general a very small contribution for this hull, for this reason these are not examined further. As the objective here is to assess contributions to parametric excitation, linear restoring moments in roll and pitch ( $\Delta GM_T \phi$  and  $\Delta GM_L \theta$ ,

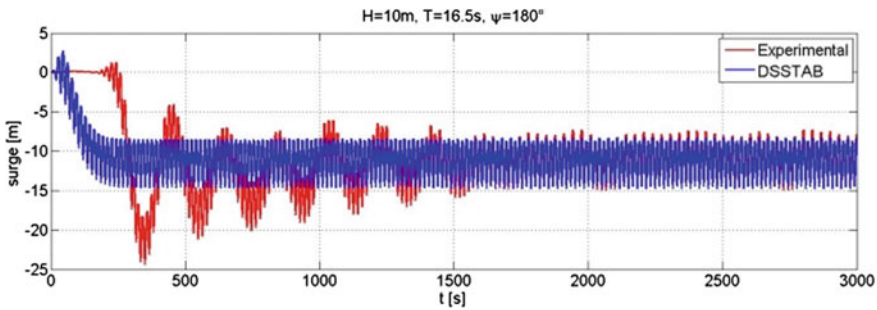


Fig. 17 Surge motion,  $T = 16.5$  s;  $H = 10$  m

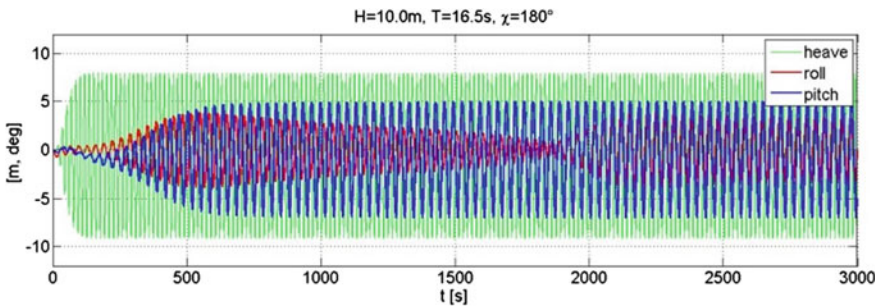


Fig. 18 Heave, roll and pitch motions, numerical simulations,  $T = 16.5$  s;  $H = 10$  m

respectively) have been excluded from the total hydrostatic moments. The non-linear parts of roll and pitch hydrostatic moments are then obtained—spectra being plotted in Fig. 19. It is observed that both moments take place as parametric actions (double wave period), pitch moment being higher. Less relevant super-harmonic contributions are observed at the 1/3 and 1/5 frequency tunings.

It is interesting to observe the qualitative distinct aspects of the Froude-Krylov contributions in the pitch and roll modes: Fig. 20 shows that the instantaneous Froude-Krylov pitch effect takes place mainly at the wave period (comparatively negligible sub-harmonics are also observed between 5 and 10 s), whereas Fig. 21 shows that Froude-Krylov roll moment has its main contribution close to twice the wave period. Then, it may be concluded that, in the pitch mode the wave field does not “notice” the pitch (parametric) motion, which exists as a sub-harmonic at twice the wave period, whereas for the roll mode (which is not externally excited), the wave field does contribute to parametric amplification. Finally, Fig. 22 shows that both roll and pitch moments associated to mooring lines loads act at double the wave period, pitch moment being higher.

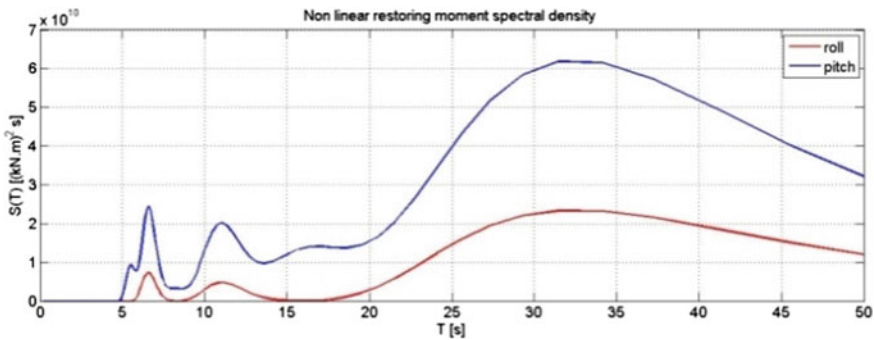


Fig. 19 Spectral density of nonlinear restoring moments,  $T = 16.5 \text{ s}$ ;  $H = 10 \text{ m}$

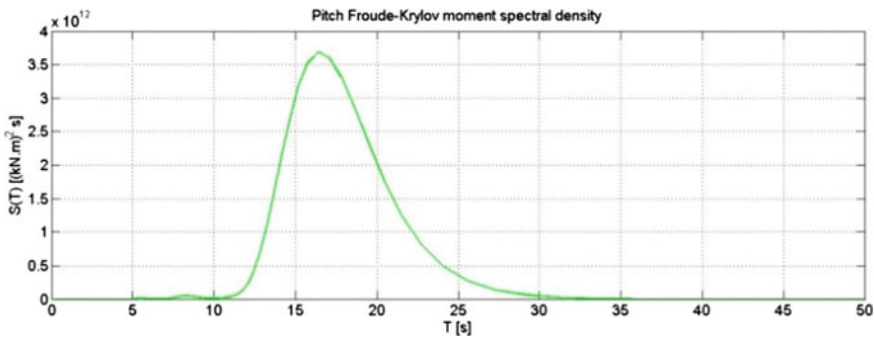


Fig. 20 Spectral density of Froude-Krylov pitch moment,  $T = 16.5 \text{ s}$ ;  $H = 10 \text{ m}$

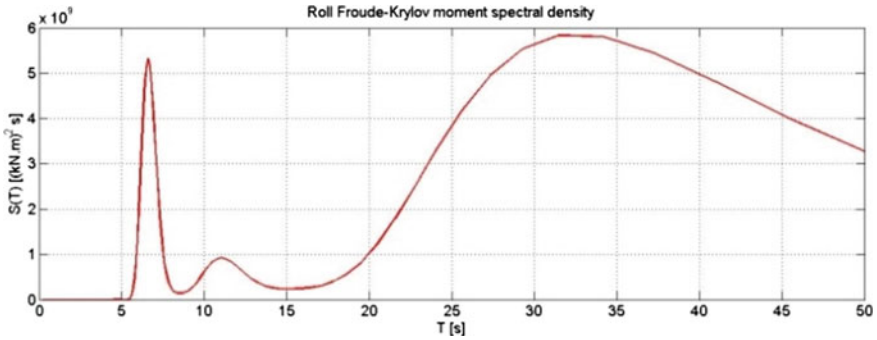


Fig. 21 Spectral density of Froude-Krylov roll moment,  $T = 16.5$  s;  $H = 10$  m

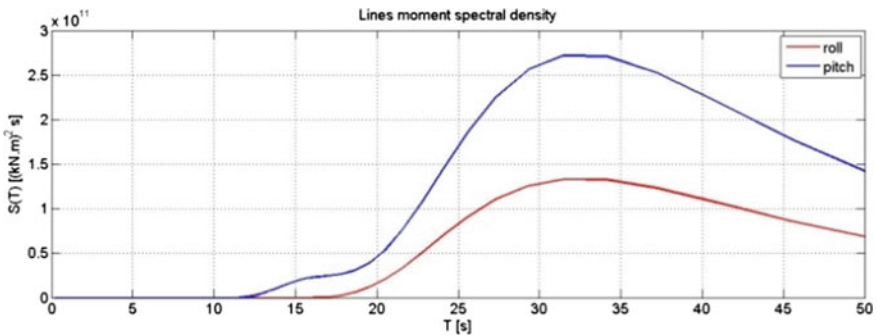
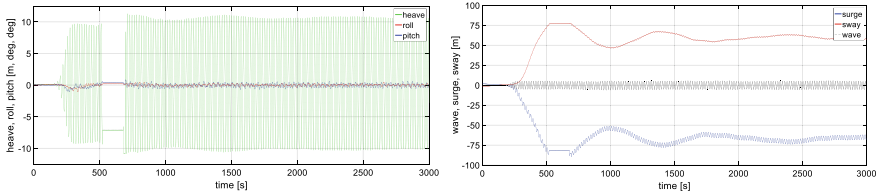


Fig. 22 Spectral density of mooring lines resultant moment,  $T = 16.5$  s;  $H = 10$  m

A summary of the parametric excitation results in Figs. 19, 20, 21 and 22 indicate that: in pitch the largest moment is introduced by mooring lines; nonlinear hydrostatic contributions comes second (one order of magnitude lower) and there is no Froude-Krylov contribution. Mooring lines moments are again the largest actions in roll, second comes hydrostatic (also one order of magnitude lower) and there exists a Froude-Krylov moment, which is the smallest contribution. In this context it is important to register that without mooring lines, no parametric motions were observed, either in pitch or roll, neither in experiments nor in numerical simulations (see the experimental results in Fig. 23). Notice that under free-floating conditions, the mono-column drifted excessively in surge and sway and reached areas of the basin not covered by the motion measurement system causing a “no visibility” problem in all the 6-dof motions of the body between time 520 s and 680 s.



**Fig. 23** Config. #0 (free-floating condition), regular wave ( $T = 18$  s,  $H = 10.0$  m): no parametric motions

## 5 Conclusions

Tests performed with a mono-column hull under different mooring arrangements in longitudinal regular and irregular waves have been presented and discussed. Tests showed physical evidence on the occurrence of undesirable parametric amplifications not only in pitch but also in roll.

Different patterns of coupled responses have been identified, depending on the mooring system arrangement. In the case of the symmetrical mooring configuration, dependence of angular responses on wave amplitude has been identified. Parametric roll requires higher levels of energy to build up than parametric pitch. Interesting nonlinear exchanges of energy between roll and pitch have been observed.

When the mooring lines are arranged such that roll and pitch natural periods become different (configurations #2 and #3), it is observed that for the same wave height, pitch motion (when tuned, Fig. 9) becomes stronger than roll motion at its respective tuning (Fig. 7). Again, this result confirms that pitch motion is more prone to parametric amplification than roll motion.

The practical relevance of parametric resonance for mono-column structures may be assessed by noting that parametric pitch amplitudes are of the same order of those resulting from direct excitation at its natural period (classical resonance).

Experimental results for the three tested mooring configurations also showed that parametric resonance (pitch and roll) also occurs in irregular waves, displaying the same patterns observed at the corresponding regular tests counterparts.

Numerical analyses of Configuration #1 for  $H = 10$  m showed that mooring lines moments are predominant in establishing the resulting parametrically excited roll and pitch motions. An interesting aspect of the different roles of roll and pitch in the coupled process arises from the Froude-Krylov moments analyses: pitch moment is not internally excited by the waves, its sub-harmonic motion depends mainly on mooring loads.

Mooring loads influence was evident in the different arrangements considered in the experiments. In the limited numerical analysis of the symmetrical configuration, it was also confirmed to be relevant. A general, yet pertinent conclusion is that the mooring arrangement should be carefully considered as an integral part of a testing program on parametric resonance of cylindrical floating platforms.

**Acknowledgements** The Authors acknowledge the contributions of LabOceano technical staff, especially Prof. Sergio Sphaier and Mr. Joel Sena Sales, for their participation in the planning and execution of the tests reported in the present paper. The Authors also acknowledge financial support from CNPq, ANP, PETROBRAS and LabOceano/UFRJ.

## References

1. Fossen TI, Nijmeijer H (Eds) (2012) *Parametric resonance in dynamical systems*, 1st edn. Springer Science International, New York. <https://doi.org/10.1007/978-1-4614-1043-0>
2. Guedes Soares C, Garbatov Y, Fonseca N, Teixeira AP (eds) (2012) *Marine technology and engineering*, 1st edn. Taylor and Francis Group, London. ISBN 978-0-415-69808-5
3. Haslum HA, Faltinsen OM (1999) Alternative shape of spar platform for use in hostile areas. In: *Proceedings of the offshore technology conference*, Paper No. OTC10953, Houston, USA
4. Hong Y, Lee D, Choi Y, Hong S, Kim S (2005) An experimental study on the extreme motion responses of a SPAR platform in the heave resonant waves. In: *Proceedings of the 15th international offshore and polar engineering conference (ISOPE'2005)*, Seoul, Korea
5. LabOceano Report 007-07 (2007) *Mono-column Technical Report* (in Portuguese)
6. Liu Y, Yan H, Yung T-W (2010) Nonlinear resonant response of deep draft platforms in surface waves, Paper OMAE2010-20823, Shanghai, China
7. Neves MAS, Sphaier SH, Mattoso BM, Rodríguez CA, Santos AL, Vileti V, Torres FGS (2008) Parametric resonance of mono-column structures. In: *Proceedings of the 6th Osaka colloquium on seakeeping and stability of ships*, 26–28th March, Osaka, Japan
8. Neves MAS, Belenky V, de Kat JO, Spyrou K, Umeda N (eds) (2011) *Contemporary ideas on ship stability and capsizing in waves*, 1st edn. Springer International, Amsterdam
9. Pasquetti E, Coelho LCG, Neves MAS, Oliveira MC, Esperança PTT, Rodríguez CA, Carbajal MAC, Polo JCF (2012) A nonlinear numerical algorithm for time-domain hydrodynamic simulations of vessel motions in the presence of waves. In: *Proceedings of 31st international conference on ocean, offshore and arctic engineering, OMAE 2012*, Rio de Janeiro
10. Rodríguez CA, Neves MAS (2012) Investigation on parametrically excited motions of spar platforms in waves. In: *Proceedings of STAB 2012 international conference*, Athens, Greece
11. Rho J, Choi H, Lee W, Shin H, Park I (2002) Heave and pitch motions of a spar platform with damping plate. In: *Proceedings of the 12th international offshore and polar engineering conference (ISOPE'2002)*, Seoul, Korea
12. Rho J, Choi H, Shin H, Park I (2003) An experimental study for mooring effects on the stability of spar platform. In: *Proceedings of the 13th international offshore and polar engineering conference (ISOPE'2003)*, Seoul, Korea



# **Special Craft**

# Validation of Simulation Tools for a RHIB Operating in Heavy Seas



Frans van Walree and William L. Thomas

**Abstract** The paper describes model test experiments representing a Rigid Hulled Inflatable Boat (RHIB) in heavy seas. A numerical simulation tool is briefly described. Simulation and experimental results are compared in a deterministic way. The cases that are compared include regular and irregular waves from various directions.

**Keywords** Small boat · Heavy seas · Numerical Simulation · Validation

## 1 Introduction

The US Coast Guard has undertaken a project to develop a standard process to define operability limits for small boats supporting naval missions. Coast Guard boats are often operated in challenging sea conditions, requiring considerable operator skill to avoid swamping, capsizing, and broaching.

Analytical tools for small boat seakeeping predictions must be developed and validated for use in the definition of operating limits. Scale model testing was chosen as one means to provide validation data and identify nonlinear behaviors for a model representing a cutter boat.

---

F. van Walree (✉)  
MARIN, Wageningen, The Netherlands  
e-mail: [F.v.Walree@marin.nl](mailto:F.v.Walree@marin.nl)

W. L. Thomas  
USCG Surface Forces Logistics Center, Baltimore, MD, USA  
e-mail: [William.L.Thomas@uscg.mil](mailto:William.L.Thomas@uscg.mil)

## 2 Model and Test Program

Considerable efforts have been made in seakeeping model tests of conventional ships during the past century. Up to now, only limited research has been performed on small boat seakeeping.

Seakeeping test facilities throughout the world are typically designed to test ship models at scale factors between 1/36 and 1/22. As a result, the wave makers in the test facility have been designed to generate moderate to large seaways at these scale ratios.

Unfortunately, small boat model testing at the aforementioned range of scale factors would require small models which are too small for instrumentation and are subject to scale effects.

The approach taken for this model test was to build a 1 m light-weight model with full instrumentation and conduct tests in moderate and steep seaways. Concerns regarding scale effects in roll damping were dealt with by comparing model scale roll damping with roll decay tests performed full-scale. Trim as a function of speed was also verified by comparing model scale data with full scale.

A carbon fiber RHIB model was constructed with main dimensions given in Table 1. Propulsion and steering is by means of a single centerline water jet unit with steerable nozzle.

The model scale was dictated by maximum wave height that can be generated in the SMB of MARIN. The required significant wave height was 3.00 m yielding scale 6.7 model with a length of 1 m.

Due to high speed and large motions in the horizontal plane the carriage cannot always follow the model. The model needs therefore to be fully free running with on-board position measurement system, autopilot computer, power supply, measurement instrumentation and data storage (Fig. 1).

The instrumentation consisted of:

- Optical motion tracking system;
- XSENS inertia and rate gyros in 6 DoF at CoG;
- Accelerometers forward and aft;

**Table 1** Main particulars

Item	Magnitude	
	Design load	Full load
Lpp (m)	6.00	6.00
B-wl (m)	2.144	2.144
Tf (m)	0.446	0.547
Ta (m)	0.646	0.689
Vol (m <sup>3</sup> )	3.762	4.559
GMt (m)	0.720	0.551
T $\varphi$ (s)	2.04	2.46

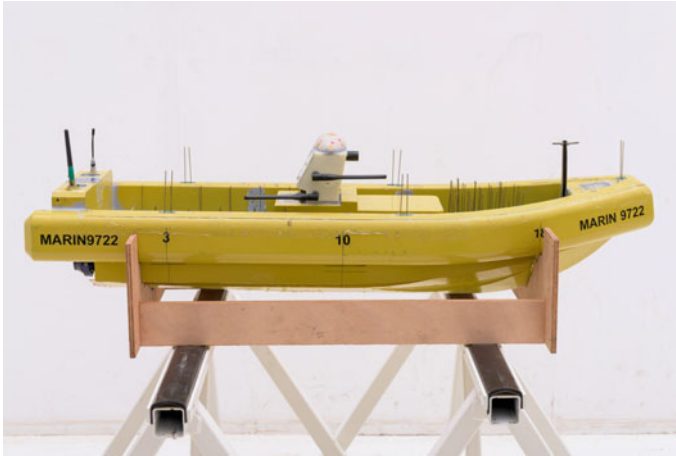


Fig. 1 Model photo

- Propulsion motor RPM;
- Steering nozzle angle;
- Cockpit and collar water level sensors;
- Incident wave sensors at three locations around the model;
- Pressure transducers to record green water impacts against steering console;
- On-board mini camera;
- miniature PC with autopilot software and hard disk for data storage;
- system for transmission of measurement data to carriage via WiFi.

The tests were performed in the Seakeeping and Manoeuvring Basin of MARIN. The basin measures  $170 \times 40 \times 5$  m in length, width and depth. It is equipped with wave makers along one long and one short side. The wave maker consists of 331 flaps that are all individually driven by an electronic engine. This facilitates generation of regular and long and short crested irregular waves from any direction. A main carriage (x-direction) and a sub-carriage (y-direction) attempt to follow the free-sailing model. The optical motion tracking system functions when the model is in the measurement window of the carriage. It sends position information to the on-board autopilot. When not in the measurement window the on-board inertia navigation system takes over.

Test conditions consisted of:

- Nominal speeds of 6 and 12 knots (Froude numbers 0.35 and 0.70) complemented with free drifting tests;
- Steep regular waves with steepness  $H/\lambda = 1/15$  and varying wave length, height and directions between and including head and following seas;
- Moderate irregular waves with  $H_{1/3} = 1.7$  m and  $T_p = 6.9$  s with directions between and including head and following seas;
- Steep (breaking) irregular waves with  $H_{1/3} = 2.5$  to 3.0 m and  $T_p = 5.2$  s with directions between and including head and following seas;

### 3 Model Test Results

The regular wave tests show that:

- Motion responses are typical for planing craft hull forms operating in the sub-planing speed ranges;
- High vertical accelerations and pitch angles are recorded in head waves, especially for the higher speeds. Transverse accelerations are substantial in beam seas;
- Some ingress of water occurred for the lower speeds in head waves;
- Impact pressures at the steering console occurred for a few head wave conditions only.

In irregular waves safe operation limits are reached occasionally in NATO Sea State 4 and more frequently in a steep Sea State 5:

- Excess horizontal and vertical accelerations occur for operation in head and bow quartering seas at 12 knots;
- Excess pitch angles are recorded prior to wave jumping, i.e. when the boat jumps out of a wave crest;
- Water ingress over the bow occurs in head and bow quartering seas, especially for the lower speed conditions;
- Surf riding occurs in Sea States 4 and 5 at 12 knots speed in stern quartering and following seas. Broaching after surf riding with accompanying high heel angles does not occur;
- Loss of course control is seen in Sea States 4 and 5 stern quartering seas;
- In stern quartering sea state 5 conditions at a 6 knots speed the boat is swamped due to breaking wave crests overtaking the boat. In these conditions capsizing may also occur due to loss of course control resulting in beam-on-breaking waves. One capsize has been observed for the design load condition and two for the full load condition for a half hour test duration for each loading condition. Figure 2 shows a swamping event.

### 4 Simulation Tools

The PanShip(NL) time domain panel methods are characterized by:

- 3D transient Green function to account for linearized free surface effects, exact forward speed effects on radiation and diffraction forces and a Kutta condition at ventilated transom sterns;
- 3D panel method to account for Froude-Krylov forces on the instantaneous submerged body;
- Cross flow drag method for viscosity effects;
- Resistance (in waves) is obtained from pressure integration each time step;



**Fig. 2** Swamping event

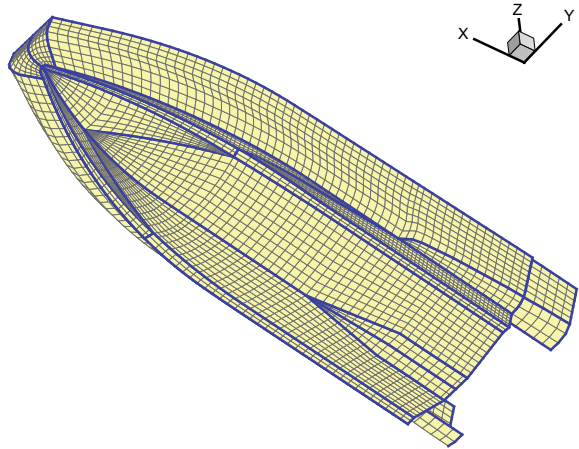
- Propulsion and steering using propeller open water characteristics, semi-empirical lifting-surface characteristics and propeller-rudder interaction coefficients. Also a semi-empirical water jet propulsion and steering method is incorporated;
- Empirical viscous roll damping by either the FDS or Ikeda methods;
- Autopilot steering.

There are two versions of the simulation tool: a semi-linear (PanShip v2.4) and a nonlinear one (PanShipNL v1.2). In PanShip, it is assumed that the motions of the craft are small, i.e. the submerged geometry does not change in time. Furthermore, the speed and heading are assumed to be constant so that the Green functions can be computed a priori for use at each time step in the simulation. In effect, the radiation and diffraction problems are then solved in a linearized manner while the wave excitation and restoring forces are treated in a nonlinear way by using the actual submerged hull geometry under the disturbed incident wave.

In PanShipNL the motions may be large while the speed and heading are not necessarily constant. The discretisation of the submerged geometry and the computation of the Green function convolution integrals are performed each time step. This approach is still not fully nonlinear due to the use of the Green functions which satisfy the linearized free surface condition. By discretising the actual submerged hull form and using the submergence relative to the undisturbed incident wave surface rather than the calm water surface, a quasi-nonlinear approach is obtained. More detailed information can be found in De Jong [1] and Van Walree and Turner [2].

The hull form of MARIN model 9722 was discretized into a surface mesh consisting of some 1900 below water and 2100 above water panels. Figure 3 shows this mesh with segment boundaries in blue. The flow streaks on the hull bottom and transom flaps were not included in the mesh. The effects of these were included empirically in PanShip(NL).

**Fig. 3** Discretized hull form  
m9722



During the simulations the ship was free running and self-propelled and kept on course through an autopilot. The impeller RPM was set such that the mean speed in waves was approximately equal to that of the model tests. The autopilot gains were the same as used for the model tests.

For all PanShip simulations the effect of forward speed on sinkage and trim was taken into account by determining the calm water equilibrium position a priori and adapting the hull mesh accordingly. For the PanShipNL simulations this was automatically achieved during the simulation since the mesh was adapted to the instantaneous motions and incident wave profile each time step.

Viscous roll damping is included by means of the FDS method, see Blok and Aalbers [3]. No tuning of the roll damping on basis of model test data has been applied.

## 5 Validation Results

Validation is based on direct time trace comparison, whereby the input wave train was reconstructed in the simulations. For regular waves this is a simple procedure. For irregular wave the procedure is more elaborate as explained in Van Walree et al. [4].

### 5.1 Regular Waves

In the steep regular waves considered here acceleration responses may be non-sinusoidal. It is noteworthy to mention that for the higher 12 knots speed the linear PanShip code could not deal with head sea conditions. In the simulation, the boat

jumps out of the steep waves to reach pitch angles over  $90^\circ$  causing the simulation to stop. The non-linear PanShipNL code however can deal with these conditions. Figures 4, 5, 6, 7 and 8 show comparisons between experimental and simulated time traces for a steep regular head wave with a frequency of 1.88 rad/s and an amplitude of 0.58 m, i.e.  $H/\lambda = 1/15$ . The waterjet RPM was set for a calm water speed of 15 knots. Figure 4 shows that in waves the speed ( $X0d$ ) varied between about 7 and 10 knots which is well predicted by PanShipNL.

The heave ( $Z0$ ) and pitch ( $\Theta$ ) time traces shown in Figs. 5 and 6 show adequate predictions as well. Note the slight trochoidal character of the pitch motion.

The longitudinal ( $Acc - \times 04$ ) and vertical ( $Acc - z04$ ) acceleration components at the bow shown in Figs. 7 and 8 show slamming peaks which are reasonably well

**Fig. 4** Comparison of forward speed

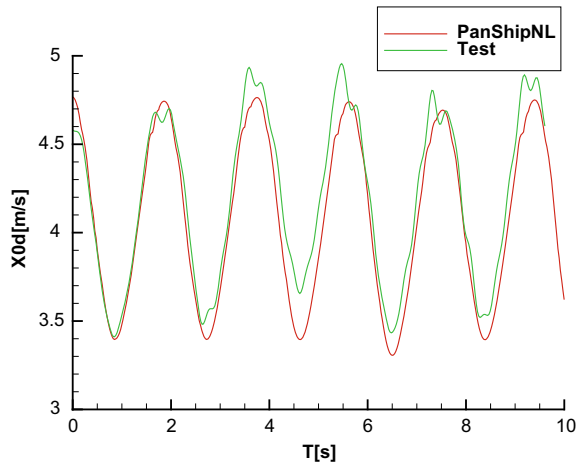


**Fig. 5** Comparison of heave

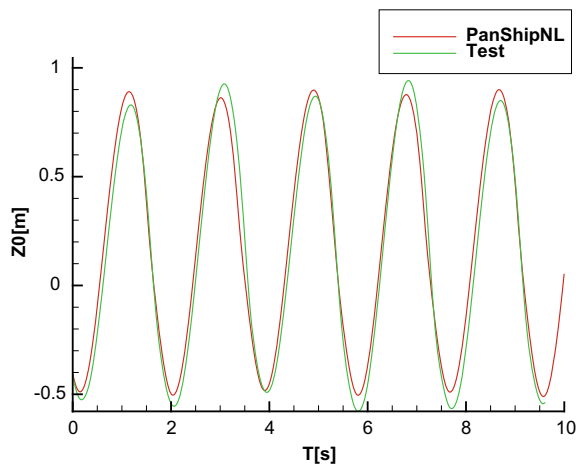




**Fig. 6** Comparison of pitch

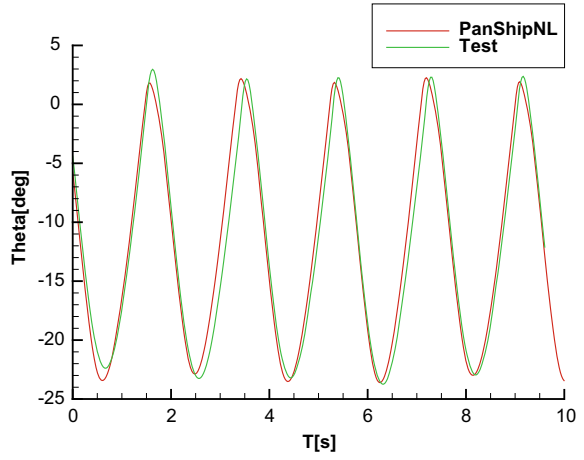


**Fig. 7** Comparison of x-acceleration

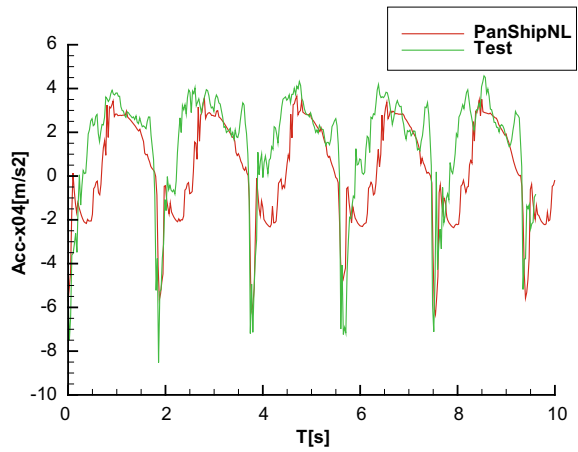
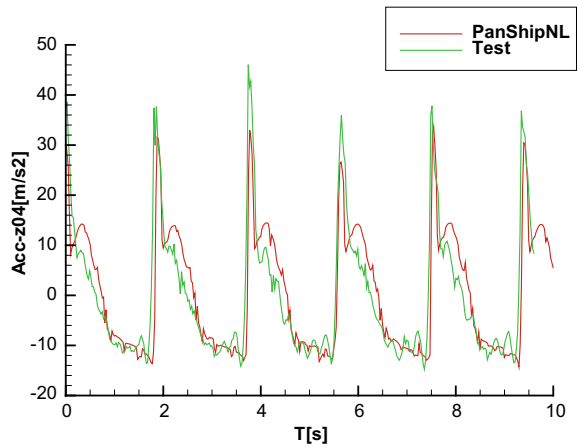


**Fig. 8** Comparison of z-acceleration



predicted. The experimental time traces show the effect of a slight variation in wave amplitude which is due to non-linear wave propagation effects in the basin.

Figures 9, 10, 11, 12, 13, 14, 15 and 16 show a comparison of time traces for a near following seas condition with a wave direction of 15° off the stern. The wave frequency is 1.88 rad/s and the wave amplitude is 0.45 m with  $H/\lambda = 1/20$ . The waterjet RPM was set for a 6 knots calm water speed, yet the speed in waves varies between about 14 and 19 knots, when the model is captured and released by the wave crest, see Fig. 9. This speed variation is well predicted by the linear PanShip code.

Figures 10, 11, 12 and 13 show that the motions are reasonably well predicted although the experimental roll and yaw motions are somewhat affected by wave reflections from the basin beaches.

The acceleration components are relatively low and the experimental signals show the noise due to the propulsion system, see Figs. 14, 15 and 16.

**Fig. 9** Comparison of forward speed

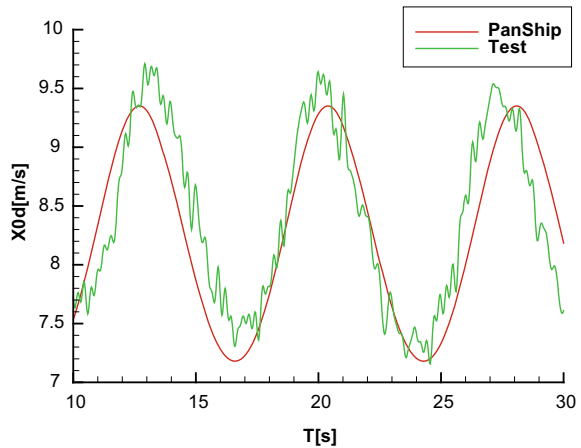


**Fig. 10** Comparison of heave

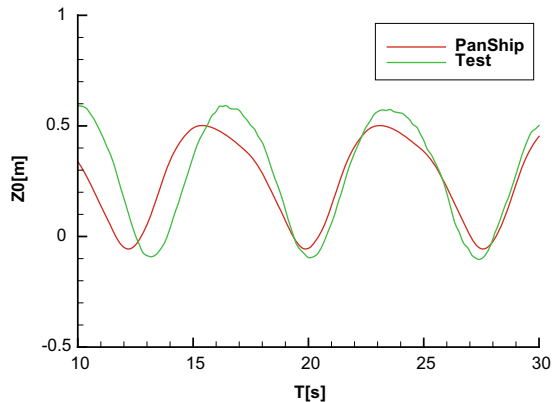


Fig. 11 Comparison of roll

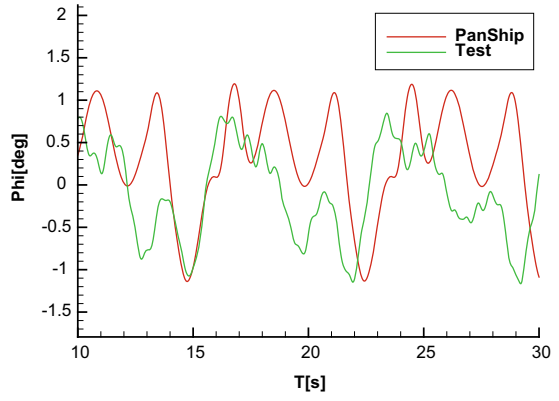


Fig. 12 Comparison of pitch

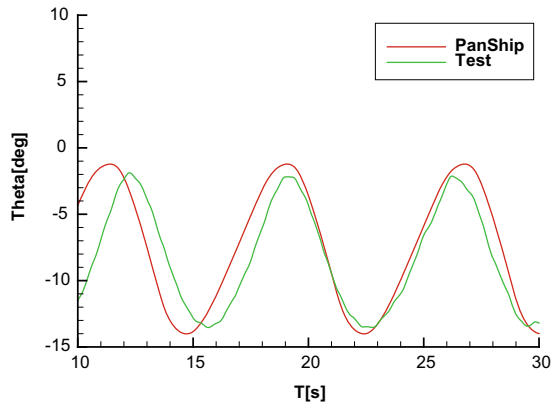
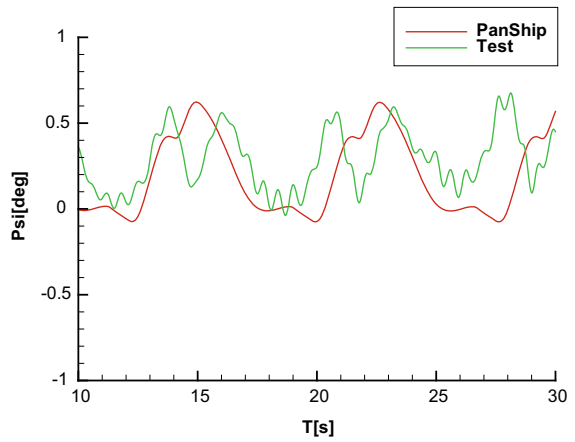
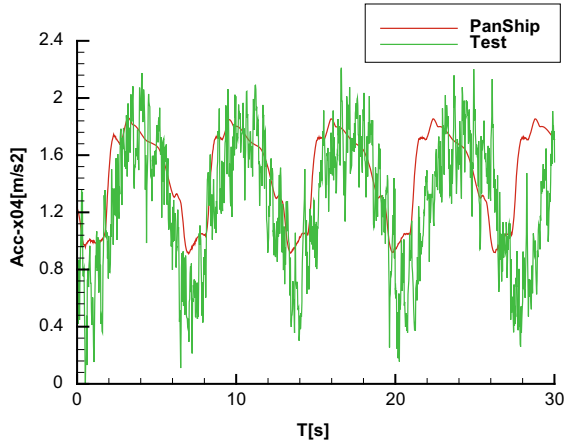


Fig. 13 Comparison of yaw



**Fig. 14** Comparison of x-acceleration



**Fig. 15** Comparison of y-acceleration

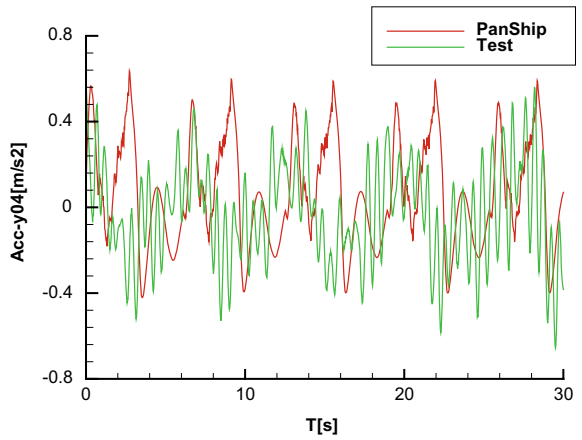
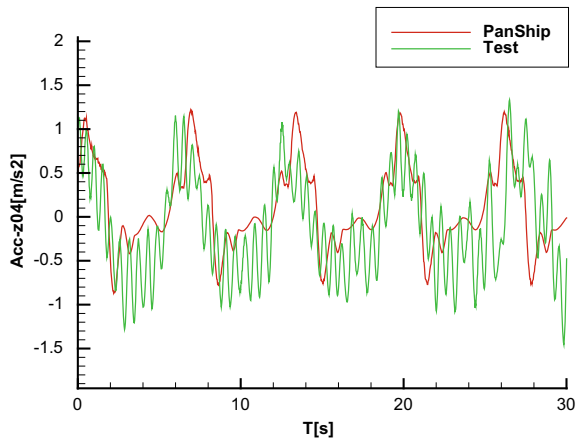


**Fig. 16** Comparison of z-acceleration



## 5.2 Irregular Waves

The first case concerns a PanShipNL simulation for a steep irregular head sea with  $H_{1/3} = 2.5$  m and  $T_p = 5.2$  s. The nominal forward speed is 12 knots ( $F_n = 0.70$ ). Figures 17, 18, 19, 20 and 21 show a comparison of time traces for forward speed, heave, pitch, and acceleration components. It is seen that the comparison is not perfect, especially for the highest wave amplitudes. One reason for this is that wave reconstruction method cannot deal with breaking waves. This is illustrated in Fig. 22 showing a comparison between the measured and reconstructed wave time traces for the time frame with the highest wave amplitudes. Figure 23 shows a detail of the pitch time traces for that time frame. The bow-up pitch amplitude is rather high: some  $35^\circ$  causing the model to fly above water for a short while, see Fig. 24. This event is reasonably well captured by PanShipNL. Even if the waves were perfectly reconstructed there would be differences because PanShipNL cannot deal with breaking waves and waterjet intake ventilation. Nevertheless, the tendency to fly out of a steep wave crest at speed is adequately predicted so that PanShipNL can be used to detect such potentially dangerous phenomena.

Interestingly, the highest vertical accelerations do not occur during the event described above. Figures 25 and 26 show a detail of the acceleration time traces. The high peak values are reasonably well captured by PanShipNL.

The second comparison concerns the same sea state ( $H_{1/3} = 2.5$  m,  $T_p = 5.2$  s) but now as a beam sea. The speed is 12 knots. Figures 27, 28, 29, 30, 31 and 32 show comparisons between experimental and simulated time traces. It is seen that the predicted yaw time traces deviate from the experimental result. This has an effect on the sway and pitch motions and forward speed as well. Heave and roll are reasonably well predicted. It is believed that the difficulty in predicting yaw is again partially due

**Fig. 17** Comparison of velocity

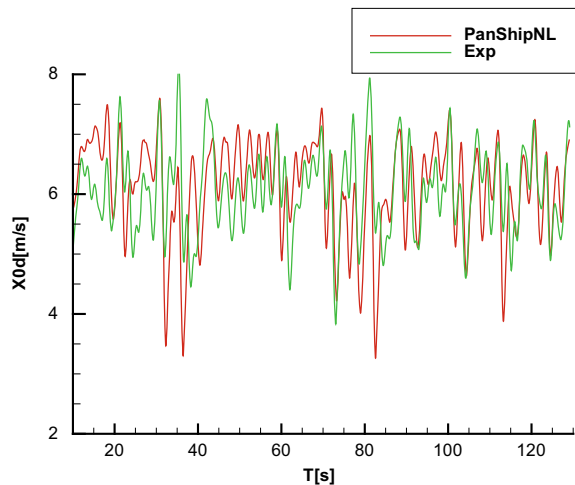


**Fig. 18** Comparison of heave

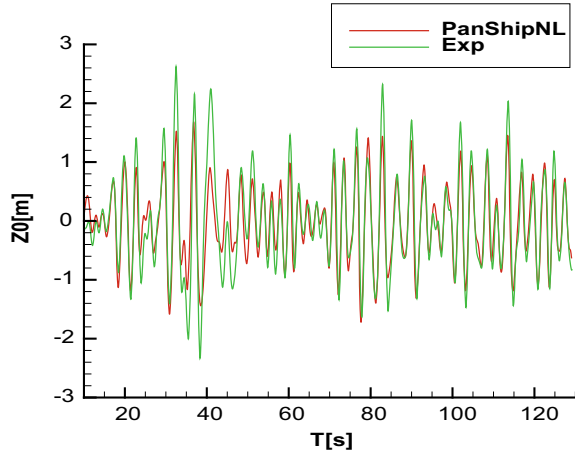
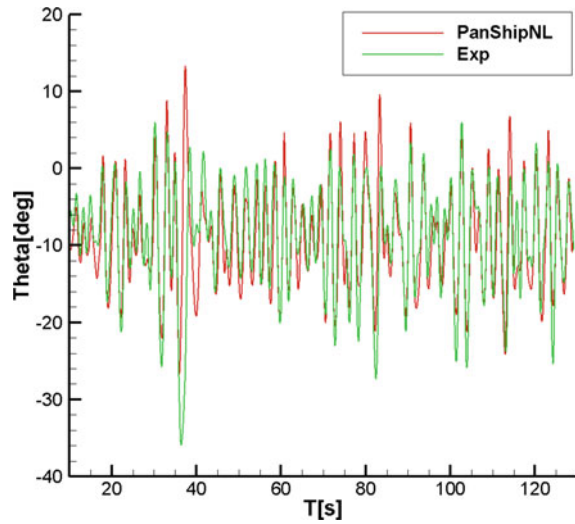
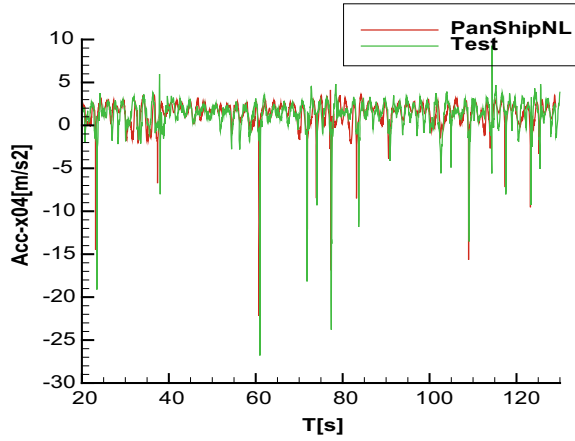


**Fig. 19** Comparison of pitch

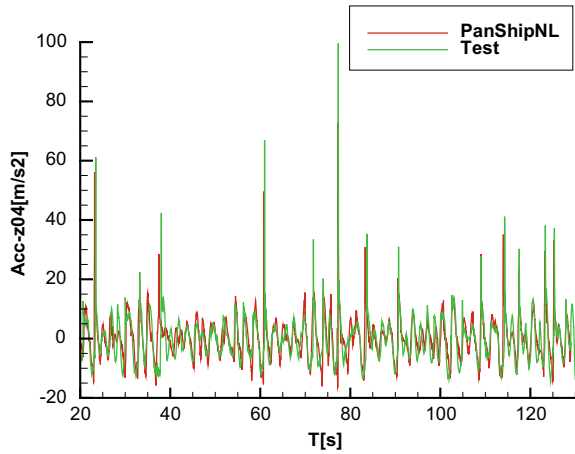


to the presence of breaking waves. Other reasons may be the use of a semi-empirical method for water jet steering in PanShipNL and the occurrence of waterjet intake ventilation.

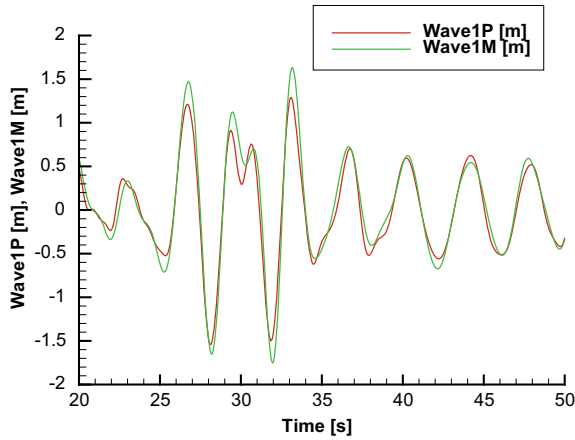
**Fig. 20** Comparison of x-acceleration



**Fig. 21** Comparison of z-acceleration



**Fig. 22** Comparison of reconstructed (Wave1P) and experimental (Wave1M) wave time trace



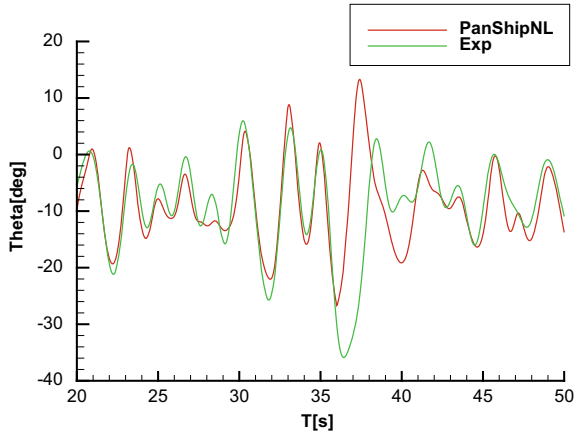


Fig. 23 Comparison of pitch time trace detail

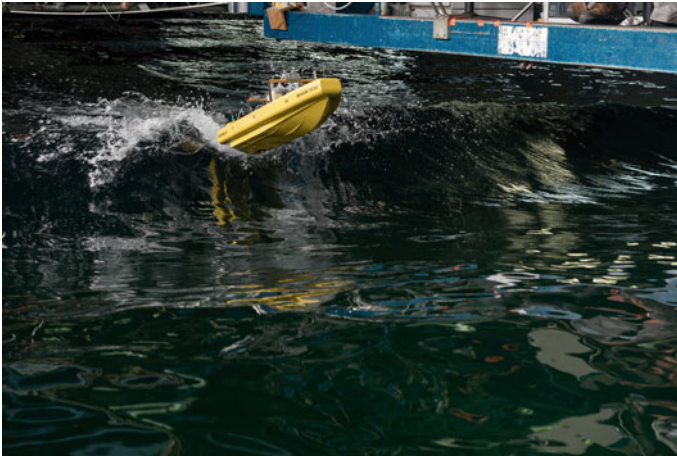


Fig. 24 Flying model

## 6 Concluding Remarks

The comparisons between experimental and simulated time traces shows that PanShip provides adequate predictions of motions and accelerations for operability analysis purposes in low amplitude yet steep regular waves.

Predictions for steep and heavy irregular seas show that non-linear events in head seas such as jumping out of wave crests and acceleration peaks are reasonably well predicted. In beam seas heave, roll and pitch are reasonably well predicted as well, however yaw and sway deviate. This is believed to be at least partially due to the



**Fig. 25** Comparison of x-acceleration (detail)

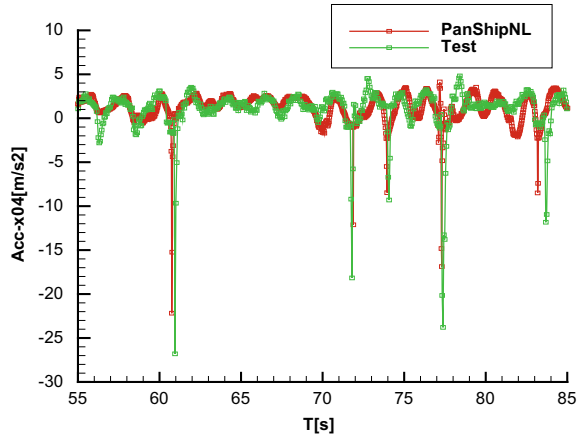


**Fig. 26** Comparison of z-acceleration (detail)

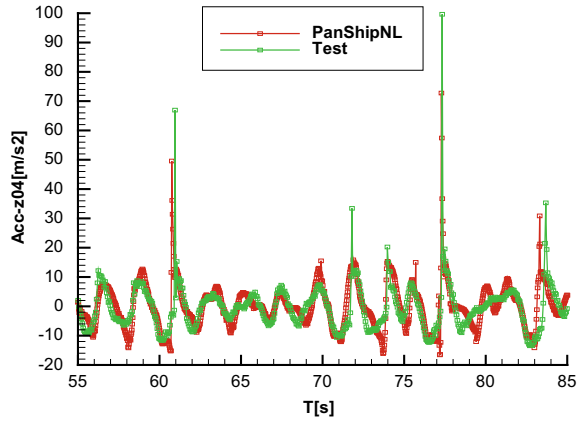


**Fig. 27** Comparison of velocity

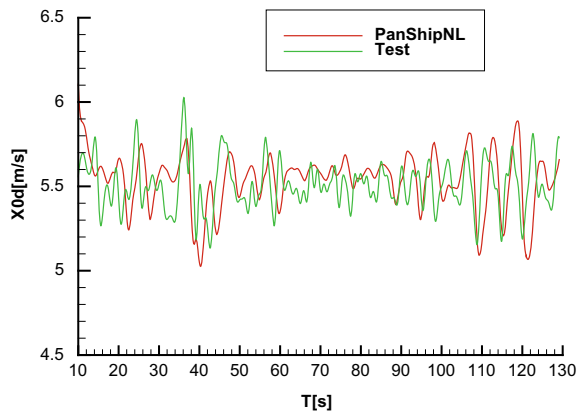


**Fig. 28** Comparison of sway

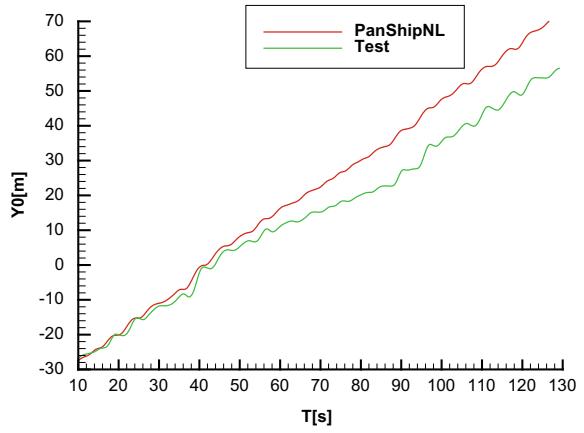


**Fig. 29** Comparison of heave

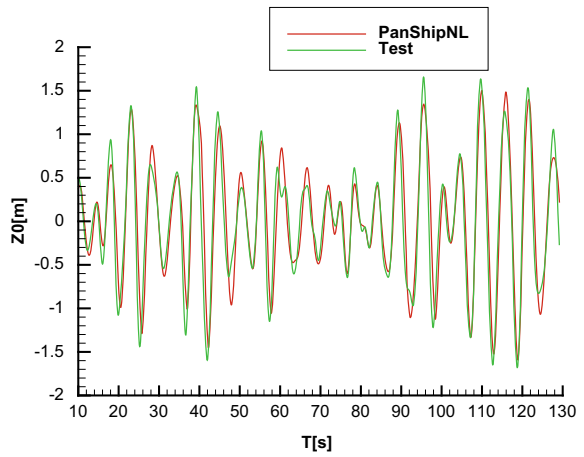


**Fig. 30** Comparison of roll

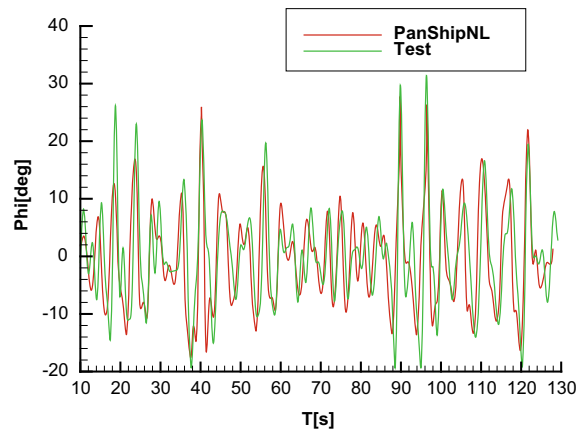


Fig. 31 Comparison of pitch

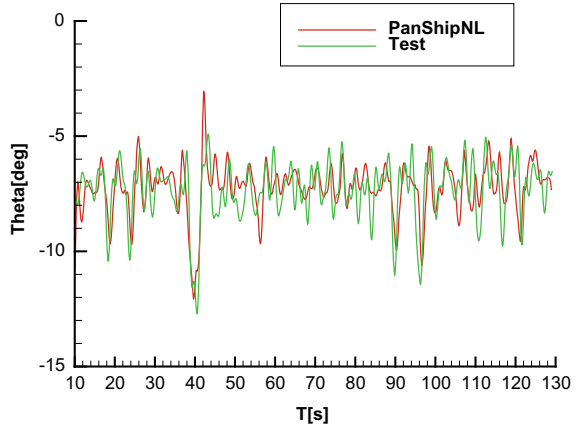
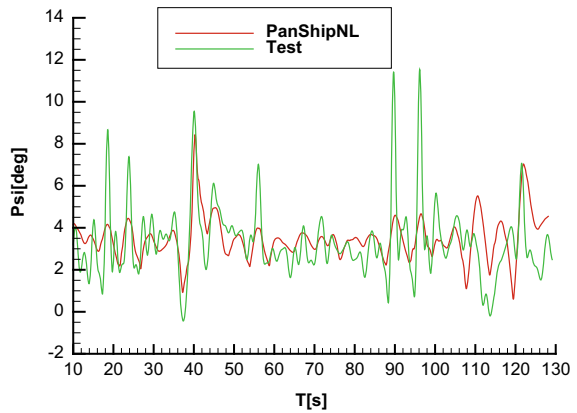


Fig. 32 Comparison of yaw



effects of breaking waves and water jet intake ventilation. Such phenomena are not included in the simulation tools.

The tests in the steep irregular waves from a stern quartering direction showed the occurrence of swamping and capsizing in breaking waves. Such events occur about two to four times per hour. It would have been of interest to show deterministic validation results for such events. This has not been attempted because the simulation methods used cannot deal with breaking waves and the resulting water ingress leading to a capsize. This remains a challenge, even for CFD based tools.

## References

1. De Jong P (2011) Seakeeping behavior of high speed ships, an experimental and numerical study. Ph. D. Thesis, Delft University of Technology
2. Van Walree F, Turner TG (2013) Development and validation of a time domain panel code for prediction of hydrodynamic loads on high speed craft. In: International conference of high speed sea transportation, FAST'2013, Amsterdam
3. Blok JJ, Aalbers AB (1991) Roll damping due to lift effects on high speed monohulls. In: Proceedings from the first international conference on fast sea transportation: FAST'91, Trondheim, June 1991
4. Van Walree F, Sgarioto D, Turner TG (2016) Validation of a time domain panel code for prediction of impulsive loads on high speed ships. In: 31th Symposium on naval hydrodynamics, Monterey, California, 11–16 Sept 2016

# Impulsive Loads on and Water Ingress in a Landing Craft: Model Tests and Simulations



F. van Walree and D. Sgarioto

**Abstract** This paper describes the use of two potential flow simulation tools, of varying degrees of non-linearity, for predicting landing craft motions, impulsive loads and water ingress. A comparison between experimental and simulation results for a landing craft hull form operating in irregular seas is provided. During the experiments, severe wave impacts against the bow door were recorded, with water ingress occurring through the bow door. Simulation results for these phenomena are compared with corresponding experimental results. The results from both non-linear and semi-linear versions of the simulation tool are discussed, together with measures adopted in the semi-linear method to yield results that approach the more representative non-linear results.

**Keywords** Model tests · Impulsive wave loads · Water ingress · Simulation methods

## 1 Introduction

For assessing the safety of ships in waves by means of simulations, advanced prediction methods are required. The advanced prediction method should be capable of handling six degrees of freedom, large motion amplitudes, non-linear waves, non-constant wetted geometry, water on deck effects, forward speed effects, impulsive wave loads and propulsion and steering.

Prediction methods that are capable of handling the above are in principle suited to simulate phenomena like resonant large roll motions, parametric roll, capsize due to loss of stability in waves, capsize after broaching and surf riding [5]. Computational Fluid Dynamics (CFD) and fully non-linear potential flow methods require

---

F. van Walree (✉)  
MARIN, Wageningen, The Netherlands  
e-mail: [F.v.Walree@marin.nl](mailto:F.v.Walree@marin.nl)

D. Sgarioto  
DST Group, Melbourne, Australia  
e-mail: [Daniel.Sgarioto@defence.gov.au](mailto:Daniel.Sgarioto@defence.gov.au)

large amounts of computer time. For safety assessment purposes, many simulations are required to cover all combinations of speed, heading, loading condition and environmental conditions. This makes fully non-linear simulation tools (i.e. body-exact) less suitable for timely safety assessment purposes. As a compromise, simulation tools that are non-linear in only certain aspects of the hydrodynamic problem, such as wave excitation and restoring forces, are typically employed.

The Landing Craft (LLC) operating out of the Australian Defence Force (ADF) Landing Helicopter Dock (LHD) were procured as a Military off The Shelf (MoTS) vessel for performing a ship to shore connector role for the LHD. LLC seakeeping is influenced by a number of challenges associated with their operation within complex non-linear wave environments as well as their requirement for delivering large payloads at relatively high speed.

The Defence Science and Technology (DST) Group were requested by the ADF to assist with an examination of the operability of the LLC. Partnering with the Maritime Research Institute Netherlands (MARIN), a scope of work was established that combined a model scale test program with numerical simulation development. The objective of the MARIN/DST collaboration was to develop a validated numerical simulation capability. This capability could be used by the ADF for determining operational guidance for LLC operations via the development of operability guidance plots. These polar plots, presented in a format similar to the Ship Helicopter Operating Limit (SHOL) polar plots, can be used to depict LLC operability over a range of vessel speeds and headings, loading conditions and sea states using a variety of limiting criteria.

Capability improvements through enhanced understanding of LLC operability will provide a force multiplier for ADF amphibious forces and deliver important safeguards for embarked personnel and materiel. Together with the provision of significant improvements to the operating envelope of the existing LLC, the ability to evaluate the operability of future LLCs will facilitate the sustainment of Australia's amphibious assault capability into the foreseeable future.

The paper discusses the model test arrangement, the main test results and the use of the simulation tools to generate operational guidance.

## 2 Model Tests

Seakeeping test facilities throughout the world are typically designed to test ship models at scale factors between  $1/36$  and  $1/22$ . As a result, the wave makers in the test facility have been designed to generate moderate to large seaways at these scale ratios.

Unfortunately, small vessel model testing at the aforementioned range of scale factors would require small models which are too small for instrumentation and are subject to scale effects.

**Table 1** Main particulars

Item	Magnitude	
	Medium load	Full load
Lpp (m)	21.3	21.3
B-wl (m)	6.40	6.40
Tf (m)	1.19	1.29
Ta (m)	1.10	1.22
Vol (m <sup>3</sup> )	117.7	131.9
GMt (m)	2.07	1.65
Tφ (s)	3.68	4.15

The model scale used for the present vessel (1/6.5) was dictated by the maximum wave height that can be generated in the seakeeping basin, space and weight considerations.

Table 1 shows the main dimensions of the landing craft. A carbon fibre model was constructed at the 1/6.5 scale ratio. Propulsion and steering was by means of twin water jet units with steerable nozzles. Figure 1 shows a photo of the model.

In order to measure global loads the model was segmented in four parts which were connected through an instrumented aluminium beam. At the three segment cuts the vertical shear force and torsional and vertical bending moments were calculated. The beam dimensions were chosen such that the natural frequencies for the one and two node mode shapes were approximately scaled. In this way hydroelastic effects are incorporated in the measured loads and accelerations.

Care has been taken to include the outer stiffener structure on the bow door since this was expected to affect the occurrence of water intake through the bow door



**Fig. 1** Model photo



**Fig. 2** Bow door detail

louver openings, see Fig. 2. Pressure gauges were used to record local pressures in the bow region.

The tests were performed in the Seakeeping and Manoeuvring Basin of MARIN. The basin measures  $170 \times 40 \times 5$  m in length, width and depth. Wave making is achieved using 331 flaps that are all individually driven by an electronic motor along the lengths of two sides of the basin. This facilitates generation of regular and long- and short-crested irregular waves from any direction. A main carriage (x-direction) and a sub-carriage (y-direction) follow the free-sailing model. An optical motion tracking system sends position information to the on-board autopilot.

Test conditions consisted of:

- Nominal speeds of 8 and 12 knots (Froude numbers 0.28 and 0.56);
- Moderate irregular waves with  $H_{1/3} = 1.25$  m and  $T_p = 5.50$  s (top Sea State 3) and  $H_{1/3} = 2.50$  m and  $T_p = 6.95$  s (top SS4) with directions between and including head and following seas.
- Two load conditions: 119 tonnes (t) and 134 t, representing 50 and 65 t cargo payloads.

### 3 Model Test Results

Model testing was performed for various combinations of loading condition, sea state, wave direction and speed to examine the operability of the LLC in terms of motions, accelerations, slamming and water ingress onto the loading deck. Occasionally, nominal operational limits are reached in Sea State 3 and more frequently in Sea State 4. Relevant notable findings arising from the test program include:



- Roll angles in SS4 exceed generic NATO STANAG 4154 limits in beam seas;
- Loss of course control was not observed, however heavy use of the steering nozzles is required for course keeping at lower speeds in stern quartering seas (SS3 and SS4) indicating that in higher sea states course keeping will be problematic;
- Water ingress through the bow door occurs in head and bow quartering seas, especially for the higher speed conditions. However the amount of water ingress did not compromise the stability of the vessel as it was discharged quickly through the freeing ports;
- In bow quartering SS4 conditions the vessel may occasionally be subject to breaking waves spilling over the side on to the loading deck;
- Slamming occurs frequently at high speed in bow and bow quartering seas. Impact pressures up to 320 kPa (full scale value) have been measured which is equivalent to a head of water of 32 m;
- The wave loads acting on the vessel are substantial in head and bow quartering seas due to wave impacts on the blunt bow shape.

## 4 Simulation Tools

The time domain panel methods are used for predicting hydrodynamic loads and seakeeping behaviour of high speed craft operating in waves. Characteristics of these simulation methods include:

- 3D transient Green functions to account for linearized free surface effects, exact forward speed effects on radiation and diffraction forces and a Kutta condition at ventilated transom sterns;
- 3D panel method to account for Froude-Krylov forces on the instantaneous submerged body;
- Cross flow drag method for viscosity effects;
- Resistance (in waves) is obtained from pressure integration at each time step;
- Propulsion and steering using propeller open water characteristics, semi-empirical lifting-surface characteristics and propeller-rudder interaction coefficients. Also a semi-empirical water jet propulsion and steering method is incorporated;
- Empirical viscous roll damping by either the FDS or Ikeda methods;
- Autopilot steering.

There are two versions of the simulation tool: a semi-linear (PanShip) and a nonlinear one (PanShipNL). In PanShip, it is assumed that the motions of the craft are small, i.e. the submerged geometry does not change in time. Furthermore, the speed and heading are assumed to be constant so that the Green functions can be computed a priori for use at each time step in the simulation. In effect, the radiation and diffraction problems are then solved in a linearised manner while the wave excitation and restoring forces are treated in a nonlinear way by using the actual submerged hull geometry under the disturbed incident wave. The disturbed wave is obtained from the pressure at waterline panels.

In PanShipNL the motions may be large while the speed and heading are not necessarily constant. The discretisation of the submerged geometry and the computation of the Green function convolution integrals are performed at each time step. This approach is still not fully nonlinear due to the use of the Green functions which satisfy the linearised free surface condition. By discretising the actual submerged hull form and using the submergence relative to the undisturbed incident wave surface rather than the calm water surface, a semi-nonlinear approach is obtained. More detailed information can be found in Van Walree et al. [6].

The hull form of MARIN model M10009 was discretised into a surface mesh consisting of 1400 panels below the still water level and 900 panels above the still water level. Figure 3 shows the mesh with a typical pressure distribution. The bow wave is clearly discernible.

During the simulations the ship was free running and self-propelled and kept on course using an autopilot. The impeller RPM was set such that the mean speed in waves was approximately equal to that of the model tests. The autopilot gains were the same as used for the model tests.

For all PanShip simulations the effect of forward speed on sinkage and trim was taken into account by determining the calm water equilibrium position a priori and adapting the hull mesh accordingly. For the PanShipNL simulations this was automatically achieved during the simulation since the mesh was adapted to the instantaneous motions and incident wave profile at each time step. The disturbed wave profile is not included in the adapted mesh; it is used for a hydrostatic correction of the pressure at each time step.

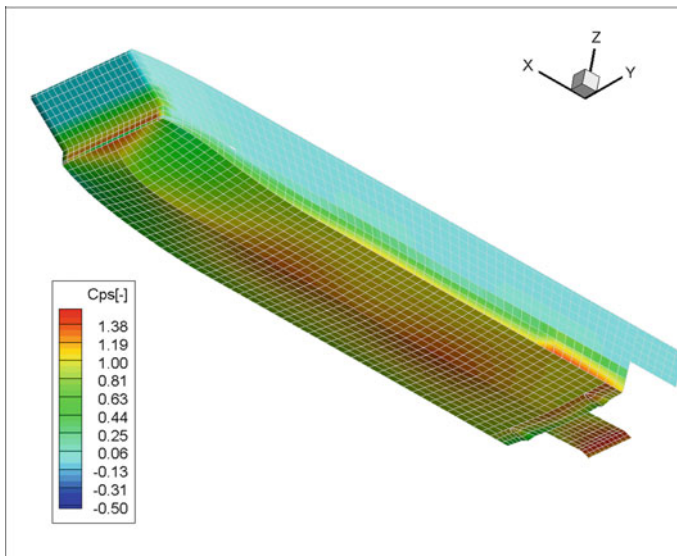


**Fig. 3** Discretised hull form M10009

Linear lift roll damping is included by means of the IHT method, see Ikeda [1]. For the Landing Craft model considered in this paper, quadratic roll damping was found to be well represented by the cross-flow drag method used to estimate viscosity effects in the horizontal plane for course keeping and manoeuvring.

## 5 Simulation Results

### 5.1 Motions

Figures 4, 5, 6 and 7 show a comparison of motion responses for the 119 t load condition in SS4 at 8 knots speed for five wave directions where 180° is head seas. The response is defined here as the standard deviation of the motion divided by that of the wave height.

The figures show that the motions are adequately predicted by the semi-linear PanShip method. As a ship-to-shore connector for the LHD, the LLC is expected to be fully loaded on 0–90° headings most often as it transits from ship to shore, then most likely unladen on 180–90° headings on its way back to the LHD.

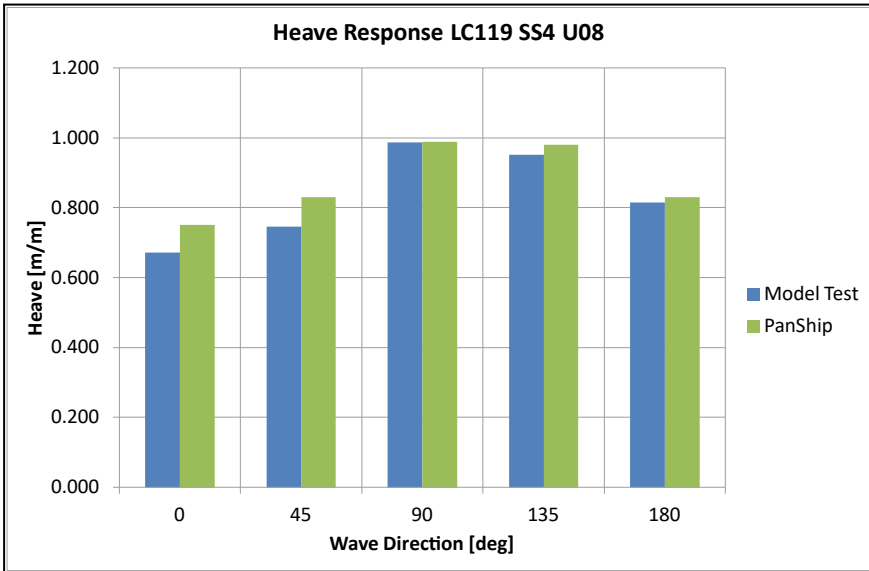


Fig. 4 Comparison of heave

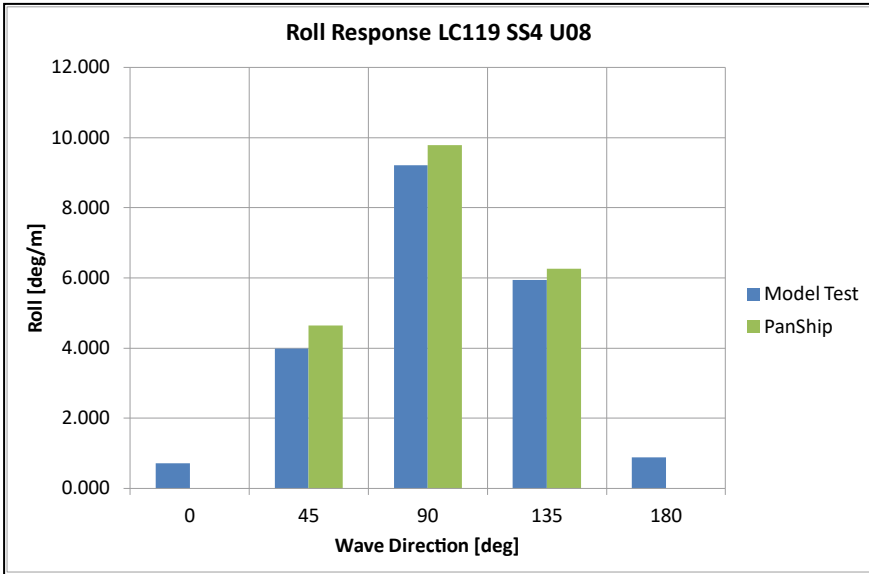


Fig. 5 Comparison of roll

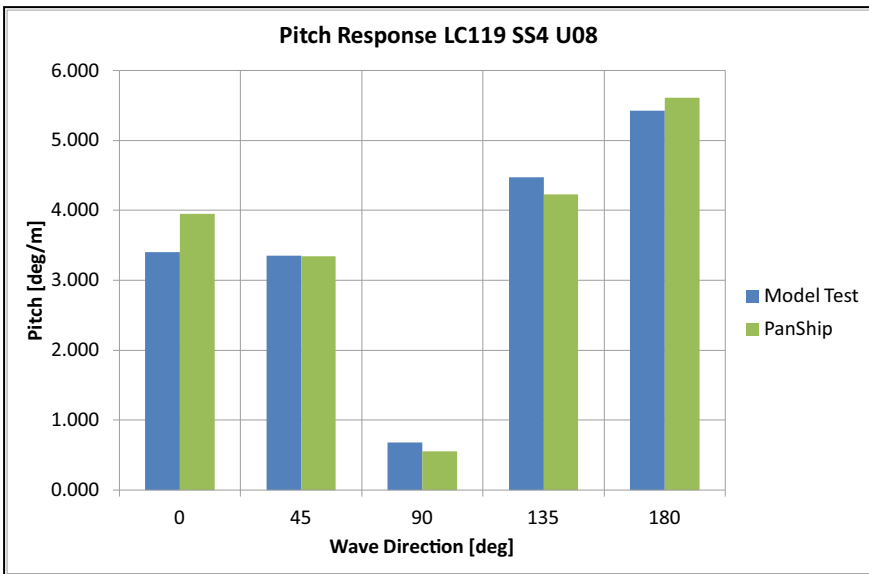


Fig. 6 Comparison of pitch

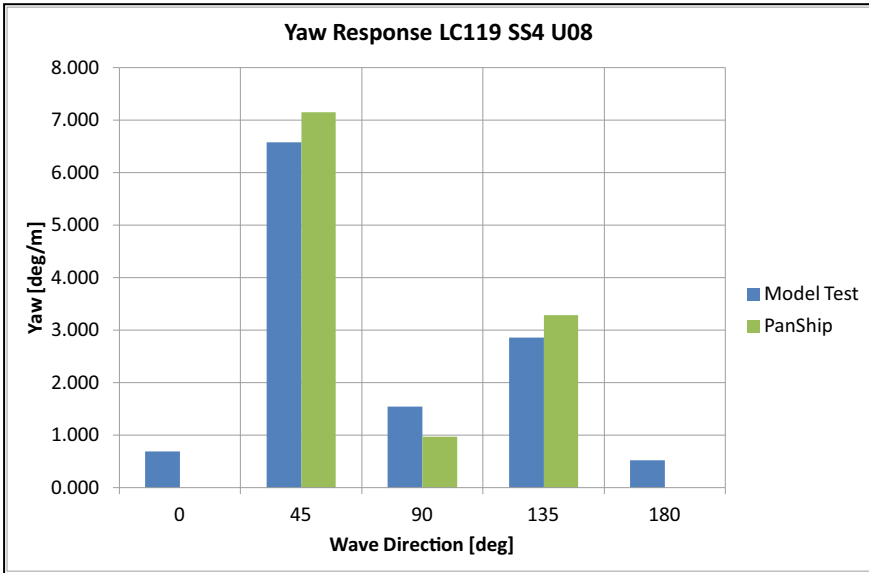


Fig. 7 Comparison of yaw

### 5.2 Wave Loads

Although there are no criteria formulated for wave loads it can be an important aspect of the operability of landing craft. Figures 8, 9 and 10 show a comparison of the mid-ship vertical shear force, torsion moment and vertical bending moment response. For this case the speed is 12 knots in SS3 and the 119 t loading condition. The uncertainty of the measurements is indicated by the error bars. It is seen that in bow seas the vertical shear force is overpredicted and the vertical bending moment is underpredicted by PanShip. This is unsurprising since the semi-linear PanShip method cannot predict wave impact and hydro-elastic effects.

The non-linear version PanShipNL does include wave impacts but still lacks hydro-elastic effects. Figures 8, 9 and 10 show improved predictions using PanShipNL for some, but not all conditions. It is expected that the inclusion of hydro-elastic effects would improve the wave impact prediction capabilities of PanShipNL.

### 5.3 Water Entry

The next item of interest is water entry through the bow door louver openings. The model tests show that water may enter through these openings in head and bow quartering seas, especially at higher speeds and for heavier load conditions, see

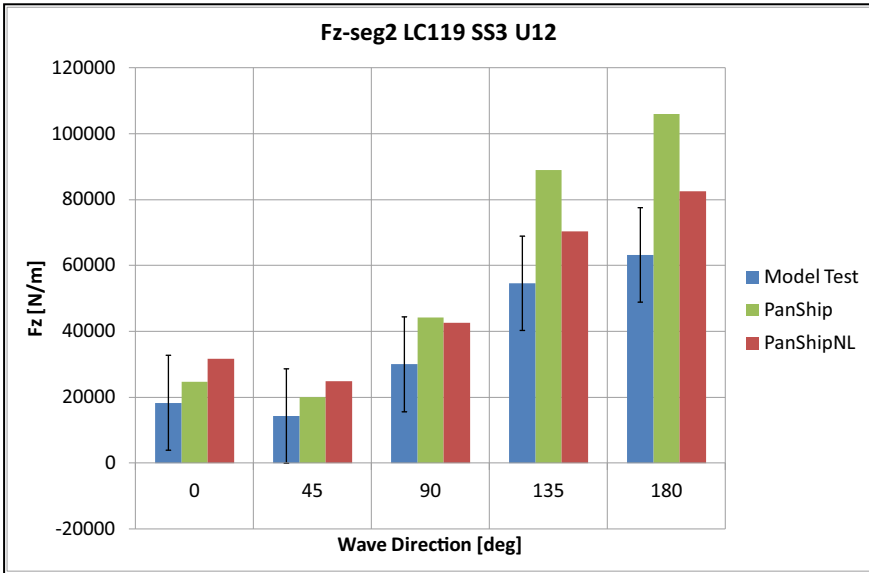


Fig. 8 Comparison of vertical shear force

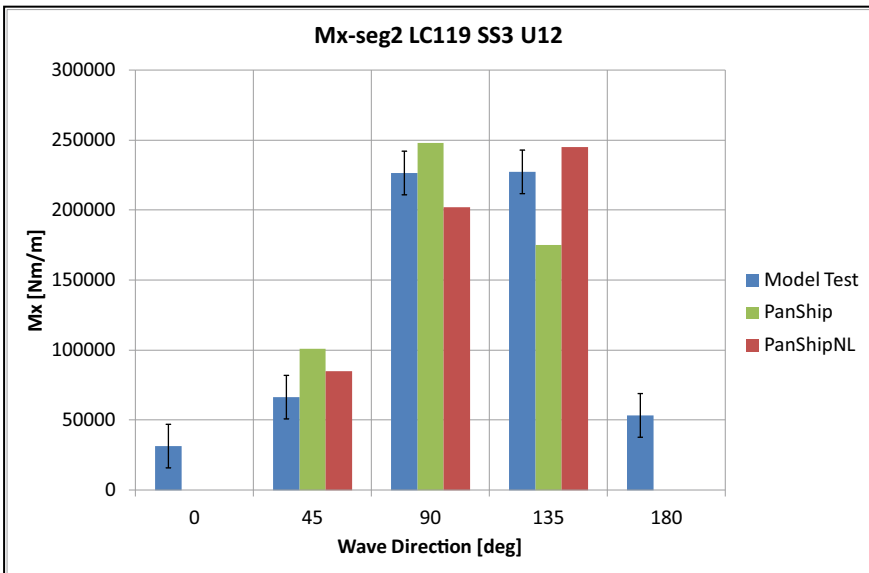


Fig. 9 Comparison of torsion moment

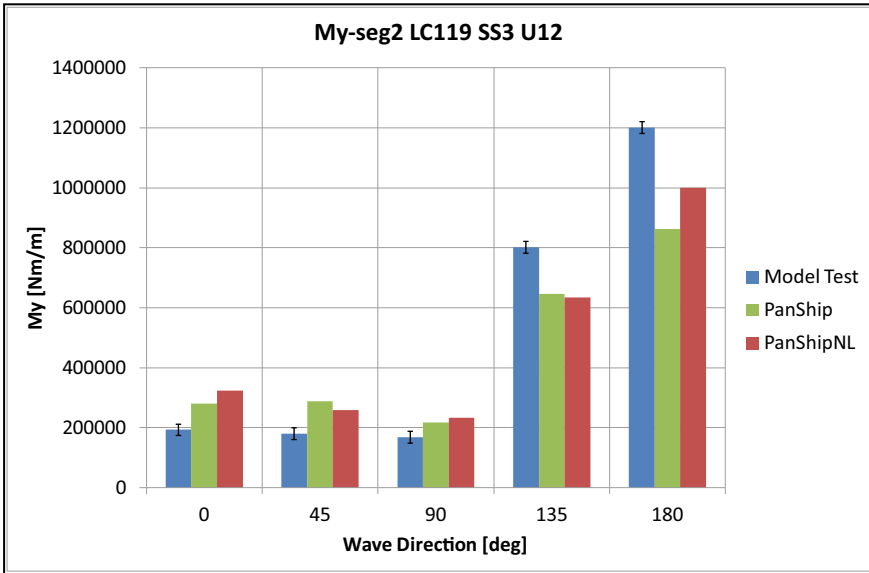


Fig. 10 Comparison of vertical bending moment

Fig. 11. This phenomenon cannot be accurately predicted by PanShip due to the massive breaking bow wave and the flow blocking effect of the bow door stiffener structure. A CFD-based method is required here but would be too time consuming for generating operability information. The same is true for the non-linear PanShipNL method.

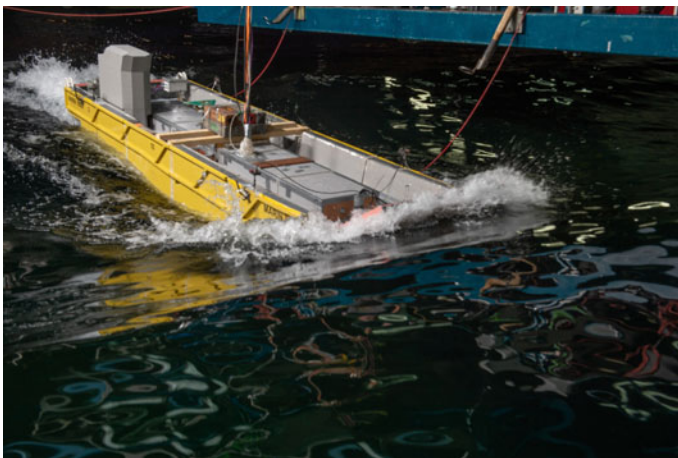
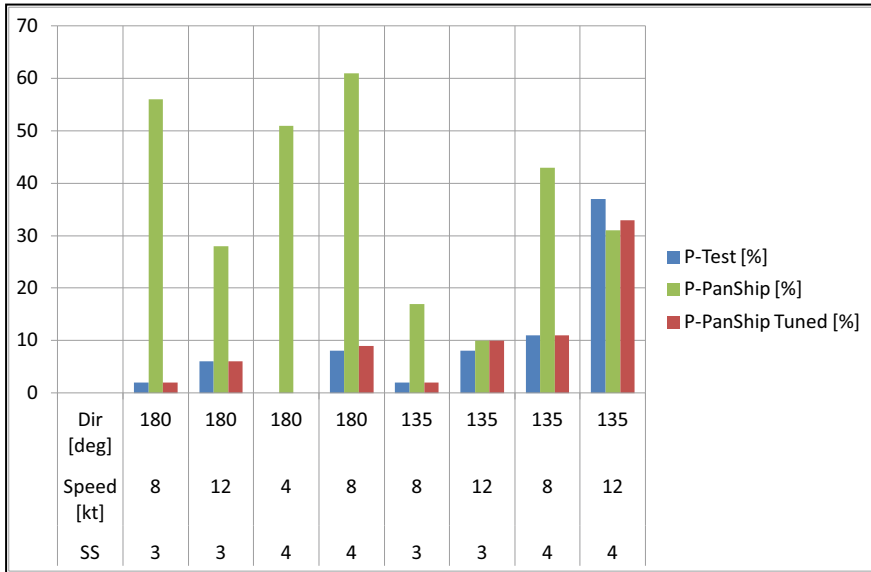


Fig. 11 Model shipping water



**Fig. 12** Water entry probabilities

As a compromise the following approach has been taken: depending on speed and wave direction, an additional factor (0.35–0.65 m) is added to the threshold relative wave height in PanShip (2.00 m above the water line) so that the predicted probability of water ingress better matches experimental observations. The probability is defined as the percentage of wave encounters that result in a water level on the deck of 0.10 m or more. Figure 12 shows a comparison between experimental, non-tuned and tuned water entry probabilities. The non-tuned simulation data are clearly much too conservative while the simple tuning does result in realistic water entry probabilities. It should be noted that the tuning is ship-specific and cannot in general be applied to other vessels.

### 5.4 Slamming

Figures 13 and 14 show the effect of a slam on the vertical acceleration and vertical bending moment. The condition is bow quartering seas SS4 at 12 knots for the 119 t loading condition. The wave frequent signal (WF) has been obtained by low-pass filtering of the measurement signal (HF). The whipping vibrations can be clearly seen in the HF signal.

For determining the effect of slamming on operability, one needs to define what a slam is and how much slamming can be allowed. To define a slam one can inspect time traces such as those shown in Figs. 13 and 14 and declare an event with a significant



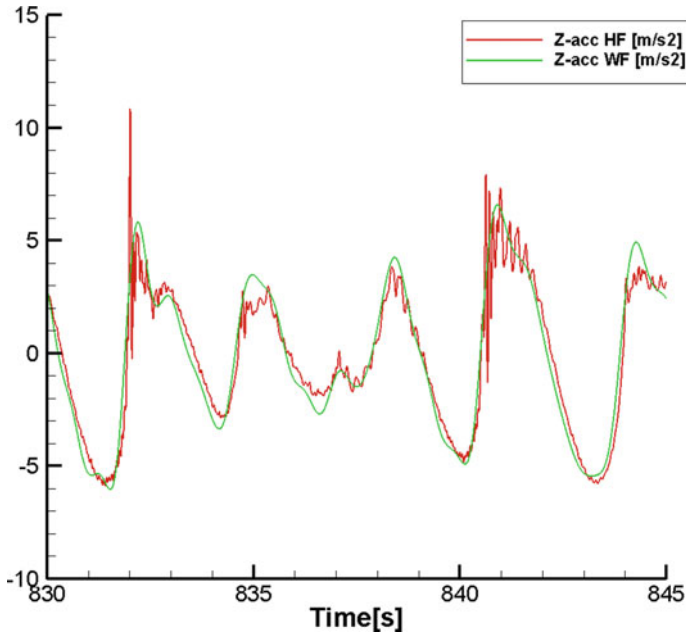


Fig. 13 Vertical acceleration at the bow

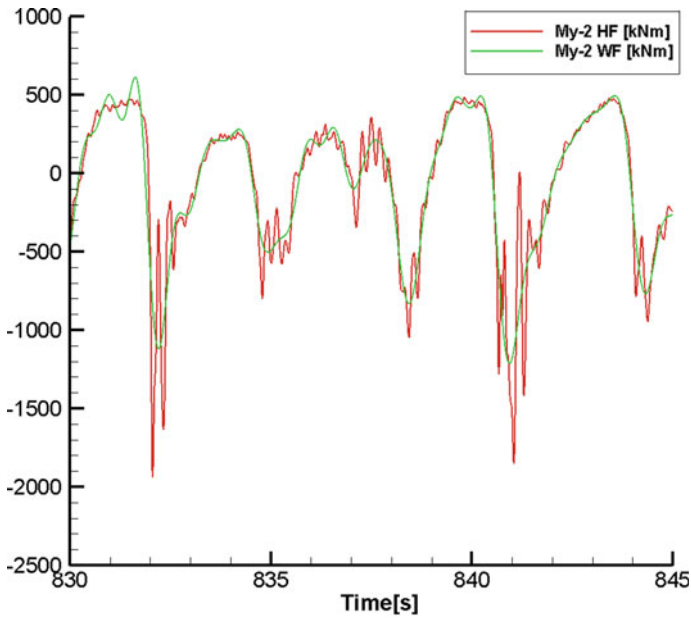


Fig. 14 Midship vertical bending moment

peak followed by whipping response to be a slam. But what is significant in this respect? Another approach is to define a pressure recording above a certain threshold a slam. This approach has been adopted here, with a threshold value of 30 kPa (full scale value), related to the forebody impact pressure specified in the relevant Classification Society structural design documentation. Although not employed in this work, alternate slam identification approaches are available, see Thomas [4] and Magoga et al. [2] for details. The semi-linear PanShip simulations have been tuned on the basis of the model test results with an Ochi-type approach, see Ochi [3]. An exceedance of a threshold value for the relative vertical velocity between the pressure gauge locations and the water surface is counted as a slam. The default Ochi threshold is  $V_{rel} = C\sqrt{gL}$  with a value for  $C$  of 0.093 and where  $L$  is the length between perpendiculars. Figure 15 shows the experimental slamming probabilities and corresponding  $C$ -values which result in the same probability in PanShip. The  $C$ -values are seen to be fairly constant and higher than the default Ochi value.

The non-linear PanShipNL method can predict impact pressures. Using the same slam determination method as utilised on the model test data, the slamming probabilities predicted by PanShipNL are shown in Fig. 16 for a selection of conditions. The correlation is considered to be satisfactory.

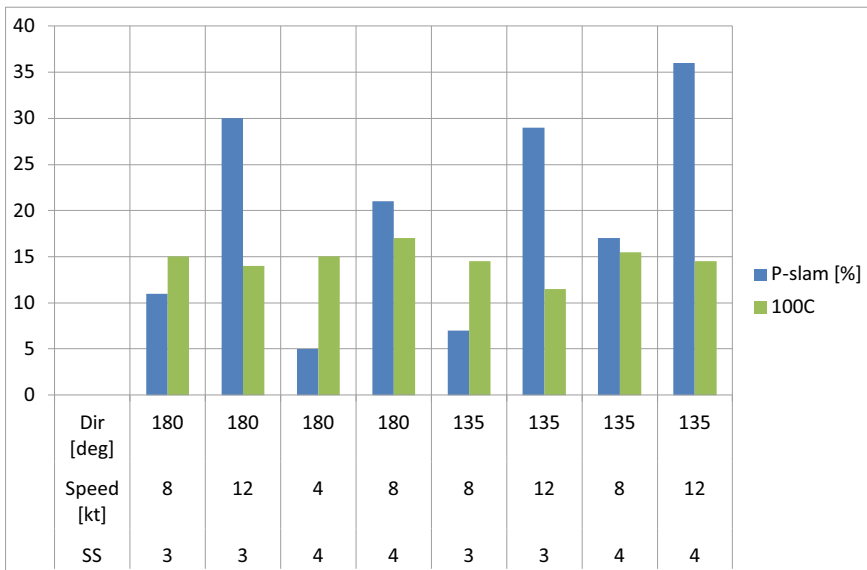


Fig. 15 Slamming probabilities using semi-linear PanShip method

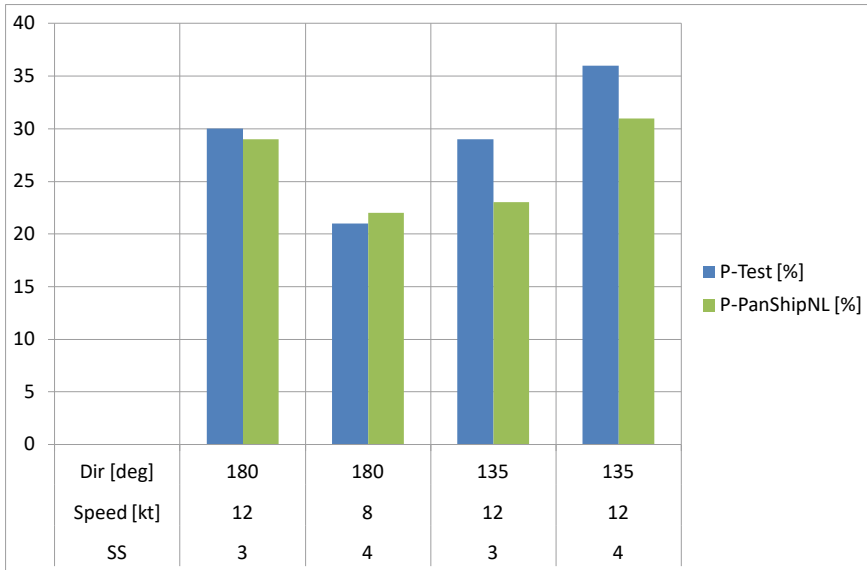


Fig. 16 Slamming probabilities using non-linear PanShipNL method

## 6 Operational Guidance

The tuned semi-linear PanShip method has been used to generate operability data for a large number of conditions. The conditions consisted of four sea states, three loading conditions, four speeds and thirteen wave directions, in total 624 conditions. For each condition half hour simulations were performed. The half hour duration is sufficient for at least 100 wave encounters which is recommended by the ITTC for reasonably accurate statistics. The challenge is to define suitable operability criteria. In consultation with a range of stakeholders the following criteria are applied to the simulation results to generate the operational guidance plots:

- Standard deviation of roll 4–8°;
- Probability of water ingress 5–10%;
- Probability of slamming 5–10%;
- Standard deviation of horizontal and vertical acceleration at pilot house 1 and 2 m/s<sup>2</sup>, respectively.

The operability guidance plots show three zones:

- Green: normal risk;
- Yellow: higher risk,
- Red: urgent operational requirement only.

An example plot is shown in Fig. 17.

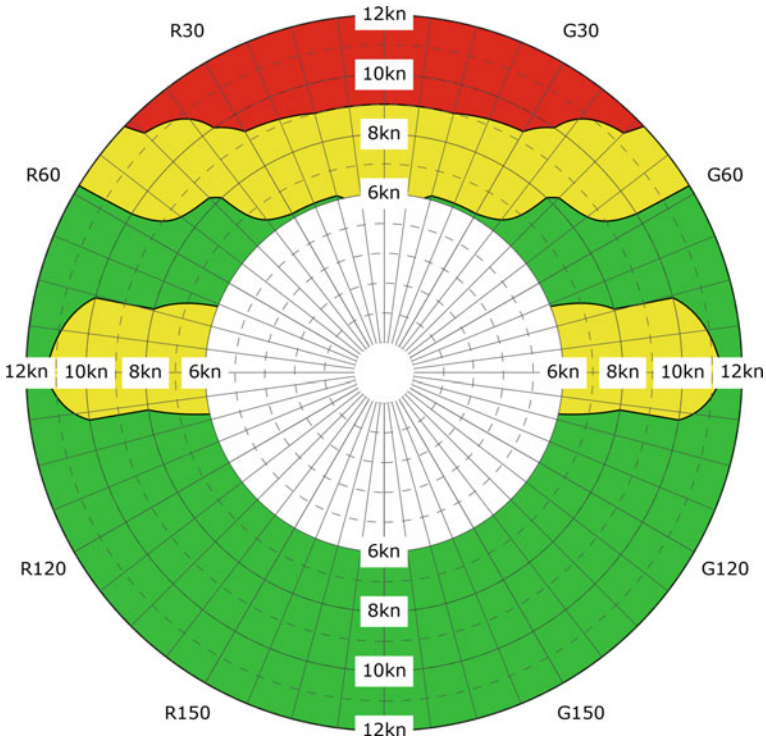


Fig. 17 Example operability guidance plot

### 7 Concluding Remarks

The paper has addressed the use of the combination of model tests and simulation tools for generating operability data for a landing craft. The semi-linear simulation tool PanShip can be used for the prediction of motions in waves. For predicting the occurrence of slamming and water entry through the bow door experimental data for tuning purposes is required. Predictions for wave loads are reasonable for conditions without slamming.

For improved wave load predictions in head seas the non-linear tool PanShipNL is required. This tool can predict slamming loads without the need for tuning by using experimental results.

For the prediction of water entry through the bow door, experimental data for tuning purposes is required when using potential flow based simulation tools. CFD based tools would be better suited for this scenario, but are not presently practical for generating operability information due to lengthy simulation runtimes.

## References

1. Ikeda Y, Himeno Y, Tanaka N (1978) Components of roll damping of ship at forward speed. ISSN 0514-8499
2. Magoga T, Aksu S, Cannon S, Ojeda R, Thomas G (2017) Identification of slam events experienced by a high-speed craft. *Ocean Eng* 140:309–321. <https://doi.org/10.1016/j.oceaneng.2016.07.017>
3. Ochi MK, Motter LE (1973) Prediction of slamming characteristics and hull responses for ship design. In: Transactions SNAME annual meeting, Nov 15–17, New York
4. Thomas G (2003) Wave slam response of large high speed catamarans. PhD thesis, University of Tasmania
5. Van Walree F, Carette NFAJ (2011) Validation of time domain seakeeping codes for a destroyer hull form operating in steep stern quartering seas. *Int J Naval Archit Ocean Eng* 3(1):9–19
6. Van Walree F, Sgarioto D, Turner TG (2016) Validation of a time domain panel code for prediction of impulsive loads on high speed ships. In: 31th symposium on naval hydrodynamics, Monterey, California, 11–16 Sept